Direct Observation of Entrained Oxides and Thermodynamic Modelling of Aluminium Alloy Melts



Sean Telford

Linacre College

University of Oxford

A thesis submitted for the degree of

Doctor of Philosophy

Hilary Term 2025

Abstract

This work aimed to provide a solid foundation to aluminium alloy melt oxidation research through a combined theoretical-experimental approach. The experimental component demonstrated the importance of this research area by directly imaging entrained oxides, including bifilms, in aluminium alloy melts for the first time. Many see these structures as the fundamental casting defect, but a lack of direct observation has caused a divide in the scientific community. By directly imaging these defects in Ca-added Al-Mg melts using synchrotron X-ray tomography, their existence in melts has been proven and a unique observation method has been established, allowing entrained oxide hypotheses to be tested directly.

The understanding of entrained oxides being bifilms encapsulating debris and gaseous atmospheres (which were observed) was found to be incomplete: the observed entrained oxide population was mostly extensive, porous oxide networks encapsulating bifilms and other debris. Porous oxide networks grew hydrogen bubbles (only in calcium-added samples), and these oxide networks were found to facilitate melt oxidation; calcium suppressed oxidation by forming a fine layer of MgO on the inner surfaces of the porous oxides.

The theoretical component established a thermodynamic framework of aluminium alloy melt oxidation. ‘Oxide stability diagrams’ were used to predict the most thermodynamically stable oxides in contact with an aluminium melt by evaluating the thermodynamics of oxidation of the melt. Non-ideal models were also implemented to allow system-specific mixing data to be incorporated: twenty-four Al-X binary systems and twelve Al-Mg-X systems were evaluated with ideal mixing, Bragg-Williams mixing, and (for binaries only) the modified quasichemical model. These diagrams were found to be a valuable tool in not only understanding oxidation products but also explaining why microalloying Al-Mg melts with Group II elements suppresses melt oxidation. These results demonstrate the effectiveness of this theoretical approach and open avenues for future modelling of aluminium alloy oxidation.

Dedicated to my parents,

my partner, and my

stubborn younger self.

Acknowledgements

I would like to express my sincere gratitude to my supervisors, Prof. Keyna O'Reilly and Prof. Marina Galano, for their invaluable guidance and mentorship throughout my project.

I am grateful to many members of the Department of Materials for their help, including Greg Cook, Richard Turner, and Gideon Ring for their technical assistance; Dr. Michael Goode for TGA; Prof. Patrick Grant and Dr. Stan Zankowski for lab space; Garry Lees for OES; Dr. Andrew Lui for XRD; Prof. James Marrow for workstations; Diana Passmore for casting equipment; Tony Wheeler for casting and sample fabrication; and Dr. Adrian Taylor for his extensive administrative assistance through my complex doctoral journey.

This research used resources of the Advanced Photon Source, a U.S. Department of Energy (DOE) Office of Science user facility operated for the DOE Office of Science by Argonne National Laboratory under Contract No. DE-AC02-06CH11357. I would like to thank Dr. Insung Han for the opportunity to use his beam time, Justin Limkaichong for invaluable assistance during the arduous experiments, and the beamline staff at 2-BM, Dr. Viktor Nikitin and Dr. Pavel Shevchenko, for their instruction and guidance.

I would like to thank the bar team at Linacre College for their professional and personal support; my quiz teams, both college and pub, for their camaraderie and friendship; and my fellow choristers in Antiphon, Arcadian Singers, Intermezzo, and the Linacre Community Choir, for wonderful music-making and a much-needed artistic release.

I would like to thank my partner for being by me through some of my most challenging years and for your unconditional love and support. Finally, I would like to thank my parents. When I became ill within six months of starting, I did not think I could make any progress. You supported me through my long, arduous recovery. I am grateful for everything you have done for me and thankful that you can both see me finish this chapter of my life.

Preface

The work here was carried out at the Department of Materials, University of Oxford, from October 2019 to April 2025, under the supervision of Prof. Keyna O'Reilly and Prof. Marina Galano. No work presented here has been previously submitted for any university degree. The work is my own, and acknowledgements are made appropriately.

Some of the work here was presented at the International Conference on Aluminum Alloys (ICAA19), held in Atlanta, GA, USA from 23-27 June 2024, in "In-situ X-ray Tomography of Entrained Oxides in Ca-added Al-Mg melts" (S. Telford, K. O'Reilly, M. Galano).

Parts of this work are being prepared for publication as a series of three journal articles:

- "Direct observation of entrained oxides in aluminium melts. Part 1: Structure and morphology", S. Telford, K.A.Q. O'Reilly, M.L. Galano
- "Direct observation of entrained oxides in aluminium melts. Part 2: Effect of calcium on oxides", S. Telford, M. Goode, K.A.Q. O'Reilly, M.L. Galano
- "Direct observation of entrained oxides in aluminium melts. Part 3: Melt deoxidation by calcium", S. Telford, K.A.Q. O'Reilly, M.L. Galano

Contents

1. Introduction

1.1. Background 1.1

1.2. Outline 1.2

1.3. References 1.4

2. Literature Review

2.1. Introduction 2.1

2.2. Oxidation of aluminium 2.1

2.2.1. Thermodynamics 2.1

2.2.2. Kinetics 2.4

2.2.3. Pure aluminium 2.7

2.2.4. Al-Mg alloys 2.9

2.2.5. Microalloying of Al-Mg alloys 2.13

2.2.6. Other aluminium alloys 2.16

2.2.6.1. Al-Cu 2.16

2.2.6.2. Al-Li 2.16

2.2.2.6.3. Al-Si 2.17

2.2.6.4. Al-Zn 2.17

2.3. Double oxide film defects 2.18

2.3.1. Entrainment 2.18

2.3.2. Gaseous nucleation 2.19

2.3.3. Nucleation of secondary phases 2.22

2.3.4. Mechanical properties 2.23

2.3.5. Observation 2.25

2.3.6. Quantification 2.27
2.3.7. Combating bifilms 2.29
2.3.8. Prospects 2.32
2.4. Thermodynamic optimisation 2.33
2.4.1. Computation 2.33
2.4.2. Solution models 2.35
2.5. Conclusions 2.35
2.6. References 2.36

3. Materials and Methods

3.1. Materials and casting 3.1
3.2. Spark OES 3.2
3.3. Metallography 3.3
3.4. Butanol dissolution 3.3
3.5. SEM/EDX 3.6
3.6. Thermogravimetric analysis (TGA) 3.6
3.7. X-ray diffraction (XRD) 3.6
3.8. Synchrotron X-ray tomography 3.7
3.9. References 3.7

4. In-situ X-ray Tomography of Ca-added Al-Mg Melts

4.1. Introduction 4.1
4.1.1. Motivation for technique 4.1
4.1.2. Choice of alloy system 4.2
4.1.3. Chapter structure 4.3

4.2. Materials and methods 4.4
4.3. Direct imaging of entrained oxides 4.6
4.3.1. Overview 4.6
4.3.2. Before melting 4.6
4.3.3. Tomography: before and after melting 4.9
4.3.4. Melt hold: oxidation 4.12
4.3.5. Tomography: solidification 4.15
4.3.6. Discussion 4.16
4.3.7. Preliminary conclusions 4.22
4.4. Effect of calcium addition on melt oxidation 4.22
4.4.1. Overview 4.22
4.4.2. Thermogravimetric analysis (TGA) 4.23
4.4.3. Before melting 4.24
4.4.4. Tomography 4.31
4.4.5. Oxidation: extracted samples 4.35
4.4.6. Discussion 4.40
4.4.7. Preliminary conclusions 4.45
4.5. Deoxidation of Al-Mg alloys by calcium 4.46
4.5.1. Overview 4.46
4.5.2. Initial melting: porosity and entrained oxide networks 4.46
4.5.3. Bubble formation from oxides 4.50
4.5.4. Bubble behaviour during solidification 4.56
4.5.5. Discussion 4.58
4.5.6. Preliminary conclusions 4.62

4.6. Further observations 4.62

4.6.1. Stacked samples 4.63

4.6.2. Image artifacts 4.67

4.7. Conclusions 4.69

4.8. References 4.70

5. Thermodynamic Modelling of Aluminium Alloy Melt Oxidation

5.1. Introduction 5.1

5.1.1. Background 5.1

5.1.2. Objectives 5.3

5.2. Theoretical basis 5.4

5.2.1. Fundamental thermodynamics 5.4

5.2.2. Pure substance oxidation and Ellingham diagrams 5.5

5.2.3. Alloy melt oxidation 5.9

5.2.4. Ideal solutions 5.12

5.2.5. Non-ideal solutions 5.13

5.2.6. Ternary systems 5.14

5.2.7. Bragg-Williams mixing 5.15

5.2.7.1. Binary systems 5.15

5.2.7.2. Ternary systems 5.17

5.2.8. Modified quasichemical model 5.19

5.3. Methodology 5.29

5.3.1. Principles 5.29

5.3.2. Data 5.31

5.4. Al-X binary systems 5.33

5.4.1. Ideal mixing 5.33
5.4.1.1. General mathematical features 5.33
5.4.1.2. Categorisation of Al-X binary systems 5.37
5.4.2. Bragg-Williams mixing 5.39
5.4.2.1. Mathematical features 5.39
5.4.2.2. Effect on oxide stability diagrams 5.42
5.4.3. Modified quasichemical model 5.46
5.4.3.1. Mathematical features 5.46
5.4.3.2. Effect on oxide stability diagrams 5.50
5.5. Al-Mg-X ternary systems 5.52
5.5.1. Ideal mixing 5.53
5.5.2. Bragg-Williams mixing 5.57
5.6. Comparison to experimental data 5.61
5.6.1. Binary systems – less reactive 5.61
5.6.2. Binary systems – more reactive 5.63
5.6.2.1. Group I elements 5.63
5.6.2.2. Group II elements 5.66
5.6.2.3. Lanthanides 5.70
5.6.3. Ternary Al-Mg-X systems: products 5.73
5.6.3.1. Group II elements 5.73
5.6.3.2. Lanthanides 5.76
5.6.4. Ternary Al-Mg-X systems: protection 5.77
5.7. Conclusions 5.84
5.8. References 5.86

6. Conclusions and Future Work

6.1. Discussion 6.1

6.1.1. Summary 6.1

6.1.2. Direct observation of entrained oxides in melts 6.1

6.1.3. Thermodynamic modelling 6.5

6.2. Conclusions 6.8

6.2.1. In-situ X-ray tomography 6.8

6.2.2. Thermodynamic modelling 6.10

6.3. Future work 6.12

Appendix A. Supplementary Mathematical Information

A.1. Overview A.1

A.1.1. List of symbols A.1

A.2. Chemical potentials A.3

A.2.1. Binary systems A.3

A.2.2. Ternary systems A.5

A.3. Bragg-Williams mixing A.8

A.3.1. Binary systems A.8

A.3.2. Ternary solutions A.11

A.4. Modified quasichemical model A.31

A.4.1. Simplification and conversion to Al-X system A.31

A.4.2. Derivative of Gibbs free energy of mixing A.35

A.4.3. Evaluation of excess relative chemical potentials A.45

A.4.4. Implicit derivative of the X-Al bond fraction A.60

A.4.5. Eliminating the derivative of the X-Al bond fraction A.65

A.5. Other mathematical derivations A.71

A.5.1. Bragg-Williams mixing: linear sums A.71

A.5.2. Modified quasichemical model: limit analysis A.73

A.5.3. Modified quasichemical model: linear sums A.77

A.5.4. Ternary oxide boundaries in ideal mixing A.78

Appendix B. Modelling: Data, Sources, and Figures

B.1. Overview B.1

B.2. Compounds and Gibbs free energy data B.2

B.3. Non-ideal solution parameters B.5

B.3.1. Bragg-Williams: Al-X binary systems B.5

B.3.2. Bragg-Williams: Al-Mg-X ternary systems B.6

B.3.3. Modified quasichemical model B.7

B.4. Binary systems: sections at constant T B.8

B.4.1. Ideal mixing B.8

B.4.2. Bragg-Williams mixing B.32

B.4.3. Modified quasichemical model B.56

B.5. Oxide stability diagrams B.66

B.5.1. Ideal Mixing B.66

B.5.2. Bragg-Williams mixing B.78

B.5.3. Modified quasichemical model B.91

B.6. Ternary systems B.98

B.6.1. Ideal mixing B.98

B.6.2. Bragg-Williams mixing B.110

B.7. Annotated oxide stability diagrams B.120

B.7.1. Binary Al-X systems B.120

B.7.1.1. Data sources B.120

B.7.1.2. Ideal mixing B.121

B.7.1.3. Bragg-Williams mixing B.127

B.7.1.4. Modified quasichemical model B.132

B.7.2. Ternary Al-X systems B.137

B.7.2.1. Data sources B.137

B.7.2.2. Products: Ideal B.138

B.7.2.3. Products: Bragg-Williams B.142

B.7.2.4. Protection: Ideal B.146

B.7.2.5. Protection: Bragg-Williams B.150

B.8. References B.155

Appendix C. Commentary on Projection Sequence Videos

Overview C.1

A. Full sequences C.1

B. Sequences from 0.01Ca sample C.3

C. Sequences from 0.03Ca sample C.4

Appendix D. Crystallographic Information

Chapter 1
Introduction

1.1. Background

Aluminium is a widely-used metal, prized for its versatility. Most uses arise from its low density whilst being able to maintain a reasonable strength when alloyed [1]. It is easy to cast [2] and properties can be tailored easily through thermomechanical processing [3], leading to widespread use in construction and automobile manufacturing. Furthermore, aluminium is easily recyclable [4], has a high corrosion resistance [5], and has high thermal and electrical conductivities, which are exploited in the electronics sector [6].

Aluminium rapidly oxidises on contact with air, both in the solid and liquid state [7,8], forming alumina (Al_2O_3). This oxide can be useful, being responsible for the high corrosion resistance of aluminium [5], but can be problematic in melts, especially in Al-Mg melts where the added magnesium greatly accelerates oxidation [9]. Melt oxidation results in dross, leading to metal losses, but oxidation causes more significant problems during casting itself [10].

The casting of aluminium involves many molten transfer steps [11], most of which involve pouring the melt. If the melt is poured turbulently, which can occur with only a 1-2 cm pour height [10,12], then the surface oxide can entrain and form entrained oxides [10]. These entrained oxides contain an unbonded interface between two oxide surfaces separated by a trapped gaseous atmosphere, therefore constituting cracks once the casting solidifies. The introduction of these effective cracks into the component degrades mechanical properties such as strength [13] and elongation to failure [10,14], and increases the scatter in these properties, rendering them less reliable [2].

Some researchers have claimed these entrained oxides to be the principal defect in aluminium alloys, being responsible for many flaws and involved in many casting phenomena [15]. These include: hydrogen porosity [16], hot tearing [15,17], weakening of intermetallics [10,18–24], silicon modification [17,25], corrosion [10,20,26], and even brittle failure in general [10].

These investigators therefore claim miraculous improvements in the quality of aluminium products should these defects be removed [15].

However, these claims have not yet been fully accepted by the wider scientific community, largely because evidence to date has only been indirect. Investigators have relied on indirect methods such as reduced pressure tests [27,28], mechanical testing on samples varying in pour turbulence [13], and microscopy [26] or tomography [29] on solid samples, but entrained oxides have yet to be directly observed in an aluminium melt. Furthermore, there is a lack of thermodynamic understanding of molten aluminium alloy oxidation: there are reports on the behaviours of individual alloying elements with justifications made by element and condition [9,30–33], and thermodynamic considerations have been used to characterise the breakaway oxidation of Al-Mg melts [9], but there has yet to be an attempt to systematically analyse the thermodynamics of aluminium alloy melt oxidation. This could be useful in being able to predict oxidation products as a function of composition and temperature, and help explain phenomena not currently understood, such as why Group II elements (specifically beryllium, calcium, and strontium) can suppress the oxidation of Al-Mg alloys in extremely small additions [34–36] but other reactive elements (such as cerium, gadolinium, and lanthanum) do not [37].

1.2. Outline

This study addresses these two major stumbling blocks, namely the absence of direct observation of entrained oxides in melts and the lack of a firm theoretical understanding of melt oxidation, through a join experimental-modelling approach. The experimental component attempts to directly observe entrained oxides in molten aluminium and put an end to the question mark over the issue. The theoretical component explores the thermodynamics of aluminium oxidation, to determine whether thermodynamics can explain observed phenomena and establish thermodynamic analysis as a tool for future metallurgical research.

Chapter 2 comprises the literature review, which gives an overview of the current state of the art. Chapter 3 details experimental methods. Chapter 4, the experimental component, explores the use of in-situ X-ray tomography, one of the few techniques that has a feasible chance of observing oxides in molten aluminium, to study the oxidation behaviour of molten calcium-added Al-Mg alloys. Since calcium greatly reduces the surface oxidation of Al-Mg melts, it is plausible that calcium also alters the behaviour of entrained oxides, so by observing both surface and entrained oxides during a melt hold, multiple experimental objectives can be completed in a single set of experiments.

The results in this chapter are presented as three main sub-chapters to consolidate findings and cement concepts as the conclusions are made: the first explores the nature of entrained oxides and oxidation, the second explores the effects of added calcium on these features, and the third focuses on the involvement of entrained oxides in bubble formation. The following sub-chapter discusses less important but noteworthy points, such as the behaviour of stacked samples and visual artefacts. Videos of the sample melting sequences are included in the supplementary material to provide more compelling evidence of the reported phenomena; commentary of these videos to highlight the important observations is included as an appendix. Readers are strongly encouraged to watch these videos, since they display the reported phenomena much more clearly than the snapshots provided in the chapter.

Chapter 5, the theoretical component, attempts to predict the oxidation products of aluminium melts through an Ellingham diagram-like approach. To begin, a range of binary systems are analysed and compared to available experimental data, first using simplistic mathematical models (ideal mixing) before proceeding to more complex ‘non-ideal’ models (Bragg-Williams mixing, modified quasichemical model). The non-ideal models contain parameters fitted to experimental data, so their purported improved accuracy is tested. After binary systems, ternary Al-Mg-X systems are modelled with ideal and Bragg-Williams mixing. The results are

compared to experimental data in two ways: a comparison of predicted and reported oxidation products, like the binary systems, and whether oxidation is suppressed by adding a third element, therefore determining if the suppression of Al-Mg oxidation by microalloying is a thermodynamic effect. Appendices contain (A) mathematical derivations, (B) parameters implemented in modelling with a full set of figures produced by modelling, (C) commentary on videos of projection sequences, and (D) crystallographic information for phases identified in X-ray diffraction analysis. The inclusion of this information as appendices is to support the conclusions of the work without cluttering the chapter with tedious detail.

Chapter 6 contains a general discussion, a summary of conclusions, and suggestions for areas of future scientific research.

1.3. References

[1] J.R. Davis, Introduction: key characteristics of aluminum, in: Corrosion of Aluminum and Aluminum Alloys, ASM International, Materials Park, OH, USA, 1999: p. 1.

[2] R. Lumley, Fundamentals of aluminium metallurgy, Woodhead Publishing Ltd., Cambridge, UK, 2011.

[3] A.K. Vasudevan, R.D. Doherty, Aluminium alloys - contemporary research and applications, Elsevier, 2012.

[4] S. Al-Alimi, N.K. Yusuf, A.M. Ghaleb, M.A. Lajis, S. Shamsudin, W. Zhou, Y.M. Altharan, H.S. Abdulwahab, Y. Saif, D.H. Didane, I.S.T. Tukiat, A. Adam, Recycling aluminium for sustainable development: A review of different processing technologies in green manufacturing, Results in Engineering 23 (2024) 102566. https://doi.org/10.1016/j.rineng.2024.102566.

[5] W.S. Tait, 28 - Corrosion prevention and control of chemical processing equipment, in: M. Kutz (Ed.), Handbook of Environmental Degradation of Materials, 2nd ed., William Andrew Publishing, Oxford, 2012: pp. 863–886. https://doi.org/10.1016/B978-1-4377-3455-3.00028-6.

[6] F. Czerwinski, Aluminum alloys for electrical engineering: a review, J Mater Sci 59 (2024) 14847–14892. https://doi.org/10.1007/s10853-024-09890-0.

[7] J. Taylor, The dark side of light metals: dealing with oxidation and dross, in: Faculty of Engineering and Industrial Sciences, Swinburne University of Technology, Swinburne University of Technology, Melbourne, Australia, 2011: pp. 34–36.

[8] B. Fateh, G.A. Brooks, M.A. Rhamdhani, J.A. Taylor, J. Davis, M. Lowe, Study of early stage interaction of oxygen with Al; methods, challenges and difficulties, in: S.J. Lindsay (Ed.), Light Metals 2011, Springer International Publishing, San Diego, California, USA, 2016: pp. 725–730. https://doi.org/10.1007/978-3-319-48160-9_126.

[9] G. Wu, K. Dash, M.L. Galano, K.A.Q. O'Reilly, Oxidation studies of Al alloys: Part II Al-Mg alloy, Corros Sci 155 (2019) 97–108. https://doi.org/10.1016/j.corsci.2019.04.018.

[10] J. Campbell, Entrainment defects, Mater Sci Technol 22 (2006) 127–145. https://doi.org/10.1179/174328406X74248.

[11] J. Campbell, Castings, 2nd ed., Elsevier Science & Technology, Oxford, UK, 2003.

[12] N.-W. Lai, The critical ingate velocity in Mg and Al alloy, PhD, School of Metallurgy and Materials, University of Birmingham, 2004.

[13] X. Dai, X. Yang, J. Campbell, J. Wood, Effects of runner system design on the mechanical strength of Al–7Si–Mg alloy castings, Materials Science and Engineering: A 354 (2003) 315–325. https://doi.org/10.1016/S0921-5093(03)00021-2.

[14] C. Cáceres, B.I. Selling, Casting defects and the tensile properties of an Al-Si-Mg alloy, Materials Science and Engineering: A 220 (1996). https://doi.org/10.1016/S0921-5093(96)10433-0.

[15] J. Campbell, Update on bifilms - the fundamental defect in metals, in: M. Tiryakioğlu, W. Griffiths, M. Jolly (Eds.), Shape Casting, Springer International Publishing, San Antonio, Texas, USA, 2019: pp. 3–15. https://doi.org/10.1007/978-3-030-06034-3_1.

[16] M. Tiryakioğlu, The myth of hydrogen pores in aluminum castings, in: M. Tiryakioğlu, W. Griffiths, M. Jolly (Eds.), Shape Casting, Springer International Publishing, San Antonio, Texas, USA, 2019: pp. 143–150. https://doi.org/10.1007/978-3-030-06034-3_14.

[17] J. Campbell, Films and bifilms - an update, in: Supplemental Proceedings: Volume 2: Materials Properties, Characterization, and Modeling, Wiley, Orlando, FL, USA, 2012: pp. 161–168.

[18] J. Campbell, The origin of Griffith cracks, Metall Mater Trans B 42 (2011) 1091–1097. https://doi.org/10.1007/s11663-011-9575-5.

[19] M. Tiryakioğlu, On the intrinsic and extrinsic microstructure-property effects in cast aluminum alloys, in: Shape Casting, Springer International Publishing, San Antonio, Texas, USA, 2019: pp. 293–302. https://doi.org/10.1007/978-3-030-06034-3_28.

[20] R. Gopalan, N.K. Prabhu, Oxide bifilms in aluminium alloy castings – a review, Mater Sci Technol 27 (2011) 1757–1769. https://doi.org/10.1179/1743284711Y.0000000033.

[21] J. Campbell, M. Tiryakioğlu, Review of effect of P and Sr on modification and porosity development in Al–Si alloys, Mater Sci Technol 26 (2010) 262–268. https://doi.org/10.1179/174328409X425227.

[22] X. Cao, J. Campbell, The nucleation of Fe-rich phases on oxide films in Al11.5Si0.4Mg cast alloys, Metallurgical and Materials Transactions A 34 (2003) 1409–1420. https://doi.org/10.1007/s11661-003-0253-3.

[23] X. Cao, J. Campbell, Morphology of β-Al5FeSi phase in Al-Si cast alloys, Mater. Trans. 47 (2006) 1303–1312. https://doi.org/10.2320/matertrans.47.1303.

[24] X. Cao, J. Campbell, Effect of precipitation of primary intermetallic compounds on tensile properties of cast Al 11.5Si 0.4Mg alloy, AFS Trans. 108 (2000) 391–400.

[25] J. Campbell, Discussion of "effect of strontium and phosphorus on eutectic Al-Si nucleation and formation of β-Al5FeSi in hypoeutectic Al-Si foundry alloys," Metall

Mater Trans A 40 (2009) 1009–1010. https://doi.org/10.1007/s11661-009-9804-6.

[26] J. Campbell, The consolidation of metals: the origin of bifilms, J. Mater. Sci. 51 (2016) 96–106. https://doi.org/10.1007/s10853-015-9399-9.

[27] D. Dispinar, J. Campbell, Critical assessment of reduced pressure test. Part 1: Porosity phenomena, Int J Cast Met Res 17 (2004) 280–286. https://doi.org/10.1179/136404604225020696.

[28] D. Dispinar, J. Campbell, Critical assessment of reduced pressure test. Part 2: Quantification, Int J Cast Met Res 17 (2004) 287–294. https://doi.org/10.1179/136404604225020704.

[29] G. Gyarmati, G. Fegyverneki, T. Mende, M. Tokár, Characterization of the double oxide film content of liquid aluminum alloys by computed tomography, Mater Charact 157 (2019) 109925. https://doi.org/10.1016/j.matchar.2019.109925.

[30] G. Wu, K. Dash, M.L. Galano, K.A.Q. O'Reilly, Oxidation studies of Al alloys: Part I Al-Cu (liquid phase) alloy, Corros Sci 157 (2019) 41–50. https://doi.org/10.1016/j.corsci.2019.05.013.

[31] I.N. Ganiev, N.I. Ganieva, D.B. Eshova, Oxidation of Aluminum Melts with Rare-Earth Metals, Russ. Metall. 2018 (2018) 458–464. https://doi.org/10.1134/S0036029518050063.

[32] W. Thiele, Die oxydation von aluminium und aluminiumlegierungs-schmelzen, PhD, Bergakademie Clausthal, 1951.

[33] I. Haginoya, T. Fukusako, Oxidation of molten Al–Mg alloys, Trans Jpn Inst Metal 24 (1983) 613–619. https://doi.org/10.2320/matertrans1960.24.613.

[34] O. Ozdemir, J.E. Gruzleski, R.A.L. Drew, Effect of low-levels of strontium on the oxidation behavior of selected molten aluminum–magnesium alloys, Oxid Met 72 (2009) 241–257. https://doi.org/10.1007/s11085-009-9158-x.

[35] C. Houska, Beryllium in aluminium and magnesium alloys, Met Mater 4 (1988) 100.

[36] S.-H. Ha, Y.-O. Yoon, B.-H. Kim, H.-K. Lim, T.-W. Lee, S.-H. Lim, S.K. Kim, Oxide scale behavior and surface protection of Al–Mg Alloys containing a trace of Ca, Inter J Metalcast 13 (2019) 121–129. https://doi.org/10.1007/s40962-018-0234-3.

[37] N. Smith-Hanssen, M. Syvertsen, A. Kvithyld, Microalloying to Inhibit Oxidation of Al–Mg Alloys, in: Light Metals 2022, Springer International Publishing, Cham, 2022: pp. 579–586. https://doi.org/10.1007/978-3-030-92529-1_76.

Chapter 2
Literature Review

2.1. Introduction

Aluminium is an abundant [1], widely-produced [2] metal used in many industries [3] due to its unique combination of desirable properties. Its structural properties, such as low density [3], high specific strength (when alloyed) [3], good castability [4], and versatility through alloying and thermomechanical processing [5] are prized in the automotive and construction sectors. Its high thermal and electrical conductivities [3] are utilised widely in the electronics sector, and its high corrosion resistance [6], from its naturally-occurring oxide layer, is useful.

This oxide layer forms through oxidation, which happens rapidly on contact with oxygen since aluminium is highly reactive [7,8]. The oxide, alumina (Al_2O_3), is stable across its solid temperature range, even in dilute air [9] and low pressures [10]. This high thermodynamic stability [11], good scale adherence [12], and near-perfect stoichiometry (of α-Al_2O_3, the most stable form of Al_2O_3 [13]) [14] gives use in protective coatings; some are formed on aluminium directly through techniques including anodising [15–19] and plasma electrolytic oxidation (PEO) [20–22], or on other metals through spraying [23]. The oxidation of molten aluminium has also been studied in the production of metal-ceramic composites (Al_2O_3/Al) through 'Directed Melt Oxidation' (DIMOX) [24–34].

However, problems can arise due to oxidation of aluminium melts. When the melt is exposed to oxygen-containing atmospheres, the melt oxidises [35], resulting in the formation of dross [36]. If oxide layers become entrained, they can form entrained oxide defects, responsible for numerous casting defects [37–39] and degradation of mechanical properties [9,40–46].

2.2. Oxidation of aluminium

2.2.1. Thermodynamics

In metallurgical contexts, oxidation is the reaction between a metal and oxygen in the

surrounding environment [47]. To determine whether oxidation can occur and whether the product is stable, the thermodynamics of the system must be analysed. The second law of thermodynamics, which states that the entropy of any isolated system must increase [48], provides a criterion for this. When considering metal oxidation, it is common to evaluate this criterion via minimisation of the Gibbs free energy, G (2.1), where H is enthalpy, T is the temperature, and S is entropy [49].

$$G = H - TS \tag{2.1}$$

In a closed system at constant temperature and pressure, a reaction is spontaneous if the change in Gibbs free energy of a reaction, ΔG, is negative [50]. Equivalently, a closed system is at chemical equilibrium when its Gibbs free energy is minimised [51]. Consider the oxidation of a moles of metal M with $b/2$ moles of oxygen gas $O_{2\,(g)}$ to form an oxide M_aO_b (2.2).

$$a\mathrm{M} + \frac{b}{2}\mathrm{O}_{2\,(g)} \rightarrow \mathrm{M}_a\mathrm{O}_b \tag{2.2}$$

The Gibbs free energy change of this reaction, ΔG, is the difference between the Gibbs energy, G_i, of the reactants and the products (2.3).

$$\Delta G = \sum_{products} n_i G_i - \sum_{reactants} n_i G_i = G_{\mathrm{M}_a\mathrm{O}_b} - \left(aG_{\mathrm{M}} + \frac{b}{2}G_{\mathrm{O}_2}\right) \tag{2.3}$$

If all species are in their standard state [52], their Gibbs free energies are termed standard Gibbs free energies, G°, and the corresponding Gibbs free energy change of reaction ΔG is termed the standard Gibbs free energy change of reaction ΔG° (2.4).

$$\Delta G^\circ = \sum_{products} n_i G_i^\circ - \sum_{reactants} n_i G_i^\circ = G^\circ_{\mathrm{M}_a\mathrm{O}_b} - \left(aG^\circ_{\mathrm{M}} + \frac{b}{2}G^\circ_{\mathrm{O}_2}\right) \tag{2.4}$$

However, oxidation often happens when species are not in their standard states. A pure solid is a standard state [52], but metals often contain multiple elements, either as impurities or as alloying. A pure gas at standard pressure (normally 100 kPa by convention [52]) is another standard state, but oxidation often occurs in multi-component atmospheres. The Gibbs free

energy change under non-standard conditions, ΔG, can be related to the standard Gibbs free energy change, ΔG°, through the reaction quotient, Q, defined as the product of the activities, a_i, of the products raised to the power of their stoichiometric coefficients, n_i, divided by those of the reactants raised to theirs (2.5).

$$\Delta G = \Delta G^\circ + RT \ln Q = \Delta G^\circ + RT \ln \left(\frac{\prod_{products} \left(a_i^{n_i} \right)}{\prod_{reactants} \left(a_i^{n_i} \right)} \right) \tag{2.5}$$

For the oxidation of a pure metal (2.2), this equation can be simplified significantly (2.6), where p_{O_2} is the partial pressure of oxygen, divided by a standard pressure (conventionally, 100 kPa [52]). In multi-component systems, more terms of the form $RT \ln(a_i)$ exist; careful evaluation of these terms are needed for accurate thermodynamic analysis.

$$\Delta G = \Delta G^\circ + RT \ln \left(\frac{a_{M_a O_b}}{a_M^a a_{O_2}^{b/2}} \right) = \Delta G^\circ - \frac{bRT}{2} \ln \left(p_{O_2} \right) \tag{2.6}$$

These equations can be used to construct Ellingham diagrams (Figure 2.1) [53], which chart the stability of compounds (most commonly oxides) through evaluation of their Gibbs free energy of formation ΔG_f°, normalised to one mole of O_2 gas [11]. An oxide is considered stable if ΔG_f° is negative, and this principle is used to predict whether one element can reduce another element's oxide: if an element's line is at a more negative value of ΔG°than another element at a given temperature, then the former element can reduce the latter element's oxide at that given temperature, since $\Delta G^\circ$of this reduction reaction will be negative, so the reaction is spontaneous. These diagrams can also be used to predict the partial pressure of oxygen at which oxides will dissociate [11]. Ellingham diagrams only consider thermodynamics and neglect kinetics, so thermodynamically favourable reactions may not be observed if the kinetics are too slow for observation on experimental timescales [54].

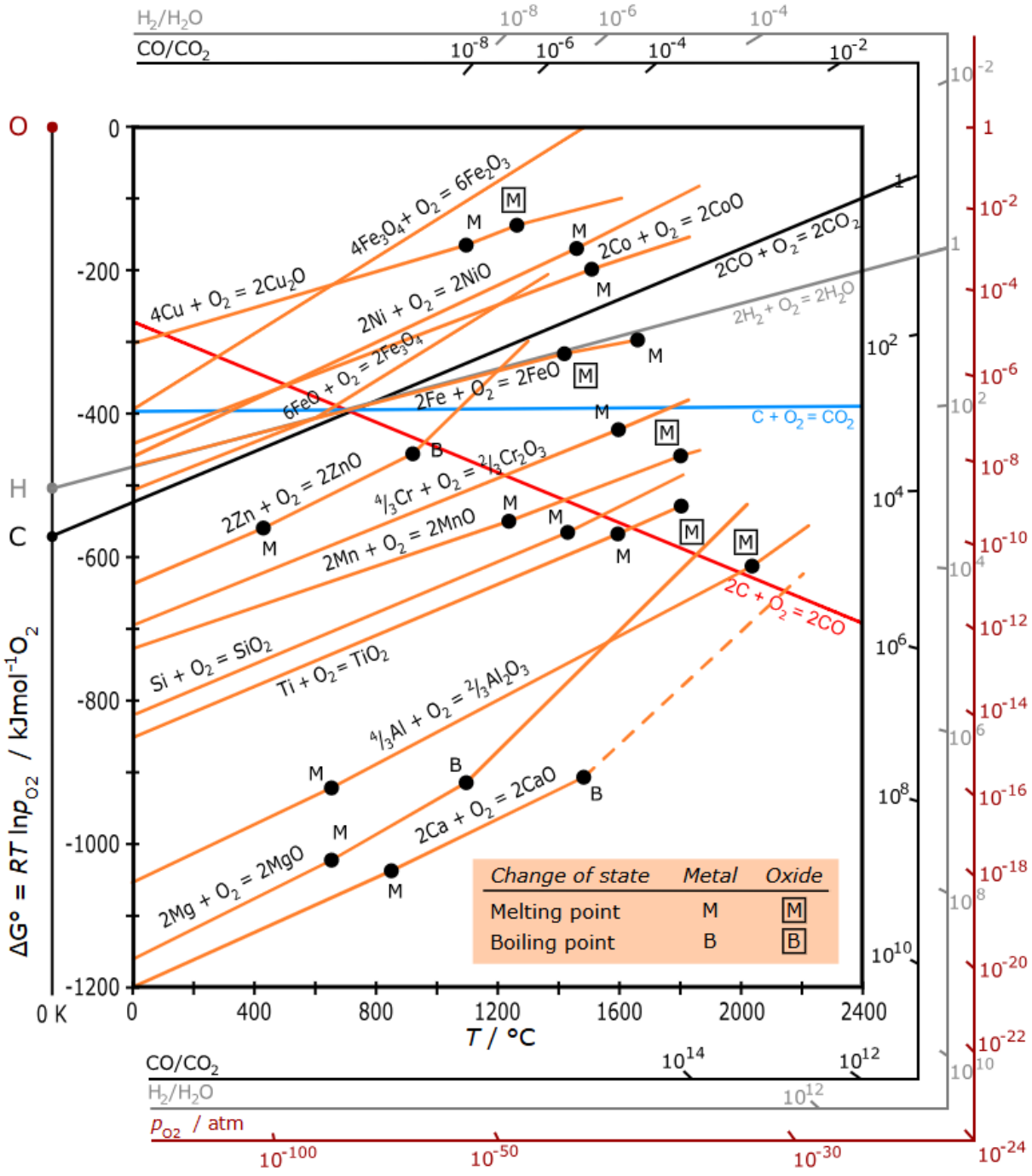


Figure 2.1. Ellingham diagram with various oxides plotted [55].

2.2.2. Kinetics

A full understanding of metal oxidation requires understanding of reaction rates, determined by kinetics [47] and affected by factors such as composition, temperature, pressure, and reaction progress [47,56]. Kinetic studies are important in characterising metal oxidation: breakaway oxidation indicates a non-protective oxide, causing excessive corrosion and

premature failure in service [57], and slow-growing, protective oxides, such as Al_2O_3 and Cr_2O_3 [47], are desirable.

Thermogravimetric Analysis (TGA) measures oxide formation directly through weight gain during metal oxidation [58], an assumption needing experimental confirmation through microscopy [35]. In isothermal oxidation [58], the shape of the weight gain-time curve allows deduction of the kinetic rate law, indicating the physical nature of oxidation [47]. Activation energies can be determined from isothermal scans at multiple temperatures and p_{O_2} measurements can indicate oxidation transport mechanisms [47]. Since different rate laws can appear similar (Figure 2.2, [59]), careful interpretation is required and some scenarios can result in rate laws with differential equations which need numerical solutions, complicating interpretation further [60].

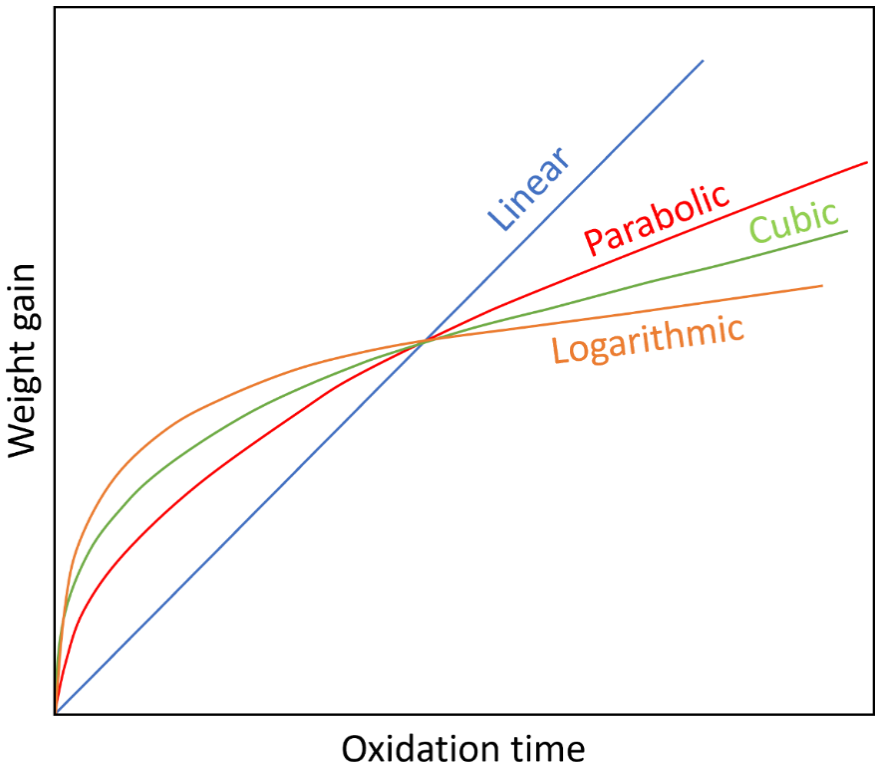


Figure 2.2. Schematic diagram of common kinetic rate laws showing similarities in appearance, especially between parabolic, cubic, and logarithmic rate laws. Adapted from [59].

Many rate laws have been observed in the oxidation of aluminium and its alloys [35,60–63], including logarithmic, parabolic, linear, (generally seen at low, intermediate, and high

temperatures respectively [59]) and paralinear laws [47]. In initial (< 100 nm) low temperature oxidation (c. < 400 °C) [47], oxide growth occurs through migration of cations outward and anions inward by an electric field from ionic separation [64]. This results in initially rapid oxidation, which slows over time, as described well by Cabrera and Mott, with logarithmic (2.7) or inverse logarithmic (2.8) laws [65].

$$x = k_{\log} \ln(t + t_0) + A \tag{2.7}$$

$$\frac{1}{x} = B - k_{\mathrm{il}} \ln(t) \tag{2.8}$$

x = oxide layer thickness; t = time; $k_{\log}$ = logarithmic rate constant; k_{il} = inverse logarithmic rate constant; t_0, A, B = experimentally fitted parameters.

At higher temperatures and thicknesses, this electric field is negligible and the oxide growth rate is limited by ionic diffusion, resulting in Wagner's parabolic law (2.9) [66]. Parabolic kinetics generally indicate a protective, continuous oxide layer [47].

$$x^2 \propto t \tag{2.9}$$

If growth is limited by the interface reaction such that growth rate is thickness-independent, linear kinetics are observed (2.10), indicating a non-protective oxide [47].

$$x \propto t \tag{2.10}$$

Linear kinetics can occur through cracking due to density differences between metals and oxides: this can be predicted (as a rule of thumb [67]) by the Pilling-Bedworth ratio, R_{PB} [68], the ratio of the elementary unit cell of the oxide to its metal (Figure 2.3). Phase transformations of the substrate, such as γ-Fe to α-Fe through chromium depletion in steels, or the oxide, such as γ-Al_2O_3 to α-Al_2O_3 in aluminium, can also cause cracking [69].

Paralinear kinetics, a combination of parabolic and linear kinetics, can be observed when duplex oxide layers exist where the inner layer is protective and outer non-protective [63] or when one component volatilises [70]. Breakaway oxidation [29,69,71–73] can also occur, in

which an initially protective oxide breaks down after a period of steady-state growth resulting in accelerated, uncontrolled oxidation [74].

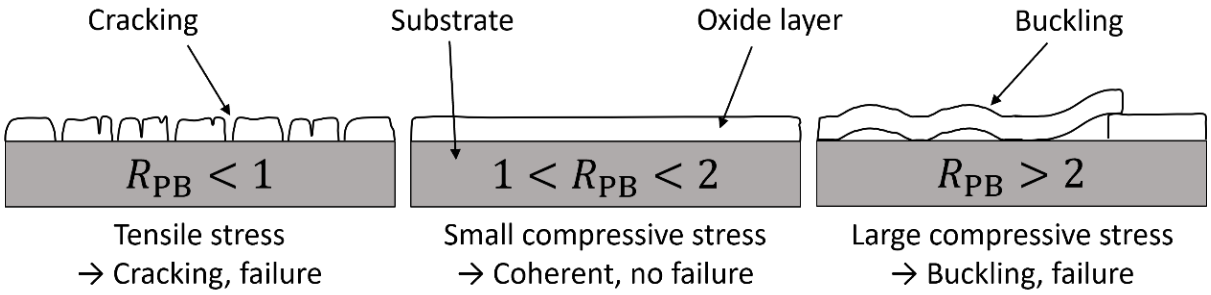


Figure 2.3. Schematic diagram of oxide growth with varying Pilling-Bedworth Ratios (R_{PB}). Low values of this ratio ($R_{PB} < 1$) indicate tensile stresses resulting in cracking; high values ($R_{PB} > 2$) indicate excessive compressive stresses resulting in buckling or detachment; and intermediate values indicate a slight compressive stress, resulting in a continuous, protective oxide layer.

2.2.3. Pure aluminium

Oxidation of pure aluminium results in alumina (Al_2O_3), three allotropes of which are commonly encountered: am-Al_2O_3, an amorphous form; γ-Al_2O_3, a defect spinel of currently undetermined structure [75]; and α-Al_2O_3, a cubic form known as corundum [76]. Oxidation of aluminium is complicated by the presence of alloying elements and impurities [77], crystal structure [62], experimental conditions [78], and temperature [61].

At low temperatures (< 300 °C), a thin am-Al_2O_3 layer grows rapidly [79] to a few nanometres [143], [161], stabilised by its surface energy [81–84]. At higher temperatures, the nucleation and (lateral then outward) growth of γ-Al_2O_3 crystals at the metal/oxide interface follows [79,85,86]. The inward diffusion of oxygen anions slows as the oxide thickens [61], and the oxide remains a duplex am-Al_2O_3/γ-Al_2O_3 layer [61,87]. There is no single accepted kinetic growth theory despite decades of research and many unsuccessful attempts [88].

Aluminium melts at 660 °C, complicating oxidation further. Convection currents enhance mass transport and thus modify kinetics and thermodynamics [89]. Turbulence can disrupt and crack the melt surface, enhancing oxidation and causing metal exudation [90], and dynamic conditions can enhance oxidation further [91].

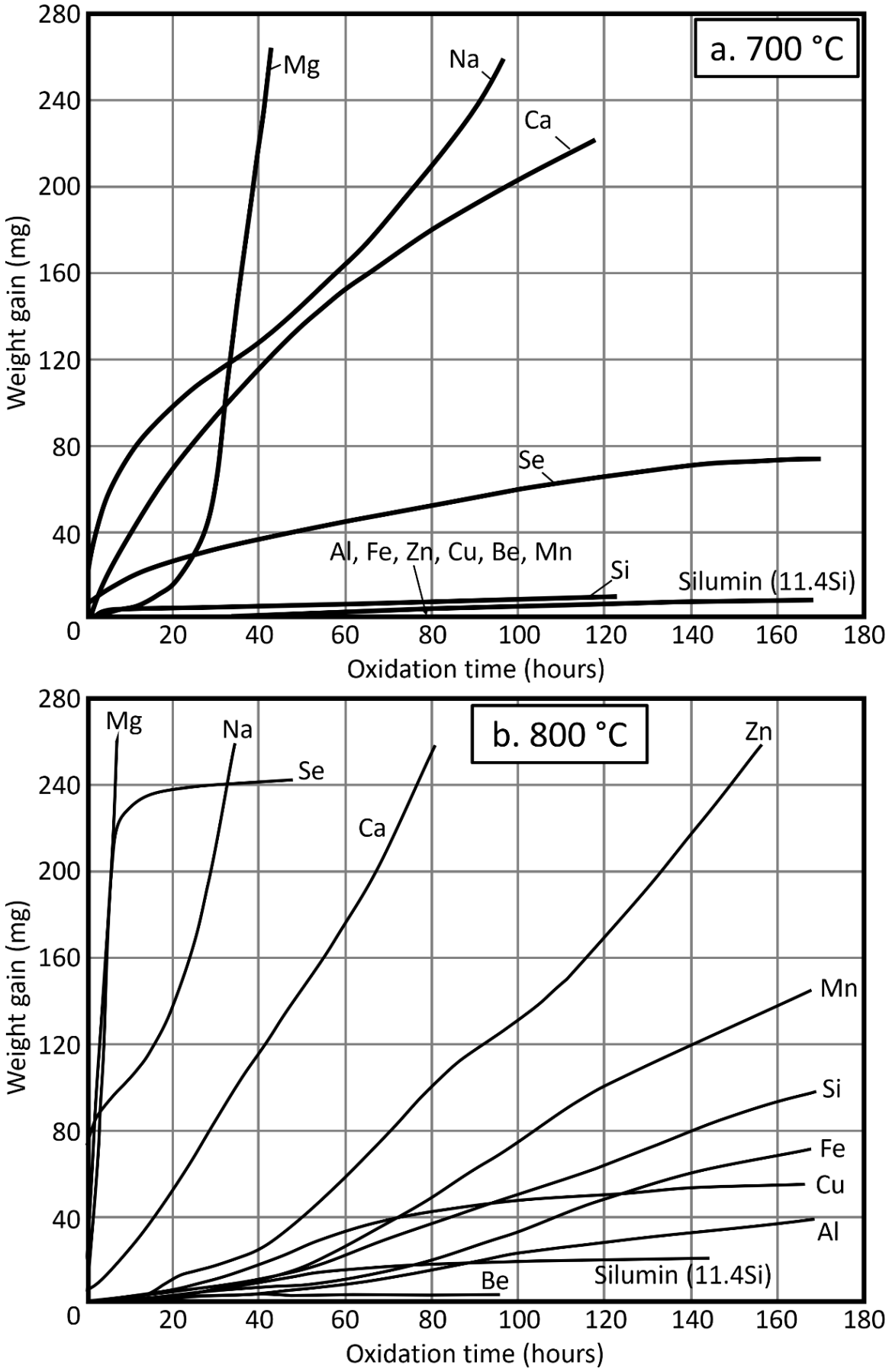


Figure 2.4. Effect of alloying additions (all 1 at.% except 'silumin', which contains 11.4 at.% Si) on the oxidation of pure aluminium (labelled Al) melts at 700 and 800 °C. Adapted from [92].

Melt oxidation is initially similar to high-temperature solid oxidation: am-Al_2O_3 forms first [34], [173], followed by nucleation and growth of γ-Al_2O_3 (after 5-10 minutes at 750 °C) [94,95]. After an incubation period dependent on many factors [69,78,96], γ-Al_2O_3 then transforms to α-Al_2O_3 [97]. Like am-Al_2O_3, γ-Al_2O_3 is stabilised by its surface energy [98], delaying the transformation to α-Al_2O_3. The γ-α transformation has an associated 24% volume contraction [69], which can cause cracking and enhance oxidation, up to 60 times more in dynamic conditions [99]. Increasing temperature increases the oxidation rate [100], lowers the γ-α transformation incubation time [99], and produces more α-Al_2O_3 over γ-Al_2O_3 [94].

Kinetic studies have produced inconsistent results: Impey [69], studying oxidation of pure aluminium at 660 – 850 °C, found logarithmic kinetics below 750 °C and parabolic above; Wu [100] found paralinear kinetics in the range 750 – 950 °C; and Hinton found two-stage sigmoidal kinetics [101]. However, aluminium is often alloyed with various elements which can greatly affect oxidation behaviour (Figure 2.4) [28,63,100,102].

2.2.4. Al-Mg alloys

Magnesium is the major alloying element of the 5xxx wrought and 5xx.x cast series of alloys. Al-Mg alloys have high strength (through work hardening), good formability, and good corrosion resistance, and are therefore used in castings, extrusions, and sheets [5]. Magnesium has the starkest effect of any common alloying addition on the oxidation of molten aluminium (Figure 2.4), vastly raising oxidation rate due to its slightly higher affinity for oxygen than aluminium [63]. Both MgO and $MgAl_2O_4$ are commonly observed, but kinetics and growth processes have been mixed and irreproducible despite decades of research. Since magnesium and aluminium have similar oxygen affinities, the most thermodynamically stable Al-Mg oxidation product is highly sensitive to both temperature and composition: at 725 °C, Al_2O_3 is most stable below 0.15 wt.% Mg, MgO above 1.5 wt.%, and $MgAl_2O_4$ between; these thresholds increase with increasing temperature [103].

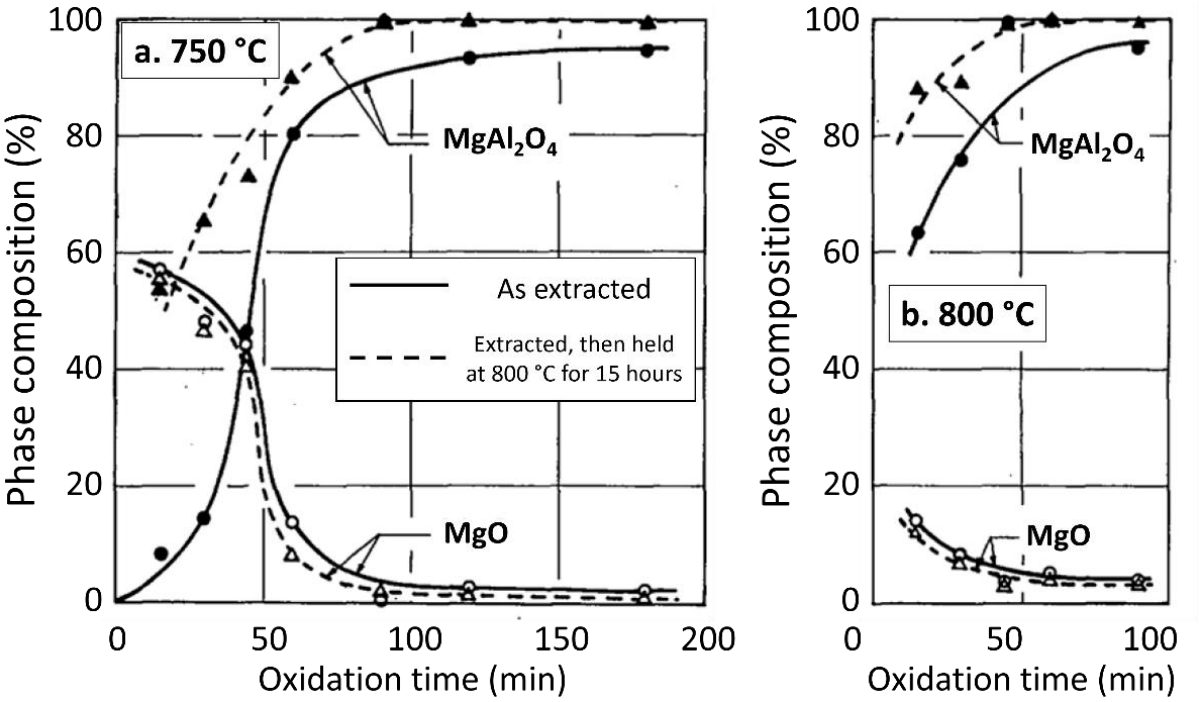


Figure 2.5. Phase compositions of oxides formed on Al-10Mg oxidised in air at (a) 750 °C and (b) 800 °C against oxidation time. $MgAl_2O_4$ forms at the expense of MgO over time, especially so when extracted from the melt and held in isolation for 15 hours. Adapted from [104].

However, Al-Mg oxidation experiments have produced both MgO and $MgAl_2O_4$ at a range of temperatures and compositions with no clear correlation to either: $MgAl_2O_4$ and MgO have been observed together from 450 °C (Al-0.5Mg) [31] to 1100 °C (Al-5Mg) [27], and from 0.4 wt.% Mg (550 °C) [105] to 12 wt.% Mg (650-900 °C) [104]. Some studies result in MgO only, such as Field (Al-4.2Mg, 520-575 °C) [106] and Tenorio (Al-4.5Mg, 550-800 °C) [107], and only $MgAl_2O_4$ in others, such as Bahadur (Al-4.5Mg, 500 °C) [108] and Wang (Al-0.49/0.7Mg, 750 °C and 920 °C) [94].

Oxidation of solid Al-Mg is broadly as follows: a continuous am-Al_2O_3 layer forms at low temperatures [109] and, as temperature increases, magnesium segregates (at c. 230 °C for Al-1.45Mg [110]). MgO then forms, followed by $MgAl_2O_4$, degrading the oxide layer [31,109]: Haginoya [104] observed $MgAl_2O_4$ content to increase with oxidation time at the expense of MgO (Figure 2.5). This increases magnesium diffusion [31] and thus the oxidation rate [109,111]. Mizuno [112] reported that magnesium evaporated in solid Al-Mg oxidation at 300-520 °C, but other researchers have only found this at higher, molten temperatures (1100-

1250 °C [27,30]). Yoon [113] attributed the oxide growth rate increase with magnesium content (0.5 to 5 wt.%) to β-Al_3Mg_2 formation, but only justified its presence through thermodynamic software, and the lack of oxide layer on Al-0.5Mg is inconsistent with other studies [31,107,109].

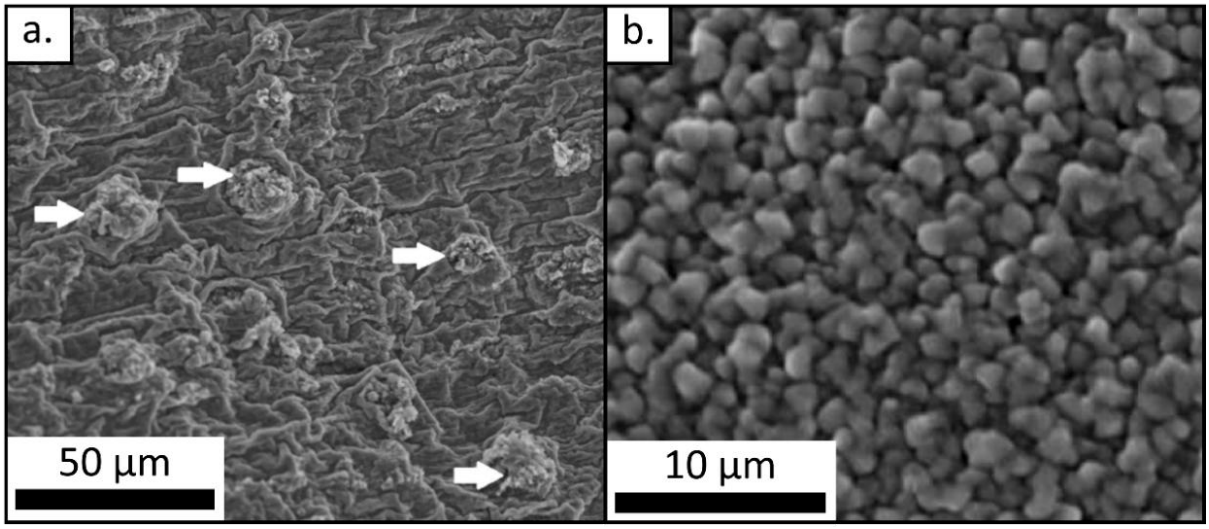


Figure 2.6. SEM (SE) images of oxides formed on Al-Mg melts (air, 750 °C, 1 hour): (a) MgO cauliflower-like bulges (see arrows) from Al-2Mg; (b) Mix of $MgAl_2O_4$ and MgO nodules from Al-0.2Mg. Adapted from [102].

Wu [63], oxidising Al-Mg melts (0.2 and 2 wt.% Mg), also observed the formation of am-Al_2O_3, MgO, then $MgAl_2O_4$, a sequence attributed to magnesium depletion. The $MgAl_2O_4$ and MgO were observed as nodules and 'cauliflower-like bulges' (Figure 2.6), consistent with previous studies [104]. This transition from MgO to $MgAl_2O_4$ was correlated with a change from parabolic to linear kinetics (Figure 2.7), also observed elsewhere [111].

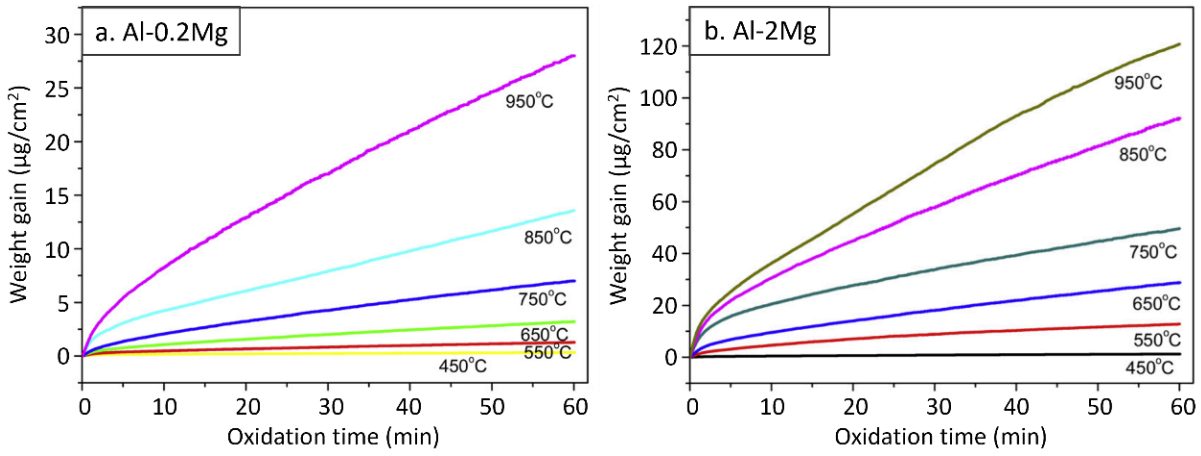


Figure 2.7. TGA of (a) Al-0.2Mg and (b) Al-2Mg alloys oxidised in air (450-950 °C). Adapted from [63].

Tenório [107] observed parabolic kinetics in Al-1Mg up to 750 °C and paralinear above 800 °C; in Al-4.5Mg, kinetics were observed to be linear at 450-500 °C and parabolic above (Figure 2.8) [107]. Both studies concluded that MgO is protective and $MgAl_2O_4$ is not.

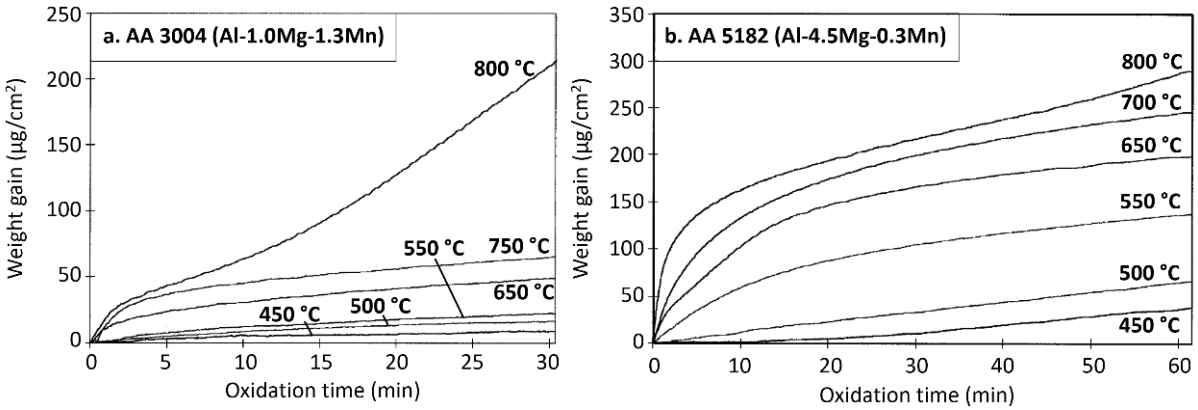


Figure 2.8. TGA results of Al-Mg-Mn alloys oxidised in air at 450-800 °C: (a) AA3004 (Al-1.0Mg-1.3Mn); (b) AA5182 (Al-4.5Mg-0.3Mn). Alloys here contain manganese, but magnesium dominates the oxidation behaviour, so the manganese content has minimal effect. Adapted from [107].

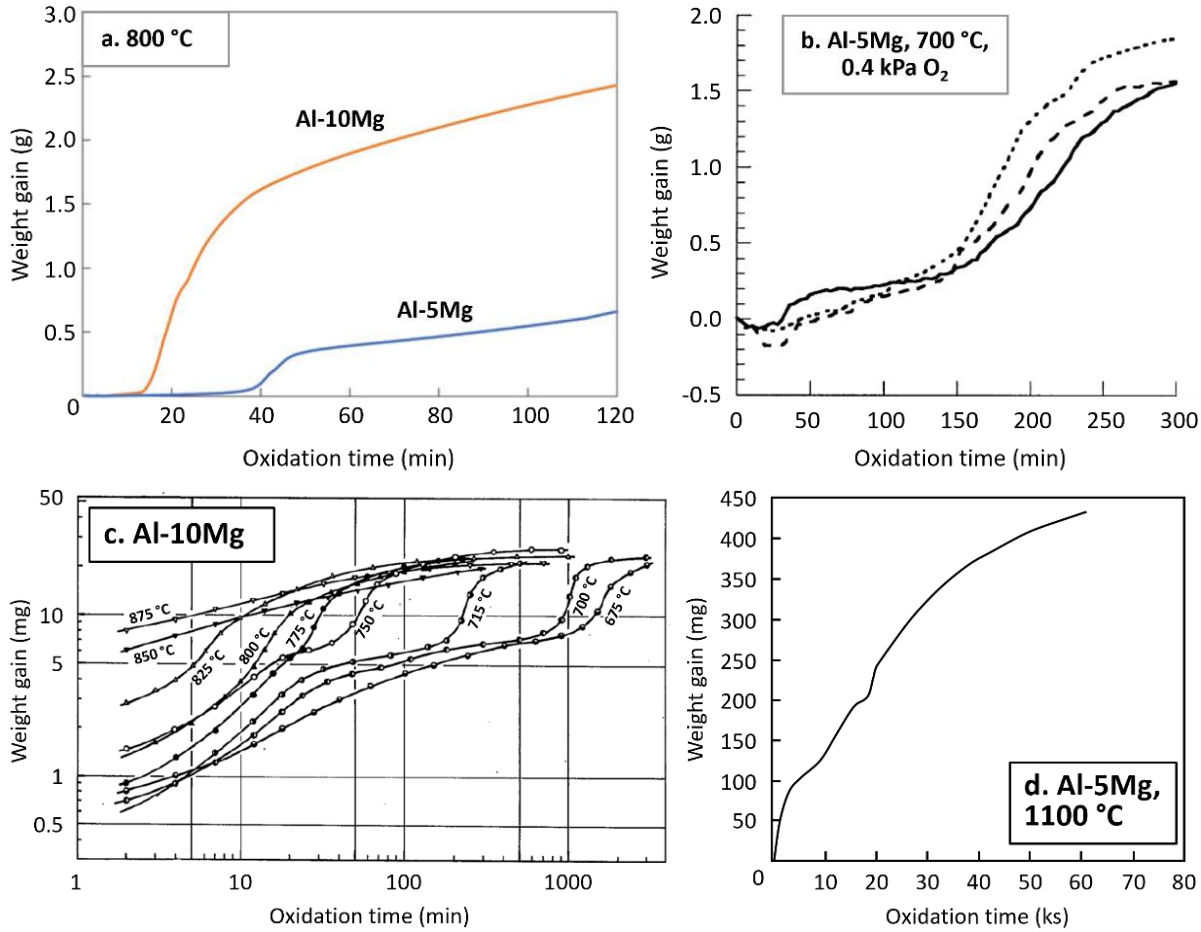


Figure 2.9. Oxidation weight gains of Al-Mg alloys, in air unless specified: (a) Sigmoidal kinetics; (b) Unreproducible results; (c) Double sigmoidal kinetics; (d) Linear, incubation, and growth. Adapted from [114] (a), [115] (b), [104] (c), and [27] (d).

However, other kinetic behaviours have been observed (Figure 2.9) such as sigmoids, double-

sigmoids associated with sequential MgO and $MgAl_2O_4$ formation [104,114] and mixed linear-sigmoidal behaviour [27]. Since observations are varying and non-reproducible [115], there is no single accepted rate law for Al-Mg oxidation.

2.2.5. Microalloying of Al-Mg alloys

Group II elements have been added to Al-Mg alloys to suppress melt oxidation. Historically, beryllium was added, since it hugely reduced oxidation with only small additions (50-500 ppm [116,117]) through the suppression of the MgO to $MgAl_2O_4$ transformation [92,118]. Smith attributed the melt protection to beryllium forming a BeO layer at the oxide-metal interface, which slowed the outward diffusion of magnesium and aluminium to the surface [119].

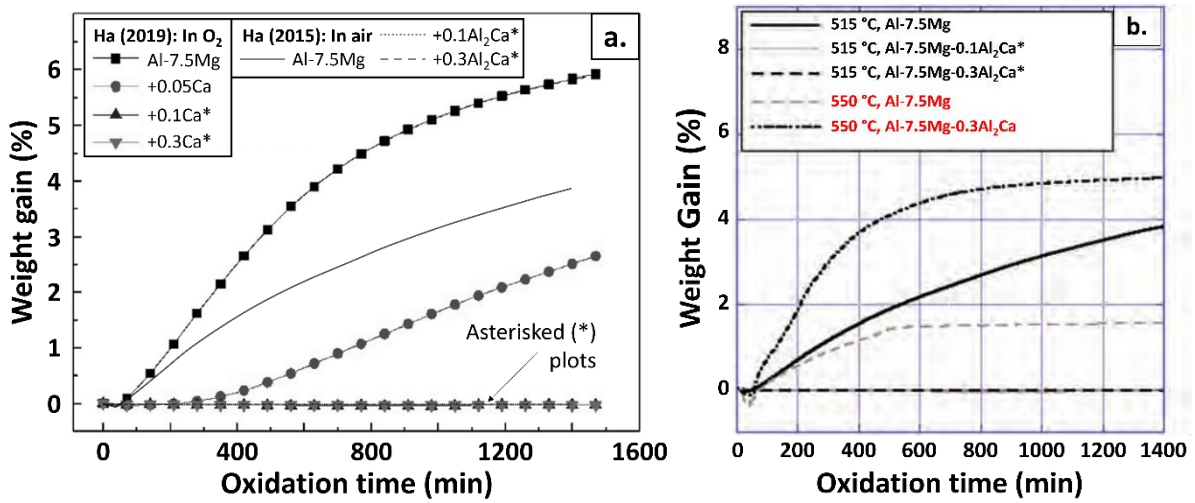


Figure 2.10. TGA results of solid Al-Mg-Ca alloy oxidation: (a) Oxidation of Al-7.5Mg (wt.%) with various Ca/Al_2Ca additions at 515 °C in O_2 and air; (b) Oxidation of Al-7.5Mg (wt.%) with various Al_2Ca additions in O_2 at 515 °C and 550 °C (red labels: from the text, it is clear that the 550 °C labels are switched). Asterisks indicate alloys with no measurable oxidation. Adapted from [120,121] (a) and [122] (b)

However, concerns over its toxicity led to alternatives being sought [123] and other Group II elements were found to be effective [124]. Trace calcium additions have been found to greatly suppress the oxidation of solid Al-Mg alloys: Kim [125], oxidising Al-5Mg and Al-5Mg-0.3Ca (wt.%) at 400/500 °C for 72 hours found no significant oxidation at 400 °C, but, at 500 °C, blistering appeared only in Al-5Mg, indicating the suppression of magnesium oxidation by calcium. Additions of Al_2Ca to Al-7.5Mg (0.1 and 0.3 wt.%) and Al-7Si-0.4Mg (0.1 wt.%) completely suppressed oxidation weight gain at 515 °C (Figure 2.10.a) [120,121], and

reductions in the oxidation of Al-7.5Mg (wt.%) at 515 °C and 550 °C were observed with additions as low as 50-100 ppm Al_2Ca [122].

This suppression was also demonstrated well by TGA studies by Ha [122], but the 550 °C curves are clearly mislabelled (Figure 2.10.b): Ha states that the weight gain of Al-7.5Mg-0.3Al_2Ca oxidised at 550 °C was 'controlled under 102%', that the weight gain of Al-7.5Mg at 550 °C showed a 'steeper slope' than at 515 °C and, latterly, the weight remained 'constant'. Furthermore, the given labels would imply that a temperature increase from 515 °C to 550 °C decreases the rate of Al-Mg oxidation, completely inconsistent with previous studies. This oxidation suppression was widely attributed to a compact mixed oxide layer [120–122,125–127], but the phase composition has yet to be conclusively identified: Kim [125] asserted the presence of $CaAl_4O_7$ through thermodynamic calculations but gave no evidence beyond EDX results confirming the presence of calcium and aluminium in the oxide.

Ha [126] reported that $CaMg_2Al_{16}O_{27}$ was present through similar reasoning, but also reported MgO_2 through the selected-area diffraction pattern (SADP) of one globular particle which is not consistent with previous experiments. Other authors label the layer as 'mixed MgO-CaO' [120–122], sometimes with Al_2O_3 also [121], but conclusive phase identification has proven difficult. Furthermore, whilst an interfilling phenomenon has been observed [122] and calcium shown to reduce magnesium loss during oxidation [121], the mechanism for oxidation resistance remains a mystery [120,122].

The suppressive effect of calcium on Al-Mg oxidation has also been observed in melts [120–122,128]: Yoon [128] found that 0.03 wt.% Ca (through Al_2Ca) reduced the oxidation weight gain (720 °C, dry air, 6 hours) of Al-5Mg (wt.%) from 10% to 0.01% (Figure 2.11), attributed to the promotion of MgO over $MgAl_2O_4$ through removal of "pores and oxide clusters caused by the MgO-$MgAl_2O_4$ transformation". Whilst the double sigmoid TGA curve (with a continued rise in weight) of the Al-5Mg (wt.%) sample is consistent with a two-stage reaction

indicative of $MgAl_2O_4$ formation [104], and the 0.03 wt.% Ca addition suppresses oxidation, it would be more complete to attribute oxidation suppression to the formation of a mixed oxide layer, not just the suppression of $MgAl_2O_4$.

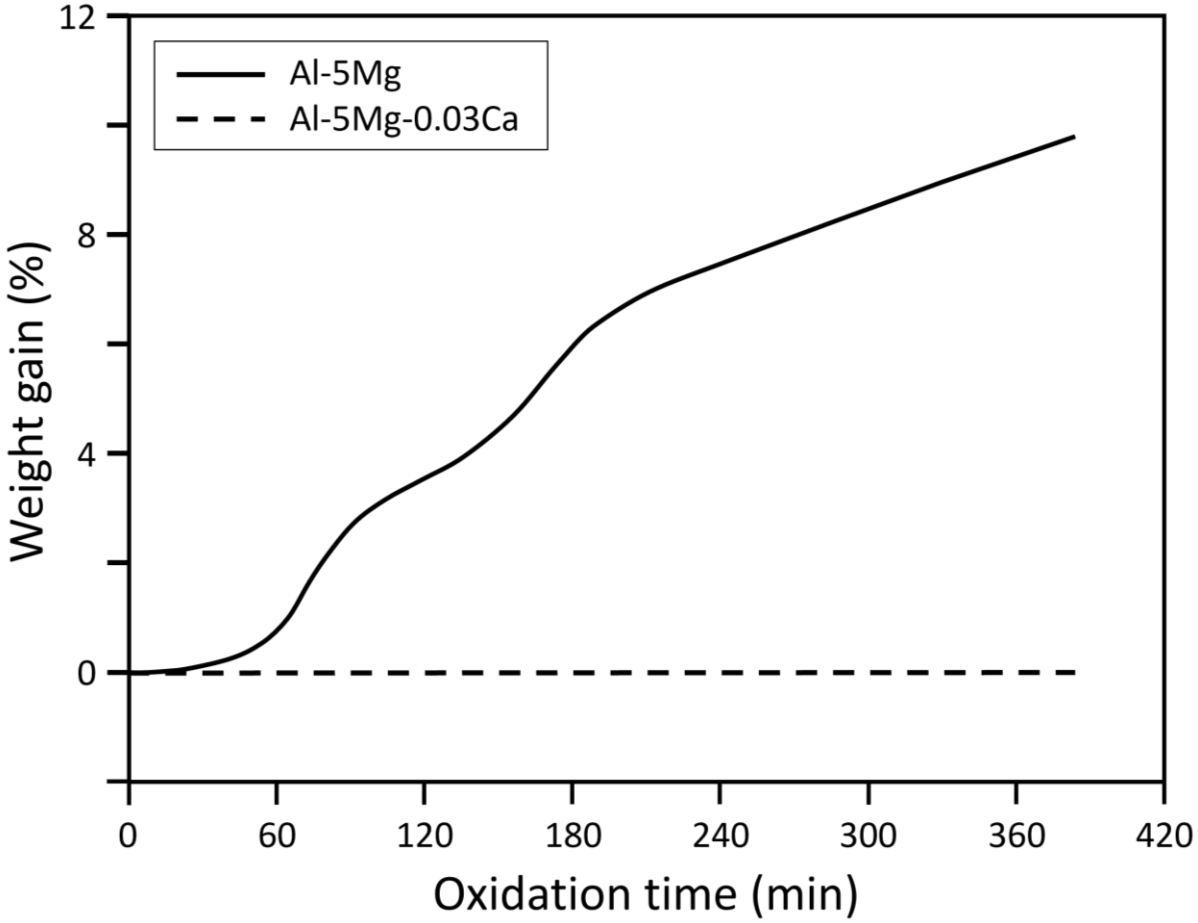


Figure 2.11. TGA results of Al-5Mg-0/0.03Ca (wt.%) oxidation (720 °C, dry air, 6 hours). Adapted from [128].

Ozdemir [71] found that small additions of strontium (250-1000 ppm) completely suppressed oxidation of low-Mg (0.5-1 wt.%) Al-Mg alloys, and partially reduced oxidation in high magnesium alloys (Figure 2.12.a-c). Like beryllium, this was attributed to the suppression of $MgAl_2O_4$ through formation of a strontium-rich surface oxide, but no strontium-containing oxides were observed (Figure 2.12.d). This was also the case in Yuen's study [129], the lack of a strontium-containing oxide being attributed to masking of XRD peaks by the much greater MgO signal. However, this suppression effect was not observed with additions of other reactive elements, such as Ce, Gd, La, or Sc [124], the reason for which has not been determined.

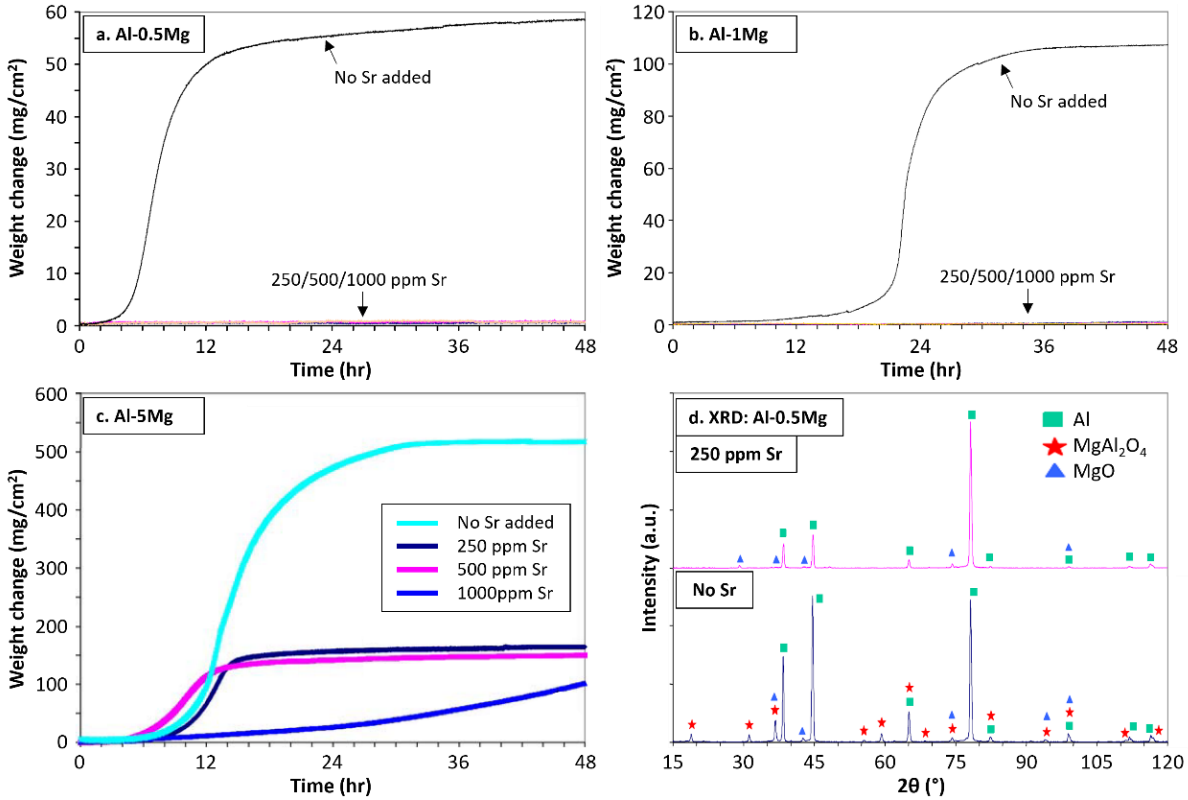


Figure 2.12. Effects of strontium additions on the oxidation of Al-Mg alloys. TGA (dry air, 750 °C) of (a) Al-0.5Mg, (b) Al-1Mg, and (c) Al-5Mg (in wt.%) with strontium additions (250/500/1000 ppm); (d) Post-TGA XRD results of oxidised Al-0.5Mg, with and without 250ppm strontium added. Adapted from [71].

2.2.6. Other aluminium alloys

2.2.6.1. Al-Cu

Aluminium alloys of the 2xxx wrought and 2xx.x cast series contain copper as their principal alloying element. The addition of copper appears to partially suppress oxidation in the liquid state [130], supressing the γ-Al_2O_3 to α-Al_2O_3 transformation, despite having a slightly higher initial oxidation rate [101]. Wu [100] also found that copper enhanced the kinetics of initial liquid state oxidation and lowered the activation energy for oxidation growth.

2.2.6.2. Al-Li

Lithium greatly accelerates oxidation of aluminium melts [131]. Gu [34], investigating the DIMOX of pure aluminium with Li_2CO_3 added to the surface, found similar results and detected mixed Li-Al oxides, such as $LiAl_5O_8$ and $LiAlO_2$ (α and γ). Mixed Li-Al oxides have also been detected in the melt oxidation of Al-Li alloys: investigators found γ-$LiAlO_2$ and α-

Al_2O_3 after oxidising Al-3Li (wt.%) in pure oxygen at 700 °C, as well as $LiAl_5O_8$ and γ-$LiAlO_2$ at 500 °C, and γ-$LiAlO_2$ after oxidising Al-0.3Li and Al-1.2Li (wt.%) in air at 750 °C ([132–134]). Jayaram [33], studying the DIMOX of Al-Li at 1050 °C in air, found an initial rapid oxidation rate which dropped over time, and observed $LiAlO_2$.

2.2.6.3. Al-Si

Silicon, a common addition and the primary alloying element of the 4xxx wrought and 4xx.x cast series, was found by Haginoya [130] to not affect weight gains at 750 °C and below but at 850 – 900 °C, silicon additions up to 4 wt.% decreased total weight gain, and further additions up to 10 wt.% Si increased it. In contrast, Thiele [92] found 1 at.% Si to increase the rate of oxidation at both 700 °C and 800 °C, but also found that 11.6 at.% Si addition increased the rate of oxidation at 700 °C and decreased it at 800 °C. Kinetic data on the oxidation of Al-Si melts is lacking: whilst Miresmaeili [135], investigating the effects of strontium and magnesium on oxidation rate, performed TGA experiments on Al-7Si at 690 °C and 730 °C, but neither kinetic laws nor data were obtained. Pritchard and Werrett [136] found evidence of aluminosilicates with inelastic electron tunnelling spectroscopy (IETS) and X-ray photospectroscopy (XPS), justified through the similarities in IETS/XPS peak positions with both zeolites and aluminosilicates. Werrett [137] found further evidence of this aluminosilicate character in solid Al-Si alloys at 25-500 °C but no aluminosilicate phases were conclusively identified in either case.

2.2.6.4. Al-Zn

Zinc appears to have little effect on melt oxidation below 700-800 °C but greatly enhances oxidation above due to its volatilisation and gas-state oxidation, resulting in various oxides including ZnO, $ZnAl_2O_4$, and Al_2O_3 [92,130]. This has been used to produce ZnO in various microstructures [138–140]. Zinc additions to Al-Mg alloys increases high-temperature melt

oxidation [26] and has resulted in various products (MgO, $MgAl_2O_4$, ZnO, and $ZnAl_2O_4$) without clear correlation to composition or temperature [26,33,140,140,141,141,142].

2.3. Double oxide film defects

2.3.1. Entrainment

Aluminium alloy production involves several molten transfer steps [40]. Should the surface break and entrain during pouring, achieved with only a 1-2 cm pour height (c. 1 m/s pour velocity) [40,143], a double oxide film defect (bifilm) can result [41], consisting of two unbonded oxide layers with an air gap (Figure 2.13).

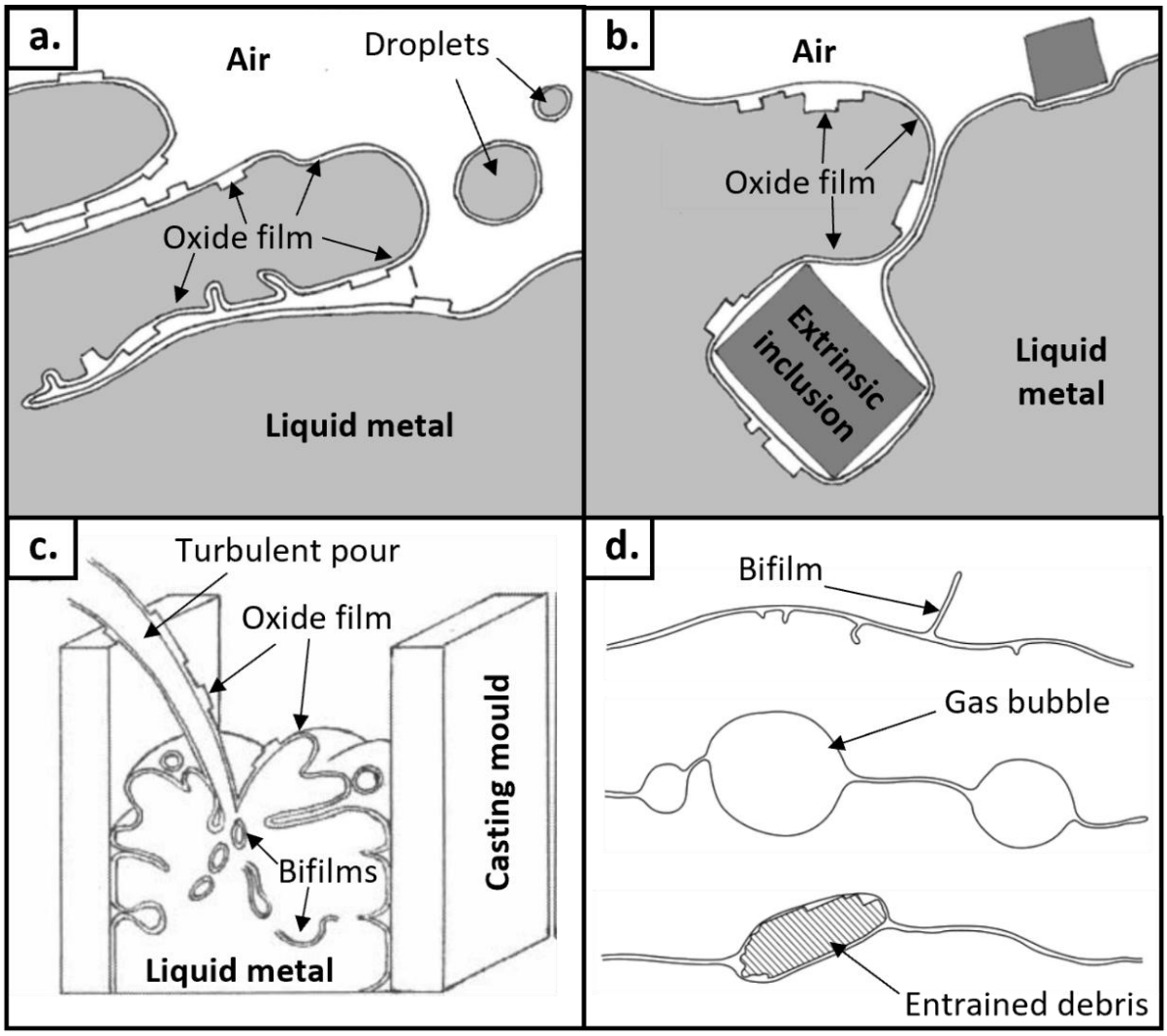


Figure 2.13. Schematic diagrams of entrained oxides, including bifilms, and their formation: (a) Folding of surface oxide film and impingement of droplets; (b) Entrainment of extrinsic inclusions; (c) Turbulent pouring of melt into casting mould resulting in bifilm formation; (d) Bifilms, including those with gaseous and solid inclusions. Adapted from [39] (a,b), [37] (c), and [144] (d).

These defects constitute cracks in the solidified component, causing many defects [40]. Oxide growth is irreversible, since melts exposed to oxygen oxidise rapidly, and the oxides remain once submerged. Bifilms have near-neutral buoyancy, making flotation impracticable [40]. Dissolved hydrogen can expand bifilms by inward diffusion, floating them to the surface, but this forms more oxide and contracts the bifilm, causing sinking into the melt [38].

Bifilms deteriorate melt quality in many ways. They are widely believed to: cause porosity by nucleation of hydrogen bubbles [40,145,146]; extrinsically weaken intermetallics, silicon precipitates, and the melt itself [43,147–153]; deteriorate mechanical properties such as strength, elongation, ductility, fatigue, and reliability [154–159]; and even contribute to corrosion [46,160] and creep [37,161]. These effects are especially prevalent from bifilms formed in the latter stages of castings (Table 2.1): thick (up to mm scale [46]), convoluted bifilms formed early in production or from ingots themselves, termed ‘old’ bifilms, pose fewer problems than latterly-formed, thin (0.1-1 μm [46,162]) bifilms, termed ‘young’ bifilms. The flexibility of ‘young’ bifilms allows straightening during melt holding, forming an engineering crack upon solidification [41].

Type	Growth time	Thickness (μm)	Visual description
Young	< 0.01 s	0.05 – 0.13	Melt surface colour change
	0.01 – 1 s	0.05 – 0.50	Transparent, creased, wrinkled films
Old	10 s – 1 min	c. 10	Flexible, extensive films
	10 min – 1 hr	c. 100	Thicker, less flexible films
	10 hr – 10 days	c. 1000	Rigid lumps and plates

Table 2.1. Young and old bifilms: comparison of formation time, thickness, and characteristics. Adapted from [163], summarising information from [144].

2.3.2. Gaseous nucleation

Bifilms easily nucleate secondary phases such as gas bubbles, intermetallics, and silicon precipitates. Gaseous nucleation causes porosity, which greatly reduces elongation, ductility,

and reliability of cast components [4]. Hydrogen bubble nucleation was originally believed to be the cause [145] due to rejection from the melt upon solidification (Figure 2.14), but classical nucleation theory shows heterogeneous and homogeneous hydrogen nucleation to be impossible [144] and that hydrogen can only contribute to a pre-existing bubble [40,145].

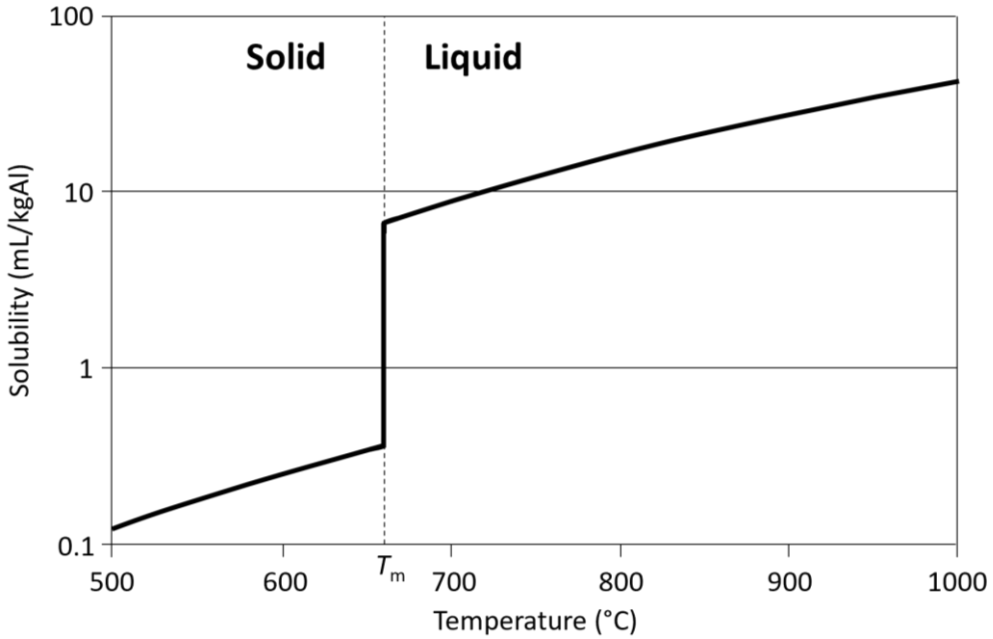


Figure 2.14. Hydrogen solubility in pure aluminium (mL of hydrogen per kg of aluminium) against temperature: there is a sharp discontinuity at the melting temperature T_m, leading to hydrogen rejection upon solidification. Plotting data from [164].

Tiryakioğlu outlines this well [146]: an aluminium melt supersaturated in hydrogen will reject excess dissolved hydrogen. According to classical nucleation theory [165], a spherical embryonic pore of radius r, surface tension σ, and pressure differential ΔP, will only grow once a critical radius r^* is reached (2.11). Applying given values of 1.03 Nm and -4 GPa for σ and ΔP respectively [146] results in a critical radius of 0.52 nm. Using the ideal gas law [166], this embryonic hydrogen bubble would contain 178 hydrogen atoms, N^* (2.12).

$$r^* = \left|\frac{2\sigma}{\Delta P}\right| = \frac{2 \times 1.03}{4 \times 10^9} \text{ m} = 0.52 \text{ nm} \tag{2.11}$$

$$N^* = \frac{P^* V^*}{k_B T_m} = \frac{4\pi P^* (r^*)^3}{3 k_B T_m} = \frac{4\pi(4 \times 10^9)(5.2 \times 10^{-10})^3}{3(1.38 \times 10^{-23})(933.5)} = 178 \tag{2.12}$$

r^* = critical pore radius ; σ = surface tension; ΔP = pressure difference between bubble and melt; N^* = number of hydrogen atoms in a bubble of radius r^*; P^* = pressure inside in a bubble of radius r^*; V^* = volume of a bubble of radius r^*; k_B = Boltzmann's constant; T_m = melting point of aluminium at atmospheric pressure.

However, this pore should immediately dissolve through an increase in the local hydrogen solubility. Using Sievert's law [167], the local hydrogen solubility of the melt $s_{\mathrm{H},P}$ due to the pore of pressure P_{Pore} and hydrogen partial pressure in equilibrium with the solution P_{H} would be around 200 times higher than the equilibrium solubility $s_{\mathrm{H,eq}}$, causing it to collapse immediately through diffusion of hydrogen from the bubble to the melt (2.13).

$$\frac{s_{\mathrm{H},P}}{s_{\mathrm{H,eq}}} = \sqrt{\frac{P_{\mathrm{Pore}}}{P_{\mathrm{H}}}} = \sqrt{\frac{4\ \mathrm{GPa}}{101.3\ \mathrm{kPa}}} = 199 \tag{2.13}$$

$s_{\mathrm{H},P}$ = local hydrogen solubility at surface of pore of pressure P_{Pore}; P_{H} = partial pressure of hydrogen in equilibrium with melt; $s_{\mathrm{H,eq}}$ = equilibrium hydrogen solubility.

Equivalently, the maximum pressure inside a hydrogen pore before its dissolution $P_{\mathrm{Pore,max}}$, calculated from the equilibrium hydrogen solubility of liquid ($s_{\mathrm{H,l}}$) and solid ($s_{\mathrm{H,s}}$) aluminium (2.14), is less than 1% of that needed for homogeneous nucleation (4 GPa [146]).

$$P_{\mathrm{Pore,max}} = P_{\mathrm{H}}\left(\frac{s_{\mathrm{H,l}}}{s_{\mathrm{H},s}}\right)^2 = 101.3\ \mathrm{kPa} \times 15.4^2 = 24\ \mathrm{MPa} \tag{2.14}$$

$P_{\mathrm{Pore,max}}$ = maximum pore pressure before immediate dissolution; $s_{\mathrm{H,l}}, s_{\mathrm{H,s}}$ = equilibrium hydrogen solubility at the melting point T_{m} in liquid and solid aluminium, respectively; P_{H} = partial pressure of hydrogen in equilibrium with melt.

Even if this were to be overcome, the vacancy concentration increase due to this pressure increase would be enough to dissolve the pore [168–171]. Therefore, homogeneous nucleation of hydrogen pores is impossible, in agreement with experimental results [172].

From this result, investigators generally concluded that heterogeneous nucleation occurred, which requires P_{Pore} to be c. 2 MPa for 2 μm oxide particles [172]. However, experiments have found P_{Pore} to be 0.1-0.3 MPa [173–175], an order of magnitude lower than required, showing heterogeneous nucleation to be impossible. Campbell also found this impossible, even at large wetting angles [144], so nucleation must have been bypassed.

Bifilms are a promising candidate [146,176], since they already contain gas inclusions; the formation of a gaseous pore therefore bypasses nucleation, allowing inward hydrogen diffusion

[40] and bifilm opening with only negligible force [144]. This is also evidenced by observations that: (i) pores occur even at low hydrogen supersaturations [177]; (ii) higher melt quality, with a lower bifilm concentration, increases the hydrogen concentration needed for pore formation [178]; and (iii) oxide films are commonly found on pore surfaces [179,180] (Figure 2.15).

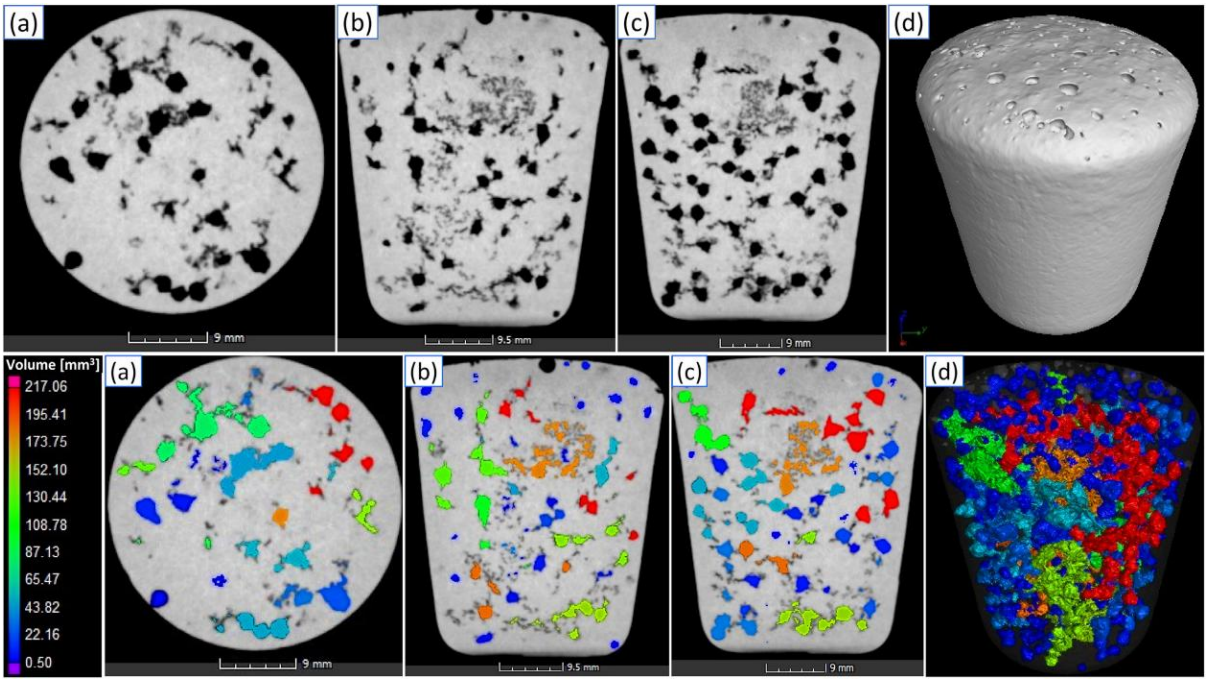


Figure 2.15. X-ray computed tomography (CT) sections of a reduced pressure test (RPT) sample showing location and volume of pores, suggesting the presence of bifilms given the complex shapes. Adapted from [179].

Furthermore, strontium-based additions, which reduce oxidation of Al-Mg melts significantly [71], increase porosity only in bad quality melts, indicating a link between porosity and oxide entrainment [180,181]. Also, hot tearing has been completely eliminated in some systems by filling design improvements which reduce entrainment and thus bifilm content [37,41]. However, the growth of hydrogen bubbles from entrained oxides has not yet been observed directly in aluminium melts, only through indirect means as detailed above.

2.3.3. Nucleation of secondary phases

Bifilms easily nucleate secondary phases such as intermetallics and silicon and in some systems they are the only observed substrate [39,40,43,46,182–185]. Whilst their observed cracking and decohesion in failed samples gives a brittle appearance, the weakening is extrinsic.

Experimental measurements and theoretical modelling have shown these secondary phases to be intrinsically strong: in silicon, strengths in bifilm-nucleated samples were found to be in 100s of MPa [151,152], but strengths orders of magnitude higher were found when measuring the silicon in isolation, such as molecular dynamics (MD) studies (8-28 GPa [148]) and in-situ micromechanical tests (up to 16 GPa, lowered to 2-15 GPa when near defects [150]).

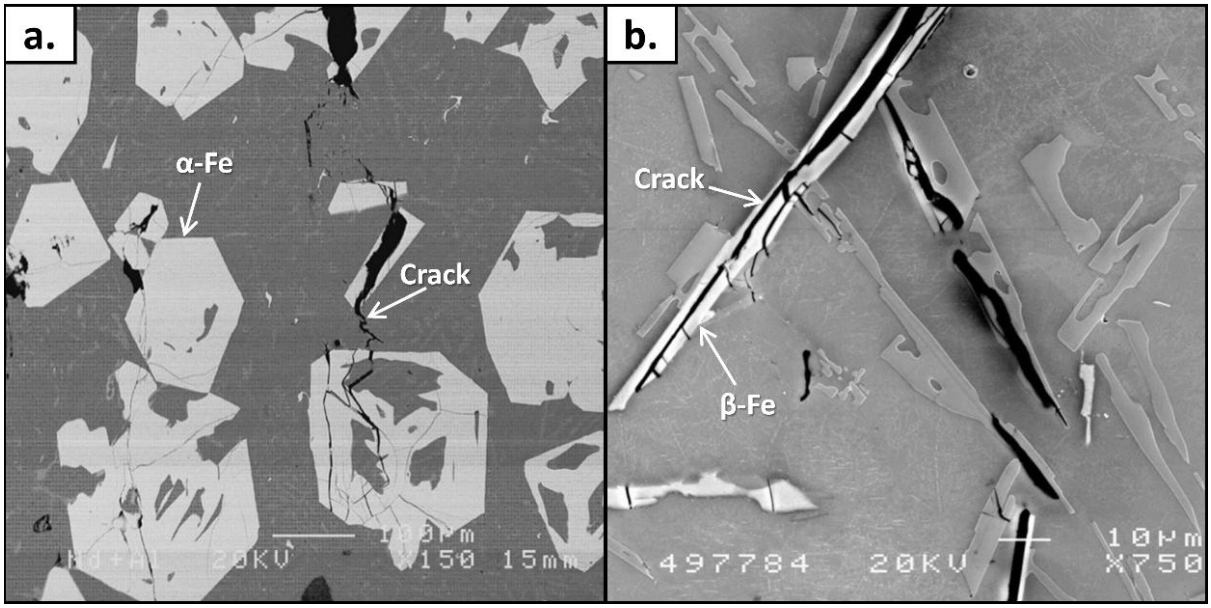


Figure 2.16. Cracked Fe-based intermetallics in an Al-Si alloy: (a) Cubic α-AlFeSi precipitates which wrap around compact bifilms; (b) Monoclinic β-AlFeSi precipitates, which grow on bifilms into platelets: cracks are nearly exclusively along the centre of the platelets giving a brittle appearance through the extrinsic weakening. Adapted from [9].

The same is true for interfaces: MD simulations have found even mismatched Al-Si interfaces to be orders of magnitude stronger (4-6 GPa [147]) than when measured experimentally (c. 240 MPa [149]). In intermetallics, cracks follow the path of pre-existing bifilms [9,43] and β-AlFeSi (Al_5FeSi) straightens bifilms during growth in the melt, resulting in large platelets (itself evidence for heterogeneous nucleation [43]).

2.3.4. Mechanical properties

Bifilms will never fully close regardless of thermomechanical treatment or working, due to inert argon within the air gap, resulting in deterioration of many mechanical properties such as strength, elongation, fatigue life, and reliability [9,41,186]. Sound metals should fail by plastic

flow and not crack under an applied stress [41], but aluminium alloys commonly show brittle failure [40]. The origin of Griffith cracks has been largely ignored, despite propagation being well-characterised [39].

Bifilms easily provide an explanation, given their morphology, behaviour, and ubiquity in metals [40,154,155]; one study found bifilms on every fracture surface, regardless of preparation [44]. Conversely, improvement in melt cleanliness can increase elongation (1-3% to 20%) and other mechanical properties [41]. Fatigue life can therefore also be improved [9], and whilst pores (and thus bifilms) were observed to initiate fatigue cracks in Al-7Si-0.4Mg [156], detection difficulties have delayed widespread recognition [40].

The chaotic nature of entrainment results in a large scatter in the mechanical properties of wrought and cast components, as bifilm populations from identically cast alloys can vary in size, morphology, and population [9]. Modifying turbulent to quiescent flow has improved Weibull moduli (i.e. reduced scatter [187]) both in elongation to failure and strength [157–159], decreased porosity [188], and reduced hydrogen content [44].

Creep may also be associated with bifilms, since the air gap provides an easy diffusion pathway [41]: improvements in nickel-based superalloys through directional solidification attributed to grain boundaries may be due to bifilms [37] [41] and counter-gravity pouring doubled creep life in magnesium alloys [161], but more research is needed to verify the connection. Surface-emergent bifilms may contribute to corrosion, as corrodants can easily travel through the air gap into the interior [9,40,46] (Figure 2.17.a). Bifilms commonly coincide with grain boundaries, often themselves cited as easy channels, but clean grain boundaries should mostly be in atomic contact and not permit corrodant penetration. Corrosion pits may indicate a surface-emergent bifilm [41] and galvanic cells may occur should intermetallics be present [46] (Figure 2.17.b). Stress corrosion cracking (SCC) [9] may be explained by bifilms, since stress corrosion cracks are often transverse cracks across inclusions (TiN, $M_{23}C_6$) in a

'beads on a string' morphology, indicative of bifilms [160]. The role of surface-emergent bifilms on melt or solid oxidation has not yet been speculated.

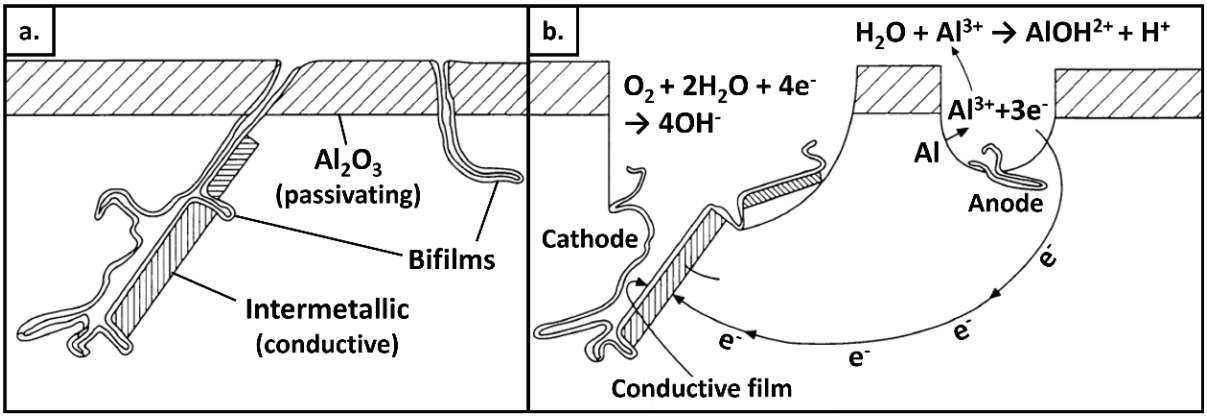


Figure 2.17. Schematic diagram of aqueous corrosion of an aluminium alloy, facilitated by bifilms: (a) Bifilms with and without intermetallics that intersect the surface; (b) Process of coupled corrosion: anode at surface-intersecting bifilm and cathode at intermetallic. Adapted from [9].

2.3.5. Observation

One reason for the recency of bifilm recognition is the difficulty of detection: whilst bifilm areas are large [145], thicknesses can be in nm and cannot be detected with even sensitive non-destructive testing (NDT) methods [40,46], such as filtration, ultrasonics, or Liquid Metal Cleanliness Analysis (LiMCA) [145]. However, even with suitable methods available they have been missed: SEM/EDX requires careful observation [90] and the liquid state has been historically neglected by metallurgists [40]. Furthermore, bifilms have not, to date, been observed in the liquid state; this lack of direct observation has proven to be a hindrance for full acceptance in the scientific community.

The Reduced Pressure Test (RPT) expands gaseous pores to an observable size by solidification under reduced pressure, often 0.1 atm (Figure 2.18) [145]. Originally a test for hydrogen content, Dispinar [176] found density (and thus porosity) to more strongly correlate with bifilm content than hydrogen content (Figure 2.18), indicating an association between bifilms and pores. However, old bifilms may remain unopened [90], RPT sample pouring may itself introduce artefactual defects [189], and bifilm content in low-hydrogen melts can be underestimated due to underinflation [179].

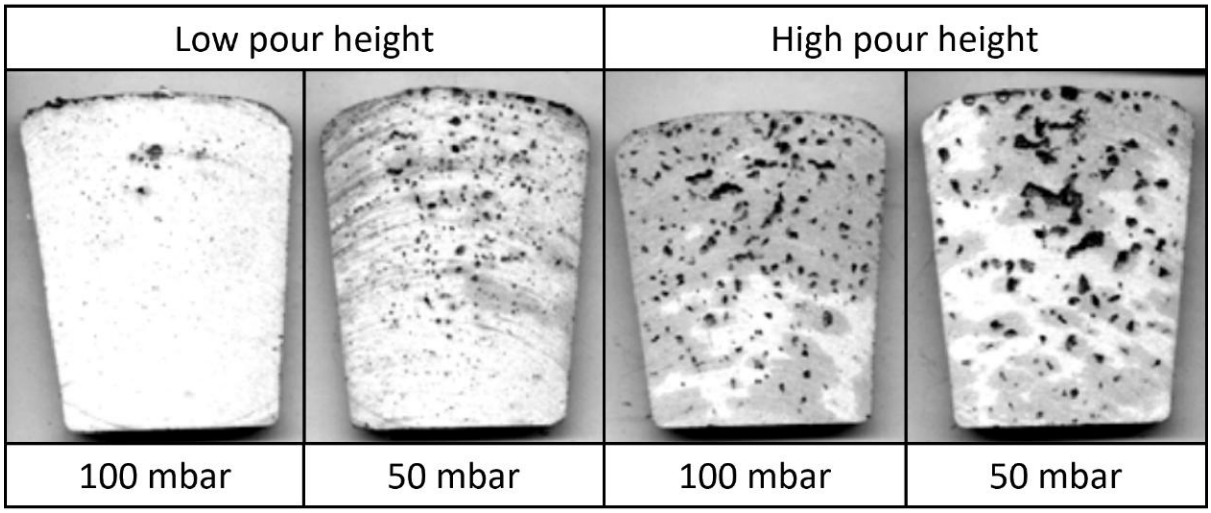


Figure 2.18. RPT samples poured from different heights to vary level of entrainment and solidified under different pressures to show enlargement of pores under reduced pressure. Pores are more visible with reduced pressure, and higher pour heights result in more pores due to more entrained defects. Adapted from [176].

X-ray computed tomography (CT) allows full 3D volume characterisation (Figure 2.15) and detection of pores (believed to be associated with bifilms) varying in shape, size, and volume [90,177,179,190], since X-rays can penetrate through metal samples. X-ray videography can also identify surface turbulence and model melt flow [159]. Tiryakioğlu [90] used X-ray CT to show that pore fraction and number increased with pouring velocity, and that below the critical pouring velocity for entrainment, there was little evidence for change in entrainment damage. However, no sample with a non-zero pouring velocity below this critical velocity was studied, so this final claim was not well-substantiated (Figure 2.19).

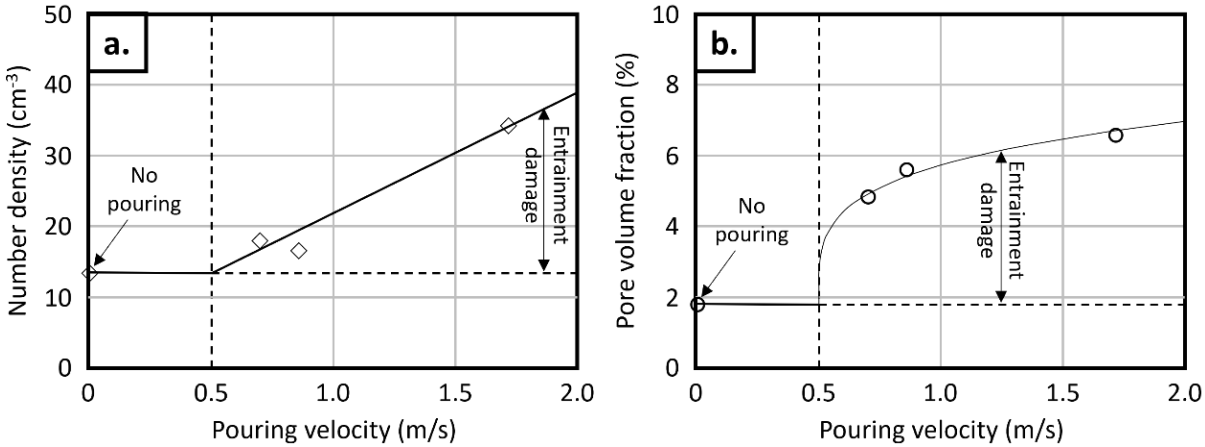


Figure 2.19. Pouring velocity vs (a) number density of pores and (b) pore volume fraction in A356 castings, showing entrainment damage to increase with pouring velocity. Adapted from [90].

2.3.6. Quantification

Since entrainment damage from bifilms depends on many factors, including morphology, size, concentration, oxide composition, and location [157–159], entrainment damage quantification and correlation against these parameters has proven difficult. Monitoring hydrogen content worked well initially [191], but Dispinar [192] showed that bifilms were more important (Figure 2.20). Researchers have therefore tried to quantify entrainment damage against bifilm metrics from RPT samples, such as pore size (length, area, volume) and number density [193], the most successful of which (Figure 2.21) is the bifilm index, the sum of the maximum pore lengths on a polished RPT sample surface [145,176].

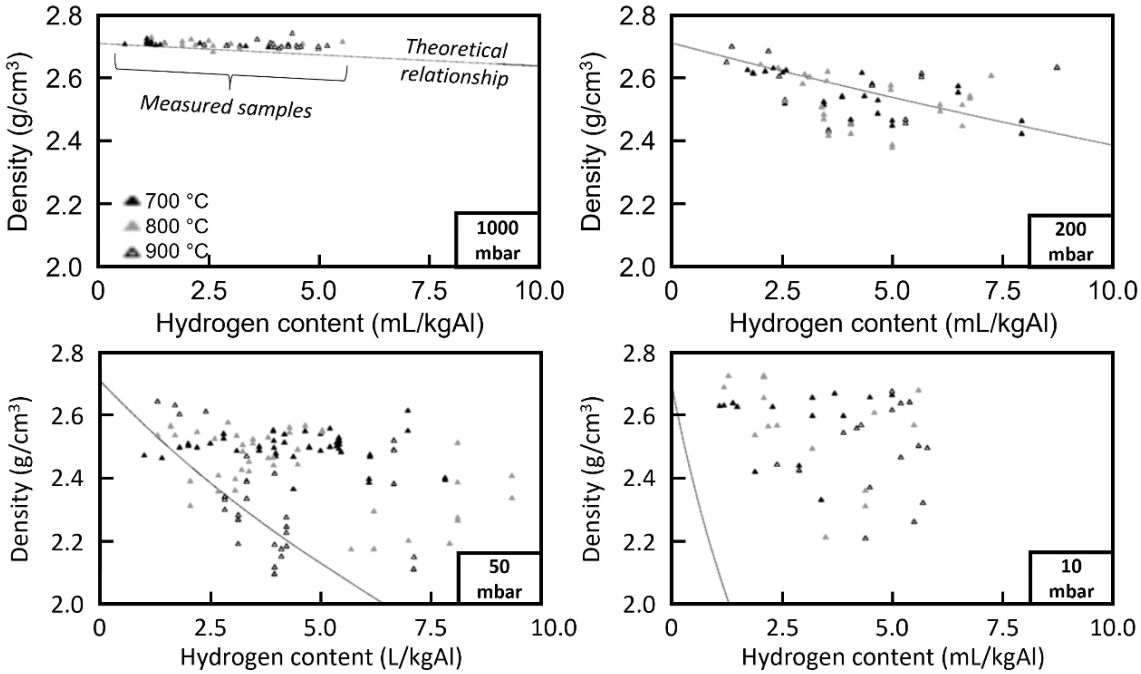


Figure 2.20. Hydrogen content vs density of LM-4 (Al-5Si-3Cu) RPT samples at various holding temperatures and solidification pressures. As solidification pressure decreases, the scatter increases, showing that hydrogen content does not correlate well with density. Adapted from [176].

The success results from the correlation between bifilm morphology and contribution to entrainment damage: less damaging old bifilms do not unfurl and expand under negative pressure but more damaging young bifilms do, and so have a greater maximum length [145]. Bifilm index also correlates well with hydrogen content on upgassing/degassing, pouring turbulence, ultimate tensile strength, and elongation to failure (Figure 2.22) [192,194].

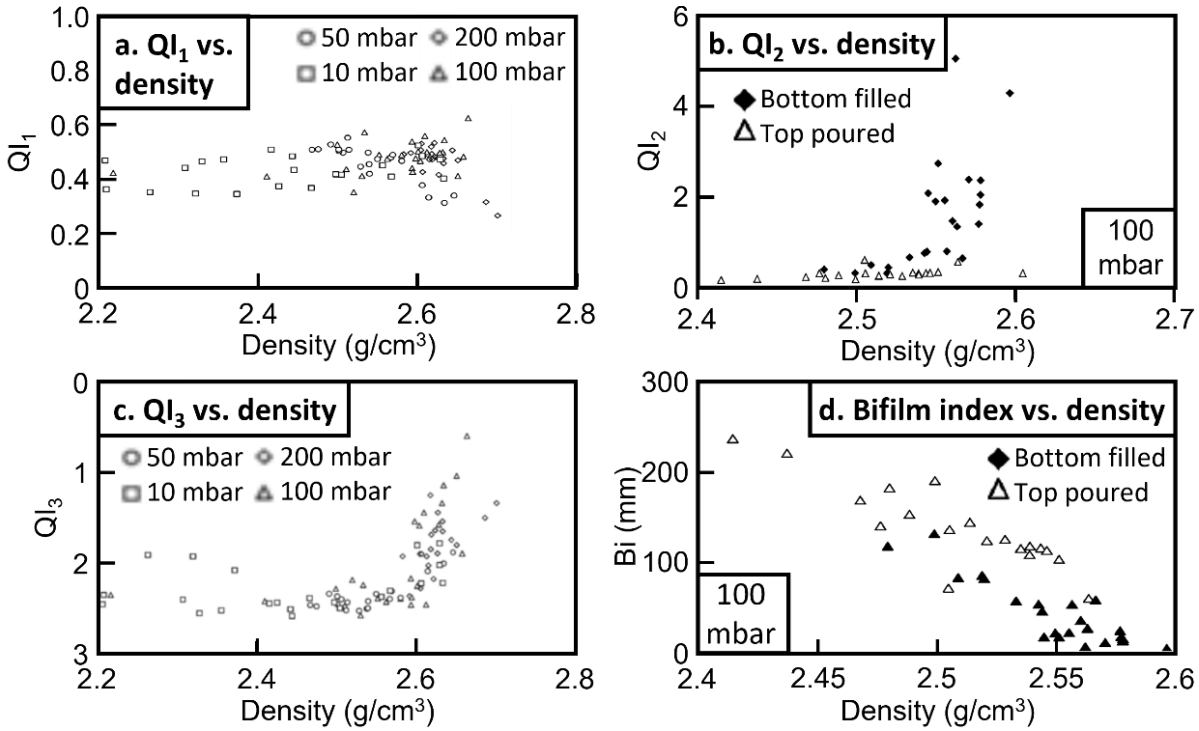


Figure 2.21. Evaluation of various quantitative bifilm metrics against sample density: (a) QI_1, pore roundness; (b) QI_2, a metric incorporating the length, shape, and number; (c) QI_3, the logarithm of the number of pores; (d) Bifilm index Bi. Each point is a different RPT sample and pressures indicated (a,c) are solidification pressures. Whilst scatter was present in each case, bifilm index showed the strongest correlation against density and so deemed the most useful metric of entrainment damage from RPT section metrics. Adapted from [145].

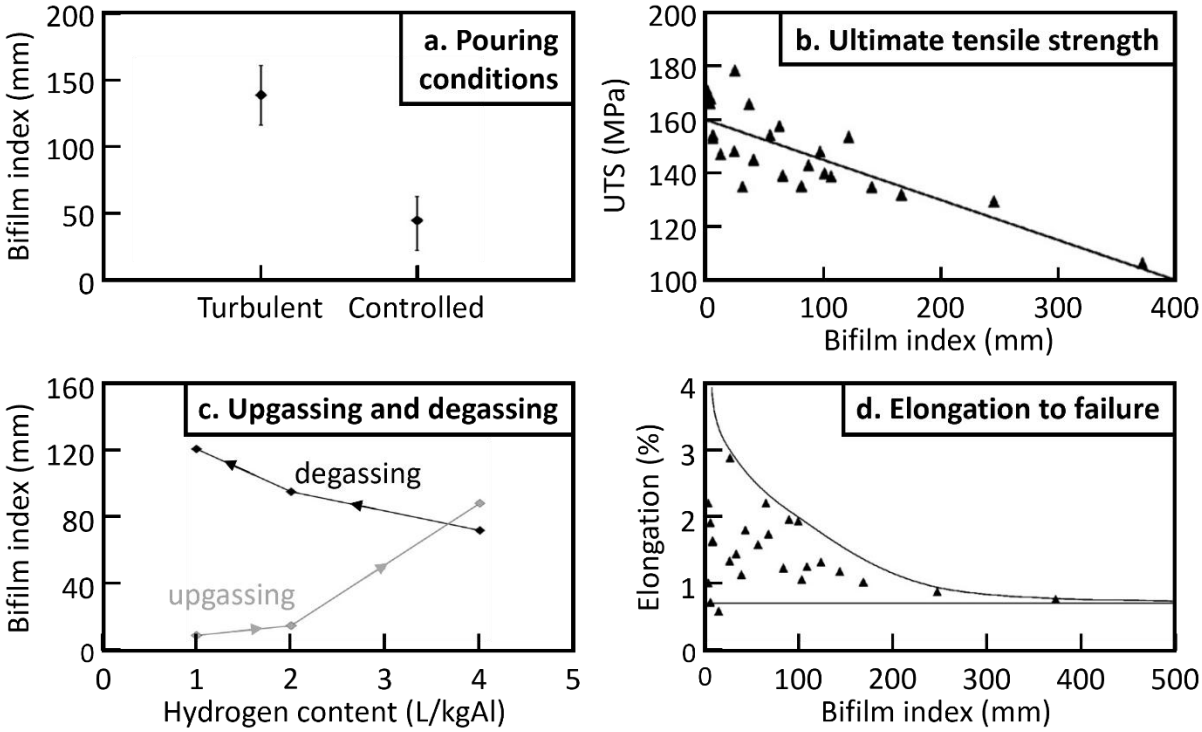


Figure 2.22. Correlation of bifilm index against: (a) Pouring conditions, showing that controlled pouring reduces bifilm content; (b) Ultimate tensile strength (UTS), which correlates negatively with bifilm index; (c) Hydrogen content with upgassing and degassing (although the hydrogen content appears to be in erroneous units, since ml/kgAl would give much more reasonable values), showing bifilm index to increase with both upgassing and degassing, and hydrogen content to not correlate well with bifilm index; (d) Elongation to failure, in which low bifilm indices show a greater scatter and higher average elongation. Adapted from [38].

2.3.7. Combating bifilms

Prevention, removal, or damage mitigation of bifilms can improve castings. Stopping entrainment is most effective and can be achieved with quiescent pouring: drop heights must not exceed 1 cm to avoid surface entrainment, so counter-gravity pouring and running design improvements [9,45] can reduce turbulence and improve castings [38,46,157,195]. Reduction of shearing stresses from electromagnetic stirring and centrifugal pumps can also reduce entrainment [41] but intensive melt shearing can break and disperse oxide films into high potency oxide inoculants, improving cast components [94]. Entrainment can also be prevented by directional solidification [9,41,195], and cutting samples to the exact shape of the crucible where possible (accounting for solidification contraction) [90].

Should entrainment occur, removal may mitigate damage. Filtering can reduce bifilm content [163,198] but pressurised melt filtration can increase it [94,145]. Holding melts can encourage bifilm flotation [181,196], but this is slow [40,41] and bifilms can unfurl and expand, worsening quality. Unfurling and flotation are therefore competing factors, such that scatter in strength and elongation varies with both holding time and alloy composition (Figure 2.23).

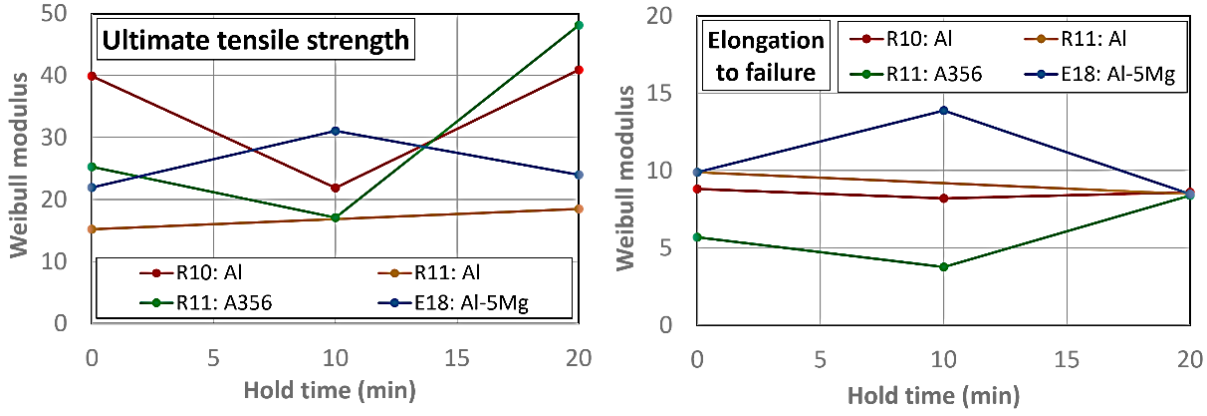


Figure 2.23. Effect of hold time (at 800 °C) on scatter in mechanical properties (Weibull moduli of UTS and elongation) of commercially pure aluminium (R10: [196], R11: [188]), Al-7Si-0.3Mg (R11: [188]), and Al-5Mg (E18: [197]). Holding for 20 minutes generally increases UTS Weibull moduli, but the competing factors of flotation, unfurling, and expansion give a range of results without clear correlation to hold time or composition.

Casting under inert atmospheres or vacuum does not help as it cannot prevent oxidation [9] and oxidising atmospheres can strengthen oxide films such that they entrain less easily than in inert

atmospheres [200]. Increasing atmospheric pressure immediately after casting can improve mechanical properties [201] and partial bonding across bifilms can mitigate damage [40]. Cracking in bifilms due to the γ-Al_2O_3 to α-Al_2O_3 transformation can allow melt to exude into the bifilm and react with oxygen and nitrogen to produce oxides and nitrides [186,197,199]. Direct observation of bifilm atmosphere consumption is difficult, but experiments on larger bubbles have proved insightful (Figure 2.24). Gas consumption rate is highly sensitive to composition and hydrogen content of the melt: oxygen is consumed first, followed by nitrogen. However, hydrogen steadily diffuses inwards, which is problematic as bifilm atmospheres must be mostly consumed before healing can occur [73,202,203].

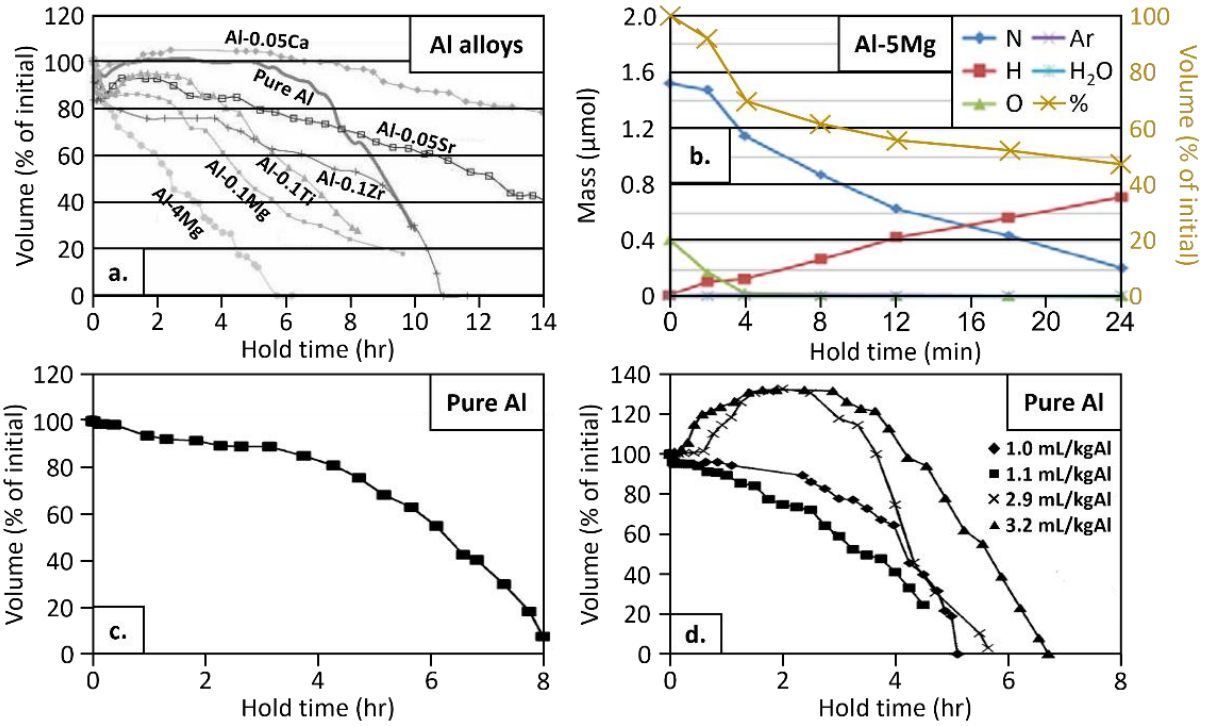


Figure 2.24. Atmospheric consumption of bubbles held in aluminium-based melts: (a) Gas consumption of air bubbles in aluminium alloys; (b) Composition and volume of air bubble held in Al-5Mg melt showing a general volume decrease caused by consumption of O_2 followed by N_2, and progressive inward hydrogen diffusion; (c) Volume of air bubble held in pure aluminium, with a gradient change at 80% volume indicating a change from oxygen consumption to nitrogen consumption; (d) Effect of melt hydrogen content on the volume of air bubble in pure aluminium. Adapted from [199] (a), [197] (b) and [186] (c, d).

The γ-Al_2O_3 to α-Al_2O_3 transformation can lead to oxide film bonding in pure Al melts (Figure 2.25), but with only negligible strength [202]. No oxide film bonding occurred in Al-4.5Mg, despite MgO formation [203], but bonding did occur in Al-7.3Si-0.3Mg [73] through

transformations from Al_2O_3 to $MgAl_2O_4$ to MgO (Figure 2.26). Therefore a reconstructive phase transformation between oxides, such as Al_2O_3 to $MgAl_2O_4$ and $MgAl_2O_4$ to MgO (Figure 2.26), is likely needed for bifilm healing, since they involve atomic rearrangement [40].

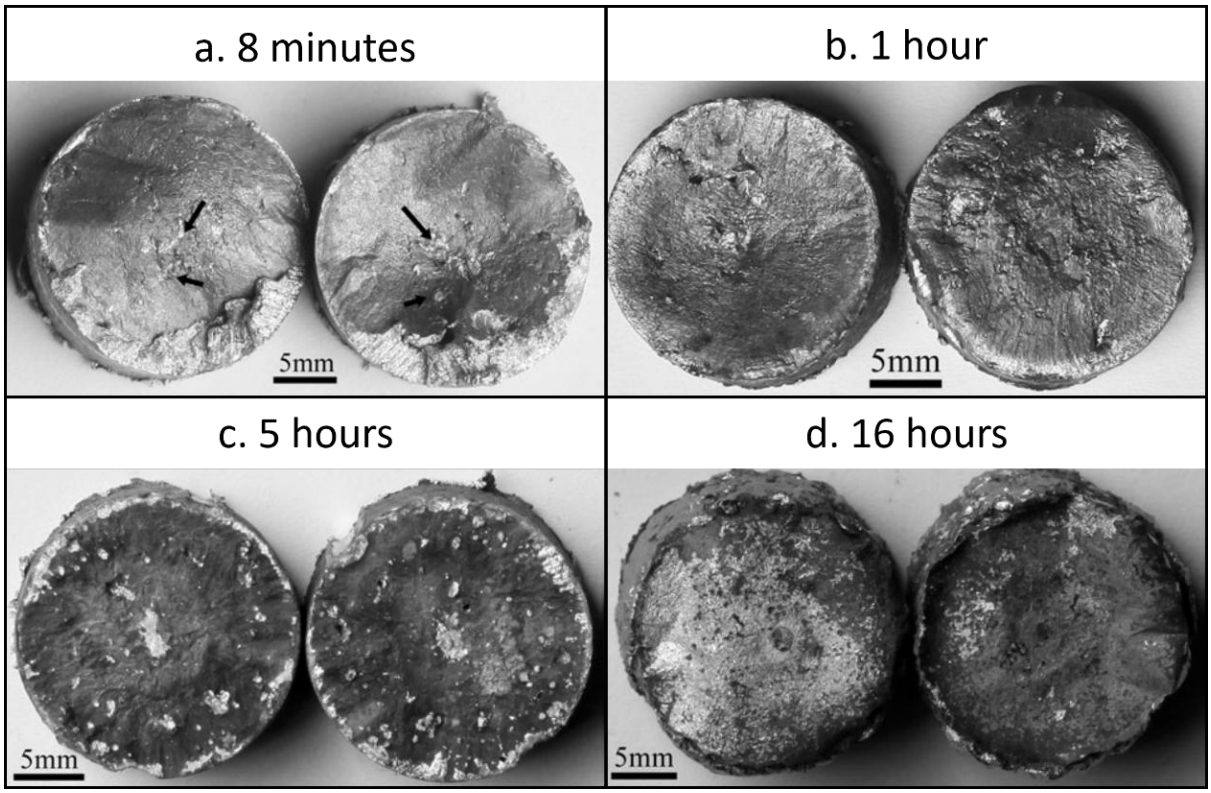


Figure 2.25. Fracture surfaces showing the development of bonding across a double alumina layer held in pure liquid aluminium. Bonding started after 5 hours and concluded after 13 hours, as shown by nodules indicating exudation and some bridging, but the force required to pull surfaces apart was negligible. Adapted from [202].

Hot isostatic pressing (HIP) can improve mechanical properties of solid components by placing them under high temperature and pressure and has vastly improved fatigue lives of Al-7.3Si-0.3Mg components. This improvement was also achieved through melt filtration before casting [204,205] and with HIP on Al-4.6Cu-0.35Mn-0.25Mg-0.2Ti in which bifilms were found at grain boundaries but not clean areas. Improvements have been limited to alloys with intermediate magnesium contents [46], consistent with the need for atomic rearrangements via a reconstructive phase transformation for the healing of bifilms.

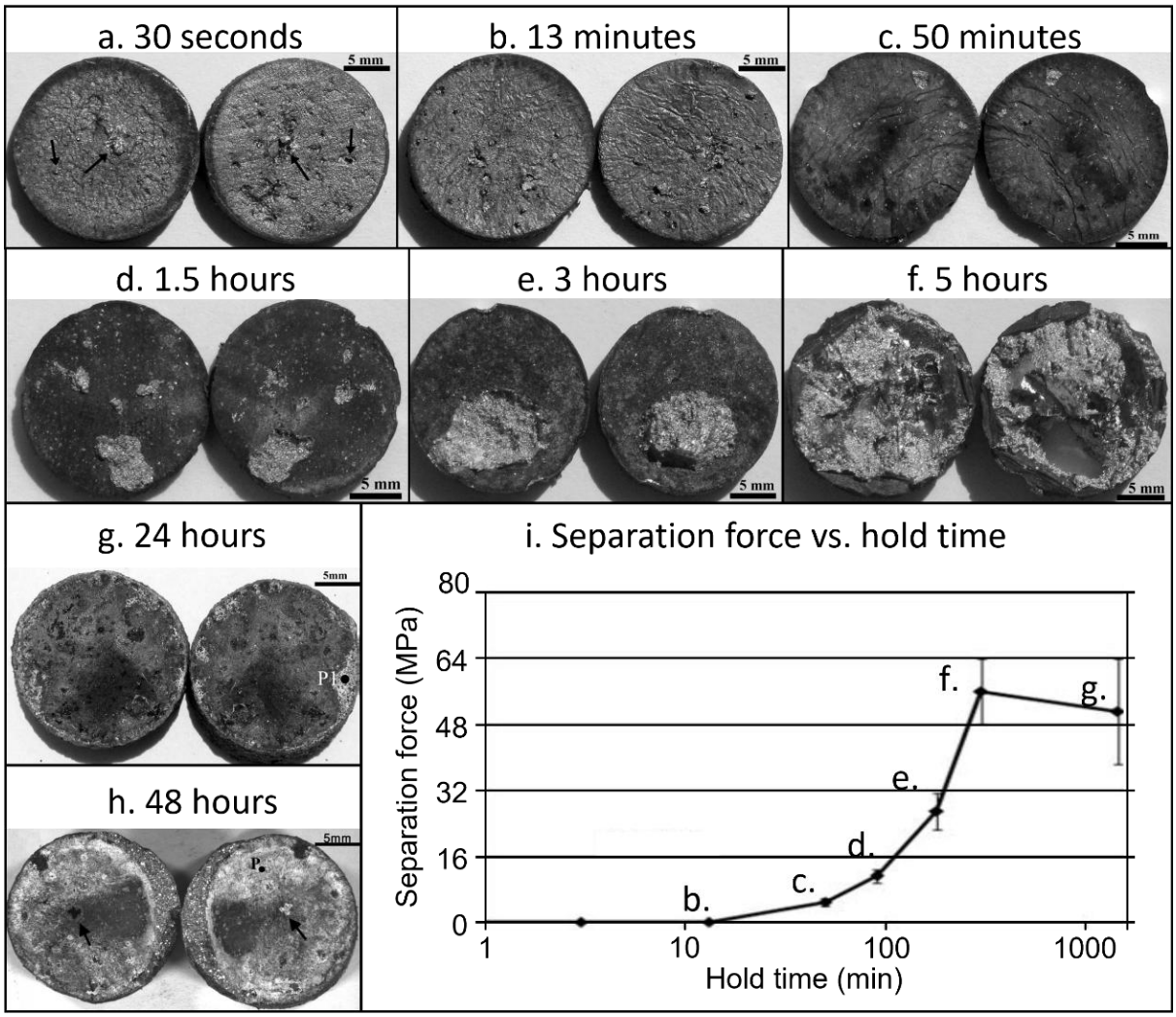


Figure 2.26. Double alumina film held in Al-7Si-0.3Mg melt: (a-h) Fracture surface appearance and (i) separation strength against hold time. Symmetrical bonding points appear at 30 seconds (a) indicating metal has exuded with limited bonding ($MgAl_2O_4$ was detected via XRD), and more bonding points appear over time (b). At around 50 minutes, MgO appears (with $MgAl_2O_4$, in c) and patches of MgO continue to grow after further holding (d-f), with a rapid rise in bond strength. At 24 hours (h), the transformation is complete, but gaps remain, indicating the existence of a residual atmosphere between the oxide layers. Adapted from [73].

2.3.8. Prospects

Eliminating bifilms could cause major improvements in engineering materials. Casting defects, intermetallic cracking, grain boundary decoherence, and premature failure by fatigue, fracture, and corrosion may be eliminated or vastly reduced [37,39,41]. Changes are simple and economic [9] and whilst improvements have already been made, bifilms are still ubiquitous, occurring from extraction to casting, so there is much to be done.

2.4. Thermodynamic optimisation

The oxidation of aluminium alloys is complicated by variations in processing, oxidation time, temperature, and atmospheric conditions, and even more so by the presence of three or more elements in commercial alloys [206] which each expand composition space exponentially. It is unfeasible to efficiently explore this space experimentally, so researchers have turned to theoretical methods, such as thermodynamic optimisation.

In thermodynamic optimisation, Gibbs free energy functions $G(T)$ of all phases in a multi-element system are evaluated through critical analysis of all relevant thermodynamic data, such that these $G(T)$ functions are self-consistent and consistent with experimental observations when back-calculated [207–209]. This should result in a small set of parameters which can efficiently model the entire system and allow calculation of phase diagrams [208,210], recognition of discrepancies [209], and determination of thermodynamic properties [209]. Binary systems are optimised first, before ternaries and higher-order systems [210]. However, thermodynamic data must be high-quality and the optimisation method carefully considered for accurate results, especially so for higher-order systems in which errors compound [211].

Thermodynamic optimisations of multicomponent oxide systems have been motivated for many areas, including metallurgical processing [207,210,212], steel deoxidisation [209,213], nuclear waste glasses [208], dental prosthetics [210], optoelectronics [214], electrodes [210], and fuel cells [208]. However, like Ellingham diagrams, thermodynamic optimisation only considers thermodynamics and neglects kinetics; discrepancies between predicted and observed experimental behaviour may therefore not just be from flawed modelling or inaccurate thermodynamic data, but also due to kinetic factors not considered [215].

2.4.1. Computation

Various powerful computational tools exist, including Thermo-Calc and FactSage [216], which can calculate material properties and phase diagrams for many common metallic and oxide

systems [217]. To model the thermodynamics of aluminium melts, data for the Gibbs free energy of each component as a function of temperature, $G(T)$, is acquired from these databases. The most common way to derive $G(T)$ values is through the 'third-law method' (2.15). This method uses thermodynamic relations between the heat capacity at constant pressure C_P, and variables H, S, and T (2.16)(2.17) [166], such that $G(T)$ can be evaluated using only C_P, T, and standard reference values $H°$ and $S°$ at a standard temperature $T°$ (2.18).

$$G(T) = H(T) - TS(T) \tag{2.15}$$

$$C_P = \left(\frac{\partial H}{\partial T}\right)_P \tag{2.16}$$

$$\left(\frac{\partial S}{\partial T}\right)_P = \frac{C_P}{T} \tag{2.17}$$

$$G(T) = H° + \int_{T°}^{T} C_P \, \mathrm{d}T - T\left(S° + \int_{T°}^{T} \frac{C_P}{T} \, \mathrm{d}T\right) \tag{2.18}$$

T = temperature; $G(T)$ = Gibbs free energy as a function of temperature T; $H(T)$ = enthalpy as a function of temperature T; $S(T)$ = entropy as a function of temperature T; C_P = heat capacity at constant pressure; $T°$ = standard temperature, $H°$ = enthalpy at standard temperature $T°$, $S°$ = entropy at standard temperature $T°$.

If C_P is independent of temperature, $G(T)$ then depends only on T and three experimental parameters (2.19) [100,215]; more polynomial terms can be added to increase accuracy and fidelity to measured values (2.20) [218].

$$G(T) = H° + C_P(T - T°) - T\left[S° + C_P \ln\left(\frac{T}{T°}\right)\right] = a + bT + cT\ln T \tag{2.19}$$

$$G(T) = a + bT + cT\ln T + dT^2 + eT^3 + fT^{-1} + \cdots \tag{2.20}$$

a, b, c, d, e, f = experimentally-determined parameters.

The standard Gibbs free energy change $\Delta G°(T)$, obtained from experiments or calculated through $G(T)$, has also been used in thermodynamic modelling [63]. Since $G(T)$ and $\Delta G°(T)$ only differ by standard reference states, the results are identical, so the choice is arbitrary.

2.4.2. Solution models

For solution phases, such as molten aluminium alloys, a mathematical description of the Gibbs free energy of mixing is required, since the components of the solution are not in their standard states [215]. The simplest model is ideal mixing, which assumes that the only thermodynamic change on mixing is a point configurational entropy change, or non-ideal, such as Bragg-Williams mixing or the modified quasichemical model [219], which include other terms. Mathematical details can be found in Chapter 5, where they are implemented in modelling aluminium alloy melt oxidation.

2.5. Conclusions

Research on liquid-state oxidation of aluminium and aluminium alloys is lacking and fragmented. Historically neglected due to perceived irrelevance, it is now recognised to be of utmost importance due to the discovery and recognition of bifilms and their effects on component quality.

The oxidation sequence of pure aluminium is well-established, but experimental results vary, and no single kinetic growth theory has been established despite numerous unsuccessful attempts. Many parameters complicate analysis, such as temperature, atmosphere, time, original microstructure, and melt quality. The presence of alloying elements complicate matters further: magnesium additions have been studied extensively since the effect is stark and whilst $MgAl_2O_4$ or MgO are known to form, observations are mixed, and no single rate law has gained full acceptance. In Al-Mg-X ternary systems, group II elements (beryllium, calcium, strontium) have been found to suppress oxidation, but other elements (cerium, gadolinium, silicon, lanthanum, zinc) do not. The reasons for this are not fully clear: with calcium, protection is attributed to a compact, mixed Ca-Mg oxide layer, and with beryllium and strontium, protection is attributed to the element forming a protective oxide layer itself. However, attempts to determine the morphology and composition of these protective layers have been flawed and

the mechanisms remain unconfirmed.

The growth of thermodynamic optimisation into multicomponent oxide systems has also allowed high-throughput screening, reducing experiments needed and giving further opportunity for the understanding of oxidation. Several models have been used for modelling complex, mixed phases to varying degrees of success.

Research into bifilms is sorely needed, given current claims of their effects, strong evidence of their ubiquity in engineering materials and inextricable association to almost all flaws in aluminium components. Their existence is widely acknowledged, thanks to careful observation and the development of modern techniques such as X-ray CT and RPT testing, but a lack of direct observation has proven to be the final roadblock to their acceptance. Strong evidence already exists for bifilms causing casting defects such as hot tearing and deterioration of mechanical properties, and bifilms easily explain other phenomena, such as corrosion and creep. Furthermore, bifilms provide the only current, scientifically sound explanations for brittle failure in metals, brittle intermetallics, and hydrogen porosity, which are all theoretically impossible in clean, inclusion-free metals.

Removal and prevention of entrained oxides are difficult, but, through increased understanding of bifilm behaviour, mitigation techniques have been developed, and entrainment damage has been reduced. Through full recognition and adoption of these practices throughout science and industry, miraculous improvements are predicted in aluminium alloys. However, this will be hindered unless the melt oxidation of aluminium and its alloys, the origin of bifilms, is properly understood, and direct, in-situ evidence of entrained oxides in aluminium melts is published.

2.6. References

[1] A.A. Yaroshevsky, Abundances of chemical elements in the Earth's crust, Geochem. Int. 44 (2006) 48–55.

[2] Mineral commodity summaries 2021, U.S. Geological Survey, Reston, VA, 2021. https://doi.org/10.3133/mcs2021.

[3] J.R. Davis, Introduction: key characteristics of aluminum, in: Corrosion of Aluminum and Aluminum Alloys, ASM International, Materials Park, OH, USA, 1999: p. 1.

[4] R. Lumley, Fundamentals of aluminium metallurgy, Woodhead Publishing Ltd., Cambridge, UK, 2011.

[5] A.K. Vasudevan, R.D. Doherty, Aluminium alloys - contemporary research and applications, Elsevier, 2012.

[6] W.S. Tait, 28 - Corrosion prevention and control of chemical processing equipment, in: M. Kutz (Ed.), Handbook of Environmental Degradation of Materials, 2nd ed., William Andrew Publishing, Oxford, 2012: pp. 863–886. https://doi.org/10.1016/B978-1-4377-3455-3.00028-6.

[7] J. Taylor, The dark side of light metals: dealing with oxidation and dross, in: Faculty of Engineering and Industrial Sciences, Swinburne University of Technology, Swinburne University of Technology, Melbourne, Australia, 2011: pp. 34–36.

[8] B. Fateh, G.A. Brooks, M.A. Rhamdhani, J.A. Taylor, J. Davis, M. Lowe, Study of early stage interaction of oxygen with Al; methods, challenges and difficulties, in: S.J. Lindsay (Ed.), Light Metals 2011, Springer International Publishing, San Diego, California, USA, 2016: pp. 725–730. https://doi.org/10.1007/978-3-319-48160-9_126.

[9] J. Campbell, The consolidation of metals: the origin of bifilms, J. Mater. Sci. 51 (2016) 96–106. https://doi.org/10.1007/s10853-015-9399-9.

[10] S. Uda, 4 - Stoichiometry of Oxide Crystals, in: T. Nishinaga (Ed.), Handbook of Crystal Growth, 2nd ed., Elsevier, Boston, 2015: pp. 175–214. https://doi.org/10.1016/B978-0-444-56369-9.00004-6.

[11] T.B. Reed, Free energy of formation of binary compounds: an atlas of charts for high-temperature chemical calculations, Biomass Energy Foundation Press, 2000.

[12] M. Groner, J. Elam, F.H. Fabreguette, S.M. George, Electrical characterization of thin Al2O3 films grown by atomic layer deposition on silicon and various metal substrates, Thin Solid Films 413 (2002) 186–197. https://doi.org/10.1016/S0040-6090(02)00438-8.

[13] S. Souza, S.P. Toledo, Standard transition aluminas. electron microscopy studies, Mater. Res. 3 (2000). https://doi.org/10.1590/S1516-14392000000400003.

[14] B. Pieraggi, 1.06.5.4.4. α-Alumina (α-Al2O3), in: Shreir's Corrosion, 4th ed., Elsevier, Amsterdam; London, 2010: pp. 129–130.

[15] M.P. Martínez-Viademonte, S.T. Abrahami, T. Hack, M. Burchardt, H. Terryn, A review on anodizing of aerospace aluminum alloys for corrosion protection, Coatings 10 (2020) 1106. https://doi.org/10.3390/coatings10111106.

[16] L.E. Fratila-Apachitei, F.D. Tichelaar, G.E. Thompson, H. Terryn, P. Skeldon, J. Duszczyk, L. Katgerman, A transmission electron microscopy study of hard anodic oxide layers on AlSi(Cu) alloys, Electrochim. Acta 49 (2004) 3169–3177. https://doi.org/10.1016/j.electacta.2004.02.030.

[17] Y. Ma, X. Zhou, G.E. Thompson, M. Curioni, P. Skeldon, X. Zhang, Z. Sun, C. Luo, Z. Tang, F. Lu, Anodic film growth on Al–Li–Cu alloy AA2099-T8, Electrochim. Acta 80 (2012) 148–159. https://doi.org/10.1016/j.electacta.2012.06.126.

[18] S. Theohari, C. Kontogeorgou, Effect of temperature on the anodizing process of aluminum alloy AA 5052, Appl Surf Sci 284 (2013) 611–618. https://doi.org/10.1016/j.apsusc.2013.07.141.

[19] H. Habazaki, K. Shimizu, P. Skeldon, G.E. Thompson, G.C. Wood, X. Zhou, Effects of alloying elements in anodizing of aluminium, Trans IMF 75 (1997) 18–23. https://doi.org/10.1080/00202967.1997.11871137.

[20] Y.-J. Oh, J.-I. Mun, J.-H. Kim, Effects of alloying elements on microstructure and protective properties of Al2O3 coatings formed on aluminum alloy substrates by plasma electrolysis, Surf Coat Technol 204 (2009) 141–148. https://doi.org/10.1016/j.surfcoat.2009.07.002.

[21] J. He, Q.Z. Cai, H.H. Luo, L. Yu, B.K. Wei, Influence of silicon on growth process of plasma electrolytic oxidation coating on Al–Si alloy, J Alloys Compd 471 (2009) 395–399. https://doi.org/10.1016/j.jallcom.2008.03.114.

[22] F. Xu, Y. Xia, G. Li, The mechanism of PEO process on Al–Si alloys with the bulk primary silicon, Appl Surf Sci 255 (2009) 9531–9538. https://doi.org/10.1016/j.apsusc.2009.07.090.

[23] D. Tejero-Martin, M. Rezvani Rad, A. McDonald, T. Hussain, Beyond traditional coatings: a review on thermal-sprayed functional and smart coatings, J Therm Spray Tech 28 (2019) 598–644. https://doi.org/10.1007/s11666-019-00857-1.

[24] H.S. Park, D.K. Kim, Effect of silica surface dopants on the formation of alumina/aluminum composites by the directed metal oxidation of an aluminum alloy, J Am Ceram Soc 84 (2004) 2526–2530. https://doi.org/10.1111/j.1151-2916.2001.tb01047.x.

[25] J. Zhao, H. Chai, F. Zhang, Formation of Al2O3/Al composites by directed melt oxidation of Al-Si-Zn alloy, J Mater Eng Perform 19 (2010) 46–51. https://doi.org/10.1007/s11665-009-9412-z.

[26] M. Hanabe, V. Jayaram, T.A. Bhaskaran, Growth of Al2O3Al composites from Al-Zn alloys, Acta Mater 44 (1996) 819–829. https://doi.org/10.1016/1359-6454(95)00185-9.

[27] H. Venugopalan, K. Tankala, T. DebRoy, Kinetics of directed oxidation of Al-Mg alloys in the initial and final stages of synthesis of Al2O3/Al composites, Mater Sci Eng A 210 (1996) 64–75. https://doi.org/10.1016/0921-5093(95)10072-5.

[28] V.S.R. Murthy, B.S. Rao, Microstructural development in the directed melt-oxidized (DIMOX) Al-Mg-Si alloys, J Mater Sci 30 (1995) 3091–3097. https://doi.org/10.1007/BF01209222.

[29] A.S. Nagelberg, Observations on the role of Mg and Si in the directed oxidation of Al–Mg–Si alloys, J Mater Sci 7 (1992) 265–268. https://doi.org/10.1557/JMR.1992.0265.

[30] L. Yang, D. Zhu, C. Xu, J. Zhang, J. Zhang, On the role of magnesium and silicon in the formation of alumina from aluminum alloys by means of DIMOX processing, Metall Mater Trans A 27 (1996) 2094–2099. https://doi.org/10.1007/BF02651863.

[31] K. Shimizu, G.M. Brown, K. Kobayashi, P. Skeldon, G.E. Thompson, G.C. Wood, The early stages of high temperature oxidation of an Al-0.5wt.% Mg alloy, Corros Sci 40 (1998) 557–575. https://doi.org/10.1016/S0010-938X(97)00153-4.

[32] X. Gu, R.J. Hand, The production of reinforced aluminium/alumina bodies by directed metal oxidation, J Eur Ceram Soc 15 (1995) 823–831. https://doi.org/10.1016/0955-2219(95)00054-X.

[33] V. Jayaram, The role of volatile solute elements in directed melt oxidation of aluminium alloys, J Mater Sci 31 (1996) 4591–4598. https://doi.org/10.1007/BF00366356.

[34] X. Gu, R.J. Hand, The use of lithium as a dopant in the directed melt oxidation of aluminium, J Eur Ceram Soc 16 (1996) 929–935. https://doi.org/10.1016/0955-2219(96)00019-2.

[35] W.C. Sleppy, Oxidation of molten high-purity aluminum in dry oxygen, Journal of the Electrochemical Society 108 (1961) 1097–1102. https://doi.org/10.1149/1.2427963.

[36] J.A. Taylor, M. Prakash, G.G. Pereira, P. Rohan, M. Lee, B. Rinderer, Predicting dross formation in aluminium melt transfer operations, Materials Science Forum 630 (2010) 37–44. https://doi.org/10.4028/www.scientific.net/MSF.630.37.

[37] J. Campbell, Films and bifilms - an update, in: Supplemental Proceedings: Volume 2: Materials Properties, Characterization, and Modeling, Wiley, Orlando, FL, USA, 2012: pp. 161–168.

[38] D. Dispinar, J. Campbell, Porosity, hydrogen and bifilm content in Al alloy castings, Mater Sci Eng A 528 (2011) 3860–3865. https://doi.org/10.1016/j.msea.2011.01.084.

[39] J. Campbell, The origin of Griffith cracks, Metall Mater Trans B 42 (2011) 1091–1097. https://doi.org/10.1007/s11663-011-9575-5.

[40] J. Campbell, Entrainment defects, Mater Sci Technol 22 (2006) 127–145. https://doi.org/10.1179/174328406X74248.

[41] J. Campbell, Update on bifilms—the fundamental defect in metals, in: M. Tiryakioğlu, W. Griffiths, M. Jolly (Eds.), Shape Casting, Springer International Publishing, San Antonio, Texas, USA, 2019: pp. 3–15. https://doi.org/10.1007/978-3-030-06034-3_1.

[42] M.A. El-Sayed, Double oxide film defects and the properties of aluminum castings. A review, Global J Mater Sci Eng 1 (2019) 5–12. https://doi.org/10.37516/global.j.mater.sci.eng.2019.0053.

[43] M. Tiryakioğlu, On the intrinsic and extrinsic microstructure-property effects in cast aluminum alloys, in: Shape Casting, Springer International Publishing, San Antonio, Texas, USA, 2019: pp. 293–302. https://doi.org/10.1007/978-3-030-06034-3_28.

[44] M.A. El-Sayed, W.D. Griffiths, Hydrogen, bifilms and mechanical properties of Al castings, Int J Cast Met Res 27 (2014) 282–287. https://doi.org/10.1179/1743133614Y.0000000113.

[45] Colin.D. Ridgeway, K. Ripplinger, D. Detwiler, A.A. Luo, A new model for predicting oxide-related defects in aluminum castings, Metall Mater Trans B 51 (2020) 1989–2002. https://doi.org/10.1007/s11663-020-01918-5.

[46] R. Gopalan, N.K. Prabhu, Oxide bifilms in aluminium alloy castings – a review, Mater Sci Technol 27 (2011) 1757–1769. https://doi.org/10.1179/1743284711Y.0000000033.

[47] N. Birks, G.H. Meier, F.S. Pettit, Introduction to the high temperature oxidation of metals, Cambridge University Press, 2006.

[48] R.K. Rajput, Second law of thermodynamics and entropy, in: Engineering Thermodynamics, 3rd ed., Laxmi Publications, Boston, USA, 2007: pp. 227–305.

[49] D.W. Rogers, The Gibbs free energy, in: Concise Physical Chemistry, John Wiley & Sons, Ltd, 2010: pp. 84–92. https://doi.org/10.1002/9780470906347.ch6.

[50] D.W. Oxtoby, H.P. Gillis, L.J. Butler, 13. Spontaneous rrocesses and thermodynamic equilibrium, in: Principles of Modern Chemistry, 8th ed., Cengage Learning, Boston, MA, USA, 2016.

[51] K.G. Denbigh, The principles of chemical equilibrium: with applications in chemistry and chemical engineering, 4th ed., Cambridge University Press, Cambridge, 1981. https://doi.org/10.1017/CBO9781139167604.

[52] V. Gold, ed., The IUPAC compendium of chemical terminology: the gold book, 4th ed., International Union of Pure and Applied Chemistry (IUPAC), Research Triangle Park, NC, 2019. https://doi.org/10.1351/goldbook.

[53] H.J.T. Ellingham, Reducibility of oxides and sulphides in metallurgical processes, Journal of the Society of Chemical Industry 63 (1944) 125–133. https://doi.org/10.1002/jctb.5000630501.

[54] P. Stratton, Ellingham diagrams – their use and misuse, International Heat Treatment and Surface Engineering 7 (2013) 70–73. https://doi.org/10.1179/1749514813Z.00000000053.

[55] DerSilberspiegel, English: The Ellingham diagram is giving the free energy of formation of metal oxides and the corresponding oxygen partial pressure at equilibrium. Labels in English., 2016. https://commons.wikimedia.org/wiki/File:Ellingham_Richardson-diagram_english.svg (accessed February 7, 2025).

[56] M. Soustelle, Chemical reaction and kinetic quantities, in: An Introduction to Chemical Kinetics, John Wiley & Sons, Ltd, 2011: pp. 1–23. https://doi.org/10.1002/9781118604243.ch1.

[57] H.E. Evans, A.T. Donaldson, T.C. Gilmour, Mechanisms of breakaway oxidation and application to a chromia-forming steel, Oxidation of Metals 52 (1999) 379–402. https://doi.org/10.1023/A:1018855914737.

[58] R. Bottom, Thermogravimetric analysis, in: Principles and Applications of Thermal Analysis, John Wiley & Sons, Ltd, 2008: pp. 87–118. https://doi.org/10.1002/9780470697702.ch3.

[59] O. Kubaschewski, B.E. Hopkins, Oxidation of metals and alloys, Butterworths Scientific Publications, London, UK, 1953.

[60] K. Patouillet, L. Davoust, O. Doche, Deal–Grove model revisited for a new insight into the oxidation of molten aluminum alloy: The A356 alloy, as a model system, AIChE 67 (2021) e17230. https://doi.org/10.1002/aic.17230.

[61] D.W. Aylmore, S.J. Gregg, W.B. Jepson, The oxidation of aluminium in dry oxygen in the temperature range 400-650 °C, J Inst Metals 88 (1960) 205–208.

[62] Y. Xu, L.P.H. Jeurgens, Y. Huang, C. Li, Y. Liu, Z. Wang, Effect of structural order on oxidation kinetics and oxide phase evolution of Al–Zr alloys, Corros Sci 165 (2020) 108407. https://doi.org/10.1016/j.corsci.2019.108407.

[63] G. Wu, K. Dash, M.L. Galano, K.A.Q. O'Reilly, Oxidation studies of Al alloys: Part II Al-Mg alloy, Corros Sci 155 (2019) 97–108. https://doi.org/10.1016/j.corsci.2019.04.018.

[64] F.P. Fehlner, N.F. Mott, Low-temperature oxidation, Oxid Met 2 (1970) 59–99. https://doi.org/10.1007/BF00603582.

[65] N. Cabrera, N.F. Mott, Theory of the oxidation of metals, Rep. Prog. Phys. 12 (1949) 163–184. https://doi.org/10.1088/0034-4885/12/1/308.

[66] C. Wagner, K. Grünewald, Beitrag zur Theorie des Anlauf Vorganges. III, Zeitschrift für Physikalische Chemie 40B (1938) 455–475. https://doi.org/10.1515/zpch-1938-4036.

[67] J. Stringer, Stress generation and relief in growing oxide films, Corrosion Science 10 (1970) 513–543. https://doi.org/10.1016/S0010-938X(70)80036-1.

[68] N.B. Pilling, R.E. Bedworth, The oxidation of metals at high temperatures, J Inst Metals 29 (1923) 529–591.

[69] S.A. Impey, D.J. Stephenson, J.R. Nicholls, Mechanism of scale growth on liquid aluminium, Mater Sci Technol 4 (1988) 1126–1132. https://doi.org/10.1179/mst.1988.4.12.1126.

[70] A.S. Ulrich, U. Glatzel, M.C. Galetz, Discontinuities in oxidation kinetics: a new model and its application to Cr–Si-base alloys, Oxid Met 95 (2021) 445–465. https://doi.org/10.1007/s11085-021-10029-8.

[71] O. Ozdemir, J.E. Gruzleski, R.A.L. Drew, Effect of low-levels of strontium on the oxidation behavior of selected molten aluminum–magnesium alloys, Oxid Met 72 (2009) 241–257. https://doi.org/10.1007/s11085-009-9158-x.

[72] S. Becker, A. Rahmel, M. Schorr, M. Schütze, Mechanism of isothermal oxidation of the intel-metallic TiAl and of TiAl alloys, Oxid Met 38 (1992) 425–464. https://doi.org/10.1007/BF00665663.

[73] M. Aryafar, R. Raiszadeh, A. Shalbafzadeh, Healing of double oxide film defects in A356 aluminium melt, J Mater Sci 45 (2010) 3041–3051. https://doi.org/10.1007/s10853-010-4308-8.

[74] H. Hindam, D.P. Whittle, Microstructure, adhesion and growth kinetics of protective scales on metals and alloys, Oxid Met 18 (1982) 245–284. https://doi.org/10.1007/BF00656571.

[75] R. Prins, On the structure of γ-Al2O3, Journal of Catalysis 392 (2020) 336–346. https://doi.org/10.1016/j.jcat.2020.10.010.

[76] M.W. Chase, NIST-JANAF thermochemical tables, 4th ed., American Chemical Society, Washington, DC, USA, 1998.

[77] K.-H. Kim, Formation of fine clusters in high-temperature oxidation of molten aluminum, Metall Mater Trans A 45 (2014) 3650–3660. https://doi.org/10.1007/s11661-014-2270-9.

[78] E. Bergsmark, C.J. Simensen, P. Kofstad, The oxidation of molten aluminum, Mater Sci Eng A 120–121 (1989) 91–95. https://doi.org/10.1016/0921-5093(89)90723-5.

[79] L.P.H. Jeurgens, W.G. Sloof, F.D. Tichelaar, E.J. Mittemeijer, Structure and morphology of aluminium-oxide films formed by thermal oxidation of aluminium, Thin Solid Films 418 (2002) 89–101. https://doi.org/10.1016/S0040-6090(02)00787-3.

[80] M.J. Pryor, The defect structure of thin oxide films on aluminum, Oxid Met 3 (1971) 523–527. https://doi.org/10.1007/BF00604998.

[81] F. Reichel, L.P.H. Jeurgens, E.J. Mittemeijer, The role of the initial oxide-film microstructure on the passivation behavior of Al metal surfaces, Surface and Interface Analysis 40 (2008) 281–284. https://doi.org/10.1002/sia.2705.

[82] F. Reichel, L.P.H. Jeurgens, E.J. Mittemeijer, The thermodynamic stability of amorphous oxide overgrowths on metals, Acta Materialia 56 (2008) 659–674. https://doi.org/10.1016/j.actamat.2007.10.023.

[83] L.P.H. Jeurgens, On the initial oxidation of aluminium in oxygen gas, PhD, Delft University of Technology, 2001.

[84] L.P.H. Jeurgens, W.G. Sloof, F.D. Tichelaar, E.J. Mittemeijer, Thermodynamic stability of amorphous oxide films on metals: Application to aluminum oxide films on aluminum substrates, Phys. Rev. B 62 (2000) 4707–4719. https://doi.org/10.1103/PhysRevB.62.4707.

[85] M.J. Dignam, W.R. Fawcett, H. Böhni, The kinetics and mechanism of oxidation of superpurity aluminum in dry oxygen, J Electrochem Soc (1966) 663–671.

[86] J.I. Eldridge, R.J. Hussey, D.F. Mitchell, M.J. Graham, Thermal oxidation of single-crystal aluminum at 550°C, Oxid Met 30 (1988) 301–328. https://doi.org/10.1007/BF00659003.

[87] W.W. Smeltzer, R.R. Haering, J.S. Kirkaldy, Oxidation of metals by short circuit and lattice diffusion of oxygen, Acta Metallurgica 9 (1961) 880–885. https://doi.org/10.1016/0001-6160(61)90192-4.

[88] F. Jin, Q. Luo, B. Zhou, Q. Li, Modeling investigation of the oxidation kinetics of copper and aluminum alloys, Adv Mater Res 402 (2012) 17–21. https://doi.org/10.4028/www.scientific.net/AMR.402.17.

[89] L. Bäckerud, G. Chai, J. Tamminen, Solidification processing, solidification characteristics of aluminum alloys. Vol. 2. foundry alloys, Skanaluminium, Oslo, Norway, 1990.

[90] M. Tiryakioğlu, P. Yousefian, P.D. Eason, Quantification of entrainment damage in A356 aluminum alloy castings, Metall Mater Trans A 49 (2018) 5815–5822. https://doi.org/10.1007/s11661-018-4865-z.

[91] M. Mehrabian, B. Nayebi, A. Bahmani, D. Dietrich, T. Lampke, E. Ahounbar, M. Shokouhimehr, Deformation, cracking and fracture behavior of dynamically-formed oxide layers on molten metals, Met Mater Int 27 (2021) 1701–1712. https://doi.org/10.1007/s12540-019-00537-3.

[92] W. Thiele, Die oxydation von aluminium und aluminiumlegierungs-schmelzen, Aluminium 38 (1962) 707–715, 780–786.

[93] S. Impey, D.J. Stephenson, J.R. Nicholls, A study of the effect of magnesium additions on the oxide growth morphologies on liquid aluminium alloys, in: Microscopy of Oxidation, The Institute of Metals, Cambridge, UK, 1990: pp. 238–244.

[94] Y. Wang, H.-T. Li, Z. Fan, Oxidation of aluminium alloy melts and inoculation by oxide particles, Trans Indian Inst Met 65 (2012) 653–661. https://doi.org/10.1007/s12666-012-0194-x.

[95] R. Fuoco, E.R. Correa, M.D.A. Bastos, Effects of grain refinement on feeding mechanisms in A356 aluminium alloy, AFS Trans. 106 (1998) 401–409.

[96] S. Impey, D.J. Stephenson, J.R. Nicholls, The influence of surface preparation and pretreatments on the oxidation of liquid aluminium and aluminium-magnesium alloys, in: Microscopy of Oxidation, Cambridge, UK, 1993: pp. 323–337.

[97] M. Drouzy, C. Mascré, The oxidation of liquid non-ferrous metals in air or oxygen, Metallurgical Reviews 14 (1969) 25–46. https://doi.org/10.1179/mtlr.1969.14.1.25.

[98] J.M. McHale, A. Auroux, A.J. Perrotta, A. Navrotsky, Surface energies and thermodynamic phase stability in nanocrystalline aluminas, Science 277 (1997) 788–791. https://doi.org/10.1126/science.277.5327.788.

[99] G. Wightman, D.J. Fray, The dynamic oxidation of aluminum and its alloys, Metall Mater Trans B 14 (1983) 625–631. https://doi.org/10.1007/BF02653948.

[100] G. Wu, K. Dash, M.L. Galano, K.A.Q. O'Reilly, Oxidation studies of Al alloys: Part I Al-Cu (liquid phase) alloy, Corros Sci 157 (2019) 41–50. https://doi.org/10.1016/j.corsci.2019.05.013.

[101] E. Hinton, W. Griffiths, N. Green, Comparison of oxide thickness of aluminium and the effects of selected alloying additions, Mater Sci Forum 765 (2013) 180–184. https://doi.org/10.4028/www.scientific.net/MSF.765.180.

[102] G. Wu, Understanding the role of oxidation in bonding of aluminium alloys, PhD, University of Oxford, 2014.

[103] M.P. Silva, D.E.J. Talbot, Oxidation of liquid aluminum - magnesium alloys, in: Light Metals 1989, TMS, Las Vegas, NV, USA, 2013.

[104] I. Haginoya, T. Fukusako, Oxidation of molten Al–Mg alloys, Trans Jpn Inst Metal 24 (1983) 613–619. https://doi.org/10.2320/matertrans1960.24.613.

[105] M.H. Zayan, O.M. Jamjoom, N.A. Razik, High-temperature oxidation of Al-Mg alloys, Oxid Met 34 (1990) 323–333. https://doi.org/10.1007/BF00665021.

[106] D.J. Field, G.M. Scanans, E.P. Butler, The high temperature oxidation of Al-4.2 Wt Pct Mg alloy, Metall Mater Trans A 18 (1987) 463–472. https://doi.org/10.1007/BF02648807.

[107] J.A.S. Tenório, D.C.R. Espinosa, High-temperature oxidation of Al–Mg alloys, Oxid Met 53 (2000) 361–373. https://doi.org/10.1023/A:1004549522648.

[108] A. Bahadur, Behaviour of Al-Mg alloys at high temperature, J Mater Sci 22 (1987) 1941–1944. https://doi.org/10.1007/BF01132920.

[109] F. Czerwinski, The reactive element effect on high-temperature oxidation of magnesium, Int Mater Rev 60 (2015) 264–296. https://doi.org/10.1179/1743280415Y.0000000001.

[110] F.J. Esposto, C.-S. Zhang, P.R. Norton, R.S. Timsit, Segregation of Mg to the surface of an Al-Mg single crystal alloy and its influence on the initial oxidation at room temperature, Surf Sci 302 (1994) 109–120. https://doi.org/10.1016/0039-6028(94)91101-0.

[111] D.H. Kim, E.P. Yoon, J.S. Kim, Oxidation of an aluminum-0.4 wt.% magnesium alloy, J Mater Sci Lett 15 (1996) 1429–1431. https://doi.org/10.1007/BF00275297.

[112] K. Mizuno, A. Nylund, I. Olefjord, Surface analysis of oxide formed during heat treatment of Al–Mg–Si alloys, Mater Sci Technol 12 (1996) 306–314. https://doi.org/10.1179/mst.1996.12.4.306.

[113] Y.-O. Yoon, S.-H. Ha, B.-H. Kim, H.-K. Lim, S.K. Kim, Experimental investigation of MgAl2O4 spinel formation in oxidation of Al–Mg alloys, in: A. Tomsett (Ed.), Light Metals 2020, Springer International Publishing, San Diego, California, USA, 2020: pp. 460–464. https://doi.org/10.1007/978-3-030-36408-3_65.

[114] T. Hiraki, H. Noguchi, N. Maruoka, T. Nagasaka, In situ observation of dross formation during melting of Al–Mg alloy, in: Light Metals, Springer International Publishing, Pheonix, Arizona, 2018: pp. 1141–1146. https://doi.org/10.1007/978-3-319-72284-9_149.

[115] K. Surla, F. Valdivieso, M. Pijolat, M. Soustelle, M. Prin, Kinetic study of the oxidation by oxygen of liquid Al–Mg 5% alloys, Solid State Ionics 143 (2001) 355–365. https://doi.org/10.1016/S0167-2738(01)00861-X.

[116] C. Houska, Beryllium in aluminium and magnesium alloys, Met Mater 4 (1988) 100.

[117] C.N. Cochran, D.L. Belitskus, D.L. Kinosz, Oxidation of aluminum-magnesium melts in air, oxygen, flue gas, and carbon dioxide, Metall Mater Trans B 8 (1977) 323–332. https://doi.org/10.1007/BF02657663.

[118] A. Dehhaghi, S.M.A. Boutorabi, Thickness estimation (folds and wrinkles) on short time dynamically formed double oxide film in Al-7Si-Mg alloyed with beryllium, Mater Res Express 6 (2019) 106574. https://doi.org/10.1088/2053-1591/ab35ed.

[119] N. Smith, A. Kvithyld, G. Tranell, The Mechanism Behind the Oxidation Protection of High Mg Al Alloys with Beryllium, Metall Mater Trans B 49 (2018) 2846–2857. https://doi.org/10.1007/s11663-018-1340-6.

[120] S.-H. Ha, Y.-O. Yoon, S.K. Kim, Distribution behavior of Al2Ca in Al-7.5Mg and Al-7Si-0.4Mg alloys and its effect on oxide scale and eutectic Si morphology, Mater Today: Proc 2 (2015) 4957–4962. https://doi.org/10.1016/j.matpr.2015.10.072.

[121] S.-H. Ha, Y.-O. Yoon, B.-H. Kim, H.-K. Lim, T.-W. Lee, S.-H. Lim, S.K. Kim, Oxide scale behavior and surface protection of Al–Mg Alloys containing a trace of Ca, Inter J Metalcast 13 (2019) 121–129. https://doi.org/10.1007/s40962-018-0234-3.

[122] S.-H. Ha, S.-Y. Lee, Y.-O. Yoon, S.K. Kim, Formation of protective oxide layer with nanometer scale and twining behavior of eutectic si in Al–Mg and Al–Si–Mg systems including a trace of Al2Ca, J Nanosci Nanotechnol 16 (2016) 11169–11172. https://doi.org/10.1166/jnn.2016.13473.

[123] R.G. Cooper, A.P. Harrison, The uses and adverse effects of beryllium on health, Indian Journal of Occupational and Environmental Medicine 13 (2009) 65. https://doi.org/10.4103/0019-5278.55122.

[124] N. Smith-Hanssen, M. Syvertsen, A. Kvithyld, Microalloying to Inhibit Oxidation of Al–Mg Alloys, in: Light Metals 2022, Springer International Publishing, Cham, 2022: pp. 579–586. https://doi.org/10.1007/978-3-030-92529-1_76.

[125] B.-H. Kim, S.-H. Ha, Y.-O. Yoon, H.-K. Lim, S.K. Kim, D.-H. Kim, Effect of Ca addition on selective oxidation of Al3Mg2 phase in Al-5 mass% Mg alloy, Mater Lett 228 (2018) 108–111. https://doi.org/10.1016/j.matlet.2018.05.132.

[126] S.-H. Ha, Y.-O. Yoon, B.-H. Kim, T.-W. Lee, S.-H. Lim, S.K. Kim, Precipitation of oxide particles in surface mixed layer of Al–Mg alloys with a trace of Ca during oxidation, J Nanosci Nanotechnol 17 (2017) 8232–8235. https://doi.org/10.1166/jnn.2017.15104.

[127] T.-W. Lee, H.-G. Kim, M.-G. So, J.-K. Lee, S.K. Kim, W.-J. Park, W.-Y. Kim, S. Kim, S.-H. Lim, Microstructural evaluation of oxide layers in CaO-added Mg alloys, J Alloys Compd 635 (2015) 5–10. https://doi.org/10.1016/j.jallcom.2015.02.101.

[128] Y.-O. Yoon, S.-H. Ha, G.-Y. Yeom, H.K. Lim, S.K. Kim, Oxidation behavior of Al2Ca added Al-5Mg alloy in the liquid state, in: B.A. Sadler (Ed.), Light Metals 2013, Springer International Publishing, San Antonio, Texas, USA, 2013: pp. 323–326. https://doi.org/10.1007/978-3-319-65136-1_56.

[129] P.K. Yuen, Effects of strontium on the oxidation of molten aluminum alloys containing silicon and magnesium, Masters, McGill University, 2001.

[130] I. Haginoya, T. Fukusako, Influence of alloying elements on oxidation of molten aluminum alloys, J Jpn Foundrym Soc 54 (1982) 664–669. https://doi.org/10.11279/imono.54.10_664.

[131] Á. Csanády, D. Marton, I. Geleji-Neubauer, S. Hofmann, J.M. Sanz, The influence of some alloying additions (Cr, Cu and Li) on the thermal oxidation of Al-Zn-Mg alloys, Corros Sci 22 (1982) 689–713. https://doi.org/10.1016/0010-938X(82)90048-8.

[132] D.J. Field, E.P. Butler, Liquid metal oxidation of Al-3wt.%Li, in: Aluminum-Lithium Alloys II: Proceedings of the Second International Aluminum-Lithium Conference, Metallurgical Society of AIME, Monterey, CA, USA, 1983: pp. 667–673.

[133] D.J. Field, G.M. Scanans, E.P. Butler, The high temperature oxidation of Al-Li alloy, in: Aluminum-Lithium Alloys II: Proceedings of the Second International Aluminum-Lithium Conference, The Metallurgical Society of AIME, Monterey, CA, USA, 1983: pp. 657–66.

[134] G.M. Scanan, E.P. Butler, Direct observation of oxidation of aluminium and aluminum alloys, in: Proceedings of the Fourth International Congress on HVEM, Toulouse, France, 1975: pp. 341–4.

[135] S.M. Miresmaeili, Effect of strontium on the oxidation behavior of liquid Al–7Si alloys, Oxid Met 71 (2009) 107–123. https://doi.org/10.1007/s11085-009-9136-3.

[136] R.G. Pritchard, C.R. Werrett, Inelastic electron tunnelling spectroscopy and XPS study of the oxides grown on three aluminium alloys, Surface and Interface Analysis 23 (1995) 705–711. https://doi.org/10.1002/sia.740231009.

[137] C.R. Werrett, D.R. Pyke, A.K. Bhattacharya, XPS studies of oxide growth and segregation in aluminium–silicon alloys, Surf Interface Anal 25 (1997) 809–816. https://doi.org/10.1002/(SICI)1096-9918(199709)25:10<809::AID-SIA304>3.0.CO;2-M.

[138] G.-H. Lee, Effect of oxygen pressure in the synthesis of ZnO nanowires through melt oxidation of Al-Zn mixture, Korean J Mater Res 24 (2014) 301–304. https://doi.org/10.3740/MRSK.2014.24.6.301.

[139] G.-H. Lee, Juniper leaf-like ZnO crystals synthesized through a melt oxidation of Al–Zn mixture in air, Jpn J Appl Phys 58 (2019) 060902. https://doi.org/10.7567/1347-4065/ab170f.

[140] G.-H. Lee, C. Allen, Synthesis of tetrapod-shaped ZnO nanowires by directive oxidation of Al-Zn mixture, J Ceramic Soc Jpn 117 (2009) 111–114. https://doi.org/10.2109/jcersj2.117.111.

[141] P. Xiao, B. Derby, Al2O3/Al composites formed by the directed oxidation of an Al-Mg-Zn alloy, Journal of the European Ceramic Society 12 (1993) 185–195. https://doi.org/10.1016/0955-2219(93)90120-G.

[142] M. Sindel, N.A. Travitzky, N. Claussen, Influence of magnesium-aluminum spinel on the directed oxidation of molten aluminum alloys, Journal of the American Ceramic Society 73 (1990) 2615–2618. https://doi.org/10.1111/j.1151-2916.1990.tb06736.x.

[143] N.-W. Lai, The critical ingate velocity in Mg and Al alloy, PhD, School of Metallurgy and Materials, University of Birmingham, 2004.

[144] J. Campbell, Castings, 2nd ed., Elsevier Science & Technology, Oxford, UK, 2003.

[145] D. Dispinar, J. Campbell, Critical assessment of reduced pressure test. Part 2: Quantification, Int J Cast Met Res 17 (2004) 287–294. https://doi.org/10.1179/136404604225020704.

[146] M. Tiryakioğlu, The myth of hydrogen pores in aluminum castings, in: M. Tiryakioğlu, W. Griffiths, M. Jolly (Eds.), Shape Casting, Springer International Publishing, San Antonio, Texas, USA, 2019: pp. 143–150. https://doi.org/10.1007/978-3-030-06034-3_14.

[147] D. Ward, W.A. Curtin, Y. Qi, Aluminum–silicon interfaces and nanocomposites: a molecular dynamics study, Composites Science and Technology 66 (2006) 1151–1161. https://doi.org/10.1016/j.compscitech.2005.10.024.

[148] S. Dubois, G.-M. Rignanese, T. Pardoen, J.-C. Charlier, Ideal strength of silicon: an ab-initio study, Physical Review B 74 (2006) 235203:1–7. https://doi.org/10.1103/PhysRevB.74.235203.

[149] S. Xia, Y. Qi, T. Perry, K.-S. Kim, Strength characterization of Al/Si interfaces: A hybrid method of nanoindentation and finite element analysis, Acta Materialia 57 (2009) 695–707. https://doi.org/10.1016/j.actamat.2008.10.011.

[150] M.G. Mueller, G. Žagar, A. Mortensen, In-situ strength of individual silicon particles within an aluminium casting alloy, Acta Materialia 143 (2018) 67–76. https://doi.org/10.1016/j.actamat.2017.09.058.

[151] S. Joseph, S. Kumar, V. Bhadram, C. Narayana, Stress states in individual Si particles of a cast Al–Si alloy: Micro-Raman analysis and microstructure based modeling, Journal of Alloys and Compounds 625 (2015). https://doi.org/10.1016/j.jallcom.2014.10.207.

[152] S. Harris, A. O'Neill, J. Boileau, W. Donlon, X. Su, B. Majumdar, Application of the Raman technique to measure stress states in individual Si particles in a cast Al–Si alloy, Acta Materialia 55 (2007) 1681–1693. https://doi.org/10.1016/j.actamat.2006.10.028.

[153] E. Erzi, M. Tiryakioğlu, On the fracture pressure of liquid metals, Mater Sci Technol 35 (2019) 1656–1659. https://doi.org/10.1080/02670836.2019.1646010.

[154] C. Cáceres, B.I. Selling, Casting defects and the tensile properties of an Al-Si-Mg alloy, Materials Science and Engineering: A 220 (1996). https://doi.org/10.1016/S0921-5093(96)10433-0.

[155] L. Liu, F. Samuel, Effect of inclusions on the tensile properties of Al–7% Si–0.35% Mg (A356.2) aluminium casting alloy, Journal of Materials Science 33 (1998) 2269–2281. https://doi.org/10.1023/A:1004331219406.

[156] H. Jiang, P. Bowen, J.F. Knott, Fatigue performance of a cast aluminium alloy Al-7Si-Mg with surface defects, Journal of Materials Science 34 (1999) 719–725. https://doi.org/10.1023/A:1004560510632.

[157] N.R. Green, J. Campbell, Statistical distributions of fracture strengths of cast Al-7Si-Mg alloy, Materials Science and Engineering: A 173 (1993) 261–266. https://doi.org/10.1016/0921-5093(93)90226-5.

[158] X. Dai, X. Yang, J. Campbell, J. Wood, Effects of runner system design on the mechanical strength of Al–7Si–Mg alloy castings, Materials Science and Engineering: A 354 (2003) 315–325. https://doi.org/10.1016/S0921-5093(03)00021-2.

[159] J. Mi, R. Harding, J. Campbell, Effects of the entrained surface film on the reliability of castings, Metallurgical and Materials Transactions A 35 (2004) 2893–2902. https://doi.org/10.1007/s11661-004-0237-y.

[160] T. Yonezawa, M. Watanabe, A. Hashimoto, The effects of metallurgical factors on PWSCC crack growth rates in TT alloy 690 in simulated PWR primary water, Metall Mater Trans A 46 (2015) 2768–2780. https://doi.org/10.1007/s11661-015-2852-1.

[161] A. Srinivasan, U.T. s Pillai, S. Jaganathan, C. Pai, Enhanced high temperature properties of low pressure cast AZ91 Mg alloy, International Journal of Cast Metals Research 19 (2006) 265–268. https://doi.org/10.1179/136404606X147774.

[162] B. Nayebi, A. Bahmani, M.S. Asl, A. Rasooli, M.G. Kakroudi, M. Shokouhimehr, Characteristics of dynamically formed oxide films in aluminum–calcium foamable alloys, J Alloys Compd 655 (2016) 433–441. https://doi.org/10.1016/j.jallcom.2015.09.200.

[163] Q. Chen, The effect of transition metal additions on double oxide film defects in Al alloy castings, PhD, University of Birmingham, 2017.

[164] C. Ransley, H. Neufeld, The solubility of hydrogen in liquid and solid aluminium, J Inst Metals 74 (1948) 599–620.

[165] C.F. Delale, J. Hruby, F. Marsik, Homogeneous bubble nucleation in liquids: The classical theory revisited, The Journal of Chemical Physics 118 (2002) 792. https://doi.org/10.1063/1.1525797.

[166] M.J. Moran, H.N. Shapiro, D.D. Boettner, M.B. Bailey, Fundamentals of engineering thermodynamics, 8th ed., Wiley, Hoboken, NJ, USA, 2014.

[167] C.K. Gupta, Chemical metallurgy: principles and practice, Wiley, Weinheim, Germany, 2003.

[168] Y. Fukai, Superabundant vacancies formed in metal–hydrogen alloys, Phys. Scr. 2003 (2003) 11. https://doi.org/10.1238/Physica.Topical.103a00011.

[169] G. Thomas, R.H. Willens, Defects in aluminum quenched from the liquid state, Acta Metallurgica 12 (1964) 191–196. https://doi.org/10.1016/0001-6160(64)90187-7.

[170] H.K. Birnbaum, C. Buckley, F. Zeides, E. Sirois, P. Rozenak, S. Spooner, J.S. Lin, Hydrogen in aluminum, Journal of Alloys and Compounds 253–254 (1997) 260–264. https://doi.org/10.1016/S0925-8388(96)02968-4.

[171] L. Ismer, M.S. Park, A. Janotti, C.G. Van de Walle, Interactions between hydrogen impurities and vacancies in Mg and Al: A comparative analysis based on density functional theory, Phys. Rev. B 80 (2009) 184110. https://doi.org/10.1103/PhysRevB.80.184110.

[172] H. Shahani, H. Fredriksson, On the mechanism of precipitation of pores in melts, Scand J Metall 14 (1985) 316:320.

[173] P. Yousefian, M. Tiryakioğlu, Pore formation during solidification of aluminum: reconciliation of experimental observations, modeling assumptions, and classical nucleation theory, Metall Mater Trans A 49 (2018) 563–575. https://doi.org/10.1007/s11661-017-4438-6.

[174] H. Lei, L. Hengcheng, P. Ye, W. Qigui, S. Guoxiong, In-situ observation of porosity formation during directional solidification of Al-Si casting alloys, China Foundry 8 (2011).

[175] A.G. Murphy, D.J. Browne, Y. Houltz, R.H. Mathiesen, In situ X-ray observations of gas porosity interactions with dendritic microstructures during solidification of Al-based alloys, IOP Conf. Ser.: Mater. Sci. Eng. 117 (2016) 012067. https://doi.org/10.1088/1757-899X/117/1/012067.

[176] D. Dispinar, J. Campbell, Critical assessment of reduced pressure test. Part 1: Porosity phenomena, Int J Cast Met Res 17 (2004) 280–286. https://doi.org/10.1179/136404604225020696.

[177] M. Tiryakioğlu, The effect of hydrogen on pore formation in aluminum alloy castings: myth versus reality, Met 10 (2020) 368. https://doi.org/10.3390/met10030368.

[178] X.-G. Chen, J.E. Gruzleski, Influence of melt cleanliness on pore formation in aluminium—silicon alloys, International Journal of Cast Metals Research 9 (1996) 17–26. https://doi.org/10.1080/13640461.1996.11819640.

[179] G. Gyarmati, G. Fegyverneki, T. Mende, M. Tokár, Characterization of the double oxide film content of liquid aluminum alloys by computed tomography, Mater Charact 157 (2019) 109925. https://doi.org/10.1016/j.matchar.2019.109925.

[180] L. Liu, A.M. Samuel, F.H. Samuel, H.W. Doty, S. Valtierra, Role of strontium oxide on porosity formation in Al-Si casting alloys, AFS Trans. (2002) 449–462.

[181] M. Uludağ, D. Dispinar, M. Tiryakioğlu, Characterization of the effect of Sr and Ti on liquid quality in Al8Si3Cu, in: M. Tiryakioğlu, W. Griffiths, M. Jolly (Eds.), Shape Casting, Springer International Publishing, San Antonio, Texas, USA, 2019: pp. 167–175. https://doi.org/10.1007/978-3-030-06034-3_17.

[182] J. Campbell, M. Tiryakioğlu, Review of effect of P and Sr on modification and porosity development in Al–Si alloys, Mater Sci Technol 26 (2010) 262–268. https://doi.org/10.1179/174328409X425227.

[183] X. Cao, J. Campbell, The nucleation of Fe-rich phases on oxide films in Al11.5Si0.4Mg cast alloys, Metallurgical and Materials Transactions A 34 (2003) 1409–1420. https://doi.org/10.1007/s11661-003-0253-3.

[184] X. Cao, J. Campbell, Morphology of β-Al5FeSi phase in Al-Si cast alloys, Mater. Trans. 47 (2006) 1303–1312. https://doi.org/10.2320/matertrans.47.1303.

[185] X. Cao, J. Campbell, Effect of precipitation of primary intermetallic compounds on tensile properties of cast Al 11.5Si 0.4Mg alloy, AFS Trans. 108 (2000) 391–400.

[186] W.D. Griffiths, R. Raiszadeh, Hydrogen, porosity and oxide film defects in liquid Al, J Mater Sci 44 (2009) 3402–3407. https://doi.org/10.1007/s10853-009-3450-7.

[187] G.E. Dieter, 11-10 Probabilistic aspects of fracture mechanics, in: Mechanical Metallurgy, SI Metric, McGraw-Hill Book Company, London, UK, 1988.

[188] R. Raiszadeh, W.D. Griffiths, The effect of holding liquid aluminum alloys on oxide film content, Metall Mater Trans B 42 (2011) 133–143. https://doi.org/10.1007/s11663-010-9439-4.

[189] G. Gyarmati, G. Fegyverneki, M. Tokár, T. Mende, Effect of the sampling method on the results of melt quality assessment of aluminum alloys with computed tomography, IOP Conf Ser: Mater Sci Eng 903 (2020) 012003. https://doi.org/10.1088/1757-899X/903/1/012003.

[190] O. Lashkari, L. Yao, S. Cockcroft, D. Maijer, X-ray microtomographic characterization of porosity in aluminum alloy A356, Metall Mater Trans A 40 (2009) 991–999. https://doi.org/10.1007/s11661-008-9778-9.

[191] S. Dasgupta, L. Parmenter, D. Apelian, Relationship between the reduced pressure test and hydrogen content of the melt, in: Proceedings of the Fifth International Conference on Molten Metal Processing, American Foundrymen's Society, Orlando, FL, USA, 1998: pp. 285–300.

[192] D. Dispinar, J. Campbell, Use of bifilm index as an assessment of liquid metal quality, Int J Cast Met Res 19 (2006) 5–17. https://doi.org/10.1179/136404606225023300.

[193] M. Uludağ, R. Çetin, D. Dişpinar, M. Tiryakioğlu, On the interpretation of melt quality assessment of A356 aluminum alloy by the reduced pressure test: the bifilm index and its physical meaning, Inter J Metalcast 12 (2018) 853–860. https://doi.org/10.1007/s40962-018-0217-4.

[194] A. Gul, Ö. Gürsoy, E. Erzi, D. Dispinar, E. Kayali, Aluminum alloy with high Mg content: casting studies for microstructural evolution, phase formation and thermophysical properties with different alloying elements, in: M. Tiryakioğlu, W. Griffiths, M. Jolly (Eds.), Shape Casting, Springer International Publishing, San Antonio, Texas, USA, 2019: pp. 337–342. https://doi.org/10.1007/978-3-030-06034-3_33.

[195] J. Campbell, M. Tiryakioğlu, Bifilm defects in Ni-based alloy castings, Metall Mater Transactions B 43 (2012) 902–914. https://doi.org/10.1007/s11663-012-9655-1.

[196] R. Raiszadeh, W.D. Griffiths, The behaviour of double oxide film defects in liquid Al alloys under atmospheric and reduced pressures, J Alloys Compd 491 (2010) 575–580. https://doi.org/10.1016/j.jallcom.2009.10.271.

[197] M. El-Sayed, An investigation of the behaviour of double oxide film defects in aluminium-magnesium cast alloys, J South Afr Inst Min Metall 118 (2018) 1225–1231. https://doi.org/10.17159/2411-9717/2018/v118n11a13.

[198] W.D. Griffiths, N.-W. Lai, Double oxide film defects in cast magnesium alloy, Metall Mater Trans A 38 (2007) 190–196. https://doi.org/10.1007/s11661-006-9048-7.

[199] R. Raiszadeh, W.D. Griffiths, A method to study the history of a double oxide film defect in liquid aluminum alloys, Metall Mater Trans B 37 (2006) 865–871. https://doi.org/10.1007/BF02735007.

[200] L. Archer, F.V. Guerra, C. Beckermann, Measurement of air entrainment during pouring of an aluminum alloy, in: M. Tiryakioğlu, W. Griffiths, M. Jolly (Eds.), Shape Casting, Springer International Publishing, San Antonio, Texas, USA, 2019: pp. 31–43. https://doi.org/10.1007/978-3-030-06034-3_3.

[201] J.T. Berry, R. Luck, R.P. Taylor, The connection between filling, feeding, and applied pressure in cast aluminum alloys, in: Shape Casting: The John Campbell Symposium, TMS, Warrendale, PA, USA, 2005: pp. 113–122.

[202] F.N. Bakhtiarani, R. Raiszadeh, Healing of double-oxide film defects in commercial purity aluminum melt, Metall Mater Trans B 42 (2011) 331–340. https://doi.org/10.1007/s11663-011-9480-y.

[203] F.N. Bakhtiarani, R. Raiszadeh, The behaviour of double oxide film defects in Al–4.5 wt.% Mg melt, J Mater Sci 46 (2011) 1305–1315. https://doi.org/10.1007/s10853-010-4916-3.

[204] C. Nyahumwa, N. Green, J. Campbell, Influence of casting technique and hot isostatic pressing on the fatigue of an Al7Si-Mg alloy, Metallurgical and Materials Transactions A 32A (2001) 349–358. https://doi.org/10.1007/s11661-001-0266-8.

[205] G. Wang, D. Apelian, D. Lados, Fatigue behavior of A356-T6 aluminum cast alloys. Part I. Effect of casting defects, Journal of Light Metals 1 (2001) 73–84. https://doi.org/10.1016/S1471-5317(00)00008-0.

[206] International alloy designations and chemical composition limits for wrought aluminum and wrought aluminum alloys, The Aluminum Association, Arlington, VA, USA, 2015.

[207] S.A. Decterov, V. Swamy, I.-H. Jung, Thermodynamic modeling of the B2O3–SiO2 and B2O3–Al2O3 systems, International Journal of Materials Research 98 (2007) 987–994. https://doi.org/10.3139/146.101555.

[208] B. Konar, M.-A. Van Ende, I.-H. Jung, Critical evaluation and thermodynamic optimization of the Li2O-Al2O3 and Li2O-MgO-Al2O3 systems, Metall Mater Trans B 49 (2018) 2917–2944. https://doi.org/10.1007/s11663-018-1349-x.

[209] S. Chatterjee, I.-H. Jung, Critical evaluation and thermodynamic modeling of the Al–Mn–O (Al2O3–MnO–Mn2O3) system, J Eur Ceram Soc 34 (2014) 1611–1621. https://doi.org/10.1016/j.jeurceramsoc.2013.12.017.

[210] B. Konar, M.-A. Van Ende, I.-H. Jung, Critical evaluation and thermodynamic optimization of the Li-O, and Li2O-SiO2 systems, J Eur Ceram Soc 37 (2017) 2189–2207. https://doi.org/10.1016/j.jeurceramsoc.2016.12.041.

[211] K.T. Jacob, A. Kumar, G. Rajitha, Y. Waseda, Thermodynamic data for Mn3O4, Mn2O3 and MnO2, High Temp Mater Process 30 (2011) 459–472. https://doi.org/10.1515/htmp.2011.069.

[212] I.-H. Jung, G. Eriksson, P. Wu, A. Pelton, Thermodynamic modeling of the Al2O3–Ti2O3–TiO2 system and its applications to the Fe–Al–Ti–O inclusion diagram, ISIJ Int 49 (2009) 1290–1297. https://doi.org/10.2355/isijinternational.49.1290.

[213] S. Panda, I.-H. Jung, Coupled experimental study and thermodynamic modeling of the Al2O3–Ti2O3–TiO2 system, J Iron Steel Inst Jpn 60 (2020) 31–41. https://doi.org/10.2355/isijinternational.ISIJINT-2019-006.

[214] H. Peelaers, J.B. Varley, J.S. Speck, C.G. Van de Walle, Structural and electronic properties of Ga2O3-Al2O3 alloys, Appl Phys Lett 112 (2018) 242101. https://doi.org/10.1063/1.5036991.

[215] N. Saunders, A.P. Miodownik, CALPHAD (calculation of phase diagrams): a comprehensive guide, 1st ed., Pergamon, 1998.

[216] I.-H. Jung, M.-A. Van Ende, Computational thermodynamic calculations: factsage from CALPHAD thermodynamic database to virtual process simulation, Metall Mater Trans B 51 (2020) 1851–1874. https://doi.org/10.1007/s11663-020-01908-7.

[217] J.-O. Andersson, T. Helander, L. Höglund, P. Shi, B. Sundman, Thermo-Calc & DICTRA, computational tools for materials science, Calphad 26 (2002) 273–312. https://doi.org/10.1016/S0364-5916(02)00037-8.

[218] R.J.D. Tilley, Understanding solids: The science of materials, John Wiley & Sons, Ltd, Chichester, UK, 2004.

[219] A.D. Pelton, Phase Diagrams and Thermodynamic Modeling of Solutions, Elsevier, Cambridge, MA, USA, 2019. https://doi.org/10.1016/C2013-0-19504-9.

Chapter 3
Materials and Methods

3.1. Materials and casting

Three Al-Mg-Ca alloys were studied: Al-5Mg, Al-5Mg-0.01Ca, and Al-5Mg-0.03Ca (all in wt.% unless specified). Commercial purity aluminium, pure magnesium ingot, and an Al-10Ca alloy were used as raw materials, and a SiC crucible, an optical emission spectroscopy (OES) mould, and an 'AVON' mould were used to make the Al-5Mg master alloy ingot (Figure 3.1). The 'AVON' mould was dammed to reduce the width of the ingot, making it more compact.

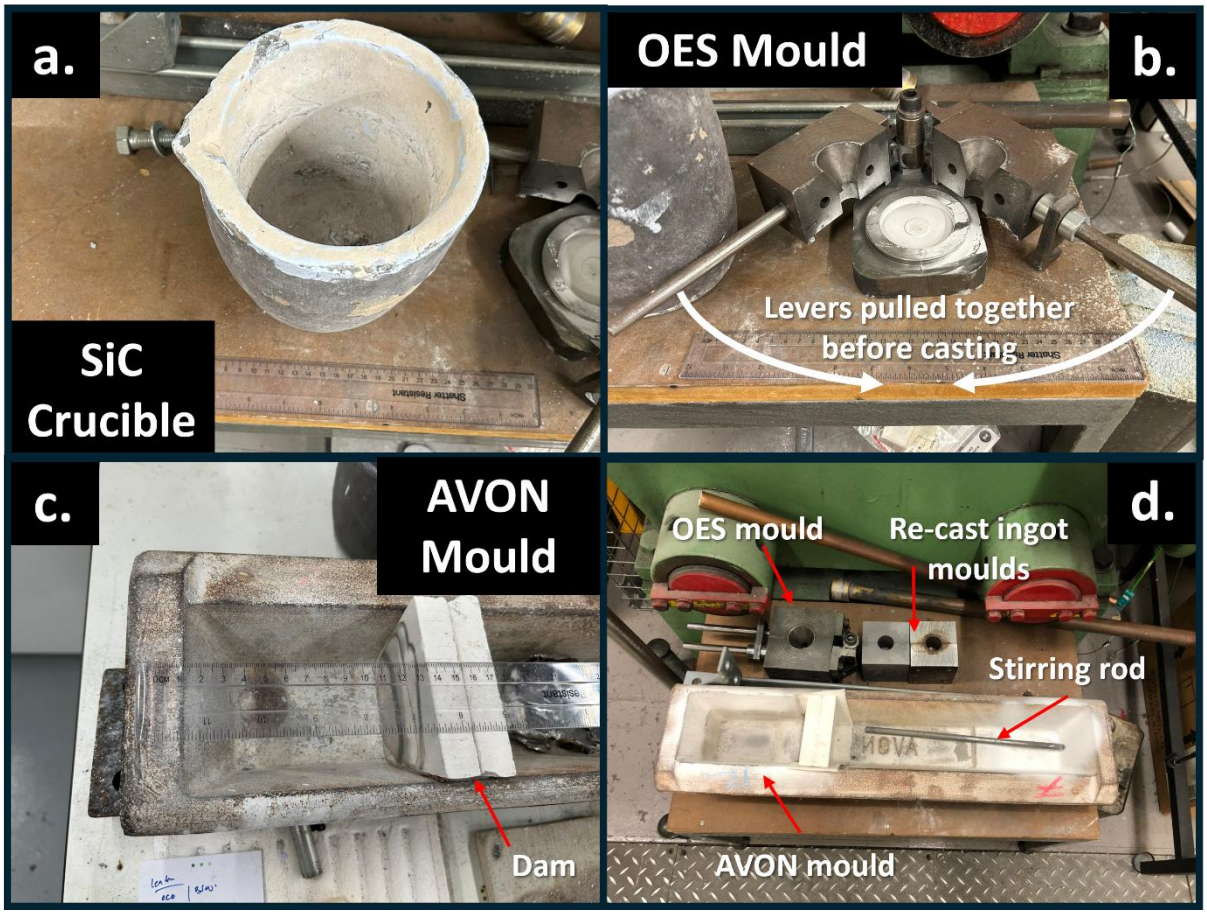


Figure 3.1. Crucibles and moulds used in master alloy casting with ruler for scale: (a) SiC crucible, (b) OES mould, (c) AVON mould, and (d) all casting equipment including stirring rod and metal moulds used for re-cast Al-Mg-Ca ingots.

A two-kilogram Al-5Mg master alloy ingot was prepared using aluminium and magnesium weighed out to composition. The pure aluminium (1.9 kg) was placed in a silicon carbide crucible (Figure 3.1.a) and inserted into an electric furnace set to 750 °C. After two hours and fifty minutes, the crucible was removed from the furnace, and the melt was stirred with a clean

stirring rod to verify that the aluminium had completely melted. The molten aluminium was placed back into the furnace. After ten minutes, the crucible was removed, the magnesium (100 g, wrapped in aluminium foil) was inserted slowly into the melt, and the crucible re-inserted into the furnace. After another ten minutes, the crucible was removed, the melt was stirred to confirm that the magnesium had dissolved, and the crucible was re-inserted into the furnace. Following a further ten minutes, the crucible was removed and the alloy cast: the OES (optical emission spectroscopy) sample mould (Figure 3.1.b) was filled first, then the remaining melt was poured into the 'AVON' mould (Figure 3.1.c) to make the master alloy ingot.

To make the three Al-Mg-Ca alloys (Al-5Mg-0.00/0.01/0.03Ca), three 250 g sections were cut from the Al-5Mg master alloy, placed into smaller crucibles, and put into an electric furnace set to 750 °C. After fifty minutes, chunks of the Al-10Ca master alloy, measured to the target compositions, were placed into two of those crucibles, which were then put back into the furnace. The crucibles were taken out after ten minutes, stirred to check that the Al-10Ca had melted, reinserted into the furnace for another ten minutes. Each melt was then poured sequentially, first filling cylindrical moulds (Figure 3.1.d), with the remaining melt poured into the AVON mould (each alloy remainder was poured separately). Discussion of this choice of alloy system is detailed in Chapter 4 (Section 4.1.2).

3.2. Spark OES

For OES testing, the remainders of the recast Al-Mg-Ca alloys were ground to 2500 grit, cleaned with ethanol, and tested with spark OES (externally) to determine their composition. Results can be found in Table 3.1, where only elements with > 50 ppm are shown.

Alloy	Composition (wt.%)				
	Al	Mg	Fe	Si	Ca
0.00Ca	Bal	5.00	0.017	0.027	0.0001
0.01Ca	Bal	5.12	0.018	0.027	0.011
0.03Ca	Bal	4.89	0.017	0.023	0.034

Table 3.1. Spark optical emission spectroscopy (OES) results for tested alloys. Only elements with > 50 ppm in any sample are shown.

3.3. Metallography

Metallographic samples of the Al-Mg-Ca alloys were prepared by embedding in bakelite, grinding with SiC grinding paper up to 4000 grit, then sequentially polishing with diamond suspension of grades 6 μm, 3 μm, and 1 μm, and 0.04 μm colloidal silica. No etchant was used, to preserve any oxide structures present.

3.4. Butanol dissolution

Al-Mg-Ca samples, both as-cast and after being subjected to a 750 °C/3-hour heat treatment, were treated with boiling 1-butanol. This technique involves using anhydrous 1-butanol to dissolve away the α-Al matrix of metallic samples to leave behind its inclusions, including intermetallics and oxides [1–3]. This works by the 1-butanol (C_4H_9OH) oxidising the α-Al matrix to aluminium butoxide ($Al(C_4H_9O)_3$), which can be carried away with the remaining unreacted 1-butanol; hydrogen gas is produced as a by-product (3.1).

$$6C_4H_9OH + 2Al \rightarrow 2Al(C_4H_9O)_3 + H_2 \quad (3.1)$$

Inclusions such as intermetallics and oxides are not oxidised by the 1-butanol, so these structures are preserved and captured by the filter. This allows observation and analysis of these inclusions of interest, including techniques such as scanning electron microscopy coupled with energy-dispersive X-ray spectroscopy (SEM/EDX) or X-ray diffraction (XRD).

Firstly, 1-butanol is refluxed under argon gas with the addition of some pure aluminium turnings to dehydrate it (Figure 3.2.a); moisture is extremely deleterious to the process, reacting with butanol to form a gel that coats inclusions and turns white upon exposure to air. The autoclaves (Figure 3.2.b) and constituent parts are cleaned thoroughly with soapy water and then with deionised water, dried, and assembled to check for leaks with argon via a gas board (Figure 3.2.d). If the autoclave leaks, joints are checked and tightened, but if it continues to leak, it is not used. A leaky autoclave results in flammable butanol gas escaping into the oven during heating, and moisture ingress, which degrades the sample quality. Next, aluminium

samples are cleaned thoroughly with soapy water, rinsed with ethanol, inserted into Schlenk tubes (Figure 3.2.c) and sealed. They are then flushed with argon and evacuated, to remove any moisture or ethanol remaining, followed by sealing again under argon. The autoclaves are fitted with a PTFE filter (47 mm diameter, 0.2 μm pore size) above the support screen. All valves are closed, then the autoclaves are flushed with argon and evacuated repeatedly.

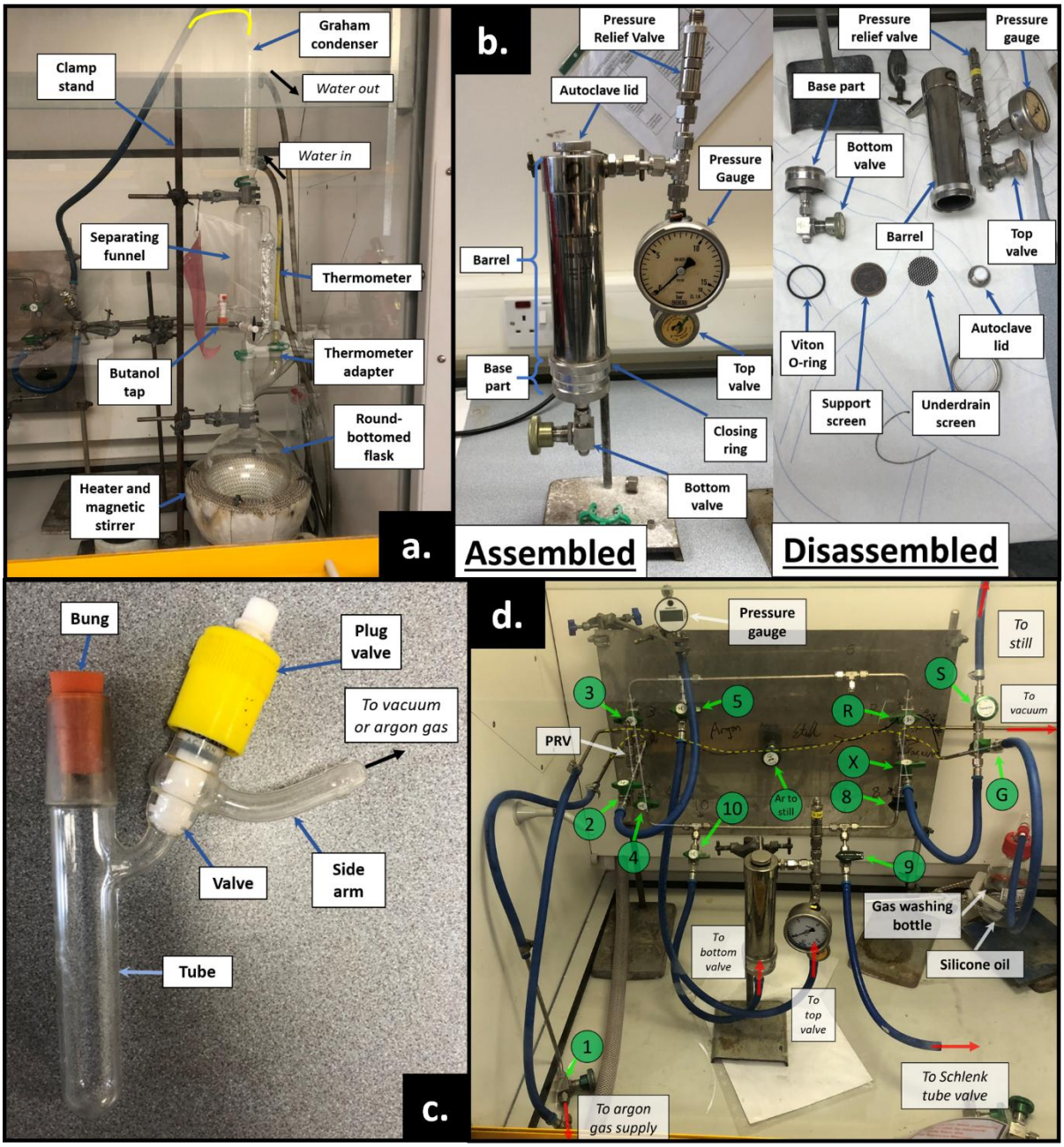


Figure 3.2. Butanol dissolution apparatus: (a) still for refluxing butanol under argon, (b) autoclaves both assembled and disassembled, (c) Schlenk tube, (d) gas board.

Once the butanol has been refluxed for at least two hours, the tap under the separating funnel

is turned to collect the anhydrous butanol. Once sufficient anhydrous butanol (80 ml per sample) has been collected, the assembled autoclave top valve (Figure 3.2.b) is connected to a continuous argon supply and the autoclave lid is removed, such that argon continuously flows from the top valve out the top of the autoclave, preventing moisture ingress.

Anhydrous butanol (80 ml) is poured into the autoclave, the sample is dropped in, the autoclave lid is reattached, and the autoclave is sealed under argon. The sample is disconnected from the gas board and placed into an oven (set at 150 °C) for at least three hours, boiling the butanol and allowing the sample to react with it in a moisture-free environment. The oven is large enough for four autoclaves, allowing four samples to be extracted simultaneously.

During this time, the pressure rises as the butanol boils, which aids reaction with the α-Al. Once enough time has passed, the autoclave is removed from the oven, placed into a fume hood, and the bottom valve opened into a glass beaker. The remaining liquid butanol is expelled by the pressure, as well as butanol vapour; argon gas is flushed through to remove any remaining butanol vapour. The autoclave lid is removed, a squirt of ethanol is added, the lid is reattached, autoclave is sealed, and the autoclave is put back into the oven for a few minutes to help clean away any remaining butanol. The autoclave is removed from the oven again and the ethanol expelled in the same manner as the butanol, firstly by its own vapour pressure, then with argon gas. The base part is then removed from the autoclave, which contains the sample on the PTFE filter paper: if successful, the aluminium will have fully dissolved, leaving behind inclusions such as intermetallics and oxides, which can be analysed further.

A key difference between the protocol followed here and the protocol used in previous studies is the omission of an acid etch on the sample before cleaning with ethanol. This was done to remove the native oxide layer to improve extraction efficiency when intermetallics were the focus of research using this technique; since oxides were the desired product, this step was omitted, but the extractions were still successful.

3.5. SEM/EDX

SEM/EDX was carried out with a Zeiss EVO MA10 fitted with a tungsten filament, secondary electron (SE) and backscattered electron (BSE) detectors, and an Oxford Instruments X-act EDX detector. Extracted samples were mounted onto SEM stubs with carbon tape and sputter coated with chromium to reduce sample charging. Metallographic samples were electrically grounded by attaching a piece of copper tape to the sample, touching both the corner of the alloy fragment and the base of the metallographic sample. Samples were observed at an operating voltage of 10 kV, and a probe current of 0.2-2 nA for extracted samples and 2-3 nA for metallographic samples. Both SE and BSE imaging were used, since SE is better for resolving topography whilst BSE gives better elemental contrast [4].

3.6. Thermogravimetric analysis (TGA)

To assess the presence of oxidation protection in Al-Mg-Ca samples, thermogravimetric analysis (TGA), which measures the changes in weight of a sample over time, was carried out in synthetic air at 750 °C. Under these conditions, the weight gain as time proceeds corresponds to oxygen pickup by oxidation, so the weight gain directly correlates with the extent of oxidation. The alloys were cut into cylinders (c. 7 mm long, 7 mm diameter), ground by hand with SiC paper up to 4000 grit, then measured (thickness and length) and put into alumina crucibles in a Netzsch STA 449 F1 Jupiter TGA. The samples were raised to temperature under argon gas and held at temperature to permit buoyancy correction. Then, the airflow was switched to synthetic air to start oxidation. Samples were held at 750 °C (melting the sample) for 8 hours, during which the weight was continuously measured and recorded.

3.7. X-ray diffraction (XRD)

Extracted samples were observed with X-ray diffraction (XRD), to identify phases present. For this, a Brucker D8 Advance Eco θ-2θ diffractometer fitted with a CuKα source was used, scanning from 10° to 80° (2θ), and indexed by manual comparison to peaks from candidate

phases using reference data from ICDD [5] and COD [6] databases.

3.8. Synchrotron X-ray tomography

X-ray tomography was carried out at the 2-BM beamline at the Advanced Photon Source (APS), Argonne National Laboratory (ANL) [7], proposal ID 80198. The set-up (Figure 3.3) consisted of an X-ray source (30 kV), an Optique Peter X-ray detector (pixel size 0.69 μm, field of view 1.41 mm x 1.41 mm), sample apparatus, and copper resistance furnace.

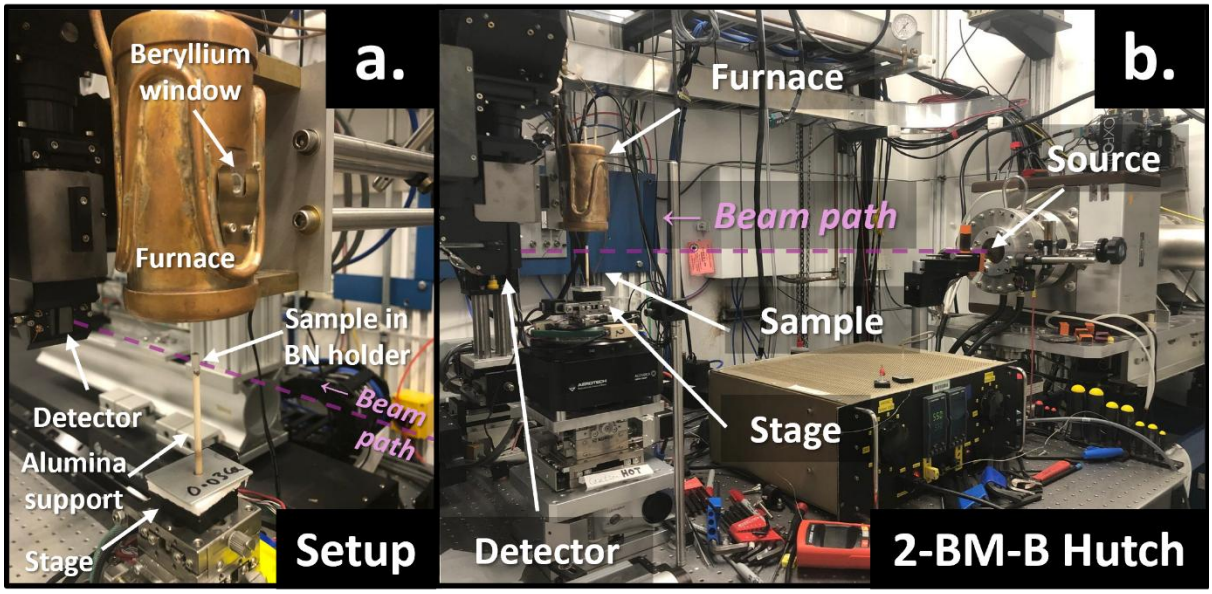


Figure 3.3. X-ray tomography at the 2-BM beamline: (a) sample setup and (b) view of hutch.

The sample apparatus (Figure 3.3.a) consisted of a small wire sample (c. 1 mm diameter, 5 mm length) placed inside a cylindrical hexagonal boron nitride (BN) holder, mounted on an alumina support attached to a stage able to translate and rotate, allowing alignment and tomography, respectively. The furnace (a copper resistance furnace) contained an X-ray transparent beryllium window on both sides and a hole at the bottom. It was connected to a support, allowing it to be lowered over the sample and raised again.

3.9. References

[1] C. Simensen, P. Fartum, A. Andersen, Analysis of intermetallic particles in aluminium by dissolution of the sample in butanol, Fresenius' Zeitschrift Für Analytische Chemie 319 (1984) 286–292. https://doi.org/10.1007/BF00487273.

[2] S. Kumar, K.A.Q. O'Reilly, Influence of Al grain structure on Fe bearing intermetallics during DC casting of an Al-Mg-Si alloy, Materials Characterization 120 (2016) 311–322. https://doi.org/10.1016/j.matchar.2016.09.017.

[3] G. Wu, Understanding the role of oxidation in bonding of aluminium alloys, PhD, University of Oxford, 2014.

[4] L. Reimer, Emission of Backscattered and Secondary Electrons, in: L. Reimer (Ed.), Scanning Electron Microscopy: Physics of Image Formation and Microanalysis, Springer, Berlin, Heidelberg, 1998: pp. 135–169. https://doi.org/10.1007/978-3-540-38967-5_4.

[5] S.N. Kabekkodu, A. Dosen, T.N. Blanton, PDF-5+: a comprehensive Powder Diffraction File for materials characterization, Powder Diffraction 39 (2024) 47–59. https://doi.org/10.1017/S0885715624000150.

[6] S. Gražulis, D. Chateigner, R.T. Downs, A.F.T. Yokochi, M. Quirós, L. Lutterotti, E. Manakova, J. Butkus, P. Moeck, A. Le Bail, Crystallography Open Database – an open-access collection of crystal structures, J Appl Cryst 42 (2009) 726–729. https://doi.org/10.1107/S0021889809016690.

[7] V. Nikitin, A. Tekawade, A. Duchkov, P. Shevchenko, F. De Carlo, Real-time streaming tomographic reconstruction with on-demand data capturing and 3D zooming to regions of interest, J Synchrotron Rad 29 (2022) 816–828. https://doi.org/10.1107/S1600577522003095.

Chapter 4
In-situ X-ray Tomography of Ca-added Al-Mg Melts

4.1. Introduction

This chapter covers investigations into the behaviour of entrained oxides in Ca-added Al-Mg melts using in-situ X-ray tomography, carried out at the 2-BM beamline at the Advanced Photon Source (APS), Argonne National Laboratory (ANL), proposal ID 80198.

4.1.1. Motivation for technique

Entrained oxides have not yet been directly imaged in aluminium melts, a key stumbling block to broader acceptance within the casting community. Evidence to date has been indirect, such as reduced pressure tests (RPT) and X-ray CT of solid samples, but direct observation of entrained oxides within aluminium melts has proven elusive. Experimental difficulties are numerous: the sample must be molten, and therefore both heated and contained; high resolution tomography requires features to be reasonably still under rotation, but the features of interest lie in a fluid medium; the fluid medium is metallic, excluding low energy electromagnetic radiation and electron methods; and the features of interest (Al/Mg-based oxides) have similar densities to the fluid medium, decreasing any potential absorption contrast.

These difficulties rule out all available experimental methods, except for highly-specialised synchrotron X-ray tomography set-ups, such as the 2-BM beamline (at APS, ANL). Other researchers have previously imaged inside molten aluminium samples using this set-up, with the caveat that the sample must be tiny (cylinders on the order of 1 mm width, 5 mm length), and therefore far smaller than the size of a casting melt. Nevertheless, this size requirement has its advantages: firstly, the sample is small enough so that the sample shape and solid features within the melt remain largely rigid. The native oxide skin is thick enough to contain the small volume of molten aluminium when it melts, as well as secure any entrained features which are in contact with this skin (by virtue of being in that location when the sample is sectioned from

the larger alloy). This simplifies containment of the melt and allows 3-D tomographs to be taken of entrained features, since they remain rigid with respect to the rotation axis.

Secondly, a smaller sample permits a higher spatial resolution (subject to the quality of the camera) for a given detector; the 0.69 μm pixel size achieved is comparable to reported thicknesses of entrained oxides, but the viewing window is large enough to observe the full sample width, including surface and sub-surface features. Thirdly, a smaller sample allows a higher frame rate, since X-rays attenuate less through the sample; this allows a higher temporal resolution, enabling observed events to be captured at faster timescales. Furthermore, phase contrast imaging was available, helping to image boundaries between oxides and the melt.

The opportunity to use this set-up therefore provided the best chance at directly imaging entrained oxides within molten aluminium and investigating predictions about the behaviour of these hypothesised objects in molten aluminium alloys.

4.1.2. Choice of alloy system

Ca-added Al-Mg alloys were chosen largely to investigate surface oxidation suppression by microalloying. As little as 0.03 wt.% can completely suppress the melt oxidation of Al-5Mg (wt.%, all compositions in wt.% unless stated) alloys at 750 °C [1], so three Al-Mg alloys were chosen, all cast in the same way (see Section 3.1): a control alloy with no additional calcium (0.00Ca), an alloy with full oxidation suppression (0.03Ca), and an alloy with an intermediate content (0.01Ca). Taking tomographs over a 3-hour melt hold of each alloy would thus allow any structural development during oxidation to be observed and characterised. Since the set-up captures the full width of the sample, the question of whether entrained oxides exist within aluminium melts can be simply answered by noting whether they appear after melting at all. In addition, the true morphologies can be deduced by tomographic reconstruction, allowing assessment of the structures hypothesised and, to date, only indirectly evidenced.

Furthermore, the development of entrained features can also be monitored by being visible

simultaneously whilst surface oxidation data is captured. Observation can be extended to the solid states before and after the melt hold, allowing comparison of features to the molten state. Taking data during melting and solidification whilst rotating the sample continuously allows snapshots of the phase transitions to be taken by partial tomographic reconstruction, giving a 3-D probe into these phase changes. Should the events happen more quickly than the time for a full tomograph (30 s), the raw radiographs, which were taken every 20 ms, still provide direct evidence of phenomena at a high temporal resolution. Although these radiographs are 2-D projections and therefore do not pinpoint the locations in 3-D, comparisons can still be made to the encompassing tomographs since the shape is generally maintained over the time of the full tomograph.

Calcium is reported to deoxidise aluminium melts, so adding calcium to the Al-5Mg alloy and observing the behaviour of oxides within the melt allows the deoxidation mechanism to be investigated. The role of surface-impinging entrained oxides on melt oxidation, whilst claimed to be involved in solid-state corrosion, has not yet been speculated, but can be investigated by this set-up and choice of alloys. A further hypothesis on entrained oxides is that hydrogen bubbles do not nucleate within melts but grow from existing gaseous atmospheres provided by entrained oxides, which this set-up allows to be evaluated.

4.1.3. Chapter structure

Since this single set of experiments monitored many different physical aspects and tested many hypotheses (in addition to supplementary experiments which were performed to consolidate the conclusions), the chapter structure is structured accordingly. The results are presented and discussed in a sequence to aid reader understanding, since many results are starkly novel even to researchers within the field. The first results sub-chapter (Chapter 4.3) focuses on the sample without added calcium (0.00Ca), discussing the structure of the entrained oxides found, and observations of melt oxidation. The second results sub-chapter (Chapter 4.4), having

established the nature of Al-Mg melt oxidation, explores the effect of calcium on Al-Mg melt oxidation, and on entrained oxides more generally. The third results sub-chapter (Chapter 4.5), having established the morphology of entrained oxides and the effect of calcium on surface oxidation, explores the nature of deoxidation by calcium, i.e. the effect of calcium on sub-surface oxides.

These are followed by a further results sub-chapter (Chapter 4.6) detailing less important but still noteworthy observations, including discussions of the stacked samples and image artifacts. Since the methods used for each chapter overlap, there is a single materials and methods subsection. Results are discussed within each sub-chapter with preliminary summaries, but there is a single conclusions section (Chapter 4.7) to consolidate the findings.

4.2. Materials and methods

Three alloys were studied using X-ray tomography: an Al-Mg alloy (0.00Ca), and two Al-Mg alloys with added calcium (0.01Ca and 0.03Ca), fabricated as described in Chapter 3. Alloys were machined into wires (c. 1 mm width, 5 mm length) and inserted into hexagonal boron nitride (BN) holders, themselves mounted onto an alumina support attached to a rotation stage (Figure 4.1.a). In testing (Figure 4.1.b), the furnace was set to 550 °C and lowered over the sample, after which the sample was allowed to get to the set temperature (as indicated by expansion of the BN holder). After the BN holder stopped expanding, an initial tomograph (0.12° step, 20 ms exposure) at the top of the sample was taken. Following this, radiographs were taken while continuously rotating the sample (0.12° step, 20 ms exposure) and raising the furnace temperature (20 K/min) to 750 °C. Over this sequence, the samples melted, and the continuous rotation allowed for tomographic reconstruction of selected 180° (1501 frame) snapshots during the sequence (Figure 4.1.b).

Samples were held in air at 750 °C for 3 hours, with tomographs taken at regular intervals to capture the oxidation of the sample over the melt hold. Afterwards, the solidification of the

sample was observed similarly to melting (continuous rotation, 0.12° step, 20 ms exposure, 20 K/min from 750 °C to 550 °C), the furnace removed, and a tomograph taken after cooling to room temperature. This was also carried out on each alloy in a 'stacked' configuration, where a wire was cut in half and inserted into the holder (with the field of view over the interface) to observe the behaviour of the interface.

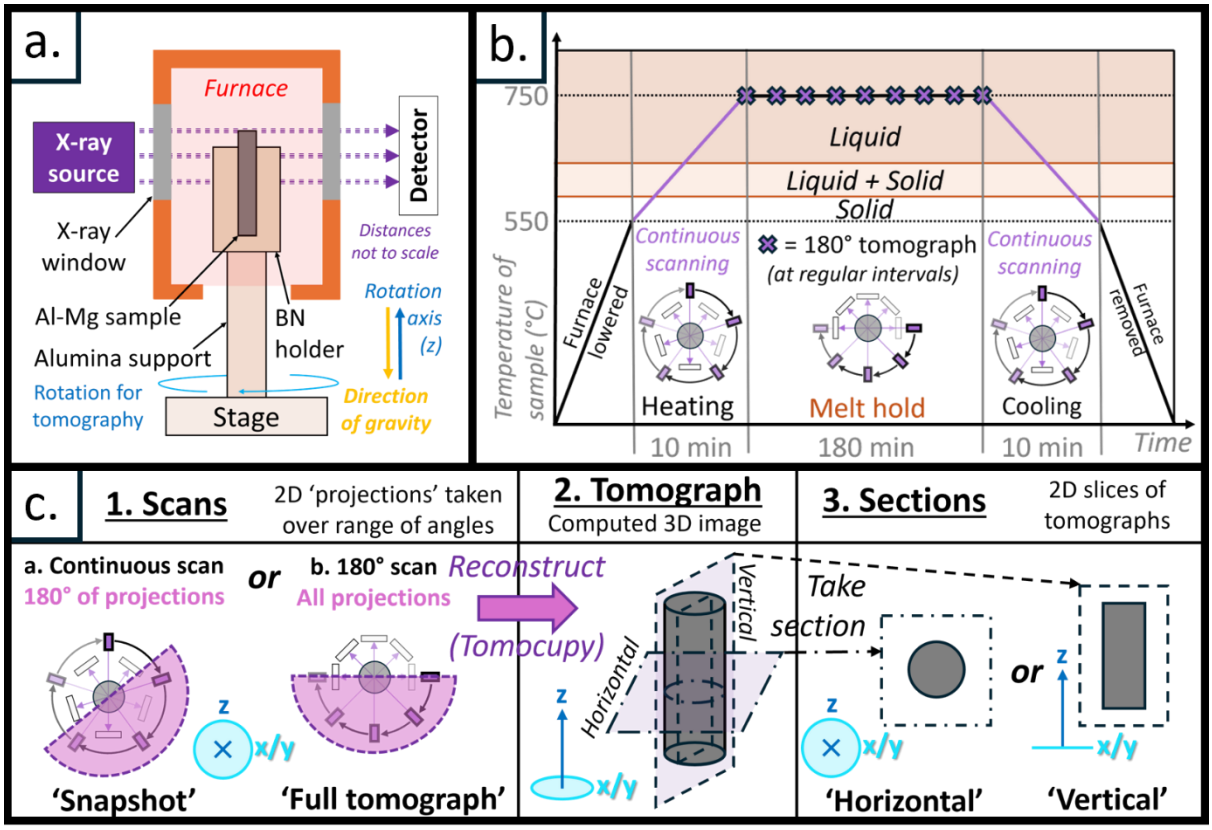


Figure 4.1. Tomography set-up and testing: (a) schematic diagram of sample apparatus, (b) testing regimen, (c) data processing for visualisation.

Data was reconstructed and analysed using tomopy (tomocupy) code provided by the 2-BM beamline [2,3] and analysed using dedicated workstations (Figure 4.1.c). Tomographs were reconstructed either from 180° tomographs or selected 180° (1501-frame) snapshots during the heating or cooling sequences to generate 3-D tomographs. These tomographs are presented in 2-D sections either perpendicular ('horizontal') or parallel ('vertical') to the rotation axis. In the vertical sections, the 'up' direction of the page is oriented opposite to gravity. As some events of interest occur over times shorter than the time for a full 180° rotation, the flat-field corrected X-ray radiographs, termed 'projections', are used to show phenomena occurring

during the melting sequences. These projections are only displayed in the 'vertical' orientation, with the rotation axis within the page and gravity pointing to the bottom of the page. Peach-coloured text is used to indicate molten samples to aid reader interpretation.

In addition, metallographic samples were cut and analysed with SEM/EDX. Other samples from the smaller ingots, both in the as-cast state and after being subjected to a 750 °C/3-hour melt treatment in dry air (analogously to the tomography), were boiled in anhydrous butanol to extract non-metallic inclusions. These residues, hereafter termed 'extracted samples', were analysed with XRD and SEM/EDX, to determine the progression of these components over the course of the melt hold. TGA was also performed on cylindrical samples (7 mm height, 8 mm diameter). Experimental particulars can be found in Chapter 3.

4.3. Direct imaging of entrained oxides

4.3.1. Overview

This sub-chapter focuses on observations of the 0.00Ca sample: the morphology of structures contained within the sample; their development after melting, during the melt hold, and during solidification; and how oxidation appears. Firstly, the results of extracted samples are discussed, then compared to metallographic and tomographic observations, to build a complete picture of the morphology and chemistry of the entrained oxides. Afterwards, the development of these oxides over the melt hold, including the effect of air oxidation, is discussed.

4.3.2. Before melting

SEM analysis of the extracted samples reveals complex oxide networks with entrained debris such as oxide films inside. Two main oxide morphologies are observed: thicker (> 1 μm) films with a rough appearance, and thin (< 1 μm) convoluted, smooth, oxide networks (Figure 4.2). Intermetallics that appear to be Al-Fe and Mg-Si based are found attached to these oxide networks, inferred from the correlation between elements in the EDX mapping (Figure 4.3).

The entrained films appear to contain more magnesium than the networks, but aluminium, magnesium, and oxygen can all be found in both the oxide films and the oxide networks.

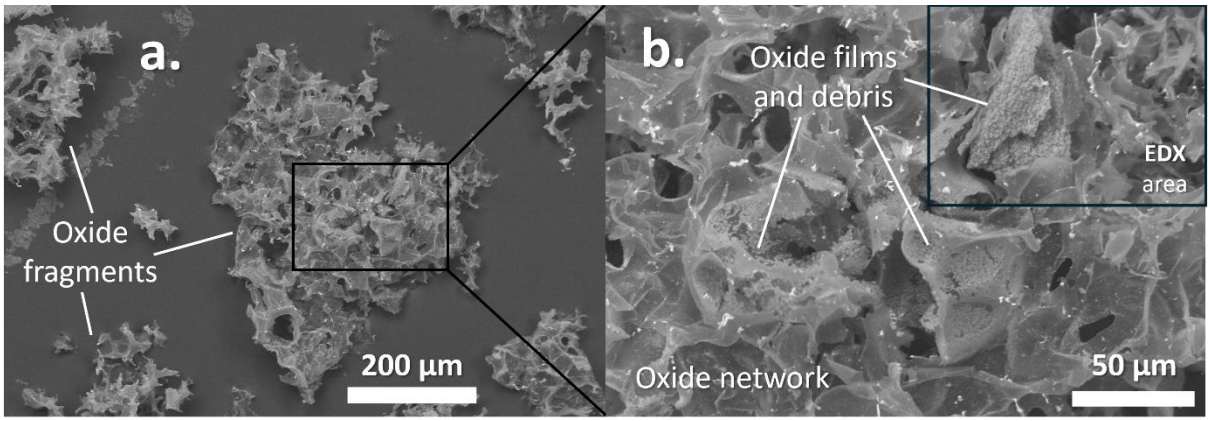


Figure 4.2. SEM (BSE) micrographs of oxide fragments found from extracted as-cast 0.00Ca samples. Many oxide fragments (a) are seen, and a closer look (b) shows the dual oxide population of the thin, convoluted oxide network and thicker, rougher oxide films and debris.

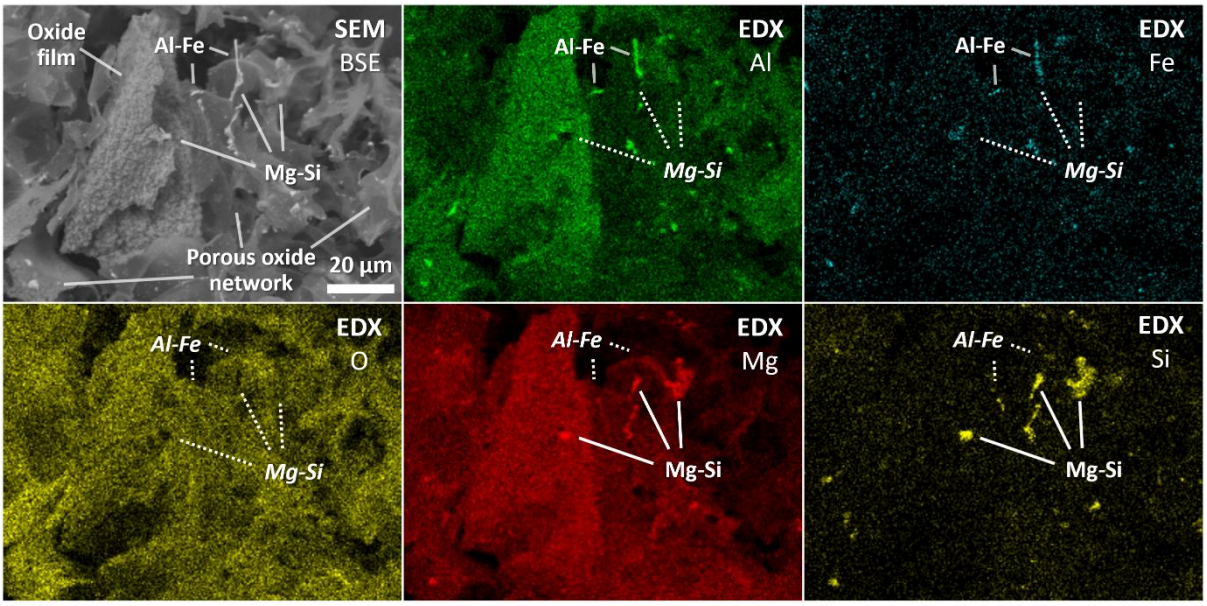


Figure 4.3. SEM/EDX of residue from butanol extraction of as-cast 0.00Ca sample. Residue consists of porous oxide networks with entrained debris, such as oxide films, and small intermetallic phases. EDX mapping indicates phases on the porous oxide networks (brighter in BSE imaging) to be Al-Fe and Mg-Si based (italicised labels and dashed lines indicate lack of presence in each element's EDX map).

Due to variation in surface orientation (Figure 4.3), quantitative EDX analysis is not reliable. Still, information can be inferred from the elemental distribution across the sample: intermetallic-forming elements, such as iron and silicon, are only found in isolated areas of the network, showing that the networks are oxide-based and not intermetallic-based.

Closer inspection of the extracted networks (Figure 4.4) reveals holes, showing them to be porous, and cracks reveal the thickness to be sub-micron. Again, small Al-Fe intermetallics,

appearing brighter in BSE (backscattered electron) imaging due to the presence of iron, are seen on the oxide surface. Larger sections of the porous oxide networks (Figure 4.5) reveal ridges and holes at regular intervals in two orthogonal directions, in a shape resembling "waffle fries"; the implications of this shape on the formation mechanism are explored later.

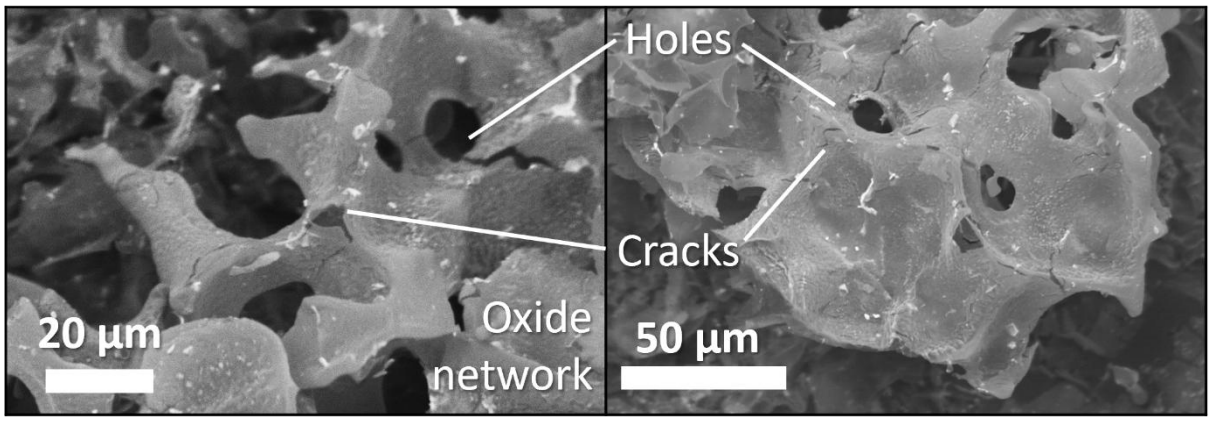


Figure 4.4. SEM (BSE) imaging of oxide networks with holes and cracks inside, revealing the thickness to be sub-micron.

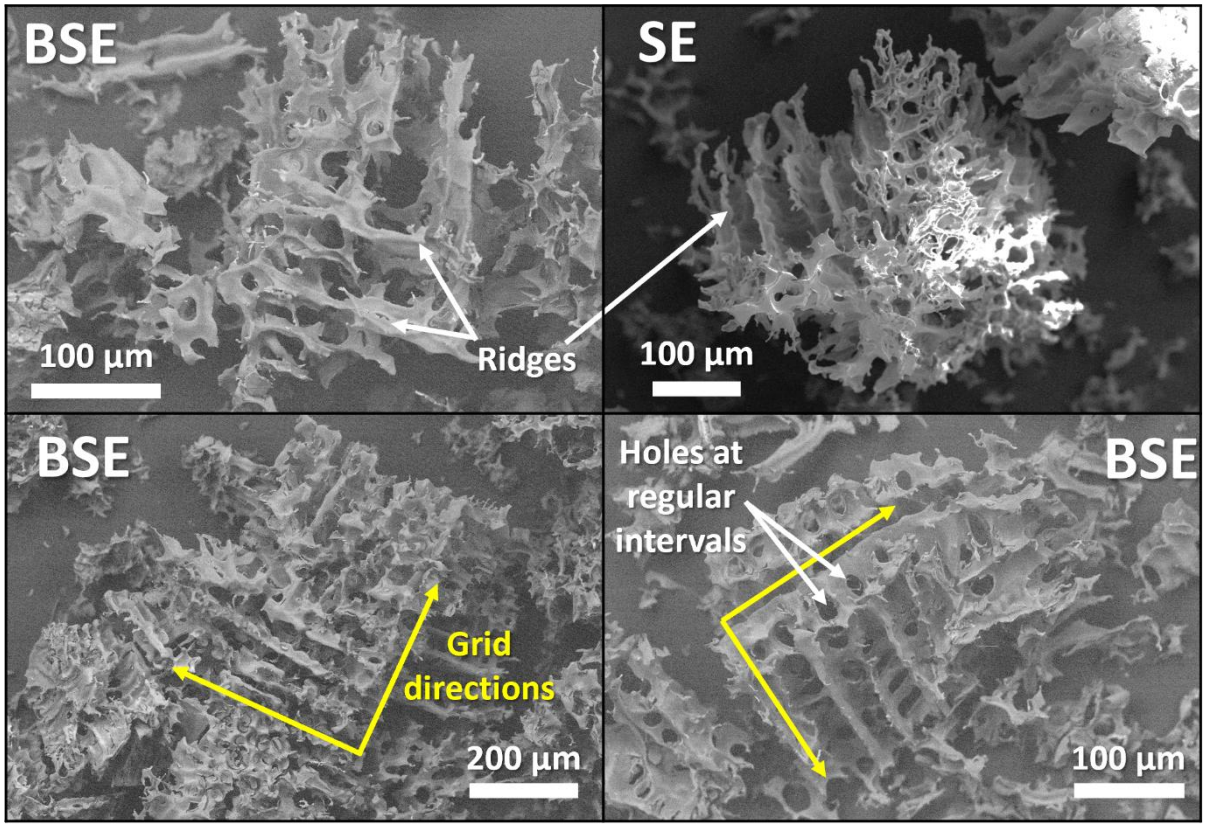


Figure 4.5. Larger extracted oxide fragments showing a 'waffle fries'-like morphology, with ridges in two orthogonal directions and holes at regular intervals.

SEM/EDX results of the metallographic samples show a uniform α-Al microstructure with porous networks (Figure 4.6). EDX analysis shows films attached to the porous networks to be

oxides. These films will be concluded to be bifilms, which will be discussed later. Whilst the shape of these porous networks is consistent with the porous oxide networks observed in the extracted samples, the presence of oxides within these pores cannot be confirmed yet: the oxide layers in the oxide networks from the extracted samples are of sub-micron thickness (Figure 4.4) and the detection of oxygen from within pores by EDX may be due to adsorption from the atmosphere or the presence of an oxide layer from the aluminium sample being exposed to the atmosphere during sample preparation.

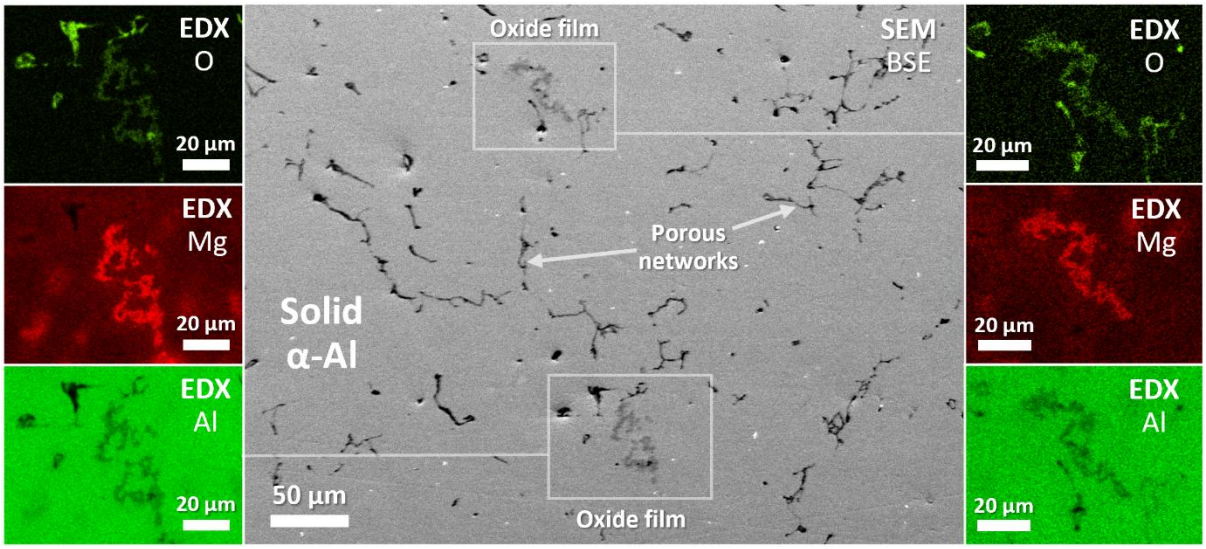


Figure 4.6. SEM/EDX imaging of 0.00Ca sample: uniform α-Al throughout, interspersed with porous networks. Some films are found attached to these networks, which are shown to be Mg-rich Al-Mg oxide films.

4.3.3. Tomography: before and after melting

Tomographs of the solid sample before melting (Figure 4.7) show a microstructure consistent with the metallographic samples: an α-Al matrix with porous networks extending through the sample. In the vertical sections, the part of the sample in the BN holder is fuzzier; this is because the field of view does not encompass the entire width of the BN holder, leading to this reconstruction artifact. Films are seen as solid white thin objects (Figure 4.8), whereas porous networks are interconnected regions of dark areas, indicating their porosity, in shapes resembling those seen in the metallographic samples (Figure 4.6). The outer oxide shell of the sample allows the macroscopic shape to remain largely intact. Films and some networks persist

after melting (Figure 4.8), indicating that within some networks there are solid objects which can coexist with an Al-Mg melt.

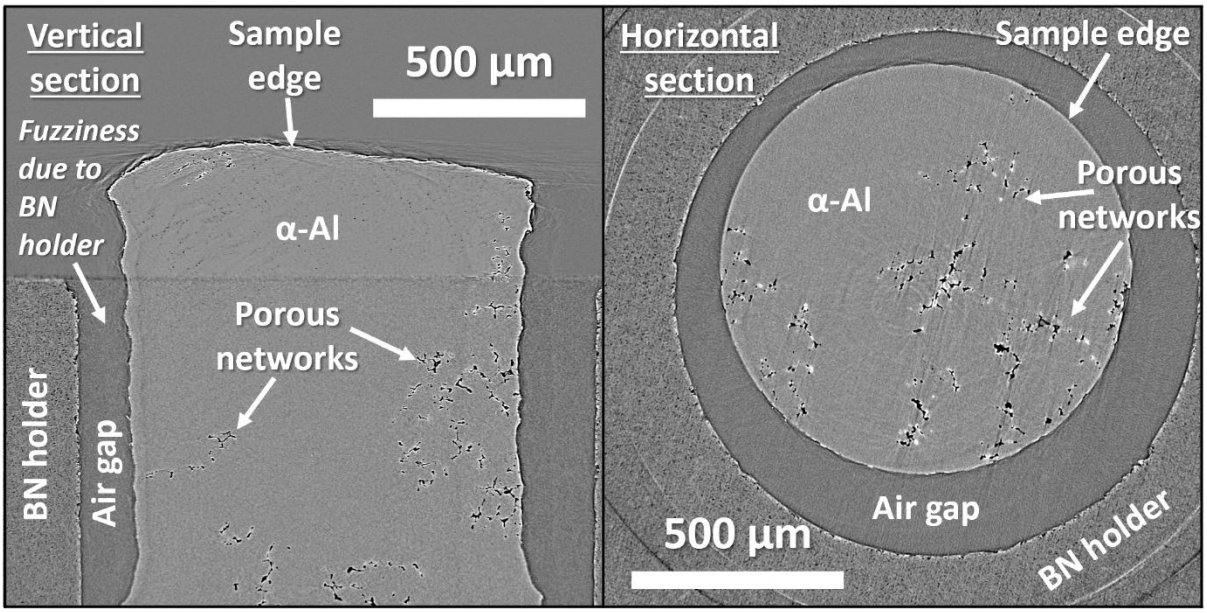


Figure 4.7. Horizontal and vertical tomographic sections of 0.00Ca sample before melting.

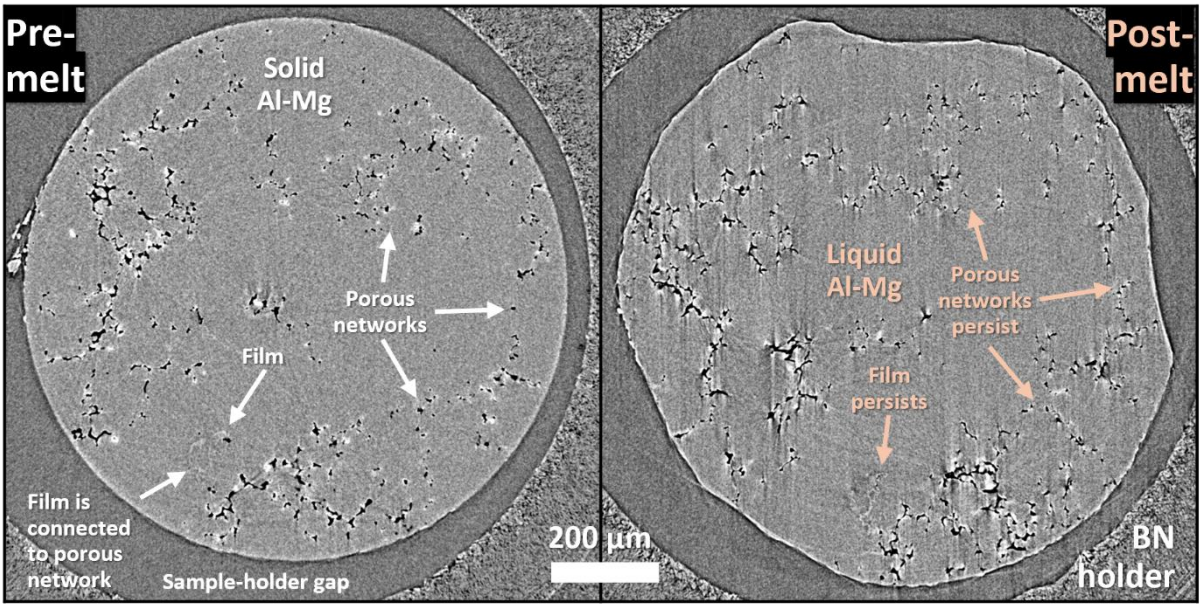


Figure 4.8. Horizontal sections of 0.00Ca sample before and after melting, showing persistence of films and porous networks within the melt and the sample shape.

All films found persist after melting (Figure 4.9) and are observed to be connected to either porous networks or the sample edge. Some porosity is found within the films, appearing as darker areas within the bright films, but generally much less porosity is found than in the porous networks to which they are attached. This porosity can also be seen in the SEM/EDX imaging, as small dark holes within the oxide films (Figure 4.6).

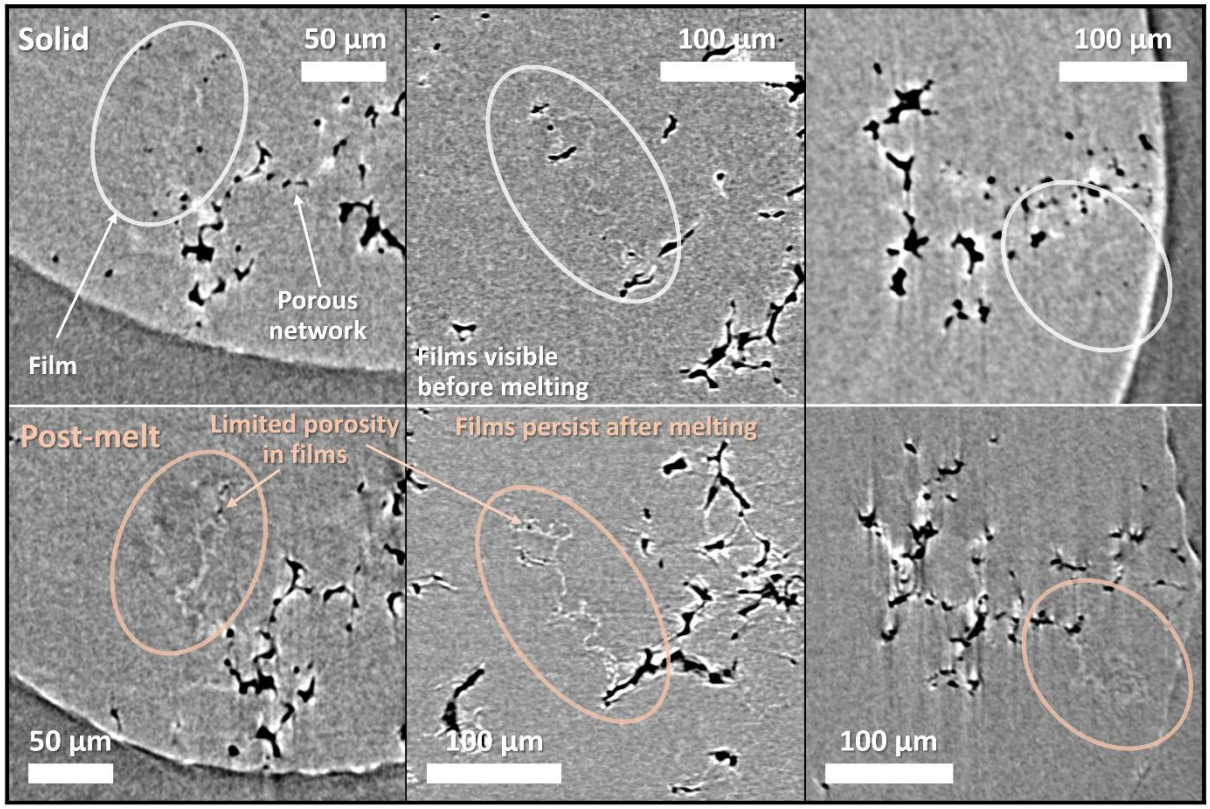


Figure 4.9. Tomographic sections showing persistence of films before and after melting in 0.00Ca sample.

Not all porous networks persist (Figure 4.10): during melting, boundaries between the solid regions become visible, and are observed to coincide with the porous networks (Figure 4.10.b). Some networks disappear after the sample melts, suggesting these networks to be interdendritic porosity, while others persist (Figure 4.10.c), indicating those networks to be solid objects.

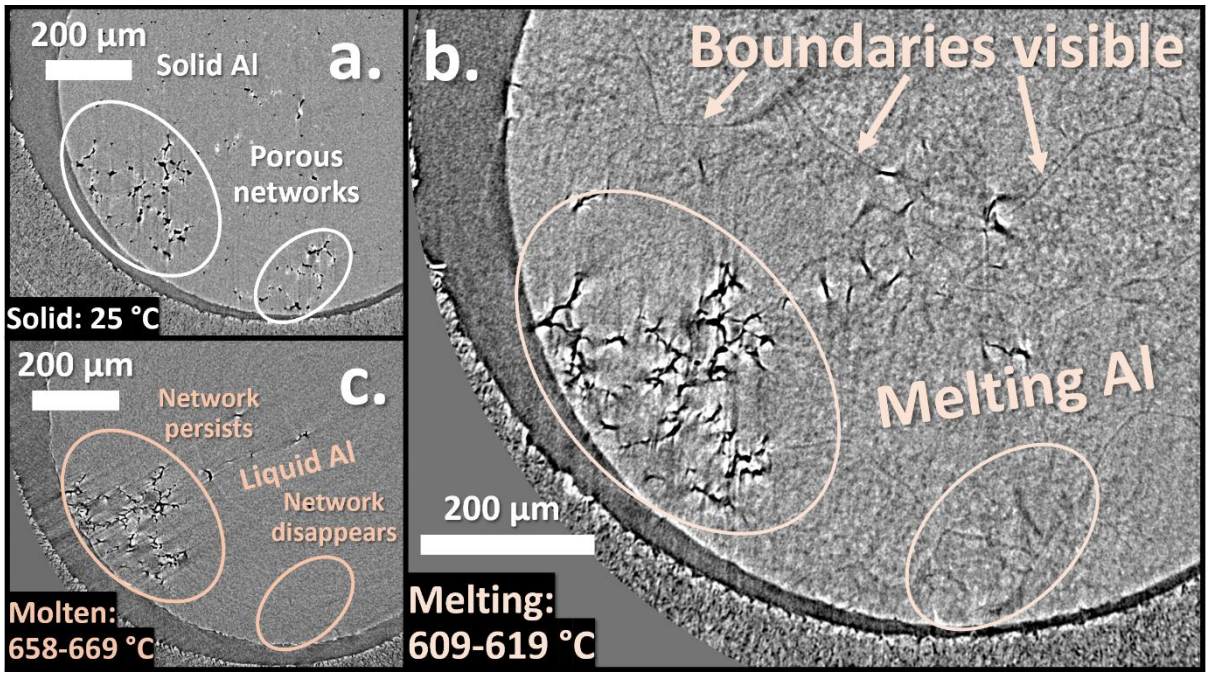


Figure 4.10. Horizontal tomographic snapshots of 0.00Ca sample (a) before, (b) during, and (c) after melting.

Since the films (Figure 4.9) and some networks persist, it is concluded that these two types of structure observed in tomography (Figure 4.8) are the oxide films and porous oxide networks found in the extracted samples, respectively (Figure 4.2).

4.3.4. Melt hold: oxidation

Over the three-hour melt hold at 750 °C, the sample oxidises. In tomography (Figure 4.11), this can be observed as the growth of more oxide via the original porous oxide networks, and an expansion of the space within the porous oxide networks. Furthermore, most of the sample surface remains intact with its shape unchanged. The lack of puncturing of the sample surface suggests melt oxidation occurs via porous oxide networks which impinge on the surface: the hollow interiors provide a path for oxygen gas to reach the melt, causing further oxidation.

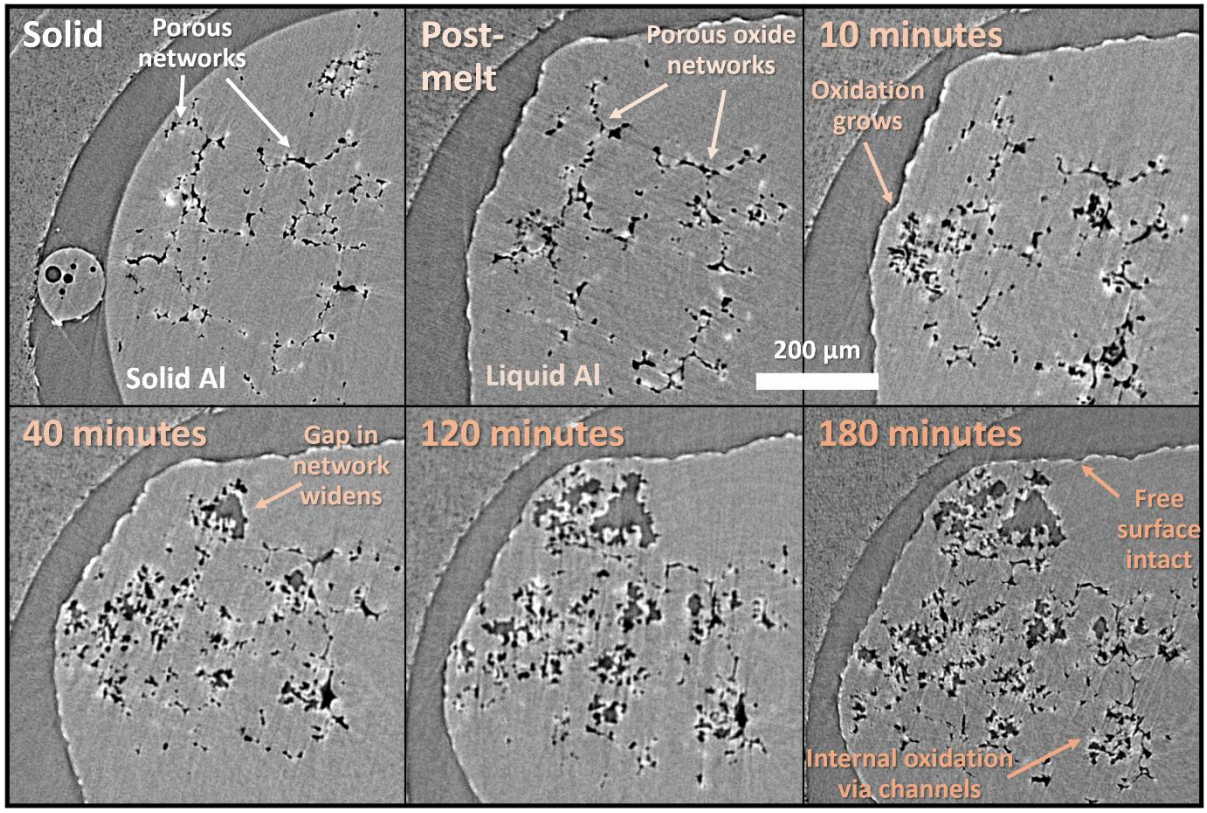


Figure 4.11. Horizontal sections of the 0.00Ca sample showing oxidation over the 3-hour melt hold.

Extracted samples imaged with SEM show consistent results (Figure 4.12): the Al-Mg oxide networks observed in the as-cast samples are seen again, but are now covered with granular, opaque Al-Mg oxides on their surface, grown during the melt hold.

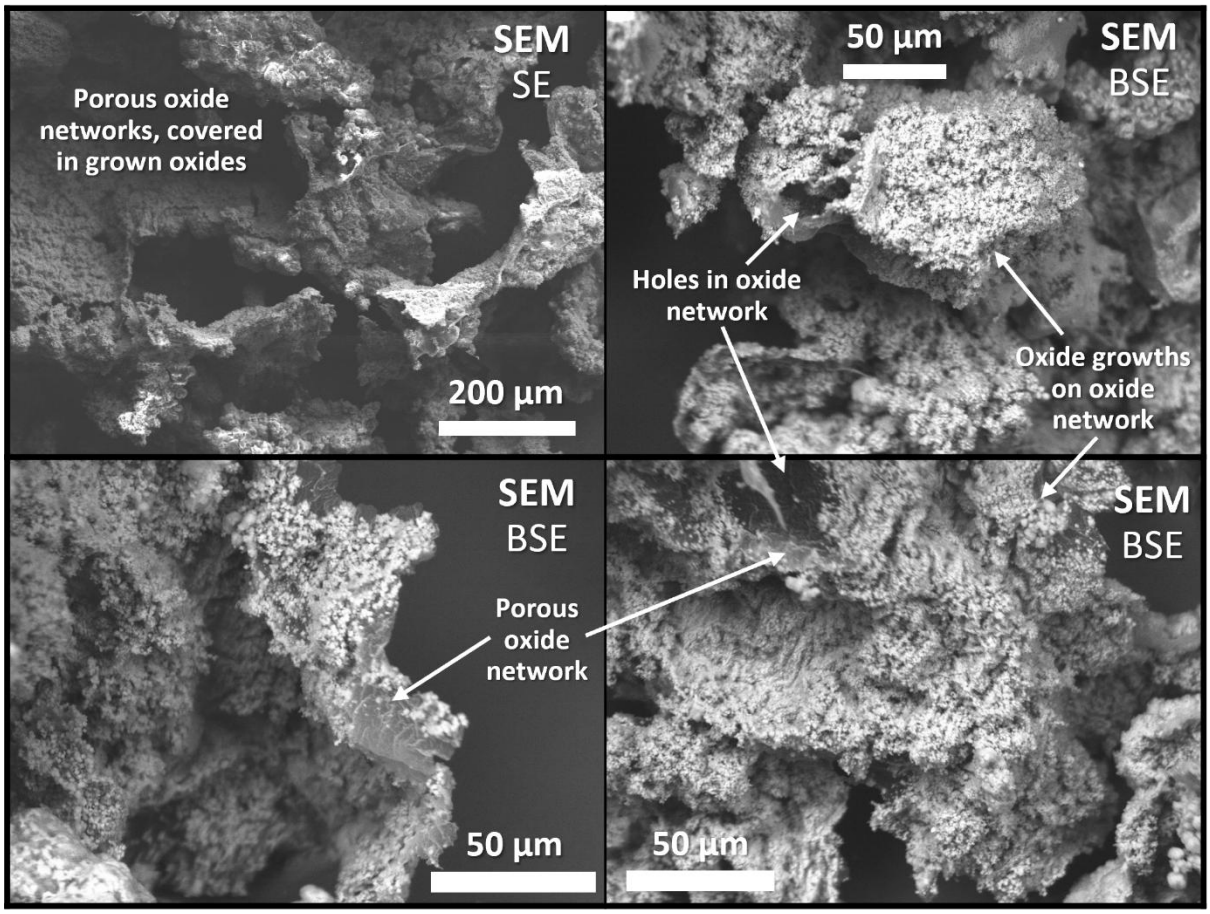


Figure 4.12. SEM imaging of 0.00Ca sample extracted after a 750 °C/3-hour melt treatment.

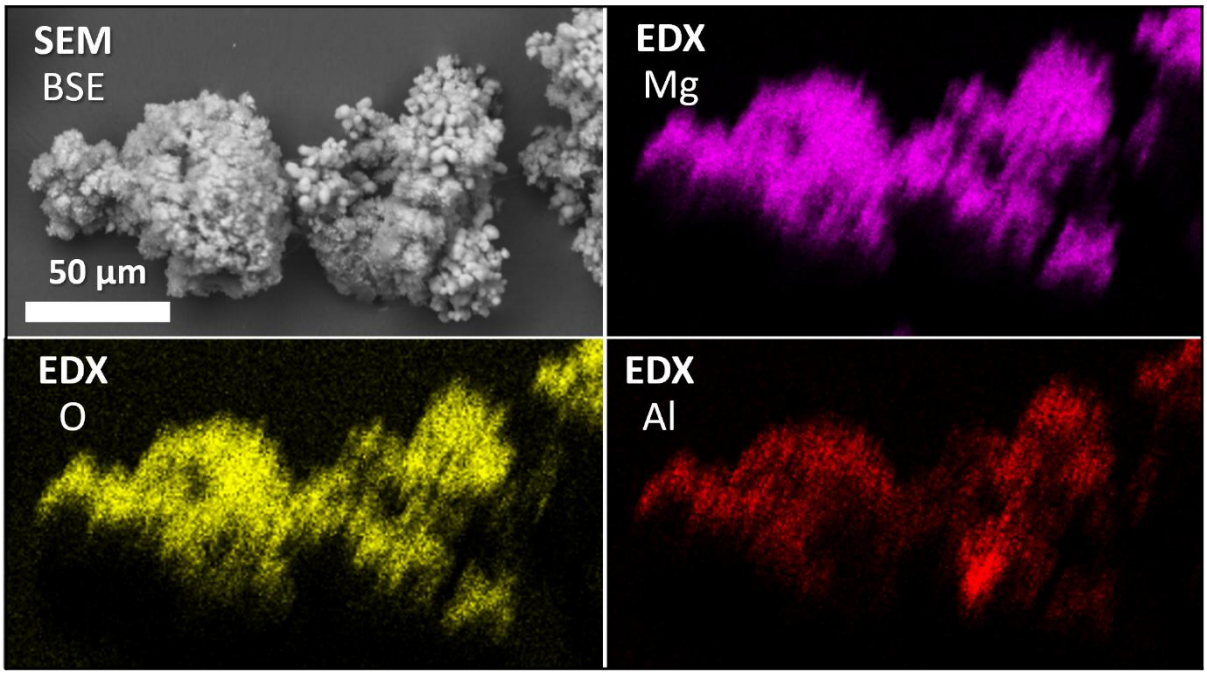


Figure 4.13. EDX mapping of residue extracted from 0.00Ca sample after 750 °C/3-hour melt treatment, showing them to be mixed Al-Mg oxides.

Holes are seen in these networks, confirming them to be porous and morphologically consistent with the samples extracted in the as-cast state (Figure 4.4). EDX analysis shows the structures

to be Al-Mg oxides (Figure 4.13), consistent with the tomographic observations of these structures forming by atmospheric oxidation.

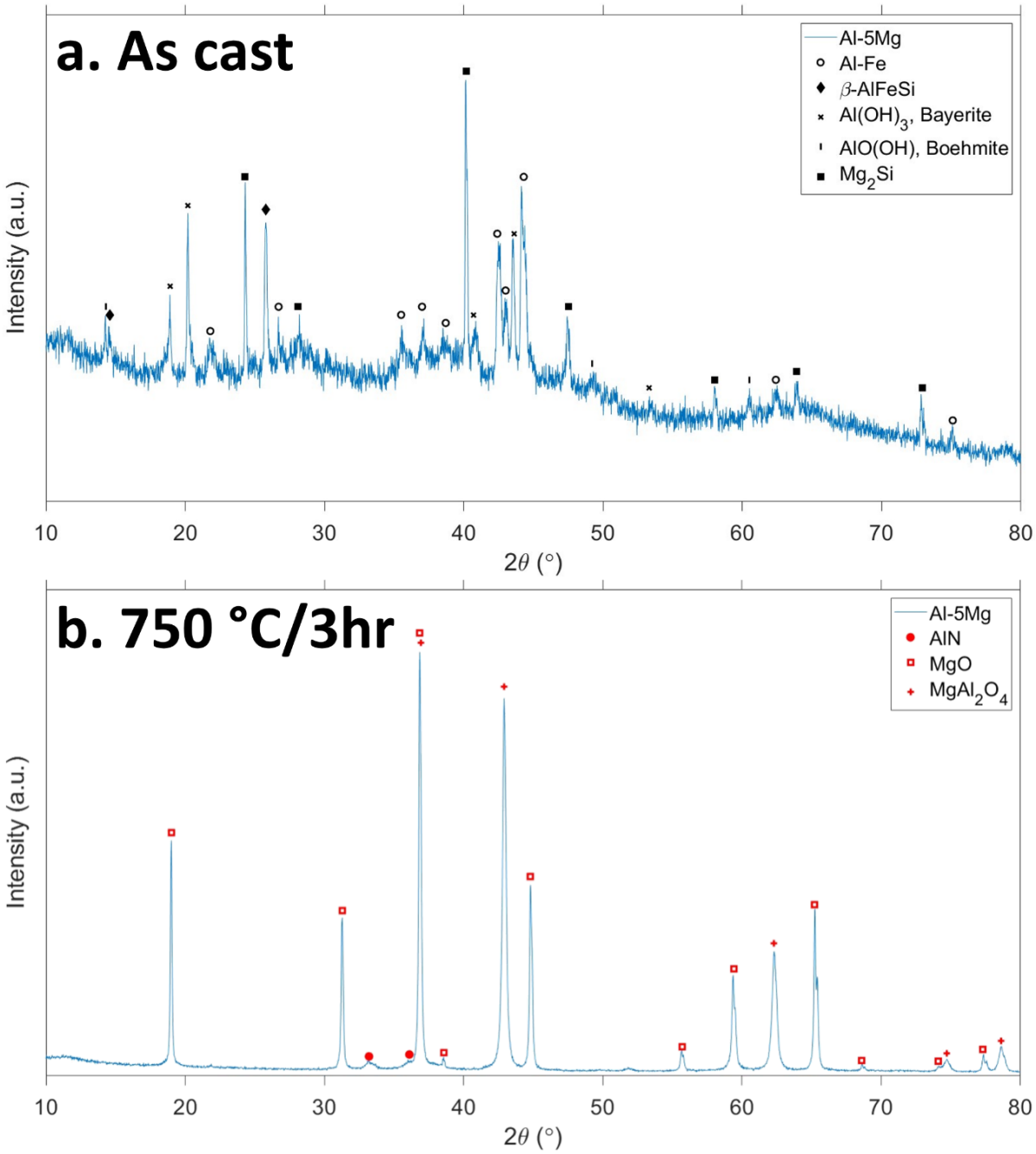


Figure 4.14. XRD analysis of (a) as-cast and (b) oxidised (750 °C, 3 hours) samples after butanol extraction. Crystallographic information can be found in Appendix D.

X-ray diffraction (XRD) performed on the samples extracted as-cast and after a 750 °C/3-hour melt treatment shows consistent results (Figure 4.14). In the XRD results of the as-cast extracted sample (Figure 4.14.a) the aluminium hydroxides bayerite ($Al(OH)_3$) and boehmite (AlO(OH)) are found, as well as both Al-Fe based ($Al_{13}Fe_4$, $Al_{13}Fe_3$, β-$Al_{4.5}FeSi$) and Mg-Si

based (Mg_2Si) intermetallics, as indicated by SEM/EDX analysis (Figure 4.3). XRD analysis of a sample extracted after 750 °C/3-hour melt hold (Figure 4.14.b) shows much more pronounced peaks, identified as MgO, $MgAl_2O_4$, and AlN. These three phases are not present in the as-cast samples, so are likely the products of oxidation (and nitridation) of the melt.

4.3.5. Tomography: solidification

Tomographs of solidification (Figure 4.15) show the dendrite boundaries forming as the sample cools, followed by porosity in the areas last to solidify.

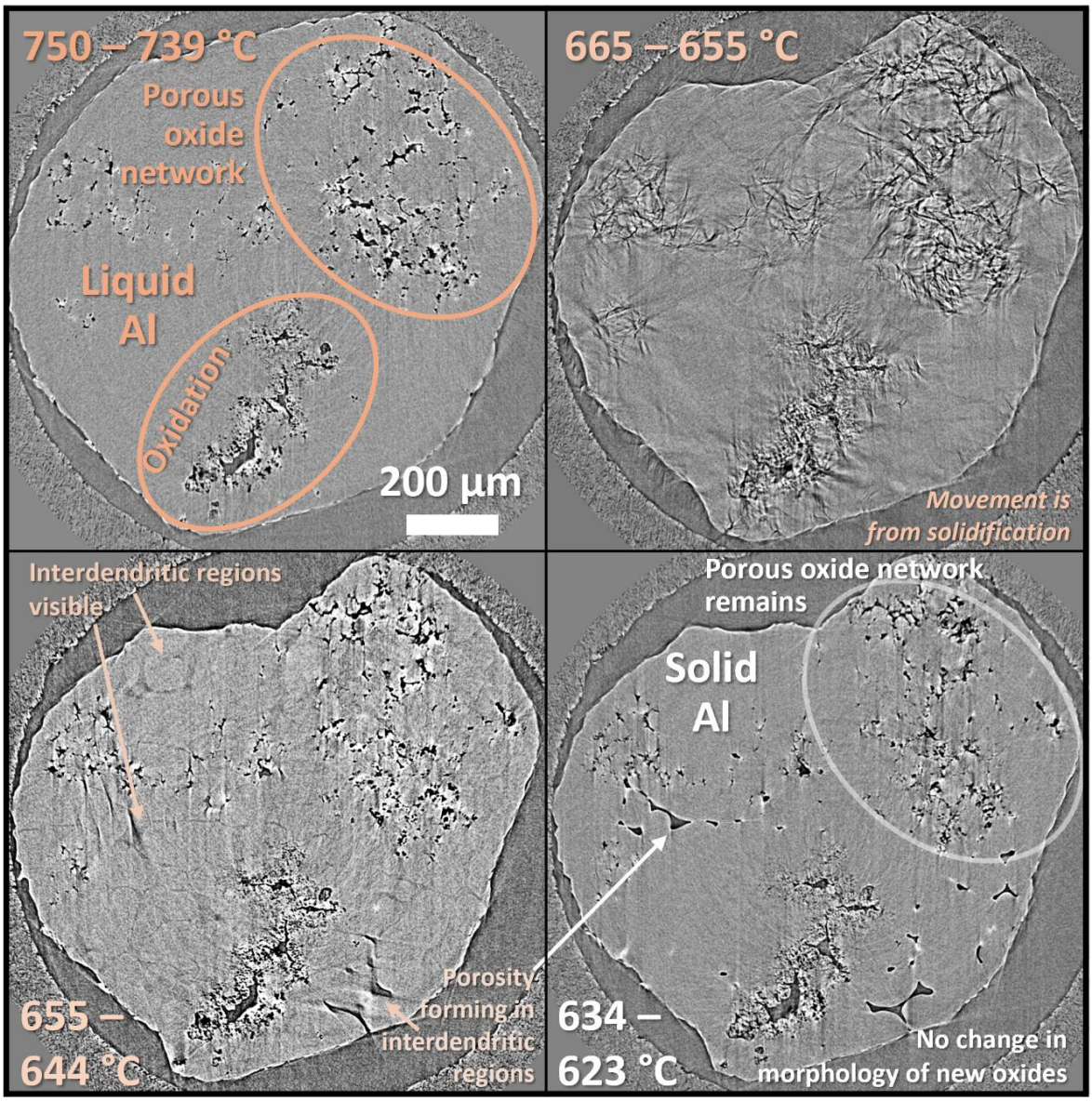


Figure 4.15. Horizontal sections of tomographic snapshots showing solidification.

No significant morphological changes are seen in the porous oxide networks, either those

existing from the cast sample or formed through oxidation. The expected solidification range in a Al-5Mg (wt.%) should be c. 640-580 °C, with some uncertainty arising from variation in composition and imprecise literature data on solidification temperature [4]; this range is similar but not exactly in the range observed by tomography (Figure 4.15), a discrepancy which could be due to the loss of magnesium over the melt hold, a lag due to the changing temperature, or a minor calibration error. However, since no conclusions are made based on the exact temperatures, only on the sequence of events over the solidification, this discrepancy is inconsequential, as is the case for melting temperatures.

4.3.6. Discussion

The observations above show that entrained oxides have been directly observed within molten aluminium melts for the first time. The persistence of porous networks after melting shows that a solid object is present in these networks (Figure 4.8): if not, the gas pockets would not maintain the complex shapes seen, since this does not minimise the surface energy between the liquid and the gas. Networks connected to interdendritic boundaries leave no discernible trace after the sample has fully melted (Figure 4.10), in contrast to the persistent porous networks, demonstrating differences between physically distinct porous networks in the sample that appear identical before melting.

Analysis of the extracted samples confirms that these persistent porous networks are oxide networks. Butanol reacts with the α-Al matrix to form aluminium butoxide and hydrogen gas through a redox reaction [5]. The formed aluminium butoxide dissolves within the excess butanol and can therefore be drained away. However, it does not react with common inclusions within aluminium samples, such as intermetallics and oxides; these are captured by the fine PTFE filter used in the process.

Historically, the dissolution of aluminium samples in butanol has been used to investigate intermetallic inclusions [5–7]. Whilst oxide particles have been found in extracted samples [7],

conventional sample preparation involves deliberate removal of the surface oxide using an acid etch [8], to allow the aluminium to react with the butanol and extract the included intermetallics more easily. This process, by design, destroys entrained oxides connected to the surface, so this step was omitted in this investigation to preserve any entrained oxides. This process alteration is a plausible explanation for the lack of prior observation of these extensive oxide networks in extracted samples.

Observing tomographic sequences during melting (Figure 4.10) and solidification (Figure 4.15) shows that it is difficult to distinguish between porous oxide networks and interdendritic porosity, which do not contain oxides, in solid samples (Figure 4.7): both exist as pore networks between dendrites, widest at the cell boundary triple points, without a discernible layer between the solid metal and the pore. The tomography pixel size (0.69 μm) is comparable to the sub-micron thickness of the oxide layer of the porous oxide networks (Figure 4.4), so the oxide layer is too thin to be resolved in tomography; it can only be revealed after melting by whether its shape is preserved, since porous oxide networks persist and regions of interdendritic porosity disappear.

Al-Mg based oxides can coexist with molten aluminium, shown by the structural integrity of the sample throughout the experiments (Figure 4.11), caused by the stiffness of the native oxide layer on the sample exterior. Intermetallic-forming elements such as iron and silicon are only seen in isolated regions of the extracted network while aluminium, magnesium, and oxygen are the only elements seen throughout the extracted networks (Figure 4.3). The morphology of the extracted networks is consistent with those observed in tomography: networks are porous with thin oxide layers, and the shapes convoluted and extensive (Figure 4.2).

X-ray diffraction confirms the phases indicated by SEM/EDX analysis (Figure 4.14). XRD peaks from Al-Fe based intermetallics are observed in the extracted as-cast sample (Figure 4.14.a), including β-$Al_{4.5}FeSi$, $Al_{13}Fe_4$, and $Al_{13}Fe_3$, the latter two being difficult to distinguish

due to many similar, overlapping peaks. Mg_2Si peaks are also found, explaining the co-existence of magnesium and silicon in the EDX mapping (Figure 4.3). The existence of boehmite and bayerite within the XRD trace from the as-cast sample can be explained by the hydration of either γ-Al_2O_3 [9] or amorphous Al_2O_3 (am-Al_2O_3) [10]. Initially-formed films on aluminium melts have been observed to be "liquid-like" [11] films of γ-Al_2O_3 or am-Al_2O_3 [12], only transforming to MgO and $MgAl_2O_4$ over a matter of minutes, as indicated by double-sigmoid curves present in thermogravimetric analysis (TGA) of Al-Mg alloys [13]. The characteristic atmospheric exposure time of the melt during pouring is significantly lower, so γ-Al_2O_3 or am-Al_2O_3 films should be expected.

The observation of boehmite and bayerite in the XRD results is therefore more likely due to atmospheric hydration between sample extraction and XRD testing: both boehmite and bayerite decompose well below the melt hold temperature of 750 °C [14], so these phases cannot coexist with molten Al-Mg. Furthermore, magnesium is found throughout the extracted networks (Figure 4.3), but no crystalline magnesium-containing oxides are observed in the XRD trace of the as-cast sample (Figure 4.14.a), which is consistent with the intercalation of magnesium into an amorphous oxide during pouring. Broad humps can be seen underneath the trace, which would be consistent with amorphous structures, but this is not conclusive. It is therefore most likely that the entrained porous oxide networks in the Al-Mg samples are γ-Al_2O_3 or am-Al_2O_3, and that boehmite and bayerite are observed in the XRD results due to hydration of γ-Al_2O_3 or am-Al_2O_3 by atmospheric moisture between butanol extraction and X-ray diffraction.

The oxide films seen are consistent with the description of bifilms [15]: whilst most of the cross-section of the observed films is closed without porosity, which would indicate that the oxide film is a single layer, small areas of porosity are seen within the films in SEM of the metallographic samples (Figure 4.6) as well as tomography (Figure 4.9), showing the presence of two distinct layers. These films are present from before the melt hold and do not form via

oxidation within the melt during the melt hold (Figure 4.11), so these films must have formed through entrainment during casting. These double-layered, entrained oxide films are therefore bifilms. Further evidence to this will be presented in later subchapters.

In general, these results show that the morphology of oxides in molten aluminium is more complex than previously believed (Figure 4.16): rather than simply bifilms, which are observed in the extracted samples (Figure 4.2), entrained oxides form extensive, porous, interdendritic networks, which contain both bifilms and intermetallics.

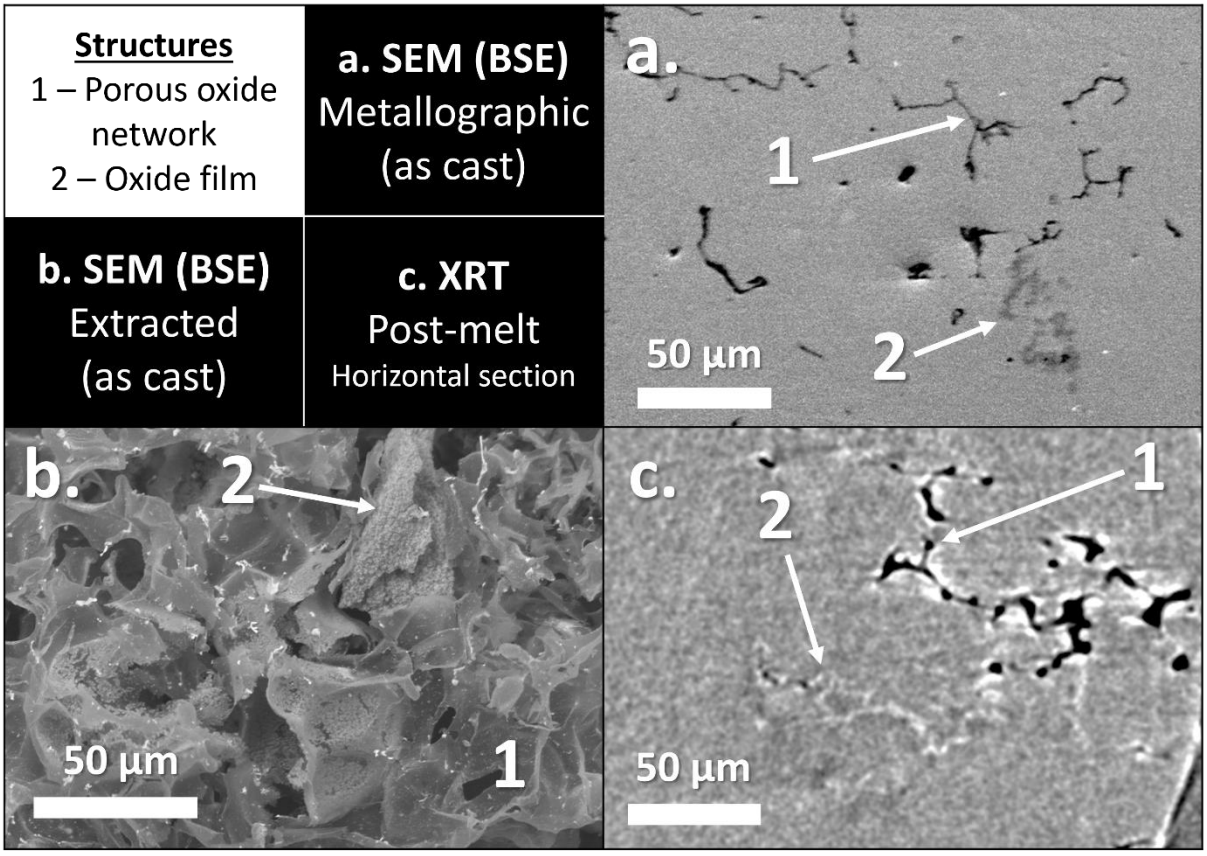


Figure 4.16. Summary of two oxide types observed within each methods used: (a) SEM of metallographic samples; (b) SEM of as-cast samples extracted with butanol, (c) X-ray tomographs post-melt. Two oxide types are (1) thin, porous oxide networks directly from the melt pour and (2) thick oxide films, from melt oxidation before pouring.

This dual oxide morphology can be explained by the entrainment process (Figure 4.17.a): while the melt to be cast is held in atmosphere, the melt reacts with oxygen to form a surface oxide skin. When the melt is poured, the surface oxide skin breaks up and is entrained with the poured metal. The breakup of the thicker surface oxide exposes the poured metal to the atmosphere, which itself reacts with atmospheric oxygen to form a thinner oxide layer.

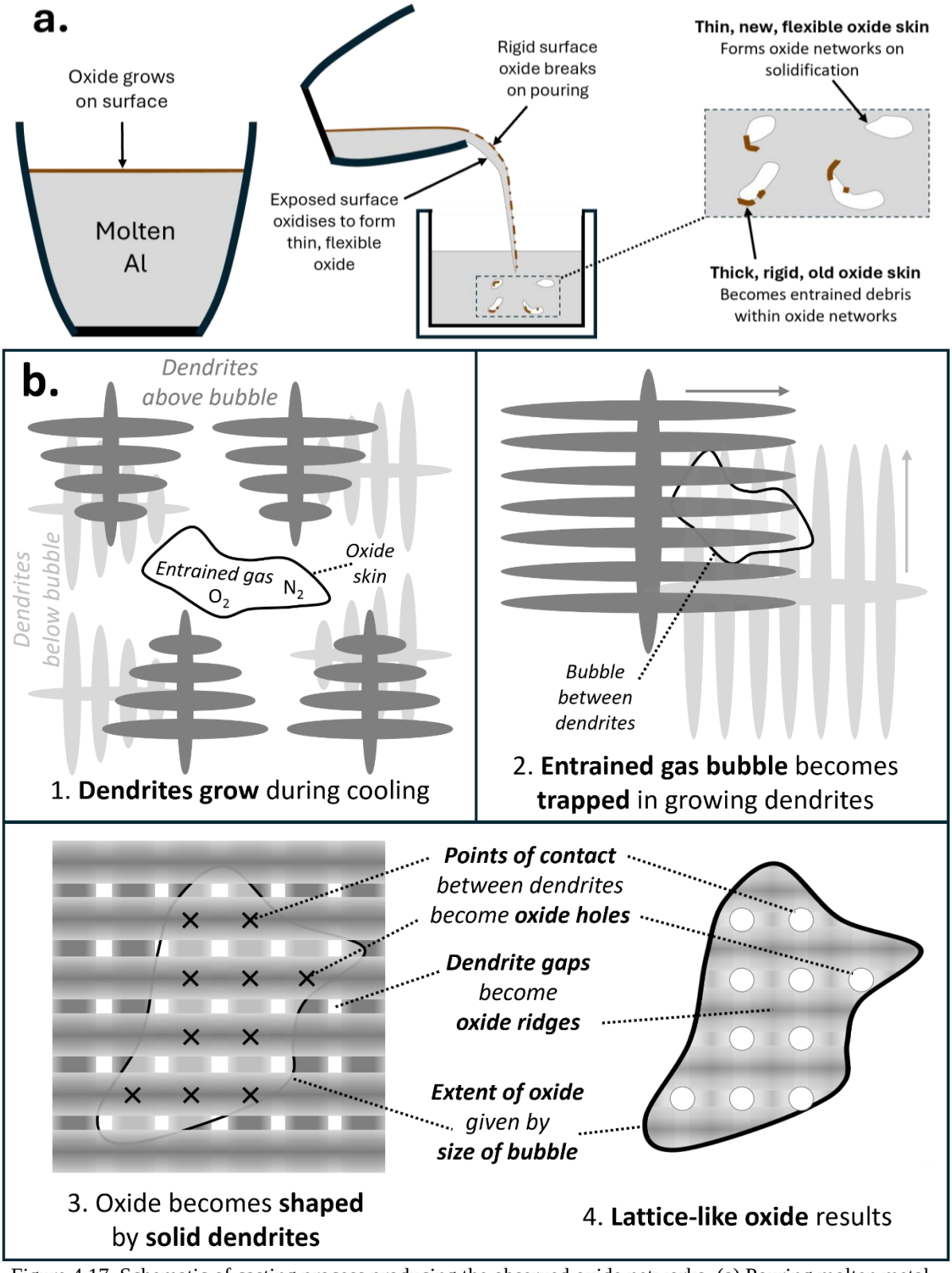


Figure 4.17. Schematic of casting process producing the observed oxide networks. (a) Pouring molten metal results in at least two types of oxide: one from exposure of the melt during melting and holding before casting, on the order of at least seconds, and one from the pouring of the metal itself, whose exposure time is orders of magnitude less than seconds. (b) Explanation of the "waffle fries"-like oxide morphology by dendrite pushing.

However, this new oxide from pouring forms over a much shorter time than the surface oxide from the melt hold and is therefore far thinner and more flexible: thicknesses of dynamically

formed films in Al-Mg melts of similar composition (5.5 wt.% Mg) at 670 °C studied by an oxide-metal-oxide sandwich technique were approximately 50 nm [16]. The oxide networks seen in the extracted samples are also of sub-micron thickness (Figure 4.4) and so cannot be resolved as layers themselves in the tomographs, whereas the oxide films (Figure 4.2) are thicker (1-10 μm) and can be resolved with tomography (Figure 4.9). This entrainment process therefore results in two distinct morphologies of oxide: thick (c. 1-10 μm) 'old' oxide skins from before pouring, and thin (< 1 μm) 'new' oxide skins formed during the pour itself.

The "waffle fries"-like shape seen in the oxide networks (Figure 4.5) can be explained by the shaping of entrained oxide bubbles by solidifying dendrites (Figure 4.17.b): entrained gas bubbles will be surrounded by a flexible oxide skin, through reaction of oxygen within the entrained gas with the melt. As dendrites form and grow during solidification, these bubbles become trapped between advancing dendrites and are pushed to the interdendritic boundaries. Owing to its flexibility from its short formation time, the entrained gas bubbles become moulded by the advancing dendrites, forming porous oxide networks.

Where the dendrites contact each other, there is a hole in the oxide, and where the gap between dendrites is greatest is a ridge. The regular spacing of the dendrites produces holes and ridges at regular intervals, which is reflected by the "waffle fries"-like shape of the oxide networks (Figure 4.5). The trapped gas inside the oxides results in an open space inside, which can be expanded by any hydrogen expelled from the liquid upon solidification. The concept of entrained oxide networks being shaped by solidifying dendrites has been previously speculated [15], but isolated oxides with this confirmatory morphology have not been observed, nor any 3-D 'waffle fries'-like shape hypothesised.

The tomographic data suggests that the melt oxidation on holding occurs primarily through entrained oxide networks (Figure 4.11). Oxides extracted after a 750 °C/3-hour melt hold also show the formation of small grainy structures on the surfaces of entrained oxide networks

(Figure 4.12), which are confirmed by EDX mapping (Figure 4.13) and XRD (Figure 4.14.b) to be oxides. It is well-established that Al-Mg melts produce MgO and $MgAl_2O_4$ when oxidised, with the most thermodynamically stable oxide at this temperature and composition being MgO [17], but the involvement of entrained oxide networks has not previously been speculated. Some researchers have speculated that the melt may move through pores by capillary action [18], acknowledging the existence of channels between the atmosphere and melt through an oxide layer, and that porous oxide networks may provide channels for corrosion through a surface oxide film [19], but the idea that porous oxides are involved in mediating melt oxidation is novel.

4.3.7. Preliminary conclusions

The observations in this subchapter constitute the first direct observation of entrained oxides and bifilms in aluminium alloy melts and therefore remove any doubt over their existence. Entrained oxides are found to be more morphologically complex than previously understood, forming extensive networks with two distinct populations of oxide: a convoluted network of thin (<1 μm), flexible, porous oxides formed by exposure of the melt to the atmosphere during the pour and shaped by solidifying dendrites which contain or are attached to thicker (1-10 μm) oxides resembling bifilms which form from melt oxidation before the final pour. Al-Mg melt oxidation is found to be facilitated by these entrained porous oxide networks which impinge on the sample exterior, since the porous interior provides a conduit for reactive gases to enter the sample and react with the melt.

4.4. Effect of calcium addition on melt oxidation

4.4.1. Overview

This sub-chapter focuses on observations of the effects of calcium addition on the oxides found in Al-Mg samples and on melt oxidation itself. Firstly, TGA results are presented to confirm

that calcium addition suppresses oxidation. Then, like the previous subchapter, findings of the as-cast samples (extracted, metallography, tomography) are presented for the 0.01Ca and 0.03Ca samples, followed by tomography of the molten samples and analysis of extracted samples to discuss structural development over the melt hold.

4.4.2. Thermogravimetric analysis (TGA)

The TGA results indicate that calcium suppresses oxidation of Al-Mg alloys (Figure 4.18). In the first few minutes (Figure 4.18.a), all samples show a mass increase which slows over time. This initial mass increase is largest for the 0.00Ca sample and smallest for the 0.03Ca sample, showing oxidation suppression to increase with calcium concentration. After this initial stage, both the 0.00Ca and 0.01Ca samples experience breakaway oxidation, with the extent of oxidation increasing significantly (Figure 4.18.b).

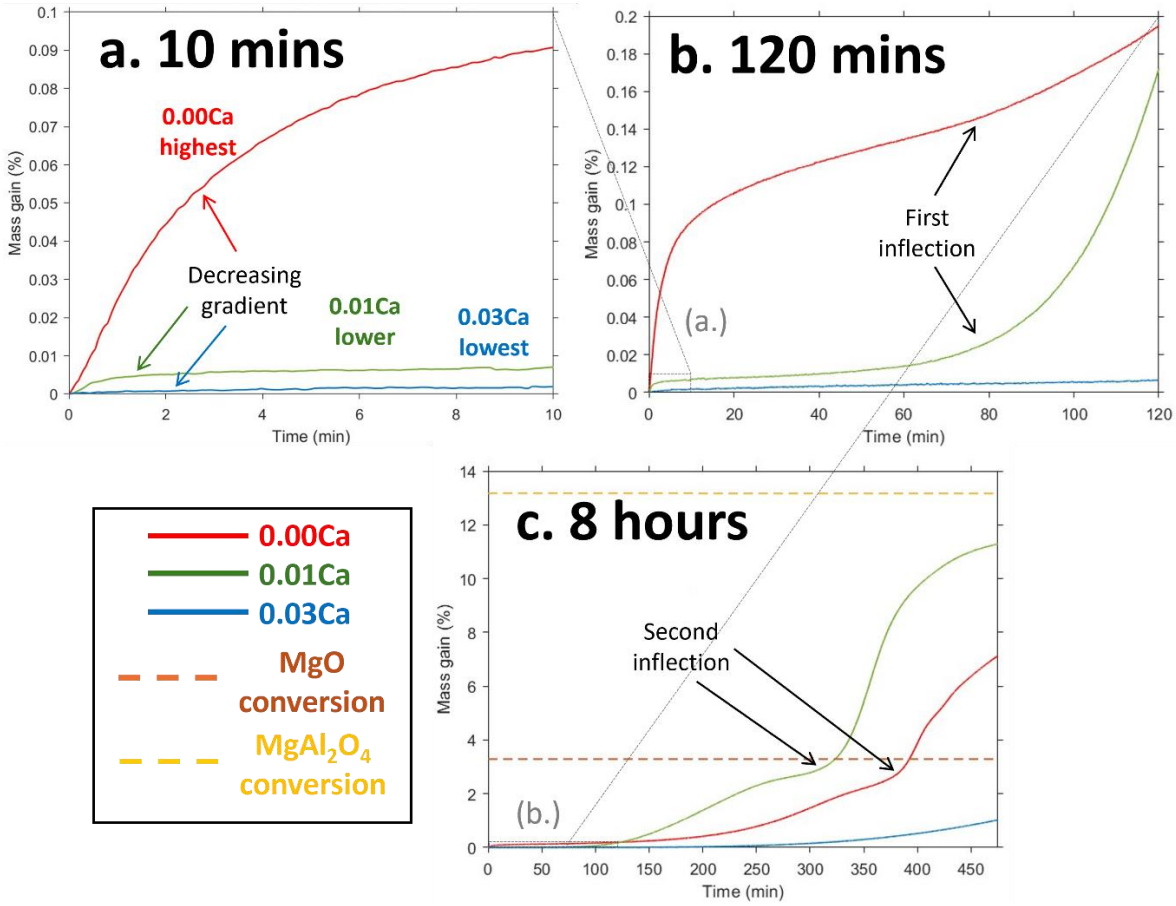


Figure 4.18. TGA results of samples held at 750 °C for eight hours in air in (a) the first two hours and (b) the full eight-hour exposure, with dashed lines indicating the expected mass gain should all the magnesium in the sample oxidise to MgO or $MgAl_2O_4$, respectively.

The 0.03Ca sample did not undergo breakaway oxidation over eight hours. Both the 0.00Ca and 0.01Ca sample curves have inflection points, at which the oxidation rate increases: the first corresponds to the formation of MgO and the second corresponds to the growth of $MgAl_2O_4$, shown by the dashed lines (Figure 4.18.c) indicating the expected mass gain should all the magnesium in the sample be converted to MgO or $MgAl_2O_4$ respectively.

4.4.3. Before melting

SEM analysis (Figure 4.19) of the extracted as-cast 0.01Ca sample shows oxide networks, like those found in the 0.00Ca sample (Figure 4.4). These networks show trapped oxide debris emerging from or completely contained within the oxide structures (Figure 4.19.b), and intermetallics on the surface, as indicated by bright areas in BSE imaging (Figure 4.19.d). Holes can also be seen in the oxide networks (Figure 4.19.e), and oxide films attached also (Figure 4.19.f).

SEM/EDX mapping (Figure 4.20) shows the networks to be Al-Mg oxides, with some parts more aluminium-rich and other parts more magnesium-rich. Elements indicating intermetallics, namely silicon and iron, are only found in limited areas, showing the networks to be oxide-based and not intermetallic-based. Silicon is associated with magnesium and aluminium with iron, indicating the presence of Mg-Si and Al-Fe phases, respectively. Calcium is hard to detect due to its small concentration but appears to be associated with silicon, suggesting Ca-Mg-Si intermetallics. In the 0.03Ca sample, extracted samples show oxide networks like those seen in the 0.00Ca and 0.01Ca samples (Figure 4.21).

The encapsulation of oxide debris is shown well by comparing SEM images taken by secondary electron (SE) imaging versus BSE imaging (Figure 4.21). In BSE imaging, elemental contrast dominates, showing intermetallics to appear brighter (due to the presence of iron) than the oxide networks, but entrained oxide debris, being of similar composition to the oxide networks, does not stand out. However, in SE imaging, topographic contrast dominates, which reveals

two main features. Firstly, large pieces of entrained oxide debris within oxide networks (e.g. red circle, Figure 4.21.a) appear rough in BSE imaging, but in SE imaging appear similar in texture to the rest of the oxide network. This shows that this piece of debris is within the oxide network, supporting the hypothesis that it is entrained.

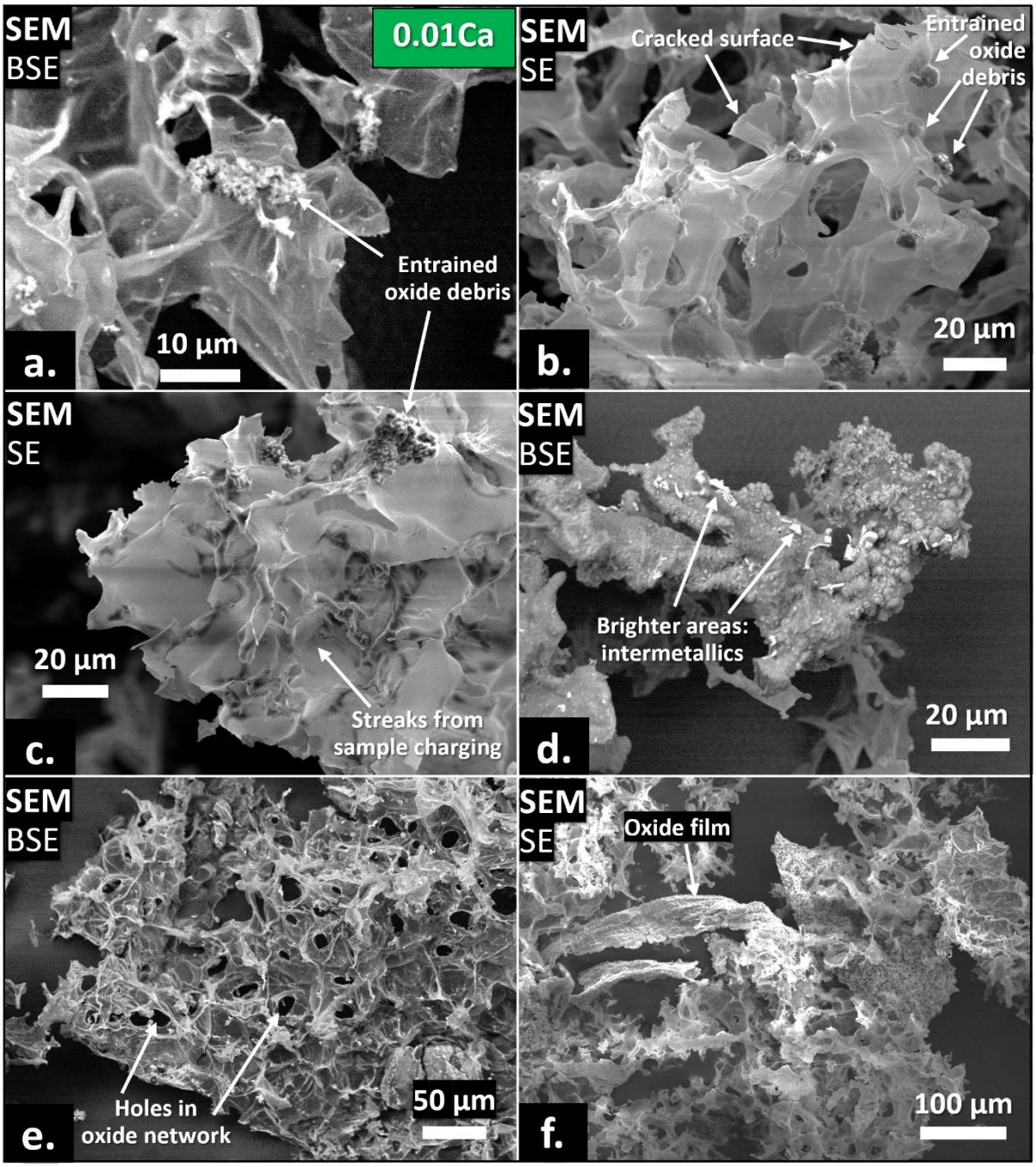


Figure 4.19. Extracted oxide networks from 0.01Ca sample showing (a, b, c) entrained oxide debris emerging from the networks, (d) intermetallics on the surface, (e) holes in the oxide network, (f) oxide films attached.

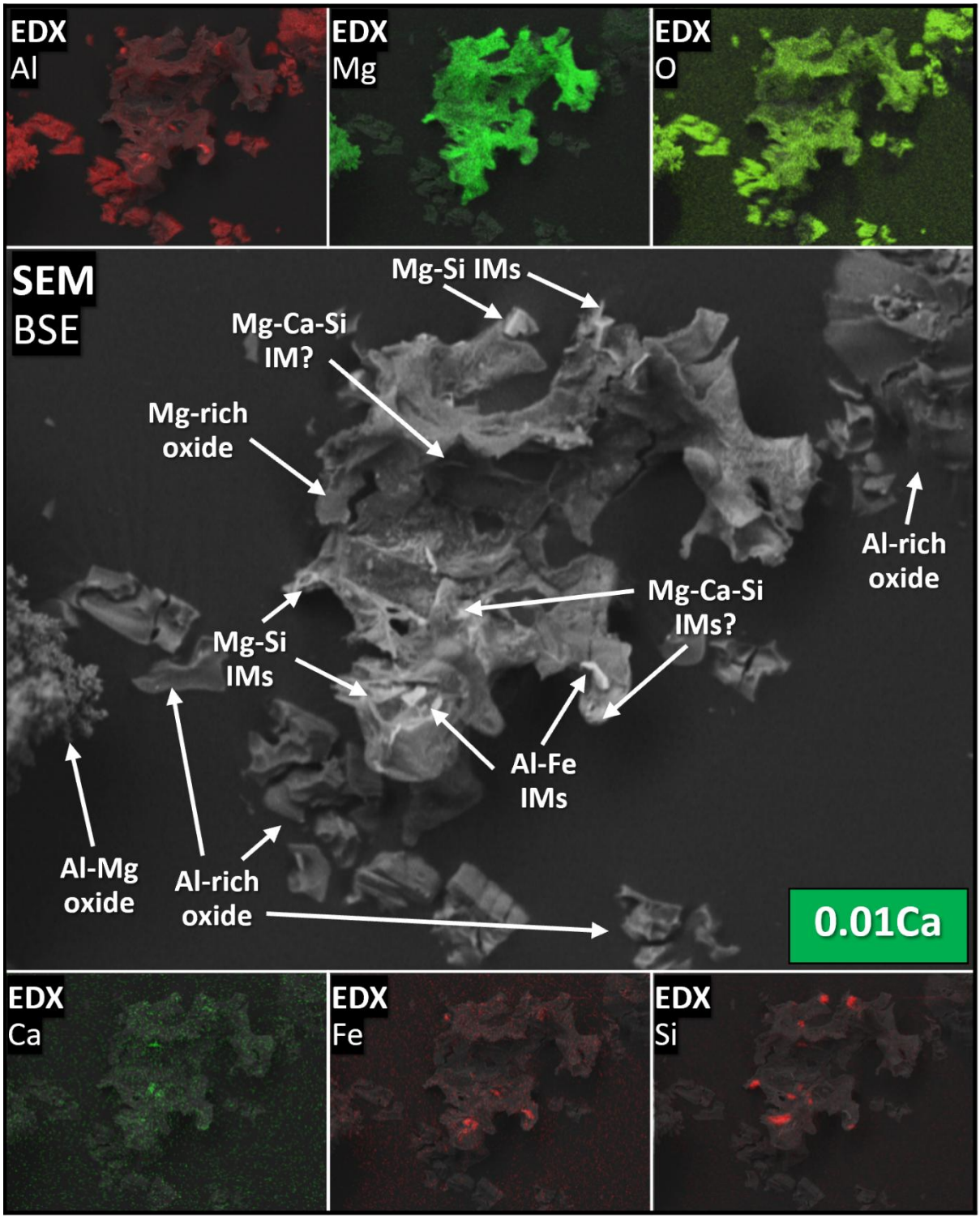


Figure 4.20. SEM/EDX mapping of an extracted oxide from the as-cast 0.01Ca sample.

Secondly, smaller pieces of trapped oxide debris (Figure 4.21.b) can be identified as dark spots in SE imaging which are not bright in BSE imaging (which would indicate an Al-Fe intermetallic). In this figure, cracks in the networks again show the sub-micron thickness of the oxide networks. Other fragments (Figure 4.22) show entrained oxide films, cracks showing the

sub-micron thickness of the network, and the 'waffle fries'-like grid pattern indicating the network to be shaped by solidifying dendrites.

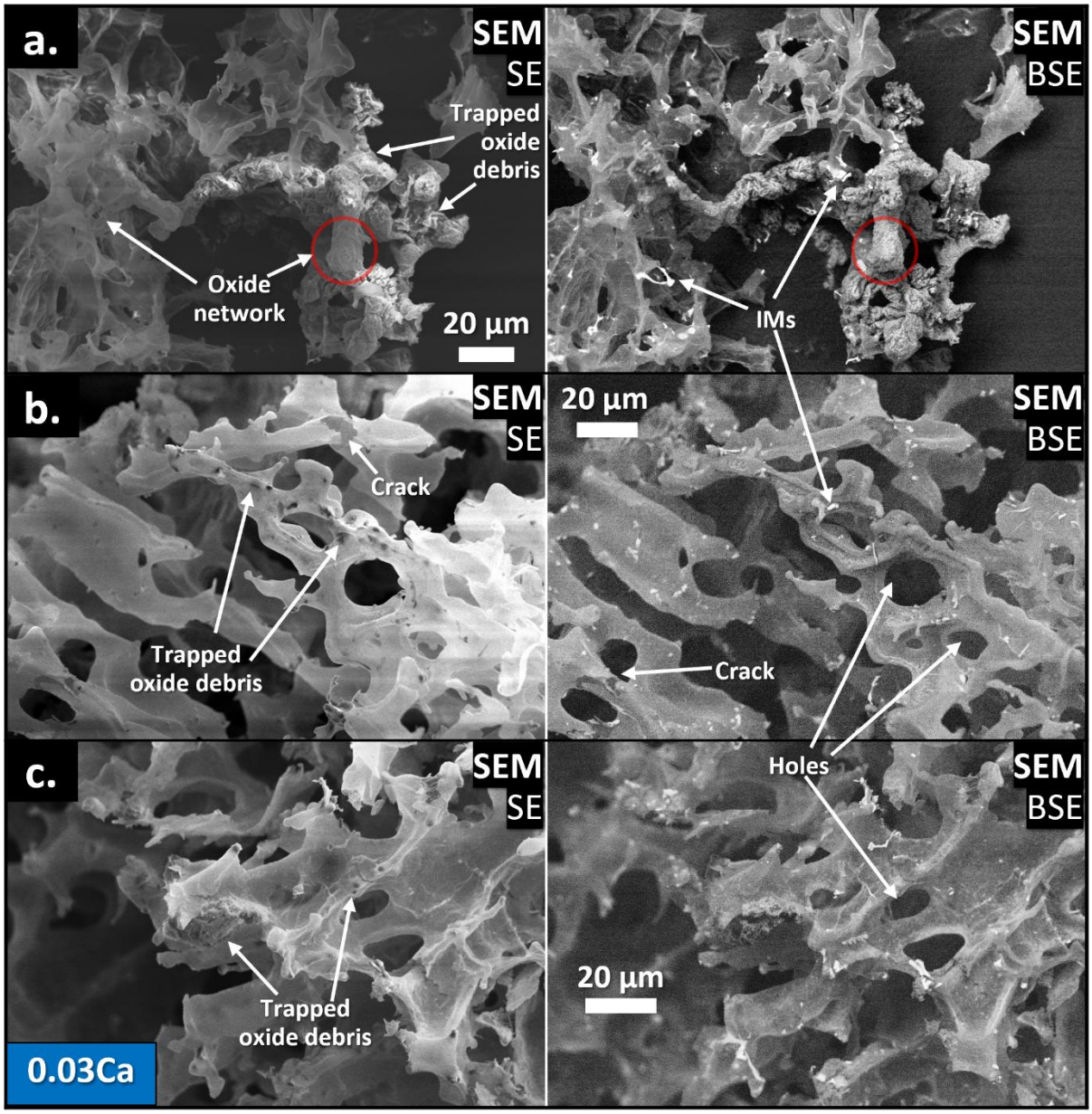


Figure 4.21. SEM imaging of oxide networks from extracted as-cast 0.03Ca samples with side-by-side comparison of SE and BSE imaging modes to show oxide entrainment in three locations (a, b, c).

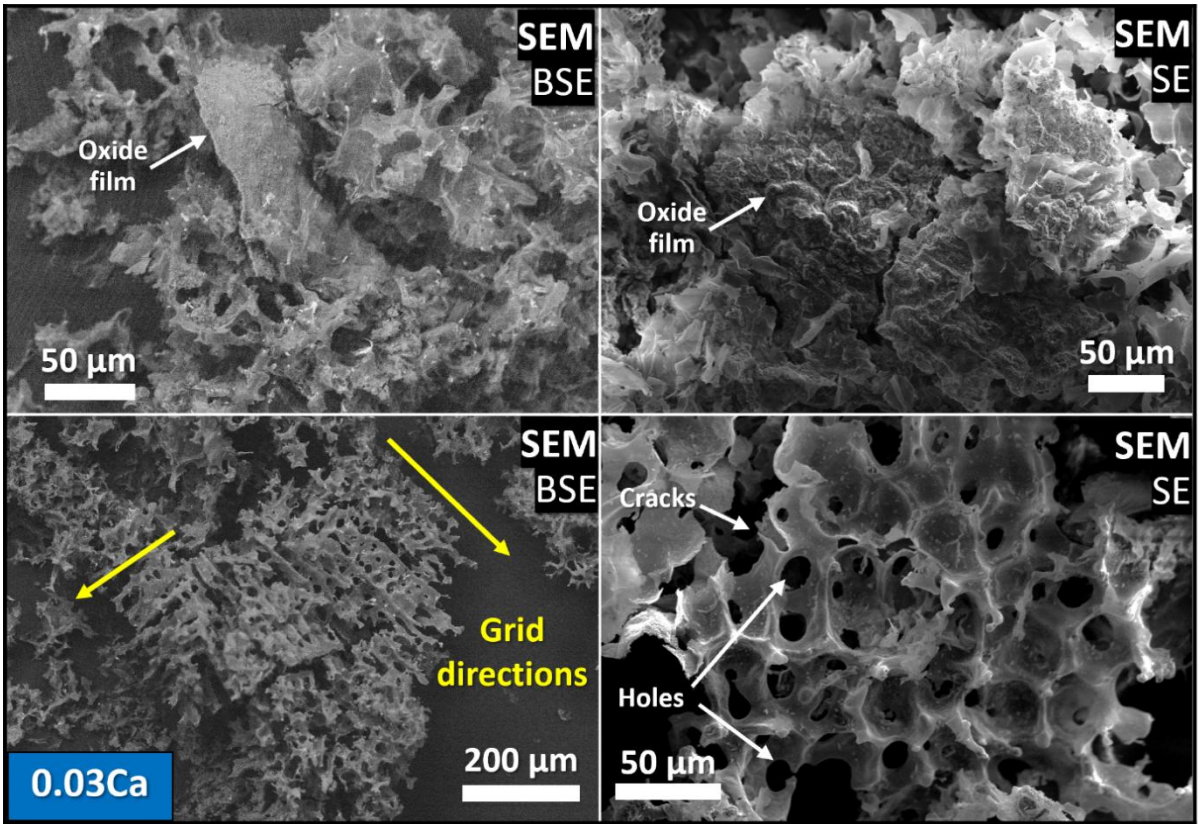


Figure 4.22. SEM imaging of the as-cast 0.03Ca sample, showing entrained oxide films (top row), holes and cracks which show the sub-micron thickness (bottom right), and the 'waffle fries' morphology (bottom left).

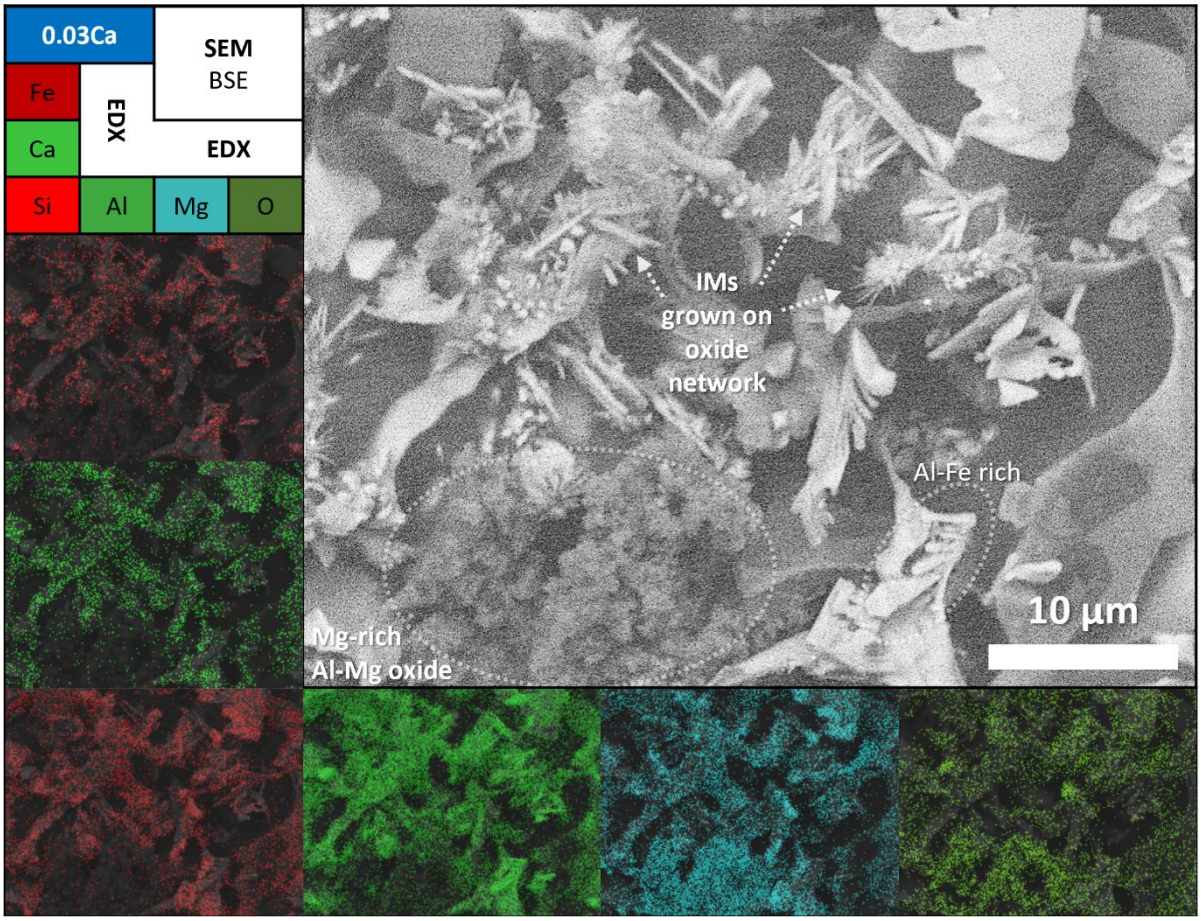


Figure 4.23. SEM/EDX mapping of extracted as-cast 0.03Ca showing intermetallics on the oxide network.

One oxide network in the 0.03Ca appears to have grown intermetallics (Figure 4.23). Needles rich in intermetallic-forming elements (Ca, Fe, Si) can be seen emanating from the networks, suggesting growth from the network, as this morphology is hard to explain if intermetallics had not grown from the networks. While the elemental distribution may indicate that this is an intermetallic network, oxide network forming elements (Al, Mg, O) are also found throughout, so it is more likely that intermetallics have formed on an oxide network.

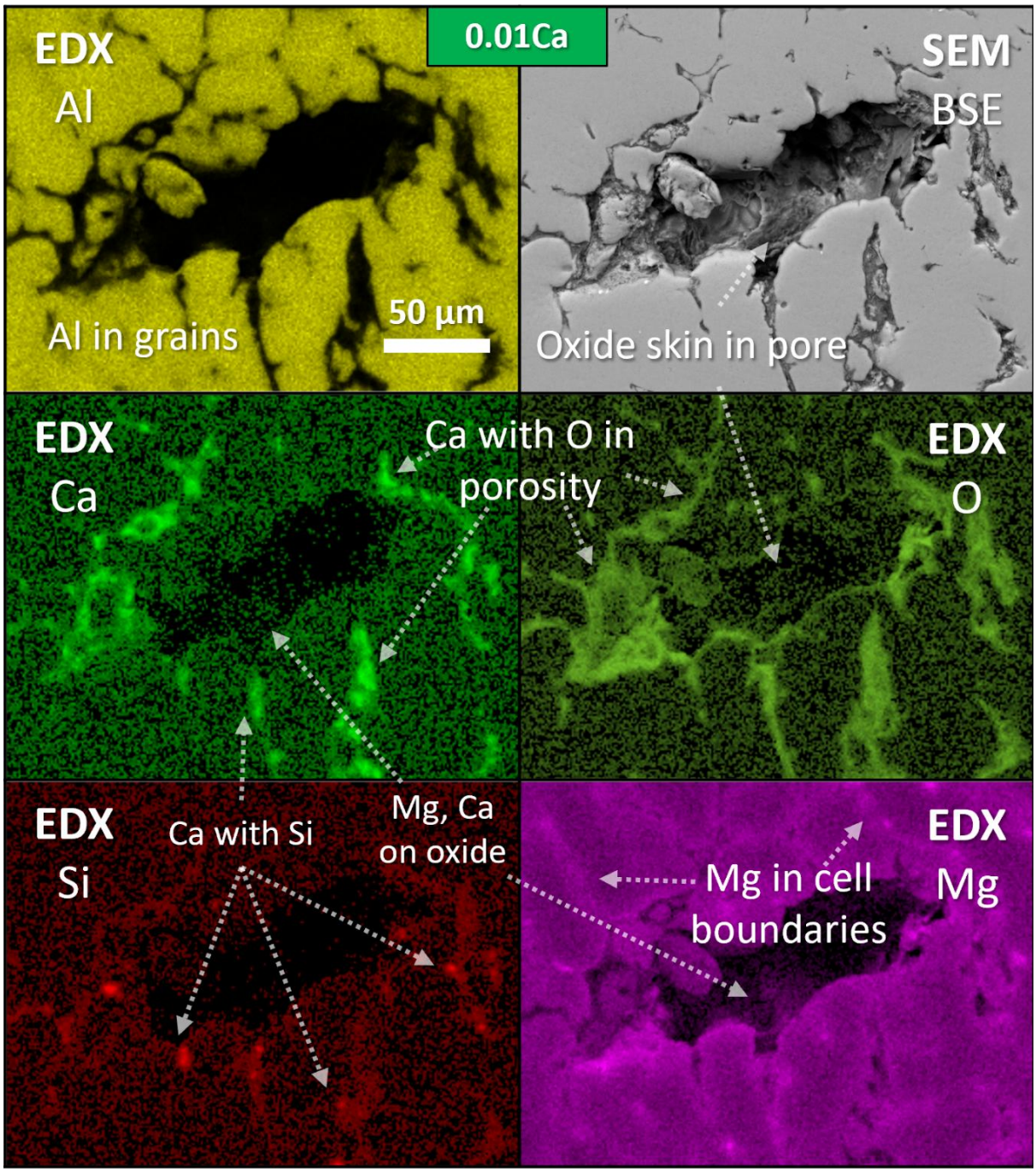


Figure 4.24: SEM/EDX mapping of pore in 0.01Ca sample.

SEM/EDX of the 0.01Ca metallographic sample show consistent results (Figure 4.24): the metal is α-Al with magnesium concentrating at the cell boundaries. In the pore highlighted, an oxide skin can be seen, consistent with the extracted oxides. Calcium is found to be concentrated in the porous areas of the cell boundaries and generally associated with oxygen and silicon. Film-like structures are found within the 0.01Ca metallographic sample, and EDX shows that these are Mg-rich films (Figure 4.25), like the 0.00Ca sample (Figure 4.6).

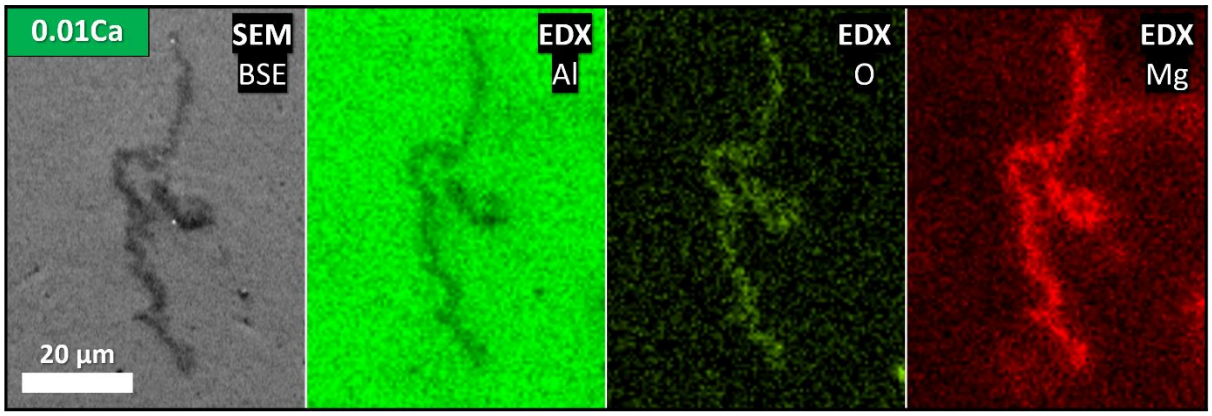


Figure 4.25. SEM/EDX of oxide film in 0.01Ca metallographic sample.

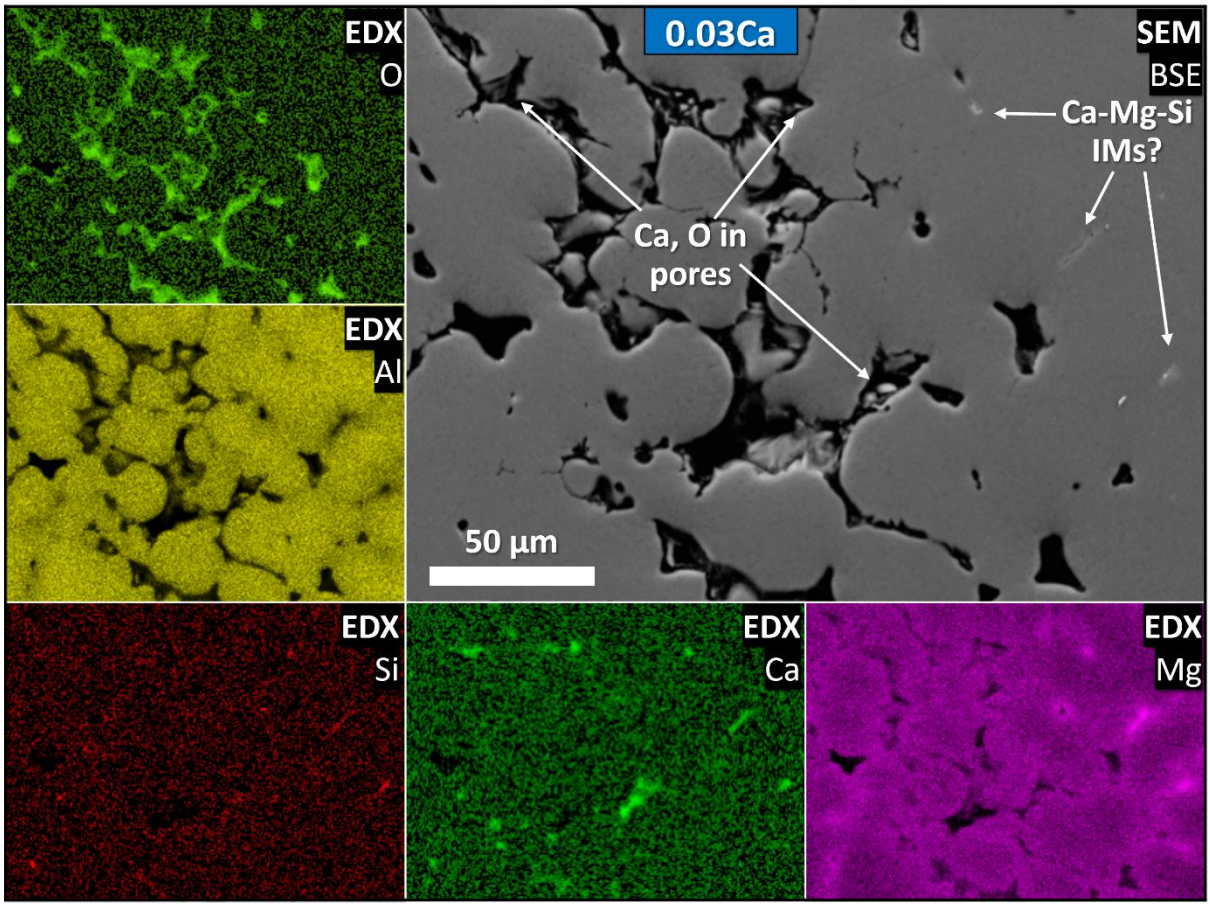


Figure 4.26. SEM/EDX imaging of 0.03Ca metallographic sample.

In the 0.03Ca sample (Figure 4.26), the metal is uniform α-Al with some magnesium alongside the aluminium, magnesium along the cell boundaries, and oxygen in the pores, like the 0.00Ca (Figure 4.6) and 0.01Ca (Figure 4.24) samples. Here, calcium is associated with silicon and magnesium in some areas, indicating Ca-Mg-Si intermetallics, but also with oxygen in some pores, which could suggest oxides. Oxide films are found attached to porosity, including one with an intermetallic (Figure 4.27).

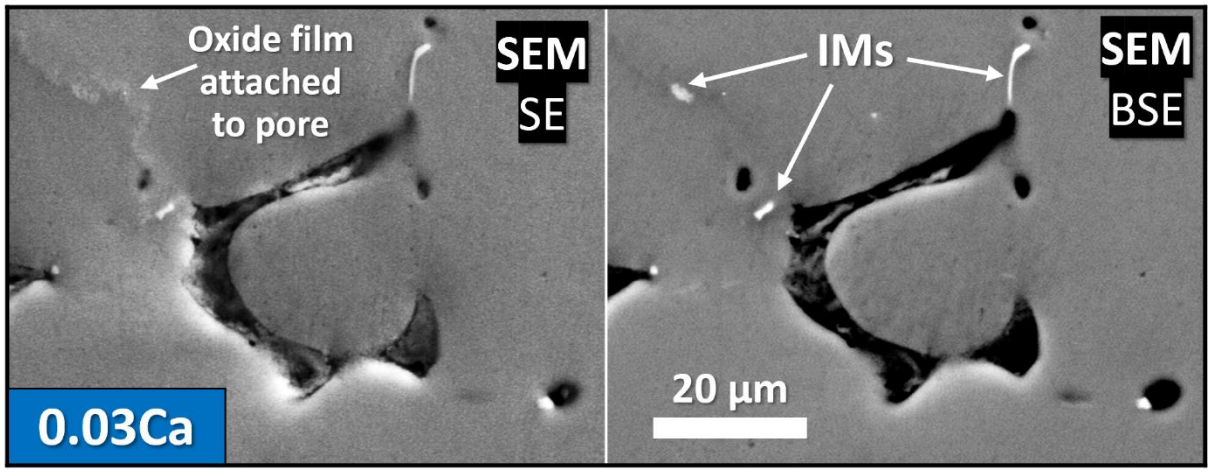


Figure 4.27. SEM (SE and BSE) imaging of film in 0.03Ca metallographic sample.

In general, the findings of 0.01Ca and 0.03Ca samples are consistent with the 0.00Ca sample: a porous α-Al microstructure with Al-Fe and Mg-Si intermetallics and oxide films. The added calcium associates mostly with the magnesium and silicon, indicating they form Ca-Mg-Si intermetallics, but is also found in pores without silicon, which may indicate oxide phases. Furthermore, an oxide network in the 0.03Ca is found to be covered with intermetallics that appear to have grown from it. The presence of aluminium, magnesium, and oxygen throughout and similarity in morphology to other oxide networks means it is unlikely that this is purely an intermetallic network.

4.4.4. Tomography

Tomographs of the solid 0.01Ca and 0.03Ca samples show a similar microstructure to 0.00Ca: α-Al with ridges indicating interdendritic regions along which porous networks (dark regions

with bright boundaries) lie, and entrained oxides such as bifilms and debris (Figure 4.28).

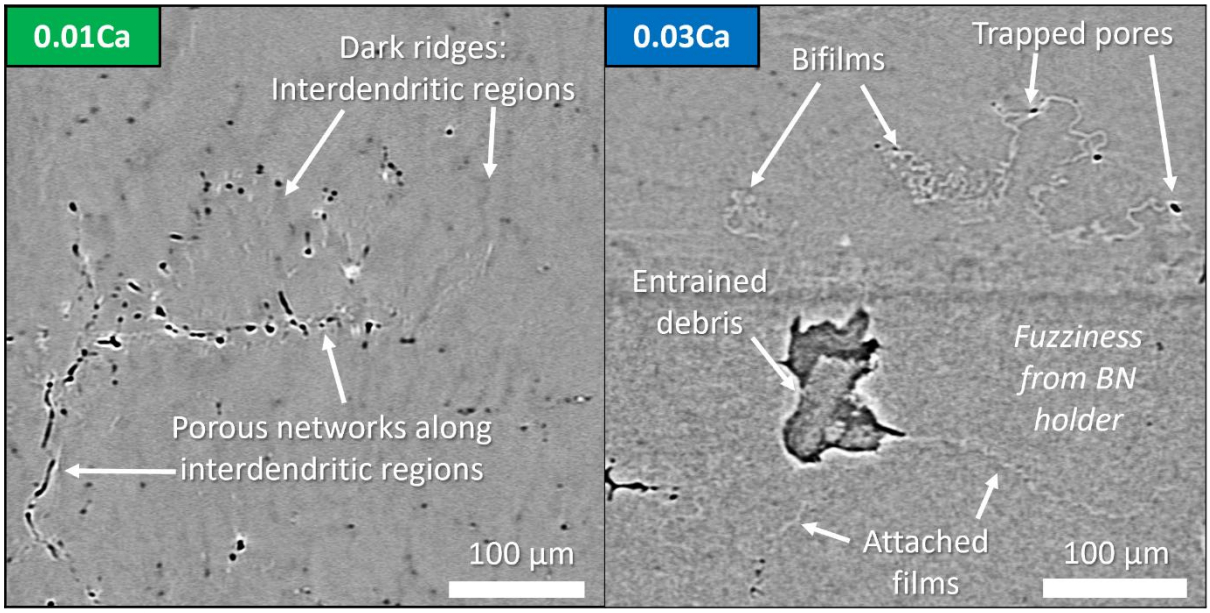


Figure 4.28. Vertical tomographic sections of solid 0.01Ca and 0.03Ca samples.

After melting, entrained oxides including oxide networks and bifilms persist in both the 0.01Ca (Figure 4.29) and 0.03Ca (Figure 4.30) samples, seen as bright, coiled, string-like features. In tomography, some oxidation can be seen (Figure 4.31). In the 0.01Ca sample (Figure 4.31.a), breakaway oxidation grows via porous oxide networks, like the 0.00Ca sample, but after a longer time (75 minutes) than the 0.00Ca sample, which itself appears to start immediately (Figure 4.11). This breakaway oxidation is seen as an increase in the extent of the high-contrast network, growing from existing porous oxide networks. In the 0.03Ca sample (Figure 4.31.b), small oxide nodules form on the surface, but no breakaway oxidation via porous oxide networks is observed. Like the 0.00Ca sample (Figure 4.9), entrained oxide networks present after melting in both the 0.01Ca and 0.03Ca samples persist throughout the melt hold.

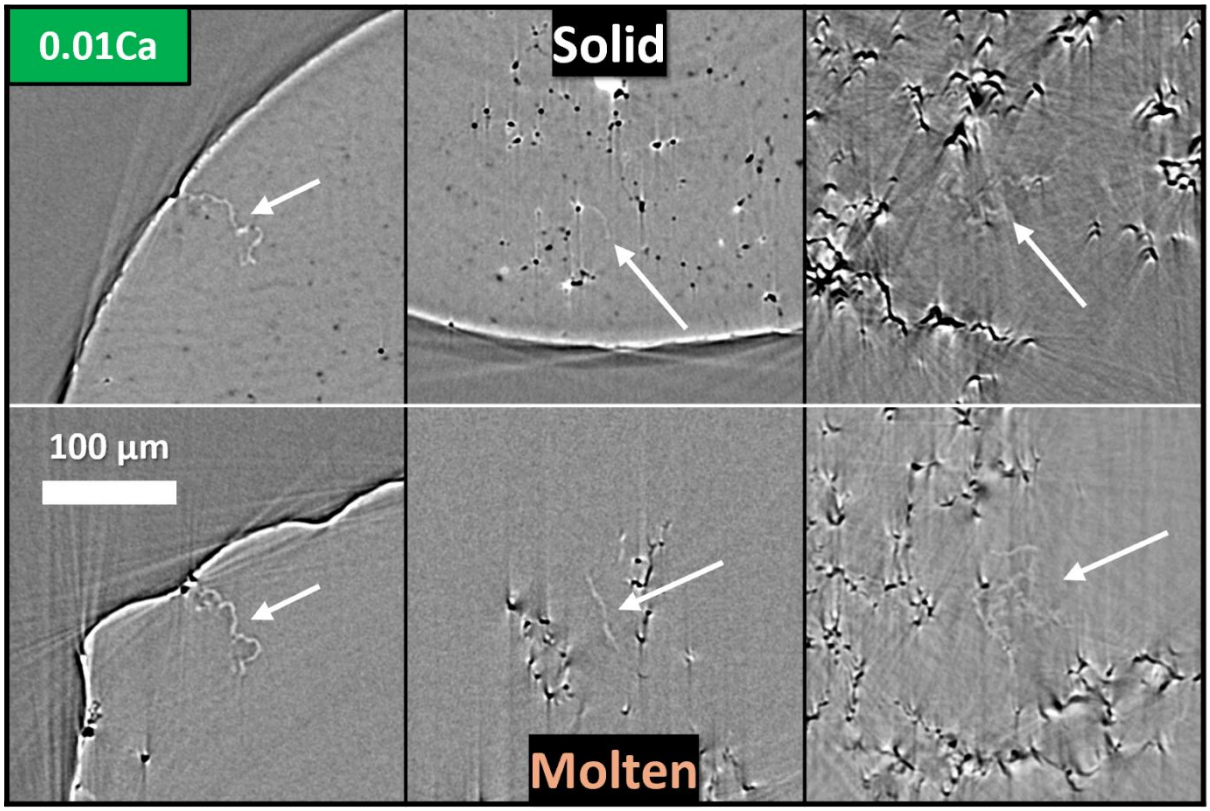


Figure 4.29. Horizontal sections of 0.01Ca sample before and after melting, showing persistence of bifilms (indicated by white arrows).

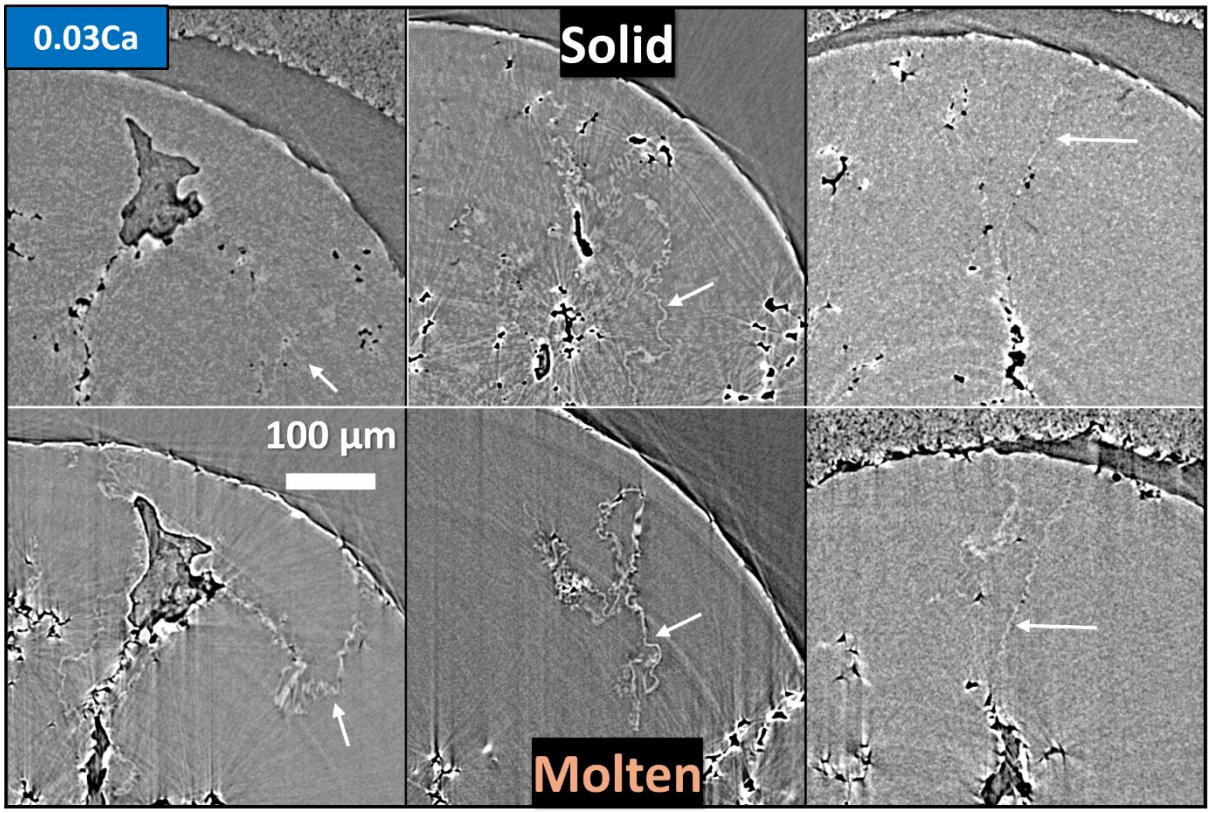


Figure 4.30. Horizontal sections of 0.03Ca sample before (top row) and after melting (bottom row), showing persistence of bifilms (indicated by white arrows).

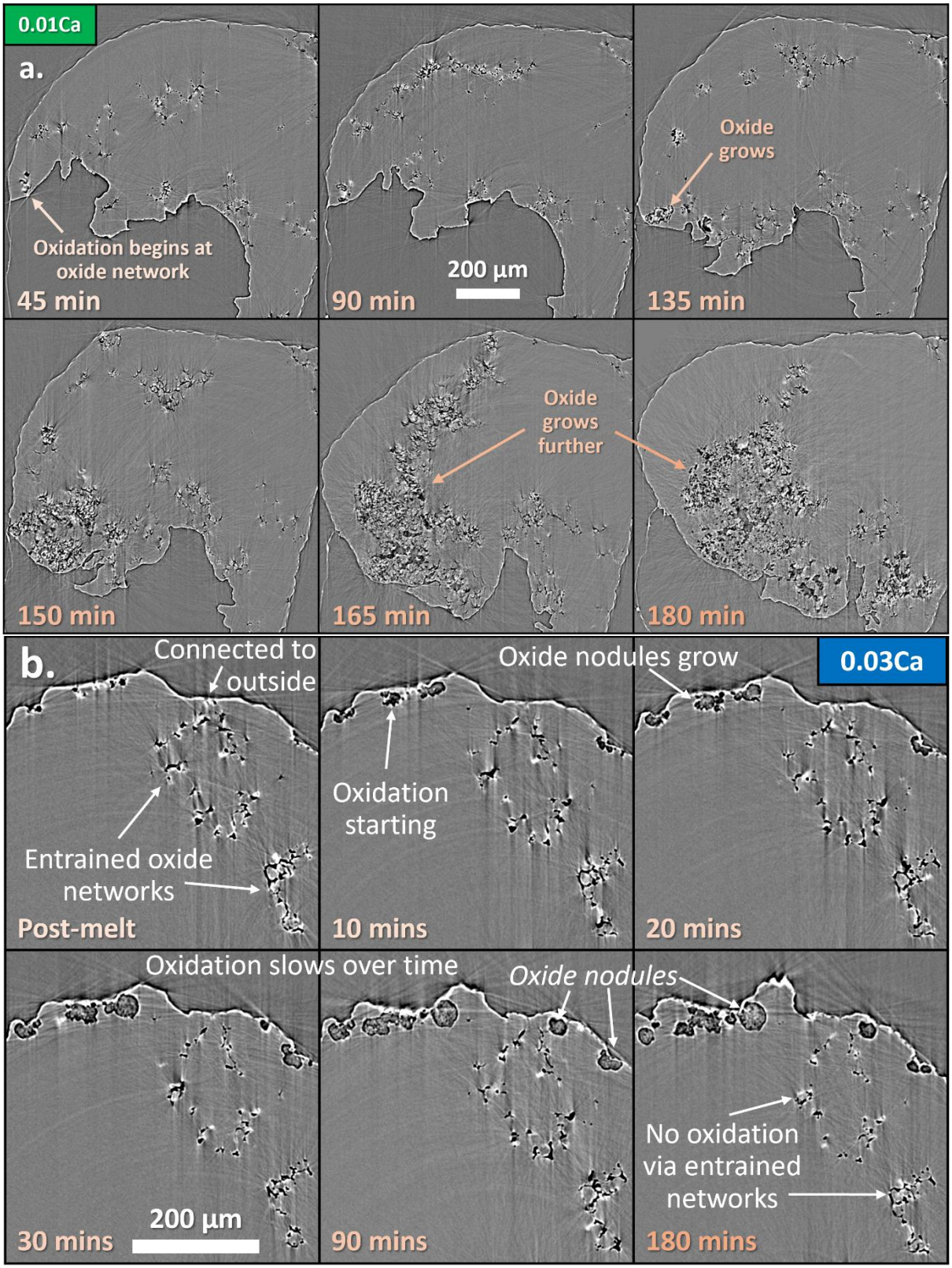


Figure 4.31. Horizontal tomographic sections of oxidation of (a) 0.01Ca and (b) 0.03Ca samples.

4.4.5. Oxidation: extracted samples

SEM analysis of the 0.01Ca sample extracted after melt oxidation (Figure 4.32) show breakaway oxide growths (Figure 4.32.a, d). These nodules appear to have grown from the porous oxide network, which is thinner and more transparent than the grown oxides. In the 0.01Ca sample, some oxides show the growth of a finer, powdery oxide on the entrained oxide network (Figure 4.32.b), as well as oxide growths emerging from the network, consistent with the morphology of breakaway oxidation observed in tomography (Figure 4.31.a). Entrained oxide debris can also be seen (Figure 4.32.c), with its entrainment indicated by a thin oxide skin encapsulating it.

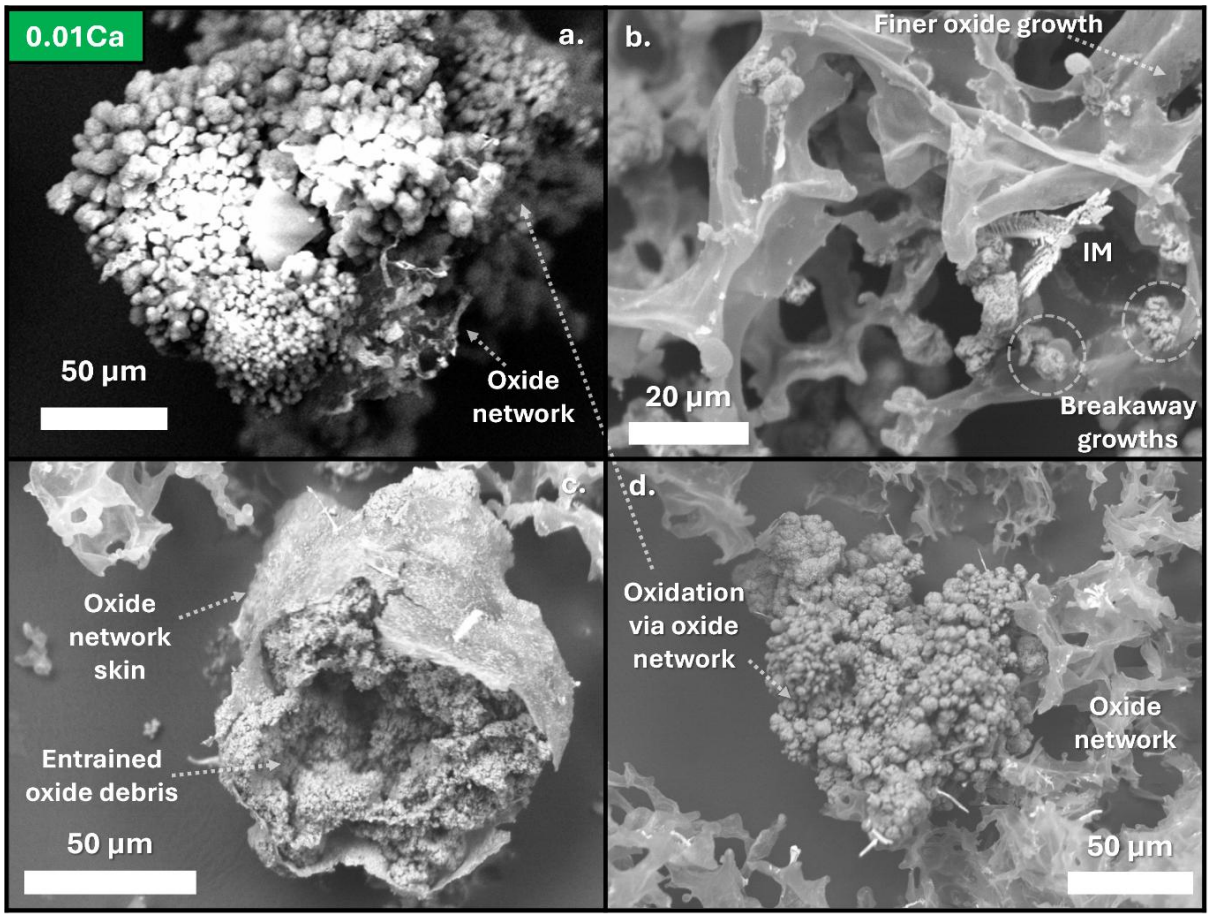


Figure 4.32. Post-melt extracted sample morphologies of the 0.01Ca sample.

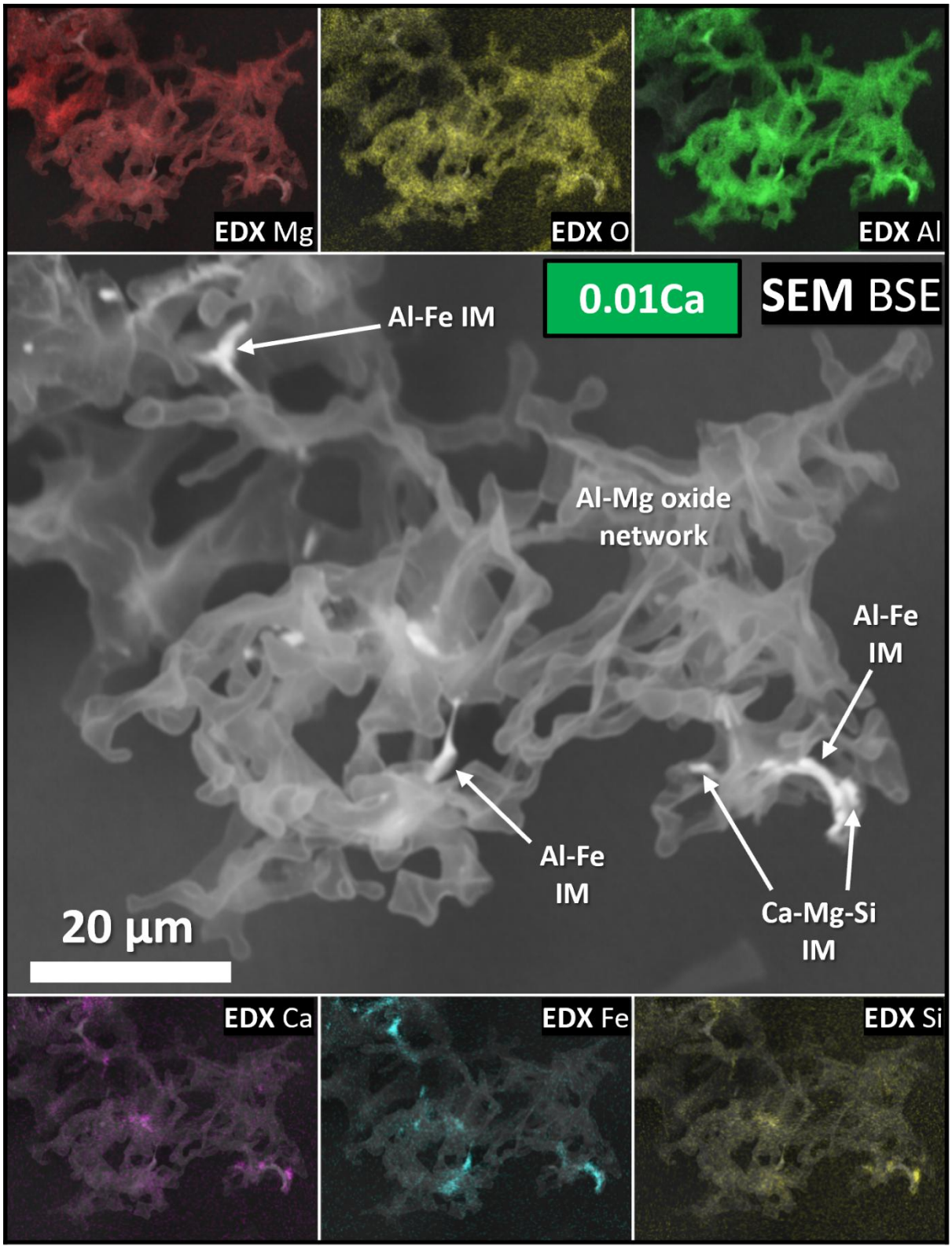


Figure 4.33. EDX mapping of fragment from extracted post-melt 0.01Ca sample.

In the oxide networks extracted from the 0.03Ca sample, no breakaway oxide growths are seen, and a fine, powdery oxide growth is seen covering the surface of the porous oxide network (Figure 4.34.a). Al-Fe intermetallics are seen on the surface of the oxides (Figure 4.34.b), and

broken surfaces reveal sub-micron fibrous structures growing from the internal surfaces.

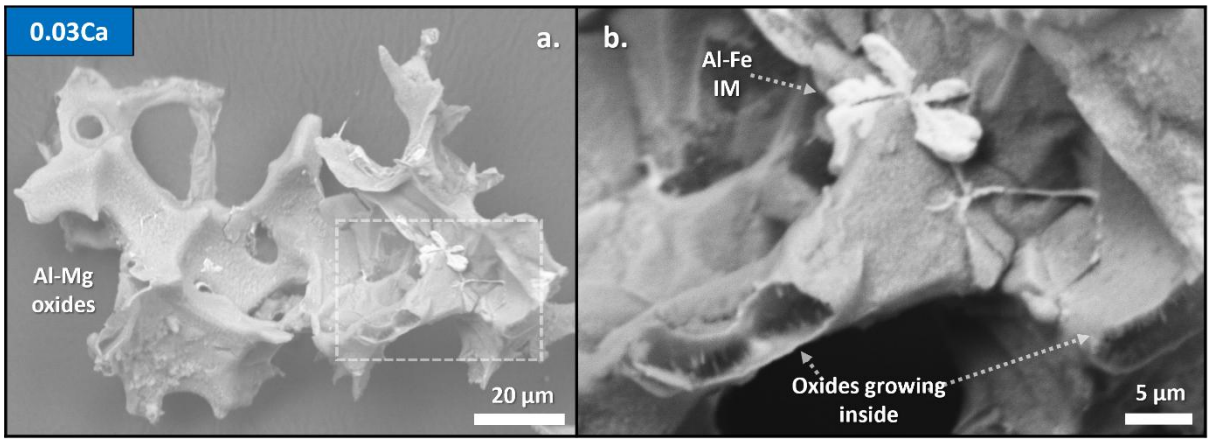


Figure 4.34. Sample morphologies of the extracted post-melt 0.03Ca sample.

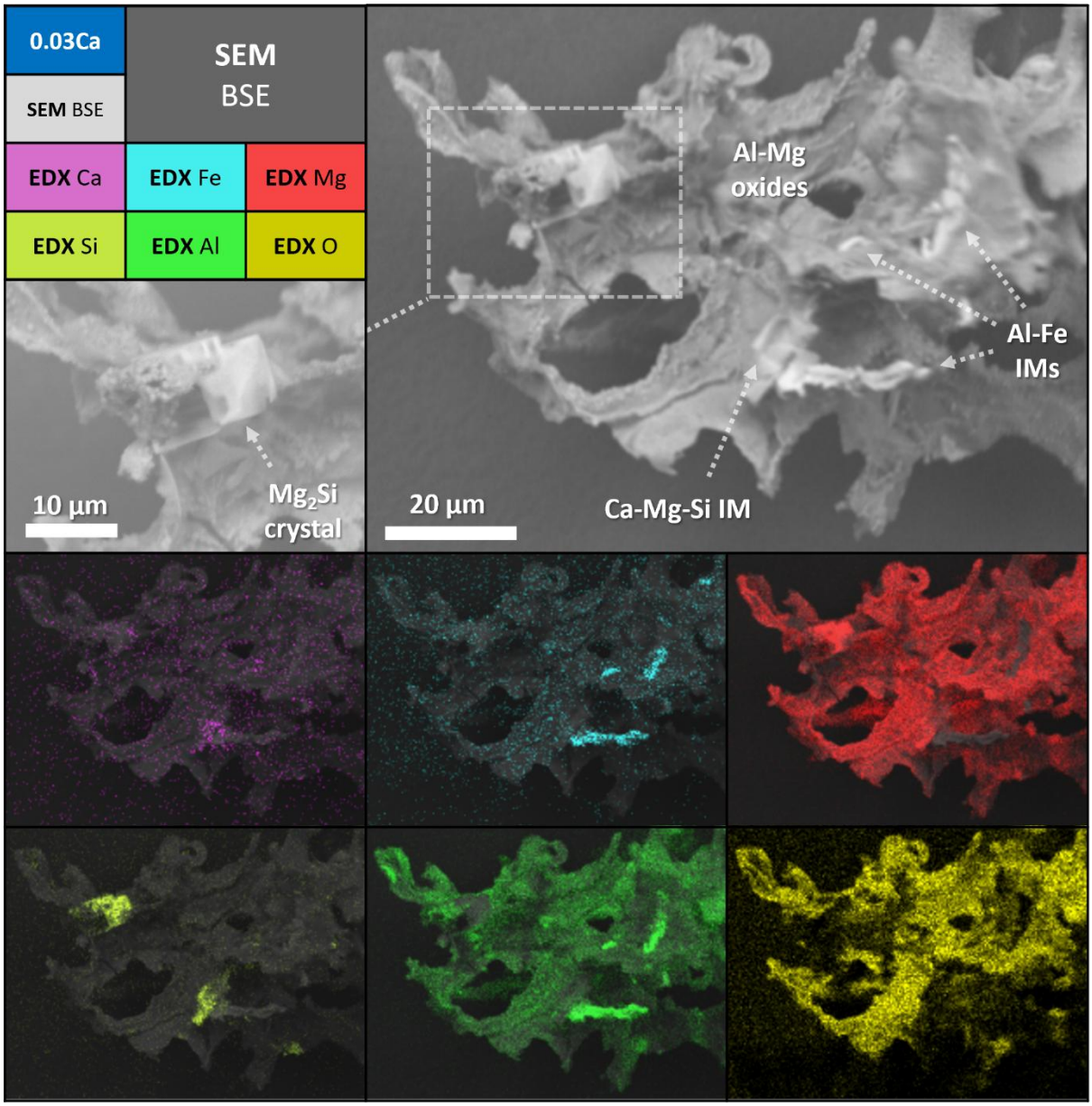


Figure 4.35. SEM/EDX analysis of the extracted post-melt 0.03Ca sample.

SEM/EDX analysis of the 0.03Ca sample after the melt oxidation (Figure 4.35) shows the entrained oxide network to be covered with fine, powdery growths. EDX results show aluminium, magnesium, and oxygen throughout, consistent with the oxide networks seen in the extracted as-cast samples. Iron is associated with aluminium, and silicon with magnesium and/or calcium, indicating the presence of Al-Fe and Mg-Ca-Si intermetallics. A faceted crystal is observed, suggesting that the Mg-Si rich region is an Mg_2Si crystal (Figure 4.35).

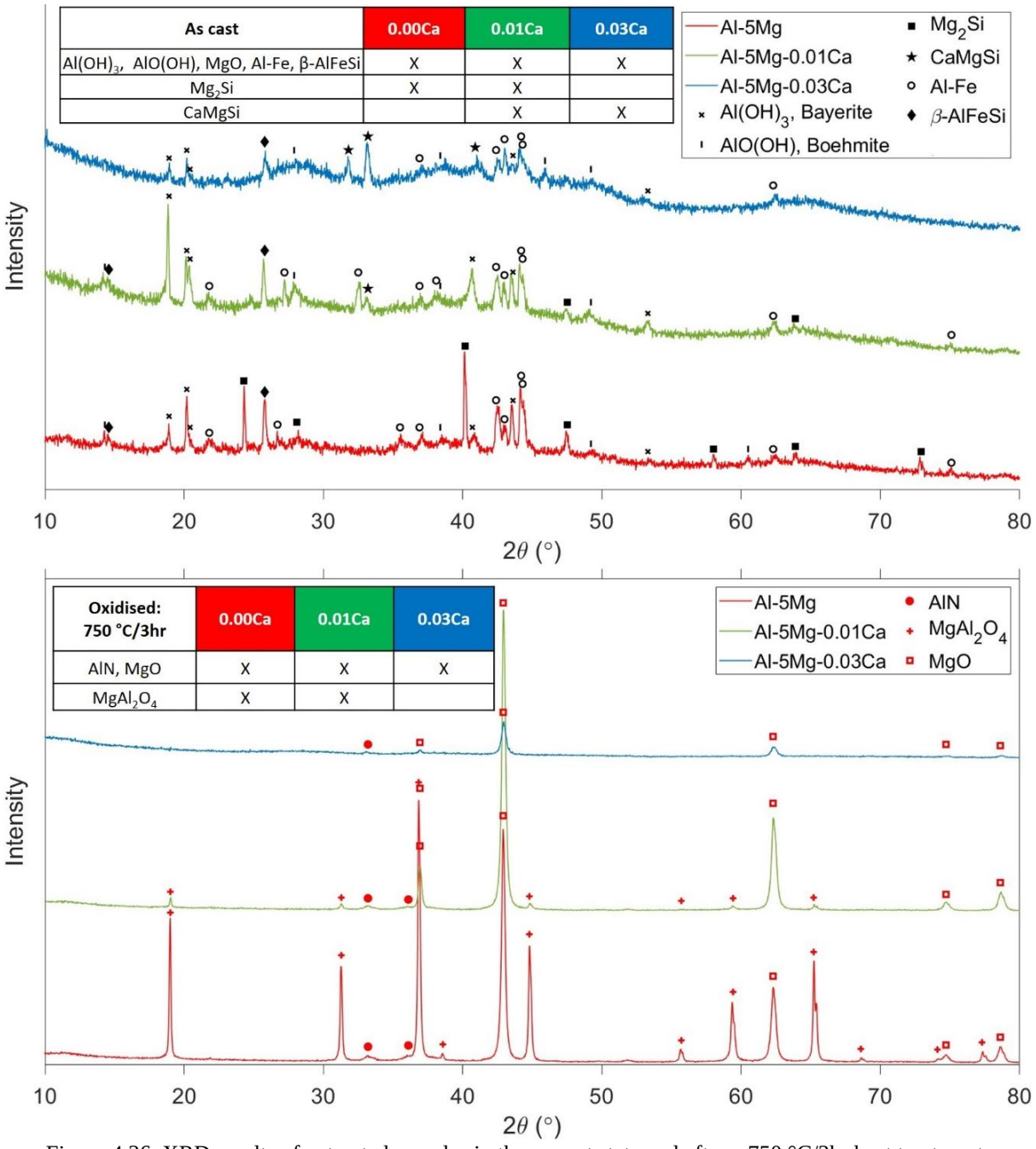


Figure 4.36. XRD results of extracted samples in the as-cast state and after a 750 °C/3hr heat treatment. Crystallographic information can be found in Appendix D.

X-ray diffraction results (Figure 4.36) reflect both the TGA (Figure 4.18) and SEM/EDX of extracted samples before (Figure 4.20, Figure 4.23) and after (Figure 4.33, Figure 4.35) melt oxidation. After oxidation, MgO forms in all samples, and $MgAl_2O_4$ in both the 0.00Ca and 0.01Ca samples. AlN is also found in all samples, likely from N_2 from gas trapped within the porous oxides reacting with the melt. In the as-cast samples, $Al(OH)_3$ (bayerite) and AlO(OH) (boehmite) are observed, likely due to hydration of either γ-Al_2O_3 [9] or am-Al_2O_3 [10]. These hydroxides are not stable at 750 °C and would dehydrate to form alumina [14], as discussed in the previous sub-chapter for the 0.00Ca sample. Intermetallics are also observed in the as-cast samples: Al-Fe ($Al_{13}Fe_3$ and $Al_{13}Fe_4$), and β-$Al_{4.5}FeSi$ are detected in all three, Mg_2Si in the 0.00Ca and 0.01Ca samples and CaMgSi detected in the 0.01Ca and 0.03Ca samples. Oxidation in the 0.01Ca sample (Figure 4.31) appears in tomography as a high-contrast network with pores inside, consistent with the 0.00Ca sample (Figure 4.11).

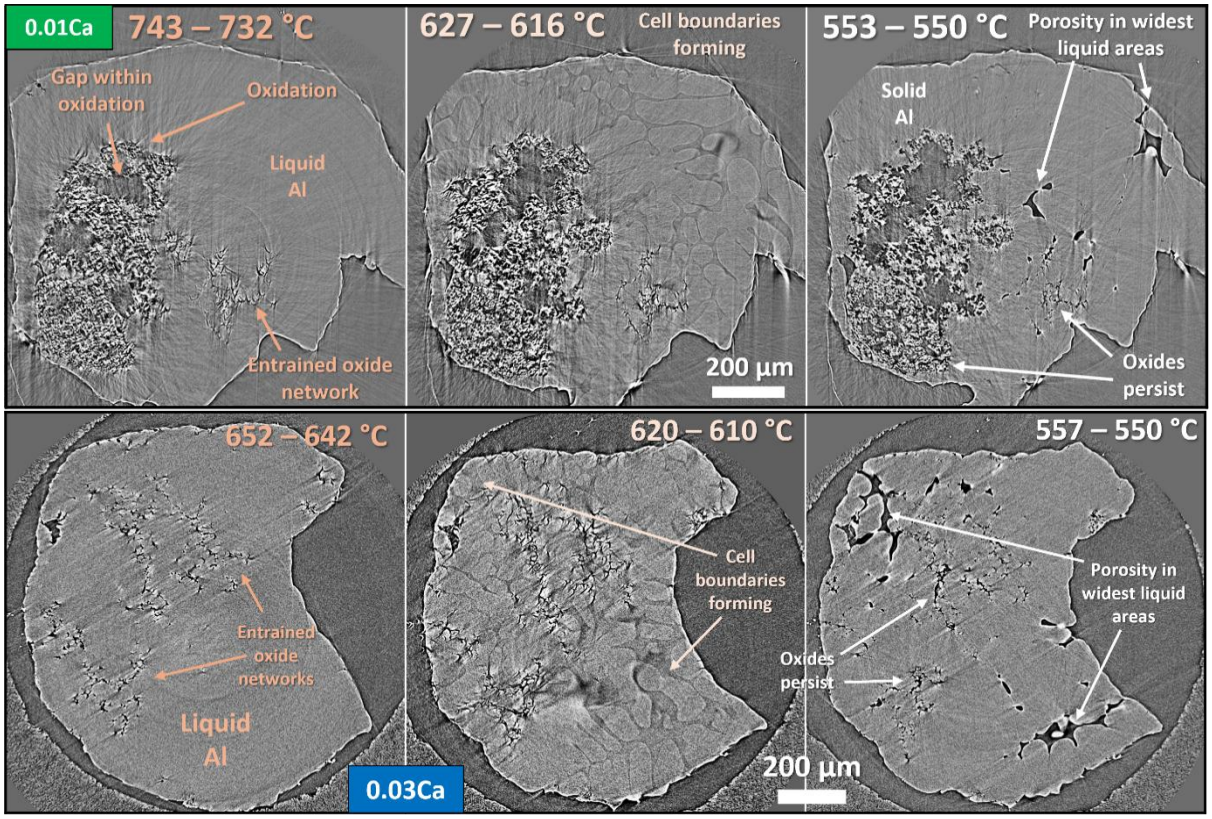


Figure 4.37. Horizontal sections of tomographic snapshots during 0.01Ca and 0.03Ca sample solidification.

During solidification of both the 0.01Ca and 0.03Ca samples (Figure 4.37), solid α-Al grains

form and are visible by a contrast with interdendritic regions, which appear darker. As solidification progresses, porosity forms in the widest interdendritic regions, and the oxides (both those grown from oxidation and entrained oxides present from before melting) persist without significant morphological change, like the 0.00Ca sample (Figure 4.15).

4.4.6. Discussion

Like the 0.00Ca sample, the porous networks seen within the 0.01Ca and 0.03Ca samples are determined to be oxide networks: the networks persist after melting with little morphological change (Figure 4.30), showing the networks to be solid objects. Chemical analysis of the extracted samples shows that the networks are oxides. The butanol extraction process only removes the aluminium metal from the extracted samples, preserving intermetallics and oxides alike, and the morphology of the networks resembles the tomographs, so it reasonable to conclude that these are the same. Entrained debris can be seen within the oxide networks, further evidencing the hypothesised origin of the oxides: in tomographs (Figure 4.30), an oxide pore connected to bifilms containing another solid object can be seen, which remains encapsulated after melting.

Oxide particles trapped within porous oxide networks can be seen in the as-cast extracted samples of both 0.01Ca (Figure 4.19) and 0.03Ca (Figure 4.21), showing that the network forms through entrainment, and the grid-like pattern with regular holes (Figure 4.22) indicates that these oxides are shaped by solidifying dendrites, as discussed in the previous subchapter (Figure 4.17). Oxide films are also found attached to the porous networks in metallographic samples (Figure 4.27) and extracted samples (Figure 4.19.f, Figure 4.22), so it is concluded that, like the 0.00Ca sample, there is a dual population of entrained oxides: thick (c. 1-10 μm) oxide skins formed from melt oxidation before pouring and oxide particles contained within a porous networks of thin (<1 μm) flexible oxide skins forming from the pouring itself. In addition, bifilms are seen throughout the tomographs in both the 0.01Ca (Figure 4.29) and

0.03Ca samples (Figure 4.30), and are observed to include debris, smaller pores, and larger bubbles (Figure 4.38). This confirms predictions made about the nature of entrained debris within bifilms [15,20] and constitutes the first direct observation and imaging of these defects within an aluminium melt.

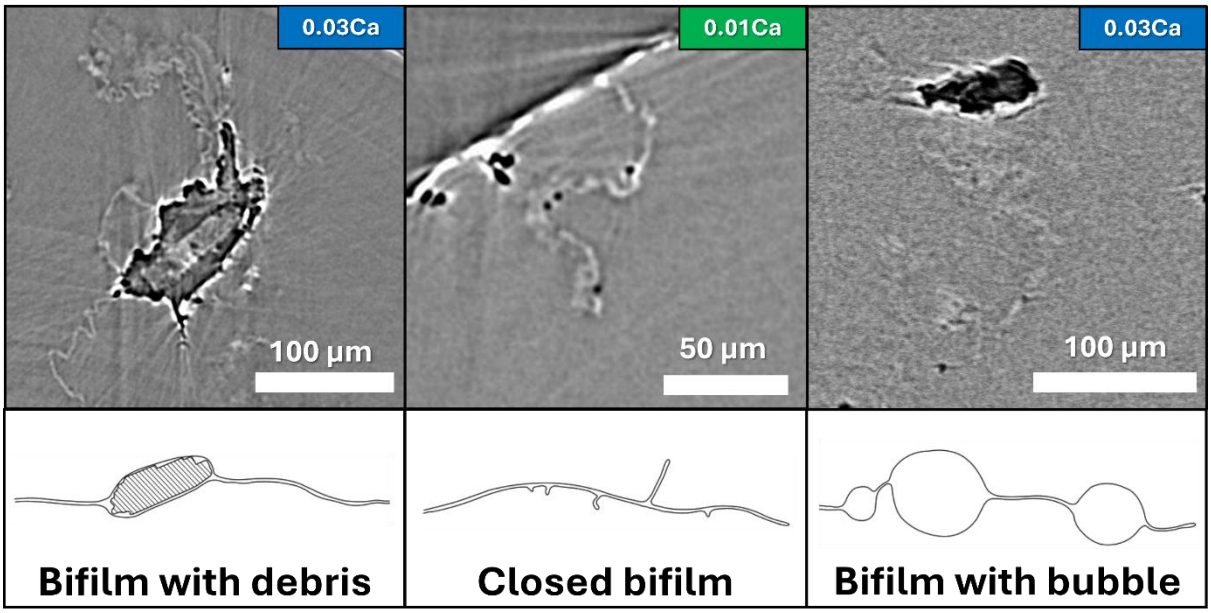


Figure 4.38. Bifilm figure comparison: tomographs of bifilms in liquid metal containing debris, small pores, and large pores compared to predicted appearance [19] by previous researchers. The association between bubble formation and entrained oxides will be discussed in the next subchapter.

Another key prediction of bifilms evidenced here is that bifilms and entrained oxides can grow intermetallics [21]. SEM/EDX mapping of the 0.03Ca metallographic sample (Figure 4.27) shows two Mg/Ca-containing intermetallics, indicated by their brighter appearance in backscattered mode, on a bifilm connected to an oxide network. Furthermore, extracted samples from the 0.03Ca as-cast sample (Figure 4.23) show many intermetallics on a porous oxide network, and their morphology of spines radiating from the oxide network indicates that they formed and grew from the entrained oxide network. These intermetallics can also be seen on samples extracted after the melt oxidation, including a clear faceted crystal, most probably Mg_2Si (Figure 4.35).

XRD results of the extracted as-cast samples (Figure 4.36) show peaks from Al-Fe intermetallics ($Al_{13}Fe_3$, $Al_{13}Fe_4$, β-$Al_{4.5}FeSi$) in all samples, Mg_2Si in the 0.00Ca and 0.01Ca

samples, and CaMgSi in the 0.01Ca and 0.03Ca samples, confirming the phases' presence. No intermetallic phases are detected in the XRD traces of the oxidised samples, which is likely due to the signal from the oxides dominating, having a much stronger signal above background than their as-cast counterparts. The morphology of the intermetallics seen in the extracted as-cast (Figure 4.23) and oxidised (Figure 4.32.b) samples are similar, and EDX mapping shows an elemental distribution which indicates intermetallic phases (Figure 4.35).

Calcium, as expected from other studies [1,22], is found to suppress melt oxidation of molten Al-Mg with only 100s ppm addition. TGA results show that calcium suppresses the initial melt oxidation, the extent increasing with calcium concentration (Figure 4.18.a). However, breakaway oxidation is observed in the 0.01Ca sample, appearing similar in tomography (Figure 4.31.a) to the 0.00Ca sample (Figure 4.11), but not in the 0.03Ca sample (Figure 4.31.b). Oxidation of the 0.03Ca sample is limited to small nodules growing from the surface, without any oxidation via porous oxide networks (Figure 4.31).

Oxidation suppression by group II elemental additions, including calcium, is generally attributed to delaying the formation of $MgAl_2O_4$ over MgO [22]. The TGA traces show a double-sigmoid curve in the 0.00Ca and 0.01Ca samples (Figure 4.18), which is characteristic of Al-Mg oxidation [13,23]. In the first regime, a thin, protective oxide layer forms, indicated by a slowing oxidation rate (Figure 4.18.a). In the second regime, this protective layer breaks, the melt is exposed to air, and further oxidation to MgO occurs; in the TGA, this can be seen as an increasing oxidation rate, before tapering off as the magnesium depletes, near the mass gain expected from full conversion of magnesium into MgO (3.3%). In the third regime, further oxidation produces $MgAl_2O_4$, possibly as a result of the depletion of magnesium which would render $MgAl_2O_4$ more thermodynamically stable than MgO when in contact with the melt [17]. Like the second regime, a sigmoid is produced by increasing oxidation rate as the MgO begins to convert to $MgAl_2O_4$, and tails off as the supply runs out, resulting in the overall double

sigmoid shape to the TGA plots of the 0.00Ca and 0.01Ca samples.

The XRD results confirm these observations (Figure 4.36): the only oxides found in the as-cast samples are AlO(OH) (boehmite) and $Al(OH)_3$ bayerite. These are likely hydration products of γ-Al_2O_3 or am-Al_2O_3 from atmospheric moisture since boehmite and bayerite are not stable at 750 °C, as discussed in the previous subchapter. However, after holding at 750 °C for three hours, $MgAl_2O_4$ and MgO are found in the 0.00Ca and 0.01Ca samples, but the only oxide found in the 0.03Ca sample is MgO (Figure 4.36). The 0.03Ca sample does not undergo breakaway oxidation over the experimental time span, as confirmed by tomography (Figure 4.31.b) and TGA (Figure 4.18). The reported correlation between protection of the melt by calcium and the hindrance of $MgAl_2O_4$ production [1,24,25] is consistent with these observations. Whether this hindrance by the presence of calcium is a kinetic or a thermodynamic effect is not yet clear. Furthermore, the presence of AlN in all samples is evidence of the reaction of trapped atmospheres within the entrained networks with the melt, since AlN only forms after the depletion of oxygen [26].

An important note to make is that breakaway times can vary greatly, being influenced by factors such as movement and sample size, and can even differ for identical samples [23–25,27]. Whilst the TGA results might imply that the conversion to $MgAl_2O_4$ in the 0.00Ca and 0.01Ca samples takes place only after 5-6 hours, which is more than the hold time of the extracted samples (3 hours), the TGA samples are substantially larger (7 mm height, 8 mm diameter) than the samples used in tomography or extracted after heat treatment (5 mm height, 1 mm diameter). Tomographic observations confirm that significant oxidation occurs within three hours in the 0.00Ca (Figure 4.11) and 0.01Ca (Figure 4.31.a) samples, so it can be concluded the post-melt extracted samples (0.00Ca and 0.01Ca) also underwent breakaway oxidation.

As previously established, melt oxidation is facilitated through the entrained oxide networks, which are porous and extensive. Like the 0.00Ca sample (Figure 4.12), breakaway growths can

be observed in the 0.01Ca post-melt extracted sample (Figure 4.32), appearing as nodular bunches surrounding the porous oxide network (Figure 4.32.a, d). These breakaway growths can be seen emerging from the porous oxide network, as well as a finer oxide layer on the surface of the porous oxide network (Figure 4.32.b).

In the 0.03Ca sample, which does not undergo breakaway oxidation, no nodular bunches forming from the porous oxide networks can be seen (Figure 4.34), but the porous oxide networks are entirely covered with a much finer oxide layer (Figure 4.35). This demonstrates the mechanism of oxidation protection: a fine MgO layer forms on the surface of the entrained oxide networks, with fractured surfaces revealing fibrous oxide structures inside (Figure 4.34.b). This compact MgO layer blocks diffusion of gases between the atmosphere and the melt, indicated by a slowing oxidation rate in the TGA results (Figure 4.18), which prevents or delays any breakaway oxidation. This is consistent with previous attributions of oxidation protection to a "mixed MgO/CaO layer" [1]; the lack of CaO peaks in post-melt XRD, which may be expected if this is the correct mechanism, is likely due to the small concentration of calcium in the alloy (0.03 wt.%) versus magnesium (5 wt.%). This hypothesis is supported by the lack of XRD peaks for Al-Fe intermetallics in the oxidised samples (Figure 4.14), despite peaks being present in XRD of the as-cast samples, and evidence of Al-Fe intermetallics in SEM/EDX analysis of both as-cast (Figure 4.23) and post-melt (Figure 4.35) extracted samples. The compact nature of the layer may also explain why the initial mass gain before breakaway decreases as the concentration of calcium increases: the more calcium present, the more quickly a compact MgO layer forms, reducing the amount of initial oxidation.

Whilst the results show that calcium greatly affects the oxidation of Al-Mg alloys in minute concentrations, the mechanism of protection is not fully established. Other studies have claimed that calcium exists within the oxides produced, either as a "mixed MgO/CaO layer" [1,28] justified by EDX mapping, or $CaMg_2Al_{16}O_{27}$, justified through thermodynamic

calculations [29]. No calcium-containing oxides appear in the XRD results (Figure 4.36), which would be the most convincing evidence for Ca-based oxides, but EDX mapping of the 0.01Ca sample indicates some pores to contain an oxide skin rich in both magnesium and calcium, and other pores to be rich in both calcium and oxygen, which could indicate the presence of calcium-containing oxides (Figure 4.24). Calcium appears to be concentrated within pores (Figure 4.26) and often appears with silicon and magnesium (Figure 4.33), which is consistent with the appearance of CaMgSi peaks in the as-cast XRD trace; therefore, the chemistry of calcium in the sample is not clear.

4.4.7. Preliminary conclusions

The results presented here, i.e. observations of the calcium-added samples and the TGA of all samples, consolidate the findings made in the first subchapter. Entrained oxides, including bifilms, have been directly observed in aluminium melts for the first time and found to be more morphologically complex than previously thought, comprising a dual population of thin, flexible, porous oxide networks produced by the melt pour shaped by growing dendrites during solidification, which are attached to thicker oxides resembling bifilms produced prior to the melt pour. Predictions that bifilms can be closed, contain bubbles, and trap debris are confirmed by direct imaging, also for the first time. There is also evidence that entrained oxide networks grow intermetallics, another bifilm prediction.

Calcium is found to suppress oxidation of aluminium melts, even in minute quantities. In an Al-Mg melt with added calcium, a fine MgO layer forms on the surface of entrained oxide networks, which are the channels for melt oxidation. This grown oxide layer blocks contact between the atmosphere and the melt.

4.5. Deoxidation of Al-Mg alloys by calcium

4.5.1. Overview

This sub-chapter covers the deoxidation of Al-Mg alloy melts by the addition of calcium, specifically observing the behaviour of entrained oxides during melting, and bubble formation that occurs in the Ca-added alloys. In this sub-chapter, tomographic data is displayed not only as horizontal and tomographic sections, but also as flat-field corrected X-ray radiographs termed 'projections', since many phenomena occur on shorter timescales than the full tomographs (30 seconds). These projections are always displayed in the 'vertical' orientation, with the 'up' direction on the page parallel to the rotation axis and against gravity. In addition, videos of the melting sequences have been produced and are available in the supplementary material. These show some of the phenomena much more clearly, and readers are encouraged to read the commentary for guidance (Appendix C).

4.5.2. Initial melting: porosity and entrained oxide networks

During melting, some porous networks, observed in projections as convoluted darker areas with a narrow bright fringe along its boundary, round off and disappear; this is shown by a series of projections at 180° intervals at two separate angles as time and temperature increases (Figure 4.39.a). In the horizontal tomographic sections (Figure 4.39.b), the porous networks appear as black regions with a rough bright boundary; upon melting, these turn into scar-like features and leave no trace after disappearing.

These scar-like structures reveal the cell boundaries within the microstructure, which pull apart and fill with molten metal, appearing as uniform regions brighter than the porosity present previously (Figure 4.40.a). As established previously (Figure 4.10), this allows porous networks and oxide networks to be distinguished: porous networks, resulting from hydrogen expulsion and shrinkage upon solidification, disappear during melting, but entrained oxide

networks persist. The metal network which appears between the cell boundaries during melting, presenting as a high contrast region around the cell boundaries (Figure 4.39.b, 616-626 °C), can be seen to be the solid remnants of the melting metal: the metal network sinks in the latter stages of melting, indicating a higher density than the liquid (Video B1).

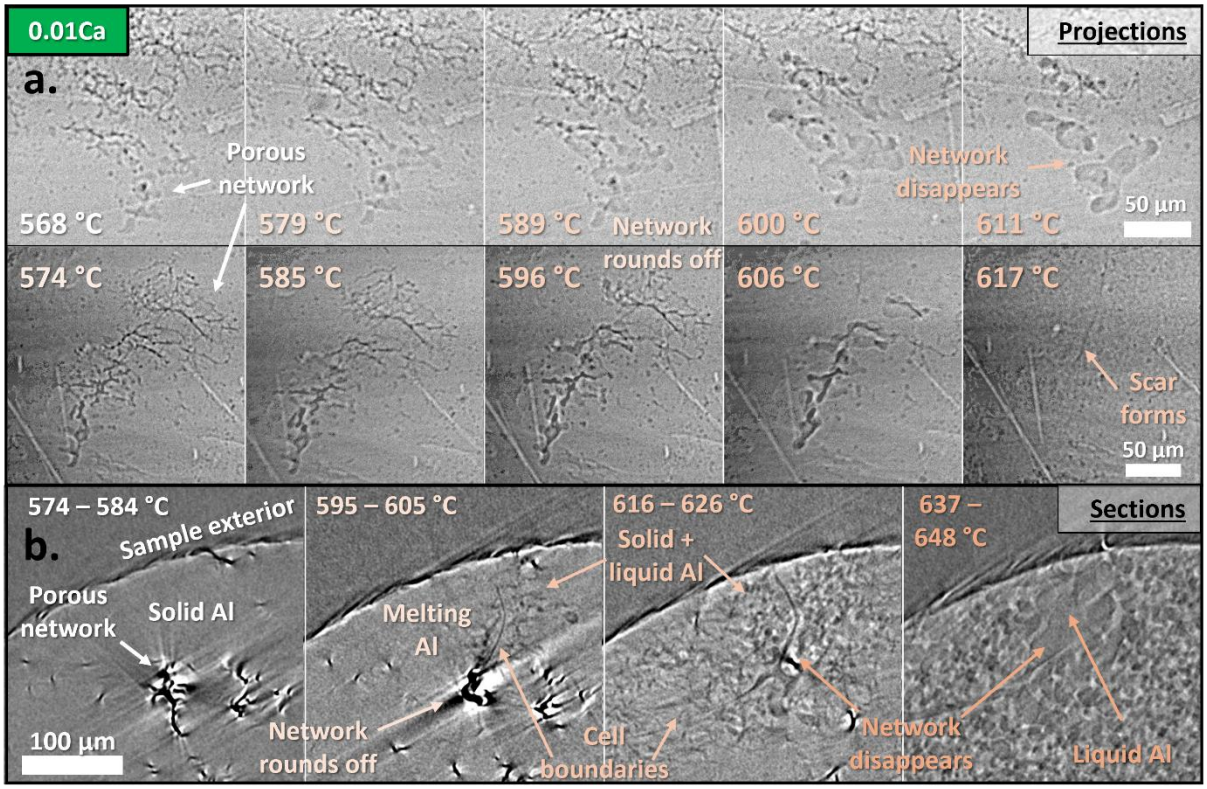


Figure 4.39. Projections and tomographs of porous networks disappearing during melting in the 0.01Ca sample: (a) Projections at 180° intervals with increasing sample temperature (left to right) at two different reference angles (top row and middle row); (b) Tomographic snapshots during melting.

In each alloy, the oxide shell expands due to pressure from the melting liquid. However, the melting metal, appearing as a bright network, does not expand into the new space, maintaining the original dimensions of the sample (Figure 4.40.b). These projections allow the entrained oxide networks, metal networks, and liquid to be distinguished: the liquid appears uniform in texture, and whilst both the oxide and metal networks are convoluted in shape, the oxide network has regions darker than the liquid whereas the metal network does not (Figure 4.40). During melting of the 0.01Ca (Figure 4.41) and 0.03Ca samples (Figure 4.42), parts of the oxide networks can be seen to break off and float upwards. Readers are encouraged to watch the videos in supplementary material, which display the flotation more clearly (Videos B1, C1,

C2). The fragments float and the other oxide networks, metal, and oxide skin do not.

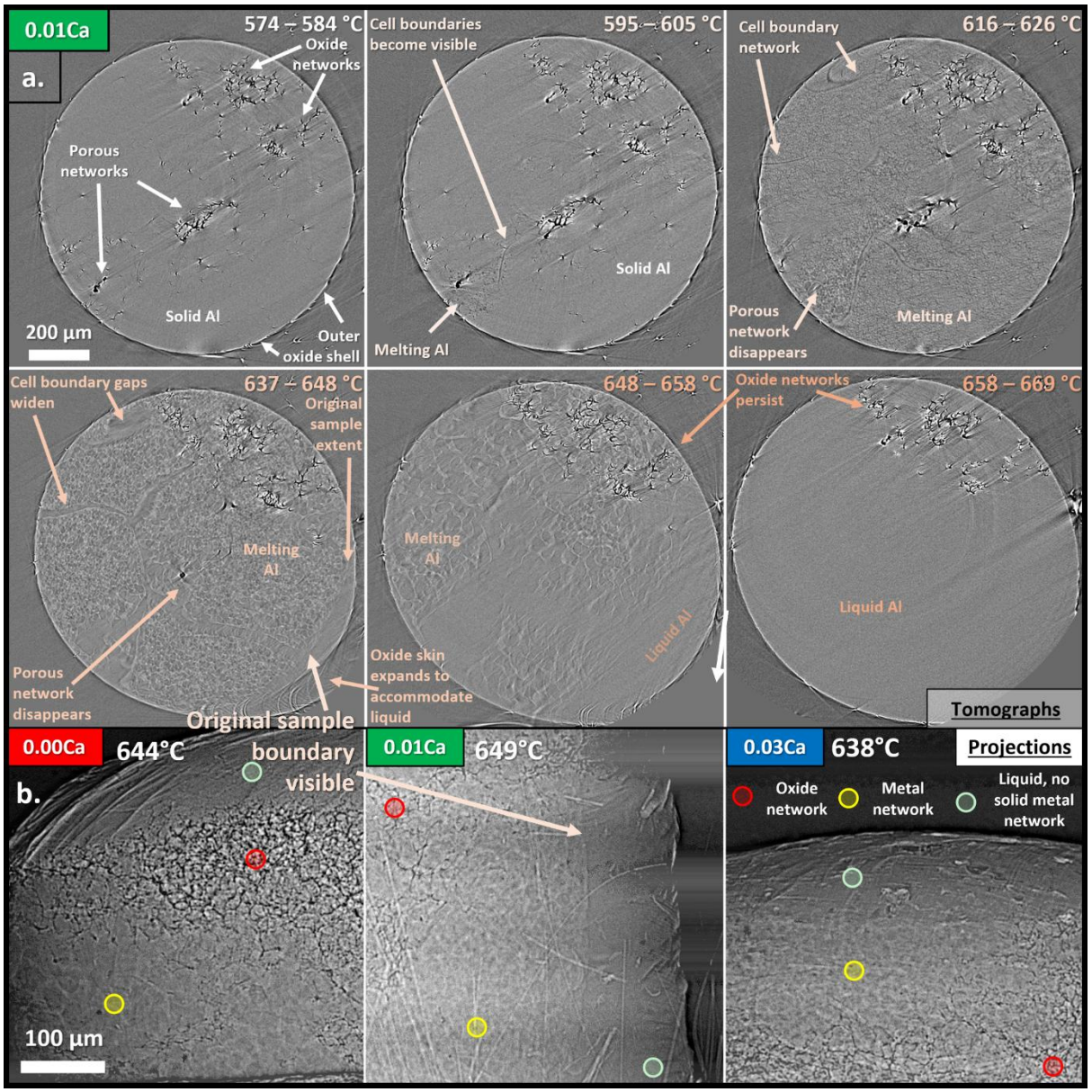


Figure 4.40. Appearance of metal networks during melting as shown by horizontal sections of tomographic snapshots of (a) the 0.01Ca sample melting sequence and (b) projections of all three samples during melting.

These fragments are entrained oxides: the maintenance of the shape in the liquid shows the objects to be solid, but the fact that they float shows that their density is lower than the liquid, showing it to be porous (in addition to the visible air gaps in the tomography). These only occur in the calcium-added samples; no such rising oxides are seen in the 0.00Ca sample.

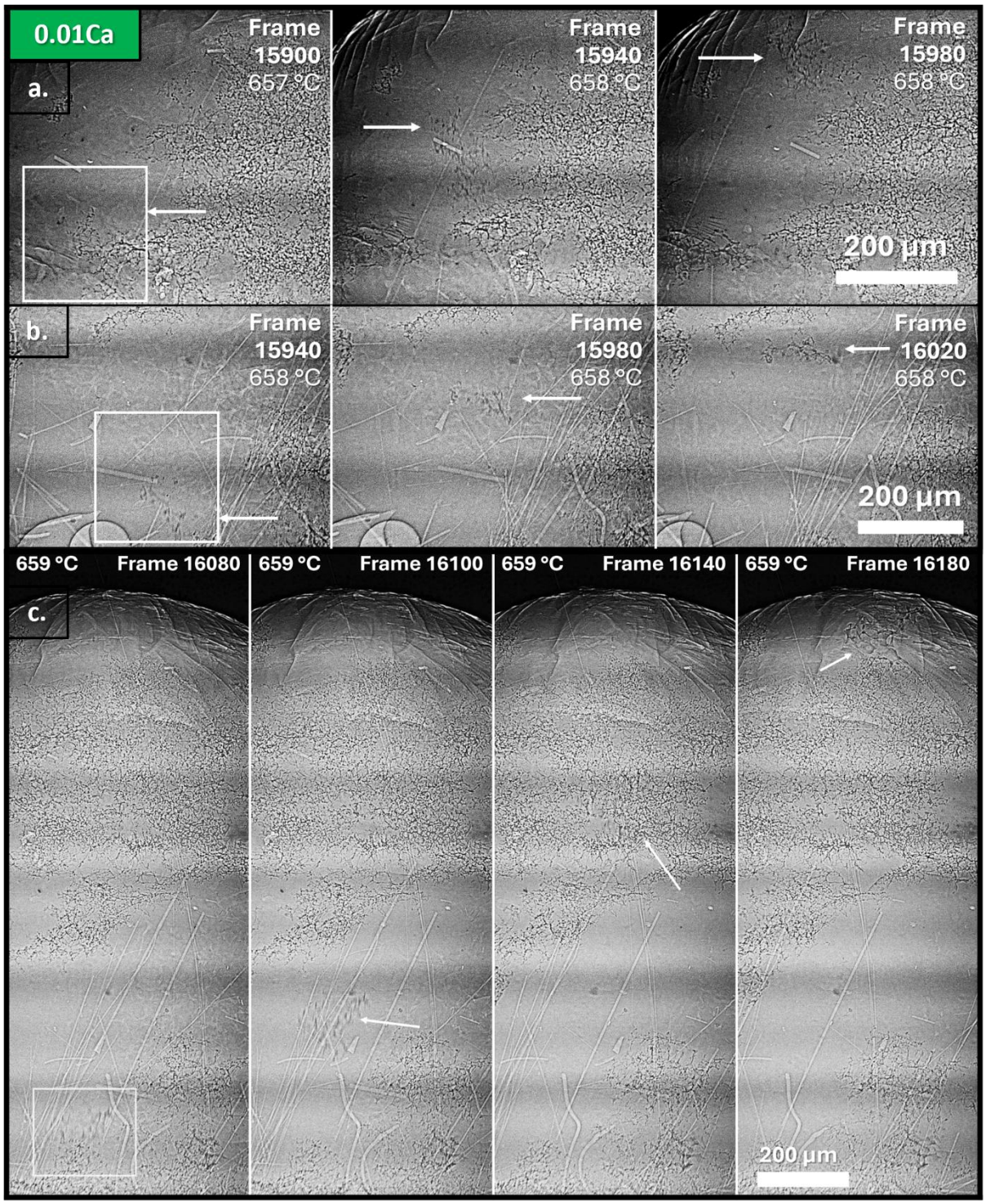


Figure 4.41. Flotation of entrained oxides following melting in the 0.01Ca sample shown by projection sequences in three views (a, b, c). The long white streaks seen in the foreground are ceramic wool fibres placed around the exterior of the metal rod to hold it in place in the BN holder and so are not sample features.

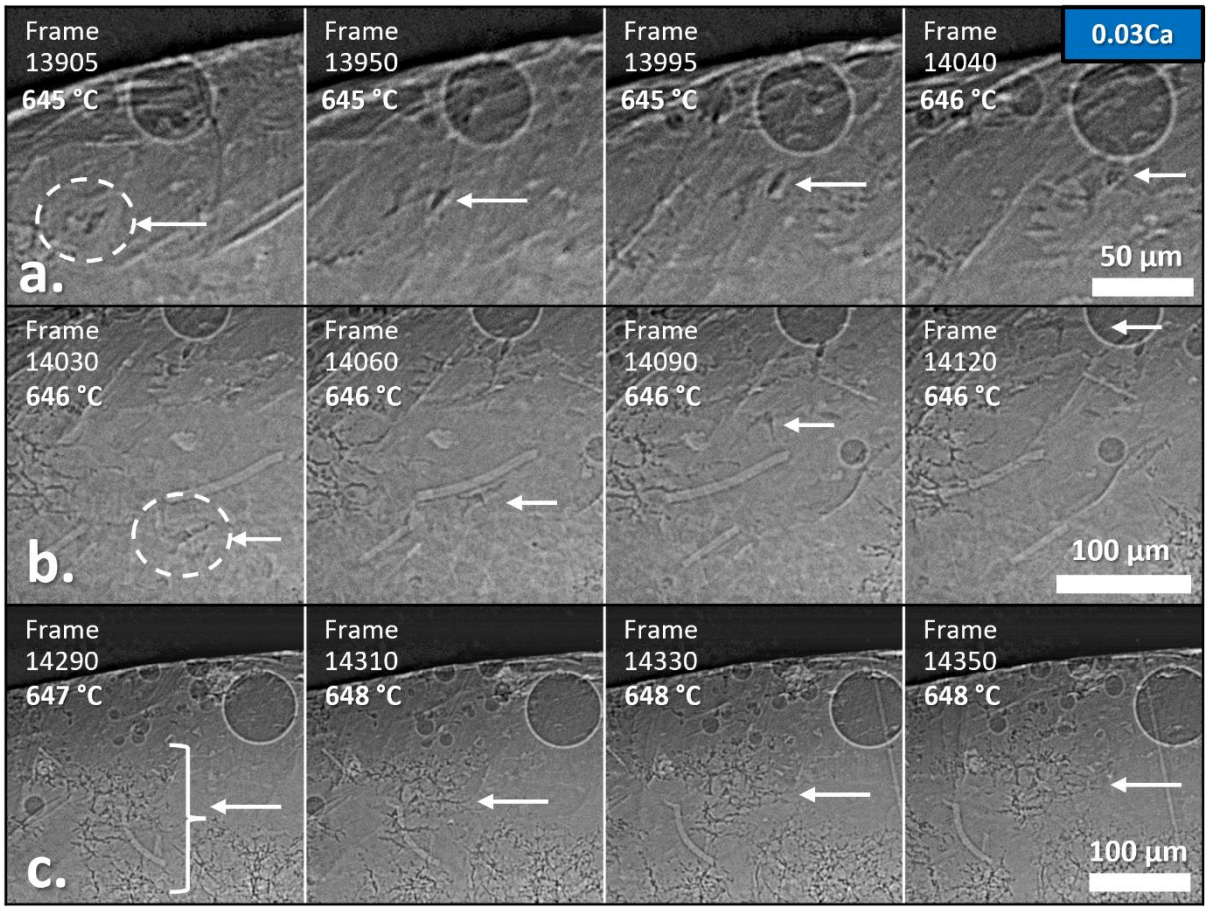


Figure 4.42. Entrained oxide flotation in 0.03Ca sample, shown by three sets of projection sequences (a, b, c).

4.5.3. Bubble formation from oxides

Bubbles form in the calcium-containing samples, but not the 0.00Ca sample (Figure 4.43). As the samples melt and after oxide fragments float upwards, bubbles begin to form. All bubbles start either from entrained oxide networks or the outer oxide shell. Bubbles also coalesce and burst on the outer shell. Readers are encouraged to view the videos of the full melting sequence of each sample (Videos A1, A2, A3) in the supplementary material, which displays this process more clearly, and use the appended commentary (Appendix C) for guidance.

No bubbles form in the 0.00Ca sample, indicating that the added calcium is responsible for this phenomenon. For bubbles originating from an entrained oxide network, the process begins as the expansion of space within the oxide network (Figure 4.44, frame 18666), which smooths out the internal surface of the entrained oxide. Afterwards, the atmosphere within the network expands into a bubble, becoming more spherical as inflation progresses (Figure 4.44, frames

18671-19101). Eventually, the bubbles dislodge from the entrained network and rise, either stopping at the top of the sample or, in the case of this highlighted bubble, lodge within an entrained oxide network (Figure 4.44, frames 19276-19291). A notable observation is that the bubble stays within the entrained oxide network and even drags along some uninflated network with it, as indicated by the lack of contrast in the area from which the bubble dislodged (Figure 4.44, frame 19281); see video B2 to see this sequence more clearly.

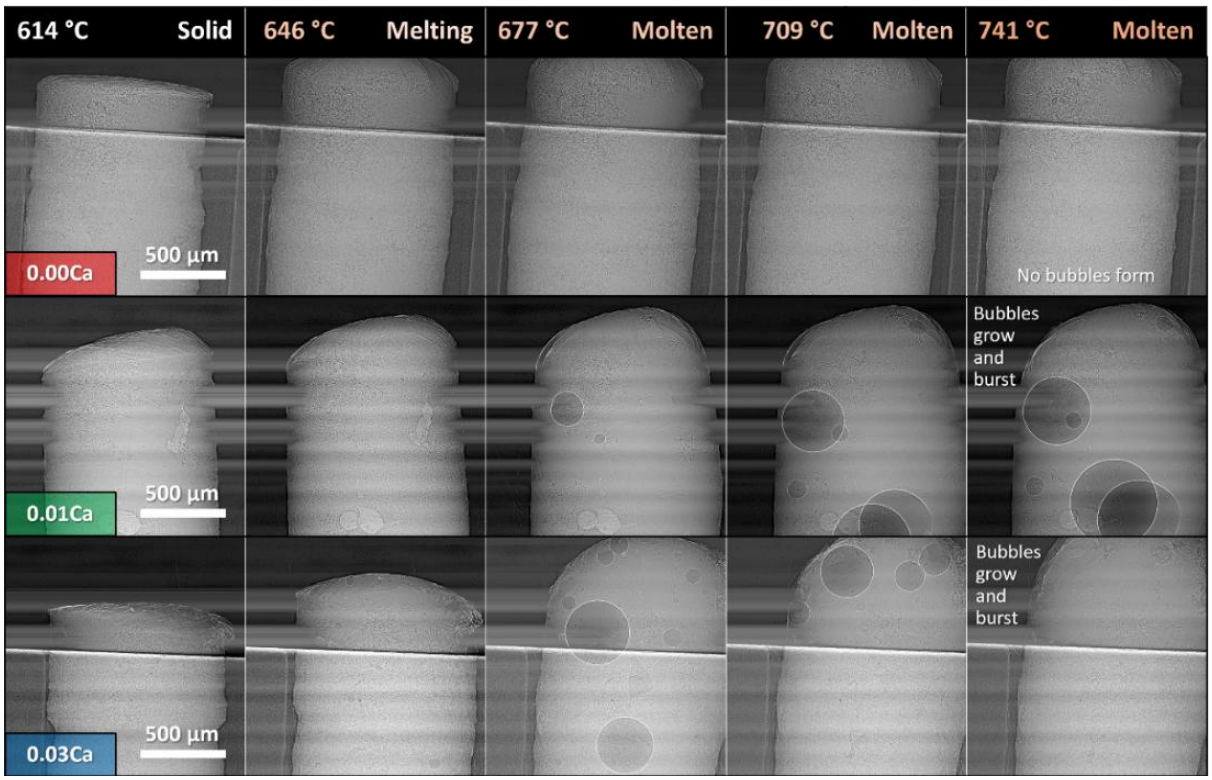


Figure 4.43. Projections taken at 180° intervals (for consistent viewing angle) of bubble formation during melting in the 0.01Ca and 0.03Ca samples, and lack of bubble formation in the 0.00Ca sample.

Tomographic snapshots confirm that bubbles form within entrained oxide networks, since these tomographs allow precise location of the bubble origin in three dimensions (Figure 4.45). During melting, porosity disappears but entrained oxide networks persist, as previously observed (Figure 4.10). Porosity networks disappear before the bubbles form, confirming that porosity networks do not grow bubbles, only entrained oxide networks. Multiple radii are seen within the snapshots of the bubbles, an image artifact caused by the bubble expanding and moving as the tomograph is taken (Figure 4.46). The bubbles grow, combine with other bubbles, and burst on the sample edge, leaving behind remnants which indicate an internal

oxide skin. Readers are strongly encouraged to view videos of the full melting sequences (Videos A1, A2, A3).

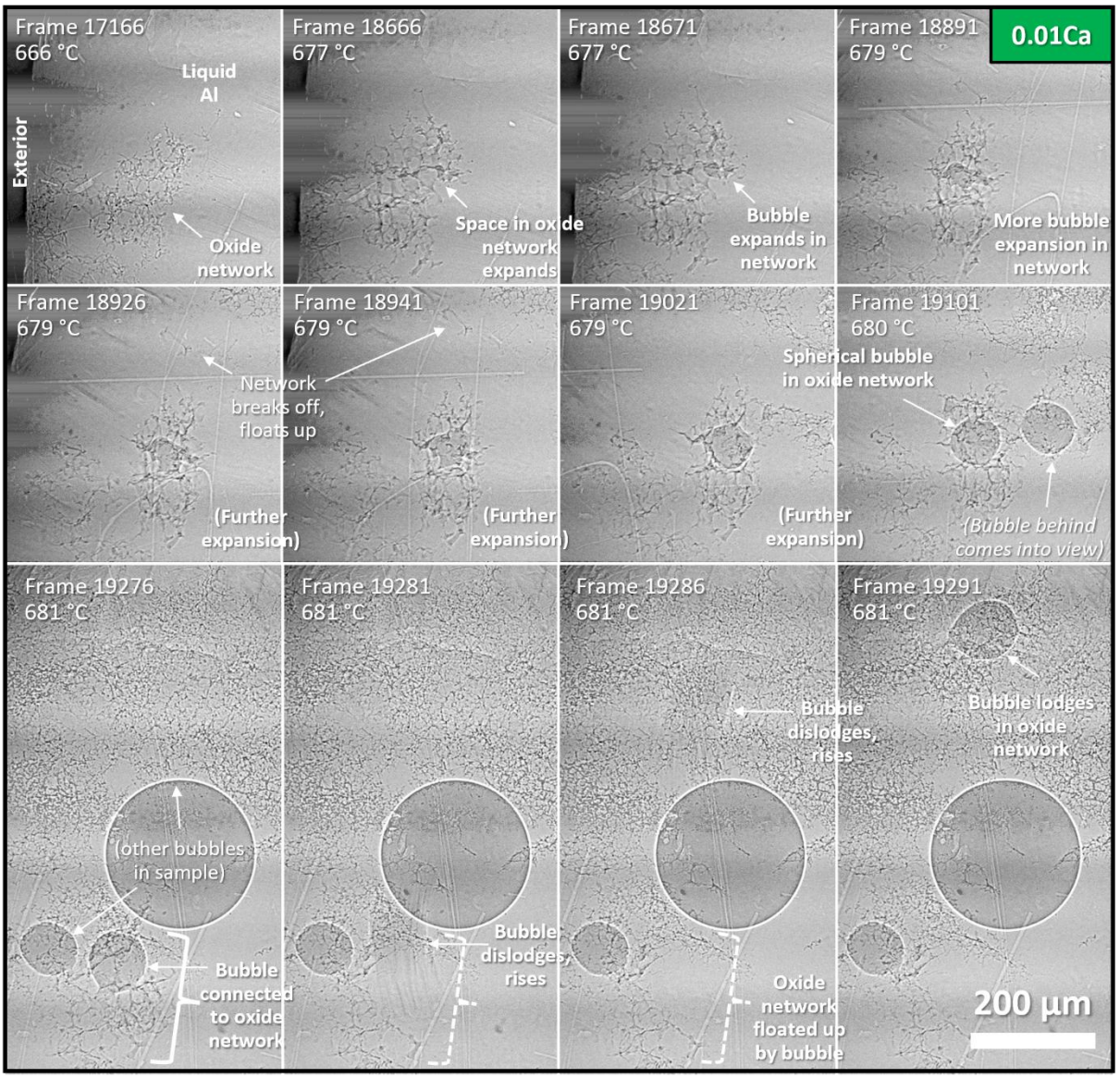


Figure 4.44. Projections showing bubble formation and growth within entrained oxide networks in 0.01Ca sample. Long white streaks in the projections are ceramic wool fibres used to secure the sample within the BN holder and so should be ignored.

The points of contact between an oxide network and a bubble leave a jagged edge (Figure 4.47, 80 min), in contrast to the smooth, concave appearance of the bubble edge where it is not in contact with an entrained oxide network. The thin oxide shell is seen to be able to hold in the bubble for a significant amount of time (more than 2 hours in the displayed case) and appears to burst only when the bubble touches an entrained oxide connected to the sample exterior.

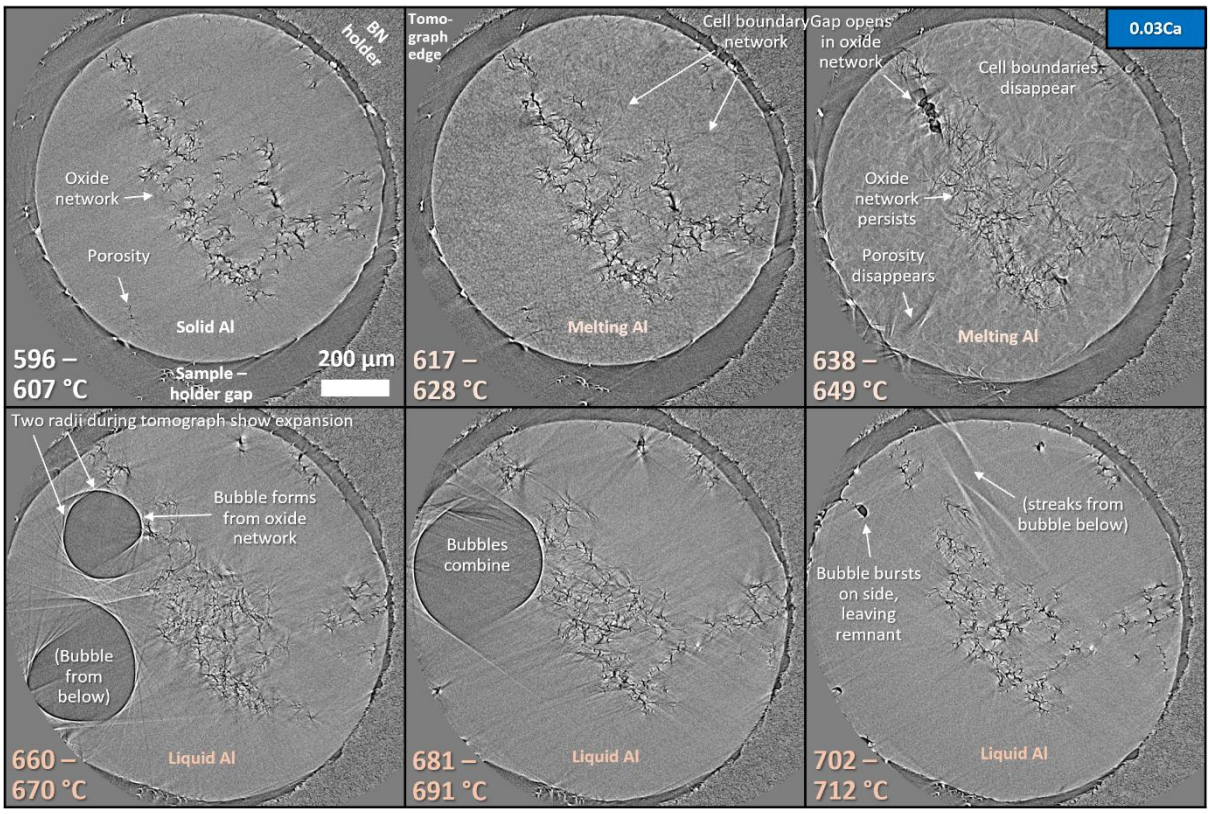


Figure 4.45. Horizontal tomographic snapshots showing bubble formation in entrained oxides in 0.03Ca sample.

It is not immediately clear whether there is a continuous oxide skin across the bubbles' curved interior surfaces. In the 0.01Ca sample, a bubble bursting on the exterior crumples immediately after bursting (within the frame rate, 20 ms), suggesting the presence of a solid skin around the bubble surface prior to deflation (Figure 4.48.a). However, when two bubbles combine within the same 0.01Ca sample, there is no crumpling or trace of the previous bubble, suggesting there is no solid layer around the bubble exterior (Figure 4.48.b). Tomographs of the 0.03Ca sample show a bubble, which formed from an oxide network after melting, leaving behind an oxide skin after deflating (Figure 4.48.c), consistent with the bubble deflating in the 0.01Ca sample on the exterior surface (Figure 4.48.a).

Oxide networks within the stacked 0.03Ca sample appear to reinflate (Figure 4.49). After melting, bubbles form via entrained oxide networks and burst on the sample exterior over time. However, likely due to a shift in the upper half of the stacked sample, bubbles form again in the lower half, via the oxide skin remnants of the samples which burst previously. This demonstrates the ability of the oxide shells within the 0.03Ca sample to maintain bubbles

within the sample, even after atmospheric exposure.

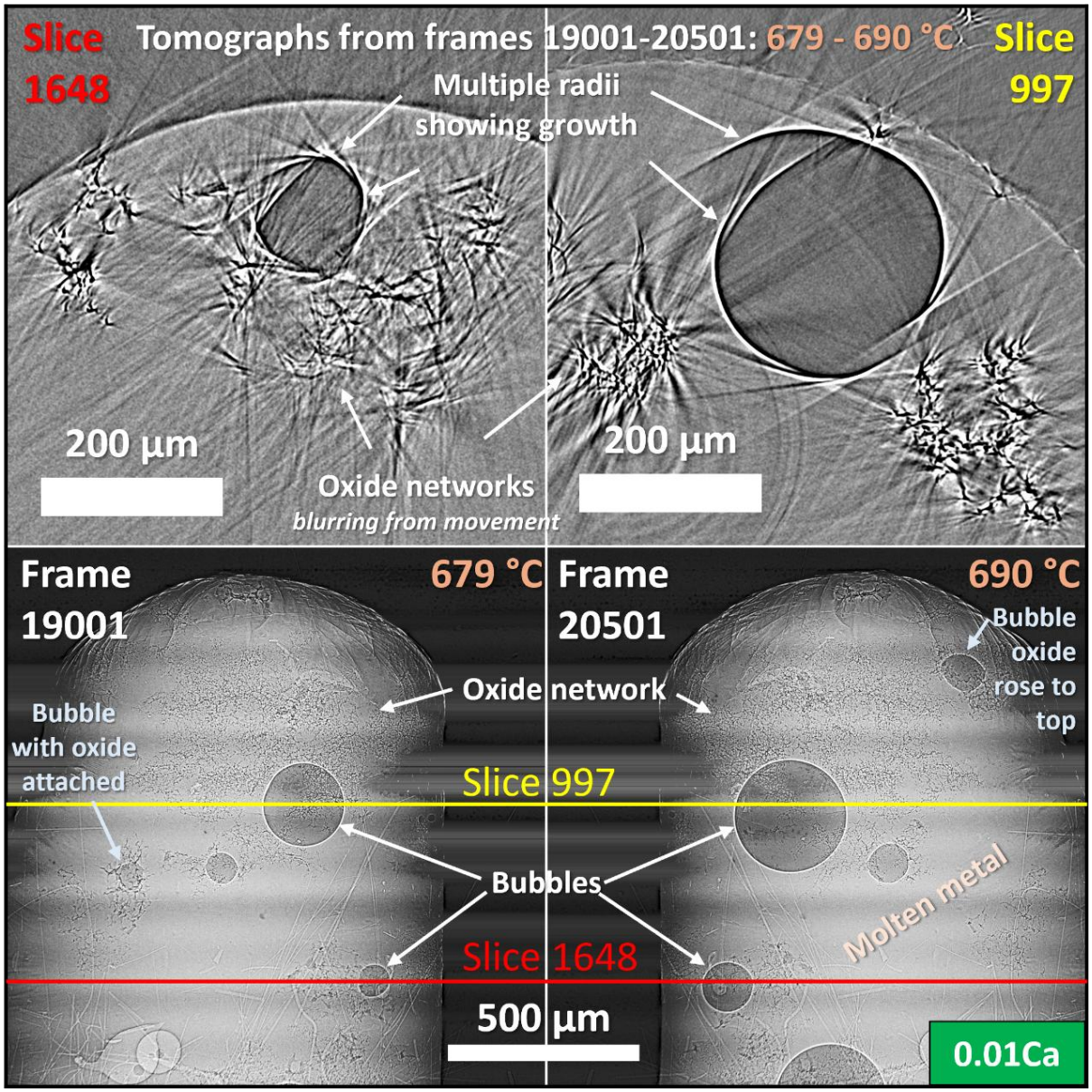


Figure 4.46. Comparison of features between tomographic snapshots and projections within the tomographic snapshots (termed 'frames') to show that bubbles form within the sample, via oxide networks.

In the same 0.03Ca sample, a bubble is found inside an entrained oxide (Figure 4.50). Here, a non-spherical bubble, indicating the presence of an oxide shell, is held down to an entrained oxide network via a bifilm. After 180 minutes, the bifilm detaches from the entrained oxide network and floats up, dragging the bifilm with it. This demonstrates the ability of a bifilm to contain a bubble, a key bifilm prediction [20].

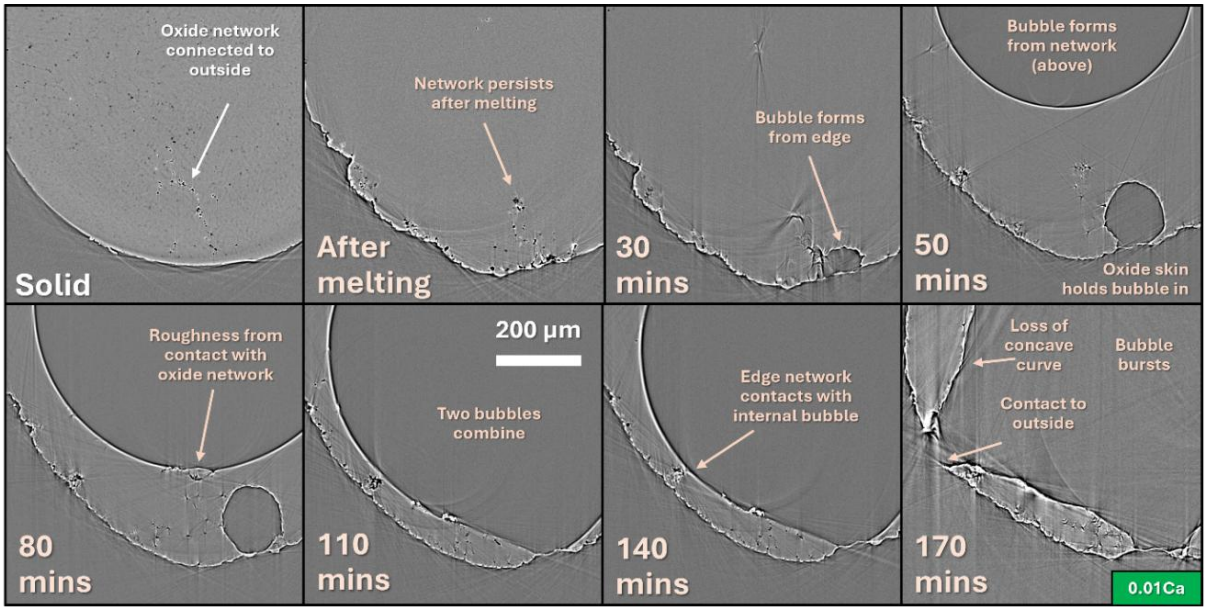


Figure 4.47. Horizontal tomographic sections showing development of bubbles in 0.01Ca sample.

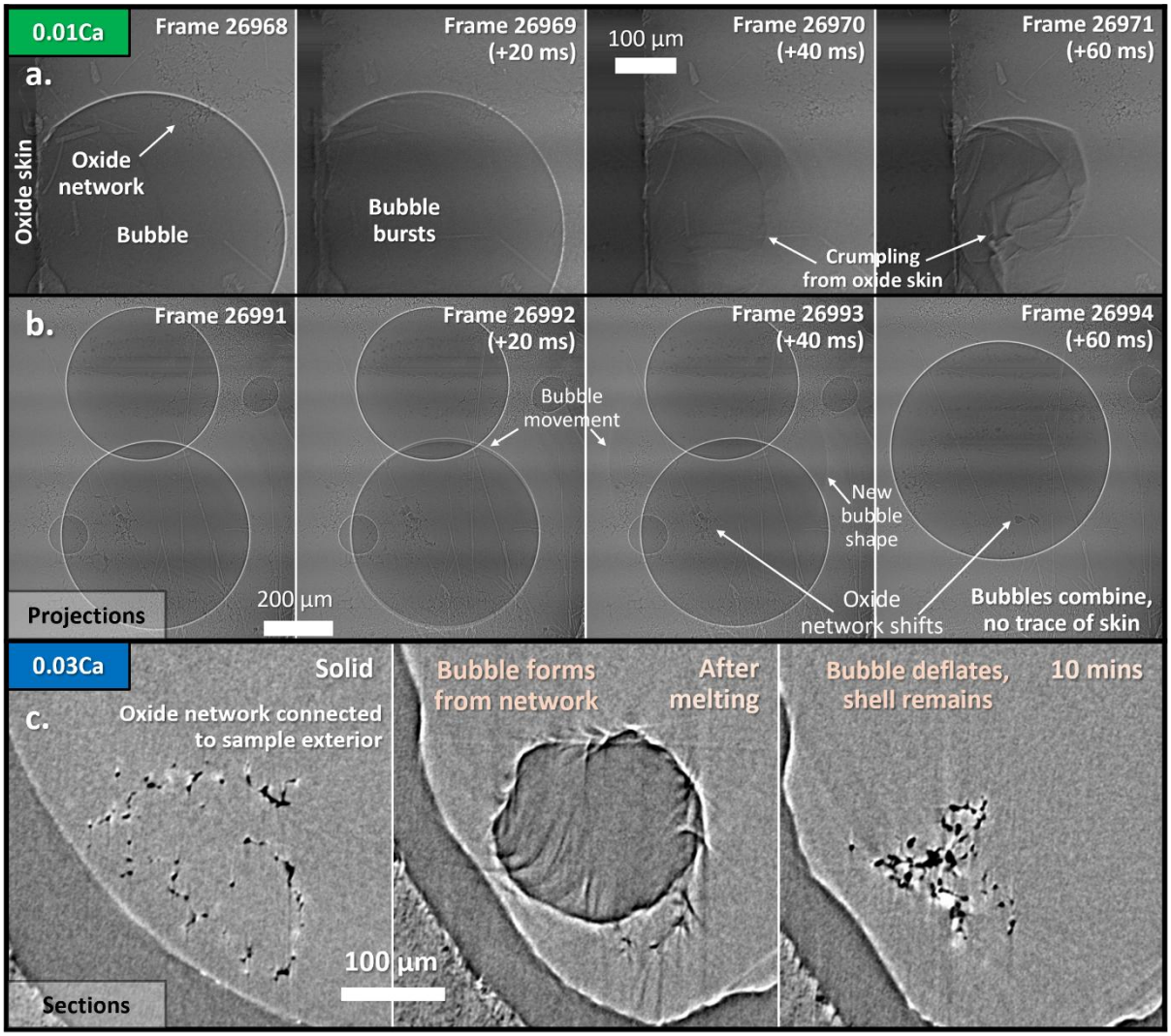


Figure 4.48. Bubbles in (a, b) 0.01Ca and (c) 0.03Ca samples shown by (a, b) projections and (c) tomographic sections.

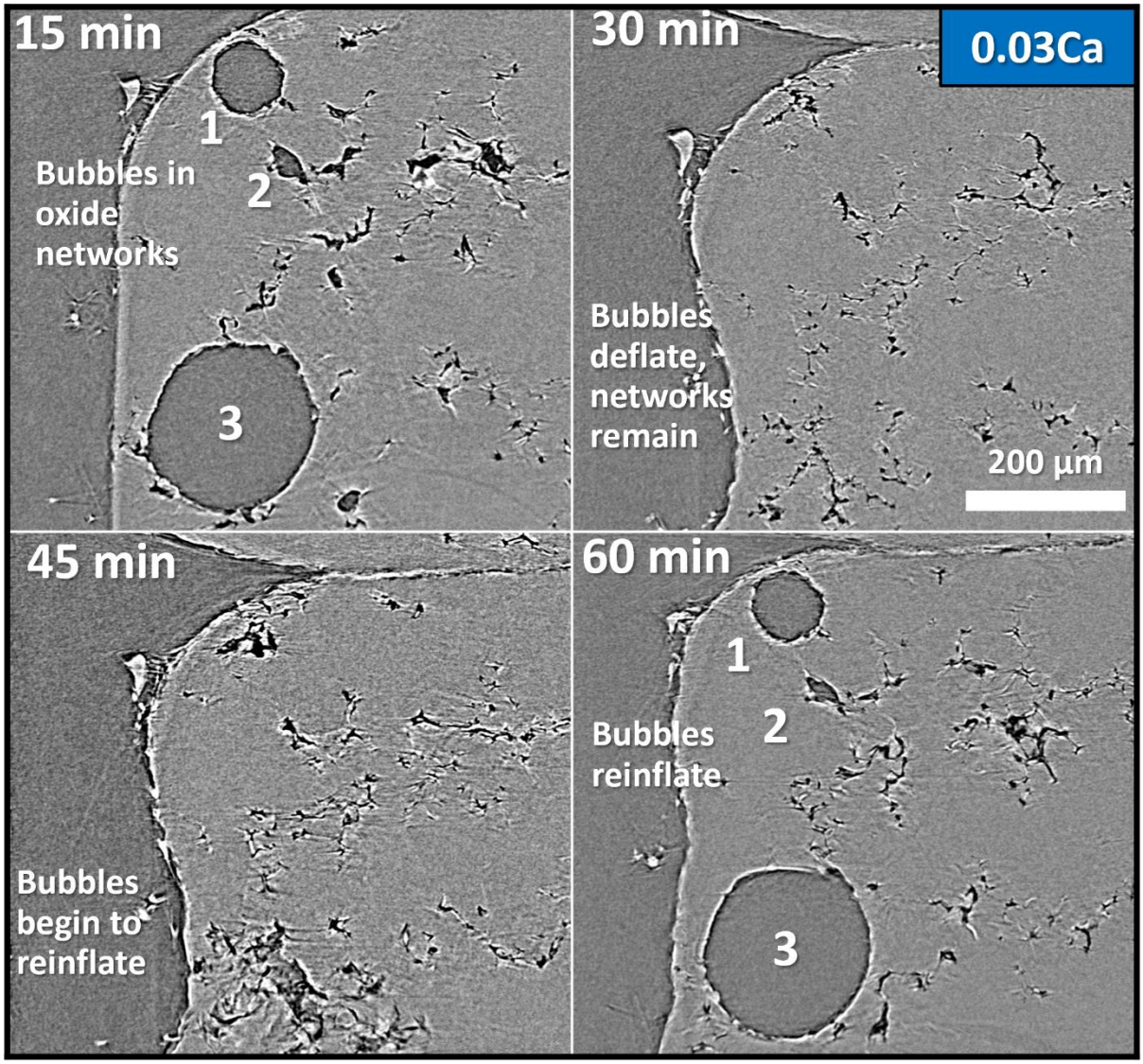


Figure 4.49. Vertical tomographic sections of stacked 0.03Ca sample (samples cut in two, fragments stacked on top of each other, then tested) showing bubble reinflation.

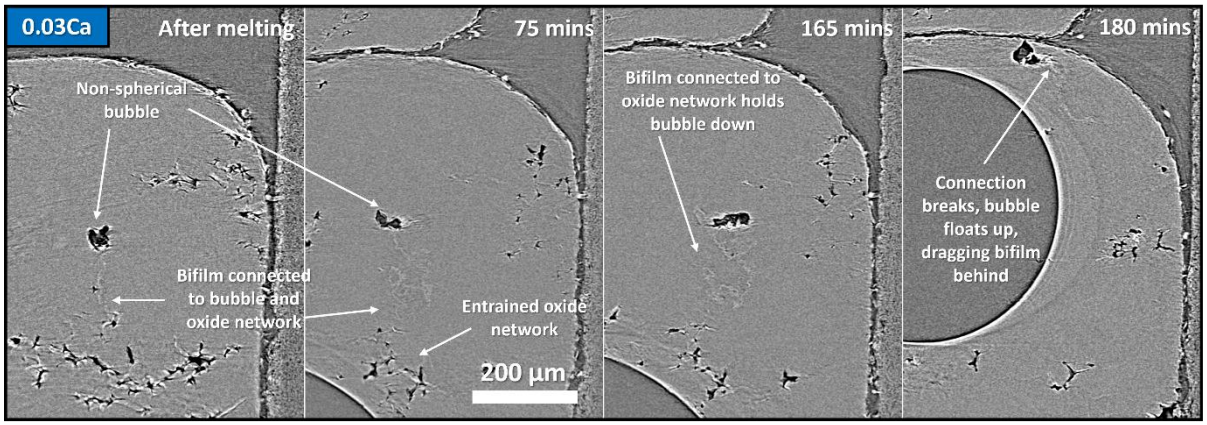


Figure 4.50. Vertical sections of the 0.03Ca stacked sample showing bifilm attachment to bubbles.

4.5.4. Bubble behaviour during solidification

During solidification, a bubble on the side of the 0.03Ca sample inflates hugely (Figure 4.51).

There is also a lack of intercellular porosity in the area near this inflated bubble, in contrast to other regions in the same sample, where porosity is seen in the last regions to solidify.

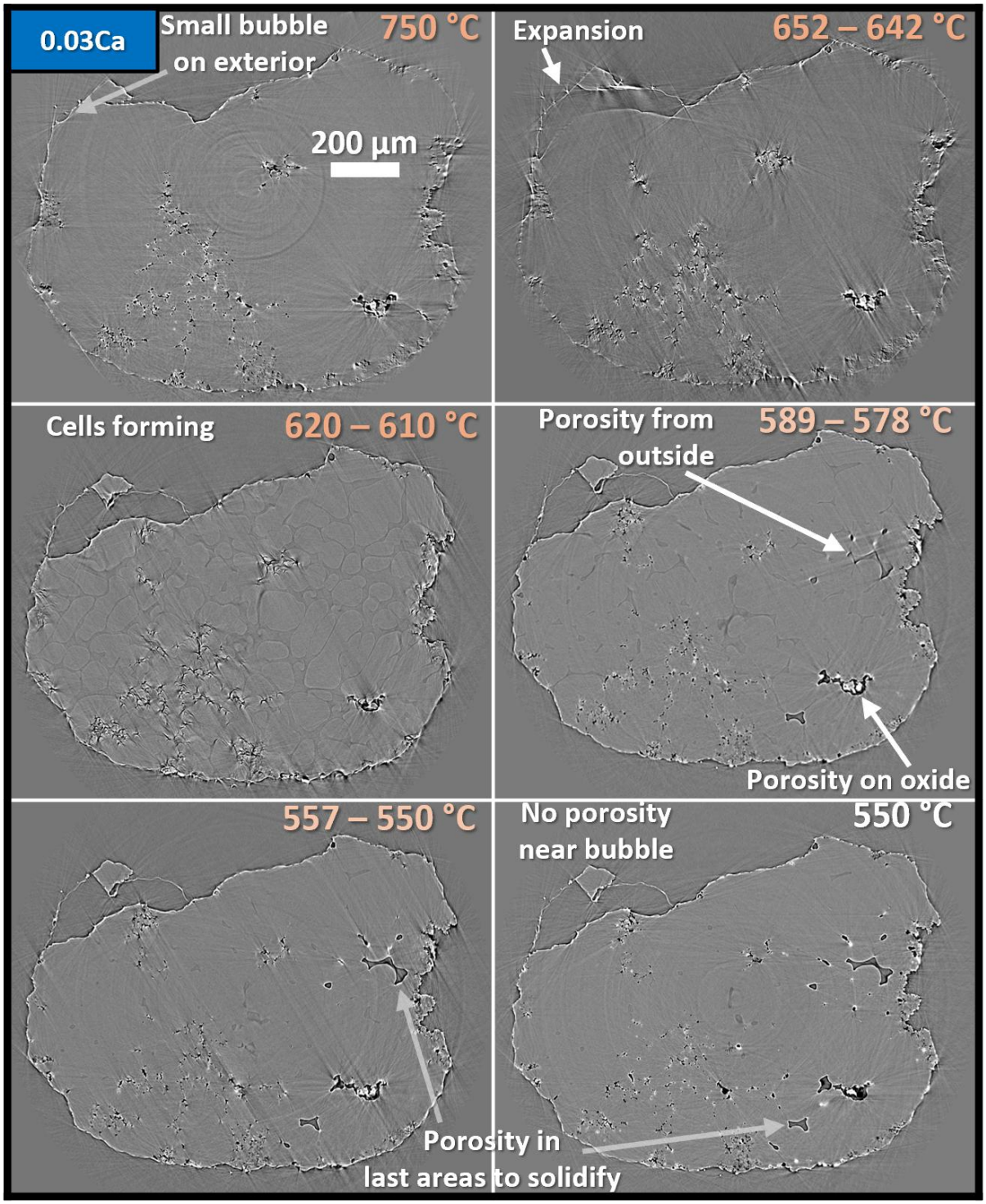


Figure 4.51. Horizontal sections of tomographic snapshots of 0.03Ca solidification showing bubble expansion.

This indicates hydrogen ejected from the melt during solidification may be ejected into the bubble, gas which would otherwise be ejected into the intercellular boundaries during the final stages of solidification. Furthermore, there is some porosity seen near an entrained oxide

(Figure 4.51, 589-478 °C), indicating that these networks may perform the same role and reinforcing the idea that entrained oxides may provide substrates for solidification porosity.

4.5.5. Discussion

The results presented here show that deoxidation of Al-Mg alloys by calcium is facilitated by the flotation and inflation of entrained oxide networks. Without the added calcium, entrained oxide networks do not break off or float upon melting. With the added calcium, fragments of the porous oxide network break off during melting and float upwards (Figure 4.41), only caught by the sample edge or another oxide network (Figure 4.42). These networks were established to be entrained oxides by the previous subchapters, and the rigidity of the shape during flotation confirms that these are not merely intercellular porosity, which disappears on melting before entrained oxide networks begin to float (Figure 4.39). The observation of flotation without expansion proves these entrained oxide fragments are porous, consistent with tomographic data and observations of extracted oxides analysed in the previous subchapters.

After network flotation, bubbles form from the entrained oxide networks, again only in the Ca-added samples (Figure 4.43). All bubbles are found to form either from entrained oxide networks (Figure 4.44) or the sample exterior (which itself is an oxide) and bubbles are observed to drag the attached oxide networks upwards with them (Figure 4.44), including bifilms (Figure 4.50). The growth of these bubbles is likely facilitated by hydrogen dissolution upon melting: as aluminium melts, the solubility of hydrogen increases significantly [30], leading to dissolution of hydrogen into the melt from the atmosphere, the extent increasing with both time and temperature. This hydrogen then diffuses through the melt and into the oxide networks (Figure 4.44), which begin to contort and expand due to the pressure of the hydrogen diffusing inwards (Figure 4.45).

As the bubbles grow, they eventually break off from the oxide networks from which they originated, float upwards, and, if they make contact with the exterior, eventually burst (Figure

4.47), sometimes combining with other bubbles in the process. Since both the initial network flotation (Figure 4.41) and subsequent bubble formation (Figure 4.44) result in flotation of the entrained oxide, it can be reasonably deduced that this is the process of deoxidation by calcium addition. Not all oxide networks in Ca-added samples undergo fracture, flotation, or expansion. The reason for this is not clear, but it could be due to variations in hydrogen concentration across the sample or differences in thicknesses and strength due to the complex morphology of the networks. However, the fact that the flotation and bubble formation only occur with added calcium (Figure 4.43) is significant and demonstrates that the added calcium is the cause.

All bubbles observed to form within the samples originate from entrained oxide networks. Classical nucleation analysis by other researchers has contended that hydrogen bubbles cannot nucleate within aluminium melts [31], either homogeneously or heterogeneously, and that an existing gaseous atmosphere is required for a bubble to form in the melt. In essence, hydrogen bubbles do not nucleate, but grow from existing gas bubbles, bypassing any thermodynamic barrier to nucleation. Entrained oxide networks give a suitable substrate: entrained oxides trap air, and reaction between trapped oxygen and the melt produces an oxide layer which prevents further diffusion of gases outwards. The addition of calcium to an Al-Mg alloy results in this oxide becoming thin and flexible [1], allowing fragments to break off and float, and hydrogen to diffuse inwards, causing expansion and subsequent flotation. Without the added calcium, the entrained oxides stay rigid, preventing any network flotation or inward hydrogen diffusion and flotation from occurring (Figure 4.43).

While there is strong evidence to show that bubbles grow from the gaseous atmospheres of entrained oxides, they are generally not observed to grow from bifilms, as previously claimed [32]. This is almost certainly because the distinction between entrained oxide networks and bifilms has only been made in this study. The distinction is somewhat akin to the difference between ‘old’ and ‘new’ bifilms [19], where ‘old’ bifilms are thicker, less rigid, and occur from

earlier processing steps than ‘new’ bifilms, but this study demonstrates that the ‘new’ bifilms (i.e. entrained oxides from the pouring itself) are not simply thinner versions of ‘old’ bifilms. The distinction is a fundamental morphological difference between extensive, convoluted, porous oxide networks and small, rigid bifilms with limited porosity.

The arguments made for the ability of ‘bifilms’ to grow hydrogen bubbles [15,31] are therefore more appropriately applied to the porous oxide networks: the oxide surfaces are observed to smooth out (Figure 4.44), akin to the hypothesised bifilm ‘unfurling’ process [15,32], and expand through inward hydrogen precipitation into the pre-existing gaseous atmospheres, resulting in bubbles which are not perfectly spherical. This expansion is permitted by a lack of bonding between the two outer surfaces of the porous oxide network and the flexibility of the oxide layer caused by the addition of calcium, as previously acknowledged [15,31]. In contrast, the ‘bifilms’ observed here contain far less porosity and have significantly more bonding across them, making them less suitable for expansion, even if connected to a large bubble (Figure 4.50); in this highlighted case where a bubble is found connected to a bifilm, the bubble does not expand throughout the bifilm, with its two sides remaining bonded over a significant area. The role of bonding across entrained oxides in permitting or prohibiting bubble expansion is indirectly acknowledged in studies into bifilm healing in Al-Mg alloys [26]: whether a bifilm would heal or not was determined to be down to a balance between the consumption of trapped oxygen and nitrogen, which closes the bifilm gap, and hydrogen ingress, which inflates the bifilm. Therefore, if a bifilm has a high degree of bonding across the interface and a low gas content compared to the oxide thickness, it will be able to resist inflation by hydrogen and so does not provide a suitable substrate for the growth of a hydrogen bubble.

Proponents of the involvement of bifilms in forming hydrogen bubbles also speculate that all hydrogen porosity is associated with bifilms [15,32]. While there is evidence that porosity can originate from entrained oxides (Figure 4.51), the formation of porosity appears to be more

strongly correlated with the regions in which the intercellular regions are widest just before final solidification. Furthermore, some porous networks are observed to disappear without trace upon melting (Figure 4.39), showing that there is not always a continuous oxide layer between the porosity and the solid in these structures. These smoother porosity regions are therefore not consistent with inflated entrained oxides, although there may be an association in the sense that these regions may start at and grow from an entrained oxide (Figure 4.51).

The gaseous composition of the bubble probably varies between bubbles. Whilst the techniques used here do not measure composition directly, inferences can be made from the tomographs. Bubbles which either contact the sample exterior during growth or initially grow from the sample exterior appear to have significant concentrations of oxygen: when bursting, oxide skin remnants are observed in tomography (Figure 4.45). This could be explained by the formation of an oxide skin upon bursting itself, were it not for the time frame over which the skin forms: projections of a bubble bursting in the 0.01Ca sample (Figure 4.48.a) show that the surface of the melt crumples within one frame (20 ms), indicating that a solid film was already present along the surface. Given the composition of the melt and the atmosphere, the most likely candidate for this solid film on the internal surface of the bubble is an oxide.

However, bubbles combining in the same sample, both of which grew from entrained oxides within the melt, do not leave an oxide skin behind (Figure 4.48.b). This also indicates that the bubbles are likely to be hydrogen bubbles, since oxygen or nitrogen would react with the surrounding melt and form solid films that would be visible during and after bubble combination. The solidification sequence also indicates that flexible oxides within the 0.03Ca sample are able to contain hydrogen bubbles: as the sample cools and solidifies, hydrogen dissolved within the melt is expelled due to the decrease in the hydrogen solubility of the melt [30]. In this sample, a small bubble on the exterior surrounded by an oxide film greatly expands (Figure 4.51), and there is a distinct lack of porosity in this area compared to other regions

within the same horizontal section, in which porosity is observed in the areas last to solidify. This demonstrates that oxide films in Ca-added Al-Mg melts can provide spaces for inward hydrogen diffusion and hydrogen bubble formation.

The flexibility of the oxide skins in the Ca-added samples and the ability to hold bubbles is further demonstrated by the reinflation of oxide networks in the 0.03Ca sample (Figure 4.49). On melting, bubbles form from entrained oxide networks but burst over time, leaving behind oxide skin shells. However, these bubbles reinflate over time, likely due to sample movement in the upper half of the stacked sample, showing the ability of these flexible oxides to contain gaseous bubbles within the melt.

4.5.6. Preliminary conclusions

In this subchapter, it is shown that calcium deoxidises through entrained oxide network flotation, either as entrained oxide fragments or bubbles attached to entrained oxides. This is because the addition of calcium results in thin, flexible oxide films which more easily contort and allow inward hydrogen diffusion, resulting in oxide network flotation and bubble formation. Without added calcium, oxide films remain rigid and unable to grow bubbles. The results here also show that hydrogen bubbles in aluminium melts grow from atmospheres trapped by entrained oxides and support the hypothesis that hydrogen bubbles cannot nucleate within aluminium melts. However, the entrained oxides from which they predominantly grow are not bifilms, but more complex entrained oxide networks established by this study.

4.6. Further observations

This additional subchapter will discuss other observations made from this study that are less scientifically significant, but still noteworthy for the purposes of a thesis, as well as some caveats which are acknowledged to start with. Firstly, these samples are much smaller than what most in the field would call a ‘melt’: the samples are c. 1 mm wide and 5 mm long, whereas a normal casting melt can be many orders of magnitude larger. Therefore, there will

be differences: the molten material in the samples here is very close to the surface, allowing hydrogen to more easily diffuse into the melt, and the temperature will be more uniform, resulting in less convective flow.

For oxidation, this is unlikely to change the conclusions significantly, since oxidation occurs at the surface anyway; a larger sample exposes a lower proportion of the sample in question to the melt, but the melt surface is unlikely be significantly different morphologically. However, a larger melt is more prone to surface disturbance through convection and liquid movement, which could alter the way that the melt is exposed to the atmosphere and alter the importance of entrained oxides in the melt oxidation process.

In terms of the effect of calcium deoxidation, a larger melt would likely enhance the effects seen: larger melts have stronger convection currents, causing more disturbance within the melt, allowing fragments to break off and float upwards. If the transport of hydrogen were also enhanced by this, then more bubbles would form, leading to increased deoxidation.

However, speculations on the effects of increasing the melt size do not alter the fact that the conclusions are based on the samples tested. The small size was necessary to allow the high resolution needed to observe the features of interest and hold them still, permitting 3-D tomographic reconstruction, and this led to some important observations. Further research is needed to confirm the speculation that this behaviour would be repeated in larger melts.

4.6.1. Stacked samples

Each alloy was tested in a ‘stacked’ configuration in which the sample was cut in half, stacked vertically within the BN holder, and observed with tomography with the field of view positioned at the interface between the two fragments. These samples were tested in the same way as the other samples, but without continuous scanning on heating and cooling: an initial scan at room temperature, scans at regular intervals whilst the sample was held at 750 °C for three hours, and a scan at room temperature after the sample had solidified.

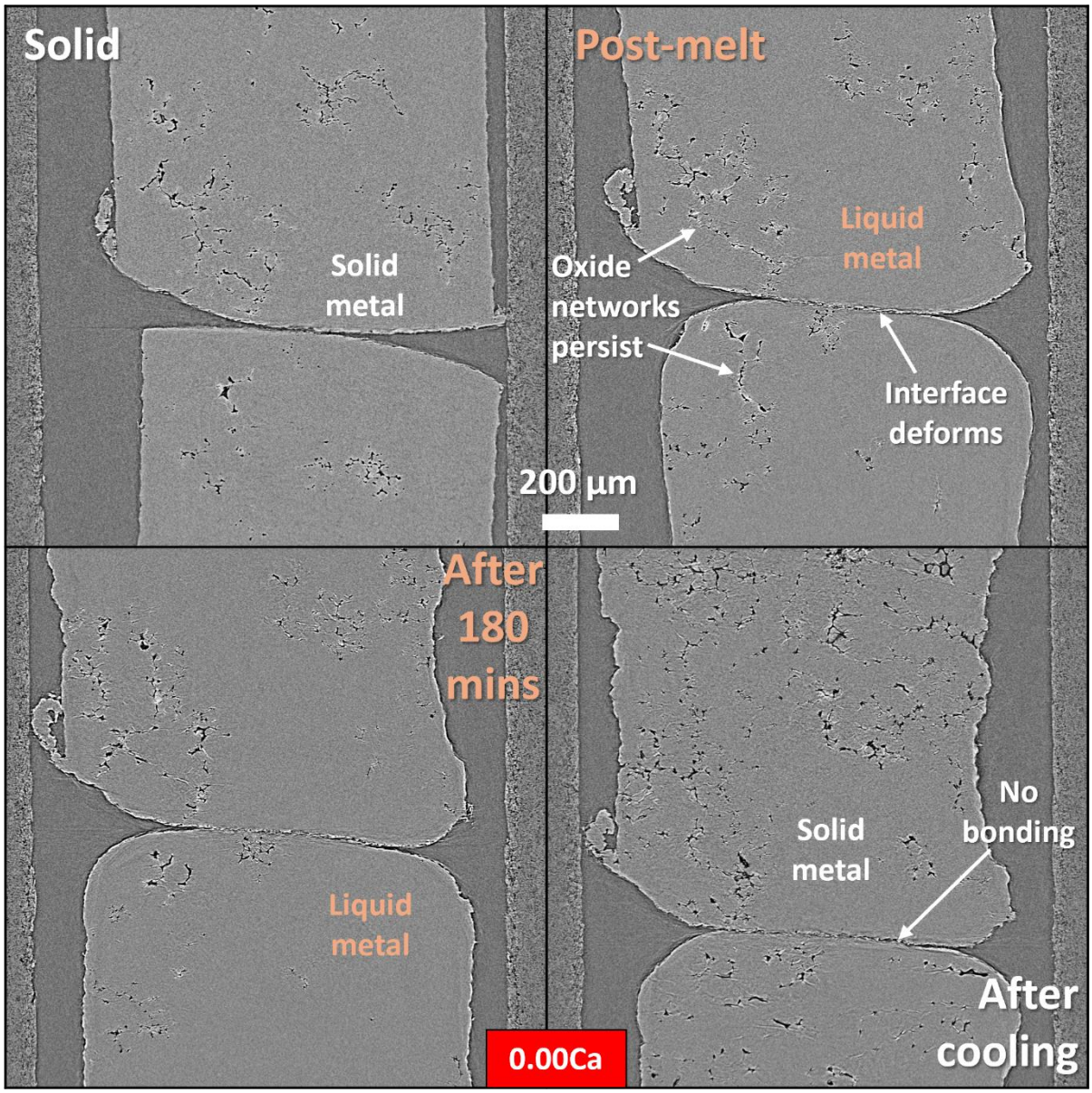


Figure 4.52. Vertical tomographic sections of 0.00Ca stacked sample before melting, after melting, after 180 minutes of a melt hold (750 °C), and after solidification.

The motivation behind testing samples in the stacked configuration was to test the melt bonding behaviour of these samples: aluminium is notoriously difficult to weld [33], a finding largely attributed to native surface oxide layers present and their persistence even when the sample is molten [34]. Other researchers have used a stacked configuration of various aluminium alloys as an analogue for a bifilm, since stacking two alloys and melting them produces a double oxide layer held in a melt with an atmosphere inside [35–37]. These studies found that when Al_2O_3 films were not the most thermodynamically stable oxide in contact with the melt, the melt would react with the native film to produce other oxides, resulting in some degree of bonding

if held for long enough.

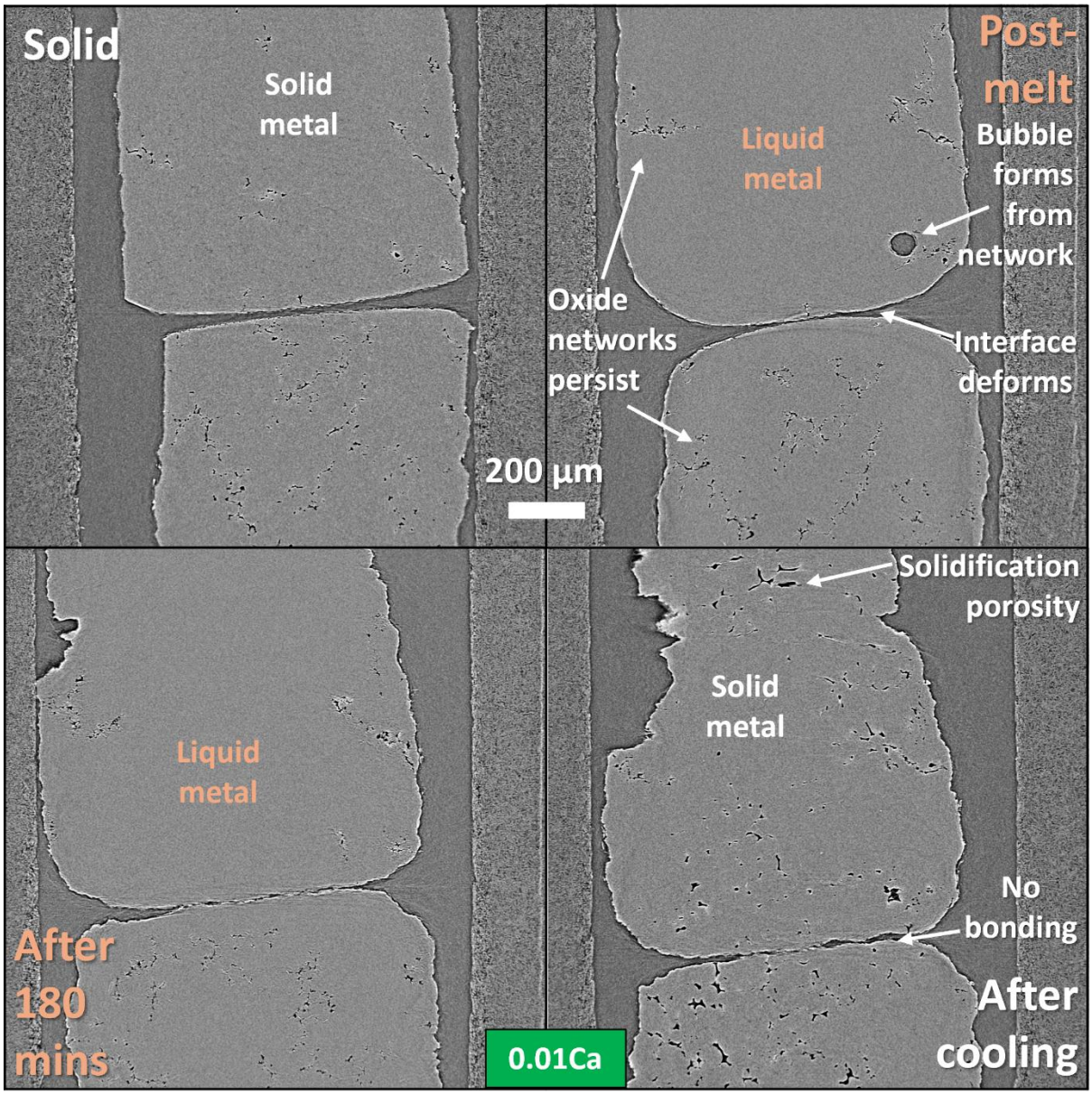


Figure 4.53. Vertical tomographic sections of 0.01Ca stacked sample before melting, after melting, after 180 minutes of a melt hold (750 °C), and after solidification.

In these samples, no bonding was achieved across the interface in any case (when removing the samples from the holders, they easily came apart), and the melt behaviour largely reflected the observations of the non-stacked samples. In the 0.00Ca stacked sample (Figure 4.52), the interface deforms after melting, and many oxide networks are seen to persist. After 180 minutes, there is very little change in the sample morphology, including a lack of visible oxidation: this is likely due to the field of view, which is below the top surface. Like the other 0.00Ca samples, no bubbles are observed to form. After solidification, some porosity can be

seen, but no bonding occurs across the interface. In the 0.01Ca stacked sample (Figure 4.53), the interface also deforms after melting, and a bubble is seen to form from an oxide network, like the non-stacked sample (Figure 4.47). No breakaway oxidation can be seen, and no bonding is observed over the interface after solidification, whilst some solidification porosity can be observed.

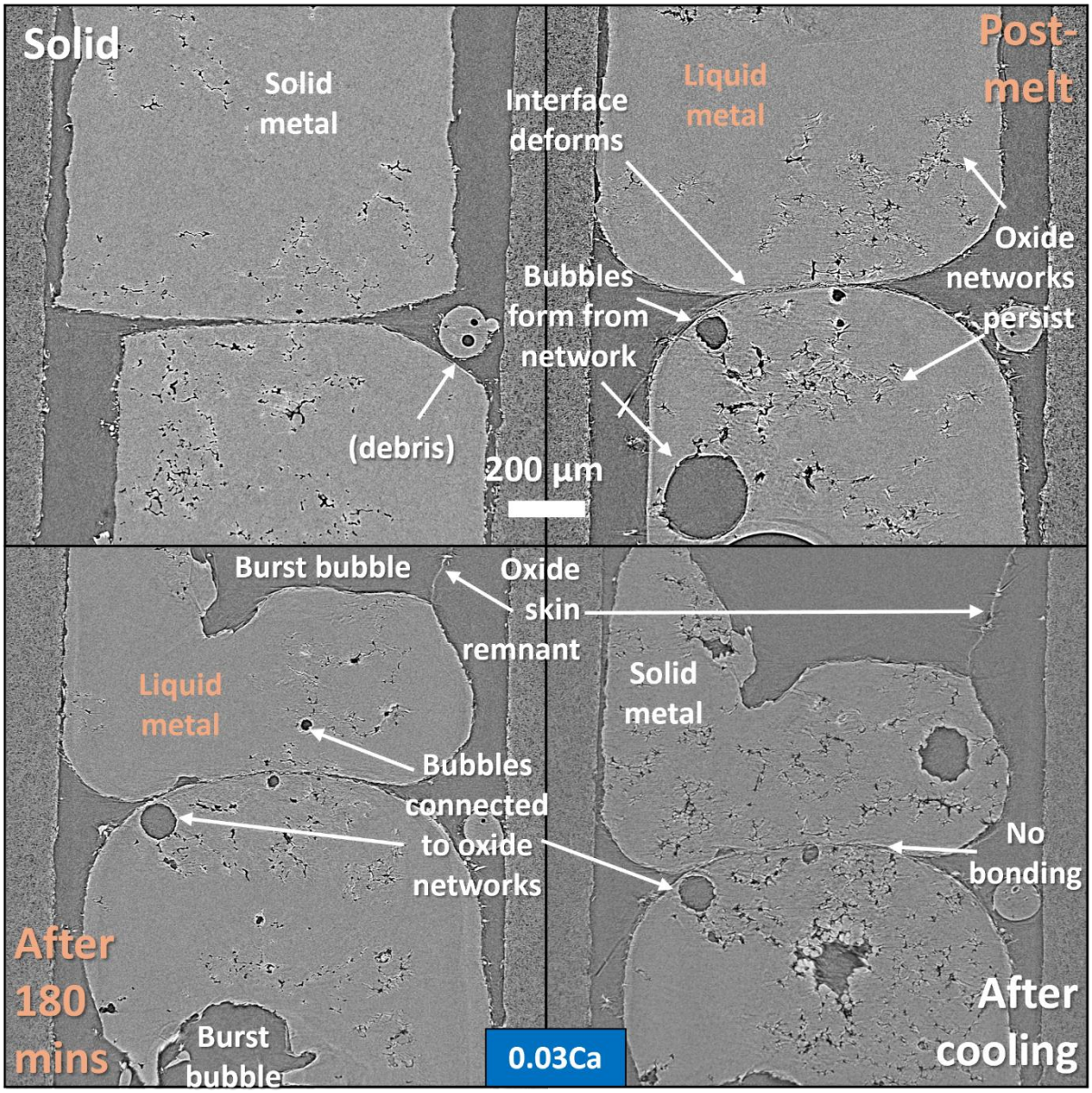


Figure 4.54. Vertical tomographic sections of 0.03Ca stacked sample before melting, after melting, after 180 minutes of a melt hold (750 °C), and after solidification.

In the 0.03Ca stacked sample (Figure 4.54), the interface deforms after melting, and many bubbles can be seen forming from oxide networks over the course of the melt hold. They are observed to form, grow, combine, burst, and even reinflate, as previously mentioned (Figure

4.49). An oxide skin remnant can be seen, left behind after a bubble bursts, and no visible oxidation was observed. After solidification, no bonding was found across the interface. The results here are consistent with previous observations that the native oxide skin prevents the joining of two molten aluminium samples in contact with each other: in each alloy, the native oxide skins are observed to deform and increase the area of contact, but the molten alloys are prevented from contact by the native oxide layer.

4.6.2. Image artifacts

Various imaging artifacts can be seen in the tomographs presented. Most of these artifacts are mitigated by the reconstruction process but are visible in the presented tomographic sections due to the high contrast required to display features, especially bifilms (Figure 4.55).

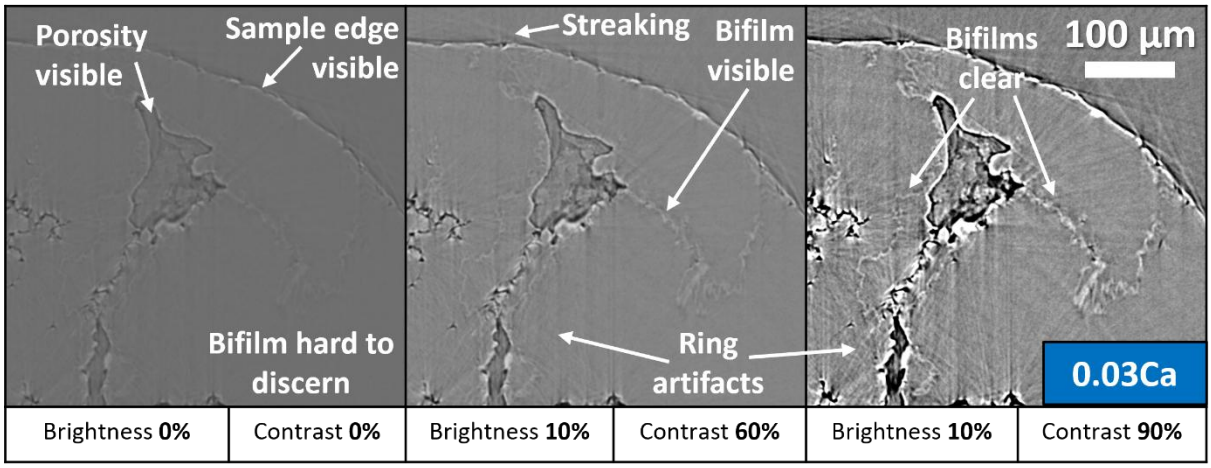


Figure 4.55. Horizontal tomographic section of bifilm in molten 0.03Ca (Figure 4.30) at different brightness and contrast values, demonstrating that the contrast levels required to discern features like bifilms end up exacerbating the prominence of artifacts seen in tomographs.

The main artifacts seen are streaks, caused by sudden changes in the density of the medium through which the beam passes through, and ring artifacts, concentric rings around the rotation centre caused by errors in detector pixel values. As mentioned, the reconstruction algorithms contain ring removal steps, which are largely successful as shown by the lack of rings visible in the image without any brightness/contrast correction (Figure 4.55); they are only visible when the contrast is increased significantly (90% in this case).

Whilst these two types of artifacts do affect the appearance of the image, they do not affect the

validity of the observations or conclusions made. Firstly, the geometry of these artifacts is clear, easily identifiable, and distinct from the other structures: ring artifacts are smooth rings around the centre and streaks are straight bright lines, whereas the features of interest are much more irregular in shape, allowing the eye to filter. Secondly, no observations or conclusions made here rely on the precise pixel values: observations are based on qualitative observations of the morphology of features of the samples. Images are therefore displayed with high contrast to make the appearance of the features of interest clear and maximise the information conveyed, at the expense of exacerbating the effects of reconstruction artifacts, which constitute superficial blemishes at most.

Some blurriness was encountered due to the field of view not capturing the whole sample apparatus width (Figure 4.7). When the field of view did not encompass the full BN holder, blurriness was introduced into the sample (Figure 4.56). This is because some parts of the holder appeared in some projections, but not others, depending on the rotation angle. This introduces errors into the reconstructed tomograph, since the reconstruction algorithms rely on the assumption that all absorbing media (i.e. not air or vacuum) encountered by the beam during the acquisition of the tomograph remains in the field of view throughout the scan. This results in blurriness below the top of the BN holder, which can be seen in the vertical tomographic sections (Figure 4.7). Luckily, since the BN was relatively homogenous and of uniform width, the blurriness was not severe, and features of interest could still be distinguished.

Sample movement also caused some blurriness, especially during melting (Figure 4.45) and solidification (Figure 4.37). These artifacts are unavoidable in such dynamic processes, and the artifacts even provide evidence: in tomographic snapshots of the 0.03Ca sample melting (Figure 4.45), the multiple radii show the bubble to grow from inside the network itself. Clearly, the bubble never has the jagged, discontinuous surface that a naïve interpretation of the tomographic snapshots would suggest; this justifies directly presenting projections in this

study since, despite providing only 2-D information, projections allow these movement artifacts to be identified and understood.

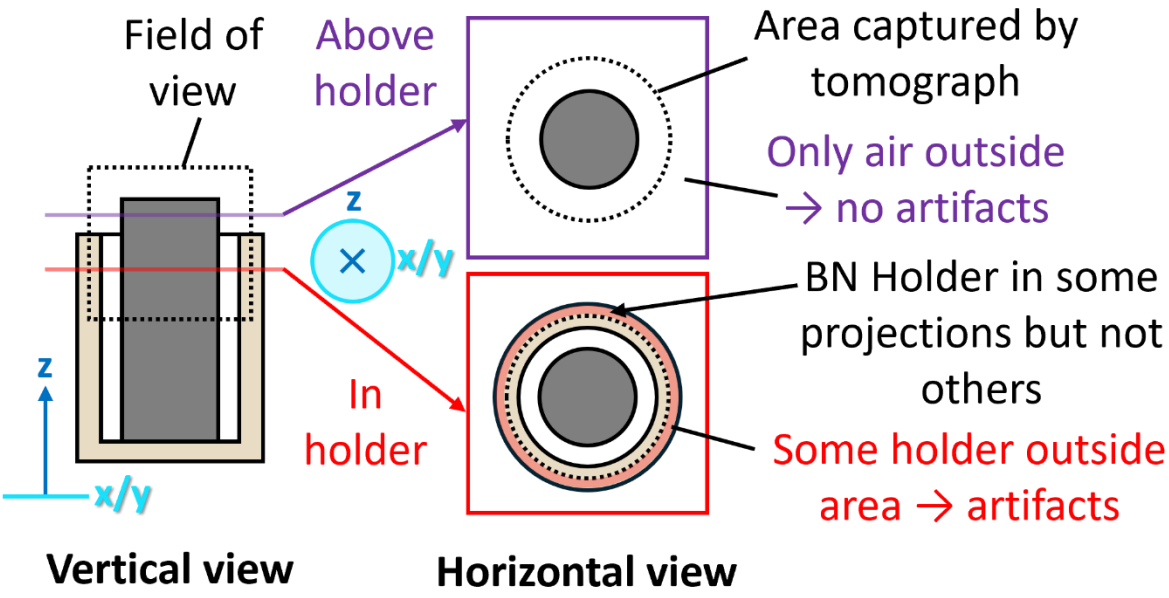


Figure 4.56. Effect of field of view on reconstruction artifacts: when field of view does not capture whole sample width, blurriness occurs in that section.

In addition, areas of saturation can be seen in the projections along the sides (e.g. Figure 4.43) of the images. This was due to the detector saturating in certain areas during acquisition, such that flat-field and dark-field correction were unable to fully correct the image, giving the banded appearance seen. This was caused by another investigator changing imaging acquisition parameters for their work and not noting this change before shift handover. There was not time to repeat these tests after this realisation; such is the nature of synchrotron experiments. Thankfully, the saturation was not too severe, and plenty is still visible within these projections. As with the tomography, observations and conclusions using these projections are qualitative in nature, so the banding caused by the ineffective flat-field and dark-field correction also is inconsequential to the validity of the conclusions made.

4.7. Conclusions

This study constitutes the first direct observations of entrained oxides within molten aluminium alloys and unambiguously proves their existence in aluminium alloy melts. Entrained oxides

are found as two morphologically distinct populations: convoluted networks of thin, flexible, porous oxides formed by oxidation of the melt on pouring which are attached to thicker oxides which resemble the traditional description of bifilms, originating from melt oxidation before the final pour. The 'waffle fries'-like shape of the entrained oxide networks is explained through its flexibility and being shaped by solidifying dendrites.

Entrained oxide networks are found to encapsulate bifilms, debris, and gas bubbles both in the solid and liquid states, proving this long-speculated behaviour of bifilms. Hydrogen bubbles originating within the melt form only from entrained oxide networks, consistent with claims that hydrogen bubbles cannot nucleate within aluminium melts but can only grow from existing gaseous atmospheres, such as those trapped by entrained oxides. Bubbles only form in samples with added calcium, which causes the oxide layer to become thinner and more flexible. Entrained oxides are found to be substrates for the growth of intermetallic phases, another key bifilm prediction.

Melt oxidation is found to be conducted through entrained oxides which impinge on the sample exterior, and breakaway oxidation occurs not at the sample surface but via these entrained oxide networks. Adding calcium suppresses the transformation from MgO to $MgAl_2O_4$, causing the formation of a fine layer of MgO particles on the interior of the entrained oxide networks which prevents contact between the atmosphere and the melt.

4.8. References

[1] Y.-O. Yoon, S.-H. Ha, G.-Y. Yeom, H.K. Lim, S.K. Kim, Oxidation behavior of Al2Ca added Al-5Mg alloy in the liquid state, in: B.A. Sadler (Ed.), Light Metals 2013, Springer International Publishing, San Antonio, Texas, USA, 2013: pp. 323–326. https://doi.org/10.1007/978-3-319-65136-1_56.

[2] D. Gürsoy, F. De Carlo, X. Xiao, C. Jacobsen, TomoPy: a framework for the analysis of synchrotron tomographic data, J Synchrotron Rad 21 (2014) 1188–1193. https://doi.org/10.1107/S1600577514013939.

[3] V. Nikitin, TomocuPy – efficient GPU-based tomographic reconstruction with asynchronous data processing, J Synchrotron Rad 30 (2023) 179–191. https://doi.org/10.1107/S1600577522010311.

[4] J.L. Murray, The Al−Mg (Aluminum−Magnesium) system, Bulletin of Alloy Phase

Diagrams 3 (1982) 60–74. https://doi.org/10.1007/BF02873413.

[5] C. Simensen, P. Fartum, A. Andersen, Analysis of intermetallic particles in aluminium by dissolution of the sample in butanol, Fresenius' Zeitschrift Für Analytische Chemie 319 (1984) 286–292. https://doi.org/10.1007/BF00487273.

[6] S. Kumar, P.S. Grant, K.A.Q. O'Reilly, Evolution of Fe Bearing Intermetallics During DC Casting and Homogenization of an Al-Mg-Si Al Alloy, Metall Mater Trans A 47 (2016) 3000–3014. https://doi.org/10.1007/s11661-016-3451-5.

[7] S. Kumar, K.A.Q. O'Reilly, Influence of Al grain structure on Fe bearing intermetallics during DC casting of an Al-Mg-Si alloy, Materials Characterization 120 (2016) 311–322. https://doi.org/10.1016/j.matchar.2016.09.017.

[8] A. Verma, Microstructural control of Al alloys using intrinsic oxides, University of Oxford, 2015.

[9] G. Lefèvre, M. Duc, P. Lepeut, R. Caplain, M. Fédoroff, Hydration of γ-Alumina in Water and Its Effects on Surface Reactivity, Langmuir 18 (2002) 7530–7537. https://doi.org/10.1021/la025651i.

[10] T. Sato, Hydration phenomena of aluminum oxides., Journal of Japan Institute of Light Metals 37 (1987) 729–735. https://doi.org/10.2464/jilm.37.729.

[11] Y. Wang, H.-T. Li, Z. Fan, Oxidation of aluminium alloy melts and inoculation by oxide particles, Trans Indian Inst Met 65 (2012) 653–661. https://doi.org/10.1007/s12666-012-0194-x.

[12] J. Qian, P. Zheng, Y. Ma, X. Zhang, J. Huang, D. Zhang, Z. Li, Y. Jiang, W. Wu, H. Li, Formation and growth kinetics of the initial amorphous oxide film on the aluminum melt: A ReaxFF molecular dynamics simulation, Computational Materials Science 220 (2023) 112035. https://doi.org/10.1016/j.commatsci.2023.112035.

[13] I. Haginoya, T. Fukusako, Oxidation of molten Al–Mg alloys, Trans Jpn Inst Metal 24 (1983) 613–619. https://doi.org/10.2320/matertrans1960.24.613.

[14] W.H. Gitzen, Alumina as a ceramic material, 1970.

[15] J. Campbell, Entrainment defects, Mater Sci Technol 22 (2006) 127–145. https://doi.org/10.1179/174328406X74248.

[16] M. Akbarifar, M. Divandari, S.M.A. Boutorabi, S.-H. Ha, Y.-O. Yoon, S.K. Kim, Short-Time Oxidation of Al–Mg in Dynamic Conditions, Oxid Met 94 (2020) 409–429. https://doi.org/10.1007/s11085-020-09999-y.

[17] G. Wu, K. Dash, M.L. Galano, K.A.Q. O'Reilly, Oxidation studies of Al alloys: Part II Al-Mg alloy, Corros Sci 155 (2019) 97–108. https://doi.org/10.1016/j.corsci.2019.04.018.

[18] E.C. Partington, P. Grieveson, B. Terry, Self-sustaining oxidation of liquid aluminium and its alloys containing magnesium and silicon, Journal of Materials Science 33 (1998) 2447–2455. https://doi.org/10.1023/A:1004372328492.

[19] J. Campbell, Castings, 2nd ed., Elsevier Science & Technology, Oxford, UK, 2003.

[20] J. Campbell, Complete casting handbook: metal casting processes, metallurgy, techniques and design, 1st ed, Elsevier Butterworth-Heinemann, Oxford, UK Waltham, MA, 2011.

[21] X. Cao, J. Campbell, Effect of precipitation of primary intermetallic compounds on

tensile properties of cast Al 11.5Si 0.4Mg alloy, AFS Trans. 108 (2000) 391–400.

[22] N. Smith-Hanssen, M. Syvertsen, A. Kvithyld, Microalloying to Inhibit Oxidation of Al–Mg Alloys, in: Light Metals 2022, Springer International Publishing, Cham, 2022: pp. 579–586. https://doi.org/10.1007/978-3-030-92529-1_76.

[23] S. Impey, D.J. Stephenson, J.R. Nicholls, A study of the effect of magnesium additions on the oxide growth morphologies on liquid aluminium alloys, in: Microscopy of Oxidation, The Institute of Metals, Cambridge, UK, 1990: pp. 238–244.

[24] O. Ozdemir, J.E. Gruzleski, R.A.L. Drew, Effect of low-levels of strontium on the oxidation behavior of selected molten aluminum–magnesium alloys, Oxid Met 72 (2009) 241–257. https://doi.org/10.1007/s11085-009-9158-x.

[25] N. Smith, A. Kvithyld, G. Tranell, The Mechanism Behind the Oxidation Protection of High Mg Al Alloys with Beryllium, Metall Mater Trans B 49 (2018) 2846–2857. https://doi.org/10.1007/s11663-018-1340-6.

[26] M. El-Sayed, An investigation of the behaviour of double oxide film defects in aluminium-magnesium cast alloys, J South Afr Inst Min Metall 118 (2018) 1225–1231. https://doi.org/10.17159/2411-9717/2018/v118n11a13.

[27] K. Surla, F. Valdivieso, M. Pijolat, M. Soustelle, M. Prin, Kinetic study of the oxidation by oxygen of liquid Al–Mg 5% alloys, Solid State Ionics 143 (2001) 355–365. https://doi.org/10.1016/S0167-2738(01)00861-X.

[28] S.-H. Ha, S.-Y. Lee, Y.-O. Yoon, S.K. Kim, Formation of protective oxide layer with nanometer scale and twining behavior of eutectic si in Al–Mg and Al–Si–Mg systems including a trace of Al2Ca, J Nanosci Nanotechnol 16 (2016) 11169–11172. https://doi.org/10.1166/jnn.2016.13473.

[29] S.-H. Ha, Y.-O. Yoon, B.-H. Kim, T.-W. Lee, S.-H. Lim, S.K. Kim, Precipitation of oxide particles in surface mixed layer of Al–Mg alloys with a trace of Ca during oxidation, J Nanosci Nanotechnol 17 (2017) 8232–8235. https://doi.org/10.1166/jnn.2017.15104.

[30] C. Ransley, H. Neufeld, The solubility of hydrogen in liquid and solid aluminium, J Inst Metals 74 (1948) 599–620.

[31] M. Tiryakioğlu, The effect of hydrogen on pore formation in aluminum alloy castings: myth versus reality, Met 10 (2020) 368. https://doi.org/10.3390/met10030368.

[32] J. Campbell, A Personal View of Microstructure and Properties of Al Alloys, Materials 14 (2021) 1297. https://doi.org/10.3390/ma14051297.

[33] R.P. Verma, K.N. Pandey, K. András, R. Khargotra, T. Singh, Difficulties and redressal in joining of aluminium alloys by GMA and GTA welding: a review, Journal of Materials Research and Technology 23 (2023) 2576–2586. https://doi.org/10.1016/j.jmrt.2023.01.183.

[34] D. Labus Zlatanovic, J. Pierre Bergmann, S. Balos, J. Hildebrand, M. Bojanic-Sejat, S. Goel, Effect of surface oxide layers in solid-state welding of aluminium alloys – review, Science and Technology of Welding and Joining 28 (2023) 331–351. https://doi.org/10.1080/13621718.2023.2165603.

[35] F.N. Bakhtiarani, R. Raiszadeh, Healing of double-oxide film defects in commercial purity aluminum melt, Metall Mater Trans B 42 (2011) 331–340. https://doi.org/10.1007/s11663-011-9480-y.

[36] F.N. Bakhtiarani, R. Raiszadeh, The behaviour of double oxide film defects in Al–4.5 wt.% Mg melt, J Mater Sci 46 (2011) 1305–1315. https://doi.org/10.1007/s10853-010-4916-3.

[37] M. Aryafar, R. Raiszadeh, A. Shalbafzadeh, Healing of double oxide film defects in A356 aluminium melt, J Mater Sci 45 (2010) 3041–3051. https://doi.org/10.1007/s10853-010-4308-8.

Chapter 5
Thermodynamic Modelling of Aluminium Alloy Melt Oxidation

5.1. Introduction

5.1.1. Background

Whilst the scientific consensus of the understanding of any natural phenomenon must be supported by repeatable and independently verifiable experimental observations and results, complete scientific understanding can only be achieved with the development and verification of theoretical models, which must be consistent both with previously validated theoretical models and relevant experimental observations. In metallurgical contexts, oxidation is largely governed by two factors, thermodynamics and kinetics [1]: thermodynamics determines whether oxidation can physically happen and kinetics determines how quickly oxidation progresses, should oxidation be thermodynamically possible. Since thermodynamics determines whether oxidation can occur at all, the logical first step to modelling oxidation behaviour would be understanding the thermodynamics.

In the case of pure substances, the thermodynamics of oxidation is visualised well using Ellingham diagrams (Figure 5.1), which plot the standard Gibbs free energy of formation of various oxides against temperature, normalised to one mole of oxygen gas [2]. These diagrams are used to make many predictions, such as whether an oxide will be stable at a given temperature, what the equilibrium partial pressure of oxygen over an oxide will be, and whether one element will reduce the oxide of another element.

These diagrams are largely sufficient to model the thermodynamic aspects of the oxidation of pure, solid substances, but the oxidation of liquid alloys is more complex for two reasons. Firstly, the liquid state alters the nature of species transfer within the oxidised sample: mass transport occurs via both convection and diffusion, instead of just diffusion; this change's ramifications are primarily kinetic [3]. Secondly, alloys are not pure substances, which changes the thermodynamics significantly: removing a solute from a melt to form an oxide incurs a

large entropic penalty, in addition to any change in enthalpy, which in turn alters the Gibbs free energy change of reaction.

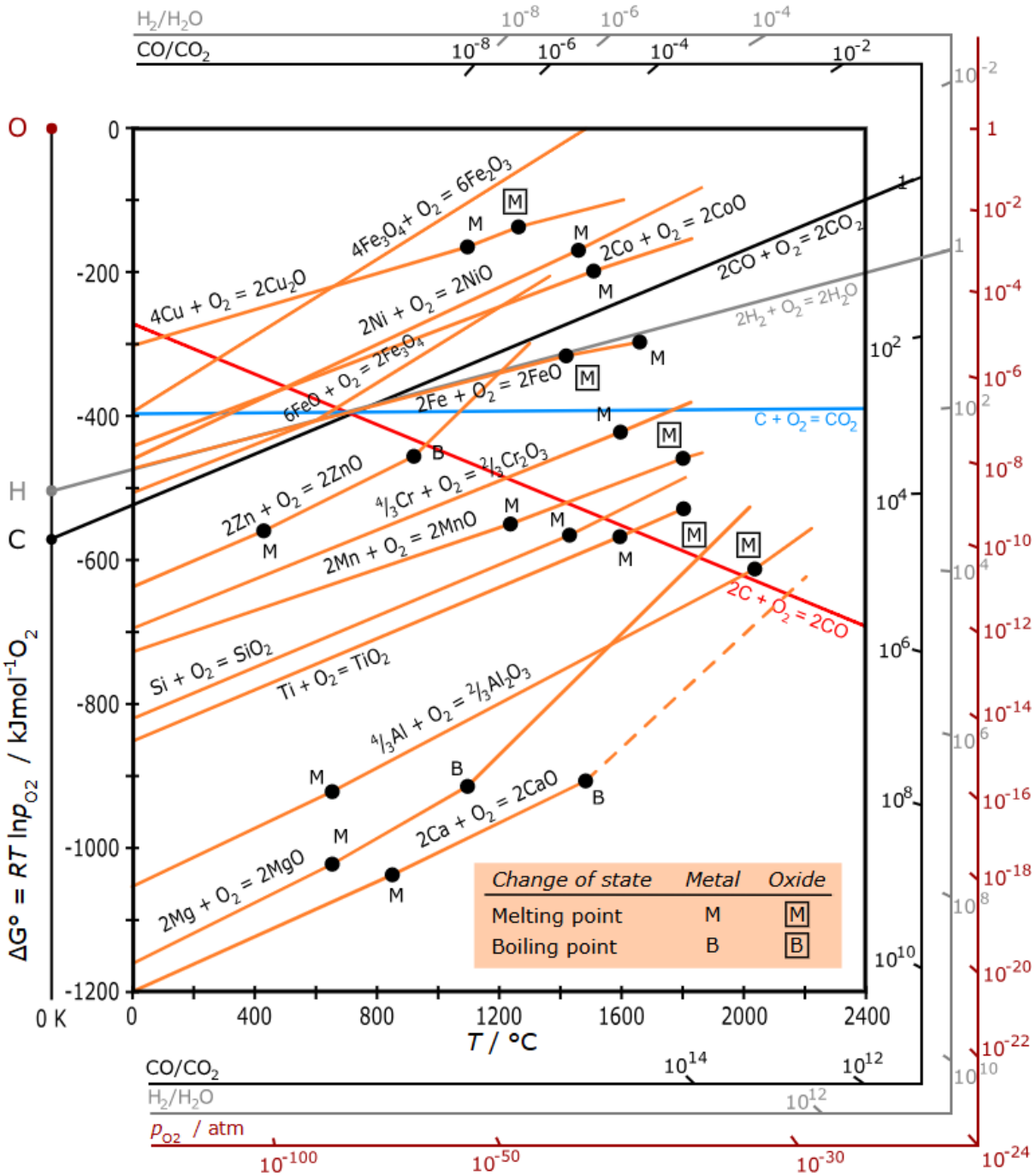


Figure 5.1. Ellingham diagram with various oxides plotted [4].

This distinction is subtle but important in characterising the thermodynamics of alloy melt oxidation. When alloy melts are oxidised, the cations in the resultant oxide do not originate from pure substances, but from multicomponent solutions. The Gibbs free energy of formation of the resultant oxide changes depending upon the composition of the melt, which is not

described by Ellingham diagrams [2]. Therefore, to make thermodynamic predictions about alloy melt oxidation in a similar manner to those used with Ellingham diagrams, such as the most thermodynamically stable oxidation product from a melt of a given composition or whether an oxide in contact with an alloy melt will be thermodynamically stable, the effect of composition must be incorporated into any thermodynamic model.

5.1.2. Objectives

This chapter attempts to gain an understanding of the role of thermodynamics in alloy melt oxidation through the incorporation of melt composition into the thermodynamic treatment of oxidation established by Ellingham diagrams. As composition space in materials science is vast, it would be helpful to predict oxidation products as a function of environmental conditions (including temperature and composition) to limit the experimental exploration of a given compositional space, should that information be desirable to researchers.

Thermodynamic modelling may also help to explain phenomena not fully understood. Group II elements such as beryllium, calcium, and strontium are found to limit the oxidation of Al-Mg alloy melts [5–8], but other reactive elements do not [5]. This phenomenon is sensitive to both temperature and composition, so the effect of these variables on oxide stability, known to be a decisive factor in the breakaway oxidation of Al-Mg alloys [9], is a logical area to explore.

There are many mathematical descriptions of solution thermodynamics, the choice of which greatly affects the predictions of the model. These range from simple treatments such as ideal mixing, which incorporates only a point entropy term, to non-ideal models such as Bragg-Williams (BW) mixing and the modified quasichemical model (MQM), which attempt to more accurately characterise the thermodynamic properties of solutions by introducing more mathematically complex terms with parameters fitted to experimental data [10,11]. As these non-ideal models are designed to characterise the thermodynamic properties of solutions more accurately, the effect of implementing these models is also assessed.

5.2. Theoretical basis

5.2.1. Fundamental thermodynamics

Whether oxidation is thermodynamically possible is determined by the second law of thermodynamics, which states that for a reaction to be spontaneous the entropy of the universe must increase due to its occurrence [12]. In the context of oxidation, this is more commonly formulated as the criterion that the Gibbs free energy change of the reaction, ΔG_r, must be negative [13]. The Gibbs free energy G of a component at temperature T is defined in terms of its enthalpy H and its entropy S (5.1).

$$G = H - TS \tag{5.1}$$

For a general reaction of reactants R_i reacting to form products P_j with stoichiometric coefficients $c_{R,i}$ and $c_{P,j}$, respectively (5.2), the Gibbs free energy change of reaction, ΔG_r, is the Gibbs free energy difference between the products G_prod and the reactants G_reac (5.3).

$$c_{R,1}R_1 + c_{R,2}R_2 + \cdots \rightarrow c_{P,1}P_1 + c_{R,2}P_2 + \cdots \tag{5.2}$$

$$\Delta G_\mathrm{r} = G_\mathrm{prod} - G_\mathrm{reac} \tag{5.3}$$

The partial derivative of the Gibbs free energy of a system G with respect to the quantity of a given species i, N_i, at constant temperature and pressure is the definition of the chemical potential, μ_i (5.4). Using the Gibbs-Duhem equation [11], G can be shown to be the quantity-weighted sum of μ_i (5.5), giving a definition of ΔG_r in terms of chemical potentials μ_i and the stoichiometric coefficients $c_{R,i}$ and $c_{P,j}$ (5.6).

$$\mu_i = \left(\frac{\partial G}{\partial N_i}\right)_{T,P,N_{i\neq j}} \tag{5.4}$$

$$G = \sum_i N_i \mu_i \tag{5.5}$$

$$\Delta G_\mathrm{r} = \sum_{j=\mathrm{products}} N_j \mu_j - \sum_{i=\mathrm{reactants}} N_i \mu_i = \sum_j c_{P,j}\mu_j - \sum_i c_{R,i}\mu_i \tag{5.6}$$

The thermodynamic activity of species i, a_i, is defined through the difference of μ_i, the

chemical potential at temperature T, and μ_i°, the chemical potential at standard conditions. This difference is termed the relative chemical potential $\Delta\mu_i$, where R is the molar gas constant (5.7).

$$a_i = \exp\left(\frac{\mu_i - \mu_i^{\circ}}{RT}\right) = \exp\left(\frac{\Delta\mu_i}{RT}\right) \tag{5.7}$$

Thus ΔG_{r} can be related to the standard Gibbs free energy of reaction, $\Delta G_{\mathrm{r}}^{\circ}$, through activities a_i and stoichiometric coefficients $c_{R,i}$ and $c_{P,j}$ (5.8). This final term is defined as the reaction quotient, Q (5.9), and at equilibrium, this becomes the equilibrium constant, K [14].

$$\begin{aligned}\Delta G_{\mathrm{r}} &= \sum_j c_{P,j}\mu_j - \sum_i c_{R,i}\mu_i = \sum_j c_{P,j}\left(\mu_j^{\circ} + RT\ln a_j\right) - \sum_i c_{R,i}(\mu_i^{\circ} + RT\ln a_i)\\ &= \left(\sum_j c_{P,j}\mu_j^{\circ} - \sum_i c_{R,i}\mu_i^{\circ}\right) + RT\left(\sum_j c_{P,j}\ln a_j - \sum_i c_{R,i}\ln a_i\right)\\ &= \Delta G_{\mathrm{r}}^{\circ} + RT\ln\left(\frac{\prod_i {a_{P_i}}^{c_{P,i}}}{\prod_j {a_{R_j}}^{c_{R,j}}}\right) = \Delta G_{\mathrm{r}}^{\circ} + RT\ln Q\end{aligned} \tag{5.8}$$

$$Q = RT\ln\left(\frac{\prod_i {a_{P_i}}^{c_{P,i}}}{\prod_j {a_{R_j}}^{c_{R,j}}}\right) = RT\ln\left(\frac{{a_{P_1}}^{c_{P,1}} \times {a_{P_2}}^{c_{P,2}} \times {a_{P_3}}^{c_{P,3}} \times \ldots}{{a_{R_1}}^{c_{R,1}} \times {a_{R_2}}^{c_{R,2}} \times {a_{R_3}}^{c_{R,3}} \times \ldots}\right) \tag{5.9}$$

The activity of a gaseous species a_{g} can be expressed as the ratio of its partial pressure p_{g} to a chosen standard pressure p_{g}° (5.10), conventionally one atmosphere, and the activity of a pure liquid or solid is unity [15]. For components in a liquid solution, the relationship between the activity a_i and composition (molar fraction) x_i is more complex and is discussed in the following sections.

$$a_{\mathrm{g}} = \frac{p_{\mathrm{g}}}{p_{\mathrm{g}}^{\circ}} \tag{5.10}$$

5.2.2. Pure substance oxidation and Ellingham diagrams

In metallurgical contexts, when a pure substance X oxidises, it reacts with oxygen gas to form an oxide (5.11). The free energy change of reaction, ΔG_{r}, is given by the difference between the Gibbs free energies of the components G_i weighted by their stoichiometric coefficients c_i

(5.12), which can then be expressed in terms of the standard free energy of reaction, $\Delta G_\mathrm{r}^\circ$, and the activities of the species a_i (5.13).

$$c_\mathrm{X}\mathrm{X} + \frac{b}{2}\mathrm{O}_2 \rightarrow \mathrm{X}_{c_\mathrm{X}}\mathrm{O}_b \tag{5.11}$$

$$\Delta G_\mathrm{r} = G_{\mathrm{X}_{c_\mathrm{X}}\mathrm{O}_b} - \left(c_\mathrm{X} G_\mathrm{X} + \frac{b}{2} G_{\mathrm{O}_2}\right) \tag{5.12}$$

$$\Delta G_\mathrm{r} = \Delta G_\mathrm{r}^\circ + RT \ln\left(\frac{a_{\mathrm{X}_{c_\mathrm{X}}\mathrm{O}_b}}{a_\mathrm{X}^{c_\mathrm{X}} a_{\mathrm{O}_2}^{b/2}}\right) \tag{5.13}$$

Since X and its oxide are pure substances, their activities are equal to one, and the activity of oxygen gas is equal to its partial pressure, p_{O_2}. In addition, since the chemical reaction (5.11) is the defining reaction for the formation of the oxide from its pure substances, the standard Gibbs free energy of reaction, $\Delta G_\mathrm{r}^\circ$, is, by definition, the standard Gibbs free energy of formation $\Delta G_\mathrm{f}^\circ$ (5.14).

$$\Delta G_\mathrm{r} = \Delta G_\mathrm{f}^\circ - \frac{b}{2} RT \ln p_{\mathrm{O}_2} \tag{5.14}$$

Normalising to one mole of O_2 (5.15), the reaction equation simplifies further, such that it is independent of the stoichiometric formula of the oxide (5.16). Ellingham diagrams (Figure 5.1) are plots for various oxides, $f_{\mathrm{X}_{c_\mathrm{X}}\mathrm{O}_b}(T)$, of the standard Gibbs free energy of formation normalised to one mole of O_2, $\Delta G_{\mathrm{f,mol}\mathrm{O}_2}^\circ$, against temperature T (5.17) [2].

$$\frac{c_\mathrm{X}}{2b}\mathrm{X} + \mathrm{O}_2 \rightarrow \frac{2}{b}\mathrm{X}_{c_\mathrm{X}}\mathrm{O}_b \tag{5.15}$$

$$\Delta G_{\mathrm{r,mol}\mathrm{O}_2} = \frac{2}{b}\Delta G_\mathrm{f}^\circ - RT \ln p_{\mathrm{O}_2} = \Delta G_{\mathrm{f,mol}\mathrm{O}_2}^\circ - RT \ln p_{\mathrm{O}_2} \tag{5.16}$$

$$f_{\mathrm{X}_{c_\mathrm{X}}\mathrm{O}_b}(T) = \Delta G_{\mathrm{f,mol}\mathrm{O}_2}^\circ \tag{5.17}$$

Metal oxides generally have a plot which starts negative and increases with temperature, which can be explained by the standard enthalpy $\Delta H_\mathrm{f}^\circ$ and entropy changes $\Delta S_\mathrm{f}^\circ$ of the formation reaction (5.18). At $T = 0$ K, the entropy-based term becomes zero, so $\Delta G_\mathrm{f}^\circ$ becomes $\Delta H_\mathrm{f}^\circ$,

which is generally negative for an oxide that is known to exist at some physical condition. As T increases, the magnitude of the entropy term begins to increase, which leads to an increase in $\Delta G_{\mathrm{f}}^{\circ}$, since $\Delta S_{\mathrm{f}}^{\circ}$ is negative: the oxidation of solid metals to form solid oxides involves capturing a gaseous species, which therefore reduces the system's entropy. Abrupt gradient changes in $f_{\mathrm{X}_{c_{\mathrm{X}}}\mathrm{O}_b}(T)$ occur when either the metal or oxide species undergoes a phase change, which are indicated on the diagram (Figure 5.1: **M** for melting point, **B** for boiling point; a square box around the letter indicates a phase change in the oxide, instead of the metal).

$$\Delta G_{\mathrm{f}}^{\circ}(T) = \Delta H_{\mathrm{f}}^{\circ}(T) - T\Delta S_{\mathrm{f}}^{\circ}(T) \tag{5.18}$$

These plots can be utilised to make thermodynamic predictions. Firstly, they can determine if an oxide is stable relative to its metal, as a function of T and p_{O_2} (5.19): if $\Delta G_{\mathrm{r,mol}\mathrm{O}_2}(T) < RT\ln\left(p_{\mathrm{O}_2}\right)$, the oxidation reaction is spontaneous, and the metal will oxidise, but if the converse is true, the metal oxide will dissociate into its metal and oxygen gas. The dissociation pressure $p_{\mathrm{O}_2,\mathrm{diss}}$, the partial pressure of oxygen below which a metal oxide will dissociate into its metal and oxygen gas, is given when $\Delta G_{\mathrm{r,mol}\mathrm{O}_2} = 0$ (5.20). Geometrically, this corresponds to the gradient of the line intercepting $(0,0)$, indicated by the capital "O" on the diagram (Figure 5.1) and the point $(f_{\mathrm{X}_{c_{\mathrm{X}}}\mathrm{O}_b}, T)$, since $p_{\mathrm{O}_2,\mathrm{diss}}$ is determined solely by the quotient of these quantities (5.21).

$$\Delta G_{\mathrm{r,mol}\mathrm{O}_2} = \Delta G_{\mathrm{f,mol}\mathrm{O}_2}^{\circ} - RT\ln p_{\mathrm{O}_2} < 0$$

$$\Delta G_{\mathrm{f,mol}\mathrm{O}_2}^{\circ} < RT\ln p_{\mathrm{O}_2} \tag{5.19}$$

$$\ln p_{\mathrm{O}_2,\mathrm{diss}} = \frac{\Delta G_{\mathrm{f,mol}\mathrm{O}_2}^{\circ}}{RT} \tag{5.20}$$

$$p_{\mathrm{O}_2,\mathrm{diss}} = \exp\left(\frac{\Delta G_{\mathrm{f,mol}\mathrm{O}_2}^{\circ}}{RT}\right) = \exp\left(\frac{f_{\mathrm{X}_{c_{\mathrm{X}}}\mathrm{O}_b}}{RT}\right) \tag{5.21}$$

Secondly, if a metal can produce multiple oxides, an Ellingham diagram can determine the most stable oxide at a given temperature. Taking the example of copper, which can form either

CuO (5.22) or Cu_2O (5.23) upon oxidation, the most stable oxide can be determined by whether ΔG_r of the reaction converting between the two oxides (5.24) is positive or negative, as this determines which direction is spontaneous (Table 5.1). On the Ellingham diagram, this corresponds to whether the difference between the functions is negative or positive at a given temperature: the species whose plot is the most negative is the most stable oxide.

	Reaction	$\Delta G_{r,molO_2}$	**Eqn.**
A	$2Cu + O_2 \rightarrow 2CuO$	$2\Delta G^{\circ}_{f,molO_2}(CuO) = f_{CuO}(T)$	(5.22)
B	$4Cu + O_2 \rightarrow 2Cu_2O$	$2\Delta G^{\circ}_{f,molO_2}(Cu_2O) = f_{Cu_2O}(T)$	(5.23)
$C = A - B$	$2Cu_2O \rightarrow 2CuO + 2Cu$	$f_{CuO}(T) - f_{Cu_2O}(T)$	(5.24)

Table 5.1. Relative thermodynamic stability of copper oxides, as determined by Ellingham Diagrams.

Similarly, these diagrams can determine whether one element can reduce another (Table 5.2). In the case of magnesium (5.25) and aluminium (5.26), magnesium will reduce alumina if the reduction reaction is spontaneous (5.27), i.e. if the Gibbs free energy change is negative, which occurs when the MgO plot, $f_{MgO}(T)$, is more negative than the Al_2O_3 plot, $f_{Al_2O_3}(T)$. Similarly, aluminium will reduce magnesia if the Al_2O_3 plot, $f_{Al_2O_3}(T)$, is lower than the MgO plot, $f_{MgO}(T)$. In this system, the former is true below c. 1500 °C, and the latter is true above this temperature. This particular use of the Ellingham diagram shows why it is necessary to normalise the functions to the quantity of oxygen: the relative reaction (5.27) does not depend on the partial pressure of oxygen, and oxides with different valencies can be compared.

	Reaction	$\Delta G_{r,molO_2}$	**Eqn.**
A	$2Mg + O_2 \rightarrow 2MgO$	$2\Delta G^{\circ}_{f,molO_2}(MgO) = f_{MgO}(T)$	(5.25)
B	$\frac{4}{3}Al + O_2 \rightarrow \frac{2}{3}Al_2O_3$	$\frac{2}{3}\Delta G^{\circ}_{f,molO_2}(Al_2O_3) = f_{Al_2O_3}(T)$	(5.26)
$C = A - B$	$\frac{2}{3}Al_2O_3 + 2Mg \rightarrow \frac{4}{3}Al + 2MgO$	$f_{MgO}(T) - f_{Al_2O_3}(T)$	(5.27)

Table 5.2. Relative thermodynamic stability of aluminium and magnesium oxides using Ellingham diagrams.

5.2.3. Alloy melt oxidation

In the case of alloy melt oxidation, an Ellingham diagram-style treatment can be applied, but an extra composition-dependent term must be incorporated. This is because the assumption that the activities of the reactants are unity no longer holds: the reactants are no longer pure substances, but components of a solution. Taking the example of an Al-X binary melt, the analogous Ellingham diagram functions $f_i(T)$ for Al_2O_3 (5.28), a general unary solute oxide $X_{c_X}O_b$ (5.29), and general binary oxide $Al_{c_{Al}}X_{c_X}O_b$ (5.30), are given as follows, and termed ΔG_i^{ox}, the Gibbs free energy of oxidation (Table 5.3).

Species	Reaction	$\Delta G_i^{ox}(a_X, a_{Al}, p_{O_2}, T)$	Eqn.
Al_2O_3	$\frac{4}{3}[Al]_{\text{in Al}} + O_{2\,(g)} \rightarrow \frac{2}{3}Al_2O_{3\,(ss)}$	$\frac{2}{3}\Delta G^{o}_{f,\,Al_2O_3}(T) - RT\ln\left({a_{Al}}^{4/3}p_{O_2}\right)$	(5.28)
$X_{c_X}O_b$	$\frac{2c_X}{b}[X]_{\text{in Al}} + O_{2\,(g)} \rightarrow \frac{2}{b}X_{c_X}O_{b\,(ss)}$	$\frac{2}{b}\Delta G^{o}_{f,\,X_{c_X}O_b}(T) - RT\ln\left({a_X}^{m_X}p_{O_2}\right)$	(5.29)
$Al_{c_{Al}}X_{c_X}O_b$	$\frac{2c_{Al}}{b}[Al]_{\text{in Al}} + \frac{2c_X}{b}[X]_{\text{in Al}} + O_{2\,(g)} \rightarrow \frac{2}{b}Al_{c_{Al}}X_{c_X}O_{b\,(ss)}$	$\frac{2}{b}\Delta G^{o}_{f,\,Al_{c_{Al}}X_{c_X}O_b}(T) - RT\ln\left({a_X}^{m_X}{a_{Al}}^{m_{Al}}p_{O_2}\right)$	(5.30)

Table 5.3. ΔG_i^{ox} terms for general oxides within an Al-X binary system, where the subscripts 'in Al', (g), and (ss) indicate dissolved in Al, gas, and standard state, respectively.

Reduced stoichiometric coefficients m_X (5.31) and m_{Al} (5.32) are introduced to simplify the expressions.

$$m_X = \frac{2c_X}{b} \tag{5.31}$$

$$m_{Al} = \frac{2c_{Al}}{b} \tag{5.32}$$

The relative stability of the oxides within the Al-X system therefore depends on the Gibbs free energy of formation $\Delta G^{o}_{f,i}(T)$, the activities of the components a_i, and the conditions of the

environment (T, p_{O_2}). To fully evaluate these ΔG^{ox} expressions, the activities of the solute and solvent, a_X and a_{Al}, respectively, must be evaluated over the entire composition-temperature range of interest. Acquiring this volume of data experimentally is unfeasible, so researchers use mathematical models with experimentally-fitted parameters [16].

The Gibbs free energy change of mixing, ΔG_{mix}, is defined as the Gibbs free energy change of a system forming a mixture of species i from their pure, standard states (5.33).

$$\Delta G_{mix} = G_{mixed} - G_{unmixed} \tag{5.33}$$

The Gibbs free energy of both the mixed G_{mixed} (5.34) and unmixed $G_{unmixed}$ (5.35) states can be defined in terms of the chemical potentials μ_i and concentrations x_i of their components i.

$$G_{mixed} = \sum_i x_i \mu_i^{mixed} = \sum_i x_i \mu_i \tag{5.34}$$

$$G_{unmixed} = \sum_i x_i \mu_i^{unmixed} = \sum_i x_i \mu_i^o \tag{5.35}$$

Since the components of the unmixed states are in their standard states, their chemical potentials μ_i are the standard chemical potentials μ_i^o, which allows ΔG_{mix} to be defined in terms of the relative chemical potentials $\Delta\mu_i$ (5.36), and so activities a_i (5.37).

$$\Delta G_{mix} = G_{mixed} - G_{unmixed} = \sum_i x_i \mu_i - \sum_i x_i \mu_i^o = \sum_i x_i \Delta\mu_i \tag{5.36}$$

$$\Delta G_{mix} = RT \sum_i x_i \ln a_i \tag{5.37}$$

The forms of ΔG_i^{ox} can therefore also be expressed in terms of $\Delta\mu_i$ instead of a_i, which simplifies the equations once the mathematical models are implemented (Table 5.4).

Species	$\Delta \boldsymbol{G_i^{ox}}(\Delta \boldsymbol{\mu_X}, \Delta \boldsymbol{\mu_{Al}}, \boldsymbol{p_{O_2}}, \boldsymbol{T})$	**Eqn.**
Al_2O_3	$\Delta G^{ox}_{Al_2O_3} = \frac{2}{3}\Delta G^o_{f,\,Al_2O_3}(T) - \frac{4}{3}\Delta\mu_{Al} - RT\ln p_{O_2}$	(5.38)
$X_{c_X}O_b$	$\Delta G^{ox}_{X_{c_X}O_b} = \frac{2}{b}\Delta G^o_{f,\,X_{c_X}O_b}(T) - m_X\Delta\mu_X - RT\ln p_{O_2}$	(5.39)

$\mathrm{Al}_{c_{\mathrm{Al}}}\mathrm{X}_{c_{\mathrm{X}}}\mathrm{O}_b$	$\Delta G^{\mathrm{ox}}_{\mathrm{Al}_{c_{\mathrm{Al}}}\mathrm{X}_{c_{\mathrm{X}}}\mathrm{O}_b} = \frac{2}{b}\Delta G^{\mathrm{o}}_{\mathrm{f},\,\mathrm{Al}_{c_{\mathrm{Al}}}\mathrm{X}_{c_{\mathrm{X}}}\mathrm{O}_b}(T) - (m_{\mathrm{Al}}\Delta\mu_{\mathrm{Al}} + m_{\mathrm{X}}\Delta\mu_{\mathrm{X}}) - RT\ln p_{\mathrm{O}_2}$	(5.40)

Table 5.4. ΔG_i^{ox} terms for oxides in an Al-X binary system, in terms of relative chemical potentials $\Delta\mu_i$.

These equations can be interpreted in terms of the oxidation process being a two-step reaction (Table 5.5).

#	**Reaction**	ΔG_{r}	**Eqn.**
A	$m_{\mathrm{Al}}[\mathrm{Al}]_{\text{in Al}} + m_{\mathrm{X}}[\mathrm{X}]_{\text{in Al}} \rightarrow m_{\mathrm{Al}}\mathrm{Al}_{(\mathrm{ss})} + m_{\mathrm{X}}\mathrm{X}_{(\mathrm{ss})}$	$\Delta G_{\mathrm{r,A}} = -(m_{\mathrm{Al}}\Delta\mu_{\mathrm{Al}} + m_{\mathrm{X}}\Delta\mu_{\mathrm{X}})$	(5.41)
B	$m_{\mathrm{Al}}\mathrm{Al}_{(\mathrm{ss})} + m_{\mathrm{X}}\mathrm{X}_{(\mathrm{ss})} + \mathrm{O}_{2\,(\mathrm{g})} \rightarrow \frac{2}{b}\mathrm{Al}_{c_{\mathrm{Al}}}\mathrm{X}_{c_{\mathrm{X}}}\mathrm{O}_b$	$\Delta G_{\mathrm{r,B}} = \frac{2}{b}\Delta G^{\mathrm{o}}_{\mathrm{f},\,\mathrm{Al}_{c_{\mathrm{Al}}}\mathrm{X}_{c_{\mathrm{X}}}\mathrm{O}_b}(T) - RT\ln p_{\mathrm{O}_2}$	(5.42)
C $= \mathrm{A} + \mathrm{B}$	$m_{\mathrm{Al}}[\mathrm{Al}]_{\text{in Al}} + m_{\mathrm{X}}[\mathrm{X}]_{\text{in Al}} + \mathrm{O}_{2\,(\mathrm{g})} \rightarrow \frac{2}{b}\mathrm{Al}_{c_{\mathrm{Al}}}\mathrm{X}_{c_{\mathrm{X}}}\mathrm{O}_b$	$\Delta G_{\mathrm{r,C}} = \Delta G_{\mathrm{r,A}} + \Delta G_{\mathrm{r,B}} = \frac{2}{b}\Delta G^{\mathrm{o}}_{\mathrm{f},\,\mathrm{Al}_{c_{\mathrm{Al}}}\mathrm{X}_{c_{\mathrm{X}}}\mathrm{O}_b}(T) - (m_{\mathrm{Al}}\Delta\mu_{\mathrm{Al}} + m_{\mathrm{X}}\Delta\mu_{\mathrm{X}}) - RT\ln p_{\mathrm{O}_2}$	(5.43)

Table 5.5. Hess' law treatment of alloy oxidation as two steps (C): separation of dissolved components into their standard states (A), and reaction at their standard states to form a compound (B).

Firstly, the components un-mix from their dissolved states at concentrations x_i into pure components in their standard states. The Gibbs free energy change of reaction of this reaction (5.41), $\Delta G_{\mathrm{r,A}}$, is the negative of the Gibbs free energy change of mixing, which is the quantity-weighted sum of the relative chemical potentials $\Delta\mu_i$ (5.36). Secondly, the components in their standard states react with oxygen at partial pressure p_{O_2} to form the oxide, completing the oxidation process.

The Gibbs free energy change of reaction of this reaction (5.42), $\Delta G_{\mathrm{r,B}}$, is the standard Gibbs free energy of formation $\Delta G_{\mathrm{f}}^{\mathrm{o}}$, normalised to one mole of O_2, with an extra term accounting for the fact that oxygen is at a partial pressure of p_{O_2}. Since Gibbs free energy is a state function,

Hess' law allows $\Delta G_{\mathrm{r,C}}$ to be determined from the sum of ΔG_{r} from these first two steps (5.43). In the case where there is no mixing involved, such as the oxidation of a pure substance, $\Delta G_{\mathrm{r,A}} = 0$, and ΔG^{ox} reduces to an Ellingham diagram plot. However, this also demonstrates why a consideration of solution thermodynamics is important for melt oxidation: the values of $\Delta\mu_i$ depend strongly on concentration x_i, so in systems where the solution components have similar reactivities, this extra contribution from unmixing can change the stability of a given oxide significantly.

5.2.4. Ideal solutions

To evaluate $\Delta\mu_i$, a mathematical model to describe the solution must be chosen. The simplest model is ideal mixing, in which the enthalpy of mixing, $\Delta H_{\mathrm{mix}}^{\mathrm{ideal}}$, is zero (5.44), and the only contribution to the entropy of mixing, $\Delta S_{\mathrm{mix}}^{\mathrm{ideal}}$, is point configurational entropy (5.45) [11].

$$\Delta H_{\mathrm{mix}}^{\mathrm{ideal}} = 0 \tag{5.44}$$

$$\Delta S_{\mathrm{mix}}^{\mathrm{ideal}} = -R\sum_i x_i \ln x_i \tag{5.45}$$

Evaluating $\Delta G_{\mathrm{mix}}^{\mathrm{ideal}}$ (5.46), which is the quantity ΔG_{mix} in ideal mixing, shows that in ideal mixing, activities a_i are equal to concentrations x_i (5.47). This is known as Raoult's law [11].

$$\Delta G_{\mathrm{mix}}^{\mathrm{ideal}} = \Delta H_{\mathrm{mix}}^{\mathrm{ideal}} - T\Delta S_{\mathrm{mix}}^{\mathrm{ideal}} = RT\sum_i x_i \ln x_i = RT\sum_i x_i \ln a_i \tag{5.46}$$

$$\therefore x_i = a_i \tag{5.47}$$

This gives a simple form of ΔG^{ox} (Table 5.6), where activities a_i reduce to compositions x_i.

Species	Reaction	$\Delta G_i^{\mathrm{ox}}(x_{\mathrm{X}}, x_{\mathrm{Al}}, p_{\mathrm{O_2}}, T)$	Eqn.
Al_2O_3	$\frac{4}{3}[\mathrm{Al}]_{\text{in Al}} + \mathrm{O_{2\,(g)}} \rightarrow \frac{2}{3}\mathrm{Al_2O_3}$	$\Delta G_{\mathrm{Al_2O_3}}^{\mathrm{ox}} = \frac{2}{3}\Delta G_{\mathrm{f,\,Al_2O_3}}^{\mathrm{o}}(T) - RT\ln\left({x_{\mathrm{Al}}}^{4/3} p\mathrm{O_2}\right)$	(5.48)

$X_{c_X}O_b$	$m_X[X]_{\text{in Al}} + O_{2\,(g)} \rightarrow \frac{2}{b}X_{c_X}O_b$	$\Delta G^{ox}_{X_{c_X}O_b} = \frac{2}{b}\Delta G^{o}_{f,\,X_{c_X}O_b}(T) - RT\ln(x_X{}^{m_X} pO_2)$	(5.49)
$Al_{c_{Al}}X_{c_X}O_b$	$m_{Al}[Al]_{\text{in Al}} + m_X[X]_{\text{in Al}} + O_{2\,(g)} \rightarrow \frac{2}{b}Al_{c_{Al}}X_{c_X}O_b$	$\Delta G^{ox}_{Al_{c_{Al}}X_{c_X}O_b} = \frac{2}{b}\Delta G^{o}_{f,\,Al_{c_{Al}}X_{c_X}O_b}(T) - RT\ln(x_X{}^{m_X} x_{Al}{}^{m_{Al}} pO_2)$	(5.50)

Table 5.6. ΔG_i^{ox} terms for oxides in an Al-X binary system evaluated with ideal mixing.

5.2.5. Non-ideal solutions

However, most systems are not adequately modelled by ideal mixing. In these systems, ΔG_{mix} is not equal to ΔG_{mix}^{ideal}, and the difference between these two quantities is termed the excess Gibbs free energy of mixing, ΔG_{mix}^{xs} (5.51).

$$\Delta G_{mix}^{xs} = \Delta G_{mix} - \Delta G_{mix}^{ideal} = RT\sum_i x_i \ln a_i - RT\sum_i x_i \ln x_i = RT\sum_i x_i \ln\left(\frac{a_i}{x_i}\right) \quad (5.51)$$

This also provides a definition for the excess relative chemical potential $\Delta\mu_i^{xs}$ (5.52), allowing ΔG_{mix}^{xs} to be defined in terms of this quantity (5.53).

$$\Delta\mu_i^{xs} = \left(\frac{\partial \Delta G_{mix}^{xs}}{\partial x_i}\right)_{P,T,x_j\neq i} = \left(\frac{\partial\left(\Delta G_{mix} - \Delta G_{mix}^{ideal}\right)}{\partial x_i}\right)_{P,T,x_j\neq i}$$

$$= \Delta\mu_i - \Delta\mu_i^{ideal} = RT\ln a_i - RT\ln x_i = RT\ln\left(\frac{a_i}{x_i}\right) \quad (5.52)$$

$$\Delta G_{mix}^{xs} = \sum_i x_i \Delta\mu_i^{xs} \quad (5.53)$$

This allows ΔG_i^{ox} to incorporate excess relative chemical potential $\Delta\mu_i^{xs}$ terms (Table 5.7).

Species	$\Delta G_i^{ox}(x_X, x_{Al}, \Delta\mu_X^{xs}, \Delta\mu_{Al}^{xs}, p_{O_2}, T)$	**Eqn.**
Al_2O_3	$\Delta G^{ox}_{Al_2O_3} = \frac{2}{3}\Delta G^{o}_{f,\,Al_2O_3}(T) - \frac{4}{3}\Delta\mu^{xs}_{Al} - RT\ln\left(x_{Al}{}^{4/3} p_{O_2}\right)$	(5.54)
$X_{c_X}O_b$	$\Delta G^{ox}_{X_{c_X}O_b} = \frac{2}{b}\Delta G^{o}_{f,\,X_{c_X}O_b}(T) - m_X\Delta\mu^{xs}_X - RT\ln\left(x_X{}^{m_X} p_{O_2}\right)$	(5.55)

$\mathrm{Al}_{c_{\mathrm{Al}}}\mathrm{X}_{c_{\mathrm{X}}}\mathrm{O}_b$	$\Delta G^{\mathrm{ox}}_{\mathrm{Al}_{c_{\mathrm{Al}}}\mathrm{X}_{c_{\mathrm{X}}}\mathrm{O}_b} = \frac{2}{b}\Delta G^{\mathrm{o}}_{\mathrm{f,\,Al}_{c_{\mathrm{Al}}}\mathrm{X}_{c_{\mathrm{X}}}\mathrm{O}_b}(T) - (m_{\mathrm{Al}}\Delta\mu^{\mathrm{xs}}_{\mathrm{Al}} + m_{\mathrm{X}}\Delta\mu^{\mathrm{xs}}_{\mathrm{X}}) - RT\ln\left({x_{\mathrm{Al}}}^{m_{\mathrm{Al}}}{x_{\mathrm{X}}}^{m_{\mathrm{X}}}p_{\mathrm{O}_2}\right)$	(5.56)

Table 5.7. ΔG_i^{ox} terms for oxides in an Al-X binary system, in terms of excess relative chemical potentials $\Delta\mu_i^{\mathrm{xs}}$.

Relative chemical potentials $\Delta\mu_i$ and excess relative chemical potentials $\Delta\mu_i^{\mathrm{xs}}$ can be defined in terms of ΔG_{mix} and $\Delta G_{\mathrm{mix}}^{\mathrm{xs}}$ respectively, where x_i is the concentration of component i (see Appendix A.2.1 for derivation). The expressions for these quantities for a binary Al-X system, $\Delta\mu_{\mathrm{X}}$ (5.57), $\Delta\mu_{\mathrm{Al}}$ (5.58), $\Delta\mu_{\mathrm{X}}^{\mathrm{xs}}$ (5.59), and $\Delta\mu_{\mathrm{X}}^{\mathrm{xs}}$ (5.60), are given below.

$$\Delta\mu_{\mathrm{X}} = \Delta G_{\mathrm{mix}} + (1 - x_{\mathrm{X}})\frac{\mathrm{d}\Delta G_{\mathrm{mix}}}{\mathrm{d}x_{\mathrm{X}}} \tag{5.57}$$

$$\Delta\mu_{\mathrm{Al}} = \Delta G_{\mathrm{mix}} - x_{\mathrm{X}}\frac{\mathrm{d}\Delta G_{\mathrm{mix}}}{\mathrm{d}x_{\mathrm{X}}} \tag{5.58}$$

$$\Delta\mu_{\mathrm{X}}^{\mathrm{xs}} = \Delta G_{\mathrm{mix}}^{\mathrm{xs}} + (1 - x_{\mathrm{X}})\frac{\mathrm{d}\Delta G_{\mathrm{mix}}^{\mathrm{xs}}}{\mathrm{d}x_{\mathrm{X}}} \tag{5.59}$$

$$\Delta\mu_{\mathrm{Al}}^{\mathrm{xs}} = \Delta G_{\mathrm{mix}}^{\mathrm{xs}} - x_{\mathrm{X}}\frac{\mathrm{d}\Delta G_{\mathrm{mix}}^{\mathrm{xs}}}{\mathrm{d}x_{\mathrm{X}}} \tag{5.60}$$

5.2.6. Ternary systems

For a ternary system with components A, B, and C, $\Delta\mu_i$ can be evaluated in terms of ΔG_{mix} and its partial derivatives with respect to x_i.

$$\Delta\mu_{\mathrm{A}} = \Delta G_{\mathrm{mix}} - x_{\mathrm{B}}\left(\frac{\partial\Delta G_{\mathrm{mix}}}{\partial x_{\mathrm{B}}}\right)_{x_{\mathrm{C}}} - x_{\mathrm{C}}\left(\frac{\partial\Delta G_{\mathrm{mix}}}{\partial x_{\mathrm{C}}}\right)_{x_{\mathrm{B}}} \tag{5.61}$$

$$\Delta\mu_{\mathrm{B}} = \Delta G_{\mathrm{mix}} - x_{\mathrm{A}}\left(\frac{\partial\Delta G_{\mathrm{mix}}}{\partial x_{\mathrm{A}}}\right)_{x_{\mathrm{C}}} - x_{\mathrm{C}}\left(\frac{\partial\Delta G_{\mathrm{mix}}}{\partial x_{\mathrm{C}}}\right)_{x_{\mathrm{A}}} \tag{5.62}$$

$$\Delta\mu_{\mathrm{C}} = \Delta G_{\mathrm{mix}} - x_{\mathrm{A}}\left(\frac{\partial\Delta G_{\mathrm{mix}}}{\partial x_{\mathrm{A}}}\right)_{x_{\mathrm{B}}} - x_{\mathrm{B}}\left(\frac{\partial\Delta G_{\mathrm{mix}}}{\partial x_{\mathrm{B}}}\right)_{x_{\mathrm{A}}} \tag{5.63}$$

Using these relations, $\Delta\mu_i$ and $\Delta\mu_i^{\mathrm{xs}}$ can be derived for a ternary Al-X_1-X_2 system (see Appendix A.2.2 for derivation).

$$\Delta\mu_1 = \Delta G_{\mathrm{mix}} + (1 - x_1)\left(\frac{\partial \Delta G_{\mathrm{mix}}}{\partial x_1}\right)_{x_2} - x_2\left(\frac{\partial \Delta G_{\mathrm{mix}}}{\partial x_2}\right)_{x_1} \tag{5.64}$$

$$\Delta\mu_2 = \Delta G_{\mathrm{mix}} - x_1\left(\frac{\partial \Delta G_{\mathrm{mix}}}{\partial x_1}\right)_{x_2} + (1 - x_2)\left(\frac{\partial \Delta G_{\mathrm{mix}}}{\partial x_2}\right)_{x_1} \tag{5.65}$$

$$\Delta\mu_{\mathrm{Al}} = \Delta G_{\mathrm{mix}} - x_1\left(\frac{\partial \Delta G_{\mathrm{mix}}}{\partial x_1}\right)_{x_2} - x_2\left(\frac{\partial \Delta G_{\mathrm{mix}}}{\partial x_2}\right)_{x_1} \tag{5.66}$$

$$\Delta\mu_1^{\mathrm{xs}} = \Delta G_{\mathrm{mix}}^{\mathrm{xs}} + (1 - x_1)\left(\frac{\partial \Delta G_{\mathrm{mix}}^{\mathrm{xs}}}{\partial x_1}\right)_{x_2} - x_2\left(\frac{\partial \Delta G_{\mathrm{mix}}^{\mathrm{xs}}}{\partial x_2}\right)_{x_1} \tag{5.67}$$

$$\Delta\mu_2^{\mathrm{xs}} = \Delta G_{\mathrm{mix}}^{\mathrm{xs}} - x_1\left(\frac{\partial \Delta G_{\mathrm{mix}}^{\mathrm{xs}}}{\partial x_1}\right)_{x_2} + (1 - x_2)\left(\frac{\partial \Delta G_{\mathrm{mix}}^{\mathrm{xs}}}{\partial x_2}\right)_{x_1} \tag{5.68}$$

$$\Delta\mu_{\mathrm{Al}}^{\mathrm{xs}} = \Delta G_{\mathrm{mix}}^{\mathrm{xs}} - x_1\left(\frac{\partial \Delta G_{\mathrm{mix}}^{\mathrm{xs}}}{\partial x_1}\right)_{x_2} - x_2\left(\frac{\partial \Delta G_{\mathrm{mix}}^{\mathrm{xs}}}{\partial x_2}\right)_{x_1} \tag{5.69}$$

For a general ternary Al-X_1-X_2 oxide, ΔG^{ox} is given as follows (5.70).

$$\Delta G^{\mathrm{ox}}_{\mathrm{Al}_{c_{\mathrm{Al}}}\mathrm{X}_{1c_1}\mathrm{X}_{2c_2}\mathrm{O}_b} = \frac{2}{b}\Delta G^{\mathrm{o}}_{\mathrm{f,\,Al}_{c_{\mathrm{Al}}}\mathrm{X}_{1c_1}\mathrm{X}_{2c_2}\mathrm{O}_b}(T)$$
$$-(m_{\mathrm{Al}}\Delta\mu_{\mathrm{Al}}^{\mathrm{xs}} + m_1\Delta\mu_1^{\mathrm{xs}} + m_2\Delta\mu_2^{\mathrm{xs}}) - RT\ln\left({x_{\mathrm{Al}}}^{m_{\mathrm{Al}}}{x_1}^{m_1}{x_2}^{m_2}p_{\mathrm{O}_2}\right) \tag{5.70}$$

5.2.7. Bragg-Williams mixing

5.2.7.1. Binary systems

In Bragg-Williams mixing (a non-ideal model), the enthalpy of mixing, ΔH_{mix}, is not equal to zero [11]. In a binary system A-B, this term is evaluated as the product of the concentrations of A and B, x_{A} and x_{B} respectively, multiplied by a parameter ω_{AB}; this product scales with the probability of a given pair (in a random mixture) being an A-B pair (5.71). The only contribution to ΔS_{mix}, like ideal mixing, is assumed to be that from point configurational entropy (5.72).

$$\Delta H_{\mathrm{mix}} = x_{\mathrm{A}}x_{\mathrm{B}}\omega_{\mathrm{AB}} \tag{5.71}$$

$$\Delta S_{\mathrm{mix}} = -R(x_{\mathrm{A}}\ln x_{\mathrm{A}} + x_{\mathrm{B}}\ln x_{\mathrm{B}}) \tag{5.72}$$

The non-zero enthalpy term gives an extra term in the expression for ΔG_{mix} (5.73), which is equal to $\Delta G_{\mathrm{mix}}^{\mathrm{xs}}$ (5.74), since it is the only extra term added compared to ideal mixing (5.46).

$$\Delta G_{\mathrm{mix}} = \Delta H_{\mathrm{mix}} - T\Delta S_{\mathrm{mix}} = RT(x_{\mathrm{A}} \ln x_{\mathrm{A}} + x_{\mathrm{B}} \ln x_{\mathrm{B}}) + x_{\mathrm{A}} x_{\mathrm{B}} \omega_{\mathrm{AB}} \tag{5.73}$$

$$\Delta G_{\mathrm{mix}}^{\mathrm{xs}} = \Delta G_{\mathrm{mix}} - \Delta G_{\mathrm{mix}}^{\mathrm{ideal}} = x_{\mathrm{A}} x_{\mathrm{B}} \omega_{\mathrm{AB}} \tag{5.74}$$

Data from the systems evaluated in this chapter expand ω_{AB} in terms of Redlich-Kister polynomials with experimentally-fitted parameters ${}^{i}L_{\mathrm{AB}}$ [11] (5.75), giving an expression for $\Delta G_{\mathrm{mix}}^{\mathrm{xs}}$ (5.76).

$$\omega_{\mathrm{AB}} = \sum_{i \geq 0} {}^{i}L_{\mathrm{AB}} (x_{\mathrm{A}} - x_{\mathrm{B}})^{i} = {}^{0}L_{\mathrm{AB}} + {}^{1}L_{\mathrm{AB}} (x_{\mathrm{A}} - x_{\mathrm{B}}) + {}^{2}L_{\mathrm{AB}} (x_{\mathrm{A}} - x_{\mathrm{B}})^{2} + \cdots \tag{5.75}$$

$$\Delta G_{\mathrm{mix}}^{\mathrm{xs}} = x_{\mathrm{X}} x_{\mathrm{Al}} \omega_{\mathrm{XAl}} = x_{\mathrm{X}} x_{\mathrm{Al}} \sum_{i \geq 0} {}^{i}L_{\mathrm{XAl}} (x_{\mathrm{X}} - x_{\mathrm{Al}})^{i} \tag{5.76}$$

This mathematical form constitutes an extension of regular solution theory, which this form reduces to if the only non-zero term present is ${}^{0}L_{\mathrm{AB}}$. The physical basis of the expansion is, according to Pelton [11], to ensure that the "distribution of species on the lattice sites should not deviate too far from a random distribution" and that the "pair-bond approximation should be reasonably valid". Evaluation of the derivative of $\Delta G_{\mathrm{mix}}^{\mathrm{xs}}$ allows evaluation of $\Delta \mu_{\mathrm{X}}^{\mathrm{xs}}$ (5.77) and $\Delta \mu_{\mathrm{Al}}^{\mathrm{xs}}$ (5.78).

$$\Delta \mu_{\mathrm{X}}^{\mathrm{xs}} = (1 - x_{\mathrm{X}})^{2} \sum_{i \geq 0} {}^{i}L_{\mathrm{XAl}} (2x_{\mathrm{X}} - 1)^{i-1} [2(i+1)x_{\mathrm{X}} - 1] \tag{5.77}$$

$$\Delta \mu_{\mathrm{Al}}^{\mathrm{xs}} = x_{\mathrm{X}}^{2} \sum_{i \geq 0} {}^{i}L_{\mathrm{XAl}} (2x_{\mathrm{X}} - 1)^{i-1} [1 - 2(i+1)(1 - x_{\mathrm{X}})] \tag{5.78}$$

This allows evaluation of ΔG^{ox} (5.79), with the Bragg-Williams binary (BWB) term (5.80), $\Delta G_{\mathrm{Al}_{c_{\mathrm{Al}}}\mathrm{X}_{c_{\mathrm{X}}}\mathrm{O}_{b}}^{\mathrm{ox,BWB}}$, defined also (see Appendix A.3.1 for derivations).

$$\Delta G_{\mathrm{Al}_{c_{\mathrm{Al}}}\mathrm{X}_{c_{\mathrm{X}}}\mathrm{O}_{b}}^{\mathrm{ox}} (x_{\mathrm{X}}, T, p\mathrm{O}_{2})$$

$$= \frac{2}{b} \Delta G_{\mathrm{f,\,Al}_{c_{\mathrm{Al}}}\mathrm{X}_{c_{\mathrm{X}}}\mathrm{O}_{b}}^{\mathrm{o}} (T) - RT \ln\left(x_{\mathrm{X}}^{m_{\mathrm{X}}} x_{\mathrm{Al}}^{m_{\mathrm{Al}}} p\mathrm{O}_{2}\right) - \Delta G_{\mathrm{Al}_{c_{\mathrm{Al}}}\mathrm{X}_{c_{\mathrm{X}}}\mathrm{O}_{b}}^{\mathrm{ox,BWB}} \tag{5.79}$$

$$\Delta G^{\mathrm{ox,BWB}}_{\mathrm{Al}_{c_{\mathrm{Al}}}\mathrm{X}_{c_{\mathrm{X}}}\mathrm{O}_b} = {}^0L_{\mathrm{XAl}}(m_{\mathrm{X}}{x_{\mathrm{Al}}}^2 + m_{\mathrm{Al}}x_{\mathrm{X}}^2)$$

$$+\sum_{i\geq 1} {}^iL_{\mathrm{XAl}}(x_{\mathrm{X}} - x_{\mathrm{Al}})^{i-1}[m_{\mathrm{X}}{x_{\mathrm{Al}}}^2(x_{\mathrm{X}} - x_{\mathrm{Al}} + 2ix_{\mathrm{X}}) + m_{\mathrm{Al}}x_{\mathrm{X}}^2(x_{\mathrm{X}} - x_{\mathrm{Al}} - 2ix_{\mathrm{Al}})] \quad (5.80)$$

5.2.7.2. Ternary systems

In ternary systems (Al-X_1- X_2), a ternary interaction parameter $\omega_{12\mathrm{Al}}$ is introduced, such that the excess free energy of mixing, $\Delta G^{\mathrm{xs}}_{\mathrm{mix}}$, is given below (5.81), where ω_{ij} are binary interaction parameters expanded as Redlich-Kister polynomials (5.75).

$$\Delta G^{\mathrm{xs}}_{\mathrm{mix}} = x_1x_2\omega_{12} + x_1x_{\mathrm{Al}}\omega_{1\mathrm{Al}} + x_2x_{\mathrm{Al}}\omega_{2\mathrm{Al}} + x_1x_2x_{\mathrm{Al}}\omega_{12\mathrm{Al}} \quad (5.81)$$

The general form for $\omega_{12\mathrm{Al}}$ is given below, where ${}^iL_{12\mathrm{Al}}$ depends on composition x_i and temperature (5.82). This form has "little theoretical justification" [11], with linear terms appearing to be chosen due to their simplicity and the $x_1x_2x_{\mathrm{Al}}$ coefficient chosen such that if any component is absent, the term is removed from the equation.

$$\omega_{12\mathrm{Al}} = x_1{}^1L_{12\mathrm{Al}} + x_2{}^2L_{12\mathrm{Al}} + x_{\mathrm{Al}}{}^{\mathrm{Al}}L_{12\mathrm{Al}} = \textstyle\sum_i x_i{}^iL_{12\mathrm{Al}} \quad (5.82)$$

From this, $\Delta\mu_1^{\mathrm{xs}}$ (5.83), $\Delta\mu_2^{\mathrm{xs}}$ (5.84), and $\Delta\mu_{\mathrm{Al}}^{\mathrm{xs}}$ (5.85) can be derived (see Appendix A.3.2 for derivation).

$$\Delta\mu_1^{\mathrm{xs}} = (1-x_1)x_2{}^0L_{12} + (1-x_1-x_2)(1-x_1){}^0L_{1\mathrm{Al}} - x_2(1-x_1-x_2){}^0L_{2\mathrm{Al}}$$
$$-x_2(1-x_1-x_2)\big((3x_1-1)\omega_{12\mathrm{Al}} - x_1{}^1L_{12\mathrm{Al}}\big)$$
$$+x_2\sum_{i\geq 1} {}^iL_{12}(x_1-x_2)^{i-1}[(1-x_1)(x_1-x_2) + ix_1(1-x_1+x_2)]$$
$$+(1-x_1-x_2)\sum_{i\geq 1} {}^iL_{1\mathrm{Al}}(2x_1+x_2-1)^{i-1}[(1-x_1)(2x_1+x_2-1) + ix_1(2-2x_1-x_2)]$$
$$-x_2(1-x_1-x_2)\sum_{i\geq 1} {}^iL_{2\mathrm{Al}}(x_1+2x_2-1)^{i-1}(1+i)(x_1+2x_2-1) \quad (5.83)$$

$$\Delta\mu_2^{\mathrm{xs}} = x_1(1-x_2){}^0L_{12} - x_1(1-x_1-x_2){}^0L_{1\mathrm{Al}} + (1-x_2)(1-x_1-x_2){}^0L_{2\mathrm{Al}}$$
$$-x_1(1-x_1-x_2)\big((3x_2-1)\omega_{12\mathrm{Al}} - x_2{}^2L_{12\mathrm{Al}}\big)$$

$$+x_1\sum_{i\geq 1}{}^{i}L_{12}(x_1-x_2)^{i-1}[(1-x_2)(x_1-x_2)-ix_2(1+x_1-x_2)]$$

$$-x_1(1-x_1-x_2)\sum_{i\geq 1}{}^{i}L_{1\mathrm{Al}}(2x_1+x_2-1)^{i-1}(2x_1+x_2-1)[1+i]$$

$$+(1-x_1-x_2)\sum_{i\geq 1}{}^{i}L_{2\mathrm{Al}}(x_1+2x_2-1)^{i-1}[(1-x_2)(x_1+2x_2-1)$$

$$+ix_2(2-x_1-2x_2)] \tag{5.84}$$

$$\Delta\mu_{\mathrm{Al}}^{\mathrm{xs}}=-x_1x_2{}^{0}L_{12}+x_1{}^{0}L_{1\mathrm{Al}}(x_1+x_2)+x_2{}^{0}L_{2\mathrm{Al}}(x_1+x_2)$$

$$+(3x_1+3x_2-2)x_1x_2\omega_{12\mathrm{Al}}+x_1x_2(1-x_1-x_2)^{\mathrm{Al}}L_{12\mathrm{Al}}$$

$$-x_1x_2\sum_{i\geq 1}{}^{i}L_{12}(x_1-x_2)^{i-1}[(1+i)(x_1-x_2)]$$

$$+x_1\sum_{i\geq 1}{}^{i}L_{1\mathrm{Al}}(2x_1+x_2-1)^{i-1}[(2x_1+x_2-1)(x_1+x_2)-i(1-x_1-x_2)(2x_1+x_2)]$$

$$+x_2\sum_{i\geq 1}{}^{i}L_{2\mathrm{Al}}(x_1+2x_2-1)^{i-1}[(x_1+2x_2-1)(x_1+x_2)$$

$$-i(1-x_1-x_2)(2x_2+x_1)] \tag{5.85}$$

This gives an expression for $\Delta G^{\mathrm{ox}}_{\mathrm{Al}_{c_{\mathrm{Al}}}\mathrm{X}_{1c_1}\mathrm{X}_{2c_2}\mathrm{O}_b}\left(x_1,x_2,T,p_{\mathrm{O}_2}\right)$ as follows (5.86), where the Bragg-Williams Ternary (BWT) term (5.87), $\Delta G^{\mathrm{ox,BWT}}_{\mathrm{Al}_{c_{\mathrm{Al}}}\mathrm{X}_{1c_1}\mathrm{X}_{2c_2}\mathrm{O}_b}$, is defined in terms of the parameters of the ternary system (${}^{i}L_{12\mathrm{Al}}$) and its constituent binary systems (${}^{i}L_{12}$, ${}^{i}L_{1\mathrm{Al}}$, ${}^{i}L_{2\mathrm{Al}}$).

$$\Delta G^{\mathrm{ox}}_{\mathrm{Al}_{c_{\mathrm{Al}}}\mathrm{X}_{1c_1}\mathrm{X}_{2c_2}\mathrm{O}_b}\left(x_1,x_2,T,p_{\mathrm{O}_2}\right)$$

$$=\frac{2}{b}\Delta G^{\mathrm{o}}_{\mathrm{f,Al}_{c_{\mathrm{Al}}}\mathrm{X}_{1c_1}\mathrm{X}_{2c_2}\mathrm{O}_b}(T)-RT\ln\left(x_{\mathrm{X}_1}^{m_1}x_{\mathrm{X}_2}^{m_2}x_{\mathrm{Al}}^{m_{\mathrm{Al}}}p_{\mathrm{O}_2}\right)-\Delta G^{\mathrm{ox,BWT}}_{\mathrm{Al}_{c_{\mathrm{Al}}}\mathrm{X}_{1c_1}\mathrm{X}_{2c_2}\mathrm{O}_b} \tag{5.86}$$

$$\Delta G^{\mathrm{ox,BWT}}_{\mathrm{Al}_{c_{\mathrm{Al}}}\mathrm{X}_{1c_1}\mathrm{X}_{2c_2}\mathrm{O}_b}=x_1x_2(1-x_1-x_2)\left(m_1{}^{1}L_{12\mathrm{Al}}+m_2{}^{2}L_{12\mathrm{Al}}+m_{\mathrm{Al}}{}^{\mathrm{Al}}L_{12\mathrm{Al}}\right)$$
$$+\omega_{12\mathrm{Al}}\left(m_1x_2(1-x_1-x_2)(1-3x_1)+m_2x_1(1-x_1-x_2)(1-3x_2)\right.$$

$$\left.+m_{\mathrm{Al}}x_1x_2(3x_1+3x_2-2)\right)$$

$$+\sum_{i\geq 0}{}^{i}L_{12}(x_1-x_2)^{i}[m_1x_2(1-x_1)+m_2x_1(1-x_2)-m_{\mathrm{Al}}x_1x_2]$$

$$+x_1x_2\sum_{i\geq 1}{}^{i}L_{12}(i)(x_1-x_2)^{i-1}[m_1(1-x_1+x_2)-m_2(1+x_1-x_2)-m_{\mathrm{Al}}(x_1-x_2)]$$
$$+\sum_{i\geq 0}{}^{i}L_{1\mathrm{Al}}(2x_1+x_2-1)^{i}[m_1(1-x_1)(1-x_1-x_2)-m_2x_1(1-x_1-x_2)$$
$$+m_{\mathrm{Al}}x_1(x_1+x_2)]$$
$$+x_1(1-x_1-x_2)\sum_{i\geq 1}{}^{i}L_{1\mathrm{Al}}(i)(2x_1+x_2-1)^{i-1}[m_1(2-2x_1-x_2)-m_2(2x_1+x_2-1)$$
$$-m_{\mathrm{Al}}(2x_1+x_2)]$$
$$+\sum_{i\geq 0}{}^{i}L_{2\mathrm{Al}}(x_1+2x_2-1)^{i}[-m_1x_2(1-x_1-x_2)+m_2(1-x_1-x_2)(1-x_2)$$
$$+m_{\mathrm{Al}}x_2(x_1+x_2)]$$
$$+x_2(1-x_1-x_2)\sum_{i\geq 1}{}^{i}L_{2\mathrm{Al}}(i)(x_1+2x_2-1)^{i-1}[-m_1(x_1+2x_2-1)$$
$$+m_2(2-x_1-2x_2)-m_{\mathrm{Al}}(2x_2+x_1)] \quad (5.87)$$

5.2.8. Modified quasichemical model

The quasichemical model [11], another non-ideal model, considers liquids in which there is a strong tendency to order at specific compositions, modified by Pelton and Blander to account for non-equiatomic ordering to produce the modified quasichemical model (MQM). For a binary A-B system, MQM considers short-range ordering of second-nearest neighbours upon mixing in terms of quasichemical reaction [11] with Gibbs free energy of reaction Δg_{AB} (5.88).

$$(\mathrm{A}-\mathrm{A})\ \text{bond}+(\mathrm{B}-\mathrm{B})\ \text{bond}\rightarrow 2(\mathrm{A}-\mathrm{B})\ \text{bonds};\ \Delta G_{\mathrm{r}}=\Delta g_{\mathrm{AB}} \quad (5.88)$$

The Gibbs free energy of the solution G_{mixed} is then given by the sum of three terms (5.89): the contributions to the Gibbs free energy from the unmixed components (n_i and g_i^0 are the number of moles and standard molar Gibbs free energies of components i), a contribution from the configurational entropy change $\Delta S^{\mathrm{config}}$, and a contribution from the interactions between second-nearest neighbours (n_{AB} is the number of A-B bonds formed on mixing).

$$G_{\text{mixed}} = (n_{\text{A}} g_{\text{A}}^{0} + n_{\text{B}} g_{\text{B}}^{0}) - T\Delta S^{\text{config}} + \frac{n_{\text{AB}}}{2}\Delta g_{\text{AB}} \tag{5.89}$$

In the pair approximation, used in modelling the Al-X systems of interest, the configurational entropy is given as the sum of contributions from point and pair configurations (5.90) [11].

$$\Delta S^{\text{config}} = \Delta S^{\text{point}} + \Delta S^{\text{pair}} \tag{5.90}$$

The point contribution is given by the Bragg-Williams formalism (5.91), and the pair contribution is based on the 1-D Ising model (5.92), where x_{ij} is the bond fraction of i-j bonds (5.93), z_i is the co-ordination number of i, and y_i is the 'co-ordination equivalent' mole fraction of i (5.94), which allows ΔS^{config} to be evaluated (5.95) [11].

$$\Delta S^{\text{point}} = -R(n_{\text{A}} \ln x_{\text{A}} + n_{\text{B}} \ln x_{\text{B}}) \tag{5.91}$$

$$\Delta S^{\text{pair}} = -R\left(n_{\text{AA}} \ln\left(\frac{x_{\text{AA}}}{y_{\text{A}}^2}\right) + n_{\text{BB}} \ln\left(\frac{x_{\text{BB}}}{y_{\text{B}}^2}\right) + n_{\text{AB}} \ln\left(\frac{x_{\text{AB}}}{2y_{\text{A}}y_{\text{B}}}\right)\right) \tag{5.92}$$

$$x_{ij} = \frac{n_{ij}}{n_{\text{AA}} + n_{\text{BB}} + n_{\text{AB}}} \tag{5.93}$$

$$y_i = \frac{z_i x_i}{z_{\text{A}} x_{\text{A}} + z_{\text{B}} x_{\text{B}}} = \frac{z_i n_i}{z_{\text{A}} n_{\text{A}} + z_{\text{B}} n_{\text{B}}} \tag{5.94}$$

$$\Delta S^{\text{config}} = \Delta S^{\text{point}} + \Delta S^{\text{pair}}$$

$$\Delta S^{\text{config}} = -R\left(n_{\text{A}} \ln x_{\text{A}} + n_{\text{B}} \ln x_{\text{B}} + n_{\text{AA}} \ln\left(\frac{x_{\text{AA}}}{y_{\text{A}}^2}\right) + n_{\text{BB}} \ln\left(\frac{x_{\text{BB}}}{y_{\text{B}}^2}\right) + n_{\text{AB}} \ln\left(\frac{x_{\text{AB}}}{2y_{\text{A}}y_{\text{B}}}\right)\right) \tag{5.95}$$

By subtracting the G_{unmixed} (5.96) and $\Delta G_{\text{mix}}^{\text{ideal}}$ (5.97) terms from G_{mixed} (5.98), the excess free energy change of mixing, $\Delta G_{\text{mix},n_i}^{\text{xs}}$ (in terms of the number of moles n_i) can be deduced (5.99).

$$G_{\text{unmixed}} = n_{\text{A}} g_{\text{A}}^{0} + n_{\text{B}} g_{\text{B}}^{0} \tag{5.96}$$

$$\Delta G_{\text{mix}}^{\text{ideal}} = RT(n_{\text{A}} \ln x_{\text{A}} + n_{\text{B}} \ln x_{\text{B}}) \tag{5.97}$$

$$G_{\text{mixed}} = (n_{\text{A}} g_{\text{A}}^{0} + n_{\text{B}} g_{\text{B}}^{0}) - T\Delta S^{\text{config}} + \frac{n_{\text{AB}}}{2}\Delta g_{\text{AB}}$$

$$= (n_{\text{A}} g_{\text{A}}^{0} + n_{\text{B}} g_{\text{B}}^{0}) + \frac{n_{\text{AB}}}{2}\Delta g_{\text{AB}}$$

$$+RT\left(n_{\mathrm{A}}\ln x_{\mathrm{A}}+n_{\mathrm{B}}\ln x_{\mathrm{B}}+n_{\mathrm{AA}}\ln\left(\frac{x_{\mathrm{AA}}}{y_{\mathrm{A}}^2}\right)+n_{\mathrm{BB}}\ln\left(\frac{x_{\mathrm{BB}}}{y_{\mathrm{B}}^2}\right)+n_{\mathrm{AB}}\ln\left(\frac{x_{\mathrm{AB}}}{2y_{\mathrm{A}}y_{\mathrm{B}}}\right)\right) \quad (5.98)$$

$$\therefore \Delta G^{\mathrm{xs}}_{\mathrm{mix},n_i}=\Delta G_{\mathrm{mix}}-\Delta G^{\mathrm{ideal}}_{\mathrm{mix}}=G_{\mathrm{mixed}}-G_{\mathrm{umixed}}-\Delta G^{\mathrm{ideal}}_{\mathrm{mix}}$$

$$=\frac{n_{\mathrm{AB}}}{2}\Delta g_{\mathrm{AB}}+(n_{\mathrm{A}}g^0_{\mathrm{A}}+n_{\mathrm{B}}g^0_{\mathrm{B}})-(n_{\mathrm{A}}g^0_{\mathrm{A}}+n_{\mathrm{B}}g^0_{\mathrm{B}})-RT(n_{\mathrm{A}}\ln x_{\mathrm{A}}+n_{\mathrm{B}}\ln x_{\mathrm{B}})$$

$$+RT\left(n_{\mathrm{A}}\ln x_{\mathrm{A}}+n_{\mathrm{B}}\ln x_{\mathrm{B}}+n_{\mathrm{AA}}\ln\left(\frac{x_{\mathrm{AA}}}{y_{\mathrm{A}}^2}\right)+n_{\mathrm{BB}}\ln\left(\frac{x_{\mathrm{BB}}}{y_{\mathrm{B}}^2}\right)+n_{\mathrm{AB}}\ln\left(\frac{x_{\mathrm{AB}}}{2y_{\mathrm{A}}y_{\mathrm{B}}}\right)\right)$$

$$\Delta G^{\mathrm{xs}}_{\mathrm{mix},n_i}=\frac{n_{\mathrm{AB}}}{2}\Delta g_{\mathrm{AB}}+RT\left(n_{\mathrm{AA}}\ln\left(\frac{x_{\mathrm{AA}}}{y_{\mathrm{A}}^2}\right)+n_{\mathrm{BB}}\ln\left(\frac{x_{\mathrm{BB}}}{y_{\mathrm{B}}^2}\right)+n_{\mathrm{AB}}\ln\left(\frac{x_{\mathrm{AB}}}{2y_{\mathrm{A}}y_{\mathrm{B}}}\right)\right) \quad (5.99)$$

Constraints arise by the definition of z_{A} (5.100) and z_{B} (5.101), from which another useful result can be derived, essentially a statement that all bonds deriving from A and B atoms must result in either A-A, B-B, or A-B bonds (5.102).

$$z_{\mathrm{A}}n_{\mathrm{A}}=2n_{\mathrm{AA}}+n_{\mathrm{AB}} \quad (5.100)$$

$$z_{\mathrm{B}}n_{\mathrm{B}}=2n_{\mathrm{BB}}+n_{\mathrm{AB}} \quad (5.101)$$

$$\frac{1}{2}(z_{\mathrm{A}}n_{\mathrm{A}}+z_{\mathrm{B}}n_{\mathrm{B}})=n_{\mathrm{AA}}+n_{\mathrm{BB}}+n_{\mathrm{AB}} \quad (5.102)$$

Another result arises (5.103), as shown by Pelton [17], by minimising G with respect to n_i.

$$\frac{x_{\mathrm{AB}}}{x_{\mathrm{AA}}x_{\mathrm{BB}}}=4\exp\left(-\frac{\Delta g_{\mathrm{AB}}}{RT}\right) \quad (5.103)$$

The parameter Δg_{AB} is often expanded in terms of pair fractions x_{ij}, with parameters g_{ij}^{mn} which are optimised to experimental data (5.104). In systems of interest, these are only first-order expansions (5.105).

$$\Delta g_{\mathrm{AB}}=\Delta g^0_{\mathrm{AB}}+\sum_{i\geq 1}g^{i0}_{\mathrm{AB}}x^i_{\mathrm{AA}}+\sum_{j\geq 1}g^{0j}_{\mathrm{AB}}x^j_{\mathrm{BB}} \quad (5.104)$$

$$\Delta g_{\mathrm{AB}}=\Delta g^0_{\mathrm{AB}}+g^{10}_{\mathrm{AB}}x_{\mathrm{AA}}+g^{01}_{\mathrm{AB}}x_{\mathrm{BB}} \quad (5.105)$$

To account for high short-range ordering at specific intermediate compositions, co-ordination numbers can be allowed to vary with concentration, resulting in composition-dependent co-ordination numbers (5.106), (5.107).

$$\frac{1}{Z_{\mathrm{A}}} = \frac{1}{Z_{\mathrm{AA}}^{\mathrm{A}}}\left(\frac{2n_{\mathrm{AA}}}{2n_{\mathrm{AA}} + n_{\mathrm{AB}}}\right) + \frac{1}{Z_{\mathrm{AB}}^{\mathrm{A}}}\left(\frac{n_{\mathrm{AB}}}{2n_{\mathrm{AA}} + n_{\mathrm{AB}}}\right) \tag{5.106}$$

$$\frac{1}{Z_{\mathrm{B}}} = \frac{1}{Z_{\mathrm{BB}}^{\mathrm{B}}}\left(\frac{2n_{\mathrm{BB}}}{2n_{\mathrm{AA}} + n_{\mathrm{AB}}}\right) + \frac{1}{Z_{\mathrm{AB}}^{\mathrm{A}}}\left(\frac{n_{\mathrm{AB}}}{2n_{\mathrm{AA}} + n_{\mathrm{AB}}}\right) \tag{5.107}$$

These allow n_{A} (5.108) and n_{B} (5.109) to be expressed in terms of n_{ij} and Z_{ij}^{i}.

$$n_{\mathrm{A}} = \frac{2n_{\mathrm{AA}}}{Z_{\mathrm{AA}}^{\mathrm{A}}} + \frac{n_{\mathrm{AB}}}{Z_{\mathrm{AB}}^{\mathrm{A}}} \tag{5.108}$$

$$n_{\mathrm{B}} = \frac{2n_{\mathrm{BB}}}{Z_{\mathrm{BB}}^{\mathrm{B}}} + \frac{n_{\mathrm{AB}}}{Z_{\mathrm{AB}}^{\mathrm{B}}} \tag{5.109}$$

By adding these expressions (5.110), molar quantities x_{A} (5.111) and x_{B} (5.112) can then be expressed in terms of x_{ij} and Z_{ij}^{i}, where β_{AA} (5.113), β_{BB} (5.114), β_{AB} (5.115), and β_{BA} (5.116), are defined in terms of Z_{ij}^{i} to simplify future calculations.

$$n_{\mathrm{A}} + n_{\mathrm{B}} = \frac{2}{Z_{\mathrm{AA}}^{\mathrm{A}}} n_{\mathrm{AA}} + \frac{2}{Z_{\mathrm{BB}}^{\mathrm{B}}} n_{\mathrm{BB}} + \left(\frac{1}{Z_{\mathrm{AB}}^{\mathrm{A}}} + \frac{1}{Z_{\mathrm{AB}}^{\mathrm{B}}}\right) n_{\mathrm{AB}} \tag{5.110}$$

$$x_{\mathrm{A}} = \frac{n_{\mathrm{A}}}{n_{\mathrm{A}} + n_{\mathrm{B}}} = \frac{\left(\frac{2}{Z_{\mathrm{AA}}^{\mathrm{A}}} n_{\mathrm{AA}} + \frac{1}{Z_{\mathrm{AB}}^{\mathrm{A}}} n_{\mathrm{AB}}\right)}{\frac{2}{Z_{\mathrm{AA}}^{\mathrm{A}}} n_{\mathrm{AA}} + \frac{2}{Z_{\mathrm{BB}}^{\mathrm{B}}} n_{\mathrm{BB}} + \left(\frac{1}{Z_{\mathrm{AB}}^{\mathrm{A}}} + \frac{1}{Z_{\mathrm{AB}}^{\mathrm{B}}}\right) n_{\mathrm{AB}}}$$

$$= \frac{\beta_{\mathrm{AA}} n_{\mathrm{AA}} + \beta_{\mathrm{AB}} n_{\mathrm{AB}}}{\beta_{\mathrm{AA}} n_{\mathrm{AA}} + \beta_{\mathrm{BB}} n_{\mathrm{BB}} + (\beta_{\mathrm{AB}} + \beta_{\mathrm{BA}}) n_{\mathrm{AB}}}$$

$$x_{\mathrm{A}} = \frac{\beta_{\mathrm{AA}} x_{\mathrm{AA}} + \beta_{\mathrm{AB}} x_{\mathrm{AB}}}{\beta_{\mathrm{AA}} x_{\mathrm{AA}} + \beta_{\mathrm{BB}} x_{\mathrm{BB}} + (\beta_{\mathrm{AB}} + \beta_{\mathrm{BA}}) x_{\mathrm{AB}}} \tag{5.111}$$

$$x_{\mathrm{B}} = \frac{n_{\mathrm{B}}}{n_{\mathrm{A}} + n_{\mathrm{B}}} = \frac{\left(\frac{2}{Z_{\mathrm{BB}}^{\mathrm{B}}} n_{\mathrm{BB}} + \frac{1}{Z_{\mathrm{AB}}^{\mathrm{B}}} n_{\mathrm{AB}}\right)}{\frac{2}{Z_{\mathrm{AA}}^{\mathrm{A}}} n_{\mathrm{AA}} + \frac{2}{Z_{\mathrm{BB}}^{\mathrm{B}}} n_{\mathrm{BB}} + \left(\frac{1}{Z_{\mathrm{AB}}^{\mathrm{A}}} + \frac{1}{Z_{\mathrm{AB}}^{\mathrm{B}}}\right) n_{\mathrm{AB}}}$$

$$= \frac{\beta_{\mathrm{BB}} n_{\mathrm{BB}} + \beta_{\mathrm{BA}} n_{\mathrm{AB}}}{\beta_{\mathrm{AA}} n_{\mathrm{AA}} + \beta_{\mathrm{BB}} n_{\mathrm{BB}} + (\beta_{\mathrm{AB}} + \beta_{\mathrm{BA}}) n_{\mathrm{AB}}}$$

$$x_{\mathrm{B}} = \frac{\beta_{\mathrm{BB}} x_{\mathrm{BB}} + \beta_{\mathrm{BA}} x_{\mathrm{AB}}}{\beta_{\mathrm{AA}} x_{\mathrm{AA}} + \beta_{\mathrm{BB}} x_{\mathrm{BB}} + (\beta_{\mathrm{AB}} + \beta_{\mathrm{BA}}) x_{\mathrm{AB}}} \tag{5.112}$$

$$\beta_{AA} = \frac{2}{Z^{A}_{AA}} \quad (5.113) \qquad \beta_{BB} = \frac{2}{Z^{B}_{BB}} \quad (5.114) \qquad \beta_{AB} = \frac{1}{Z^{A}_{AB}} \quad (5.115) \qquad \beta_{BA} = \frac{1}{Z^{A}_{BA}} \quad (5.116)$$

The terms x_{AA} (5.117) and x_{BB} (5.118) can be expressed in terms of x_i, β_{ij}, and x_{AB}.

$$x_A = \frac{\beta_{AA}x_{AA} + \beta_{AB}x_{AB}}{\beta_{AA}x_{AA} + \beta_{BB}x_{BB} + (\beta_{AB} + \beta_{BA})x_{AB}}$$

$$= \frac{\beta_{AA}x_{AA} + \beta_{AB}x_{AB}}{\beta_{AA}x_{AA} + \beta_{BB}(1 - x_{AA} - x_{AB}) + (\beta_{AB} + \beta_{BA})x_{AB}}$$

$$\beta_{AA}x_{AA} + \beta_{AB}x_{AB} = x_A(\beta_{AA}x_{AA} + \beta_{BB}(1 - x_{AA} - x_{AB}) + (\beta_{AB} + \beta_{BA})x_{AB})$$

$$x_{AA}(\beta_{AA} - x_A\beta_{AA} + x_A\beta_{BB}) = x_A(\beta_{BB}(1 - x_{AB}) + (\beta_{AB} + \beta_{BA})x_{AB}) - \beta_{AB}x_{AB}$$

$$x_{AA}((1 - x_A)\beta_{AA} + x_A\beta_{BB}) = x_{AB}(x_A(\beta_{AB} + \beta_{BA} - \beta_{BB}) - \beta_{AB}) + \beta_{BB}x_A$$

$$x_{AA} = \frac{(x_A(\beta_{AB} + \beta_{BA} - \beta_{BB}) - \beta_{AB})x_{AB} + \beta_{BB}x_A}{(1 - x_A)\beta_{AA} + x_A\beta_{BB}}$$

$$x_{AA} = \frac{(x_A\beta_{BA} - (1 - x_A)\beta_{AB})x_{AB} + x_A\beta_{BB}(1 - x_{AB})}{(1 - x_A)\beta_{AA} + x_A\beta_{BB}} \quad (5.117)$$

$$x_{BB} = \frac{(x_B(\beta_{AB} + \beta_{BA} - \beta_{AA}) - \beta_{BA})x_{AB} + \beta_{AA}x_B}{(1 - x_A)\beta_{AA} + x_A\beta_{BB}}$$

$$= \frac{\big((1 - x_A)(\beta_{AB} + \beta_{BA} - \beta_{AA}) - \beta_{BA}\big)x_{AB} + \beta_{AA}(1 - x_A)}{(1 - x_A)\beta_{AA} + x_A\beta_{BB}}$$

$$x_{BB} = \frac{\big((1 - x_A)\beta_{AB} - x_A\beta_{BA}\big)x_{AB} + \beta_{AA}(1 - x_A)(1 - x_{AB})}{(1 - x_A)\beta_{AA} + x_A\beta_{BB}} \quad (5.118)$$

This allows x_{AB} (5.119) to be expressed in terms of x_A, Δg^0_{AB}, g^{ij}_{AB}, and β_{ij}.

$$\frac{x_{AB}}{x_{AA}x_{BB}} = 4\exp\left(-\frac{\Delta g_{AB}}{RT}\right)$$

$$x_{AB} = 4x_{AA}x_{BB}\exp\left(-\frac{\Delta g^0_{AB} + g^{10}_{AB}x_{AA} + g^{01}_{AB}x_{BB}}{RT}\right)$$

$$= 4\exp\left(-\frac{\Delta g^0_{AB}}{RT}\right)x_{AA}x_{BB}\exp\left(-\frac{g^{10}_{AB}x_{AA} + g^{01}_{AB}x_{BB}}{RT}\right)$$

$$x_{\mathrm{AB}} = 4\exp\left(-\frac{\Delta g^0_{\mathrm{AB}}}{RT}\right) \times \left[(x_{\mathrm{A}}(\beta_{\mathrm{AB}} + \beta_{\mathrm{BA}} - \beta_{\mathrm{BB}}) - \beta_{\mathrm{AB}})x_{\mathrm{AB}} + \beta_{\mathrm{BB}}x_{\mathrm{A}}\right]$$
$$\times \left[\left((1 - x_{\mathrm{A}})(\beta_{\mathrm{AB}} + \beta_{\mathrm{BA}} - \beta_{\mathrm{AA}}) - \beta_{\mathrm{BA}}\right)x_{\mathrm{AB}} + \beta_{\mathrm{AA}}(1 - x_{\mathrm{A}})\right]$$
$$\div \left[(1 - x_{\mathrm{A}})\beta_{\mathrm{AA}} + x_{\mathrm{A}}\beta_{\mathrm{BB}}\right]^2$$
$$\times \exp\Big(-\big(g^{10}_{\mathrm{AB}}\left[(x_{\mathrm{A}}(\beta_{\mathrm{AB}} + \beta_{\mathrm{BA}} - \beta_{\mathrm{BB}}) - \beta_{\mathrm{AB}})x_{\mathrm{AB}} + \beta_{\mathrm{BB}}x_{\mathrm{A}}\right]$$
$$+ g^{01}_{\mathrm{AB}}\left[\left((1 - x_{\mathrm{A}})(\beta_{\mathrm{AB}} + \beta_{\mathrm{BA}} - \beta_{\mathrm{AA}}) - \beta_{\mathrm{BA}}\right)x_{\mathrm{AB}} + \beta_{\mathrm{AA}}(1 - x_{\mathrm{A}})\right]\big)$$
$$\div \Big(RT\big((1 - x_{\mathrm{A}})\beta_{\mathrm{AA}} + x_{\mathrm{A}}\beta_{\mathrm{BB}}\big)\Big)\Big) \tag{5.119}$$

This implicit equation must be solved via numerical methods, giving the quantities x_{ij} as functions of the variables x_i and optimised parameters Z^i_{ij} , Δg^0_{ij}, and g^{nm}_{ij}. This allows evaluation of $\Delta G^{\mathrm{xs}}_{\mathrm{mix}}$, in molar quantities (5.120).

$$\Delta G^{\mathrm{xs}}_{\mathrm{mix}} = \frac{\Delta G^{\mathrm{xs},n_i}_{\mathrm{mix}}}{n_{\mathrm{A}} + n_{\mathrm{B}}} = \frac{\left(\frac{n_{\mathrm{AB}}}{2}\Delta g_{\mathrm{AB}} + RT\left(n_{\mathrm{AA}}\ln\frac{x_{\mathrm{AA}}}{y^2_{\mathrm{A}}} + n_{\mathrm{BB}}\ln\frac{x_{\mathrm{BB}}}{y^2_{\mathrm{B}}} + n_{\mathrm{AB}}\ln\frac{x_{\mathrm{AB}}}{2y_{\mathrm{A}}y_{\mathrm{B}}}\right)\right)}{\beta_{\mathrm{AA}}n_{\mathrm{AA}} + \beta_{\mathrm{BB}}n_{\mathrm{BB}} + (\beta_{\mathrm{AB}} + \beta_{\mathrm{BA}})n_{\mathrm{AB}}}$$

$$= \frac{\left(\frac{x_{\mathrm{AB}}}{2}(\Delta g^0_{\mathrm{AB}} + g^{10}_{\mathrm{AB}}x_{\mathrm{AA}} + g^{01}_{\mathrm{AB}}x_{\mathrm{BB}}) + RT\left(x_{\mathrm{AA}}\ln\frac{x_{\mathrm{AA}}}{y^2_{\mathrm{A}}} + x_{\mathrm{BB}}\ln\frac{x_{\mathrm{BB}}}{y^2_{\mathrm{B}}} + x_{\mathrm{AB}}\ln\frac{x_{\mathrm{AB}}}{2y_{\mathrm{A}}y_{\mathrm{B}}}\right)\right)}{\beta_{\mathrm{AA}}x_{\mathrm{AA}} + \beta_{\mathrm{BB}}x_{\mathrm{BB}} + (\beta_{\mathrm{AB}} + \beta_{\mathrm{BA}})x_{\mathrm{AB}}} \tag{5.120}$$

Converting to an Al-X system and simplifying terms (see Appendix A.4.1 for derivation), $\Delta G^{\mathrm{xs}}_{\mathrm{mix}}$ (5.121) can be expressed in terms of ε_i and β_{ij}.

$$\Delta G^{\mathrm{xs}}_{\mathrm{mix}} = \frac{x_{\mathrm{XAl}}}{2\varepsilon_6}\left(\Delta g^0_{\mathrm{XAl}}\varepsilon_1 + g^{10}_{\mathrm{XAl}}\varepsilon_2 + g^{01}_{\mathrm{XAl}}\varepsilon_3\right)$$
$$+ \frac{RT}{\varepsilon_6}\left(\varepsilon_1\ln\varepsilon_1 + \varepsilon_2\ln\varepsilon_2 + \varepsilon_3\ln\varepsilon_3 + \varepsilon_1 x_{\mathrm{XAl}}\ln\left(\frac{\varepsilon_1 x_{\mathrm{XAl}}}{2}\right) - \left(\varepsilon_4\ln\left(\frac{\varepsilon_4}{2}\right) + \varepsilon_5\ln\left(\frac{\varepsilon_5}{2}\right)\right)\right) \tag{5.121}$$

$$\varepsilon_1 = (1 - x_{\mathrm{X}})\beta_{\mathrm{XX}} + x_{\mathrm{X}}\beta_{\mathrm{AlAl}} \tag{5.122}$$

$$\varepsilon_2 = \varepsilon_1 x_{\mathrm{XX}} = (x_{\mathrm{X}}\beta_{\mathrm{AlX}} - (1 - x_{\mathrm{X}})\beta_{\mathrm{XAl}})x_{\mathrm{XAl}} + x_{\mathrm{X}}\beta_{\mathrm{AlAl}}(1 - x_{\mathrm{XAl}}) \tag{5.123}$$

$$\varepsilon_3 = \varepsilon_1 x_{\mathrm{AlAl}} = \left((1 - x_{\mathrm{X}})\beta_{\mathrm{XAl}} - x_{\mathrm{X}}\beta_{\mathrm{AlX}}\right)x_{\mathrm{XAl}} + \beta_{\mathrm{XX}}(1 - x_{\mathrm{X}})(1 - x_{\mathrm{XAl}}) \tag{5.124}$$

$$\varepsilon_4 = 2\varepsilon_1 y_{\mathrm{X}} = x_{\mathrm{XAl}}\big((2\beta_{\mathrm{AlX}} - \beta_{\mathrm{AlAl}})x_{\mathrm{X}} + (\beta_{\mathrm{XX}} - 2\beta_{\mathrm{XAl}})(1 - x_{\mathrm{X}})\big) + 2x_{\mathrm{X}}\beta_{\mathrm{AlAl}} \tag{5.125}$$

$$\varepsilon_5 = 2\varepsilon_1 y_{\mathrm{Al}} = x_{\mathrm{XAl}}\big((\beta_{\mathrm{AlAl}} - 2\beta_{\mathrm{AlX}})x_{\mathrm{X}} + (2\beta_{\mathrm{XAl}} - \beta_{\mathrm{XX}})(1 - x_{\mathrm{X}})\big) + 2\beta_{\mathrm{XX}}(1 - x_{\mathrm{X}}) \tag{5.126}$$

$$\varepsilon_6 = \beta_{\mathrm{XX}}\beta_{\mathrm{AlAl}} + x_{\mathrm{XAl}}(\beta_{\mathrm{XX}}\beta_{\mathrm{AlX}} + \beta_{\mathrm{AlAl}}\beta_{\mathrm{XAl}} - \beta_{\mathrm{XX}}\beta_{\mathrm{AlAl}}) \quad (5.127)$$

$$\beta_{\mathrm{XX}} = \frac{2}{Z^{\mathrm{X}}_{\mathrm{XX}}} \quad (5.128) \qquad \beta_{\mathrm{AlAl}} = \frac{2}{Z^{\mathrm{Al}}_{\mathrm{AlAl}}} \quad (5.129) \qquad \beta_{\mathrm{XAl}} = \frac{1}{Z^{\mathrm{X}}_{\mathrm{AlX}}} \quad (5.130) \qquad \beta_{\mathrm{AlX}} = \frac{1}{Z^{\mathrm{X}}_{\mathrm{AlX}}} \quad (5.131)$$

The derivative $\frac{\mathrm{d}\Delta G^{\mathrm{xs}}_{\mathrm{mix}}}{\mathrm{d}x_{\mathrm{X}}}$ (5.132) can then be evaluated in terms of these quantities and x'_{XAl}, the derivative of x_{XAl} with respect to x_{X} (see Appendix A.4.2 for derivation).

$$\begin{aligned}
\frac{\mathrm{d}\Delta G^{\mathrm{xs}}_{\mathrm{mix}}}{\mathrm{d}x_{\mathrm{X}}} &= \frac{\Delta g^{0}_{\mathrm{XAl}}}{2\varepsilon_6^2}\left(x'_{\mathrm{XAl}}(\varepsilon_1\beta_{\mathrm{XX}}\beta_{\mathrm{AlAl}}) + (\beta_{\mathrm{AlAl}} - \beta_{\mathrm{XX}})\varepsilon_6 x_{\mathrm{XAl}}\right) \\
&+ \frac{g^{10}_{\mathrm{XAl}}}{2\varepsilon_6^2}\left(x'_{\mathrm{XAl}}(\varepsilon_2(\beta_{\mathrm{XX}}\beta_{\mathrm{AlAl}} + \varepsilon_6) - x_{\mathrm{X}}\beta_{\mathrm{AlAl}}\varepsilon_6) + \frac{\varepsilon_6}{x_{\mathrm{X}}}(\varepsilon_2 + \beta_{\mathrm{XAl}}x_{\mathrm{XAl}})x_{\mathrm{XAl}}\right) \\
&+ \frac{g^{01}_{\mathrm{XAl}}}{2\varepsilon_6^2}\left(x'_{\mathrm{XAl}}(\varepsilon_3(\beta_{\mathrm{XX}}\beta_{\mathrm{AlAl}} + \varepsilon_6) - (1 - x_{\mathrm{X}})\beta_{\mathrm{XX}}\varepsilon_6) - \frac{\varepsilon_6}{1 - x_{\mathrm{X}}}(\varepsilon_3 + \beta_{\mathrm{AlX}}x_{\mathrm{XAl}})x_{\mathrm{XAl}}\right) \\
&+ \frac{RT}{\varepsilon_6^2}\ln\varepsilon_1\left((\beta_{\mathrm{AlAl}} - \beta_{\mathrm{XX}})\varepsilon_6 - \varepsilon_1(\beta_{\mathrm{XX}}\beta_{\mathrm{AlX}} + \beta_{\mathrm{AlAl}}\beta_{\mathrm{XAl}} - \beta_{\mathrm{XX}}\beta_{\mathrm{AlAl}})x'_{\mathrm{XAl}}\right) \\
&+ \frac{RT}{\varepsilon_6^2}\ln\varepsilon_2\left(\frac{\varepsilon_6}{x_{\mathrm{X}}}(\varepsilon_2 + \beta_{\mathrm{XAl}}x_{\mathrm{XAl}}) - \beta_{\mathrm{AlAl}}\beta_{\mathrm{XAl}}\varepsilon_1 x'_{\mathrm{XAl}}\right) \\
&+ \frac{RT}{\varepsilon_6^2}\ln\varepsilon_3\left(-\frac{\varepsilon_6}{1 - x_{\mathrm{X}}}(\varepsilon_3 + \beta_{\mathrm{AlX}}x_{\mathrm{XAl}}) - \beta_{\mathrm{XX}}\beta_{\mathrm{AlX}}\varepsilon_1 x'_{\mathrm{XAl}}\right) \\
&- \frac{RT}{\varepsilon_6^2}\ln\left(\frac{\varepsilon_4}{2}\right)\left(\frac{\varepsilon_6}{x_{\mathrm{X}}}\left(\varepsilon_4 + x_{\mathrm{XAl}}(2\beta_{\mathrm{XAl}} - \beta_{\mathrm{XX}})\right) - \varepsilon_1\beta_{\mathrm{AlAl}}(2\beta_{\mathrm{XAl}} - \beta_{\mathrm{XX}})x'_{\mathrm{XAl}}\right) \\
&- \frac{RT}{\varepsilon_6^2}\ln\left(\frac{\varepsilon_5}{2}\right)\left(-\frac{\varepsilon_6}{1 - x_{\mathrm{X}}}\left(\varepsilon_5 + x_{\mathrm{XAl}}(2\beta_{\mathrm{AlX}} - \beta_{\mathrm{AlAl}})\right) - \varepsilon_1\beta_{\mathrm{XX}}(2\beta_{\mathrm{AlX}} - \beta_{\mathrm{AlAl}})x'_{\mathrm{XAl}}\right) \\
&+ \frac{RT}{\varepsilon_6^2}\ln\left(\frac{\varepsilon_1 x_{\mathrm{XAl}}}{2}\right)\left(\left(\beta_{\mathrm{XX}}\beta_{\mathrm{AlAl}}x'_{\mathrm{XAl}}\varepsilon_1 + x_{\mathrm{XAl}}\varepsilon_6(\beta_{\mathrm{AlAl}} - \beta_{\mathrm{XX}})\right)\right)
\end{aligned} \quad (5.132)$$

This allows $\Delta\mu^{\mathrm{xs}}_{\mathrm{X}}$ (5.133) and $\Delta\mu^{\mathrm{xs}}_{\mathrm{Al}}$ to be calculated (5.134), where ε_{X} (5.135) and $\varepsilon_{\mathrm{Al}}$ (5.136) are groupings of the logarithm-based terms (see Appendix A.4.3 for derivation).

$$\Delta\mu^{\mathrm{xs}}_{\mathrm{X}} = \frac{1}{2\varepsilon_1\varepsilon_6}\left(x_{\mathrm{XAl}}\varepsilon_6(1 - x_{\mathrm{X}})\left(g^{10}_{\mathrm{XAl}} - g^{01}_{\mathrm{XAl}}\right) + RT\varepsilon_1\left(2\beta_{\mathrm{AlAl}}\varepsilon_{\mathrm{X}} + x_{\mathrm{XAl}}(2\beta_{\mathrm{AlX}} - \beta_{\mathrm{AlAl}})(\varepsilon_{\mathrm{X}} - \varepsilon_{\mathrm{Al}})\right)\right)$$

$$-\frac{x'_{\mathrm{XAl}}(1-x_{\mathrm{X}})}{2\varepsilon_6^2}\Big(RT\varepsilon_1\big(\beta_{\mathrm{XX}}\varepsilon_{\mathrm{Al}}(2\beta_{\mathrm{AlX}}-\beta_{\mathrm{AlAl}})+\beta_{\mathrm{AlAl}}\varepsilon_{\mathrm{X}}(2\beta_{\mathrm{XAl}}-\beta_{\mathrm{XX}})\big)$$

$$-\varepsilon_6\left((\varepsilon_3-(1-x_{\mathrm{X}})\beta_{\mathrm{XX}})g^{01}_{\mathrm{XAl}}+(\varepsilon_2-x_{\mathrm{X}}\beta_{\mathrm{AlAl}})g^{10}_{\mathrm{XAl}}\right)\Big) \tag{5.133}$$

$$\Delta\mu^{\mathrm{xs}}_{\mathrm{Al}}=\frac{1}{2\varepsilon_1\varepsilon_6}\left[\varepsilon_6 x_{\mathrm{X}}x_{\mathrm{XAl}}\left(g^{01}_{\mathrm{XAl}}-g^{10}_{\mathrm{XAl}}\right)+RT\varepsilon_1\left(2\beta_{\mathrm{XX}}\varepsilon_{\mathrm{Al}}+x_{\mathrm{XAl}}(2\beta_{\mathrm{XAl}}-\beta_{\mathrm{XX}})(\varepsilon_{\mathrm{Al}}-\varepsilon_{\mathrm{X}})\right)\right]$$

$$+\frac{x_{\mathrm{X}}x'_{\mathrm{XAl}}}{2\varepsilon_6^2}\Big[RT\varepsilon_1\big(\beta_{\mathrm{AlAl}}\varepsilon_{\mathrm{X}}(2\beta_{\mathrm{XAl}}-\beta_{\mathrm{XX}})+\beta_{\mathrm{XX}}\varepsilon_{\mathrm{Al}}(2\beta_{\mathrm{AlX}}-\beta_{\mathrm{AlAl}})\big)$$

$$-\varepsilon_6\left((\varepsilon_2-x_{\mathrm{X}}\beta_{\mathrm{AlAl}})g^{10}_{\mathrm{XAl}}+(\varepsilon_3-(1-x_{\mathrm{X}})\beta_{\mathrm{XX}})g^{01}_{\mathrm{XAl}}\right)\Big] \tag{5.134}$$

$$\varepsilon_{\mathrm{X}}=\ln\varepsilon_1+\ln\varepsilon_2-2\ln\left(\frac{\varepsilon_4}{2}\right)=\ln\left(\frac{4\varepsilon_1\varepsilon_2}{\varepsilon_4^2}\right)=\ln\left(\frac{4\varepsilon_1^2x_{\mathrm{XX}}}{(2\varepsilon_1y_{\mathrm{X}})^2}\right)=\ln\left(\frac{x_{\mathrm{XX}}}{{y_{\mathrm{X}}}^2}\right) \tag{5.135}$$

$$\varepsilon_{\mathrm{Al}}=\ln\varepsilon_1+\ln\varepsilon_2-2\ln\left(\frac{\varepsilon_5}{2}\right)=\ln\left(\frac{4\varepsilon_1\varepsilon_3}{\varepsilon_5^2}\right)=\ln\left(\frac{4\varepsilon_1^2x_{\mathrm{AlAl}}}{(2\varepsilon_1y_{\mathrm{Al}})^2}\right)=\ln\left(\frac{x_{\mathrm{AlAl}}}{{y_{\mathrm{Al}}}^2}\right) \tag{5.136}$$

Whilst x_{XAl} (5.137) must be evaluated numerically, x'_{XAl} can be expressed in terms of x_{XAl} (5.138) and the other parameters of the system by implicit differentiation (see Appendix A.4.4 for derivation).

$$x_{\mathrm{XAl}}(x_{\mathrm{X}})=\left(\frac{4\varepsilon_2\varepsilon_3}{\varepsilon_1^2}\right)\exp\left(-\frac{\varepsilon_1\Delta g^0_{\mathrm{XAl}}+\varepsilon_2g^{10}_{\mathrm{XAl}}+\varepsilon_3g^{01}_{\mathrm{XAl}}}{\varepsilon_1RT}\right) \tag{5.137}$$

$$x'_{\mathrm{XAl}}=\frac{\varepsilon_6x_{\mathrm{XAl}}}{\varepsilon_1}\times\left(\varepsilon_1(\varepsilon_3-\varepsilon_2)RT-\varepsilon_2\varepsilon_3\left(g^{10}_{\mathrm{XAl}}-g^{01}_{\mathrm{XAl}}\right)\right)$$

$$\div\Big(RT\varepsilon_1\big(\beta_{\mathrm{AlAl}}\beta_{\mathrm{XX}}x_{\mathrm{X}}(1-x_{\mathrm{X}})-(\varepsilon_2-x_{\mathrm{X}}\beta_{\mathrm{AlAl}})(\varepsilon_3-(1-x_{\mathrm{X}})\beta_{\mathrm{XX}})\big)$$

$$+\varepsilon_2\varepsilon_3\left((\varepsilon_2-x_{\mathrm{X}}\beta_{\mathrm{AlAl}})g^{10}_{\mathrm{XAl}}+(\varepsilon_3-(1-x_{\mathrm{X}})\beta_{\mathrm{XX}})g^{01}_{\mathrm{XAl}}\right)\Big) \tag{5.138}$$

This can be used to simplify expressions for $\Delta\mu^{\mathrm{xs}}_{\mathrm{X}}$ (5.139) and $\Delta\mu^{\mathrm{xs}}_{\mathrm{Al}}$ (5.140), where σ_{X} (5.141), σ_{Al} (5.142), σ_1 (5.143), σ_2 (5.144), and σ_3 (5.145) are defined below (see Appendix A.4.5 for derivation).

$$\Delta\mu^{\mathrm{xs}}_{\mathrm{X}}(x_{\mathrm{X}})=\frac{RT}{2\varepsilon_6}\sigma_{\mathrm{X}}+(1-x_{\mathrm{X}})\frac{RTx_{\mathrm{XAl}}}{2\sigma_1}\left(\frac{\sigma_2}{\varepsilon_6}+\sigma_3\right) \tag{5.139}$$

$$\Delta\mu_{\mathrm{Al}}^{\mathrm{xs}}(x_{\mathrm{X}}) = \frac{RT}{2\varepsilon_6}\sigma_{\mathrm{Al}} - x_{\mathrm{X}}\frac{RTx_{\mathrm{XAl}}}{2\sigma_1}\left(\frac{\sigma_2}{\varepsilon_6} + \sigma_3\right) \tag{5.140}$$

$$\sigma_{\mathrm{X}} = 2\beta_{\mathrm{AlAl}}\varepsilon_{\mathrm{X}} + x_{\mathrm{XAl}}(2\beta_{\mathrm{AlX}} - \beta_{\mathrm{AlAl}})(\varepsilon_{\mathrm{X}} - \varepsilon_{\mathrm{Al}}) \tag{5.141}$$

$$\sigma_{\mathrm{Al}} = 2\beta_{\mathrm{XX}}\varepsilon_{\mathrm{Al}} + x_{\mathrm{XAl}}(2\beta_{\mathrm{XAl}} - \beta_{\mathrm{XX}})(\varepsilon_{\mathrm{Al}} - \varepsilon_{\mathrm{X}}) \tag{5.142}$$

$$\begin{aligned}\sigma_1 = {} & RT\varepsilon_1\big(\beta_{\mathrm{AlAl}}\beta_{\mathrm{XX}}x_{\mathrm{X}}(1-x_{\mathrm{X}}) - (\varepsilon_2 - x_{\mathrm{X}}\beta_{\mathrm{AlAl}})(\varepsilon_3 - (1-x_{\mathrm{X}})\beta_{\mathrm{XX}})\big) \\ & + \varepsilon_2\varepsilon_3\left((\varepsilon_2 - x_{\mathrm{X}}\beta_{\mathrm{AlAl}})g_{\mathrm{XAl}}^{10} + (\varepsilon_3 - (1-x_{\mathrm{X}})\beta_{\mathrm{XX}})g_{\mathrm{XAl}}^{01}\right)\end{aligned} \tag{5.143}$$

$$\begin{aligned}\sigma_2 = {} & \left(\varepsilon_1(\varepsilon_2 - \varepsilon_3)RT + \varepsilon_2\varepsilon_3\big(g_{\mathrm{XAl}}^{10} - g_{\mathrm{XAl}}^{01}\big)\right)\big(\beta_{\mathrm{XX}}\varepsilon_{\mathrm{Al}}(2\beta_{\mathrm{AlX}} - \beta_{\mathrm{AlAl}}) \\ & + \beta_{\mathrm{AlAl}}\varepsilon_{\mathrm{X}}(2\beta_{\mathrm{XAl}} - \beta_{\mathrm{XX}})\big)\end{aligned} \tag{5.144}$$

$$\sigma_3 = \varepsilon_2(\varepsilon_1 - \varepsilon_2)g_{\mathrm{XAl}}^{10} - \varepsilon_3(\varepsilon_1 - \varepsilon_3)g_{\mathrm{XAl}}^{01} \tag{5.145}$$

These expressions can be used to evaluate the excess free energy term of ΔG^{ox} (5.146).

$$\begin{aligned}& [m_{\mathrm{X}}\Delta\mu_{\mathrm{X}}^{\mathrm{xs}} + m_{\mathrm{Al}}\Delta\mu_{\mathrm{Al}}^{\mathrm{xs}}] \\ & = m_{\mathrm{X}}\left[\frac{RT}{2\varepsilon_6}\sigma_{\mathrm{X}} + (1-x_{\mathrm{X}})\frac{RTx_{\mathrm{XAl}}}{2\sigma_1}\left(\frac{\sigma_2}{\varepsilon_6} + \sigma_3\right)\right] \\ & + m_{\mathrm{Al}}\left[\frac{RT}{2\varepsilon_6}\sigma_{\mathrm{Al}} - x_{\mathrm{X}}\frac{RTx_{\mathrm{XAl}}}{2\sigma_1}\left(\frac{\sigma_2}{\varepsilon_6} + \sigma_3\right)\right] \\ & = \frac{RT}{2\varepsilon_6}(m_{\mathrm{X}}\sigma_{\mathrm{X}} + m_{\mathrm{Al}}\sigma_{\mathrm{Al}}) + \frac{RTx_{\mathrm{XAl}}}{2\sigma_1}\left(\frac{\sigma_2}{\varepsilon_6} + \sigma_3\right)(m_{\mathrm{X}}(1-x_{\mathrm{X}}) - m_{\mathrm{Al}}x_{\mathrm{X}})\end{aligned} \tag{5.146}$$

This allows evaluation of ΔG^{ox} (5.147).

$$\begin{aligned}& \Delta G_{\mathrm{Al}_{c_{\mathrm{Al}}}\mathrm{X}_{c_{\mathrm{X}}}\mathrm{O}_b}^{\mathrm{ox}}(x_{\mathrm{X}}, T, p_{\mathrm{O}_2}) \\ & = \frac{2}{b}\Delta G_{\mathrm{f,\,Al}_{c_{\mathrm{Al}}}\mathrm{X}_{c_{\mathrm{X}}}\mathrm{O}_b}^{\mathrm{o}}(T) - [m_{\mathrm{X}}\Delta\mu_{\mathrm{X}}^{\mathrm{xs}} + m_{\mathrm{Al}}\Delta\mu_{\mathrm{Al}}^{\mathrm{xs}}] - RT\ln\big(x_{\mathrm{X}}^{m_{\mathrm{X}}}x_{\mathrm{Al}}^{m_{\mathrm{Al}}}p_{\mathrm{O}_2}\big) \\ & = \frac{2}{b}\Delta G_{\mathrm{f,\,Al}_{c_{\mathrm{Al}}}\mathrm{X}_{c_{\mathrm{X}}}\mathrm{O}_b}^{\mathrm{o}}(T) - RT\big(m_{\mathrm{X}}\ln x_{\mathrm{X}} + m_{\mathrm{Al}}\ln(1-x_{\mathrm{X}}) + \ln p_{\mathrm{O}_2}\big) \\ & - \frac{RT}{2\varepsilon_6}(m_{\mathrm{X}}\sigma_{\mathrm{X}} + m_{\mathrm{Al}}\sigma_{\mathrm{Al}}) - \frac{RTx_{\mathrm{XAl}}}{2\sigma_1}\left(\frac{\sigma_2}{\varepsilon_6} + \sigma_3\right)(m_{\mathrm{X}}(1-x_{\mathrm{X}}) - m_{\mathrm{Al}}x_{\mathrm{X}}) \\ & = \frac{2}{b}\Delta G_{\mathrm{f,\,Al}_{c_{\mathrm{Al}}}\mathrm{X}_{c_{\mathrm{X}}}\mathrm{O}_b}^{\mathrm{o}}(T) - RT\big(m_{\mathrm{X}}\ln x_{\mathrm{X}} + m_{\mathrm{Al}}\ln(1-x_{\mathrm{X}}) + \ln p_{\mathrm{O}_2}\big)\end{aligned}$$

$$-\frac{RT}{2\sigma_1\varepsilon_6}\left(\sigma_1(m_{\mathrm{X}}\sigma_{\mathrm{X}}+m_{\mathrm{Al}}\sigma_{\mathrm{Al}})+x_{\mathrm{XAl}}(\sigma_2+\sigma_3\varepsilon_6)(m_{\mathrm{X}}(1-x_{\mathrm{X}})-m_{\mathrm{Al}}x_{\mathrm{X}})\right) \quad (5.147)$$

Therefore, $\Delta G^{\mathrm{ox}}_{\mathrm{Al}_{c_{\mathrm{Al}}}\mathrm{X}_{c_{\mathrm{X}}}\mathrm{O}_b}$ is given as below (5.148), with the modified quasichemical model (MQM) term $\Delta G^{\mathrm{ox,MQM}}_{\mathrm{Al}_{c_{\mathrm{Al}}}\mathrm{X}_{c_{\mathrm{X}}}\mathrm{O}_b}$ also defined (5.149).

$$\Delta G^{\mathrm{ox}}_{\mathrm{Al}_{c_{\mathrm{Al}}}\mathrm{X}_{c_{\mathrm{X}}}\mathrm{O}_b}(x_{\mathrm{X}},T,p_{\mathrm{O}_2})$$

$$=\frac{2}{b}\Delta G^{\mathrm{o}}_{\mathrm{f,Al}_{c_{\mathrm{Al}}}\mathrm{X}_{c_{\mathrm{X}}}\mathrm{O}_b}(T)-RT\ln\left(x_{\mathrm{X}}^{m_{\mathrm{X}}}x_{\mathrm{Al}}^{m_{\mathrm{Al}}}p_{\mathrm{O}_2}\right)-\Delta G^{\mathrm{ox,MQM}}_{\mathrm{Al}_{c_{\mathrm{Al}}}\mathrm{X}_{c_{\mathrm{X}}}\mathrm{O}_b} \quad (5.148)$$

$$\Delta G^{\mathrm{ox,MQM}}_{\mathrm{Al}_{c_{\mathrm{Al}}}\mathrm{X}_{c_{\mathrm{X}}}\mathrm{O}_b}=\frac{RT}{2\sigma_1\varepsilon_6}\left(\sigma_1(m_{\mathrm{X}}\sigma_{\mathrm{X}}+m_{\mathrm{Al}}\sigma_{\mathrm{Al}})+x_{\mathrm{XAl}}(\sigma_2+\sigma_3\varepsilon_6)(m_{\mathrm{X}}(1-x_{\mathrm{X}})-m_{\mathrm{Al}}x_{\mathrm{X}})\right) \quad (5.149)$$

Terms in the above expressions are defined below, repeated here for convenience, noting that x_{XAl} is defined implicitly and must be evaluated numerically (5.137).

$$\beta_{\mathrm{XX}}=\frac{2}{Z^{\mathrm{X}}_{\mathrm{XX}}}\ (5.128)\quad \beta_{\mathrm{AlAl}}=\frac{2}{Z^{\mathrm{Al}}_{\mathrm{AlAl}}}\ (5.129)\quad \beta_{\mathrm{XAl}}=\frac{1}{Z^{\mathrm{X}}_{\mathrm{AlX}}}\ (5.130)\quad \beta_{\mathrm{AlX}}=\frac{1}{Z^{\mathrm{Al}}_{\mathrm{AlX}}}\ (5.131)$$

$$\varepsilon_1=(1-x_{\mathrm{X}})\beta_{\mathrm{XX}}+x_{\mathrm{X}}\beta_{\mathrm{AlAl}} \quad (5.122)$$

$$\varepsilon_2=\varepsilon_1x_{\mathrm{XX}}=(x_{\mathrm{X}}\beta_{\mathrm{AlX}}-(1-x_{\mathrm{X}})\beta_{\mathrm{XAl}})x_{\mathrm{XAl}}+x_{\mathrm{X}}\beta_{\mathrm{AlAl}}(1-x_{\mathrm{XAl}}) \quad (5.123)$$

$$\varepsilon_3=\varepsilon_1x_{\mathrm{AlAl}}=\left((1-x_{\mathrm{X}})\beta_{\mathrm{XAl}}-x_{\mathrm{X}}\beta_{\mathrm{AlX}}\right)x_{\mathrm{XAl}}+\beta_{\mathrm{XX}}(1-x_{\mathrm{X}})(1-x_{\mathrm{XAl}}) \quad (5.124)$$

$$\varepsilon_4=2\varepsilon_1y_{\mathrm{X}}=x_{\mathrm{XAl}}\left((2\beta_{\mathrm{AlX}}-\beta_{\mathrm{AlAl}})x_{\mathrm{X}}+(\beta_{\mathrm{XX}}-2\beta_{\mathrm{XAl}})(1-x_{\mathrm{X}})\right)+2x_{\mathrm{X}}\beta_{\mathrm{AlAl}} \quad (5.125)$$

$$\varepsilon_5=2\varepsilon_1y_{\mathrm{Al}}=x_{\mathrm{XAl}}\left((\beta_{\mathrm{AlAl}}-2\beta_{\mathrm{AlX}})x_{\mathrm{X}}+(2\beta_{\mathrm{XAl}}-\beta_{\mathrm{XX}})(1-x_{\mathrm{X}})\right)+2\beta_{\mathrm{XX}}(1-x_{\mathrm{X}}) \quad (5.126)$$

$$\varepsilon_6=\beta_{\mathrm{XX}}\beta_{\mathrm{AlAl}}+x_{\mathrm{XAl}}(\beta_{\mathrm{XX}}\beta_{\mathrm{AlX}}+\beta_{\mathrm{AlAl}}\beta_{\mathrm{XAl}}-\beta_{\mathrm{XX}}\beta_{\mathrm{AlAl}}) \quad (5.127)$$

$$\varepsilon_{\mathrm{X}}=\ln\varepsilon_1+\ln\varepsilon_2-2\ln\left(\frac{\varepsilon_4}{2}\right)=\ln\left(\frac{4\varepsilon_1\varepsilon_2}{\varepsilon_4^2}\right)=\ln\left(\frac{4\varepsilon_1^2x_{\mathrm{XX}}}{(2\varepsilon_1y_{\mathrm{X}})^2}\right)=\ln\left(\frac{x_{\mathrm{XX}}}{{y_{\mathrm{X}}}^2}\right) \quad (5.135)$$

$$\varepsilon_{\mathrm{Al}}=\ln\varepsilon_1+\ln\varepsilon_3-2\ln\left(\frac{\varepsilon_5}{2}\right)=\ln\left(\frac{4\varepsilon_1\varepsilon_3}{\varepsilon_5^2}\right)=\ln\left(\frac{4\varepsilon_1^2x_{\mathrm{AlAl}}}{(2\varepsilon_1y_{\mathrm{Al}})^2}\right)=\ln\left(\frac{x_{\mathrm{AlAl}}}{{y_{\mathrm{Al}}}^2}\right) \quad (5.136)$$

$$\sigma_{\mathrm{X}}=2\beta_{\mathrm{AlAl}}\varepsilon_{\mathrm{X}}+x_{\mathrm{XAl}}(2\beta_{\mathrm{AlX}}-\beta_{\mathrm{AlAl}})(\varepsilon_{\mathrm{X}}-\varepsilon_{\mathrm{Al}}) \quad (5.141)$$

$$\sigma_{\mathrm{Al}}=2\beta_{\mathrm{XX}}\varepsilon_{\mathrm{Al}}+x_{\mathrm{XAl}}(2\beta_{\mathrm{XAl}}-\beta_{\mathrm{XX}})(\varepsilon_{\mathrm{Al}}-\varepsilon_{\mathrm{X}}) \quad (5.142)$$

$$\begin{aligned}\sigma_1=RT\varepsilon_1\big(&\beta_{\mathrm{AlAl}}\beta_{\mathrm{XX}}x_{\mathrm{X}}(1-x_{\mathrm{X}})-(\varepsilon_2-x_{\mathrm{X}}\beta_{\mathrm{AlAl}})(\varepsilon_3-(1-x_{\mathrm{X}})\beta_{\mathrm{XX}})\big)\\&+\varepsilon_2\varepsilon_3\left((\varepsilon_2-x_{\mathrm{X}}\beta_{\mathrm{AlAl}})g^{10}_{\mathrm{XAl}}+(\varepsilon_3-(1-x_{\mathrm{X}})\beta_{\mathrm{XX}})g^{01}_{\mathrm{XAl}}\right)\end{aligned} \quad (5.143)$$

$$\sigma_2 = \left(\varepsilon_1(\varepsilon_2 - \varepsilon_3)RT + \varepsilon_2\varepsilon_3\left(g_{\mathrm{XAl}}^{10} - g_{\mathrm{XAl}}^{01}\right)\right)\left(\beta_{\mathrm{XX}}\varepsilon_{\mathrm{Al}}(2\beta_{\mathrm{AlX}} - \beta_{\mathrm{AlAl}})\right.$$
$$\left. + \beta_{\mathrm{AlAl}}\varepsilon_{\mathrm{X}}(2\beta_{\mathrm{XAl}} - \beta_{\mathrm{XX}})\right) \quad (5.144)$$

$$\sigma_3 = \varepsilon_2(\varepsilon_1 - \varepsilon_2)g_{\mathrm{XAl}}^{10} - \varepsilon_3(\varepsilon_1 - \varepsilon_3)g_{\mathrm{XAl}}^{01} \quad (5.145)$$

5.3. Methodology

5.3.1. Principles

In this chapter, ΔG^{ox} functions are used to predict which oxide is expected to form from the oxidation of an aluminium alloy melt. From the thermodynamics discussed above, it can be seen that ΔG^{ox} (for a chosen model) depends only on the free energy of formation of the oxide, $\Delta G_{\mathrm{f}}^{\mathrm{o}}$, the conditions of the environment (T, $p_{\mathrm{O_2}}$), and the composition of the melt x_i. In fact, when comparing relative stabilities of oxides, $p_{\mathrm{O_2}}$ is irrelevant (assuming $p_{\mathrm{O_2}}$ is greater than the dissociation pressure for all oxides in the system over the conditions of interest), since each ΔG^{ox} function only depends on $p_{\mathrm{O_2}}$ by the subtraction of a $RT \ln p_{\mathrm{O_2}}$ term, which is the same for all ΔG^{ox} functions. In any case, $p_{\mathrm{O_2}}$ is taken to be 0.21 atm for all calculations, to model oxidation in ambient conditions.

In an Al-X binary system, ΔG^{ox} depends on only two variables: the solute concentration x_i, and temperature, T. Binary systems are therefore visualised in two ways: firstly, $\Delta G^{\mathrm{ox}}(x_{\mathrm{X}})$ curves at selected temperatures T_i are plotted across the compositional range to demonstrate how the ΔG^{ox} curves change with temperature (Figure 5.2.a-c). Secondly, these $\Delta G^{\mathrm{ox}}(x_{\mathrm{X}})$ plots are used to map out, as a function of x_{X} and T, the oxide with the lowest ΔG^{ox}, and so determine which oxide is the most stable when in contact with the melt (Figure 5.2.d); these are termed 'oxide stability diagrams'.

This treatment is carried out first with the assumption of ideal mixing, then implementing non-ideal models to assess how the results change. Since elemental additions to aluminium melts can be as low as parts per million, a logarithmic compositional axis is used to capture the

behaviour of trace additions.

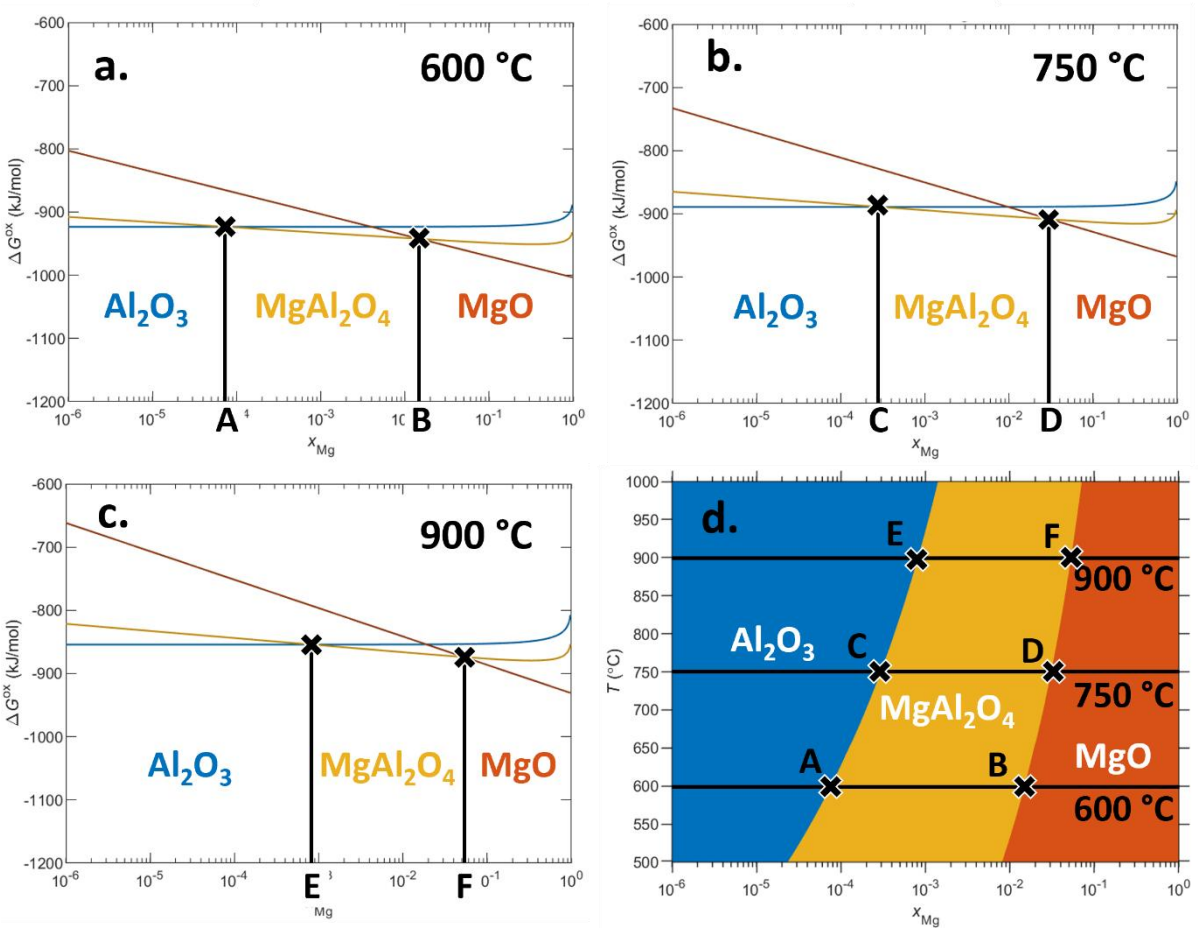


Figure 5.2. Visualisation of ΔG^{ox} for an Al-X binary system: using the Al-Mg binary system as an example, $\Delta G^{ox}(x_{Mg})$ plotted for all candidate oxides within the system (α-Al_2O_3, MgO, $MgAl_2O_4$) at selected temperatures of (a) 600 °C, (b) 750 °C, and (c) 900 °C. These plots can be used to make an oxide stability diagram (d), which charts the oxide with the lowest ΔG^{ox} as a function of composition x_{Mg} and temperature T. Points of correspondence between $\Delta G^{ox}(x_{Mg})$ plots and the x_{Mg}-T map are indicated by capital letters A-F.

In Al-X_1-X_2 ternary systems, there are two independent compositional variables, x_1 and x_2, so maps of the oxide with the lowest ΔG^{ox} are plotted as a function of the two compositional variables, x_1 and x_2, at selected temperatures. Like the binary systems, an ideal model is first assumed and then a Bragg-Williams mixing model is applied. Since the form of ΔG^{ox} for a binary system assuming the modified quasichemical model was found to be extremely cumbersome to derive (see Appendix A.4), a derivation for the equivalent expression for a ternary system, which will be somewhat more complex, was not attempted. In this study, all ternary systems are Al-Mg-X ternary systems: magnesium greatly enhances oxidation, a rise which can be suppressed by some ternary additions (Be, Ca, Sr) in quantities as low as ppm

additions, but other elements do not [5], so investigation of ternary Al-Mg-X systems using this method should help to establish whether the oxidation suppression can be plausibly explained by thermodynamic considerations.

One key caveat when interpreting these diagrams is that the treatment is only valid for fully mixed solutions. In ideal mixing, this validity applies to both solid and liquid solutions, but for non-ideal models, including the ones presented here, the parameters implemented here are for liquid solutions; the predictions are therefore only valid when the alloy is molten.

5.3.2. Data

Twenty-four Al-X binary systems and twelve ternary systems were chosen and analysed in this study (Table 5.8). For each system, a literature search was conducted to find all stable oxides, and thermodynamic data was acquired for each; a full list of compounds and data references can be found in Appendix B.2.

	Model	Ag	B	Be	Ca	Ce	Co	Cr	Cu	Fe	Gd	Ge	K
Binary Al-X	Ideal	X	X	X	X	X	X	X	X	X	X	X	X
	BW	X	X	X	X	X	X	X	X	X	X	X	X
	MQM				X	X					X		
Ternary Al-Mg-X	Ideal			X	X	X			X		X		
	BW			X	X	X			X		X		

	Model	La	Li	Mg	Mn	Na	Ni	Sc	Si	Sr	Ti	Zn	Zr
Binary Al-X	Ideal	X	X	X	X	X	X	X	X	X	X	X	X
	BW	X	X	X	X	X	X	X	X	X	X	X	X
	MQM	X	X	X		X		X	X	X			
Ternary Al-Mg-X	Ideal	X		n/a	X			X	X	X		X	
	BW	X		n/a	X				X	X		X	

Table 5.8. Systems investigated in this study, including choice of solution model.

All binary systems were assessed with ideal and Bragg-Williams mixing, and ten with the modified quasichemical model. Experimental data of oxidation products against melt composition and temperature were then compared to these diagrams to evaluate them. For Al-Mg-X ternary systems, eleven systems of interest were modelled with ideal mixing, and ten of those with Bragg-Williams (data for Al-Sc was not available). Like the binary systems,

experimental data of oxidation products against melt composition and temperature was compared to these ternary Al-Mg-X diagrams, but also the presence of oxidation protection.

Data for $\Delta G_{\mathrm{f}}^{\mathrm{o}}$ of candidate oxides was mostly determined via the Reaction module from the FactSage thermochemical software and databases [18], which allowed direct calculation of $\Delta G_{\mathrm{f}}^{\mathrm{o}}$ across the temperature range of interest. For some oxides, including all ternary Al-Mg-X oxides and some binary Al-X oxides, this method was not available and $\Delta G_{\mathrm{f}}^{\mathrm{o}}$ data was calculated using the 'G-method', where $G(T)$ data for a compound was combined with $\Delta G_{\mathrm{f}}^{\mathrm{o}}$ and $G(T)$ data from the unary Al and X oxides to produce $\Delta G_{\mathrm{f}}^{\mathrm{o}}$ functions (Table 5.9).

#	**Reaction**	$\Delta \boldsymbol{G}_{\mathbf{r}}$
R_1	$\mathrm{Al}_{\,(\mathrm{ss})} + \mathrm{Sc}_{\,(\mathrm{ss})} + \frac{3}{2}\mathrm{O}_{2\,(\mathrm{g})} \rightarrow \mathrm{ScAlO}_{3\,(\mathrm{s})}$	$\Delta G_{\mathrm{f,\,ScAlO_3}}^{\mathrm{o}}$
R_2	$\mathrm{Al}_{\,(\mathrm{ss})} + \frac{3}{4}\mathrm{O}_{2\,(\mathrm{g})} \rightarrow \frac{1}{2}\mathrm{Al_2O}_{3\,(\mathrm{s})}$	$\frac{1}{2}\Delta G_{\mathrm{f,\,Al_2O_3}}^{\mathrm{o}}$
R_3	$\mathrm{Sc}_{\,(\mathrm{ss})} + \frac{3}{4}\mathrm{O}_{2\,(\mathrm{g})} \rightarrow \frac{1}{2}\mathrm{Sc_2O}_{3\,(\mathrm{s})}$	$\frac{1}{2}\Delta G_{\mathrm{f,\,Sc_2O_3}}^{\mathrm{o}}$
R_4	$\frac{1}{2}\mathrm{Al_2O}_{3\,(\mathrm{s})} + \frac{1}{2}\mathrm{Sc_2O}_{3\,(\mathrm{s})} \rightarrow \mathrm{ScAlO}_{3\,(\mathrm{s})}$	$G_{\mathrm{ScAlO_3}} - \left(\frac{1}{2}G_{\mathrm{Al_2O_3}} + \frac{1}{2}G_{\mathrm{Sc_2O_3}}\right)$

Table 5.9. Summary of constituent reactions for determining $\Delta G_{\mathrm{f}}^{\mathrm{o}}$, using $\mathrm{ScAlO_3}$ as an example.

Since the first reaction R_1 can be expressed as the sum of the three beneath it (R_2, R_3, R_4), the Gibbs free energies of reaction ΔG_{r} can be equated similarly, since G is a state variable (5.150).

$$\Delta G_{\mathrm{r},1} = \Delta G_{\mathrm{r},2} + \Delta G_{\mathrm{r},3} + \Delta G_{\mathrm{r},4}$$

$$\therefore \Delta G_{\mathrm{f,\,ScAlO_3}}^{\mathrm{o}} = \frac{1}{2}\Delta G_{\mathrm{f,\,Al_2O_3}}^{\mathrm{o}} + \frac{1}{2}\Delta G_{\mathrm{f,\,Sc_2O_3}}^{\mathrm{o}} + G_{\mathrm{ScAlO_3}} - \left(\frac{1}{2}G_{\mathrm{Al_2O_3}} + \frac{1}{2}G_{\mathrm{Sc_2O_3}}\right) \qquad (5.150)$$

Parameters for non-ideal solutions (e.g. ${}^{i}L_{12}$ for Bragg-Williams, Z_{AlX}^{i} for MQM) were taken directly from thermodynamic optimisations; a list can be found in Appendix B.3.

5.4. Al-X binary systems

5.4.1. Ideal mixing

5.4.1.1. General mathematical features

In ideal mixing, $\Delta G^{\mathrm{ox}}(x_{\mathrm{X}})$ plots have consistent general features (Al-Mg is used as an example in Table 5.10 and Figure 5.3): for Al_2O_3 (5.151), the plot tends to a minimum value as $x_{\mathrm{X}} \to 0$, but as $x_{\mathrm{X}} \to 1$, $\Delta G^{\mathrm{ox}}(x_{\mathrm{X}}) \to +\infty$, since $\ln(1 - x_{\mathrm{X}}) \to -\infty$, producing an asymptote.

Species	$\boldsymbol{\Delta G_i^{\mathrm{ox}}(x_{\mathrm{X}}, p_{\mathrm{O_2}}, T)}$	**Eqn.**
Al_2O_3	$\frac{2}{3}\Delta G^{\mathrm{o}}_{\mathrm{f,\,Al_2O_3}}(T) - RT\ln p_{\mathrm{O_2}} - \frac{4}{3}RT\ln(1 - x_{\mathrm{X}})$	(5.151)
MgO	$\Delta G^{\mathrm{o}}_{\mathrm{f,MgO}}(T) - RT\ln p_{\mathrm{O_2}} - RT\ln x_{\mathrm{X}}$	(5.152)
$MgAl_2O_4$	$\frac{1}{2}\Delta G^{\mathrm{o}}_{\mathrm{f,MgAl_2O_4}}(T) - RT\ln p_{\mathrm{O_2}} - \frac{1}{2}RT\ln x_{\mathrm{X}} - RT\ln(1 - x_{\mathrm{X}})$	(5.153)

Table 5.10. ΔG^{ox} equations for the Al-Mg system, assuming ideal mixing.

The converse is true for the solute-containing unary oxide (e.g. MgO in Al-Mg): the plot tends to a minimum value as $x_{\mathrm{X}} \to 1$, but as $x_{\mathrm{X}} \to 0$, there is an asymptote: $\Delta G^{\mathrm{ox}} \to +\infty$, since $\ln x_{\mathrm{X}} \to -\infty$ (5.152). However, since this a logarithmic plot, this appears as a straight line (e.g. MgO, Figure 5.3). For binary Al-X oxides (e.g. $MgAl_2O_4$ in Al-Mg, Figure 5.3), asymptotes are seen at both $x_{\mathrm{X}} \to 0$ and $x_{\mathrm{X}} \to 1$, since both $\ln x_{\mathrm{X}}$ and $\ln(1 - x_{\mathrm{X}})$ terms are present (5.153). As temperature increases, each plot becomes less negative, since $\Delta G_{\mathrm{f}}^{\mathrm{o}}(T)$ becomes less negative, and the gradients become steeper, because the coefficient of the logarithm-based terms scale with temperature (Figure 5.3.b). This causes the crossovers between curves to shift to higher x_{X} (Figure 5.3.b).

The positions of the crossovers depend on the relative values of $\Delta G^{\mathrm{o}}_{\mathrm{f\,mol\,O_2}}$ across the oxides in the system. If the solute has a similar reactivity to aluminium, such as the Al-Mg system, then crossovers occur at values of x_{X} that are easily visualised in the compositional range (Figure

5.2). A full collection of $\Delta G_f^o(x_X)$ plots assuming ideal mixing at selected temperatures (500 – 1000 °C, in 100 °C intervals) can be found in Appendix B.4.1.

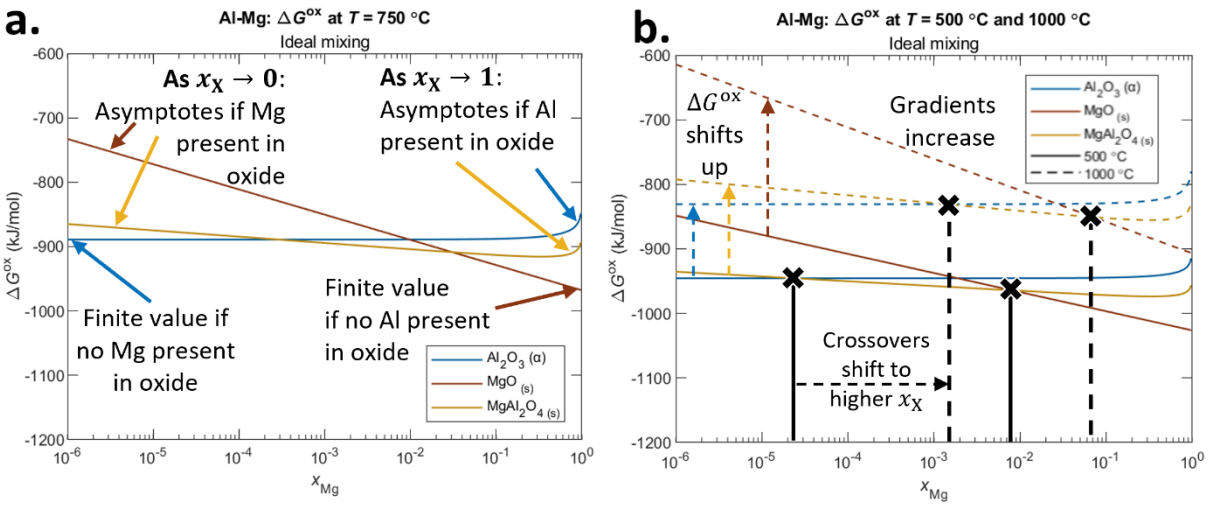


Figure 5.3. $\Delta G^{ox}(x_X)$ at selected T in the Al-Mg system, assuming ideal mixing: (a) Plots at 750 °C, showing general shapes of plots; (b) Effect of raising temperature (from 500 °C to 1000 °C), where plots increase in value and become steeper, causing crossovers to shift to higher solute concentrations.

However, if the solute is far less reactive than aluminium (such as iron, Figure 5.4.a), or there is a binary Al-X oxide which has a significantly lower $\Delta G^o_{f\,molO_2}$ value (such as $ScAlO_3$ in the Al-Sc system, Figure 5.4.b), then one species will dominate across the composition range. In the case of the less reactive solute, e.g. Al-Fe (Figure 5.4.a), there will be a crossover very close to $x_X = 1$ due to the asymptote in $\Delta G^{ox}_{Al_2O_3}(x_X)$, but this is not relevant in this study, which focuses on melts where aluminium is the dominant species. This is the result for many solutes studied here, namely Ag, B, Co, Cr, Cu, Fe, Ge, Mn, Ni, Si, and Zn; a full collection of oxide stability diagrams which implement ideal mixing can be found in Appendix B.5.1. When an oxide species is considered but does not appear on the oxide stability diagram, e.g. all Fe-containing oxides in Al-Fe (Figure 5.4), they are included in the key with a white box, to show that these phases have been incorporated into the analysis.

When the solute is more reactive, oxides other than Al_2O_3 are seen in the oxide stability diagrams (Figure 5.5). These elements are grouped as follows: Group I elements (Figure 5.5, row 1), Group II elements (Figure 5.5, row 2, and Al-Mg in Figure 5.2), lanthanides (Figure 5.5, row 3), and more reactive transition metals (Figure 5.5, row 4). Horizontal lines exist where

there is an allomorphic phase change (e.g. $AlLiO_2$ in Al-Li, or $SrAl_2O_4$ in Al-Sr), since the relative stability of the two allotropes depends only on temperature and not composition. Sudden gradient changes in the phase boundaries occur when one of the components undergoes a phase change e.g. potassium boiling at 759 °C in Al-K or aluminium melting at 660 °C, which present in all systems but more easily visible in the diagrams for Al-Gd, Al-La, and Al-Zr.

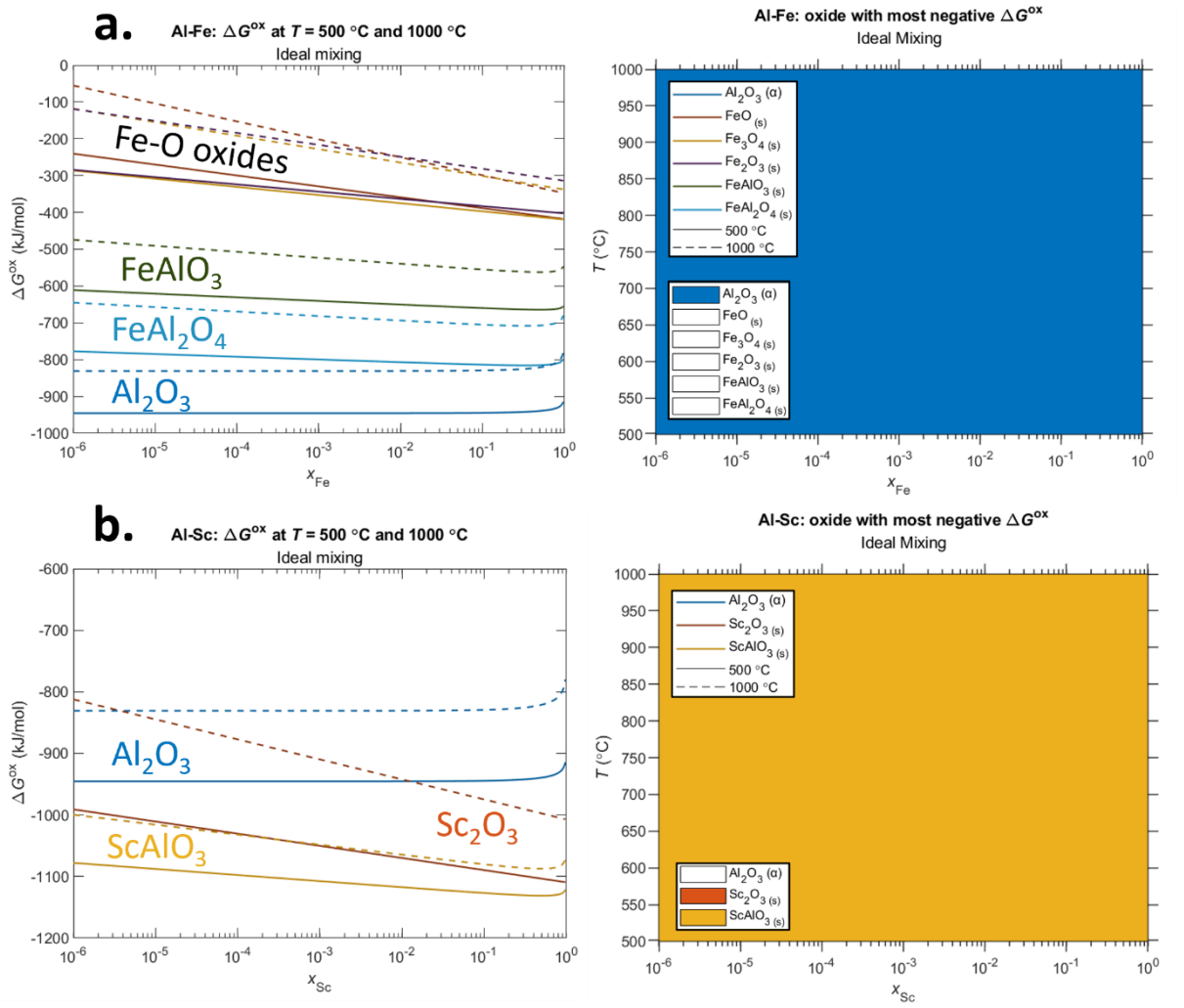


Figure 5.4. $\Delta G^{ox}(x_X)$ at 500 °C and 1000 °C and their resultant oxide stability diagrams for (a) Fe, where Al_2O_3 is the most stable oxide throughout the composition range and (b) Sc, where $ScAlO_3$ is the most stable. See Appendix B for larger versions: B.4.1.9&19 for $\Delta G^{ox}(x_X)$ plots and B.5.1.9&19 for oxide stability diagrams.

In these systems with more reactive solutes, the diagrams follow a trend: as x_X increases, or as temperature decreases, oxides with a higher proportion of the solute element become more stable (Figure 5.5). The compositional trend can be justified by considering the entropy change of removing the solute from the solution to form the compound: as the solute concentration increases, the entropic penalty for removing the solute decreases, so compounds containing

more of the solute element become more stable relative to those with less. A full collection of binary oxide stability diagrams assuming ideal mixing can be found in Appendix B.5.1.

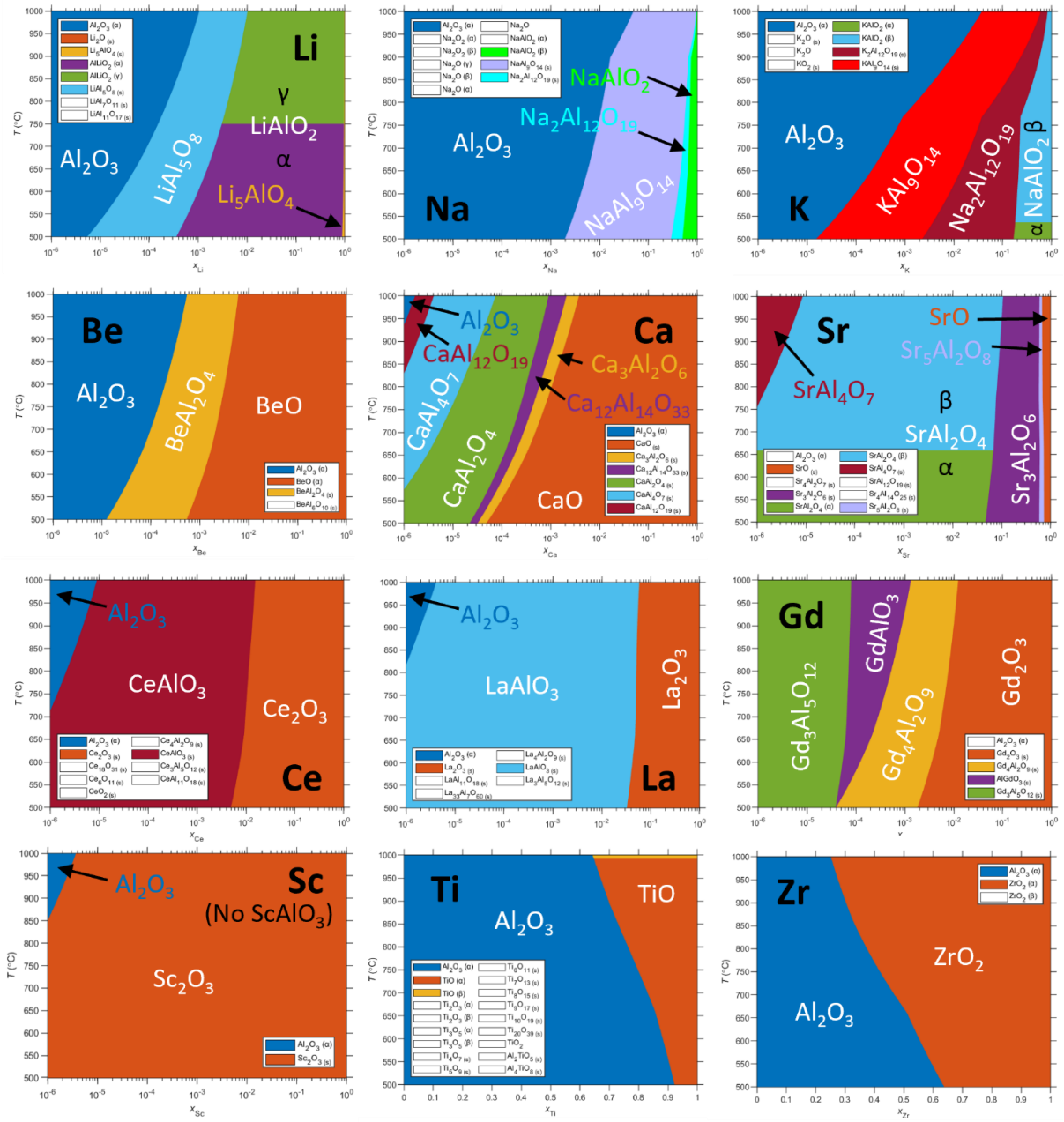


Figure 5.5. Oxide stability diagrams, assuming ideal mixing, for Al-X systems which display oxides other than Al_2O_3. These elements are from Group I (row 1), Group II (row 2), lanthanides (row 3), and more reactive transition elements (row 4). A linear scale is used for Ti and Zr for clarity of display. Al-Sc is displayed without $ScAlO_3$, in contrast to Figure 5.4, since the quality of the data for $ScAlO_3$ is not clear. See Appendix B.5.1 for larger versions of the oxide stability diagrams assuming ideal mixing.

As temperature increases, the entropic term in ΔG^{ox} becomes greater in magnitude, so any entropic penalty for removing the solute from the melt increases in magnitude, shifting the boundaries on the diagram to higher concentrations. Where there are no binary Al-X oxides, such as Al-Sc (if $ScAlO_3$ is not considered), Al-Ti (Table 5.11), and Al-Zr, the boundary

depends purely on how the $\Delta G_{\mathrm{f}}^{\mathrm{o}}$ values change with temperature (5.156).

Species	$\boldsymbol{\Delta G_i^{ox}(x_X, p_{O_2}, T)}$	**Eqn.**
Al_2O_3	$\frac{2}{3}\Delta G_{\mathrm{f,\,Al_2O_3}}^{\mathrm{o}}(T) - RT\ln p_{O_2} - \frac{4}{3}RT\ln(1-x_X)$	(5.154)
TiO	$\Delta G_{\mathrm{f,TiO}}^{\mathrm{o}}(T) - RT\ln p_{O_2} - RT\ln x_X$	(5.155)

Table 5.11. ΔG^{ox} equations for Al-Ti system (only Al_2O_3 and TiO).

$$\Delta G_{Al_2O_3}^{ox}(x_{X,eq}, p_{O_2}, T) = \Delta G_{TiO}^{ox}(x_{X,eq}, p_{O_2}, T)$$

$$\frac{2}{3}\Delta G_{\mathrm{f,\,Al_2O_3}}^{\mathrm{o}}(T) - RT\ln p_{O_2} - \frac{4}{3}RT\ln(1-x_{X,eq}) = \Delta G_{\mathrm{f,TiO}}^{\mathrm{o}}(T) - RT\ln p_{O_2} - RT\ln x_{X,eq}$$

$$\frac{(1-x_{X,eq})^{\frac{4}{3}}}{x_{X,eq}} = \exp\left(\frac{2\Delta G_{\mathrm{f,\,Al_2O_3}}^{\mathrm{o}}(T) - 3\Delta G_{\mathrm{f,TiO}}^{\mathrm{o}}(T)}{3RT}\right) \quad (5.156)$$

5.4.1.2. Categorisation of Al-X binary systems

The elements can be categorised by the features of their oxide stability diagrams (Figure 5.6):

- Less reactive (only Al_2O_3): Ag, B, Co, Cr, Cu, Fe, Ge, Mn, Ni, Si, and Zn
- More reactive (not only Al_2O_3):
    - Non-mixed (no binary Al-X oxides): Sc, Ti, Zr
    - Mixed (binary Al-X oxides present):
        - Group 1 (forms binary Al-X oxides with 1+ ions): Li, Na, K
        - Group 2 (forms binary Al-X oxides with 2+ ions): Be, Mg, Ca, Sr
        - Lanthanides (forms binary Al-X oxides with 3+ ions): Ce, La, Gd

Oxides within 'less reactive' systems contain neither unary nor binary oxides whose $\Delta G_{\mathrm{f,\,mol\,O_2}}^{\mathrm{o}\ 298\mathrm{K}}$ value is sufficiently close to that of Al_2O_3 for the entropic stabilisation effect of low solute concentration to make any oxide other than Al_2O_3 stable across the temperature-solute

range of interest (Figure 5.7).

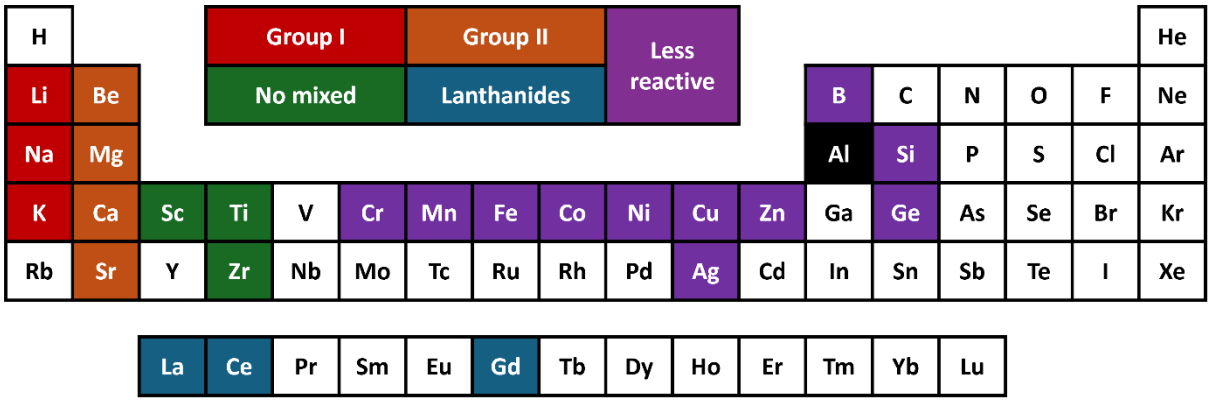


Figure 5.6. Categorisation of Al-X systems on the periodic table (first five rows plus lanthanides).

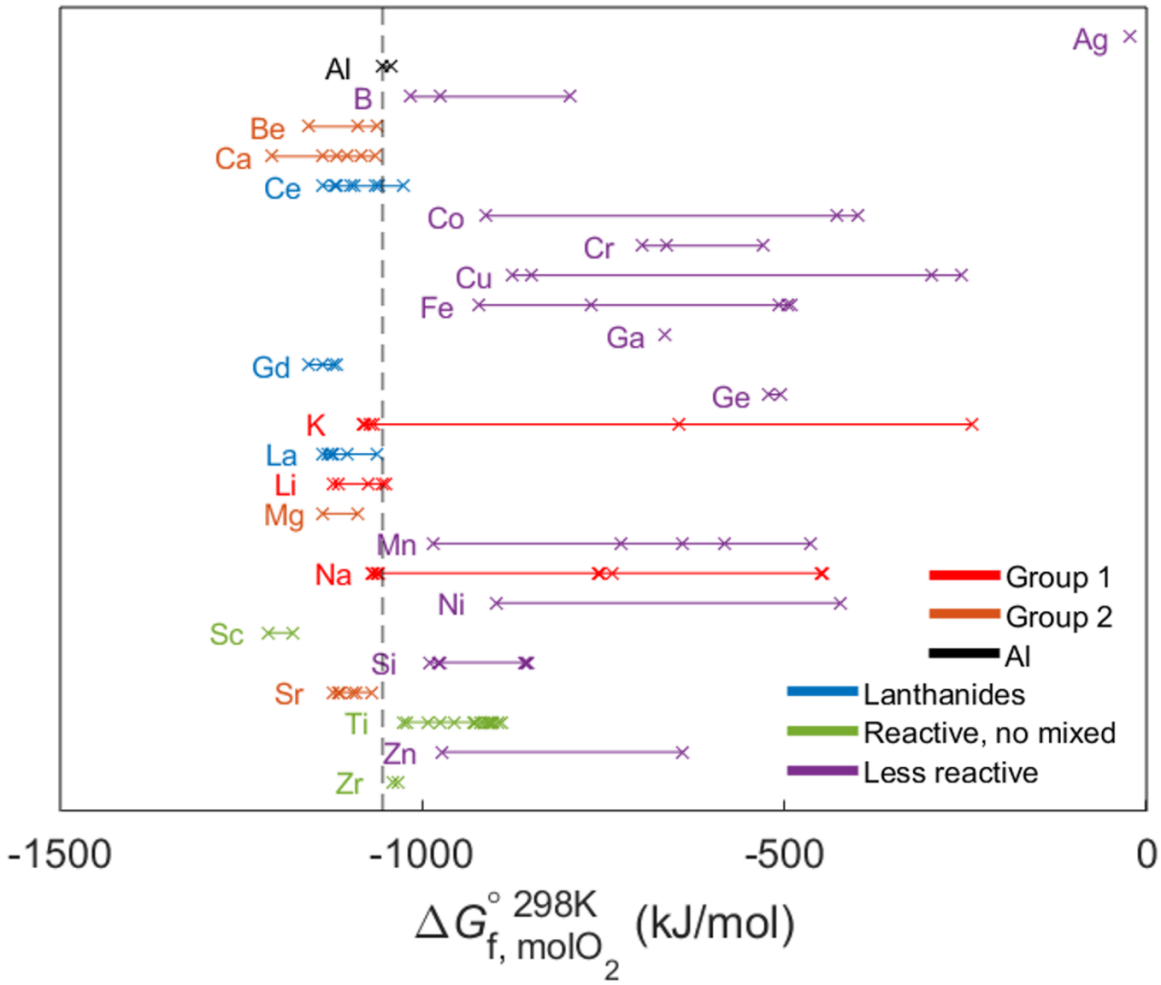


Figure 5.7. Plots of standard ΔG_f° at 298 K of (solid) oxides within Al-X systems

Conversely, more reactive systems have either unary solute oxides with a more negative $\Delta G^{o\ 298K}_{f,\ mol\ O_2}$ than Al_2O_3 (e.g. CaO, MgO) which also results in binary oxides having a more negative $\Delta G^{o\ 298K}_{f,\ mol\ O_2}$ than Al_2O_3 (e.g. $CaAl_2O_4$, $MgAl_2O_4$), or binary oxides which have a sufficiently high content of Al to have a more negative $\Delta G^{o\ 298K}_{f,\ mol\ O_2}$ than Al_2O_3 (e.g. KAl_9O_{14} or

$NaAl_9O_{14}$), despite the solute oxide having a significantly less negative $\Delta G^{\circ\,298K}_{f,\,mol\,O_2}$ than Al_2O_3 (e.g. K_2O or Na_2O). If there are no binary Al-X oxides, $\Delta G^{\circ\,298K}_{f,\,mol\,O_2}$ of the solute oxide must be close to that of Al_2O_3 (e.g. TiO, ZrO_2), or only Al_2O_3 will be present (e.g. Cr_2O_3, Ag_2O).

5.4.2. Bragg-Williams mixing

5.4.2.1. Mathematical features

In Bragg-Williams mixing, an extra enthalpy term is introduced (5.71) which scales with the concentrations of both components. The coefficient of this term, ω_{XAl}, is expanded in terms of Redlich-Kister polynomials (5.76), whose terms ${}^{i}L_{XAl}$ are fitted to data. This gives an extra term to ΔG^{ox}, termed $\Delta G^{ox,BWB}$ (5.80), plotted below for Al-Cu (Figure 5.8, Table 5.12).

Species	$\Delta G_i^{ox,BWB}$	**Eqn.**
Al_2O_3	$\Delta G^{ox,BWB}_{Al_2O_3} = \frac{4}{3}\sum_{i\geq 0} {}^{i}L_{CuAl}(2x_X - 1)^{i-1}\left[x_X^2\left(2x_X - 1 - 2i(1-x_X)\right)\right]$	(5.157)
CuO	$\Delta G^{ox,BWB}_{CuO} = 2\sum_{i\geq 0} {}^{i}L_{CuAl}(2x_X - 1)^{i-1}[(1-x_X)^2(2x_X - 1 + 2ix_X)]$	(5.158)
Cu_2O	$\Delta G^{ox,BWB}_{Cu_2O} = 4\sum_{i\geq 0} {}^{i}L_{CuAl}(2x_X - 1)^{i-1}[(1-x_X)^2(2x_X - 1 + 2ix_X)]$	(5.159)
$CuAlO_2$	$\Delta G^{ox,BWB}_{CuAlO_2} = \frac{3}{4}\Delta G^{ox,BWB}_{Al_2O_3} + \frac{1}{4}\Delta G^{ox,BWB}_{Cu_2O}$	(5.160)
$CuAl_2O_4$	$\Delta G^{ox,BWB}_{CuAl_2O_4} = \frac{3}{4}\Delta G^{ox,BWB}_{Al_2O_3} + \frac{1}{4}\Delta G^{ox,BWB}_{CuO}$	(5.161)

Table 5.12. Bragg-Williams contributions to ΔG^{ox}, $\Delta G_i^{ox,BWB}$, for each oxide considered in the Al-Cu system.

In all cases, $\Delta G^{ox,BWB}$ is zero at $x_X = 1$ for unary solute oxides (e.g. CuO, Cu_2O), and zero at $x_X = 0$ for Al_2O_3. This is because each term has a coefficient of either $m_X(1-x_X)^2$ or $m_{Al}{x_X}^2$: in unary solute oxides, $m_{Al} = 0$, so $\Delta G^{ox,BWB} = 0$ when $x_X = 0$, and in Al_2O_3, $m_X = 0$, so $\Delta G^{ox,BWB} = 0$ when $x_X = 1$.

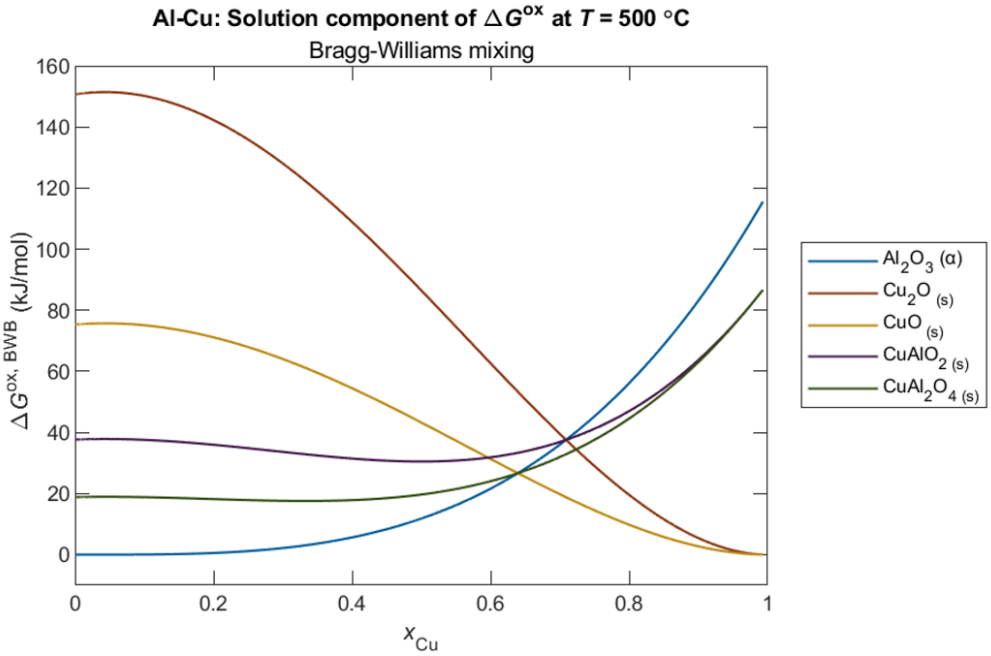


Figure 5.8. $\Delta G^{\mathrm{ox,BWB}}(x_{\mathrm{X}})$ for the Al-Cu system.

In addition, the $\Delta G^{\mathrm{ox,BWB}}$ term for a binary Al-X oxide $\Delta G^{\mathrm{ox,BWB}}_{\mathrm{Al}_{c_{\mathrm{Al}}}\mathrm{X}_{c_{\mathrm{X}}}\mathrm{O}_b}$ made up of α_{Al} formula units of Al_2O_3 and α_{X} formula units of the unary solute oxide with equivalent valency $\mathrm{X}_2\mathrm{O}_z$ (5.175) is the sum of the terms of the respective unary oxides, $\Delta G^{\mathrm{ox,BWB}}_{\mathrm{Al_2O_3}}$ and $\Delta G^{\mathrm{ox,BWB}}_{\mathrm{X_2O_z}}$, weighted by the proportion of oxygen atoms contributed to the formula unit of the binary oxide, which are $z\alpha_{\mathrm{X}}$ and $3\alpha_{\mathrm{Al}}$ for $\mathrm{X}_2\mathrm{O}_z$ and $\mathrm{Al}_2\mathrm{O}_3$, respectively (see Appendix A.5.1 for derivation).

$$\Delta G^{\mathrm{ox,BW}}_{\mathrm{Al}_{c_{\mathrm{Al}}}\mathrm{X}_{c_{\mathrm{X}}}\mathrm{O}_b} = \frac{z\alpha_{\mathrm{X}}}{z\alpha_{\mathrm{X}} + 3\alpha_{\mathrm{Al}}}\Delta G^{\mathrm{ox,BW}}_{\mathrm{X_2O_z}} + \frac{3\alpha_{\mathrm{Al}}}{z\alpha_{\mathrm{X}} + 3\alpha_{\mathrm{Al}}}\Delta G^{\mathrm{ox,BW}}_{\mathrm{Al_2O_3}} \tag{5.162}$$

For example, in the case of Al-Cu, $\Delta G^{\mathrm{ox,BWB}}_{\mathrm{CuAlO_2}}$ is the sum of $\Delta G^{\mathrm{ox,BWB}}_{\mathrm{Al_2O_3}}$ and $\Delta G^{\mathrm{ox,BWB}}_{\mathrm{Cu_2O}}$, weighted by the number of oxygen atoms contributed to the formula unit (3 and 1, respectively), and the same is true for $\Delta G^{\mathrm{ox,BWB}}_{\mathrm{CuAl_2O_4}}$, except it is a 3:1 weighting between $\Delta G^{\mathrm{ox,BWB}}_{\mathrm{Al_2O_3}}$ and $\Delta G^{\mathrm{ox,BWB}}_{\mathrm{CuO}}$, the $\Delta G^{\mathrm{ox,BWB}}$ term with copper oxide with the same valency (2+), which is CuO, instead of Cu_2O (1+). This demonstrates why the graphs intersect at two points $x_{\mathrm{Cu,eq}}$ (Figure 5.8), namely Al_2O_3, Cu_2O, and $CuAlO_2$ at $x_{\mathrm{Cu,eq1}} = 0.72$, and Al_2O_3, CuO, and $CuAl_2O_4$ at $x_{\mathrm{Cu,eq2}} = 0.65$: when the plots for alumina and a copper oxide intersect, e.g. Al_2O_3 and Cu_2O, the value for the corresponding binary oxide, e.g. $CuAlO_2$, is also equal (5.163).

$$\Delta G^{\mathrm{ox,BWB}}_{\mathrm{Al_2O_3}}(x_{\mathrm{Cu,eq1}}) = \Delta G^{\mathrm{ox,BWB}}_{\mathrm{Cu_2O}}(x_{\mathrm{Cu,eq1}})$$

$$\Delta G^{\mathrm{ox,BWB}}_{\mathrm{CuAlO_2}}(x_{\mathrm{Cu,eq1}}) = \frac{3}{4}\Delta G^{\mathrm{ox,BWB}}_{\mathrm{Al_2O_3}}(x_{\mathrm{Cu,eq1}}) + \frac{1}{4}\Delta G^{\mathrm{ox,BWB}}_{\mathrm{Cu_2O}}(x_{\mathrm{Cu,eq1}})$$

$$= \left(\frac{1}{4}+\frac{3}{4}\right)\Delta G^{\mathrm{ox,BWB}}_{\mathrm{Al_2O_3}}(x_{\mathrm{Cu,eq1}}) = \Delta G^{\mathrm{ox,BWB}}_{\mathrm{Al_2O_3}}(x_{\mathrm{Cu,eq1}})$$

$$\therefore \Delta G^{\mathrm{ox,BWB}}_{\mathrm{Al_2O_3}}(x_{\mathrm{Cu,eq1}}) = \Delta G^{\mathrm{ox,BWB}}_{\mathrm{Cu_2O}}(x_{\mathrm{Cu,eq1}}) = \Delta G^{\mathrm{ox,BWB}}_{\mathrm{CuAlO_2}}(x_{\mathrm{Cu,eq1}}) \quad (5.163)$$

The same can be shown for $CuAl_2O_4$ (5.164), which also demonstrates why the curves intersect only if the solute element present in the formula unit of each oxide has the same valency: for this to be true, the intersection of $\Delta G^{\mathrm{ox,BWB}}$ plots for the two solute oxides must coincide with each other and Al_2O_3. $\Delta G^{\mathrm{ox,BWB}}$ plots for solute oxides only coincide when the value of the summation term is zero, which generally only occurs at $x_{\mathrm{X}} = 0$.

$$\Delta G^{\mathrm{ox,BWB}}_{\mathrm{Al_2O_3}}(x_{\mathrm{Cu,eq2}}) = \Delta G^{\mathrm{ox,BWB}}_{\mathrm{CuO}}(x_{\mathrm{Cu,eq2}})$$

$$\Delta G^{\mathrm{ox,BWB}}_{\mathrm{CuAl_2O_4}}(x_{\mathrm{Cu,eq2}}) = \frac{3}{4}\Delta G^{\mathrm{ox,BWB}}_{\mathrm{Al_2O_3}}(x_{\mathrm{Cu,eq2}}) + \frac{1}{4}\Delta G^{\mathrm{ox,BWB}}_{\mathrm{CuO}}(x_{\mathrm{Cu,eq2}})$$

$$= \left(\frac{1}{4}+\frac{3}{4}\right)\Delta G^{\mathrm{ox,BWB}}_{\mathrm{Al_2O_3}}(x_{\mathrm{Cu,eq2}}) = \Delta G^{\mathrm{ox,BWB}}_{\mathrm{Al_2O_3}}(x_{\mathrm{Cu,eq2}})$$

$$\therefore \Delta G^{\mathrm{ox,BWB}}_{\mathrm{Al_2O_3}}(x_{\mathrm{Cu,eq2}}) = \Delta G^{\mathrm{ox,BWB}}_{\mathrm{CuO}}(x_{\mathrm{Cu,eq2}}) = \Delta G^{\mathrm{ox,BWB}}_{\mathrm{CuAl_2O_4}}(x_{\mathrm{Cu,eq2}}) \quad (5.164)$$

The $\Delta G^{\mathrm{ox,BWB}}$ term is roughly the sum of two parabolae, one centred at $x_{\mathrm{X}} = 0$ which scales with m_{Al}, and another centred at $x_{\mathrm{X}} = 1$ which scales with m_{X}. This is strictly true when only zeroth-order ${}^{i}L_{\mathrm{CuAl}}$ terms are present, but most systems are optimised such that the contribution from successive terms diminishes, so the contributions are largely encapsulated by the sign of ${}^{0}L_{\mathrm{XAl}}$. A negative ${}^{0}L_{\mathrm{XAl}}$ value at a given temperature indicates that the enthalpy of solution is negative (Bragg-Williams mixing reduces to a regular solution if only the zeroth order term is present), such that mixing is always favourable, and a positive ${}^{0}L_{\mathrm{XAl}}$ value indicates a positive enthalpy of solution. As temperature changes, the values of ${}^{i}L_{\mathrm{XAl}}$ change slightly, depending upon the temperature coefficients in each Al-X system (Appendix B.3.1).

5.4.2.2. Effect on oxide stability diagrams

The effect of the implementation of Bragg-Williams mixing on the oxide stability diagrams (Figure 5.9) is a shift in boundaries. A full collection of $\Delta G^{\mathrm{ox}}(x_{\mathrm{X}})$ plots and oxide stability diagrams can be found in Appendix B (B.4.2 and B.5.2, respectively).

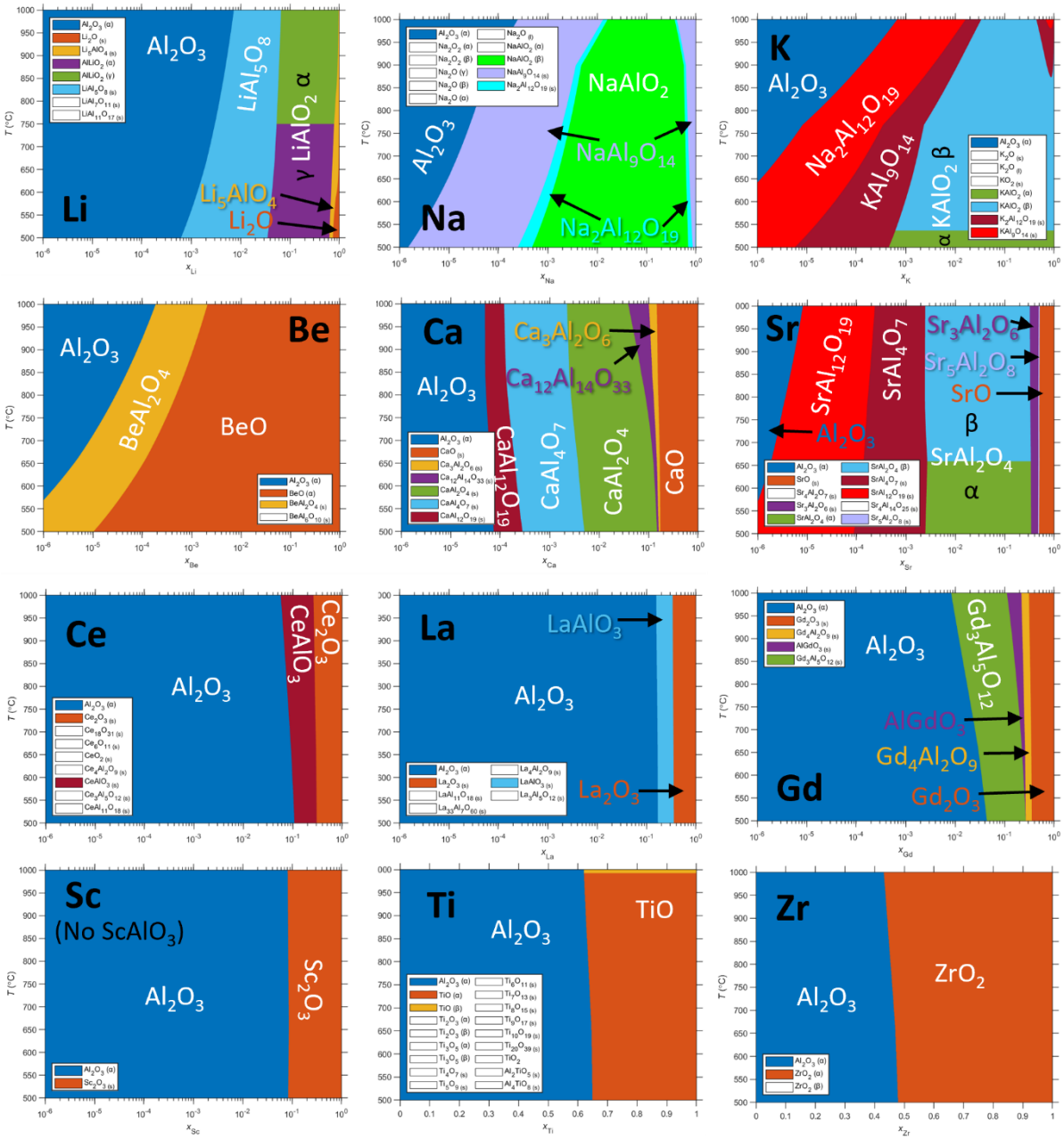


Figure 5.9. Oxide stability diagrams of Al-X systems with more reactive solutes, assuming Bragg-Williams mixing, sorted into rows by group: group 1, group 2, lanthanides, and more reactive transition elements. See Appendix B.5.2 for larger versions of the oxide stability diagrams.

'Less Reactive' elements (Figure 5.6), whose stability diagrams only contain Al_2O_3 in ideal mixing are not changed. The Bragg-Williams term is simply not large enough to overcome the

differences in ΔG^{ox} from ideal mixing due to the large difference in $\Delta G^{\mathrm{o}}_{\mathrm{f,\,mol\,O_2}}$ between Al_2O_3 and any solute-containing oxide in the Al-X system. In more reactive systems, the change manifests as a shift in the boundaries between oxides. In most cases, phase boundaries shift towards $x_{\mathrm{X}} = 0.5$, with the effect being stronger at lower temperatures (Figure 5.10).

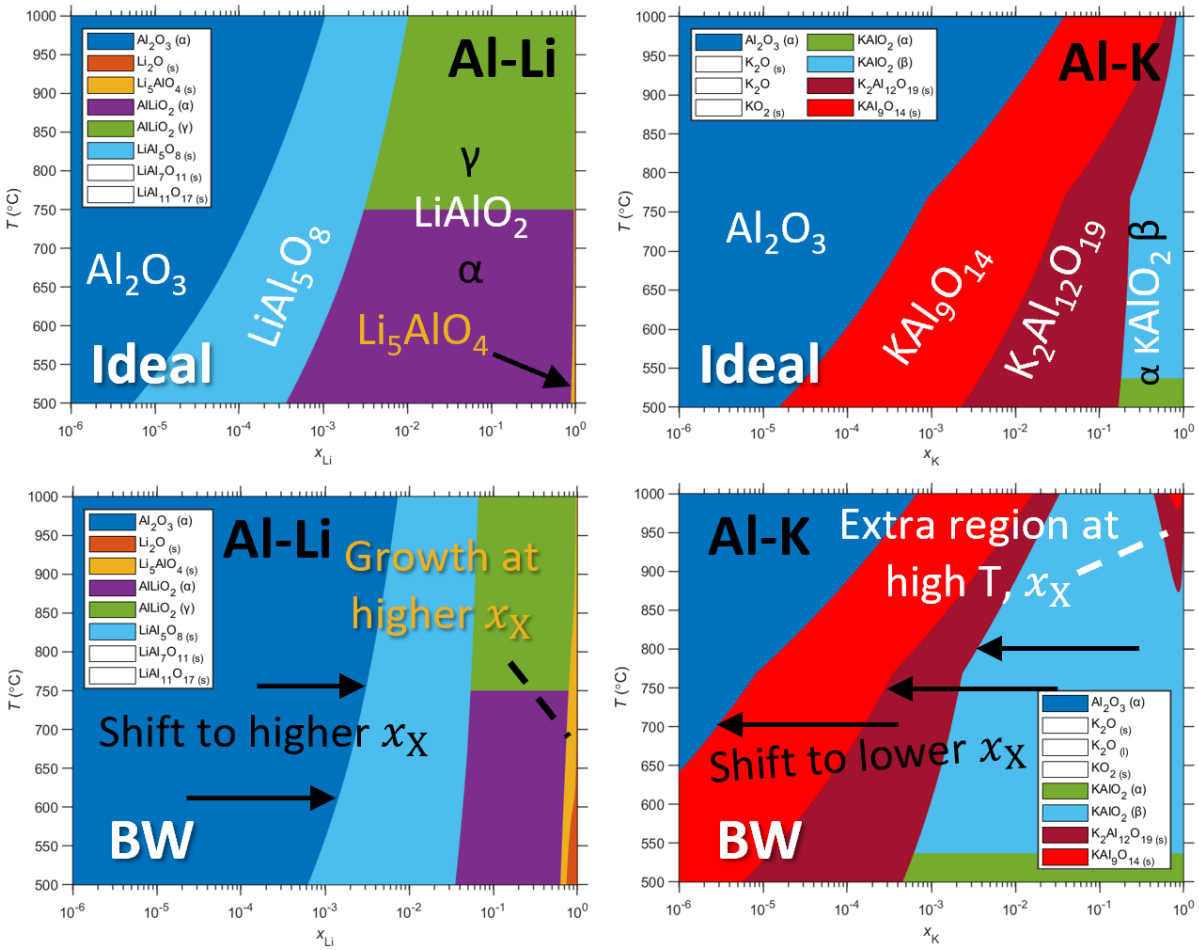


Figure 5.10. Effect of incorporation of $\Delta G^{\mathrm{ox,BWB}}$ on oxide stability diagrams. In some systems (e.g. Al-Li), boundaries at low x_{X} shift to higher x_{X} and boundaries at high x_{X} shift to lower x_{X}, but the converse is true in some other systems e.g. Al-K. In some systems, extra regions appear at higher x_{X} and temperature of phases found at lower x_{X}, such as $K_2Al_{12}O_{19}$ and KAl_9O_{14} in the Al-K system. See Appendix B for larger versions (B.5.1.12&14 for ideal, B.5.2.12&14 for Bragg-Williams).

The exceptions to this are beryllium, potassium, and sodium, whose boundaries shift away from $x_{\mathrm{X}} = 0.5$, with a stronger effect at lower temperatures. This can be explained by considering the limit of $\Delta G^{\mathrm{ox,BWB}}$ at low x_{X}, which is proportional to m_{X} (5.165). The sign of $\Delta G^{\mathrm{ox,BWB}}$ is determined by the sign of the alternating sum $L_{\mathrm{XAl,alt}}$ (5.166).

$$\Delta G^{\mathrm{ox,BWB}} = \sum_{i\geq 0} {}^{i}L_{\mathrm{XAl}}(x_{\mathrm{X}} - x_{\mathrm{Al}})^{i-1}[m_{\mathrm{X}}x_{\mathrm{Al}}{}^{2}(x_{\mathrm{X}} - x_{\mathrm{Al}} + 2ix_{\mathrm{X}}) + m_{\mathrm{Al}}x_{\mathrm{X}}^{2}(x_{\mathrm{X}} - x_{\mathrm{Al}} - 2ix_{\mathrm{Al}})]$$

$$\Delta G^{\mathrm{ox,BWB}}\left(x_{\mathrm{X,low}}\right) \approx \sum_{i\geq 0} {}^{i}L_{\mathrm{XAl}}(x_{\mathrm{X}}-1)^{i-1}\left[m_{\mathrm{X}}\left((1+2i)x_{\mathrm{X}}-1\right)+m_{\mathrm{Al}}x_{\mathrm{X}}^{2}\left(x_{\mathrm{X}}-(1+2i)\right)\right]$$

$$\approx m_{\mathrm{X}}\sum_{i\geq 0} {}^{i}L_{\mathrm{XAl}}(x_{\mathrm{X}}-1)^{i-1}[(1+2i)x_{\mathrm{X}}-1]$$

$$\approx m_{\mathrm{X}}({}^{0}L_{\mathrm{XAl}}-{}^{1}L_{\mathrm{XAl}}(1-3x_{\mathrm{X}})+{}^{2}L_{\mathrm{XAl}}(1-x_{\mathrm{X}})(1-5x_{\mathrm{X}})+\cdots)$$

$$\approx m_{\mathrm{X}}\sum_{i\geq 0} {}^{i}L_{\mathrm{XAl}}(-1)^{i}=m_{\mathrm{X}}({}^{0}L_{\mathrm{XAl}}-{}^{1}L_{\mathrm{XAl}}+{}^{2}L_{\mathrm{XAl}}-{}^{3}L_{\mathrm{XAl}}+\cdots)=m_{\mathrm{X}}L_{\mathrm{XAl,alt}} \tag{5.165}$$

$$L_{\mathrm{XAl,alt}}=\sum_{i\geq 0} {}^{i}L_{\mathrm{XAl}}(-1)^{i}={}^{0}L_{\mathrm{XAl}}-{}^{1}L_{\mathrm{XAl}}+{}^{2}L_{\mathrm{XAl}}-{}^{3}L_{\mathrm{XAl}}+\cdots \tag{5.166}$$

If $L_{\mathrm{XAl,alt}}$ is negative, then $\Delta G^{\mathrm{ox}}\left(x_{\mathrm{X,low}}\right)$ increases, but due to the proportionality with m_{X}, the higher the value of m_{X}, the more $\Delta G^{\mathrm{ox}}\left(x_{\mathrm{X,low}}\right)$ increases. Therefore, boundaries will shift to higher x_{X} as oxides containing less solute become more favourable.

X	Shift to $x_{\mathrm{X}}=0.5$?	$L_{\mathrm{XAl,alt}}$		First term		First two terms		First three terms	
		500 °C	1000 °C	500 °C	1000 °C	500 °C	1000 °C	500 °C	1000 °C
Be	No	45147	31147	35291	21291	45147	31147	45147	31147
Ca	Yes	-28691	-17560	-64041	-46294	-26584	-24934	-8043	-5276
Ce	Yes	-75241	-57128	-100587	-81325	-69176	-53095	-75241	-57128
Gd	Yes	-80615	-52435	-126018	-99838	-102228	-76048	-80615	-52435
K	No	38349	42703	38349	42703	38349	42703	38349	42703
La	Yes	-82631	-72581	-144905	-144146	-82631	-72581	-82631	-72581
Li	Yes	-6340	1605	-29583	-20583	-17515	-9570	-6340	1605
Mg	Yes	-2952	2831	-5377	-1094	-4952	831	-2952	2831
Na	No	46113	56113	46113	56113	46113	56113	46113	56113
Sc	Yes	-83981	-99059	-128965	-127145	-115702	-118321	-83981	-99059
Sr	Yes	-23856	-18352	-56526	-44683	-31346	-23777	-23856	-18352
Ti	Yes	-101824	-88572	-86129	-69029	-101824	-88572	-101824	-88572

Table 5.13. L_{alt} and its partial sums for reactive Al-X systems, compared to shifts in phase boundaries seen in oxide stability diagrams when Bragg-Williams mixing is considered (either to or away from $x_{\mathrm{X}}=0.5$). Positive values are shaded red, as well as whether a system has boundary shifts away from $x_{\mathrm{X}}=0.5$.

The converse is true if $L_{\mathrm{XAl,alt}}$ is positive: $\Delta G^{\mathrm{ox}}\left(x_{\mathrm{X,low}}\right)$ decreases due to the $\Delta G^{\mathrm{ox,BWB}}$ term, the magnitude scaling with m_{X}, so boundaries shift to lower x_{X} as oxides containing more solute become more favourable. Physically, this term $L_{\mathrm{XAl,alt}}$ is analogous to the enthalpy of solution: if the enthalpy of solution is positive, then unmixing is more favourable (compared to an ideal solution). This means that solutes more readily come out of solution to form solute-

containing oxides, leading to boundaries shifting to lower x_X, since less solute is required for a solute-containing oxide to form. Conversely, a negative enthalpy of solution means unmixing is less favourable, therefore oxidation favours oxides with less solute, shifting boundaries to higher x_X. Comparing $L_{XAl,alt}$ values for reactive Al-X systems to the trends seen in the oxide stability diagrams (Table 5.13), a direct correlation between the sign of the $L_{XAl,alt}$ value and the shift in boundaries seen in the oxide stability diagrams is seen (see Appendix B.5.2).

At 500 °C, the pattern is perfect, but at 1000 °C, there are sign changes in Li and Mg: this can be attributed to the breakdown of the assumptions made for low x_X. As x_X increases, the contributions from higher order ${}^{i}L_{XAl}$ terms diminish, such that the lower order terms dominate. Taking only the first term ${}^{0}L_{XAl}$, the correlation is much improved, and it remains for Li when the second term is added.

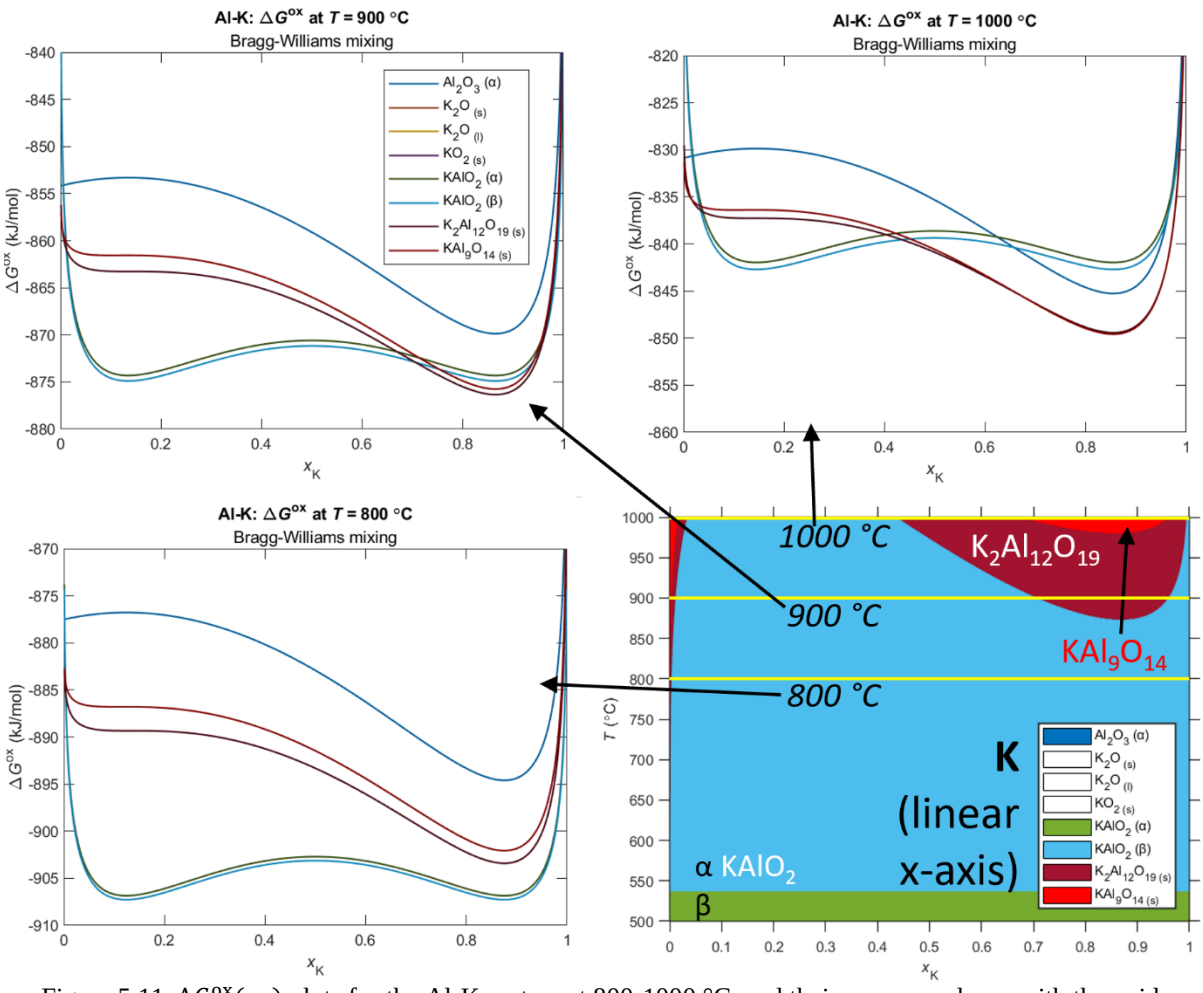


Figure 5.11. $\Delta G^{ox}(x_X)$ plots for the Al-K system at 800-1000 °C, and their correspondence with the oxide stability diagram, assuming Bragg-Williams mixing.

By symmetry, this analysis also applies to the limit of high x_{X}, which explains why boundaries at high x_{X}, such as $AlLiO_2$ and Li_5AlO_4, shift to lower x_{X} whilst the boundaries at lower x_{X} shift to higher x_{X}. The magnitudes of the boundary shifts diminish as temperature increases, which can be attributed to the growing magnitude of the ideal entropy term, which masks the effect of incorporating $\Delta G^{\mathrm{ox,BWB}}$. The extra regions which appear on Al-K and Al-Na can be more easily visualised using plots with a linear x_{X} axis, showing that these regions appear due to the $\Delta G^{\mathrm{ox}}(x_{\mathrm{X}})$ curves crossing over as temperature increases (Figure 5.11).

5.4.3. Modified quasichemical model

5.4.3.1. Mathematical features

In the modified quasichemical model, two terms are added in comparison to ideal mixing: an enthalpy term which roughly scales with the A-B bond fraction x_{AB}, and an extra entropy term to model ordering between second-nearest neighbours. This extra contribution, $\Delta G^{\mathrm{ox,MQM}}$, has distinct features: firstly, its value is zero at $x_{\mathrm{X}} = 0$ for Al_2O_3, and zero at $x_{\mathrm{X}} = 1$ for any unary solute oxide. In the case of an unary solute oxide (5.167), $m_{\mathrm{Al}} = 0$, and at $x_{\mathrm{X}} = 1$, $x_{\mathrm{XAl}} = 0$, and $x_{\mathrm{XX}} = y_{\mathrm{X}} = 1$, resulting in $\Delta G^{\mathrm{ox,MQM}}_{\mathrm{X}_{c_{\mathrm{X}}}\mathrm{O}_b}$ being equal to zero (5.168).

$$\Delta G^{\mathrm{ox,MQM}}_{\mathrm{X}_{c_{\mathrm{X}}}\mathrm{O}_b} = m_{\mathrm{X}} \frac{RT}{2\sigma_1\varepsilon_6}\left(\sigma_1\sigma_{\mathrm{X}} + x_{\mathrm{XAl}}(\sigma_2 + \sigma_3\varepsilon_6)(1 - x_{\mathrm{X}})\right) \tag{5.167}$$

$$\Delta G^{\mathrm{ox,MQM}}_{\mathrm{X}_{c_{\mathrm{X}}}\mathrm{O}_b}(x_{\mathrm{X}} = 1) = m_{\mathrm{X}} \frac{RT}{2\sigma_1\varepsilon_6}\sigma_1\sigma_{\mathrm{X}}$$

$$= \frac{RTm_{\mathrm{X}}}{2\varepsilon_6}\left(2\beta_{\mathrm{AlAl}}\varepsilon_{\mathrm{X}} + x_{\mathrm{XAl}}(2\beta_{\mathrm{AlX}} - \beta_{\mathrm{AlAl}})(\varepsilon_{\mathrm{X}} - \varepsilon_{\mathrm{Al}})\right) = \frac{RTm_{\mathrm{X}}}{2\varepsilon_6}(2\beta_{\mathrm{AlAl}}\varepsilon_{\mathrm{X}})$$

$$= \frac{RTm_{\mathrm{X}}\beta_{\mathrm{AlAl}}}{\varepsilon_6}\varepsilon_{\mathrm{X}} = \frac{RTm_{\mathrm{X}}\beta_{\mathrm{AlAl}}}{\varepsilon_6}\ln\left(\frac{x_{\mathrm{XX}}}{{y_{\mathrm{X}}}^2}\right) = \frac{RTm_{\mathrm{X}}\beta_{\mathrm{AlAl}}}{\varepsilon_6}\ln\left(\frac{1}{1}\right) = 0 \tag{5.168}$$

Equivalently, for Al_2O_3, $m_{\mathrm{X}} = 0$ (5.169), and at $x_{\mathrm{X}} = 0$, $x_{\mathrm{XAl}} = 0$ and $x_{\mathrm{AlAl}} = y_{\mathrm{Al}} = 1$, resulting in $\Delta G^{\mathrm{ox,MQM}}_{\mathrm{Al_2O_3}}$ being equal to zero (5.170). Physically, this can be justified as when

there is no second component, this is simply a case of a pure substance oxidising to form its unary oxide, so the thermodynamics of mixing with a second component is irrelevant.

$$\Delta G^{\mathrm{ox,MQM}}_{\mathrm{Al_2O_3}} = \frac{RTm_{\mathrm{Al}}}{2\sigma_1\varepsilon_6}\left(\sigma_1(\sigma_{\mathrm{Al}}) - x_{\mathrm{X}}x_{\mathrm{XAl}}(\sigma_2 + \sigma_3\varepsilon_6)\right) \tag{5.169}$$

$$\Delta G^{\mathrm{ox,MQM}}_{\mathrm{Al_2O_3}}(x_{\mathrm{X}} = 0) = \frac{RTm_{\mathrm{Al}}}{2\varepsilon_6}\sigma_{\mathrm{Al}}$$

$$= \frac{RTm_{\mathrm{Al}}}{2\varepsilon_6}\left(2\beta_{\mathrm{XX}}\varepsilon_{\mathrm{Al}} + x_{\mathrm{XAl}}(2\beta_{\mathrm{XAl}} - \beta_{\mathrm{XX}})(\varepsilon_{\mathrm{Al}} - \varepsilon_{\mathrm{X}})\right) = \frac{RTm_{\mathrm{Al}}}{2\varepsilon_6}(2\beta_{\mathrm{XX}}\varepsilon_{\mathrm{Al}})$$

$$= \frac{RTm_{\mathrm{Al}}\beta_{\mathrm{XX}}}{2\varepsilon_6}\varepsilon_{\mathrm{Al}} = \frac{RTm_{\mathrm{Al}}\beta_{\mathrm{XX}}}{2\varepsilon_6}\ln\left(\frac{x_{\mathrm{AlAl}}}{{y_{\mathrm{Al}}}^2}\right) = \frac{RTm_{\mathrm{Al}}\beta_{\mathrm{XX}}}{\varepsilon_6}\ln\left(\frac{1}{1}\right) = 0 \tag{5.170}$$

Secondly, in the other limit, e.g. as $x_{\mathrm{X}} \to 0$ for an unary solute oxide, $\Delta G^{\mathrm{ox,MQM}}$ has an asymptote: in this limit, $\Delta G^{\mathrm{ox,MQM}}_{\mathrm{X}_{c_{\mathrm{X}}}\mathrm{O}_b}$ is proportional to both m_{X} and $\ln(x_{\mathrm{X}})$ (5.171), where the constant of proportionality δ_{X} (5.172) is positive (see Appendix A.5.2 for derivation of this limit and proof that $\delta_{\mathrm{X}} > 0$).

$$\Delta G^{\mathrm{ox,MQM}}_{\mathrm{X}_{c_{\mathrm{X}}}\mathrm{O}_b}(x_{\mathrm{X,low}}) \approx \delta_{\mathrm{X}} m_{\mathrm{X}} \ln x_{\mathrm{X}} \tag{5.171}$$

$$\delta_{\mathrm{X}} = \frac{2RT}{\beta_{\mathrm{XX}}} \times \frac{\beta_{\mathrm{XX}} + 4\exp\left(-\frac{g^{01}_{\mathrm{XAl}} + \Delta g^{0}_{\mathrm{XAl}}}{RT}\right)\left(\beta_{\mathrm{XX}}\beta_{\mathrm{AlAl}} + \beta_{\mathrm{XAl}}(1 - 2\beta_{\mathrm{AlAl}})\right)}{\left(\beta_{\mathrm{XX}} + \beta_{\mathrm{XAl}}4\exp\left(-\frac{g^{01}_{\mathrm{XAl}} + \Delta g^{0}_{\mathrm{XAl}}}{RT}\right)\right)} \tag{5.172}$$

This proportionality with m_{X} and $\ln(x_{\mathrm{X}})$ can be seen in $\Delta G^{\mathrm{ox,MQM}}(x_{\mathrm{X}})$ plots with a logarithmic compositional axis, where plots tend to a straight line as $x_{\mathrm{X}} \to 0$, with gradient increasing with m_{X} and T (Figure 5.12): m_{X} is highest for the unary solute (La_2O_3 in the featured Al-La system) and lowest ($m_{\mathrm{X}} = 0$) for alumina. By symmetry, in the limit $x_{\mathrm{X}} \to 1$, $\Delta G^{\mathrm{ox,MQM}}_{\mathrm{Al_2O_3}}$ has an asymptote, since the limit is proportional to both m_{Al} and $\ln(1 - x_{\mathrm{X}})$ (5.173), with the proportionality constant δ_{Al} being positive since $Z^{\mathrm{X}}_{\mathrm{XX}} = 6$ for all systems of interest (5.174).

$$\Delta G^{\mathrm{ox,MQM}}_{\mathrm{Al_2O_3}}(x_{\mathrm{X,low}}) \approx \delta_{\mathrm{Al}} m_{\mathrm{Al}} \ln(1 - x_{\mathrm{X}}) \tag{5.173}$$

$$\delta_{\mathrm{Al}} = \frac{2RT}{\beta_{\mathrm{AlAl}}} \times \frac{\beta_{\mathrm{AlAl}} + 4\exp\left(-\frac{g^{10}_{\mathrm{XAl}} + \Delta g^{0}_{\mathrm{XAl}}}{RT}\right)\left(\beta_{\mathrm{XX}}\beta_{\mathrm{AlAl}} + \beta_{\mathrm{AlX}}(1 - 2\beta_{\mathrm{XX}})\right)}{\left(\beta_{\mathrm{AlAl}} + \beta_{\mathrm{AlX}} 4\exp\left(-\frac{g^{10}_{\mathrm{XAl}} + \Delta g^{0}_{\mathrm{XAl}}}{RT}\right)\right)} \tag{5.174}$$

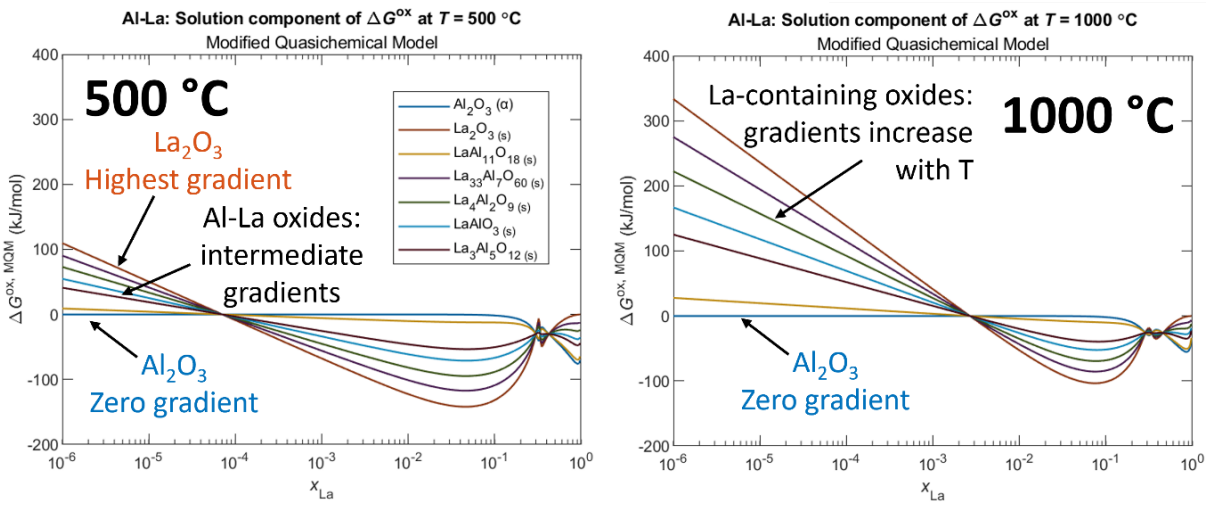


Figure 5.12. $\Delta G^{\mathrm{ox,MQM}}$ plots at 500 °C and 1000 °C for the Al-La system, showing linearity as $x_{\mathrm{X}} \to 0$, gradients scaling with m_{X} and increasing with temperature.

Thirdly, like the Bragg-Williams model, the term for a binary Al-X oxide $\Delta G^{\mathrm{ox,MQM}}_{\mathrm{Al}_{c_{\mathrm{Al}}}\mathrm{X}_{c_{\mathrm{X}}}\mathrm{O}_b}$ made up α_{Al} formula units of Al_2O_3 and α_{X} formula units of the solute oxide with equivalent valency X_2O_z, is the sum of the terms of the respective unary oxides, $\Delta G^{\mathrm{ox,MQM}}_{\mathrm{Al_2O_3}}$ and $\Delta G^{\mathrm{ox,MQM}}_{\mathrm{X_2O_z}}$, weighted by the proportion of oxygen atoms contributed to the formula unit of the binary oxide (5.175), $z\alpha_{\mathrm{X}}$ and $3\alpha_{\mathrm{Al}}$ for X_2O_z and Al_2O_3, respectively (see Appendix A.5.3 for derivation).

$$\Delta G^{\mathrm{ox,MQM}}_{\mathrm{Al}_{c_{\mathrm{Al}}}\mathrm{X}_{c_{\mathrm{X}}}\mathrm{O}_b} = \frac{z\alpha_{\mathrm{X}}}{z\alpha_{\mathrm{X}} + 3\alpha_{\mathrm{Al}}} \Delta G^{\mathrm{ox,MQM}}_{\mathrm{X_2O_z}} + \frac{3\alpha_{\mathrm{Al}}}{z\alpha_{\mathrm{X}} + 3\alpha_{\mathrm{Al}}} \Delta G^{\mathrm{ox,MQM}}_{\mathrm{Al_2O_3}} \tag{5.175}$$

The forms of $\Delta G^{\mathrm{ox,MQM}}$ of an Al-X system can therefore be understood by considering only the unary oxides. Each $\Delta G^{\mathrm{ox,MQM}}$ curve can be considered as the sum of two terms (5.176): a logarithm-based term $\Delta G^{\mathrm{ox,MQM,log}}_{\mathrm{Al}_{c_{\mathrm{Al}}}\mathrm{X}_{c_{\mathrm{X}}}\mathrm{O}_b}$ (5.177), and a polynomial term $\Delta G^{\mathrm{ox,MQM,poly}}_{\mathrm{Al}_{c_{\mathrm{Al}}}\mathrm{X}_{c_{\mathrm{X}}}\mathrm{O}_b}$ (5.178).

$$\Delta G^{\mathrm{ox,MQM}}_{\mathrm{Al}_{c_{\mathrm{Al}}}\mathrm{X}_{c_{\mathrm{X}}}\mathrm{O}_b} = \frac{RT}{2\sigma_1\varepsilon_6}\left(\sigma_1(m_{\mathrm{X}}\sigma_{\mathrm{X}} + m_{\mathrm{Al}}\sigma_{\mathrm{Al}}) + x_{\mathrm{XAl}}(\sigma_2 + \sigma_3\varepsilon_6)(m_{\mathrm{X}}(1 - x_{\mathrm{X}}) - m_{\mathrm{Al}}x_{\mathrm{X}})\right)$$

$$= \frac{RT}{2\sigma_1\varepsilon_6}\left(\sigma_1(m_{\mathrm{X}}\sigma_{\mathrm{X}} + m_{\mathrm{Al}}\sigma_{\mathrm{Al}}) + x_{\mathrm{XAl}}\sigma_2(m_{\mathrm{X}}(1 - x_{\mathrm{X}}) - m_{\mathrm{Al}}x_{\mathrm{X}})\right)$$

$$+ \frac{RTx_{\mathrm{XAl}}\sigma_3}{2\sigma_1}(m_{\mathrm{X}}(1 - x_{\mathrm{X}}) - m_{\mathrm{Al}}x_{\mathrm{X}})$$

$$= \frac{RT}{2\sigma_1\varepsilon_6}\left(m_{\mathrm{X}}(\sigma_1\sigma_{\mathrm{X}} + (1-x_{\mathrm{X}})x_{\mathrm{XAl}}\sigma_2) + m_{\mathrm{Al}}(\sigma_1\sigma_{\mathrm{Al}} - x_{\mathrm{X}}\sigma_2)\right) + \frac{RTx_{\mathrm{XAl}}\sigma_3}{2\sigma_1}(m_{\mathrm{X}}(1-x_{\mathrm{X}}) - m_{\mathrm{Al}}x_{\mathrm{X}})$$

$$\Delta G^{\mathrm{ox,MQM}}_{\mathrm{Al}_{c_{\mathrm{Al}}}\mathrm{X}_{c_{\mathrm{X}}}\mathrm{O}_b} = \Delta G^{\mathrm{ox,MQM,log}}_{\mathrm{Al}_{c_{\mathrm{Al}}}\mathrm{X}_{c_{\mathrm{X}}}\mathrm{O}_b} + \Delta G^{\mathrm{ox,MQM,poly}}_{\mathrm{Al}_{c_{\mathrm{Al}}}\mathrm{X}_{c_{\mathrm{X}}}\mathrm{O}_b} \tag{5.176}$$

$$\Delta G^{\mathrm{ox,MQM,log}}_{\mathrm{Al}_{c_{\mathrm{Al}}}\mathrm{X}_{c_{\mathrm{X}}}\mathrm{O}_b} = \frac{RT}{2\sigma_1\varepsilon_6}\left(m_{\mathrm{X}}(\sigma_1\sigma_{\mathrm{X}} + (1-x_{\mathrm{X}})x_{\mathrm{XAl}}\sigma_2) + m_{\mathrm{Al}}(\sigma_1\sigma_{\mathrm{Al}} - x_{\mathrm{X}}\sigma_2)\right) \tag{5.177}$$

$$\Delta G^{\mathrm{ox,MQM,poly}}_{\mathrm{Al}_{c_{\mathrm{Al}}}\mathrm{X}_{c_{\mathrm{X}}}\mathrm{O}_b} = \frac{RTx_{\mathrm{XAl}}\sigma_3}{2\sigma_1}(m_{\mathrm{X}}(1-x_{\mathrm{X}}) - m_{\mathrm{Al}}x_{\mathrm{X}}) \tag{5.178}$$

Demonstrating using Al-Gd at 700 °C (Figure 5.13), the logarithm-based term $\Delta G^{\mathrm{ox,MQM,log}}_{\mathrm{Al}_{c_{\mathrm{Al}}}\mathrm{X}_{c_{\mathrm{X}}}\mathrm{O}_b}$ has asymptotes at the composition limits (at $x_{\mathrm{X}} = 0$ for solute-containing oxides and $x_{\mathrm{X}} = 1$ for aluminium-containing oxides), and a crossover in the centre. In contrast, the polynomial-based term $\Delta G^{\mathrm{ox,MQM,poly}}_{\mathrm{Al}_{c_{\mathrm{Al}}}\mathrm{X}_{c_{\mathrm{X}}}\mathrm{O}_b}$ is zero at the composition limits for all oxides and crosses over in the centre at a slightly different composition. This difference in crossover composition, and difference in gradients in this region, leads to a complex form with multiple turning points when added together.

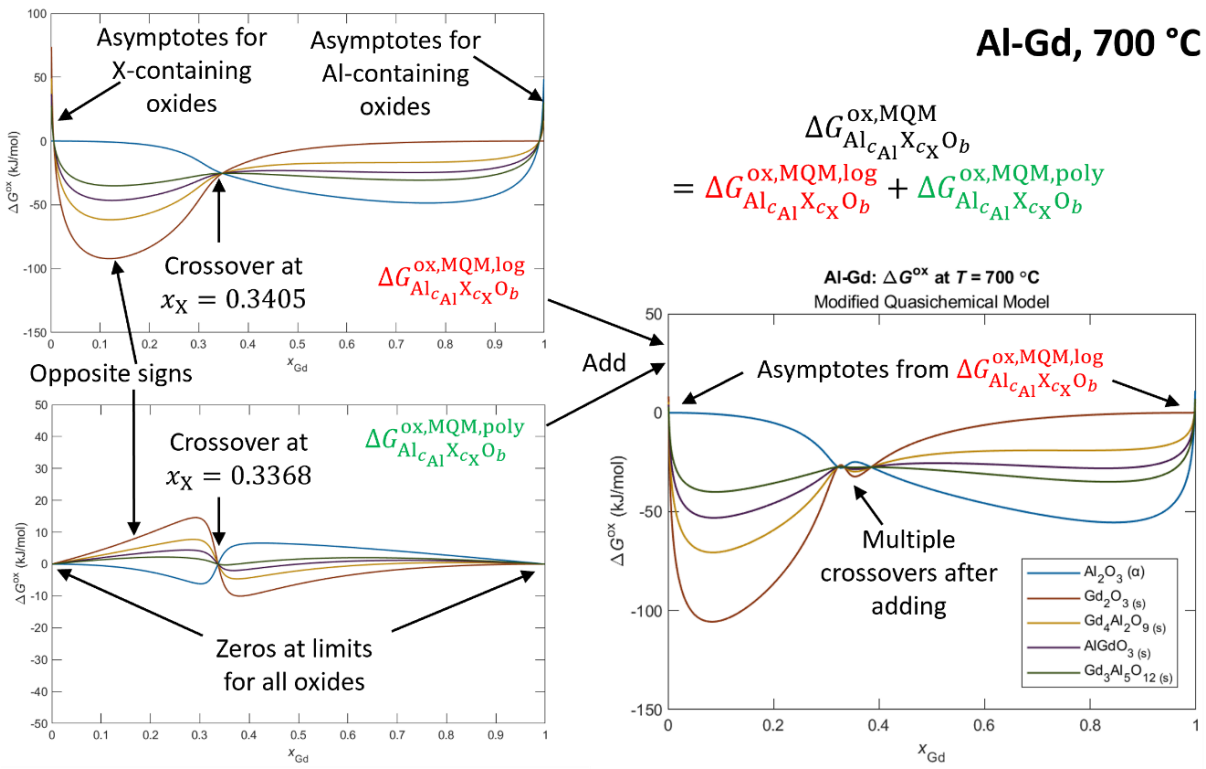


Figure 5.13: $\Delta G^{\mathrm{ox,MQM}}$ curves for Al-Gd at 700 °C split into logarithm-based terms ($\Delta G^{\mathrm{ox,MQM,log}}$) and polynomial terms $\Delta G^{\mathrm{ox,MQM,poly}}$, using a linear composition axis.

The asymptotes can be interpreted physically as an extra configurational entropic contribution from the consideration of second-nearest neighbour ordering. Like the case of point entropy considered in ideal mixing, the entropic penalty for removing a solute atom increases hugely as composition decreases.

5.4.3.2. Effect on oxide stability diagrams

The effect on oxide stability diagrams (Figure 5.14), like Bragg-Williams Mixing, is largely a shift in the boundaries between regions and, in some cases, the appearance of extra regions (see Appendix B.5.3 for a full set of diagrams).

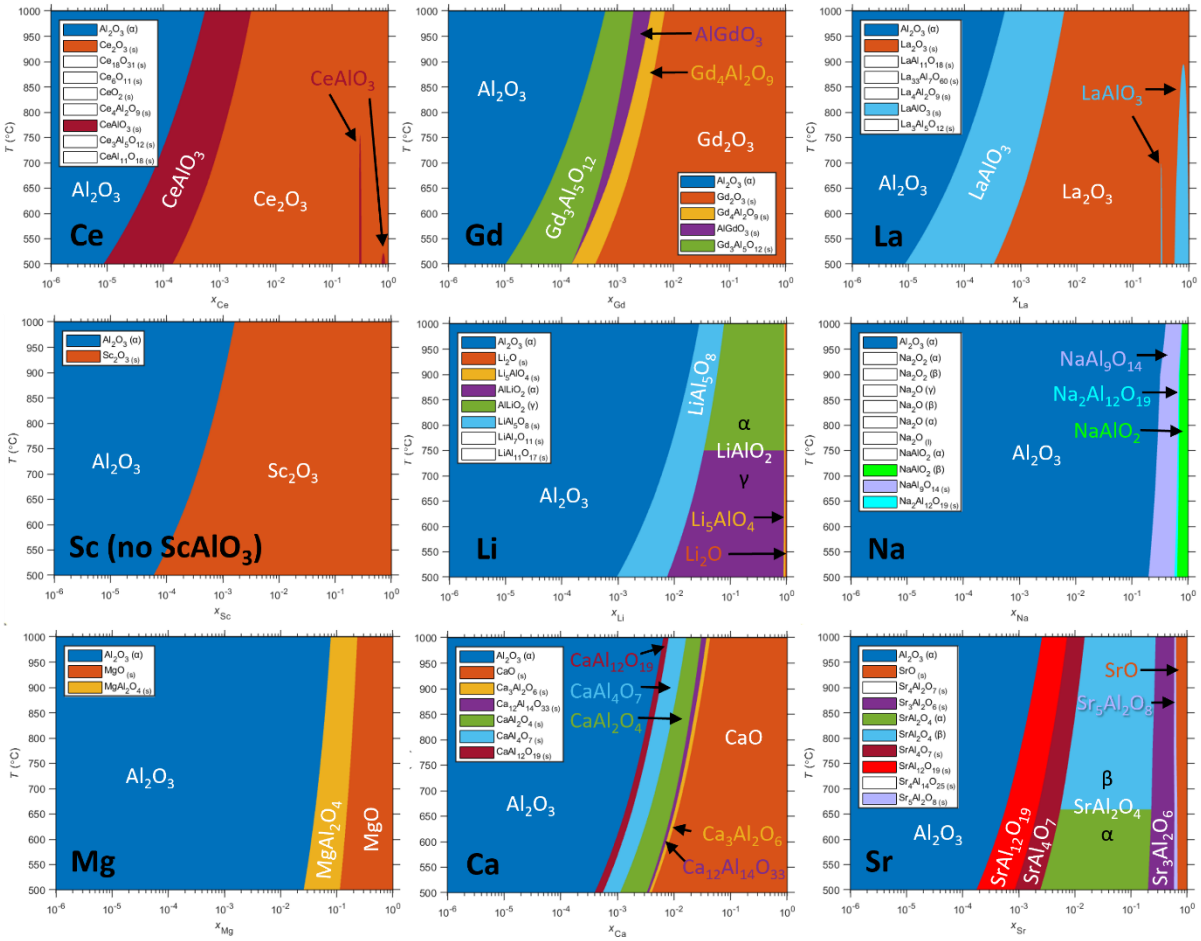


Figure 5.14. Oxide stability diagrams incorporating MQM mixing. See Appendix B.5.3 for larger versions.

In the case of Al-Si, there is still only Al_2O_3 across the temperature-composition range, since the contribution from $\Delta G^{\mathrm{ox,MQM}}$ is not enough to overcome the difference in $\Delta G^{\circ}_{\mathrm{f\,mol\,O_2}}$ between Al_2O_3 and the Si-containing oxides. In all 'more reactive' Al-X systems, there is a narrowing

of the binary Al-X oxide regions. This is due to the increase in gradients of ΔG^{ox} at low x_{X}, through the incorporation of the second-order entropy term (Figure 5.15): the increase in gradient (with a logarithmic x_{X} axis) at low x_{X} scales with m_{X} (5.171) and (roughly) with temperature T (5.172), which is also the case for the ideal term (5.50).

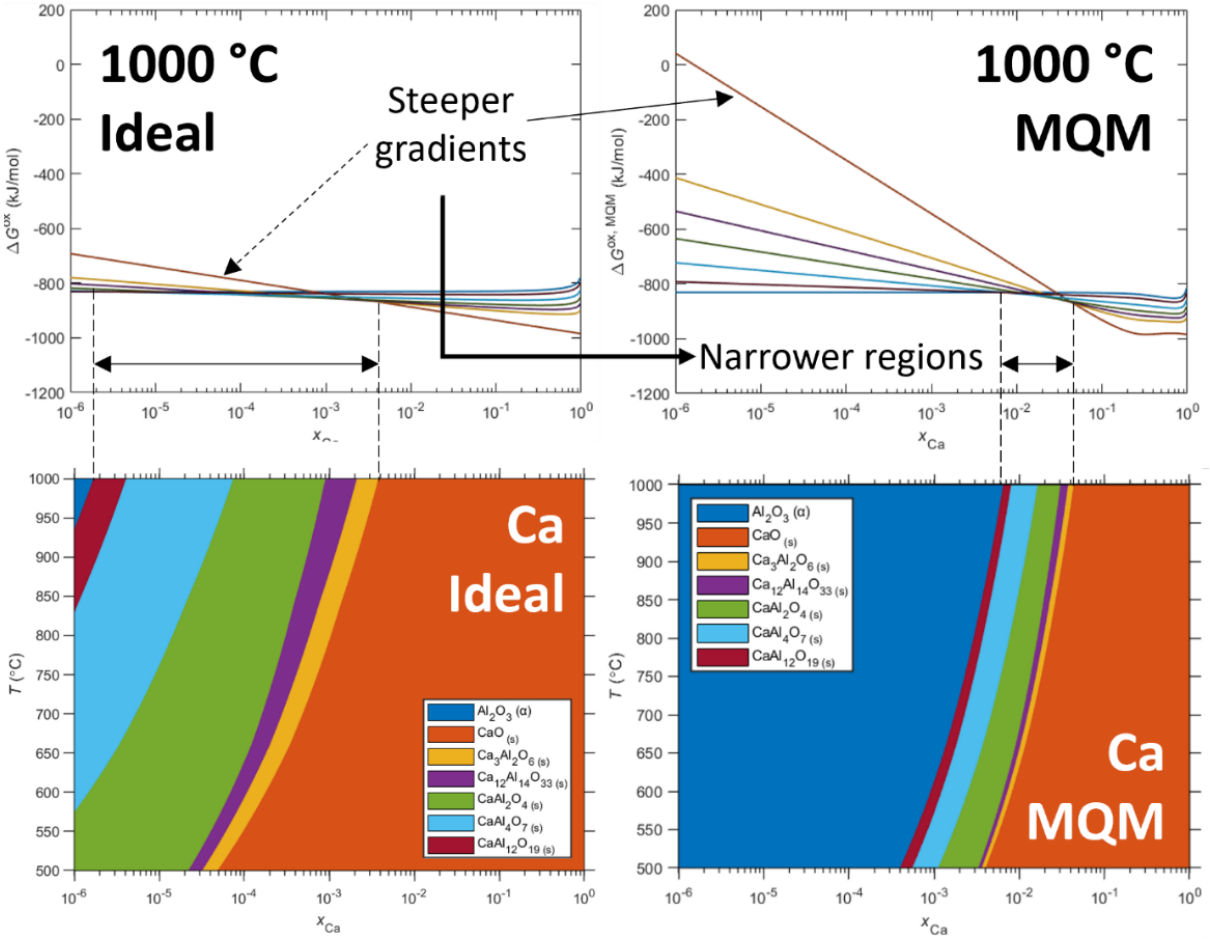


Figure 5.15. Narrowing of regions in oxide stability diagrams with incorporation of MQM due to increased ΔG^{ox} gradients at low x_{X} demonstrated with the Al-Ca system. Figure contains $\Delta G^{\mathrm{ox}}(x_{\mathrm{X}})$ plots at 1000 °C, and their correspondence with the oxide stability diagrams, plotted for both ideal mixing and MQM mixing: an increase in gradients of $\Delta G^{\mathrm{ox}}(x_{\mathrm{X}})$ at low x_{X}, which itself scales with m_{X}, leads to a narrowing of regions.

In addition, boundaries become steeper, since the entropy terms are more dominant generally compared to the $\Delta G^{\mathrm{o}}_{\mathrm{f\,mol}O_2}$ terms. These two factors cause boundaries for oxides with low m_{X} (including Al_2O_3) to shift to higher x_{X}. However, some boundaries between oxides with high m_{X}, e.g. Ce_2O_3 and La_2O_3, shift to lower x_{X}; the difference between the behaviours is due to the general narrowing of the intermediate oxide regions.

In some systems, such as Al-Ce and Al-La, extra regions appear (Figure 5.14), due to the

undulations of the $\Delta G^{\mathrm{ox,MQM}}(x_{\mathrm{X}})$ term. Oxides with approximately equal m_{X} and m_{Al} have flatter shapes than those with unequal m_i, leading to the prevalence of crossovers in regions where the $\Delta G^{\mathrm{ox,MQM}}(x_{\mathrm{X}})$ terms have turning points. By design, since MQM mixing was developed to favour ordering at compositions slightly away from 0.5, these turning points occur on the order of $x_{\mathrm{X}} = 10^{-1}$ (i.e. 0.1-0.9), thus resulting in extra regions for binary oxides (e.g. $LaAlO_3$ and $CeAlO_3$) around these compositions. As temperature increases, the entropic terms dominate more and mask the effects of these turning points, narrowing the regions and eventually removing them from the stability diagram (Figure 5.16).

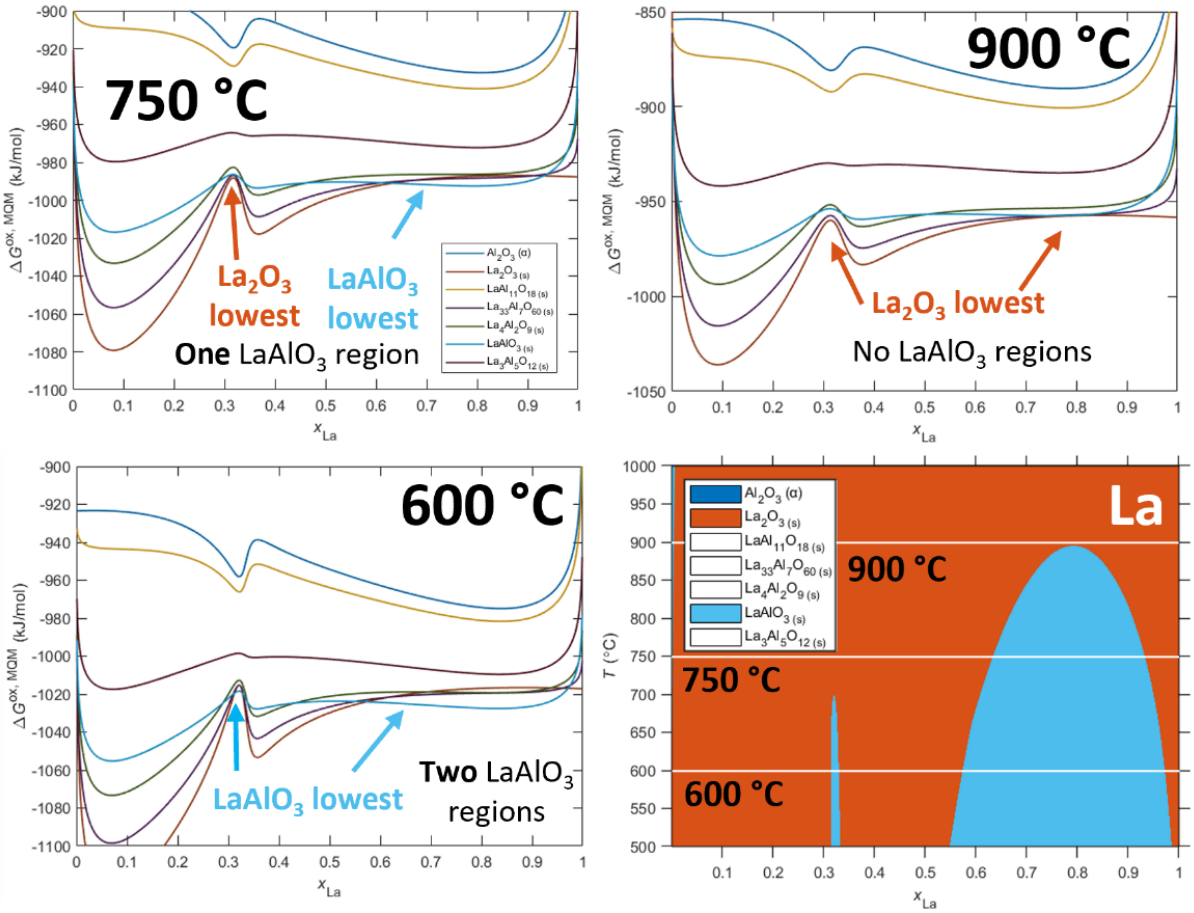


Figure 5.16. Extra $LaAlO_3$ regions Al-La oxide stability diagrams due to undulations of plots, shown by correspondence with $\Delta G^{\mathrm{ox}}(x_{\mathrm{X}})$ plots at 600 °C, 750 °C, and 900 °C. Note the use of a linear composition axis, to demonstrate the formation of these regions more clearly.

5.5. Al-Mg-X ternary systems

In ternary Al-Mg-X systems there are two independent composition variables: one for the solute element X, x_{X}, and another for magnesium, x_{Mg}, which is reflected in the ΔG^{ox}

expressions for a general Al-Mg-X system (Table 5.14). Since there are three variables of interest for a given Al-Mg-X system, $\{x_{\mathrm{X}}, x_{\mathrm{Mg}}, T\}$, but only two axes on an oxide stability diagram, temperature is chosen to be fixed and the changes shown by multiple sections at various temperatures.

Species	$\Delta G_i^{\mathrm{ox}}(x_{\mathrm{Mg}}, x_{\mathrm{X}}, p_{\mathrm{O_2}}, T)$	**Eqn.**
$\mathrm{Al_2O_3}$	$\frac{2}{3}\Delta G^{\mathrm{o}}_{\mathrm{f,\,Al_2O_3}}(T) - RT\ln p_{\mathrm{O_2}} - \frac{4}{3}\left(\Delta\mu^{\mathrm{xs}}_{\mathrm{Al}} + RT\ln\left(1 - x_{\mathrm{X}} - x_{\mathrm{Mg}}\right)\right)$	(5.179)
MgO	$\Delta G^{\mathrm{o}}_{\mathrm{f,MgO}}(T) - RT\ln p_{\mathrm{O_2}} - \frac{1}{2}\left(\Delta\mu^{\mathrm{xs}}_{\mathrm{Mg}} + RT\ln x_{\mathrm{Mg}}\right)$	(5.180)
$\mathrm{MgAl_2O_4}$	$\frac{1}{2}\Delta G^{\mathrm{o}}_{\mathrm{f,MgAl_2O_4}}(T) - RT\ln p_{\mathrm{O_2}} - \frac{1}{2}\left(\Delta\mu^{\mathrm{xs}}_{\mathrm{Mg}} + RT\ln x_{\mathrm{Mg}}\right) - \left(\Delta\mu^{\mathrm{xs}}_{\mathrm{Al}} + RT\ln\left(1 - x_{\mathrm{X}} - x_{\mathrm{Mg}}\right)\right)$	(5.181)
$\mathrm{X}_{c_{\mathrm{X}}}\mathrm{O}_b$	$\frac{2}{b}\Delta G^{\mathrm{o}}_{\mathrm{f,\,X}_{c_{\mathrm{X}}}\mathrm{O}_b}(T) - m_{\mathrm{X}}\Delta\mu^{\mathrm{xs}}_{\mathrm{X}} - RT\ln\left(x_{\mathrm{X}}{}^{m_{\mathrm{X}}} p_{\mathrm{O_2}}\right)$	(5.182)
$\mathrm{Al}_{c_{\mathrm{Al}}}\mathrm{X}_{c_{\mathrm{X}}}\mathrm{O}_b$	$\frac{2}{b}\Delta G^{\mathrm{o}}_{\mathrm{f,\,Al}_{c_{\mathrm{Al}}}\mathrm{X}_{c_{\mathrm{X}}}\mathrm{O}_b}(T) - (m_{\mathrm{Al}}\Delta\mu^{\mathrm{xs}}_{\mathrm{Al}} + m_{\mathrm{X}}\Delta\mu^{\mathrm{xs}}_{\mathrm{X}}) - RT\ln\left(\left(1 - x_{\mathrm{X}} - x_{\mathrm{Mg}}\right)^{m_{\mathrm{Al}}} x_{\mathrm{X}}{}^{m_{\mathrm{X}}} p_{\mathrm{O_2}}\right)$	(5.183)
$\mathrm{Al}_{c_{\mathrm{Al}}}\mathrm{Mg}_{c_{\mathrm{Mg}}}\mathrm{X}_{c_{\mathrm{X}}}\mathrm{O}_b$	$\frac{2}{b}\Delta G^{\mathrm{o}}_{\mathrm{f,\,Al}_{c_{\mathrm{Al}}}\mathrm{Mg}_{c_{\mathrm{Mg}}}\mathrm{X}_{c_{\mathrm{X}}}\mathrm{O}_b}(T) - \left(m_{\mathrm{Al}}\Delta\mu^{\mathrm{xs}}_{\mathrm{Al}} + m_{\mathrm{X}}\Delta\mu^{\mathrm{xs}}_{\mathrm{X}} + m_{\mathrm{Mg}}\Delta\mu^{\mathrm{xs}}_{\mathrm{Mg}}\right) - RT\ln\left(\left(1 - x_{\mathrm{X}} - x_{\mathrm{Mg}}\right)^{m_{\mathrm{Al}}} x_{\mathrm{X}}{}^{m_{\mathrm{X}}} x_{\mathrm{Mg}}{}^{m_{\mathrm{Mg}}} p_{\mathrm{O_2}}\right)$	(5.184)

Table 5.14. ΔG^{ox} equations for a general Al-Mg-X system.

5.5.1. Ideal mixing

In ideal mixing, like in the binary case, the enthalpy of mixing is set to zero. Any variation in ΔG^{ox} with temperature is therefore only due to changes in configurational entropy, which manifests as $m_i \ln(x_i)$ terms in ΔG^{ox} expressions (Table 5.15). When the solute element is an

element that is "less reactive" in the binary classification (Figure 5.6), only Al_2O_3, $MgAl_2O_4$, and MgO are present (Figure 5.17, see Zn) and the boundaries depend only on the Al:Mg ratio. These boundaries appear as horizontal lines at low x_X and curve downwards as $x_X \to 1$, following lines of constant $x_{Al}: x_{Mg}$.

Species	$\Delta G_i^{ox}(x_{Mg}, x_X, p_{O_2}, T)$	**Eqn.**
Al_2O_3	$\frac{2}{3}\Delta G^o_{f,\,Al_2O_3}(T) - RT\ln p_{O_2} - \frac{4}{3}RT\ln(1 - x_X - x_{Mg})$	(5.185)
MgO	$\Delta G^o_{f,MgO}(T) - RT\ln p_{O_2} - RT\ln x_X$	(5.186)
$MgAl_2O_4$	$\frac{1}{2}\Delta G^o_{f,MgAl_2O_4}(T) - RT\ln pO_2 - \frac{1}{2}RT\ln x_{Mg} - RT\ln(1 - x_X - x_{Mg})$	(5.187)
$X_{c_X}O_b$	$\frac{2}{b}\Delta G^o_{f,\,X_{c_X}O_b}(T) - RT\ln({x_X}^{m_X} pO_2)$	(5.188)
$Al_{c_{Al}}X_{c_X}O_b$	$\frac{2}{b}\Delta G^o_{f,\,Al_{c_{Al}}X_{c_X}O_b}(T) - RT\ln pO_2 - RTm_X\ln x_X - RTm_{Al}\ln(1 - x_X - x_{Mg})$	(5.189)
$Al_{c_{Al}}Mg_{c_{Mg}}X_{c_X}O_b$	$\frac{2}{b}\Delta G^o_{f,\,Al_{c_{Al}}Mg_{c_{Mg}}X_{c_X}O_b}(T) - RT\ln pO_2 - RTm_X\ln x_X - RTm_{Mg}\ln x_{Mg} - RTm_{Al}\ln(1 - x_X - x_{Mg})$	(5.190)

Table 5.15. ΔG^{ox} equations for a general Al-Mg-X system, assuming ideal mixing.

In the case of more reactive elements in which the only solute-containing oxide is a unary oxide, such as Sc_2O_3, then there is an extra region for this oxide (Figure 5.17). The boundary between Al_2O_3 and this unary oxide is vertical, since the two oxides' relative stability is independent of x_{Mg}. This is also the case when there are binary Al-X oxides present, such as Al-Be: the relative stability of $BeAl_2O_4$ and BeO does not depend on x_{Mg}.

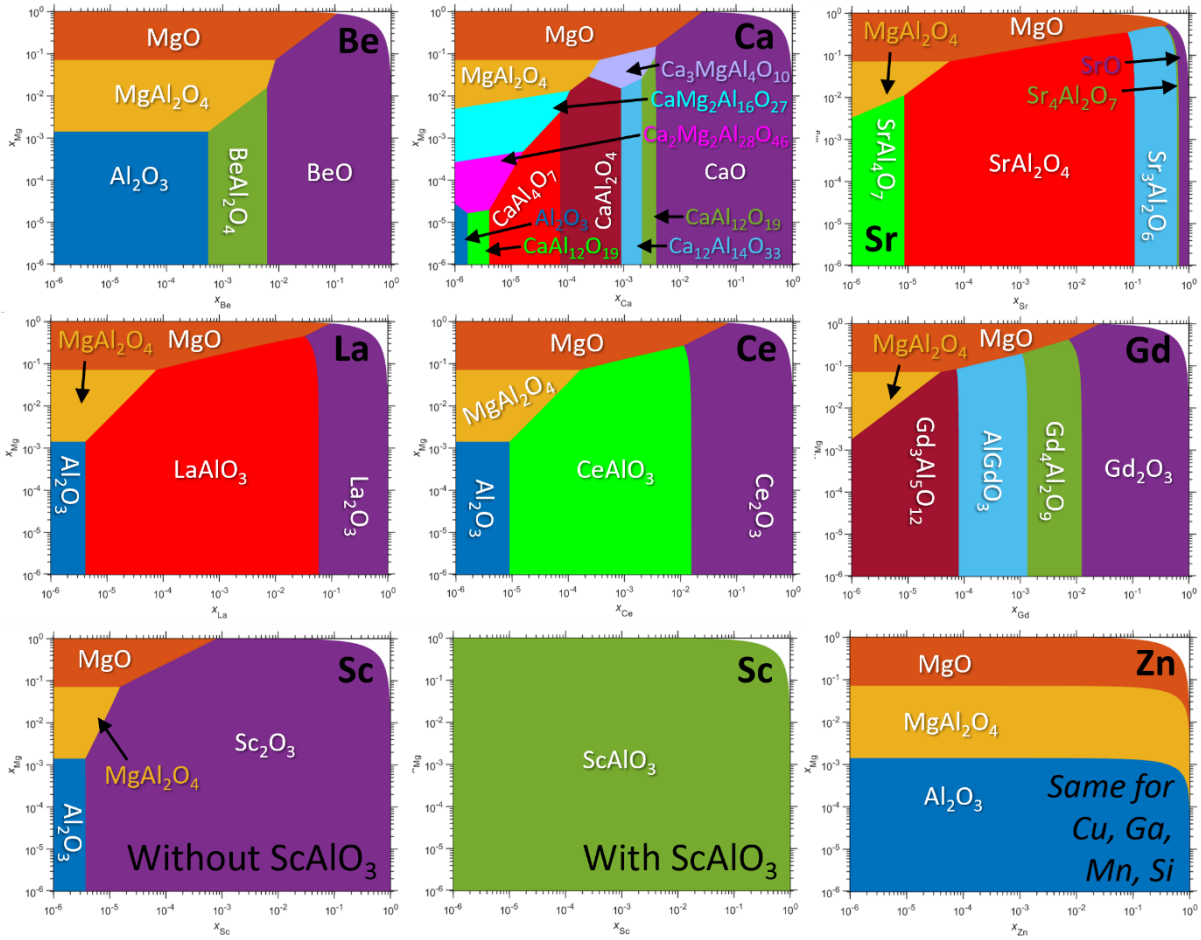


Figure 5.17. Al-Mg-X ternary oxide stability diagrams at 1000 °C, assuming ideal mixing. This temperature is chosen to display the most different regions in the diagrams (for the composition ranges considered), but diagrams from 500 – 1000 °C, as larger versions, can be found in Appendix B.6.1.

When Al-X unary or binary oxide regions coincide with the regions for $MgAl_2O_4$ or MgO, the boundary is diagonal: the gradient (5.191) is given by the ratio of the non-zero m_X and m_{Mg} values (see Appendix A.5.4 for derivation).

$$g_{\text{plot}} = \frac{m_X}{m_{Mg}} \tag{5.191}$$

Since m_X and m_{Mg} are positive, all gradients in these cases are positive, which is observed on the plots (Figure 5.17). This linearity only holds strictly true when $x_{Al} \gg x_X, x_{Mg}$, so for boundaries at higher compositions, the boundaries curve (e.g. MgO and $Sr_3Al_2O_6$), but this approximation holds well for most boundaries seen. The exception to this condition is between two oxides for which $m_{Al} = 0$, where this condition holds true even outside of this limit (e.g. the MgO-SrO boundary). If there are ternary Al-Mg-X oxides present, such as the Al-Ca

system, then the gradient depends on the ratio of the differences between m_X and m_{Mg} values (5.192), so some gradients can be negative, such as the boundary between $CaAl_2O_4$ and $Ca_3MgAl_4O_{10}$ (5.193).

$$g_{plot} = \frac{m_{X1} - m_{X2}}{m_{Mg2} - m_{Mg1}} \tag{5.192}$$

$$g_{plot}(CaAl_2O_4/Ca_3MgAl_4O_{10}) = \frac{m_{X1} - m_{X2}}{m_{Mg2} - m_{Mg1}} = \frac{\frac{1}{2} - \frac{3}{5}}{\frac{1}{5} - 0} = -\frac{1}{2} < 0 \tag{5.193}$$

For Al-Mg-Ca, the ternary Al-Mg-X oxide regions lie in a similar pattern to the binary systems: the higher the m_{Mg}, the higher value of x_{Mg} at which the region is found e.g. $Ca_2Mg_2Al_{28}O_{46}$ and $CaMg_2Al_{16}O_{27}$, and equivalently for x_X, e.g. $CaMg_2Al_{16}O_{27}$ and $Ca_3MgAl_4O_{10}$.

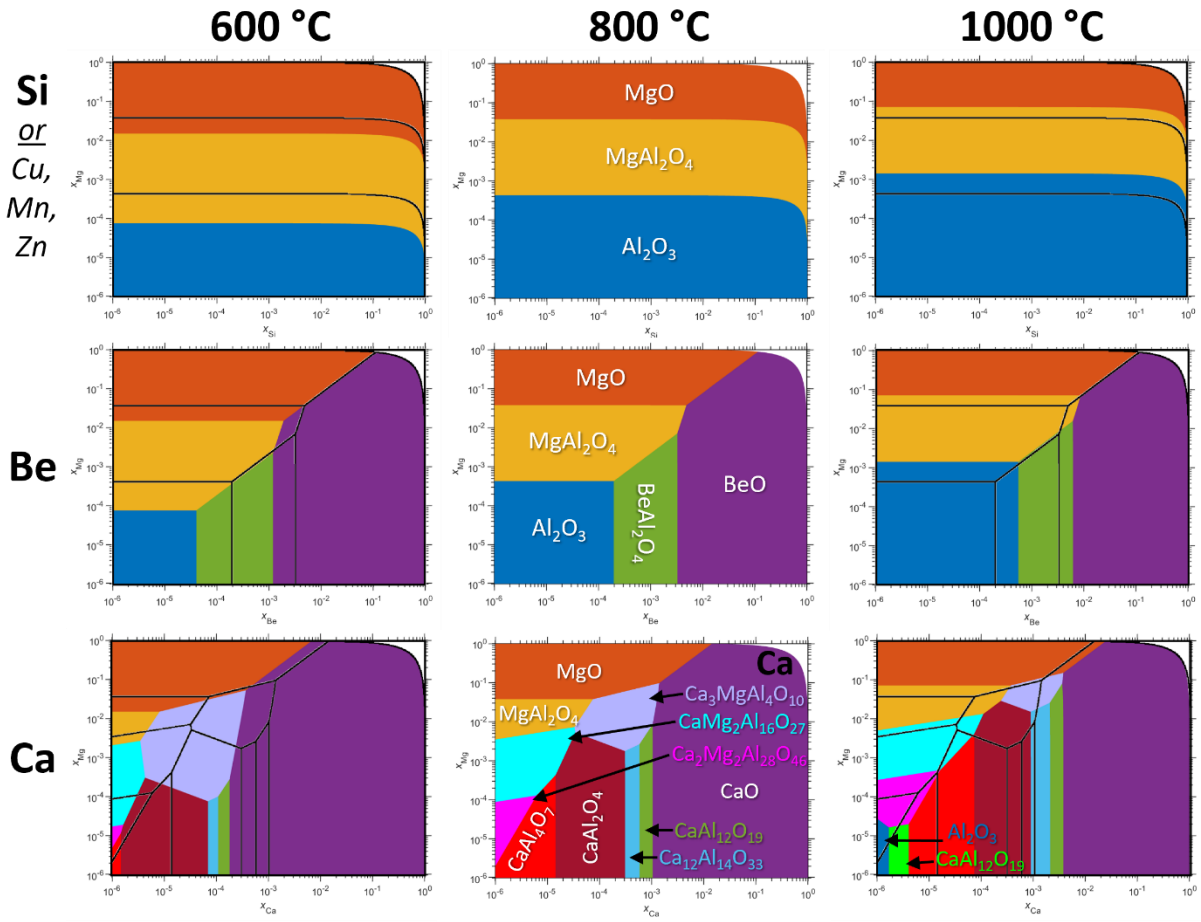


Figure 5.18. Change in ternary oxide stability diagrams with temperature: selected systems (Be, Ca, Si) at 600 °C, 800 °C, and 1000 °C. The boundaries for 800 °C are laid over the stability diagrams for 600 °C and 1000 °C to show the changes. Larger versions can be found in Appendix B.6.1.

The variation in these ternary plots with temperature is the same as the constituent binaries:

boundaries shift to higher x_{X} as temperature increases (Figure 5.18). For less reactive solutes (Cu, Mn, Si, Zn), for which only Al_2O_3, $MgAl_2O_4$, and MgO are present, the boundaries shift to higher x_{Mg} as temperature increases, due to the shift in stability of the Al-Mg unary and binary oxides. For more reactive solutes without any ternary Al-Mg-X oxides (e.g. Al-Mg-Be), the boundaries shift to higher x_{Mg} and x_{X} as temperature increases, due to the shift in stability of Al-Mg and Al-Be unary and binary oxides, but the gradients of the boundaries stay constant, as they are only determined by m_i values (5.192). For Al-Mg-Ca, which contains ternary oxides that do appear on the oxide stability diagrams, the ternary Al-Mg-Ca oxide regions also shift to higher x_{Mg} and x_{X} as temperature increases.

5.5.2. Bragg-Williams mixing

In Bragg-Williams mixing, an extra ΔH_{mix} term is added in (5.81), including parameters fitted to experimental data (5.82), resulting in an extra term $\Delta G^{\mathrm{ox,BWT}}_{\mathrm{Al}_{c_{\mathrm{Al}}}\mathrm{X}_{1c_1}\mathrm{X}_{2c_2}\mathrm{O}_b}$ (5.87). For an Al-Mg-X system, $\Delta G^{\mathrm{ox}}_{\mathrm{Al}_{c_{\mathrm{Al}}}\mathrm{Mg}_{c_{\mathrm{Mg}}}\mathrm{X}_{c_{\mathrm{X}}}\mathrm{O}_b}$ (5.194) and the Bragg-Williams ternary term $\Delta G^{\mathrm{ox,BWT}}_{\mathrm{Al}_{c_{\mathrm{Al}}}\mathrm{Mg}_{c_{\mathrm{Mg}}}\mathrm{X}_{c_{\mathrm{X}}}\mathrm{O}_b}$ (5.195), are expressed as follows.

$$\Delta G^{\mathrm{ox}}_{\mathrm{Al}_{c_{\mathrm{Al}}}\mathrm{Mg}_{c_{\mathrm{Mg}}}\mathrm{X}_{c_{\mathrm{X}}}\mathrm{O}_b}(x_1, x_2, T, pO_2)$$

$$= \frac{2}{b}\Delta G^{\mathrm{o}}_{\mathrm{f,Al}_{c_{\mathrm{Al}}}\mathrm{Mg}_{c_{\mathrm{Mg}}}\mathrm{X}_{c_{\mathrm{X}}}\mathrm{O}_b}(T) - RT\ln\left(x_{\mathrm{Mg}}^{m_{\mathrm{Mg}}} x_{\mathrm{X}}^{m_{\mathrm{X}}} x_{\mathrm{Al}}^{m_{\mathrm{Al}}} pO_2\right) - \Delta G^{\mathrm{ox,BWT}}_{\mathrm{Al}_{c_{\mathrm{Al}}}\mathrm{Mg}_{c_{\mathrm{Mg}}}\mathrm{X}_{c_{\mathrm{X}}}\mathrm{O}_b} \qquad (5.194)$$

$$\begin{aligned}
\Delta G^{\mathrm{ox,BWT}}_{\mathrm{Al}_{c_{\mathrm{Al}}}\mathrm{Mg}_{c_{\mathrm{Mg}}}\mathrm{X}_{c_{\mathrm{X}}}\mathrm{O}_b} &= x_{\mathrm{Al}}x_{\mathrm{Mg}}x_{\mathrm{X}}\left(m_{\mathrm{Al}}{}^{\mathrm{Al}}L_{\mathrm{AlMgX}} + m_{\mathrm{Mg}}{}^{\mathrm{Mg}}L_{\mathrm{AlMgX}} + m_{\mathrm{X}}{}^{\mathrm{X}}L_{\mathrm{AlMgX}}\right) \\
&+\omega_{\mathrm{AlMgX}}\left(m_{\mathrm{Al}}x_{\mathrm{Mg}}x_{\mathrm{X}}(1-3x_{\mathrm{Al}}) + m_{\mathrm{Mg}}x_{\mathrm{Al}}x_{\mathrm{X}}\left(1-3x_{\mathrm{Mg}}\right) + m_{\mathrm{X}}x_{\mathrm{Al}}x_{\mathrm{Mg}}(1-3x_{\mathrm{X}})\right) \\
&+\sum_{i\geq 0}{}^{i}L_{\mathrm{AlMg}}\left(x_{\mathrm{Al}}-x_{\mathrm{Mg}}\right)^{i}\left[m_{\mathrm{Al}}x_{\mathrm{Mg}}\left(x_{\mathrm{Mg}}+x_{\mathrm{X}}\right) + m_{\mathrm{Mg}}x_{\mathrm{Al}}(x_{\mathrm{Al}}+x_{\mathrm{X}}) - m_{\mathrm{X}}x_{\mathrm{Al}}x_{\mathrm{Mg}}\right] \\
&+x_{\mathrm{Al}}x_{\mathrm{Mg}}\sum_{i\geq 1}{}^{i}L_{\mathrm{AlMg}}(i)\left(x_{\mathrm{Al}}-x_{\mathrm{Mg}}\right)^{i-1}\left[m_{Al}\left(2x_{\mathrm{Mg}}+x_{\mathrm{X}}\right) - m_{\mathrm{Mg}}(2x_{\mathrm{Al}}+x_{\mathrm{X}})\right. \\
&\qquad \left. - m_{\mathrm{X}}\left(x_{\mathrm{Al}}-x_{\mathrm{Mg}}\right)\right] \\
&+\sum_{i\geq 0}{}^{i}L_{\mathrm{AlX}}(x_{\mathrm{Al}}-x_{\mathrm{X}})^{i}\left[m_{\mathrm{Al}}x_{\mathrm{X}}\left(x_{\mathrm{Mg}}+x_{\mathrm{X}}\right) - m_{\mathrm{Mg}}x_{\mathrm{Al}}x_{\mathrm{X}} + m_{\mathrm{X}}x_{\mathrm{Al}}\left(x_{\mathrm{Al}}+x_{\mathrm{Mg}}\right)\right]
\end{aligned}$$

$$+x_{\mathrm{Al}}x_{\mathrm{X}}\sum_{i\geq 1}{}^{i}L_{\mathrm{AlX}}(i)(x_{\mathrm{Al}}-x_{\mathrm{X}})^{i-1}\left[m_{\mathrm{Al}}\left(x_{\mathrm{Mg}}+2x_{\mathrm{X}}\right)-m_{\mathrm{Mg}}(x_{\mathrm{Al}}-x_{\mathrm{X}})-m_{\mathrm{X}}\left(2x_{\mathrm{Al}}+x_{\mathrm{Mg}}\right)\right]$$

$$+\sum_{i\geq 0}{}^{i}L_{\mathrm{MgX}}\left(x_{\mathrm{Mg}}-x_{\mathrm{X}}\right)^{i}\left[-m_{\mathrm{Al}}x_{\mathrm{Mg}}x_{\mathrm{X}}+m_{\mathrm{Mg}}x_{\mathrm{X}}(x_{\mathrm{Al}}+x_{\mathrm{X}})+m_{\mathrm{X}}x_{\mathrm{Mg}}\left(x_{\mathrm{Al}}+x_{\mathrm{Mg}}\right)\right]$$

$$+x_{\mathrm{Mg}}x_{\mathrm{X}}\sum_{i\geq 1}{}^{i}L_{\mathrm{MgX}}(i)\left(x_{\mathrm{Mg}}-x_{\mathrm{X}}\right)^{i-1}\left[-m_{\mathrm{Al}}\left(x_{\mathrm{Mg}}-x_{\mathrm{X}}\right)+m_{\mathrm{Mg}}(x_{\mathrm{Al}}+2x_{\mathrm{X}})\right.$$
$$\left.-m_{\mathrm{X}}\left(2x_{\mathrm{Mg}}+x_{\mathrm{Al}}\right)\right] \qquad (5.195)$$

In the systems where the solute is a 'more reactive' element (Figure 5.6), the shifts in boundaries reflect those of the binary Al-X system (see Appendix B.6.2 for a full collection of plots). When the alternating sum L_{alt} (5.166) of the binary component is positive, such as Be, the phase boundaries shift to lower x_{X} (technically, from $x_{\mathrm{X}}=0.5$), but where the alternating sum is negative, such as Gd (see Appendix B.6.2), the boundaries shift to higher x_{X}, which also occurs in the binary systems (Figure 5.9).

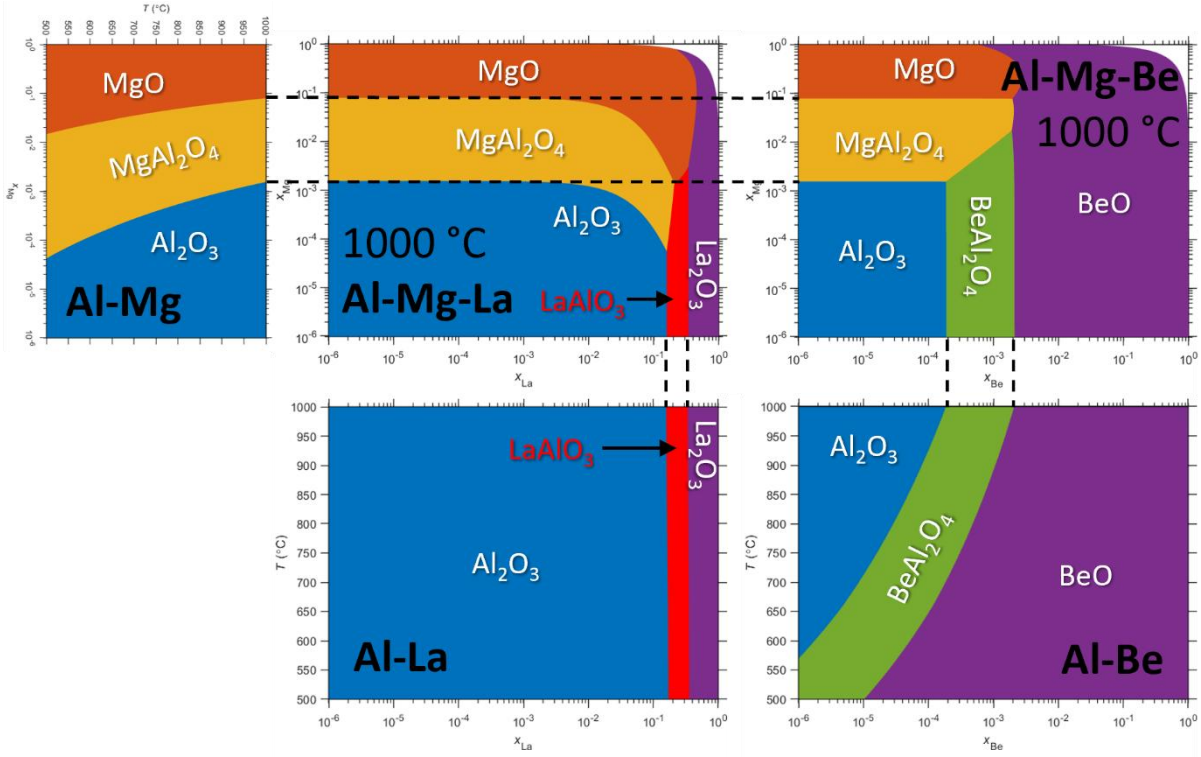


Figure 5.19. Correspondence between binary and ternary oxide stability diagrams in the Al-Mg-Be and Al-Mg-La systems, assuming Bragg-Williams Mixing.

This is demonstrated by the correspondence between binary and ternary oxide stability diagrams (Figure 5.19), which also holds when assuming ideal mixing. The binary limits of the

ternary oxide stability diagrams (i.e. either $x_X \to 0$ or $x_{Mg} \to 0$) correspond with the respective binary oxide stability diagram: the regions at 1000 °C for Al-Mg match with the regions at $x_X = 10^{-6}$ for the ternary oxide stability diagram calculated at 1000 °C for both Al-Mg-La and Al-Mg-Be, and equivalently the regions at $x_{Mg} = 10^{-6}$ for the ternary oxide stability diagrams of Al-Mg-La and Al-Mg-Be calculated at 1000 °C correspond with the binary oxide stability diagram regions at 1000 °C for Al-La and Al-Be respectively.

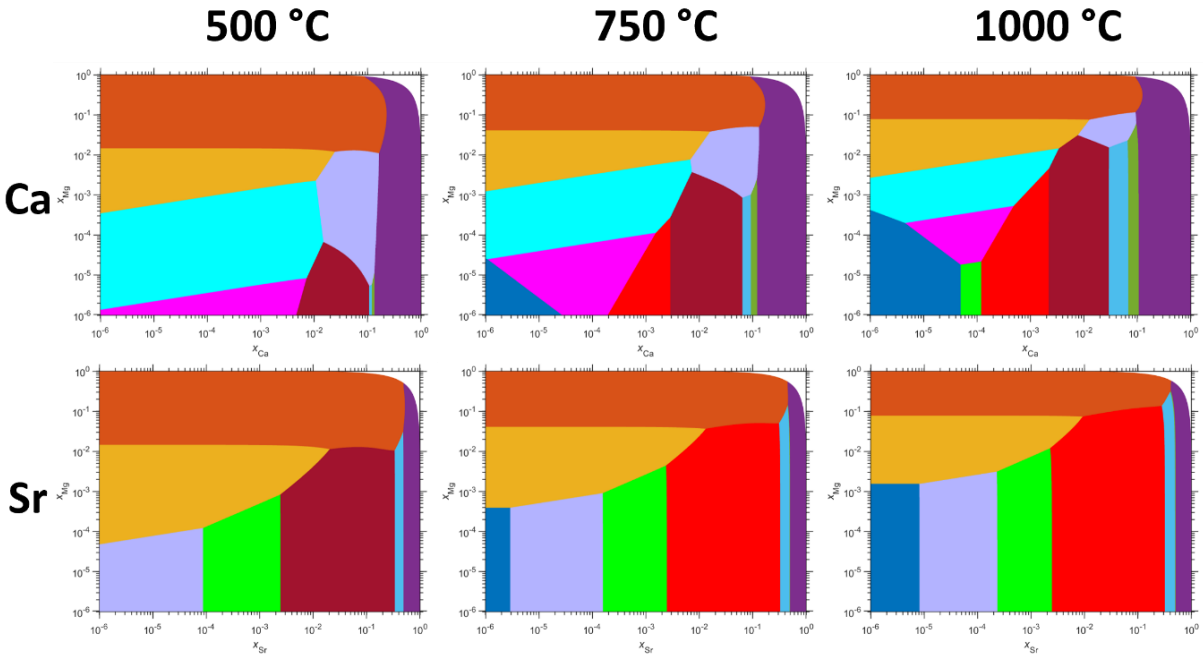


Figure 5.20. Comparison of boundaries in Al-Mg-Ca and Al-Mg-Sr ternary systems assuming Bragg-Williams mixing at 500 °C, 750 °C, and 1000 °C. As temperature increases, boundaries become less curved, especially so at lower compositions, due to increasing dominance of entropy term over the enthalpic term. Larger versions can be found in Appendix B.6.2.

In addition, the boundaries between regions are no longer strictly straight lines due to the addition of the extra $\Delta G^{ox,BWT}$ term, an effect which is stronger at higher x_X and x_{Mg} (due to the breakdown of the assumption of $x_{Al} \gg x_X, x_{Mg}$ required for linear boundaries in the ideal case) and at lower temperatures, where the entropy term dominates less. The curvature is less pronounced at higher temperatures since the ideal entropy term becomes more dominant compared to the extra enthalpy term from Bragg-Williams mixing (Figure 5.20). Notably, these trends also apply to the less reactive systems, in which only Al-Mg unary and binary oxides are observed in the ternary oxide stability diagrams (Figure 5.21). In the limit of $x_X \to 0$, there

is a shift in Al-Mg oxide boundaries due to the binary Al-Mg Bragg Williams parameters which, as the figure shows, becomes less prominent.

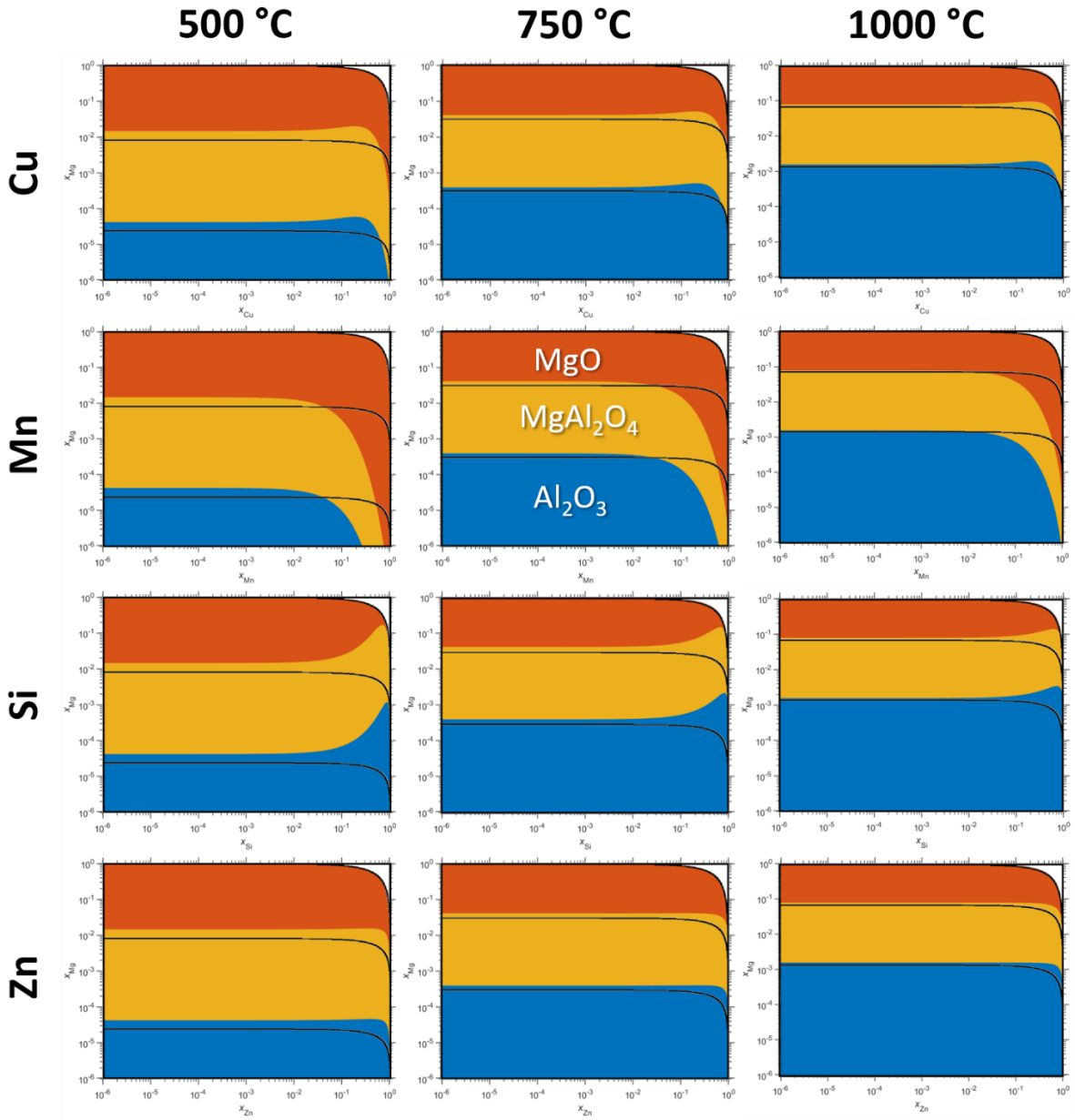


Figure 5.21. Ternary Al-Mg-X oxide stability diagrams for less reactive solutes (Cu, Si, Mn, Zn) at 500 °C, 750 °C, and 1000 °C, with boundaries of stability diagrams of systems with ideal mixing superimposed. Larger versions, without superimposition, can be found in Appendix B.6.2.

There are additional alterations to the shapes of the boundaries which can be explained by the signs of the alternating sum, L_{alt} (5.166), of the Al-X and Mg-X binary systems (Table 5.16).

X_1	**Al**	**Al**	**Al**	**Al**	**Al**	**Mg**	**Mg**	**Mg**	**Mg**
X_2	**Cu**	**Mn**	**Si**	**Zn**	**Mg**	**Cu**	**Mn**	**Si**	**Zn**
500 °C	-88710	-43064	-7209	8387	-2952	-49325	36379	-43170	-20035
1000 °C	-79060	-33864	-7821	6634	2831	-46330	40897	-30680	-18660

Table 5.16. L_{alt} values, roughly corresponding to enthalpy of mixing, for Al-X and Mg-X systems in less reactive ternary systems (Cu, Mn, Si, Zn) at 500 °C and 1000 °C. Positive values are shaded red.

The sign of L_{alt} indicates whether mixing is enthalpically favourable (if negative) or unfavourable (if positive). As x_{X} increases (at constant x_{Mg}), aluminium becomes replaced by the solute X in the solution: in the Al-Mg-Cu, Al-Mg-Si, and Al-Mg-Zn systems, where $L_{\mathrm{alt,MgX}} < 0$, this means that magnesium is more strongly bound within the melt, since $L_{\mathrm{alt,MgX}}$ is more negative than $L_{\mathrm{alt,AlMg}}$. Therefore, a higher x_{Mg} is required to produce an Mg-containing oxide, resulting in the boundaries shifting to higher x_{Mg}. Conversely, in the Al-Mg-Mn system, where $L_{\mathrm{alt,MgX}} > 0$, a replacement of X for aluminium causes the magnesium to be less tightly bound within the melt, so a lower x_{Mg} is required to produce an Mg-containing oxide, shifting the boundaries to lower x_{Mg}. These effects become less pronounced as temperature increases, due to the increasing dominance of the entropy term (which is present in ideal mixing) over the enthalpy term added by Bragg-Williams Mixing.

5.6. Comparison to experimental data

Any theoretical model which claims to capture physical behaviour must be tested against experimental data to assess its validity. For binary Al-X (Appendix B.7.1) and ternary Al-Mg-X (Appendix B.7.2.2-3) systems, oxidation products of melts at a given composition and temperature are compared to oxide stability diagrams to see how the actual and predicted products and behaviour correlate. Additionally, in ternary Al-Mg-X systems, the presence of oxidation protection by microalloying is compared to these diagrams (Appendix B.7.2.4-5), to determine whether oxidation suppression by microalloying is a thermodynamic effect.

5.6.1. Binary systems – less reactive

In the case of less reactive solutes (Figure 5.6), namely Ag, B, Co, Cr, Cu, Fe, Ge, Mn, Ni, Si, and Zn, only Al_2O_3 is predicted throughout the composition-temperature range of interest. This is reflected in the literature data: in many systems there are direct experimental observations of Al_2O_3 films on Al-X melts without any unary or binary solute-containing oxides, namely Co

[19], Cu [7,20–22], Fe [7,21,23], Mn [7,23], but in other areas only data on solid alloy oxidation was available (Ag [24], B [25], Cr [26], Ni [27]), and in some cases no data was available at all (Ge). For Al-Si, most studies suggested that only Al_2O_3 formed [7,22,23], but other cases suggested that some silicon was incorporated into the oxide layer [21,28,29]; however, no silicon-containing oxide crystal structures were definitively identified.

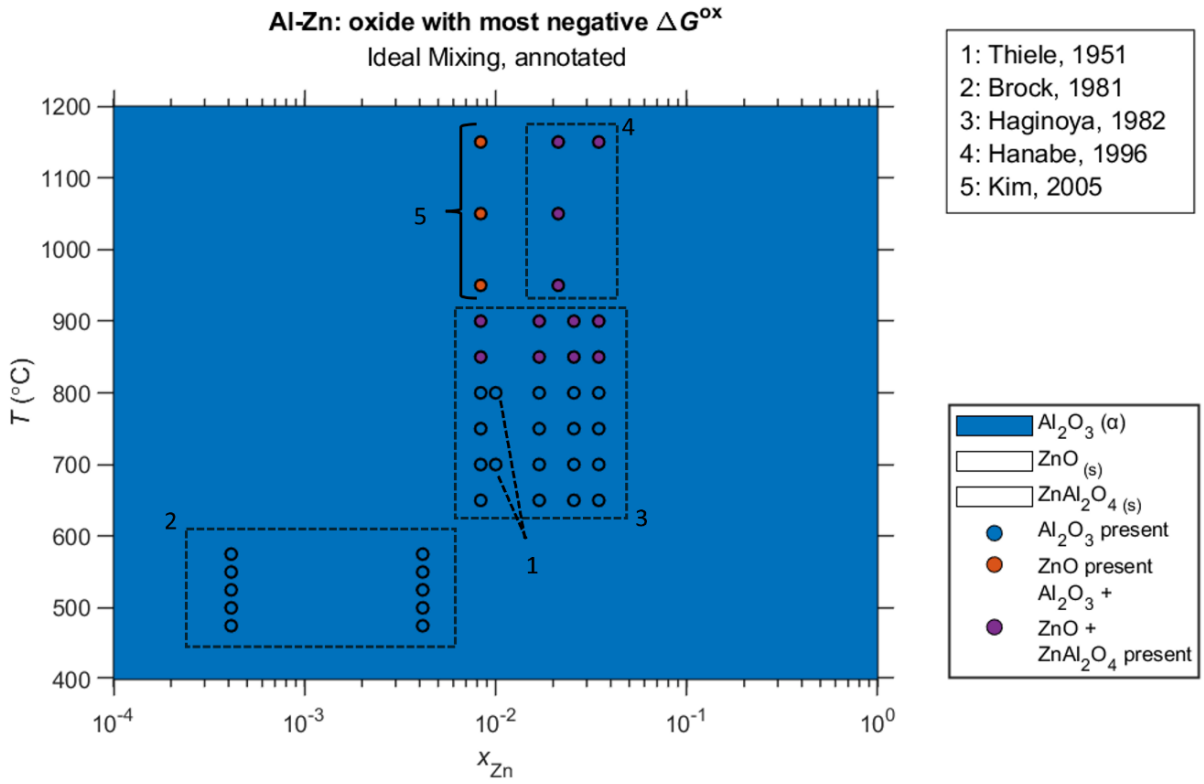


Figure 5.22. Al-Zn oxide stability diagram annotated with experimental data of products produced by melt oxidation (data from: 1 [7], 2 [30], 3 [23], 4 [31], 5 [32]).

The one notable exception in the 'less reactive' elements is the Al-Zn system (Figure 5.22). Below 800 °C, only Al_2O_3 is observed, but above this temperature, Zn-containing products are regularly identified, such as ZnO or $ZnAl_2O_4$. This can be attributed to the volatility of zinc in Al-Zn melts: zinc readily vaporises, reacts with oxygen in the atmosphere away from the melt to form ZnO [32–34], and then falls back onto the surface of the melt, where it reacts with the oxide skin on the melt to form $ZnAl_2O_4$, resulting in the three products observed [31]. However, this is not a discrepancy with the model: the model considers the most thermodynamically stable oxide which is in contact with the melt. ZnO only forms upon volatilisation of zinc, and

$ZnAl_2O_4$ only forms when this ZnO reacts with Al_2O_3; the oxide skin which forms by direct oxidation of the melt is Al_2O_3, as predicted. Additionally, ZnO or $ZnAl_2O_4$ that comes into contact with the melt is reduced to Al_2O_3 [31].

5.6.2. Binary systems – more reactive

In more reactive systems, products other than Al_2O_3 are predicted in the temperature-composition range of interest. In some systems, data could not be found (K, Gd, Zr), but in other systems, a range of oxidation products were found.

5.6.2.1. Group I elements

In Al-Li, a variety of oxidation products are observed in the experimental data, due to the high reactivity and volatility of lithium (Figure 5.23). All oxides predicted by the oxide stability diagrams (Li_2O, Li_5AlO_4, $AlLiO_2$, $AlLi_5AlO_8$) are observed somewhere in the temperature-composition range, those predicted not to be stable enough are not observed ($LiAl_7O_{11}$, $LiAl_{11}O_{17}$), and a carbonate, Li_2CO_3, is also reported. To predict the stability of carbonates on oxide stability diagrams, the ambient pressure of CO_2 must be known, since it is one of the decomposition products and therefore will affect its relative stability to oxides [35]. Carbonates are therefore excluded from this analysis, as well as the fact that, of the systems incorporated into this study, carbonates are only reported in the Al-Li system.

While there is not a clear correlation of oxidation products with either temperature or composition ($AlLiO_2$ is reported at each data point) there are some trends to note: at lower temperatures, products with a higher lithium content (Li_2CO_3, Li_2O, Li_5AlO_4) are reported alongside $AlLiO_2$, whereas observations at higher temperatures or lower lithium compositions either report Al_2O_3 alongside (ref. 1 on Figure 5.23) or do not report an additional lithium-rich oxide (refs. 8, 9 on Figure 5.23). However, some points go against this trend, such as the presence of $LiAl_5O_8$ at lower temperature/higher lithium content in Field/Scanans [36] (ref. 3

on Figure 5.23) or Li_2O at higher temperature in Field/Butler [37] (ref. 2 on Figure 5.23). Another caveat is that points below 600 °C, the alloy is solid: this is still relevant in the case of ideal mixing, since these lithium concentrations are below the solubility limits at this temperature, but the values of the Bragg-Williams parameters are only valid for liquids.

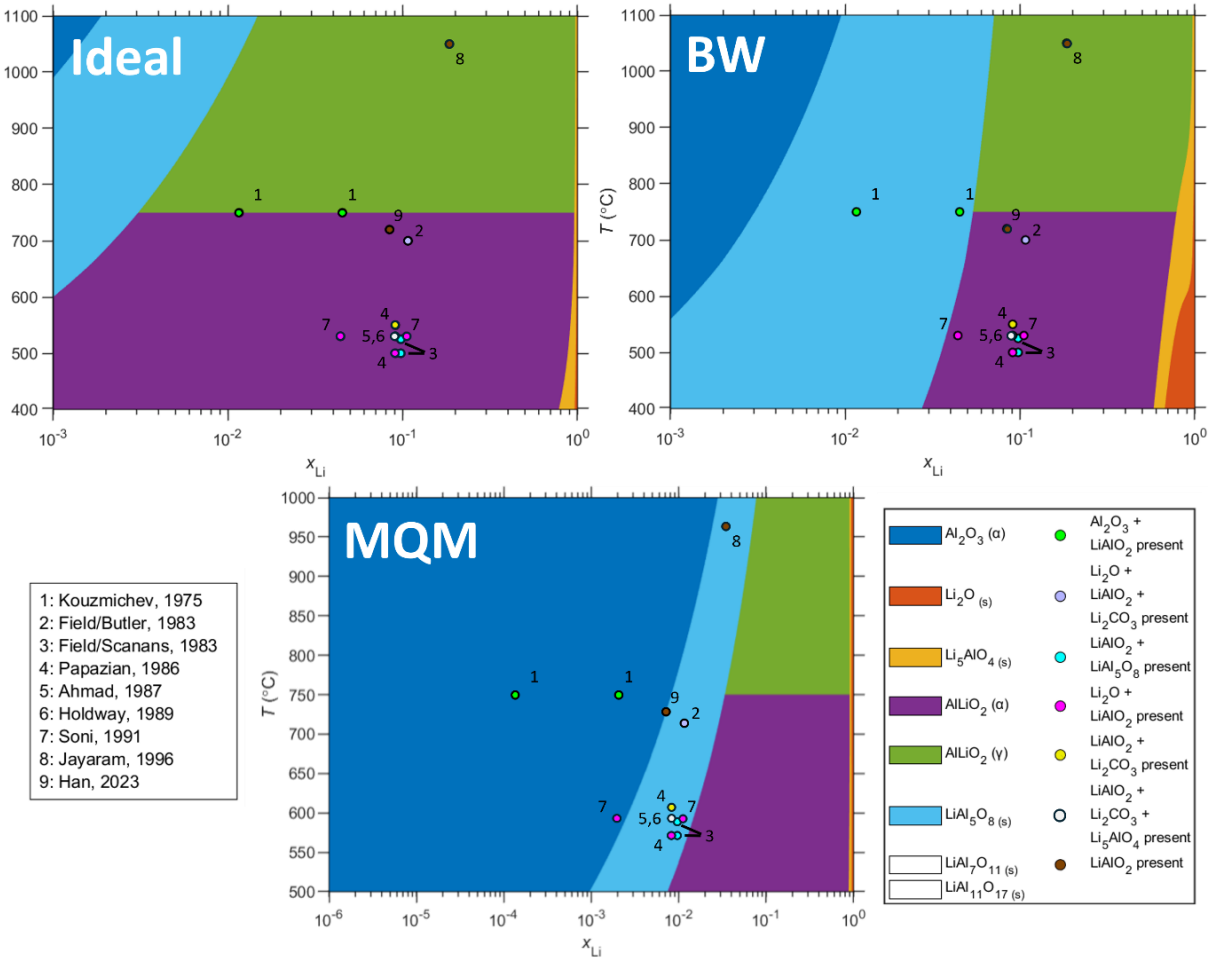


Figure 5.23. Al-Li oxide stability diagrams modelled with Ideal mixing, Bragg-Williams (BW) mixing, and the modified quasichemical model (MQM), annotated with data from literature (data from: 1 [38], 2 [37], 3 [36], 4 [39], 5 [40], 6 [41], 7 [42], 8 [43], 9 [44]). Larger versions can be found in Appendix B (B.7.1.2.5, B.7.1.3.5, and B.7.1.4.4 for ideal, Bragg-Williams, and MQM, respectively).

Despite these inconsistencies, it can be concluded that the oxide stability diagrams using ideal or Bragg-Williams mixing explain the presence of $AlLiO_2$ (α and γ) in the results well: with ideal mixing, all points lie in the $AlLiO_2$ region, whereas with Bragg-Williams Mixing, only two points, which report Al_2O_3 and $AlLiO_2$, lie outside the $AlLiO_2$ region. However, these lie in the $LiAl_5O_8$ region, which exists between the two products reported (Al_2O_3 and $AlLiO_2$), so this result is not inconsistent with the predictions. The modified quasichemical model does not

predict the trends well, with all points lying outside the $AlLiO_2$ region.

There is limited data on the Al-Na system, despite the widespread use of sodium as a silicon modifier. The only data found was the detection of $NaAlO_2$ at 1050 °C in an Al-3.2 wt.%Na alloy, which is consistent with the oxide stability diagram using Bragg-Williams mixing, but not ideal mixing or the modified quasichemical model (Figure 5.24). While the prediction of a mixed Al-Na oxide at only 3.2 wt.% sodium is good evidence for the validity of this theoretical approach, more data would be needed to definitively assess the merits of the chosen solution model in the Al-Na system.

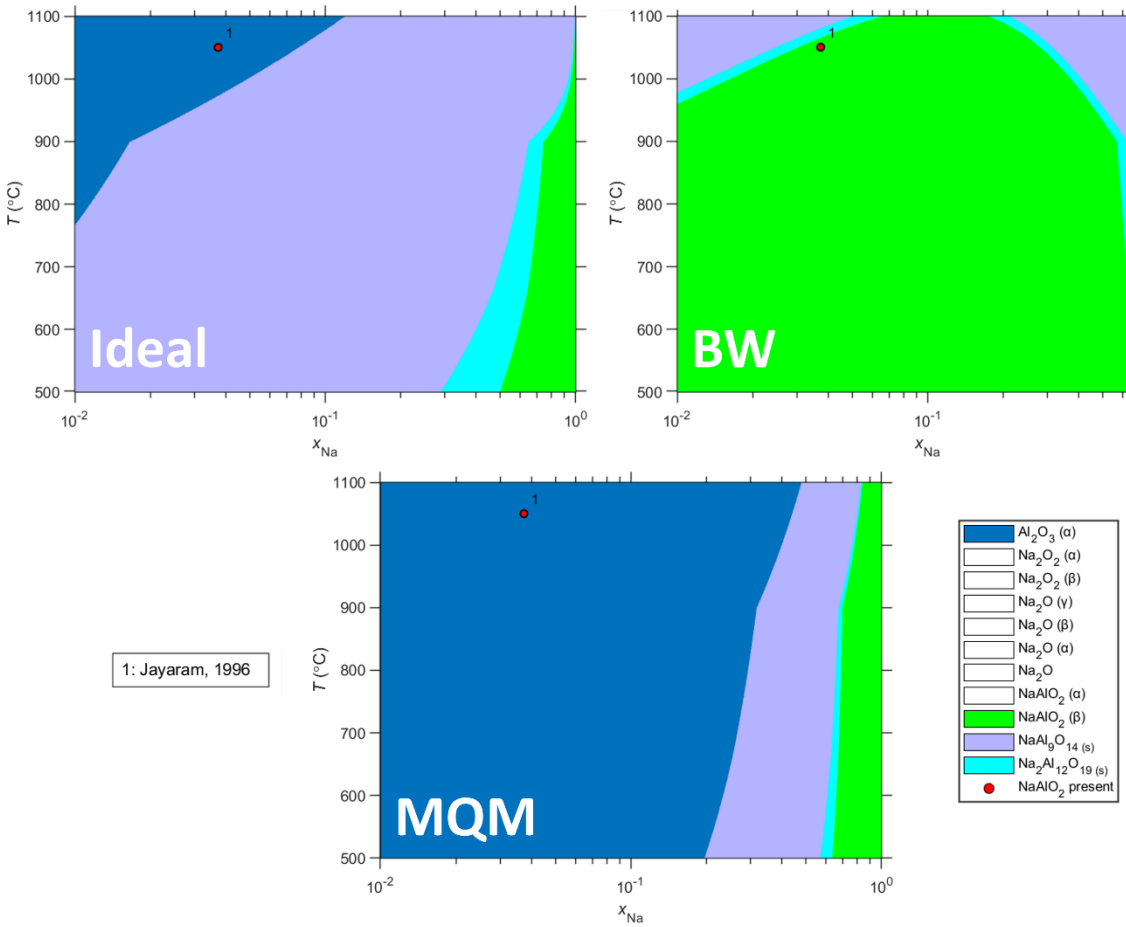


Figure 5.24. Al-Na oxide stability diagrams modelled with Ideal mixing, Bragg-Williams (BW) mixing, and the modified quasichemical model (MQM), annotated with data from literature (data from: 1 [43]). Larger diagrams can be found in Appendix B (B.7.1.2.7, B.7.1.3.7, and B.7.1.4.6 for ideal, BW, and MQM, respectively).

Therefore, for Group I elements, oxide stability diagrams best match the data with Bragg-Williams mixing. Ideal mixing is reasonably good for Al-Li but inaccurate for Al-Na (noting that there is only one data point for the Al-Na system) and the modified quasichemical model

overestimates the amount of solute required to form mixed Al-X oxides. However, more data would be needed to confirm these conclusions (especially in Al-Na and Al-K).

5.6.2.2. Group II elements

In the Al-Be system, BeO is found as the product of Al-Be melt oxidation in melts containing as little as 1-4 at.% Be [7,45], which is the predicted product in both ideal and Bragg-Williams mixing (Figure 5.25). The implementation of Bragg-Williams mixing shifts boundaries to lower x_X, which is not applicable to the data found.

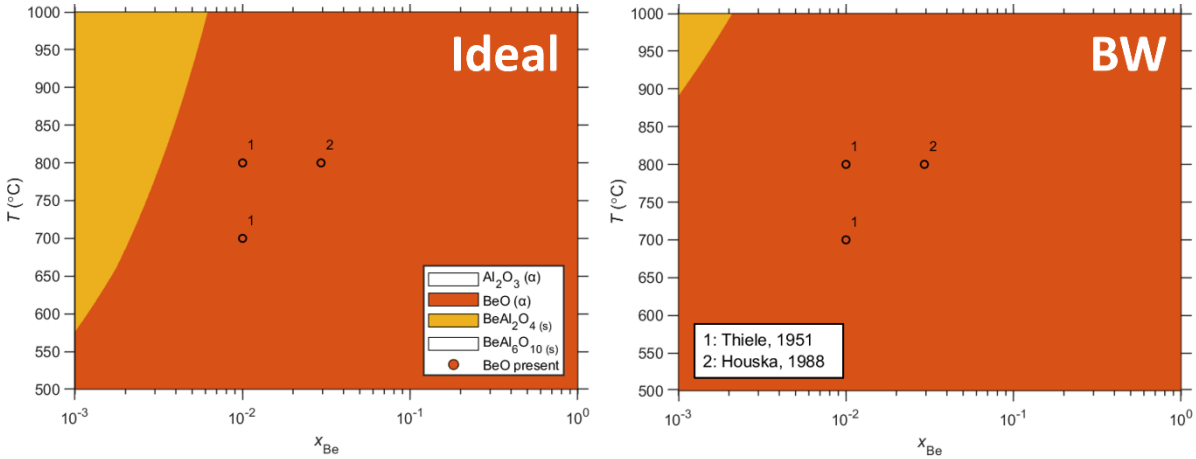


Figure 5.25. Al-Be oxide stability diagrams modelled with Ideal and Bragg-Williams (BW) mixing, annotated with data from literature (data from: 1 [7], 2 [45]). Larger diagrams can be found in Appendix B (B.7.1.2.1 and B.7.1.3.1 for ideal and BW respectively).

In the Al-Ca system, experimental data reports a variety of calcium aluminates even when the calcium concentration is in the 10^{-5}-10^{-4} range. The correspondence between experimental data and predictions by the oxide stability diagrams (Figure 5.26) appears to be best with Bragg-Williams mixing, which match the findings of $CaAl_4O_7$ and $CaAl_{12}O_{19}$ in the data from Khaleghifar [46], and are close to the reports of $CaAl_2O_4$ by Shevchenko [47]. MQM mixing comes closest to the reports of $Ca_3Al_2O_6$ by Thiele [7], a product justified by a limited number of diffraction rings from a (by modern standards) elementary set-up, but only predicts Al_2O_3 in all other cases.

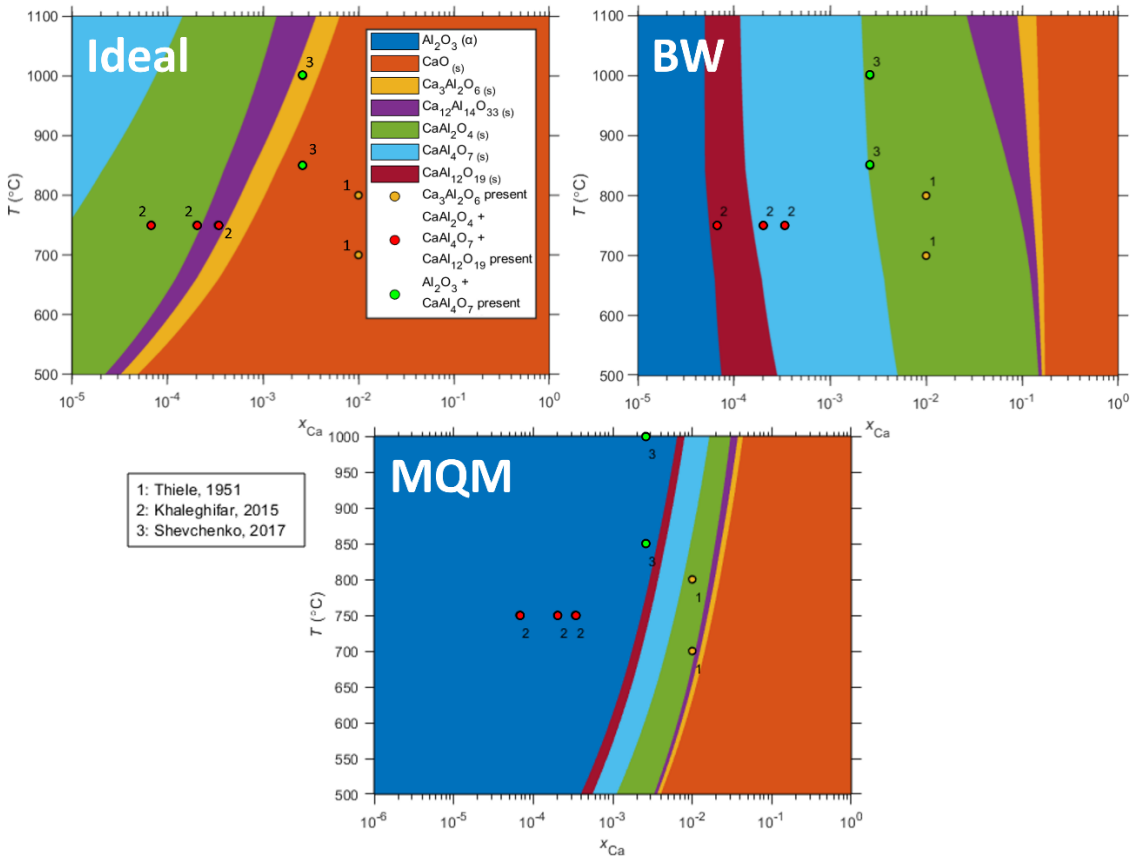


Figure 5.26. Al-Ca oxide stability diagrams modelled with Ideal mixing, Bragg-Williams (BW) mixing, and the modified quasichemical model (MQM), annotated with data from literature (data from: 1 [7], 2 [46], 3 [47]). Larger diagrams can be found in Appendix B (B.7.1.2.2, B.7.1.3.2, and B.7.1.4.1 for ideal, BW, and MQM, respectively).

In the case of Al-Mg, likely the most studied binary system studied in terms of melt oxidation, it is widely accepted that as the concentration of magnesium increases, MgO becomes favoured over $MgAl_2O_4$ as a melt oxidation product [9]. Equivalently, as oxidation progresses in an Al-Mg melt and the concentration of Mg decreases, $MgAl_2O_4$ becomes favoured over MgO, a transition which is attributed to the breakaway oxidation of Al-Mg alloys and the 'double sigmoid' shape in TGA studies [5,7,48].

Indeed, the approach and analysis in this chapter is inspired by, and based on the principles of, this justification: previous investigators have constructed diagrams mapping out regions of stability of $MgAl_2O_4$ and MgO as a function of melt concentration and temperature [9,49,50], or referenced a critical concentration of magnesium for the change between MgO and $MgAl_2O_4$, thus using these principles indirectly [51,52]. However, in all cases, only ideal mixing was assumed, and the approach was not applied to other aluminium alloy systems.

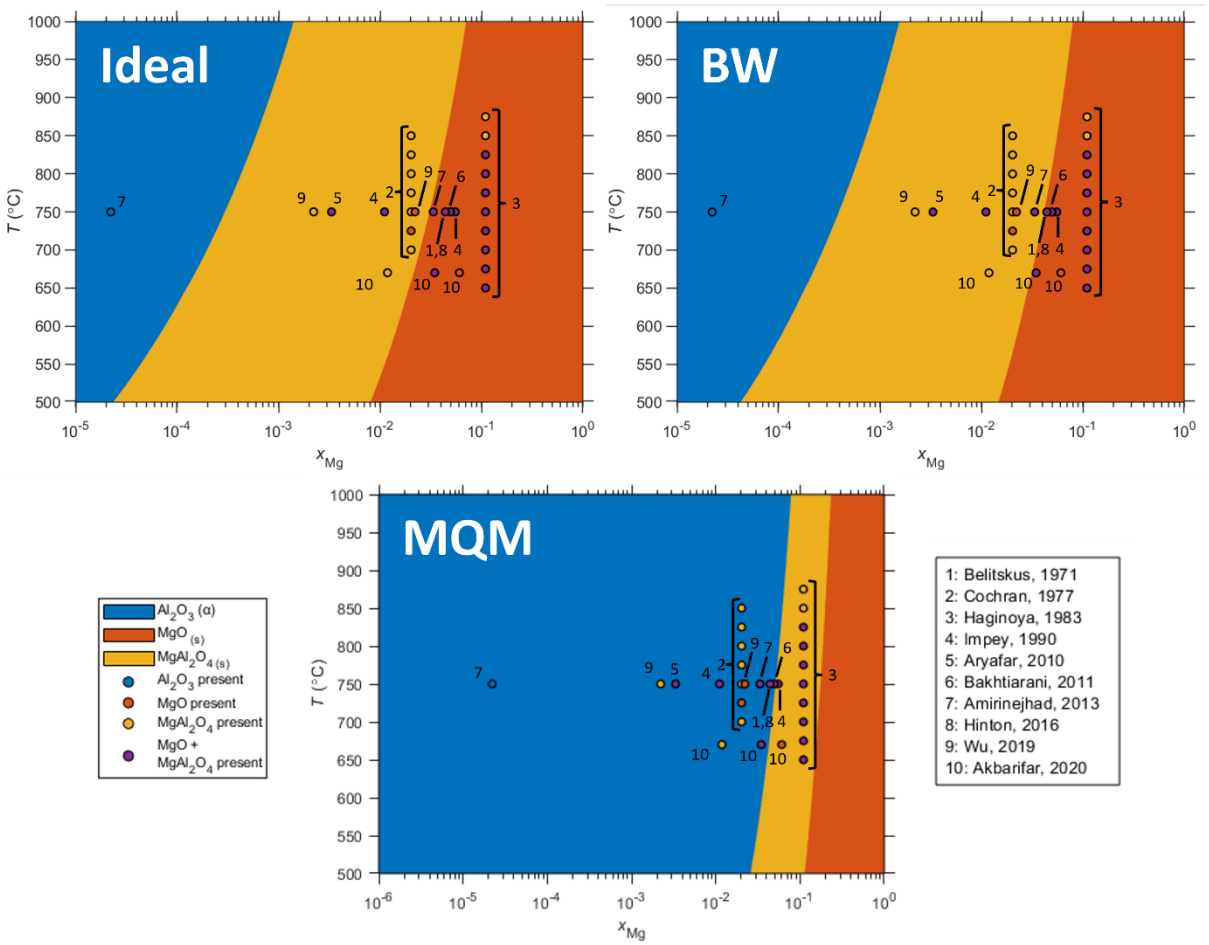


Figure 5.27. Al-Mg oxide stability diagrams modelled with Ideal mixing, Bragg-Williams (BW) mixing, and the modified quasichemical model (MQM), annotated with data from literature (data from: 1 [53], 2 [8], 3 [48], 4 [54], 5 [55], 6 [56], 7 [57], 8 [21], 9 [9], 10 [58]). Larger diagrams can be found in Appendix B (B.7.1.2.6, B.7.1.3.6, and B.7.1.4.5 for ideal, BW, and MQM, respectively).

Both ideal and Bragg-Williams mixing correlate well with the data (Figure 5.27), with the $MgAl_2O_4$+MgO data lying largely in the MgO region and the $MgAl_2O_4$ data lying largely in the $MgAl_2O_4$ region; there is little difference between ideal and Bragg-Williams Mixing due to the small magnitude of the ${}^{i}L_{\mathrm{AlMg}}$ parameters, so it is difficult to assess which one is superior. Like Al-Ca, the diagram assuming MQM mixing does not correlate well, with many data points reporting Mg-containing oxides lying in the Al_2O_3 region.

In the Al-Sr system, a variety of Sr-containing oxides are reported: Miresmaeili [59] speculates on the existence of "Sr-containing oxides", but the only Al-Sr oxides mentioned are SrO and $SrAl_2O_4$. The same is true for Nateghian [60], whose results show four distinct oxides, likely to be SrO, Al_2O_3, and two intermediate Al-Sr binary oxides based on EDX data. Hinton's

conclusions [21] of the presence of SrO are based on XRD peaks barely above background or masked by larger alumina peaks; the EDX data indicates the presence of a mixed Al-Sr oxide. Therefore, the points presented are likely to be mixed SrO-Al_2O_3 oxides, showing the MQM prediction to once again be off the mark (Figure 5.28). Diagrams with ideal and Bragg-Williams mixing predict mixed Al-Sr oxides in the region of the collected data, but the relative merits cannot be determined without precise phase identification, which is lacking in the data.

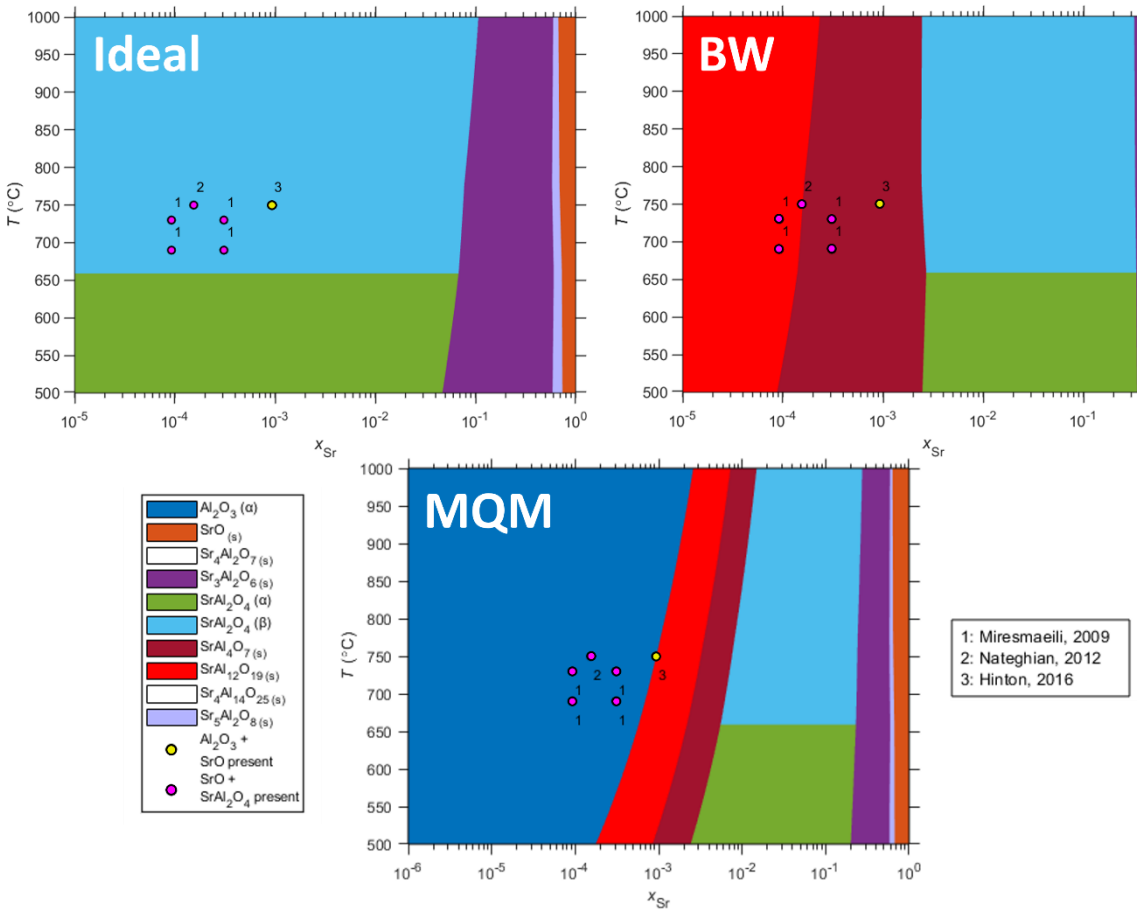


Figure 5.28. Al-Sr oxide stability diagrams modelled with Ideal mixing, Bragg-Williams (BW) mixing, and the modified quasichemical model (MQM), annotated with data from literature (data from: 1 [59], 2 [60], 3 [21]). Larger diagrams can be found in Appendix B (B.7.1.2.9, B.7.1.3.9, and B.7.1.4.8 for ideal, BW, and MQM, respectively).

In summary, for group II elements, oxide stability diagrams using Bragg-Williams mixing predict melt oxidation products well and explain the existence of mixed Al-X oxides in experimental results. Ideal mixing is an acceptable approximation, but MQM mixing overestimates the amount of solute required to produce a mixed Al-X oxide.

5.6.2.3. Lanthanides

In Al-Ce, melt oxidation data comes from Ganiev et al. [61], which reports $CeAlO_3$ as the main oxidation product. However, counterintuitively, a decrease in cerium concentration results in the prevalence of CeO_2 over $CeAlO_3$; as the temperature is raised, both CeO_2 and $CeAlO_3$ are observed (Figure 5.29). The prevalence of CeO_2 over Ce_2O_3 is justified by Ganiev et al. [61] by acknowledging that Ce_2O_3 is 'unstable in air', and rapidly oxidises to form CeO_2. While the predictions and results of unary oxides are inconsistent, there is some consistency in the Bragg-Williams diagram with the $CeAlO_3$ points.

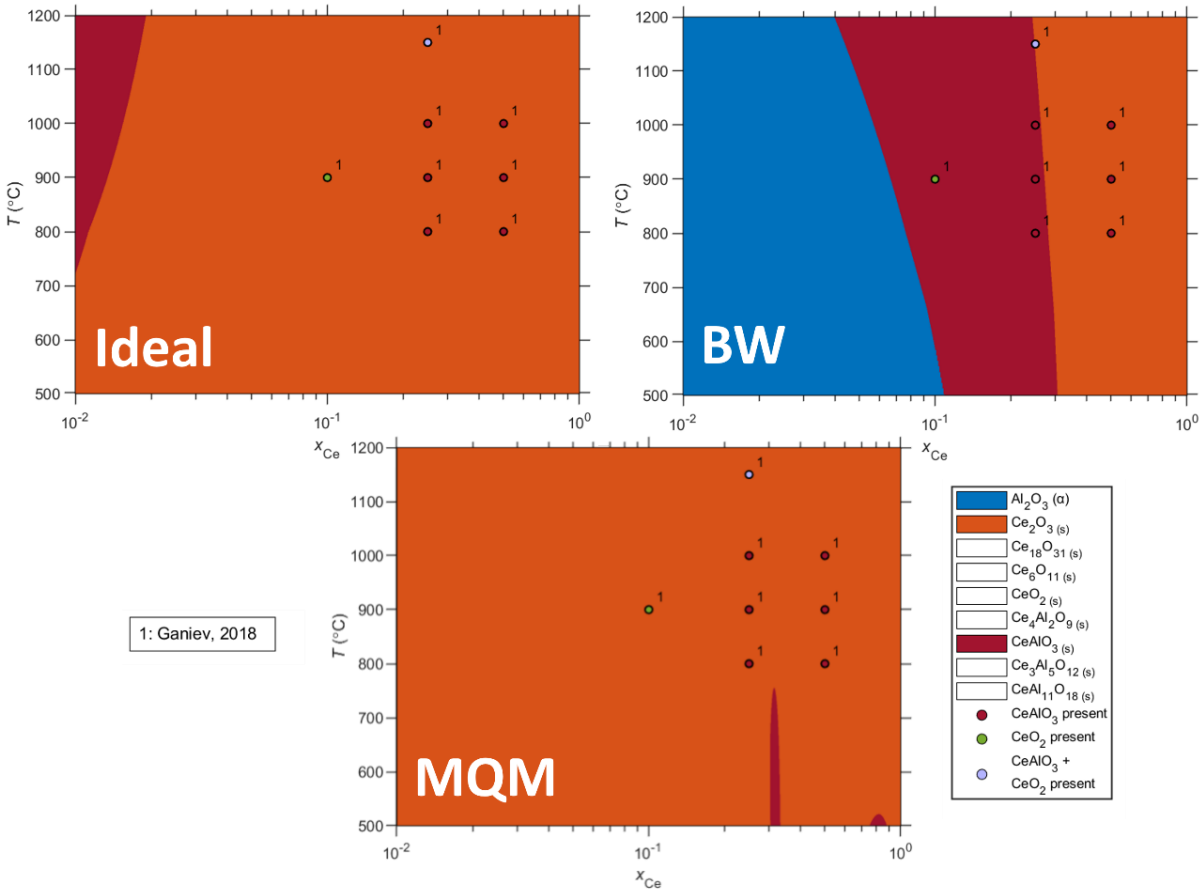


Figure 5.29. Al-Ce oxide stability diagrams modelled with Ideal mixing, Bragg-Williams (BW) mixing, and the modified quasichemical model (MQM), annotated with data from literature (data from: 1 [61]). Larger diagrams can be found in Appendix B (B.7.1.2.3, B.7.1.3.3, and B.7.1.4.2 for ideal, BW, and MQM, respectively).

In addition, the reverse trend where a ceria becomes favoured over a cerium aluminate (CeO_2 over $CeAlO_3$) with decreasing cerium concentration is captured by the modified quasichemical model (the small $CeAlO_3$ region at $x_{Ce} = 0.3 - 0.4$), but the diagram predicts this occurring

at a lower temperature than observed (Figure 5.29).

In Al-La (Figure 5.30), a mixture of Al_2O_3 and La_2O_3 is seen at lower x_{La}, and at higher x_{La}, a mixture of La_2O_3 and $LaAl_{11}O_{18}$. In the oxide stability diagrams, $LaAlO_3$ is the predicted binary oxide, which is inconsistent with the experimental results, but the presence of La_2O_3 in all points is consistent with most of the diagrams. However, there are not enough data points to determine which solution model is best.

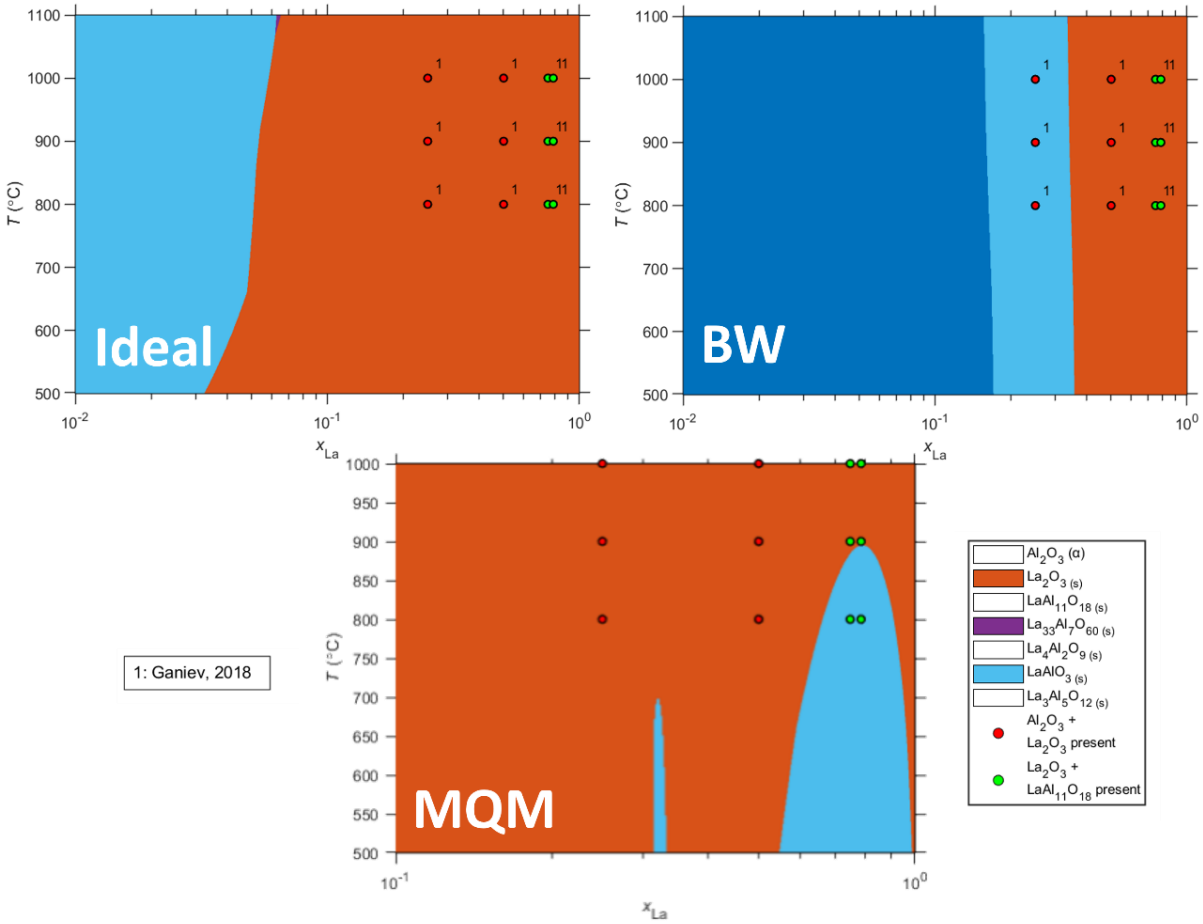


Figure 5.30. Al-La oxide stability diagrams modelled with Ideal mixing, Bragg-Williams (BW) mixing, and the modified quasichemical model (MQM), annotated with data from literature (data from: 1 [61]). Larger diagrams can be found in Appendix B (B.7.1.2.4, B.7.1.3.4, and B.7.1.4.3 for ideal, BW, and MQM, respectively).

The Al-Sc system (scandium is not technically a lanthanide, but is a trivalent rare earth element, so best included in this section) is modelled with and without $ScAlO_3$, since the data for $ScAlO_3$ [62] is questionable due to its very low ΔG_f value that causes it to dominate the stability diagrams when included. However, due to a lack of available data, the accuracy of this $\Delta G_f(T)$ fit cannot be verified. Without the inclusion of $ScAlO_3$, the stability diagram using Bragg-

Williams mixing corresponds well to the data; in ideal mixing, all Al_2O_3+$ScAlO_3$ points lie in the Sc_2O_3 region, and with MQM mixing, some of them do. When $ScAlO_3$ is included, all data points lie in the $ScAlO_3$ region but, of all the models tested, the Bragg-Williams model has Sc_2O_3 regions closest to the Sc_2O_3 data points.

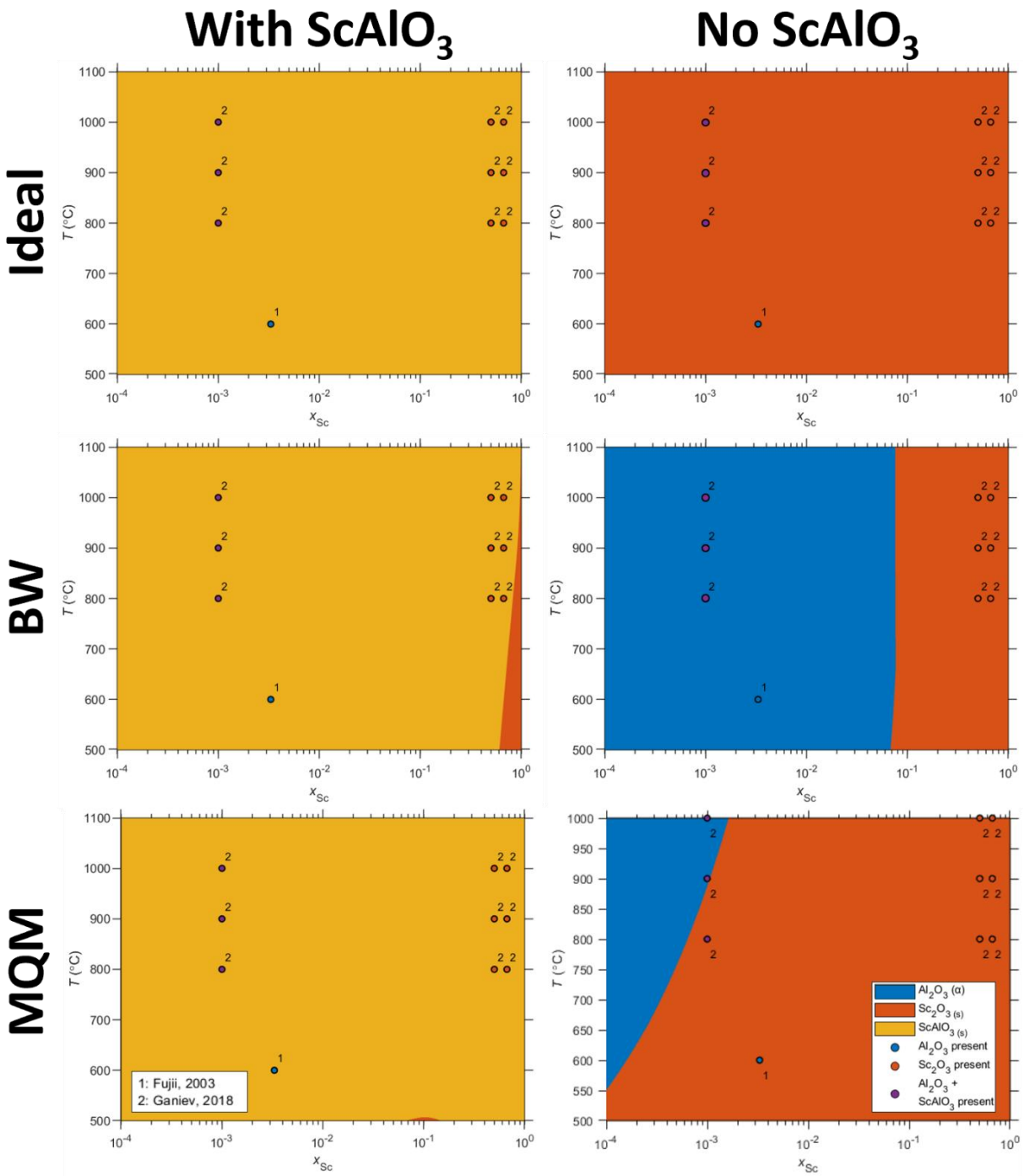


Figure 5.31. Al-Sc oxide stability diagrams modelled with Ideal mixing, Bragg-Williams (BW) mixing, and the modified quasichemical model (MQM), annotated with data from literature (data from: 1 [63], 2 [61]). Larger diagrams can be found in Appendix B (B.7.1.2.8, B.7.1.3.8, and B.7.1.4.7 for ideal, BW, and MQM, respectively).

In general, the products of oxidation of these systems are most accurately predicted by the Bragg-Williams model. However, there are significant discrepancies in terms of the products predicted, such as Ce_2O_3 instead of CeO_2, and $LaAlO_3$ instead of $LaAl_{11}O_{18}$, and issues with the reliability of available thermodynamic and experimental data: the ΔG_f fit for $ScAlO_3$ cannot be verified, and the data is almost entirely from one study [61].

5.6.3. Ternary Al-Mg-X systems: products

Ternary Al-Mg-X systems are evaluated in two ways. Firstly, like the binary systems, products of melt oxidation are compared to the predictions from the oxide stability diagrams (Appendix B.7.2.2-3). Secondly, the prevalence of 'melt oxidation protection', i.e. where microalloying has suppressed oxidation of Al-Mg alloys, is plotted against melt composition and temperature to determine correlations with the oxide stability diagrams (Appendix B.7.2.4-5).

5.6.3.1. Group II elements

In the Al-Mg-Be system, the data generally match the oxide stability diagrams: all data found reports the presence of MgO, and in some there are also reports of BeO and $BeAl_2O_4$, or BeO, Al_2O_3, and $BeAl_2O_4$ alongside (Figure 5.32).

With ideal mixing, all points fall within the MgO region, and in Bragg-Williams mixing this is also true, except for two MgO points at 700 °C falling within the $MgAl_2O_4$ region. Additionally, one mixed BeO/$BeAl_2O_4$/MgO point falls on the MgO/BeO boundary. The oxide stability diagrams do not predict $BeAl_2O_4$ at these composition-temperature points, but there is a region of $BeAl_2O_4$ at lower magnesium concentrations, so a depletion of magnesium may cause $BeAl_2O_4$ to become stable as oxidation progresses. Generally, both models predict the presence of MgO (and the lack of $MgAl_2O_4$) well, with ideal mixing matching against data slightly better than Bragg-Williams mixing.

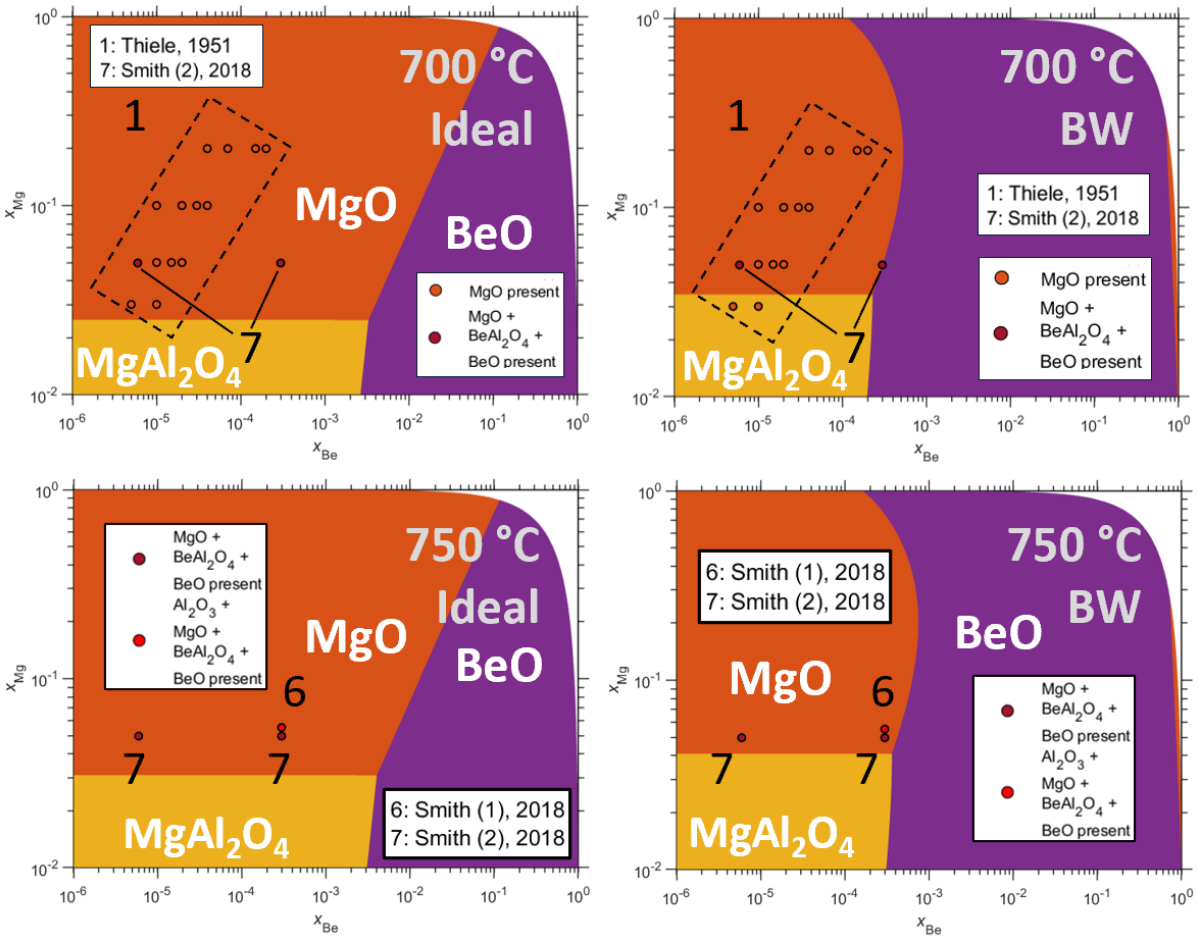


Figure 5.32. Al-Mg-Be ternary oxide stability diagrams modelled with Ideal mixing and Bragg-Williams (BW) mixing, annotated with data from literature (data from: 1 [7], 6 [65], 7 [66]) showing products produced from oxidising Al-Mg-Be melts. Larger diagrams can be found in Appendix B (B.7.2.2.1 and B.7.2.3.1 for ideal and BW, respectively).

In the Al-Mg-Ca system, all points again contain MgO, which are mostly consistent with the diagrams (Figure 5.33). In the ideal system, one of the points lies in the CaO region, but CaO is not reported. However, the claims of the ternary oxide $CaMg_2Al_{16}O_{27}$ from Ha [64] are based on thermodynamic calculations and not on direct experimentation: it is only established that there is a Ca-containing oxide in their experimental results.

The data at 750 °C shows a correlation with the region of $Ca_3MgAl_4O_{10}$, a different ternary oxide: in ideal mixing, the points which report only MgO lie either on or close to this ternary oxide region, whereas the points which report MgO and $MgAl_2O_4$ lie in the MgO region. In the Bragg-Williams diagram at 750 °C, all points lie in the MgO region. Therefore, diagrams predict the presence of MgO well but differ in which ternary oxide is predicted.

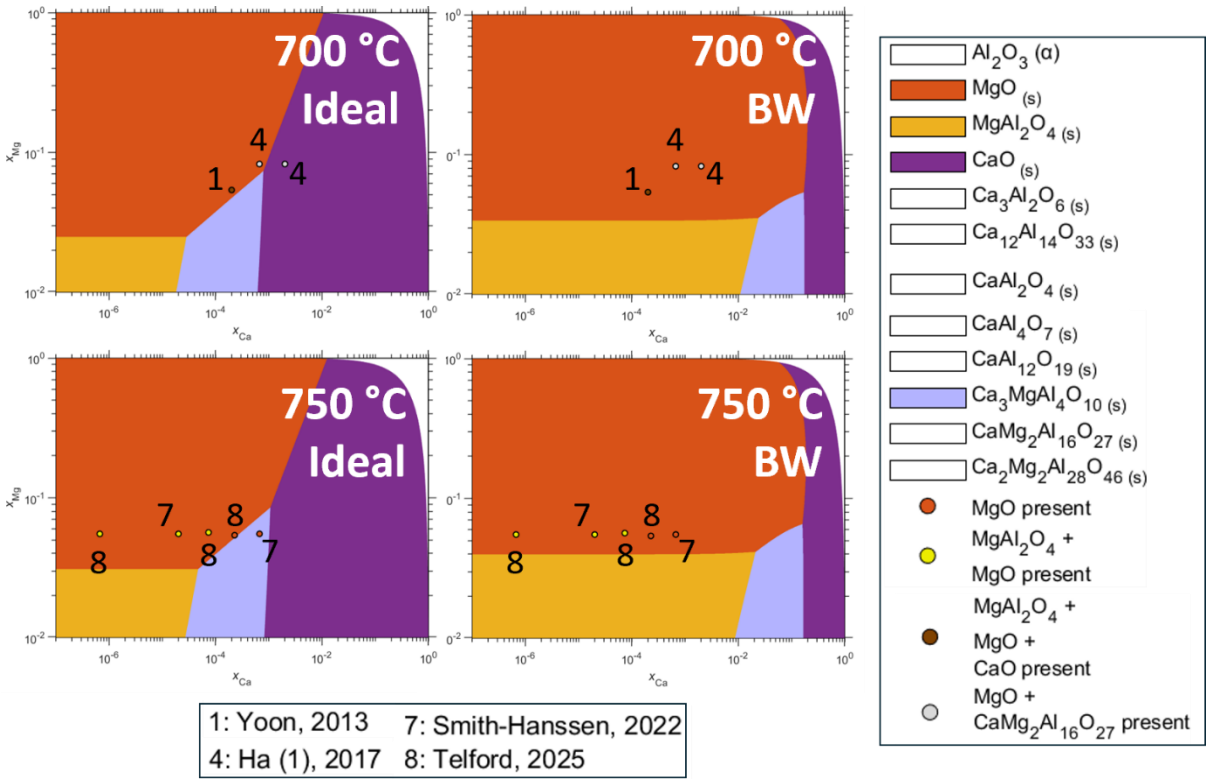


Figure 5.33. Al-Mg-Ca ternary oxide stability diagrams modelled with Ideal mixing and Bragg-Williams (BW) mixing, annotated with data from literature (data from: 1 [67], 4 [64], 7 [5], 8 [present work]) showing products produced from oxidising Al-Mg-Ca melts. Larger diagrams can be found in Appendix B (B.7.2.2.2 and B.7.2.3.2 for ideal and BW, respectively).

In the Al-Mg-Sr system (Figure 5.34), the oxide stability diagrams do not match up well with the products. With ideal mixing, all points lie in the $SrAl_2O_4$ region, but this phase is not reported; the only Sr-containing oxide reported is $SrAl_4O_7$, which is predicted at lower x_{Mg}.

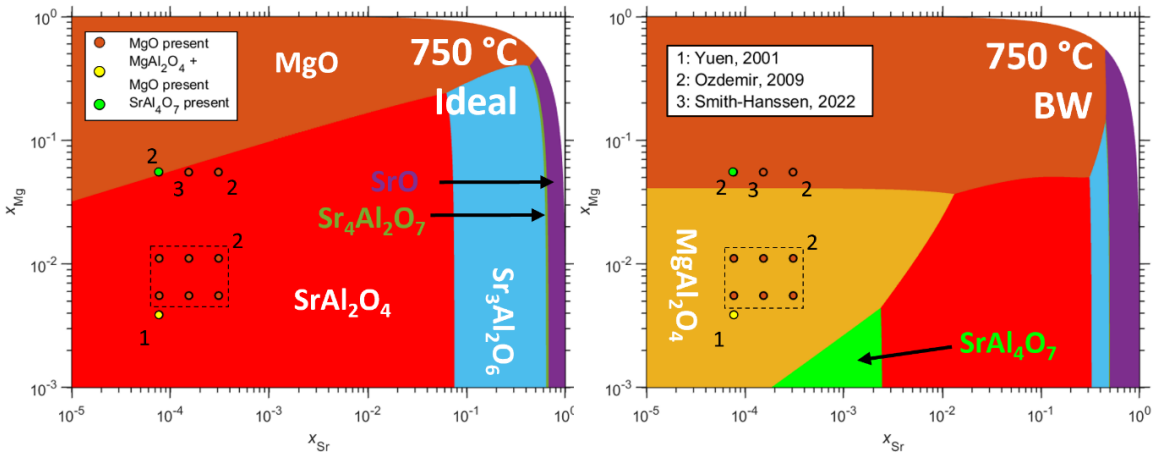


Figure 5.34. Al-Mg-Sr ternary oxide stability diagrams modelled with ideal and Bragg-Williams (BW) mixing, annotated with literature data (data from: 1 [68], 2 [69], 3 [5]) showing products produced from oxidising Al-Mg-Sr melts. Larger diagrams can be found in Appendix B (B.7.2.2.6 and B.7.2.3.6 for Ideal and BW).

Most of the points where MgO is reported lie at a lower x_{Mg} than the MgO region. In Bragg-Williams mixing, the MgO points lie either in the MgO or $MgAl_2O_4$ regions; there is therefore

some correspondence, but the diagrams are generally inconsistent with the data.

Overall, the oxide stability diagrams match the reported products well in the Al-Mg-Be and Al-Mg-Ca systems, but there are significant discrepancies in the Al-Mg-Sr system.

5.6.3.2. Lanthanides

For lanthanides (Figure 5.35), data from Smith-Hanssen's study on the microalloying of Al-Mg melts [5] was used, specifically cerium, lanthanum, and gadolinium.

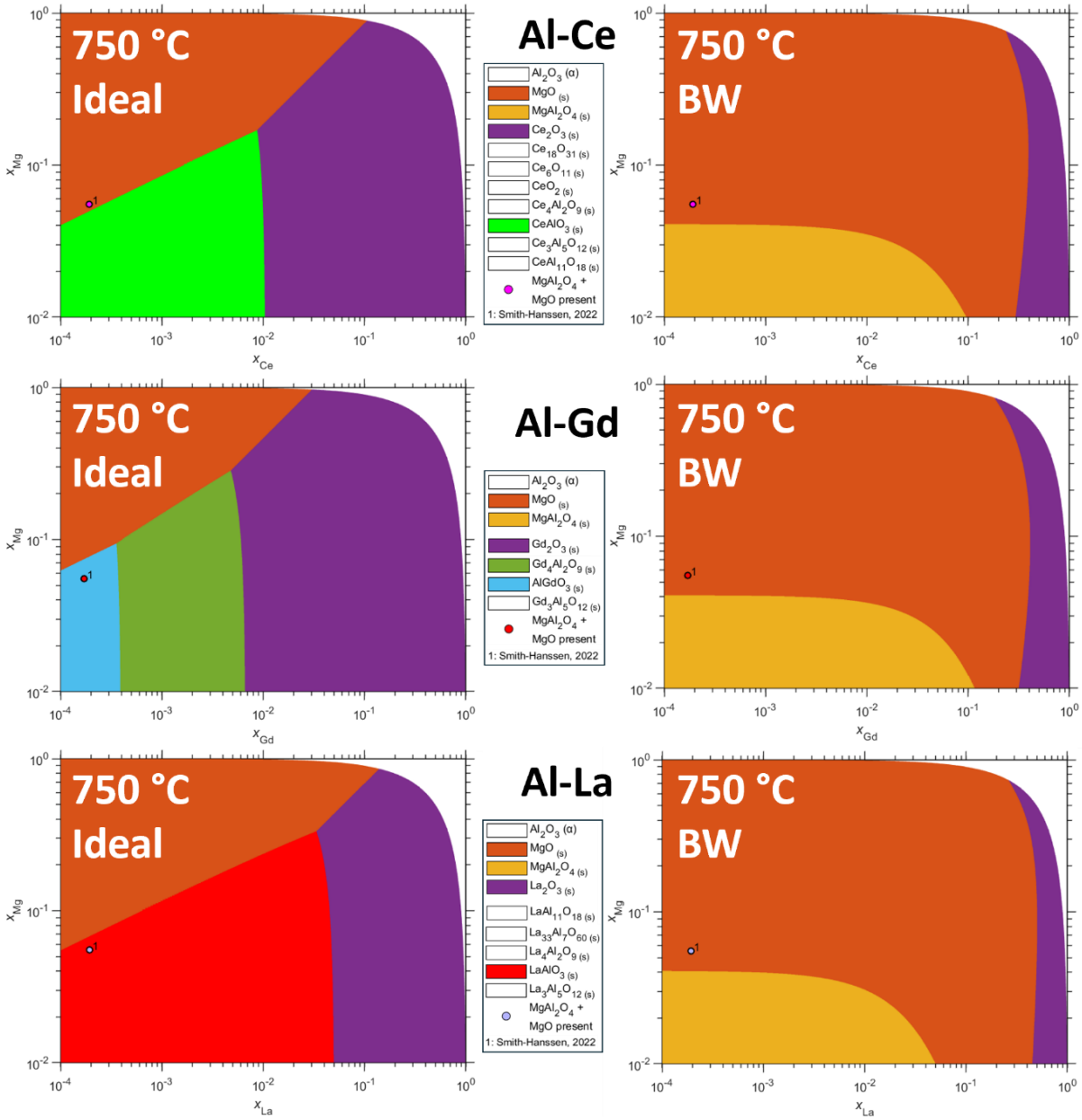


Figure 5.35. Al-Mg-X ternary oxide stability diagrams for lanthanides (Ce, La, Gd) modelled with Ideal mixing and Bragg-Williams (BW) mixing, annotated with data from literature (data from: 1 [5]) showing products produced from oxidising Al-Mg-X (X = Ce, La, Gd) melts. Larger diagrams can be found in Appendix B (B.7.2.2.3-5 and B.7.2.3.3-5 for ideal and BW, respectively).

In each case, the addition did not suppress oxidation, producing both MgO and $MgAl_2O_4$. In these cases, the products are described well by the diagrams with Bragg-Williams mixing, with the points lying in the MgO region, near to the $MgAl_2O_4$ region, but in the ideal case, points lie near the boundary between MgO and the $AlXO_3$ oxide. In these systems, the $AlXO_3$ oxide is not observed, so the ideal case is not consistent.

5.6.4. Ternary Al-Mg-X systems: protection

It has been commonly reported that small additions of group II elements (Be [5,7,8,65,66], Ca [5,64,67], Sr [5,64,68]) can suppress the oxidation of Al-Mg alloys, whereas lanthanide elements (Ce, Gd, La [5]) do not. Since the onset of breakaway oxidation is associated with the formation of $MgAl_2O_4$, and the protection with the formation of a mixed MgO-BeO/CaO/SrO layer, it follows that these oxide stability diagrams should be compared to the presence of melt oxidation protection to determine whether the thermodynamic stability of oxides in contact with the melt can explain the observed phenomena.

In the Al-Mg-Be system, there does not appear to be a clear correlation between the presence of oxidation protection and the regions in the oxide stability diagrams, either with ideal or Bragg-Williams mixing (Figure 5.36). The cut-off for protection appears to be a line of increasing x_{Mg} and x_{Be}, i.e. more beryllium is needed to suppress oxidation as x_{Mg} increases, but this line (Figure 5.36, yellow dashed line) does not correspond to any region boundaries on the oxide stability diagrams.

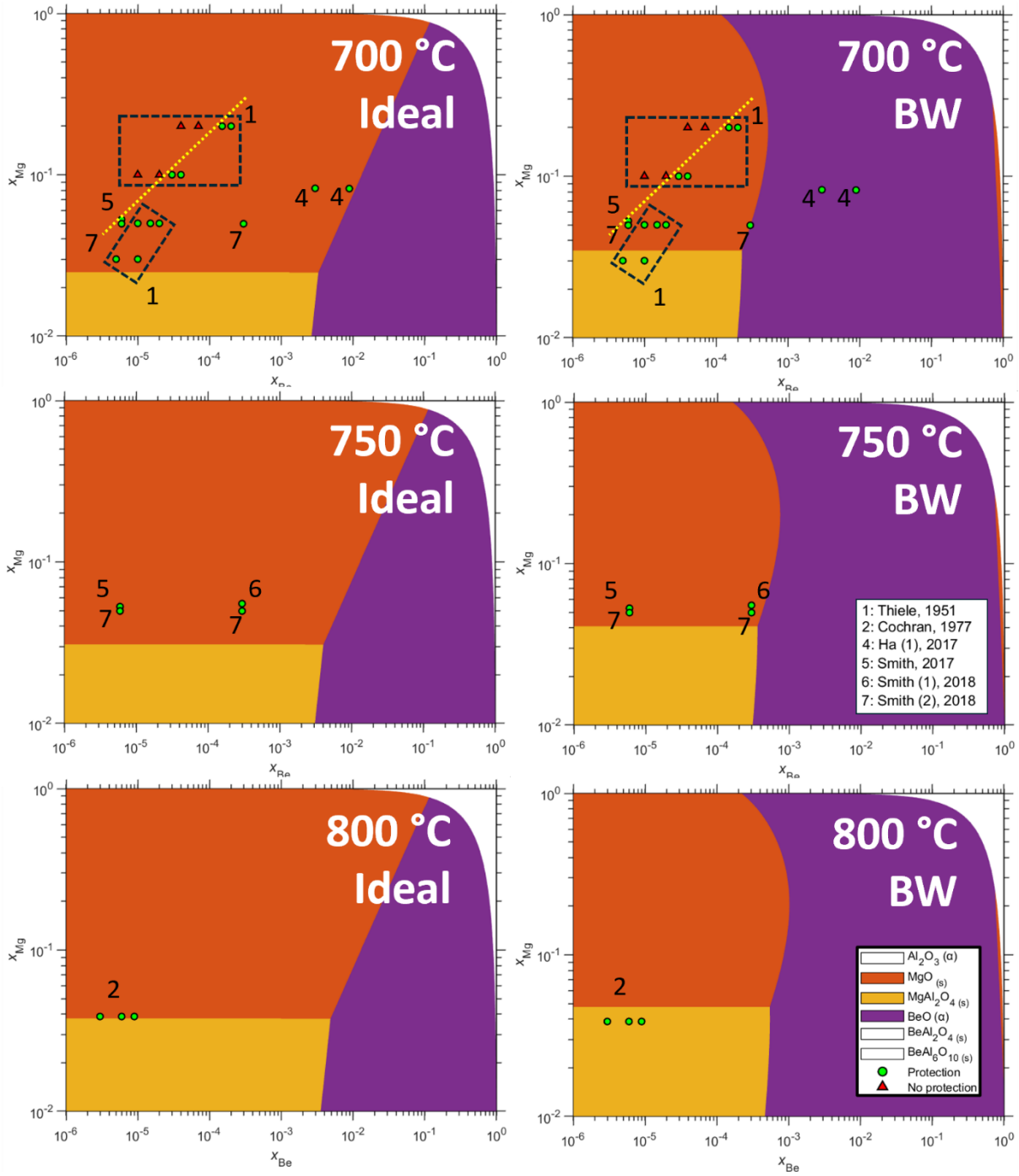


Figure 5.36. Al-Mg-Be ternary oxide stability diagrams modelled with Ideal mixing and Bragg-Williams (BW) mixing, annotated with literature data (data from: 1 [7], 2 [8], 4 [6], 5 [66], 6 [65], 7 [70]) indicating oxidation protection. A yellow line indicates the approximate critical x_{Mg}-x_{Be} concentrations for oxidation protection. Larger diagrams can be found in Appendix B (B.7.2.4.1 and B.7.2.5.1 for ideal and BW, respectively).

In the Al-Mg-Ca system (Figure 5.37), there is a plausible explanation to the presence of protection (Figure 5.38). As oxides are produced from the oxidation of a melt, its composition will change depending on the composition of the oxide produced: if MgO is produced, then x_{Mg} will decrease while x_{Ca} (to a first approximation, since $x_{\mathrm{Al}} \gg x_{\mathrm{Mg}} \gg x_{\mathrm{Ca}}$) remains

constant; on the oxide stability diagram, this means the composition of the point goes downwards. Similarly, if CaO is produced, x_{Ca} will decrease while x_{Mg} remains constant, so the point will shift to the left. In the $MgAl_2O_4$ and $Ca_3MgAl_4O_{10}$ regions, production of these oxides means a shift downwards and to the left respectively (Figure 5.38, top left).

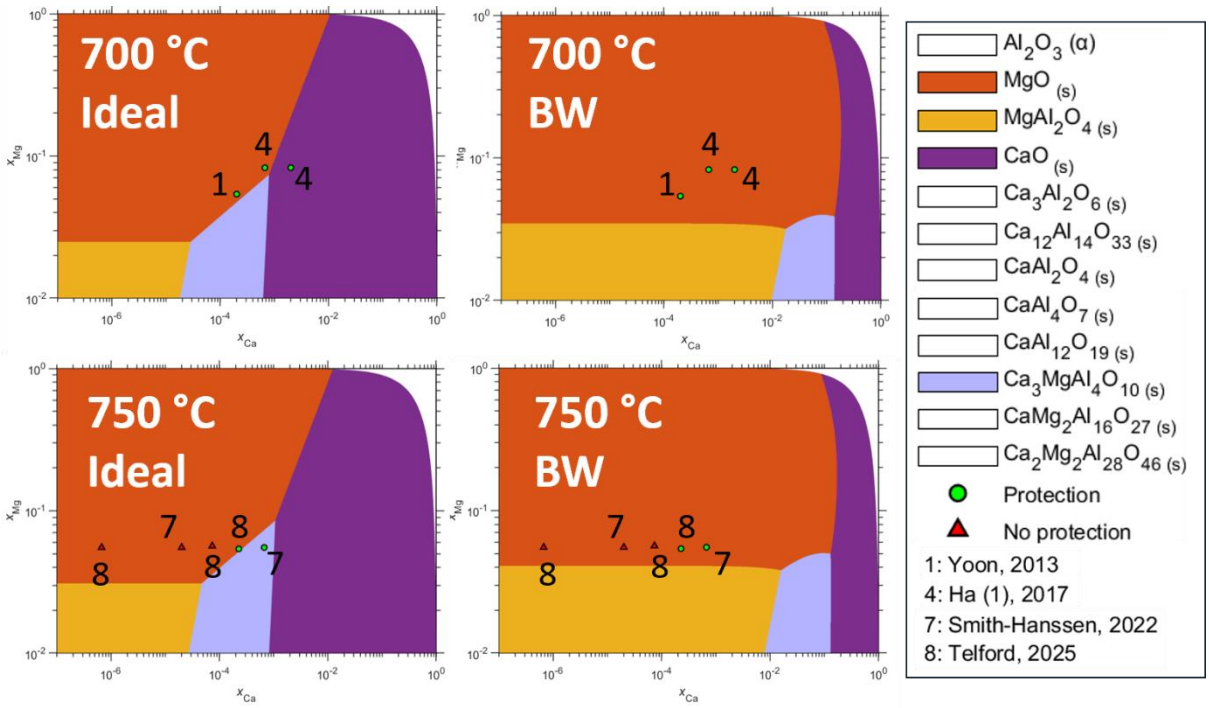


Figure 5.37. Al-Mg-Ca ternary oxide stability diagrams modelled with Ideal and Bragg-Williams (BW) mixing, annotated with data from literature (data from: 1 [67], 4 [6], 7 [5], 8 [present work]) indicating presence of oxidation protection. Larger diagrams can be found in Appendix B (B.7.2.4.2 and B.7.2.5.2 for ideal and BW).

When the melt composition hits a boundary, the direction may change (Figure 5.38, top left). If the point was previously in the CaO region but hits the MgO region, then both MgO and CaO will be produced: any deviation away from the boundary will lead to the production of the oxide that will move the composition back to the boundary (Figure 5.38, top right), which is also the case for MgO and $Ca_3MgAl_4O_{10}$ regions. However, on the MgO-$MgAl_2O_4$ boundary, both the production of MgO and $MgAl_2O_4$ depletes the melt of magnesium while not affecting the calcium concentration, so the melt continues to deplete in magnesium when the MgO-$MgAl_2O_4$ boundary is crossed. The same occurs for the CaO-$Ca_3MgAl_4O_{10}$ boundary, where the melt composition continues to move away from the boundary (Figure 5.38, top right), except that it is calcium that is depleted, and the composition moves to the left instead of down.

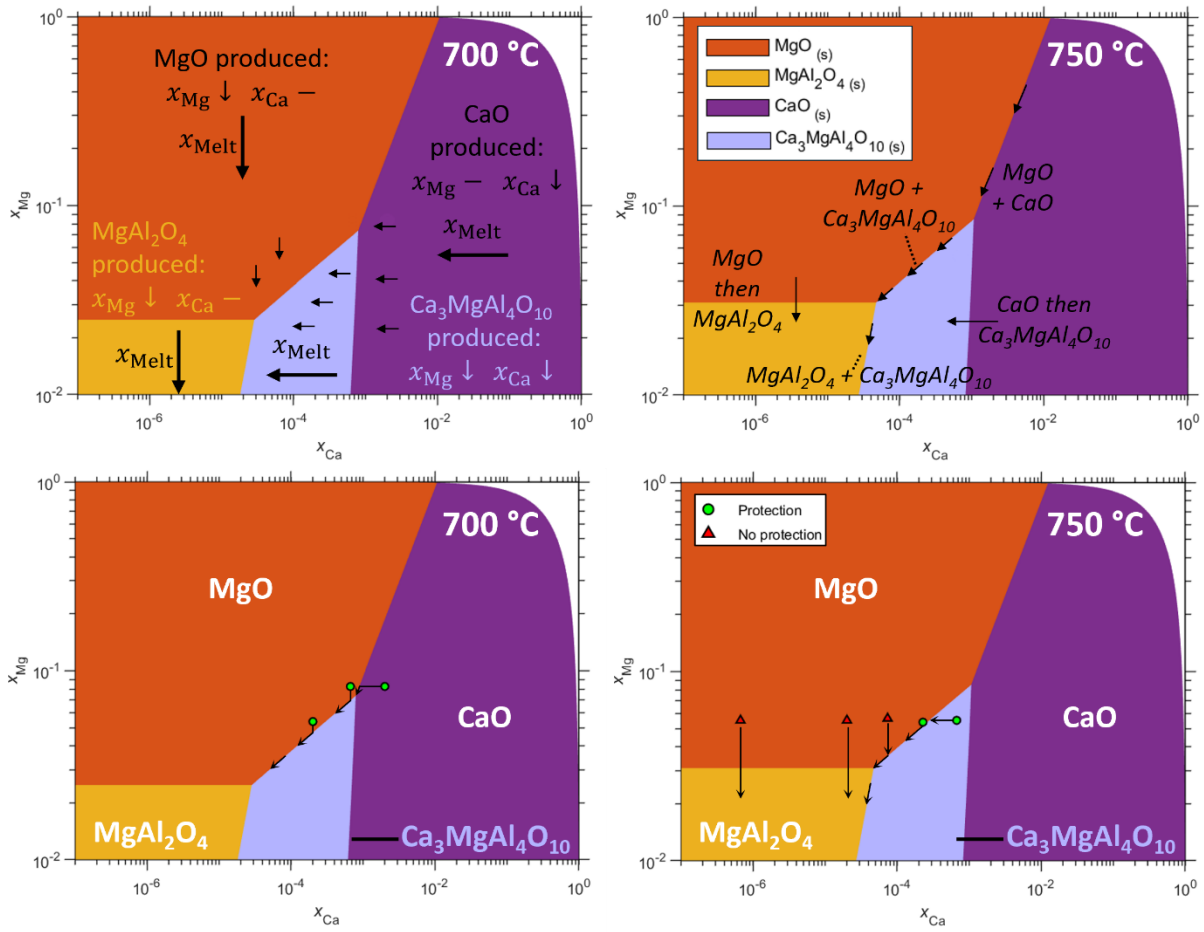


Figure 5.38. Change in melt composition, x_{melt}, when predicted oxidation products are produced in the Al-Mg-Ca system, based on oxide stability diagram assuming ideal mixing: directions of changes in x_{melt} in each region when predicted oxide is produced (top left), direction of x_{melt} at boundaries (top right), and predicted paths of x_{melt} for (x_{Mg}, x_{Ca},T) points in literature annotated with the presence or lack of oxidation protection at 700 °C (bottom left) and 750 °C (bottom right).

The points which show protection in the Al-Mg-Ca diagrams at 700 °C and 750 °C involve a step in which there is simultaneous production of MgO and $Ca_3MgAl_4O_{10}$, regardless of whether the points start in the MgO, CaO, or $Ca_3MgAl_4O_{10}$ region. In Ha's study providing two of the points at 700 °C [6], the oxidation protection effect is attributed to 'interfilling' by a ternary oxide, $CaMg_2Al_{16}O_{27}$. This differs from the ternary oxide predicted here, $Ca_3MgAl_4O_{10}$, but the identification of the ternary oxide in Ha's study is only justified through theoretical calculations and not direct crystallographic identification; it is therefore still consistent with the idea of simultaneous growth of MgO and a ternary Al-Mg-Ca oxide. Furthermore, Yoon's study [67] attributes the protection to a 'mixed MgO-CaO layer', which is consistent.

Between the three points which do not show oxidation protection at 750 °C, the two points with the lowest x_{Ca} go straight from MgO to $MgAl_2O_4$ (Figure 5.38, bottom right). The production of $MgAl_2O_4$ is associated with breakaway oxidation, explaining why there is no oxidation suppression: there is no stage at which a calcium-containing oxide is produced. The third point shows some limited oxidation suppression (Figure 4.18) but then breaks away: this is consistent with the composition going downwards through the MgO region to the MgO-$Ca_3MgAl_4O_{10}$ boundary, going down along the boundary (along which oxidation is slow) to the tripoint with $MgAl_2O_4$, at which point the sample undergoes breakaway oxidation when $MgAl_2O_4$ is produced. The XRD results from the current study are consistent with these products (Figure 4.36): MgO is observed in all three samples, but $MgAl_2O_4$ only in the two with the lowest calcium concentrations. The calcium-containing oxides are not observed, which is likely due to the low concentration of calcium within the samples (0.01 wt.% and 0.03 wt.%).

In the Al-Mg-Sr system, the presence of oxidation protection correlates well with the MgO-$SrAl_2O_4$ boundary in the diagram with ideal mixing (Figure 5.39): points with protection (except for one in Ozdemir's study [69]) lie in the $SrAl_2O_4$ region, whereas points without protection lie in the MgO region. In Yuen's study [68] only MgO could be found, and the absence of Sr-containing oxide was attributed to masking by the predominance of MgO; other studies have attributed the protection to be due to the formation of Sr-containing oxides, such as $SrAl_2O_4$ and $SrAl_4O_7$ [71,72].

Smith-Hanssen's study [5] does not speculate on the involvement of Sr-containing phases, but Ozdemir's study proposes an entirely different mechanism (a difference noted in the paper itself), attributing the protection to a continuous layer of Al_4Sr [69]. The evidence for the continuous layer at the sample surface being an intermetallic is not convincing: the phase is justified through "EDS and WDS analyses", but EDS or WDS results indicating an Al:Sr ratio of 4:1 could just as easily indicate $SrAl_4O_7$, since oxygen measurements on metallographic

samples are often unreliable due to surface oxidation during sample preparation. Furthermore, as noted by the authors, the layer in question is underneath a thick layer of MgO, and the interaction volume of the electron beam could easily overestimate the aluminium content, meaning that the layer, whose thickness is on the order of μm, could in fact be $SrAl_2O_4$.

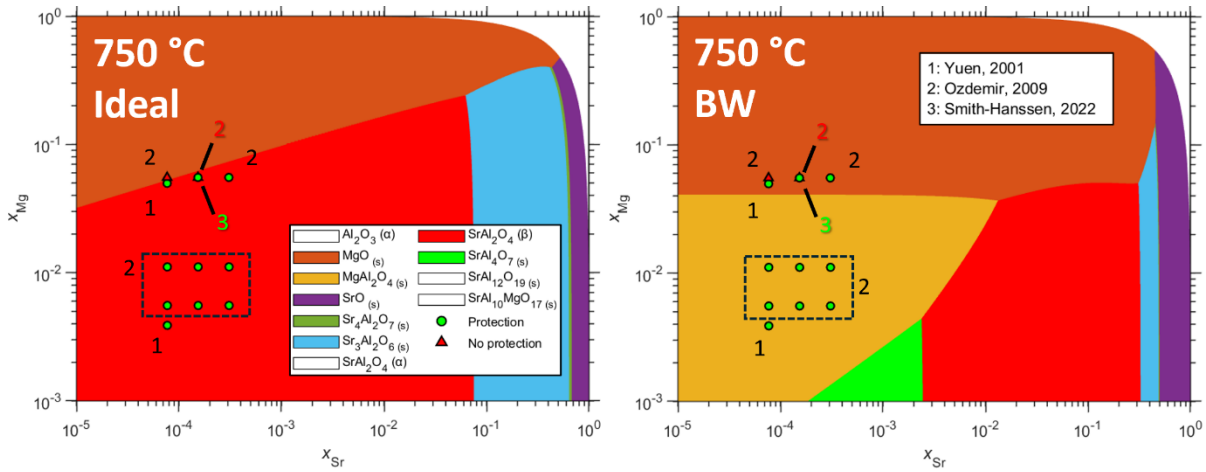


Figure 5.39. Al-Mg-Sr ternary oxide stability diagrams modelled with Ideal and Bragg-Williams (BW) mixing, annotated with data from literature (data from: 1 [68], 2 [69], 3 [5]) indicating presence of oxidation protection. Larger diagrams can be found in Appendix B (B.7.2.4.6 and B.7.2.5.6 for ideal and BW, respectively).

The literature therefore suggests that the initial formation of a strontium aluminate before MgO is the key to oxidation protection of Al-Mg alloys by strontium and explains why the oxide stability diagram boundary between the MgO and $SrAl_2O_4$ correlates well with the presence of protection: if $SrAl_2O_4$ is the first oxide to form, oxidation is suppressed, but if MgO forms first, it is not. This is different to the apparent interfilling effect of CaO and Al-Mg-Ca oxides in MgO layers, where samples which initially produce MgO still appear protected if the composition of the melt eventually hits a MgO-CaO or MgO-$Ca_3MgAl_4O_{10}$ boundary before any production of $MgAl_2O_4$ is thermodynamically favourable. Despite being from the same group as each other (and magnesium), the mechanisms are subtly different: protection of Al-Mg-Sr relies on the most stable product to be a strontium aluminate, but protection of Al-Mg-Ca relies on a Ca-containing oxide being produced before $MgAl_2O_4$, regardless of if the initial oxide is MgO.

Revisiting the Al-Mg-Be system, it is entirely possible that the MgO-BeO boundary lies closer

to the line between protection/non-protection (yellow line, Figure 5.36), which would be consistent with Smith's speculated mechanism of protection [70] that a uniform layer of BeO forming first slows diffusion of magnesium to the surface. Furthermore, since beryllium and aluminium mixing is enthalpically unfavourable, as shown by the positive L_{alt} value in the binary system (Table 5.13), beryllium tends to concentrate at the melt surface, as acknowledged by Smith-Hanssen as an 'increased beryllium activity' at the surface [70]. The beryllium concentration of the melt at the surface (which is the relevant concentration for surface oxidation) may therefore be higher than the average concentration of beryllium in the melt, which would move the data points closer to the MgO-BeO boundary.

Therefore, it is possible that the Al-Mg-Be system could have its oxidation protection mechanism explained by these oxide stability diagrams in a similar manner to Al-Mg-Ca and Al-Mg-Sr, but this cannot be firmly concluded without knowing the solution thermodynamics of the system or the extent to which beryllium concentrates at the melt surface.

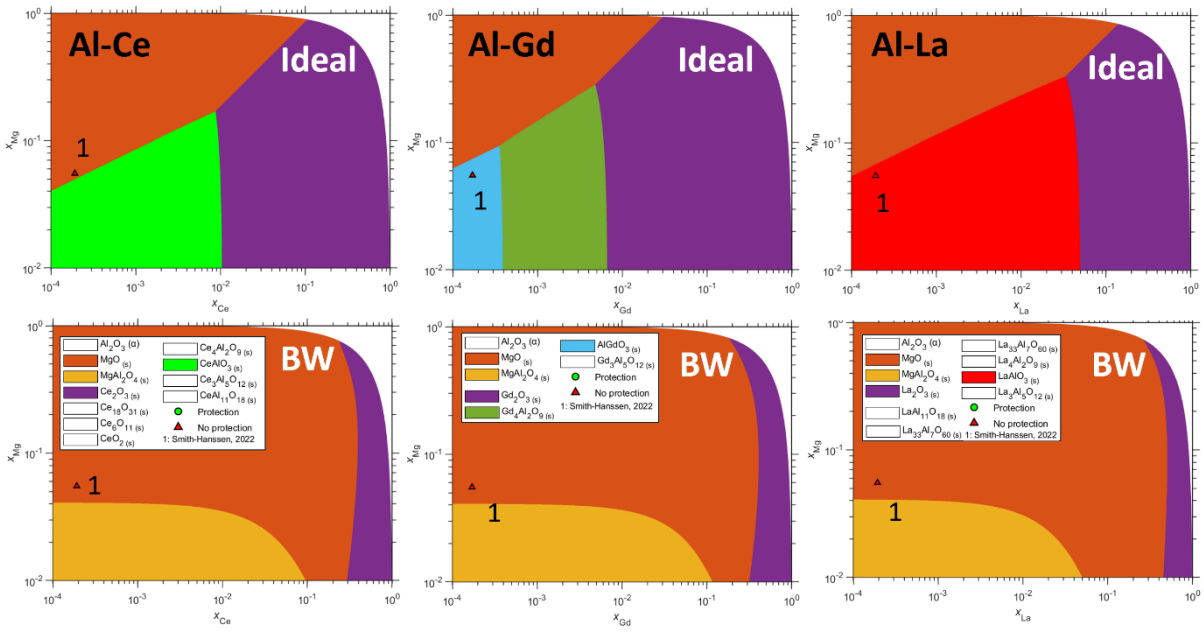


Figure 5.40. Al-Mg-X ternary oxide stability diagrams for lanthanides (Ce, La, Gd) at 750 °C modelled with Ideal mixing and Bragg-Williams (BW) mixing, annotated with data from literature (data from: 1 [5]) indicating lack of oxidation protection. Larger diagrams can be found in Appendix B (B.7.2.4.3-5 and B.7.2.5.3-5 for ideal and BW, respectively).

For lanthanides, it is difficult to draw any conclusions since there is one data point for each system, in each case indicating lack of oxidation protection (Figure 5.40). In the ideal diagrams,

one data point lies in the MgO region (Ce) and two in $AlXO_3$ regions (Gd, La), which could indicate that $AlXO_3$ oxides are non-protective: if the oxidation products are as predicted by the diagrams, then all cases end up going along a MgO-$AlXO_3$ boundary, so there is neither interfilling protection as seen in Al-Mg-Ca nor an initial X-aluminate layer protection as seen in Al-Mg-Sr. If the Bragg-Williams diagrams more accurately represent the thermodynamics then the lack of protection is simpler to explain: each point lies in an MgO region above an $MgAl_2O_4$ region, and therefore oxidation progresses as MgO then $MgAl_2O_4$, resulting in breakaway oxidation.

5.7. Conclusions

The results presented here establish the importance of thermodynamic analysis in the scientific understanding of aluminium melt oxidation. Without incorporating the effect of solute concentration on the stability of oxides in contact with an aluminium melt, it is not possible to explain the change in prevalence of oxide products with a change in solute concentration. This pioneering approach of oxide stability diagrams uses this missing thermodynamic approach to predict oxidation products with a reasonable degree of accuracy.

In binary systems, solute elements are classified into 'less reactive' elements, where only Al_2O_3 is predicted across the temperature-composition range of interest, and 'more reactive' elements, where elements other than Al_2O_3 appear. This classification correlates well with the presence of an oxide in the Al-X system with an oxide with similar or less negative Gibbs free energy of formation (normalised to one mole of O_2) to Al_2O_3. Within more reactive elements, systems are further classified into whether there are no mixed Al-X binary oxides (Ti, Zr) and whether the mixed oxides are univalent (Group I: Li, Na, K), divalent (Group II: Be, Ca, Mg, Sr), or trivalent (Lanthanides: Ce, La, Gd). The implementation of non-ideal solution models such as Bragg-Williams mixing and the modified quasichemical model affects the oxide stability diagrams of the more reactive systems but does not affect the less reactive systems. The

changes are explained by the mathematical features of the models and the physical characteristics of the binary solutions.

In ternary systems, 'less reactive' systems show only Al-Mg oxides (Al_2O_3, $MgAl_2O_4$, and MgO), whereas 'more reactive' elements show other unary or binary Al-X oxides, and even ternary Al-Mg-X oxides in the Al-Mg-Ca system. The implementation of Bragg-Williams mixing shifts the boundaries of the oxide stability diagrams of 'more reactive' elements in the same manner as the corresponding Al-Mg and Al-X binary systems, but also the 'less reactive' elements depending on the thermodynamics of mixing of the constituent binary systems of the Al-Mg-X ternary system.

Comparing oxidation products to the binary oxide stability diagrams, the diagrams predict the oxidation products well. For less reactive elements, the prediction of only Al_2O_3 is accurate for all systems except Al-Zn, whose extra products can be explained by the evaporation and subsequent gas-state oxidation of the dissolved zinc. In more reactive systems, the oxidation products for Group I and Group II elements correlate best with Bragg-Williams mixing; ideal mixing is an acceptable approximation, but the modified quasichemical model consistently overestimates the amount of solute needed to produce solute-containing oxides. For lanthanides, Bragg-Williams mixing is also best, but the modified quasichemical model is the only model which accounts for the anomalous trend of a unary solute oxide becoming more stable with decreasing solute concentration.

In ternary Al-Mg-X diagrams, ideal mixing is found to have the best correlation between predicted and observed products in the Al-Mg-Be and Al-Mg-Ca systems, but not with Al-Mg-Sr. The prevalence of oxidation protection with the addition of group II elements to Al-Mg is explained well by the ternary oxide stability diagrams. By considering the change in composition of the melt as oxidation progresses, calcium is found to protect melts by the simultaneous production of MgO along with either CaO or a ternary Al-Mg-Ca oxide, as

observed experimentally; if a point is predicted to form MgO and then $MgAl_2O_4$, then there is no protection. For strontium, the condition for oxidation protection is the initial formation of a strontium aluminate before MgO, which has been reported by other investigators. In Al-Mg-Be, the line demarcating points which do and do not have oxidation protection does not correspond with a boundary in the oxide stability diagrams, but this discrepancy may be due to an underestimation of the beryllium concentration at the melt surface, caused by the mixing of beryllium and aluminium being enthalpically unfavourable.

Therefore, these diagrams comprise a useful tool for predicting and understanding the oxidation of aluminium melts, and open avenues for future targeted research.

5.8. References

[1] N. Birks, G.H. Meier, F.S. Pettit, Introduction to the high temperature oxidation of metals, Cambridge University Press, 2006.

[2] H.J.T. Ellingham, Reducibility of oxides and sulphides in metallurgical processes, Journal of the Society of Chemical Industry 63 (1944) 125–133. https://doi.org/10.1002/jctb.5000630501.

[3] L. Bäckerud, G. Chai, J. Tamminen, Solidification processing, solidification characteristics of aluminum alloys. Vol. 2. foundry alloys, Skanaluminium, Oslo, Norway, 1990.

[4] DerSilberspiegel, English: The Ellingham diagram is giving the free energy of formation of metal oxides and the corresponding oxygen partial pressure at equilibrium. Labels in English., 2016. https://commons.wikimedia.org/wiki/File:Ellingham_Richardson-diagram_english.svg (accessed February 7, 2025).

[5] N. Smith-Hanssen, M. Syvertsen, A. Kvithyld, Microalloying to Inhibit Oxidation of Al–Mg Alloys, in: Light Metals 2022, Springer International Publishing, Cham, 2022: pp. 579–586. https://doi.org/10.1007/978-3-030-92529-1_76.

[6] S.-H. Ha, Y.-O. Yoon, N.-S. Kim, S.-H. Lim, S.K. Kim, Oxide scale behavior and its effect on oxidation resistance in Al alloys containing alkaline earth metal elements, Defect and Diffusion Forum 380 (2017) 120–123. https://doi.org/10.4028/www.scientific.net/DDF.380.120.

[7] W. Thiele, Die oxydation von aluminium und aluminiumlegierungs-schmelzen, PhD, Bergakademie Clausthal, 1951.

[8] C.N. Cochran, D.L. Belitskus, D.L. Kinosz, Oxidation of aluminum-magnesium melts in air, oxygen, flue gas, and carbon dioxide, Metall Mater Trans B 8 (1977) 323–332. https://doi.org/10.1007/BF02657663.

[9] G. Wu, K. Dash, M.L. Galano, K.A.Q. O'Reilly, Oxidation studies of Al alloys: Part II Al-Mg alloy, Corros Sci 155 (2019) 97–108. https://doi.org/10.1016/j.corsci.2019.04.018.

[10] A.D. Pelton, S.A. Degterov, G. Eriksson, C. Robelin, Y. Dessureault, The modified quasichemical model I—Binary solutions, Metall Mater Trans B 31 (2000) 651–659. https://doi.org/10.1007/s11663-000-0103-2.

[11] A.D. Pelton, Phase Diagrams and Thermodynamic Modeling of Solutions, Elsevier, Cambridge, MA, USA, 2019. https://doi.org/10.1016/C2013-0-19504-9.

[12] R.K. Rajput, Second law of thermodynamics and entropy, in: Engineering Thermodynamics, 3rd ed., Laxmi Publications, Boston, USA, 2007: pp. 227–305.

[13] D.W. Rogers, The Gibbs free energy, in: Concise Physical Chemistry, John Wiley & Sons, Ltd, 2010: pp. 84–92. https://doi.org/10.1002/9780470906347.ch6.

[14] IUPAC, Compendium of Chemical Terminology (the "Gold Book"), 2nd ed., Blackwell Scientific Publications, Oxford, 1997.

[15] V. Gold, ed., The IUPAC compendium of chemical terminology: the gold book, 4th ed., International Union of Pure and Applied Chemistry (IUPAC), Research Triangle Park, NC, 2019. https://doi.org/10.1351/goldbook.

[16] N. Saunders, A.P. Miodownik, CALPHAD (calculation of phase diagrams): a comprehensive guide, 1st ed., Pergamon, 1998.

[17] A.D. Pelton, M. Blander, Computer-assisted analysis of the thermodynamic properties and phase diagrams of slags, in: Proceedings of the Second International Symposium on Metallurgical Slags and Fluxes, TMS-AIME, Warrendale, PA, USA, 1984: pp. 281–94.

[18] C.W. Bale, E. Bélisle, P. Chartrand, S.A. Decterov, G. Eriksson, A.E. Gheribi, K. Hack, I.-H. Jung, Y.-B. Kang, J. Melançon, A.D. Pelton, S. Petersen, C. Robelin, J. Sangster, P. Spencer, M.-A. Van Ende, FactSage thermochemical software and databases, 2010–2016, Calphad 54 (2016) 35–53. https://doi.org/10.1016/j.calphad.2016.05.002.

[19] P. Šulhánek, M. Drienovský, I. Černičková, L. Ďuriška, R. Skaudžius, Ž. Gerhátová, M. Palcut, Oxidation of Al-Co Alloys at high temperatures, Mater 13 (2020) 3152. https://doi.org/10.3390/ma13143152.

[20] G. Wu, K. Dash, M.L. Galano, K.A.Q. O'Reilly, Oxidation studies of Al alloys: Part I Al-Cu (liquid phase) alloy, Corros Sci 157 (2019) 41–50. https://doi.org/10.1016/j.corsci.2019.05.013.

[21] E.M. Hinton, The oxidation of liquid aluminium and the potential for oxides in grain refinement of aluminium alloys, PhD, University of Birmingham, 2016. https://etheses.bham.ac.uk/id/eprint/6508/ (accessed July 14, 2021).

[22] E. Hinton, W. Griffiths, N. Green, Comparison of oxide thickness of aluminium and the effects of selected alloying additions, Mater Sci Forum 765 (2013) 180–184. https://doi.org/10.4028/www.scientific.net/MSF.765.180.

[23] I. Haginoya, T. Fukusako, Influence of alloying elements on oxidation of molten aluminum alloys, J Jpn Foundrym Soc 54 (1982) 664–669. https://doi.org/10.11279/imono.54.10_664.

[24] B. Xiong, Z.L. Yu, G. Xu, L. Miao, J.F. Shi, X.D. Xiao, Ag Behaviors of Ag-Al Alloy Annealed in Air Atmosphere, Advanced Materials Research 557–559 (2012) 1247–1250. https://doi.org/10.4028/www.scientific.net/AMR.557-559.1247.

[25] H.D. Alamdari, D. Dubé, P. Tessier, Behavior of Boron in Molten Aluminum and its Grain Refinement Mechanism, Metall Mater Trans A 44 (2013) 388–394. https://doi.org/10.1007/s11661-012-1388-x.

[26] J.K. Parle, A. Beni, V.R. Dhanak, J.A. Smerdon, P. Schmutz, M. Wardé, M.-G. Barthés-Labrousse, B. Bauer, P. Gille, H.R. Sharma, R. McGrath, STM and XPS investigation of the oxidation of the Al 4 (Cr,Fe) quasicrystal approximant, Applied Surface Science 283 (2013) 276–282. https://doi.org/10.1016/j.apsusc.2013.06.101.

[27] I.N. Ganiev, J.Kh. Dzhaloev, A.R. Rashidov, U.Sh. Yakubov, F.Z. Zuvaidullozoda, Oxidation Kinetics of Aluminum-Nickel Alloys in the Solid State, Bulletin of St. Petersburg State University of Technology and Design 1 (2020) 104–108.

[28] C.R. Werrett, D.R. Pyke, A.K. Bhattacharya, XPS studies of oxide growth and segregation in aluminium–silicon alloys, Surf Interface Anal 25 (1997) 809–816. https://doi.org/10.1002/(SICI)1096-9918(199709)25:10<809::AID-SIA304>3.0.CO;2-M.

[29] R.G. Pritchard, C.R. Werrett, Inelastic electron tunnelling spectroscopy and XPS study of the oxides grown on three aluminium alloys, Surface and Interface Analysis 23 (1995) 705–711. https://doi.org/10.1002/sia.740231009.

[30] A.J. Brock, G.R. Irani, M.J. Pryor, The kinetics of the oxidation of aluminum-zinc alloys in oxygen at high temperature, Oxid Met 15 (1981) 77–100. https://doi.org/10.1007/BF00603756.

[31] M. Hanabe, V. Jayaram, T.A. Bhaskaran, Growth of Al2O3Al composites from Al-Zn alloys, Acta Mater 44 (1996) 819–829. https://doi.org/10.1016/1359-6454(95)00185-9.

[32] S.-J. Kim, W.-J. Lee, B.-C. Shin, I.-S. Kim, G.-H. Lee, Effect of oxidation temperature on the morphology of ZnO nanowires fabricated by directed melt oxidation of Al-Zn alloy, Jpn J Appl Phys 44 (2005) 739–741. https://doi.org/10.1143/JJAP.44.739.

[33] G.-H. Lee, Effect of oxygen pressure in the synthesis of ZnO nanowires through melt oxidation of Al-Zn mixture, Korean J Mater Res 24 (2014) 301–304. https://doi.org/10.3740/MRSK.2014.24.6.301.

[34] G.-H. Lee, C. Allen, Synthesis of tetrapod-shaped ZnO nanowires by directive oxidation of Al-Zn mixture, J Ceramic Soc Jpn 117 (2009) 111–114. https://doi.org/10.2109/jcersj2.117.111.

[35] L. Shi, T. Qu, D. Liu, Y. Deng, B. Yang, Y. Dai, Process of Thermal Decomposition of Lithium Carbonate, in: J. Lee, S. Wagstaff, G. Lambotte, A. Allanore, F. Tesfaye (Eds.), Materials Processing Fundamentals 2020, Springer International Publishing, Cham, 2020: pp. 107–116. https://doi.org/10.1007/978-3-030-36556-1_10.

[36] D.J. Field, G.M. Scanans, E.P. Butler, The high temperature oxidation of Al-Li alloy, in: Aluminum-Lithium Alloys II: Proceedings of the Second International Aluminum-Lithium Conference, The Metallurgical Society of AIME, Monterey, CA, USA, 1983: pp. 657–66.

[37] D.J. Field, E.P. Butler, Liquid metal oxidation of Al-3wt.%Li, in: Aluminum-Lithium Alloys II: Proceedings of the Second International Aluminum-Lithium Conference, Metallurgical Society of AIME, Monterey, CA, USA, 1983: pp. 667–673.

[38] L.V. Kouzmichev, L.Y. Myzlin, A.Y. Radin, B.D. Goopiev, Oxidation of Aluminium/Lithium Alloys and Methods of Protection, Tekhnol. Legk. Splavov, Nauchno-Tekh Byul VILSa. 8 (1975) 18–22.

[39] J.M. Papazian, R.L. Schulte, P.N. Adler, Lithium depletion during heat treatment of aluminum-lithium alloys, Metall Trans A 17 (1986) 635–643. https://doi.org/10.1007/BF02643982.

[40] M. Ahmad, Thermal oxidation behavior of an Al-Li-Cu-Mg-Zr alloy, Metallurgical Transactions A 18 (1987) 681–689. https://doi.org/10.1007/BF02649484.

[41] P. Holdway, A.W. Bowen, The measurement of lithium depletion in aluminium-lithium alloys using X-ray diffraction, J Mater Sci 24 (1989) 3841–3849. https://doi.org/10.1007/BF01168945.

[42] K.K. Soni, D.B. Williams, J.M. Chabala, R. Levi-Setti, D.E. Newbury, Morphological and microchemical phenomena in the high-temperature oxidation of binary Al-Li alloys, Oxidation of Metals 36 (1991) 361–378. https://doi.org/10.1007/BF01151586.

[43] V. Jayaram, The role of volatile solute elements in directed melt oxidation of aluminium alloys, J Mater Sci 31 (1996) 4591–4598. https://doi.org/10.1007/BF00366356.

[44] W. Han, X. Hu, Corrosion of Al-Li alloy melt on oxide refractories, Anti-Corrosion Methods and Materials 70 (2023) 229–235. https://doi.org/10.1108/ACMM-03-2023-2779.

[45] C. Houska, Beryllium in aluminium and magnesium alloys, Met Mater 4 (1988) 100.

[46] F. Khaleghifar, R. Raiszadeh, H. Doostmohammadi, Effect of Ca on the behavior of double oxide film defects in commercially pure aluminum melt, Metall Mater Trans B 46 (2015) 1044–1051. https://doi.org/10.1007/s11663-014-0240-7.

[47] V.G. Shevchenko, D.A. Eselevich, A.I. Ancharov, B.P. Tolochko, In Situ Investigation of Oxidation of Aluminum Alloy Powders with Calcium and Barium by Synchrotron Radiation, Universal Journal of Physics and Application 11 (2017) 115–120. https://doi.org/10.13189/ujpa.2017.110404.

[48] I. Haginoya, T. Fukusako, Oxidation of molten Al–Mg alloys, Trans Jpn Inst Metal 24 (1983) 613–619. https://doi.org/10.2320/matertrans1960.24.613.

[49] B. Hu, D. Li, T. Ying, N. Yu, X. Zeng, Oxidation mechanism of molten Al–5Mg–2Si–Mn alloy, J Mater Sci 55 (2020) 12554–12567. https://doi.org/10.1007/s10853-020-04874-2.

[50] G. Wu, Understanding the role of oxidation in bonding of aluminium alloys, PhD, University of Oxford, 2014.

[51] M.P. Silva, D.E.J. Talbot, Oxidation of liquid aluminum - magnesium alloys, in: Light Metals 1989, TMS, Las Vegas, NV, USA, 2013.

[52] K. Surla, F. Valdivieso, M. Pijolat, M. Soustelle, M. Prin, Kinetic study of the oxidation by oxygen of liquid Al–Mg 5% alloys, Solid State Ionics 143 (2001) 355–365. https://doi.org/10.1016/S0167-2738(01)00861-X.

[53] D.L. Belitskus, Oxidation of molten AI-Mg alloy in air, air-SO2, and air-H2S atmospheres, Oxid Met 3 (1971) 313–317.

[54] S. Impey, D.J. Stephenson, J.R. Nicholls, A study of the effect of magnesium additions on the oxide growth morphologies on liquid aluminium alloys, in: Microscopy of Oxidation, The Institute of Metals, Cambridge, UK, 1990: pp. 238–244.

[55] M. Aryafar, R. Raiszadeh, A. Shalbafzadeh, Healing of double oxide film defects in A356 aluminium melt, J Mater Sci 45 (2010) 3041–3051. https://doi.org/10.1007/s10853-010-4308-8.

[56] F.N. Bakhtiarani, R. Raiszadeh, The behaviour of double oxide film defects in Al–4.5

wt.% Mg melt, J Mater Sci 46 (2011) 1305–1315. https://doi.org/10.1007/s10853-010-4916-3.

[57] S. Amirinejhad, R. Raiszadeh, H. Doostmohammadi, Calorimetric study of the oxidation of Al–Mg alloys for the prediction of healing of the double oxide film defect, J Therm Anal Calorim 113 (2013) 769–777. https://doi.org/10.1007/s10973-012-2810-8.

[58] M. Akbarifar, M. Divandari, S.M.A. Boutorabi, S.-H. Ha, Y.-O. Yoon, S.K. Kim, Short-Time Oxidation of Al–Mg in Dynamic Conditions, Oxid Met 94 (2020) 409–429. https://doi.org/10.1007/s11085-020-09999-y.

[59] S.M. Miresmaeili, Effect of strontium on the oxidation behavior of liquid Al–7Si alloys, Oxid Met 71 (2009) 107–123. https://doi.org/10.1007/s11085-009-9136-3.

[60] M. Nateghian, R. Raiszadeh, H. Doostmohammadi, Behavior of Double-Oxide Film Defects in Al-0.05 wt pct Sr Alloy, Metall and Materi Trans B 43 (2012) 1540–1549. https://doi.org/10.1007/s11663-012-9708-5.

[61] I.N. Ganiev, N.I. Ganieva, D.B. Eshova, Oxidation of Aluminum Melts with Rare-Earth Metals, Russ. Metall. 2018 (2018) 458–464. https://doi.org/10.1134/S0036029518050063.

[62] W. Zhi, F. Wang, X. Chen, Y. Tian, B. Yang, Thermodynamic assessment of the CaO–Al2O3–Sc2O3 ternary system, Calphad 78 (2022) 102454. https://doi.org/10.1016/j.calphad.2022.102454.

[63] H. Fujii, H. Akiyama, J. Kaneko, M. Sugamata, L. Blaz, Al-Sc Master Alloy Prepared by Mechanical Alloying of Aluminum with Addition of Sc2O3, Mater. Trans. 44 (2003) 1049–1052. https://doi.org/10.2320/matertrans.44.1049.

[64] S.-H. Ha, Y.-O. Yoon, B.-H. Kim, T.-W. Lee, S.-H. Lim, S.K. Kim, Precipitation of oxide particles in surface mixed layer of Al–Mg alloys with a trace of Ca during oxidation, J Nanosci Nanotechnol 17 (2017) 8232–8235. https://doi.org/10.1166/jnn.2017.15104.

[65] N. Smith, A. Kvithyld, G. Tranell, XPS Examination of the Oxide-Metal Interface of an Aluminum–Magnesium Alloy Containing Beryllium, in: O. Martin (Ed.), Light Metals 2018, Springer International Publishing, Cham, 2018: pp. 913–919. https://doi.org/10.1007/978-3-319-72284-9_119.

[66] N. Smith, B. Gleeson, A. Kvithyld, G. Tranell, Effects of 2 ppm Beryllium on the Oxidation of a 5XXX Aluminum Alloy at Temperatures Between 500 and 750 °C, in: A.P. Ratvik (Ed.), Light Metals 2017, Springer International Publishing, Cham, 2017: pp. 1465–1474. https://doi.org/10.1007/978-3-319-51541-0_175.

[67] Y.-O. Yoon, S.-H. Ha, G.-Y. Yeom, H.K. Lim, S.K. Kim, Oxidation behavior of Al2Ca added Al-5Mg alloy in the liquid state, in: B.A. Sadler (Ed.), Light Metals 2013, Springer International Publishing, San Antonio, Texas, USA, 2013: pp. 323–326. https://doi.org/10.1007/978-3-319-65136-1_56.

[68] P.K. Yuen, Effects of strontium on the oxidation of molten aluminum alloys containing silicon and magnesium, Masters, McGill University, 2001.

[69] O. Ozdemir, J.E. Gruzleski, R.A.L. Drew, Effect of low-levels of strontium on the oxidation behavior of selected molten aluminum–magnesium alloys, Oxid Met 72 (2009) 241–257. https://doi.org/10.1007/s11085-009-9158-x.

[70] N. Smith, A. Kvithyld, G. Tranell, The Mechanism Behind the Oxidation Protection

of High Mg Al Alloys with Beryllium, Metall Mater Trans B 49 (2018) 2846–2857. https://doi.org/10.1007/s11663-018-1340-6.

[71] R.A.L. Drew, J.E. Gruzleski, Effects of Strontium on the Oxidation Behavior of an A356 alloy, Aluminum Trans 3 (2000) 31–39.

[72] P.K. Yuen, R.A.L. Drew, J.E. Gruzleski, K. Dennis, Effects of Strontium on the Oxidation Behavior of Molten Aluminum Alloys Containing Silicon and Magnesium, in: Molten Aluminum Processing, Orlando, FL, USA, 2001: p. 179.

Chapter 6
General Discussion, Conclusions, and Future Work

6.1. Discussion

6.1.1. Summary

This study aimed to tackle two major issues within the field of aluminium casting using a combined experimental-theoretical approach: to confirm that entrained oxide films exist in liquid aluminium alloys by directly observing them in-situ for the first time, and to establish a theoretical framework for predicting the products of aluminium melt oxidation through thermodynamic modelling. This would therefore establish a key motivation for studying the melt oxidation of aluminium alloys, by removing any doubt over a defect likely responsible for many casting problems, and getting a head start on future analysis by establishing the appropriate theoretical approach. Both goals were achieved to a reasonable degree of success: entrained oxide films were directly imaged in aluminium melts, oxidation products were predicted well by the theoretical modelling, and even previously unexplained phenomena such as oxidation suppression by microalloying were explained using this approach.

6.1.2. Direct observation of entrained oxides in melts

The most major finding of this work was the direct observation of entrained oxides in molten aluminium, done for the first time. Whilst evidence for the existence of entrained oxides and their effects on the quality of the aluminium melts has been well documented, direct observation in the liquid state has proven problematic: it is extremely difficult to image thin oxide films in a liquid metal due to the numerous logistical challenges. This previous lack of direct observation appears to be the main, if not the only, barrier to wider acceptance of entrained oxide theories; a picture of a bifilm is harder to dismiss than a multi-step explanation of why only entrained oxides could explain observed phenomena, however accurate the hypothesis turns out to be.

Whilst the structures deduced to be oxides were directly observed, the conclusion of the observed structures being entrained oxides did require some piecing together. Diffraction was not available for the in-situ tomography, so deduction of the chemistry was done by lab-based analysis. The morphologies of the extracted and metallographic samples were consistent with tomographic observations (Figure 4.16), so it was deemed that there was enough evidence to make those conclusions. Repeating this experiment with diffraction would decisively determine the veracity of these claims and provide insights into the chemical interactions of the entrained oxides and the melt.

The need for direct observation was underlined by the findings in this thesis: bifilms were observed, but a different, morphologically distinct entrained oxide population dominated. The difference in the formation mechanism and in-melt behaviour between the oxide networks and bifilms was akin to the distinctions previously made between ‘young’ and ‘old’ bifilms. Firstly, porous oxide networks grew hydrogen bubbles, contorting and smoothing out during inflation, which is similar to the description of bifilms ‘unfurling’ in which mostly ‘young’ bifilms unravel and inflate. Secondly, bifilms were (mostly) found not to inflate due to bonding across the inner interface, similar to the idea that ‘old’ bifilms are less likely to unfurl than ‘young’ bifilms due to their thickness and degree of bonding across the inner surfaces. Lastly, porous oxide networks were concluded to be derived from the melt pour itself, and bifilms from pre-pour oxidation, a distinction previously made between ‘young’ and ‘old’ bifilms.

The results here are therefore consistent with the previous understanding that there are two distinct populations of entrained oxide, one from oxidation during the melt pour and the other from prior melt oxidation, which generally do and do not act as the sites for hydrogen bubble formation, respectively. Direct observation allowed this description to validated and refined: rather than both oxide populations being bifilms differing only by thickness, the two oxide populations are morphologically distinct. ‘Young’ entrained oxides are extensive, convoluted

networks of thin oxide layer, and 'old' entrained oxides are consistent with descriptions of bifilms. Porous oxide networks and bifilms are both closed oxide surfaces encapsulating a gas atmosphere in a melt, but there is enough of a difference in appearance to categorise these structures into two types, for the purposes of a metallurgical description.

Another reason for the lack of previous recognition of porous oxide networks is their apparent similarity to interdendritic porosity in microscopy. Porous oxide networks are very thin (sub-micron, Figure 4.4) and shaped by solidifying dendrites, as evidenced by their 'waffle fries' morphology[1] (Figure 4.5). They are therefore hard to distinguish by most available observation methods: SEM/EDX of metallographic samples only provided hints of an oxide layer in interdendritic pores (Figure 4.24), and any oxygen pickup may be from sample exposure to the atmosphere during preparation, complicating interpretation of EDX results. Furthermore, even the high-resolution X-ray tomography employed in this study could only distinguish between interdendritic porosity and porous oxide networks by whether the networks persisted after melting (Figure 4.10): oxide networks did, but porosity did not.

The most important technique in formulating the idea of porous oxide networks was the butanol extraction. Previously used for extracting intermetallic inclusions, one simple step is probably responsible for the destruction of oxide structures and therefore lack of previous recognition: the use of an acid etch. If attempting to observe intermetallics, this step is justified: removing the oxide layer helps the butanol react with the aluminium more efficiently whilst preserving intermetallic structures of interest. However, this destroys any oxides not only on the surface but within the sample. Oxide networks are now known to form extensive networks which can impinge on the sample surface, providing channels that carry corrodants into the sample. Without knowledge of this caveat, under the assumption that the butanol dissolution process

[1] Whilst the object of comparison was not intended to be a fast-food item, the morphological similarity was uncanny, and no other object came close to resembling the observed structures.

only removes the α-Al grains, it is easy to see how a scientist performing regular extractions can assume that oxides do not exist as inclusions, and for this systematic error in understanding to propagate through the literature.

This modified process was therefore attempted, in case an extraction without an acid etch were possible. Contrary to the predictions of a more senior colleague who predicted it would be impossible to find bifilms this way due to their small size, the process worked first time. The butanol process appears to be falling out of fashion, as it is quite dangerous and unsociable to others working in the laboratory, which could also explain why these results (from a relatively simple idea) are novel. Phenol seems to be the solvent of choice, being more efficient in dissolving aluminium, so phenol should be used to dissolve similar aluminium samples, and the extracted samples analysed to determine whether they are oxides, to fully confirm that this is not an artefact of the butanol dissolution process[2].

Overall, this combined methodology proved to be an effective way of observing entrained oxides and therefore should be used to test other bifilm hypotheses. The growth of intermetallics on entrained oxides was evidenced by the extracted oxides, especially the spine-like growths from the 0.03Ca sample (Figure 4.23), but intermetallic growth could not be seen in the tomography, likely due to the concentrations of intermetallic-forming elements and the size of the features. Therefore, alloys with higher concentrations of iron and silicon should be tested, to visualise intermetallic growth in real time in three dimensions and so determine whether entrained oxides can nucleate and grow intermetallic phases. Continuous scanning during solidification of a eutectic Al-Si alloy could determine whether irregular eutectic growth is caused by growth of silicon platelets on entrained oxides, since partial reconstructions can

[2] The author notes that an investigator at ICAA19 presented images of inclusions extracted with phenol from an aluminium sample that resembled the morphology of entrained oxide networks. The investigator did not analyse these structures, instead focusing on the intermetallics in the foreground, so they were not confirmed to be oxides; these images remain unpublished at the time of writing. This observation gave the author confidence that the oxides were not an experimental artefact, but more robust investigations are clearly needed to establish this to an satisfactory scientific standard.

visualise real-time growth in 3-D. Although the synchrotron XRT set-up is specialised and beamline time valuable, it provides a unique opportunity to test long-disputed hypotheses.

6.1.3. Thermodynamic modelling

Having demonstrated the importance of understanding the oxidation of aluminium alloy melts by directly observing entrained oxides, a logical next step is establishing a theoretical network through thermodynamic modelling. Commercial aluminium alloys contain multiple elements, with the compositional space to explore increasing exponentially with each element added, and the literature shows that even trace elements in ppm quantities can have a significant impact on oxidation. A way of predicting oxidation products as a function of the properties of the system, such as melt composition and temperature, would therefore be useful for understanding observed oxidation behaviour and high-throughput screening, if searching for a particular oxidation behaviour.

Ellingham diagrams are the established method of assessing the oxidation thermodynamics of pure metals, so applying a similar treatment to aluminium melts was thought to be appropriate. The effect of melt composition on the thermodynamics of oxidation is subtle, but important to recognise: for a solute-containing oxide to be formed (e.g. $MgAl_2O_4$ from an Al-Mg melt), it is a requirement that the solute element be present, but if this were the only consideration, then the favoured oxidation product would not change with composition, since the Gibbs free energy of formation of the oxide (from standard states) would remain constant.

Oxidising a melt is not thermodynamically equivalent to oxidising a mixture of two non-interacting elements, which itself is analogous to a pure element powder mixture: solute elements in an aluminium melt are stabilised by the configurational entropy penalty required to remove the element from solution, in addition to any enthalpic changes from the interactions between the differing elements. Since Gibbs free energy is a state variable, Hess' law allows the Gibbs free energy change of this reaction to be evaluated as the addition of two separate

steps: (a) the removal of the elements from a solution to form pure elements in their standard states and (b) the reaction of the pure elements in their standard states with atmospheric oxygen to make the oxide. The first step (the removal of elements from solution) gives us the compositional dependence that we observe experimentally: assuming ideal mixing for a binary alloy, which incorporates only a point configurational entropy change, the Gibbs free energy change of unmixing scales with the logarithm of concentration, producing an asymptote as concentration approaches zero. It is therefore appropriate to display compositional dependence with a logarithmic composition axis, as even minute concentrations can affect oxide stability.

The concept was validated by other investigators' previous use of this thermodynamic treatment to explain the oxidation of Al-Mg alloys. Both MgO and $MgAl_2O_4$ are commonly observed in Al-Mg melt oxidation, often MgO first followed by $MgAl_2O_4$, a sequence justified by $MgAl_2O_4$ becoming thermodynamically favoured over MgO as magnesium in the melt depletes during oxidation. Researchers have calculated lines of equilibrium between MgO and $MgAl_2O_4$ and even presented maps of which oxide was favoured as a function of composition and temperature, but there appears not to have been an extension to other aluminium alloy systems or the use of non-ideal models, which use more complex mathematical forms to allow system-specific parameters to be incorporated.

This oversight may be due to many factors. Firstly, there may have been a lack of motivation: without the problems of entrained oxides, thermodynamic modelling of aluminium alloy oxidation could be regarded as a purely academic exercise, a stance this work shows to be misguided. Secondly, lots of thermodynamic data required by this modelling has only recently become available: modelling the thermodynamics of oxidation of a binary system requires the Gibbs free energy of each candidate oxide in the system to be calculated across the temperature range of interest, data which, for many systems, has only been published within the last decade. This problem is worse for parameters from solution models, such as Bragg-Williams mixing

and the modified quasichemical model, and for data required for ternary or higher order systems. A systematic approach in the manner presented here (twenty-four Al-X binary systems and twelve Al-Mg-X systems) may therefore have been impossible.

Thirdly, deriving expressions for non-ideal models was not trivial. The binary and ternary Bragg-Williams expressions required some thought, but the complexity of the modified quasichemical model greatly increased the effort required to derive the relevant mathematical expressions. These quantities could have been determined by numerical solution (indeed, the quantity x_{XAl} could only be solved numerically), but it is good scientific practice to derive analytical expressions where possible, however cumbersome it may be. Expressions were derived by hand and verified using software since computational tools could not feasibly derive the equations when attempted: the software frequently failed to spot substitutions required for cancellation and full expansion gave unwieldy mathematical expressions that would inevitably cause transcription errors.

For binary systems, the oxide stability diagrams were quite successful in predicting oxidation products, with observations of oxides for a given melt composition and temperature generally lining up well with the diagrams, especially when the Bragg-Williams model was applied. Discrepancies and multiple oxidation products could be justified by recognising the limitations of the analysis: oxidation of melts is a complex, dynamic process, requiring kinetic considerations for full scientific understanding, and this treatment, like Ellingham diagrams, considers only equilibrium thermodynamics.

The analysis of microalloying to prevent Al-Mg oxidation justifies the representation of ternary (Al-Mg-X) melt oxidation in this way. Using this thermodynamic treatment, the mechanism of oxidation protection in Al-Mg alloys with added group II elements could be understood by considering the change in composition of the melt as oxidation progressed, showing this protection to be a predominantly thermodynamic effect, and not a kinetic effect. In the case of

Al-Mg-Ca, which was studied in the experimental component, the formation sequence of various oxides observed correlated well with the thermodynamic modelling, providing a satisfying link between the two components of the study.

6.2. Conclusions

6.2.1. In-situ X-ray tomography

The conclusions from the experimental chapter, involving the in-situ X-ray tomography of Ca-added Al-Mg melts and relevant complementary experimental work, are as follows:

1. Entrained oxides, including ‘bifilms’, were directly imaged and identified in molten aluminium melts for the first time, removing any lingering doubt over their existence. Entrained oxides were found not just to be ‘bifilms’, as previously thought, but consist of two distinct populations, whose behaviour resembled prior descriptions of ‘young’ and ‘old’ bifilms, respectively. Convoluted networks of thin, flexible, porous oxides, which originate from the oxidation of the melt on pouring itself, were found to dominate the samples and behaved in a similar manner to ‘young’ bifilms. In contrast, thicker films resembling bifilms arising from melt oxidation before the pour were within the porous oxide networks and were consistent with ‘old’ bifilms.
2. Many entrained oxide networks had a ‘waffle fries’ morphology, consisting of two sets of parallel ridges, each set oriented orthogonally to the other, containing holes at the intersections of the gaps in each set of ridges. This was explained by the oxides being shaped by growing dendrites, evidencing their origin as products of entrainment.
3. Entrained oxide networks were also found to contain debris such as oxide particles and gas bubbles, further evidencing their origin from entrainment. These debris remained encapsulated even after the sample was melted, showing the stability of the porous oxide networks when in contact with the melt, proving this long-speculated behaviour of entrained oxides.

4. Evidence presented here suggests that entrained oxide networks and bifilms grow intermetallics, another bifilm prediction, by observing their associations with oxide structures on extracted oxide samples. However, this could not be confirmed by direct observation and requires further investigation to firmly establish.
5. Hydrogen bubbles formed only from inside entrained oxide networks, not from 'bifilms'. These observations are consistent with previous assertions that hydrogen bubbles cannot nucleate within aluminium melts but grow from pre-existing atmospheres provided by entrained oxides. These bubbles were not found to grow from the entrained oxide structures resembling bifilms, but from the thinner, porous oxide networks discovered by this study. The arguments previously applied to bifilms and their ability to unfurl when growing a hydrogen bubble are therefore more appropriately applied to the contortion of entrained oxide networks during inflation.
6. Hydrogen bubbles only formed in Al-Mg samples with added calcium. The finding that hydrogen bubbles do not form in the sample without added calcium further evidences the involvement of oxides in hydrogen bubble formation.
7. Deoxidation of aluminium melts by calcium addition was found to be facilitated by porous oxide network flotation, both with and without the growth of hydrogen bubbles. Neither bubble formation nor oxide network flotation was observed in the sample without added calcium.
8. Entrained oxides which impinge on the melt surface were found to facilitate melt oxidation, implicating them in melt oxidation for the first time despite previous speculation of their involvement in solid-state corrosion.
9. The addition of calcium helped protect Al-Mg melts from oxidation by suppressing the transformation of MgO to $MgAl_2O_4$ and forming a fine MgO layer on the interior of entrained oxide networks, limiting contact between the atmosphere and the melt.

6.2.2. Thermodynamic modelling

The conclusions of the theoretical component, involving the thermodynamic modelling of aluminium melt oxidation through an Ellingham diagram-style approach, are as follows:

1. A method of predicting the most stable oxidation product of an aluminium alloy melt as a function of temperature and composition was established using oxide stability diagrams. The results demonstrate that incorporating the thermodynamics of solute concentration is necessary for predicting multicomponent oxides, and for justifying why solute concentration affects the composition of the oxidation product at all.
2. In binary Al-X systems, where aluminium is the majority component, solute elements are classified based on their predicted oxidation products within the temperature-composition range of interest. Solute elements that do not affect the predicted stability of Al_2O_3 are classed as 'non-reactive', and solute elements that do are classed as 'reactive'. Reactive solute elements are further divided into whether mixed Al-X binary oxides are absent the oxide stability diagram (e.g. Ti, Zr) and if not, whether the cations within the mixed oxides are generally univalent (Group I: Li, Na, K), divalent (Group II: Be, Ca, Mg, Sr), or trivalent (Lanthanides: Ce, La, Gd). Whether solute elements are classified as non-reactive or reactive correlates well with the presence of an oxide within the Al-X system which has a Gibbs free energy of formation (normalised to one mole of O_2) which is close to or less than Al_2O_3.
3. Equations allowing implementation of non-ideal models (Bragg-Williams mixing and the modified quasichemical model) were derived from first principles and incorporated into the binary oxide stability diagrams. Non-ideal models were found to affect the oxide stability diagrams of more reactive elements but not the less reactive elements. The changes were explained by the physical characteristics of the solute elements in Al-X solutions and the mathematics of the solution models.

4. In ternary Al-Mg-X systems, oxide stability diagrams of solute elements (X) classified as less reactive in the binary case only showed Al-Mg unary and binary oxides (Al_2O_3, $MgAl_2O_4$, and MgO), whereas more reactive solute elements showed solute-containing oxides also. The implementation of Bragg-Williams mixing shifted the boundaries of more reactive elements in the same way as the corresponding binary systems, but boundaries were also shifted in the less reactive systems. The shift for less reactive systems could be explained by considering the thermodynamics of mixing of the constituent elements.
5. Comparison to experimental data allowed evaluation of the utility and effectiveness of this approach. For less reactive binary systems, the prediction of only Al_2O_3 is reasonably accurate for all considered systems except Al-Zn, whose oxidation products are explained by the evaporation and gas-phase oxidation of zinc. In more reactive systems, products for Group I and Group II solute elements correlated best with Bragg-Williams mixing and were described well by ideal mixing. However, the modified quasichemical model consistently overestimated the amount of solute required to produce a solute-containing oxide, due to an additional second nearest neighbour ordering term introduced by the model. For lanthanides, Bragg-Williams mixing was again found to be the most effective but the modified quasichemical model did account for an anomalous trend of a unary solute oxide becoming more stable with decreasing solute concentration, despite missing the mark on the precise composition.
6. In ternary Al-Mg-X systems, ideal mixing gives the best correlation between predicted and observed products in the Al-Mg-Be and Al-Mg-Ca systems, but not in Al-Mg-Sr.
7. The prevalence of oxidation protection of Al-Mg melts by Group II oxides is explained well by the ternary oxide stability diagrams, by considering the change in melt composition as oxidation develops. This novel approach accounts for observations of

the joint formation of MgO and either CaO or a mixed ternary oxide in the Al-Mg-Ca system when the calcium concentration is high enough to give oxidation protection, as well as the initial formation of an $SrAl_2O_4$ layer before other oxides in protected Al-Mg-Sr alloys. In the Al-Mg-Be system, the experimentally observed boundary (as a function of melt composition) between alloys that are and are not protected does not align with any boundary on the ternary oxide stability diagrams. Still, this discrepancy may be accounted for by preferential segregation of beryllium to the melt surface.

6.3. Future work

This study opens the door to many areas of future research, some of which are listed below:

1. The in-situ X-ray tomography observation approach should be applied more widely for investigating oxides in aluminium melts, namely:
    a. Repeats of the experiments presented but switching calcium for elements which do (Be, Sr) and do not (Ce, La, Gd) cause oxidation suppression in Al-Mg alloys, to determine whether the oxidation protection mechanism is the same, and if these elements have the same effect on entrained oxides, such as the formation of hydrogen bubbles.
    b. Investigating whether entrained oxides (or lack thereof) are responsible for the irregular eutectic solidification behaviour of Al-Si alloys, by directly observing the formation of the Al-Si eutectic and comparing the location of platelets to entrained oxides.
    c. By using an alloy with higher concentrations of intermetallic-forming elements (Fe, Si, Mn…), attempting to directly observe intermetallic nucleation and growth on entrained oxides, another bifilm prediction.
    d. Repeating the Al-Mg-Ca experiments but on larger samples with a larger field of view, firstly to ensure reproducibility but also to confirm that this is not just

a surface effect.

e. Any of the above investigations with a diffraction set-up, to also provide phase identification in real time.

2. For strengthening the theoretical approach:

   a. Carrying out melt oxidation experiments on more Al-X and Al-Mg-X systems, to provide further experimental evidence for the theoretical approach.

   b. Deriving equations for the modified quasichemical model for ternary Al-Mg-X systems (not recommended, given how onerous the binary derivation was, but it is a logical next step).

   c. Implementing the ability for the oxide composition to vary: only stoichiometric oxides were implemented, which is a reasonable assumption at the temperature ranges considered, but this would produce more accurate results.

   d. Adding in other products, such as nitrides and carbonates, if the experimental conditions are known well enough.

   e. Extending to other alloy systems, since this approach is not exclusive to aluminium.

Appendix A
Supplementary Mathematical Information

A.1. Overview

This appendix contains supplementary mathematical information for Chapter 5, including derivations of equations and a comprehensive list of symbols used in the analysis.

A.1.1. List of symbols

Below is a comprehensive list of symbols used in Chapter 5 and this appendix. Some symbols, such as β_{ij}, are not named, but are defined in the chapter.

Symbol	Description
a_i	Thermodynamic activity of species i
$\mathrm{Al}_{c_{\mathrm{Al}}}\mathrm{X}_{c_{\mathrm{X}}}\mathrm{O}_b$	General binary oxide for solute element X
$\mathrm{Al}_{c_{\mathrm{Al}}}\mathrm{X}_{1c_1}\mathrm{X}_{2c_2}\mathrm{O}_b$	General ternary oxide for solute elements X_1 and X_2
b	Stoichiometric coefficient of oxygen in an oxide
$c_{R,i}$	Stoichiometric coefficient of reactant i
$c_{R,j}$	Stoichiometric coefficient of product j
c_{Al}	Stoichiometric coefficient of aluminium in an oxide
c_{Mg}	Stoichiometric coefficient of magnesium in an oxide
c_{X}	Stoichiometric coefficient of element X in an oxide
$\exp(x)$	Exponential function of x
$f_i(T)$	Ellingham diagram plot of substance i as a function of temperature T
g_i^0	Standard molar Gibbs free energy of component i
G	Gibbs free energy
G_i	Gibbs free energy of component i
G_{prod}	Total Gibbs free energy of the products
G_{reac}	Total Gibbs free energy of the reactants
Δg_{AB}	Gibbs free energy change of reaction when two A-B bonds are formed from an A-A bond and a B-B bond
Δg_{AB}^0	Composition-independent component of Δg_{AB}
$\Delta G_{\mathrm{f}}^{\circ}$	Standard Gibbs free energy change of formation
$\Delta G_{\mathrm{f},i}^{\mathrm{o}}$	Standard Gibbs free energy change of formation of component i
$\Delta G_{\mathrm{f,mol}\mathrm{O}_2}^{\circ}$	Standard Gibbs free energy change of formation, normalised to one mole of O_2 gas
$\Delta G_{\mathrm{f,\,mol\,O_2}}^{\mathrm{o\ 298K}}$	Standard Gibbs free energy change of formation, normalised to one mole of O_2 gas at a temperature of 298 K
g_{ij}^{mn}	m-nth order parameter for Δg_{AB}
g_{plot}	Oxide stability diagram boundary gradient
ΔG_{mix}	Gibbs free energy change of mixing
$\Delta G_{\mathrm{mix}}^{\mathrm{ideal}}$	Gibbs free energy change of mixing, assuming ideal mixing
G_{mixed}	Gibbs free energy of a mixture

ΔG^{ox}	Gibbs free energy of oxidation
ΔG_i^{ox}	Gibbs free energy of oxidation of component i
$\Delta G_i^{\mathrm{ox,BWB}}$	Bragg-Williams contribution to the Gibbs free energy of oxidation of component i in a binary system
$\Delta G_i^{\mathrm{ox,BWT}}$	Bragg-Williams contribution to the Gibbs free energy of oxidation of component i in a ternary system
$\Delta G_i^{\mathrm{ox,MQM}}$	Modified quasichemical model contribution to the Gibbs free energy of oxidation of component i (in a binary system)
$\Delta G_{\mathrm{Al}_{c_{\mathrm{Al}}}\mathrm{X}_{c_{\mathrm{X}}}\mathrm{O}_b}^{\mathrm{ox,MQM,log}}$	Logarithm-based terms of $\Delta G_{\mathrm{Al}_{c_{\mathrm{Al}}}\mathrm{X}_{c_{\mathrm{X}}}\mathrm{O}_b}^{\mathrm{ox,MQM}}$
$\Delta G_{\mathrm{Al}_{c_{\mathrm{Al}}}\mathrm{X}_{c_{\mathrm{X}}}\mathrm{O}_b}^{\mathrm{ox,MQM,poly}}$	Polynomial-based terms of $\Delta G_{\mathrm{Al}_{c_{\mathrm{Al}}}\mathrm{X}_{c_{\mathrm{X}}}\mathrm{O}_b}^{\mathrm{ox,MQM}}$
ΔG_{r}	Gibbs free energy change of reaction
$\Delta G_{\mathrm{r,mol}\mathrm{O}_2}$	Gibbs free energy change of reaction, normalised to one mole of O_2 gas
$\Delta G_{\mathrm{r}}^{o}$	Standard Gibbs free energy change of reaction
G_{unmixed}	Gibbs free energy of unmixed components
$\Delta G_{\mathrm{mix}}^{\mathrm{xs}}$	Excess Gibbs free energy of mixing
$\Delta G_{\mathrm{mix},n_i}^{\mathrm{xs}}$ or $\Delta G_{\mathrm{mix}}^{\mathrm{xs},n_i}$	Excess Gibbs free energy of mixing in terms of number of moles n_i
H	Enthalpy
$\Delta H_{\mathrm{f}}^{\circ}$	Standard enthalpy of formation
ΔH_{mix}	Enthalpy change of mixing
$\Delta H_{\mathrm{mix}}^{\mathrm{ideal}}$	Enthalpy change of mixing, assuming ideal mixing
K	Equilibrium constant
L_{alt}	Alternating sum of ${}^{i}L_{jk}$ terms
$L_{\mathrm{alt,AB}}$	Alternating sum of ${}^{i}L_{jk}$ terms for the A-B binary system
${}^{i}L_{jk}$	i-th order Bragg-Williams interaction parameter for the binary system j-k
${}^{i}L_{jkl}$	i-th order Bragg-Williams interaction parameter for the ternary system j-k-l
$\ln(x)$	Natural logarithm of x
m_{Al}	Reduced stoichiometric coefficient of aluminium in an oxide
m_{Mg}	Reduced stoichiometric coefficient of magnesium in an oxide
m_{X}	Reduced stoichiometric coefficient of element X in an oxide
n_i	Number of moles of species i
n_{ij}	Number of i-j bonds
N_i	Quantity of species i
p_{g}	Partial pressure of a gas
p_{g}°	Standard partial pressure of a gas
p_{O_2}	Partial pressure of O_2 gas
$p_{\mathrm{O}_2,\mathrm{diss}}$	Oxygen dissociation pressure
P_j	Product j
Q	Reaction quotient
R_i	Reactant i
R	Molar gas constant
S	Entropy
$\Delta S^{\mathrm{config}}$	Configurational entropy cahnge
$\Delta S_{\mathrm{f}}^{\circ}$	Standard entropy change of formation

ΔS_{mix}	Entropy change of mixing
$\Delta S_{\mathrm{mix}}^{\mathrm{ideal}}$	Entropy change of mixing, assuming ideal mixing
$\Delta S^{\mathrm{point}}$	Point contribution to Gibbs free energy of mixing
ΔS^{pair}	Pair contribution to Gibbs free energy of mixing
T	Temperature
x_i	Composition (molar fraction) of component i
x_{ij}	Bond fraction of i-j bonds
x'_{XAl}	Derivative of x_{XAl} with respect to x_{X}
$x_{\mathrm{X},\mathrm{eq}i}$	i-th intersection point (context-specific) in an Al-X system
$f(x_{\mathrm{X,low}})$	Limit of $f(x_{\mathrm{X}})$ as $x_{\mathrm{X}} \to 0$
$\mathrm{X}_2\mathrm{O}_z$	Unary oxide for solute element X where X has valency z
$\mathrm{X}_{c_{\mathrm{X}}}\mathrm{O}_b$	General unary oxide for solute element X
y_i	Co-ordination-equivalent mole fraction of component i
z	Valency of element X in oxide $\mathrm{X}_2\mathrm{O}_z$
z_i	Co-ordination number of component i
Z_{ij}^k	Co-ordination number of component k in the i-j binary system when all the nearest neighbours of k are j
α_{Al}	Number of formula units of $\mathrm{Al}_2\mathrm{O}_3$ in a binary oxide $\mathrm{Al}_{c_{\mathrm{Al}}}\mathrm{X}_{c_{\mathrm{X}}}\mathrm{O}_b$
α_{X}	Number of formula units of a unary solute oxide $\mathrm{X}_2\mathrm{O}_z$ in a binary oxide $\mathrm{Al}_{c_{\mathrm{Al}}}\mathrm{X}_{c_{\mathrm{X}}}\mathrm{O}_b$
β_{ij}	(not named – symbols used in modified quasichemical model)
δ_{X}	Proportionality constant of $\Delta G_{\mathrm{X}_{c_{\mathrm{X}}}\mathrm{O}_b}^{\mathrm{ox,MQM}}$ (with $m_{\mathrm{X}} \ln x_{\mathrm{X}}$) as $x_{\mathrm{X}} \to 0$
δ_{Al}	Proportionality constant of $\Delta G_{\mathrm{Al}_2\mathrm{O}_3}^{\mathrm{ox,MQM}}$ (with $m_{\mathrm{Al}} \ln(1 - x_{\mathrm{X}})$) as $x_{\mathrm{X}} \to 1$
$\left(\frac{\partial f(x_i)}{\partial x_j}\right)_k$	Partial derivative of multivariate function $f(x_i)$ (x_i are independent variables) with respect to variable x_j at constant conditions k
ε_i	(not named – symbols used in modified quasichemical model)
μ_i	Chemical potential of component i
μ_i^{o}	Standard chemical potential of component i
$\Delta\mu_i$	Excess chemical potential of component i
$\Delta\mu_i^{\mathrm{ideal}}$	Excess chemical potential of component i assuming ideal mixing
$\Delta\mu_i^{\mathrm{xs}}$	Excess relative chemical potential of component i
$\prod_i f(x_i)$	Product of $f(x_i)$ over all i
σ_i	(not named – symbols used in modified quasichemical model)
$\sum_i f(x_i)$	Sum of $f(x_i)$ over all i
ω_{ij}	Bragg-Williams interaction parameter for the binary system i-j
ω_{ijk}	Bragg-Williams interaction parameter for the ternary system i-j-k

Table A.1. Comprehensive list of symbols used in Chapter 5.

A.2. Chemical potentials

A.2.1. Binary systems

For a binary solution of species A and B with concentrations x_{A} and x_{B}, the relative chemical

potential of component A, $\Delta\mu_{\mathrm{A}}$, can be defined through Gibbs free energy of mixing ΔG_{mix}, using the fact that their concentrations sum to unity (A.1).

$$\Delta G_{\mathrm{mix}} = \sum_i x_i(\mu_i - \mu_i^{\mathrm{o}}) = x_{\mathrm{A}}\mu_{\mathrm{A}} + x_{\mathrm{B}}\mu_{\mathrm{B}} - (x_{\mathrm{A}}\mu_{\mathrm{A}}^{\mathrm{o}} + x_{\mathrm{B}}\mu_{\mathrm{B}}^{\mathrm{o}})$$

$$\therefore \Delta G_{\mathrm{mix}} + x_{\mathrm{B}}\frac{\mathrm{d}\Delta G_{\mathrm{mix}}}{\mathrm{d}x_{\mathrm{A}}}$$

$$= x_{\mathrm{A}}\mu_{\mathrm{A}} + x_{\mathrm{B}}\mu_{\mathrm{B}} - (x_{\mathrm{A}}\mu_{\mathrm{A}}^{\mathrm{o}} + x_{\mathrm{B}}\mu_{\mathrm{B}}^{\mathrm{o}}) + x_{\mathrm{B}}\frac{\mathrm{d}}{\mathrm{d}x_{\mathrm{A}}}\left(x_{\mathrm{A}}\mu_{\mathrm{A}} + x_{\mathrm{B}}\mu_{\mathrm{B}} - (x_{\mathrm{A}}\mu_{\mathrm{A}}^{\mathrm{o}} + x_{\mathrm{B}}\mu_{\mathrm{B}}^{\mathrm{o}})\right)$$

$$= x_{\mathrm{A}}\mu_{\mathrm{A}} + x_{\mathrm{B}}\mu_{\mathrm{B}} - (x_{\mathrm{A}}\mu_{\mathrm{A}}^{\mathrm{o}} + x_{\mathrm{B}}\mu_{\mathrm{B}}^{\mathrm{o}}) + x_{\mathrm{B}}(\mu_{\mathrm{A}} - \mu_{\mathrm{B}}) - x_{\mathrm{B}}(\mu_{\mathrm{A}}^{\mathrm{o}} - \mu_{\mathrm{B}}^{\mathrm{o}})$$

$$= (x_{\mathrm{A}} + x_{\mathrm{B}})\mu_{\mathrm{A}} + (x_{\mathrm{B}} - x_{\mathrm{B}})\mu_{\mathrm{B}} - (x_{\mathrm{A}} + x_{\mathrm{B}})\mu_{\mathrm{A}}^{\mathrm{o}} - (x_{\mathrm{B}} - x_{\mathrm{B}})\mu_{\mathrm{B}}^{\mathrm{o}}$$

$$= (x_{\mathrm{A}} + x_{\mathrm{B}})(\mu_{\mathrm{A}} - \mu_{\mathrm{A}}^{\mathrm{o}}) = \Delta\mu_{\mathrm{A}}$$

$$\therefore \Delta\mu_{\mathrm{A}} = \Delta G_{\mathrm{mix}} + x_{\mathrm{B}}\frac{\mathrm{d}\Delta G_{\mathrm{mix}}}{\mathrm{d}x_{\mathrm{A}}} = \Delta G_{\mathrm{mix}} + (1 - x_{\mathrm{A}})\frac{\mathrm{d}\Delta G_{\mathrm{mix}}}{\mathrm{d}x_{\mathrm{A}}} \tag{A.1}$$

Using symmetry and the chain rule (A.2), $\Delta\mu_{\mathrm{B}}$ can also be evaluated (A.3).

$$\frac{\mathrm{d}}{\mathrm{d}x_{\mathrm{B}}} = \frac{\mathrm{d}x_{\mathrm{A}}}{\mathrm{d}x_{\mathrm{B}}} \times \frac{\mathrm{d}}{\mathrm{d}x_{\mathrm{A}}} = \frac{\mathrm{d}}{\mathrm{d}x_{\mathrm{B}}}(1 - x_{\mathrm{B}}) \times \frac{\mathrm{d}}{\mathrm{d}x_{\mathrm{A}}} = -\frac{\mathrm{d}}{\mathrm{d}x_{\mathrm{A}}} \tag{A.2}$$

$$\Delta\mu_{\mathrm{B}} = \Delta G_{\mathrm{mix}} + x_{\mathrm{A}}\frac{\mathrm{d}\Delta G_{\mathrm{mix}}}{\mathrm{d}x_{\mathrm{B}}} = \Delta G_{\mathrm{mix}} - x_{\mathrm{A}}\frac{\mathrm{d}\Delta G_{\mathrm{mix}}}{\mathrm{d}x_{\mathrm{A}}} \tag{A.3}$$

This also applies to $\Delta\mu_i^{\mathrm{xs}}$, where replacing ΔG_{mix} with $\Delta G_{\mathrm{mix}}^{\mathrm{xs}}$ gives expressions for $\Delta\mu_{\mathrm{A}}^{\mathrm{xs}}$ (A.4) and $\Delta\mu_{\mathrm{B}}^{\mathrm{xs}}$ (A.5).

$$\Delta\mu_{\mathrm{A}}^{\mathrm{xs}} = \Delta\mu_{\mathrm{A}} - \Delta\mu_{\mathrm{A}}^{\mathrm{ideal}} = \Delta G_{\mathrm{mix}} + x_{\mathrm{B}}\frac{\mathrm{d}\Delta G_{\mathrm{mix}}}{\mathrm{d}x_{\mathrm{A}}} - \left(\Delta G_{\mathrm{mix}}^{\mathrm{ideal}} + x_{\mathrm{B}}\frac{\mathrm{d}\Delta G_{\mathrm{mix}}^{\mathrm{ideal}}}{\mathrm{d}x_{\mathrm{A}}}\right)$$

$$= \left(\Delta G_{\mathrm{mix}} - \Delta G_{\mathrm{mix}}^{\mathrm{ideal}}\right) + x_{\mathrm{B}}\frac{\mathrm{d}}{\mathrm{d}x_{\mathrm{A}}}\left(\Delta G_{\mathrm{mix}} - \Delta G_{\mathrm{mix}}^{\mathrm{ideal}}\right) = \Delta G_{\mathrm{mix}}^{\mathrm{xs}} + x_{\mathrm{B}}\frac{\mathrm{d}\Delta G_{\mathrm{mix}}^{\mathrm{xs}}}{\mathrm{d}x_{\mathrm{A}}}$$

$$\Delta\mu_{\mathrm{A}}^{\mathrm{xs}} = \Delta G_{\mathrm{mix}}^{\mathrm{xs}} + (1 - x_{\mathrm{A}})\frac{\mathrm{d}\Delta G_{\mathrm{mix}}^{\mathrm{xs}}}{\mathrm{d}x_{\mathrm{A}}} \tag{A.4}$$

$$\Delta\mu_{\mathrm{B}}^{\mathrm{xs}} = \Delta G_{\mathrm{mix}}^{\mathrm{xs}} - x_{\mathrm{A}}\frac{\mathrm{d}\Delta G_{\mathrm{mix}}^{\mathrm{xs}}}{\mathrm{d}x_{\mathrm{A}}} \tag{A.5}$$

Switching A and B with X and Al, expressions for $\Delta\mu_{\mathrm{X}}$ (A.6), $\Delta\mu_{\mathrm{Al}}$ (A.7), $\Delta\mu_{\mathrm{X}}^{\mathrm{xs}}$ (A.8), and $\Delta\mu_{\mathrm{Al}}^{\mathrm{xs}}$

(A.9) can be written.

$$\Delta\mu_{\mathrm{X}} = \Delta G_{\mathrm{mix}} + (1 - x_{\mathrm{X}})\frac{\mathrm{d}\Delta G_{\mathrm{mix}}}{\mathrm{d}x_{\mathrm{X}}} \tag{A.6}$$

$$\Delta\mu_{\mathrm{Al}} = \Delta G_{\mathrm{mix}} - x_{\mathrm{X}}\frac{\mathrm{d}\Delta G_{\mathrm{mix}}}{\mathrm{d}x_{\mathrm{X}}} \tag{A.7}$$

$$\Delta\mu_{\mathrm{X}}^{\mathrm{xs}} = \Delta G_{\mathrm{mix}}^{\mathrm{xs}} + (1 - x_{\mathrm{X}})\frac{\mathrm{d}\Delta G_{\mathrm{mix}}^{\mathrm{xs}}}{\mathrm{d}x_{\mathrm{X}}} \tag{A.8}$$

$$\Delta\mu_{\mathrm{Al}}^{\mathrm{xs}} = \Delta G_{\mathrm{mix}}^{\mathrm{xs}} - x_{\mathrm{X}}\frac{\mathrm{d}\Delta G_{\mathrm{mix}}^{\mathrm{xs}}}{\mathrm{d}x_{\mathrm{X}}} \tag{A.9}$$

A.2.2. Ternary systems

For ternary systems, the chemical potential of each component $\Delta\mu_i$ can be determined graphically by finding the intersections of the plane tangent to the function $\Delta G_{\mathrm{mix}}(x_{\mathrm{A}}, x_{\mathrm{B}})$ at the pure compositions $x_i = 1$, analogously to the binary system (Figure A.1).

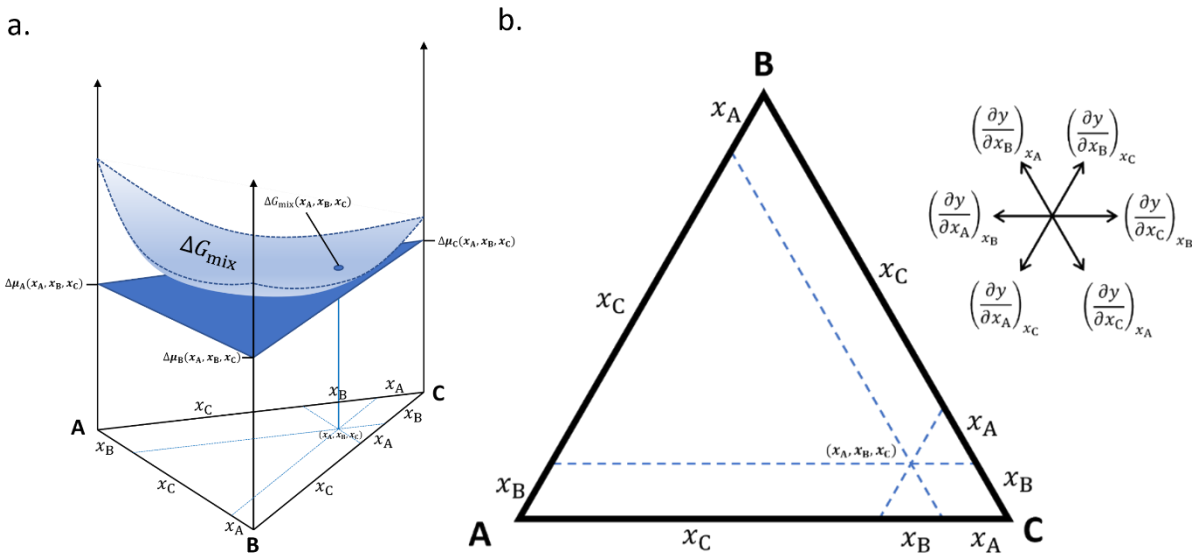


Figure A.1. Graphical representation of ΔG_{mix} in ternary systems. (a) The relationship between ΔG_{mix} and $\Delta\mu_{\mathrm{i}}$ in a ternary system ($\mathrm{i} \in \{\mathrm{A}, \mathrm{B}, \mathrm{C}\}$): the tangent plane to $\Delta G_{\mathrm{mix}}(x_{\mathrm{A}}, x_{\mathrm{B}}, x_{\mathrm{C}})$ intercepts the vertical axes x_{i} at $\Delta\mu_{\mathrm{i}}(x_{\mathrm{A}}, x_{\mathrm{B}}, x_{\mathrm{C}})$; (b) The relationship between derivatives in the three directions, constrained by the fact they must sum to unity.

For a ternary system with components A, B, and C, $\Delta\mu_{\mathrm{A}}$ (A.10), $\Delta\mu_{\mathrm{B}}$ (A.11), and $\Delta\mu_{\mathrm{C}}$ (A.12) can be evaluated in terms of ΔG_{mix} and its partial derivatives with respect to x_i.

$$\Delta\mu_{\mathrm{A}} = \Delta G_{\mathrm{mix}} - x_{\mathrm{B}}\left(\frac{\partial \Delta G_{\mathrm{mix}}}{\partial x_{\mathrm{B}}}\right)_{x_{\mathrm{C}}} - x_{\mathrm{C}}\left(\frac{\partial \Delta G_{\mathrm{mix}}}{\partial x_{\mathrm{C}}}\right)_{x_{\mathrm{B}}} \tag{A.10}$$

$$\Delta\mu_{\mathrm{B}} = \Delta G_{\mathrm{mix}} - x_{\mathrm{A}}\left(\frac{\partial \Delta G_{\mathrm{mix}}}{\partial x_{\mathrm{A}}}\right)_{x_{\mathrm{C}}} - x_{\mathrm{C}}\left(\frac{\partial \Delta G_{\mathrm{mix}}}{\partial x_{\mathrm{C}}}\right)_{x_{\mathrm{A}}} \tag{A.11}$$

$$\Delta\mu_{\mathrm{C}} = \Delta G_{\mathrm{mix}} - x_{\mathrm{A}}\left(\frac{\partial \Delta G_{\mathrm{mix}}}{\partial x_{\mathrm{A}}}\right)_{x_{\mathrm{B}}} - x_{\mathrm{B}}\left(\frac{\partial \Delta G_{\mathrm{mix}}}{\partial x_{\mathrm{B}}}\right)_{x_{\mathrm{A}}} \tag{A.12}$$

Since there is the constraint $x_{\mathrm{A}} + x_{\mathrm{B}} + x_{\mathrm{C}} = 1$, two useful relations can be derived. For a general function of the concentration of the three components $y(x_{\mathrm{A}}, x_{\mathrm{B}}, x_{\mathrm{C}})$, the increment $\mathrm{d}y$ can be expressed in terms of the increments of two of the variables $\mathrm{d}x_i$, since the constraint leaves only two independent variables x_i (A.13).

$$\begin{aligned}\mathrm{d}y &= \mathrm{d}x_{\mathrm{A}}\left(\frac{\partial y}{\partial x_{\mathrm{A}}}\right)_{x_{\mathrm{B}}} + \mathrm{d}x_{\mathrm{B}}\left(\frac{\partial y}{\partial x_{\mathrm{B}}}\right)_{x_{\mathrm{A}}} = \mathrm{d}x_{\mathrm{A}}\left(\frac{\partial y}{\partial x_{\mathrm{A}}}\right)_{x_{\mathrm{C}}} + \mathrm{d}x_{\mathrm{C}}\left(\frac{\partial y}{\partial x_{\mathrm{C}}}\right)_{x_{\mathrm{A}}} \\ &= \mathrm{d}x_{\mathrm{B}}\left(\frac{\partial y}{\partial x_{\mathrm{B}}}\right)_{x_{\mathrm{C}}} + \mathrm{d}x_{\mathrm{C}}\left(\frac{\partial y}{\partial x_{\mathrm{C}}}\right)_{x_{\mathrm{B}}}\end{aligned} \tag{A.13}$$

Using the relation $x_{\mathrm{A}} + x_{\mathrm{B}} + x_{\mathrm{C}} = 1$, dx_{C} can be eliminated and substituted.

$$\mathrm{d}x_{\mathrm{A}} + \mathrm{d}x_{\mathrm{B}} + \mathrm{d}x_{\mathrm{C}} = 0 \tag{A.14}$$

$$\mathrm{d}y = \mathrm{d}x_{\mathrm{A}}\left(\frac{\partial y}{\partial x_{\mathrm{A}}}\right)_{x_{\mathrm{B}}} + \mathrm{d}x_{\mathrm{B}}\left(\frac{\partial y}{\partial x_{\mathrm{B}}}\right)_{x_{\mathrm{A}}} = \mathrm{d}x_{\mathrm{A}}\left(\frac{\partial y}{\partial x_{\mathrm{A}}}\right)_{x_{\mathrm{C}}} - (\mathrm{d}x_{\mathrm{A}} + \mathrm{d}x_{\mathrm{B}})\left(\frac{\partial y}{\partial x_{\mathrm{C}}}\right)_{x_{\mathrm{A}}}$$

$$\mathrm{d}y = \mathrm{d}x_{\mathrm{B}}\left(\frac{\partial y}{\partial x_{\mathrm{B}}}\right)_{x_{\mathrm{C}}} - (\mathrm{d}x_{\mathrm{A}} + \mathrm{d}x_{\mathrm{B}})\left(\frac{\partial y}{\partial x_{\mathrm{C}}}\right)_{x_{\mathrm{B}}} \tag{A.15}$$

$$\mathrm{d}y = dx_{\mathrm{A}}\left(\frac{\partial y}{\partial x_{\mathrm{A}}}\right)_{x_{\mathrm{B}}} + \mathrm{d}x_{\mathrm{B}}\left(\frac{\partial y}{\partial x_{\mathrm{B}}}\right)_{x_{\mathrm{A}}}$$

$$= \mathrm{d}x_{\mathrm{A}}\left(\left(\frac{\partial y}{\partial x_{\mathrm{A}}}\right)_{x_{\mathrm{C}}} - \left(\frac{\partial y}{\partial x_{\mathrm{C}}}\right)_{x_{\mathrm{A}}}\right) - \mathrm{d}x_{\mathrm{B}}\left(\frac{\partial y}{\partial x_{\mathrm{C}}}\right)_{x_{\mathrm{A}}}$$

$$\mathrm{d}y = -\mathrm{d}x_{\mathrm{A}}\left(\frac{\partial y}{\partial x_{\mathrm{C}}}\right)_{x_{\mathrm{B}}} + \mathrm{d}x_{\mathrm{B}}\left(\left(\frac{\partial y}{\partial x_{\mathrm{B}}}\right)_{x_{\mathrm{C}}} - \left(\frac{\partial y}{\partial x_{\mathrm{C}}}\right)_{x_{\mathrm{B}}}\right) \tag{A.16}$$

Since the coefficients of $\mathrm{d}x_{\mathrm{A}}$ and $\mathrm{d}x_{\mathrm{B}}$ are equal, two other relations can be derived.

$$\left(\frac{\partial y}{\partial x_{\mathrm{A}}}\right)_{x_{\mathrm{B}}} = \left(\frac{\partial y}{\partial x_{\mathrm{A}}}\right)_{x_{\mathrm{C}}} - \left(\frac{\partial y}{\partial x_{\mathrm{C}}}\right)_{x_{\mathrm{A}}} = -\left(\frac{\partial y}{\partial x_{\mathrm{C}}}\right)_{x_{\mathrm{B}}} \tag{A.17}$$

$$\left(\frac{\partial y}{\partial x_{\mathrm{B}}}\right)_{x_{\mathrm{A}}} = \left(\frac{\partial y}{\partial x_{\mathrm{B}}}\right)_{x_{\mathrm{C}}} - \left(\frac{\partial y}{\partial x_{\mathrm{C}}}\right)_{x_{\mathrm{B}}} = -\left(\frac{\partial y}{\partial x_{\mathrm{C}}}\right)_{x_{\mathrm{A}}} \tag{A.18}$$

This gives the first relation (A.18) from which two others can be derived by cyclic permutation.

$$\left(\frac{\partial y}{\partial x_{\mathrm{B}}}\right)_{x_{\mathrm{A}}} + \left(\frac{\partial y}{\partial x_{\mathrm{C}}}\right)_{x_{\mathrm{A}}} = 0 \tag{A.19}$$

$$\left(\frac{\partial y}{\partial x_{\mathrm{A}}}\right)_{x_{\mathrm{B}}} + \left(\frac{\partial y}{\partial x_{\mathrm{C}}}\right)_{x_{\mathrm{B}}} = 0 \tag{A.20}$$

$$\left(\frac{\partial y}{\partial x_{\mathrm{A}}}\right)_{x_{\mathrm{C}}} + \left(\frac{\partial y}{\partial x_{\mathrm{B}}}\right)_{x_{\mathrm{C}}} = 0 \tag{A.21}$$

Two more relations can be derived from these equations.

$$\left(\frac{\partial y}{\partial x_{\mathrm{A}}}\right)_{x_{\mathrm{C}}} + \left(\frac{\partial y}{\partial x_{\mathrm{B}}}\right)_{x_{\mathrm{A}}} + \left(\frac{\partial y}{\partial x_{\mathrm{C}}}\right)_{x_{\mathrm{B}}} = 0 \tag{A.22}$$

$$\left(\frac{\partial y}{\partial x_{\mathrm{A}}}\right)_{x_{\mathrm{B}}} + \left(\frac{\partial y}{\partial x_{\mathrm{B}}}\right)_{x_{\mathrm{C}}} + \left(\frac{\partial y}{\partial x_{\mathrm{C}}}\right)_{x_{\mathrm{A}}} = 0 \tag{A.23}$$

These relations can be seen geometrically using the ternary diagram (Figure A.1). These relations allow the chemical potentials to be described in terms of two variables x_{A} and x_{B}.

$$\Delta\mu_{\mathrm{A}} = \Delta G_{\mathrm{mix}} - x_{\mathrm{B}}\left(\frac{\partial \Delta G_{\mathrm{mix}}}{\partial x_{\mathrm{B}}}\right)_{x_{\mathrm{C}}} - x_{\mathrm{C}}\left(\frac{\partial \Delta G_{\mathrm{mix}}}{\partial x_{\mathrm{C}}}\right)_{x_{\mathrm{B}}}$$

$$= \Delta G_{\mathrm{mix}} + x_{\mathrm{B}}\left(\left(\frac{\partial \Delta G_{\mathrm{mix}}}{\partial x_{\mathrm{A}}}\right)_{x_{\mathrm{B}}} + \left(\frac{\partial \Delta G_{\mathrm{mix}}}{\partial x_{\mathrm{C}}}\right)_{x_{\mathrm{A}}}\right) + x_{\mathrm{C}}\left(\frac{\partial \Delta G_{\mathrm{mix}}}{\partial x_{\mathrm{A}}}\right)_{x_{\mathrm{B}}}$$

$$= \Delta G_{\mathrm{mix}} - x_{\mathrm{B}}\left(\frac{\partial \Delta G_{\mathrm{mix}}}{\partial x_{\mathrm{B}}}\right)_{x_{\mathrm{A}}} + (x_{\mathrm{B}} + x_{\mathrm{C}})\left(\frac{\partial \Delta G_{\mathrm{mix}}}{\partial x_{\mathrm{A}}}\right)_{x_{\mathrm{B}}}$$

$$\Delta\mu_{\mathrm{A}} = \Delta G_{\mathrm{mix}} + (1 - x_{\mathrm{A}})\left(\frac{\partial \Delta G_{\mathrm{mix}}}{\partial x_{\mathrm{A}}}\right)_{x_{\mathrm{B}}} - x_{\mathrm{B}}\left(\frac{\partial \Delta G_{\mathrm{mix}}}{\partial x_{\mathrm{B}}}\right)_{x_{\mathrm{A}}} \tag{A.24}$$

$$\Delta\mu_{\mathrm{B}} = \Delta G_{\mathrm{mix}} - x_{\mathrm{A}}\left(\frac{\partial \Delta G_{\mathrm{mix}}}{\partial x_{\mathrm{A}}}\right)_{x_{\mathrm{C}}} - x_{\mathrm{C}}\left(\frac{\partial \Delta G_{\mathrm{mix}}}{\partial x_{\mathrm{C}}}\right)_{x_{\mathrm{A}}}$$

$$= \Delta G_{\mathrm{mix}} + x_{\mathrm{A}}\left(\left(\frac{\partial \Delta G_{\mathrm{mix}}}{\partial x_{\mathrm{B}}}\right)_{x_{\mathrm{A}}} + \left(\frac{\partial \Delta G_{\mathrm{mix}}}{\partial x_{\mathrm{C}}}\right)_{x_{\mathrm{B}}}\right) + x_{\mathrm{C}}\left(\frac{\partial \Delta G_{\mathrm{mix}}}{\partial x_{\mathrm{B}}}\right)_{x_{\mathrm{A}}}$$

$$= \Delta G_{\mathrm{mix}} - x_{\mathrm{A}}\left(\frac{\partial \Delta G_{\mathrm{mix}}}{\partial x_{\mathrm{A}}}\right)_{x_{\mathrm{B}}} + (x_{\mathrm{A}} + x_{\mathrm{C}})\left(\frac{\partial \Delta G_{\mathrm{mix}}}{\partial x_{\mathrm{B}}}\right)_{x_{\mathrm{A}}}$$

$$\Delta\mu_{\mathrm{B}} = \Delta G_{\mathrm{mix}} - x_{\mathrm{A}}\left(\frac{\partial \Delta G_{\mathrm{mix}}}{\partial x_{\mathrm{A}}}\right)_{x_{\mathrm{B}}} + (1 - x_{\mathrm{B}})\left(\frac{\partial \Delta G_{\mathrm{mix}}}{\partial x_{\mathrm{B}}}\right)_{x_{\mathrm{A}}} \tag{A.25}$$

$$\Delta\mu_{\mathrm{C}} = \Delta G_{\mathrm{mix}} - x_{\mathrm{A}}\left(\frac{\partial \Delta G_{\mathrm{mix}}}{\partial x_{\mathrm{A}}}\right)_{x_{\mathrm{B}}} - x_{\mathrm{B}}\left(\frac{\partial \Delta G_{\mathrm{mix}}}{\partial x_{\mathrm{B}}}\right)_{x_{\mathrm{A}}} \tag{A.26}$$

Therefore, for a ternary Al-X_1-X_2 system, $\Delta\mu_i$ are given below.

$$\Delta\mu_1 = \Delta G_{\mathrm{mix}} + (1 - x_1)\left(\frac{\partial \Delta G_{\mathrm{mix}}}{\partial x_1}\right)_{x_2} - x_2\left(\frac{\partial \Delta G_{\mathrm{mix}}}{\partial x_2}\right)_{x_1} \tag{A.27}$$

$$\Delta\mu_2 = \Delta G_{\mathrm{mix}} - x_1\left(\frac{\partial \Delta G_{\mathrm{mix}}}{\partial x_1}\right)_{x_2} + (1 - x_2)\left(\frac{\partial \Delta G_{\mathrm{mix}}}{\partial x_2}\right)_{x_1} \tag{A.28}$$

$$\Delta\mu_{\mathrm{Al}} = \Delta G_{\mathrm{mix}} - x_1\left(\frac{\partial \Delta G_{\mathrm{mix}}}{\partial x_1}\right)_{x_2} - x_2\left(\frac{\partial \Delta G_{\mathrm{mix}}}{\partial x_2}\right)_{x_1} \tag{A.29}$$

The excess quantities $\Delta\mu_i^{\mathrm{xs}}$ can also be evaluated.

$$\Delta\mu_1^{\mathrm{xs}} = \Delta G_{\mathrm{mix}}^{\mathrm{xs}} + (1 - x_1)\left(\frac{\partial \Delta G_{\mathrm{mix}}^{\mathrm{xs}}}{\partial x_1}\right)_{x_2} - x_2\left(\frac{\partial \Delta G_{\mathrm{mix}}^{\mathrm{xs}}}{\partial x_2}\right)_{x_1} \tag{A.30}$$

$$\Delta\mu_2^{\mathrm{xs}} = \Delta G_{\mathrm{mix}}^{\mathrm{xs}} - x_1\left(\frac{\partial \Delta G_{\mathrm{mix}}^{\mathrm{xs}}}{\partial x_1}\right)_{x_2} + (1 - x_2)\left(\frac{\partial \Delta G_{\mathrm{mix}}^{\mathrm{xs}}}{\partial x_2}\right)_{x_1} \tag{A.31}$$

$$\Delta\mu_{\mathrm{Al}}^{\mathrm{xs}} = \Delta G_{\mathrm{mix}}^{\mathrm{xs}} - x_1\left(\frac{\partial \Delta G_{\mathrm{mix}}^{\mathrm{xs}}}{\partial x_1}\right)_{x_2} - x_2\left(\frac{\partial \Delta G_{\mathrm{mix}}^{\mathrm{xs}}}{\partial x_2}\right)_{x_1} \tag{A.32}$$

A.3. Bragg-Williams mixing

A.3.1. Binary systems

In Bragg-Williams mixing, $\Delta G_{\mathrm{mix}}^{\mathrm{xs}}$ is expanded in terms of Redlich-Kister Polynomials, whose parameters can be fitted to experimental data (A.33).

$$\Delta G_{\mathrm{mix}}^{\mathrm{xs}} = x_{\mathrm{X}} x_{\mathrm{Al}} \omega_{\mathrm{XAl}} = x_{\mathrm{X}} x_{\mathrm{Al}} \sum_{i \geq 0} {}^{i}L_{\mathrm{XAl}} (x_{\mathrm{X}} - x_{\mathrm{Al}})^{i} \tag{A.33}$$

The expressions for $\Delta G_{\mathrm{mix}}^{\mathrm{xs}}$ (A.34) and its derivative (A.35) can be evaluated.

$$\Delta G_{\mathrm{mix}}^{\mathrm{xs}} = x_{\mathrm{X}}(1 - x_{\mathrm{X}}) \sum_{i \geq 0} {}^{i}L_{\mathrm{XAl}} (2x_{\mathrm{X}} - 1)^{i} = \sum_{i \geq 0} {}^{i}L_{\mathrm{XAl}} (2x_{\mathrm{X}} - 1)^{i} (x_{\mathrm{X}} - x_{\mathrm{X}}^{2}) \tag{A.34}$$

$$\frac{\mathrm{d}\Delta G_{\mathrm{mix}}^{\mathrm{xs}}}{\mathrm{d}x_{\mathrm{X}}} = \sum_{i \geq 0} {}^{i}L_{\mathrm{XAl}} (2x_{\mathrm{X}} - 1)^{i-1} [(4 + 2i)(x_{\mathrm{X}} - x_{\mathrm{X}}^{2}) - 1] \tag{A.35}$$

Evaluation of the terms $x_{\mathrm{X}} \frac{\mathrm{d}\Delta G_{\mathrm{mix}}^{\mathrm{xs}}}{\mathrm{d}x_{\mathrm{X}}}$ (A.36) and $(1 - x_{\mathrm{X}}) \frac{\mathrm{d}\Delta G_{\mathrm{mix}}^{\mathrm{xs}}}{\mathrm{d}x_{\mathrm{X}}}$ (A.37) allows calculation of $\Delta \mu_{\mathrm{X}}^{\mathrm{xs}}$ (A.38) and $\Delta \mu_{\mathrm{Al}}^{\mathrm{xs}}$ (A.39).

$$x_{\mathrm{X}} \frac{\mathrm{d}\Delta G_{\mathrm{mix}}^{\mathrm{xs}}}{\mathrm{d}x_{\mathrm{X}}} = x_{\mathrm{X}} \sum_{i \geq 0} {}^{i}L_{\mathrm{XAl}} (2x_{\mathrm{X}} - 1)^{i-1} [(4 + 2i)(x_{\mathrm{X}} - x_{\mathrm{X}}^{2}) - 1]$$

$$= \sum_{i \geq 0} {}^{i}L_{\mathrm{XAl}} (2x_{\mathrm{X}} - 1)^{i-1} [(4 + 2i)(x_{\mathrm{X}}^{2} - x_{\mathrm{X}}^{3}) - x_{\mathrm{X}}] \tag{A.36}$$

$$(1 - x_{\mathrm{X}}) \frac{\mathrm{d}\Delta G_{\mathrm{mix}}^{\mathrm{xs}}}{\mathrm{d}x_{\mathrm{X}}} = (1 - x_{\mathrm{X}}) \sum_{i \geq 0} {}^{i}L_{\mathrm{XAl}} (2x_{\mathrm{X}} - 1)^{i-1} [(4 + 2i)(x_{\mathrm{X}} - x_{\mathrm{X}}^{2}) - 1]$$

$$= \sum_{i \geq 0} {}^{i}L_{\mathrm{XAl}} (2x_{\mathrm{X}} - 1)^{i-1} (1 - x_{\mathrm{X}}) [(x_{\mathrm{X}}(4 + 2i)(1 - x_{\mathrm{X}}) - 1)] \tag{A.37}$$

$$\Delta \mu_{\mathrm{X}}^{\mathrm{xs}} = \Delta G_{\mathrm{mix}}^{\mathrm{xs}} + (1 - x_{\mathrm{X}}) \frac{\mathrm{d}\Delta G_{\mathrm{mix}}^{\mathrm{xs}}}{\mathrm{d}x_{\mathrm{X}}}$$

$$= x_{\mathrm{X}}(1 - x_{\mathrm{X}}) \sum_{i \geq 0} {}^{i}L_{\mathrm{XAl}} (2x_{\mathrm{X}} - 1)^{i}$$

$$+ \sum_{i \geq 0} {}^{i}L_{\mathrm{XAl}} (2x_{\mathrm{X}} - 1)^{i-1} (1 - x_{\mathrm{X}}) [(x_{\mathrm{X}}(4 + 2i)(1 - x_{\mathrm{X}}) - 1)]$$

$$= (1 - x_{\mathrm{X}}) \sum_{i \geq 0} {}^{i}L_{\mathrm{XAl}} (2x_{\mathrm{X}} - 1)^{i-1} (x_{\mathrm{X}}(2x_{\mathrm{X}} - 1) + x_{\mathrm{X}}(4 + 2i)(1 - x_{\mathrm{X}}) - 1)$$

$$= (1 - x_{\mathrm{X}}) \sum_{i \geq 0} {}^{i}L_{\mathrm{XAl}} (2x_{\mathrm{X}} - 1)^{i-1} (2x_{\mathrm{X}}^{2} - x_{\mathrm{X}} + 4x_{\mathrm{X}} + 2ix_{\mathrm{X}} - 4x_{\mathrm{X}}^{2} - 2ix_{\mathrm{X}}^{2} - 1)$$

$$\Delta \mu_{\mathrm{X}}^{\mathrm{xs}} = (1 - x_{\mathrm{X}})^{2} \sum_{i \geq 0} {}^{i}L_{\mathrm{XAl}} (2x_{\mathrm{X}} - 1)^{i-1} [2(i + 1)x_{\mathrm{X}} - 1] \tag{A.38}$$

$$\Delta \mu_{\mathrm{Al}}^{\mathrm{xs}} = \Delta G_{\mathrm{mix}}^{\mathrm{xs}} - x_{\mathrm{X}} \frac{\mathrm{d}\Delta G_{\mathrm{mix}}^{\mathrm{xs}}}{\mathrm{d}x_{\mathrm{X}}}$$

$$= \sum_{i\geq 0} {}^{i}L_{\mathrm{XAl}}(2x_{\mathrm{X}}-1)^{i}(x_{\mathrm{X}}-x_{\mathrm{X}}^{2}) - \sum_{i\geq 0} {}^{i}L_{\mathrm{XAl}}(2x_{\mathrm{X}}-1)^{i-1}\left((4+2i)(x_{\mathrm{X}}^{2}-x_{\mathrm{X}}^{3})-x_{\mathrm{X}}\right)$$

$$= \sum_{i\geq 0} {}^{i}L_{\mathrm{XAl}}(2x_{\mathrm{X}}-1)^{i-1}\left((2x_{\mathrm{X}}-1)(x_{\mathrm{X}}-x_{\mathrm{X}}^{2}) - \left((4+2i)(x_{\mathrm{X}}^{2}-x_{\mathrm{X}}^{3})-x_{\mathrm{X}}\right)\right)$$

$$= \sum_{i\geq 0} {}^{i}L_{\mathrm{XAl}}(2x_{\mathrm{X}}-1)^{i-1}(2x_{\mathrm{X}}^{2}-x_{\mathrm{X}}+x_{\mathrm{X}}^{2}-2x_{\mathrm{X}}^{3}-4x_{\mathrm{X}}^{2}+4x_{\mathrm{X}}^{3}-2ix_{\mathrm{X}}^{2}+2ix_{\mathrm{X}}^{3}+x_{\mathrm{X}})$$

$$= \sum_{i\geq 0} {}^{i}L_{\mathrm{XAl}}(2x_{\mathrm{X}}-1)^{i-1}(-x_{\mathrm{X}}^{2}+2x_{\mathrm{X}}^{3}-2ix_{\mathrm{X}}^{2}+2ix_{\mathrm{X}}^{3})$$

$$= x_{\mathrm{X}}^{2}\sum_{i\geq 0} {}^{i}L_{\mathrm{XAl}}(2x_{\mathrm{X}}-1)^{i-1}(-1+2x_{\mathrm{X}}-2i+2ix_{\mathrm{X}})$$

$$\Delta\mu_{\mathrm{Al}}^{\mathrm{xs}} = x_{\mathrm{X}}^{2}\sum_{i\geq 0} {}^{i}L_{\mathrm{XAl}}(2x_{\mathrm{X}}-1)^{i-1}[1-2(i+1)(1-x_{\mathrm{X}})] \tag{A.39}$$

The combined $\Delta\mu_{i}^{\mathrm{xs}}$ term can then be evaluated (A.40), allowing evaluation of ΔG^{ox} (A.41).

$$m_{\mathrm{X}}\Delta\mu_{\mathrm{X}}^{\mathrm{xs}} + m_{\mathrm{Al}}\Delta\mu_{\mathrm{Al}}^{\mathrm{xs}}$$

$$= m_{\mathrm{X}}(1-x_{\mathrm{X}})^{2}\sum_{i\geq 0} {}^{i}L_{\mathrm{XAl}}(2x_{\mathrm{X}}-1)^{i-1}(2x_{\mathrm{X}}(i+1)-1)$$

$$+ m_{\mathrm{Al}}x_{\mathrm{X}}^{2}\sum_{i\geq 0} {}^{i}L_{\mathrm{XAl}}(2x_{\mathrm{X}}-1)^{i-1}\left(1-2(i+1)(1-x_{\mathrm{X}})\right)$$

$$= \sum_{i\geq 0} {}^{i}L_{\mathrm{XAl}}(2x_{\mathrm{X}}-1)^{i-1}\left[m_{\mathrm{X}}(1-x_{\mathrm{X}})^{2}(2x_{\mathrm{X}}(i+1)-1) + m_{\mathrm{Al}}x_{\mathrm{X}}^{2}\left(1-2(i+1)(1-x_{\mathrm{X}})\right)\right]$$

$$= \sum_{i\geq 0} {}^{i}L_{\mathrm{XAl}}(2x_{\mathrm{X}}-1)^{i-1}\left[m_{\mathrm{X}}(1-x_{\mathrm{X}})^{2}(2x_{\mathrm{X}}-1+2ix_{\mathrm{X}})\right.$$

$$\left. + m_{\mathrm{Al}}x_{\mathrm{X}}^{2}\left(2x_{\mathrm{X}}-1-2i(1-x_{\mathrm{X}})\right)\right] \tag{A.40}$$

$$\Delta G^{\mathrm{ox}}_{\mathrm{Al}_{c_{\mathrm{Al}}}\mathrm{X}_{c_{\mathrm{X}}}\mathrm{O}_{b}}(x_{\mathrm{X}},T,p\mathrm{O}_{2})$$

$$= \frac{2}{b}\Delta G^{\mathrm{o}}_{\mathrm{f,\,Al}_{c_{\mathrm{Al}}}\mathrm{X}_{c_{\mathrm{X}}}\mathrm{O}_{b}}(T) - [m_{\mathrm{X}}\Delta\mu_{\mathrm{X}}^{\mathrm{xs}} + m_{\mathrm{Al}}\Delta\mu_{\mathrm{Al}}^{\mathrm{xs}}] - RT\ln\left(x_{\mathrm{X}}^{m_{\mathrm{X}}}x_{\mathrm{Al}}^{m_{\mathrm{Al}}}p\mathrm{O}_{2}\right)$$

$$= \frac{2}{b}\Delta G^{\mathrm{o}}_{\mathrm{f,\,Al}_{c_{\mathrm{Al}}}\mathrm{X}_{c_{\mathrm{X}}}\mathrm{O}_{b}}(T) - RT\ln\left(x_{\mathrm{X}}^{m_{\mathrm{X}}}x_{\mathrm{Al}}^{m_{\mathrm{Al}}}p\mathrm{O}_{2}\right) - \Delta G^{\mathrm{ox,BWB}}_{\mathrm{Al}_{c_{\mathrm{Al}}}\mathrm{X}_{c_{\mathrm{X}}}\mathrm{O}_{b}} \tag{A.41}$$

Where m_{X} (A.42), m_{Al} (A.43), and $\Delta G^{\mathrm{ox,BWB}}_{\mathrm{Al}_{c_{\mathrm{Al}}}\mathrm{X}_{c_{\mathrm{X}}}\mathrm{O}_{\mathrm{b}}}$ (A.44), the Bragg-Williams binary (BWB)

term, are defined as follows.

$$m_{\mathrm{X}} = \frac{2a}{b} \qquad \text{(A.42)} \qquad m_{\mathrm{Al}} = \frac{2c}{b} \qquad \text{(A.43)}$$

$$\Delta G^{\mathrm{ox,BWB}}_{\mathrm{Al}_{c_{\mathrm{Al}}}\mathrm{X}_{c_{\mathrm{X}}}\mathrm{O}_{\mathrm{b}}} = {}^{0}L_{\mathrm{XAl}}(m_{\mathrm{X}}(1-x_{\mathrm{X}})^2 + m_{\mathrm{Al}}x_{\mathrm{X}}^2)$$

$$+\sum_{i\geq 1} {}^{i}L_{\mathrm{XAl}}(2x_{\mathrm{X}}-1)^{i-1}\left[m_{\mathrm{X}}(1-x_{\mathrm{X}})^2(2x_{\mathrm{X}}-1+2ix_{\mathrm{X}}) + m_{\mathrm{Al}}x_{\mathrm{X}}^2\left(2x_{\mathrm{X}}-1-2i(1-x_{\mathrm{X}})\right)\right]$$

$$=\sum_{i\geq 0} {}^{i}L_{\mathrm{XAl}}(x_{\mathrm{X}}-x_{\mathrm{Al}})^{i-1}[(m_{\mathrm{X}}{x_{\mathrm{Al}}}^2 + m_{\mathrm{Al}}x_{\mathrm{X}}^2)(x_{\mathrm{X}}-x_{\mathrm{Al}})$$

$$+ 2ix_{\mathrm{X}}x_{\mathrm{Al}}(m_{\mathrm{X}}x_{\mathrm{Al}} - m_{\mathrm{Al}}x_{\mathrm{X}})] \qquad \text{(A.44)}$$

A.3.2. Ternary solutions

In ternary systems (Al-X_1- X_2), a ternary interaction parameter $\omega_{12\mathrm{Al}}$ is introduced, such that the excess free energy of mixing, $\Delta G^{\mathrm{xs}}_{\mathrm{mix}}$, is given below (A.45), where ω_{ij} are binary interaction parameters expanded as Redlich-Kister polynomials.

$$\Delta G^{\mathrm{xs}}_{\mathrm{mix}} = x_1x_2\omega_{12} + x_1x_{\mathrm{Al}}\omega_{1\mathrm{Al}} + x_2x_{\mathrm{Al}}\omega_{2\mathrm{Al}} + x_1x_2x_{\mathrm{Al}}\omega_{12\mathrm{Al}} \qquad \text{(A.45)}$$

The general form for $\omega_{12\mathrm{Al}}$ is given below, where ${}^{i}L_{12\mathrm{Al}}$ depends on temperature and compositions x_i (A.46).

$$\omega_{12\mathrm{Al}} = x_1{}^{1}L_{12\mathrm{Al}} + x_2{}^{2}L_{12\mathrm{Al}} + x_{\mathrm{Al}}{}^{\mathrm{Al}}L_{12\mathrm{Al}} = \textstyle\sum_i x_i{}^{i}L_{12\mathrm{Al}} \qquad \text{(A.46)}$$

The partial derivatives of ω_{ij} and ω_{ijk} can be evaluated with respect to x_i.

$$\left(\frac{\partial\omega_{12}}{\partial x_1}\right)_{x_2} = \omega_{12,x_1} = \left(\frac{\partial}{\partial x_1}\sum_{i\geq 0} {}^{i}L_{12}(x_1-x_2)^i\right)_{x_2} = \sum_{i\geq 1} i\,{}^{i}L_{12}(x_1-x_2)^{i-1} \qquad \text{(A.47)}$$

$$\left(\frac{\partial\omega_{12}}{\partial x_2}\right)_{x_1} = \omega_{12,x_2} = \left(\frac{\partial}{\partial x_2}\sum_{i\geq 0} {}^{i}L_{12}(x_1-x_2)^i\right)_{x_1} = \sum_{i\geq 1} -i\,{}^{i}L_{12}(x_1-x_2)^{i-1} \qquad \text{(A.48)}$$

$$\left(\frac{\partial\omega_{1\mathrm{Al}}}{\partial x_1}\right)_{x_2} = \omega_{1\mathrm{Al},x_1} = \left(\frac{\partial}{\partial x_1}\sum_{i\geq 0} {}^{i}L_{1\mathrm{Al}}(x_1-x_{\mathrm{Al}})^i\right)_{x_2}$$

$$= \left(\frac{\partial}{\partial x_1}\sum_{i\geq 0} {}^{i}L_{1\mathrm{Al}}\big(x_1-(1-x_1-x_2)\big)^{i}\right)_{x_2}$$

$$= \left(\frac{\partial}{\partial x_1}\sum_{i\geq 0} {}^{i}L_{1\mathrm{Al}}(2x_1+x_2-1)^{i}\right)_{x_2} = \sum_{i\geq 1} 2i\,{}^{i}L_{1\mathrm{Al}}(2x_1+x_2-1)^{i-1} \tag{A.49}$$

$$\left(\frac{\partial \omega_{1\mathrm{Al}}}{\partial x_2}\right)_{x_1} = \omega_{1\mathrm{Al},x_2} = \left(\frac{\partial}{\partial x_2}\sum_{i\geq 0} {}^{i}L_{1\mathrm{Al}}(2x_1+x_2-1)^{i}\right)_{x_1}$$

$$= \sum_{i\geq 1} i\,{}^{i}L_{1\mathrm{Al}}(2x_1+x_2-1)^{i-1} \tag{A.50}$$

$$\left(\frac{\partial \omega_{2\mathrm{Al}}}{\partial x_1}\right)_{x_2} = \omega_{2\mathrm{Al},x_1} = \left(\frac{\partial}{\partial x_1}\sum_{i\geq 0} {}^{i}L_{2\mathrm{Al}}(x_2-x_{\mathrm{Al}})^{i}\right)_{x_2}$$

$$= \left(\frac{\partial}{\partial x_1}\sum_{i\geq 0} {}^{i}L_{2\mathrm{Al}}\big(x_2-(1-x_1-x_2)\big)^{i}\right)_{x_2}$$

$$= \left(\frac{\partial}{\partial x_1}\sum_{i\geq 0} {}^{i}L_{2\mathrm{Al}}(x_1+2x_2-1)^{i}\right)_{x_2} = \sum_{i\geq 1} i\,{}^{i}L_{2\mathrm{Al}}(x_1+2x_2-1)^{i-1} \tag{A.51}$$

$$\left(\frac{\partial \omega_{2\mathrm{Al}}}{\partial x_2}\right)_{x_1} = \omega_{2\mathrm{Al},x_2} = \left(\frac{\partial}{\partial x_2}\sum_{i\geq 0} {}^{i}L_{2\mathrm{Al}}(x_1+2x_2-1)^{i}\right)_{x_1}$$

$$= \sum_{i\geq 1} 2i\,{}^{i}L_{2\mathrm{Al}}(2x_1+x_2-1)^{i-1} \tag{A.52}$$

$$\left(\frac{\partial \omega_{12\mathrm{Al}}}{\partial x_1}\right)_{x_2} = \omega_{12\mathrm{Al},x_1} = \left(\frac{\partial}{\partial x_1}\left(x_1\,{}^{1}L_{12\mathrm{Al}} + x_2\,{}^{2}L_{12\mathrm{Al}} + (1-x_1-x_2)\,{}^{\mathrm{Al}}L_{12\mathrm{Al}}\right)\right)_{x_2}$$

$$= {}^{1}L_{12\mathrm{Al}} - {}^{\mathrm{Al}}L_{12\mathrm{Al}} \tag{A.53}$$

$$\left(\frac{\partial \omega_{12\mathrm{Al}}}{\partial x_2}\right)_{x_1} = \omega_{12\mathrm{Al},x_2} = \left(\frac{\partial}{\partial x_2}\left(x_1\,{}^{1}L_{12\mathrm{Al}} + x_2\,{}^{2}L_{12\mathrm{Al}} + (1-x_1-x_2)\,{}^{\mathrm{Al}}L_{12\mathrm{Al}}\right)\right)_{x_1}$$

$$= {}^{2}L_{12\mathrm{Al}} - {}^{\mathrm{Al}}L_{12\mathrm{Al}} \tag{A.54}$$

The partial derivatives of $\Delta G_{\mathrm{mix}}^{\mathrm{xs}}$ with respect to x_1 (A.55) and x_2 (A.56) can then be found.

$$\Delta G_{\mathrm{mix}}^{\mathrm{xs}} = x_1x_2\omega_{12} + x_1\omega_{1\mathrm{Al}} - x_1(x_1+x_2)\omega_{1\mathrm{Al}} + x_2\omega_{2\mathrm{Al}} - x_2(x_1+x_2)\omega_{2\mathrm{Al}} + x_1x_2\omega_{12\mathrm{Al}}$$
$$- x_1x_2(x_1+x_2)\omega_{12\mathrm{Al}}$$

$$\left(\frac{\partial \Delta G_{\mathrm{mix}}^{\mathrm{xs}}}{\partial x_1}\right)_{x_2} = x_2\omega_{12} + x_1x_2\omega_{12,x_1} + \omega_{1\mathrm{Al}} + x_1\omega_{1\mathrm{Al},x_1} - (x_1+x_2)\omega_{1\mathrm{Al}} - x_1\omega_{1\mathrm{Al}}$$
$$- x_1(x_1+x_2)\omega_{1\mathrm{Al},x_1} + x_2\omega_{2\mathrm{Al},x_1} - x_2\omega_{2\mathrm{Al}} - x_2(x_1+x_2)\omega_{2\mathrm{Al},x_1} + x_2\omega_{12\mathrm{Al}}$$
$$+ x_1x_2\omega_{12\mathrm{Al},x_1} - x_2(x_1+x_2)\omega_{12\mathrm{Al}} - x_1x_2\omega_{12\mathrm{Al}} - x_1x_2(x_1+x_2)\omega_{12\mathrm{Al},x_1}$$
$$= x_2\big(\omega_{12} + x_1\omega_{12,x_1}\big) + \omega_{1\mathrm{Al}}(1-(x_1+x_2)-x_1) + x_1\omega_{1\mathrm{Al},x_1}\big(1-(x_1+x_2)\big) - x_2\omega_{2\mathrm{Al}}$$
$$+ x_2\omega_{2\mathrm{Al},x_1}\big(1-(x_1+x_2)\big) + x_2\omega_{12\mathrm{Al}}(1-(x_1+x_2)-x_1)$$
$$+ x_1x_2\omega_{12\mathrm{Al},x_1}\big(1-(x_1+x_2)\big)$$
$$= x_2\big(\omega_{12} + x_1\omega_{12,x_1}\big) + \omega_{1\mathrm{Al}}(1-2x_1-x_2) + x_1\omega_{1\mathrm{Al},x_1}(1-x_1-x_2) - x_2\omega_{2\mathrm{Al}}$$
$$+ x_2\omega_{2\mathrm{Al},x_1}(1-x_1-x_2) + x_2\omega_{12\mathrm{Al}}(1-2x_1-x_2)$$
$$+ x_1x_2\omega_{12\mathrm{Al},x_1}(1-x_1-x_2)$$
$$= x_2\big(\omega_{12} - \omega_{2\mathrm{Al}} + x_1\omega_{12,x_1}\big) + (1-2x_1-x_2)(\omega_{1\mathrm{Al}} + x_2\omega_{12\mathrm{Al}})$$
$$+ (1-x_1-x_2)\big(x_1\omega_{1\mathrm{Al},x_1} + x_2\omega_{2\mathrm{Al},x_1} + x_1x_2\omega_{12\mathrm{Al},x_1}\big)$$
$$= x_2\left(\sum_{i\geq 0} {}^{i}L_{12}(x_1-x_2)^i - \sum_{i\geq 0} {}^{i}L_{2\mathrm{Al}}(x_1+2x_2-1)^i + \sum_{i\geq 1} i x_1 {}^{i}L_{12}(x_1-x_2)^{i-1}\right)$$
$$+(1-2x_1-x_2)\left(\sum_{i\geq 0} {}^{i}L_{1\mathrm{Al}}(2x_1+x_2-1)^i\right.$$
$$\left. + x_2\big(x_1 {}^{1}L_{12\mathrm{Al}} + x_2 {}^{2}L_{12\mathrm{Al}} + (1-x_1-x_2) {}^{\mathrm{Al}}L_{12\mathrm{Al}}\big)\right)$$
$$+(1-x_1-x_2)\left(\sum_{i\geq 1} 2i x_1 {}^{i}L_{1\mathrm{Al}}(2x_1+x_2-1)^{i-1} + \sum_{i\geq 1} i x_2 {}^{i}L_{2\mathrm{Al}}(x_1+2x_2-1)^{i-1}\right.$$
$$\left. + x_1x_2\big({}^{1}L_{12\mathrm{Al}} - {}^{\mathrm{Al}}L_{12\mathrm{Al}}\big)\right)$$

$$= x_2({}^0L_{12} - {}^0L_{2\mathrm{Al}}) + (1 - 2x_1 - x_2){}^0L_{1\mathrm{Al}}$$

$$+(1 - x_1 - x_2)x_1x_2\left({}^1L_{12\mathrm{Al}} - {}^{\mathrm{Al}}L_{12\mathrm{Al}}\right)$$

$$+ (1 - 2x_1 - x_2)x_2\left(x_1{}^1L_{12\mathrm{Al}} + x_2{}^2L_{12\mathrm{Al}} + (1 - x_1 - x_2){}^{\mathrm{Al}}L_{12\mathrm{Al}}\right)$$

$$+x_2\sum_{i\geq 1}{}^iL_{12}(x_1 - x_2)^{i-1}\left(ix_1 + (x_1 - x_2)\right)$$

$$+\sum_{i\geq 1}{}^iL_{1\mathrm{Al}}(2x_1 + x_2 - 1)^{i-1}\left(2ix_1(1 - x_1 - x_2) + (1 - 2x_1 - x_2)(2x_1 + x_2 - 1)\right)$$

$$+x_2\sum_{i\geq 1}{}^iL_{2\mathrm{Al}}(x_1 + 2x_2 - 1)^{i-1}\left(i(1 - x_1 - x_2) - (x_1 + 2x_2 - 1)\right)$$

$$= x_2({}^0L_{12} - {}^0L_{2\mathrm{Al}}) + (1 - 2x_1 - x_2){}^0L_{1\mathrm{Al}}$$

$$+x_2\left({}^1L_{12\mathrm{Al}}x_1\left((1 - x_1 - x_2) + (1 - 2x_1 - x_2)\right) + {}^2L_{12\mathrm{Al}}x_2(1 - 2x_1 - x_2)\right.$$

$$\left. + {}^{\mathrm{Al}}L_{12\mathrm{Al}}(1 - x_1 - x_2)(1 - 2x_1 - x_2 - x_1)\right)$$

$$+x_2\sum_{i\geq 1}{}^iL_{12}(x_1 - x_2)^{i-1}\left(ix_1 + (x_1 - x_2)\right)$$

$$+\sum_{i\geq 1}{}^iL_{1\mathrm{Al}}(2x_1 + x_2 - 1)^{i-1}(2ix_1(1 - x_1 - x_2) - (1 - 2x_1 - x_2)^2)$$

$$+\sum_{i\geq 1}{}^iL_{2\mathrm{Al}}(x_1 + 2x_2 - 1)^{i-1}\,x_2\left(i(1 - x_1 - x_2) + (1 - x_1 - 2x_2)\right)$$

$$\left(\frac{\partial \Delta G^{\mathrm{xs}}_{\mathrm{mix}}}{\partial x_1}\right)_{x_2} = x_2({}^0L_{12} - {}^0L_{2\mathrm{Al}}) + (1 - 2x_1 - x_2){}^0L_{1\mathrm{Al}}$$

$$+x_2\left({}^1L_{12\mathrm{Al}}x_1(2 - 3x_1 - 2x_2) + {}^2L_{12\mathrm{Al}}x_2(1 - 2x_1 - x_2)\right.$$

$$\left. + {}^{\mathrm{Al}}L_{12\mathrm{Al}}(1 - x_1 - x_2)(1 - 3x_1 - x_2)\right)$$

$$+x_2\sum_{i\geq 1}{}^iL_{12}(x_1 - x_2)^{i-1}\left(ix_1 + (x_1 - x_2)\right)$$

$$+\sum_{i\geq 1}{}^iL_{1\mathrm{Al}}(2x_1 + x_2 - 1)^{i-1}(2ix_1(1 - x_1 - x_2) - (1 - 2x_1 - x_2)^2)$$

$$+x_2\sum_{i\geq 1}{}^{i}L_{2\mathrm{Al}}(x_1+2x_2-1)^{i-1}\left(i(1-x_1-x_2)+(1-x_1-2x_2)\right) \tag{A.55}$$

$$\left(\frac{\partial \Delta G_{\mathrm{mix}}^{\mathrm{xs}}}{\partial x_2}\right)_{x_1} = x_1\omega_{12}+x_1x_2\omega_{12,x_2}+x_1\omega_{1\mathrm{Al},x_2}-x_1\omega_{1\mathrm{Al}}-x_1(x_1+x_2)\omega_{1\mathrm{Al},x_2}+$$

$$\omega_{2\mathrm{Al}}+x_2\omega_{2\mathrm{Al},x_2}-(x_1+x_2)\omega_{2\mathrm{Al}}-x_2\omega_{2\mathrm{Al}}-x_2(x_1+x_2)\omega_{2\mathrm{Al},x_2}+x_1\omega_{12\mathrm{Al}}+$$

$$x_1x_2\omega_{12\mathrm{Al},x_2}-x_1(x_1+x_2)\omega_{12\mathrm{Al}}-x_1x_2\omega_{12\mathrm{Al}}-x_1x_2(x_1+x_2)\omega_{12\mathrm{Al},x_2}$$

$$= x_1\left(\omega_{12}+x_2\omega_{12,x_2}\right)+x_1\left((1-x_1-x_2)\omega_{1\mathrm{Al},x_2}-\omega_{1\mathrm{Al}}\right)$$

$$+(1-x_1-2x_2)\omega_{2\mathrm{Al}}+x_2(1-x_1-x_2)\omega_{2\mathrm{Al},x_2}$$

$$+x_1\left((1-x_1-2x_2)\omega_{12\mathrm{Al}}+x_2(1-x_1-x_2)\omega_{12\mathrm{Al},x_2}\right)$$

$$= x_1\left(\omega_{12}-\omega_{1\mathrm{Al}}+x_2\omega_{12,x_2}\right)+(1-x_1-2x_2)(\omega_{2\mathrm{Al}}+x_1\omega_{12\mathrm{Al}})$$

$$+(1-x_1-x_2)\left(x_1\omega_{1\mathrm{Al},x_2}+x_2\omega_{2\mathrm{Al},x_2}+x_1x_2\omega_{12\mathrm{Al},x_2}\right)$$

$$= x_1\left({}^{0}L_{12}+\sum_{i\geq 1}{}^{i}L_{12}(x_1-x_2)^i-{}^{0}L_{1\mathrm{Al}}-\sum_{i\geq 1}{}^{i}L_{1\mathrm{Al}}(2x_1+x_2-1)^i\right.$$

$$\left.-x_2\sum_{i\geq 1}{}^{i}L_{12}i(x_1-x_2)^{i-1}\right)$$

$$+(1-x_1-2x_2)\left({}^{0}L_{2\mathrm{Al}}+\sum_{i\geq 1}{}^{i}L_{2\mathrm{Al}}(x_1+2x_2-1)^i\right.$$

$$\left.+x_1\left(x_1{}^{1}L_{12\mathrm{Al}}+x_2{}^{2}L_{12\mathrm{Al}}+(1-x_1-x_2){}^{\mathrm{Al}}L_{12\mathrm{Al}}\right)\right)$$

$$+(1-x_1-x_2)\left(x_1\sum_{i\geq 1}i{}^{i}L_{1\mathrm{Al}}(2x_1+x_2-1)^{i-1}\right.$$

$$\left.+x_2\sum_{i\geq 1}2i{}^{i}L_{2\mathrm{Al}}(x_1+2x_2-1)^{i-1}+x_1x_2\left({}^{2}L_{12\mathrm{Al}}-{}^{\mathrm{Al}}L_{12\mathrm{Al}}\right)\right)$$

$$= x_1({}^{0}L_{12}-{}^{0}L_{1\mathrm{Al}})+(1-x_1-2x_2){}^{0}L_{2\mathrm{Al}}$$

$$+x_1\Big({}^1L_{12\mathrm{Al}}x_1(1-x_1-2x_2)+{}^2L_{12\mathrm{Al}}x_2\big((1-x_1-2x_2)+(1-x_1-x_2)\big)$$

$$+{}^{\mathrm{Al}}L_{12\mathrm{Al}}(1-x_1-x_2)\big((1-x_1-2x_2)-x_2\big)\Big)$$

$$+x_1\sum_{i\geq 1}{}^iL_{12}(x_1-x_2)^{i-1}(x_1-x_2-ix_2)$$

$$+x_1\sum_{i\geq 1}{}^iL_{1\mathrm{Al}}(2x_1+x_2-1)^{i-1}\big(i(1-x_1-x_2)-(2x_1+x_2-1)\big)$$

$$+\sum_{i\geq 1}{}^iL_{2\mathrm{Al}}(x_1+2x_2-1)^{i-1}\big(2ix_2(1-x_1-x_2)$$

$$+(1-x_1-2x_2)(x_1+2x_2-1)\big)$$

$$\left(\frac{\partial\Delta G_{\mathrm{mix}}^{\mathrm{xs}}}{\partial x_2}\right)_{x_1}=x_1({}^0L_{12}-{}^0L_{1\mathrm{Al}})+(1-x_1-2x_2){}^0L_{2\mathrm{Al}}$$

$$+x_1\Big({}^1L_{12\mathrm{Al}}x_1(1-x_1-2x_2)+{}^2L_{12\mathrm{Al}}x_2(2-2x_1-3x_2)$$

$$+{}^{\mathrm{Al}}L_{12\mathrm{Al}}(1-x_1-x_2)(1-x_1-3x_2)\Big)$$

$$+x_1\sum_{i\geq 1}{}^iL_{12}(x_1-x_2)^{i-1}(x_1-x_2-ix_2)$$

$$+x_1\sum_{i\geq 1}{}^iL_{1\mathrm{Al}}(2x_1+x_2-1)^{i-1}\big(i(1-x_1-x_2)+(1-2x_1-x_2)\big)$$

$$+\sum_{i\geq 1}{}^iL_{2\mathrm{Al}}(x_1+2x_2-1)^{i-1}(2ix_2(1-x_1-x_2)-(1-x_1-2x_2)^2) \tag{A.56}$$

$\Delta G_{\mathrm{mix}}^{\mathrm{xs}}$ can be expressed in terms of the summations seen in the partial derivatives (A.57).

$$\Delta G_{\mathrm{mix}}^{\mathrm{xs}}=x_1x_2\omega_{12}+x_1\big(1-(x_1+x_2)\big)\omega_{1\mathrm{Al}}+x_2\big(1-(x_1+x_2)\big)\omega_{2\mathrm{Al}}$$

$$+x_1x_2\big(1-(x_1+x_2)\big)\omega_{12\mathrm{Al}}$$

$$=x_1x_2\sum_{i\geq 0}{}^iL_{12}(x_1-x_2)^i+x_1\big(1-(x_1+x_2)\big)\sum_{i\geq 0}{}^iL_{1\mathrm{Al}}(2x_1+x_2-1)^i$$

$$+x_2\big(1-(x_1+x_2)\big)\sum_{i\geq 0}{}^iL_{2\mathrm{Al}}(x_1+2x_2-1)^i+x_1x_2\big(1-(x_1+x_2)\big)\omega_{12\mathrm{Al}}$$

$$= x_1x_2{}^0L_{12} + x_1\big(1-(x_1+x_2)\big){}^0L_{1\mathrm{Al}} + x_2\big(1-(x_1+x_2)\big){}^0L_{2\mathrm{Al}}$$

$$+ x_1x_2\big(1-(x_1+x_2)\big)\omega_{12\mathrm{Al}}$$

$$+\sum_{i\geq 1} {}^iL_{12}(x_1-x_2)^{i-1}\big(x_1x_2(x_1-x_2)\big)$$

$$+\sum_{i\geq 1} {}^iL_{1\mathrm{Al}}(2x_1+x_2-1)^{i-1}\Big(x_1\big(1-(x_1+x_2)\big)(2x_1+x_2-1)\Big)$$

$$+\sum_{i\geq 1} {}^iL_{2\mathrm{Al}}(x_1+2x_2-1)^{i-1}\Big(x_2\big(1-(x_1+x_2)\big)(x_1+2x_2-1)\Big)$$

$$\Delta G_{\mathrm{mix}}^{\mathrm{xs}} = x_1x_2{}^0L_{12} + (1-x_1-x_2)(x_1{}^0L_{1\mathrm{Al}} + x_2{}^0L_{2\mathrm{Al}} + x_1x_2\omega_{12\mathrm{Al}})$$

$$+\sum_{i\geq 1} {}^iL_{12}(x_1-x_2)^{i-1}\big(x_1x_2(x_1-x_2)\big)$$

$$+\sum_{i\geq 1} {}^iL_{1\mathrm{Al}}(2x_1+x_2-1)^{i-1}\big(x_1(1-x_1-x_2)(2x_1+x_2-1)\big)$$

$$+\sum_{i\geq 1} {}^iL_{2\mathrm{Al}}(x_1+2x_2-1)^{i-1}\big(x_2(1-x_1-x_2)(x_1+2x_2-1)\big) \qquad \text{(A.57)}$$

$\Delta\mu_1^{\mathrm{xs}}$ can be evaluated (A.58).

$$\Delta\mu_1^{\mathrm{xs}} = \Delta G_{\mathrm{mix}}^{\mathrm{xs}} + (1-x_1)\left(\frac{\partial\Delta G_{\mathrm{mix}}^{\mathrm{xs}}}{\partial x_1}\right)_{x_2} - x_2\left(\frac{\partial\Delta G_{\mathrm{mix}}^{\mathrm{xs}}}{\partial x_2}\right)_{x_1}$$

$$= x_1x_2{}^0L_{12} + (1-x_1-x_2)(x_1{}^0L_{1\mathrm{Al}} + x_2{}^0L_{2\mathrm{Al}})$$

$$+x_1x_2(1-x_1-x_2)\big(x_1{}^1L_{12\mathrm{Al}} + x_2{}^2L_{12\mathrm{Al}} + (1-x_1-x_2)^{\mathrm{Al}}L_{12\mathrm{Al}}\big)$$

$$+\sum_{i\geq 1} {}^iL_{12}(x_1-x_2)^{i-1}\big(x_1x_2(x_1-x_2)\big)$$

$$+\sum_{i\geq 1} {}^iL_{1\mathrm{Al}}(2x_1+x_2-1)^{i-1}\big(x_1(1-x_1-x_2)(2x_1+x_2-1)\big)$$

$$+\sum_{i\geq 1} {}^iL_{2\mathrm{Al}}(x_1+2x_2-1)^{i-1}\big(x_2(1-x_1-x_2)(x_1+2x_2-1)\big)$$

$$+(1-x_1)(x_2({}^0L_{12} - {}^0L_{2\mathrm{Al}}) + (1-2x_1-x_2){}^0L_{1\mathrm{Al}})$$

$$+(1-x_1)x_2\left({}^{1}L_{12\mathrm{Al}}x_1(2-3x_1-2x_2)+{}^{2}L_{12\mathrm{Al}}x_2(1-2x_1-x_2)\right.$$
$$\left.+{}^{\mathrm{Al}}L_{12\mathrm{Al}}(1-x_1-x_2)(1-3x_1-x_2)\right)$$
$$+(1-x_1)x_2\sum_{i\geq 1}{}^{i}L_{12}(x_1-x_2)^{i-1}\big(ix_1+(x_1-x_2)\big)$$
$$+(1-x_1)\sum_{i\geq 1}{}^{i}L_{1\mathrm{Al}}(2x_1+x_2-1)^{i-1}(2ix_1(1-x_1-x_2)-(1-2x_1-x_2)^2)$$
$$+(1-x_1)x_2\sum_{i\geq 1}{}^{i}L_{2\mathrm{Al}}(x_1+2x_2-1)^{i-1}\left(i(1-x_1-x_2)+(1-x_1-2x_2)\right)$$
$$-x_2(x_1({}^{0}L_{12}-{}^{0}L_{1\mathrm{Al}})+(1-x_1-2x_2){}^{0}L_{2\mathrm{Al}})$$
$$-x_1x_2\left({}^{1}L_{12\mathrm{Al}}x_1(1-x_1-2x_2)+{}^{2}L_{12\mathrm{Al}}x_2(2-2x_1-3x_2)\right.$$
$$\left.+{}^{\mathrm{Al}}L_{12\mathrm{Al}}(1-x_1-x_2)(1-x_1-3x_2)\right)$$
$$+x_1x_2\sum_{i\geq 1}{}^{i}L_{12}(x_1-x_2)^{i-1}(ix_2-x_1+x_2)$$
$$-x_1x_2\sum_{i\geq 1}{}^{i}L_{1\mathrm{Al}}(2x_1+x_2-1)^{i-1}\big(i(1-x_1-x_2)+(1-2x_1-x_2)\big)$$
$$-x_2\sum_{i\geq 1}{}^{i}L_{2\mathrm{Al}}(x_1+2x_2-1)^{i-1}(2ix_2(1-x_1-x_2)-(1-x_1-2x_2)^2)$$
$$=x_1x_2{}^{0}L_{12}+(1-x_1-x_2)(x_1{}^{0}L_{1\mathrm{Al}}+x_2{}^{0}L_{2\mathrm{Al}})$$
$$+(1-x_1)(x_2({}^{0}L_{12}-{}^{0}L_{2\mathrm{Al}})+(1-2x_1-x_2){}^{0}L_{1\mathrm{Al}})$$
$$-x_2(x_1({}^{0}L_{12}-{}^{0}L_{1\mathrm{Al}})+(1-x_1-2x_2){}^{0}L_{2\mathrm{Al}})$$
$$+x_1x_2(1-x_1-x_2)\big(x_1{}^{1}L_{12\mathrm{Al}}+x_2{}^{2}L_{12\mathrm{Al}}+(1-x_1-x_2){}^{\mathrm{Al}}L_{12\mathrm{Al}}\big)$$
$$+(1-x_1)x_2\left({}^{1}L_{12\mathrm{Al}}x_1(2-3x_1-2x_2)+{}^{2}L_{12\mathrm{Al}}x_2(1-2x_1-x_2)\right.$$
$$\left.+{}^{\mathrm{Al}}L_{12\mathrm{Al}}(1-x_1-x_2)(1-3x_1-x_2)\right)$$
$$-x_1x_2\left({}^{1}L_{12\mathrm{Al}}x_1(1-x_1-2x_2)+{}^{2}L_{12\mathrm{Al}}x_2(2-2x_1-3x_2)\right.$$
$$\left.+{}^{\mathrm{Al}}L_{12\mathrm{Al}}(1-x_1-x_2)(1-x_1-3x_2)\right)$$

$$+\sum_{i\geq 1} {}^{i}L_{12}(x_1-x_2)^{i-1}\big[x_1x_2(x_1-x_2)+(1-x_1)x_2\big(ix_1+(x_1-x_2)\big)$$

$$+x_1x_2(ix_2-x_1+x_2)\big]$$

$$+\sum_{i\geq 1} {}^{i}L_{1\mathrm{Al}}(2x_1+x_2-1)^{i-1}\big[x_1(1-x_1-x_2)(2x_1+x_2-1)$$

$$+(1-x_1)(2ix_1(1-x_1-x_2)-(1-2x_1-x_2)^2)$$

$$-x_1x_2\big(i(1-x_1-x_2)+(1-2x_1-x_2)\big)\big]$$

$$+\sum_{i\geq 1} {}^{i}L_{2\mathrm{Al}}(x_1+2x_2-1)^{i-1}\big[x_2(1-x_1-x_2)(x_1+2x_2-1)$$

$$+(1-x_1)x_2\big(i(1-x_1-x_2)+(1-x_1-2x_2)\big)$$

$$-x_2(2ix_2(1-x_1-x_2)-(1-x_1-2x_2)^2)\big]$$

$$={}^{0}L_{12}(x_1x_2+x_2(1-x_1)-x_1x_2)$$

$$+{}^{0}L_{1\mathrm{Al}}(x_1(1-x_1-x_2)+(1-x_1)(1-2x_1-x_2)+x_1x_2)$$

$$+{}^{0}L_{2\mathrm{Al}}\big(x_2(1-x_1-x_2)-x_2(1-x_1)-x_2(1-x_1-2x_2)\big)$$

$$+x_1{}^{1}L_{12\mathrm{Al}}\big(x_1x_2(1-x_1-x_2)+(1-x_1)x_2(2-3x_1-2x_2)-x_1x_2(1-x_1-2x_2)\big)$$

$$+x_2{}^{2}L_{12\mathrm{Al}}\big(x_1x_2(1-x_1-x_2)+(1-x_1)x_2(1-2x_1-x_2)-x_1x_2(2-2x_1-3x_2)\big)$$

$$+(1-x_1-x_2)^{\mathrm{Al}}L_{12\mathrm{Al}}\big(x_1x_2(1-x_1-x_2)+(1-x_1)x_2(1-3x_1-x_2)$$

$$-x_1x_2(1-x_1-3x_2)\big)$$

$$+x_2\sum_{i\geq 1} {}^{i}L_{12}(x_1-x_2)^{i-1}[ix_1(1-x_1+x_2)+(1-x_1)(x_1-x_2)]$$

$$+(1-x_1-x_2)\sum_{i\geq 1} {}^{i}L_{1\mathrm{Al}}(2x_1+x_2-1)^{i-1}[ix_1(2-2x_1-x_2)-(1-x_1)(1-2x_1-x_2)]$$

$$+(1-x_1-x_2)x_2\sum_{i\geq 1} {}^{i}L_{2\mathrm{Al}}(x_1+2x_2-1)^{i-1}\big[(1-x_1-2x_2)[1+i]\big]$$

$$=(1-x_1)x_2{}^{0}L_{12}+(1-x_1-x_2)(1-x_1){}^{0}L_{1\mathrm{Al}}-x_2(1-x_1-x_2){}^{0}L_{2\mathrm{Al}}$$

$$-x_1x_2(1-x_1-x_2)^1L_{12\mathrm{Al}}(3x_1-2)-x_2^2(1-x_1-x_2)^2L_{12\mathrm{Al}}(3x_1-1)$$

$$-x_2(1-x_1-x_2)^{2\,\mathrm{Al}}L_{12\mathrm{Al}}(3x_1-1)$$

$$+x_2\sum_{i\geq 1}{}^iL_{12}(x_1-x_2)^{i-1}[ix_1(1-x_1+x_2)+(1-x_1)(x_1-x_2)]$$

$$+(1-x_1-x_2)\sum_{i\geq 1}{}^iL_{1\mathrm{Al}}(2x_1+x_2-1)^{i-1}[ix_1(2-2x_1-x_2)-(1-x_1)(1-2x_1-x_2)]$$

$$+(1-x_1-x_2)x_2\sum_{i\geq 1}{}^iL_{2\mathrm{Al}}(x_1+2x_2-1)^{i-1}\big[(1-x_1-2x_2)[1+i]\big]$$

$$=(1-x_1)x_2{}^0L_{12}+(1-x_1-x_2)(1-x_1)^0L_{1\mathrm{Al}}-x_2(1-x_1-x_2)^0L_{2\mathrm{Al}}$$

$$-x_2(1-x_1-x_2)\Big(x_1{}^1L_{12\mathrm{Al}}(3x_1-2)+x_2{}^2L_{12\mathrm{Al}}(3x_1-1)$$

$$+(1-x_1-x_2)^{\mathrm{Al}}L_{12\mathrm{Al}}(3x_1-1)\Big)$$

$$+x_2\sum_{i\geq 1}{}^iL_{12}(x_1-x_2)^{i-1}[ix_1(1-x_1+x_2)+(1-x_1)(x_1-x_2)]$$

$$+(1-x_1-x_2)\sum_{i\geq 1}{}^iL_{1\mathrm{Al}}(2x_1+x_2-1)^{i-1}[ix_1(2-2x_1-x_2)+(1-x_1)(2x_1+x_2-1)]$$

$$-(1-x_1-x_2)x_2\sum_{i\geq 1}{}^iL_{2\mathrm{Al}}(x_1+2x_2-1)^{i-1}(1+i)(x_1+2x_2-1)$$

$$\Delta\mu_1^{\mathrm{xs}}=(1-x_1)x_2{}^0L_{12}+(1-x_1-x_2)(1-x_1)^0L_{1\mathrm{Al}}-x_2(1-x_1-x_2)^0L_{2\mathrm{Al}}$$

$$-x_2(1-x_1-x_2)\big((3x_1-1)\omega_{12\mathrm{Al}}-x_1{}^1L_{12\mathrm{Al}}\big)$$

$$+x_2\sum_{i\geq 1}{}^iL_{12}(x_1-x_2)^{i-1}[(1-x_1)(x_1-x_2)+ix_1(1-x_1+x_2)]$$

$$+(1-x_1-x_2)\sum_{i\geq 1}{}^iL_{1\mathrm{Al}}(2x_1+x_2-1)^{i-1}[(1-x_1)(2x_1+x_2-1)+ix_1(2-2x_1-x_2)]$$

$$-x_2(1-x_1-x_2)\sum_{i\geq 1}{}^iL_{2\mathrm{Al}}(x_1+2x_2-1)^{i-1}(1+i)(x_1+2x_2-1) \qquad \text{(A.58)}$$

$\Delta\mu_2^{\mathrm{xs}}$ can also be evaluated (A.59).

$$\Delta\mu_2^{\mathrm{xs}}=\Delta G_{\mathrm{mix}}^{\mathrm{xs}}-x_1\left(\frac{\partial\Delta G_{\mathrm{mix}}^{\mathrm{xs}}}{\partial x_1}\right)_{x_2}+(1-x_2)\left(\frac{\partial\Delta G_{\mathrm{mix}}^{\mathrm{xs}}}{\partial x_2}\right)_{x_1}$$

$$= x_1x_2{}^0L_{12} + (1 - x_1 - x_2)(x_1{}^0L_{1\mathrm{Al}} + x_2{}^0L_{2\mathrm{Al}})$$

$$+x_1x_2(1 - x_1 - x_2)\big(x_1{}^1L_{12\mathrm{Al}} + x_2{}^2L_{12\mathrm{Al}} + (1 - x_1 - x_2)^{\mathrm{Al}}L_{12\mathrm{Al}}\big)$$

$$+\sum_{i\geq 1}{}^iL_{12}(x_1 - x_2)^{i-1}\big(x_1x_2(x_1 - x_2)\big)$$

$$+\sum_{i\geq 1}{}^iL_{1\mathrm{Al}}(2x_1 + x_2 - 1)^{i-1}\big(x_1(1 - x_1 - x_2)(2x_1 + x_2 - 1)\big)$$

$$+\sum_{i\geq 1}{}^iL_{2\mathrm{Al}}(x_1 + 2x_2 - 1)^{i-1}\big(x_2(1 - x_1 - x_2)(x_1 + 2x_2 - 1)\big)$$

$$-x_1(x_2({}^0L_{12} - {}^0L_{2\mathrm{Al}}) + (1 - 2x_1 - x_2){}^0L_{1\mathrm{Al}})$$

$$-x_1x_2\Big({}^1L_{12\mathrm{Al}}x_1(2 - 3x_1 - 2x_2) + {}^2L_{12\mathrm{Al}}x_2(1 - 2x_1 - x_2)$$

$$+ {}^{\mathrm{Al}}L_{12\mathrm{Al}}(1 - x_1 - x_2)(1 - 3x_1 - x_2)\Big)$$

$$-x_1x_2\sum_{i\geq 1}{}^iL_{12}(x_1 - x_2)^{i-1}\big(ix_1 + (x_1 - x_2)\big)$$

$$-x_1\sum_{i\geq 1}{}^iL_{1\mathrm{Al}}(2x_1 + x_2 - 1)^{i-1}(2ix_1(1 - x_1 - x_2) - (1 - 2x_1 - x_2)^2)$$

$$-x_1x_2\sum_{i\geq 1}{}^iL_{2\mathrm{Al}}(x_1 + 2x_2 - 1)^{i-1}\big(i(1 - x_1 - x_2) + (1 - x_1 - 2x_2)\big)$$

$$+(1 - x_2)(x_1({}^0L_{12} - {}^0L_{1\mathrm{Al}}) + (1 - x_1 - 2x_2){}^0L_{2\mathrm{Al}})$$

$$+(1 - x_2)x_1\Big({}^1L_{12\mathrm{Al}}x_1(1 - x_1 - 2x_2) + {}^2L_{12\mathrm{Al}}x_2(2 - 2x_1 - 3x_2)$$

$$+ {}^{\mathrm{Al}}L_{12\mathrm{Al}}(1 - x_1 - x_2)(1 - x_1 - 3x_2)\Big)$$

$$-(1 - x_2)x_1\sum_{i\geq 1}{}^iL_{12}(x_1 - x_2)^{i-1}(ix_2 - x_1 + x_2)$$

$$+(1 - x_2)x_1\sum_{i\geq 1}{}^iL_{1\mathrm{Al}}(2x_1 + x_2 - 1)^{i-1}\big(i(1 - x_1 - x_2) + (1 - 2x_1 - x_2)\big)$$

$$+(1 - x_2)\sum_{i\geq 1}{}^iL_{2\mathrm{Al}}(x_1 + 2x_2 - 1)^{i-1}(2ix_2(1 - x_1 - x_2) - (1 - x_1 - 2x_2)^2)$$

$$= x_1x_2{}^0L_{12} + (1 - x_1 - x_2)(x_1{}^0L_{1\mathrm{Al}} + x_2{}^0L_{2\mathrm{Al}})$$

$$
\begin{aligned}
&-x_1(x_2({}^0L_{12} - {}^0L_{2\mathrm{Al}}) + (1 - 2x_1 - x_2){}^0L_{1\mathrm{Al}}) \\
&+(1 - x_2)(x_1({}^0L_{12} - {}^0L_{1\mathrm{Al}}) + (1 - x_1 - 2x_2){}^0L_{2\mathrm{Al}}) \\
&+x_1x_2(1 - x_1 - x_2)\big(x_1{}^1L_{12\mathrm{Al}} + x_2{}^2L_{12\mathrm{Al}} + (1 - x_1 - x_2){}^{\mathrm{Al}}L_{12\mathrm{Al}}\big) \\
&-x_1x_2\Big({}^1L_{12\mathrm{Al}}x_1(2 - 3x_1 - 2x_2) + {}^2L_{12\mathrm{Al}}x_2(1 - 2x_1 - x_2) \\
&\qquad + {}^{\mathrm{Al}}L_{12\mathrm{Al}}(1 - x_1 - x_2)(1 - 3x_1 - x_2)\Big) \\
&+(1 - x_2)x_1\Big({}^1L_{12\mathrm{Al}}x_1(1 - x_1 - 2x_2) + {}^2L_{12\mathrm{Al}}x_2(2 - 2x_1 - 3x_2) \\
&\qquad + {}^{\mathrm{Al}}L_{12\mathrm{Al}}(1 - x_1 - x_2)(1 - x_1 - 3x_2)\Big) \\
&+\sum_{i\geq 1} {}^iL_{12}(x_1 - x_2)^{i-1}\big[x_1x_2(x_1 - x_2) - x_1x_2\big(ix_1 + (x_1 - x_2)\big) \\
&\qquad - (1 - x_2)x_1(ix_2 - x_1 + x_2)\big] \\
&+\sum_{i\geq 1} {}^iL_{1\mathrm{Al}}(2x_1 + x_2 - 1)^{i-1}\big[x_1(1 - x_1 - x_2)(2x_1 + x_2 - 1) \\
&\qquad - x_1(2ix_1(1 - x_1 - x_2) - (1 - 2x_1 - x_2)^2) \\
&\qquad + (1 - x_2)x_1\big(i(1 - x_1 - x_2) + (1 - 2x_1 - x_2)\big)\big] \\
&+\sum_{i\geq 1} {}^iL_{2\mathrm{Al}}(x_1 + 2x_2 - 1)^{i-1}\big[x_2(1 - x_1 - x_2)(x_1 + 2x_2 - 1) \\
&\qquad - x_1x_2\big(i(1 - x_1 - x_2) + (1 - x_1 - 2x_2)\big) \\
&\qquad + (1 - x_2)(2ix_2(1 - x_1 - x_2) - (1 - x_1 - 2x_2)^2)\big] \\
&= {}^0L_{12}\big(x_1x_2 - x_1x_2 + x_1(1 - x_2)\big) \\
&+{}^0L_{1\mathrm{Al}}\big(x_1(1 - x_1 - x_2) - x_1(1 - 2x_1 - x_2) - x_1(1 - x_2)\big) \\
&+{}^0L_{2\mathrm{Al}}\big(x_2(1 - x_1 - x_2) + x_1x_2 + (1 - x_2)(1 - x_1 - 2x_2)\big) \\
&+x_1{}^1L_{12\mathrm{Al}}\big(x_1x_2(1 - x_1 - x_2) - x_1x_2(2 - 3x_1 - 2x_2) + (1 - x_2)x_1(1 - x_1 - 2x_2)\big) \\
&+x_2{}^2L_{12\mathrm{Al}}\big(x_1x_2(1 - x_1 - x_2) - x_1x_2(1 - 2x_1 - x_2) + (1 - x_2)x_1(2 - 2x_1 - 3x_2)\big)
\end{aligned}
$$

$$+(1-x_1-x_2)^{\mathrm{Al}}L_{12\mathrm{Al}}\big(x_1x_2(1-x_1-x_2)-x_1x_2(1-3x_1-x_2)$$
$$+(1-x_2)x_1(1-x_1-3x_2)\big)$$
$$+\sum_{i\geq 1}{}^{i}L_{12}(x_1-x_2)^{i-1}\big[x_1x_2(x_1-x_2)-x_1x_2(x_1-x_2)-(1-x_2)x_1(x_2-x_1)$$
$$-ix_1x_2\big(x_1+(1-x_2)\big)\big]$$
$$+\sum_{i\geq 1}{}^{i}L_{1\mathrm{Al}}(2x_1+x_2-1)^{i-1}\big[x_1(1-x_1-x_2)(2x_1+x_2-1)+x_1(1-2x_1-x_2)^2$$
$$+(1-x_2)x_1(1-2x_1-x_2)+ix_1(1-x_1-x_2)\big((1-x_2)-2x_1\big)\big]$$
$$+\sum_{i\geq 1}{}^{i}L_{2\mathrm{Al}}(x_1+2x_2-1)^{i-1}\big[x_2(1-x_1-x_2)(x_1+2x_2-1)-x_1x_2(1-x_1-2x_2)-(1$$
$$-x_2)(1-x_1-2x_2)^2+i\big(2x_2(1-x_2)(1-x_1-x_2)-x_1x_2(1-x_1-x_2)\big)\big]$$
$$={}^{0}L_{12}x_1(1-x_2)-{}^{0}L_{1\mathrm{Al}}x_1(1-x_1-x_2)+{}^{0}L_{2\mathrm{Al}}(1-x_2)(1-x_1-x_2)$$
$$-x_1^2\,{}^{1}L_{12\mathrm{Al}}(3x_2-1)(1-x_1-x_2)$$
$$-x_1x_2\,{}^{2}L_{12\mathrm{Al}}(3x_2-2)(1-x_1-x_2)$$
$$-x_1(1-x_1-x_2)^{\mathrm{Al}}L_{12\mathrm{Al}}(3x_2-1)(1-x_1-x_2)$$
$$+x_1\sum_{i\geq 1}{}^{i}L_{12}(x_1-x_2)^{i-1}[(1-x_2)(x_1-x_2)-ix_2(1+x_1-x_2)]$$
$$+x_1(1-x_1-x_2)\sum_{i\geq 1}{}^{i}L_{1\mathrm{Al}}(2x_1+x_2-1)^{i-1}(1-2x_1-x_2)[1+i]$$
$$+(1-x_1-x_2)\sum_{i\geq 1}{}^{i}L_{2\mathrm{Al}}(x_1+2x_2-1)^{i-1}[ix_2(2-x_1-2x_2)+(x_1+2x_2-1)(1-x_2)]$$
$$={}^{0}L_{12}x_1(1-x_2)-{}^{0}L_{1\mathrm{Al}}x_1(1-x_1-x_2)+{}^{0}L_{2\mathrm{Al}}(1-x_2)(1-x_1-x_2)$$
$$-x_1(1-x_1-x_2)\Big(x_1\,{}^{1}L_{12\mathrm{Al}}(3x_2-1)+x_2\,{}^{2}L_{12\mathrm{Al}}(3x_2-2)+(1-x_1$$
$$-x_2)^{\mathrm{Al}}L_{12\mathrm{Al}}(3x_2-1)\Big)$$
$$+x_1\sum_{i\geq 1}{}^{i}L_{12}(x_1-x_2)^{i-1}[(1-x_2)(x_1-x_2)-ix_2(1+x_1-x_2)]$$

$$+x_1(1-x_1-x_2)\sum_{i\geq 1} {}^{i}L_{1\mathrm{Al}}(2x_1+x_2-1)^{i-1}(1-2x_1-x_2)[1+i]$$

$$+(1-x_1-x_2)\sum_{i\geq 1} {}^{i}L_{2\mathrm{Al}}(x_1+2x_2-1)^{i-1}[(x_1+2x_2-1)(1-x_2)+ix_2(2-x_1-2x_2)]$$

$$\Delta\mu_2^{\mathrm{xs}} = x_1(1-x_2)^{0}L_{12} - x_1(1-x_1-x_2)^{0}L_{1\mathrm{Al}} + (1-x_2)(1-x_1-x_2)^{0}L_{2\mathrm{Al}}$$

$$-x_1(1-x_1-x_2)\left((3x_2-1)\omega_{12\mathrm{Al}} - {x_2}^{2}L_{12\mathrm{Al}}\right)$$

$$+x_1\sum_{i\geq 1} {}^{i}L_{12}(x_1-x_2)^{i-1}[(1-x_2)(x_1-x_2)-ix_2(1+x_1-x_2)]$$

$$-x_1(1-x_1-x_2)\sum_{i\geq 1} {}^{i}L_{1\mathrm{Al}}(2x_1+x_2-1)^{i-1}(2x_1+x_2-1)[1+i]$$

$$+(1-x_1-x_2)\sum_{i\geq 1} {}^{i}L_{2\mathrm{Al}}(x_1+2x_2-1)^{i-1}[(1-x_2)(x_1+2x_2-1)$$

$$+ix_2(2-x_1-2x_2)] \qquad \text{(A.59)}$$

Finally, $\Delta\mu_{\mathrm{Al}}^{\mathrm{xs}}$ can also be evaluated (A.60).

$$\Delta\mu_{\mathrm{Al}}^{\mathrm{xs}} = \Delta G_{\mathrm{mix}}^{\mathrm{xs}} - x_1\left(\frac{\partial\Delta G_{\mathrm{mix}}^{\mathrm{xs}}}{\partial x_1}\right)_{x_2} - x_2\left(\frac{\partial\Delta G_{\mathrm{mix}}^{\mathrm{xs}}}{\partial x_2}\right)_{x_1}$$

$$= x_1x_2{}^{0}L_{12} + (1-x_1-x_2)(x_1{}^{0}L_{1\mathrm{Al}} + x_2{}^{0}L_{2\mathrm{Al}})$$

$$+x_1x_2(1-x_1-x_2)\left(x_1{}^{1}L_{12\mathrm{Al}} + x_2{}^{2}L_{12\mathrm{Al}} + (1-x_1-x_2)^{\mathrm{Al}}L_{12\mathrm{Al}}\right)$$

$$+\sum_{i\geq 1} {}^{i}L_{12}(x_1-x_2)^{i-1}\left(x_1x_2(x_1-x_2)\right)$$

$$+\sum_{i\geq 1} {}^{i}L_{1\mathrm{Al}}(2x_1+x_2-1)^{i-1}\left(x_1(1-x_1-x_2)(2x_1+x_2-1)\right)$$

$$+\sum_{i\geq 1} {}^{i}L_{2\mathrm{Al}}(x_1+2x_2-1)^{i-1}\left(x_2(1-x_1-x_2)(x_1+2x_2-1)\right)$$

$$-x_1(x_2({}^{0}L_{12} - {}^{0}L_{2\mathrm{Al}}) + (1-2x_1-x_2)^{0}L_{1\mathrm{Al}})$$

$$-x_1x_2\left({}^{1}L_{12\mathrm{Al}}x_1(2-3x_1-2x_2) + {}^{2}L_{12\mathrm{Al}}x_2(1-2x_1-x_2)\right.$$

$$\left.+{}^{\mathrm{Al}}L_{12\mathrm{Al}}(1-x_1-x_2)(1-3x_1-x_2)\right)$$

$$-x_1x_2\sum_{i\geq 1}{}^{i}L_{12}(x_1-x_2)^{i-1}\big(ix_1+(x_1-x_2)\big)$$

$$-x_1\sum_{i\geq 1}{}^{i}L_{1\mathrm{Al}}(2x_1+x_2-1)^{i-1}(2ix_1(1-x_1-x_2)-(1-2x_1-x_2)^2)$$

$$-x_1x_2\sum_{i\geq 1}{}^{i}L_{2\mathrm{Al}}(x_1+2x_2-1)^{i-1}\left(i(1-x_1-x_2)+(1-x_1-2x_2)\right)$$

$$-x_2(x_1({}^{0}L_{12}-{}^{0}L_{1\mathrm{Al}})+(1-x_1-2x_2){}^{0}L_{2\mathrm{Al}})$$

$$-x_1x_2\Big({}^{1}L_{12\mathrm{Al}}x_1(1-x_1-2x_2)+{}^{2}L_{12\mathrm{Al}}x_2(2-2x_1-3x_2)$$

$$+{}^{\mathrm{Al}}L_{12\mathrm{Al}}(1-x_1-x_2)(1-x_1-3x_2)\Big)$$

$$+x_1x_2\sum_{i\geq 1}{}^{i}L_{12}(x_1-x_2)^{i-1}(ix_2-x_1+x_2)$$

$$-x_1x_2\sum_{i\geq 1}{}^{i}L_{1\mathrm{Al}}(2x_1+x_2-1)^{i-1}\big(i(1-x_1-x_2)+(1-2x_1-x_2)\big)$$

$$-x_2\sum_{i\geq 1}{}^{i}L_{2\mathrm{Al}}(x_1+2x_2-1)^{i-1}(2ix_2(1-x_1-x_2)-(1-x_1-2x_2)^2)$$

$$=x_1x_2{}^{0}L_{12}+(1-x_1-x_2)(x_1{}^{0}L_{1\mathrm{Al}}+x_2{}^{0}L_{2\mathrm{Al}})$$

$$-x_1(x_2({}^{0}L_{12}-{}^{0}L_{2\mathrm{Al}})+(1-2x_1-x_2){}^{0}L_{1\mathrm{Al}})$$

$$-x_2(x_1({}^{0}L_{12}-{}^{0}L_{1\mathrm{Al}})+(1-x_1-2x_2){}^{0}L_{2\mathrm{Al}})$$

$$+x_1x_2(1-x_1-x_2)\big(x_1{}^{1}L_{12\mathrm{Al}}+x_2{}^{2}L_{12\mathrm{Al}}+(1-x_1-x_2){}^{\mathrm{Al}}L_{12\mathrm{Al}}\big)$$

$$-x_1x_2\Big({}^{1}L_{12\mathrm{Al}}x_1(2-3x_1-2x_2)+{}^{2}L_{12\mathrm{Al}}x_2(1-2x_1-x_2)$$

$$+{}^{\mathrm{Al}}L_{12\mathrm{Al}}(1-x_1-x_2)(1-3x_1-x_2)\Big)$$

$$-x_1x_2\Big({}^{1}L_{12\mathrm{Al}}x_1(1-x_1-2x_2)+{}^{2}L_{12\mathrm{Al}}x_2(2-2x_1-3x_2)$$

$$+{}^{\mathrm{Al}}L_{12\mathrm{Al}}(1-x_1-x_2)(1-x_1-3x_2)\Big)$$

$$+\sum_{i\geq 1}{}^{i}L_{12}(x_1-x_2)^{i-1}\left(x_1x_2(x_1-x_2)-x_1x_2\big(ix_1+(x_1-x_2)\big)+x_1x_2(ix_2-x_1+x_2)\right)$$

$$+\sum_{i\geq 1} {}^{i}L_{1\mathrm{Al}}(2x_1+x_2-1)^{i-1}\Big(x_1(1-x_1-x_2)(2x_1+x_2-1)$$

$$-x_1(2ix_1(1-x_1-x_2)-(1-2x_1-x_2)^2)$$

$$-x_1x_2\big(i(1-x_1-x_2)+(1-2x_1-x_2)\big)\Big)$$

$$+\sum_{i\geq 1} {}^{i}L_{2\mathrm{Al}}(x_1+2x_2-1)^{i-1}\Big(x_2(1-x_1-x_2)(x_1+2x_2-1)$$

$$-x_1x_2\big(i(1-x_1-x_2)+(1-x_1-2x_2)\big)$$

$$-x_2(2ix_2(1-x_1-x_2)-(1-x_1-2x_2)^2)\Big)$$

$$={}^{0}L_{12}(x_1x_2-x_1x_2-x_1x_2)$$

$$+{}^{0}L_{1\mathrm{Al}}(x_1(1-x_1-x_2)-x_1(1-2x_1-x_2)+x_1x_2)$$

$$+{}^{0}L_{2\mathrm{Al}}\big(x_2(1-x_1-x_2)+x_1x_2-x_2(1-x_1-2x_2)\big)$$

$$+x_1{}^{1}L_{12\mathrm{Al}}\big(x_1x_2(1-x_1-x_2)-x_1x_2(2-3x_1-2x_2)-x_1x_2(1-x_1-2x_2)\big)$$

$$+x_2{}^{2}L_{12\mathrm{Al}}\big(x_1x_2(1-x_1-x_2)-x_1x_2(1-2x_1-x_2)-x_1x_2(2-2x_1-3x_2)\big)$$

$$+(1-x_1-x_2)^{\mathrm{Al}}L_{12\mathrm{Al}}\big(x_1x_2(1-x_1-x_2)-x_1x_2(1-3x_1-x_2)-x_1x_2(1-x_1-3x_2)\big)$$

$$+\sum_{i\geq 1} {}^{i}L_{12}(x_1-x_2)^{i-1}\big(x_1x_2(x_1-x_2)-x_1x_2(x_1-x_2)+x_1x_2(-x_1+x_2)$$

$$+x_1x_2i(x_2-x_1)\big)$$

$$+\sum_{i\geq 1} {}^{i}L_{1\mathrm{Al}}(2x_1+x_2-1)^{i-1}\Big(x_1(1-x_1-x_2)(2x_1+x_2-1)+x_1(1-2x_1-x_2)^2$$

$$-x_1x_2(1-2x_1-x_2)-x_1i\big(2x_1(1-x_1-x_2)+x_2(1-x_1-x_2)\big)\Big)$$

$$+\sum_{i\geq 1} {}^{i}L_{2\mathrm{Al}}(x_1+2x_2-1)^{i-1}\Big(x_2(1-x_1-x_2)(x_1+2x_2-1)-x_1x_2(1-x_1-2x_2)$$

$$+x_2(1-x_1-2x_2)^2-x_2i\big(x_1(1-x_1-x_2)+2x_2(1-x_1-x_2)\big)\Big)$$

$$=-x_1x_2{}^{0}L_{12}+x_1{}^{0}L_{1\mathrm{Al}}(x_1+x_2)+x_2{}^{0}L_{2\mathrm{Al}}(x_1+x_2)$$

$$+x_1x_2\Big(x_1{}^1L_{12\mathrm{Al}}(3x_1+3x_2-2)+x_2{}^2L_{12\mathrm{Al}}(3x_1+3x_2-2)$$

$$+(1-x_1-x_2)^{\mathrm{Al}}L_{12\mathrm{Al}}(3x_1+3x_2-1)\Big)$$

$$-x_1x_2\sum_{i\geq 1}{}^iL_{12}(x_1-x_2)^{i-1}[(1+i)(x_1-x_2)]$$

$$-x_1\sum_{i\geq 1}{}^iL_{1\mathrm{Al}}(2x_1+x_2-1)^{i-1}[(2x_1+x_2-1)(x_1+x_2)+(1-x_1-x_2)(2x_1+x_2)i]$$

$$+x_2\sum_{i\geq 1}{}^iL_{2\mathrm{Al}}(x_1+2x_2-1)^{i-1}[(x_1+2x_2-1)(x_1+x_2)-(1-x_1-x_2)(2x_2+x_1)i]$$

$$\Delta\mu_{\mathrm{Al}}^{\mathrm{xs}}=-x_1x_2{}^0L_{12}+x_1{}^0L_{1\mathrm{Al}}(x_1+x_2)+x_2{}^0L_{2\mathrm{Al}}(x_1+x_2)$$

$$+(3x_1+3x_2-2)x_1x_2\omega_{12\mathrm{Al}}+x_1x_2(1-x_1-x_2)^{\mathrm{Al}}L_{12\mathrm{Al}}$$

$$-x_1x_2\sum_{i\geq 1}{}^iL_{12}(x_1-x_2)^{i-1}[(1+i)(x_1-x_2)]$$

$$+x_1\sum_{i\geq 1}{}^iL_{1\mathrm{Al}}(2x_1+x_2-1)^{i-1}[(2x_1+x_2-1)(x_1+x_2)-(1-x_1-x_2)(2x_1+x_2)i]$$

$$+x_2\sum_{i\geq 1}{}^iL_{2\mathrm{Al}}(x_1+2x_2-1)^{i-1}[(x_1+2x_2-1)(x_1+x_2)$$

$$-(1-x_1-x_2)(2x_2+x_1)i] \qquad \text{(A.60)}$$

The excess free energy term in ΔG^{ox} can be evaluated (A.61).

$$m_1\Delta\mu_1^{\mathrm{xs}}+m_2\Delta\mu_2^{\mathrm{xs}}+m_{\mathrm{Al}}\Delta\mu_{\mathrm{Al}}^{\mathrm{xs}}$$
$$=m_1\Bigg((1-x_1)x_2{}^0L_{12}+(1-x_1-x_2)(1-x_1)^0L_{1\mathrm{Al}}-x_2(1-x_1-x_2)^0L_{2\mathrm{Al}}$$
$$-x_2(1-x_1-x_2)\big((3x_1-1)\omega_{12\mathrm{Al}}-x_1{}^1L_{12\mathrm{Al}}\big)$$
$$+x_2\sum_{i\geq 1}{}^iL_{12}(x_1-x_2)^{i-1}[(1-x_1)(x_1-x_2)+ix_1(1-x_1+x_2)]$$
$$+(1-x_1$$
$$-x_2)\sum_{i\geq 1}{}^iL_{1\mathrm{Al}}(2x_1+x_2-1)^{i-1}[(1-x_1)(2x_1+x_2-1)$$
$$+ix_1(2-2x_1-x_2)]$$
$$-x_2(1-x_1-x_2)\sum_{i\geq 1}{}^iL_{2\mathrm{Al}}(x_1+2x_2-1)^{i-1}(1+i)(x_1+2x_2-1)\Bigg)$$

$$
\begin{aligned}
&+m_2\Big(x_1(1-x_2)^0L_{12}-x_1(1-x_1-x_2)^0L_{1\mathrm{Al}}+(1-x_2)(1-x_1-x_2)^0L_{2\mathrm{Al}}\\
&\qquad -x_1(1-x_1-x_2)\big((3x_2-1)\omega_{12\mathrm{Al}}-{x_2}^2L_{12\mathrm{Al}}\big)\\
&\qquad +x_1\sum_{i\geq 1}{}^iL_{12}(x_1-x_2)^{i-1}[(1-x_2)(x_1-x_2)-ix_2(1+x_1-x_2)]\\
&\qquad -x_1(1-x_1-x_2)\sum_{i\geq 1}{}^iL_{1\mathrm{Al}}(2x_1+x_2-1)^{i-1}(2x_1+x_2-1)[1+i]\\
&\qquad +(1-x_1\\
&\qquad -x_2)\sum_{i\geq 1}{}^iL_{2\mathrm{Al}}(x_1+2x_2-1)^{i-1}[(1-x_2)(x_1+2x_2-1)\\
&\qquad +ix_2(2-x_1-2x_2)]\Big)\\
&+m_{\mathrm{Al}}\Big(-x_1{x_2}^0L_{12}+{x_1}^0L_{1\mathrm{Al}}(x_1+x_2)+{x_2}^0L_{2\mathrm{Al}}(x_1+x_2)+(3x_1+3x_2-2)x_1x_2\omega_{12\mathrm{Al}}\\
&\qquad +x_1x_2(1-x_1-x_2)^{\mathrm{Al}}L_{12\mathrm{Al}}-x_1x_2\sum_{i\geq 1}{}^iL_{12}(x_1-x_2)^{i-1}[(1+i)(x_1-x_2)]\\
&\qquad +x_1\sum_{i\geq 1}{}^iL_{1\mathrm{Al}}(2x_1+x_2-1)^{i-1}[(2x_1+x_2-1)(x_1+x_2)\\
&\qquad -(1-x_1-x_2)(2x_1+x_2)i]\\
&\qquad +x_2\sum_{i\geq 1}{}^iL_{2\mathrm{Al}}(x_1+2x_2-1)^{i-1}[(x_1+2x_2-1)(x_1+x_2)\\
&\qquad -(1-x_1-x_2)(2x_2+x_1)i]\Big)\\
&={}^0L_{12}(m_1x_2(1-x_1)+m_2x_1(1-x_2)-m_{\mathrm{Al}}x_1x_2)\\
&+{}^0L_{1\mathrm{Al}}\big(m_1(1-x_1-x_2)(1-x_1)-m_2x_1(1-x_1-x_2)+m_{\mathrm{Al}}x_1(x_1+x_2)\big)\\
&+{}^0L_{2\mathrm{Al}}\big(-m_1x_2(1-x_1-x_2)+m_2(1-x_2)(1-x_1-x_2)+m_{\mathrm{Al}}x_2(x_1+x_2)\big)\\
&+\omega_{12\mathrm{Al}}(-m_1x_2(1-x_1-x_2)(3x_1-1)-m_2x_1(1-x_1-x_2)(3x_2-1)\\
&\qquad +m_{\mathrm{Al}}(3x_1+3x_2-2)x_1x_2)\\
&+x_1x_2(1-x_1-x_2)\big(m_1{}^1L_{12\mathrm{Al}}+m_2{}^2L_{12\mathrm{Al}}+m_{\mathrm{Al}}{}^{\mathrm{Al}}L_{12\mathrm{Al}}\big)\\
&+\sum_{i\geq 1}{}^iL_{12}(x_1-x_2)^{i-1}([m_1x_2(1-x_1)(x_1-x_2)+m_2x_1(1-x_2)(x_1-x_2)\\
&\qquad -m_{\mathrm{Al}}x_1x_2(x_1-x_2)]\\
&\qquad +i[m_1x_1x_2(1-x_1+x_2)-m_2x_1x_2(1+x_1-x_2)-m_{\mathrm{Al}}x_1x_2(x_1-x_2)])\\
&+\sum_{i\geq 1}{}^iL_{1\mathrm{Al}}(2x_1+x_2-1)^{i-1}([m_1(1-x_1)(2x_1+x_2-1)(1-x_1-x_2)\\
&\qquad -m_2x_1(1-x_1-x_2)(2x_1+x_2-1)+m_{\mathrm{Al}}x_1(2x_1+x_2-1)(x_1+x_2)]\\
&\qquad +i[m_1x_1(2-2x_1-x_2)(1-x_1-x_2)-m_2x_1(1-x_1-x_2)(2x_1+x_2-1)\\
&\qquad -m_{\mathrm{Al}}x_1(1-x_1-x_2)(2x_1+x_2)])
\end{aligned}
$$

$$+\sum_{i\geq 1} {}^{i}L_{2\mathrm{Al}}(x_1+2x_2-1)^{i-1}([-m_1x_2(1-x_1-x_2)(x_1+2x_2-1)$$

$$+m_2(1-x_1-x_2)(1-x_2)(x_1+2x_2-1)$$

$$+m_{\mathrm{Al}}x_2(x_1+2x_2-1)(x_1+x_2)]$$

$$+i[-m_1x_2(1-x_1-x_2)(x_1+2x_2-1)$$

$$+m_2(1-x_1-x_2)x_2(2-x_1-2x_2)-m_{\mathrm{Al}}x_2(1-x_1-x_2)(2x_2+x_1)])$$

$$= {}^{0}L_{12}(m_1x_2(1-x_1)+m_2x_1(1-x_2)-m_{\mathrm{Al}}x_1x_2)$$
$$+{}^{0}L_{1\mathrm{Al}}\big(m_1(1-x_1-x_2)(1-x_1)-m_2x_1(1-x_1-x_2)+m_{\mathrm{Al}}x_1(x_1+x_2)\big)$$
$$+{}^{0}L_{2\mathrm{Al}}\big(-m_1x_2(1-x_1-x_2)+m_2(1-x_2)(1-x_1-x_2)+m_{\mathrm{Al}}x_2(x_1+x_2)\big)$$
$$+\omega_{12\mathrm{Al}}(m_1x_2(1-x_1-x_2)(1-3x_1)+m_2x_1(1-x_1-x_2)(1-3x_2)$$
$$+m_{\mathrm{Al}}(3x_1+3x_2-2)x_1x_2)$$
$$+x_1x_2(1-x_1-x_2)\big(m_1{}^{1}L_{12\mathrm{Al}}+m_2{}^{2}L_{12\mathrm{Al}}+m_{\mathrm{Al}}{}^{\mathrm{Al}}L_{12\mathrm{Al}}\big)$$
$$+\sum_{i\geq 1} {}^{i}L_{12}(x_1-x_2)^{i}[m_1x_2(1-x_1)+m_2x_1(1-x_2)-m_{\mathrm{Al}}x_1x_2]$$
$$+x_1x_2\sum_{i\geq 1} {}^{i}L_{12}(i)(x_1-x_2)^{i-1}[m_1(1-x_1+x_2)-m_2(1+x_1-x_2)-m_{\mathrm{Al}}(x_1-x_2)]$$
$$+\sum_{i\geq 1} {}^{i}L_{1\mathrm{Al}}(2x_1+x_2-1)^{i}([m_1(1-x_1)(1-x_1-x_2)-m_2x_1(1-x_1-x_2)$$

$$+m_{\mathrm{Al}}x_1(x_1+x_2)])$$

$$+x_1(1-x_1-x_2)\sum_{i\geq 1} {}^{i}L_{1\mathrm{Al}}(i)(2x_1+x_2-1)^{i-1}([m_1(2-2x_1-x_2)-m_2(2x_1+x_2-1)$$

$$-m_{\mathrm{Al}}(2x_1+x_2)])$$

$$+\sum_{i\geq 1} {}^{i}L_{2\mathrm{Al}}(x_1+2x_2-1)^{i}[-m_1x_2(1-x_1-x_2)+m_2(1-x_1-x_2)(1-x_2)$$

$$+m_{\mathrm{Al}}x_2(x_1+x_2)]$$

$$+x_2(1-x_1-x_2)\sum_{i\geq 1} {}^{i}L_{2\mathrm{Al}}(i)(x_1+2x_2-1)^{i-1}[-m_1(x_1+2x_2-1)+m_2(2-x_1-2x_2)$$
$$-m_{\mathrm{Al}}(2x_2+x_1)]$$
$$m_1\Delta\mu_1^{\mathrm{xs}}+m_2\Delta\mu_2^{\mathrm{xs}}+m_{\mathrm{Al}}\Delta\mu_{\mathrm{Al}}^{\mathrm{xs}}$$
$$=\omega_{12\mathrm{Al}}(m_1x_2(1-x_1-x_2)(1-3x_1)+m_2x_1(1-x_1-x_2)(1-3x_2)$$

$$+m_{\mathrm{Al}}(3x_1+3x_2-2)x_1x_2)$$

$$+x_1x_2(1-x_1-x_2)\big(m_1{}^{1}L_{12\mathrm{Al}}+m_2{}^{2}L_{12\mathrm{Al}}+m_{\mathrm{Al}}{}^{\mathrm{Al}}L_{12\mathrm{Al}}\big)$$

$$+\sum_{i\geq 0} {}^{i}L_{12}(x_1-x_2)^i[m_1x_2(1-x_1)+m_2x_1(1-x_2)-m_{\mathrm{Al}}x_1x_2]$$
$$+x_1x_2\sum_{i\geq 1} {}^{i}L_{12}(i)(x_1-x_2)^{i-1}[m_1(1-x_1+x_2)-m_2(1+x_1-x_2)-m_{\mathrm{Al}}(x_1-x_2)]$$
$$+\sum_{i\geq 0} {}^{i}L_{1\mathrm{Al}}(2x_1+x_2-1)^i[m_1(1-x_1)(1-x_1-x_2)-m_2x_1(1-x_1-x_2)$$
$$+m_{\mathrm{Al}}x_1(x_1+x_2)]$$
$$+x_1(1-x_1-x_2)\sum_{i\geq 1} {}^{i}L_{1\mathrm{Al}}(i)(2x_1+x_2-1)^{i-1}[m_1(2-2x_1-x_2)-m_2(2x_1+x_2-1)$$
$$-m_{\mathrm{Al}}(2x_1+x_2)]$$
$$+\sum_{i\geq 0} {}^{i}L_{2\mathrm{Al}}(x_1+2x_2-1)^i[-m_1x_2(1-x_1-x_2)+m_2(1-x_1-x_2)(1-x_2)$$
$$+m_{\mathrm{Al}}x_2(x_1+x_2)]$$
$$+x_2(1-x_1-x_2)\sum_{i\geq 1} {}^{i}L_{2\mathrm{Al}}(i)(x_1+2x_2-1)^{i-1}[-m_1(x_1+2x_2-1)$$
$$+m_2(2-x_1-2x_2)-m_{\mathrm{Al}}(2x_2+x_1)] \qquad \text{(A.61)}$$

Therefore $\Delta G^{\mathrm{ox}}_{\mathrm{Al}_{c_{\mathrm{Al}}}\mathrm{X}_{1c_1}\mathrm{X}_{2c_2}\mathrm{O}_{\mathrm{b}}}(x_{\mathrm{X}},T,p\mathrm{O}_2)$ is given as follows (A.62), where the Bragg-Williams Ternary (BWT) term (A.63), $\Delta G^{\mathrm{ox,BWT}}_{\mathrm{Al}_{c_{\mathrm{Al}}}\mathrm{X}_{1c_1}\mathrm{X}_{2c_2}\mathrm{O}_{\mathrm{b}}}$, defined in terms of the parameters of the ternary system ($^{i}L_{12\mathrm{Al}}$) and its constituent binary systems ($^{i}L_{12}$, $^{i}L_{1\mathrm{Al}}$, $^{i}L_{2\mathrm{Al}}$).

$$\Delta G^{\mathrm{ox}}_{\mathrm{Al}_{c_{\mathrm{Al}}}\mathrm{X}_{1c_1}\mathrm{X}_{2c_2}\mathrm{O}_{\mathrm{b}}}(x_1,x_2,T,p\mathrm{O}_2)$$
$$=\frac{2}{b}\Delta G^{\mathrm{o}}_{\mathrm{f,Al}_{c_{\mathrm{Al}}}\mathrm{X}_{1c_1}\mathrm{X}_{2c_2}\mathrm{O}_{\mathrm{b}}}(T)-RT\ln\left(x_{\mathrm{X}_1}^{m_1}x_{\mathrm{X}_2}^{m_2}x_{\mathrm{Al}}^{m_{\mathrm{Al}}}p\mathrm{O}_2\right)-\Delta G^{\mathrm{ox,BWT}}_{\mathrm{Al}_{c_{\mathrm{Al}}}\mathrm{X}_{1c_1}\mathrm{X}_{2c_2}\mathrm{O}_{\mathrm{b}}} \qquad \text{(A.62)}$$

$$\Delta G^{\mathrm{ox,BWT}}_{\mathrm{Al}_{c_{\mathrm{Al}}}\mathrm{X}_{1c_1}\mathrm{X}_{2c_2}\mathrm{O}_{\mathrm{b}}}=x_1x_2x_{\mathrm{Al}}\left(m_1\,{}^{1}L_{12\mathrm{Al}}+m_2\,{}^{2}L_{12\mathrm{Al}}+m_{\mathrm{Al}}\,{}^{\mathrm{Al}}L_{12\mathrm{Al}}\right)$$
$$+\omega_{12\mathrm{Al}}\left(m_1x_2x_{\mathrm{Al}}(1-3x_1)+m_2x_1x_{\mathrm{Al}}(1-3x_2)+m_{\mathrm{Al}}x_1x_2(1-3x_{\mathrm{Al}})\right)$$
$$+\sum_{i\geq 0} {}^{i}L_{12}(x_1-x_2)^i[m_1x_2(x_2+x_{\mathrm{Al}})+m_2x_1(x_1+x_{\mathrm{Al}})-m_{\mathrm{Al}}x_1x_2]$$
$$+x_1x_2\sum_{i\geq 1} {}^{i}L_{12}(i)(x_1-x_2)^{i-1}[m_1(2x_2+x_{\mathrm{Al}})-m_2(2x_1+x_{\mathrm{Al}})-m_{\mathrm{Al}}(x_1-x_2)]$$
$$+\sum_{i\geq 0} {}^{i}L_{1\mathrm{Al}}(x_1-x_{\mathrm{Al}})^i[m_1x_{\mathrm{Al}}(x_2+x_{\mathrm{Al}})-m_2x_1x_{\mathrm{Al}}+m_{\mathrm{Al}}x_1(x_1+x_2)]$$

$$+x_1x_{\mathrm{Al}}\sum_{i\geq 1}{}^{i}L_{1\mathrm{Al}}(i)(x_1-x_{\mathrm{Al}})^{i-1}[m_1(x_2+2x_{\mathrm{Al}})-m_2(x_1-x_{\mathrm{Al}})-m_{\mathrm{Al}}(2x_1+x_2)]$$

$$+\sum_{i\geq 0}{}^{i}L_{2\mathrm{Al}}(x_2-x_{\mathrm{Al}})^{i}[-m_1x_2x_{\mathrm{Al}}+m_2x_{\mathrm{Al}}(x_1+x_{\mathrm{Al}})+m_{\mathrm{Al}}x_2(x_1+x_2)]$$

$$+x_2x_{\mathrm{Al}}\sum_{i\geq 1}{}^{i}L_{2\mathrm{Al}}(i)(x_2-x_{\mathrm{Al}})^{i-1}[-m_1(x_2-x_{\mathrm{Al}})+m_2(x_1+2x_{\mathrm{Al}})-m_{\mathrm{Al}}(2x_2+x_1)]$$

$$\Delta G^{\mathrm{ox,BWT}}_{\mathrm{Al}_{c_{\mathrm{Al}}}\mathrm{X}_{1c_1}\mathrm{X}_{2c_2}\mathrm{O}_{\mathrm{b}}}=x_1x_2(1-x_1-x_2)\left(m_1{}^{1}L_{12\mathrm{Al}}+m_2{}^{2}L_{12\mathrm{Al}}+m_{\mathrm{Al}}{}^{\mathrm{Al}}L_{12\mathrm{Al}}\right)$$
$$+\omega_{12\mathrm{Al}}\big(m_1x_2(1-x_1-x_2)(1-3x_1)+m_2x_1(1-x_1-x_2)(1-3x_2)$$
$$+m_{\mathrm{Al}}x_1x_2(3x_1+3x_2-2)\big)$$

$$+\sum_{i\geq 0}{}^{i}L_{12}(x_1-x_2)^{i}[m_1x_2(1-x_1)+m_2x_1(1-x_2)-m_{\mathrm{Al}}x_1x_2]$$
$$+x_1x_2\sum_{i\geq 1}{}^{i}L_{12}(i)(x_1-x_2)^{i-1}[m_1(1-x_1+x_2)-m_2(1+x_1-x_2)-m_{\mathrm{Al}}(x_1-x_2)]$$
$$+\sum_{i\geq 0}{}^{i}L_{1\mathrm{Al}}(2x_1+x_2-1)^{i}[m_1(1-x_1)(1-x_1-x_2)-m_2x_1(1-x_1-x_2)$$
$$+m_{\mathrm{Al}}x_1(x_1+x_2)]$$
$$+x_1(1-x_1-x_2)\sum_{i\geq 1}{}^{i}L_{1\mathrm{Al}}(i)(2x_1+x_2-1)^{i-1}[m_1(2-2x_1-x_2)-m_2(2x_1+x_2-1)$$
$$-m_{\mathrm{Al}}(2x_1+x_2)]$$
$$+\sum_{i\geq 0}{}^{i}L_{2\mathrm{Al}}(x_1+2x_2-1)^{i}[-m_1x_2(1-x_1-x_2)+m_2(1-x_1-x_2)(1-x_2)$$
$$+m_{\mathrm{Al}}x_2(x_1+x_2)]$$
$$+x_2(1-x_1-x_2)\sum_{i\geq 1}{}^{i}L_{2\mathrm{Al}}(i)(x_1+2x_2-1)^{i-1}[-m_1(x_1+2x_2-1)$$
$$+m_2(2-x_1-2x_2)-m_{\mathrm{Al}}(2x_2+x_1)] \qquad \text{(A.63)}$$

A.4. Modified quasichemical model

A.4.1. Simplification and conversion to Al-X system

This section covers the simplification of $\Delta G^{\mathrm{xs}}_{\mathrm{mix}}$ and conversion into an X-Al system. The excess free energy of mixing in terms of molar fraction, $\Delta G^{\mathrm{xs}}_{\mathrm{mix}}(x_i)$, is given as follows (A.64):

$$\Delta G_{\mathrm{mix}}^{\mathrm{xs}}$$

$$= \frac{\left(\frac{x_{\mathrm{AB}}}{2}\left(\Delta g_{\mathrm{AB}}^{0} + g_{\mathrm{AB}}^{10}x_{\mathrm{AA}} + g_{\mathrm{AB}}^{01}x_{\mathrm{BB}}\right) + RT\left(x_{\mathrm{AA}}\ln\left(\frac{x_{\mathrm{AA}}}{y_{\mathrm{A}}^{2}}\right) + x_{\mathrm{BB}}\ln\left(\frac{x_{\mathrm{BB}}}{y_{\mathrm{B}}^{2}}\right) + x_{\mathrm{AB}}\ln\left(\frac{x_{\mathrm{AB}}}{2y_{\mathrm{A}}y_{\mathrm{B}}}\right)\right)\right)}{\beta_{\mathrm{AA}}x_{\mathrm{AA}} + \beta_{\mathrm{BB}}x_{\mathrm{BB}} + (\beta_{\mathrm{AB}} + \beta_{\mathrm{BA}})x_{\mathrm{AB}}} \quad \text{(A.64)}$$

Evaluating y_{A} (A.65) and y_{B} (A.66) in terms of x_{A}, x_{AB}, and β_{ij}:

$$y_{\mathrm{A}} = \frac{z_{\mathrm{A}}n_{\mathrm{A}}}{z_{\mathrm{A}}n_{\mathrm{A}} + z_{\mathrm{B}}n_{\mathrm{B}}} = \frac{2n_{\mathrm{AA}} + n_{\mathrm{AB}}}{2n_{\mathrm{AA}} + n_{\mathrm{AB}} + 2n_{\mathrm{BB}} + n_{\mathrm{AB}}} = \frac{2x_{\mathrm{AA}} + x_{\mathrm{AB}}}{2(x_{\mathrm{AA}} + x_{\mathrm{BB}} + x_{\mathrm{AB}})} = x_{\mathrm{AA}} + \frac{1}{2}x_{\mathrm{AB}}$$

$$= \frac{(x_{\mathrm{A}}\beta_{\mathrm{BA}} - (1-x_{\mathrm{A}})\beta_{\mathrm{AB}})x_{\mathrm{AB}} + x_{\mathrm{A}}\beta_{\mathrm{BB}}(1-x_{\mathrm{AB}})}{(1-x_{\mathrm{A}})\beta_{\mathrm{AA}} + x_{\mathrm{A}}\beta_{\mathrm{BB}}} + \frac{x_{\mathrm{AB}}\big((1-x_{\mathrm{A}})\beta_{\mathrm{AA}} + x_{\mathrm{A}}\beta_{\mathrm{BB}}\big)}{2\big((1-x_{\mathrm{A}})\beta_{\mathrm{AA}} + x_{\mathrm{A}}\beta_{\mathrm{BB}}\big)}$$

$$= \frac{2\big((x_{\mathrm{A}}\beta_{\mathrm{BA}} - (1-x_{\mathrm{A}})\beta_{\mathrm{AB}})x_{\mathrm{AB}} + x_{\mathrm{A}}\beta_{\mathrm{BB}}(1-x_{\mathrm{AB}})\big) + x_{\mathrm{AB}}\big((1-x_{\mathrm{A}})\beta_{\mathrm{AA}} + x_{\mathrm{A}}\beta_{\mathrm{BB}}\big)}{2\big((1-x_{\mathrm{A}})\beta_{\mathrm{AA}} + x_{\mathrm{A}}\beta_{\mathrm{BB}}\big)}$$

$$y_{\mathrm{A}} = \frac{x_{\mathrm{AB}}\big((2\beta_{\mathrm{BA}} - \beta_{\mathrm{BB}})x_{\mathrm{A}} + (\beta_{\mathrm{AA}} - 2\beta_{\mathrm{AB}})(1-x_{\mathrm{A}})\big) + 2x_{\mathrm{A}}\beta_{\mathrm{BB}}}{2\big((1-x_{\mathrm{A}})\beta_{\mathrm{AA}} + x_{\mathrm{A}}\beta_{\mathrm{BB}}\big)} \quad \text{(A.65)}$$

$$y_{\mathrm{B}} = x_{\mathrm{BB}} + \frac{1}{2}x_{\mathrm{AB}} = \frac{\big((1-x_{\mathrm{A}})\beta_{\mathrm{AB}} - x_{\mathrm{A}}\beta_{\mathrm{BA}}\big)x_{\mathrm{AB}} + \beta_{\mathrm{AA}}(1-x_{\mathrm{A}})(1-x_{\mathrm{AB}})}{(1-x_{\mathrm{A}})\beta_{\mathrm{AA}} + x_{\mathrm{A}}\beta_{\mathrm{BB}}} + \frac{x_{\mathrm{AB}}}{2}$$

$$= \frac{2x_{\mathrm{AB}}\big((1-x_{\mathrm{A}})\beta_{\mathrm{AB}} - x_{\mathrm{A}}\beta_{\mathrm{BA}}\big) + 2\beta_{\mathrm{AA}}(1-x_{\mathrm{A}})(1-x_{\mathrm{AB}}) + x_{\mathrm{AB}}\big((1-x_{\mathrm{A}})\beta_{\mathrm{AA}} + x_{\mathrm{A}}\beta_{\mathrm{BB}}\big)}{2\big((1-x_{\mathrm{A}})\beta_{\mathrm{AA}} + x_{\mathrm{A}}\beta_{\mathrm{BB}}\big)}$$

$$= \frac{2x_{\mathrm{AB}}\big((1-x_{\mathrm{A}})\beta_{\mathrm{AB}} - x_{\mathrm{A}}\beta_{\mathrm{BA}}\big) + \beta_{\mathrm{AA}}(1-x_{\mathrm{A}})(2-x_{\mathrm{AB}}) + x_{\mathrm{A}}\beta_{\mathrm{BB}}x_{\mathrm{AB}}}{2\big((1-x_{\mathrm{A}})\beta_{\mathrm{AA}} + x_{\mathrm{A}}\beta_{\mathrm{BB}}\big)}$$

$$y_{\mathrm{B}} = \frac{x_{\mathrm{AB}}\big(x_{\mathrm{A}}(\beta_{\mathrm{BB}} - 2\beta_{\mathrm{BA}}) + (2\beta_{\mathrm{AB}} - \beta_{\mathrm{AA}})(1-x_{\mathrm{A}})\big) + 2\beta_{\mathrm{AA}}(1-x_{\mathrm{A}})}{2\big((1-x_{\mathrm{A}})\beta_{\mathrm{AA}} + x_{\mathrm{A}}\beta_{\mathrm{BB}}\big)} \quad \text{(A.66)}$$

Simplifying the log-based terms (A.67):

$$x_{\mathrm{AA}}\ln\frac{x_{\mathrm{AA}}}{y_{\mathrm{A}}^{2}} + x_{\mathrm{BB}}\ln\frac{x_{\mathrm{BB}}}{y_{\mathrm{B}}^{2}} + x_{\mathrm{AB}}\ln\frac{x_{\mathrm{AB}}}{2y_{\mathrm{A}}y_{\mathrm{B}}}$$

$$= x_{\mathrm{AA}}\ln x_{\mathrm{AA}} + x_{\mathrm{BB}}\ln x_{\mathrm{BB}} + x_{\mathrm{AB}}\ln\frac{x_{\mathrm{AB}}}{2} - 2x_{\mathrm{AA}}\ln y_{\mathrm{A}} - 2x_{\mathrm{BB}}\ln y_{\mathrm{B}} - x_{\mathrm{AB}}\ln y_{\mathrm{A}} - x_{\mathrm{AB}}\ln y_{\mathrm{B}}$$

$$= x_{\mathrm{AA}}\ln x_{\mathrm{AA}} + x_{\mathrm{BB}}\ln x_{\mathrm{BB}} + x_{\mathrm{AB}}\ln\frac{x_{\mathrm{AB}}}{2} - 2\ln y_{\mathrm{A}}\left(x_{\mathrm{AA}} + \frac{x_{\mathrm{AB}}}{2}\right) - 2\ln y_{\mathrm{B}}\left(x_{\mathrm{BB}} + \frac{x_{\mathrm{AB}}}{2}\right)$$

$$= x_{\mathrm{AA}}\ln x_{\mathrm{AA}} + x_{\mathrm{BB}}\ln x_{\mathrm{BB}} + x_{\mathrm{AB}}\ln\frac{x_{\mathrm{AB}}}{2} - 2(y_{\mathrm{A}}\ln y_{\mathrm{A}} + y_{\mathrm{B}}\ln y_{\mathrm{B}}) \quad \text{(A.67)}$$

Expressing x_{AA} (A.68), x_{BB} (A.69), y_{A} (A.70), and y_{B} (A.71) in simplified terms δ_i:

$$x_{\mathrm{AA}} = \frac{(x_{\mathrm{A}}\beta_{\mathrm{BA}} - (1-x_{\mathrm{A}})\beta_{\mathrm{AB}})x_{\mathrm{AB}} + x_{\mathrm{A}}\beta_{\mathrm{BB}}(1-x_{\mathrm{AB}})}{(1-x_{\mathrm{A}})\beta_{\mathrm{AA}} + x_{\mathrm{A}}\beta_{\mathrm{BB}}} = \frac{\delta_2}{\delta_1} \tag{A.68}$$

$$x_{\mathrm{BB}} = \frac{\big((1-x_{\mathrm{A}})\beta_{\mathrm{AB}} - x_{\mathrm{A}}\beta_{\mathrm{BA}}\big)x_{\mathrm{AB}} + \beta_{\mathrm{AA}}(1-x_{\mathrm{A}})(1-x_{\mathrm{AB}})}{(1-x_{\mathrm{A}})\beta_{\mathrm{AA}} + x_{\mathrm{A}}\beta_{\mathrm{BB}}} = \frac{\delta_3}{\delta_1} \tag{A.69}$$

$$y_{\mathrm{A}} = \frac{x_{\mathrm{AB}}\big((2\beta_{\mathrm{BA}} - \beta_{\mathrm{BB}})x_{\mathrm{A}} + (\beta_{\mathrm{AA}} - 2\beta_{\mathrm{AB}})(1-x_{\mathrm{A}})\big) + 2x_{\mathrm{A}}\beta_{\mathrm{BB}}}{2\big((1-x_{\mathrm{A}})\beta_{\mathrm{AA}} + x_{\mathrm{A}}\beta_{\mathrm{BB}}\big)} = \frac{\delta_4}{2\delta_1} \tag{A.70}$$

$$y_{\mathrm{B}} = \frac{x_{\mathrm{AB}}\big(x_{\mathrm{A}}(\beta_{\mathrm{BB}} - 2\beta_{\mathrm{BA}}) + (2\beta_{\mathrm{AB}} - \beta_{\mathrm{AA}})(1-x_{\mathrm{A}})\big) + 2\beta_{\mathrm{AA}}(1-x_{\mathrm{A}})}{2\big((1-x_{\mathrm{A}})\beta_{\mathrm{AA}} + x_{\mathrm{A}}\beta_{\mathrm{BB}}\big)} = \frac{\delta_5}{2\delta_1} \tag{A.71}$$

Where δ_i are defined as follows:

$$\delta_1 = (1-x_{\mathrm{A}})\beta_{\mathrm{AA}} + x_{\mathrm{A}}\beta_{\mathrm{BB}} \tag{A.72}$$

$$\delta_2 = \delta_1 x_{\mathrm{AA}} = (x_{\mathrm{A}}\beta_{\mathrm{BA}} - (1-x_{\mathrm{A}})\beta_{\mathrm{AB}})x_{\mathrm{AB}} + x_{\mathrm{A}}\beta_{\mathrm{BB}}(1-x_{\mathrm{AB}}) \tag{A.73}$$

$$\delta_3 = \delta_1 x_{\mathrm{BB}} = \big((1-x_{\mathrm{A}})\beta_{\mathrm{AB}} - x_{\mathrm{A}}\beta_{\mathrm{BA}}\big)x_{\mathrm{AB}} + \beta_{\mathrm{AA}}(1-x_{\mathrm{A}})(1-x_{\mathrm{AB}}) \tag{A.74}$$

$$\delta_4 = 2\delta_1 y_{\mathrm{A}} = x_{\mathrm{AB}}\big((2\beta_{\mathrm{BA}} - \beta_{\mathrm{BB}})x_{\mathrm{A}} + (\beta_{\mathrm{AA}} - 2\beta_{\mathrm{AB}})(1-x_{\mathrm{A}})\big) + 2x_{\mathrm{A}}\beta_{\mathrm{BB}} \tag{A.75}$$

$$\delta_5 = 2\delta_1 y_{\mathrm{B}} = x_{\mathrm{AB}}\big(x_{\mathrm{A}}(\beta_{\mathrm{BB}} - 2\beta_{\mathrm{BA}}) + (2\beta_{\mathrm{AB}} - \beta_{\mathrm{AA}})(1-x_{\mathrm{A}})\big) + 2\beta_{\mathrm{AA}}(1-x_{\mathrm{A}}) \tag{A.76}$$

Putting the log-based terms (A.67) in terms of δ_i (A.72)-(A.76) to simplify (A.77):

$$x_{\mathrm{AA}}\ln x_{\mathrm{AA}} + x_{\mathrm{BB}}\ln x_{\mathrm{BB}} + x_{\mathrm{AB}}\ln\frac{x_{\mathrm{AB}}}{2} - 2(y_{\mathrm{A}}\ln y_{\mathrm{A}} + y_{\mathrm{B}}\ln y_{\mathrm{B}})$$

$$= \frac{\delta_2}{\delta_1}\ln\frac{\delta_2}{\delta_1} + \frac{\delta_3}{\delta_1}\ln\frac{\delta_3}{\delta_1} + x_{\mathrm{AB}}\ln\frac{x_{\mathrm{AB}}}{2} - 2\left(\frac{\delta_4}{2\delta_1}\ln\frac{\delta_4}{2\delta_1} + \frac{\delta_5}{2\delta_1}\ln\frac{\delta_5}{2\delta_1}\right)$$

$$= \left(\frac{1}{\delta_1}\right)\left(\delta_2\ln\frac{\delta_2}{\delta_1} + \delta_3\ln\frac{\delta_3}{\delta_1} + \delta_1 x_{\mathrm{AB}}\ln\frac{x_{\mathrm{AB}}}{2} - \left(\delta_4\ln\frac{\delta_4}{2\delta_1} + \delta_5\ln\frac{\delta_5}{2\delta_1}\right)\right)$$

$$= \left(\frac{1}{\delta_1}\right)\left(\delta_2\ln\delta_2 + \delta_3\ln\delta_3 + \delta_1 x_{\mathrm{AB}}\ln\frac{x_{\mathrm{AB}}}{2} - \left(\delta_4\ln\frac{\delta_4}{2} + \delta_5\ln\frac{\delta_5}{2}\right)\right.$$

$$\left. + \big(\delta_4 + \delta_5 - (\delta_2 + \delta_3)\big)\ln\delta_1\right)$$

$$= x_{\mathrm{AA}}\ln\delta_2 + x_{\mathrm{BB}}\ln\delta_3 + x_{\mathrm{AB}}\ln\frac{x_{\mathrm{AB}}}{2} - 2\left(y_{\mathrm{A}}\ln\frac{\delta_4}{2} + y_{\mathrm{B}}\ln\frac{\delta_5}{2}\right)$$

$$+ \big(2(y_{\mathrm{A}} + y_{\mathrm{B}}) - (x_{\mathrm{AA}} + x_{\mathrm{BB}})\big)\ln\delta_1$$

$$= x_{\mathrm{AA}}\ln\delta_2 + x_{\mathrm{BB}}\ln\delta_3 + x_{\mathrm{AB}}\ln\frac{x_{\mathrm{AB}}}{2} - 2\left(y_{\mathrm{A}}\ln\frac{\delta_4}{2} + y_{\mathrm{B}}\ln\frac{\delta_5}{2}\right) + \big(2 - (1-x_{\mathrm{AB}})\big)\ln\delta_1$$

$$= (1 + x_{\mathrm{AB}}) \ln \delta_1 + x_{\mathrm{AA}} \ln \delta_2 + x_{\mathrm{BB}} \ln \delta_3 + x_{\mathrm{AB}} \ln \frac{x_{\mathrm{AB}}}{2} - 2\left(y_{\mathrm{A}} \ln \frac{\delta_4}{2} + y_{\mathrm{B}} \ln \frac{\delta_5}{2}\right)$$

$$= \ln \delta_1 + x_{\mathrm{AA}} \ln \delta_2 + x_{\mathrm{BB}} \ln \delta_3 + x_{\mathrm{AB}} \ln\left(\frac{\delta_1 x_{\mathrm{AB}}}{2}\right) - 2\left(y_{\mathrm{A}} \ln \frac{\delta_4}{2} + y_{\mathrm{B}} \ln \frac{\delta_5}{2}\right)$$

$$= \frac{1}{\delta_1}\left(\delta_1 \ln \delta_1 + \delta_2 \ln \delta_2 + \delta_3 \ln \delta_3 + \delta_1 x_{\mathrm{AB}} \ln\left(\frac{\delta_1 x_{\mathrm{AB}}}{2}\right) - \left(\delta_4 \ln \frac{\delta_4}{2} + \delta_5 \ln \frac{\delta_5}{2}\right)\right) \quad \text{(A.77)}$$

Implementing this into $\Delta G_{\mathrm{mix}}^{\mathrm{xs}}$ (A.78):

$$\Delta G_{\mathrm{mix}}^{\mathrm{xs}} = \frac{\left(\frac{x_{\mathrm{AB}}}{2}(\Delta g_{\mathrm{AB}}^{0} + g_{\mathrm{AB}}^{10} x_{\mathrm{AA}} + g_{\mathrm{AB}}^{01} x_{\mathrm{BB}}) + RT\left(x_{\mathrm{AA}} \ln\left(\frac{x_{\mathrm{AA}}}{y_{\mathrm{A}}^2}\right) + x_{\mathrm{BB}} \ln\left(\frac{x_{\mathrm{BB}}}{y_{\mathrm{B}}^2}\right) + x_{\mathrm{AB}} \ln\left(\frac{x_{\mathrm{AB}}}{2 y_{\mathrm{A}} y_{\mathrm{B}}}\right)\right)\right)}{\beta_{\mathrm{AA}} x_{\mathrm{AA}} + \beta_{\mathrm{BB}} x_{\mathrm{BB}} + (\beta_{\mathrm{AB}} + \beta_{\mathrm{BA}}) x_{\mathrm{AB}}}$$

$$= \frac{\left(\frac{x_{\mathrm{AB}}}{2}(\delta_1 \Delta g_{\mathrm{AB}}^{0} + g_{\mathrm{AB}}^{10} \delta_1 x_{\mathrm{AA}} + g_{\mathrm{AB}}^{01} \delta_1 x_{\mathrm{BB}}) + RT\delta_1\left(x_{\mathrm{AA}} \ln\left(\frac{x_{\mathrm{AA}}}{y_{\mathrm{A}}^2}\right) + x_{\mathrm{BB}} \ln\left(\frac{x_{\mathrm{BB}}}{y_{\mathrm{B}}^2}\right) + x_{\mathrm{AB}} \ln\left(\frac{x_{\mathrm{AB}}}{2 y_{\mathrm{A}} y_{\mathrm{B}}}\right)\right)\right)}{\beta_{\mathrm{AA}} \delta_1 x_{\mathrm{AA}} + \beta_{\mathrm{BB}} \delta_1 x_{\mathrm{BB}} + \delta_1 (\beta_{\mathrm{AB}} + \beta_{\mathrm{BA}}) x_{\mathrm{AB}}}$$

$$\Delta G_{\mathrm{mix}}^{\mathrm{xs}} = \left(\frac{x_{\mathrm{AB}}}{2}\left(\Delta g_{\mathrm{AB}}^{0} \delta_1 + g_{\mathrm{AB}}^{10} \delta_2 + g_{\mathrm{AB}}^{01} \delta_3\right)\right.$$

$$+ RT\left(\delta_1 \ln \delta_1 + \delta_2 \ln \delta_2 + \delta_3 \ln \delta_3 + \delta_1 x_{\mathrm{AB}} \ln\left(\frac{\delta_1 x_{\mathrm{AB}}}{2}\right)\right.$$

$$\left.\left. - \left(\delta_4 \ln \frac{\delta_4}{2} + \delta_5 \ln \frac{\delta_5}{2}\right)\right)\right) \div (\beta_{\mathrm{AA}} \delta_2 + \beta_{\mathrm{BB}} \delta_3 + \delta_1 (\beta_{\mathrm{AB}} + \beta_{\mathrm{BA}}) x_{\mathrm{AB}}) \quad \text{(A.78)}$$

Simplifying the denominator and defining as δ_6 (A.79):

$$\delta_6 = \beta_{\mathrm{AA}} \delta_2 + \beta_{\mathrm{BB}} \delta_3 + \delta_1 (\beta_{\mathrm{AB}} + \beta_{\mathrm{BA}}) x_{\mathrm{AB}}$$

$$= \beta_{\mathrm{AA}}\big((x_{\mathrm{A}} \beta_{\mathrm{BA}} - (1 - x_{\mathrm{A}}) \beta_{\mathrm{AB}}) x_{\mathrm{AB}} + x_{\mathrm{A}} \beta_{\mathrm{BB}} (1 - x_{\mathrm{AB}})\big)$$

$$+ \beta_{\mathrm{BB}}\left(\big((1 - x_{\mathrm{A}}) \beta_{\mathrm{AB}} - x_{\mathrm{A}} \beta_{\mathrm{BA}}\big) x_{\mathrm{AB}} + \beta_{\mathrm{AA}} (1 - x_{\mathrm{A}})(1 - x_{\mathrm{AB}})\right)$$

$$+ x_{\mathrm{AB}} (\beta_{\mathrm{AB}} + \beta_{\mathrm{BA}})\big((1 - x_{\mathrm{A}}) \beta_{\mathrm{AA}} + x_{\mathrm{A}} \beta_{\mathrm{BB}}\big)$$

$$= (\beta_{\mathrm{AA}} - \beta_{\mathrm{BB}})(x_{\mathrm{A}} \beta_{\mathrm{BA}} - (1 - x_{\mathrm{A}}) \beta_{\mathrm{AB}}) x_{\mathrm{AB}} + \beta_{\mathrm{AA}} \beta_{\mathrm{BB}} (1 - x_{\mathrm{AB}})$$

$$+ x_{\mathrm{AB}} (\beta_{\mathrm{AB}} + \beta_{\mathrm{BA}})\big((1 - x_{\mathrm{A}}) \beta_{\mathrm{AA}} + x_{\mathrm{A}} \beta_{\mathrm{BB}}\big)$$

$$= x_{\mathrm{AB}}(\beta_{\mathrm{AA}} \beta_{\mathrm{BA}} x_{\mathrm{A}} - \beta_{\mathrm{BB}} \beta_{\mathrm{BA}} x_{\mathrm{A}} - \beta_{\mathrm{AA}} \beta_{\mathrm{AB}} (1 - x_{\mathrm{A}}) + \beta_{\mathrm{BB}} \beta_{\mathrm{AB}} (1 - x_{\mathrm{A}}) + \beta_{\mathrm{AA}} \beta_{\mathrm{AB}} (1 - x_{\mathrm{A}})$$

$$+ \beta_{\mathrm{AA}} \beta_{\mathrm{BA}} (1 - x_{\mathrm{A}}) + \beta_{\mathrm{BB}} \beta_{\mathrm{BA}} x_{\mathrm{A}} + \beta_{\mathrm{BB}} \beta_{\mathrm{AB}} x_{\mathrm{A}}) + \beta_{\mathrm{AA}} \beta_{\mathrm{BB}} (1 - x_{\mathrm{AB}})$$

$$= x_{\mathrm{AB}}\Big(\beta_{\mathrm{AA}}\beta_{\mathrm{AB}}\big((1-x_{\mathrm{A}})-(1-x_{\mathrm{A}})\big)+\beta_{\mathrm{AA}}\beta_{\mathrm{BA}}\big((1-x_{\mathrm{A}})+x_{\mathrm{A}}\big)$$

$$+\beta_{\mathrm{BB}}\beta_{\mathrm{AB}}\big((1-x_{\mathrm{A}})+x_{\mathrm{A}}\big)+\beta_{\mathrm{BB}}\beta_{\mathrm{BA}}(x_{\mathrm{A}}-x_{\mathrm{A}})\Big)+\beta_{\mathrm{AA}}\beta_{\mathrm{BB}}(1-x_{\mathrm{AB}})$$

$$\delta_6 = \beta_{\mathrm{AA}}\beta_{\mathrm{BB}} + x_{\mathrm{AB}}(\beta_{\mathrm{AA}}\beta_{\mathrm{BA}} + \beta_{\mathrm{BB}}\beta_{\mathrm{AB}} - \beta_{\mathrm{AA}}\beta_{\mathrm{BB}}) \tag{A.79}$$

Implementing this into $\Delta G_{\mathrm{mix}}^{\mathrm{xs}}$ (A.80):

$$\Delta G_{\mathrm{mix}}^{\mathrm{xs}} = \frac{x_{\mathrm{AB}}}{2\delta_6}(\Delta g_{\mathrm{AB}}^{0}\delta_1 + g_{\mathrm{AB}}^{10}\delta_2 + g_{\mathrm{AB}}^{01}\delta_3)$$

$$+\frac{RT}{\delta_6}\left(\delta_1\ln\delta_1+\delta_2\ln\delta_2+\delta_3\ln\delta_3+\delta_1 x_{\mathrm{AB}}\ln\left(\frac{\delta_1 x_{\mathrm{AB}}}{2}\right)-\left(\delta_4\ln\frac{\delta_4}{2}+\delta_5\ln\frac{\delta_5}{2}\right)\right) \tag{A.80}$$

Converting to an Al-X system (A = X, B = Al) (A.81):

$$\Delta G_{\mathrm{mix}}^{\mathrm{xs}} = \frac{x_{\mathrm{XAl}}}{2\varepsilon_6}\big(\Delta g_{\mathrm{XAl}}^{0}\varepsilon_1 + g_{\mathrm{XAl}}^{10}\varepsilon_2 + g_{\mathrm{XAl}}^{01}\varepsilon_3\big)$$

$$+\frac{RT}{\varepsilon_6}\left(\varepsilon_1\ln\varepsilon_1+\varepsilon_2\ln\varepsilon_2+\varepsilon_3\ln\varepsilon_3+\varepsilon_1 x_{\mathrm{XAl}}\ln\left(\frac{\varepsilon_1 x_{\mathrm{XAl}}}{2}\right)-\left(\varepsilon_4\ln\frac{\varepsilon_4}{2}+\varepsilon_5\ln\frac{\varepsilon_5}{2}\right)\right) \tag{A.81}$$

Where ε_i and β_{ij} are defined as follows:

$$\varepsilon_1 = (1-x_{\mathrm{X}})\beta_{\mathrm{XX}} + x_{\mathrm{X}}\beta_{\mathrm{AlAl}} \tag{A.82}$$

$$\varepsilon_2 = \varepsilon_1 x_{\mathrm{XX}} = (x_{\mathrm{X}}\beta_{\mathrm{AlX}} - (1-x_{\mathrm{X}})\beta_{\mathrm{XAl}})x_{\mathrm{XAl}} + x_{\mathrm{X}}\beta_{\mathrm{AlAl}}(1-x_{\mathrm{XAl}}) \tag{A.83}$$

$$\varepsilon_3 = \varepsilon_1 x_{\mathrm{AlAl}} = \big((1-x_{\mathrm{X}})\beta_{\mathrm{XAl}} - x_{\mathrm{X}}\beta_{\mathrm{AlX}}\big)x_{\mathrm{XAl}} + \beta_{\mathrm{XX}}(1-x_{\mathrm{X}})(1-x_{\mathrm{XAl}}) \tag{A.84}$$

$$\varepsilon_4 = 2\varepsilon_1 y_{\mathrm{X}} = x_{\mathrm{XAl}}\big((2\beta_{\mathrm{AlX}} - \beta_{\mathrm{AlAl}})x_{\mathrm{X}} + (\beta_{\mathrm{XX}} - 2\beta_{\mathrm{XAl}})(1-x_{\mathrm{X}})\big) + 2x_{\mathrm{X}}\beta_{\mathrm{AlAl}} \tag{A.85}$$

$$\varepsilon_5 = 2\varepsilon_1 y_{\mathrm{Al}} = x_{\mathrm{XAl}}\big((\beta_{\mathrm{AlAl}} - 2\beta_{\mathrm{AlX}})x_{\mathrm{X}} + (2\beta_{\mathrm{XAl}} - \beta_{\mathrm{XX}})(1-x_{\mathrm{X}})\big) + 2\beta_{\mathrm{XX}}(1-x_{\mathrm{X}}) \tag{A.86}$$

$$\varepsilon_6 = \beta_{\mathrm{XX}}\beta_{\mathrm{AlAl}} + x_{\mathrm{XAl}}(\beta_{\mathrm{XX}}\beta_{\mathrm{AlX}} + \beta_{\mathrm{AlAl}}\beta_{\mathrm{XAl}} - \beta_{\mathrm{XX}}\beta_{\mathrm{AlAl}}) \tag{A.87}$$

$$\beta_{\mathrm{XX}} = \frac{2}{Z_{\mathrm{XX}}^{\mathrm{X}}} \quad \text{(A.88)} \qquad \beta_{\mathrm{AlAl}} = \frac{2}{Z_{\mathrm{AlAl}}^{\mathrm{Al}}} \quad \text{(A.89)} \qquad \beta_{\mathrm{XAl}} = \frac{1}{Z_{\mathrm{XAl}}^{\mathrm{X}}} \quad \text{(A.90)} \qquad \beta_{\mathrm{AlX}} = \frac{1}{Z_{\mathrm{AlX}}^{\mathrm{X}}} \quad \text{(A.91)}$$

A.4.2. Derivative of Gibbs free energy of mixing

Evaluating the derivative of ε_i with respect to x_{X}, as well as other useful relations:

$$\varepsilon_1' = \frac{\mathrm{d}\varepsilon_1}{\mathrm{d}x_{\mathrm{X}}} = \frac{\mathrm{d}}{\mathrm{d}x_{\mathrm{X}}}\big((1-x_{\mathrm{X}})\beta_{\mathrm{XX}} + x_{\mathrm{X}}\beta_{\mathrm{AlAl}}\big) = \beta_{\mathrm{AlAl}} - \beta_{\mathrm{XX}} = \frac{\varepsilon_1 - \beta_{\mathrm{XX}}}{x_{\mathrm{X}}} \tag{A.92}$$

$$\varepsilon_2' = \frac{\mathrm{d}\varepsilon_2}{\mathrm{d}x_\mathrm{X}} = \frac{\mathrm{d}}{\mathrm{d}x_\mathrm{X}}\big((x_\mathrm{X}\beta_\mathrm{AlX} - (1-x_\mathrm{X})\beta_\mathrm{XAl})x_\mathrm{XAl} + x_\mathrm{X}\beta_\mathrm{AlAl}(1-x_\mathrm{XAl})\big)$$

$$= (x_\mathrm{X}\beta_\mathrm{AlX} - (1-x_\mathrm{X})\beta_\mathrm{XAl})x_\mathrm{XAl}' + x_\mathrm{XAl}(\beta_\mathrm{AlX} + \beta_\mathrm{XAl}) + \beta_\mathrm{AlAl}\big((1-x_\mathrm{XAl}) - x_\mathrm{X}x_\mathrm{XAl}'\big)$$

$$= x_\mathrm{XAl}'(x_\mathrm{X}\beta_\mathrm{AlX} - (1-x_\mathrm{X})\beta_\mathrm{XAl} - x_\mathrm{X}\beta_\mathrm{AlAl}) + x_\mathrm{XAl}(\beta_\mathrm{AlX} + \beta_\mathrm{XAl}) + \beta_\mathrm{AlAl}(1-x_\mathrm{XAl})$$

$$\varepsilon_2' = x_\mathrm{XAl}'(x_\mathrm{X}(\beta_\mathrm{AlX} + \beta_\mathrm{XAl} - \beta_\mathrm{AlAl}) - \beta_\mathrm{XAl}) + x_\mathrm{XAl}(\beta_\mathrm{AlX} + \beta_\mathrm{XAl} - \beta_\mathrm{AlAl}) + \beta_\mathrm{AlAl} \tag{A.93}$$

$$\varepsilon_3' = \frac{\mathrm{d}\varepsilon_3}{\mathrm{d}x_\mathrm{X}} = \frac{\mathrm{d}}{\mathrm{d}x_\mathrm{X}}\Big(\big((1-x_\mathrm{X})\beta_\mathrm{XAl} - x_\mathrm{X}\beta_\mathrm{AlX}\big)x_\mathrm{XAl} + \beta_\mathrm{XX}(1-x_\mathrm{X})(1-x_\mathrm{XAl})\Big)$$

$$= \big((1-x_\mathrm{X})\beta_\mathrm{XAl} - x_\mathrm{X}\beta_\mathrm{AlX}\big)x_\mathrm{XAl}' - x_\mathrm{XAl}(\beta_\mathrm{XAl} + \beta_\mathrm{AlX})$$
$$- \beta_\mathrm{XX}\big((1-x_\mathrm{X})x_\mathrm{XAl}' + (1-x_\mathrm{XAl})\big)$$

$$= x_\mathrm{XAl}'\big((1-x_\mathrm{X})\beta_\mathrm{XAl} - x_\mathrm{X}\beta_\mathrm{AlX} - \beta_\mathrm{XX}(1-x_\mathrm{X})\big) - x_\mathrm{XAl}(\beta_\mathrm{XAl} + \beta_\mathrm{AlX}) - \beta_\mathrm{XX}(1-x_\mathrm{XAl})$$

$$\varepsilon_3' = x_\mathrm{XAl}'\big((1-x_\mathrm{X})(\beta_\mathrm{XAl} + \beta_\mathrm{AlX} - \beta_\mathrm{XX}) - \beta_\mathrm{AlX}\big) - x_\mathrm{XAl}(\beta_\mathrm{XAl} + \beta_\mathrm{AlX} - \beta_\mathrm{XX}) - \beta_\mathrm{XX} \tag{A.94}$$

$$\varepsilon_4' = \frac{\mathrm{d}\varepsilon_4}{\mathrm{d}x_\mathrm{X}} = \frac{\mathrm{d}}{\mathrm{d}x_\mathrm{X}}\big(x_\mathrm{XAl}\big((2\beta_\mathrm{AlX} - \beta_\mathrm{AlAl})x_\mathrm{X} + (\beta_\mathrm{XX} - 2\beta_\mathrm{XAl})(1-x_\mathrm{X})\big) + 2x_\mathrm{X}\beta_\mathrm{AlAl}\big)$$

$$= x_\mathrm{XAl}'\big((2\beta_\mathrm{AlX} - \beta_\mathrm{AlAl})x_\mathrm{X} + (\beta_\mathrm{XX} - 2\beta_\mathrm{XAl})(1-x_\mathrm{X})\big)$$
$$+ x_\mathrm{XAl}\big((2\beta_\mathrm{AlX} - \beta_\mathrm{AlAl}) - (\beta_\mathrm{XX} - 2\beta_\mathrm{XAl})\big) + 2\beta_\mathrm{AlAl}$$

$$\varepsilon_4' = 2\varepsilon_2' + \mathrm{x}_\mathrm{XAl}\varepsilon_1' + \mathrm{x}_\mathrm{XAl}'\varepsilon_1 \tag{A.95}$$

$$\varepsilon_5' = \frac{\mathrm{d}\varepsilon_5}{\mathrm{d}x_\mathrm{X}} = \frac{\mathrm{d}}{\mathrm{d}x_\mathrm{X}}\Big(x_\mathrm{XAl}\big(x_\mathrm{X}(\beta_\mathrm{AlAl} - 2\beta_\mathrm{AlX}) + (2\beta_\mathrm{XAl} - \beta_\mathrm{XX})(1-x_\mathrm{X})\big) + 2\beta_\mathrm{XX}(1-x_\mathrm{X})\Big)$$

$$= x_\mathrm{XAl}'\big(x_\mathrm{X}(\beta_\mathrm{AlAl} - 2\beta_\mathrm{AlX}) + (2\beta_\mathrm{XAl} - \beta_\mathrm{XX})(1-x_\mathrm{X})\big)$$
$$+ x_\mathrm{XAl}\big(\beta_\mathrm{AlAl} - 2\beta_\mathrm{AlX} - (2\beta_\mathrm{XAl} - \beta_\mathrm{XX})\big) - 2\beta_\mathrm{XX}$$

$$\varepsilon_5' = 2\varepsilon_3' + x_\mathrm{XAl}\varepsilon_1' + x_\mathrm{XAl}'\varepsilon_1 \tag{A.96}$$

$$\varepsilon_6' = \frac{\mathrm{d}\varepsilon_6}{\mathrm{d}x_\mathrm{X}} = \frac{\mathrm{d}}{\mathrm{d}x_\mathrm{X}}\big(\beta_\mathrm{XX}\beta_\mathrm{AlAl} + x_\mathrm{XAl}(\beta_\mathrm{XX}\beta_\mathrm{AlX} + \beta_\mathrm{AlAl}\beta_\mathrm{XAl} - \beta_\mathrm{XX}\beta_\mathrm{AlAl})\big)$$

$$= (\beta_\mathrm{XX}\beta_\mathrm{AlX} + \beta_\mathrm{AlAl}\beta_\mathrm{XAl} - \beta_\mathrm{XX}\beta_\mathrm{AlAl})x_\mathrm{XAl}'$$

$$\varepsilon_6' = \frac{x_\mathrm{XAl}'}{x_\mathrm{XAl}}(\varepsilon_6 - \beta_\mathrm{XX}\beta_\mathrm{AlAl}) \tag{A.97}$$

$$\frac{\mathrm{d}}{\mathrm{d}x_\mathrm{X}}\left(\frac{RT}{\varepsilon_6}\right) = \frac{\mathrm{d}}{\mathrm{d}x_\mathrm{X}}\left(\frac{RT}{\beta_\mathrm{XX}\beta_\mathrm{AlAl} + x_\mathrm{XAl}(\beta_\mathrm{XX}\beta_\mathrm{AlX} + \beta_\mathrm{AlAl}\beta_\mathrm{XAl} - \beta_\mathrm{XX}\beta_\mathrm{AlAl})}\right) \tag{A.98}$$

$$\frac{\mathrm{d}}{\mathrm{d}x_\mathrm{X}}\left(\frac{RT}{\varepsilon_6}\right)=\frac{-RT(\beta_{\mathrm{XX}}\beta_{\mathrm{AlX}}+\beta_{\mathrm{AlAl}}\beta_{\mathrm{XAl}}-\beta_{\mathrm{XX}}\beta_{\mathrm{AlAl}})x'_{\mathrm{XAl}}}{\left(\beta_{\mathrm{XX}}\beta_{\mathrm{AlAl}}+x_{\mathrm{XAl}}(\beta_{\mathrm{XX}}\beta_{\mathrm{AlX}}+\beta_{\mathrm{AlAl}}\beta_{\mathrm{XAl}}-\beta_{\mathrm{XX}}\beta_{\mathrm{AlAl}})\right)^2}=\frac{-RT\varepsilon'_6}{\varepsilon_6^2}$$

$$\frac{\mathrm{d}}{\mathrm{d}x_\mathrm{X}}\left(\frac{x_{\mathrm{XAl}}}{2\varepsilon_6}\right)=\frac{1}{2}\frac{\mathrm{d}}{\mathrm{d}x_\mathrm{X}}\left(\frac{x_{\mathrm{XAl}}}{\beta_{\mathrm{XX}}\beta_{\mathrm{AlAl}}+x_{\mathrm{XAl}}(\beta_{\mathrm{XX}}\beta_{\mathrm{AlX}}+\beta_{\mathrm{AlAl}}\beta_{\mathrm{XAl}}-\beta_{\mathrm{XX}}\beta_{\mathrm{AlAl}})}\right)$$

$$=\frac{x'_{\mathrm{XAl}}}{2\left(\beta_{\mathrm{XX}}\beta_{\mathrm{AlAl}}+x_{\mathrm{XAl}}(\beta_{\mathrm{XX}}\beta_{\mathrm{AlX}}+\beta_{\mathrm{AlAl}}\beta_{\mathrm{XAl}}-\beta_{\mathrm{XX}}\beta_{\mathrm{AlAl}})\right)}$$

$$-\frac{(\beta_{\mathrm{XX}}\beta_{\mathrm{AlX}}+\beta_{\mathrm{AlAl}}\beta_{\mathrm{XAl}}-\beta_{\mathrm{XX}}\beta_{\mathrm{AlAl}})x'_{\mathrm{XAl}}}{2\left(\beta_{\mathrm{XX}}\beta_{\mathrm{AlAl}}+x_{\mathrm{XAl}}(\beta_{\mathrm{XX}}\beta_{\mathrm{AlX}}+\beta_{\mathrm{AlAl}}\beta_{\mathrm{XAl}}-\beta_{\mathrm{XX}}\beta_{\mathrm{AlAl}})\right)^2}$$

$$\frac{\mathrm{d}}{\mathrm{d}x_\mathrm{X}}\left(\frac{x_{\mathrm{XAl}}}{2\varepsilon_6}\right)=\frac{x'_{\mathrm{XAl}}\left(\beta_{\mathrm{XX}}\beta_{\mathrm{AlAl}}-(1-x_{\mathrm{XAl}})(\beta_{\mathrm{XX}}\beta_{\mathrm{AlX}}+\beta_{\mathrm{AlAl}}\beta_{\mathrm{XAl}}-\beta_{\mathrm{XX}}\beta_{\mathrm{AlAl}})\right)}{2\left(\beta_{\mathrm{XX}}\beta_{\mathrm{AlAl}}+x_{\mathrm{XAl}}(\beta_{\mathrm{XX}}\beta_{\mathrm{AlX}}+\beta_{\mathrm{AlAl}}\beta_{\mathrm{XAl}}-\beta_{\mathrm{XX}}\beta_{\mathrm{AlAl}})\right)^2}$$

$$=\frac{x'_{\mathrm{XAl}}}{2\varepsilon_6}-\frac{x_{\mathrm{XAl}}\varepsilon'_6}{2\varepsilon_6^2}=\frac{x'_{\mathrm{XAl}}\varepsilon_6-x_{\mathrm{XAl}}\varepsilon'_6}{2\varepsilon_6^2} \tag{A.99}$$

$$\frac{\mathrm{d}}{\mathrm{d}x_\mathrm{X}}(x_{\mathrm{XAl}}\varepsilon_1)=\frac{\mathrm{d}}{\mathrm{d}x_\mathrm{X}}\left(x_{\mathrm{XAl}}\left((1-x_\mathrm{X})\beta_{\mathrm{XX}}+x_\mathrm{X}\beta_{\mathrm{AlAl}}\right)\right)$$

$$=x'_{\mathrm{XAl}}\left((1-x_\mathrm{X})\beta_{\mathrm{XX}}+x_\mathrm{X}\beta_{\mathrm{AlAl}}\right)+x_{\mathrm{XAl}}(\beta_{\mathrm{AlAl}}-\beta_{\mathrm{XX}})=x'_{\mathrm{XAl}}\varepsilon_1+x_{\mathrm{XAl}}\varepsilon'_1 \tag{A.100}$$

$$\frac{\mathrm{d}}{\mathrm{d}x_\mathrm{X}}(f(x_\mathrm{X})\ln f(x_\mathrm{X}))=f'(x_\mathrm{X})\ln f(x_\mathrm{X})+\frac{f(x_\mathrm{X})f'(x_\mathrm{X})}{f(x_\mathrm{X})}=f'(x_\mathrm{X})(\ln f(x_\mathrm{X})+1) \tag{A.101}$$

$$\frac{\mathrm{d}}{\mathrm{d}x_\mathrm{X}}\left(f(x_\mathrm{X})\ln\frac{f(x_\mathrm{X})}{2}\right)=f'(x_\mathrm{X})\ln\frac{f(x_\mathrm{X})}{2}+f(x_\mathrm{X})\frac{\frac{f'(x_\mathrm{X})}{2}}{\frac{f(x_\mathrm{X})}{2}}=f'(x_\mathrm{X})\left(\ln\frac{f(x_\mathrm{X})}{2}+1\right) \tag{A.102}$$

Taking the derivative of $\Delta G^{\mathrm{xs}}_{\mathrm{mix}}$ (A.103):

$$\frac{\mathrm{d}\Delta G^{\mathrm{xs}}_{\mathrm{mix}}}{\mathrm{d}x_\mathrm{X}}=\frac{\mathrm{d}}{\mathrm{d}x_\mathrm{X}}\left(\frac{x_{\mathrm{XAl}}}{2\varepsilon_6}\left(\Delta g^0_{\mathrm{XAl}}\varepsilon_1+g^{10}_{\mathrm{XAl}}\varepsilon_2+g^{01}_{\mathrm{XAl}}\varepsilon_3\right)\right)$$

$$+\frac{\mathrm{d}}{\mathrm{d}x_\mathrm{X}}\left(\frac{RT}{\varepsilon_6}\left(\varepsilon_1\ln\varepsilon_1+\varepsilon_2\ln\varepsilon_2+\varepsilon_3\ln\varepsilon_3+\varepsilon_1x_{\mathrm{XAl}}\ln\left(\frac{\varepsilon_1x_{\mathrm{XAl}}}{2}\right)-\left(\varepsilon_4\ln\frac{\varepsilon_4}{2}+\varepsilon_5\ln\frac{\varepsilon_5}{2}\right)\right)\right)$$

$$=\frac{\mathrm{d}}{\mathrm{d}x_\mathrm{X}}\left(\frac{x_{\mathrm{XAl}}}{2\varepsilon_6}\right)\left(\Delta g^0_{\mathrm{XAl}}\varepsilon_1+g^{10}_{\mathrm{XAl}}\varepsilon_2+g^{01}_{\mathrm{XAl}}\varepsilon_3\right)+\frac{x_{\mathrm{XAl}}}{2\varepsilon_6}\left(\Delta g^0_{\mathrm{XAl}}\varepsilon'_1+g^{10}_{\mathrm{XAl}}\varepsilon'_2+g^{01}_{\mathrm{XAl}}\varepsilon'_3\right)$$

$$+\frac{\mathrm{d}}{\mathrm{d}x_\mathrm{X}}\left(\frac{RT}{\varepsilon_6}\right)\left(\varepsilon_1\ln\varepsilon_1+\varepsilon_2\ln\varepsilon_2+\varepsilon_3\ln\varepsilon_3+\varepsilon_1x_{\mathrm{XAl}}\ln\left(\frac{\varepsilon_1x_{\mathrm{XAl}}}{2}\right)-\left(\varepsilon_4\ln\frac{\varepsilon_4}{2}+\varepsilon_5\ln\frac{\varepsilon_5}{2}\right)\right)$$

$$+\frac{RT}{\varepsilon_6}\left(\varepsilon_1'(1+\ln\varepsilon_1)+\varepsilon_2'(1+\ln\varepsilon_2)+\varepsilon_3'(1+\ln\varepsilon_3)+\frac{\mathrm{d}}{\mathrm{d}x_\mathrm{X}}(\varepsilon_1 x_\mathrm{XAl})\left(1+\ln\left(\frac{\varepsilon_1 x_\mathrm{XAl}}{2}\right)\right)\right.$$

$$\left.-\left(\varepsilon_4'\left(1+\ln\frac{\varepsilon_4}{2}\right)+\varepsilon_5'\left(1+\ln\frac{\varepsilon_5}{2}\right)\right)\right)$$

$$=\frac{\Delta g^0_\mathrm{XAl}}{2}\left(\varepsilon_1\frac{\mathrm{d}}{\mathrm{d}x_\mathrm{X}}\left(\frac{x_\mathrm{XAl}}{\varepsilon_6}\right)+\varepsilon_1'\frac{x_\mathrm{XAl}}{\varepsilon_6}\right)+\frac{g^{10}_\mathrm{XAl}}{2}\left(\varepsilon_2\frac{\mathrm{d}}{\mathrm{d}x_\mathrm{X}}\left(\frac{x_\mathrm{XAl}}{\varepsilon_6}\right)+\varepsilon_2'\frac{x_\mathrm{XAl}}{\varepsilon_6}\right)$$

$$+\frac{g^{01}_\mathrm{XAl}}{2}\left(\varepsilon_3\frac{\mathrm{d}}{\mathrm{d}x_\mathrm{X}}\left(\frac{x_\mathrm{XAl}}{\varepsilon_6}\right)+\varepsilon_3'\frac{x_\mathrm{XAl}}{\varepsilon_6}\right)+RT\ln\varepsilon_1\left(\varepsilon_1\frac{\mathrm{d}}{\mathrm{d}x_\mathrm{X}}\left(\frac{1}{\varepsilon_6}\right)+\frac{\varepsilon_1'}{\varepsilon_6}\right)$$

$$+RT\ln\varepsilon_2\left(\varepsilon_2\frac{\mathrm{d}}{\mathrm{d}x_\mathrm{X}}\left(\frac{1}{\varepsilon_6}\right)+\frac{\varepsilon_2'}{\varepsilon_6}\right)+RT\ln\varepsilon_3\left(\varepsilon_3\frac{\mathrm{d}}{\mathrm{d}x_\mathrm{X}}\left(\frac{1}{\varepsilon_6}\right)+\frac{\varepsilon_3'}{\varepsilon_6}\right)$$

$$+RT\ln\left(\frac{\varepsilon_1 x_\mathrm{XAl}}{2}\right)\left(\varepsilon_1 x_\mathrm{XAl}\frac{\mathrm{d}}{\mathrm{d}x_\mathrm{X}}\left(\frac{1}{\varepsilon_6}\right)+\frac{1}{\varepsilon_6}\frac{\mathrm{d}}{\mathrm{d}x_\mathrm{X}}(\varepsilon_1 x_\mathrm{XAl})\right)-RT\ln\frac{\varepsilon_4}{2}\left(\varepsilon_4\frac{\mathrm{d}}{\mathrm{d}x_\mathrm{X}}\left(\frac{1}{\varepsilon_6}\right)+\frac{\varepsilon_4'}{\varepsilon_6}\right)$$

$$-RT\ln\frac{\varepsilon_5}{2}\left(\varepsilon_5\frac{\mathrm{d}}{\mathrm{d}x_\mathrm{X}}\left(\frac{1}{\varepsilon_6}\right)+\frac{\varepsilon_5'}{\varepsilon_6}\right)+\frac{RT}{\varepsilon_6}\left(\varepsilon_1'+\varepsilon_2'+\varepsilon_3'+\frac{\mathrm{d}}{\mathrm{d}x_\mathrm{X}}(\varepsilon_1 x_\mathrm{XAl})-\varepsilon_4'-\varepsilon_5'\right)$$

$$=\frac{\Delta g^0_\mathrm{XAl}}{2}\left(\varepsilon_1\left(\frac{x_\mathrm{XAl}'\varepsilon_6-x_\mathrm{XAl}\varepsilon_6'}{\varepsilon_6^2}\right)+\varepsilon_1'\frac{x_\mathrm{XAl}}{\varepsilon_6}\right)+\frac{g^{10}_\mathrm{XAl}}{2}\left(\varepsilon_2\left(\frac{x_\mathrm{XAl}'\varepsilon_6-x_\mathrm{XAl}\varepsilon_6'}{\varepsilon_6^2}\right)+\varepsilon_2'\frac{x_\mathrm{XAl}}{\varepsilon_6}\right)$$

$$+\frac{g^{01}_\mathrm{XAl}}{2}\left(\varepsilon_3\left(\frac{x_\mathrm{XAl}'\varepsilon_6-x_\mathrm{XAl}\varepsilon_6'}{\varepsilon_6^2}\right)+\varepsilon_3'\frac{x_\mathrm{XAl}}{\varepsilon_6}\right)+RT\ln\varepsilon_1\left(\varepsilon_1\frac{-\varepsilon_6'}{\varepsilon_6^2}+\frac{\varepsilon_1'}{\varepsilon_6}\right)$$

$$+RT\ln\varepsilon_2\left(\varepsilon_2\frac{-\varepsilon_6'}{\varepsilon_6^2}+\frac{\varepsilon_2'}{\varepsilon_6}\right)+RT\ln\varepsilon_3\left(\varepsilon_3\frac{-\varepsilon_6'}{\varepsilon_6^2}+\frac{\varepsilon_3'}{\varepsilon_6}\right)$$

$$+RT\ln\left(\frac{\varepsilon_1 x_\mathrm{XAl}}{2}\right)\left(\varepsilon_1 x_\mathrm{XAl}\frac{-\varepsilon_6'}{\varepsilon_6^2}+\frac{1}{\varepsilon_6}(x_\mathrm{XAl}'\varepsilon_1+x_\mathrm{XAl}\varepsilon_1')\right)-RT\ln\frac{\varepsilon_4}{2}\left(\varepsilon_4\frac{-\varepsilon_6'}{\varepsilon_6^2}+\frac{\varepsilon_4'}{\varepsilon_6}\right)$$

$$-RT\ln\frac{\varepsilon_5}{2}\left(\varepsilon_5\frac{-\varepsilon_6'}{\varepsilon_6^2}+\frac{\varepsilon_5'}{\varepsilon_6}\right)+\frac{RT}{\varepsilon_6}(\varepsilon_1'+\varepsilon_2'+\varepsilon_3'+(x_\mathrm{XAl}'\varepsilon_1+x_\mathrm{XAl}\varepsilon_1')-\varepsilon_4'-\varepsilon_5')$$

$$\frac{\mathrm{d}\Delta G^\mathrm{xs}_\mathrm{mix}}{\mathrm{d}x_\mathrm{X}}=\frac{\Delta g^0_\mathrm{XAl}}{2\varepsilon_6^2}(\varepsilon_1(x_\mathrm{XAl}'\varepsilon_6-x_\mathrm{XAl}\varepsilon_6')+\varepsilon_1'\varepsilon_6 x_\mathrm{XAl})$$

$$+\frac{g^{10}_\mathrm{XAl}}{2\varepsilon_6^2}(\varepsilon_2(x_\mathrm{XAl}'\varepsilon_6-x_\mathrm{XAl}\varepsilon_6')+\varepsilon_2'\varepsilon_6 x_\mathrm{XAl})+\frac{g^{01}_\mathrm{XAl}}{2\varepsilon_6^2}(\varepsilon_3(x_\mathrm{XAl}'\varepsilon_6-x_\mathrm{XAl}\varepsilon_6')+\varepsilon_3'\varepsilon_6 x_\mathrm{XAl})$$

$$+\frac{RT}{\varepsilon_6^2}\ln\varepsilon_1\,(\varepsilon_1'\varepsilon_6-\varepsilon_1\varepsilon_6')+\frac{RT}{\varepsilon_6^2}\ln\varepsilon_2\,(\varepsilon_2'\varepsilon_6-\varepsilon_2\varepsilon_6')+\frac{RT}{\varepsilon_6^2}\ln\varepsilon_3\,(\varepsilon_3'\varepsilon_6-\varepsilon_3\varepsilon_6')$$

$$+\frac{RT}{\varepsilon_6^2}\ln\left(\frac{\varepsilon_1 x_\mathrm{XAl}}{2}\right)(\varepsilon_6(x_\mathrm{XAl}'\varepsilon_1+x_\mathrm{XAl}\varepsilon_1')-\varepsilon_1 x_\mathrm{XAl}\varepsilon_6')\;-\frac{RT}{\varepsilon_6^2}\ln\frac{\varepsilon_4}{2}(\varepsilon_4'\varepsilon_6-\varepsilon_4\varepsilon_6')$$

$$-\frac{RT}{\varepsilon_6^2}\ln\frac{\varepsilon_5}{2}(\varepsilon_5'\varepsilon_6-\varepsilon_5\varepsilon_6')+\frac{RT}{\varepsilon_6}\left(\varepsilon_1'-\varepsilon_2'-\varepsilon_3'-(x_{\mathrm{XAl}}'\varepsilon_1+x_{\mathrm{XAl}}\varepsilon_1')\right) \tag{A.103}$$

Evaluating $x_{\mathrm{XAl}}'\varepsilon_6-x_{\mathrm{XAl}}\varepsilon_6'$ (A.104):

$$x_{\mathrm{XAl}}'\varepsilon_6-x_{\mathrm{XAl}}\varepsilon_6'=x_{\mathrm{XAl}}'\varepsilon_6-x_{\mathrm{XAl}}\left(\frac{x_{\mathrm{XAl}}'}{x_{\mathrm{XAl}}}(\varepsilon_6-\beta_{\mathrm{XX}}\beta_{\mathrm{AlAl}})\right)$$

$$=x_{\mathrm{XAl}}'\varepsilon_6-x_{\mathrm{XAl}}'(\varepsilon_6-\beta_{\mathrm{XX}}\beta_{\mathrm{AlAl}})=\beta_{\mathrm{XX}}\beta_{\mathrm{AlAl}}x_{\mathrm{XAl}}' \tag{A.104}$$

Evaluating $\varepsilon_6(x_{\mathrm{XAl}}'\varepsilon_1+x_{\mathrm{XAl}}\varepsilon_1')-\varepsilon_1x_{\mathrm{XAl}}\varepsilon_6'$ (A.105):

$$\varepsilon_6(x_{\mathrm{XAl}}'\varepsilon_1+x_{\mathrm{XAl}}\varepsilon_1')-\varepsilon_1x_{\mathrm{XAl}}\varepsilon_6'=\varepsilon_6\left(x_{\mathrm{XAl}}'\varepsilon_1+x_{\mathrm{XAl}}(\beta_{\mathrm{AlAl}}-\beta_{\mathrm{XX}})\right)-\varepsilon_1x_{\mathrm{XAl}}\varepsilon_6'$$

$$=\varepsilon_1(\varepsilon_6x_{\mathrm{XAl}}'-x_{\mathrm{XAl}}\varepsilon_6')+x_{\mathrm{XAl}}\varepsilon_6(\beta_{\mathrm{AlAl}}-\beta_{\mathrm{XX}})$$

$$=\beta_{\mathrm{XX}}\beta_{\mathrm{AlAl}}x_{\mathrm{XAl}}'\varepsilon_1+x_{\mathrm{XAl}}\varepsilon_6(\beta_{\mathrm{AlAl}}-\beta_{\mathrm{XX}}) \tag{A.105}$$

Evaluating the last term (A.106) in $\frac{\mathrm{d}\Delta G_{\mathrm{mix}}^{\mathrm{xs}}}{\mathrm{d}x_{\mathrm{X}}}$ (A.103):

$$\varepsilon_1'-\varepsilon_2'-\varepsilon_3'-(x_{\mathrm{XAl}}'\varepsilon_1+x_{\mathrm{XAl}}\varepsilon_1')=\left(\varepsilon_1(1-x_{\mathrm{XAl}})-(\varepsilon_2+\varepsilon_3)\right)'$$

$$=\Big(\big((1-x_{\mathrm{X}})\beta_{\mathrm{XX}}+x_{\mathrm{X}}\beta_{\mathrm{AlAl}}\big)(1-x_{\mathrm{XAl}})-(1-x_{\mathrm{XAl}})(x_{\mathrm{X}}\beta_{\mathrm{AlAl}}+\beta_{\mathrm{XX}}(1-x_{\mathrm{X}}))\Big)'$$

$$=(0)'=0 \tag{A.106}$$

Simplifying $\frac{\mathrm{d}\Delta G_{\mathrm{mix}}^{\mathrm{xs}}}{\mathrm{d}x_{\mathrm{X}}}$ (A.107) using these results:

$$\frac{\mathrm{d}\Delta G_{\mathrm{mix}}^{\mathrm{xs}}}{\mathrm{d}x_{\mathrm{X}}}=\frac{\Delta g_{\mathrm{XAl}}^{0}}{2\varepsilon_6^2}(\varepsilon_1\beta_{\mathrm{XX}}\beta_{\mathrm{AlAl}}x_{\mathrm{XAl}}'+\varepsilon_1'\varepsilon_6x_{\mathrm{XAl}})+\frac{g_{\mathrm{XAl}}^{10}}{2\varepsilon_6^2}(\varepsilon_2\beta_{\mathrm{XX}}\beta_{\mathrm{AlAl}}x_{\mathrm{XAl}}'+\varepsilon_2'\varepsilon_6x_{\mathrm{XAl}})$$

$$+\frac{g_{\mathrm{XAl}}^{01}}{2\varepsilon_6^2}(\varepsilon_3\beta_{\mathrm{XX}}\beta_{\mathrm{AlAl}}x_{\mathrm{XAl}}'+\varepsilon_3'\varepsilon_6x_{\mathrm{XAl}})$$

$$+\frac{RT}{\varepsilon_6^2}\Bigg((\varepsilon_1'\varepsilon_6-\varepsilon_1\varepsilon_6')\ln\varepsilon_1+(\varepsilon_2'\varepsilon_6-\varepsilon_2\varepsilon_6')\ln\varepsilon_2+(\varepsilon_3'\varepsilon_6-\varepsilon_3\varepsilon_6')\ln\varepsilon_3-(\varepsilon_4'\varepsilon_6-\varepsilon_4\varepsilon_6')\ln\frac{\varepsilon_4}{2}$$

$$-(\varepsilon_5'\varepsilon_6-\varepsilon_5\varepsilon_6')\ln\frac{\varepsilon_5}{2}\Bigg)$$

$$+\frac{RT}{\varepsilon_6^2}\left(\left(\beta_{\mathrm{XX}}\beta_{\mathrm{AlAl}}x_{\mathrm{XAl}}'\varepsilon_1+x_{\mathrm{XAl}}\varepsilon_6(\beta_{\mathrm{AlAl}}-\beta_{\mathrm{XX}})\right)\ln\left(\frac{\varepsilon_1x_{\mathrm{XAl}}}{2}\right)\right) \tag{A.107}$$

Evaluating $\varepsilon_1'\varepsilon_6-\varepsilon_1\varepsilon_6'$ (A.108):

$$\varepsilon_1'\varepsilon_6 - \varepsilon_1\varepsilon_6' = \varepsilon_1'\varepsilon_6 - \varepsilon_1(\beta_{\mathrm{XX}}\beta_{\mathrm{AlX}} + \beta_{\mathrm{AlAl}}\beta_{\mathrm{XAl}} - \beta_{\mathrm{XX}}\beta_{\mathrm{AlAl}})x_{\mathrm{XAl}}'$$

$$= (\beta_{\mathrm{AlAl}} - \beta_{\mathrm{XX}})\varepsilon_6 - \varepsilon_1(\beta_{\mathrm{XX}}\beta_{\mathrm{AlX}} + \beta_{\mathrm{AlAl}}\beta_{\mathrm{XAl}} - \beta_{\mathrm{XX}}\beta_{\mathrm{AlAl}})x_{\mathrm{XAl}}' \quad \text{(A.108)}$$

Evaluating $\varepsilon_2'\varepsilon_6 - \varepsilon_2\varepsilon_6'$ (A.109):

$$\varepsilon_2'\varepsilon_6 - \varepsilon_2\varepsilon_6' = \varepsilon_2'\varepsilon_6 - \varepsilon_2(\beta_{\mathrm{XX}}\beta_{\mathrm{AlX}} + \beta_{\mathrm{AlAl}}\beta_{\mathrm{XAl}} - \beta_{\mathrm{XX}}\beta_{\mathrm{AlAl}})x_{\mathrm{XAl}}'$$

$$= \varepsilon_6(x_{\mathrm{XAl}}'(x_{\mathrm{X}}(\beta_{\mathrm{AlX}} + \beta_{\mathrm{XAl}} - \beta_{\mathrm{AlAl}}) - \beta_{\mathrm{XAl}}) + x_{\mathrm{XAl}}(\beta_{\mathrm{AlX}} + \beta_{\mathrm{XAl}} - \beta_{\mathrm{AlAl}}) + \beta_{\mathrm{AlAl}})$$

$$- \varepsilon_2(\beta_{\mathrm{XX}}\beta_{\mathrm{AlX}} + \beta_{\mathrm{AlAl}}\beta_{\mathrm{XAl}} - \beta_{\mathrm{XX}}\beta_{\mathrm{AlAl}})x_{\mathrm{XAl}}'$$

$$= \varepsilon_6(x_{\mathrm{XAl}}(\beta_{\mathrm{AlX}} + \beta_{\mathrm{XAl}}) + (1 - x_{\mathrm{XAl}})\beta_{\mathrm{AlAl}})$$

$$+x_{\mathrm{XAl}}'\big(\varepsilon_6(x_{\mathrm{X}}(\beta_{\mathrm{AlX}} + \beta_{\mathrm{XAl}} - \beta_{\mathrm{AlAl}}) - \beta_{\mathrm{XAl}}) - \varepsilon_2(\beta_{\mathrm{XX}}\beta_{\mathrm{AlX}} + \beta_{\mathrm{AlAl}}\beta_{\mathrm{XAl}} - \beta_{\mathrm{XX}}\beta_{\mathrm{AlAl}})\big)$$

$$= \varepsilon_6(x_{\mathrm{XAl}}(\beta_{\mathrm{AlX}} + \beta_{\mathrm{XAl}}) + (1 - x_{\mathrm{XAl}})\beta_{\mathrm{AlAl}})$$

$$+x_{\mathrm{XAl}}'\Big(\big(\beta_{\mathrm{XX}}\beta_{\mathrm{AlAl}} + x_{\mathrm{XAl}}(\beta_{\mathrm{XX}}\beta_{\mathrm{AlX}} + \beta_{\mathrm{AlAl}}\beta_{\mathrm{XAl}} - \beta_{\mathrm{XX}}\beta_{\mathrm{AlAl}})\big)(x_{\mathrm{X}}(\beta_{\mathrm{AlX}} + \beta_{\mathrm{XAl}} - \beta_{\mathrm{AlAl}}) - \beta_{\mathrm{XAl}})$$

$$- \big((x_{\mathrm{X}}\beta_{\mathrm{AlX}} - (1 - x_{\mathrm{X}})\beta_{\mathrm{XAl}})x_{\mathrm{XAl}} + x_{\mathrm{X}}\beta_{\mathrm{AlAl}}(1 - x_{\mathrm{XAl}})\big)(\beta_{\mathrm{XX}}\beta_{\mathrm{AlX}} + \beta_{\mathrm{AlAl}}\beta_{\mathrm{XAl}}$$

$$- \beta_{\mathrm{XX}}\beta_{\mathrm{AlAl}})\Big)$$

$$= \varepsilon_6(x_{\mathrm{XAl}}(\beta_{\mathrm{AlX}} + \beta_{\mathrm{XAl}}) + (1 - x_{\mathrm{XAl}})\beta_{\mathrm{AlAl}})$$

$$+x_{\mathrm{XAl}}'\Big(\big(\beta_{\mathrm{XX}}\beta_{\mathrm{AlAl}} + x_{\mathrm{XAl}}(\beta_{\mathrm{XX}}\beta_{\mathrm{AlX}} + \beta_{\mathrm{AlAl}}\beta_{\mathrm{XAl}} - \beta_{\mathrm{XX}}\beta_{\mathrm{AlAl}})\big)(x_{\mathrm{X}}(\beta_{\mathrm{AlX}} + \beta_{\mathrm{XAl}} - \beta_{\mathrm{AlAl}}) - \beta_{\mathrm{XAl}})$$

$$- \big((x_{\mathrm{X}}(\beta_{\mathrm{AlX}} + \beta_{\mathrm{XAl}} - \beta_{\mathrm{AlAl}}) - \beta_{\mathrm{XAl}})x_{\mathrm{XAl}} + x_{\mathrm{X}}\beta_{\mathrm{AlAl}}\big)(\beta_{\mathrm{XX}}\beta_{\mathrm{AlX}} + \beta_{\mathrm{AlAl}}\beta_{\mathrm{XAl}}$$

$$- \beta_{\mathrm{XX}}\beta_{\mathrm{AlAl}})\Big)$$

$$= \varepsilon_6(x_{\mathrm{XAl}}(\beta_{\mathrm{AlX}} + \beta_{\mathrm{XAl}}) + (1 - x_{\mathrm{XAl}})\beta_{\mathrm{AlAl}})$$

$$+x_{\mathrm{XAl}}'\big(\beta_{\mathrm{XX}}\beta_{\mathrm{AlAl}}(x_{\mathrm{X}}(\beta_{\mathrm{AlX}} + \beta_{\mathrm{XAl}} - \beta_{\mathrm{AlAl}}) - \beta_{\mathrm{XAl}})\big)$$

$$+x_{\mathrm{XAl}}'\big(x_{\mathrm{XAl}}(\beta_{\mathrm{XX}}\beta_{\mathrm{AlX}} + \beta_{\mathrm{AlAl}}\beta_{\mathrm{XAl}} - \beta_{\mathrm{XX}}\beta_{\mathrm{AlAl}})(x_{\mathrm{X}}(\beta_{\mathrm{AlX}} + \beta_{\mathrm{XAl}} - \beta_{\mathrm{AlAl}}) - \beta_{\mathrm{XAl}})\big)$$

$$-x_{\mathrm{XAl}}'\big((\beta_{\mathrm{XX}}\beta_{\mathrm{AlX}} + \beta_{\mathrm{AlAl}}\beta_{\mathrm{XAl}} - \beta_{\mathrm{XX}}\beta_{\mathrm{AlAl}})(x_{\mathrm{X}}(\beta_{\mathrm{AlX}} + \beta_{\mathrm{XAl}} - \beta_{\mathrm{AlAl}}) - \beta_{\mathrm{XAl}})x_{\mathrm{XAl}}\big)$$

$$-x_{\mathrm{XAl}}'\big(x_{\mathrm{X}}\beta_{\mathrm{AlAl}}(\beta_{\mathrm{XX}}\beta_{\mathrm{AlX}} + \beta_{\mathrm{AlAl}}\beta_{\mathrm{XAl}} - \beta_{\mathrm{XX}}\beta_{\mathrm{AlAl}})\big)$$

$$= \varepsilon_6(x_{\mathrm{XAl}}(\beta_{\mathrm{AlX}} + \beta_{\mathrm{XAl}}) + (1 - x_{\mathrm{XAl}})\beta_{\mathrm{AlAl}})$$

$$+x_{\mathrm{XAl}}'\beta_{\mathrm{AlAl}}\big(\beta_{\mathrm{XX}}(x_{\mathrm{X}}(\beta_{\mathrm{AlX}} + \beta_{\mathrm{XAl}} - \beta_{\mathrm{AlAl}}) - \beta_{\mathrm{XAl}}) - x_{\mathrm{X}}(\beta_{\mathrm{XX}}\beta_{\mathrm{AlX}} + \beta_{\mathrm{AlAl}}\beta_{\mathrm{XAl}} - \beta_{\mathrm{XX}}\beta_{\mathrm{AlAl}})\big)$$

$$= \varepsilon_6(x_{\mathrm{XAl}}(\beta_{\mathrm{AlX}} + \beta_{\mathrm{XAl}}) + (1 - x_{\mathrm{XAl}})\beta_{\mathrm{AlAl}})$$

$$+x'_{\mathrm{XAl}}\beta_{\mathrm{AlAl}}\big((x_{\mathrm{X}}(\beta_{\mathrm{XX}}\beta_{\mathrm{AlX}}+\beta_{\mathrm{XX}}\beta_{\mathrm{XAl}}-\beta_{\mathrm{XX}}\beta_{\mathrm{AlAl}})-\beta_{\mathrm{XX}}\beta_{\mathrm{XAl}})$$

$$-x_{\mathrm{X}}(\beta_{\mathrm{XX}}\beta_{\mathrm{AlX}}+\beta_{\mathrm{AlAl}}\beta_{\mathrm{XAl}}-\beta_{\mathrm{XX}}\beta_{\mathrm{AlAl}})\big)$$

$$=\varepsilon_6(x_{\mathrm{XAl}}(\beta_{\mathrm{AlX}}+\beta_{\mathrm{XAl}})+(1-x_{\mathrm{XAl}})\beta_{\mathrm{AlAl}})$$

$$+x'_{\mathrm{XAl}}\beta_{\mathrm{AlAl}}\big((x_{\mathrm{X}}\beta_{\mathrm{XX}}\beta_{\mathrm{XAl}}-\beta_{\mathrm{XX}}\beta_{\mathrm{XAl}})-x_{\mathrm{X}}(\beta_{\mathrm{AlAl}}\beta_{\mathrm{XAl}})\big)$$

$$=\varepsilon_6(x_{\mathrm{XAl}}(\beta_{\mathrm{AlX}}+\beta_{\mathrm{XAl}})+(1-x_{\mathrm{XAl}})\beta_{\mathrm{AlAl}})-x'_{\mathrm{XAl}}\beta_{\mathrm{XAl}}\beta_{\mathrm{AlAl}}(\beta_{\mathrm{AlAl}}x_{\mathrm{X}}+(1-x_{\mathrm{X}})\beta_{\mathrm{XX}})$$

$$=\varepsilon_6\left(\frac{\varepsilon_2+\beta_{\mathrm{XAl}}x_{\mathrm{XAl}}}{x_{\mathrm{X}}}\right)-x'_{\mathrm{XAl}}\beta_{\mathrm{XAl}}\beta_{\mathrm{AlAl}}\varepsilon_1$$

$$\varepsilon'_2\varepsilon_6-\varepsilon_2\varepsilon'_6=\frac{\varepsilon_6}{x_{\mathrm{X}}}(\varepsilon_2+\beta_{\mathrm{XAl}}x_{\mathrm{XAl}})-x'_{\mathrm{XAl}}\beta_{\mathrm{XAl}}\beta_{\mathrm{AlAl}}\varepsilon_1 \tag{A.109}$$

Evaluating $\varepsilon'_3\varepsilon_6-\varepsilon_3\varepsilon'_6$ (A.110):

$$\varepsilon'_3\varepsilon_6-\varepsilon_3\varepsilon'_6$$

$$=\varepsilon_6\big(x'_{\mathrm{XAl}}\big((1-x_{\mathrm{X}})(\beta_{\mathrm{XAl}}+\beta_{\mathrm{AlX}}-\beta_{\mathrm{XX}})-\beta_{\mathrm{AlX}}\big)-x_{\mathrm{XAl}}(\beta_{\mathrm{XAl}}+\beta_{\mathrm{AlX}}-\beta_{\mathrm{XX}})-\beta_{\mathrm{XX}}\big)$$

$$-\varepsilon_3(\beta_{\mathrm{XX}}\beta_{\mathrm{AlX}}+\beta_{\mathrm{AlAl}}\beta_{\mathrm{XAl}}-\beta_{\mathrm{XX}}\beta_{\mathrm{AlAl}})x'_{\mathrm{XAl}}$$

$$=x'_{\mathrm{XAl}}\Big(\varepsilon_6\big((1-x_{\mathrm{X}})(\beta_{\mathrm{XAl}}+\beta_{\mathrm{AlX}}-\beta_{\mathrm{XX}})-\beta_{\mathrm{AlX}}\big)-\varepsilon_3(\beta_{\mathrm{XX}}\beta_{\mathrm{AlX}}+\beta_{\mathrm{AlAl}}\beta_{\mathrm{XAl}}-\beta_{\mathrm{XX}}\beta_{\mathrm{AlAl}})\Big)$$

$$-\varepsilon_6(x_{\mathrm{XAl}}(\beta_{\mathrm{XAl}}+\beta_{\mathrm{AlX}}-\beta_{\mathrm{XX}})+\beta_{\mathrm{XX}})$$

$$=-\varepsilon_6(x_{\mathrm{XAl}}(\beta_{\mathrm{XAl}}+\beta_{\mathrm{AlX}}-\beta_{\mathrm{XX}})+\beta_{\mathrm{XX}})$$

$$+x'_{\mathrm{XAl}}\Big(\big(\beta_{\mathrm{XX}}\beta_{\mathrm{AlAl}}+x_{\mathrm{XAl}}(\beta_{\mathrm{XX}}\beta_{\mathrm{AlX}}+\beta_{\mathrm{AlAl}}\beta_{\mathrm{XAl}}-\beta_{\mathrm{XX}}\beta_{\mathrm{AlAl}})\big)\big((1-x_{\mathrm{X}})(\beta_{\mathrm{XAl}}+\beta_{\mathrm{AlX}}-\beta_{\mathrm{XX}})-\beta_{\mathrm{AlX}}\big)$$

$$-\Big(\big((1-x_{\mathrm{X}})\beta_{\mathrm{XAl}}-x_{\mathrm{X}}\beta_{\mathrm{AlX}}\big)x_{\mathrm{XAl}}+\beta_{\mathrm{XX}}(1-x_{\mathrm{X}})(1-x_{\mathrm{XAl}})\Big)(\beta_{\mathrm{XX}}\beta_{\mathrm{AlX}}+\beta_{\mathrm{AlAl}}\beta_{\mathrm{XAl}}$$

$$-\beta_{\mathrm{XX}}\beta_{\mathrm{AlAl}})\Big)$$

$$=-\varepsilon_6(x_{\mathrm{XAl}}(\beta_{\mathrm{XAl}}+\beta_{\mathrm{AlX}}-\beta_{\mathrm{XX}})+\beta_{\mathrm{XX}})$$

$$+x'_{\mathrm{XAl}}\Big(\big(\beta_{\mathrm{XX}}\beta_{\mathrm{AlAl}}+x_{\mathrm{XAl}}(\beta_{\mathrm{XX}}\beta_{\mathrm{AlX}}+\beta_{\mathrm{AlAl}}\beta_{\mathrm{XAl}}-\beta_{\mathrm{XX}}\beta_{\mathrm{AlAl}})\big)\big(\beta_{\mathrm{XAl}}-\beta_{\mathrm{XX}}-x_{\mathrm{X}}(\beta_{\mathrm{XAl}}+\beta_{\mathrm{AlX}}-\beta_{\mathrm{XX}})\big)$$

$$-\Big(\big(\beta_{\mathrm{XAl}}-\beta_{\mathrm{XX}}-x_{\mathrm{X}}(\beta_{\mathrm{AlX}}+\beta_{\mathrm{XAl}}-\beta_{\mathrm{XX}})\big)x_{\mathrm{XAl}}+\beta_{\mathrm{XX}}(1-x_{\mathrm{X}})\Big)(\beta_{\mathrm{XX}}\beta_{\mathrm{AlX}}$$

$$+\beta_{\mathrm{AlAl}}\beta_{\mathrm{XAl}}-\beta_{\mathrm{XX}}\beta_{\mathrm{AlAl}})\Big)$$

$$=-\varepsilon_6(x_{\mathrm{XAl}}(\beta_{\mathrm{XAl}}+\beta_{\mathrm{AlX}}-\beta_{\mathrm{XX}})+\beta_{\mathrm{XX}})$$

$$+x'_{\mathrm{XAl}}\Big(\beta_{\mathrm{XX}}\beta_{\mathrm{AlAl}}\big(\beta_{\mathrm{XAl}}-\beta_{\mathrm{XX}}-x_{\mathrm{X}}(\beta_{\mathrm{XAl}}+\beta_{\mathrm{AlX}}-\beta_{\mathrm{XX}})\big)\Big)$$

$$+x'_{\mathrm{XAl}}\left(x_{\mathrm{XAl}}(\beta_{\mathrm{XX}}\beta_{\mathrm{AlX}}+\beta_{\mathrm{AlAl}}\beta_{\mathrm{XAl}}-\beta_{\mathrm{XX}}\beta_{\mathrm{AlAl}})\left(\beta_{\mathrm{XAl}}-\beta_{\mathrm{XX}}-x_{\mathrm{X}}(\beta_{\mathrm{XAl}}+\beta_{\mathrm{AlX}}-\beta_{\mathrm{XX}})\right)\right)$$

$$-x'_{\mathrm{XAl}}\left(\left(\beta_{\mathrm{XAl}}-\beta_{\mathrm{XX}}-x_{\mathrm{X}}(\beta_{\mathrm{AlX}}+\beta_{\mathrm{XAl}}-\beta_{\mathrm{XX}})\right)x_{\mathrm{XAl}}(\beta_{\mathrm{XX}}\beta_{\mathrm{AlX}}+\beta_{\mathrm{AlAl}}\beta_{\mathrm{XAl}}-\beta_{\mathrm{XX}}\beta_{\mathrm{AlAl}})\right)$$

$$-x'_{\mathrm{XAl}}\left(\beta_{\mathrm{XX}}(1-x_{\mathrm{X}})(\beta_{\mathrm{XX}}\beta_{\mathrm{AlX}}+\beta_{\mathrm{AlAl}}\beta_{\mathrm{XAl}}-\beta_{\mathrm{XX}}\beta_{\mathrm{AlAl}})\right)$$

$$=-\varepsilon_6(x_{\mathrm{XAl}}(\beta_{\mathrm{XAl}}+\beta_{\mathrm{AlX}}-\beta_{\mathrm{XX}})+\beta_{\mathrm{XX}})$$

$$+x'_{\mathrm{XAl}}\beta_{\mathrm{XX}}\left(\beta_{\mathrm{AlAl}}\left(\beta_{\mathrm{XAl}}-\beta_{\mathrm{XX}}-x_{\mathrm{X}}(\beta_{\mathrm{XAl}}+\beta_{\mathrm{AlX}}-\beta_{\mathrm{XX}})\right)-(1-x_{\mathrm{X}})(\beta_{\mathrm{XX}}\beta_{\mathrm{AlX}}+\beta_{\mathrm{AlAl}}\beta_{\mathrm{XAl}}-\beta_{\mathrm{XX}}\beta_{\mathrm{AlAl}})\right)$$

$$=-\varepsilon_6(x_{\mathrm{XAl}}(\beta_{\mathrm{XAl}}+\beta_{\mathrm{AlX}}-\beta_{\mathrm{XX}})+\beta_{\mathrm{XX}})$$

$$+x'_{\mathrm{XAl}}\beta_{\mathrm{XX}}\left(\beta_{\mathrm{AlAl}}\left((1-x_{\mathrm{X}})(\beta_{\mathrm{XAl}}-\beta_{\mathrm{XX}})-x_{\mathrm{X}}\beta_{\mathrm{AlX}}-(1-x_{\mathrm{X}})(\beta_{\mathrm{XAl}}-\beta_{\mathrm{XX}})\right)-(1-x_{\mathrm{X}})\beta_{\mathrm{XX}}\beta_{\mathrm{AlX}}\right)$$

$$=\varepsilon_6(-x_{\mathrm{XAl}}(\beta_{\mathrm{XAl}}+\beta_{\mathrm{AlX}}-\beta_{\mathrm{XX}})-\beta_{\mathrm{XX}})+x'_{\mathrm{XAl}}\beta_{\mathrm{XX}}\beta_{\mathrm{AlX}}(\beta_{\mathrm{AlAl}}(-x_{\mathrm{X}})-(1-x_{\mathrm{X}})\beta_{\mathrm{XX}})$$

$$=-\varepsilon_6\left(x_{\mathrm{XAl}}(\beta_{\mathrm{XAl}}+\beta_{\mathrm{AlX}})+\beta_{\mathrm{XX}}(1-x_{\mathrm{XAl}})\right)-x'_{\mathrm{XAl}}\beta_{\mathrm{XX}}\beta_{\mathrm{AlX}}\varepsilon_1$$

$$\varepsilon'_3\varepsilon_6-\varepsilon_3\varepsilon'_6=-\frac{\varepsilon_6}{1-x_{\mathrm{X}}}(\varepsilon_3+\beta_{\mathrm{AlX}}x_{\mathrm{XAl}})-x'_{\mathrm{XAl}}\beta_{\mathrm{XX}}\beta_{\mathrm{AlX}}\varepsilon_1 \qquad \text{(A.110)}$$

Evaluating $\varepsilon'_4\varepsilon_6-\varepsilon_4\varepsilon'_6$ (A.111):

$$\varepsilon_4=2\varepsilon_1y_{\mathrm{X}}=\varepsilon_1(2x_{\mathrm{XX}}+x_{\mathrm{XAl}})=2\varepsilon_2+x_{\mathrm{XAl}}\varepsilon_1$$

$$\varepsilon'_4=2\varepsilon'_2+x'_{\mathrm{XAl}}\varepsilon_1+x_{\mathrm{XAl}}\varepsilon'_1$$

$$\varepsilon'_4\varepsilon_6-\varepsilon_4\varepsilon'_6=\varepsilon_6(2\varepsilon'_2+x'_{\mathrm{XAl}}\varepsilon_1+x_{\mathrm{XAl}}\varepsilon'_1)-\varepsilon'_6(2\varepsilon_2+x_{\mathrm{XAl}}\varepsilon_1)$$

$$=2(\varepsilon'_2\varepsilon_6-\varepsilon_2\varepsilon'_6)+x_{\mathrm{XAl}}(\varepsilon'_1\varepsilon_6-\varepsilon_1\varepsilon'_6)+x'_{\mathrm{XAl}}\varepsilon_1\varepsilon_6$$

$$=\frac{2\varepsilon_6}{x_{\mathrm{X}}}(\varepsilon_2+\beta_{\mathrm{XAl}}x_{\mathrm{XAl}})-2x'_{\mathrm{XAl}}\beta_{\mathrm{XAl}}\beta_{\mathrm{AlAl}}\varepsilon_1+x'_{\mathrm{XAl}}\varepsilon_1\varepsilon_6$$

$$+x_{\mathrm{XAl}}\left((\beta_{\mathrm{AlAl}}-\beta_{\mathrm{XX}})\varepsilon_6-\varepsilon_1(\beta_{\mathrm{XX}}\beta_{\mathrm{AlX}}+\beta_{\mathrm{AlAl}}\beta_{\mathrm{XAl}}-\beta_{\mathrm{XX}}\beta_{\mathrm{AlAl}})x'_{\mathrm{XAl}}\right)$$

$$=\varepsilon_1x'_{\mathrm{XAl}}\left(\varepsilon_6-2\beta_{\mathrm{XAl}}\beta_{\mathrm{AlAl}}-x_{\mathrm{XAl}}(\beta_{\mathrm{XX}}\beta_{\mathrm{AlX}}+\beta_{\mathrm{AlAl}}\beta_{\mathrm{XAl}}-\beta_{\mathrm{XX}}\beta_{\mathrm{AlAl}})\right)$$

$$+\frac{2\varepsilon_6}{x_{\mathrm{X}}}(\varepsilon_2+\beta_{\mathrm{XAl}}x_{\mathrm{XAl}})+(\beta_{\mathrm{AlAl}}-\beta_{\mathrm{XX}})\varepsilon_6x_{\mathrm{XAl}}$$

$$=\varepsilon_1x'_{\mathrm{XAl}}(\beta_{\mathrm{XX}}\beta_{\mathrm{AlAl}}-2\beta_{\mathrm{XAl}}\beta_{\mathrm{AlAl}})+\frac{\varepsilon_6}{x_{\mathrm{X}}}(2\varepsilon_2+2\beta_{\mathrm{XAl}}x_{\mathrm{XAl}}+x_{\mathrm{X}}(\beta_{\mathrm{AlAl}}-\beta_{\mathrm{XX}})x_{\mathrm{XAl}})$$

$$=\varepsilon_1\beta_{\mathrm{AlAl}}x'_{\mathrm{XAl}}(\beta_{\mathrm{XX}}-2\beta_{\mathrm{XAl}})$$

$$+\frac{\varepsilon_6}{x_{\mathrm{X}}}\big(2\big((x_{\mathrm{X}}\beta_{\mathrm{AlX}}-(1-x_{\mathrm{X}})\beta_{\mathrm{XAl}})x_{\mathrm{XAl}}+x_{\mathrm{X}}\beta_{\mathrm{AlAl}}(1-x_{\mathrm{XAl}})\big)+2\beta_{\mathrm{XAl}}x_{\mathrm{XAl}}$$

$$+x_{\mathrm{X}}(\beta_{\mathrm{AlAl}}-\beta_{\mathrm{XX}})x_{\mathrm{XAl}}\big)$$

$$=\varepsilon_1\beta_{\mathrm{AlAl}}x'_{\mathrm{XAl}}(\beta_{\mathrm{XX}}-2\beta_{\mathrm{XAl}})$$

$$+\varepsilon_6\big(2\big((\beta_{\mathrm{AlX}}+\beta_{\mathrm{XAl}})x_{\mathrm{XAl}}+\beta_{\mathrm{AlAl}}(1-x_{\mathrm{XAl}})\big)+(\beta_{\mathrm{AlAl}}-\beta_{\mathrm{XX}})x_{\mathrm{XAl}}\big)$$

$$=\varepsilon_1\beta_{\mathrm{AlAl}}x'_{\mathrm{XAl}}(\beta_{\mathrm{XX}}-2\beta_{\mathrm{XAl}})+\varepsilon_6(x_{\mathrm{XAl}}(2(\beta_{\mathrm{AlX}}+\beta_{\mathrm{XAl}})-\beta_{\mathrm{AlAl}}-\beta_{\mathrm{XX}})+2\beta_{\mathrm{AlAl}})$$

$$=\varepsilon_1\beta_{\mathrm{AlAl}}x'_{\mathrm{XAl}}(\beta_{\mathrm{XX}}-2\beta_{\mathrm{XAl}})+\frac{\varepsilon_6}{x_{\mathrm{X}}}(\varepsilon_4-(\beta_{\mathrm{XX}}-2\beta_{\mathrm{XAl}})x_{\mathrm{XAl}})$$

$$\varepsilon'_4\varepsilon_6-\varepsilon_4\varepsilon'_6=\frac{\varepsilon_6}{x_{\mathrm{X}}}(\varepsilon_4+(2\beta_{\mathrm{XAl}}-\beta_{\mathrm{XX}})x_{\mathrm{XAl}})-\varepsilon_1\beta_{\mathrm{AlAl}}(2\beta_{\mathrm{XAl}}-\beta_{\mathrm{XX}})x'_{\mathrm{XAl}} \qquad \text{(A.111)}$$

Evaluating $\varepsilon'_5\varepsilon_6-\varepsilon_5\varepsilon'_6$ (A.112):

$$\varepsilon_5=2\varepsilon_1y_{\mathrm{Al}}=\varepsilon_1(2x_{\mathrm{AlAl}}+x_{\mathrm{XAl}})=2\varepsilon_3+x_{\mathrm{XAl}}\varepsilon_1$$

$$\varepsilon'_5=2\varepsilon'_3+x'_{\mathrm{XAl}}\varepsilon_1+x_{\mathrm{XAl}}\varepsilon'_1$$

$$\varepsilon'_5\varepsilon_6-\varepsilon_5\varepsilon'_6=\varepsilon_6(2\varepsilon'_3+x'_{\mathrm{XAl}}\varepsilon_1+x_{\mathrm{XAl}}\varepsilon'_1)-\varepsilon'_6(2\varepsilon_3+x_{\mathrm{XAl}}\varepsilon_1)$$

$$=2(\varepsilon'_3\varepsilon_6-\varepsilon_3\varepsilon'_6)+x_{\mathrm{XAl}}(\varepsilon'_1\varepsilon_6-\varepsilon_1\varepsilon'_6)+x'_{\mathrm{XAl}}\varepsilon_1\varepsilon_6$$

$$=-\frac{2\varepsilon_6}{1-x_{\mathrm{X}}}(\varepsilon_3+\beta_{\mathrm{AlX}}x_{\mathrm{XAl}})-2x'_{\mathrm{XAl}}\beta_{\mathrm{XX}}\beta_{\mathrm{AlX}}\varepsilon_1+x'_{\mathrm{XAl}}\varepsilon_1\varepsilon_6$$

$$+x_{\mathrm{XAl}}\big((\beta_{\mathrm{AlAl}}-\beta_{\mathrm{XX}})\varepsilon_6-\varepsilon_1(\beta_{\mathrm{XX}}\beta_{\mathrm{AlX}}+\beta_{\mathrm{AlAl}}\beta_{\mathrm{XAl}}-\beta_{\mathrm{XX}}\beta_{\mathrm{AlAl}})x'_{\mathrm{XAl}}\big)$$

$$=\varepsilon_6\left((\beta_{\mathrm{AlAl}}-\beta_{\mathrm{XX}})x_{\mathrm{XAl}}-\frac{2}{1-x_{\mathrm{X}}}(\varepsilon_3+\beta_{\mathrm{AlX}}x_{\mathrm{XAl}})\right)$$

$$+\varepsilon_1x'_{\mathrm{XAl}}\big(\varepsilon_6-2\beta_{\mathrm{XX}}\beta_{\mathrm{AlX}}-x_{\mathrm{XAl}}(\beta_{\mathrm{XX}}\beta_{\mathrm{AlX}}+\beta_{\mathrm{AlAl}}\beta_{\mathrm{XAl}}-\beta_{\mathrm{XX}}\beta_{\mathrm{AlAl}})\big)$$

$$=\varepsilon_6\left((\beta_{\mathrm{AlAl}}-\beta_{\mathrm{XX}})x_{\mathrm{XAl}}-2\big((\beta_{\mathrm{XAl}}+\beta_{\mathrm{AlX}})x_{\mathrm{XAl}}+\beta_{\mathrm{XX}}(1-x_{\mathrm{XAl}})\big)\right)$$

$$+\varepsilon_1x'_{\mathrm{XAl}}(\beta_{\mathrm{XX}}\beta_{\mathrm{AlAl}}-2\beta_{\mathrm{XX}}\beta_{\mathrm{AlX}})$$

$$=\varepsilon_6(x_{\mathrm{XAl}}(\beta_{\mathrm{AlAl}}-\beta_{\mathrm{XX}}-2\beta_{\mathrm{XAl}}-2\beta_{\mathrm{AlX}}+2\beta_{\mathrm{XX}})-2\beta_{\mathrm{XX}})-\varepsilon_1\beta_{\mathrm{XX}}x'_{\mathrm{XAl}}(2\beta_{\mathrm{AlX}}-\beta_{\mathrm{AlAl}})$$

$$=\varepsilon_6(x_{\mathrm{XAl}}(\beta_{\mathrm{AlAl}}+\beta_{\mathrm{XX}}-2\beta_{\mathrm{XAl}}-2\beta_{\mathrm{AlX}})-2\beta_{\mathrm{XX}})-\varepsilon_1\beta_{\mathrm{XX}}x'_{\mathrm{XAl}}(2\beta_{\mathrm{AlX}}-\beta_{\mathrm{AlAl}})$$

$$\varepsilon'_5\varepsilon_6-\varepsilon_5\varepsilon'_6=-\frac{\varepsilon_6}{1-x_{\mathrm{X}}}(\varepsilon_5+(2\beta_{\mathrm{AlX}}-\beta_{\mathrm{AlAl}})x_{\mathrm{XAl}})-\varepsilon_1\beta_{\mathrm{XX}}(2\beta_{\mathrm{AlX}}-\beta_{\mathrm{AlAl}})x'_{\mathrm{XAl}} \qquad \text{(A.112)}$$

Evaluating $\varepsilon_1\beta_{\mathrm{XX}}\beta_{\mathrm{AlAl}}x'_{\mathrm{XAl}} + \varepsilon'_1\varepsilon_6 x_{\mathrm{XAl}}$ (A.113):

$$\varepsilon_1\beta_{\mathrm{XX}}\beta_{\mathrm{AlAl}}x'_{\mathrm{XAl}} + \varepsilon'_1\varepsilon_6 x_{\mathrm{XAl}} = \varepsilon_1\beta_{\mathrm{XX}}\beta_{\mathrm{AlAl}}x'_{\mathrm{XAl}} + (\beta_{\mathrm{AlAl}} - \beta_{\mathrm{XX}})\varepsilon_6 x_{\mathrm{XAl}} \tag{A.113}$$

Evaluating $\varepsilon_2\beta_{\mathrm{XX}}\beta_{\mathrm{AlAl}}x'_{\mathrm{XAl}} + \varepsilon'_2\varepsilon_6 x_{\mathrm{XAl}}$ (A.114):

$$\begin{aligned}
&\varepsilon_2\beta_{\mathrm{XX}}\beta_{\mathrm{AlAl}}x'_{\mathrm{XAl}} + \varepsilon'_2\varepsilon_6 x_{\mathrm{XAl}} \\
&= \varepsilon_2\beta_{\mathrm{XX}}\beta_{\mathrm{AlAl}}x'_{\mathrm{XAl}} + \varepsilon_6 x_{\mathrm{XAl}}x'_{\mathrm{XAl}}(x_{\mathrm{X}}(\beta_{\mathrm{AlX}} + \beta_{\mathrm{XAl}} - \beta_{\mathrm{AlAl}}) - \beta_{\mathrm{XAl}}) \\
&+\varepsilon_6 x_{\mathrm{XAl}}(x_{\mathrm{XAl}}(\beta_{\mathrm{AlX}} + \beta_{\mathrm{XAl}} - \beta_{\mathrm{AlAl}}) + \beta_{\mathrm{AlAl}}) \\
&= x'_{\mathrm{XAl}}\big(\varepsilon_2\beta_{\mathrm{XX}}\beta_{\mathrm{AlAl}} + \varepsilon_6(x_{\mathrm{XAl}}(x_{\mathrm{X}}\beta_{\mathrm{AlX}} - (1 - x_{\mathrm{X}})\beta_{\mathrm{XAl}}) - x_{\mathrm{X}}x_{\mathrm{XAl}}\beta_{\mathrm{AlAl}})\big) \\
&+\varepsilon_6 x_{\mathrm{XAl}}(x_{\mathrm{XAl}}(\beta_{\mathrm{AlX}} + \beta_{\mathrm{XAl}}) + (1 - x_{\mathrm{XAl}})\beta_{\mathrm{AlAl}}) \\
&= x'_{\mathrm{XAl}}\big(\varepsilon_2\beta_{\mathrm{XX}}\beta_{\mathrm{AlAl}} + \varepsilon_6(\varepsilon_2 - x_{\mathrm{X}}\beta_{\mathrm{AlAl}})\big) \\
&+\varepsilon_6 x_{\mathrm{XAl}}(x_{\mathrm{XAl}}(\beta_{\mathrm{AlX}} + \beta_{\mathrm{XAl}}) + (1 - x_{\mathrm{XAl}})\beta_{\mathrm{AlAl}}) \\
&= x'_{\mathrm{XAl}}(\varepsilon_2(\beta_{\mathrm{XX}}\beta_{\mathrm{AlAl}} + \varepsilon_6) - x_{\mathrm{X}}\beta_{\mathrm{AlAl}}\varepsilon_6) + \frac{\varepsilon_6 x_{\mathrm{XAl}}}{x_{\mathrm{X}}}(\varepsilon_2 + \beta_{\mathrm{XAl}}x_{\mathrm{XAl}})
\end{aligned} \tag{A.114}$$

Evaluating $\varepsilon_3\beta_{\mathrm{XX}}\beta_{\mathrm{AlAl}}x'_{\mathrm{XAl}} + \varepsilon'_3\varepsilon_6 x_{\mathrm{XAl}}$ (A.115):

$$\begin{aligned}
&\varepsilon_3\beta_{\mathrm{XX}}\beta_{\mathrm{AlAl}}x'_{\mathrm{XAl}} + \varepsilon'_3\varepsilon_6 x_{\mathrm{XAl}} \\
&= \varepsilon_3\beta_{\mathrm{XX}}\beta_{\mathrm{AlAl}}x'_{\mathrm{XAl}} \\
&\qquad + \varepsilon_6 x_{\mathrm{XAl}}\big(x'_{\mathrm{XAl}}\big((1 - x_{\mathrm{X}})(\beta_{\mathrm{XAl}} + \beta_{\mathrm{AlX}} - \beta_{\mathrm{XX}}) - \beta_{\mathrm{AlX}}\big) - x_{\mathrm{XAl}}(\beta_{\mathrm{XAl}} + \beta_{\mathrm{AlX}} - \beta_{\mathrm{XX}}) \\
&\qquad - \beta_{\mathrm{XX}}\big) \\
&= x'_{\mathrm{XAl}}\left(\varepsilon_3\beta_{\mathrm{XX}}\beta_{\mathrm{AlAl}} + \varepsilon_6 x_{\mathrm{XAl}}\big((1 - x_{\mathrm{X}})(\beta_{\mathrm{XAl}} + \beta_{\mathrm{AlX}} - \beta_{\mathrm{XX}}) - \beta_{\mathrm{AlX}}\big)\right) \\
&\qquad - \varepsilon_6 x_{\mathrm{XAl}}(x_{\mathrm{XAl}}(\beta_{\mathrm{XAl}} + \beta_{\mathrm{AlX}} - \beta_{\mathrm{XX}}) + \beta_{\mathrm{XX}}) \\
&= x'_{\mathrm{XAl}}\left(\varepsilon_3\beta_{\mathrm{XX}}\beta_{\mathrm{AlAl}} + \varepsilon_6 x_{\mathrm{XAl}}\big((1 - x_{\mathrm{X}})\beta_{\mathrm{XAl}} - x_{\mathrm{X}}\beta_{\mathrm{AlX}} - \beta_{\mathrm{XX}}(1 - x_{\mathrm{X}})\big)\right) \\
&\qquad - \varepsilon_6 x_{\mathrm{XAl}}(x_{\mathrm{XAl}}(\beta_{\mathrm{XAl}} + \beta_{\mathrm{AlX}}) + (1 - x_{\mathrm{XAl}})\beta_{\mathrm{XX}}) \\
&= x'_{\mathrm{XAl}}\big(\varepsilon_3\beta_{\mathrm{XX}}\beta_{\mathrm{AlAl}} + \varepsilon_6(\varepsilon_3 - (1 - x_{\mathrm{X}})\beta_{\mathrm{XX}})\big) - \varepsilon_6 x_{\mathrm{XAl}}(x_{\mathrm{XAl}}(\beta_{\mathrm{XAl}} + \beta_{\mathrm{AlX}}) + (1 - x_{\mathrm{XAl}})\beta_{\mathrm{XX}}) \\
&= x'_{\mathrm{XAl}}(\varepsilon_3(\beta_{\mathrm{XX}}\beta_{\mathrm{AlAl}} + \varepsilon_6) - (1 - x_{\mathrm{X}})\beta_{\mathrm{XX}}\varepsilon_6) - \frac{\varepsilon_6 x_{\mathrm{XAl}}}{1 - x_{\mathrm{X}}}(\varepsilon_3 + \beta_{\mathrm{AlX}}x_{\mathrm{XAl}})
\end{aligned} \tag{A.115}$$

Simplifying $\frac{\mathrm{d}\Delta G^{\mathrm{xs}}_{\mathrm{mix}}}{\mathrm{d}x_{\mathrm{X}}}$ using the results above (A.116):

$$\frac{\mathrm{d}\Delta G_{\mathrm{mix}}^{\mathrm{xs}}}{\mathrm{d}x_{\mathrm{X}}} = \frac{\Delta g_{\mathrm{XAl}}^{0}}{2\varepsilon_6^2}\left(x'_{\mathrm{XAl}}(\varepsilon_1\beta_{\mathrm{XX}}\beta_{\mathrm{AlAl}}) + (\beta_{\mathrm{AlAl}} - \beta_{\mathrm{XX}})\varepsilon_6 x_{\mathrm{XAl}}\right)$$
$$+\frac{g_{\mathrm{XAl}}^{10}}{2\varepsilon_6^2}\left(x'_{\mathrm{XAl}}(\varepsilon_2(\beta_{\mathrm{XX}}\beta_{\mathrm{AlAl}} + \varepsilon_6) - x_{\mathrm{X}}\beta_{\mathrm{AlAl}}\varepsilon_6) + \frac{\varepsilon_6}{x_{\mathrm{X}}}(\varepsilon_2 + \beta_{\mathrm{XAl}}x_{\mathrm{XAl}})x_{\mathrm{XAl}}\right)$$
$$+\frac{g_{\mathrm{XAl}}^{01}}{2\varepsilon_6^2}\left(x'_{\mathrm{XAl}}(\varepsilon_3(\beta_{\mathrm{XX}}\beta_{\mathrm{AlAl}} + \varepsilon_6) - (1 - x_{\mathrm{X}})\beta_{\mathrm{XX}}\varepsilon_6) - \frac{\varepsilon_6}{1 - x_{\mathrm{X}}}(\varepsilon_3 + \beta_{\mathrm{AlX}}x_{\mathrm{XAl}})x_{\mathrm{XAl}}\right)$$
$$+\frac{RT}{\varepsilon_6^2}\ln\varepsilon_1\left((\beta_{\mathrm{AlAl}} - \beta_{\mathrm{XX}})\varepsilon_6 - \varepsilon_1(\beta_{\mathrm{XX}}\beta_{\mathrm{AlX}} + \beta_{\mathrm{AlAl}}\beta_{\mathrm{XAl}} - \beta_{\mathrm{XX}}\beta_{\mathrm{AlAl}})x'_{\mathrm{XAl}}\right)$$
$$+\frac{RT}{\varepsilon_6^2}\ln\varepsilon_2\left(\frac{\varepsilon_6}{x_{\mathrm{X}}}(\varepsilon_2 + \beta_{\mathrm{XAl}}x_{\mathrm{XAl}}) - \beta_{\mathrm{AlAl}}\beta_{\mathrm{XAl}}\varepsilon_1 x'_{\mathrm{XAl}}\right)$$
$$+\frac{RT}{\varepsilon_6^2}\ln\varepsilon_3\left(-\frac{\varepsilon_6}{1 - x_{\mathrm{X}}}(\varepsilon_3 + \beta_{\mathrm{AlX}}x_{\mathrm{XAl}}) - \beta_{\mathrm{XX}}\beta_{\mathrm{AlX}}\varepsilon_1 x'_{\mathrm{XAl}}\right)$$
$$-\frac{RT}{\varepsilon_6^2}\ln\frac{\varepsilon_4}{2}\left(\frac{\varepsilon_6}{x_{\mathrm{X}}}\left(\varepsilon_4 + x_{\mathrm{XAl}}(2\beta_{\mathrm{XAl}} - \beta_{\mathrm{XX}})\right) - \varepsilon_1\beta_{\mathrm{AlAl}}(2\beta_{\mathrm{XAl}} - \beta_{\mathrm{XX}})x'_{\mathrm{XAl}}\right)$$
$$-\frac{RT}{\varepsilon_6^2}\ln\frac{\varepsilon_5}{2}\left(-\frac{\varepsilon_6}{1 - x_{\mathrm{X}}}\left(\varepsilon_5 + x_{\mathrm{XAl}}(2\beta_{\mathrm{AlX}} - \beta_{\mathrm{AlAl}})\right) - \varepsilon_1\beta_{\mathrm{XX}}(2\beta_{\mathrm{AlX}} - \beta_{\mathrm{AlAl}})x'_{\mathrm{XAl}}\right)$$
$$+\frac{RT}{\varepsilon_6^2}\ln\left(\frac{\varepsilon_1 x_{\mathrm{XAl}}}{2}\right)\left(\left(\beta_{\mathrm{XX}}\beta_{\mathrm{AlAl}}x'_{\mathrm{XAl}}\varepsilon_1 + x_{\mathrm{XAl}}\varepsilon_6(\beta_{\mathrm{AlAl}} - \beta_{\mathrm{XX}})\right)\right) \qquad \text{(A.116)}$$

A.4.3. Evaluation of excess relative chemical potentials

A.4.3.1. Excess relative chemical potential of X

Evaluating $\Delta\mu_{\mathrm{X}}^{\mathrm{xs}}$ (A.117):

$$\Delta\mu_{\mathrm{X}}^{\mathrm{xs}} = \Delta G_{\mathrm{mix}}^{\mathrm{xs}} + (1 - x_{\mathrm{X}})\frac{\mathrm{d}\Delta G_{\mathrm{mix}}^{\mathrm{xs}}}{\mathrm{d}x_{\mathrm{X}}}$$

$$= \frac{\Delta g_{\mathrm{XAl}}^{0}}{2\varepsilon_6^2}\left[(1 - x_{\mathrm{X}})\left(x'_{\mathrm{XAl}}(\varepsilon_1\beta_{\mathrm{XX}}\beta_{\mathrm{AlAl}}) + \left((\beta_{\mathrm{AlAl}} - \beta_{\mathrm{XX}})\varepsilon_6\right)x_{\mathrm{XAl}}\right) + \varepsilon_6\varepsilon_1 x_{\mathrm{XAl}}\right]$$

$$+\frac{g_{\mathrm{XAl}}^{10}}{2\varepsilon_6^2}\left[(1 - x_{\mathrm{X}})\left(x'_{\mathrm{XAl}}(\varepsilon_2(\beta_{\mathrm{XX}}\beta_{\mathrm{AlAl}} + \varepsilon_6) - x_{\mathrm{X}}\beta_{\mathrm{AlAl}}\varepsilon_6) + \frac{\varepsilon_6}{x_{\mathrm{X}}}(\varepsilon_2 + \beta_{\mathrm{XAl}}x_{\mathrm{XAl}})x_{\mathrm{XAl}}\right) + \varepsilon_6\varepsilon_2 x_{\mathrm{XAl}}\right]$$

$$+\frac{g_{\mathrm{XAl}}^{01}}{2\varepsilon_6^2}\left[(1 - x_{\mathrm{X}})\left(x'_{\mathrm{XAl}}(\varepsilon_3(\beta_{\mathrm{XX}}\beta_{\mathrm{AlAl}} + \varepsilon_6) - (1 - x_{\mathrm{X}})\beta_{\mathrm{XX}}\varepsilon_6) - \frac{\varepsilon_6}{1 - x_{\mathrm{X}}}(\varepsilon_3 + \beta_{\mathrm{AlX}}x_{\mathrm{XAl}})x_{\mathrm{XAl}}\right)\right.$$
$$\left. + \varepsilon_6\varepsilon_3 x_{\mathrm{XAl}}\right]$$

$$+\frac{RT}{\varepsilon_6^2}\ln\varepsilon_1\left[(1 - x_{\mathrm{X}})\left((\beta_{\mathrm{AlAl}} - \beta_{\mathrm{XX}})\varepsilon_6 - \varepsilon_1(\beta_{\mathrm{XX}}\beta_{\mathrm{AlX}} + \beta_{\mathrm{AlAl}}\beta_{\mathrm{XAl}} - \beta_{\mathrm{XX}}\beta_{\mathrm{AlAl}})x'_{\mathrm{XAl}}\right) + \varepsilon_6\varepsilon_1\right]$$

$$+\frac{RT}{\varepsilon_6^2}\ln\varepsilon_2\left[(1 - x_{\mathrm{X}})\left(\frac{\varepsilon_6}{x_{\mathrm{X}}}(\varepsilon_2 + \beta_{\mathrm{XAl}}x_{\mathrm{XAl}}) - \beta_{\mathrm{AlAl}}\beta_{\mathrm{XAl}}\varepsilon_1 x'_{\mathrm{XAl}}\right) + \varepsilon_6\varepsilon_2\right]$$

$$+\frac{RT}{\varepsilon_6^2}\ln\varepsilon_3\left[(1-x_{\mathrm{X}})\left(-\frac{\varepsilon_6}{1-x_{\mathrm{X}}}(\varepsilon_3+\beta_{\mathrm{AlX}}x_{\mathrm{XAl}})-\beta_{\mathrm{XX}}\beta_{\mathrm{AlX}}\varepsilon_1x'_{\mathrm{XAl}}\right)+\varepsilon_6\varepsilon_3\right]$$

$$+\frac{RT}{\varepsilon_6^2}\ln\frac{\varepsilon_4}{2}\left[(1-x_{\mathrm{X}})\left(-\frac{\varepsilon_6}{x_{\mathrm{X}}}\left(\varepsilon_4+x_{\mathrm{XAl}}(2\beta_{\mathrm{XAl}}-\beta_{\mathrm{XX}})\right)+\varepsilon_1\beta_{\mathrm{AlAl}}(2\beta_{\mathrm{XAl}}-\beta_{\mathrm{XX}})x'_{\mathrm{XAl}}\right)-\varepsilon_6\varepsilon_4\right]$$

$$+\frac{RT}{\varepsilon_6^2}\ln\frac{\varepsilon_5}{2}\left[(1-x_{\mathrm{X}})\left(\frac{\varepsilon_6}{1-x_{\mathrm{X}}}\left(\varepsilon_5+x_{\mathrm{XAl}}(2\beta_{\mathrm{AlX}}-\beta_{\mathrm{AlAl}})\right)+\varepsilon_1\beta_{\mathrm{XX}}(2\beta_{\mathrm{AlX}}-\beta_{\mathrm{AlAl}})x'_{\mathrm{XAl}}\right)-\varepsilon_6\varepsilon_5\right]$$

$$+\frac{RT}{\varepsilon_6^2}\ln\left(\frac{\varepsilon_1x_{\mathrm{XAl}}}{2}\right)\left[(1-x_{\mathrm{X}})\left(\beta_{\mathrm{XX}}\beta_{\mathrm{AlAl}}x'_{\mathrm{XAl}}\varepsilon_1+x_{\mathrm{XAl}}\varepsilon_6(\beta_{\mathrm{AlAl}}-\beta_{\mathrm{XX}})\right)+\varepsilon_1\varepsilon_6x_{\mathrm{XAl}}\right]$$

$$\Delta\mu_{\mathrm{X}}^{\mathrm{xs}}=\frac{\Delta g_{\mathrm{XAl}}^{0}}{2\varepsilon_6^2}\left[\varepsilon_1\beta_{\mathrm{XX}}\beta_{\mathrm{AlAl}}(1-x_{\mathrm{X}})x'_{\mathrm{XAl}}+\varepsilon_6x_{\mathrm{XAl}}\left(\varepsilon_1+(1-x_{\mathrm{X}})(\beta_{\mathrm{AlAl}}-\beta_{\mathrm{XX}})\right)\right]$$

$$+\frac{g_{\mathrm{XAl}}^{10}}{2\varepsilon_6^2}\left[(1-x_{\mathrm{X}})x'_{\mathrm{XAl}}(\varepsilon_2(\beta_{\mathrm{XX}}\beta_{\mathrm{AlAl}}+\varepsilon_6)-x_{\mathrm{X}}\beta_{\mathrm{AlAl}}\varepsilon_6)+x_{\mathrm{XAl}}\varepsilon_6\left(\frac{1-x_{\mathrm{X}}}{x_{\mathrm{X}}}(\varepsilon_2+\beta_{\mathrm{XAl}}x_{\mathrm{XAl}})+\varepsilon_2\right)\right]$$

$$+\frac{g_{\mathrm{XAl}}^{01}}{2\varepsilon_6^2}\left[(1-x_{\mathrm{X}})x'_{\mathrm{XAl}}(\varepsilon_3(\beta_{\mathrm{XX}}\beta_{\mathrm{AlAl}}+\varepsilon_6)-(1-x_{\mathrm{X}})\beta_{\mathrm{XX}}\varepsilon_6)+x_{\mathrm{XAl}}\varepsilon_6(-(\varepsilon_3+\beta_{\mathrm{AlX}}x_{\mathrm{XAl}})+\varepsilon_3)\right]$$

$$+\frac{RT}{\varepsilon_6^2}\ln\varepsilon_1\left[(1-x_{\mathrm{X}})(-\varepsilon_1(\beta_{\mathrm{XX}}\beta_{\mathrm{AlX}}+\beta_{\mathrm{AlAl}}\beta_{\mathrm{XAl}}-\beta_{\mathrm{XX}}\beta_{\mathrm{AlAl}})x'_{\mathrm{XAl}})\right.$$

$$\left.+\varepsilon_6\left(\varepsilon_1+(1-x_{\mathrm{X}})(\beta_{\mathrm{AlAl}}-\beta_{\mathrm{XX}})\right)\right]$$

$$+\frac{RT}{\varepsilon_6^2}\ln\varepsilon_2\left[(1-x_{\mathrm{X}})(-\beta_{\mathrm{AlAl}}\beta_{\mathrm{XAl}}\varepsilon_1x'_{\mathrm{XAl}})+\varepsilon_6\left(\varepsilon_2+\frac{1-x_{\mathrm{X}}}{x_{\mathrm{X}}}(\varepsilon_2+\beta_{\mathrm{XAl}}x_{\mathrm{XAl}})\right)\right]$$

$$+\frac{RT}{\varepsilon_6^2}\ln\varepsilon_3\left[(1-x_{\mathrm{X}})(-\beta_{\mathrm{XX}}\beta_{\mathrm{AlX}}\varepsilon_1x'_{\mathrm{XAl}})+\varepsilon_6\left(\varepsilon_3-(\varepsilon_3+\beta_{\mathrm{AlX}}x_{\mathrm{XAl}})\right)\right]$$

$$+\frac{RT}{\varepsilon_6^2}\ln\frac{\varepsilon_4}{2}\left[(1-x_{\mathrm{X}})(\varepsilon_1\beta_{\mathrm{AlAl}}(2\beta_{\mathrm{XAl}}-\beta_{\mathrm{XX}})x'_{\mathrm{XAl}})-\varepsilon_6\left(\varepsilon_4+\frac{1-x_{\mathrm{X}}}{x_{\mathrm{X}}}\left(\varepsilon_4+x_{\mathrm{XAl}}(2\beta_{\mathrm{XAl}}-\beta_{\mathrm{XX}})\right)\right)\right]$$

$$+\frac{RT}{\varepsilon_6^2}\ln\frac{\varepsilon_5}{2}\left[(1-x_{\mathrm{X}})(\varepsilon_1\beta_{\mathrm{XX}}(2\beta_{\mathrm{AlX}}-\beta_{\mathrm{AlAl}})x'_{\mathrm{XAl}})-\varepsilon_6\left(\varepsilon_5-\left(\varepsilon_5+x_{\mathrm{XAl}}(2\beta_{\mathrm{AlX}}-\beta_{\mathrm{AlAl}})\right)\right)\right]$$

$$+\frac{RT}{\varepsilon_6^2}\ln\left(\frac{\varepsilon_1x_{\mathrm{XAl}}}{2}\right)\left[(1-x_{\mathrm{X}})(\beta_{\mathrm{XX}}\beta_{\mathrm{AlAl}}x'_{\mathrm{XAl}}\varepsilon_1)+\varepsilon_6x_{\mathrm{XAl}}\left(\varepsilon_1+(1-x_{\mathrm{X}})(\beta_{\mathrm{AlAl}}-\beta_{\mathrm{XX}})\right)\right] \tag{A.117}$$

Simplifying terms as possible:

$$\begin{aligned}\varepsilon_1+(1-x_{\mathrm{X}})(\beta_{\mathrm{AlAl}}-\beta_{\mathrm{XX}})&=\left((1-x_{\mathrm{X}})\beta_{\mathrm{XX}}+x_{\mathrm{X}}\beta_{\mathrm{AlAl}}\right)+(1-x_{\mathrm{X}})(\beta_{\mathrm{AlAl}}-\beta_{\mathrm{XX}})\\&=\beta_{\mathrm{AlAl}}\end{aligned} \tag{A.118}$$

$$\frac{1-x_{\mathrm{X}}}{x_{\mathrm{X}}}(\varepsilon_2+\beta_{\mathrm{XAl}}x_{\mathrm{XAl}})+\varepsilon_2$$

$$=\frac{1-x_{\mathrm{X}}}{x_{\mathrm{X}}}\big((x_{\mathrm{X}}\beta_{\mathrm{AlX}}-(1-x_{\mathrm{X}})\beta_{\mathrm{XAl}})x_{\mathrm{XAl}}+x_{\mathrm{X}}\beta_{\mathrm{AlAl}}(1-x_{\mathrm{XAl}})+\beta_{\mathrm{XAl}}x_{\mathrm{XAl}}\big)+\varepsilon_2$$

$$=\frac{1-x_{\mathrm{X}}}{x_{\mathrm{X}}}\big((x_{\mathrm{X}}\beta_{\mathrm{AlX}}+x_{\mathrm{X}}\beta_{\mathrm{XAl}})x_{\mathrm{XAl}}+x_{\mathrm{X}}\beta_{\mathrm{AlAl}}(1-x_{\mathrm{XAl}})\big)+(x_{\mathrm{X}}\beta_{\mathrm{AlX}}-(1-x_{\mathrm{X}})\beta_{\mathrm{XAl}})x_{\mathrm{XAl}}$$
$$+x_{\mathrm{X}}\beta_{\mathrm{AlAl}}(1-x_{\mathrm{XAl}})$$

$$=(1-x_{\mathrm{X}})\big((\beta_{\mathrm{AlX}}+\beta_{\mathrm{XAl}})x_{\mathrm{XAl}}+\beta_{\mathrm{AlAl}}(1-x_{\mathrm{XAl}})\big)+(x_{\mathrm{X}}\beta_{\mathrm{AlX}}-(1-x_{\mathrm{X}})\beta_{\mathrm{XAl}})x_{\mathrm{XAl}}$$
$$+x_{\mathrm{X}}\beta_{\mathrm{AlAl}}(1-x_{\mathrm{XAl}})$$

$$=\beta_{\mathrm{AlX}}x_{\mathrm{XAl}}(1-x_{\mathrm{X}}+x_{\mathrm{X}})+\beta_{\mathrm{XAl}}x_{\mathrm{XAl}}\big((1-x_{\mathrm{X}})-(1-x_{\mathrm{X}})\big)+\beta_{\mathrm{AlAl}}(1-x_{\mathrm{XAl}})\big((1-x_{\mathrm{X}})+x_{\mathrm{X}}\big)$$

$$=\beta_{\mathrm{AlX}}x_{\mathrm{XAl}}+\beta_{\mathrm{AlAl}}(1-x_{\mathrm{XAl}})=\beta_{\mathrm{AlAl}}+x_{\mathrm{XAl}}(\beta_{\mathrm{AlX}}-\beta_{\mathrm{AlAl}}) \tag{A.119}$$

$$-(\varepsilon_3+\beta_{\mathrm{AlX}}x_{\mathrm{XAl}})+\varepsilon_3=-\beta_{\mathrm{AlX}}x_{\mathrm{XAl}} \tag{A.120}$$

$$-\frac{1-x_{\mathrm{X}}}{x_{\mathrm{X}}}\big(\varepsilon_4+x_{\mathrm{XAl}}(2\beta_{\mathrm{XAl}}-\beta_{\mathrm{XX}})\big)-\varepsilon_4$$

$$=-\frac{1-x_{\mathrm{X}}}{x_{\mathrm{X}}}\Big(x_{\mathrm{XAl}}\big((2\beta_{\mathrm{AlX}}-\beta_{\mathrm{AlAl}})x_{\mathrm{X}}+(\beta_{\mathrm{XX}}-2\beta_{\mathrm{XAl}})(1-x_{\mathrm{X}})\big)+2x_{\mathrm{X}}\beta_{\mathrm{AlAl}}+x_{\mathrm{XAl}}(2\beta_{\mathrm{XAl}}-\beta_{\mathrm{XX}})\Big)$$
$$-\varepsilon_4$$

$$=-\frac{1-x_{\mathrm{X}}}{x_{\mathrm{X}}}\big(x_{\mathrm{XAl}}\big(\beta_{\mathrm{XX}}(1-x_{\mathrm{X}}-1)-x_{\mathrm{X}}\beta_{\mathrm{AlAl}}+\beta_{\mathrm{AlX}}(2x_{\mathrm{X}})-2\beta_{\mathrm{XAl}}(1-x_{\mathrm{X}}-1)\big)+2x_{\mathrm{X}}\beta_{\mathrm{AlAl}}\big)-\varepsilon_4$$

$$=-(1-x_{\mathrm{X}})(x_{\mathrm{XAl}}(-\beta_{\mathrm{XX}}-\beta_{\mathrm{AlAl}}+2\beta_{\mathrm{AlX}}+2\beta_{\mathrm{XAl}})+2\beta_{\mathrm{AlAl}})$$
$$-\big(x_{\mathrm{XAl}}\big((2\beta_{\mathrm{AlX}}-\beta_{\mathrm{AlAl}})x_{\mathrm{X}}+(\beta_{\mathrm{XX}}-2\beta_{\mathrm{XAl}})(1-x_{\mathrm{X}})\big)+2x_{\mathrm{X}}\beta_{\mathrm{AlAl}}\big)$$

$$=x_{\mathrm{XAl}}\Big(\beta_{\mathrm{XX}}\big((1-x_{\mathrm{X}})-(1-x_{\mathrm{X}})\big)+\beta_{\mathrm{AlAl}}\big((1-x_{\mathrm{X}})+x_{\mathrm{X}}\big)+\beta_{\mathrm{XAl}}\big(-2(1-x_{\mathrm{X}})+2(1-x_{\mathrm{X}})\big)$$
$$+\beta_{\mathrm{AlX}}(-2(1-x_{\mathrm{X}})-2x_{\mathrm{X}})\Big)+\beta_{\mathrm{AlAl}}(-2(1-x_{\mathrm{X}})-2x_{\mathrm{X}})$$

$$=x_{\mathrm{XAl}}(\beta_{\mathrm{AlAl}}-2\beta_{\mathrm{AlX}})-2\beta_{\mathrm{AlAl}} \tag{A.121}$$

$$\big(\varepsilon_5+x_{\mathrm{XAl}}(2\beta_{\mathrm{AlX}}-\beta_{\mathrm{AlAl}})\big)-\varepsilon_5=x_{\mathrm{XAl}}(2\beta_{\mathrm{AlX}}-\beta_{\mathrm{AlAl}}) \tag{A.122}$$

Simplifying $\Delta\mu_{\mathrm{X}}^{\mathrm{xs}}$ using these relations (A.123):

$$\Delta\mu_{\mathrm{X}}^{\mathrm{xs}}=\frac{\Delta g_{\mathrm{XAl}}^{0}}{2\varepsilon_{\zeta}^{2}}[\varepsilon_1\beta_{\mathrm{XX}}\beta_{\mathrm{AlAl}}(1-x_{\mathrm{X}})x'_{\mathrm{XAl}}+\varepsilon_6x_{\mathrm{XAl}}\beta_{\mathrm{AlAl}}]$$

$$+\frac{g_{\mathrm{XAl}}^{10}}{2\varepsilon_6^2}\left[(1-x_{\mathrm{X}})x'_{\mathrm{XAl}}(\varepsilon_2(\beta_{\mathrm{XX}}\beta_{\mathrm{AlAl}}+\varepsilon_6)-x_{\mathrm{X}}\beta_{\mathrm{AlAl}}\varepsilon_6)\right.$$

$$\left.+x_{\mathrm{XAl}}\varepsilon_6\left(\beta_{\mathrm{AlAl}}+x_{\mathrm{XAl}}(\beta_{\mathrm{AlX}}-\beta_{\mathrm{AlAl}})\right)\right]$$

$$+\frac{g_{\mathrm{XAl}}^{01}}{2\varepsilon_6^2}\left[(1-x_{\mathrm{X}})x'_{\mathrm{XAl}}(\varepsilon_3(\beta_{\mathrm{XX}}\beta_{\mathrm{AlAl}}+\varepsilon_6)-(1-x_{\mathrm{X}})\beta_{\mathrm{XX}}\varepsilon_6)-x_{\mathrm{XAl}}\varepsilon_6(\beta_{\mathrm{AlX}}x_{\mathrm{XAl}})\right]$$

$$+\frac{RT}{\varepsilon_6^2}\ln\varepsilon_1\left[(1-x_{\mathrm{X}})(-\varepsilon_1(\beta_{\mathrm{XX}}\beta_{\mathrm{AlX}}+\beta_{\mathrm{AlAl}}\beta_{\mathrm{XAl}}-\beta_{\mathrm{XX}}\beta_{\mathrm{AlAl}})x'_{\mathrm{XAl}})+\varepsilon_6\beta_{\mathrm{AlAl}}\right]$$

$$+\frac{RT}{\varepsilon_6^2}\ln\varepsilon_2\left[(1-x_{\mathrm{X}})(-\beta_{\mathrm{AlAl}}\beta_{\mathrm{XAl}}\varepsilon_1x'_{\mathrm{XAl}})+\varepsilon_6\left(\beta_{\mathrm{AlAl}}+x_{\mathrm{XAl}}(\beta_{\mathrm{AlX}}-\beta_{\mathrm{AlAl}})\right)\right]$$

$$+\frac{RT}{\varepsilon_6^2}\ln\varepsilon_3\left[(1-x_{\mathrm{X}})(-\beta_{\mathrm{XX}}\beta_{\mathrm{AlX}}\varepsilon_1x'_{\mathrm{XAl}}x'_{\mathrm{XAl}})-\varepsilon_6\beta_{\mathrm{AlX}}x_{\mathrm{XAl}}\right]$$

$$+\frac{RT}{\varepsilon_6^2}\ln\frac{\varepsilon_4}{2}\left[(1-x_{\mathrm{X}})(\varepsilon_1\beta_{\mathrm{AlAl}}(2\beta_{\mathrm{XAl}}-\beta_{\mathrm{XX}})x'_{\mathrm{XAl}})+\varepsilon_6(x_{\mathrm{XAl}}(\beta_{\mathrm{AlAl}}-2\beta_{\mathrm{AlX}})-2\beta_{\mathrm{AlAl}})\right]$$

$$+\frac{RT}{\varepsilon_6^2}\ln\frac{\varepsilon_5}{2}\left[(1-x_{\mathrm{X}})(\varepsilon_1\beta_{\mathrm{XX}}(2\beta_{\mathrm{AlX}}-\beta_{\mathrm{AlAl}})x'_{\mathrm{XAl}})+\varepsilon_6x_{\mathrm{XAl}}(2\beta_{\mathrm{AlX}}-\beta_{\mathrm{AlAl}})\right]$$

$$+\frac{RT}{\varepsilon_6^2}\ln\left(\frac{\varepsilon_1x_{\mathrm{XAl}}}{2}\right)\left[(1-x_{\mathrm{X}})(\beta_{\mathrm{XX}}\beta_{\mathrm{AlAl}}x'_{\mathrm{XAl}}\varepsilon_1)+\beta_{\mathrm{AlAl}}\varepsilon_6x_{\mathrm{XAl}}\right]$$

$$=\frac{x'_{\mathrm{XAl}}(1-x_{\mathrm{X}})\beta_{\mathrm{XX}}\beta_{\mathrm{AlAl}}}{2\varepsilon_6^2}\left(\varepsilon_1\Delta g_{\mathrm{XAl}}^{0}+\varepsilon_2g_{\mathrm{XAl}}^{10}+\varepsilon_3g_{\mathrm{XAl}}^{01}\right)$$

$$+\frac{x'_{\mathrm{XAl}}(1-x_{\mathrm{X}})}{2\varepsilon_6}\left((\varepsilon_2-x_{\mathrm{X}}\beta_{\mathrm{AlAl}})g_{\mathrm{XAl}}^{10}+(\varepsilon_3-(1-x_{\mathrm{X}})\beta_{\mathrm{XX}})g_{\mathrm{XAl}}^{01}\right)$$

$$+\frac{x_{\mathrm{XAl}}\beta_{\mathrm{AlAl}}}{2\varepsilon_6}\left(\Delta g_{\mathrm{XAl}}^{0}+g_{\mathrm{XAl}}^{10}\right)+\frac{x_{\mathrm{XAl}}^2}{2\varepsilon_6}\left((\beta_{\mathrm{AlX}}-\beta_{\mathrm{AlAl}})g_{\mathrm{XAl}}^{10}-\beta_{\mathrm{AlX}}g_{\mathrm{XAl}}^{01}\right)$$

$$-\frac{RT(1-x_{\mathrm{X}})x'_{\mathrm{XAl}}\varepsilon_1}{\varepsilon_6^2}\left[(\beta_{\mathrm{XX}}\beta_{\mathrm{AlX}}+\beta_{\mathrm{AlAl}}\beta_{\mathrm{XAl}}-\beta_{\mathrm{XX}}\beta_{\mathrm{AlAl}})\ln\varepsilon_1+\beta_{\mathrm{AlAl}}\beta_{\mathrm{XAl}}\ln\varepsilon_2+\beta_{\mathrm{XX}}\beta_{\mathrm{AlX}}\ln\varepsilon_3\right.$$

$$\left.-\beta_{\mathrm{AlAl}}(2\beta_{\mathrm{XAl}}-\beta_{\mathrm{XX}})\ln\frac{\varepsilon_4}{2}-\beta_{\mathrm{XX}}(2\beta_{\mathrm{AlX}}-\beta_{\mathrm{AlAl}})\ln\frac{\varepsilon_5}{2}-\beta_{\mathrm{XX}}\beta_{\mathrm{AlAl}}\ln\left(\frac{\varepsilon_1x_{\mathrm{XAl}}}{2}\right)\right]$$

$$+\frac{RT}{\varepsilon_6}\left[\beta_{\mathrm{AlAl}}\ln\varepsilon_1+\beta_{\mathrm{AlAl}}\ln\varepsilon_2-2\beta_{\mathrm{AlAl}}\ln\frac{\varepsilon_4}{2}\right]$$

$$+\frac{RTx_{\mathrm{XAl}}}{\varepsilon_6}\left[(\beta_{\mathrm{AlX}}-\beta_{\mathrm{AlAl}})\ln\varepsilon_2-\beta_{\mathrm{AlX}}\ln\varepsilon_3+(\beta_{\mathrm{AlAl}}-2\beta_{\mathrm{AlX}})\ln\frac{\varepsilon_4}{2}+(2\beta_{\mathrm{AlX}}-\beta_{\mathrm{AlAl}})\ln\frac{\varepsilon_5}{2}\right.$$

$$\left.+\beta_{\mathrm{AlAl}}\ln\left(\frac{\varepsilon_1x_{\mathrm{XAl}}}{2}\right)\right]$$

$$\Delta\mu_{\mathrm{X}}^{\mathrm{xs}}=\frac{x'_{\mathrm{XAl}}(1-x_{\mathrm{X}})\beta_{\mathrm{XX}}\beta_{\mathrm{AlAl}}}{2\varepsilon_6^2}\left(\varepsilon_1\Delta g_{\mathrm{XAl}}^{0}+\varepsilon_2g_{\mathrm{XAl}}^{10}+\varepsilon_3g_{\mathrm{XAl}}^{01}\right)$$

$$+\frac{x'_{\mathrm{XAl}}(1-x_{\mathrm{X}})}{2\varepsilon_6}\left((\varepsilon_2-x_{\mathrm{X}}\beta_{\mathrm{AlAl}})g_{\mathrm{XAl}}^{10}+(\varepsilon_3-(1-x_{\mathrm{X}})\beta_{\mathrm{XX}})g_{\mathrm{XAl}}^{01}\right)$$

$$+\frac{x_{\mathrm{XAl}}\beta_{\mathrm{AlAl}}}{2\varepsilon_6}\left(\Delta g_{\mathrm{XAl}}^{0}+g_{\mathrm{XAl}}^{10}\right)+\frac{x_{\mathrm{XAl}}^2}{2\varepsilon_6}\left((\beta_{\mathrm{AlX}}-\beta_{\mathrm{AlAl}})g_{\mathrm{XAl}}^{10}-\beta_{\mathrm{AlX}}g_{\mathrm{XAl}}^{01}\right)$$

$$-\frac{RT(1-x_{\mathrm{X}})x'_{\mathrm{XAl}}\varepsilon_1}{\varepsilon_6^2}\Big[-\beta_{\mathrm{XX}}\beta_{\mathrm{AlAl}}\left(\ln\varepsilon_1-\ln\frac{\varepsilon_4}{2}-\ln\frac{\varepsilon_5}{2}+\ln\left(\frac{\varepsilon_1 x_{\mathrm{XAl}}}{2}\right)\right)$$

$$+\beta_{\mathrm{XX}}\beta_{\mathrm{AlX}}\left(\ln\varepsilon_1+\ln\varepsilon_3-2\ln\frac{\varepsilon_5}{2}\right)+\beta_{\mathrm{AlAl}}\beta_{\mathrm{XAl}}\left(\ln\varepsilon_1+\ln\varepsilon_2-2\ln\frac{\varepsilon_4}{2}\right)\Big]$$

$$+\frac{RT}{\varepsilon_6}\Big[\beta_{\mathrm{AlAl}}\left(\ln\varepsilon_1+\ln\varepsilon_2-2\ln\frac{\varepsilon_4}{2}\right)\Big]$$

$$+\frac{RTx_{\mathrm{XAl}}}{\varepsilon_6}\Big[\beta_{\mathrm{AlX}}\left(\ln\varepsilon_2-\ln\varepsilon_3-2\ln\frac{\varepsilon_4}{2}+2\ln\frac{\varepsilon_5}{2}\right)$$

$$+\beta_{\mathrm{AlAl}}\left(\ln\left(\frac{\varepsilon_1 x_{\mathrm{XAl}}}{2}\right)-\ln\varepsilon_2+\ln\frac{\varepsilon_4}{2}-\ln\frac{\varepsilon_5}{2}\right)\Big] \qquad \text{(A.123)}$$

Evaluating $\ln\left(\frac{\varepsilon_1 x_{\mathrm{XAl}}}{2}\right)$ (A.124):

$$\frac{x_{\mathrm{XAl}}^2}{x_{\mathrm{XX}}x_{\mathrm{AlAl}}}=4\exp\left(-\frac{\Delta g_{\mathrm{XAl}}}{RT}\right)=\frac{x_{\mathrm{XAl}}^2}{\left(\frac{\varepsilon_2}{\varepsilon_1}\right)\left(\frac{\varepsilon_3}{\varepsilon_1}\right)}=\frac{x_{\mathrm{XAl}}^2\varepsilon_1^2}{\varepsilon_2\varepsilon_3}$$

$$\frac{x_{\mathrm{XAl}}^2\varepsilon_1^2}{4}=\varepsilon_2\varepsilon_3\exp\left(-\frac{\Delta g_{\mathrm{XAl}}^0+g_{\mathrm{XAl}}^{10}x_{\mathrm{XX}}+g_{\mathrm{XAl}}^{01}x_{\mathrm{AlAl}}}{RT}\right)$$

$$2\ln\left(\frac{\varepsilon_1 x_{\mathrm{XAl}}}{2}\right)=\ln\varepsilon_2+\ln\varepsilon_3-\frac{\Delta g_{\mathrm{XAl}}^0\varepsilon_1+g_{\mathrm{XAl}}^{10}\varepsilon_2+g_{\mathrm{XAl}}^{01}\varepsilon_3}{RT\varepsilon_1}$$

$$\ln\left(\frac{\varepsilon_1 x_{\mathrm{XAl}}}{2}\right)=\frac{\ln\varepsilon_2}{2}+\frac{\ln\varepsilon_3}{2}-\frac{\Delta g_{\mathrm{XAl}}^0\varepsilon_1+g_{\mathrm{XAl}}^{10}\varepsilon_2+g_{\mathrm{XAl}}^{01}\varepsilon_3}{2RT\varepsilon_1}$$

$$-\frac{\Delta g_{\mathrm{XAl}}^0\varepsilon_1+g_{\mathrm{XAl}}^{10}\varepsilon_2+g_{\mathrm{XAl}}^{01}\varepsilon_3}{2RT\varepsilon_1}=\frac{1}{2}\left(\ln\varepsilon_1+\ln\frac{x_{\mathrm{XAl}}}{2}-\frac{\ln\varepsilon_2}{2}-\frac{\ln\varepsilon_3}{2}\right) \qquad \text{(A.124)}$$

Eliminating $\ln\left(\frac{\varepsilon_1 x_{\mathrm{XAl}}}{2}\right)$ (A.124) to simplify $\Delta\mu_{\mathrm{X}}^{\mathrm{xs}}$ (A.125):

$$\Delta\mu_{\mathrm{X}}^{\mathrm{xs}}=\frac{x'_{\mathrm{XAl}}(1-x_{\mathrm{X}})\beta_{\mathrm{XX}}\beta_{\mathrm{AlAl}}}{2\varepsilon_6^2}\left(\varepsilon_1\Delta g_{\mathrm{XAl}}^0+\varepsilon_2 g_{\mathrm{XAl}}^{10}+\varepsilon_3 g_{\mathrm{XAl}}^{01}\right)$$

$$+\frac{x'_{\mathrm{XAl}}(1-x_{\mathrm{X}})}{2\varepsilon_6}\left((\varepsilon_2-x_{\mathrm{X}}\beta_{\mathrm{AlAl}})g_{\mathrm{XAl}}^{10}+(\varepsilon_3-(1-x_{\mathrm{X}})\beta_{\mathrm{XX}})g_{\mathrm{XAl}}^{01}\right)$$

$$+\frac{x_{\mathrm{XAl}}\beta_{\mathrm{AlAl}}}{2\varepsilon_6}\left(\Delta g_{\mathrm{XAl}}^0+g_{\mathrm{XAl}}^{10}\right)+\frac{x_{\mathrm{XAl}}^2}{2\varepsilon_6}\left((\beta_{\mathrm{AlX}}-\beta_{\mathrm{AlAl}})g_{\mathrm{XAl}}^{10}-\beta_{\mathrm{AlX}}g_{\mathrm{XAl}}^{01}\right)$$

$$-\frac{RT(1-x_{\mathrm{X}})x'_{\mathrm{XAl}}\varepsilon_1}{\varepsilon_6^2}\Bigg[-\beta_{\mathrm{XX}}\beta_{\mathrm{AlAl}}\Bigg(\ln\varepsilon_1+\frac{\ln\varepsilon_2}{2}+\frac{\ln\varepsilon_3}{2}-\ln\frac{\varepsilon_4}{2}-\ln\frac{\varepsilon_5}{2}$$

$$-\frac{\Delta g^0_{\mathrm{XAl}}\varepsilon_1+g^{10}_{\mathrm{XAl}}\varepsilon_2+g^{01}_{\mathrm{XAl}}\varepsilon_3}{2RT\varepsilon_1}\Bigg)+\beta_{\mathrm{XX}}\beta_{\mathrm{AlX}}\left(\ln\varepsilon_1+\ln\varepsilon_3-2\ln\frac{\varepsilon_5}{2}\right)$$

$$+\beta_{\mathrm{AlAl}}\beta_{\mathrm{XAl}}\left(\ln\varepsilon_1+\ln\varepsilon_2-2\ln\frac{\varepsilon_4}{2}\right)\Bigg]+\frac{RT}{\varepsilon_6}\left[\beta_{\mathrm{AlAl}}\left(\ln\varepsilon_1+\ln\varepsilon_2-2\ln\frac{\varepsilon_4}{2}\right)\right]$$

$$+\frac{RTx_{\mathrm{XAl}}}{\varepsilon_6}\Bigg[\beta_{\mathrm{AlX}}\left(\ln\varepsilon_2-\ln\varepsilon_3-2\ln\frac{\varepsilon_4}{2}+2\ln\frac{\varepsilon_5}{2}\right)$$

$$+\beta_{\mathrm{AlAl}}\left(\frac{\ln\varepsilon_2}{2}+\frac{\ln\varepsilon_3}{2}-\frac{\Delta g^0_{\mathrm{XAl}}\varepsilon_1+g^{10}_{\mathrm{XAl}}\varepsilon_2+g^{01}_{\mathrm{XAl}}\varepsilon_3}{2RT\varepsilon_1}-\ln\varepsilon_2+\ln\frac{\varepsilon_4}{2}-\ln\frac{\varepsilon_5}{2}\right)\Bigg]$$

$$\Delta\mu^{\mathrm{xs}}_{\mathrm{X}}=\frac{x'_{\mathrm{XAl}}(1-x_{\mathrm{X}})\beta_{\mathrm{XX}}\beta_{\mathrm{AlAl}}}{2\varepsilon_6^2}\left(\varepsilon_1\Delta g^0_{\mathrm{XAl}}+\varepsilon_2 g^{10}_{\mathrm{XAl}}+\varepsilon_3 g^{01}_{\mathrm{XAl}}\right)$$

$$+\frac{x'_{\mathrm{XAl}}(1-x_{\mathrm{X}})}{2\varepsilon_6}\left((\varepsilon_2-x_{\mathrm{X}}\beta_{\mathrm{AlAl}})g^{10}_{\mathrm{XAl}}+(\varepsilon_3-(1-x_{\mathrm{X}})\beta_{\mathrm{XX}})g^{01}_{\mathrm{XAl}}\right)$$

$$+\frac{x_{\mathrm{XAl}}\beta_{\mathrm{AlAl}}}{2\varepsilon_6}\left(\Delta g^0_{\mathrm{XAl}}+g^{10}_{\mathrm{XAl}}\right)+\frac{x^2_{\mathrm{XAl}}}{2\varepsilon_6}\left((\beta_{\mathrm{AlX}}-\beta_{\mathrm{AlAl}})g^{10}_{\mathrm{XAl}}-\beta_{\mathrm{AlX}}g^{01}_{\mathrm{XAl}}\right)$$

$$-\frac{RT(1-x_{\mathrm{X}})x'_{\mathrm{XAl}}\varepsilon_1}{\varepsilon_6^2}\Bigg[-\beta_{\mathrm{XX}}\beta_{\mathrm{AlAl}}\left(\ln\varepsilon_1+\frac{\ln\varepsilon_2}{2}+\frac{\ln\varepsilon_3}{2}-\ln\frac{\varepsilon_4}{2}-\ln\frac{\varepsilon_5}{2}\right)$$

$$+\beta_{\mathrm{XX}}\beta_{\mathrm{AlX}}\left(\ln\varepsilon_1+\ln\varepsilon_3-2\ln\frac{\varepsilon_5}{2}\right)+\beta_{\mathrm{AlAl}}\beta_{\mathrm{XAl}}\left(\ln\varepsilon_1+\ln\varepsilon_2-2\ln\frac{\varepsilon_4}{2}\right)\Bigg]$$

$$+\frac{RT}{\varepsilon_6}\left[\beta_{\mathrm{AlAl}}\left(\ln\varepsilon_1+\ln\varepsilon_2-2\ln\frac{\varepsilon_4}{2}\right)\right]$$

$$+\frac{RTx_{\mathrm{XAl}}}{\varepsilon_6}\left[\beta_{\mathrm{AlX}}\left(\ln\varepsilon_2-\ln\varepsilon_3-2\ln\frac{\varepsilon_4}{2}+2\ln\frac{\varepsilon_5}{2}\right)+\beta_{\mathrm{AlAl}}\left(-\frac{\ln\varepsilon_2}{2}+\frac{\ln\varepsilon_3}{2}+\ln\frac{\varepsilon_4}{2}-\ln\frac{\varepsilon_5}{2}\right)\right]$$

$$-\frac{RT(1-x_{\mathrm{X}})x'_{\mathrm{XAl}}\varepsilon_1}{\varepsilon_6^2}\left[\beta_{\mathrm{XX}}\beta_{\mathrm{AlAl}}\frac{\Delta g^0_{\mathrm{XAl}}\varepsilon_1+g^{10}_{\mathrm{XAl}}\varepsilon_2+g^{01}_{\mathrm{XAl}}\varepsilon_3}{2RT\varepsilon_1}\right]$$

$$-\frac{RTx_{\mathrm{XAl}}}{\varepsilon_6}\beta_{\mathrm{AlAl}}\frac{\Delta g^0_{\mathrm{XAl}}\varepsilon_1+g^{10}_{\mathrm{XAl}}\varepsilon_2+g^{01}_{\mathrm{XAl}}\varepsilon_3}{2RT\varepsilon_1}$$

$$\Delta\mu^{\mathrm{xs}}_{\mathrm{X}}=\frac{x'_{\mathrm{XAl}}(1-x_{\mathrm{X}})}{2\varepsilon_6}\left((\varepsilon_2-x_{\mathrm{X}}\beta_{\mathrm{AlAl}})g^{10}_{\mathrm{XAl}}+(\varepsilon_3-(1-x_{\mathrm{X}})\beta_{\mathrm{XX}})g^{01}_{\mathrm{XAl}}\right)$$

$$+\frac{x_{\mathrm{XAl}}\beta_{\mathrm{AlAl}}}{2\varepsilon_6}\left(\Delta g^0_{\mathrm{XAl}}+g^{10}_{\mathrm{XAl}}\right)+\frac{x^2_{\mathrm{XAl}}}{2\varepsilon_6}\left((\beta_{\mathrm{AlX}}-\beta_{\mathrm{AlAl}})g^{10}_{\mathrm{XAl}}-\beta_{\mathrm{AlX}}g^{01}_{\mathrm{XAl}}\right)$$

$$-\frac{RT(1-x_{\mathrm{X}})x'_{\mathrm{XAl}}\varepsilon_1}{\varepsilon_6^2}\Big[-\beta_{\mathrm{XX}}\beta_{\mathrm{AlAl}}\Big(\ln\varepsilon_1+\frac{\ln\varepsilon_2}{2}+\frac{\ln\varepsilon_3}{2}-\ln\frac{\varepsilon_4}{2}-\ln\frac{\varepsilon_5}{2}\Big)$$

$$+\beta_{\mathrm{XX}}\beta_{\mathrm{AlX}}\Big(\ln\varepsilon_1+\ln\varepsilon_3-2\ln\frac{\varepsilon_5}{2}\Big)+\beta_{\mathrm{AlAl}}\beta_{\mathrm{XAl}}\Big(\ln\varepsilon_1+\ln\varepsilon_2-2\ln\frac{\varepsilon_4}{2}\Big)\Big]$$

$$+\frac{RT}{\varepsilon_6}\Big[\beta_{\mathrm{AlAl}}\Big(\ln\varepsilon_1+\ln\varepsilon_2-2\ln\frac{\varepsilon_4}{2}\Big)\Big]$$

$$+\frac{RTx_{\mathrm{XAl}}}{\varepsilon_6}\Big[\beta_{\mathrm{AlX}}\Big(\ln\varepsilon_2-\ln\varepsilon_3-2\ln\frac{\varepsilon_4}{2}+2\ln\frac{\varepsilon_5}{2}\Big)+\beta_{\mathrm{AlAl}}\Big(-\frac{\ln\varepsilon_2}{2}+\frac{\ln\varepsilon_3}{2}+\ln\frac{\varepsilon_4}{2}-\ln\frac{\varepsilon_5}{2}\Big)\Big]$$

$$-\frac{x_{\mathrm{XAl}}\beta_{\mathrm{AlAl}}}{2\varepsilon_1\varepsilon_6}\big(\Delta g^0_{\mathrm{XAl}}\varepsilon_1+g^{10}_{\mathrm{XAl}}\varepsilon_2+g^{01}_{\mathrm{XAl}}\varepsilon_3\big) \tag{A.125}$$

Grouping $\ln\varepsilon_i$ terms as ε_{X} (A.126) and $\varepsilon_{\mathrm{Al}}$ (A.127) to simplify $\Delta\mu^{\mathrm{xs}}_{\mathrm{X}}$ (A.128):

$$\varepsilon_{\mathrm{X}}=\ln\varepsilon_1+\ln\varepsilon_2-2\ln\frac{\varepsilon_4}{2} \tag{A.126}$$

$$\varepsilon_{\mathrm{Al}}=\ln\varepsilon_1+\ln\varepsilon_3-2\ln\frac{\varepsilon_5}{2} \tag{A.127}$$

$$\Delta\mu^{\mathrm{xs}}_{\mathrm{X}}=\frac{x'_{\mathrm{XAl}}(1-x_{\mathrm{X}})}{2\varepsilon_6}\Big((\varepsilon_2-x_{\mathrm{X}}\beta_{\mathrm{AlAl}})g^{10}_{\mathrm{XAl}}+(\varepsilon_3-(1-x_{\mathrm{X}})\beta_{\mathrm{XX}})g^{01}_{\mathrm{XAl}}\Big)$$

$$+\frac{x_{\mathrm{XAl}}\beta_{\mathrm{AlAl}}}{2\varepsilon_6}\big(\Delta g^0_{\mathrm{XAl}}+g^{10}_{\mathrm{XAl}}\big)+\frac{x^2_{\mathrm{XAl}}}{2\varepsilon_6}\Big((\beta_{\mathrm{AlX}}-\beta_{\mathrm{AlAl}})g^{10}_{\mathrm{XAl}}-\beta_{\mathrm{AlX}}g^{01}_{\mathrm{XAl}}\Big)$$

$$-\frac{RT(1-x_{\mathrm{X}})x'_{\mathrm{XAl}}\varepsilon_1}{2\varepsilon_6^2}[-\beta_{\mathrm{XX}}\beta_{\mathrm{AlAl}}(\varepsilon_{\mathrm{X}}+\varepsilon_{\mathrm{Al}})+2\beta_{\mathrm{XX}}\beta_{\mathrm{AlX}}(\varepsilon_{\mathrm{Al}})+2\beta_{\mathrm{AlAl}}\beta_{\mathrm{XAl}}(\varepsilon_{\mathrm{X}})]$$

$$+\frac{RT}{\varepsilon_6}[\beta_{\mathrm{AlAl}}(\varepsilon_{\mathrm{X}})]$$

$$+\frac{RTx_{\mathrm{XAl}}}{2\varepsilon_6}[2\beta_{\mathrm{AlX}}(\varepsilon_{\mathrm{X}}-\varepsilon_{\mathrm{Al}})+\beta_{\mathrm{AlAl}}(\varepsilon_{\mathrm{Al}}-\varepsilon_{\mathrm{X}})]-\frac{x_{\mathrm{XAl}}\beta_{\mathrm{AlAl}}}{2\varepsilon_1\varepsilon_6}\big(\Delta g^0_{\mathrm{XAl}}\varepsilon_1+g^{10}_{\mathrm{XAl}}\varepsilon_2+g^{01}_{\mathrm{XAl}}\varepsilon_3\big)$$

$$=\frac{x_{\mathrm{XAl}}\beta_{\mathrm{AlAl}}}{2\varepsilon_6}\big(\Delta g^0_{\mathrm{XAl}}+g^{10}_{\mathrm{XAl}}\big)+\frac{x^2_{\mathrm{XAl}}}{2\varepsilon_6}\Big((\beta_{\mathrm{AlX}}-\beta_{\mathrm{AlAl}})g^{10}_{\mathrm{XAl}}-\beta_{\mathrm{AlX}}g^{01}_{\mathrm{XAl}}\Big)$$

$$+\frac{RTx_{\mathrm{XAl}}}{2\varepsilon_6}[2\beta_{\mathrm{AlX}}(\varepsilon_{\mathrm{X}}-\varepsilon_{\mathrm{Al}})+\beta_{\mathrm{AlAl}}(\varepsilon_{\mathrm{Al}}-\varepsilon_{\mathrm{X}})]-\frac{x_{\mathrm{XAl}}\beta_{\mathrm{AlAl}}}{2\varepsilon_1\varepsilon_6}\big(\Delta g^0_{\mathrm{XAl}}\varepsilon_1+g^{10}_{\mathrm{XAl}}\varepsilon_2+g^{01}_{\mathrm{XAl}}\varepsilon_3\big)$$

$$+\frac{x'_{\mathrm{XAl}}(1-x_{\mathrm{X}})}{2\varepsilon_6}\Big((\varepsilon_2-x_{\mathrm{X}}\beta_{\mathrm{AlAl}})g^{10}_{\mathrm{XAl}}+(\varepsilon_3-(1-x_{\mathrm{X}})\beta_{\mathrm{XX}})g^{01}_{\mathrm{XAl}}\Big)$$

$$-\frac{RT(1-x_{\mathrm{X}})x'_{\mathrm{XAl}}\varepsilon_1}{2\varepsilon_6^2}[-\beta_{\mathrm{XX}}\beta_{\mathrm{AlAl}}(\varepsilon_{\mathrm{X}}+\varepsilon_{\mathrm{Al}})+2\beta_{\mathrm{XX}}\beta_{\mathrm{AlX}}(\varepsilon_{\mathrm{Al}})+2\beta_{\mathrm{AlAl}}\beta_{\mathrm{XAl}}(\varepsilon_{\mathrm{X}})]$$

$$+\frac{RT}{\varepsilon_6}[\beta_{\mathrm{AlAl}}(\varepsilon_{\mathrm{X}})]$$

$$=\frac{x_{\mathrm{XAl}}\beta_{\mathrm{AlAl}}}{2\varepsilon_1\varepsilon_6}\left(\varepsilon_1\Delta g^0_{\mathrm{XAl}}+\varepsilon_1 g^{10}_{\mathrm{XAl}}-\left(\Delta g^0_{\mathrm{XAl}}\varepsilon_1+g^{10}_{\mathrm{XAl}}\varepsilon_2+g^{01}_{\mathrm{XAl}}\varepsilon_3\right)\right)$$

$$+\frac{x^2_{\mathrm{XAl}}}{2\varepsilon_6}\left((\beta_{\mathrm{AlX}}-\beta_{\mathrm{AlAl}})g^{10}_{\mathrm{XAl}}-\beta_{\mathrm{AlX}}g^{01}_{\mathrm{XAl}}\right)+\frac{RT}{2\varepsilon_6}[x_{\mathrm{XAl}}(2\beta_{\mathrm{AlX}}-\beta_{\mathrm{AlAl}})(\varepsilon_{\mathrm{X}}-\varepsilon_{\mathrm{Al}})+2\beta_{\mathrm{AlAl}}\varepsilon_{\mathrm{X}}]$$

$$+\frac{x'_{\mathrm{XAl}}(1-x_{\mathrm{X}})}{2\varepsilon_6}\left((\varepsilon_2-x_{\mathrm{X}}\beta_{\mathrm{AlAl}})g^{10}_{\mathrm{XAl}}+(\varepsilon_3-(1-x_{\mathrm{X}})\beta_{\mathrm{XX}})g^{01}_{\mathrm{XAl}}\right)$$

$$-\frac{RT(1-x_{\mathrm{X}})x'_{\mathrm{XAl}}\varepsilon_1}{2\varepsilon_6^2}[\beta_{\mathrm{AlAl}}\varepsilon_{\mathrm{X}}(2\beta_{\mathrm{XAl}}-\beta_{\mathrm{XX}})+\beta_{\mathrm{XX}}\varepsilon_{\mathrm{Al}}(2\beta_{\mathrm{AlX}}-\beta_{\mathrm{AlAl}})]$$

$$=\frac{x_{\mathrm{XAl}}\beta_{\mathrm{AlAl}}}{2\varepsilon_1\varepsilon_6}\left((\varepsilon_1-\varepsilon_2)g^{10}_{\mathrm{XAl}}-g^{01}_{\mathrm{XAl}}\varepsilon_3\right)+\frac{x^2_{\mathrm{XAl}}}{2\varepsilon_6}\left((\beta_{\mathrm{AlX}}-\beta_{\mathrm{AlAl}})g^{10}_{\mathrm{XAl}}-\beta_{\mathrm{AlX}}g^{01}_{\mathrm{XAl}}\right)$$

$$+\frac{RT}{2\varepsilon_6}[x_{\mathrm{XAl}}(2\beta_{\mathrm{AlX}}-\beta_{\mathrm{AlAl}})(\varepsilon_{\mathrm{X}}-\varepsilon_{\mathrm{Al}})+2\beta_{\mathrm{AlAl}}\varepsilon_{\mathrm{Al}}]$$

$$+\frac{x'_{\mathrm{XAl}}(1-x_{\mathrm{X}})}{2\varepsilon_6}\left((\varepsilon_2-x_{\mathrm{X}}\beta_{\mathrm{AlAl}})g^{10}_{\mathrm{XAl}}+(\varepsilon_3-(1-x_{\mathrm{X}})\beta_{\mathrm{XX}})g^{01}_{\mathrm{XAl}}\right)$$

$$-\frac{RT(1-x_{\mathrm{X}})x'_{\mathrm{XAl}}\varepsilon_1}{2\varepsilon_6^2}[\beta_{\mathrm{AlAl}}\varepsilon_{\mathrm{X}}(2\beta_{\mathrm{XAl}}-\beta_{\mathrm{XX}})+\beta_{\mathrm{XX}}\varepsilon_{\mathrm{Al}}(2\beta_{\mathrm{AlX}}-\beta_{\mathrm{AlAl}})]$$

$$=\frac{x_{\mathrm{XAl}}}{2\varepsilon_1\varepsilon_6}\left(\beta_{\mathrm{AlAl}}\left((\varepsilon_1-\varepsilon_2)g^{10}_{\mathrm{XAl}}-g^{01}_{\mathrm{XAl}}\varepsilon_3\right)+\varepsilon_1 x_{\mathrm{XAl}}\left((\beta_{\mathrm{AlX}}-\beta_{\mathrm{AlAl}})g^{10}_{\mathrm{XAl}}-\beta_{\mathrm{AlX}}g^{01}_{\mathrm{XAl}}\right)\right)$$

$$+\frac{RT}{2\varepsilon_6}[x_{\mathrm{XAl}}(2\beta_{\mathrm{AlX}}-\beta_{\mathrm{AlAl}})(\varepsilon_{\mathrm{X}}-\varepsilon_{\mathrm{Al}})+2\beta_{\mathrm{AlAl}}\varepsilon_{\mathrm{X}}]$$

$$+\frac{x'_{\mathrm{XAl}}(1-x_{\mathrm{X}})}{2\varepsilon_6}\left((\varepsilon_2-x_{\mathrm{X}}\beta_{\mathrm{AlAl}})g^{10}_{\mathrm{XAl}}+(\varepsilon_3-(1-x_{\mathrm{X}})\beta_{\mathrm{XX}})g^{01}_{\mathrm{XAl}}\right)$$

$$-\frac{RT(1-x_{\mathrm{X}})x'_{\mathrm{XAl}}\varepsilon_1}{2\varepsilon_6^2}[\beta_{\mathrm{AlAl}}\varepsilon_{\mathrm{X}}(2\beta_{\mathrm{XAl}}-\beta_{\mathrm{XX}})+\beta_{\mathrm{XX}}\varepsilon_{\mathrm{Al}}(2\beta_{\mathrm{AlX}}-\beta_{\mathrm{AlAl}})]$$

$$\Delta\mu^{\mathrm{xs}}_{\mathrm{X}}=\frac{x_{\mathrm{XAl}}}{2\varepsilon_1\varepsilon_6}\left(\beta_{\mathrm{AlAl}}\left((\varepsilon_1-\varepsilon_2)g^{10}_{\mathrm{XAl}}-g^{01}_{\mathrm{XAl}}\varepsilon_3\right)+\varepsilon_1 x_{\mathrm{XAl}}\left((\beta_{\mathrm{AlX}}-\beta_{\mathrm{AlAl}})g^{10}_{\mathrm{XAl}}-\beta_{\mathrm{AlX}}g^{01}_{\mathrm{XAl}}\right)\right)$$

$$+\frac{RT}{2\varepsilon_6}[x_{\mathrm{XAl}}(2\beta_{\mathrm{AlX}}-\beta_{\mathrm{AlAl}})(\varepsilon_{\mathrm{X}}-\varepsilon_{\mathrm{Al}})+2\beta_{\mathrm{AlAl}}\varepsilon_{\mathrm{X}}]$$

$$+\frac{x'_{\mathrm{XAl}}(1-x_{\mathrm{X}})}{2\varepsilon_6}\Big((\varepsilon_2-x_{\mathrm{X}}\beta_{\mathrm{AlAl}})g^{10}_{\mathrm{XAl}}+(\varepsilon_3-(1-x_{\mathrm{X}})\beta_{\mathrm{XX}})g^{01}_{\mathrm{XAl}}\Big)$$

$$-\frac{RT(1-x_{\mathrm{X}})x'_{\mathrm{XAl}}\varepsilon_1}{2\varepsilon_6^2}[\beta_{\mathrm{AlAl}}\varepsilon_{\mathrm{X}}(2\beta_{\mathrm{XAl}}-\beta_{\mathrm{XX}})+\beta_{\mathrm{XX}}\varepsilon_{\mathrm{Al}}(2\beta_{\mathrm{AlX}}-\beta_{\mathrm{AlAl}})] \tag{A.128}$$

Simplifying the first term (A.129):

$$\beta_{\mathrm{AlAl}}\Big((\varepsilon_1-\varepsilon_2)g^{10}_{\mathrm{XAl}}-g^{01}_{\mathrm{XAl}}\varepsilon_3\Big)+\varepsilon_1x_{\mathrm{XAl}}\Big((\beta_{\mathrm{AlX}}-\beta_{\mathrm{AlAl}})g^{10}_{\mathrm{XAl}}-\beta_{\mathrm{AlX}}g^{01}_{\mathrm{XAl}}\Big)$$

$$=g^{10}_{\mathrm{XAl}}\big((\varepsilon_1-\varepsilon_2)\beta_{\mathrm{AlAl}}+\varepsilon_1x_{\mathrm{XAl}}(\beta_{\mathrm{AlX}}-\beta_{\mathrm{AlAl}})\big)-g^{01}_{\mathrm{XAl}}(\beta_{\mathrm{AlAl}}\varepsilon_3+\beta_{\mathrm{AlX}}\varepsilon_1x_{\mathrm{XAl}})$$

$$=g^{10}_{\mathrm{XAl}}\big((\beta_{\mathrm{AlAl}}(1-x_{\mathrm{XAl}})+x_{\mathrm{XAl}}\beta_{\mathrm{AlX}})\varepsilon_1-\varepsilon_2\beta_{\mathrm{AlAl}}\big)-g^{01}_{\mathrm{XAl}}(\beta_{\mathrm{AlAl}}\varepsilon_3+\beta_{\mathrm{AlX}}\varepsilon_1x_{\mathrm{XAl}})$$

$$=g^{10}_{\mathrm{XAl}}\Big((\beta_{\mathrm{AlAl}}(1-x_{\mathrm{XAl}})+x_{\mathrm{XAl}}\beta_{\mathrm{AlX}})\big((1-x_{\mathrm{X}})\beta_{\mathrm{XX}}+x_{\mathrm{X}}\beta_{\mathrm{AlAl}}\big)$$

$$-\beta_{\mathrm{AlAl}}\big((x_{\mathrm{X}}\beta_{\mathrm{AlX}}-(1-x_{\mathrm{X}})\beta_{\mathrm{XAl}})x_{\mathrm{XAl}}+x_{\mathrm{X}}\beta_{\mathrm{AlAl}}(1-x_{\mathrm{XAl}})\big)\Big)$$

$$-g^{01}_{\mathrm{XAl}}\Big(\beta_{\mathrm{AlAl}}\Big(\big((1-x_{\mathrm{X}})\beta_{\mathrm{XAl}}-x_{\mathrm{X}}\beta_{\mathrm{AlX}}\big)x_{\mathrm{XAl}}+\beta_{\mathrm{XX}}(1-x_{\mathrm{X}})(1-x_{\mathrm{XAl}})\Big)$$

$$+\beta_{\mathrm{AlX}}\big((1-x_{\mathrm{X}})\beta_{\mathrm{XX}}+x_{\mathrm{X}}\beta_{\mathrm{AlAl}}\big)x_{\mathrm{XAl}}\Big)$$

$$=g^{10}_{\mathrm{XAl}}\big(\beta_{\mathrm{AlAl}}\beta_{\mathrm{XX}}(1-x_{\mathrm{X}})(1-x_{\mathrm{XAl}})+\beta_{\mathrm{AlX}}\beta_{\mathrm{XX}}(1-x_{\mathrm{X}})x_{\mathrm{XAl}}+\beta_{\mathrm{AlAl}}\beta_{\mathrm{AlAl}}x_{\mathrm{X}}(1-x_{\mathrm{XAl}})$$

$$+\beta_{\mathrm{AlAl}}\beta_{\mathrm{AlX}}x_{\mathrm{X}}x_{\mathrm{XAl}}-\beta_{\mathrm{AlX}}\beta_{\mathrm{AlAl}}x_{\mathrm{X}}x_{\mathrm{XAl}}+\beta_{\mathrm{XAl}}\beta_{\mathrm{AlAl}}(1-x_{\mathrm{X}})x_{\mathrm{XAl}}$$

$$-\beta_{\mathrm{AlAl}}\beta_{\mathrm{AlAl}}x_{\mathrm{X}}(1-x_{\mathrm{XAl}})\big)$$

$$-g^{01}_{\mathrm{XAl}}(\beta_{\mathrm{XAl}}\beta_{\mathrm{AlAl}}(1-x_{\mathrm{X}})x_{\mathrm{XAl}}-\beta_{\mathrm{AlX}}\beta_{\mathrm{AlAl}}x_{\mathrm{X}}x_{\mathrm{XAl}}+\beta_{\mathrm{AlAl}}\beta_{\mathrm{XX}}(1-x_{\mathrm{X}})(1-x_{\mathrm{XAl}})$$

$$+\beta_{\mathrm{XX}}\beta_{\mathrm{AlX}}(1-x_{\mathrm{X}})x_{\mathrm{XAl}}+\beta_{\mathrm{AlAl}}\beta_{\mathrm{AlX}}x_{\mathrm{X}}x_{\mathrm{XAl}})$$

$$=g^{10}_{\mathrm{XAl}}(\beta_{\mathrm{AlAl}}\beta_{\mathrm{XX}}(1-x_{\mathrm{X}})(1-x_{\mathrm{XAl}})+\beta_{\mathrm{AlX}}\beta_{\mathrm{XX}}(1-x_{\mathrm{X}})x_{\mathrm{XAl}}+\beta_{\mathrm{XAl}}\beta_{\mathrm{AlAl}}(1-x_{\mathrm{X}})x_{\mathrm{XAl}})$$

$$-g^{01}_{\mathrm{XAl}}(\beta_{\mathrm{XAl}}\beta_{\mathrm{AlAl}}(1-x_{\mathrm{X}})x_{\mathrm{XAl}}+\beta_{\mathrm{AlAl}}\beta_{\mathrm{XX}}(1-x_{\mathrm{X}})(1-x_{\mathrm{XAl}})+\beta_{\mathrm{XX}}\beta_{\mathrm{AlX}}(1-x_{\mathrm{X}})x_{\mathrm{XAl}})$$

$$=(1-x_{\mathrm{X}})\big(g^{10}_{\mathrm{XAl}}-g^{01}_{\mathrm{XAl}}\big)(\beta_{\mathrm{AlAl}}\beta_{\mathrm{XX}}(1-x_{\mathrm{XAl}})+\beta_{\mathrm{AlX}}\beta_{\mathrm{XX}}x_{\mathrm{XAl}}+\beta_{\mathrm{XAl}}\beta_{\mathrm{AlAl}}x_{\mathrm{XAl}})$$

$$=(1-x_{\mathrm{X}})\big(g^{10}_{\mathrm{XAl}}-g^{01}_{\mathrm{XAl}}\big)\varepsilon_6 \tag{A.129}$$

Substituting into $\Delta\mu^{\mathrm{xs}}_{\mathrm{X}}$ (A.130):

$$\Delta\mu^{\mathrm{xs}}_{\mathrm{X}}=\frac{x_{\mathrm{XAl}}}{2\varepsilon_1\varepsilon_6}\Big((1-x_{\mathrm{X}})\big(g^{10}_{\mathrm{XAl}}-g^{01}_{\mathrm{XAl}}\big)\varepsilon_6\Big)+\frac{RT}{2\varepsilon_6}[x_{\mathrm{XAl}}(2\beta_{\mathrm{AlX}}-\beta_{\mathrm{AlAl}})(\varepsilon_{\mathrm{X}}-\varepsilon_{\mathrm{Al}})+2\beta_{\mathrm{AlAl}}\varepsilon_{\mathrm{X}}]$$

$$+\frac{x'_{\mathrm{XAl}}(1-x_{\mathrm{X}})}{2\varepsilon_6}\Big((\varepsilon_2-x_{\mathrm{X}}\beta_{\mathrm{AlAl}})g^{10}_{\mathrm{XAl}}+(\varepsilon_3-(1-x_{\mathrm{X}})\beta_{\mathrm{XX}})g^{01}_{\mathrm{XAl}}\Big)$$

$$-\frac{RT(1-x_{\mathrm{X}})x'_{\mathrm{XAl}}\varepsilon_1}{2\varepsilon_6^2}[\beta_{\mathrm{AlAl}}(2\beta_{\mathrm{XAl}}-\beta_{\mathrm{XX}})\varepsilon_{\mathrm{X}}+\beta_{\mathrm{XX}}(2\beta_{\mathrm{AlX}}-\beta_{\mathrm{AlAl}})\varepsilon_{\mathrm{Al}}]$$

$$\Delta\mu_{\mathrm{X}}^{\mathrm{xs}}=\frac{1}{2\varepsilon_1\varepsilon_6}\Big(x_{\mathrm{XAl}}\varepsilon_6(1-x_{\mathrm{X}})\big(g_{\mathrm{XAl}}^{10}-g_{\mathrm{XAl}}^{01}\big)+RT\varepsilon_1\big(2\beta_{\mathrm{AlAl}}\varepsilon_{\mathrm{X}}+x_{\mathrm{XAl}}(2\beta_{\mathrm{AlX}}-\beta_{\mathrm{AlAl}})(\varepsilon_{\mathrm{X}}-\varepsilon_{\mathrm{Al}})\big)\Big)$$

$$-\frac{x'_{\mathrm{XAl}}(1-x_{\mathrm{X}})}{2\varepsilon_6^2}\Big(RT\varepsilon_1\big(\beta_{\mathrm{XX}}\varepsilon_{\mathrm{Al}}(2\beta_{\mathrm{AlX}}-\beta_{\mathrm{AlAl}})+\beta_{\mathrm{AlAl}}\varepsilon_{\mathrm{X}}(2\beta_{\mathrm{XAl}}-\beta_{\mathrm{XX}})\big)$$

$$-\varepsilon_6\Big((\varepsilon_3-(1-x_{\mathrm{X}})\beta_{\mathrm{XX}})g_{\mathrm{XAl}}^{01}+(\varepsilon_2-x_{\mathrm{X}}\beta_{\mathrm{AlAl}})g_{\mathrm{XAl}}^{10}\Big)\Big) \qquad \text{(A.130)}$$

A.4.3.2. Excess relative chemical potential of Al

Evaluating $\Delta\mu_{\mathrm{Al}}^{\mathrm{xs}}$ (A.131):

$$\Delta\mu_{\mathrm{Al}}^{\mathrm{xs}}=\Delta G_{\mathrm{mix}}^{\mathrm{xs}}-x_{\mathrm{X}}\frac{\mathrm{d}\Delta G_{\mathrm{mix}}^{\mathrm{xs}}}{\mathrm{d}x_{\mathrm{X}}}$$

$$=\frac{\Delta g_{\mathrm{XAl}}^{0}}{2\varepsilon_6^2}[-x_{\mathrm{X}}(x'_{\mathrm{XAl}}(\varepsilon_1\beta_{\mathrm{XX}}\beta_{\mathrm{AlAl}})+(\beta_{\mathrm{AlAl}}-\beta_{\mathrm{XX}})\varepsilon_6x_{\mathrm{XAl}})+\varepsilon_6\varepsilon_1x_{\mathrm{XAl}}]$$

$$+\frac{g_{\mathrm{XAl}}^{10}}{2\varepsilon_6^2}\Big[-x_{\mathrm{X}}\Big(x'_{\mathrm{XAl}}(\varepsilon_2(\beta_{\mathrm{XX}}\beta_{\mathrm{AlAl}}+\varepsilon_6)-x_{\mathrm{X}}\beta_{\mathrm{AlAl}}\varepsilon_6)+\frac{\varepsilon_6}{x_{\mathrm{X}}}(\varepsilon_2+\beta_{\mathrm{XAl}}x_{\mathrm{XAl}})x_{\mathrm{XAl}}\Big)+\varepsilon_6\varepsilon_2x_{\mathrm{XAl}}\Big]$$

$$+\frac{g_{\mathrm{XAl}}^{01}}{2\varepsilon_6^2}\Big[-x_{\mathrm{X}}\Big(x'_{\mathrm{XAl}}(\varepsilon_3(\beta_{\mathrm{XX}}\beta_{\mathrm{AlAl}}+\varepsilon_6)-(1-x_{\mathrm{X}})\beta_{\mathrm{XX}}\varepsilon_6)-\frac{\varepsilon_6}{1-x_{\mathrm{X}}}(\varepsilon_3+\beta_{\mathrm{AlX}}x_{\mathrm{XAl}})x_{\mathrm{XAl}}\Big)+\varepsilon_6\varepsilon_3x_{\mathrm{XAl}}\Big]$$

$$+\frac{RT}{\varepsilon_6^2}\ln\varepsilon_1\left[-x_{\mathrm{X}}\big((\beta_{\mathrm{AlAl}}-\beta_{\mathrm{XX}})\varepsilon_6-\varepsilon_1(\beta_{\mathrm{XX}}\beta_{\mathrm{AlX}}+\beta_{\mathrm{AlAl}}\beta_{\mathrm{XAl}}-\beta_{\mathrm{XX}}\beta_{\mathrm{AlAl}})x'_{\mathrm{XAl}}\big)+\varepsilon_6\varepsilon_1\right]$$

$$+\frac{RT}{\varepsilon_6^2}\ln\varepsilon_2\left[-x_{\mathrm{X}}\left(\frac{\varepsilon_6}{x_{\mathrm{X}}}(\varepsilon_2+\beta_{\mathrm{XAl}}x_{\mathrm{XAl}})-\beta_{\mathrm{AlAl}}\beta_{\mathrm{XAl}}\varepsilon_1x'_{\mathrm{XAl}}\right)+\varepsilon_6\varepsilon_2\right]$$

$$+\frac{RT}{\varepsilon_6^2}\ln\varepsilon_3\left[-x_{\mathrm{X}}\left(-\frac{\varepsilon_6}{1-x_{\mathrm{X}}}(\varepsilon_3+\beta_{\mathrm{AlX}}x_{\mathrm{XAl}})-\beta_{\mathrm{XX}}\beta_{\mathrm{AlX}}\varepsilon_1x'_{\mathrm{XAl}}\right)+\varepsilon_6\varepsilon_3\right]$$

$$+\frac{RT}{\varepsilon_6^2}\ln\frac{\varepsilon_4}{2}\left[-x_{\mathrm{X}}\left(-\frac{\varepsilon_6}{x_{\mathrm{X}}}\big(\varepsilon_4+x_{\mathrm{XAl}}(2\beta_{\mathrm{XAl}}-\beta_{\mathrm{XX}})\big)+\varepsilon_1\beta_{\mathrm{AlAl}}(2\beta_{\mathrm{XAl}}-\beta_{\mathrm{XX}})x'_{\mathrm{XAl}}\right)-\varepsilon_6\varepsilon_4\right]$$

$$+\frac{RT}{\varepsilon_6^2}\ln\frac{\varepsilon_5}{2}\left[-x_{\mathrm{X}}\left(\frac{\varepsilon_6}{1-x_{\mathrm{X}}}\big(\varepsilon_5+x_{\mathrm{XAl}}(2\beta_{\mathrm{AlX}}-\beta_{\mathrm{AlAl}})\big)+\varepsilon_1\beta_{\mathrm{XX}}(2\beta_{\mathrm{AlX}}-\beta_{\mathrm{AlAl}})x'_{\mathrm{XAl}}\right)-\varepsilon_6\varepsilon_5\right]$$

$$+\frac{RT}{\varepsilon_6^2}\ln\left(\frac{\varepsilon_1x_{\mathrm{XAl}}}{2}\right)\left[-x_{\mathrm{X}}\big(\beta_{\mathrm{XX}}\beta_{\mathrm{AlAl}}x'_{\mathrm{XAl}}\varepsilon_1+x_{\mathrm{XAl}}\varepsilon_6(\beta_{\mathrm{AlAl}}-\beta_{\mathrm{XX}})\big)+\varepsilon_1\varepsilon_6x_{\mathrm{XAl}}\right]$$

$$\Delta\mu_{\mathrm{Al}}^{\mathrm{xs}}=\frac{\Delta g_{\mathrm{XAl}}^{0}}{2\varepsilon_6^2}\left[-x_{\mathrm{X}}\varepsilon_1\beta_{\mathrm{XX}}\beta_{\mathrm{AlAl}}x'_{\mathrm{XAl}}+\varepsilon_6x_{\mathrm{XAl}}\big(\varepsilon_1-x_{\mathrm{X}}(\beta_{\mathrm{AlAl}}-\beta_{\mathrm{XX}})\big)\right]$$

$$+\frac{g_{\mathrm{XAl}}^{10}}{2\varepsilon_6^2}\left[-x_{\mathrm{X}}x'_{\mathrm{XAl}}(\varepsilon_2(\beta_{\mathrm{XX}}\beta_{\mathrm{AlAl}}+\varepsilon_6)-x_{\mathrm{X}}\beta_{\mathrm{AlAl}}\varepsilon_6)+x_{\mathrm{XAl}}\varepsilon_6(-(\varepsilon_2+\beta_{\mathrm{XAl}}x_{\mathrm{XAl}})+\varepsilon_2)\right]$$

$$+\frac{g_{\mathrm{XAl}}^{01}}{2\varepsilon_6^2}\left[-x_{\mathrm{X}}x'_{\mathrm{XAl}}(\varepsilon_3(\beta_{\mathrm{XX}}\beta_{\mathrm{AlAl}}+\varepsilon_6)-(1-x_{\mathrm{X}})\beta_{\mathrm{XX}}\varepsilon_6)+x_{\mathrm{XAl}}\varepsilon_6\left(\frac{x_{\mathrm{X}}}{1-x_{\mathrm{X}}}(\varepsilon_3+\beta_{\mathrm{AlX}}x_{\mathrm{XAl}})+\varepsilon_3\right)\right]$$

$$+\frac{RT}{\varepsilon_6^2}\ln\varepsilon_1\left[-x_{\mathrm{X}}(-\varepsilon_1(\beta_{\mathrm{XX}}\beta_{\mathrm{AlX}}+\beta_{\mathrm{AlAl}}\beta_{\mathrm{XAl}}-\beta_{\mathrm{XX}}\beta_{\mathrm{AlAl}})x'_{\mathrm{XAl}})+\varepsilon_6(\varepsilon_1-x_{\mathrm{X}}(\beta_{\mathrm{AlAl}}-\beta_{\mathrm{XX}}))\right]$$

$$+\frac{RT}{\varepsilon_6^2}\ln\varepsilon_2\left[-x_{\mathrm{X}}(-\beta_{\mathrm{AlAl}}\beta_{\mathrm{XAl}}\varepsilon_1x'_{\mathrm{XAl}})+\varepsilon_6(\varepsilon_2-(\varepsilon_2+\beta_{\mathrm{XAl}}x_{\mathrm{XAl}}))\right]$$

$$+\frac{RT}{\varepsilon_6^2}\ln\varepsilon_3\left[-x_{\mathrm{X}}(-\beta_{\mathrm{XX}}\beta_{\mathrm{AlX}}\varepsilon_1x'_{\mathrm{XAl}})+\varepsilon_6\left(\varepsilon_3+\frac{x_{\mathrm{X}}}{1-x_{\mathrm{X}}}(\varepsilon_3+\beta_{\mathrm{AlX}}x_{\mathrm{XAl}})\right)\right]$$

$$+\frac{RT}{\varepsilon_6^2}\ln\frac{\varepsilon_4}{2}\left[-x_{\mathrm{X}}(\varepsilon_1\beta_{\mathrm{AlAl}}(2\beta_{\mathrm{XAl}}-\beta_{\mathrm{XX}})x'_{\mathrm{XAl}})-\varepsilon_6\left(\varepsilon_4-\left(\varepsilon_4+x_{\mathrm{XAl}}(2\beta_{\mathrm{XAl}}-\beta_{\mathrm{XX}})\right)\right)\right]$$

$$+\frac{RT}{\varepsilon_6^2}\ln\frac{\varepsilon_5}{2}\left[-x_{\mathrm{X}}(\varepsilon_1\beta_{\mathrm{XX}}(2\beta_{\mathrm{AlX}}-\beta_{\mathrm{AlAl}})x'_{\mathrm{XAl}})-\varepsilon_6\left(\varepsilon_5+\frac{x_{\mathrm{X}}}{1-x_{\mathrm{X}}}\left(\varepsilon_5+x_{\mathrm{XAl}}(2\beta_{\mathrm{AlX}}-\beta_{\mathrm{AlAl}})\right)\right)\right]$$

$$+\frac{RT}{\varepsilon_6^2}\ln\left(\frac{\varepsilon_1x_{\mathrm{XAl}}}{2}\right)\left[-x_{\mathrm{X}}(\beta_{\mathrm{XX}}\beta_{\mathrm{AlAl}}x'_{\mathrm{XAl}}\varepsilon_1)+\varepsilon_6x_{\mathrm{XAl}}\left(\varepsilon_1-x_{\mathrm{X}}(\beta_{\mathrm{AlAl}}-\beta_{\mathrm{XX}})\right)\right] \tag{A.131}$$

Simplifying terms as possible:

$$\varepsilon_1-x_{\mathrm{X}}(\beta_{\mathrm{AlAl}}-\beta_{\mathrm{XX}})=\left((1-x_{\mathrm{X}})\beta_{\mathrm{XX}}+x_{\mathrm{X}}\beta_{\mathrm{AlAl}}\right)-x_{\mathrm{X}}(\beta_{\mathrm{AlAl}}-\beta_{\mathrm{XX}})=\beta_{\mathrm{XX}} \tag{A.132}$$

$$-(\varepsilon_2+\beta_{\mathrm{XAl}}x_{\mathrm{XAl}})+\varepsilon_2=-\beta_{\mathrm{XAl}}x_{\mathrm{XAl}} \tag{A.133}$$

$$\frac{x_{\mathrm{X}}}{1-x_{\mathrm{X}}}(\varepsilon_3+\beta_{\mathrm{AlX}}x_{\mathrm{XAl}})+\varepsilon_3=\frac{x_{\mathrm{X}}(\varepsilon_3+\beta_{\mathrm{AlX}}x_{\mathrm{XAl}})+(1-x_{\mathrm{X}})\varepsilon_3}{1-x_{\mathrm{X}}}=\frac{\varepsilon_3+x_{\mathrm{X}}\beta_{\mathrm{AlX}}x_{\mathrm{XAl}}}{1-x_{\mathrm{X}}}$$

$$=\frac{1}{1-x_{\mathrm{X}}}\left(\left((1-x_{\mathrm{X}})\beta_{\mathrm{XAl}}-x_{\mathrm{X}}\beta_{\mathrm{AlX}}\right)x_{\mathrm{XAl}}+\beta_{\mathrm{XX}}(1-x_{\mathrm{X}})(1-x_{\mathrm{XAl}})+x_{\mathrm{X}}\beta_{\mathrm{AlX}}x_{\mathrm{XAl}}\right)$$

$$=\frac{(1-x_{\mathrm{X}})\left(\beta_{\mathrm{XAl}}x_{\mathrm{XAl}}+\beta_{\mathrm{XX}}(1-x_{\mathrm{XAl}})\right)}{1-x_{\mathrm{X}}}$$

$$=\beta_{\mathrm{XAl}}x_{\mathrm{XAl}}+\beta_{\mathrm{XX}}(1-x_{\mathrm{XAl}}) \tag{A.134}$$

$$\varepsilon_4-\left(\varepsilon_4+x_{\mathrm{XAl}}(2\beta_{\mathrm{XAl}}-\beta_{\mathrm{XX}})\right)=-(2\beta_{\mathrm{XAl}}-\beta_{\mathrm{XX}})x_{\mathrm{XAl}} \tag{A.135}$$

$$\varepsilon_5+\frac{x_{\mathrm{X}}}{1-x_{\mathrm{X}}}\left(\varepsilon_5+x_{\mathrm{XAl}}(2\beta_{\mathrm{AlX}}-\beta_{\mathrm{AlAl}})\right)=\frac{\varepsilon_5+x_{\mathrm{X}}x_{\mathrm{XAl}}(2\beta_{\mathrm{AlX}}-\beta_{\mathrm{AlAl}})}{1-x_{\mathrm{X}}}$$

$$=\frac{1}{1-x_{\mathrm{X}}}\Big(x_{\mathrm{XAl}}\left((\beta_{\mathrm{AlAl}}-2\beta_{\mathrm{AlX}})x_{\mathrm{X}}+(2\beta_{\mathrm{XAl}}-\beta_{\mathrm{XX}})(1-x_{\mathrm{X}})\right)+2\beta_{\mathrm{XX}}(1-x_{\mathrm{X}})$$

$$+x_{\mathrm{X}}x_{\mathrm{XAl}}(2\beta_{\mathrm{AlX}}-\beta_{\mathrm{AlAl}})\Big)$$

$$= \frac{1}{1-x_{\mathrm{X}}}\left(x_{\mathrm{XAl}}(2\beta_{\mathrm{XAl}}-\beta_{\mathrm{XX}})(1-x_{\mathrm{X}})+2\beta_{\mathrm{XX}}(1-x_{\mathrm{X}})\right)$$

$$= (2\beta_{\mathrm{XAl}}-\beta_{\mathrm{XX}})x_{\mathrm{XAl}}+2\beta_{\mathrm{XX}} \qquad \text{(A.136)}$$

Simplifying $\Delta\mu_{\mathrm{Al}}^{\mathrm{xs}}$ (A.137):

$$\Delta\mu_{\mathrm{Al}}^{\mathrm{xs}} = \frac{\Delta g_{\mathrm{XAl}}^{0}}{2\varepsilon_6^2}[-x_{\mathrm{X}}\varepsilon_1\beta_{\mathrm{XX}}\beta_{\mathrm{AlAl}}x'_{\mathrm{XAl}}+\varepsilon_6\beta_{\mathrm{XX}}x_{\mathrm{XAl}}]$$

$$+\frac{g_{\mathrm{XAl}}^{10}}{2\varepsilon_6^2}[-x_{\mathrm{X}}x'_{\mathrm{XAl}}(\varepsilon_2(\beta_{\mathrm{XX}}\beta_{\mathrm{AlAl}}+\varepsilon_6)-x_{\mathrm{X}}\beta_{\mathrm{AlAl}}\varepsilon_6)-\beta_{\mathrm{XAl}}x_{\mathrm{XAl}}x_{\mathrm{XAl}}\varepsilon_6]$$

$$+\frac{g_{\mathrm{XAl}}^{01}}{2\varepsilon_6^2}\left[-x_{\mathrm{X}}x'_{\mathrm{XAl}}(\varepsilon_3(\beta_{\mathrm{XX}}\beta_{\mathrm{AlAl}}+\varepsilon_6)-(1-x_{\mathrm{X}})\beta_{\mathrm{XX}}\varepsilon_6)+x_{\mathrm{XAl}}\varepsilon_6\left(\beta_{\mathrm{XAl}}x_{\mathrm{XAl}}+\beta_{\mathrm{XX}}(1-x_{\mathrm{XAl}})\right)\right]$$

$$+\frac{RT}{\varepsilon_6^2}\ln\varepsilon_1\,[-x_{\mathrm{X}}(-\varepsilon_1(\beta_{\mathrm{XX}}\beta_{\mathrm{AlX}}+\beta_{\mathrm{AlAl}}\beta_{\mathrm{XAl}}-\beta_{\mathrm{XX}}\beta_{\mathrm{AlAl}})x'_{\mathrm{XAl}})+\varepsilon_6\beta_{\mathrm{XX}}]$$

$$+\frac{RT}{\varepsilon_6^2}\ln\varepsilon_2\,[-x_{\mathrm{X}}(-\beta_{\mathrm{AlAl}}\beta_{\mathrm{XAl}}\varepsilon_1x'_{\mathrm{XAl}})-\beta_{\mathrm{XAl}}x_{\mathrm{XAl}}\varepsilon_6]$$

$$+\frac{RT}{\varepsilon_6^2}\ln\varepsilon_3\left[-x_{\mathrm{X}}(-\beta_{\mathrm{XX}}\beta_{\mathrm{AlX}}\varepsilon_1x'_{\mathrm{XAl}})+\varepsilon_6\left(\beta_{\mathrm{XAl}}x_{\mathrm{XAl}}+\beta_{\mathrm{XX}}(1-x_{\mathrm{XAl}})\right)\right]$$

$$+\frac{RT}{\varepsilon_6^2}\ln\frac{\varepsilon_4}{2}\,[-x_{\mathrm{X}}(\varepsilon_1\beta_{\mathrm{AlAl}}(2\beta_{\mathrm{XAl}}-\beta_{\mathrm{XX}})x'_{\mathrm{XAl}})-\varepsilon_6(-(2\beta_{\mathrm{XAl}}-\beta_{\mathrm{XX}})x_{\mathrm{XAl}})]$$

$$+\frac{RT}{\varepsilon_6^2}\ln\frac{\varepsilon_5}{2}\left[-x_{\mathrm{X}}(\varepsilon_1\beta_{\mathrm{XX}}(2\beta_{\mathrm{AlX}}-\beta_{\mathrm{AlAl}})x'_{\mathrm{XAl}})-\varepsilon_6\left((2\beta_{\mathrm{XAl}}-\beta_{\mathrm{XX}})x_{\mathrm{XAl}}+2\beta_{\mathrm{XX}}\right)\right]$$

$$+\frac{RT}{\varepsilon_6^2}\ln\left(\frac{\varepsilon_1x_{\mathrm{XAl}}}{2}\right)[-x_{\mathrm{X}}(\beta_{\mathrm{XX}}\beta_{\mathrm{AlAl}}x'_{\mathrm{XAl}}\varepsilon_1)+\varepsilon_6\beta_{\mathrm{XX}}x_{\mathrm{XAl}}]$$

$$= \frac{-x_{\mathrm{X}}\beta_{\mathrm{XX}}\beta_{\mathrm{AlAl}}x'_{\mathrm{XAl}}}{2\varepsilon_6^2}\left[\varepsilon_1\Delta g_{\mathrm{XAl}}^{0}+\varepsilon_2g_{\mathrm{XAl}}^{10}+\varepsilon_3g_{\mathrm{XAl}}^{01}\right]$$

$$-\frac{x_{\mathrm{X}}x'_{\mathrm{XAl}}}{2\varepsilon_6}\left[(\varepsilon_2-x_{\mathrm{X}}\beta_{\mathrm{AlAl}})g_{\mathrm{XAl}}^{10}+(\varepsilon_3-(1-x_{\mathrm{X}})\beta_{\mathrm{XX}})g_{\mathrm{XAl}}^{01}\right]$$

$$+\frac{x_{\mathrm{XAl}}}{2\varepsilon_6}\left[\beta_{\mathrm{XX}}\Delta g_{\mathrm{XAl}}^{0}+\beta_{\mathrm{XX}}g_{\mathrm{XAl}}^{01}+x_{\mathrm{XAl}}\left(-\beta_{\mathrm{XAl}}g_{\mathrm{XAl}}^{10}+g_{\mathrm{XAl}}^{01}(\beta_{\mathrm{XAl}}-\beta_{\mathrm{XX}})\right)\right]$$

$$+\frac{RTx_{\mathrm{X}}x'_{\mathrm{XAl}}\varepsilon_1}{\varepsilon_6^2}\left[(\beta_{\mathrm{XX}}\beta_{\mathrm{AlX}}+\beta_{\mathrm{AlAl}}\beta_{\mathrm{XAl}}-\beta_{\mathrm{XX}}\beta_{\mathrm{AlAl}})\ln\varepsilon_1+\beta_{\mathrm{AlAl}}\beta_{\mathrm{XAl}}\ln\varepsilon_2+\beta_{\mathrm{XX}}\beta_{\mathrm{AlX}}\ln\varepsilon_3\right.$$

$$\left.-\beta_{\mathrm{AlAl}}(2\beta_{\mathrm{XAl}}-\beta_{\mathrm{XX}})\ln\frac{\varepsilon_4}{2}-\beta_{\mathrm{XX}}(2\beta_{\mathrm{AlX}}-\beta_{\mathrm{AlAl}})\ln\frac{\varepsilon_5}{2}-\beta_{\mathrm{XX}}\beta_{\mathrm{AlAl}}\ln\left(\frac{\varepsilon_1x_{\mathrm{XAl}}}{2}\right)\right]$$

$$+\frac{RT}{\varepsilon_6}\left[\beta_{\mathrm{XX}}\ln\varepsilon_1+\beta_{\mathrm{XX}}\ln\varepsilon_3-2\ln\frac{\varepsilon_5}{2}\right]$$

$$+\frac{RTx_{\mathrm{XAl}}}{\varepsilon_6}\Big[-\beta_{\mathrm{XAl}}\ln\varepsilon_2+(\beta_{\mathrm{XAl}}-\beta_{\mathrm{XX}})\ln\varepsilon_3+(2\beta_{\mathrm{XAl}}-\beta_{\mathrm{XX}})\ln\frac{\varepsilon_4}{2}-(2\beta_{\mathrm{XAl}}-\beta_{\mathrm{XX}})\ln\frac{\varepsilon_5}{2}$$

$$+\beta_{\mathrm{XX}}\ln\Big(\frac{\varepsilon_1 x_{\mathrm{XAl}}}{2}\Big)\Big]$$

$$=\frac{-x_{\mathrm{X}}\beta_{\mathrm{XX}}\beta_{\mathrm{AlAl}}x'_{\mathrm{XAl}}}{2\varepsilon_6^2}\big[\varepsilon_1\Delta g^0_{\mathrm{XAl}}+\varepsilon_2 g^{10}_{\mathrm{XAl}}+\varepsilon_3 g^{01}_{\mathrm{XAl}}\big]$$

$$-\frac{x_{\mathrm{X}}x'_{\mathrm{XAl}}}{2\varepsilon_6}\big[(\varepsilon_2-x_{\mathrm{X}}\beta_{\mathrm{AlAl}})g^{10}_{\mathrm{XAl}}+(\varepsilon_3-(1-x_{\mathrm{X}})\beta_{\mathrm{XX}})g^{01}_{\mathrm{XAl}}\big]$$

$$+\frac{x_{\mathrm{XAl}}\beta_{\mathrm{XX}}}{2\varepsilon_6}\big[\Delta g^0_{\mathrm{XAl}}+g^{01}_{\mathrm{XAl}}\big]+\frac{x^2_{\mathrm{XAl}}}{2\varepsilon_6}\big[(\beta_{\mathrm{XAl}}-\beta_{\mathrm{XX}})g^{01}_{\mathrm{XAl}}-\beta_{\mathrm{XAl}}g^{10}_{\mathrm{XAl}}\big]$$

$$+\frac{RTx_{\mathrm{X}}x'_{\mathrm{XAl}}\varepsilon_1}{\varepsilon_6^2}\Big[\beta_{\mathrm{XX}}\beta_{\mathrm{AlX}}\Big(\ln\varepsilon_1+\ln\varepsilon_3-2\ln\frac{\varepsilon_5}{2}\Big)+\beta_{\mathrm{AlAl}}\beta_{\mathrm{XAl}}\Big(\ln\varepsilon_1+\ln\varepsilon_2-2\ln\frac{\varepsilon_4}{2}\Big)$$

$$-\beta_{\mathrm{XX}}\beta_{\mathrm{AlAl}}\Big(\ln\varepsilon_1-\ln\frac{\varepsilon_4}{2}-\ln\frac{\varepsilon_5}{2}+\ln\Big(\frac{\varepsilon_1 x_{\mathrm{XAl}}}{2}\Big)\Big)\Big]+\frac{RT}{\varepsilon_6}\beta_{\mathrm{XX}}\Big[\ln\varepsilon_1+\ln\varepsilon_3-2\ln\frac{\varepsilon_5}{2}\Big]$$

$$+\frac{RTx_{\mathrm{XAl}}}{\varepsilon_6}\Big[\beta_{\mathrm{XX}}\Big(\ln\Big(\frac{\varepsilon_1 x_{\mathrm{XAl}}}{2}\Big)-\ln\varepsilon_3-\ln\frac{\varepsilon_4}{2}+\ln\frac{\varepsilon_5}{2}\Big)+\beta_{\mathrm{XAl}}\Big(-\ln\varepsilon_2+\ln\varepsilon_3+2\ln\frac{\varepsilon_4}{2}-2\ln\frac{\varepsilon_5}{2}\Big)\Big]$$

$$=\frac{-x_{\mathrm{X}}\beta_{\mathrm{XX}}\beta_{\mathrm{AlAl}}x'_{\mathrm{XAl}}}{2\varepsilon_6^2}\big[\varepsilon_1\Delta g^0_{\mathrm{XAl}}+\varepsilon_2 g^{10}_{\mathrm{XAl}}+\varepsilon_3 g^{01}_{\mathrm{XAl}}\big]$$

$$-\frac{x_{\mathrm{X}}x'_{\mathrm{XAl}}}{2\varepsilon_6}\big[(\varepsilon_2-x_{\mathrm{X}}\beta_{\mathrm{AlAl}})g^{10}_{\mathrm{XAl}}+(\varepsilon_3-(1-x_{\mathrm{X}})\beta_{\mathrm{XX}})g^{01}_{\mathrm{XAl}}\big]$$

$$+\frac{x_{\mathrm{XAl}}\beta_{\mathrm{XX}}}{2\varepsilon_6}\big[\Delta g^0_{\mathrm{XAl}}+g^{01}_{\mathrm{XAl}}\big]+\frac{x^2_{\mathrm{XAl}}}{2\varepsilon_6}\big[(\beta_{\mathrm{XAl}}-\beta_{\mathrm{XX}})g^{01}_{\mathrm{XAl}}-\beta_{\mathrm{XAl}}g^{10}_{\mathrm{XAl}}\big]$$

$$+\frac{RTx_{\mathrm{X}}x'_{\mathrm{XAl}}\varepsilon_1}{\varepsilon_6^2}\Big[\beta_{\mathrm{XX}}\beta_{\mathrm{AlX}}\Big(\ln\varepsilon_1+\ln\varepsilon_3-2\ln\frac{\varepsilon_5}{2}\Big)+\beta_{\mathrm{AlAl}}\beta_{\mathrm{XAl}}\Big(\ln\varepsilon_1+\ln\varepsilon_2-2\ln\frac{\varepsilon_4}{2}\Big)$$

$$-\beta_{\mathrm{XX}}\beta_{\mathrm{AlAl}}\Big(\ln\varepsilon_1+\frac{\ln\varepsilon_2}{2}+\frac{\ln\varepsilon_3}{2}-\ln\frac{\varepsilon_4}{2}-\ln\frac{\varepsilon_5}{2}\Big)\Big]+\frac{RT}{\varepsilon_6}\beta_{\mathrm{XX}}\Big[\ln\varepsilon_1+\ln\varepsilon_3-2\ln\frac{\varepsilon_5}{2}\Big]$$

$$+\frac{RTx_{\mathrm{XAl}}}{\varepsilon_6}\Big[\beta_{\mathrm{XX}}\Big(\frac{\ln\varepsilon_2}{2}-\frac{\ln\varepsilon_3}{2}-\ln\frac{\varepsilon_4}{2}+\ln\frac{\varepsilon_5}{2}\Big)+\beta_{\mathrm{XAl}}\Big(-\ln\varepsilon_2+\ln\varepsilon_3+2\ln\frac{\varepsilon_4}{2}-2\ln\frac{\varepsilon_5}{2}\Big)\Big]$$

$$-\frac{\beta_{\mathrm{XX}}\beta_{\mathrm{AlAl}}RTx_{\mathrm{X}}x'_{\mathrm{XAl}}\varepsilon_1}{\varepsilon_6^2}\Big[-\frac{\Delta g^0_{\mathrm{XAl}}\varepsilon_1+g^{10}_{\mathrm{XAl}}\varepsilon_2+g^{01}_{\mathrm{XAl}}\varepsilon_3}{2RT\varepsilon_1}\Big]$$

$$+\frac{RTx_{\mathrm{XAl}}\beta_{\mathrm{XX}}}{\varepsilon_6}\Big[-\frac{\Delta g^0_{\mathrm{XAl}}\varepsilon_1+g^{10}_{\mathrm{XAl}}\varepsilon_2+g^{01}_{\mathrm{XAl}}\varepsilon_3}{2RT\varepsilon_1}\Big]$$

$$=\frac{-x_{\mathrm{X}}\beta_{\mathrm{XX}}\beta_{\mathrm{AlAl}}x'_{\mathrm{XAl}}}{2\varepsilon_6^2}\big[\varepsilon_1\Delta g^0_{\mathrm{XAl}}+\varepsilon_2 g^{10}_{\mathrm{XAl}}+\varepsilon_3 g^{01}_{\mathrm{XAl}}\big]$$

$$-\frac{x_{\mathrm{X}}x'_{\mathrm{XAl}}}{2\varepsilon_6}\left[(\varepsilon_2-x_{\mathrm{X}}\beta_{\mathrm{AlAl}})g^{10}_{\mathrm{XAl}}+(\varepsilon_3-(1-x_{\mathrm{X}})\beta_{\mathrm{XX}})g^{01}_{\mathrm{XAl}}\right]$$

$$+\frac{x_{\mathrm{XAl}}\beta_{\mathrm{XX}}}{2\varepsilon_6}\left[\Delta g^{0}_{\mathrm{XAl}}+g^{01}_{\mathrm{XAl}}\right]+\frac{x^2_{\mathrm{XAl}}}{2\varepsilon_6}\left[(\beta_{\mathrm{XAl}}-\beta_{\mathrm{XX}})g^{01}_{\mathrm{XAl}}-\beta_{\mathrm{XAl}}g^{10}_{\mathrm{XAl}}\right]$$

$$+\frac{RTx_{\mathrm{X}}x'_{\mathrm{XAl}}\varepsilon_1}{2\varepsilon_6^2}[2\beta_{\mathrm{XX}}\beta_{\mathrm{AlX}}(\varepsilon_{\mathrm{Al}})+2\beta_{\mathrm{AlAl}}\beta_{\mathrm{XAl}}(\varepsilon_{\mathrm{X}})-\beta_{\mathrm{XX}}\beta_{\mathrm{AlAl}}(\varepsilon_{\mathrm{X}}+\varepsilon_{\mathrm{Al}})]+\frac{RT}{\varepsilon_6}\beta_{\mathrm{XX}}[\varepsilon_{\mathrm{Al}}]$$

$$+\frac{RTx_{\mathrm{XAl}}}{2\varepsilon_6}[\beta_{\mathrm{XX}}(\varepsilon_{\mathrm{X}}-\varepsilon_{\mathrm{Al}})+2\beta_{\mathrm{XAl}}(\varepsilon_{\mathrm{Al}}-\varepsilon_{\mathrm{X}})]$$

$$+\frac{\beta_{\mathrm{XX}}\beta_{\mathrm{AlAl}}x_{\mathrm{X}}x'_{\mathrm{XAl}}}{2\varepsilon_6^2}\left[\Delta g^{0}_{\mathrm{XAl}}\varepsilon_1+g^{10}_{\mathrm{XAl}}\varepsilon_2+g^{01}_{\mathrm{XAl}}\varepsilon_3\right]-\frac{x_{\mathrm{XAl}}\beta_{\mathrm{XX}}}{2\varepsilon_6\varepsilon_1}\left[\Delta g^{0}_{\mathrm{XAl}}\varepsilon_1+g^{10}_{\mathrm{XAl}}\varepsilon_2+g^{01}_{\mathrm{XAl}}\varepsilon_3\right]$$

$$=-\frac{x_{\mathrm{X}}x'_{\mathrm{XAl}}}{2\varepsilon_6}\left[(\varepsilon_2-x_{\mathrm{X}}\beta_{\mathrm{AlAl}})g^{10}_{\mathrm{XAl}}+(\varepsilon_3-(1-x_{\mathrm{X}})\beta_{\mathrm{XX}})g^{01}_{\mathrm{XAl}}\right]$$

$$+\frac{x_{\mathrm{XAl}}\beta_{\mathrm{XX}}}{2\varepsilon_6}\left[\Delta g^{0}_{\mathrm{XAl}}+g^{01}_{\mathrm{XAl}}\right]+\frac{x^2_{\mathrm{XAl}}}{2\varepsilon_6}\left[(\beta_{\mathrm{XAl}}-\beta_{\mathrm{XX}})g^{01}_{\mathrm{XAl}}-\beta_{\mathrm{XAl}}g^{10}_{\mathrm{XAl}}\right]$$

$$-\frac{x_{\mathrm{XAl}}\beta_{\mathrm{XX}}}{2\varepsilon_6\varepsilon_1}\left[\Delta g^{0}_{\mathrm{XAl}}\varepsilon_1+g^{10}_{\mathrm{XAl}}\varepsilon_2+g^{01}_{\mathrm{XAl}}\varepsilon_3\right]$$

$$+\frac{RTx_{\mathrm{X}}x'_{\mathrm{XAl}}\varepsilon_1}{2\varepsilon_6^2}[\beta_{\mathrm{AlAl}}\varepsilon_{\mathrm{X}}(2\beta_{\mathrm{XAl}}-\beta_{\mathrm{XX}})+\beta_{\mathrm{XX}}\varepsilon_{\mathrm{Al}}(2\beta_{\mathrm{AlX}}-\beta_{\mathrm{AlAl}})]$$

$$+\frac{RT}{2\varepsilon_6}[2\beta_{\mathrm{XX}}\varepsilon_{\mathrm{Al}}+x_{\mathrm{XAl}}(2\beta_{\mathrm{XAl}}-\beta_{\mathrm{XX}})(\varepsilon_{\mathrm{Al}}-\varepsilon_{\mathrm{X}})]$$

$$\Delta\mu^{\mathrm{xs}}_{\mathrm{Al}}=-\frac{x_{\mathrm{X}}x'_{\mathrm{XAl}}}{2\varepsilon_6}\left[(\varepsilon_2-x_{\mathrm{X}}\beta_{\mathrm{AlAl}})g^{10}_{\mathrm{XAl}}+(\varepsilon_3-(1-x_{\mathrm{X}})\beta_{\mathrm{XX}})g^{01}_{\mathrm{XAl}}\right]$$

$$+\frac{x_{\mathrm{XAl}}}{2\varepsilon_6\varepsilon_1}\Big[\beta_{\mathrm{XX}}\varepsilon_1\left(\Delta g^{0}_{\mathrm{XAl}}+g^{01}_{\mathrm{XAl}}\right)+\varepsilon_1x_{\mathrm{XAl}}\left((\beta_{\mathrm{XAl}}-\beta_{\mathrm{XX}})g^{01}_{\mathrm{XAl}}-\beta_{\mathrm{XAl}}g^{10}_{\mathrm{XAl}}\right)$$

$$-\beta_{\mathrm{XX}}\left[\Delta g^{0}_{\mathrm{XAl}}\varepsilon_1+g^{10}_{\mathrm{XAl}}\varepsilon_2+g^{01}_{\mathrm{XAl}}\varepsilon_3\right]\Big]$$

$$+\frac{RTx_{\mathrm{X}}x'_{\mathrm{XAl}}\varepsilon_1}{2\varepsilon_6^2}[\beta_{\mathrm{AlAl}}\varepsilon_{\mathrm{X}}(2\beta_{\mathrm{XAl}}-\beta_{\mathrm{XX}})+\beta_{\mathrm{XX}}\varepsilon_{\mathrm{Al}}(2\beta_{\mathrm{AlX}}-\beta_{\mathrm{AlAl}})]$$

$$+\frac{RT}{2\varepsilon_6}[2\beta_{\mathrm{XX}}\varepsilon_{\mathrm{Al}}+x_{\mathrm{XAl}}(2\beta_{\mathrm{XAl}}-\beta_{\mathrm{XX}})(\varepsilon_{\mathrm{Al}}-\varepsilon_{\mathrm{X}})] \tag{A.137}$$

Simplifying terms (A.138):

$$\beta_{\mathrm{XX}}\varepsilon_1\left(\Delta g^{0}_{\mathrm{XAl}}+g^{01}_{\mathrm{XAl}}\right)+\varepsilon_1x_{\mathrm{XAl}}\left((\beta_{\mathrm{XAl}}-\beta_{\mathrm{XX}})g^{01}_{\mathrm{XAl}}-\beta_{\mathrm{XAl}}g^{10}_{\mathrm{XAl}}\right)-\beta_{\mathrm{XX}}\left[\Delta g^{0}_{\mathrm{XAl}}\varepsilon_1+g^{10}_{\mathrm{XAl}}\varepsilon_2+g^{01}_{\mathrm{XAl}}\varepsilon_3\right]$$

$$=\beta_{\mathrm{XX}}\Delta g^{0}_{\mathrm{XAl}}(\varepsilon_1-\varepsilon_1)+g^{10}_{\mathrm{XAl}}(-\beta_{\mathrm{XAl}}\varepsilon_1x_{\mathrm{XAl}}-\beta_{\mathrm{XX}}\varepsilon_2)+g^{01}_{\mathrm{XAl}}(\beta_{\mathrm{XX}}\varepsilon_1+(\beta_{\mathrm{XAl}}-\beta_{\mathrm{XX}})\varepsilon_1x_{\mathrm{XAl}}-\beta_{\mathrm{XX}}\varepsilon_3)$$

$$= g_{\mathrm{XAl}}^{10}\Big(-\beta_{\mathrm{XAl}}x_{\mathrm{XAl}}\big((1-x_{\mathrm{X}})\beta_{\mathrm{XX}}+x_{\mathrm{X}}\beta_{\mathrm{AlAl}}\big)$$

$$-\beta_{\mathrm{XX}}\big((x_{\mathrm{X}}\beta_{\mathrm{AlX}}-(1-x_{\mathrm{X}})\beta_{\mathrm{XAl}})x_{\mathrm{XAl}}+x_{\mathrm{X}}\beta_{\mathrm{AlAl}}(1-x_{\mathrm{XAl}})\big)\Big)$$

$$+g_{\mathrm{XAl}}^{01}\Big((\beta_{\mathrm{XX}}(1-x_{\mathrm{XAl}})+\beta_{\mathrm{XAl}}x_{\mathrm{XAl}})\big((1-x_{\mathrm{X}})\beta_{\mathrm{XX}}+x_{\mathrm{X}}\beta_{\mathrm{AlAl}}\big)$$

$$-\beta_{\mathrm{XX}}\Big(\big((1-x_{\mathrm{X}})\beta_{\mathrm{XAl}}-x_{\mathrm{X}}\beta_{\mathrm{AlX}}\big)x_{\mathrm{XAl}}+\beta_{\mathrm{XX}}(1-x_{\mathrm{X}})(1-x_{\mathrm{XAl}})\Big)\Big)$$

$$= g_{\mathrm{XAl}}^{10}\Big(\beta_{\mathrm{XX}}\beta_{\mathrm{XAl}}\big(-x_{\mathrm{XAl}}(1-x_{\mathrm{X}})\big)-\beta_{\mathrm{AlAl}}\beta_{\mathrm{XAl}}x_{\mathrm{X}}x_{\mathrm{XAl}}-\beta_{\mathrm{XX}}\beta_{\mathrm{AlX}}x_{\mathrm{X}}x_{\mathrm{XAl}}+\beta_{\mathrm{XX}}\beta_{\mathrm{XAl}}(1-x_{\mathrm{X}})x_{\mathrm{XAl}}$$

$$-\beta_{\mathrm{XX}}\beta_{\mathrm{AlAl}}x_{\mathrm{X}}(1-x_{\mathrm{XAl}})\Big)$$

$$+g_{\mathrm{XAl}}^{01}\big(\beta_{\mathrm{XX}}\beta_{\mathrm{XX}}(1-x_{\mathrm{X}})(1-x_{\mathrm{XAl}})+\beta_{\mathrm{XX}}\beta_{\mathrm{AlAl}}x_{\mathrm{X}}(1-x_{\mathrm{XAl}})+\beta_{\mathrm{XAl}}\beta_{\mathrm{XX}}(1-x_{\mathrm{X}})x_{\mathrm{XAl}}$$

$$+\beta_{\mathrm{XAl}}\beta_{\mathrm{AlAl}}x_{\mathrm{X}}x_{\mathrm{XAl}}-\beta_{\mathrm{XAl}}\beta_{\mathrm{XX}}(1-x_{\mathrm{X}})x_{\mathrm{XAl}}+\beta_{\mathrm{XAl}}\beta_{\mathrm{XX}}x_{\mathrm{X}}x_{\mathrm{XAl}}$$

$$-\beta_{\mathrm{XX}}\beta_{\mathrm{XX}}(1-x_{\mathrm{X}})(1-x_{\mathrm{XAl}})\big)$$

$$= g_{\mathrm{XAl}}^{10}\big(-\beta_{\mathrm{AlAl}}\beta_{\mathrm{XAl}}x_{\mathrm{X}}x_{\mathrm{XAl}}-\beta_{\mathrm{XX}}\beta_{\mathrm{AlX}}x_{\mathrm{X}}x_{\mathrm{XAl}}-\beta_{\mathrm{XX}}\beta_{\mathrm{AlAl}}x_{\mathrm{X}}(1-x_{\mathrm{XAl}})\big)$$

$$+g_{\mathrm{XAl}}^{01}(\beta_{\mathrm{XX}}\beta_{\mathrm{AlAl}}x_{\mathrm{X}}(1-x_{\mathrm{XAl}})+\beta_{\mathrm{XAl}}\beta_{\mathrm{AlAl}}x_{\mathrm{X}}x_{\mathrm{XAl}}+\beta_{\mathrm{XAl}}\beta_{\mathrm{XX}}x_{\mathrm{X}}x_{\mathrm{XAl}})$$

$$= x_{\mathrm{X}}\big(\beta_{\mathrm{XX}}\beta_{\mathrm{AlAl}}+x_{\mathrm{XAl}}(\beta_{\mathrm{XX}}\beta_{\mathrm{AlX}}+\beta_{\mathrm{AlAl}}\beta_{\mathrm{XAl}}-\beta_{\mathrm{XX}}\beta_{\mathrm{AlAl}})\big)\big(g_{\mathrm{XAl}}^{01}-g_{\mathrm{XAl}}^{10}\big)$$

$$= \varepsilon_6 x_{\mathrm{X}}\big(g_{\mathrm{XAl}}^{01}-g_{\mathrm{XAl}}^{10}\big) \tag{A.138}$$

Simplifying $\Delta\mu_{\mathrm{Al}}^{\mathrm{xs}}$ (A.139):

$$\Delta\mu_{\mathrm{Al}}^{\mathrm{xs}} = \frac{x_{\mathrm{XAl}}}{2\varepsilon_6\varepsilon_1}\big[\varepsilon_6 x_{\mathrm{X}}\big(g_{\mathrm{XAl}}^{01}-g_{\mathrm{XAl}}^{10}\big)\big]-\frac{x_{\mathrm{X}}x'_{\mathrm{XAl}}}{2\varepsilon_6}\big[(\varepsilon_2-x_{\mathrm{X}}\beta_{\mathrm{AlAl}})g_{\mathrm{XAl}}^{10}+(\varepsilon_3-(1-x_{\mathrm{X}})\beta_{\mathrm{XX}})g_{\mathrm{XAl}}^{01}\big]$$

$$+\frac{RTx_{\mathrm{X}}x'_{\mathrm{XAl}}\varepsilon_1}{2\varepsilon_6^2}[\beta_{\mathrm{AlAl}}\varepsilon_{\mathrm{X}}(2\beta_{\mathrm{XAl}}-\beta_{\mathrm{XX}})+\beta_{\mathrm{XX}}\varepsilon_{\mathrm{Al}}(2\beta_{\mathrm{AlX}}-\beta_{\mathrm{AlAl}})]$$

$$+\frac{RT}{2\varepsilon_6}[2\beta_{\mathrm{XX}}\varepsilon_{\mathrm{Al}}+x_{\mathrm{XAl}}(2\beta_{\mathrm{XAl}}-\beta_{\mathrm{XX}})(\varepsilon_{\mathrm{Al}}-\varepsilon_{\mathrm{X}})]$$

$$\Delta\mu_{\mathrm{Al}}^{\mathrm{xs}} = \frac{1}{2\varepsilon_1\varepsilon_6}\big[\varepsilon_6 x_{\mathrm{X}}x_{\mathrm{XAl}}\big(g_{\mathrm{XAl}}^{01}-g_{\mathrm{XAl}}^{10}\big)+RT\varepsilon_1\big(2\beta_{\mathrm{XX}}\varepsilon_{\mathrm{Al}}+x_{\mathrm{XAl}}(2\beta_{\mathrm{XAl}}-\beta_{\mathrm{XX}})(\varepsilon_{\mathrm{Al}}-\varepsilon_{\mathrm{X}})\big)\big]$$

$$+\frac{x_{\mathrm{X}}x'_{\mathrm{XAl}}}{2\varepsilon_6^2}\Big[RT\varepsilon_1\big(\beta_{\mathrm{AlAl}}\varepsilon_{\mathrm{X}}(2\beta_{\mathrm{XAl}}-\beta_{\mathrm{XX}})+\beta_{\mathrm{XX}}\varepsilon_{\mathrm{Al}}(2\beta_{\mathrm{AlX}}-\beta_{\mathrm{AlAl}})\big)$$

$$-\varepsilon_6\Big((\varepsilon_2-x_{\mathrm{X}}\beta_{\mathrm{AlAl}})g_{\mathrm{XAl}}^{10}+(\varepsilon_3-(1-x_{\mathrm{X}})\beta_{\mathrm{XX}})g_{\mathrm{XAl}}^{01}\Big)\Big] \tag{A.139}$$

A.4.4. Implicit derivative of the X-Al bond fraction

Evaluating the derivative implicitly (A.140):

$$x_{\mathrm{XAl}} = \left(\frac{4\varepsilon_2\varepsilon_3}{\varepsilon_1^2}\right)\exp\left(-\frac{\varepsilon_1\Delta g^0_{\mathrm{XAl}} + \varepsilon_2 g^{10}_{\mathrm{XAl}} + \varepsilon_3 g^{01}_{\mathrm{XAl}}}{\varepsilon_1 RT}\right)$$

$$x_{\mathrm{XAl}} = 4\exp\left(-\frac{\Delta g^0_{\mathrm{XAl}}}{RT}\right)\left(\frac{\varepsilon_2\varepsilon_3}{\varepsilon_1^2}\right)\exp\left(-\frac{\varepsilon_2 g^{10}_{\mathrm{XAl}} + \varepsilon_3 g^{01}_{\mathrm{XAl}}}{\varepsilon_1 RT}\right) \tag{A.140}$$

Evaluating the derivative of a product of functions $f_i(x_{\mathrm{X}})$ in a variety of ways, to provide useful relations to simplify x'_{XAl} (A.141):

$$y = f_1(x_{\mathrm{X}})f_2(x_{\mathrm{X}})f_3(x_{\mathrm{X}})\ldots$$

$$y' = f_1'(x_{\mathrm{X}})f_2(x_{\mathrm{X}})f_3(x_{\mathrm{X}})\ldots + f_1(x_{\mathrm{X}})f_2'(x_{\mathrm{X}})f_3(x_{\mathrm{X}})\ldots + f_1(x_{\mathrm{X}})f_2(x_{\mathrm{X}})f_3'(x_{\mathrm{X}})\ldots$$

$$= f_1(x_{\mathrm{X}})f_2(x_{\mathrm{X}})f_3(x_{\mathrm{X}})\ldots\left(\frac{f_1'(x_{\mathrm{X}})}{f_1(x_{\mathrm{X}})} + \frac{f_2'(x_{\mathrm{X}})}{f_2(x_{\mathrm{X}})} + \frac{f_3'(x_{\mathrm{X}})}{f_3(x_{\mathrm{X}})} + \cdots\right)$$

$$= y\left(\frac{f_1'(x_{\mathrm{X}})}{f_1(x_{\mathrm{X}})} + \frac{f_2'(x_{\mathrm{X}})}{f_2(x_{\mathrm{X}})} + \frac{f_3'(x_{\mathrm{X}})}{f_3(x_{\mathrm{X}})} + \cdots\right)$$

$$= y\left(\frac{\mathrm{d}\ln\left(f_1(x_{\mathrm{X}})\right)}{\mathrm{d}x_{\mathrm{X}}} + \frac{\mathrm{d}\ln\left(f_2(x_{\mathrm{X}})\right)}{\mathrm{d}x_{\mathrm{X}}} + \frac{\mathrm{d}\ln\left(f_3(x_{\mathrm{X}})\right)}{\mathrm{d}x_{\mathrm{X}}} + \cdots\right)$$

$$= y\left(\frac{\mathrm{d}}{\mathrm{d}x_{\mathrm{X}}}\left(\ln\left(f_1(x_{\mathrm{X}})\right) + \ln\left(f_2(x_{\mathrm{X}})\right) + \ln\left(f_3(x_{\mathrm{X}})\right) + \cdots\right)\right) =$$

$$= y\left(\frac{\mathrm{d}}{dx_{\mathrm{X}}}\left(\ln(f_1(x_{\mathrm{X}})f_2(x_{\mathrm{X}})f_3(x_{\mathrm{X}})\ldots)\right)\right) = y\frac{\mathrm{d}}{dx_{\mathrm{X}}}(\ln y) \tag{A.141}$$

Evaluating the derivative implicitly (A.142):

$$x_{\mathrm{XAl}} = 4\exp\left(-\frac{\Delta g^0_{\mathrm{XAl}}}{RT}\right)\left(\frac{\varepsilon_2\varepsilon_3}{\varepsilon_1^2}\right)\exp\left(-\frac{\varepsilon_2 g^{10}_{\mathrm{XAl}} + \varepsilon_3 g^{01}_{\mathrm{XAl}}}{RT\varepsilon_1}\right)$$

$$x'_{\mathrm{XAl}} = 4\exp\left(-\frac{\Delta g^0_{\mathrm{XAl}}}{RT}\right)\frac{\mathrm{d}}{\mathrm{d}x_{\mathrm{X}}}\left[\left(\frac{\varepsilon_2\varepsilon_3}{\varepsilon_1^2}\right)\exp\left(-\frac{\varepsilon_2 g^{10}_{\mathrm{XAl}} + \varepsilon_3 g^{01}_{\mathrm{XAl}}}{RT\varepsilon_1}\right)\right]$$

$$x'_{\mathrm{XAl}} = 4\exp\left(-\frac{\Delta g^0_{\mathrm{XAl}}}{RT}\right)\left(\frac{\varepsilon_2\varepsilon_3}{\varepsilon_1^2}\right)\exp\left(-\frac{\varepsilon_2 g^{10}_{\mathrm{XAl}} + \varepsilon_3 g^{01}_{\mathrm{XAl}}}{\varepsilon_1}\right)$$

$$\times\frac{\mathrm{d}}{\mathrm{d}x_{\mathrm{X}}}\left[\ln\left(\left(\frac{\varepsilon_2\varepsilon_3}{\varepsilon_1^2}\right)\exp\left(-\frac{\varepsilon_2 g^{10}_{\mathrm{XAl}} + \varepsilon_3 g^{01}_{\mathrm{XAl}}}{RT\varepsilon_1}\right)\right)\right]$$

$$\frac{x'_{\mathrm{XAl}}}{x_{\mathrm{XAl}}} = \frac{\mathrm{d}}{\mathrm{d}x_{\mathrm{X}}}\left[\ln\varepsilon_2 + \ln\varepsilon_3 - 2\ln\varepsilon_1 - \frac{\varepsilon_2 g^{10}_{\mathrm{XAl}} + \varepsilon_3 g^{01}_{\mathrm{XAl}}}{RT\varepsilon_1}\right]$$

$$= \frac{\varepsilon'_2}{\varepsilon_2} + \frac{\varepsilon'_3}{\varepsilon_3} - 2\frac{\varepsilon'_1}{\varepsilon_1} - \frac{g^{10}_{\mathrm{XAl}}}{RT}\frac{\mathrm{d}}{\mathrm{d}x_{\mathrm{X}}}\left(\frac{\varepsilon_2}{\varepsilon_1}\right) - \frac{g^{01}_{\mathrm{XAl}}}{RT}\frac{\mathrm{d}}{\mathrm{d}x_{\mathrm{X}}}\left(\frac{\varepsilon_3}{\varepsilon_1}\right)$$

$$= \frac{\varepsilon'_2}{\varepsilon_2} + \frac{\varepsilon'_3}{\varepsilon_3} - 2\frac{\varepsilon'_1}{\varepsilon_1} - \frac{g^{10}_{\mathrm{XAl}}}{RT}\frac{\varepsilon_2}{\varepsilon_1}\frac{\mathrm{d}}{\mathrm{d}x_{\mathrm{X}}}(\ln\varepsilon_2 - \ln\varepsilon_1) - \frac{g^{01}_{\mathrm{XAl}}}{RT}\frac{\varepsilon_3}{\varepsilon_1}\frac{\mathrm{d}}{\mathrm{d}x_{\mathrm{X}}}(\ln\varepsilon_3 - \ln\varepsilon_1)$$

$$= \frac{\varepsilon'_2}{\varepsilon_2} + \frac{\varepsilon'_3}{\varepsilon_3} - 2\frac{\varepsilon'_1}{\varepsilon_1} - \frac{g^{10}_{\mathrm{XAl}}}{RT}\frac{\varepsilon_2}{\varepsilon_1}\left(\frac{\varepsilon'_2}{\varepsilon_2} - \frac{\varepsilon'_1}{\varepsilon_1}\right) - \frac{g^{01}_{\mathrm{XAl}}}{RT}\frac{\varepsilon_3}{\varepsilon_1}\left(\frac{\varepsilon'_3}{\varepsilon_3} - \frac{\varepsilon'_1}{\varepsilon_1}\right)$$

$$= \left(\frac{\varepsilon'_2}{\varepsilon_2} - \frac{\varepsilon'_1}{\varepsilon_1}\right) + \left(\frac{\varepsilon'_3}{\varepsilon_3} - \frac{\varepsilon'_1}{\varepsilon_1}\right) - \frac{g^{10}_{\mathrm{XAl}}}{RT}\left(\frac{\varepsilon_1\varepsilon'_2 - \varepsilon'_1\varepsilon_2}{\varepsilon_1^2}\right) - \frac{g^{01}_{\mathrm{XAl}}}{RT}\left(\frac{\varepsilon_1\varepsilon'_3 - \varepsilon'_1\varepsilon_3}{\varepsilon_1^2}\right)$$

$$= \frac{\varepsilon_1\varepsilon'_2 - \varepsilon'_1\varepsilon_2}{\varepsilon_1\varepsilon_2} + \frac{\varepsilon_1\varepsilon'_3 - \varepsilon'_1\varepsilon_3}{\varepsilon_1\varepsilon_3} - \frac{g^{10}_{\mathrm{XAl}}}{RT}\left(\frac{\varepsilon_1\varepsilon'_2 - \varepsilon'_1\varepsilon_2}{\varepsilon_1^2}\right) - \frac{g^{01}_{\mathrm{XAl}}}{RT}\left(\frac{\varepsilon_1\varepsilon'_3 - \varepsilon'_1\varepsilon_3}{\varepsilon_1^2}\right)$$

$$\frac{x'_{\mathrm{XAl}}}{x_{\mathrm{XAl}}} = \frac{\varepsilon_1\varepsilon'_2 - \varepsilon'_1\varepsilon_2}{\varepsilon_1^2\varepsilon_2}\left(\varepsilon_1 - \varepsilon_2\frac{g^{10}_{\mathrm{XAl}}}{RT}\right) + \frac{\varepsilon_1\varepsilon'_3 - \varepsilon'_1\varepsilon_3}{\varepsilon_1^2\varepsilon_3}\left(\varepsilon_1 - \varepsilon_3\frac{g^{01}_{\mathrm{XAl}}}{RT}\right)$$

$$\frac{x'_{\mathrm{XAl}}}{x_{\mathrm{XAl}}}\varepsilon_1^2\varepsilon_2\varepsilon_3 = (\varepsilon_1\varepsilon'_2 - \varepsilon'_1\varepsilon_2)\varepsilon_3\left(\varepsilon_1 - \varepsilon_2\frac{g^{10}_{\mathrm{XAl}}}{RT}\right) + (\varepsilon_1\varepsilon'_3 - \varepsilon'_1\varepsilon_3)\varepsilon_2\left(\varepsilon_1 - \varepsilon_3\frac{g^{01}_{\mathrm{XAl}}}{RT}\right) \qquad \text{(A.142)}$$

Evaluating $\varepsilon_1\varepsilon'_2 - \varepsilon'_1\varepsilon_2$ (A.143):

$$\varepsilon_1\varepsilon'_2 - \varepsilon'_1\varepsilon_2 = \varepsilon_1\big(x'_{\mathrm{XAl}}(x_{\mathrm{X}}\beta_{\mathrm{AlX}} - (1-x_{\mathrm{X}})\beta_{\mathrm{XAl}} - x_{\mathrm{X}}\beta_{\mathrm{AlAl}}) + x_{\mathrm{XAl}}(\beta_{\mathrm{AlX}} + \beta_{\mathrm{XAl}})$$

$$+ \beta_{\mathrm{AlAl}}(1 - x_{\mathrm{XAl}})\big)$$

$$- (\beta_{\mathrm{AlAl}} - \beta_{\mathrm{XX}})\big((x_{\mathrm{X}}\beta_{\mathrm{AlX}} - (1-x_{\mathrm{X}})\beta_{\mathrm{XAl}})x_{\mathrm{XAl}} + x_{\mathrm{X}}\beta_{\mathrm{AlAl}}(1 - x_{\mathrm{XAl}})\big)$$

$$= \varepsilon_1\frac{x'_{\mathrm{XAl}}}{x_{\mathrm{XAl}}}(\varepsilon_2 - x_{\mathrm{X}}\beta_{\mathrm{AlAl}}) + \varepsilon_1\big(x_{\mathrm{XAl}}(\beta_{\mathrm{AlX}} + \beta_{\mathrm{XAl}}) + \beta_{\mathrm{AlAl}}(1 - x_{\mathrm{XAl}})\big)$$

$$- (\beta_{\mathrm{AlAl}} - \beta_{\mathrm{XX}})\big((x_{\mathrm{X}}\beta_{\mathrm{AlX}} - (1-x_{\mathrm{X}})\beta_{\mathrm{XAl}})x_{\mathrm{XAl}} + x_{\mathrm{X}}\beta_{\mathrm{AlAl}}(1 - x_{\mathrm{XAl}})\big)$$

$$= \varepsilon_1 \frac{x'_{\mathrm{XAl}}}{x_{\mathrm{XAl}}}(\varepsilon_2 - x_{\mathrm{X}}\beta_{\mathrm{AlAl}}) + \beta_{\mathrm{AlX}}x_{\mathrm{XAl}}(\varepsilon_1 - (\beta_{\mathrm{AlAl}} - \beta_{\mathrm{XX}})x_{\mathrm{X}})$$

$$+ \beta_{\mathrm{XAl}}x_{\mathrm{XAl}}\big(\varepsilon_1 + (\beta_{\mathrm{AlAl}} - \beta_{\mathrm{XX}})(1 - x_{\mathrm{X}})\big) + \varepsilon_1\beta_{\mathrm{AlAl}}(1 - x_{\mathrm{XAl}})$$

$$- (\beta_{\mathrm{AlAl}} - \beta_{\mathrm{XX}})x_{\mathrm{X}}\beta_{\mathrm{AlAl}}(1 - x_{\mathrm{XAl}})$$

$$= \varepsilon_1 \frac{x'_{\mathrm{XAl}}}{x_{\mathrm{XAl}}}(\varepsilon_2 - x_{\mathrm{X}}\beta_{\mathrm{AlAl}}) + \beta_{\mathrm{XX}}\beta_{\mathrm{AlX}}x_{\mathrm{XAl}} + \beta_{\mathrm{AlAl}}\beta_{\mathrm{XAl}}x_{\mathrm{XAl}}$$

$$+ \beta_{\mathrm{AlAl}}(\varepsilon_1 - (\beta_{\mathrm{AlAl}} - \beta_{\mathrm{XX}})x_{\mathrm{X}})(1 - x_{\mathrm{XAl}})$$

$$= \varepsilon_1 \frac{x'_{\mathrm{XAl}}}{x_{\mathrm{XAl}}}(\varepsilon_2 - x_{\mathrm{X}}\beta_{\mathrm{AlAl}}) + \beta_{\mathrm{XX}}\beta_{\mathrm{AlX}}x_{\mathrm{XAl}} + \beta_{\mathrm{AlAl}}\beta_{\mathrm{XAl}}x_{\mathrm{XAl}} + \beta_{\mathrm{AlAl}}\beta_{\mathrm{XX}}(1 - x_{\mathrm{XAl}})$$

$$\varepsilon_1\varepsilon'_2 - \varepsilon'_1\varepsilon_2 = \varepsilon_1 \frac{x'_{\mathrm{XAl}}}{x_{\mathrm{XAl}}}(\varepsilon_2 - x_{\mathrm{X}}\beta_{\mathrm{AlAl}}) + \varepsilon_6 \tag{A.143}$$

Evaluating $\varepsilon_1\varepsilon'_3 - \varepsilon'_1\varepsilon_3$ (A.144):

$$\varepsilon_1\varepsilon'_3 - \varepsilon'_1\varepsilon_3 = \varepsilon_1\big(x'_{\mathrm{XAl}}\big((1 - x_{\mathrm{X}})(\beta_{\mathrm{XAl}} + \beta_{\mathrm{AlX}} - \beta_{\mathrm{XX}}) - \beta_{\mathrm{AlX}}\big) - x_{\mathrm{XAl}}(\beta_{\mathrm{XAl}} + \beta_{\mathrm{AlX}} - \beta_{\mathrm{XX}})$$

$$- \beta_{\mathrm{XX}}\big)$$

$$- (\beta_{\mathrm{AlAl}} - \beta_{\mathrm{XX}})\Big(\big((1 - x_{\mathrm{X}})\beta_{\mathrm{XAl}} - x_{\mathrm{X}}\beta_{\mathrm{AlX}}\big)x_{\mathrm{XAl}} + \beta_{\mathrm{XX}}(1 - x_{\mathrm{X}})(1 - x_{\mathrm{XAl}})\Big)$$

$$= \varepsilon_1 x'_{\mathrm{XAl}}\big((1 - x_{\mathrm{X}})\beta_{\mathrm{XAl}} - x_{\mathrm{X}}\beta_{\mathrm{AlX}} - \beta_{\mathrm{XX}}(1 - x_{\mathrm{X}})\big) - \varepsilon_1(x_{\mathrm{XAl}}(\beta_{\mathrm{XAl}} + \beta_{\mathrm{AlX}}) + (1 - x_{\mathrm{XAl}})\beta_{\mathrm{XX}})$$

$$- (\beta_{\mathrm{AlAl}} - \beta_{\mathrm{XX}})\Big(\big((1 - x_{\mathrm{X}})\beta_{\mathrm{XAl}} - x_{\mathrm{X}}\beta_{\mathrm{AlX}}\big)x_{\mathrm{XAl}} + \beta_{\mathrm{XX}}(1 - x_{\mathrm{X}})(1 - x_{\mathrm{XAl}})\Big)$$

$$= \varepsilon_1 \frac{x'_{\mathrm{XAl}}}{x_{\mathrm{XAl}}}(\varepsilon_3 - (1 - x_{\mathrm{X}})\beta_{\mathrm{XX}}) - \beta_{\mathrm{XAl}}x_{\mathrm{XAl}}\big(\varepsilon_1 + (\beta_{\mathrm{AlAl}} - \beta_{\mathrm{XX}})(1 - x_{\mathrm{X}})\big)$$

$$- \beta_{\mathrm{AlX}}x_{\mathrm{XAl}}(\varepsilon_1 - (\beta_{\mathrm{AlAl}} - \beta_{\mathrm{XX}})x_{\mathrm{X}})$$

$$- (1 - x_{\mathrm{XAl}})\beta_{\mathrm{XX}}\big(\varepsilon_1 + (\beta_{\mathrm{AlAl}} - \beta_{\mathrm{XX}})(1 - x_{\mathrm{X}})\big)$$

$$= \varepsilon_1 \frac{x'_{\mathrm{XAl}}}{x_{\mathrm{XAl}}}(\varepsilon_3 - (1 - x_{\mathrm{X}})\beta_{\mathrm{XX}}) - \beta_{\mathrm{XAl}}\beta_{\mathrm{AlAl}}x_{\mathrm{XAl}} - \beta_{\mathrm{AlX}}x_{\mathrm{XAl}}\beta_{\mathrm{XX}} - (1 - x_{\mathrm{XAl}})\beta_{\mathrm{XX}}\beta_{\mathrm{AlAl}}$$

$$\varepsilon_1\varepsilon'_3 - \varepsilon'_1\varepsilon_3 = \varepsilon_1 \frac{x'_{\mathrm{XAl}}}{x_{\mathrm{XAl}}}(\varepsilon_3 - (1 - x_{\mathrm{X}})\beta_{\mathrm{XX}}) - \varepsilon_6 \tag{A.144}$$

Simplifying the expression for x'_{XAl} (A.145):

$$\frac{x'_{\mathrm{XAl}}}{x_{\mathrm{XAl}}}\varepsilon_1^2\varepsilon_2\varepsilon_3 = (\varepsilon_1\varepsilon'_2 - \varepsilon'_1\varepsilon_2)\varepsilon_3\left(\varepsilon_1 - \varepsilon_2\frac{g^{10}_{\mathrm{XAl}}}{RT}\right) + (\varepsilon_1\varepsilon'_3 - \varepsilon'_1\varepsilon_3)\varepsilon_2\left(\varepsilon_1 - \varepsilon_3\frac{g^{01}_{\mathrm{XAl}}}{RT}\right)$$

$$= \left(\varepsilon_1\frac{x'_{\mathrm{XAl}}}{x_{\mathrm{XAl}}}(\varepsilon_2 - x_{\mathrm{X}}\beta_{\mathrm{AlAl}}) + \varepsilon_6\right)\varepsilon_3\left(\varepsilon_1 - \varepsilon_2\frac{g^{10}_{\mathrm{XAl}}}{RT}\right)$$

$$+ \left(\varepsilon_1\frac{x'_{\mathrm{XAl}}}{x_{\mathrm{XAl}}}(\varepsilon_3 - (1-x_{\mathrm{X}})\beta_{\mathrm{XX}}) - \varepsilon_6\right)\varepsilon_2\left(\varepsilon_1 - \varepsilon_3\frac{g^{01}_{\mathrm{XAl}}}{RT}\right)$$

$$= \frac{x'_{\mathrm{XAl}}}{x_{\mathrm{XAl}}}\left(\varepsilon_1\varepsilon_3(\varepsilon_2 - x_{\mathrm{X}}\beta_{\mathrm{AlAl}})\left(\varepsilon_1 - \varepsilon_2\frac{g^{10}_{\mathrm{XAl}}}{RT}\right) + \varepsilon_1\varepsilon_2(\varepsilon_3 - (1-x_{\mathrm{X}})\beta_{\mathrm{XX}})\left(\varepsilon_1 - \varepsilon_3\frac{g^{01}_{\mathrm{XAl}}}{RT}\right)\right)$$

$$+ \varepsilon_6\left(\varepsilon_3\left(\varepsilon_1 - \varepsilon_2\frac{g^{10}_{\mathrm{XAl}}}{RT}\right) - \varepsilon_2\left(\varepsilon_1 - \varepsilon_3\frac{g^{01}_{\mathrm{XAl}}}{RT}\right)\right)$$

$$= \frac{x'_{\mathrm{XAl}}}{x_{\mathrm{XAl}}}\left(\varepsilon_1\varepsilon_3(\varepsilon_2 - x_{\mathrm{X}}\beta_{\mathrm{AlAl}})(\varepsilon_1) + \varepsilon_1\varepsilon_2(\varepsilon_3 - (1-x_{\mathrm{X}})\beta_{\mathrm{XX}})(\varepsilon_1) - \frac{g^{10}_{\mathrm{XAl}}}{RT}\varepsilon_1\varepsilon_2\varepsilon_3(\varepsilon_2 - x_{\mathrm{X}}\beta_{\mathrm{AlAl}})\right.$$

$$\left. - \frac{g^{01}_{\mathrm{XAl}}}{RT}\varepsilon_1\varepsilon_2\varepsilon_3(\varepsilon_3 - (1-x_{\mathrm{X}})\beta_{\mathrm{XX}})\right) + \varepsilon_6\left(\varepsilon_3\left(\varepsilon_1 - \varepsilon_2\frac{g^{10}_{\mathrm{XAl}}}{RT}\right) - \varepsilon_2\left(\varepsilon_1 - \varepsilon_3\frac{g^{01}_{\mathrm{XAl}}}{RT}\right)\right)$$

$$= \varepsilon_1^2\frac{x'_{\mathrm{XAl}}}{x_{\mathrm{XAl}}}\left(\varepsilon_3(\varepsilon_2 - x_{\mathrm{X}}\beta_{\mathrm{AlAl}}) + \varepsilon_2(\varepsilon_3 - (1-x_{\mathrm{X}})\beta_{\mathrm{XX}})\right) + \varepsilon_6\left(\varepsilon_1(\varepsilon_3 - \varepsilon_2) - \frac{\varepsilon_2\varepsilon_3}{RT}\left(g^{10}_{\mathrm{XAl}} - g^{01}_{\mathrm{XAl}}\right)\right)$$

$$- \varepsilon_1\varepsilon_2\varepsilon_3\frac{x'_{\mathrm{XAl}}}{RTx_{\mathrm{XAl}}}\left((\varepsilon_2 - x_{\mathrm{X}}\beta_{\mathrm{AlAl}})g^{10}_{\mathrm{XAl}} + (\varepsilon_3 - (1-x_{\mathrm{X}})\beta_{\mathrm{XX}})g^{01}_{\mathrm{XAl}}\right)$$

$$\frac{x'_{\mathrm{XAl}}}{x_{\mathrm{XAl}}}\left(\varepsilon_1^2\varepsilon_2\varepsilon_3 - \varepsilon_1^2\left(\varepsilon_3(\varepsilon_2 - x_{\mathrm{X}}\beta_{\mathrm{AlAl}}) + \varepsilon_2(\varepsilon_3 - (1-x_{\mathrm{X}})\beta_{\mathrm{XX}})\right)\right)$$

$$= \varepsilon_6\left(\varepsilon_1(\varepsilon_3 - \varepsilon_2) - \frac{\varepsilon_2\varepsilon_3}{RT}\left(g^{10}_{\mathrm{XAl}} - g^{01}_{\mathrm{XAl}}\right)\right)$$

$$- \varepsilon_1\varepsilon_2\varepsilon_3\frac{x'_{\mathrm{XAl}}}{RTx_{\mathrm{XAl}}}\left((\varepsilon_2 - x_{\mathrm{X}}\beta_{\mathrm{AlAl}})g^{10}_{\mathrm{XAl}} + (\varepsilon_3 - (1-x_{\mathrm{X}})\beta_{\mathrm{XX}})g^{01}_{\mathrm{XAl}}\right)$$

$$\varepsilon_1^2\frac{x'_{\mathrm{XAl}}}{x_{\mathrm{XAl}}}\left(\varepsilon_2\varepsilon_3 - \left(\varepsilon_3(\varepsilon_2 - x_{\mathrm{X}}\beta_{\mathrm{AlAl}}) + \varepsilon_2(\varepsilon_3 - (1-x_{\mathrm{X}})\beta_{\mathrm{XX}})\right)\right)$$

$$= \varepsilon_6\left(\varepsilon_1(\varepsilon_3 - \varepsilon_2) - \frac{\varepsilon_2\varepsilon_3}{RT}\left(g^{10}_{\mathrm{XAl}} - g^{01}_{\mathrm{XAl}}\right)\right)$$

$$- \varepsilon_1\varepsilon_2\varepsilon_3\frac{x'_{\mathrm{XAl}}}{RTx_{\mathrm{XAl}}}\left((\varepsilon_2 - x_{\mathrm{X}}\beta_{\mathrm{AlAl}})g^{10}_{\mathrm{XAl}} + (\varepsilon_3 - (1-x_{\mathrm{X}})\beta_{\mathrm{XX}})g^{01}_{\mathrm{XAl}}\right)$$

$$\varepsilon_1^2 \frac{x'_{\mathrm{XAl}}}{x_{\mathrm{XAl}}}(\beta_{\mathrm{XX}}(1-x_{\mathrm{X}})\varepsilon_2 + x_{\mathrm{X}}\beta_{\mathrm{AlAl}}\varepsilon_3 - \varepsilon_2\varepsilon_3)$$

$$= \varepsilon_6\left(\varepsilon_1(\varepsilon_3-\varepsilon_2) - \frac{\varepsilon_2\varepsilon_3}{RT}\left(g^{10}_{\mathrm{XAl}} - g^{01}_{\mathrm{XAl}}\right)\right)$$

$$- \varepsilon_1\varepsilon_2\varepsilon_3\frac{x'_{\mathrm{XAl}}}{RTx_{\mathrm{XAl}}}\left((\varepsilon_2 - x_{\mathrm{X}}\beta_{\mathrm{AlAl}})g^{10}_{\mathrm{XAl}} + (\varepsilon_3 - (1-x_{\mathrm{X}})\beta_{\mathrm{XX}})g^{01}_{\mathrm{XAl}}\right)$$

$$\varepsilon_1\frac{x'_{\mathrm{XAl}}}{x_{\mathrm{XAl}}}\Bigg(\varepsilon_1(\beta_{\mathrm{XX}}(1-x_{\mathrm{X}})\varepsilon_2 + x_{\mathrm{X}}\beta_{\mathrm{AlAl}}\varepsilon_3 - \varepsilon_2\varepsilon_3)$$

$$+ \frac{\varepsilon_2\varepsilon_3}{RT}\left((\varepsilon_2 - x_{\mathrm{X}}\beta_{\mathrm{AlAl}})g^{10}_{\mathrm{XAl}} + (\varepsilon_3 - (1-x_{\mathrm{X}})\beta_{\mathrm{XX}})g^{01}_{\mathrm{XAl}}\right)\Bigg)$$

$$= \varepsilon_6\left(\varepsilon_1(\varepsilon_3-\varepsilon_2) - \frac{\varepsilon_2\varepsilon_3}{RT}\left(g^{10}_{\mathrm{XAl}} - g^{01}_{\mathrm{XAl}}\right)\right)$$

$$x'_{\mathrm{XAl}} = \frac{\varepsilon_6 x_{\mathrm{XAl}}}{\varepsilon_1} \times \left(\varepsilon_1(\varepsilon_3-\varepsilon_2)RT - \varepsilon_2\varepsilon_3\left(g^{10}_{\mathrm{XAl}} - g^{01}_{\mathrm{XAl}}\right)\right)$$

$$\div \Bigg(RT\varepsilon_1(\beta_{\mathrm{XX}}(1-x_{\mathrm{X}})\varepsilon_2 + x_{\mathrm{X}}\beta_{\mathrm{AlAl}}\varepsilon_3 - \varepsilon_2\varepsilon_3)$$

$$+ \varepsilon_2\varepsilon_3\left((\varepsilon_2 - x_{\mathrm{X}}\beta_{\mathrm{AlAl}})g^{10}_{\mathrm{XAl}} + (\varepsilon_3 - (1-x_{\mathrm{X}})\beta_{\mathrm{XX}})g^{01}_{\mathrm{XAl}}\right)\Bigg) \qquad \text{(A.145)}$$

Simplifying $\beta_{\mathrm{XX}}(1-x_{\mathrm{X}})\varepsilon_2 + x_{\mathrm{X}}\beta_{\mathrm{AlAl}}\varepsilon_3 - \varepsilon_2\varepsilon_3$ (A.146):

$$\beta_{\mathrm{XX}}(1-x_{\mathrm{X}})\varepsilon_2 + x_{\mathrm{X}}\beta_{\mathrm{AlAl}}\varepsilon_3 - \varepsilon_2\varepsilon_3$$

$$= \beta_{\mathrm{AlAl}}\beta_{\mathrm{XX}}x_{\mathrm{X}}(1-x_{\mathrm{X}})$$

$$+x^2_{\mathrm{XAl}}\left(\beta_{\mathrm{XAl}}(x_{\mathrm{X}}-1) + x_{\mathrm{X}}(\beta_{\mathrm{AlX}} - \beta_{\mathrm{AlAl}})\right)\left(\beta_{\mathrm{XX}} + \beta_{\mathrm{XAl}}(x_{\mathrm{X}}-1) + x_{\mathrm{X}}(\beta_{\mathrm{AlX}} - \beta_{\mathrm{XX}})\right)$$

$$= \beta_{\mathrm{AlAl}}\beta_{\mathrm{XX}}x_{\mathrm{X}}(1-x_{\mathrm{X}})$$

$$-x_{\mathrm{XAl}}(x_{\mathrm{X}}\beta_{\mathrm{AlX}} - \beta_{\mathrm{XAl}}(1-x_{\mathrm{X}}) - \beta_{\mathrm{AlAl}}x_{\mathrm{X}})x_{\mathrm{XAl}}\left(\beta_{\mathrm{XAl}}(1-x_{\mathrm{X}}) - x_{\mathrm{X}}\beta_{\mathrm{AlX}} + \beta_{\mathrm{XX}}(1-x_{\mathrm{X}})\right)$$

$$= \beta_{\mathrm{AlAl}}\beta_{\mathrm{XX}}x_{\mathrm{X}}(1-x_{\mathrm{X}}) - (\varepsilon_2 - x_{\mathrm{X}}\beta_{\mathrm{AlAl}})(\varepsilon_3 - (1-x_{\mathrm{X}})\beta_{\mathrm{XX}}) \qquad \text{(A.146)}$$

Putting into x'_{XAl} (A.147):

$$x'_{\mathrm{XAl}} = \frac{\varepsilon_6 x_{\mathrm{XAl}}}{\varepsilon_1} \times \left(\varepsilon_1(\varepsilon_3-\varepsilon_2)RT - \varepsilon_2\varepsilon_3\left(g^{10}_{\mathrm{XAl}} - g^{01}_{\mathrm{XAl}}\right)\right)$$

$$\div \Bigg(RT\varepsilon_1\left(\beta_{\mathrm{AlAl}}\beta_{\mathrm{XX}}x_{\mathrm{X}}(1-x_{\mathrm{X}}) - (\varepsilon_2 - x_{\mathrm{X}}\beta_{\mathrm{AlAl}})(\varepsilon_3 - (1-x_{\mathrm{X}})\beta_{\mathrm{XX}})\right)$$

$$+ \varepsilon_2\varepsilon_3\left((\varepsilon_2 - x_{\mathrm{X}}\beta_{\mathrm{AlAl}})g^{10}_{\mathrm{XAl}} + (\varepsilon_3 - (1-x_{\mathrm{X}})\beta_{\mathrm{XX}})g^{01}_{\mathrm{XAl}}\right)\Bigg) \qquad \text{(A.147)}$$

A.4.5. Eliminating the derivative of the X-Al bond fraction

Putting into the expression for $\Delta\mu_{\mathrm{X}}^{\mathrm{xs}}$ (A.148):

$$\Delta\mu_{\mathrm{X}}^{\mathrm{xs}}(x_{\mathrm{X}}) = \frac{1}{2\varepsilon_1\varepsilon_6}\Big[x_{\mathrm{XAl}}\varepsilon_6(1-x_{\mathrm{X}})\big(g_{\mathrm{XAl}}^{10}-g_{\mathrm{XAl}}^{01}\big) + RT\varepsilon_1\big(2\beta_{\mathrm{AlAl}}\varepsilon_{\mathrm{X}} + x_{\mathrm{XAl}}(2\beta_{\mathrm{AlX}}-\beta_{\mathrm{AlAl}})(\varepsilon_{\mathrm{X}}-\varepsilon_{\mathrm{Al}})\big)\Big]$$

$$-\frac{x'_{\mathrm{XAl}}(1-x_{\mathrm{X}})}{2\varepsilon_6^2}\Big[RT\varepsilon_1\big(\beta_{\mathrm{XX}}\varepsilon_{\mathrm{Al}}(2\beta_{\mathrm{AlX}}-\beta_{\mathrm{AlAl}}) + \beta_{\mathrm{AlAl}}\varepsilon_{\mathrm{X}}(2\beta_{\mathrm{XAl}}-\beta_{\mathrm{XX}})\big) - \varepsilon_6\Big((\varepsilon_3-(1-x_{\mathrm{X}})\beta_{\mathrm{XX}})g_{\mathrm{XAl}}^{01} + (\varepsilon_2-x_{\mathrm{X}}\beta_{\mathrm{AlAl}})g_{\mathrm{XAl}}^{10}\Big)\Big]$$

$$\Delta\mu_{\mathrm{X}}^{\mathrm{xs}}(x_{\mathrm{X}}) = \frac{x_{\mathrm{XAl}}}{2\varepsilon_1}(1-x_{\mathrm{X}})\big(g_{\mathrm{XAl}}^{10}-g_{\mathrm{XAl}}^{01}\big) + \frac{RT}{2\varepsilon_6}\big(2\beta_{\mathrm{AlAl}}\varepsilon_{\mathrm{X}} + x_{\mathrm{XAl}}(2\beta_{\mathrm{AlX}}-\beta_{\mathrm{AlAl}})(\varepsilon_{\mathrm{X}}-\varepsilon_{\mathrm{Al}})\big)$$

$$+\frac{x_{\mathrm{XAl}}(1-x_{\mathrm{X}})}{2\varepsilon_1\varepsilon_6}\times\Big(\varepsilon_1(\varepsilon_3-\varepsilon_2)RT - \varepsilon_2\varepsilon_3\big(g_{\mathrm{XAl}}^{10}-g_{\mathrm{XAl}}^{01}\big)\Big) \times\Big[\varepsilon_6\Big((\varepsilon_3-(1-x_{\mathrm{X}})\beta_{\mathrm{XX}})g_{\mathrm{XAl}}^{01} + (\varepsilon_2-x_{\mathrm{X}}\beta_{\mathrm{AlAl}})g_{\mathrm{XAl}}^{10}\Big)\Big] \div\Big(RT\varepsilon_1\big(\beta_{\mathrm{AlAl}}\beta_{\mathrm{XX}}x_{\mathrm{X}}(1-x_{\mathrm{X}}) - (\varepsilon_2-x_{\mathrm{X}}\beta_{\mathrm{AlAl}})(\varepsilon_3-(1-x_{\mathrm{X}})\beta_{\mathrm{XX}})\big) + \varepsilon_2\varepsilon_3\Big((\varepsilon_2-x_{\mathrm{X}}\beta_{\mathrm{AlAl}})g_{\mathrm{XAl}}^{10} + (\varepsilon_3-(1-x_{\mathrm{X}})\beta_{\mathrm{XX}})g_{\mathrm{XAl}}^{01}\Big)\Big)$$

$$-\frac{x_{\mathrm{XAl}}(1-x_{\mathrm{X}})}{2\varepsilon_1\varepsilon_6}\times\Big(\varepsilon_1(\varepsilon_3-\varepsilon_2)RT - \varepsilon_2\varepsilon_3\big(g_{\mathrm{XAl}}^{10}-g_{\mathrm{XAl}}^{01}\big)\Big) \times\Big[RT\varepsilon_1\big(\beta_{\mathrm{XX}}\varepsilon_{\mathrm{Al}}(2\beta_{\mathrm{AlX}}-\beta_{\mathrm{AlAl}}) + \beta_{\mathrm{AlAl}}\varepsilon_{\mathrm{X}}(2\beta_{\mathrm{XAl}}-\beta_{\mathrm{XX}})\big)\Big] \div\Big(RT\varepsilon_1\big(\beta_{\mathrm{AlAl}}\beta_{\mathrm{XX}}x_{\mathrm{X}}(1-x_{\mathrm{X}}) - (\varepsilon_2-x_{\mathrm{X}}\beta_{\mathrm{AlAl}})(\varepsilon_3-(1-x_{\mathrm{X}})\beta_{\mathrm{XX}})\big) + \varepsilon_2\varepsilon_3\Big((\varepsilon_2-x_{\mathrm{X}}\beta_{\mathrm{AlAl}})g_{\mathrm{XAl}}^{10} + (\varepsilon_3-(1-x_{\mathrm{X}})\beta_{\mathrm{XX}})g_{\mathrm{XAl}}^{01}\Big)\Big)$$

$$\Delta\mu_{\mathrm{X}}^{\mathrm{xs}}(x_{\mathrm{X}}) = \frac{x_{\mathrm{XAl}}}{2\varepsilon_1}(1-x_{\mathrm{X}})\big(g_{\mathrm{XAl}}^{10}-g_{\mathrm{XAl}}^{01}\big)$$

$$+\frac{x_{\mathrm{XAl}}(1-x_{\mathrm{X}})}{2\varepsilon_1}\times\left(\varepsilon_1(\varepsilon_3-\varepsilon_2)RT-\varepsilon_2\varepsilon_3\left(g_{\mathrm{XAl}}^{10}-g_{\mathrm{XAl}}^{01}\right)\right)$$

$$\times\left((\varepsilon_2-x_{\mathrm{X}}\beta_{\mathrm{AlAl}})g_{\mathrm{XAl}}^{10}+(\varepsilon_3-(1-x_{\mathrm{X}})\beta_{\mathrm{XX}})g_{\mathrm{XAl}}^{01}\right)$$

$$\div\left(RT\varepsilon_1\left(\beta_{\mathrm{AlAl}}\beta_{\mathrm{XX}}x_{\mathrm{X}}(1-x_{\mathrm{X}})-(\varepsilon_2-x_{\mathrm{X}}\beta_{\mathrm{AlAl}})(\varepsilon_3-(1-x_{\mathrm{X}})\beta_{\mathrm{XX}})\right)\right.$$

$$\left.+\varepsilon_2\varepsilon_3\left((\varepsilon_2-x_{\mathrm{X}}\beta_{\mathrm{AlAl}})g_{\mathrm{XAl}}^{10}+(\varepsilon_3-(1-x_{\mathrm{X}})\beta_{\mathrm{XX}})g_{\mathrm{XAl}}^{01}\right)\right)$$

$$+\frac{RT}{2\varepsilon_6}\left(2\beta_{\mathrm{AlAl}}\varepsilon_{\mathrm{X}}+x_{\mathrm{XAl}}(2\beta_{\mathrm{AlX}}-\beta_{\mathrm{AlAl}})(\varepsilon_{\mathrm{X}}-\varepsilon_{\mathrm{Al}})\right)$$

$$-\frac{RTx_{\mathrm{XAl}}(1-x_{\mathrm{X}})}{2\varepsilon_6}\times\left(\varepsilon_1(\varepsilon_3-\varepsilon_2)RT-\varepsilon_2\varepsilon_3\left(g_{\mathrm{XAl}}^{10}-g_{\mathrm{XAl}}^{01}\right)\right)$$

$$\times\left(\beta_{\mathrm{XX}}\varepsilon_{\mathrm{Al}}(2\beta_{\mathrm{AlX}}-\beta_{\mathrm{AlAl}})+\beta_{\mathrm{AlAl}}\varepsilon_{\mathrm{X}}(2\beta_{\mathrm{XAl}}-\beta_{\mathrm{XX}})\right)$$

$$\div\left(RT\varepsilon_1\left(\beta_{\mathrm{AlAl}}\beta_{\mathrm{XX}}x_{\mathrm{X}}(1-x_{\mathrm{X}})-(\varepsilon_2-x_{\mathrm{X}}\beta_{\mathrm{AlAl}})(\varepsilon_3-(1-x_{\mathrm{X}})\beta_{\mathrm{XX}})\right)\right.$$

$$\left.+\varepsilon_2\varepsilon_3\left((\varepsilon_2-x_{\mathrm{X}}\beta_{\mathrm{AlAl}})g_{\mathrm{XAl}}^{10}+(\varepsilon_3-(1-x_{\mathrm{X}})\beta_{\mathrm{XX}})g_{\mathrm{XAl}}^{01}\right)\right) \quad \text{(A.148)}$$

Simplifying the first term (A.149):

$$\left(g_{\mathrm{XAl}}^{10}-g_{\mathrm{XAl}}^{01}\right)\times\left(RT\varepsilon_1\left(\beta_{\mathrm{AlAl}}\beta_{\mathrm{XX}}x_{\mathrm{X}}(1-x_{\mathrm{X}})-(\varepsilon_2-x_{\mathrm{X}}\beta_{\mathrm{AlAl}})(\varepsilon_3-(1-x_{\mathrm{X}})\beta_{\mathrm{XX}})\right)\right.$$

$$\left.+\varepsilon_2\varepsilon_3\left((\varepsilon_2-x_{\mathrm{X}}\beta_{\mathrm{AlAl}})g_{\mathrm{XAl}}^{10}+(\varepsilon_3-(1-x_{\mathrm{X}})\beta_{\mathrm{XX}})g_{\mathrm{XAl}}^{01}\right)\right)$$

$$+\left(\varepsilon_1(\varepsilon_3-\varepsilon_2)RT-\varepsilon_2\varepsilon_3\left(g_{\mathrm{XAl}}^{10}-g_{\mathrm{XAl}}^{01}\right)\right)\left((\varepsilon_2-x_{\mathrm{X}}\beta_{\mathrm{AlAl}})g_{\mathrm{XAl}}^{10}\right.$$

$$\left.+(\varepsilon_3-(1-x_{\mathrm{X}})\beta_{\mathrm{XX}})g_{\mathrm{XAl}}^{01}\right)$$

$$=RT\varepsilon_1\left(g_{\mathrm{XAl}}^{10}-g_{\mathrm{XAl}}^{01}\right)\left(\beta_{\mathrm{AlAl}}\beta_{\mathrm{XX}}x_{\mathrm{X}}(1-x_{\mathrm{X}})-(\varepsilon_2-x_{\mathrm{X}}\beta_{\mathrm{AlAl}})(\varepsilon_3-(1-x_{\mathrm{X}})\beta_{\mathrm{XX}})\right)$$

$$+\left(g_{\mathrm{XAl}}^{10}-g_{\mathrm{XAl}}^{01}\right)\varepsilon_2\varepsilon_3\left((\varepsilon_2-x_{\mathrm{X}}\beta_{\mathrm{AlAl}})g_{\mathrm{XAl}}^{10}+(\varepsilon_3-(1-x_{\mathrm{X}})\beta_{\mathrm{XX}})g_{\mathrm{XAl}}^{01}\right)$$

$$+\varepsilon_1(\varepsilon_3-\varepsilon_2)RT\left((\varepsilon_2-x_{\mathrm{X}}\beta_{\mathrm{AlAl}})g_{\mathrm{XAl}}^{10}+(\varepsilon_3-(1-x_{\mathrm{X}})\beta_{\mathrm{XX}})g_{\mathrm{XAl}}^{01}\right)$$

$$-\varepsilon_2\varepsilon_3\left(g_{\mathrm{XAl}}^{10}-g_{\mathrm{XAl}}^{01}\right)\left((\varepsilon_2-x_{\mathrm{X}}\beta_{\mathrm{AlAl}})g_{\mathrm{XAl}}^{10}+(\varepsilon_3-(1-x_{\mathrm{X}})\beta_{\mathrm{XX}})g_{\mathrm{XAl}}^{01}\right)$$

$$=RT\varepsilon_1\left(g_{\mathrm{XAl}}^{10}-g_{\mathrm{XAl}}^{01}\right)\left(\beta_{\mathrm{AlAl}}\beta_{\mathrm{XX}}x_{\mathrm{X}}(1-x_{\mathrm{X}})-(\varepsilon_2-x_{\mathrm{X}}\beta_{\mathrm{AlAl}})(\varepsilon_3-(1-x_{\mathrm{X}})\beta_{\mathrm{XX}})\right)$$

$$+\varepsilon_1(\varepsilon_3-\varepsilon_2)RT\left((\varepsilon_2-x_{\mathrm{X}}\beta_{\mathrm{AlAl}})g_{\mathrm{XAl}}^{10}+(\varepsilon_3-(1-x_{\mathrm{X}})\beta_{\mathrm{XX}})g_{\mathrm{XAl}}^{01}\right)$$

$$= RT\varepsilon_1 \Big(\big(g^{10}_{\mathrm{XAl}} - g^{01}_{\mathrm{XAl}}\big)\big(\beta_{\mathrm{AlAl}}\beta_{\mathrm{XX}}x_{\mathrm{X}}(1-x_{\mathrm{X}}) - (\varepsilon_2 - x_{\mathrm{X}}\beta_{\mathrm{AlAl}})(\varepsilon_3 - (1-x_{\mathrm{X}})\beta_{\mathrm{XX}})\big)$$

$$+ (\varepsilon_3 - \varepsilon_2)\Big((\varepsilon_2 - x_{\mathrm{X}}\beta_{\mathrm{AlAl}})g^{10}_{\mathrm{XAl}} + (\varepsilon_3 - (1-x_{\mathrm{X}})\beta_{\mathrm{XX}})g^{01}_{\mathrm{XAl}}\Big)\Big)$$

$$= RT\varepsilon_1 \Big(g^{10}_{\mathrm{XAl}}\big(\beta_{\mathrm{AlAl}}\beta_{\mathrm{XX}}x_{\mathrm{X}}(1-x_{\mathrm{X}}) - (\varepsilon_2 - x_{\mathrm{X}}\beta_{\mathrm{AlAl}})(\varepsilon_3 - (1-x_{\mathrm{X}})\beta_{\mathrm{XX}})$$

$$+ (\varepsilon_3 - \varepsilon_2)(\varepsilon_2 - x_{\mathrm{X}}\beta_{\mathrm{AlAl}})\big)$$

$$+ g^{01}_{\mathrm{XAl}}\Big((\varepsilon_3 - \varepsilon_2)(\varepsilon_3 - (1-x_{\mathrm{X}})\beta_{\mathrm{XX}})$$

$$- \big(\beta_{\mathrm{AlAl}}\beta_{\mathrm{XX}}x_{\mathrm{X}}(1-x_{\mathrm{X}}) - (\varepsilon_2 - x_{\mathrm{X}}\beta_{\mathrm{AlAl}})(\varepsilon_3 - (1-x_{\mathrm{X}})\beta_{\mathrm{XX}})\big)\Big)\Big)$$

$$= RT\varepsilon_1 \Big(g^{10}_{\mathrm{XAl}}\Big(\beta_{\mathrm{AlAl}}\beta_{\mathrm{XX}}x_{\mathrm{X}}(1-x_{\mathrm{X}}) + \big(\varepsilon_3 - \varepsilon_2 - (\varepsilon_3 - (1-x_{\mathrm{X}})\beta_{\mathrm{XX}})\big)(\varepsilon_2 - x_{\mathrm{X}}\beta_{\mathrm{AlAl}})\Big)$$

$$+ g^{01}_{\mathrm{XAl}}\big((\varepsilon_3 - (1-x_{\mathrm{X}})\beta_{\mathrm{XX}})(\varepsilon_3 - \varepsilon_2 + \varepsilon_2 - x_{\mathrm{X}}\beta_{\mathrm{AlAl}}) - \beta_{\mathrm{AlAl}}\beta_{\mathrm{XX}}x_{\mathrm{X}}(1-x_{\mathrm{X}})\big)\Big)$$

$$= RT\varepsilon_1 \Big(g^{10}_{\mathrm{XAl}}\big(\beta_{\mathrm{AlAl}}\beta_{\mathrm{XX}}x_{\mathrm{X}}(1-x_{\mathrm{X}}) - (\varepsilon_2 - (1-x_{\mathrm{X}})\beta_{\mathrm{XX}})(\varepsilon_2 - x_{\mathrm{X}}\beta_{\mathrm{AlAl}})\big)$$

$$+ g^{01}_{\mathrm{XAl}}\big((\varepsilon_3 - (1-x_{\mathrm{X}})\beta_{\mathrm{XX}})(\varepsilon_3 - x_{\mathrm{X}}\beta_{\mathrm{AlAl}}) - \beta_{\mathrm{AlAl}}\beta_{\mathrm{XX}}x_{\mathrm{X}}(1-x_{\mathrm{X}})\big)\Big)$$

$$= RT\varepsilon_1 \Big(g^{10}_{\mathrm{XAl}}\Big(\beta_{\mathrm{AlAl}}\beta_{\mathrm{XX}}x_{\mathrm{X}}(1-x_{\mathrm{X}}) - \big(\varepsilon_2^2 - \varepsilon_1\varepsilon_2 + \beta_{\mathrm{AlAl}}\beta_{\mathrm{XX}}x_{\mathrm{X}}(1-x_{\mathrm{X}})\big)\Big)$$

$$+ g^{01}_{\mathrm{XAl}}\Big(\varepsilon_3^2 - \varepsilon_3\varepsilon_1 + \beta_{\mathrm{AlAl}}\beta_{\mathrm{XX}}x_{\mathrm{X}}(1-x_{\mathrm{X}}) - \beta_{\mathrm{AlAl}}\beta_{\mathrm{XX}}x_{\mathrm{X}}(1-x_{\mathrm{X}})\Big)\Big)$$

$$= RT\varepsilon_1 \Big(\varepsilon_2 g^{10}_{\mathrm{XAl}}(\varepsilon_1 - \varepsilon_2) + \varepsilon_3 g^{01}_{\mathrm{XAl}}(\varepsilon_3 - \varepsilon_1)\Big)$$

$$= RT\varepsilon_1 \Big(\varepsilon_2 g^{10}_{\mathrm{XAl}}(\varepsilon_1 - \varepsilon_2) - \varepsilon_3 g^{01}_{\mathrm{XAl}}(\varepsilon_1 - \varepsilon_3)\Big) \qquad \text{(A.149)}$$

Putting into $\Delta\mu^{\mathrm{xs}}_{\mathrm{X}}$ (A.150):

$$\Delta\mu^{\mathrm{xs}}_{\mathrm{X}}(x_{\mathrm{X}}) = \frac{x_{\mathrm{XAl}}}{2\varepsilon_1}(1-x_{\mathrm{X}})\big(g^{10}_{\mathrm{XAl}} - g^{01}_{\mathrm{XAl}}\big)$$

$$+ \frac{x_{\mathrm{XAl}}(1-x_{\mathrm{X}})}{2\varepsilon_1} \times \Big(\varepsilon_1(\varepsilon_3 - \varepsilon_2)RT - \varepsilon_2\varepsilon_3\big(g^{10}_{\mathrm{XAl}} - g^{01}_{\mathrm{XAl}}\big)\Big)$$

$$\times \Big((\varepsilon_2 - x_{\mathrm{X}}\beta_{\mathrm{AlAl}})g^{10}_{\mathrm{XAl}} + (\varepsilon_3 - (1-x_{\mathrm{X}})\beta_{\mathrm{XX}})g^{01}_{\mathrm{XAl}}\Big)$$

$$\div \Big(RT\varepsilon_1\big(\beta_{\mathrm{AlAl}}\beta_{\mathrm{XX}}x_{\mathrm{X}}(1-x_{\mathrm{X}}) - (\varepsilon_2 - x_{\mathrm{X}}\beta_{\mathrm{AlAl}})(\varepsilon_3 - (1-x_{\mathrm{X}})\beta_{\mathrm{XX}})\big)$$

$$+ \varepsilon_2\varepsilon_3\Big((\varepsilon_2 - x_{\mathrm{X}}\beta_{\mathrm{AlAl}})g^{10}_{\mathrm{XAl}} + (\varepsilon_3 - (1-x_{\mathrm{X}})\beta_{\mathrm{XX}})g^{01}_{\mathrm{XAl}}\Big)\Big)$$

$$+\frac{RT}{2\varepsilon_6}\left(2\beta_{\mathrm{AlAl}}\varepsilon_{\mathrm{X}}+x_{\mathrm{XAl}}(2\beta_{\mathrm{AlX}}-\beta_{\mathrm{AlAl}})(\varepsilon_{\mathrm{X}}-\varepsilon_{\mathrm{Al}})\right)$$

$$-\frac{RTx_{\mathrm{XAl}}(1-x_{\mathrm{X}})}{2\varepsilon_6}\times\left(\varepsilon_1(\varepsilon_3-\varepsilon_2)RT-\varepsilon_2\varepsilon_3\left(g_{\mathrm{XAl}}^{10}-g_{\mathrm{XAl}}^{01}\right)\right)$$

$$\times\left(\beta_{\mathrm{XX}}\varepsilon_{\mathrm{Al}}(2\beta_{\mathrm{AlX}}-\beta_{\mathrm{AlAl}})+\beta_{\mathrm{AlAl}}\varepsilon_{\mathrm{X}}(2\beta_{\mathrm{XAl}}-\beta_{\mathrm{XX}})\right)$$

$$\div\left(RT\varepsilon_1\left(\beta_{\mathrm{AlAl}}\beta_{\mathrm{XX}}x_{\mathrm{X}}(1-x_{\mathrm{X}})-(\varepsilon_2-x_{\mathrm{X}}\beta_{\mathrm{AlAl}})(\varepsilon_3-(1-x_{\mathrm{X}})\beta_{\mathrm{XX}})\right)\right.$$

$$\left.+\varepsilon_2\varepsilon_3\left((\varepsilon_2-x_{\mathrm{X}}\beta_{\mathrm{AlAl}})g_{\mathrm{XAl}}^{10}+(\varepsilon_3-(1-x_{\mathrm{X}})\beta_{\mathrm{XX}})g_{\mathrm{XAl}}^{01}\right)\right)$$

$$\Delta\mu_{\mathrm{X}}^{\mathrm{xs}}(x_{\mathrm{X}})=x_{\mathrm{XAl}}(1-x_{\mathrm{X}})RT\left(\varepsilon_2(\varepsilon_1-\varepsilon_2)g_{\mathrm{XAl}}^{10}-\varepsilon_3(\varepsilon_1-\varepsilon_3)g_{\mathrm{XAl}}^{01}\right)$$

$$\div\left(2\left(RT\varepsilon_1\left(\beta_{\mathrm{AlAl}}\beta_{\mathrm{XX}}x_{\mathrm{X}}(1-x_{\mathrm{X}})-(\varepsilon_2-x_{\mathrm{X}}\beta_{\mathrm{AlAl}})(\varepsilon_3-(1-x_{\mathrm{X}})\beta_{\mathrm{XX}})\right)\right.\right.$$

$$\left.\left.+\varepsilon_2\varepsilon_3\left((\varepsilon_2-x_{\mathrm{X}}\beta_{\mathrm{AlAl}})g_{\mathrm{XAl}}^{10}+(\varepsilon_3-(1-x_{\mathrm{X}})\beta_{\mathrm{XX}})g_{\mathrm{XAl}}^{01}\right)\right)\right)$$

$$+\frac{RT}{2\varepsilon_6}\left(2\beta_{\mathrm{AlAl}}\varepsilon_{\mathrm{X}}+x_{\mathrm{XAl}}(2\beta_{\mathrm{AlX}}-\beta_{\mathrm{AlAl}})(\varepsilon_{\mathrm{X}}-\varepsilon_{\mathrm{Al}})\right)$$

$$+\frac{RTx_{\mathrm{XAl}}(1-x_{\mathrm{X}})}{2\varepsilon_6}\times\left(\varepsilon_1(\varepsilon_2-\varepsilon_3)RT+\varepsilon_2\varepsilon_3\left(g_{\mathrm{XAl}}^{10}-g_{\mathrm{XAl}}^{01}\right)\right)$$

$$\times\left(\beta_{\mathrm{XX}}\varepsilon_{\mathrm{Al}}(2\beta_{\mathrm{AlX}}-\beta_{\mathrm{AlAl}})+\beta_{\mathrm{AlAl}}\varepsilon_{\mathrm{X}}(2\beta_{\mathrm{XAl}}-\beta_{\mathrm{XX}})\right)$$

$$\div\left(RT\varepsilon_1\left(\beta_{\mathrm{AlAl}}\beta_{\mathrm{XX}}x_{\mathrm{X}}(1-x_{\mathrm{X}})-(\varepsilon_2-x_{\mathrm{X}}\beta_{\mathrm{AlAl}})(\varepsilon_3-(1-x_{\mathrm{X}})\beta_{\mathrm{XX}})\right)\right.$$

$$\left.+\varepsilon_2\varepsilon_3\left((\varepsilon_2-x_{\mathrm{X}}\beta_{\mathrm{AlAl}})g_{\mathrm{XAl}}^{10}+(\varepsilon_3-(1-x_{\mathrm{X}})\beta_{\mathrm{XX}})g_{\mathrm{XAl}}^{01}\right)\right) \tag{A.150}$$

Putting into the expression for $\Delta\mu_{\mathrm{Al}}^{\mathrm{xs}}$ (A.151):

$$\Delta\mu_{\mathrm{Al}}^{\mathrm{xs}}=\frac{1}{2\varepsilon_1\varepsilon_6}\left[\varepsilon_6x_{\mathrm{X}}x_{\mathrm{XAl}}\left(g_{\mathrm{XAl}}^{01}-g_{\mathrm{XAl}}^{10}\right)+RT\varepsilon_1\left(2\beta_{\mathrm{XX}}\varepsilon_{\mathrm{Al}}+x_{\mathrm{XAl}}(2\beta_{\mathrm{XAl}}-\beta_{\mathrm{XX}})(\varepsilon_{\mathrm{Al}}-\varepsilon_{\mathrm{X}})\right)\right]$$

$$+\frac{x_{\mathrm{X}}x'_{\mathrm{XAl}}}{2\varepsilon_6^2}\left[RT\varepsilon_1\left(\beta_{\mathrm{AlAl}}\varepsilon_{\mathrm{X}}(2\beta_{\mathrm{XAl}}-\beta_{\mathrm{XX}})+\beta_{\mathrm{XX}}\varepsilon_{\mathrm{Al}}(2\beta_{\mathrm{AlX}}-\beta_{\mathrm{AlAl}})\right)\right.$$

$$\left.-\varepsilon_6\left((\varepsilon_2-x_{\mathrm{X}}\beta_{\mathrm{AlAl}})g_{\mathrm{XAl}}^{10}+(\varepsilon_3-(1-x_{\mathrm{X}})\beta_{\mathrm{XX}})g_{\mathrm{XAl}}^{01}\right)\right]$$

$$\Delta\mu_{\mathrm{Al}}^{\mathrm{xs}}=\frac{x_{\mathrm{XAl}}}{2\varepsilon_1}x_{\mathrm{X}}\left(g_{\mathrm{XAl}}^{01}-g_{\mathrm{XAl}}^{10}\right)+\frac{RT}{2\varepsilon_6}\left(2\beta_{\mathrm{XX}}\varepsilon_{\mathrm{Al}}+x_{\mathrm{XAl}}(2\beta_{\mathrm{XAl}}-\beta_{\mathrm{XX}})(\varepsilon_{\mathrm{Al}}-\varepsilon_{\mathrm{X}})\right)$$

$$-\frac{x_{\mathrm{X}}x_{\mathrm{XAl}}}{2\varepsilon_1\varepsilon_6}\times\Big(\varepsilon_1(\varepsilon_3-\varepsilon_2)RT-\varepsilon_2\varepsilon_3\big(g^{10}_{\mathrm{XAl}}-g^{01}_{\mathrm{XAl}}\big)\Big)$$

$$\times\,\varepsilon_6\Big((\varepsilon_2-x_{\mathrm{X}}\beta_{\mathrm{AlAl}})g^{10}_{\mathrm{XAl}}+(\varepsilon_3-(1-x_{\mathrm{X}})\beta_{\mathrm{XX}})g^{01}_{\mathrm{XAl}}\Big)$$

$$\div\Big(RT\varepsilon_1\big(\beta_{\mathrm{AlAl}}\beta_{\mathrm{XX}}x_{\mathrm{X}}(1-x_{\mathrm{X}})-(\varepsilon_2-x_{\mathrm{X}}\beta_{\mathrm{AlAl}})(\varepsilon_3-(1-x_{\mathrm{X}})\beta_{\mathrm{XX}})\big)$$

$$+\,\varepsilon_2\varepsilon_3\Big((\varepsilon_2-x_{\mathrm{X}}\beta_{\mathrm{AlAl}})g^{10}_{\mathrm{XAl}}+(\varepsilon_3-(1-x_{\mathrm{X}})\beta_{\mathrm{XX}})g^{01}_{\mathrm{XAl}}\Big)\Big)$$

$$+\frac{x_{\mathrm{X}}x_{\mathrm{XAl}}}{2\varepsilon_1\varepsilon_6}\times\Big(\varepsilon_1(\varepsilon_3-\varepsilon_2)RT-\varepsilon_2\varepsilon_3\big(g^{10}_{\mathrm{XAl}}-g^{01}_{\mathrm{XAl}}\big)\Big)$$

$$\times\,RT\varepsilon_1\big(\beta_{\mathrm{AlAl}}\varepsilon_{\mathrm{X}}(2\beta_{\mathrm{XAl}}-\beta_{\mathrm{XX}})+\beta_{\mathrm{XX}}\varepsilon_{\mathrm{Al}}(2\beta_{\mathrm{AlX}}-\beta_{\mathrm{AlAl}})\big)$$

$$\div\Big(RT\varepsilon_1\big(\beta_{\mathrm{AlAl}}\beta_{\mathrm{XX}}x_{\mathrm{X}}(1-x_{\mathrm{X}})-(\varepsilon_2-x_{\mathrm{X}}\beta_{\mathrm{AlAl}})(\varepsilon_3-(1-x_{\mathrm{X}})\beta_{\mathrm{XX}})\big)$$

$$+\,\varepsilon_2\varepsilon_3\Big((\varepsilon_2-x_{\mathrm{X}}\beta_{\mathrm{AlAl}})g^{10}_{\mathrm{XAl}}+(\varepsilon_3-(1-x_{\mathrm{X}})\beta_{\mathrm{XX}})g^{01}_{\mathrm{XAl}}\Big)\Big)$$

$$\Delta\mu^{\mathrm{xs}}_{\mathrm{Al}}(x_{\mathrm{X}})=-\frac{x_{\mathrm{XAl}}}{2\varepsilon_1}x_{\mathrm{X}}\big(g^{10}_{\mathrm{XAl}}-g^{01}_{\mathrm{XAl}}\big)$$

$$-\frac{x_{\mathrm{X}}x_{\mathrm{XAl}}}{2\varepsilon_1}\times\Big(\varepsilon_1(\varepsilon_3-\varepsilon_2)RT-\varepsilon_2\varepsilon_3\big(g^{10}_{\mathrm{XAl}}-g^{01}_{\mathrm{XAl}}\big)\Big)$$

$$\times\Big((\varepsilon_2-x_{\mathrm{X}}\beta_{\mathrm{AlAl}})g^{10}_{\mathrm{XAl}}+(\varepsilon_3-(1-x_{\mathrm{X}})\beta_{\mathrm{XX}})g^{01}_{\mathrm{XAl}}\Big)$$

$$\div\Big(RT\varepsilon_1\big(\beta_{\mathrm{AlAl}}\beta_{\mathrm{XX}}x_{\mathrm{X}}(1-x_{\mathrm{X}})-(\varepsilon_2-x_{\mathrm{X}}\beta_{\mathrm{AlAl}})(\varepsilon_3-(1-x_{\mathrm{X}})\beta_{\mathrm{XX}})\big)$$

$$+\,\varepsilon_2\varepsilon_3\Big((\varepsilon_2-x_{\mathrm{X}}\beta_{\mathrm{AlAl}})g^{10}_{\mathrm{XAl}}+(\varepsilon_3-(1-x_{\mathrm{X}})\beta_{\mathrm{XX}})g^{01}_{\mathrm{XAl}}\Big)\Big)$$

$$+\frac{RT}{2\varepsilon_6}\big(2\beta_{\mathrm{XX}}\varepsilon_{\mathrm{Al}}+x_{\mathrm{XAl}}(2\beta_{\mathrm{XAl}}-\beta_{\mathrm{XX}})(\varepsilon_{\mathrm{Al}}-\varepsilon_{\mathrm{X}})\big)$$

$$+\frac{RTx_{\mathrm{X}}x_{\mathrm{XAl}}}{2\varepsilon_6}\times\Big(\varepsilon_1(\varepsilon_3-\varepsilon_2)RT-\varepsilon_2\varepsilon_3\big(g^{10}_{\mathrm{XAl}}-g^{01}_{\mathrm{XAl}}\big)\Big)$$

$$\times\,\big(\beta_{\mathrm{AlAl}}\varepsilon_{\mathrm{X}}(2\beta_{\mathrm{XAl}}-\beta_{\mathrm{XX}})+\beta_{\mathrm{XX}}\varepsilon_{\mathrm{Al}}(2\beta_{\mathrm{AlX}}-\beta_{\mathrm{AlAl}})\big)$$

$$\div\Big(RT\varepsilon_1\big(\beta_{\mathrm{AlAl}}\beta_{\mathrm{XX}}x_{\mathrm{X}}(1-x_{\mathrm{X}})-(\varepsilon_2-x_{\mathrm{X}}\beta_{\mathrm{AlAl}})(\varepsilon_3-(1-x_{\mathrm{X}})\beta_{\mathrm{XX}})\big)$$

$$+\,\varepsilon_2\varepsilon_3\Big((\varepsilon_2-x_{\mathrm{X}}\beta_{\mathrm{AlAl}})g^{10}_{\mathrm{XAl}}+(\varepsilon_3-(1-x_{\mathrm{X}})\beta_{\mathrm{XX}})g^{01}_{\mathrm{XAl}}\Big)\Big)$$

$$\Delta\mu_{\mathrm{Al}}^{\mathrm{xs}}(x_{\mathrm{X}}) = -x_{\mathrm{XAl}}x_{\mathrm{X}}RT\left(\varepsilon_2(\varepsilon_1-\varepsilon_2)g_{\mathrm{XAl}}^{10}-\varepsilon_3(\varepsilon_1-\varepsilon_3)g_{\mathrm{XAl}}^{01}\right)$$
$$\div\left(2\left(RT\varepsilon_1\left(\beta_{\mathrm{AlAl}}\beta_{\mathrm{XX}}x_{\mathrm{X}}(1-x_{\mathrm{X}})-(\varepsilon_2-x_{\mathrm{X}}\beta_{\mathrm{AlAl}})(\varepsilon_3-(1-x_{\mathrm{X}})\beta_{\mathrm{XX}})\right)\right.\right.$$
$$\left.\left.+\varepsilon_2\varepsilon_3\left((\varepsilon_2-x_{\mathrm{X}}\beta_{\mathrm{AlAl}})g_{\mathrm{XAl}}^{10}+(\varepsilon_3-(1-x_{\mathrm{X}})\beta_{\mathrm{XX}})g_{\mathrm{XAl}}^{01}\right)\right)\right)$$
$$+\frac{RT}{2\varepsilon_6}\left(2\beta_{\mathrm{XX}}\varepsilon_{\mathrm{Al}}+x_{\mathrm{XAl}}(2\beta_{\mathrm{XAl}}-\beta_{\mathrm{XX}})(\varepsilon_{\mathrm{Al}}-\varepsilon_{\mathrm{X}})\right)$$
$$-\frac{RTx_{\mathrm{XAl}}x_{\mathrm{X}}}{2\varepsilon_6}\times\left(\varepsilon_1(\varepsilon_2-\varepsilon_3)RT+\varepsilon_2\varepsilon_3\left(g_{\mathrm{XAl}}^{10}-g_{\mathrm{XAl}}^{01}\right)\right)$$
$$\times\left(\beta_{\mathrm{XX}}\varepsilon_{\mathrm{Al}}(2\beta_{\mathrm{AlX}}-\beta_{\mathrm{AlAl}})+\beta_{\mathrm{AlAl}}\varepsilon_{\mathrm{X}}(2\beta_{\mathrm{XAl}}-\beta_{\mathrm{XX}})\right)$$
$$\div\left(RT\varepsilon_1\left(\beta_{\mathrm{AlAl}}\beta_{\mathrm{XX}}x_{\mathrm{X}}(1-x_{\mathrm{X}})-(\varepsilon_2-x_{\mathrm{X}}\beta_{\mathrm{AlAl}})(\varepsilon_3-(1-x_{\mathrm{X}})\beta_{\mathrm{XX}})\right)\right.$$
$$\left.+\varepsilon_2\varepsilon_3\left((\varepsilon_2-x_{\mathrm{X}}\beta_{\mathrm{AlAl}})g_{\mathrm{XAl}}^{10}+(\varepsilon_3-(1-x_{\mathrm{X}})\beta_{\mathrm{XX}})g_{\mathrm{XAl}}^{01}\right)\right) \quad \text{(A.151)}$$

Simplifying expressions for $\Delta\mu_{\mathrm{X}}^{\mathrm{xs}}$ (A.152) and $\Delta\mu_{\mathrm{Al}}^{\mathrm{xs}}$ (A.153):

$$\Delta\mu_{\mathrm{X}}^{\mathrm{xs}}(x_{\mathrm{X}}) = \frac{RT}{2\varepsilon_6}\sigma_{\mathrm{X}}+(1-x_{\mathrm{X}})\frac{RTx_{\mathrm{XAl}}}{2\sigma_1}\left(\frac{\sigma_2}{\varepsilon_6}+\sigma_3\right) \quad \text{(A.152)}$$

$$\Delta\mu_{\mathrm{Al}}^{\mathrm{xs}}(x_{\mathrm{X}}) = \frac{RT}{2\varepsilon_6}\sigma_{\mathrm{Al}}-x_{\mathrm{X}}\frac{RTx_{\mathrm{XAl}}}{2\sigma_1}\left(\frac{\sigma_2}{\varepsilon_6}+\sigma_3\right) \quad \text{(A.153)}$$

Where σ_{X} (A.154), σ_{Al} (A.155), σ_1 (A.156), σ_2 (A.157), and σ_3 (A.158) are defined as follows:

$$\sigma_{\mathrm{X}} = 2\beta_{\mathrm{AlAl}}\varepsilon_{\mathrm{X}}+x_{\mathrm{XAl}}(2\beta_{\mathrm{AlX}}-\beta_{\mathrm{AlAl}})(\varepsilon_{\mathrm{X}}-\varepsilon_{\mathrm{Al}}) \quad \text{(A.154)}$$

$$\sigma_{\mathrm{Al}} = 2\beta_{\mathrm{XX}}\varepsilon_{\mathrm{Al}}+x_{\mathrm{XAl}}(2\beta_{\mathrm{XAl}}-\beta_{\mathrm{XX}})(\varepsilon_{\mathrm{Al}}-\varepsilon_{\mathrm{X}}) \quad \text{(A.155)}$$

$$\sigma_1 = RT\varepsilon_1\left(\beta_{\mathrm{AlAl}}\beta_{\mathrm{XX}}x_{\mathrm{X}}(1-x_{\mathrm{X}})-(\varepsilon_2-x_{\mathrm{X}}\beta_{\mathrm{AlAl}})(\varepsilon_3-(1-x_{\mathrm{X}})\beta_{\mathrm{XX}})\right)$$
$$+\varepsilon_2\varepsilon_3\left((\varepsilon_2-x_{\mathrm{X}}\beta_{\mathrm{AlAl}})g_{\mathrm{XAl}}^{10}+(\varepsilon_3-(1-x_{\mathrm{X}})\beta_{\mathrm{XX}})g_{\mathrm{XAl}}^{01}\right) \quad \text{(A.156)}$$

$$\sigma_2 = \left(\varepsilon_1(\varepsilon_2-\varepsilon_3)RT+\varepsilon_2\varepsilon_3\left(g_{\mathrm{XAl}}^{10}-g_{\mathrm{XAl}}^{01}\right)\right)\left(\beta_{\mathrm{XX}}\varepsilon_{\mathrm{Al}}(2\beta_{\mathrm{AlX}}-\beta_{\mathrm{AlAl}})\right.$$
$$\left.+\beta_{\mathrm{AlAl}}\varepsilon_{\mathrm{X}}(2\beta_{\mathrm{XAl}}-\beta_{\mathrm{XX}})\right) \quad \text{(A.157)}$$

$$\sigma_3 = \varepsilon_2(\varepsilon_1-\varepsilon_2)g_{\mathrm{XAl}}^{10}-\varepsilon_3(\varepsilon_1-\varepsilon_3)g_{\mathrm{XAl}}^{01} \quad \text{(A.158)}$$

A.5. Other mathematical derivations

A.5.1. Bragg-Williams mixing: linear sums

The extra term added to ΔG^{ox} for a ternary compound $\mathrm{Al}_{c_{\mathrm{Al}}}\mathrm{X}_{c_{\mathrm{X}}}\mathrm{O}_b$ by a Bragg-Williams Model over an ideal model, $\Delta G^{\mathrm{ox,BWB}}_{\mathrm{Al}_{c_{\mathrm{Al}}}\mathrm{X}_{c_{\mathrm{X}}}\mathrm{O}_b}$ (A.159), can be expressed in terms of the stoichiometry-weighted sum of two functions $f_{\mathrm{X}}\left({}^{i}L_{\mathrm{XAl}}, x_{\mathrm{X}}\right)$ (A.160) and $f_{\mathrm{Al}}\left({}^{i}L_{\mathrm{XAl}}, x_{\mathrm{X}}\right)$ (A.161).

$$\Delta G^{\mathrm{ox,BWB}}_{\mathrm{Al}_{c_{\mathrm{Al}}}\mathrm{X}_{c_{\mathrm{X}}}\mathrm{O}_b} = {}^{0}L_{\mathrm{XAl}}(m_{\mathrm{X}}{x_{\mathrm{Al}}}^{2} + m_{\mathrm{Al}}x_{\mathrm{X}}^{2})$$

$$+\sum_{i\geq 1} {}^{i}L_{\mathrm{XAl}}(x_{\mathrm{X}} - x_{\mathrm{Al}})^{i-1}[m_{\mathrm{X}}{x_{\mathrm{Al}}}^{2}(x_{\mathrm{X}} - x_{\mathrm{Al}} + 2ix_{\mathrm{X}}) + m_{\mathrm{Al}}x_{\mathrm{X}}^{2}(x_{\mathrm{X}} - x_{\mathrm{Al}} - 2ix_{\mathrm{Al}})]$$

$$= \sum_{i\geq 0} {}^{i}L_{\mathrm{XAl}}(2x_{\mathrm{X}} - 1)^{i-1}\left[m_{\mathrm{X}}(1 - x_{\mathrm{X}})^{2}(2x_{\mathrm{X}} - 1 + 2ix_{\mathrm{X}}) + m_{\mathrm{Al}}x_{\mathrm{X}}^{2}\left(2x_{\mathrm{X}} - 1 - 2i(1 - x_{\mathrm{X}})\right)\right]$$

$$= m_{\mathrm{X}}\sum_{i\geq 0} {}^{i}L_{\mathrm{XAl}}(2x_{\mathrm{X}} - 1)^{i-1}[(1 - x_{\mathrm{X}})^{2}(2x_{\mathrm{X}} - 1 + 2ix_{\mathrm{X}})]$$

$$+ m_{\mathrm{Al}}\sum_{i\geq 0} {}^{i}L_{\mathrm{XAl}}(2x_{\mathrm{X}} - 1)^{i-1}\left[x_{\mathrm{X}}^{2}\left(2x_{\mathrm{X}} - 1 - 2i(1 - x_{\mathrm{X}})\right)\right]$$

$$\Delta G^{\mathrm{ox,BWB}}_{\mathrm{Al}_{c_{\mathrm{Al}}}\mathrm{X}_{c_{\mathrm{X}}}\mathrm{O}_b} = m_{\mathrm{X}}f_{\mathrm{X}}\left({}^{i}L_{\mathrm{XAl}}, x_{\mathrm{X}}\right) + m_{\mathrm{Al}}f_{\mathrm{Al}}\left({}^{i}L_{\mathrm{XAl}}, x_{\mathrm{X}}\right) \tag{A.159}$$

$$f_{\mathrm{X}}\left({}^{i}L_{\mathrm{XAl}}, x_{\mathrm{X}}\right) = \sum_{i\geq 0} {}^{i}L_{\mathrm{XAl}}(2x_{\mathrm{X}} - 1)^{i-1}[(1 - x_{\mathrm{X}})^{2}(2x_{\mathrm{X}} - 1 + 2ix_{\mathrm{X}})] \tag{A.160}$$

$$f_{\mathrm{Al}}\left({}^{i}L_{\mathrm{XAl}}, x_{\mathrm{X}}\right) = \sum_{i\geq 0} {}^{i}L_{\mathrm{XAl}}(2x_{\mathrm{X}} - 1)^{i-1}\left[x_{\mathrm{X}}^{2}\left(2x_{\mathrm{X}} - 1 - 2i(1 - x_{\mathrm{X}})\right)\right] \tag{A.161}$$

The $\Delta G^{\mathrm{ox,BWB}}$ contribution for unary oxides Al_2O_3 (A.162) and $\mathrm{X}_{c_{\mathrm{X}}}\mathrm{O}_b$ (A.163), can be evaluated in terms of only $f_{\mathrm{X}}\left({}^{i}L_{\mathrm{XAl}}, x_{\mathrm{X}}\right)$ and $f_{\mathrm{Al}}\left({}^{i}L_{\mathrm{XAl}}, x_{\mathrm{X}}\right)$.

$$\Delta G^{\mathrm{ox,BWB}}_{\mathrm{X}_{c_{\mathrm{X}}}\mathrm{O}_b} = m_{\mathrm{X}}f_{\mathrm{X}}\left({}^{i}L_{\mathrm{XAl}}, x_{\mathrm{X}}\right) \tag{A.162}$$

$$\Delta G^{\mathrm{ox,BWB}}_{\mathrm{Al_2O_3}} = \frac{4}{3}f_{\mathrm{Al}}\left({}^{i}L_{\mathrm{XAl}}, x_{\mathrm{X}}\right) \tag{A.163}$$

If the solute forms a z+ ion upon oxidation, giving the solute oxide the formula $\mathrm{X_2O_z}$, then by charge neutrality (A.164):

$$c_{\mathrm{X}} z = 2b$$

$$m_{\mathrm{X}} = \frac{2c_{\mathrm{X}}}{b} = \frac{4}{z}$$

$$\Delta G^{\mathrm{ox,BWB}}_{\mathrm{X}_{c_{\mathrm{X}}}\mathrm{O}_b} = \frac{4}{z} f_{\mathrm{X}}\left({}^{i}L_{\mathrm{XAl}}, x_{\mathrm{X}}\right) \tag{A.164}$$

Therefore, $\Delta G^{\mathrm{ox,BWB}}_{\mathrm{Al}_{c_{\mathrm{Al}}}\mathrm{X}_{c_{\mathrm{X}}}\mathrm{O}_b}$ can be expressed as a linear sum of the two unary oxides (A.165).

$$\Delta G^{\mathrm{ox,BWB}}_{\mathrm{Al}_{c_{\mathrm{Al}}}\mathrm{X}_{c_{\mathrm{X}}}\mathrm{O}_b} = m_{\mathrm{X}} f_{\mathrm{X}}\left({}^{i}L_{\mathrm{XAl}}, x_{\mathrm{X}}\right) + m_{\mathrm{Al}} f_{\mathrm{Al}}\left({}^{i}L_{\mathrm{XAl}}, x_{\mathrm{X}}\right)$$

$$\Delta G^{\mathrm{ox,BWB}}_{\mathrm{Al}_{c_{\mathrm{Al}}}\mathrm{X}_{c_{\mathrm{X}}}\mathrm{O}_b} = \frac{z m_{\mathrm{X}}}{4} \Delta G^{\mathrm{ox,BWB}}_{\mathrm{X}_{c_{\mathrm{X}}}\mathrm{O}_b} + \frac{3 m_{\mathrm{Al}}}{4} \Delta G^{\mathrm{ox,BWB}}_{\mathrm{Al_2O_3}} \tag{A.165}$$

If the binary oxide is comprised of α_{X} formula units of $\mathrm{X_2O_z}$ and α_{Al} formula units of $\mathrm{Al_2O_3}$, m_{X} (A.169) and m_{Al} (A.170) can be expressed in terms of α_i, which also shows that the contribution to the number of oxygen atoms in the formula unit from X and Al is $z\alpha_{\mathrm{X}}$ and $3\alpha_{\mathrm{Al}}$, respectively (A.167).

$$\mathrm{Al}_{c_{\mathrm{Al}}}\mathrm{X}_{c_{\mathrm{X}}}\mathrm{O}_b = \alpha_{\mathrm{X}}\mathrm{X_2O_z} + \alpha_{\mathrm{Al}}\mathrm{Al_2O_3} = \mathrm{Al}_{2\alpha_{\mathrm{Al}}}\mathrm{X}_{2\alpha_{\mathrm{X}}}\mathrm{O}_{z\alpha_{\mathrm{X}}+3\alpha_{\mathrm{Al}}}$$

$$c_{\mathrm{X}} = 2\alpha_{\mathrm{X}} \tag{A.166}$$

$$b = z\alpha_{\mathrm{X}} + 3\alpha_{\mathrm{Al}} \tag{A.167}$$

$$c_{\mathrm{Al}} = 2\alpha_{\mathrm{Al}} \tag{A.168}$$

$$m_{\mathrm{X}} = \frac{2a}{b} = \frac{4\alpha_{\mathrm{X}}}{z\alpha_{\mathrm{X}} + 3\alpha_{\mathrm{Al}}} \tag{A.169}$$

$$m_{\mathrm{Al}} = \frac{2c}{b} = \frac{4\alpha_{\mathrm{Al}}}{z\alpha_{\mathrm{X}} + 3\alpha_{\mathrm{Al}}} \tag{A.170}$$

Putting these results into $\Delta G^{\mathrm{ox,BWB}}_{\mathrm{Al}_{c_{\mathrm{Al}}}\mathrm{X}_{c_{\mathrm{X}}}\mathrm{O}_b}$ (A.171) shows that the contribution to ΔG^{ox} made by the assumption of Bragg-Williams mixing for a binary Al-X oxide, $\Delta G^{\mathrm{ox,BWB}}_{\mathrm{Al}_{c_{\mathrm{Al}}}\mathrm{X}_{c_{\mathrm{X}}}\mathrm{O}_b}$, is the sum of the $\Delta G^{\mathrm{ox,BWB}}$ terms for the solute oxide (with the same valency as the solute in the binary oxide) $\Delta G^{\mathrm{ox,BWB}}_{\mathrm{X_2O_z}}$, and for alumina, $\Delta G^{\mathrm{ox,BWB}}_{\mathrm{Al_2O_3}}$, weighted by the relative contributions of oxygen atoms to the formula unit of the binary oxide.

$$\Delta G^{\mathrm{ox,BWB}}_{\mathrm{Al}_{c_{\mathrm{Al}}}\mathrm{X}_{c_{\mathrm{X}}}\mathrm{O}_b} = \frac{z\alpha_{\mathrm{X}}}{z\alpha_{\mathrm{X}} + 3\alpha_{\mathrm{Al}}}\Delta G^{\mathrm{ox,BWB}}_{\mathrm{X_2O}_z} + \frac{3\alpha_{\mathrm{Al}}}{z\alpha_{\mathrm{X}} + 3\alpha_{\mathrm{Al}}}\Delta G^{\mathrm{ox,BWB}}_{\mathrm{Al_2O_3}} \tag{A.171}$$

A.5.2. Modified quasichemical model: limit analysis

This section contains derivations of the forms of $\Delta G^{\mathrm{ox,MQM}}$ for unary oxides $\mathrm{X}_{c_{\mathrm{X}}}\mathrm{O}_b$ and Al_2O_3 in the limit of $x_{\mathrm{X}} \to 0$ and $x_{\mathrm{X}} \to 1$, respectively. In general, the Al-X bond fraction, x_{XAl}, is given below:

$$x_{\mathrm{XAl}} = 4x_{\mathrm{XX}}x_{\mathrm{AlAl}} \exp\frac{\left(-\Delta g^0_{\mathrm{XAl}} - x_{\mathrm{XX}}g^{10}_{\mathrm{XAl}} - x_{\mathrm{AlAl}}g^{01}_{\mathrm{XAl}}\right)}{RT} \tag{A.172}$$

As $x_{\mathrm{X}} \to 0, x_{\mathrm{AlAl}} \to 1$, resulting in x_{XAl} becoming proportional to x_{XX} (A.173), with proportionality constant δ_1 (A.174).

$$x_{\mathrm{XAl}}\left(x_{\mathrm{X,low}}\right) = 4x_{\mathrm{XX}}(1 - x_{\mathrm{XX}}) \exp -\frac{\left(\Delta g^0_{\mathrm{XAl}} - g^{01}_{\mathrm{XAl}} + x_{\mathrm{XX}}\left(g^{10}_{\mathrm{XAl}} - g^{01}_{\mathrm{XAl}}\right)\right)}{RT}$$

$$\approx 4x_{\mathrm{XX}} \exp -\frac{g^{01}_{\mathrm{XAl}} + \Delta g^0_{\mathrm{XAl}}}{RT} \approx \delta_1 x_{\mathrm{XX}} \tag{A.173}$$

$$\delta_1 = 4 \exp\left(-\frac{g^{01}_{\mathrm{XAl}} + \Delta g^0_{\mathrm{XAl}}}{RT}\right) \tag{A.174}$$

Evaluating x_{XX} in terms of x_{X} (A.175) shows it to scale with x_{X} with proportionality constant δ_2 (A.176).

$$\varepsilon_1 = (1 - x_{\mathrm{X}})\beta_{\mathrm{XX}} + x_{\mathrm{X}}\beta_{\mathrm{AlAl}} \approx \beta_{\mathrm{XX}}$$

$$\varepsilon_2 = \varepsilon_1 x_{\mathrm{XX}} = (x_{\mathrm{X}}\beta_{\mathrm{AlX}} - (1 - x_{\mathrm{X}})\beta_{\mathrm{XAl}})x_{\mathrm{XAl}} + x_{\mathrm{X}}\beta_{\mathrm{AlAl}}(1 - x_{\mathrm{XAl}})$$

$$\beta_{\mathrm{XX}}x_{\mathrm{XX}} = (x_{\mathrm{X}}\beta_{\mathrm{AlX}} - (1 - x_{\mathrm{X}})\beta_{\mathrm{XAl}})\delta_1 x_{\mathrm{XX}} + x_{\mathrm{X}}\beta_{\mathrm{AlAl}}(1 - \delta_1 x_{\mathrm{XX}})$$

$$\beta_{\mathrm{XX}}x_{\mathrm{XX}} = -\beta_{\mathrm{XAl}}\delta_1 x_{\mathrm{XX}} + x_{\mathrm{X}}\beta_{\mathrm{AlAl}}$$

$$x_{\mathrm{XX}} \approx \frac{\beta_{\mathrm{AlAl}}}{\beta_{\mathrm{XX}} + \beta_{\mathrm{XAl}}\alpha_1}x_{\mathrm{X}} = \delta_2 x_{\mathrm{X}} \tag{A.175}$$

$$\delta_2 = \frac{\beta_{\mathrm{AlAl}}}{\beta_{\mathrm{XX}} + \beta_{\mathrm{XAl}}\delta_1} = \frac{\beta_{\mathrm{AlAl}}}{\beta_{\mathrm{XX}} + 4\beta_{\mathrm{XAl}} \exp\left(-\frac{g^{01}_{\mathrm{XAl}} + \Delta g^0_{\mathrm{XAl}}}{RT}\right)} \tag{A.176}$$

Evaluating other terms ε_3 (A.177), ε_4 (A.178), ε_5 (A.179), ε_6 (A.180), ε_{X} (A.181), $\varepsilon_{\mathrm{Al}}$ (A.182), σ_{X} (A.183), and σ_{Al} (A.184):

$$\varepsilon_3 = \varepsilon_1 x_{\mathrm{AlAl}} = \varepsilon_1(1 - x_{\mathrm{XX}} - x_{\mathrm{XAl}}) \approx \beta_{\mathrm{XX}}(1 - \delta_2 x_{\mathrm{X}} - \delta_1\delta_2 x_{\mathrm{X}}) \approx \beta_{\mathrm{XX}} \tag{A.177}$$

$$\varepsilon_4 = 2\varepsilon_1 y_{\mathrm{X}} = \varepsilon_1(2x_{\mathrm{XX}} + x_{\mathrm{XAl}}) = \beta_{\mathrm{XX}}(2\delta_2 + \delta_1\delta_2)x_{\mathrm{X}} = \beta_{\mathrm{XX}}\delta_2(2 + \delta_1)x_{\mathrm{X}} \tag{A.178}$$

$$\varepsilon_5 = 2\varepsilon_1 y_{\mathrm{Al}} = \varepsilon_1(2x_{\mathrm{AlAl}} + x_{\mathrm{XAl}}) = \varepsilon_1(2(1 - x_{\mathrm{XAl}} - x_{\mathrm{XX}}) + x_{\mathrm{XAl}}) \tag{A.179}$$

$$= \varepsilon_1(2 - x_{\mathrm{XAl}} - 2x_{\mathrm{XX}}) \approx \beta_{\mathrm{XX}}$$

$$\varepsilon_6 = \beta_{\mathrm{XX}}\beta_{\mathrm{AlAl}} + x_{\mathrm{XAl}}(\beta_{\mathrm{XX}}\beta_{\mathrm{AlX}} + \beta_{\mathrm{AlAl}}\beta_{\mathrm{XAl}}) \approx \beta_{\mathrm{XX}}\beta_{\mathrm{AlAl}} \tag{A.180}$$

$$\varepsilon_{\mathrm{X}} = \ln\frac{4\varepsilon_1\varepsilon_2}{\varepsilon_4^2} = \ln\frac{(4\beta_{\mathrm{XX}})(\beta_{\mathrm{XX}}\delta_2 x_{\mathrm{X}})}{(\beta_{\mathrm{XX}}\delta_2(2 + \delta_1)x_{\mathrm{X}})^2} = -\ln\frac{(\beta_{\mathrm{XX}}\delta_2(2 + \delta_1)x_{\mathrm{X}})^2}{(4\beta_{\mathrm{XX}})(\beta_{\mathrm{XX}}\delta_2 x_{\mathrm{X}})} \tag{A.181}$$

$$= -\ln\frac{\delta_2}{4}(2 + \delta_1)^2 x_{\mathrm{X}} = -\ln\frac{\delta_2}{4}(2 + \delta_1)^2 - \ln x_{\mathrm{X}} \approx -\ln x_{\mathrm{X}}$$

$$\varepsilon_{\mathrm{Al}} = \ln\frac{4\varepsilon_1\varepsilon_3}{\varepsilon_5^2} \approx \ln 4 \tag{A.182}$$

$$\sigma_{\mathrm{X}} \approx 2\beta_{\mathrm{AlAl}}(-\ln x_{\mathrm{X}}) + \delta_1\delta_2 x_{\mathrm{X}}(2\beta_{\mathrm{AlX}} - \beta_{\mathrm{AlAl}})(-\ln x_{\mathrm{X}} - \ln 4) \approx -2\beta_{\mathrm{AlAl}}\ln x_{\mathrm{X}} \tag{A.183}$$

$$\sigma_{\mathrm{Al}} \approx 2\beta_{\mathrm{XX}}\ln 4 + \delta_1\delta_2 x_{\mathrm{X}}(2\beta_{\mathrm{XAl}} - \beta_{\mathrm{XX}})(\ln 4 + \ln x_{\mathrm{X}}) \approx 2\beta_{\mathrm{XX}}\ln 4 \tag{A.184}$$

Using these results to evaluate σ_1 (A.185), σ_2 (A.186), and σ_3 (A.187):

$$\sigma_1 = RT\varepsilon_1\big(\beta_{\mathrm{AlAl}}\beta_{\mathrm{XX}}x_{\mathrm{X}}(1 - x_{\mathrm{X}}) - (\varepsilon_2 - x_{\mathrm{X}}\beta_{\mathrm{AlAl}})(\varepsilon_3 - (1 - x_{\mathrm{X}})\beta_{\mathrm{XX}})\big)$$

$$+\varepsilon_2\varepsilon_3\left((\varepsilon_2 - x_{\mathrm{X}}\beta_{\mathrm{AlAl}})g_{\mathrm{XAl}}^{10} + (\varepsilon_3 - (1 - x_{\mathrm{X}})\beta_{\mathrm{XX}})g_{\mathrm{XAl}}^{01}\right)$$

$$\sigma_1 = RT\varepsilon_1\big(\beta_{\mathrm{AlAl}}\beta_{\mathrm{XX}}x_{\mathrm{X}}(1 - x_{\mathrm{X}})$$

$$- (x_{\mathrm{X}}\beta_{\mathrm{AlX}} - (1 - x_{\mathrm{X}})\beta_{\mathrm{XAl}} - x_{\mathrm{X}}\beta_{\mathrm{AlAl}})\big((1 - x_{\mathrm{X}})\beta_{\mathrm{XAl}} - x_{\mathrm{X}}\beta_{\mathrm{AlX}}$$

$$- \beta_{\mathrm{XX}}(1 - x_{\mathrm{X}})\big)x_{\mathrm{XAl}}^2\big)$$

$$+\varepsilon_2\varepsilon_3 x_{\mathrm{XAl}}\left((x_{\mathrm{X}}\beta_{\mathrm{AlX}} - (1 - x_{\mathrm{X}})\beta_{\mathrm{XAl}} - x_{\mathrm{X}}\beta_{\mathrm{AlAl}})g_{\mathrm{XAl}}^{10}\right.$$

$$\left. + \big((1 - x_{\mathrm{X}})\beta_{\mathrm{XAl}} - x_{\mathrm{X}}\beta_{\mathrm{AlX}} - \beta_{\mathrm{XX}}(1 - x_{\mathrm{X}})\big)g_{\mathrm{XAl}}^{01}\right)$$

$$= RT\varepsilon_1\big(\beta_{\mathrm{AlAl}}\beta_{\mathrm{XX}}x_{\mathrm{X}}(1-x_{\mathrm{X}}) - (x_{\mathrm{X}}(\beta_{\mathrm{AlX}}+\beta_{\mathrm{XAl}}-\beta_{\mathrm{AlAl}})-\beta_{\mathrm{XAl}})(x_{\mathrm{X}}(\beta_{\mathrm{XX}}-\beta_{\mathrm{XAl}}-\beta_{\mathrm{AlX}})+\beta_{\mathrm{XAl}} - \beta_{\mathrm{XX}})x_{\mathrm{XAl}}^2\big) + \varepsilon_2\varepsilon_3 x_{\mathrm{XAl}}\Big((x_{\mathrm{X}}(\beta_{\mathrm{AlX}}+\beta_{\mathrm{XAl}}-\beta_{\mathrm{AlAl}})-\beta_{\mathrm{XAl}})g_{\mathrm{XAl}}^{10} + \big(\beta_{\mathrm{XAl}}-\beta_{\mathrm{XX}}+x_{\mathrm{X}}(\beta_{\mathrm{XX}}-\beta_{\mathrm{XAl}}-\beta_{\mathrm{AlX}})\big)g_{\mathrm{XAl}}^{01}\Big)$$

$$\approx RT\beta_{\mathrm{XX}}(\beta_{\mathrm{AlAl}}\beta_{\mathrm{XX}}x_{\mathrm{X}}(1-x_{\mathrm{X}}) - (x_{\mathrm{X}}(\beta_{\mathrm{AlX}}+\beta_{\mathrm{XAl}}-\beta_{\mathrm{AlAl}})-\beta_{\mathrm{XAl}})(x_{\mathrm{X}}(\beta_{\mathrm{XX}}-\beta_{\mathrm{XAl}}-\beta_{\mathrm{AlX}})+\beta_{\mathrm{XAl}} - \beta_{\mathrm{XX}})(\delta_1\delta_2x_{\mathrm{X}})^2) + \beta_{\mathrm{XX}}^2\delta_1\delta_2^2x_{\mathrm{X}}^2\Big((x_{\mathrm{X}}(\beta_{\mathrm{AlX}}+\beta_{\mathrm{XAl}}-\beta_{\mathrm{AlAl}})-\beta_{\mathrm{XAl}})g_{\mathrm{XAl}}^{10} + \big(\beta_{\mathrm{XAl}}-\beta_{\mathrm{XX}}+x_{\mathrm{X}}(\beta_{\mathrm{XX}}-\beta_{\mathrm{XAl}}-\beta_{\mathrm{AlX}})\big)g_{\mathrm{XAl}}^{01}\Big)$$

$$\sigma_1 \approx RT\beta_{\mathrm{XX}}^2\beta_{\mathrm{AlAl}}x_{\mathrm{X}} \tag{A.185}$$

$$\sigma_2 = \Big(\varepsilon_1(\varepsilon_2-\varepsilon_3)RT + \varepsilon_2\varepsilon_3\big(g_{\mathrm{XAl}}^{10}-g_{\mathrm{XAl}}^{01}\big)\Big)\big(\beta_{\mathrm{XX}}\varepsilon_{\mathrm{Al}}(2\beta_{\mathrm{AlX}}-\beta_{\mathrm{AlAl}}) + \beta_{\mathrm{AlAl}}\varepsilon_{\mathrm{X}}(2\beta_{\mathrm{XAl}}-\beta_{\mathrm{XX}})\big)$$

$$\sigma_2 \approx \Big(\beta_{\mathrm{XX}}(\beta_{\mathrm{XX}}\delta_2x_{\mathrm{X}}-\beta_{\mathrm{XX}})RT + \beta_{\mathrm{XX}}\delta_2x_{\mathrm{X}}\beta_{\mathrm{XX}}\big(g_{\mathrm{XAl}}^{10}-g_{\mathrm{XAl}}^{01}\big)\Big)\big(\beta_{\mathrm{XX}}\ln 4\,(2\beta_{\mathrm{AlX}}-\beta_{\mathrm{AlAl}}) - 2\beta_{\mathrm{AlAl}}\ln x_{\mathrm{X}}\,\beta_{\mathrm{AlAl}}(2\beta_{\mathrm{XAl}}-\beta_{\mathrm{XX}})\big)$$

$$\sigma_2 \approx 2\beta_{\mathrm{XX}}^2\beta_{\mathrm{AlAl}}^2(2\beta_{\mathrm{XAl}}-\beta_{\mathrm{XX}})RT\ln x_{\mathrm{X}} \tag{A.186}$$

$$\sigma_3 = \varepsilon_2(\varepsilon_1-\varepsilon_2)g_{\mathrm{XAl}}^{10} - \varepsilon_3(\varepsilon_1-\varepsilon_3)g_{\mathrm{XAl}}^{01} \approx \beta_{\mathrm{XX}}\delta_2x_{\mathrm{X}}(\beta_{\mathrm{XX}}-\beta_{\mathrm{XX}}\alpha_2x_{\mathrm{X}})g_{\mathrm{XAl}}^{10} - \beta_{\mathrm{XX}}(\varepsilon_1-\varepsilon_3)g_{\mathrm{XAl}}^{01}$$

$$\varepsilon_1-\varepsilon_3 = \varepsilon_1(1-x_{\mathrm{AlAl}}) = \varepsilon_1(x_{\mathrm{XAl}}+x_{\mathrm{XX}}) = \beta_{\mathrm{XX}}\delta_2(1+\delta_1)x_{\mathrm{X}}$$

$$\sigma_3 \approx \beta_{\mathrm{XX}}\delta_2x_{\mathrm{X}}(\beta_{\mathrm{XX}}-\beta_{\mathrm{XX}}\delta_2x_{\mathrm{X}})g_{\mathrm{XAl}}^{10} - \beta_{\mathrm{XX}}^2\delta_2(1+\delta_1)x_{\mathrm{X}}g_{\mathrm{XAl}}^{01} \approx x_{\mathrm{X}}\beta_{\mathrm{XX}}^2\delta_2\big(g_{\mathrm{XAl}}^{10}-(1+\delta_1)g_{\mathrm{XAl}}^{01}\big)$$

$$\sigma_3 \approx x_{\mathrm{X}}\beta_{\mathrm{XX}}^2\delta_2\big(g_{\mathrm{XAl}}^{10}-(1+\delta_1)g_{\mathrm{XAl}}^{01}\big) \tag{A.187}$$

Using these results to evaluate terms within $\Delta G^{\text{ox,MQM}}_{\text{X}_{c_\text{X}}\text{O}_b}$, $\varepsilon_6\sigma_1$ (A.188), $m_\text{X}\sigma_\text{X}$ (A.189), and $\sigma_2 + \varepsilon_6\sigma_3$ (A.190), and then $\Delta G^{\text{ox,MQM}}_{\text{X}_{c_\text{X}}\text{O}_b}$ (A.191) shows that the term is proportional to $\ln(x_\text{X})$ and m_X with constant δ_3 (A.192).

$$\varepsilon_6\sigma_1 \approx \beta_{\text{XX}}\beta_{\text{AlAl}}RT\beta^2_{\text{XX}}\beta_{\text{AlAl}}x_\text{X} = RT\beta^3_{\text{XX}}\beta^2_{\text{AlAl}}x_\text{X} \tag{A.188}$$

$$m_\text{X}\sigma_\text{X} \approx -2m_\text{X}\beta_{\text{AlAl}}\ln x_\text{X} \tag{A.189}$$

$$\sigma_2 + \varepsilon_6\sigma_3 \approx 2\beta^2_{\text{XX}}\beta^2_{\text{AlAl}}(2\beta_{\text{XAl}} - \beta_{\text{XX}})RT\ln x_\text{X} + \beta_{\text{XX}}\beta_{\text{AlAl}}x_\text{X}\beta^2_{\text{XX}}\delta_2\left(g^{10}_{\text{XAl}} - (1+\delta_1)g^{01}_{\text{XAl}}\right)$$

$$\sigma_2 + \varepsilon_6\sigma_3 \approx 2\beta^2_{\text{XX}}\beta^2_{\text{AlAl}}(2\beta_{\text{XAl}} - \beta_{\text{XX}})RT\ln x_\text{X} \tag{A.190}$$

$$\Delta G^{\text{ox,MQM}}_{\text{X}_{c_\text{X}}\text{O}_b} = -\frac{m_\text{X}RT}{\varepsilon_6\sigma_1}\left(\sigma_1\sigma_\text{X} + x_{\text{XAl}}(\sigma_2 + \varepsilon_6\sigma_3)(1 - x_\text{X})\right)$$

$$\Delta G^{\text{ox,MQM}}_{\text{X}_{c_\text{X}}\text{O}_b}\left(x_{\text{X,low}}\right)$$

$$\approx -\frac{m_\text{X}RT}{RT\beta^3_{\text{XX}}\beta^2_{\text{AlAl}}x_\text{X}}\Big((RT\beta^2_{\text{XX}}\beta_{\text{AlAl}}x_\text{X})(-2\beta_{\text{AlAl}}\ln x_\text{X}) + \delta_1\delta_2 x_\text{X}\left(2\beta^2_{\text{XX}}\beta^2_{\text{AlAl}}(2\beta_{\text{XAl}} - \beta_{\text{XX}})RT\ln x_\text{X}\right)\Big)$$

$$\Delta G^{\text{ox,MQM}}_{\text{X}_{c_\text{X}}\text{O}_b} \approx m_\text{X}\ln x_\text{X}\frac{2RT}{\beta_{\text{XX}}}\left(1 - \delta_1\delta_2(2\beta_{\text{XAl}} - \beta_{\text{XX}})\right) = \delta_\text{X}m_\text{X}\ln x_\text{X} \tag{A.191}$$

$$\delta_\text{X} = \frac{2RT}{\beta_{\text{XX}}}\left(1 - \delta_1\delta_2(2\beta_{\text{XAl}} - \beta_{\text{XX}})\right) \tag{A.192}$$

Using the facts that $Z^{\text{Al}}_{\text{AlAl}} = 6$ (A.193), $\delta_1 > 0$ (A.194), and that β_{ij}, R, and T are positive, it can be shown that δ_X term is always positive (A.195).

$$\beta_{\text{AlAl}} = \frac{2}{Z^{\text{Al}}_{\text{AlAl}}} = \frac{2}{6} = \frac{1}{3} \tag{A.193}$$

$$\delta_1 = 4\exp\left(-\frac{g^{01}_{\text{XAl}} + \Delta g^0_{\text{XAl}}}{RT}\right)$$

$$-\frac{g^{01}_{\text{XAl}} + \Delta g^0_{\text{XAl}}}{RT} \in \mathbf{R} \therefore \delta_1 > 0 \tag{A.194}$$

$$\delta_\text{X} = \frac{2RT}{\beta_{\text{XX}}}\left(1 - \delta_1\delta_2(2\beta_{\text{XAl}} - \beta_{\text{XX}})\right)$$

$$= \frac{2RT}{\beta_{\mathrm{XX}}}\left(1 - \delta_1\left(\frac{\beta_{\mathrm{AlAl}}}{\beta_{\mathrm{XX}} + \beta_{\mathrm{XAl}}\delta_1}\right)(2\beta_{\mathrm{XAl}} - \beta_{\mathrm{XX}})\right)$$

$$= \frac{2RT}{\beta_{\mathrm{XX}}(\beta_{\mathrm{XX}} + \beta_{\mathrm{XAl}}\delta_1)}\left(\beta_{\mathrm{XX}} + \beta_{\mathrm{XAl}}\delta_1 - \delta_1\beta_{\mathrm{AlAl}}(2\beta_{\mathrm{XAl}} - \beta_{\mathrm{XX}})\right)$$

$$= \frac{2RT}{\beta_{\mathrm{XX}}(\beta_{\mathrm{XX}} + \beta_{\mathrm{XAl}}\delta_1)}\left(\beta_{\mathrm{XX}} + \delta_1\left(\beta_{\mathrm{XX}}\beta_{\mathrm{AlAl}} + \beta_{\mathrm{XAl}}(1 - 2\beta_{\mathrm{AlAl}})\right)\right)$$

$$\delta_{\mathrm{X}} = \frac{2RT}{\beta_{\mathrm{XX}}(\beta_{\mathrm{XX}} + \beta_{\mathrm{XAl}}\delta_1)}\left(\beta_{\mathrm{XX}} + \delta_1\left(\beta_{\mathrm{XX}}\beta_{\mathrm{AlAl}} + \frac{2}{3}\beta_{\mathrm{XAl}}\right)\right) > 0 \tag{A.195}$$

A.5.3. Modified quasichemical model: linear sums

For a solute oxide with valency z, $\Delta G^{\mathrm{ox,MQM}}_{\mathrm{X_2O_z}}$ is given as follows (A.196):

$$\Delta G^{\mathrm{ox,MQM}}_{\mathrm{X_2O_z}} = \frac{4RT}{z\varepsilon_6\sigma_1}\left(\sigma_1\sigma_{\mathrm{X}} + x_{\mathrm{XAl}}(\sigma_2 + \varepsilon_6\sigma_3)(1 - x_{\mathrm{X}})\right) \tag{A.196}$$

For Al_2O_3, $\Delta G^{\mathrm{ox,MQM}}_{\mathrm{Al_2O_3}}$ is given by (A.197):

$$\Delta G^{\mathrm{ox,MQM}}_{\mathrm{Al_2O_3}} = \frac{4RT}{3\varepsilon_6\sigma_1}\left(\sigma_1\sigma_{\mathrm{Al}} - x_{\mathrm{X}}x_{\mathrm{XAl}}(\sigma_2 + \varepsilon_6\sigma_3)\right) \tag{A.197}$$

Therefore, the term for a binary Al-X oxide $\Delta G^{\mathrm{ox,MQM}}_{\mathrm{Al}_{c_{\mathrm{Al}}}\mathrm{X}_{c_{\mathrm{X}}}\mathrm{O}_b}$ can be expressed in terms of its constituent binaries (A.198).

$$\Delta G^{\mathrm{ox,MQM}}_{\mathrm{Al}_{c_{\mathrm{Al}}}\mathrm{X}_{c_{\mathrm{X}}}\mathrm{O}_b} = \frac{RT}{\varepsilon_6\sigma_1}\left(\sigma_1(m_{\mathrm{X}}\sigma_{\mathrm{X}} + m_{\mathrm{Al}}\sigma_{\mathrm{Al}}) + x_{\mathrm{XAl}}(\sigma_2 + \varepsilon_6\sigma_3)(m_{\mathrm{X}}(1 - x_{\mathrm{X}}) - m_{\mathrm{Al}}x_{\mathrm{X}})\right)$$

$$= m_{\mathrm{X}}\frac{RT}{\varepsilon_6\sigma_1}\left(\sigma_1\sigma_{\mathrm{X}} + x_{\mathrm{XAl}}(\sigma_2 + \varepsilon_6\sigma_3)(1 - x_{\mathrm{X}})\right) + m_{\mathrm{Al}}\frac{RT}{\varepsilon_6\sigma_1}\left(\sigma_1\sigma_{\mathrm{Al}} - x_{\mathrm{X}}x_{\mathrm{XAl}}(\sigma_2 + \varepsilon_6\sigma_3)\right)$$

$$\Delta G^{\mathrm{ox,MQM}}_{\mathrm{Al}_{c_{\mathrm{Al}}}\mathrm{X}_{c_{\mathrm{X}}}\mathrm{O}_b} = \frac{z}{4}m_{\mathrm{X}}\Delta G^{\mathrm{ox,MQM}}_{\mathrm{X_2O_z}} + \frac{3}{4}m_{\mathrm{Al}}\Delta G^{\mathrm{ox,MQM}}_{\mathrm{X_2O_z}} \tag{A.198}$$

Expressing the binary oxide $\mathrm{Al}_{c_{\mathrm{Al}}}\mathrm{X}_{c_{\mathrm{X}}}\mathrm{O}_b$ as the sum of α_{X} formula units of $\mathrm{X_2O_z}$ and α_{Al} formula units of $\mathrm{Al_2O_3}$, previously derived relations for m_{X} (A.169) and m_{Al} (A.170) show that $\Delta G^{\mathrm{ox,MQM}}_{\mathrm{Al}_{c_{\mathrm{Al}}}\mathrm{X}_{c_{\mathrm{X}}}\mathrm{O}_b}$ (A.199) is the sum of the equivalent terms for the solute oxide with the equivalent valency, $\Delta G^{\mathrm{ox,MQM}}_{\mathrm{X_2O_z}}$, and Al_2O_3, $\Delta G^{\mathrm{ox,MQM}}_{\mathrm{Al_2O_3}}$, weighted by the number of oxygen atoms

contributed to the formula unit ($z\alpha_{\mathrm{X}}$ and $3\alpha_{\mathrm{Al}}$ for $\mathrm{X_2O}_z$ and $\mathrm{Al_2O_3}$, respectively).

$$\Delta G^{\mathrm{ox,MQM}}_{\mathrm{Al}_{c_{\mathrm{Al}}}\mathrm{X}_{c_{\mathrm{X}}}\mathrm{O}_b} = \frac{z\alpha_{\mathrm{X}}}{z\alpha_{\mathrm{X}} + 3\alpha_{\mathrm{Al}}}\Delta G^{\mathrm{ox,MQM}}_{\mathrm{X_2O}_z} + \frac{3\alpha_{\mathrm{Al}}}{z\alpha_{\mathrm{X}} + 3\alpha_{\mathrm{Al}}}\Delta G^{\mathrm{ox,MQM}}_{\mathrm{Al_2O_3}} \tag{A.199}$$

A.5.4. Ternary oxide boundaries in ideal mixing

The boundary on a ternary oxide stability diagram between two ternary Al-Mg-X oxides $\mathrm{Al}_{c_{\mathrm{Al1}}}\mathrm{Mg}_{c_{\mathrm{X1}}}\mathrm{X}_{c_{\mathrm{X1}}}\mathrm{O}_{b1}$ and $\mathrm{Al}_{c_{\mathrm{Al2}}}\mathrm{Mg}_{c_{\mathrm{X2}}}\mathrm{X}_{c_{\mathrm{X2}}}\mathrm{O}_{b2}$ occurs when their ΔG^{ox} values are equal. At low solute and Mg concentrations, $x_{\mathrm{Al}} \approx 1$. In this case, the $\Delta G^{\mathrm{ox,ideal}}$ values for ternary Al-Mg-X oxides $\mathrm{Al}_{c_{\mathrm{Al1}}}\mathrm{Mg}_{c_{\mathrm{X1}}}\mathrm{X}_{c_{\mathrm{X1}}}\mathrm{O}_{b1}$ (A.200) and $\mathrm{Al}_{c_{\mathrm{Al2}}}\mathrm{Mg}_{c_{\mathrm{X2}}}\mathrm{X}_{c_{\mathrm{X2}}}\mathrm{O}_{b2}$ (A.201) can be simplified.

$$\begin{aligned}\Delta G^{\mathrm{ox,ideal}}_{\mathrm{Al}_{c_{\mathrm{Al1}}}\mathrm{Mg}_{c_{\mathrm{X1}}}\mathrm{X}_{c_{\mathrm{X1}}}\mathrm{O}_{b1}} &= \Delta G^{\mathrm{o}}_{\mathrm{f,molO_2},1}(T) - RT\ln\left({x_{\mathrm{Al}}}^{m_{\mathrm{Al1}}}{x_{\mathrm{Mg}}}^{m_{\mathrm{Mg1}}}{x_{\mathrm{X}}}^{m_{\mathrm{X1}}}p_{\mathrm{O_2}}\right)\\ &\approx \Delta G^{\mathrm{o}}_{\mathrm{f,molO_2}1}(T) - RT\ln p_{\mathrm{O_2}} - RT\left(m_{\mathrm{Mg1}}\ln x_{\mathrm{Mg}} + m_{\mathrm{X1}}\ln x_{\mathrm{X}}\right)\end{aligned} \tag{A.200}$$

$$\begin{aligned}\Delta G^{\mathrm{ox,ideal}}_{\mathrm{Al}_{c_{\mathrm{Al2}}}\mathrm{Mg}_{c_{\mathrm{X2}}}\mathrm{X}_{c_{\mathrm{X2}}}\mathrm{O}_{b2}} &= \Delta G^{\mathrm{o}}_{\mathrm{f,molO_2},2}(T) - RT\ln\left({x_{\mathrm{Al}}}^{m_{\mathrm{Al2}}}{x_{\mathrm{Mg}}}^{m_{\mathrm{Mg2}}}{x_{\mathrm{X}}}^{m_{\mathrm{X2}}}p_{\mathrm{O_2}}\right)\\ &\approx \Delta G^{\mathrm{o}}_{\mathrm{f,molO_2},2}(T) - RT\ln p_{\mathrm{O_2}} - RT\left(m_{\mathrm{Mg2}}\ln x_{\mathrm{Mg}} + m_{\mathrm{X2}}\ln x_{\mathrm{X}}\right)\end{aligned} \tag{A.201}$$

Equating these expressions (A.202), it can be shown that in the case of $x_{\mathrm{Al}} \gg x_{\mathrm{X}}, x_{\mathrm{Mg}}$, the boundary between ternary Al-Mg-X oxides $\mathrm{Al}_{c_{\mathrm{Al1}}}\mathrm{Mg}_{c_{\mathrm{X1}}}\mathrm{X}_{c_{\mathrm{X1}}}\mathrm{O}_{b1}$ and $\mathrm{Al}_{c_{\mathrm{Al2}}}\mathrm{Mg}_{c_{\mathrm{X2}}}\mathrm{X}_{c_{\mathrm{X2}}}\mathrm{O}_{b2}$ on an $x_{\mathrm{Mg}} - x_{\mathrm{X}}$ plot with a logarithmic scale is linear, with a gradient g_{plot} (A.203) dependent only on $m_{\mathrm{X}i}$ and $m_{\mathrm{Al}i}$, and intercept c_{plot} (A.204).

$$\Delta G^{\mathrm{ox,ideal}}_{\mathrm{Al}_{c_{\mathrm{Al1}}}\mathrm{Mg}_{c_{\mathrm{X1}}}\mathrm{X}_{c_{\mathrm{X1}}}\mathrm{O}_{b1}} = \Delta G^{\mathrm{ox,ideal}}_{\mathrm{Al}_{c_{\mathrm{Al2}}}\mathrm{Mg}_{c_{\mathrm{X2}}}\mathrm{X}_{c_{\mathrm{X2}}}\mathrm{O}_{b2}}$$

$$\Delta G^{\mathrm{o}}_{\mathrm{f,molO_2}1}(T) - RT\ln(p\mathrm{O_2}) - RT\left(m_{\mathrm{Mg1}}\ln\left(x_{\mathrm{Mg}}\right) + m_{\mathrm{X1}}\ln(x_{\mathrm{X}})\right)$$

$$= \Delta G^{\mathrm{o}}_{\mathrm{f,molO_2},2}(T) - RT\ln(p\mathrm{O_2}) - RT\left(m_{\mathrm{Mg2}}\ln\left(x_{\mathrm{Mg}}\right) + m_{\mathrm{X2}}\ln(x_{\mathrm{X}})\right)$$

$$\frac{\Delta G^{\mathrm{o}}_{\mathrm{f,molO_2}1}(T) - \Delta G^{\mathrm{o}}_{\mathrm{f,molO_2},2}(T)}{RT} = \left(m_{\mathrm{Mg1}} - m_{\mathrm{Mg2}}\right)\ln\left(x_{\mathrm{Mg}}\right) + (m_{\mathrm{X1}} - m_{\mathrm{X2}})\ln(x_{\mathrm{X}})$$

$$\ln\left(x_{\mathrm{Mg}}\right) = \frac{m_{\mathrm{X1}} - m_{\mathrm{X2}}}{m_{\mathrm{Mg2}} - m_{\mathrm{Mg1}}}\ln(x_{\mathrm{X}}) + \frac{\Delta G^{\mathrm{o}}_{\mathrm{f,molO_2}1}(T) - \Delta G^{\mathrm{o}}_{\mathrm{f,molO_2},2}(T)}{RT\left(m_{\mathrm{Mg2}} - m_{\mathrm{Mg1}}\right)}$$

$$\log_{10}(x_{\mathrm{Mg}}) = \frac{m_{\mathrm{X1}} - m_{\mathrm{X2}}}{m_{\mathrm{Mg2}} - m_{\mathrm{Mg1}}} \log_{10}(x_{\mathrm{X}}) + \frac{\Delta G^{\mathrm{o}}_{\mathrm{f,mol}\mathrm{O}_2 1}(T) - \Delta G^{\mathrm{o}}_{\mathrm{f,mol}\mathrm{O}_2,2}(T)}{\ln(10)\, RT\left(m_{\mathrm{Mg2}} - m_{\mathrm{Mg1}}\right)}$$

$$\log_{10}(x_{\mathrm{Mg}}) = g_{\mathrm{plot}} \log_{10}(x_{\mathrm{X}}) + c_{\mathrm{plot}} \tag{A.202}$$

$$g_{\mathrm{plot}} = \frac{m_{\mathrm{X1}} - m_{\mathrm{X2}}}{m_{\mathrm{Mg2}} - m_{\mathrm{Mg1}}} \tag{A.203}$$

$$c_{\mathrm{plot}} = \frac{\Delta G^{\mathrm{o}}_{\mathrm{f,mol}\mathrm{O}_2 1}(T) - \Delta G^{\mathrm{o}}_{\mathrm{f,mol}\mathrm{O}_2,2}(T)}{\ln(10)\, RT\left(m_{\mathrm{Mg2}} - m_{\mathrm{Mg1}}\right)} \tag{A.204}$$

For the boundary between two Al-X binary or unary oxides, $m_{\mathrm{Mg1}} = m_{\mathrm{Mg2}} = 0$, therefore $1/g_{\mathrm{plot}} = 0$, resulting in vertical boundaries. Between two Al-Mg binary or unary oxides, $m_{\mathrm{X1}} = m_{\mathrm{X2}} = 0$, therefore $g_{\mathrm{plot}} = 0$, resulting in horizontal boundaries. In the case of a boundary between a unary or binary Al-X oxide and a unary or binary Al-Mg oxide, $m_{\mathrm{Mg1}} = m_{\mathrm{X2}} = 0$, the gradient will be the ratio of the non-zero m_{X} and m_{Mg} values, which are positive since m_{X} and m_{Mg} are positive (A.205).

$$g_{\mathrm{plot}} = \frac{m_{\mathrm{X1}} - m_{\mathrm{X2}}}{m_{\mathrm{Mg2}} - m_{\mathrm{Mg1}}} = \frac{m_{\mathrm{X1}}}{m_{\mathrm{Mg2}}} \tag{A.205}$$

Appendix B
Modelling: Data, Sources, and Figures

B.1. Overview

This appendix contains details of data used in thermodynamic modelling, including sources, and a collection of plots generated in thermodynamic modelling, including:

- For binary systems:
    - $\Delta G^{\mathrm{ox}}(x_{\mathrm{X}})$ plots at temperatures between 500 °C and 1000 °C, using:
        - Ideal mixing
        - Bragg-Williams mixing
        - Modified quasichemical model
    - Oxide stability diagrams (plots of oxide with lowest $\Delta G^{\mathrm{ox}}(x_{\mathrm{X}}, T)$), using:
        - Ideal mixing
        - Bragg-Williams mixing
        - Modified quasichemical model
- For Al-Mg-X ternary systems:
    - Oxide stability diagrams (plots of oxide with lowest $\Delta G^{\mathrm{ox}}(x_{\mathrm{X}}, x_{\mathrm{Mg}})$ at selected temperatures), using:
        - Ideal mixing
        - Bragg-Williams mixing

In addition, there are diagrams annotated with experimental data, where available, for Al-X binary systems (Be, Ca, Ce, La, Li, Mg, Na, Sc, Sr, Zn) and ternary Al-Mg-X systems (Be, Ca, Ce, Gd, La, Sr). Data is annotated by compounds produced on oxidation, as function of temperature and initial melt composition, for both Al-X binary and Al-Mg-X systems and, in Al-Mg-X ternary systems, by whether the solute element imparts oxidation protection.

B.2. Compounds and Gibbs free energy data

Below is a table summarising all compounds used in the modelling chapter. Column 1 specifies the element, column 2 specifies the compound of interest, and column 3 specifies the phases. Most standard Gibbs free energy of formation ΔG_f^o data of binary oxides (Al_2O_3 and X-O oxides) was acquired through the 'Reaction' Module from FactSage [1] via the FACT pure substances (FactPS) database or FACT oxide database (FTOxid), and others calculated via the 'G-method' with data directly from published thermodynamic optimisations [2–5]. For ternary oxides (Al-Mg-X-O), the reaction module was unavailable, so these were calculated via the 'G-method' from data taken from FactPS database.

X	Compound	Code	Label	Phase	Method	Source
Ag	Ag2O	sol	(s)	Solid	RM	FactPS
Ag	Ag2O	liq	(l)	Liquid	RM	FactPS
Al	Al2O3	alp	(α)	Alpha	RM	FactPS
Al	Al2O3	gam	(γ)	Gamma	RM	FactPS
B	B2O	gas	(g)	Gas	RM	FactPS
B	BO	gas	(g)	Gas	RM	FactPS
B	B2O3	sol	(s)	Solid	RM	FactPS
B	B2O3	liq	(l)	Liquid	RM	FactPS
B	BO2	gas	(g)	Gas	RM	FactPS
B	AlBO2	gas	(g)	Gas	RM	FactPS
B	Al4B2O9	sol	(s)	Solid	RM	FactPS
B	Al18B4O33	sol	(s)	Solid	RM	FactPS
Be	Be2O	gas	(g)	Gas	RM	FactPS
Be	BeO	alp	(α)	Alpha	RM	FactPS
Be	BeAl2O4	sol	(s)	Solid	RM	FactPS
Be	BeAl6O10	sol	(s)	Solid	RM	FactPS
Ca	CaO	sol	(s)	Solid	RM	FactPS
Ca	Ca3Al2O6	sol	(s)	Solid	RM	FactPS
Ca	Ca12Al14O33	sol	(s)	Solid	G method	[2]
Ca	CaAl2O4	sol	(s)	Solid	RM	FactPS
Ca	CaAl4O7	sol	(s)	Solid	RM	FactPS
Ca	CaAl12O19	sol	(s)	Solid	RM	FactPS
Ca	Ca3MgAl4O10	sol	(s)	Solid	G method	FactPS
Ca	CaMg2Al16O27	sol	(s)	Solid	G method	FactPS
Ca	Ca2Mg2Al28O46	sol	(s)	Solid	G method	FactPS
Ce	Ce2O3	sol	(s)	Solid	RM	FactPS
Ce	Ce18O31	sol	(s)	Solid	RM	FactPS
Ce	Ce6O11	sol	(s)	Solid	RM	FactPS
Ce	CeO2	sol	(s)	Solid	RM	FactPS
Ce	Ce4Al2O9	sol	(s)	Solid	RM	FactPS

Ce	CeAlO3	sol	(s)	Solid	RM	FactPS
Ce	Ce3Al5O12	sol	(s)	Solid	RM	FactPS
Ce	CeAl11O18	sol	(s)	Solid	RM	FactPS
Co	CoO	sol	(s)	Solid	RM	FactPS
Co	Co3O4	sol	(s)	Solid	RM	FactPS
Co	CoAl2O4	sol	(s)	Solid	G method	[3]
Cr	CrO	liq	(l)	Liquid	RM	FactPS
Cr	Cr3O4	sol	(s)	Solid	RM	FactPS
Cr	Cr2O3	sol	(s)	Solid	RM	FactPS
Cr	CrO2	sol	(s)	Solid	RM	FactPS
Cu	Cu2O	sol	(s)	Solid	RM	FactPS
Cu	CuO	sol	(s)	Solid	RM	FactPS
Cu	CuAlO2	sol	(s)	Solid	RM	FactPS
Cu	CuAl2O4	sol	(s)	Solid	G method	[4]
Fe	FeO	sol	(s)	Solid	RM	FactPS
Fe	Fe3O4	sol	(s)	Solid	RM	FactPS
Fe	Fe2O3	sol	(s)	Solid	RM	FactPS
Fe	FeAlO3	sol	(s)	Solid	RM	FactPS
Fe	FeAl2O4	sol	(s)	Solid	RM	FactPS
Gd	Gd2O3	sol	(s)	Solid	RM	FactPS
Gd	Gd4Al2O9	sol	(s)	Solid	RM	FactPS
Gd	AlGdO3	sol	(s)	Solid	RM	FactPS
Gd	Gd3Al5O12	sol	(s)	Solid	RM	FactPS
Ge	GeO2	tet	(tet)	Tetragonal	RM	FactPS
Ge	GeO2	hex	(hex)	Hexagonal	RM	FactPS
Ge	GeO2	liq	(l)	Liquid	RM	FactPS
K	K2O	sol	(s)	Solid	RM	FactPS
K	K2O	liq	(l)	Liquid	RM	FactPS
K	KO2	sol	(s)	Solid	RM	FactPS
K	KAlO2	alp	(α)	Alpha	RM	FactPS
K	KAlO2	bet	(β)	Beta	RM	FactPS
K	K2Al12O19	sol	(s)	Solid	RM	FactPS
K	KAl9O14	sol	(s)	Solid	RM	FactPS
La	La2O	gas	(g)	Gas	RM	FactPS
La	LaO	gas	(g)	Gas	RM	FactPS
La	La2O3	sol	(s)	Solid	RM	FactPS
La	LaAl11O18	sol	(s)	Solid	RM	FactPS
La	La33Al7O60	sol	(s)	Solid	RM	FactPS
La	La4Al2O9	sol	(s)	Solid	RM	FactPS
La	LaAlO3	sol	(s)	Solid	RM	FactPS
La	La3Al5O12	sol	(s)	Solid	RM	FactPS
Li	Li2O	sol	(s)	Solid	RM	FactPS
Li	LiO	gas	(g)	Gas	RM	FactPS
Li	Li5AlO4	sol	(s)	Solid	RM	FactPS
Li	AlLiO2	alp	(α)	Alpha	RM	FTOxid
Li	AlLiO2	gam	(γ)	Gamma	RM	FTOxid
Li	LiAl5O8	sol	(s)	Solid	RM	FactPS
Li	LiAl7O11	sol	(s)	Solid	RM	FactPS

Li	LiAl11O17	sol	(s)	Solid	RM	FactPS
Mg	MgO	sol	(s)	Solid	RM	FactPS
Mg	MgAl2O4	sol	(s)	Solid	RM	FactPS
Mn	MnO	sol	(s)	Solid	RM	FactPS
Mn	Mn2O3	sol	(s)	Solid	RM	FactPS
Mn	Mn3O4	sol	(s)	Solid	RM	FactPS
Mn	MnO2	sol	(s)	Solid	RM	FactPS
Mn	MnAl2O4	sol	(s)	Solid	RM	FactPS
Na	Na2O2	alp	(α)	Alpha	RM	FactPS
Na	Na2O2	bet	(β)	Beta	RM	FactPS
Na	Na2O	gam	(γ)	Gamma	RM	FactPS
Na	Na2O	bet	(β)	Beta	RM	FactPS
Na	Na2O	alp	(α)	Alpha	RM	FactPS
Na	Na2O	liq	(l)	Liquid	RM	FactPS
Na	NaAlO2	alp	(α)	Alpha	RM	FactPS
Na	NaAlO2	bet	(β)	Beta	RM	FactPS
Na	NaAl9O14	sol	(s)	Solid	RM	FTOxid
Na	Na2Al12O19	sol	(s)	Solid	RM	FactPS
Ni	NiO	sol	(s)	Solid	RM	FactPS
Ni	NiAl2O4	sol	(s)	Solid	RM	FactPS
Sc	Sc2O3	sol	(s)	Solid	RM	FactPS
Sc	ScAlO3	sol	(s)	Solid	dG directly	[5]
Si	SiO2	qlo	(qlo)	Quartz - low T	RM	FactPS
Si	SiO2	qhi	(qhi)	Quartz - high T	RM	FactPS
Si	SiO2	thi	(thi)	Tridymite - high T	RM	FactPS
Si	Al2Si2O7	sol	(s)	Solid	RM	FactPS
Si	Al2SiO5	and	(and)	Andalusite	RM	FactPS
Si	Al2SiO5	kya	(kya)	Kyanite	RM	FactPS
Si	Al2SiO5	sil	(sil)	Sillimanite	RM	FactPS
Si	Al6Si2O13	sol	(s)	Solid	RM	FactPS
Si	MgSiO3	cli	(cli)	Clino-enstatite	RM	FactPS
Si	MgSiO3	ens	(ens)	Ortho-enstatite	RM	FactPS
Si	MgSiO3	pro	(pro)	Proto-enstatite	RM	FactPS
Si	Mg2SiO4	sol	(s)	Solid	RM	FactPS
Si	Mg2Al4Si5O18	sol	(s)	Solid	G method	FactPS
Si	Mg3Al2Si3O12	sol	(s)	Solid	G method	FactPS
Si	Mg4Al10Si2O23	sol	(s)	Solid	G method	FactPS
Sr	Sr2O	gas	(g)	Gas	RM	FactPS
Sr	SrO	sol	(s)	Solid	RM	FactPS
Sr	Sr4Al2O7	sol	(s)	Solid	RM	FTOxid
Sr	Sr3Al2O6	sol	(s)	Solid	RM	FTOxid
Sr	SrAl2O4	alp	(α)	Alpha	RM	FTOxid
Sr	SrAl2O4	bet	(β)	Beta	RM	FTOxid
Sr	SrAl4O7	sol	(s)	Solid	RM	FTOxid
Sr	SrAl12O19	sol	(s)	Solid	RM	FTOxid
Sr	Sr5Al2O8	sol	(s)	Solid	RM	FTOxid
Sr	Sr4Al14O25	sol	(s)	Solid	RM	FTOxid
Sr	SrAl10MgO17	sol	(s)	Solid	G method	FactPS

Ti	TiO	alp	(α)	Alpha	RM	FactPS
Ti	TiO	bet	(β)	Beta	RM	FactPS
Ti	Ti2O3	alp	(α)	Alpha	RM	FactPS
Ti	Ti2O3	bet	(β)	Beta	RM	FactPS
Ti	Ti3O5	alp	(α)	Alpha	RM	FactPS
Ti	Ti3O5	bet	(β)	Beta	RM	FactPS
Ti	Ti4O7	sol	(s)	Solid	RM	FactPS
Ti	Ti5O9	sol	(s)	Solid	RM	FactPS
Ti	Ti6O11	sol	(s)	Solid	RM	FactPS
Ti	Ti7O13	sol	(s)	Solid	RM	FactPS
Ti	Ti8O15	sol	(s)	Solid	RM	FactPS
Ti	Ti9O17	sol	(s)	Solid	RM	FactPS
Ti	Ti10O19	sol	(s)	Solid	RM	FactPS
Ti	Ti20O39	sol	(s)	Solid	RM	FactPS
Ti	TiO2	rut	(rut)	Rutile	RM	FactPS
Ti	Al2TiO5	sol	(s)	Solid	RM	FactPS
Ti	Al4TiO8	sol	(s)	Solid	RM	FactPS
Zn	ZnO	sol	(s)	Solid	RM	FactPS
Zn	ZnAl2O4	sol	(s)	Solid	RM	FactPS
Zr	ZrO2	alp	(α)	Alpha	RM	FactPS
Zr	ZrO2	bet	(β)	Beta	RM	FactPS

Table B.1. Summary of compounds and data sources. RM refers to the Reaction Module from FactSage [1].

B.3. Non-ideal solution parameters

B.3.1. Bragg-Williams: Al-X binary systems

The data used to model Al-X binary systems, ${}^{i}L_{\mathrm{Al-X}}$ parameters, is shown below (Table B.2).

X	**Ref**	${}^{0}L_{\mathrm{Al-X}}$		${}^{1}L_{\mathrm{Al-X}}$		${}^{2}L_{\mathrm{Al-X}}$		${}^{3}L_{\mathrm{Al-X}}$	
		$a_i(\mathrm{cst.})$	$b_i(T)$	$a_i(\mathrm{cst.})$	$b_i(T)$	$a_i(\mathrm{cst.})$	$b_i(T)$	$a_i(\mathrm{cst.})$	$b_i(T)$
Ag	[6]	-13224.15	-7.67	17133.55	3.27	-493.86			
B	[7]	-927.53	-5.11	31961.6		-12992			
Be	[8]	56939	-28	-9856					
Ca	[9]	-91481.9	35.49	-62344.5	32.19	16815.5	2.23	33581	-16.73
Ce	[10]	-13371	38.52	-3633	6.36	-928	4.65		
Co	[11]	-1551	33.73	-29294.9	12.5	3374.5	-3.41		
Cr	[12]	-37139.1	2.11	-15698.7	7.46				
Cu	[13]	-68236	9.43	33155	-9.87	-2241			
Fe	[14]	-84735.6	17.57	-13643	7.7	-2484			
Gd	[15]	-1665	52.36	-2379		1852	4		
Ge	[16]	-14869	-1.1	3325	-3.67				
K	[17]	31616	8.78						
La	[18]	-14679	1.52	-4798	-18.58				
Li	[19]	-435	18	-137	2.11	11175			
Mg	[20]	-12	8.57	1894	-3	2			

Mn	[21]	-7584.9	28.23	-13293.5	9.83				
Na	[22]	30650	20						
Ni	[23]	-194177	28.66	4829		5342	-9.12		
Sc	[24]	-131778	3.64	-2126	8.88	5985	-24.92		
Si	[25]	-11655.93	-0.93	-2873.45	0.29	252			
Sr	[26]	-74839	23.69	-3179	8.55	1683	-4.13		
Ti	[27]	-11257	34.2	9746.9	7.69				
Zn	[28]	1465.55	-3.39						
Zr	[29]	-186477.95	49.86	-38386.64	25.91	48183.91	-7.4		

Table B.2. Summary of ${}^{i}L_{\mathrm{Al-X}}$ parameters used in Al-X binary systems, given in (a) J/mol and (b) J/mol/K.

Each ${}^{i}L_{\mathrm{Al-X}}$ parameter is linearly dependent on temperature, where a_i is the constant term and b_i is the coefficient of T (B.1).

$$ {}^{i}L(T) = a_i + b_i T \tag{B.1}$$

B.3.2. Bragg-Williams: Al-Mg-X ternary systems

Below are tables of the Bragg-Williams parameters, both binary ${}^{i}L_{12}$ (Table B.3) and ternary ${}^{i}L_{12\mathrm{Al}}$ (Table B.4), used in modelling the Al-Mg-X ternary systems. Like the Al-X binary systems, ${}^{i}L_{12}$ and ${}^{i}L_{12\mathrm{Al}}$ values are given as a constant term a_i and a linear coefficient of temperature, b_i (B.1).

System		Ref	${}^{0}L_{12}$		${}^{1}L_{12}$		${}^{2}L_{12}$		${}^{3}L_{12}$	
1	2		$a_i(\mathrm{cst.})$	$b_i(T)$	$a_i(\mathrm{cst.})$	$b_i(T)$	$a_i(\mathrm{cst.})$	$b_i(T)$	$a_i(\mathrm{cst.})$	$b_i(T)$
Al	Be	[8]	56939	-28	-9856					
Al	Ca	[9]	-91481.9	35.49298	-62344.5	32.19103	16815.5	2.23255	33581	-16.7272
Al	Ce	[10]	-130371	38.523	-36330	6.362	-9208	4.065		
Al	Cu	[13]	-68236	9.43	33155	-9.87	-2241			
Al	Gd	[15]	-166500	52.36	-23790		18520			
Al	La	[18]	-146079	1.518	47908	18.582				
Al	Mg	[20]	-12000	8.566	1894	-3	2000			
Al	Mn	[21]	-70584.9	28.22693	-13293.5	9.82551				
Al	Si	[25]	-11655.9	-0.92934	-2873.45	0.2945	2520			
Al	Sr	[26]	-74839	23.686	-31790	8.549	10683	-4.13		
Al	Zn	[28]	10288	-3.035	-810	0.471				
Mg	Be	[30]	57000							
Mg	Ca	[31]	-32322.4	16.7211	-60.3	-6.549	-5742.3	2.7596		
Mg	Ce	[32]	-39381.2	16.3405	-25338.6	11.8689	-15106.9			
Mg	Cu	[13]	-33546	-11.09	20410	-17.08				
Mg	Gd	[15]	-25000	0.3089	-23600	4.521				
Mg	La	[32]	-36462.5	12.1291	-26159	14.9613	-13283.1			
Mg	Mn	[33]	25922.4	9.0357	-3470.8					

Mg	Si	[34]	-70055	24.98	-1300		6272			
Mg	Sr	[35]	-20858	6.358	-13008	4.715				
Mg	Zn	[20]	-81439.7	518.25	2627.54	2.93061	-1637.28			

Table B.3. Binary ${}^{i}L_{12}$ parameters used in Al-Mg-X ternary systems, given in (a) J/mol and (b) J/mol/K.

		${}^{\mathbf{Al}}\boldsymbol{L}_{\mathbf{AlMgX}}$		${}^{\mathbf{Mg}}\boldsymbol{L}_{\mathbf{AlMgX}}$		${}^{\mathbf{X}}\boldsymbol{L}_{\mathbf{AlMgX}}$	
X	Ref	$a_i(\text{cst.})$	$b_i(T)$	$a_i(\text{cst.})$	$b_i(T)$	$a_i(\text{cst.})$	$b_i(T)$
Be	[30]	0	0	0	0	0	0
Ca	[36]	-22000	3	-22000	3	-22000	3
Ce	[37]	0	0	0	0	0	0
Cu	[13]	-32641	0	-92074	0	172393	0
Gd	[38]	50000	0	-90000	0	-180000	0
La	[39]	0	0	0	0	0	0
Mn	[21]	28000	0	0	0	0	0
Si	[37]	147000	-113	-14000	0	-95000	0
Sr	[36]	0	0	-25000	0	0	0
Zn	[20]	-4094.48	0	-39973.74	0	-1137.52	0

Table B.4. Ternary ${}^{i}L_{AlMgX}$ parameters used in Al-Mg-X ternary systems, given in (a) J/mol and (b) J/mol/K.

B.3.3. Modified quasichemical model

Below is a table of the parameters used in the Al-X systems evaluated with the modified quasichemical model (Table B.5).

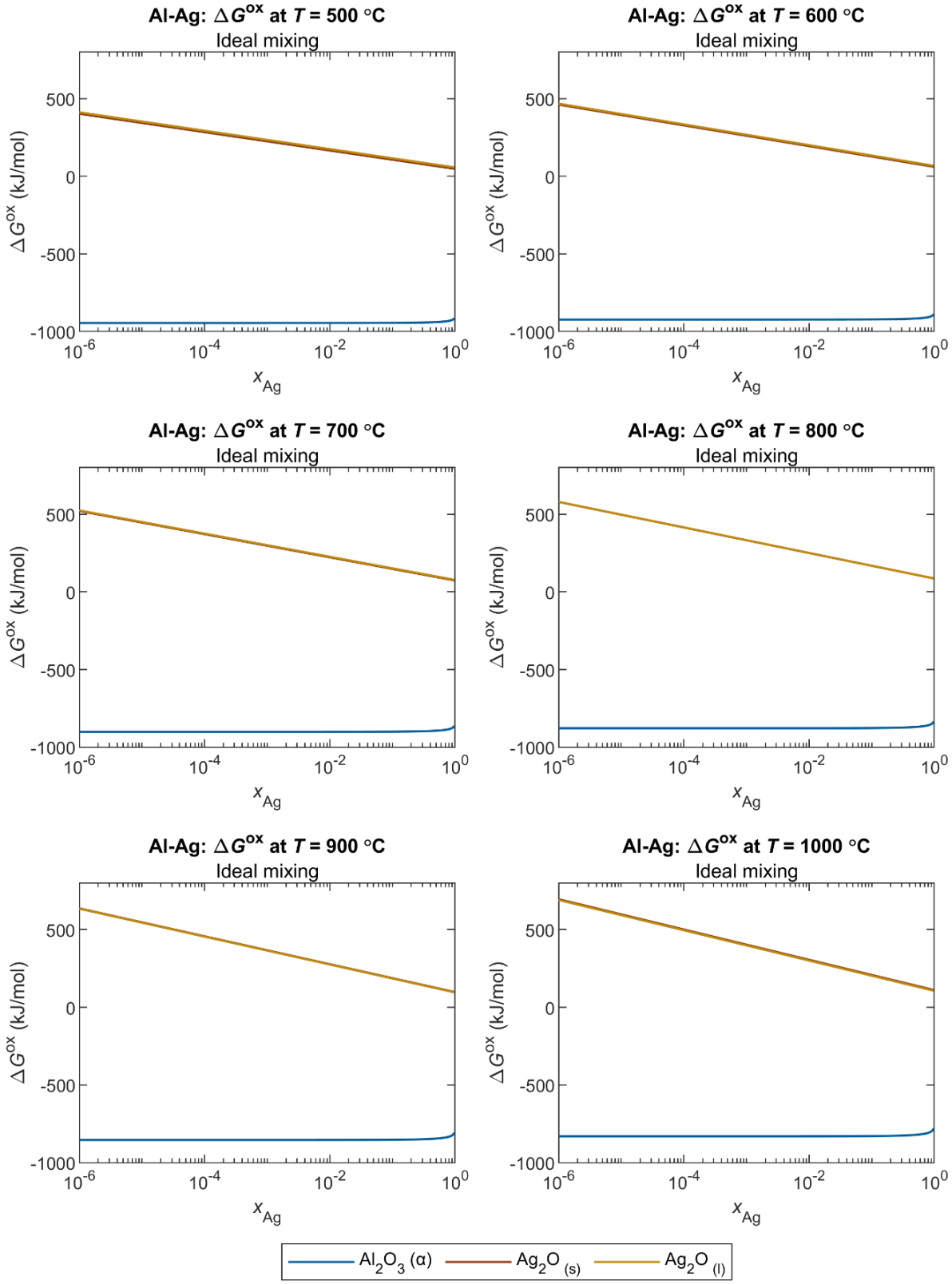
X	Ref	Z^{i}_{jk}				$\Delta g^{0}_{\mathrm{AlX}}$		g^{10}_{AlX}		g^{01}_{AlX}	
		$Z^{\mathrm{A}}_{\mathrm{AlAl}}$	$Z^{\mathrm{Al}}_{\mathrm{AlX}}$	$Z^{\mathrm{X}}_{\mathrm{AlX}}$	$Z^{\mathrm{X}}_{\mathrm{XX}}$	$a_i(\text{cst.})$	$b_i(T)$	$a_i(\text{cst.})$	$b_i(T)$	$a_i(\text{cst.})$	$b_i(T)$
Ca	[40]	6	3	6	6	-30572	10.58	0	1.32	-4890.6	-0.38
Ce	[41]	6	3	6	6	-46024	5.65	-17364	-1.13	-10460	0
Gd	[42]	6	3	6	6	-48116	5.02	-3264	-1.8	-7113	0
La	[41]	6	3	6	6	-48116	4.6	-11088	-1.674	-15732	0
Li	[43]	6	2	2	6	-25480	14	0	0	0	0
Mg	[44]	6	6	6	6	-2761.44	1.53	-418.4	0.63	0	0
Na	[45]	6	6	6	6	203509	5.90	-193133	0.00	0	0
Sc	[46]	6	6	6	6	-30543	0	-5858	-2.1	0	0
Si	[44]	6	5	5	6	-4622.28	-0.03	836.8	-1.17	836.8	-1.17
Sr	[47]	6	6	4	6	-1511.50	0.54	442.76	-0.108	-187.10	-0.27

Table B.5. Optimised parameters for Al-X systems evaluated with the modified quasichemical model, with g^{ij}_{AlX} parameters given in (a) J/mol and (b) J/mol/K.

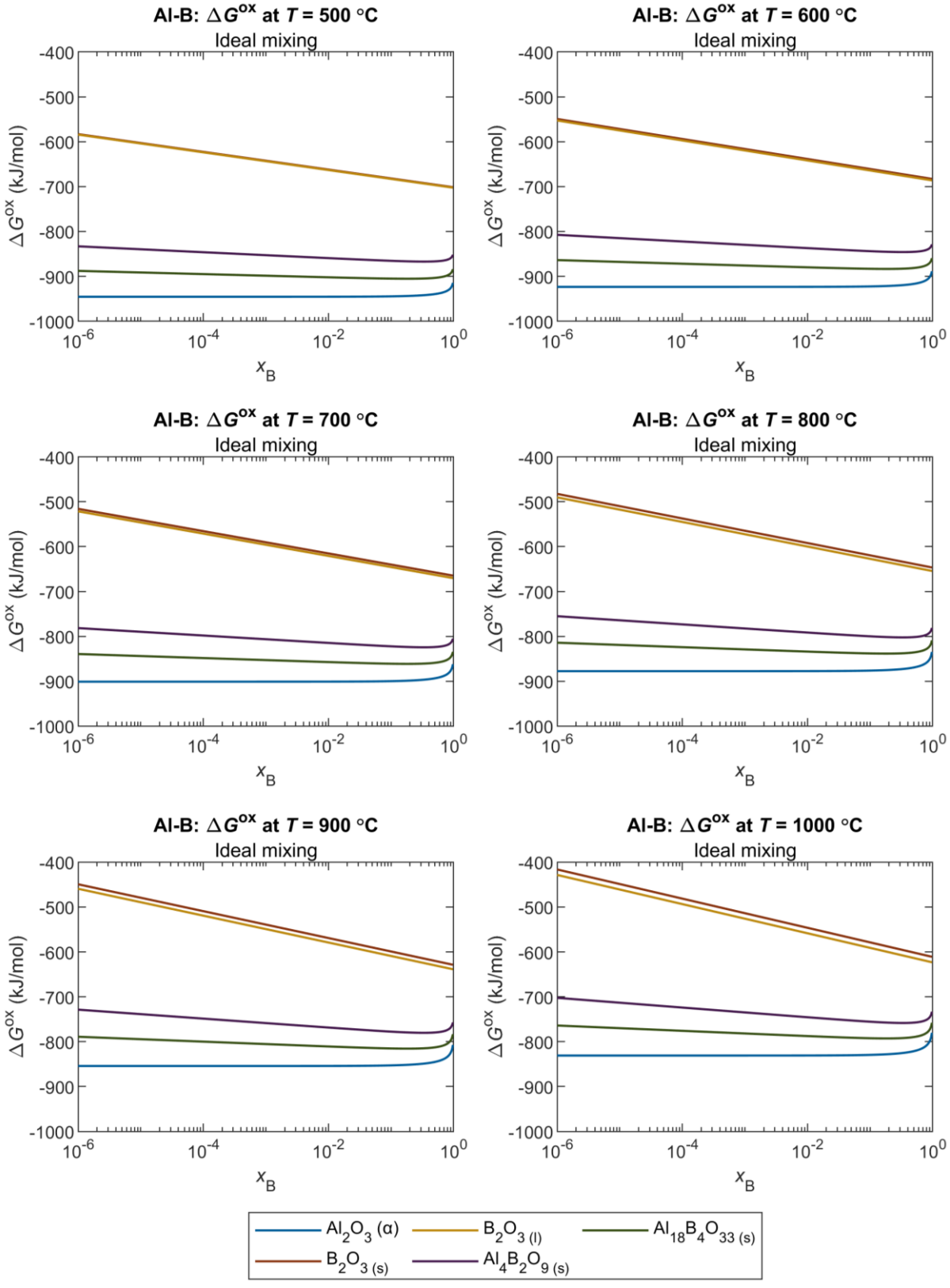
B.4. Binary systems: sections at constant T

B.4.1. Ideal mixing

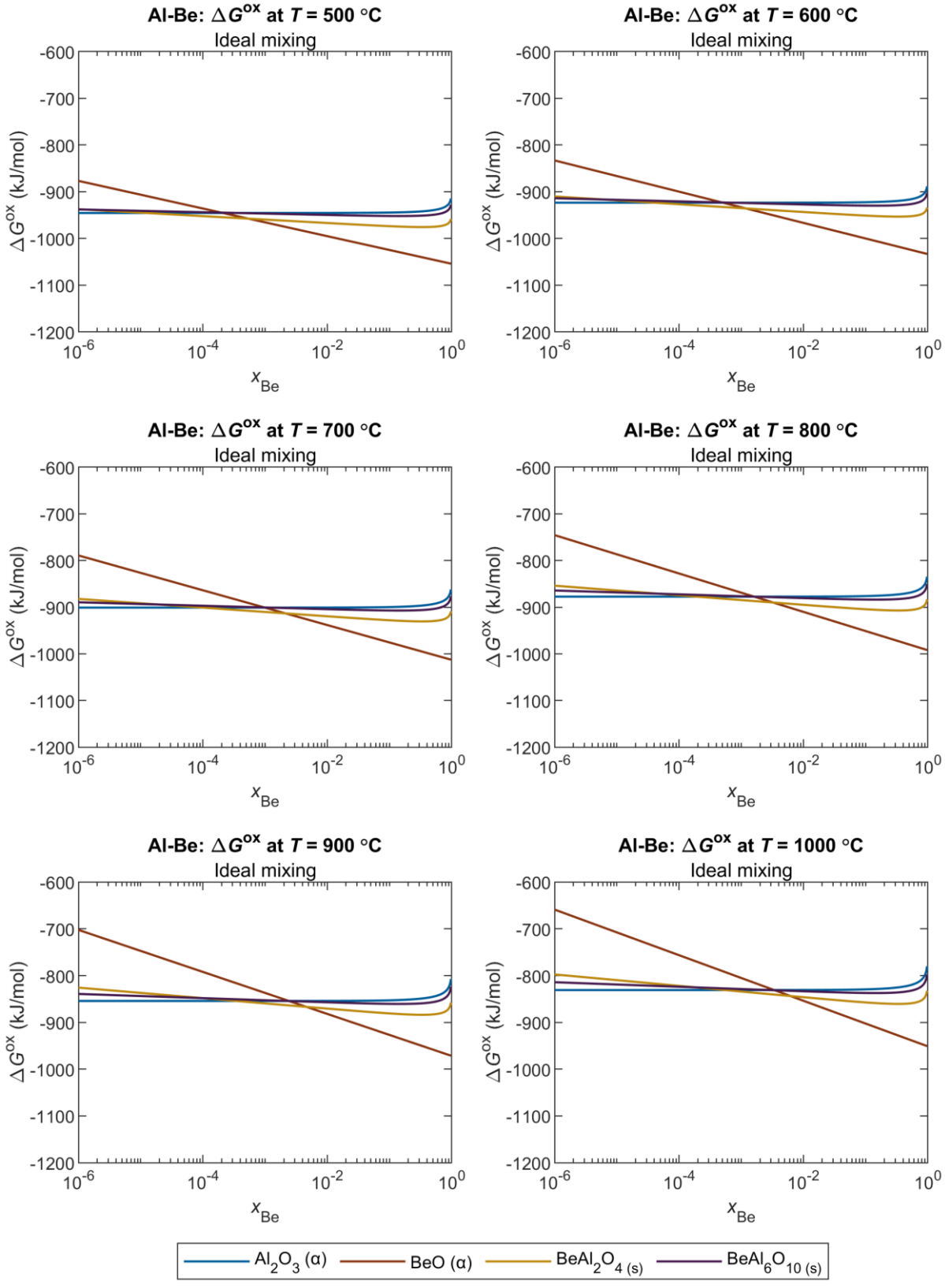
B.4.1.1. Al-Ag



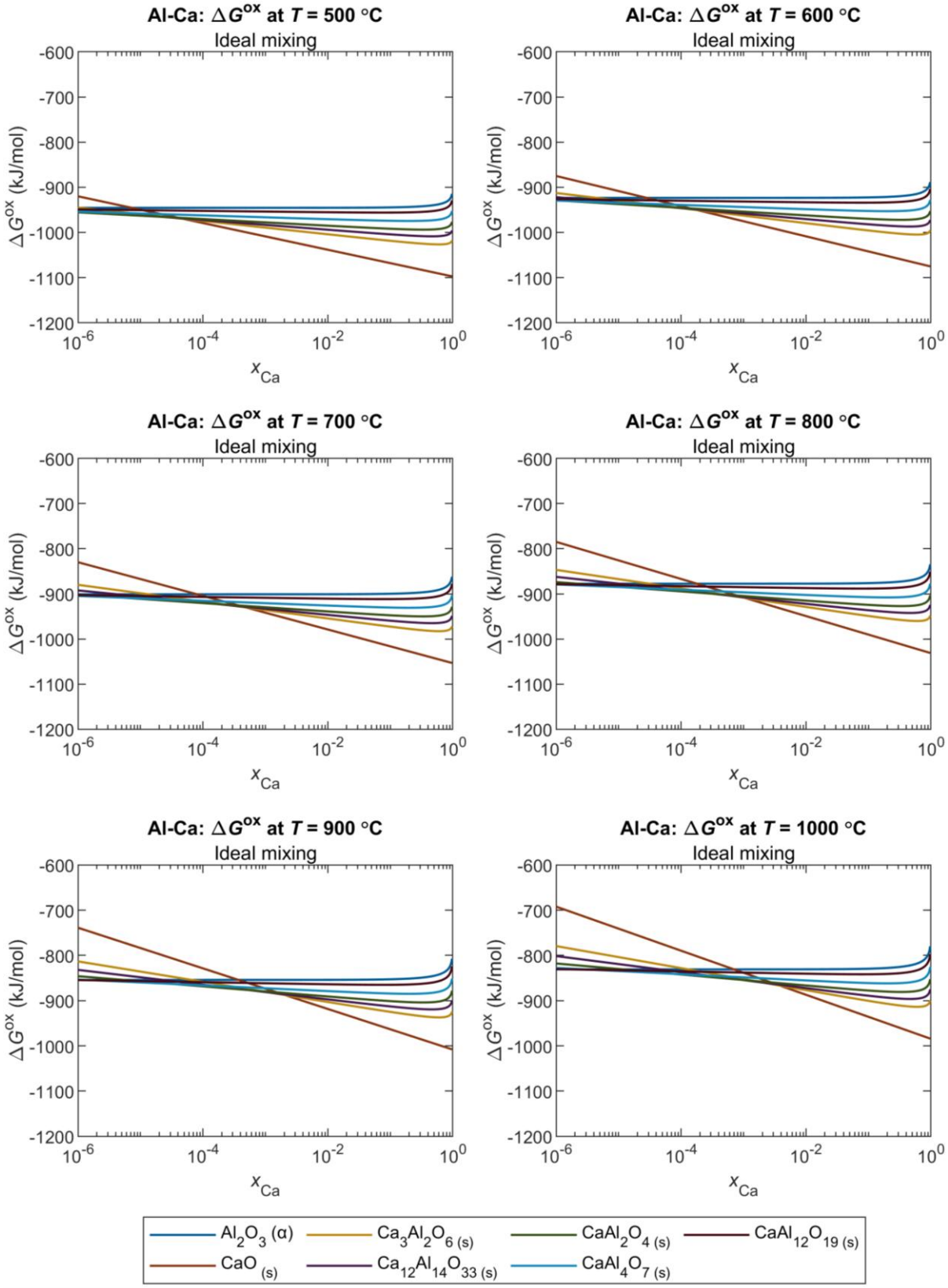
B.4.1.2. Al-B


Al-B: ΔG^ox at T = 500 °C
Ideal mixing
Al-B: ΔG^ox at T = 600 °C
Ideal mixing
Al-B: ΔG^ox at T = 700 °C
Ideal mixing
Al-B: ΔG^ox at T = 800 °C
Ideal mixing
Al-B: ΔG^ox at T = 900 °C
Ideal mixing
Al-B: ΔG^ox at T = 1000 °C
Ideal mixing
ΔG^ox (kJ/mol)
-400
-500
-600
-700
-800
-900
-1000
10^-6
10^-4
10^-2
10^0
x_B
Al2O3 (α)
B2O3 (l)
Al18B4O33 (s)
B2O3 (s)
Al4B2O9 (s)

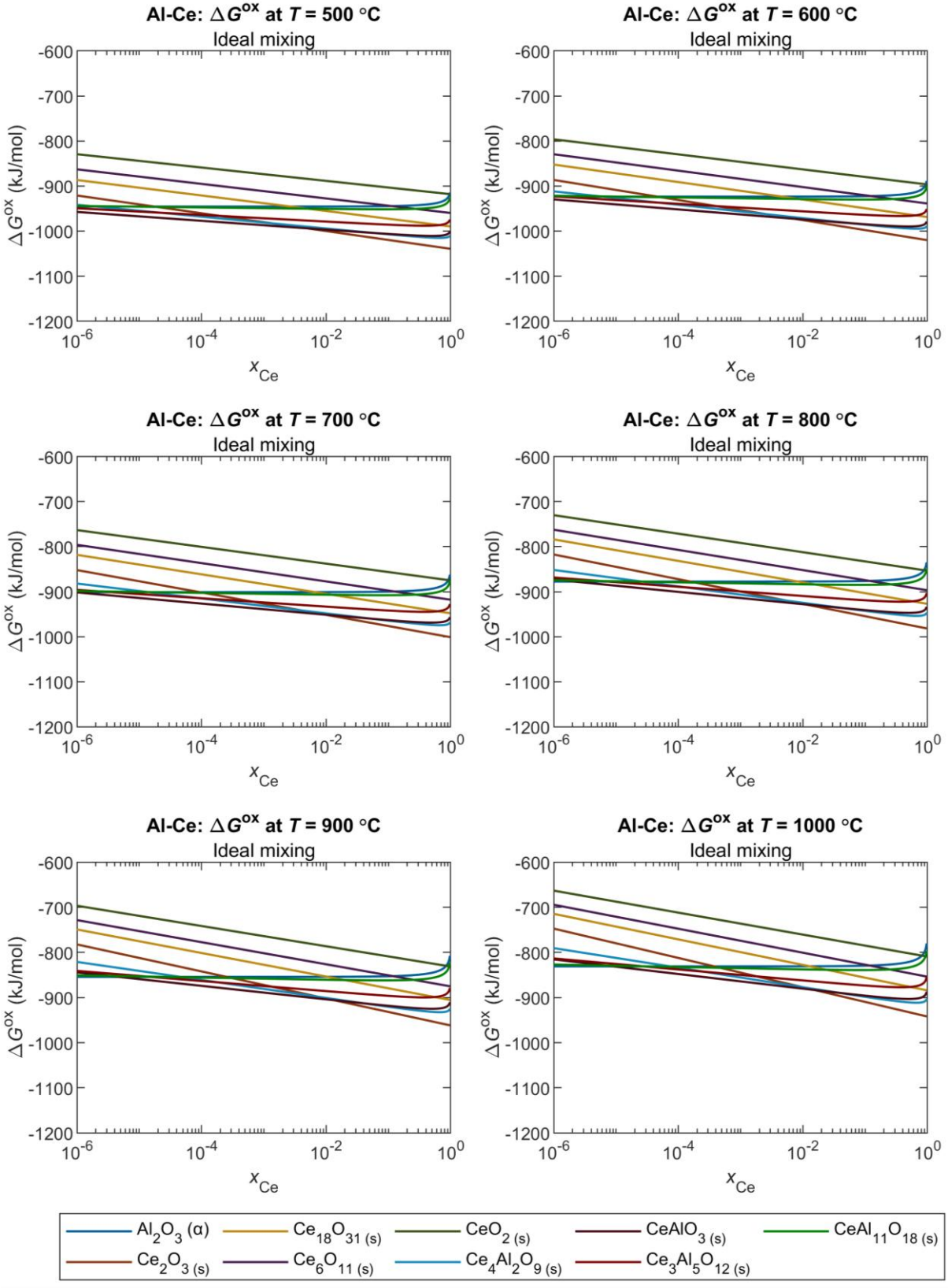
B.4.1.3. Al-Be


Al-Be: ΔG^ox at T = 500 °C
Ideal mixing
Al-Be: ΔG^ox at T = 600 °C
Ideal mixing
Al-Be: ΔG^ox at T = 700 °C
Ideal mixing
Al-Be: ΔG^ox at T = 800 °C
Ideal mixing
Al-Be: ΔG^ox at T = 900 °C
Ideal mixing
Al-Be: ΔG^ox at T = 1000 °C
Ideal mixing
ΔG^ox (kJ/mol)
-600
-700
-800
-900
-1000
-1100
-1200
10^-6
10^-4
10^-2
10^0
x_Be
Al2O3 (α)
BeO (α)
BeAl2O4 (s)
BeAl6O10 (s)

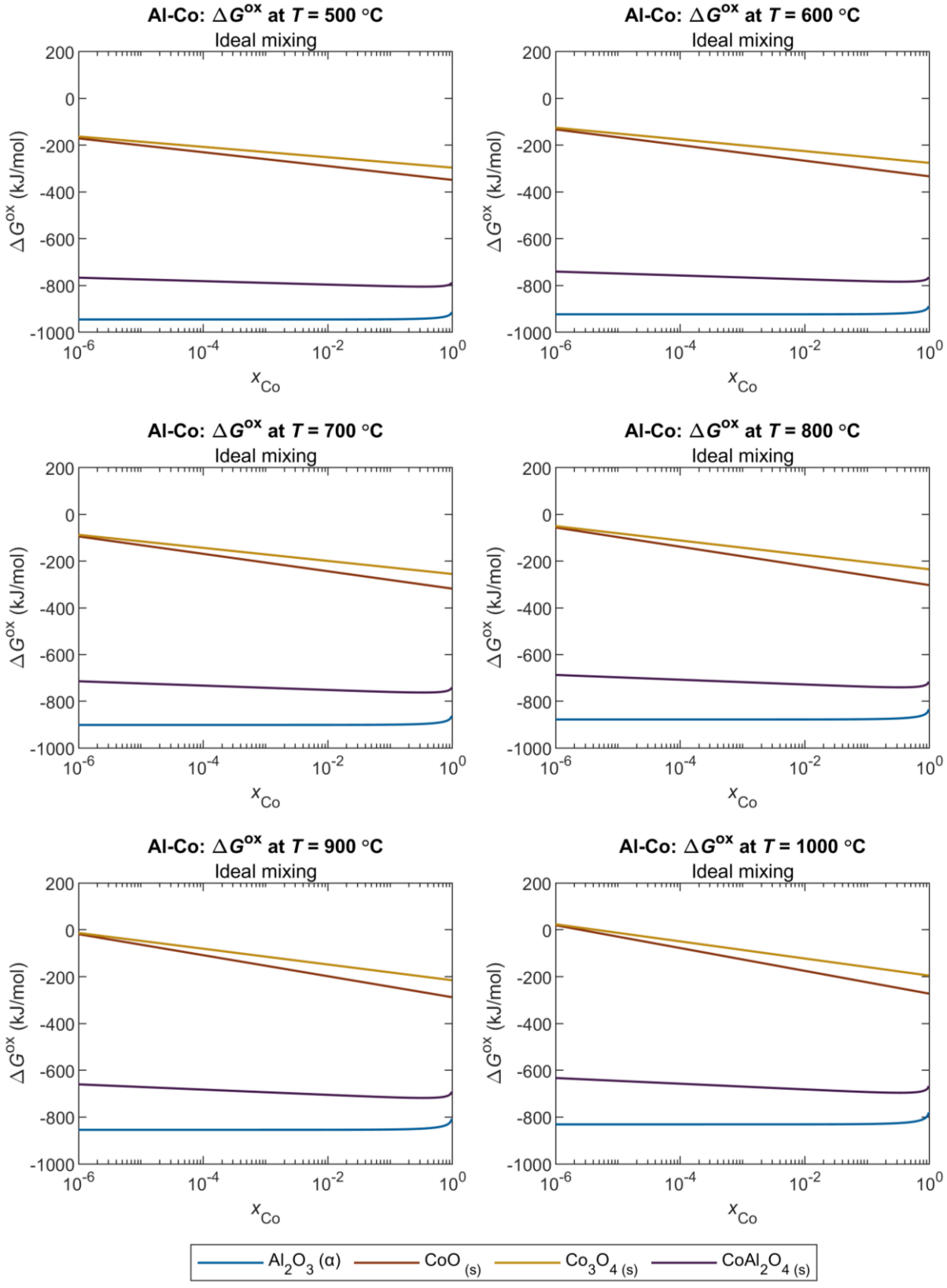
B.4.1.4. Al-Ca


Al-Ca: ΔG^ox at T = 500 °C
Ideal mixing
Al-Ca: ΔG^ox at T = 600 °C
Ideal mixing
Al-Ca: ΔG^ox at T = 700 °C
Ideal mixing
Al-Ca: ΔG^ox at T = 800 °C
Ideal mixing
Al-Ca: ΔG^ox at T = 900 °C
Ideal mixing
Al-Ca: ΔG^ox at T = 1000 °C
Ideal mixing
ΔG^ox (kJ/mol)
x_Ca
-600
-700
-800
-900
-1000
-1100
-1200
10^-6
10^-4
10^-2
10^0
Al2O3 (α)
Ca3Al2O6 (s)
CaAl2O4 (s)
CaAl12O19 (s)
CaO (s)
Ca12Al14O33 (s)
CaAl4O7 (s)

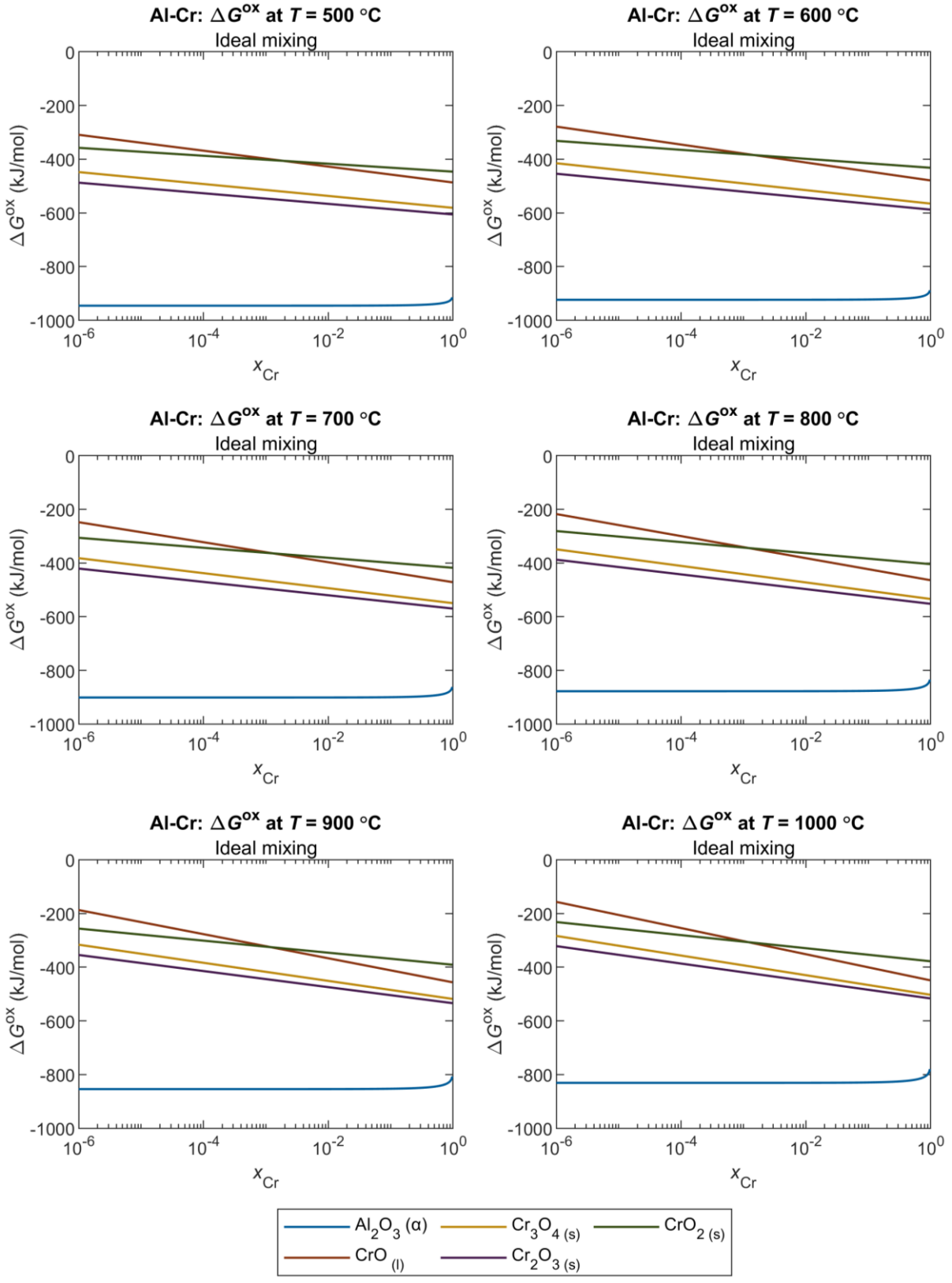
B.4.1.5. Al-Ce


Al-Ce: ΔG^ox at T = 500 °C
Ideal mixing
Al-Ce: ΔG^ox at T = 600 °C
Ideal mixing
Al-Ce: ΔG^ox at T = 700 °C
Ideal mixing
Al-Ce: ΔG^ox at T = 800 °C
Ideal mixing
Al-Ce: ΔG^ox at T = 900 °C
Ideal mixing
Al-Ce: ΔG^ox at T = 1000 °C
Ideal mixing
ΔG^ox (kJ/mol)
x_Ce
-600
-700
-800
-900
-1000
-1100
-1200
10^-6
10^-4
10^-2
10^0
Al2O3 (α)
Ce18O31 (s)
CeO2 (s)
CeAlO3 (s)
CeAl11O18 (s)
Ce2O3 (s)
Ce6O11 (s)
Ce4Al2O9 (s)
Ce3Al5O12 (s)

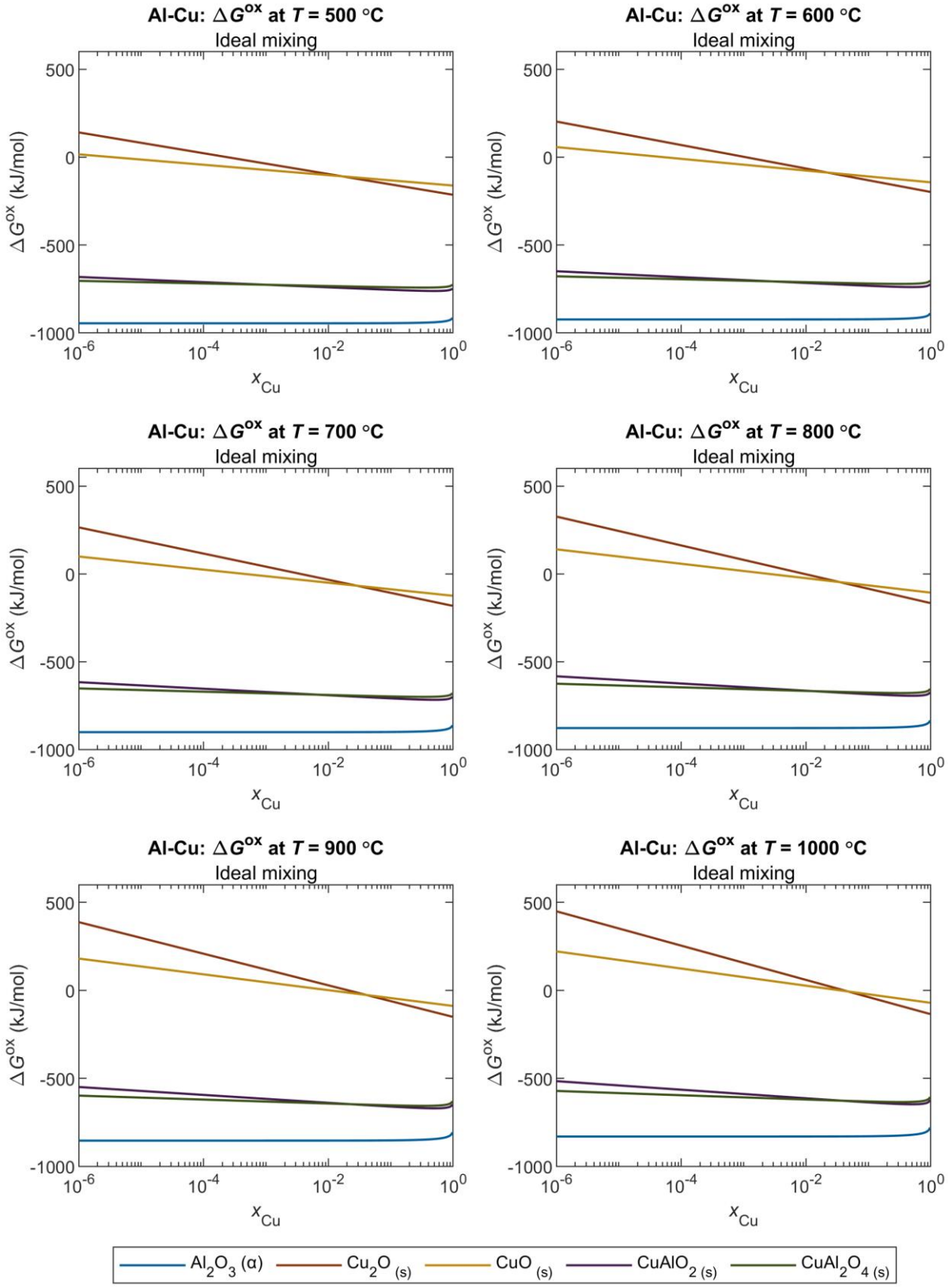
B.4.1.6. Al-Co


Al-Co: ΔG^ox at T = 500 °C
Ideal mixing
Al-Co: ΔG^ox at T = 600 °C
Ideal mixing
Al-Co: ΔG^ox at T = 700 °C
Ideal mixing
Al-Co: ΔG^ox at T = 800 °C
Ideal mixing
Al-Co: ΔG^ox at T = 900 °C
Ideal mixing
Al-Co: ΔG^ox at T = 1000 °C
Ideal mixing
ΔG^ox (kJ/mol)
x_Co
Al2O3 (α)
CoO (s)
Co3O4 (s)
CoAl2O4 (s)

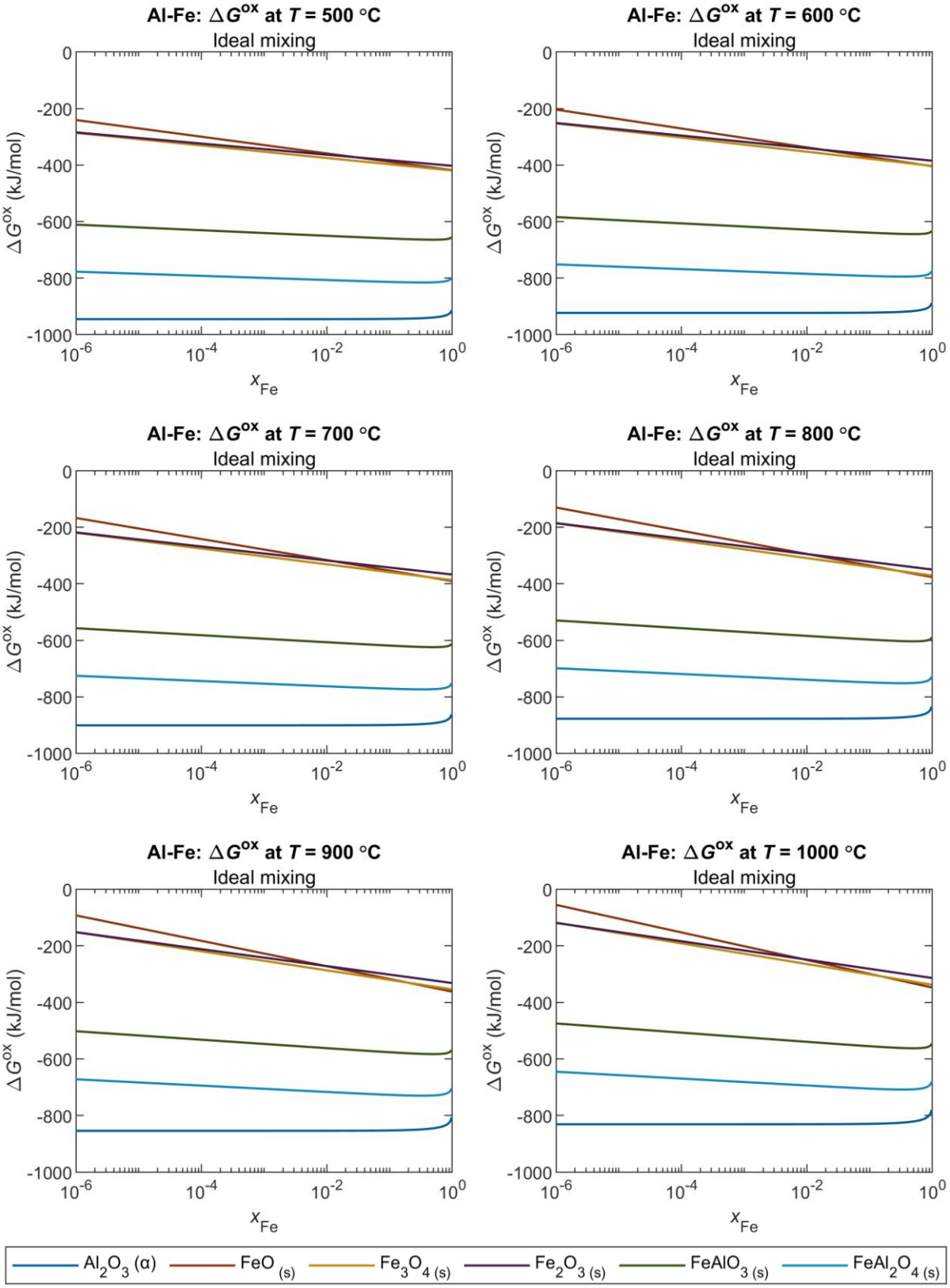
B.4.1.7. Al-Cr


Al-Cr: ΔG^ox at T = 500 °C
Ideal mixing
Al-Cr: ΔG^ox at T = 600 °C
Ideal mixing
Al-Cr: ΔG^ox at T = 700 °C
Ideal mixing
Al-Cr: ΔG^ox at T = 800 °C
Ideal mixing
Al-Cr: ΔG^ox at T = 900 °C
Ideal mixing
Al-Cr: ΔG^ox at T = 1000 °C
Ideal mixing
ΔG^ox (kJ/mol)
x_Cr
0
-200
-400
-600
-800
-1000
10^-6
10^-4
10^-2
10^0
Al2O3 (α)
Cr3O4 (s)
CrO2 (s)
CrO (l)
Cr2O3 (s)

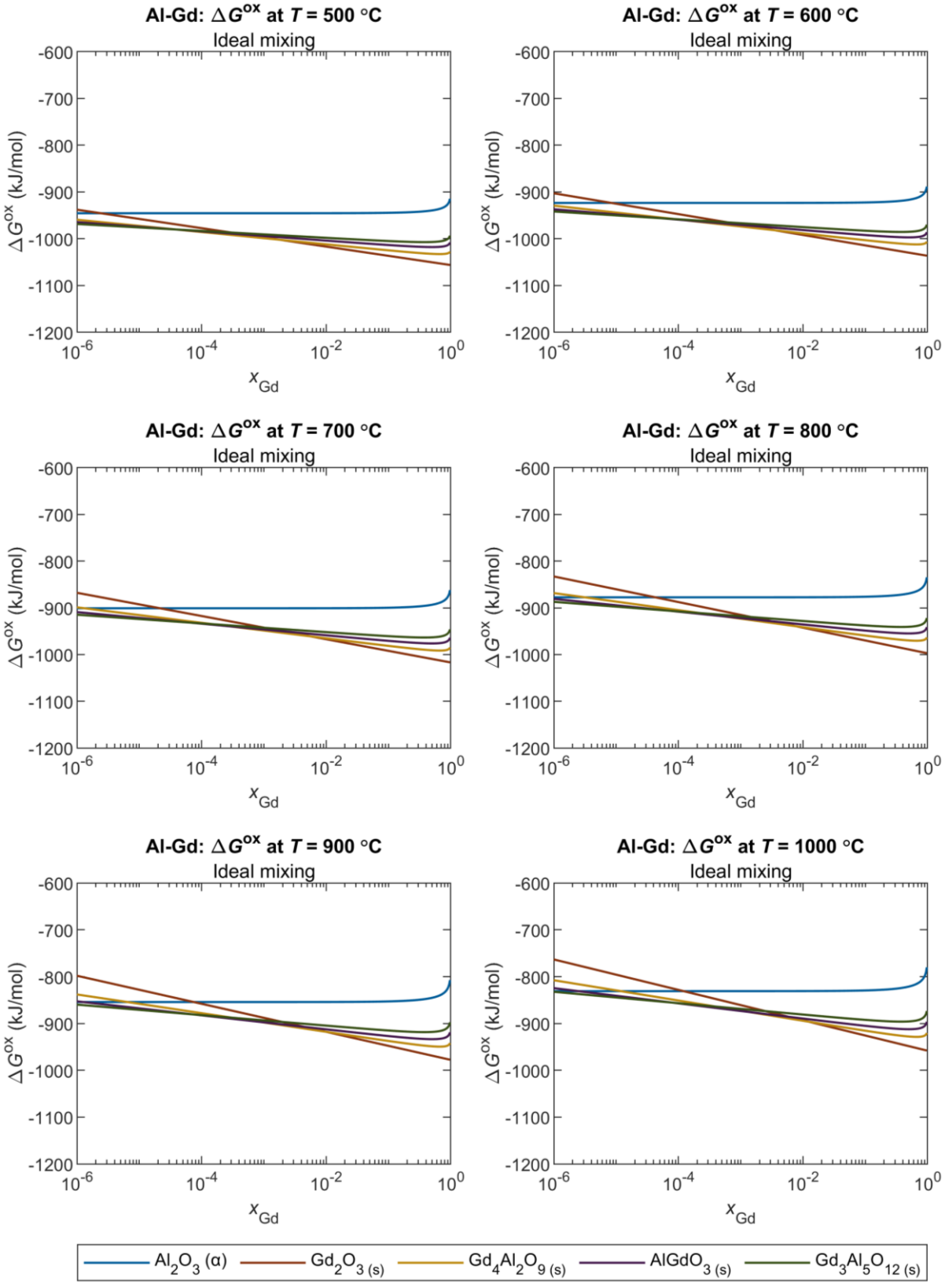
B.4.1.8. Al-Cu


Al-Cu: ΔG^ox at T = 500 °C
Ideal mixing
Al-Cu: ΔG^ox at T = 600 °C
Ideal mixing
Al-Cu: ΔG^ox at T = 700 °C
Ideal mixing
Al-Cu: ΔG^ox at T = 800 °C
Ideal mixing
Al-Cu: ΔG^ox at T = 900 °C
Ideal mixing
Al-Cu: ΔG^ox at T = 1000 °C
Ideal mixing
ΔG^ox (kJ/mol)
500
0
-500
-1000
10^-6
10^-4
10^-2
10^0
x_Cu
Al2O3 (α)
Cu2O (s)
CuO (s)
CuAlO2 (s)
CuAl2O4 (s)

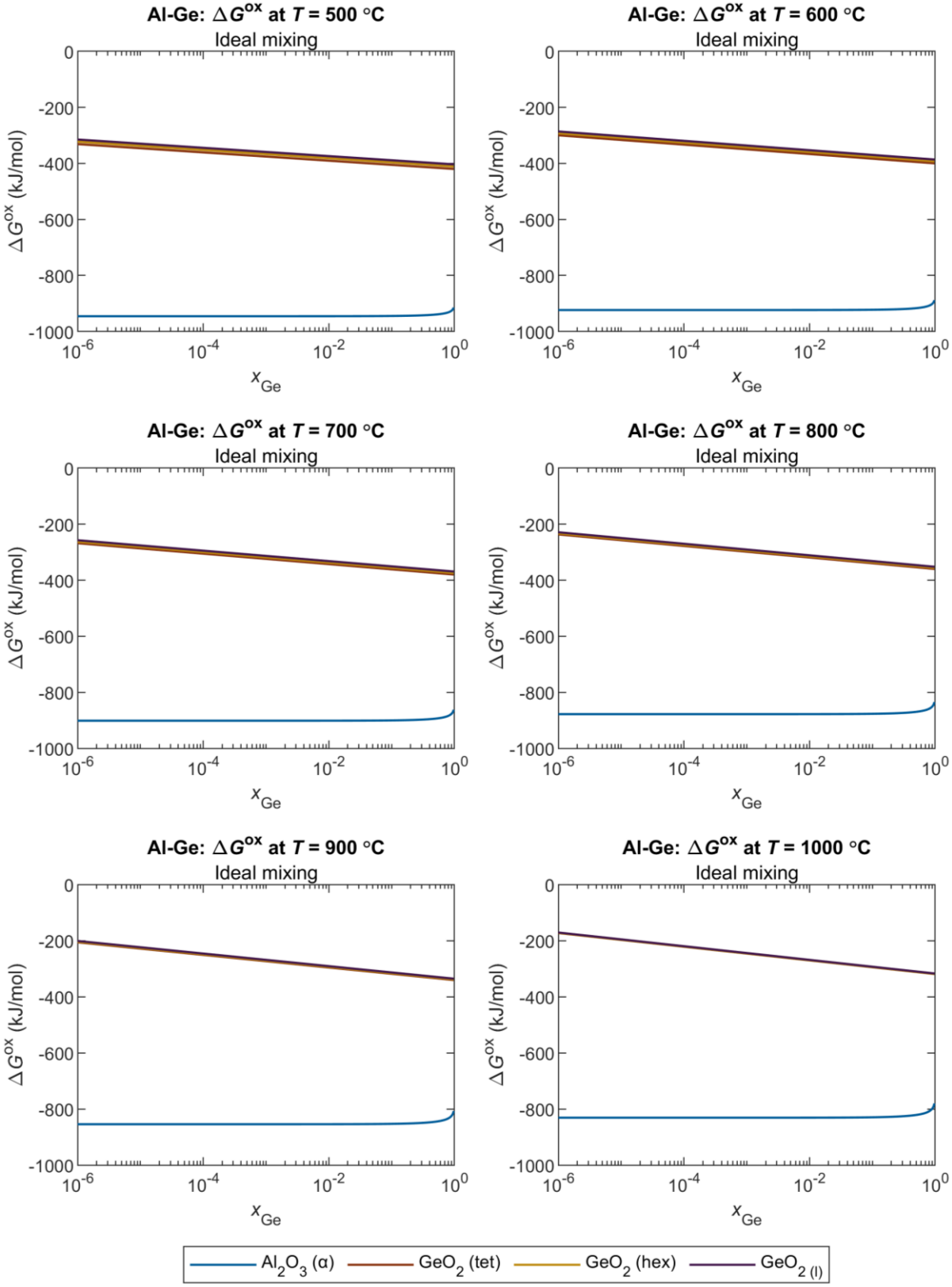
B.4.1.9. Al-Fe


Al-Fe: ΔG^ox at T = 500 °C
Ideal mixing
Al-Fe: ΔG^ox at T = 600 °C
Ideal mixing
Al-Fe: ΔG^ox at T = 700 °C
Ideal mixing
Al-Fe: ΔG^ox at T = 800 °C
Ideal mixing
Al-Fe: ΔG^ox at T = 900 °C
Ideal mixing
Al-Fe: ΔG^ox at T = 1000 °C
Ideal mixing
ΔG^ox (kJ/mol)
x_Fe
0
-200
-400
-600
-800
-1000
10^-6
10^-4
10^-2
10^0
Al2O3 (α)
FeO (s)
Fe3O4 (s)
Fe2O3 (s)
FeAlO3 (s)
FeAl2O4 (s)

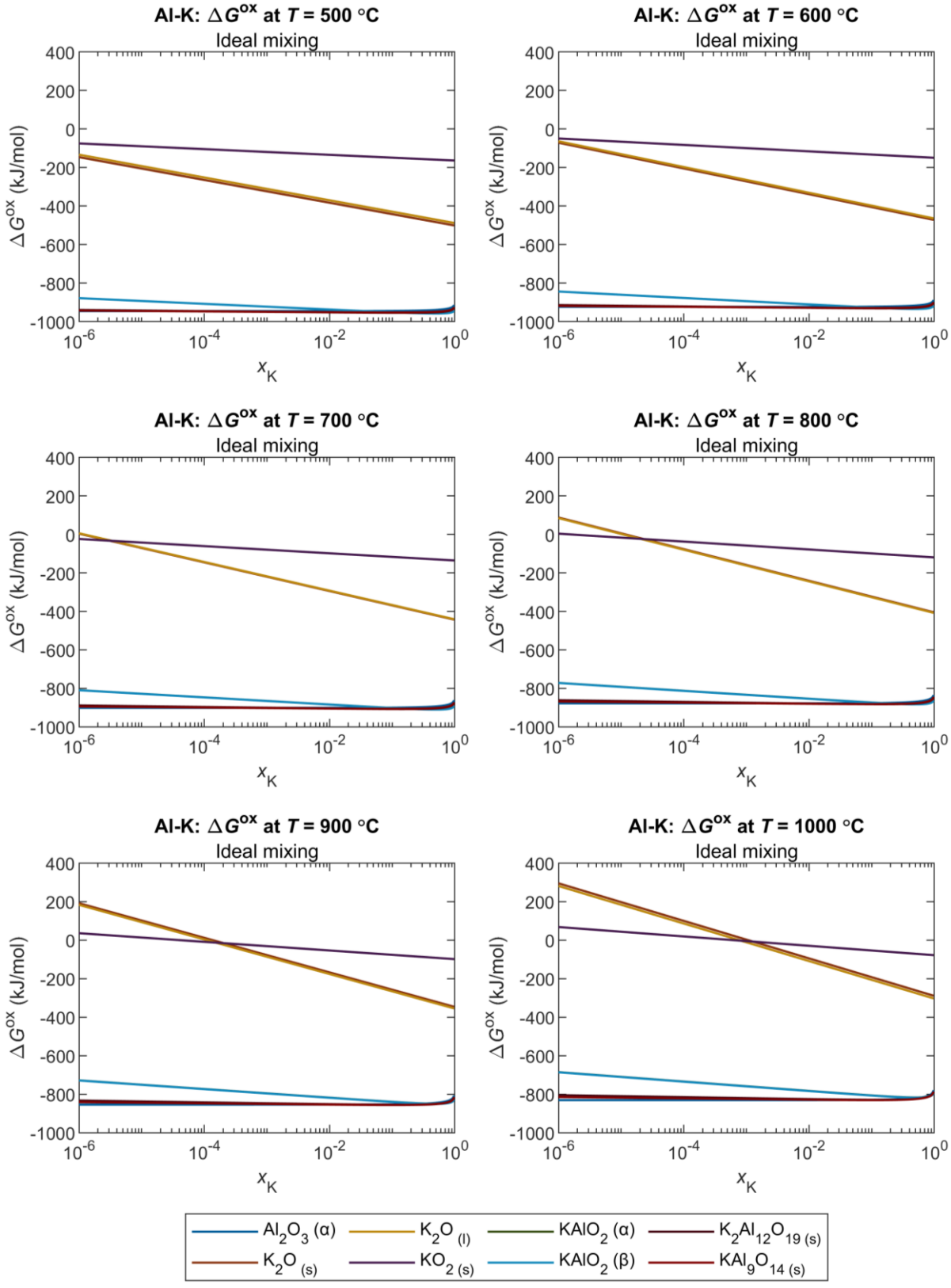
B.4.1.10. Al-Gd


Al-Gd: ΔG^ox at T = 500 °C
Ideal mixing
Al-Gd: ΔG^ox at T = 600 °C
Ideal mixing
Al-Gd: ΔG^ox at T = 700 °C
Ideal mixing
Al-Gd: ΔG^ox at T = 800 °C
Ideal mixing
Al-Gd: ΔG^ox at T = 900 °C
Ideal mixing
Al-Gd: ΔG^ox at T = 1000 °C
Ideal mixing
ΔG^ox (kJ/mol)
-600
-700
-800
-900
-1000
-1100
-1200
10^-6
10^-4
10^-2
10^0
x_Gd
Al2O3 (α)
Gd2O3 (s)
Gd4Al2O9 (s)
AlGdO3 (s)
Gd3Al5O12 (s)

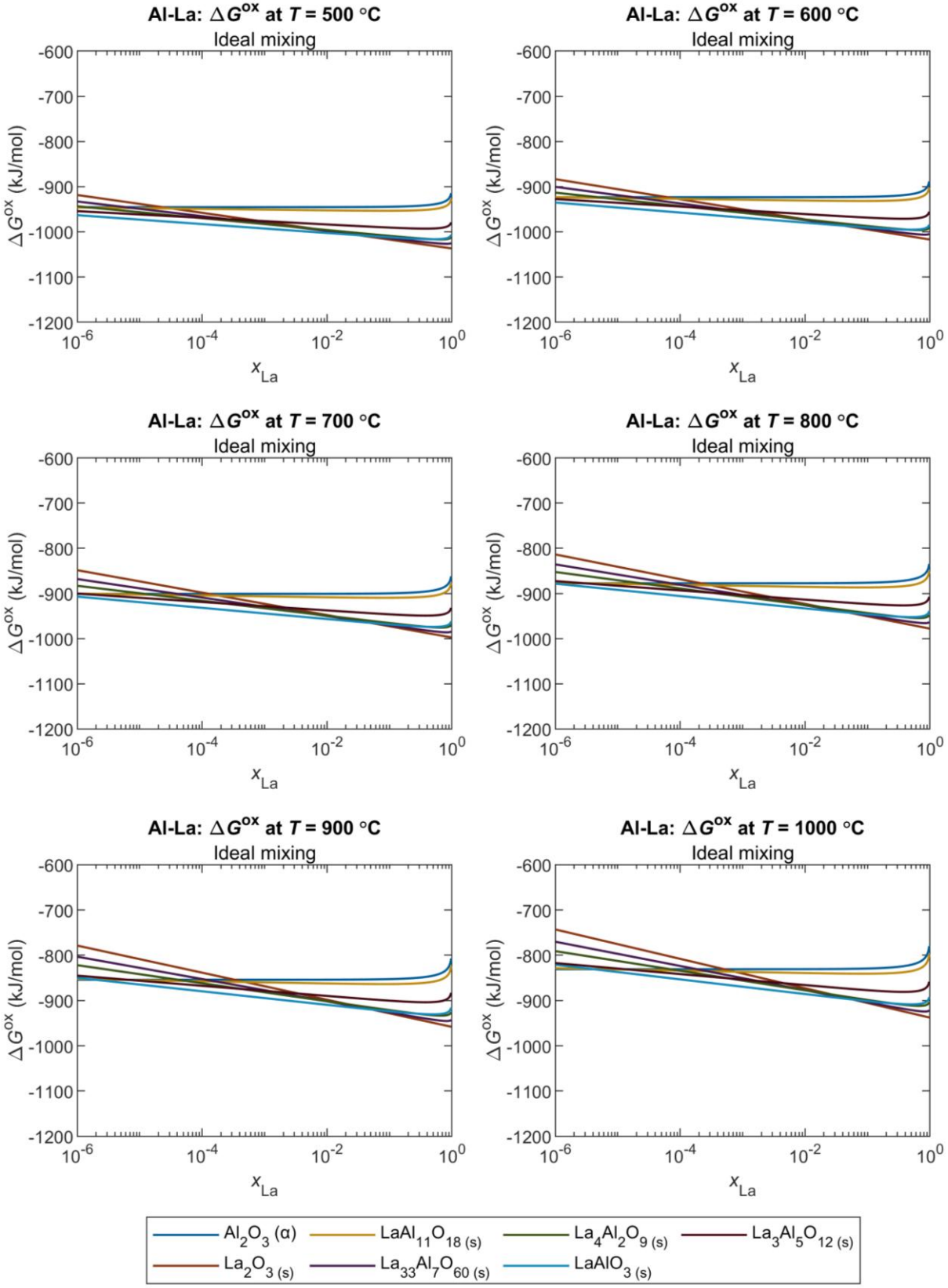
B.4.1.11. Al-Ge


Al-Ge: ΔG^ox at T = 500 °C
Ideal mixing
Al-Ge: ΔG^ox at T = 600 °C
Ideal mixing
Al-Ge: ΔG^ox at T = 700 °C
Ideal mixing
Al-Ge: ΔG^ox at T = 800 °C
Ideal mixing
Al-Ge: ΔG^ox at T = 900 °C
Ideal mixing
Al-Ge: ΔG^ox at T = 1000 °C
Ideal mixing
ΔG^ox (kJ/mol)
0
-200
-400
-600
-800
-1000
10^-6
10^-4
10^-2
10^0
x_Ge
Al2O3 (α)
GeO2 (tet)
GeO2 (hex)
GeO2 (l)

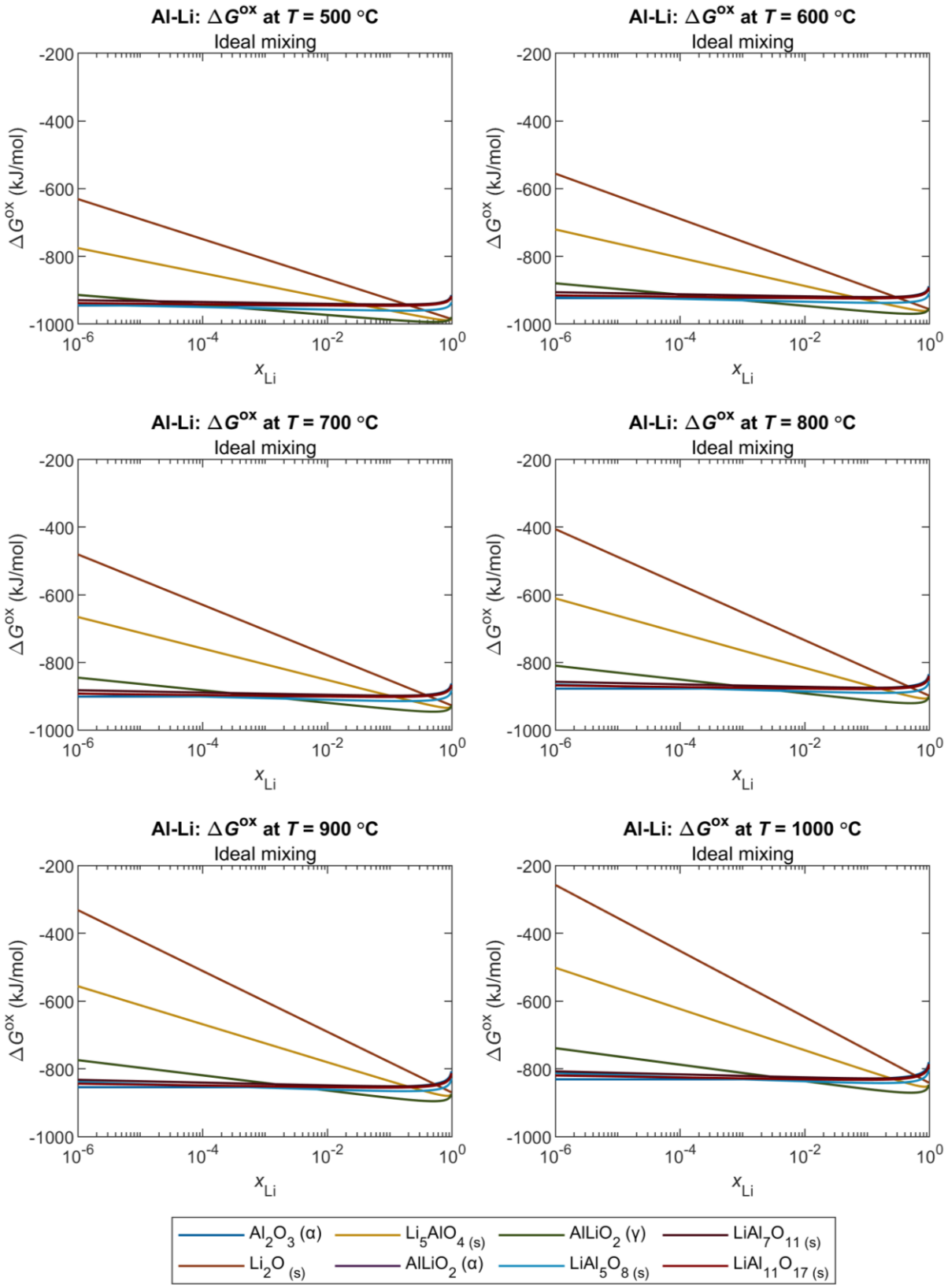
B.4.1.12. Al-K


Al-K: ΔG^ox at T = 500 °C
Ideal mixing
Al-K: ΔG^ox at T = 600 °C
Ideal mixing
Al-K: ΔG^ox at T = 700 °C
Ideal mixing
Al-K: ΔG^ox at T = 800 °C
Ideal mixing
Al-K: ΔG^ox at T = 900 °C
Ideal mixing
Al-K: ΔG^ox at T = 1000 °C
Ideal mixing
ΔG^ox (kJ/mol)
x_K
Al2O3 (α)
K2O (l)
KAlO2 (α)
K2Al12O19 (s)
K2O (s)
KO2 (s)
KAlO2 (β)
KAl9O14 (s)

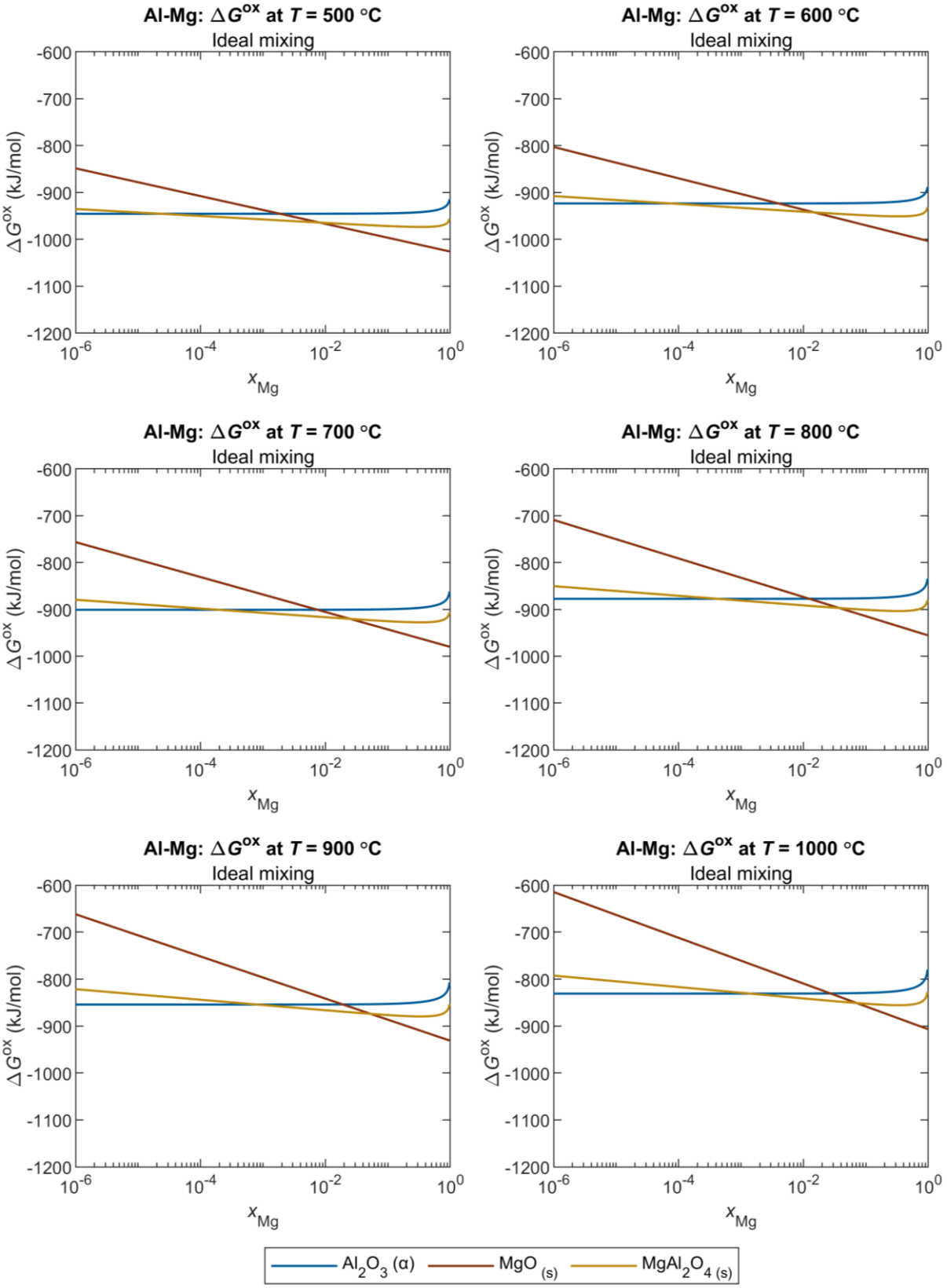
B.4.1.13. Al-La


Al-La: ΔG^ox at T = 500 °C
Ideal mixing
Al-La: ΔG^ox at T = 600 °C
Ideal mixing
Al-La: ΔG^ox at T = 700 °C
Ideal mixing
Al-La: ΔG^ox at T = 800 °C
Ideal mixing
Al-La: ΔG^ox at T = 900 °C
Ideal mixing
Al-La: ΔG^ox at T = 1000 °C
Ideal mixing
ΔG^ox (kJ/mol)
-600
-700
-800
-900
-1000
-1100
-1200
10^-6
10^-4
10^-2
10^0
x_La
Al2O3 (α)
LaAl11O18 (s)
La4Al2O9 (s)
La3Al5O12 (s)
La2O3 (s)
La33Al7O60 (s)
LaAlO3 (s)

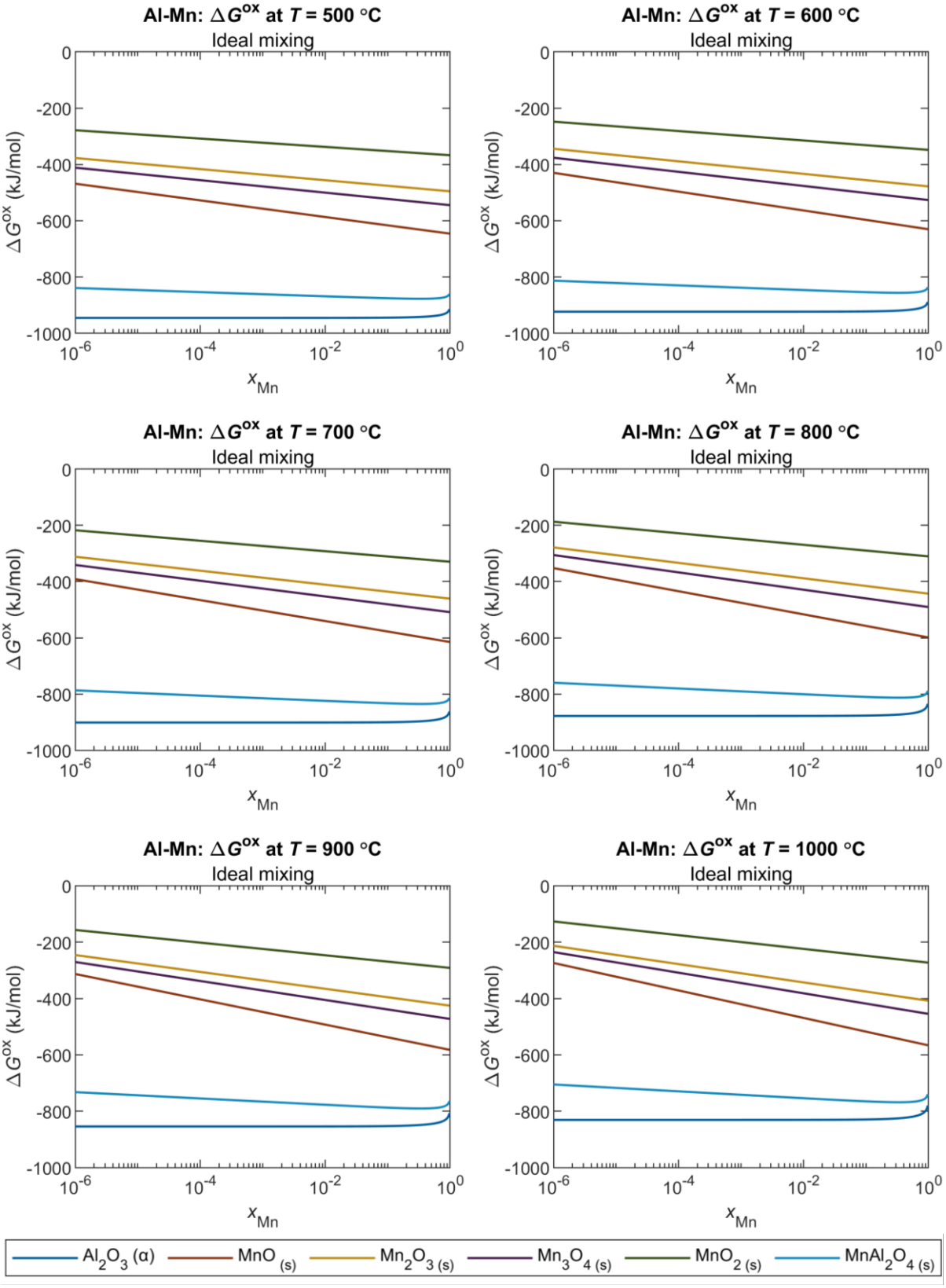
B.4.1.14. Al-Li


Al-Li: ΔG^ox at T = 500 °C
Ideal mixing
Al-Li: ΔG^ox at T = 600 °C
Ideal mixing
Al-Li: ΔG^ox at T = 700 °C
Ideal mixing
Al-Li: ΔG^ox at T = 800 °C
Ideal mixing
Al-Li: ΔG^ox at T = 900 °C
Ideal mixing
Al-Li: ΔG^ox at T = 1000 °C
Ideal mixing
ΔG^ox (kJ/mol)
x_Li
-200
-400
-600
-800
-1000
10^-6
10^-4
10^-2
10^0
Al2O3 (α)
Li5AlO4 (s)
AlLiO2 (γ)
LiAl7O11 (s)
Li2O (s)
AlLiO2 (α)
LiAl5O8 (s)
LiAl11O17 (s)

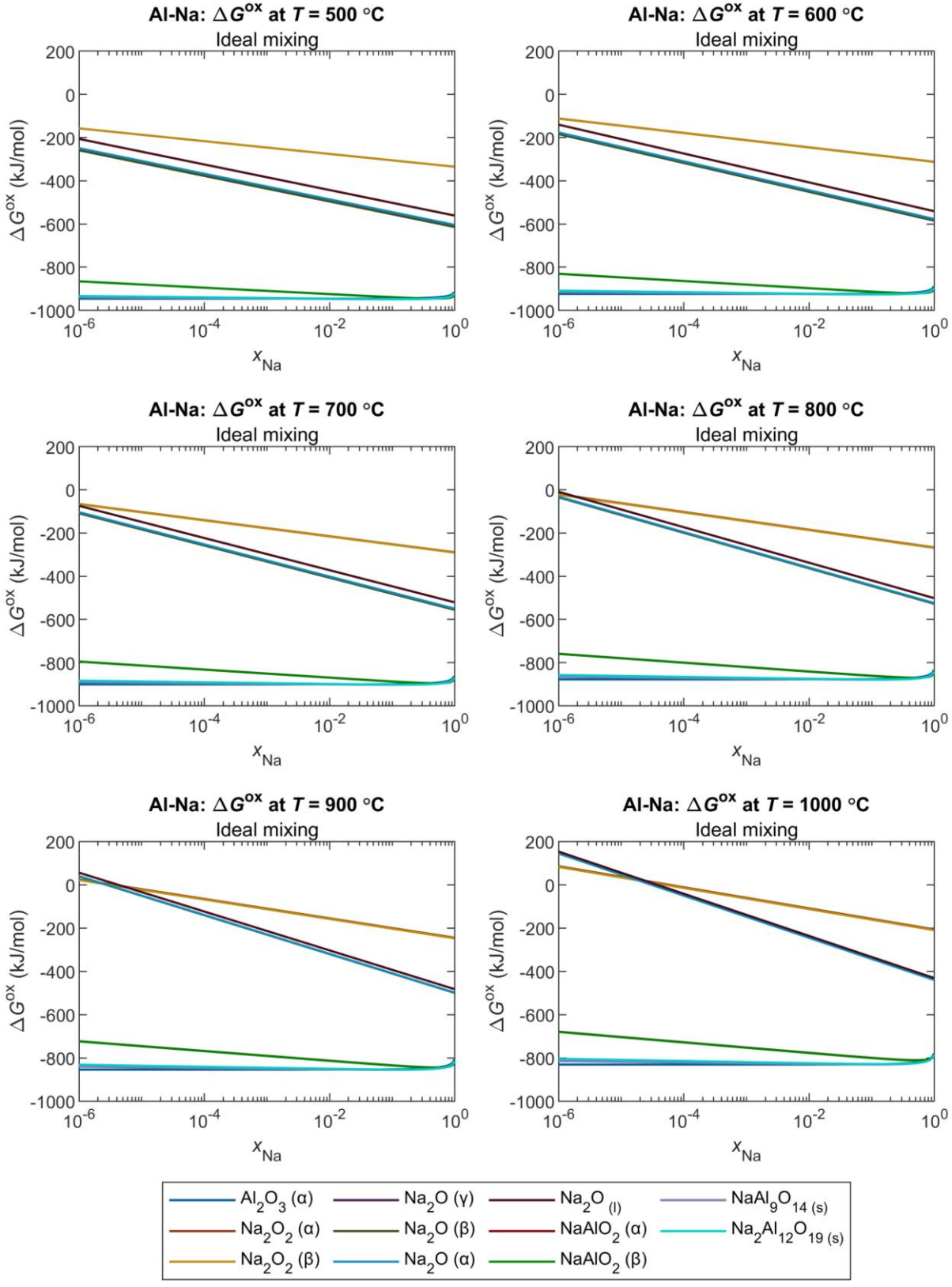
B.4.1.15. Al-Mg


Al-Mg: ΔG^ox at T = 500 °C
Ideal mixing
Al-Mg: ΔG^ox at T = 600 °C
Ideal mixing
Al-Mg: ΔG^ox at T = 700 °C
Ideal mixing
Al-Mg: ΔG^ox at T = 800 °C
Ideal mixing
Al-Mg: ΔG^ox at T = 900 °C
Ideal mixing
Al-Mg: ΔG^ox at T = 1000 °C
Ideal mixing
ΔG^ox (kJ/mol)
-600
-700
-800
-900
-1000
-1100
-1200
10^-6
10^-4
10^-2
10^0
x_Mg
Al2O3 (α)
MgO (s)
MgAl2O4 (s)

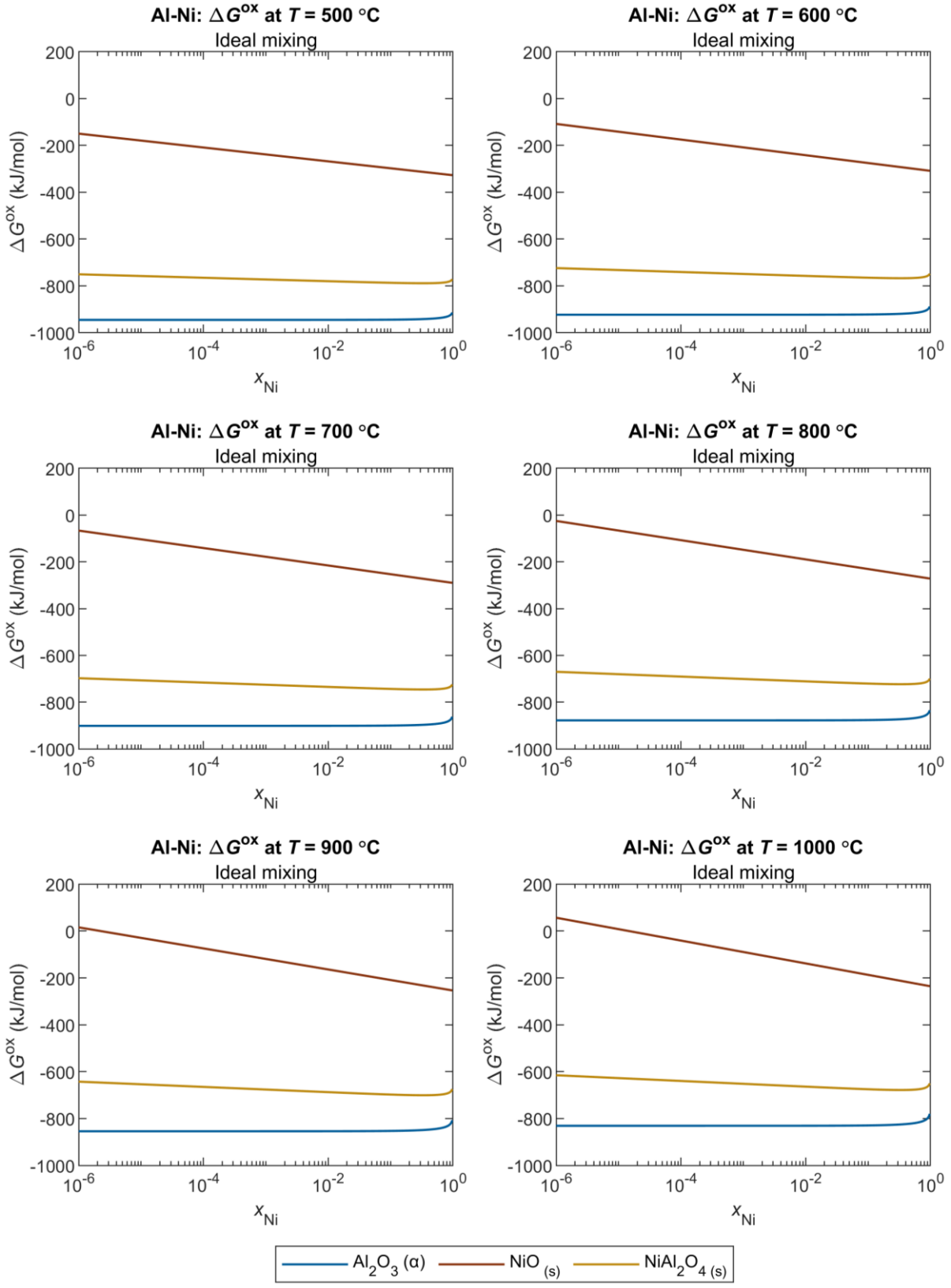
B.4.1.16. Al-Mn


Al-Mn: ΔG^ox at T = 500 °C
Ideal mixing
Al-Mn: ΔG^ox at T = 600 °C
Ideal mixing
Al-Mn: ΔG^ox at T = 700 °C
Ideal mixing
Al-Mn: ΔG^ox at T = 800 °C
Ideal mixing
Al-Mn: ΔG^ox at T = 900 °C
Ideal mixing
Al-Mn: ΔG^ox at T = 1000 °C
Ideal mixing
ΔG^ox (kJ/mol)
x_Mn
0
-200
-400
-600
-800
-1000
10^-6
10^-4
10^-2
10^0
Al2O3 (α)
MnO (s)
Mn2O3 (s)
Mn3O4 (s)
MnO2 (s)
MnAl2O4 (s)

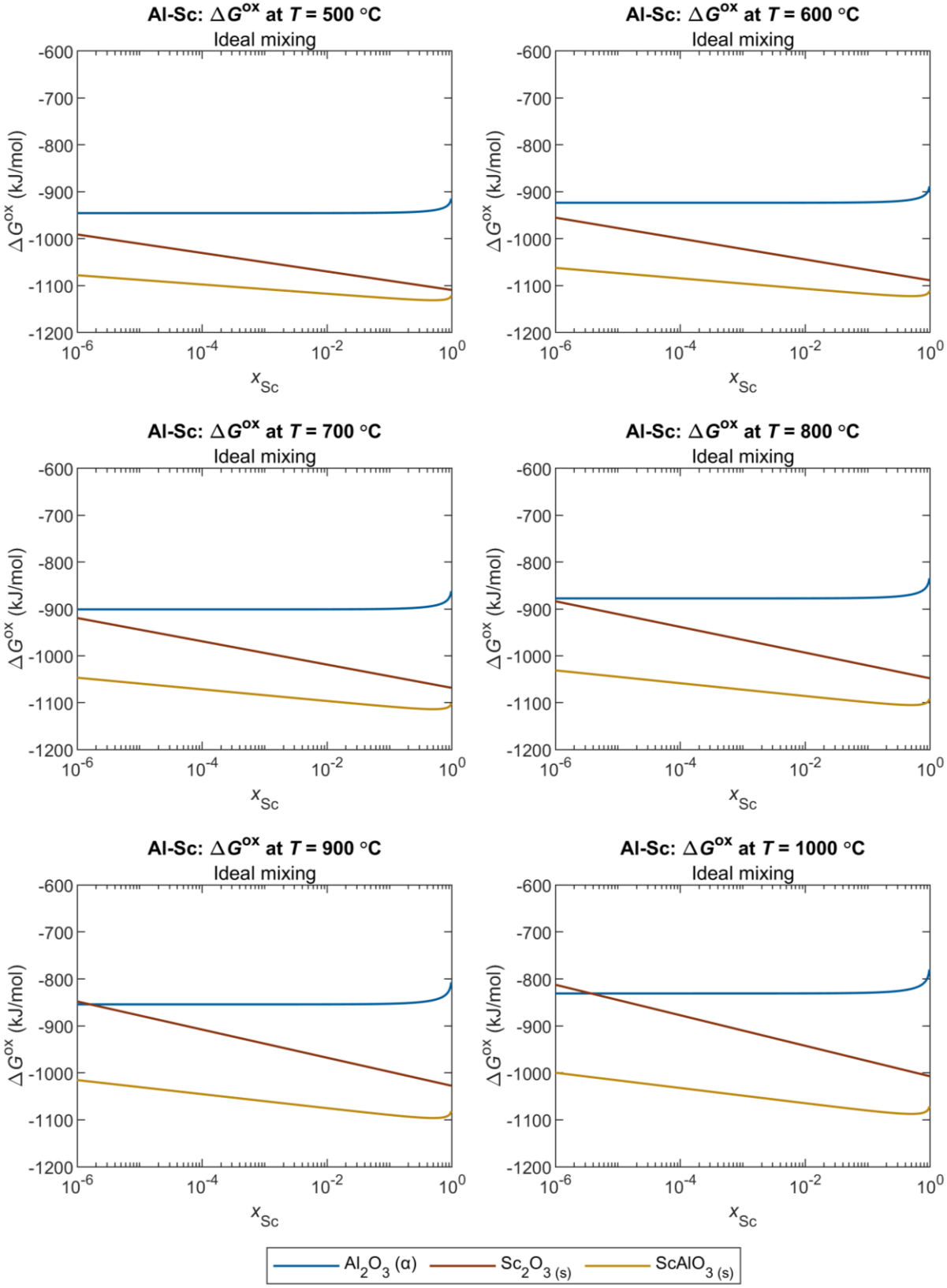
B.4.1.17. Al-Na


Al-Na: ΔG^ox at T = 500 °C
Ideal mixing
Al-Na: ΔG^ox at T = 600 °C
Ideal mixing
Al-Na: ΔG^ox at T = 700 °C
Ideal mixing
Al-Na: ΔG^ox at T = 800 °C
Ideal mixing
Al-Na: ΔG^ox at T = 900 °C
Ideal mixing
Al-Na: ΔG^ox at T = 1000 °C
Ideal mixing
ΔG^ox (kJ/mol)
x_Na
Al2O3 (α)
Na2O (γ)
Na2O (l)
NaAl9O14 (s)
Na2O2 (α)
Na2O (β)
NaAlO2 (α)
Na2Al12O19 (s)
Na2O2 (β)
Na2O (α)
NaAlO2 (β)

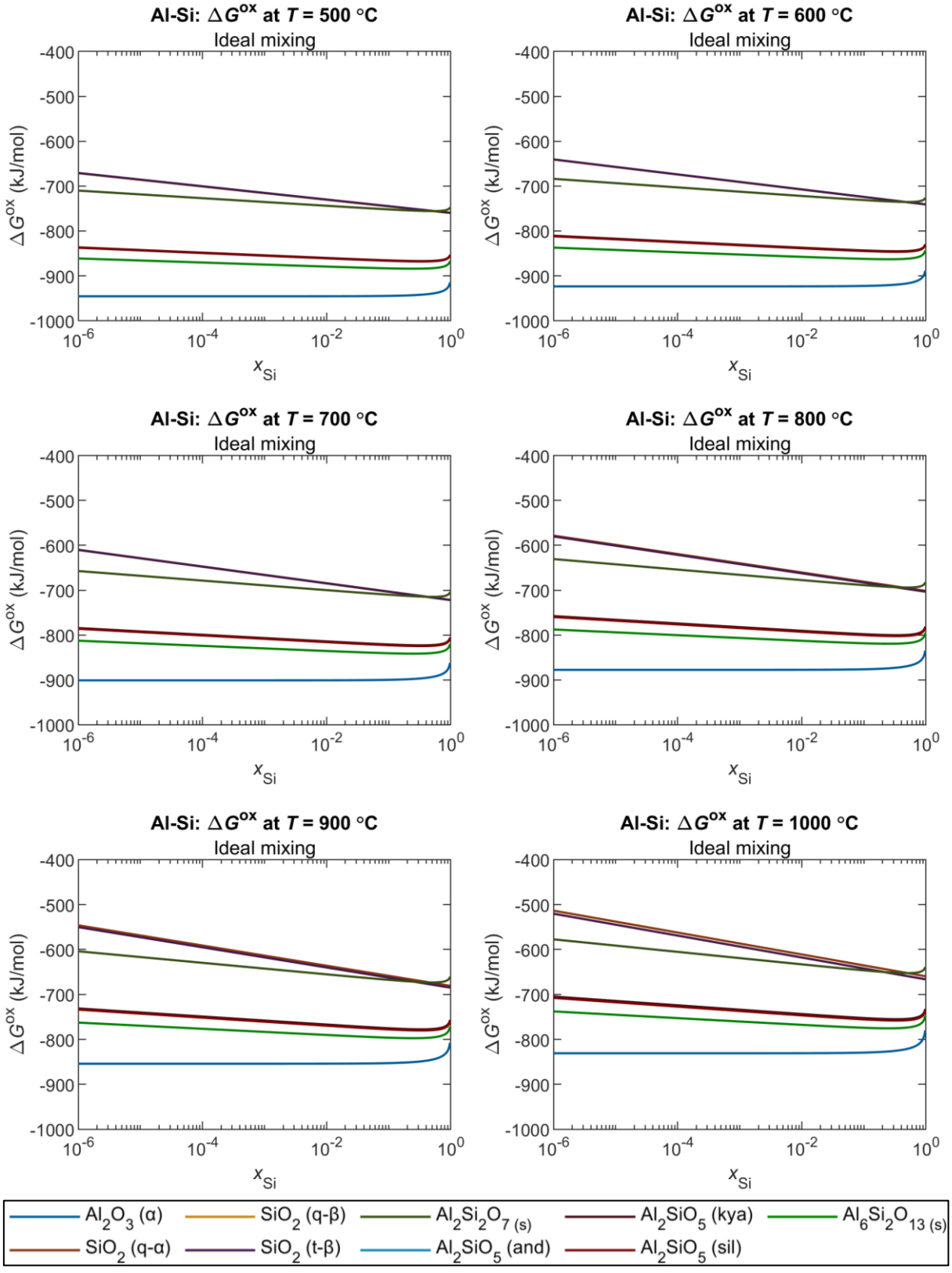
B.4.1.18. Al-Ni


Al-Ni: ΔG^ox at T = 500 °C
Ideal mixing
Al-Ni: ΔG^ox at T = 600 °C
Ideal mixing
Al-Ni: ΔG^ox at T = 700 °C
Ideal mixing
Al-Ni: ΔG^ox at T = 800 °C
Ideal mixing
Al-Ni: ΔG^ox at T = 900 °C
Ideal mixing
Al-Ni: ΔG^ox at T = 1000 °C
Ideal mixing
ΔG^ox (kJ/mol)
x_Ni
200
0
-200
-400
-600
-800
-1000
10^-6
10^-4
10^-2
10^0
Al2O3 (α)
NiO (s)
NiAl2O4 (s)

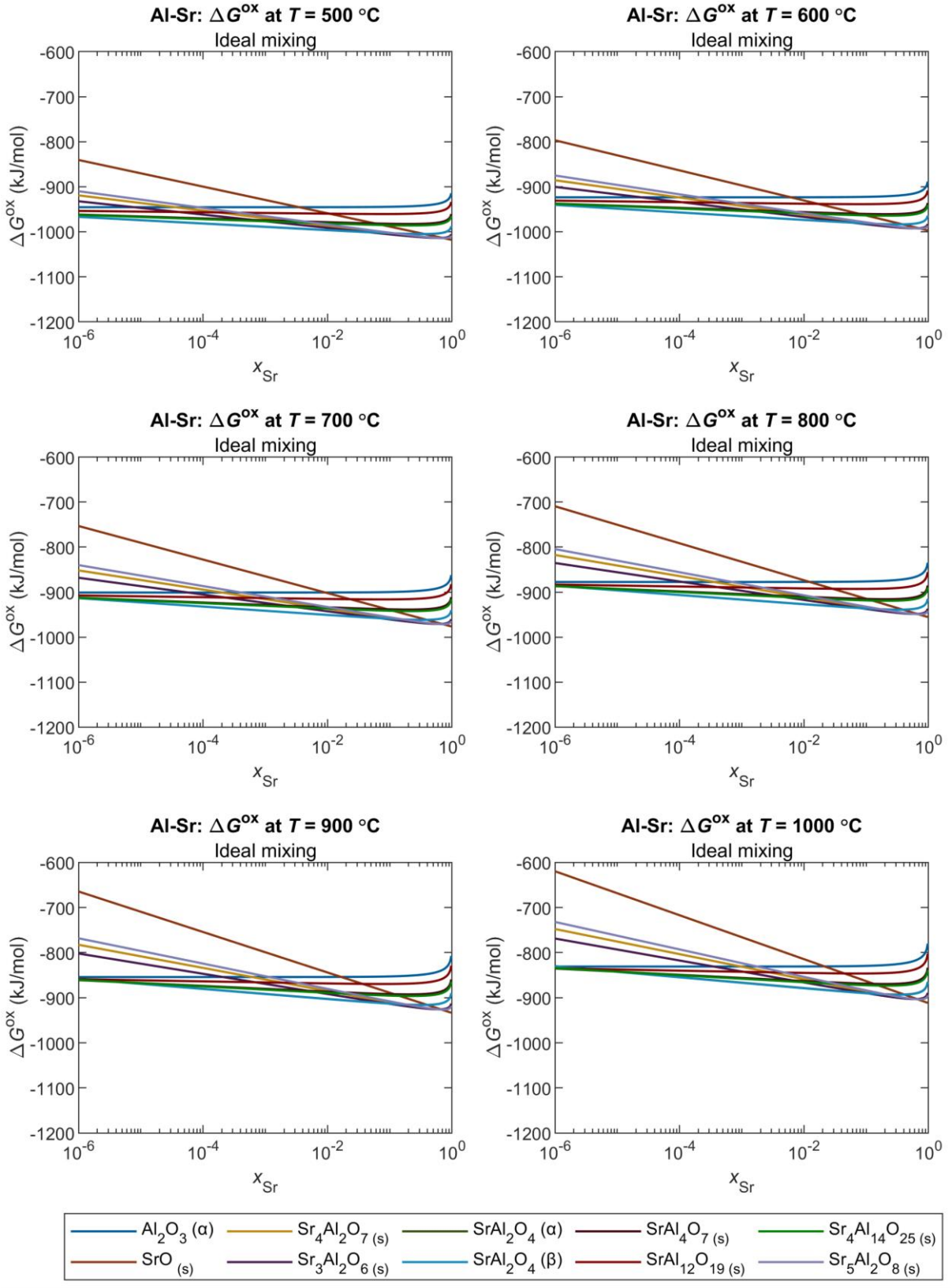
B.4.1.19. Al-Sc


Al-Sc: ΔG^ox at T = 500 °C
Ideal mixing
Al-Sc: ΔG^ox at T = 600 °C
Ideal mixing
Al-Sc: ΔG^ox at T = 700 °C
Ideal mixing
Al-Sc: ΔG^ox at T = 800 °C
Ideal mixing
Al-Sc: ΔG^ox at T = 900 °C
Ideal mixing
Al-Sc: ΔG^ox at T = 1000 °C
Ideal mixing
ΔG^ox (kJ/mol)
x_Sc
-600
-700
-800
-900
-1000
-1100
-1200
10^-6
10^-4
10^-2
10^0
Al2O3 (α)
Sc2O3 (s)
ScAlO3 (s)

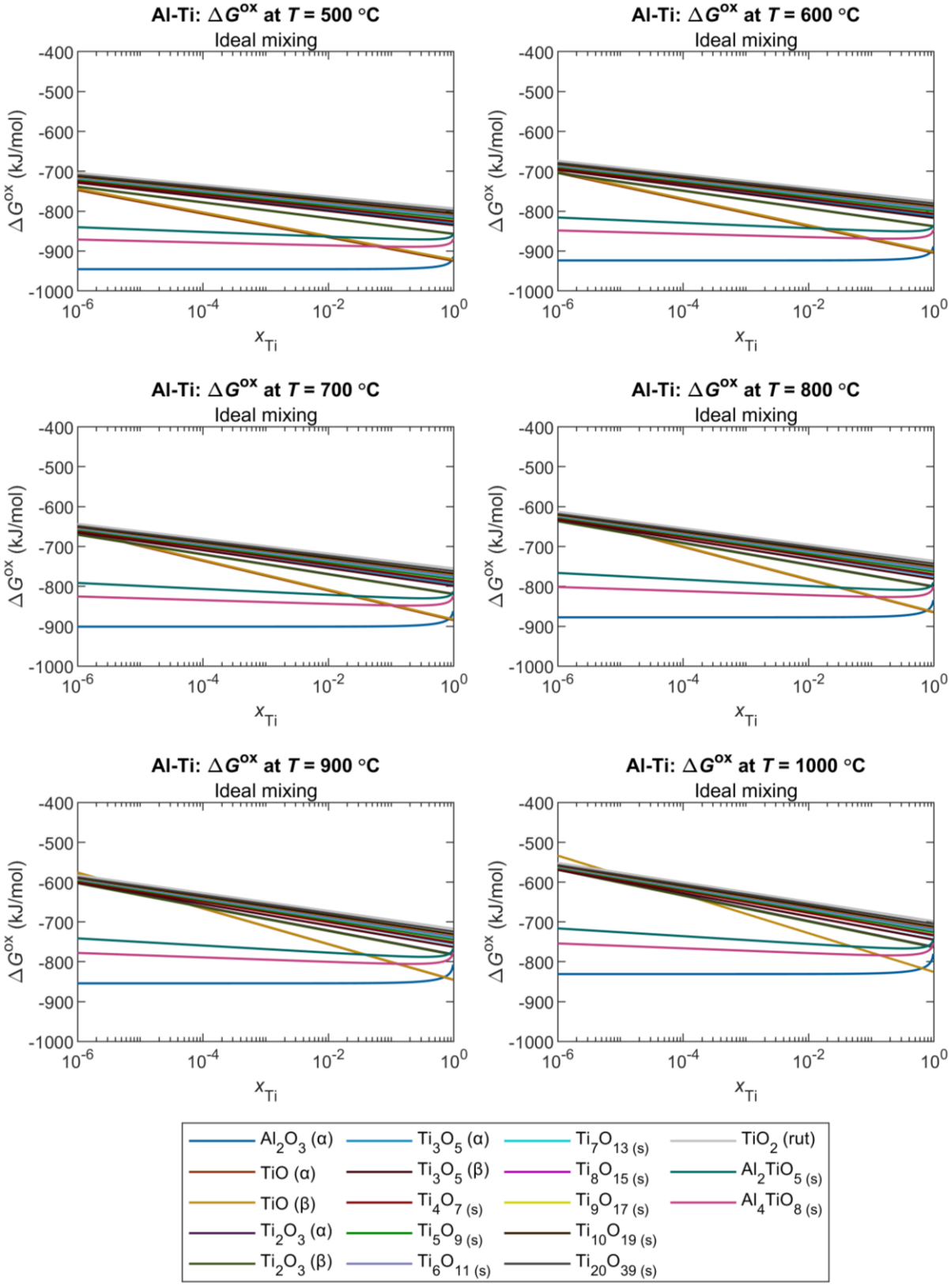
B.4.1.20. Al-Si


Al-Si: ΔG^ox at T = 500 °C
Ideal mixing
Al-Si: ΔG^ox at T = 600 °C
Ideal mixing
Al-Si: ΔG^ox at T = 700 °C
Ideal mixing
Al-Si: ΔG^ox at T = 800 °C
Ideal mixing
Al-Si: ΔG^ox at T = 900 °C
Ideal mixing
Al-Si: ΔG^ox at T = 1000 °C
Ideal mixing
ΔG^ox (kJ/mol)
x_Si
-400
-500
-600
-700
-800
-900
-1000
10^-6
10^-4
10^-2
10^0
Al2O3 (α)
SiO2 (q-β)
Al2Si2O7 (s)
Al2SiO5 (kya)
Al6Si2O13 (s)
SiO2 (q-α)
SiO2 (t-β)
Al2SiO5 (and)
Al2SiO5 (sil)

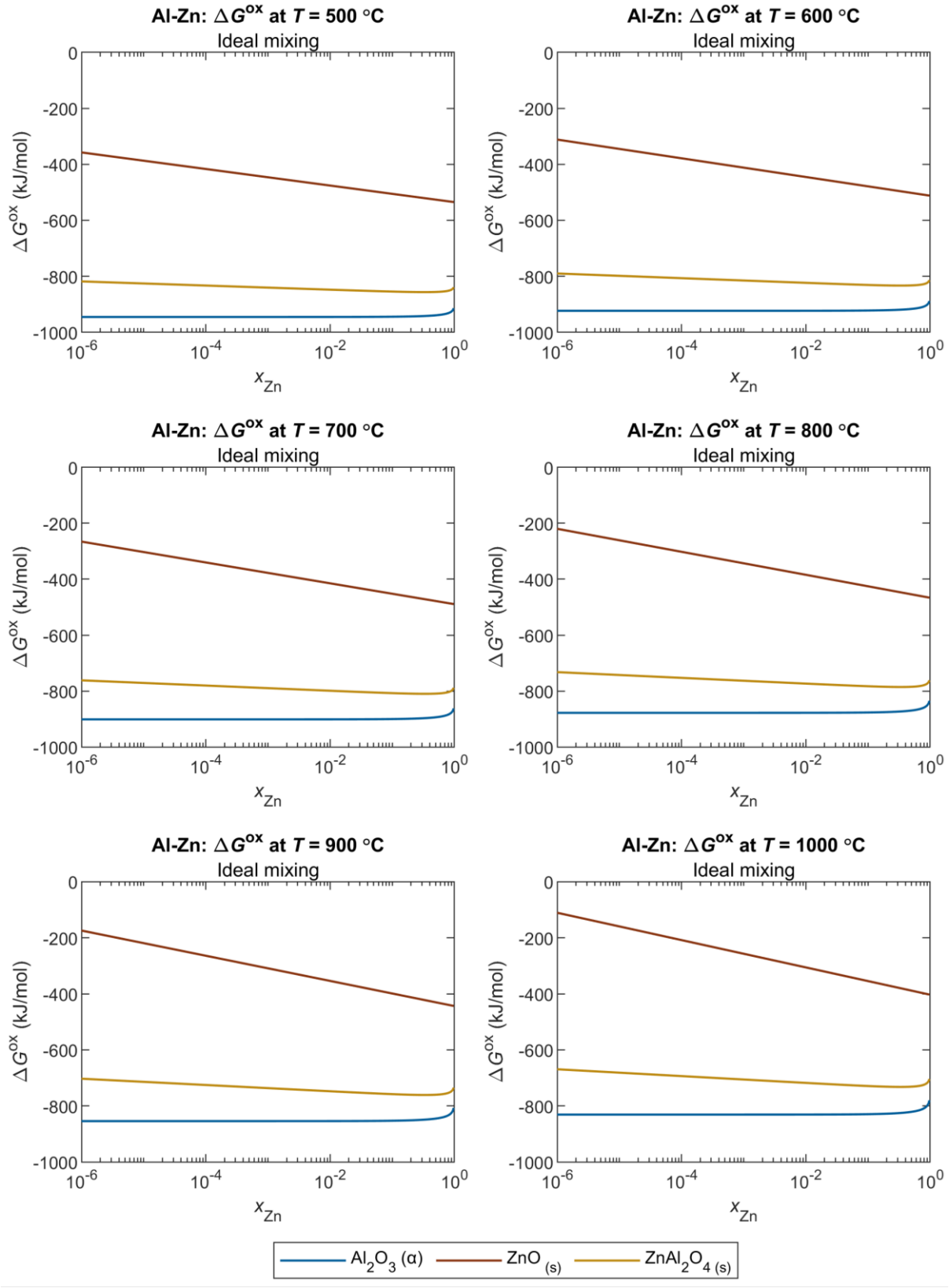
B.4.1.21. Al-Sr


Al-Sr: ΔG^ox at T = 500 °C
Ideal mixing
Al-Sr: ΔG^ox at T = 600 °C
Ideal mixing
Al-Sr: ΔG^ox at T = 700 °C
Ideal mixing
Al-Sr: ΔG^ox at T = 800 °C
Ideal mixing
Al-Sr: ΔG^ox at T = 900 °C
Ideal mixing
Al-Sr: ΔG^ox at T = 1000 °C
Ideal mixing
ΔG^ox (kJ/mol)
x_Sr
-600
-700
-800
-900
-1000
-1100
-1200
10^-6
10^-4
10^-2
10^0
Al2O3 (α)
Sr4Al2O7 (s)
SrAl2O4 (α)
SrAl4O7 (s)
Sr4Al14O25 (s)
SrO (s)
Sr3Al2O6 (s)
SrAl2O4 (β)
SrAl12O19 (s)
Sr5Al2O8 (s)

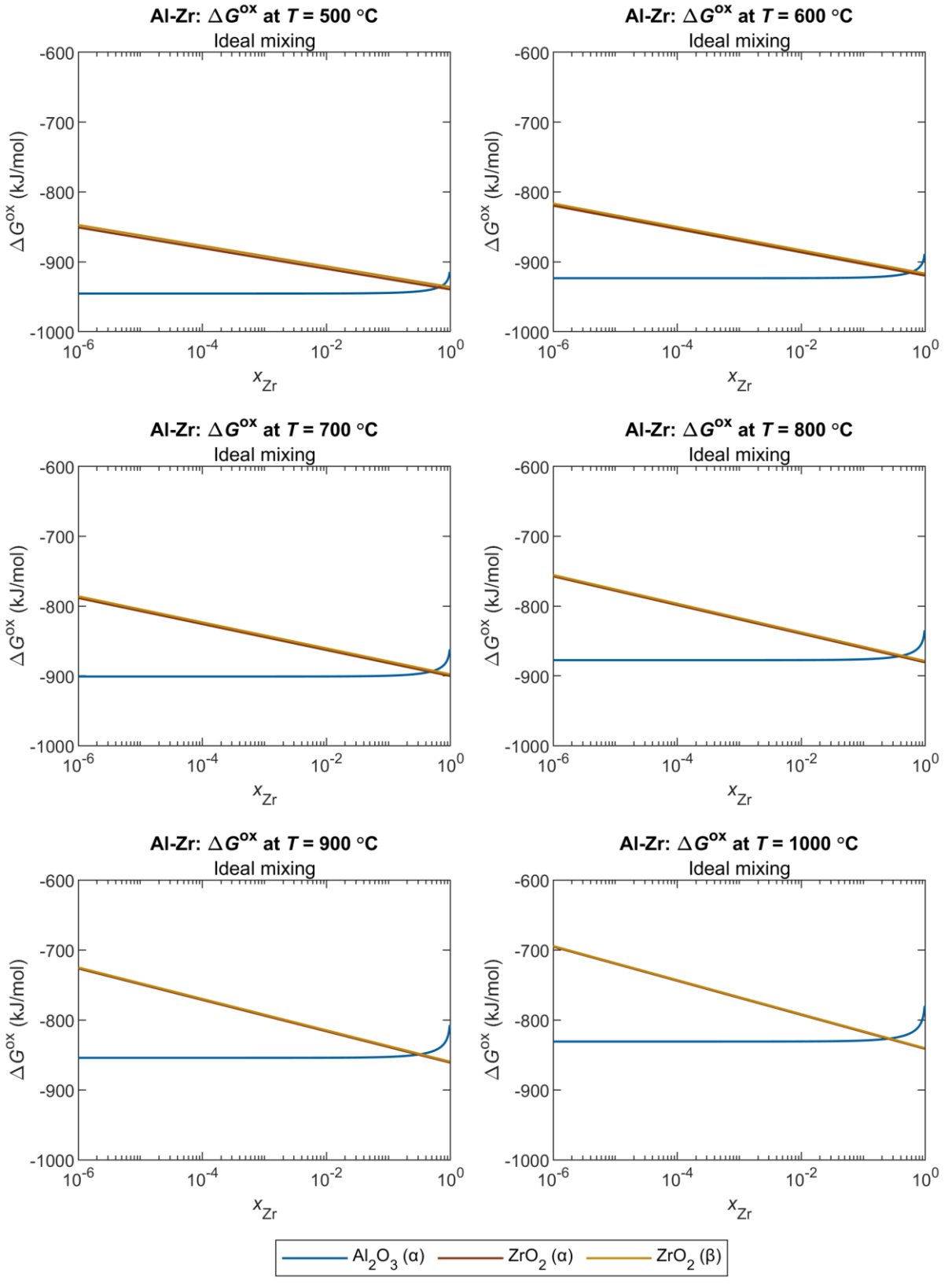
B.4.1.22. Al-Ti


Al-Ti: ΔG^ox at T = 500 °C
Ideal mixing
Al-Ti: ΔG^ox at T = 600 °C
Ideal mixing
Al-Ti: ΔG^ox at T = 700 °C
Ideal mixing
Al-Ti: ΔG^ox at T = 800 °C
Ideal mixing
Al-Ti: ΔG^ox at T = 900 °C
Ideal mixing
Al-Ti: ΔG^ox at T = 1000 °C
Ideal mixing
ΔG^ox (kJ/mol)
x_Ti
-400
-500
-600
-700
-800
-900
-1000
10^-6
10^-4
10^-2
10^0
Al2O3 (α)
Ti3O5 (α)
Ti7O13 (s)
TiO2 (rut)
TiO (α)
Ti3O5 (β)
Ti8O15 (s)
Al2TiO5 (s)
TiO (β)
Ti4O7 (s)
Ti9O17 (s)
Al4TiO8 (s)
Ti2O3 (α)
Ti5O9 (s)
Ti10O19 (s)
Ti2O3 (β)
Ti6O11 (s)
Ti20O39 (s)

B.4.1.23. Al-Zn

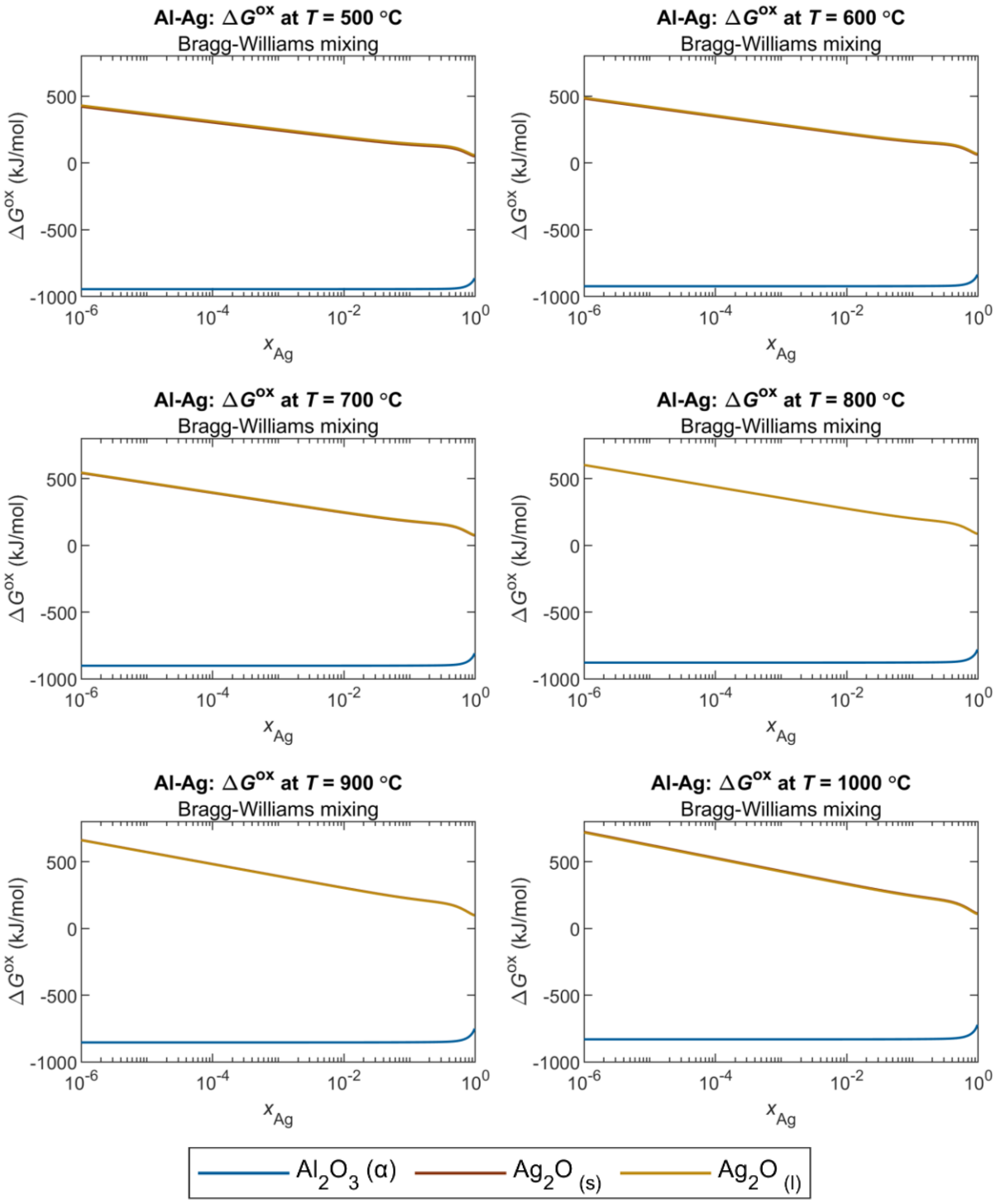

Al-Zn: ΔG^ox at T = 500 °C
Ideal mixing
Al-Zn: ΔG^ox at T = 600 °C
Ideal mixing
Al-Zn: ΔG^ox at T = 700 °C
Ideal mixing
Al-Zn: ΔG^ox at T = 800 °C
Ideal mixing
Al-Zn: ΔG^ox at T = 900 °C
Ideal mixing
Al-Zn: ΔG^ox at T = 1000 °C
Ideal mixing
ΔG^ox (kJ/mol)
x_Zn
0
-200
-400
-600
-800
-1000
10^-6
10^-4
10^-2
10^0
Al2O3 (α)
ZnO (s)
ZnAl2O4 (s)

B.4.1.24. Al-Zr

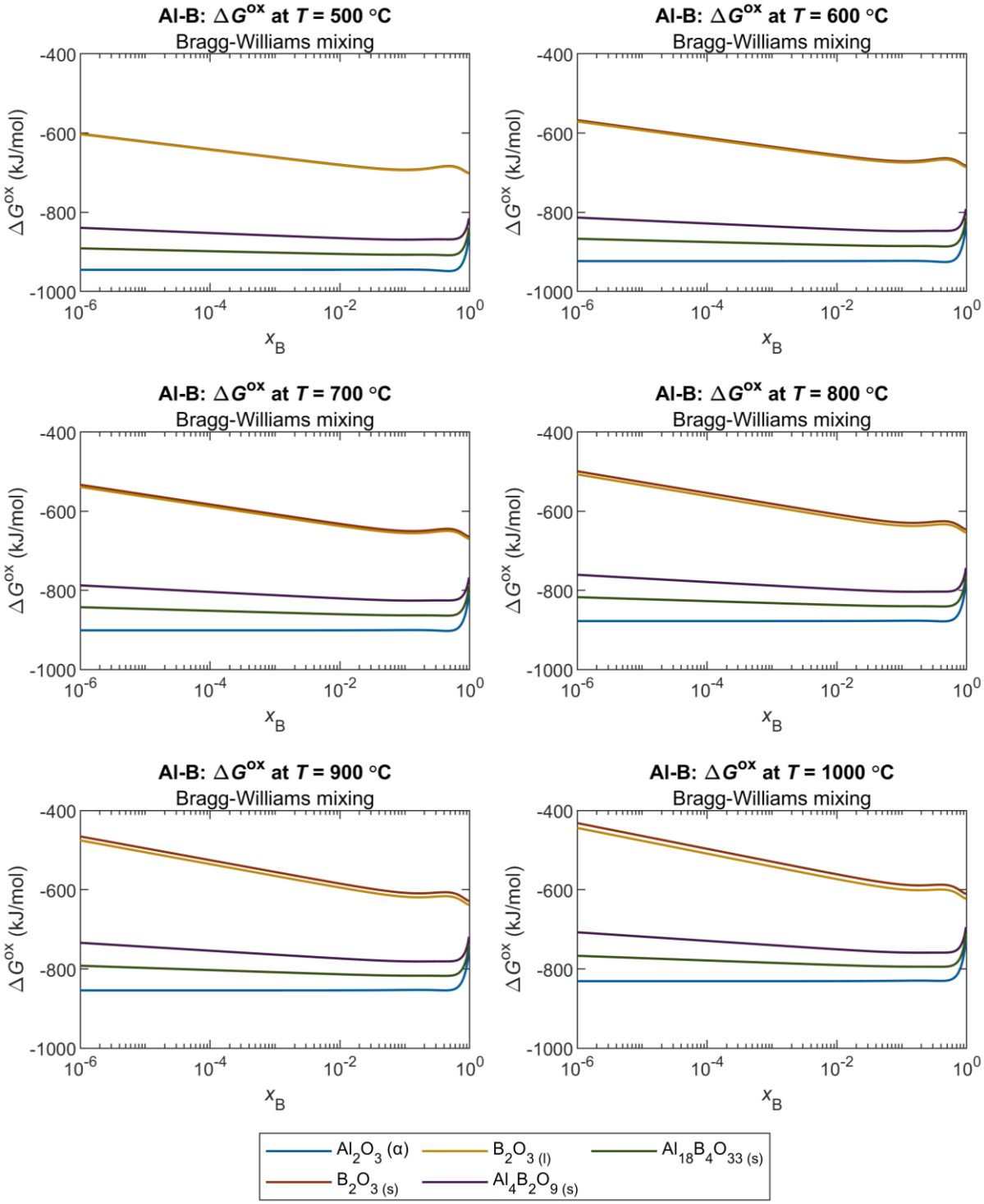

Al-Zr: ΔG^ox at T = 500 °C
Ideal mixing
Al-Zr: ΔG^ox at T = 600 °C
Ideal mixing
Al-Zr: ΔG^ox at T = 700 °C
Ideal mixing
Al-Zr: ΔG^ox at T = 800 °C
Ideal mixing
Al-Zr: ΔG^ox at T = 900 °C
Ideal mixing
Al-Zr: ΔG^ox at T = 1000 °C
Ideal mixing
ΔG^ox (kJ/mol)
-600
-700
-800
-900
-1000
10^-6
10^-4
10^-2
10^0
x_Zr
Al2O3 (α)
ZrO2 (α)
ZrO2 (β)

B.4.2. Bragg-Williams mixing

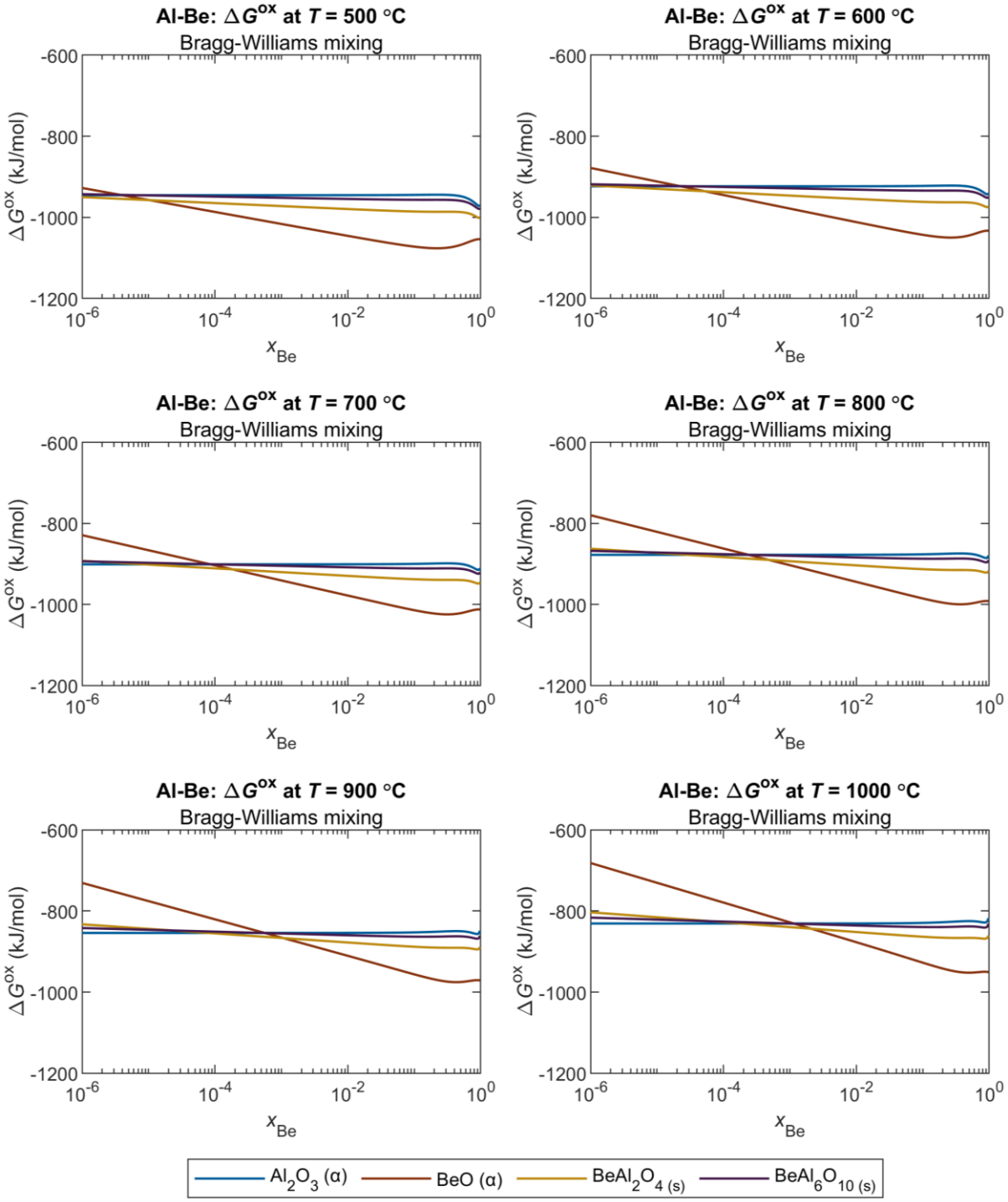
B.4.2.1. Al-Ag



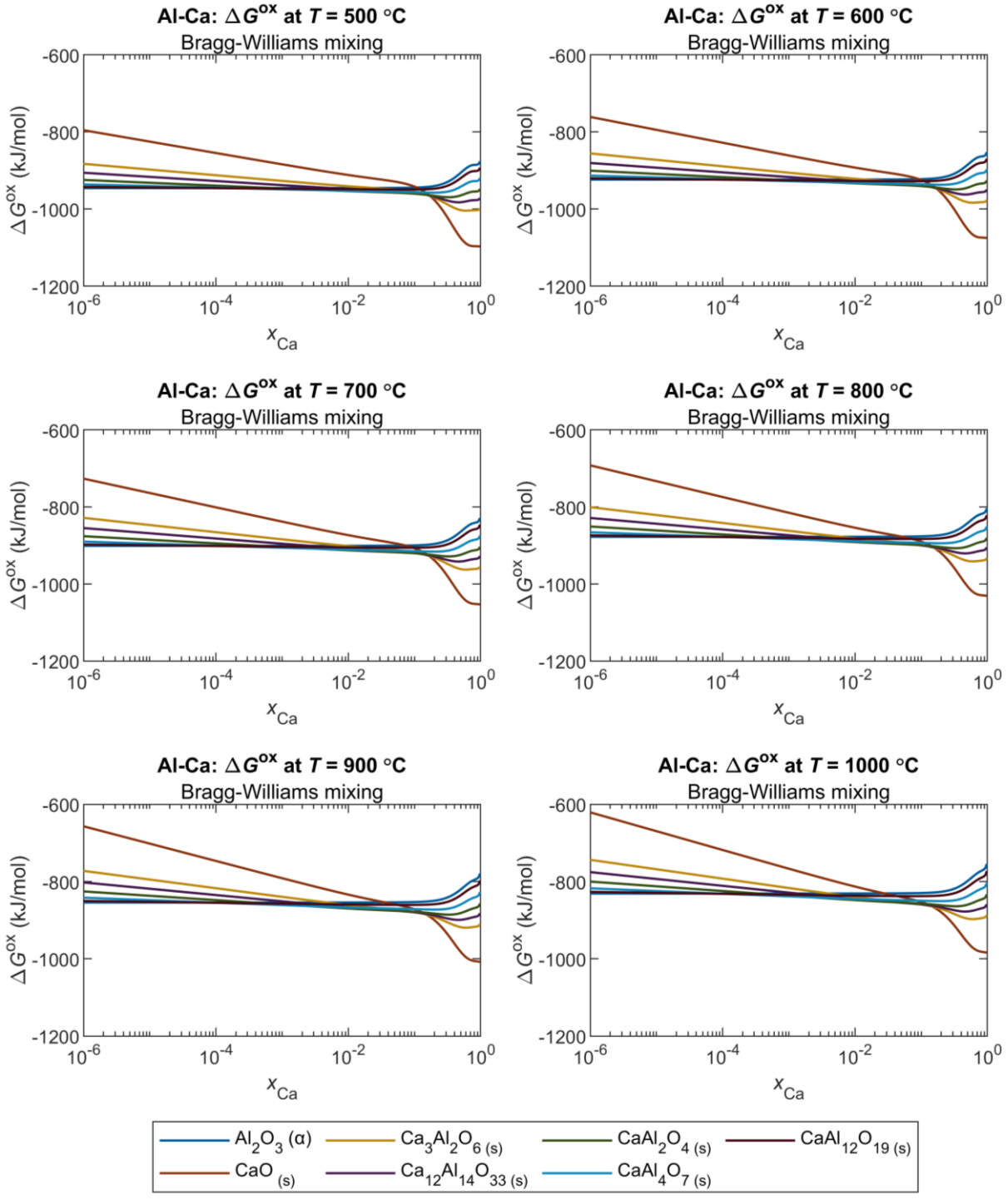
B.4.2.2. Al-B


Al-B: ΔG^ox at T = 500 °C
Bragg-Williams mixing
Al-B: ΔG^ox at T = 600 °C
Bragg-Williams mixing
Al-B: ΔG^ox at T = 700 °C
Bragg-Williams mixing
Al-B: ΔG^ox at T = 800 °C
Bragg-Williams mixing
Al-B: ΔG^ox at T = 900 °C
Bragg-Williams mixing
Al-B: ΔG^ox at T = 1000 °C
Bragg-Williams mixing
ΔG^ox (kJ/mol)
-400
-600
-800
-1000
10^-6
10^-4
10^-2
10^0
x_B
Al2O3 (α)
B2O3 (l)
Al18B4O33 (s)
B2O3 (s)
Al4B2O9 (s)

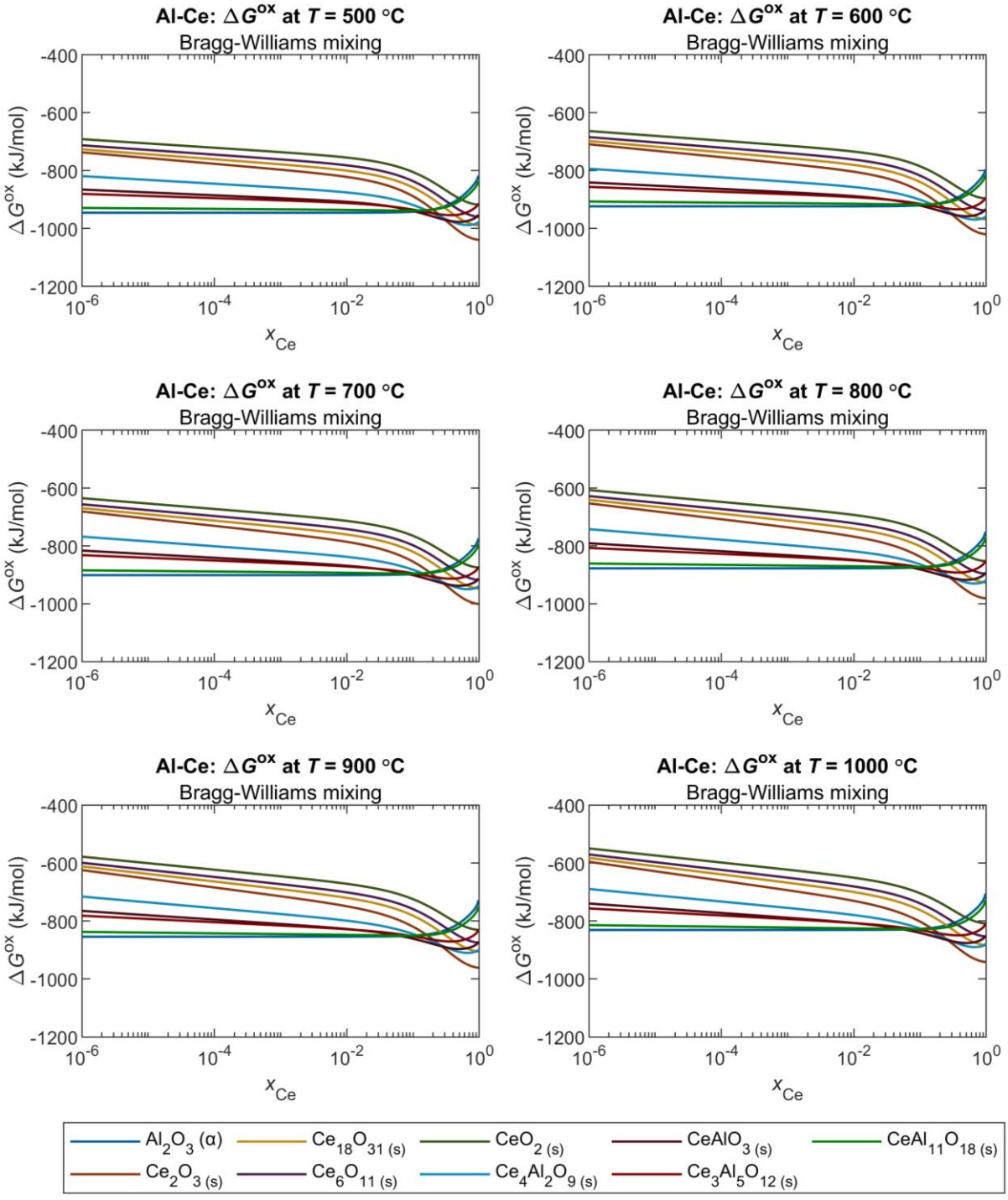
B.4.2.3. Al-Be


Al-Be: ΔG^ox at T = 500 °C
Bragg-Williams mixing
Al-Be: ΔG^ox at T = 600 °C
Bragg-Williams mixing
Al-Be: ΔG^ox at T = 700 °C
Bragg-Williams mixing
Al-Be: ΔG^ox at T = 800 °C
Bragg-Williams mixing
Al-Be: ΔG^ox at T = 900 °C
Bragg-Williams mixing
Al-Be: ΔG^ox at T = 1000 °C
Bragg-Williams mixing
ΔG^ox (kJ/mol)
-600
-800
-1000
-1200
10^-6
10^-4
10^-2
10^0
x_Be
Al2O3 (α)
BeO (α)
BeAl2O4 (s)
BeAl6O10 (s)

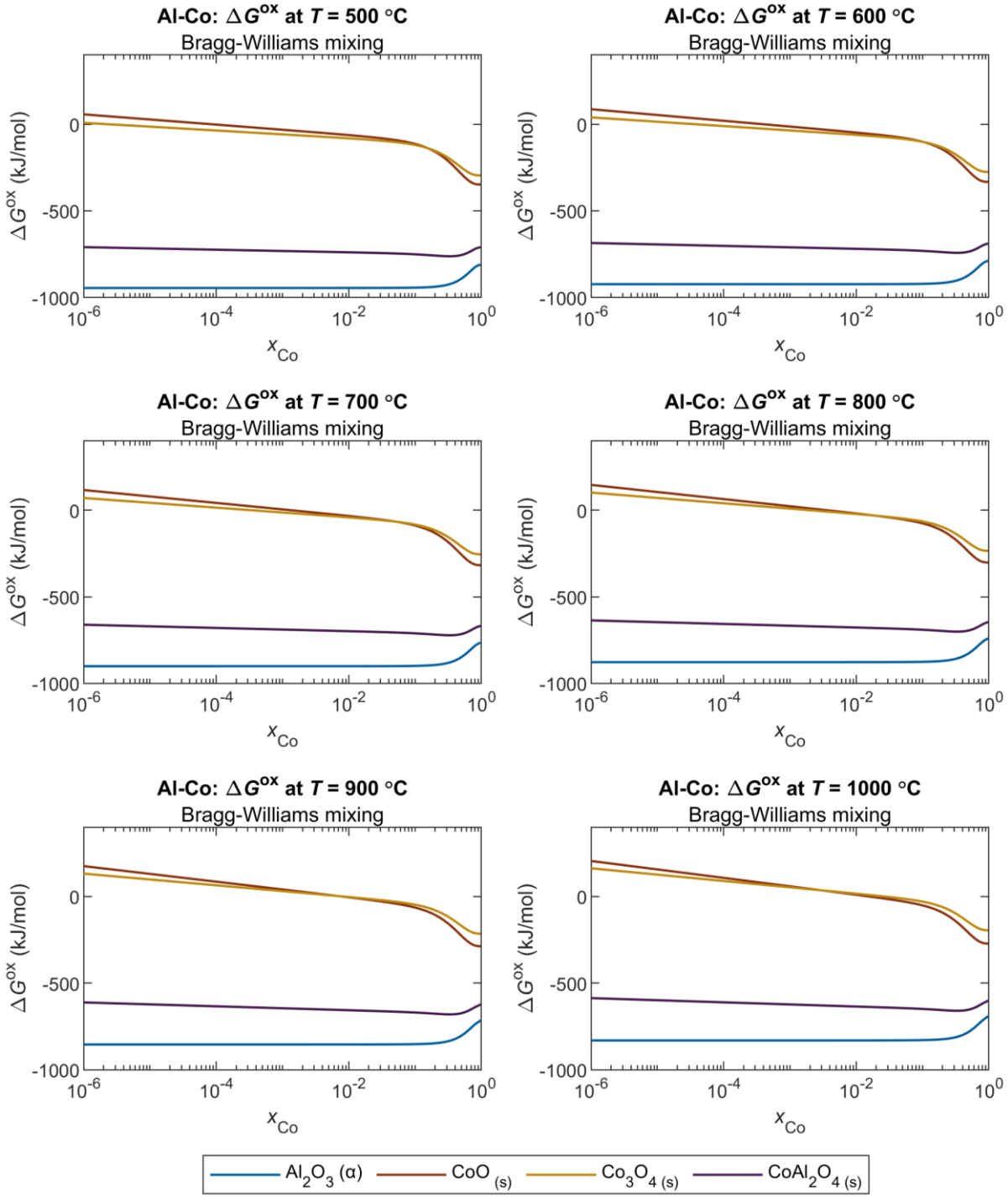
B.4.2.4. Al-Ca


Al-Ca: ΔG^ox at T = 500 °C
Bragg-Williams mixing
Al-Ca: ΔG^ox at T = 600 °C
Bragg-Williams mixing
Al-Ca: ΔG^ox at T = 700 °C
Bragg-Williams mixing
Al-Ca: ΔG^ox at T = 800 °C
Bragg-Williams mixing
Al-Ca: ΔG^ox at T = 900 °C
Bragg-Williams mixing
Al-Ca: ΔG^ox at T = 1000 °C
Bragg-Williams mixing
ΔG^ox (kJ/mol)
-600
-800
-1000
-1200
10^-6
10^-4
10^-2
10^0
x_Ca
Al2O3 (α)
Ca3Al2O6 (s)
CaAl2O4 (s)
CaAl12O19 (s)
CaO (s)
Ca12Al14O33 (s)
CaAl4O7 (s)

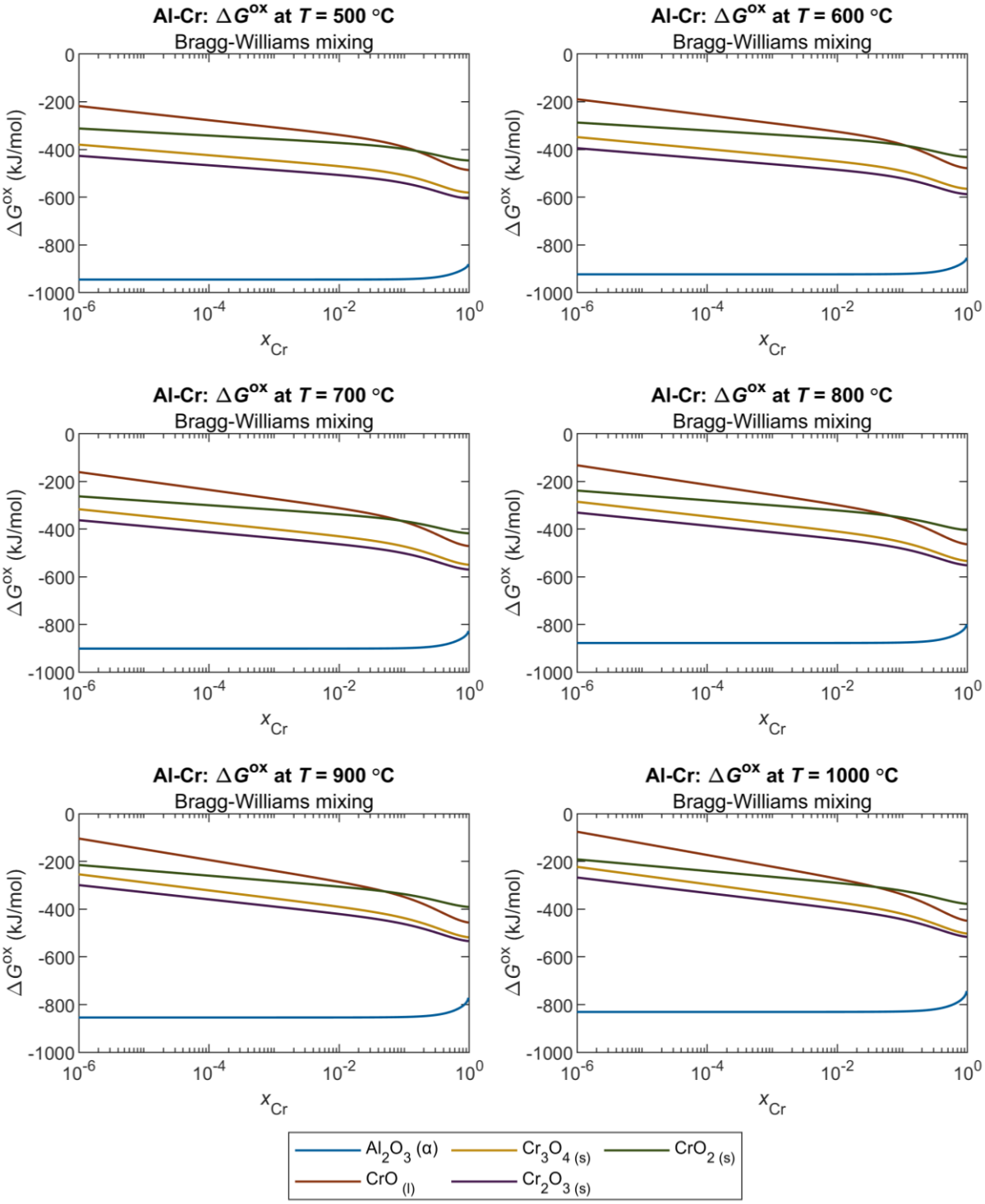
B.4.2.5. Al-Ce


Al-Ce: ΔG^ox at T = 500 °C
Bragg-Williams mixing
Al-Ce: ΔG^ox at T = 600 °C
Bragg-Williams mixing
Al-Ce: ΔG^ox at T = 700 °C
Bragg-Williams mixing
Al-Ce: ΔG^ox at T = 800 °C
Bragg-Williams mixing
Al-Ce: ΔG^ox at T = 900 °C
Bragg-Williams mixing
Al-Ce: ΔG^ox at T = 1000 °C
Bragg-Williams mixing
ΔG^ox (kJ/mol)
-400
-600
-800
-1000
-1200
10^-6
10^-4
10^-2
10^0
x_Ce
Al2O3 (α)
Ce18O31 (s)
CeO2 (s)
CeAlO3 (s)
CeAl11O18 (s)
Ce2O3 (s)
Ce6O11 (s)
Ce4Al2O9 (s)
Ce3Al5O12 (s)

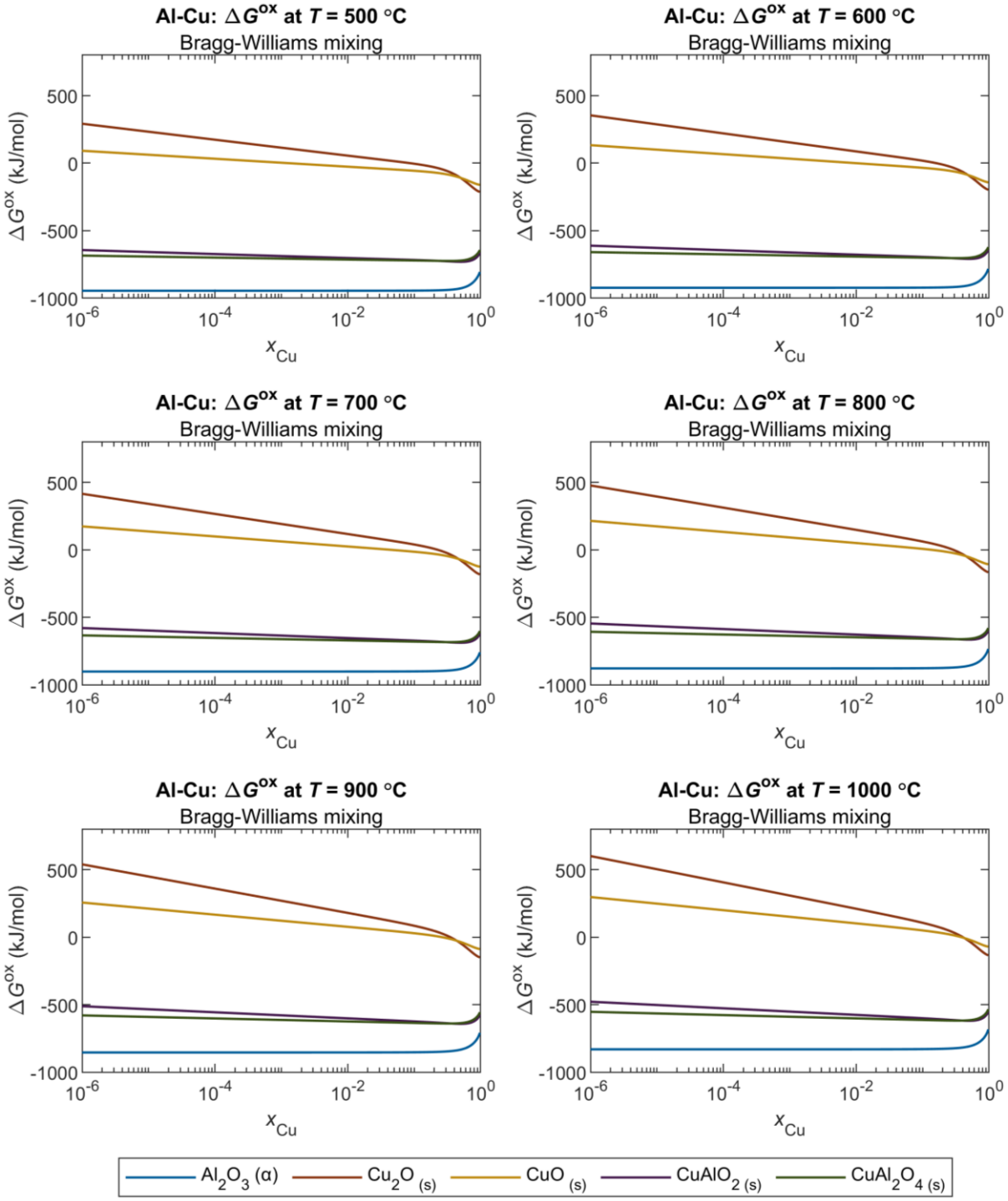
B.4.2.6. Al-Co


Al-Co: ΔG^ox at T = 500 °C
Bragg-Williams mixing
Al-Co: ΔG^ox at T = 600 °C
Bragg-Williams mixing
Al-Co: ΔG^ox at T = 700 °C
Bragg-Williams mixing
Al-Co: ΔG^ox at T = 800 °C
Bragg-Williams mixing
Al-Co: ΔG^ox at T = 900 °C
Bragg-Williams mixing
Al-Co: ΔG^ox at T = 1000 °C
Bragg-Williams mixing
ΔG^ox (kJ/mol)
0
-500
-1000
10^-6
10^-4
10^-2
10^0
x_Co
Al2O3 (α)
CoO (s)
Co3O4 (s)
CoAl2O4 (s)

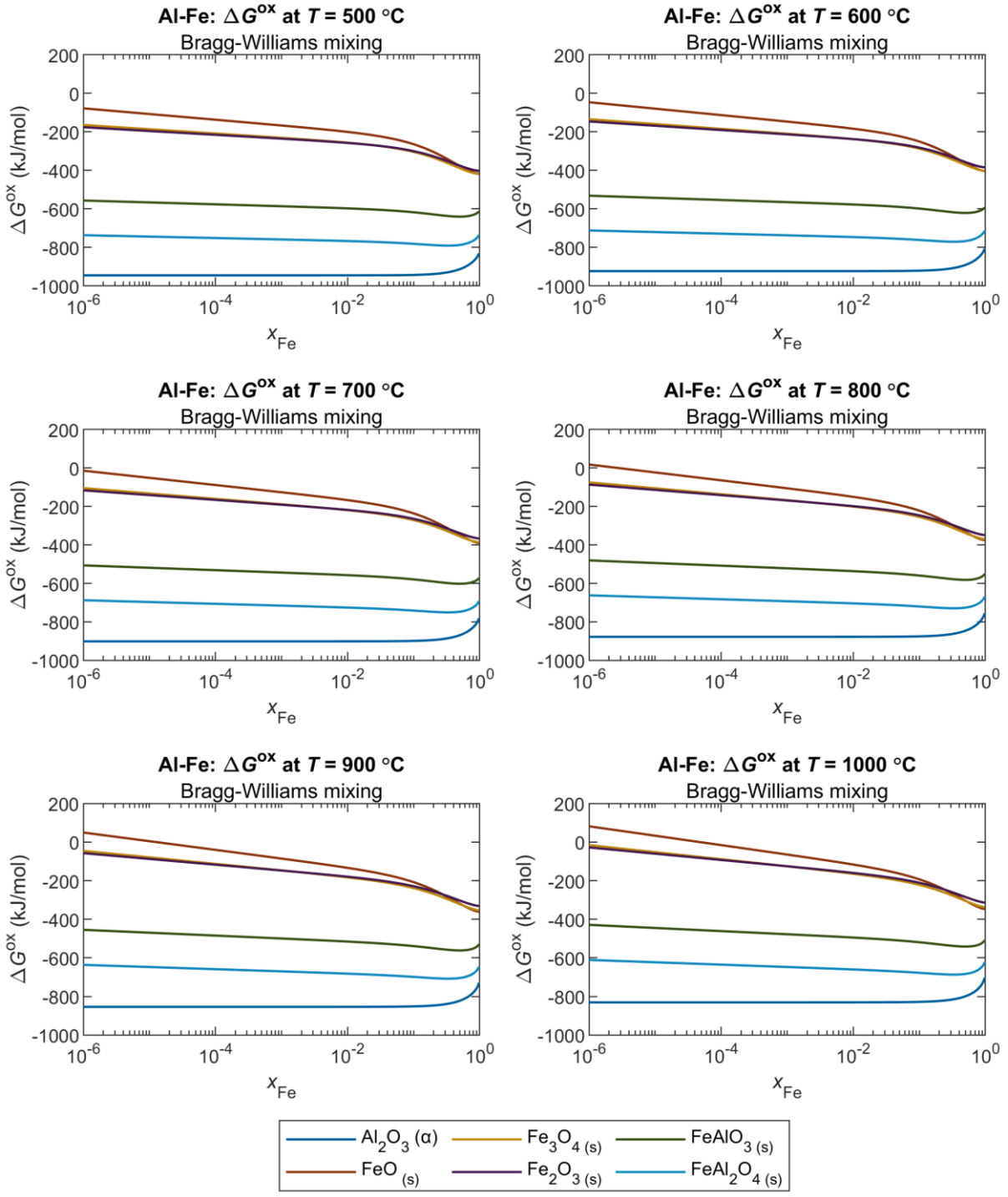
B.4.2.7. Al-Cr


Al-Cr: ΔG^ox at T = 500 °C
Bragg-Williams mixing
Al-Cr: ΔG^ox at T = 600 °C
Bragg-Williams mixing
Al-Cr: ΔG^ox at T = 700 °C
Bragg-Williams mixing
Al-Cr: ΔG^ox at T = 800 °C
Bragg-Williams mixing
Al-Cr: ΔG^ox at T = 900 °C
Bragg-Williams mixing
Al-Cr: ΔG^ox at T = 1000 °C
Bragg-Williams mixing
ΔG^ox (kJ/mol)
0
-200
-400
-600
-800
-1000
10^-6
10^-4
10^-2
10^0
x_Cr
Al2O3 (α)
Cr3O4 (s)
CrO2 (s)
CrO (l)
Cr2O3 (s)

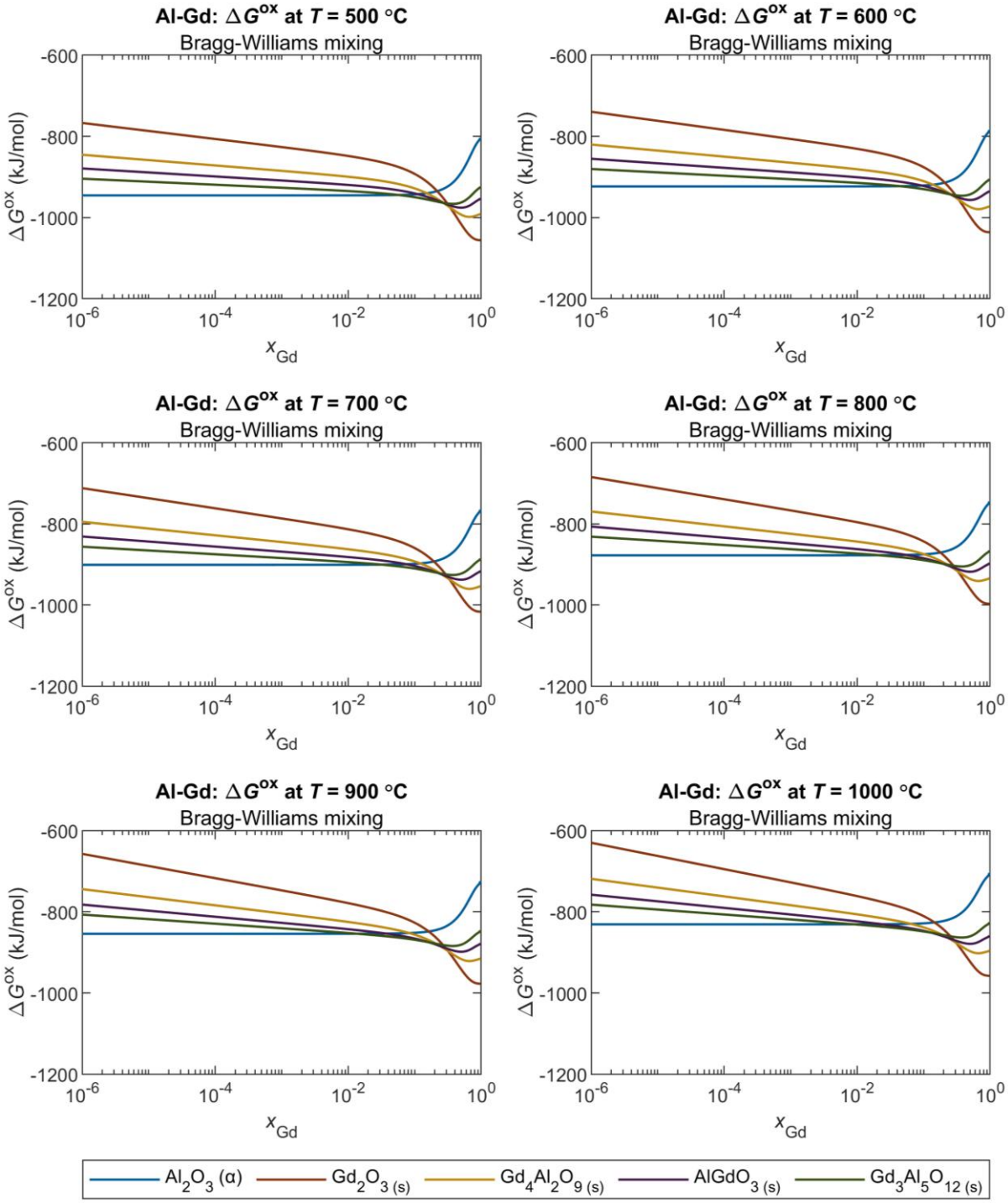
B.4.2.8. Al-Cu


Al-Cu: ΔG^ox at T = 500 °C
Bragg-Williams mixing
Al-Cu: ΔG^ox at T = 600 °C
Bragg-Williams mixing
Al-Cu: ΔG^ox at T = 700 °C
Bragg-Williams mixing
Al-Cu: ΔG^ox at T = 800 °C
Bragg-Williams mixing
Al-Cu: ΔG^ox at T = 900 °C
Bragg-Williams mixing
Al-Cu: ΔG^ox at T = 1000 °C
Bragg-Williams mixing
ΔG^ox (kJ/mol)
500
0
-500
-1000
10^-6
10^-4
10^-2
10^0
x_Cu
Al2O3 (α)
Cu2O (s)
CuO (s)
CuAlO2 (s)
CuAl2O4 (s)

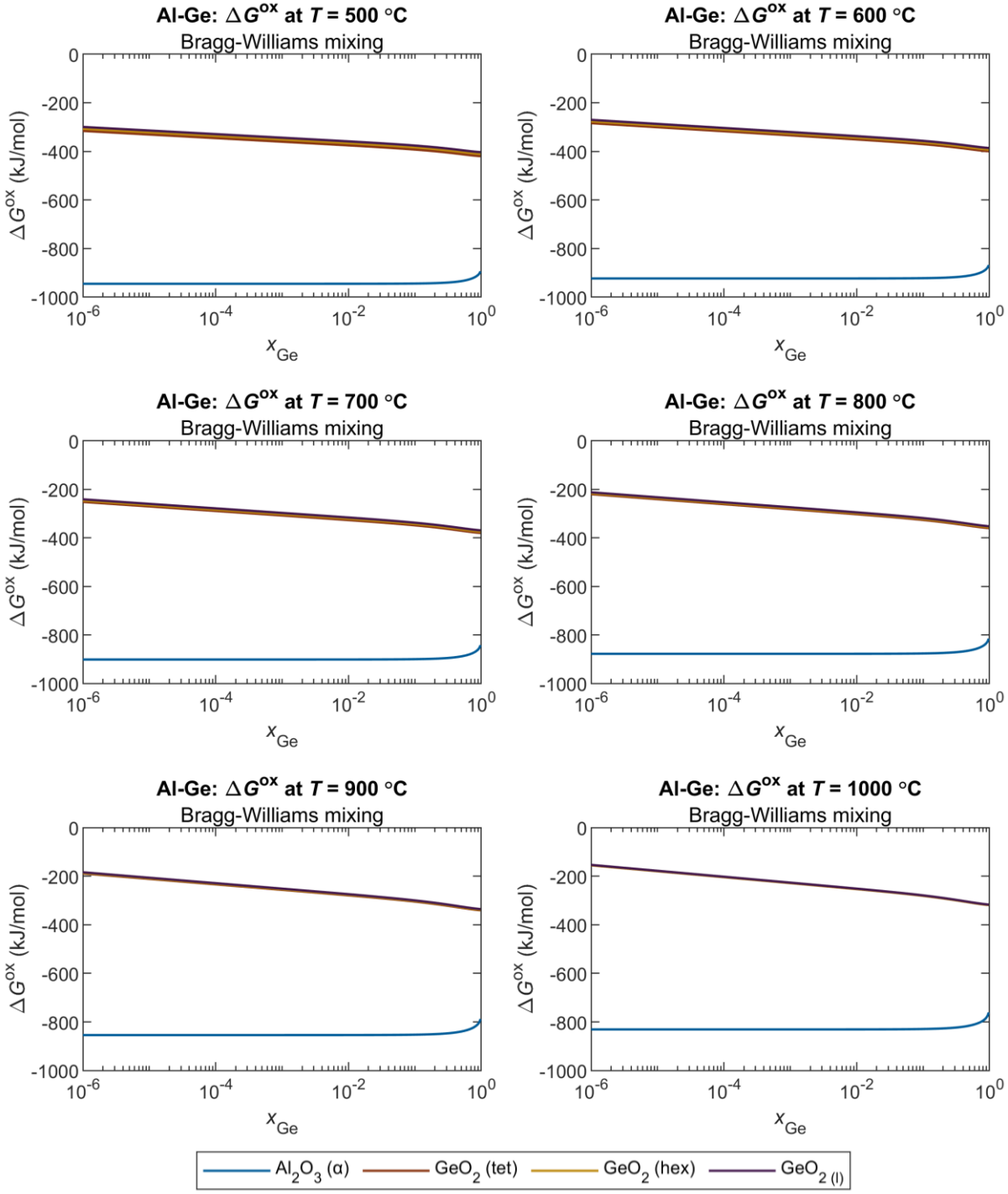
B.4.2.9. Al-Fe


Al-Fe: ΔG^ox at T = 500 °C
Bragg-Williams mixing
Al-Fe: ΔG^ox at T = 600 °C
Bragg-Williams mixing
Al-Fe: ΔG^ox at T = 700 °C
Bragg-Williams mixing
Al-Fe: ΔG^ox at T = 800 °C
Bragg-Williams mixing
Al-Fe: ΔG^ox at T = 900 °C
Bragg-Williams mixing
Al-Fe: ΔG^ox at T = 1000 °C
Bragg-Williams mixing
ΔG^ox (kJ/mol)
x_Fe
Al2O3 (α)
Fe3O4 (s)
FeAlO3 (s)
FeO (s)
Fe2O3 (s)
FeAl2O4 (s)

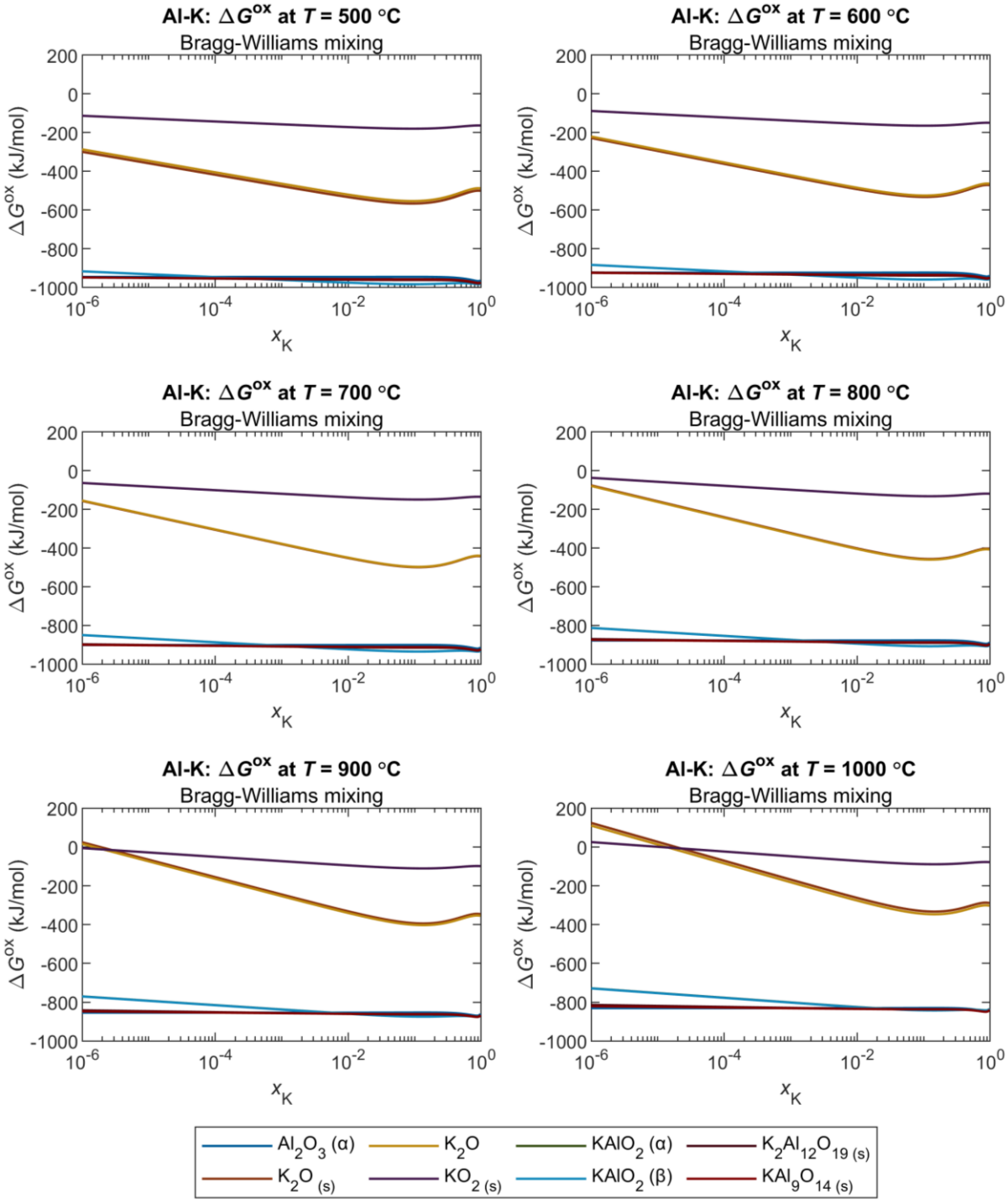
B.4.2.10. Al-Gd


Al-Gd: ΔG^ox at T = 500 °C
Bragg-Williams mixing
Al-Gd: ΔG^ox at T = 600 °C
Bragg-Williams mixing
Al-Gd: ΔG^ox at T = 700 °C
Bragg-Williams mixing
Al-Gd: ΔG^ox at T = 800 °C
Bragg-Williams mixing
Al-Gd: ΔG^ox at T = 900 °C
Bragg-Williams mixing
Al-Gd: ΔG^ox at T = 1000 °C
Bragg-Williams mixing
ΔG^ox (kJ/mol)
-600
-800
-1000
-1200
10^-6
10^-4
10^-2
10^0
x_Gd
Al2O3 (α)
Gd2O3 (s)
Gd4Al2O9 (s)
AlGdO3 (s)
Gd3Al5O12 (s)

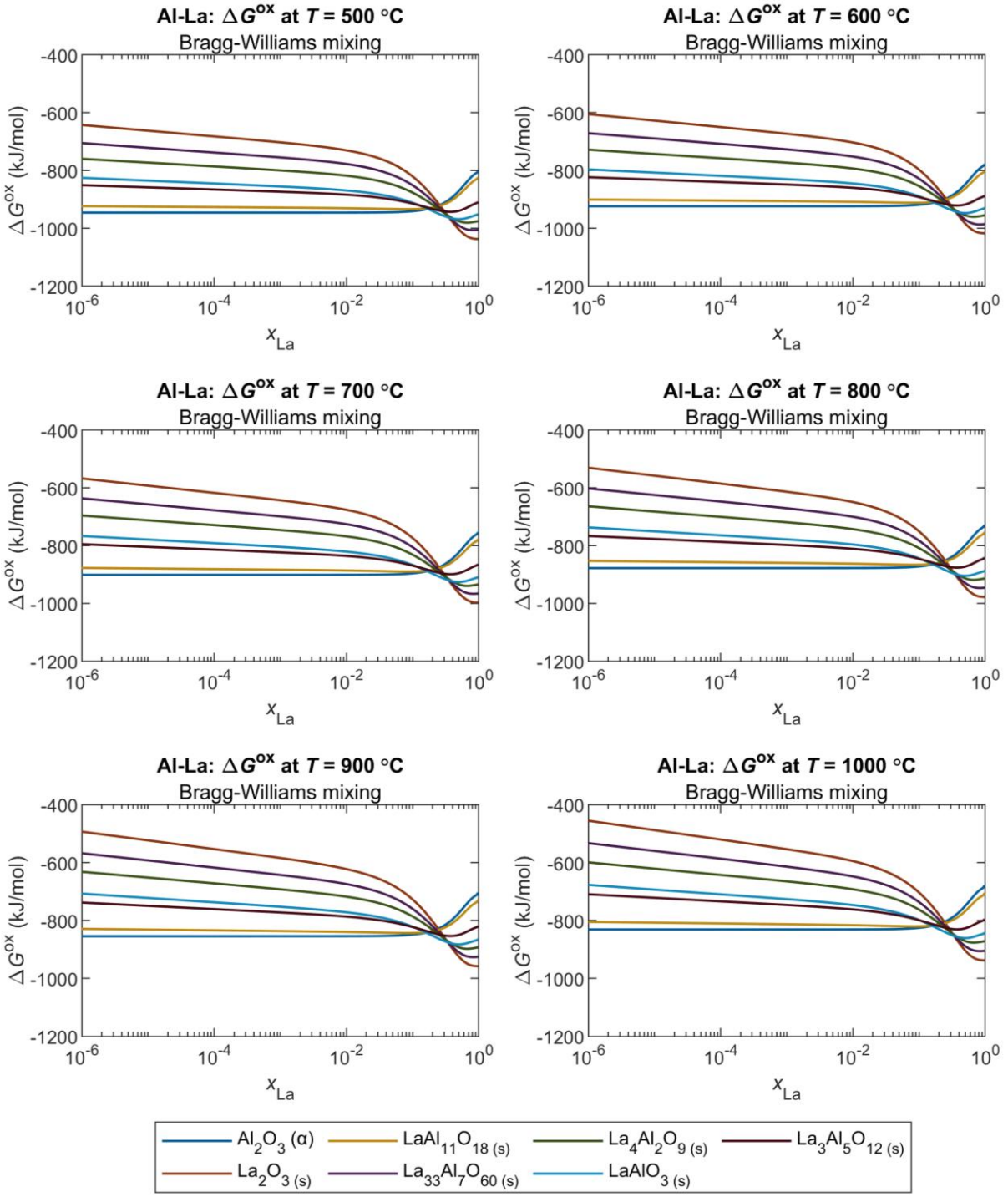
B.4.2.11. Al-Ge


Al-Ge: ΔG^ox at T = 500 °C
Bragg-Williams mixing
Al-Ge: ΔG^ox at T = 600 °C
Bragg-Williams mixing
Al-Ge: ΔG^ox at T = 700 °C
Bragg-Williams mixing
Al-Ge: ΔG^ox at T = 800 °C
Bragg-Williams mixing
Al-Ge: ΔG^ox at T = 900 °C
Bragg-Williams mixing
Al-Ge: ΔG^ox at T = 1000 °C
Bragg-Williams mixing
ΔG^ox (kJ/mol)
0
-200
-400
-600
-800
-1000
10^-6
10^-4
10^-2
10^0
x_Ge
Al2O3 (α)
GeO2 (tet)
GeO2 (hex)
GeO2 (l)

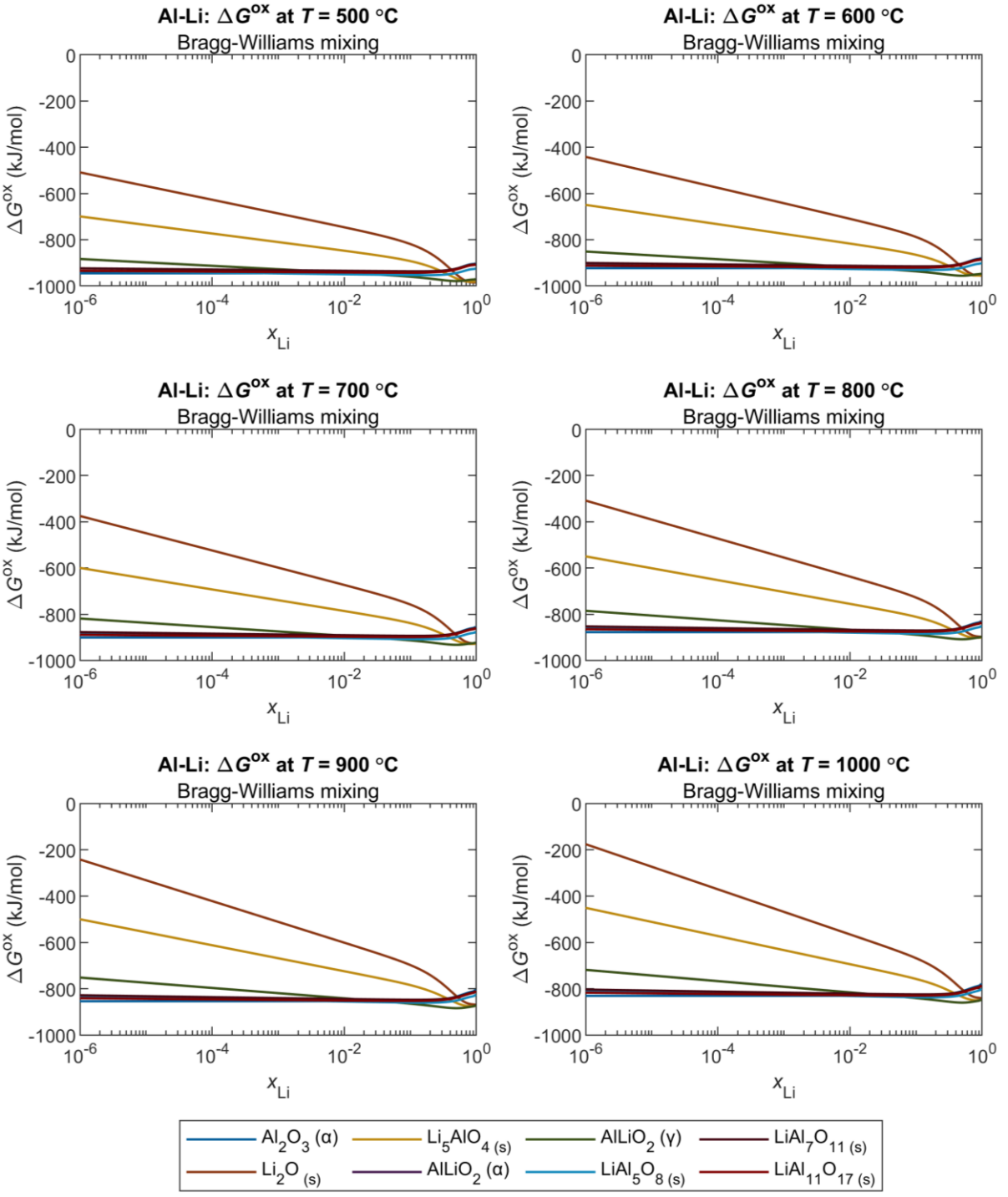
B.4.2.12. Al-K


Al-K: ΔG^ox at T = 500 °C
Bragg-Williams mixing
Al-K: ΔG^ox at T = 600 °C
Bragg-Williams mixing
Al-K: ΔG^ox at T = 700 °C
Bragg-Williams mixing
Al-K: ΔG^ox at T = 800 °C
Bragg-Williams mixing
Al-K: ΔG^ox at T = 900 °C
Bragg-Williams mixing
Al-K: ΔG^ox at T = 1000 °C
Bragg-Williams mixing
ΔG^ox (kJ/mol)
x_K
Al2O3 (α)
K2O
KAlO2 (α)
K2Al12O19 (s)
K2O (s)
KO2 (s)
KAlO2 (β)
KAl9O14 (s)

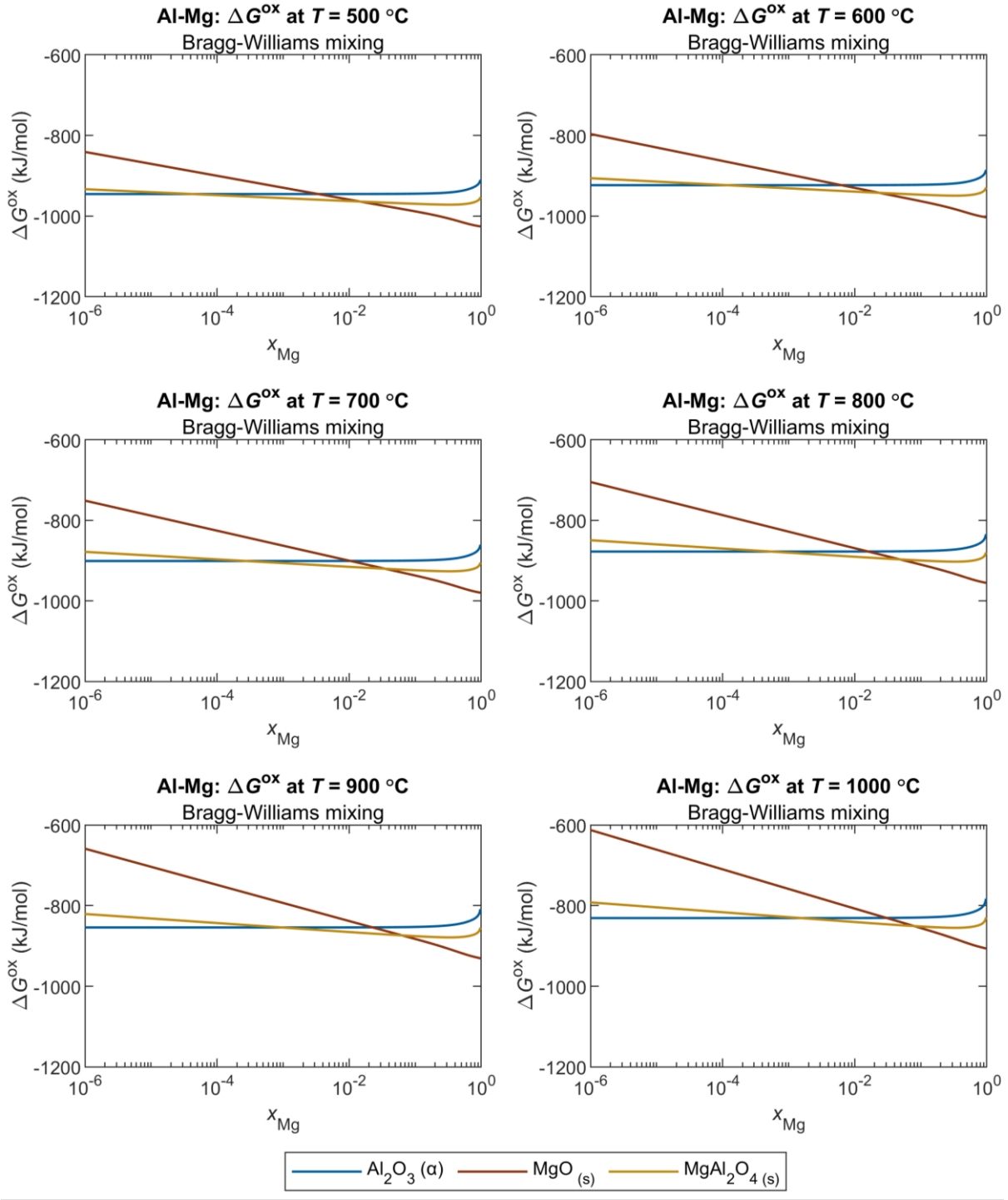
B.4.2.13. Al-La


Al-La: ΔG^ox at T = 500 °C
Bragg-Williams mixing
Al-La: ΔG^ox at T = 600 °C
Bragg-Williams mixing
Al-La: ΔG^ox at T = 700 °C
Bragg-Williams mixing
Al-La: ΔG^ox at T = 800 °C
Bragg-Williams mixing
Al-La: ΔG^ox at T = 900 °C
Bragg-Williams mixing
Al-La: ΔG^ox at T = 1000 °C
Bragg-Williams mixing
ΔG^ox (kJ/mol)
-400
-600
-800
-1000
-1200
10^-6
10^-4
10^-2
10^0
x_La
Al2O3 (α)
LaAl11O18 (s)
La4Al2O9 (s)
La3Al5O12 (s)
La2O3 (s)
La33Al7O60 (s)
LaAlO3 (s)

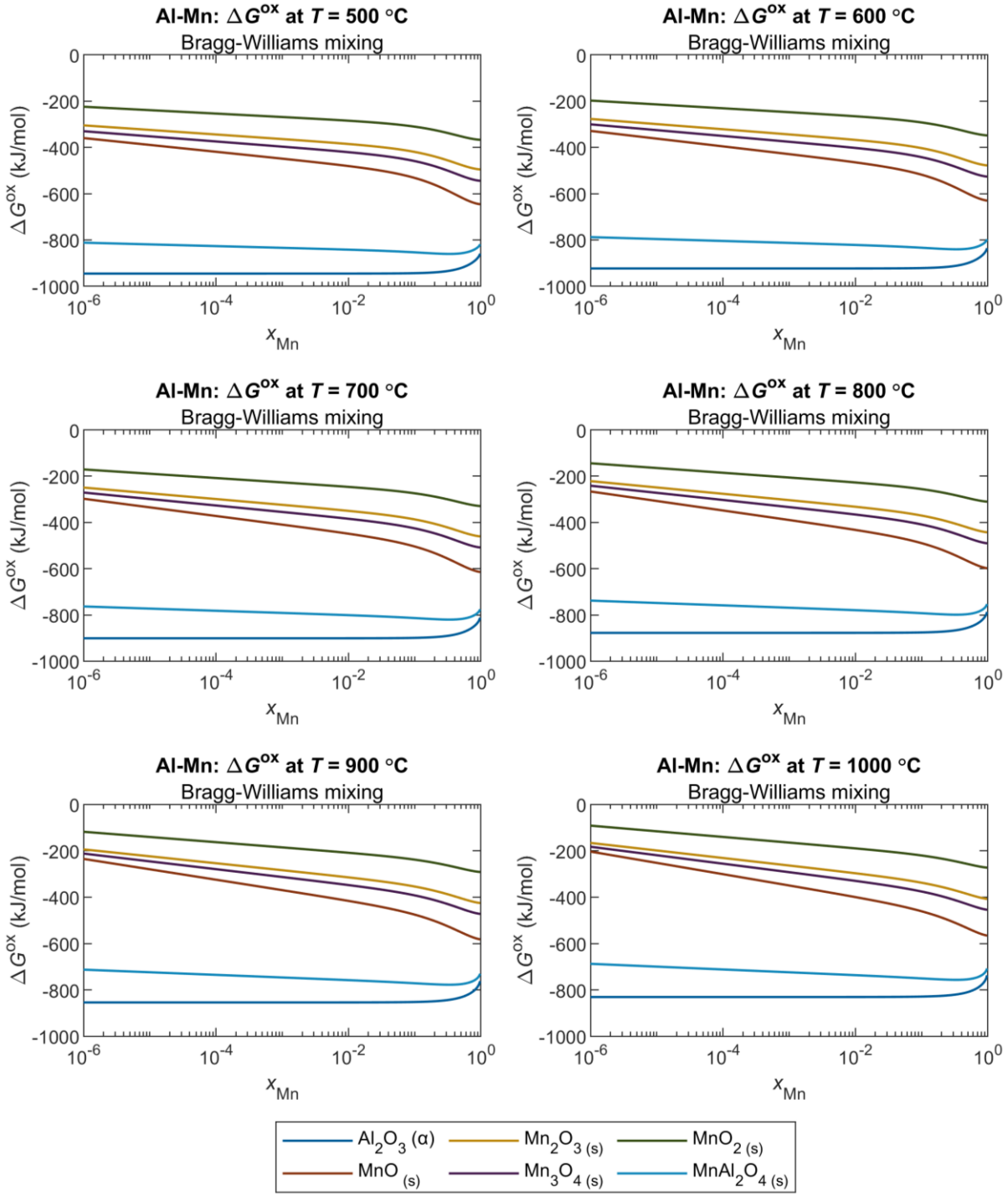
B.4.2.14. Al-Li


Al-Li: ΔG^ox at T = 500 °C
Bragg-Williams mixing
Al-Li: ΔG^ox at T = 600 °C
Bragg-Williams mixing
Al-Li: ΔG^ox at T = 700 °C
Bragg-Williams mixing
Al-Li: ΔG^ox at T = 800 °C
Bragg-Williams mixing
Al-Li: ΔG^ox at T = 900 °C
Bragg-Williams mixing
Al-Li: ΔG^ox at T = 1000 °C
Bragg-Williams mixing
ΔG^ox (kJ/mol)
0
-200
-400
-600
-800
-1000
10^-6
10^-4
10^-2
10^0
x_Li
Al2O3 (α)
Li5AlO4 (s)
AlLiO2 (γ)
LiAl7O11 (s)
Li2O (s)
AlLiO2 (α)
LiAl5O8 (s)
LiAl11O17 (s)

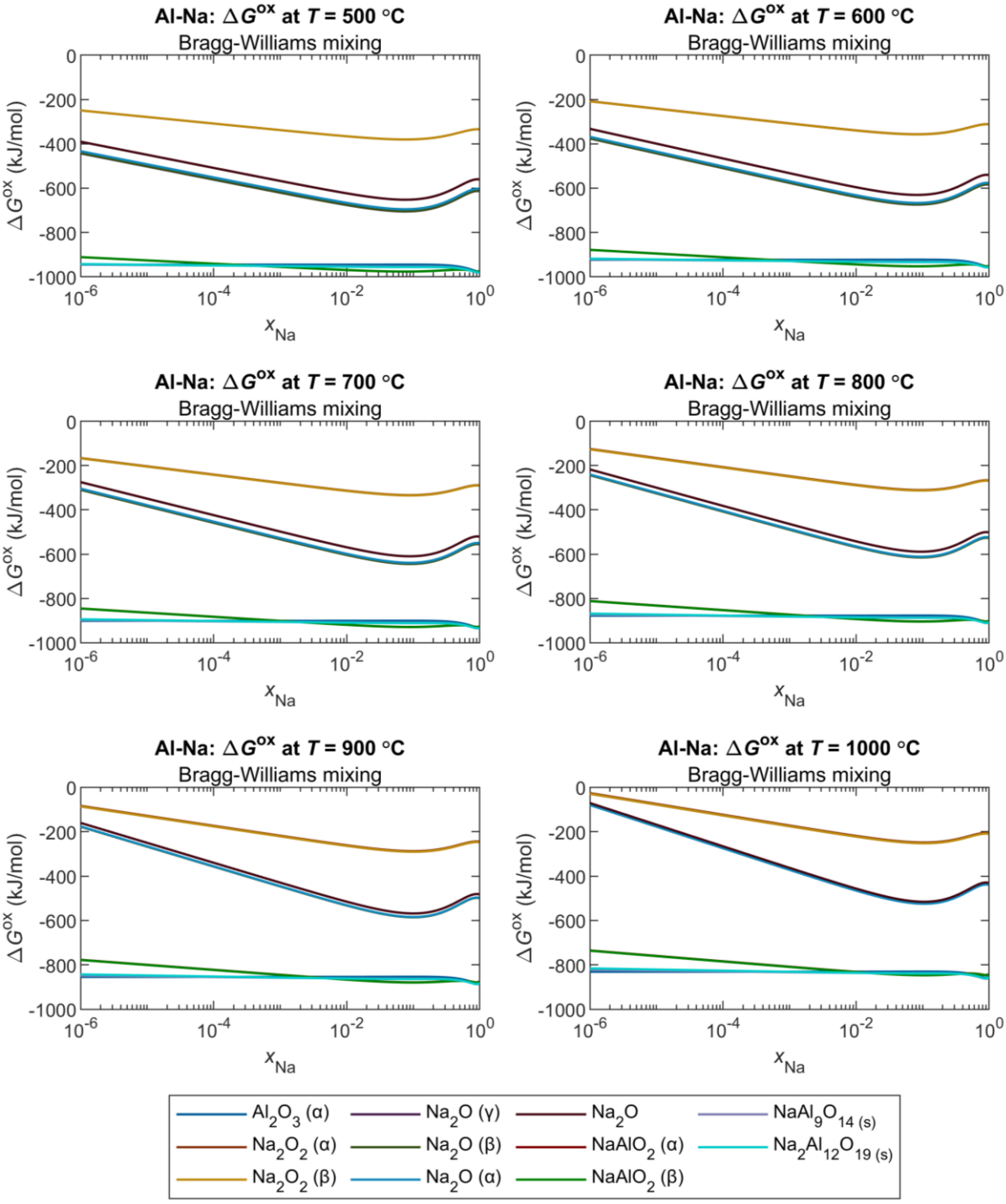
B.4.2.15. Al-Mg


Al-Mg: ΔG^ox at T = 500 °C
Bragg-Williams mixing
Al-Mg: ΔG^ox at T = 600 °C
Bragg-Williams mixing
Al-Mg: ΔG^ox at T = 700 °C
Bragg-Williams mixing
Al-Mg: ΔG^ox at T = 800 °C
Bragg-Williams mixing
Al-Mg: ΔG^ox at T = 900 °C
Bragg-Williams mixing
Al-Mg: ΔG^ox at T = 1000 °C
Bragg-Williams mixing
ΔG^ox (kJ/mol)
-600
-800
-1000
-1200
10^-6
10^-4
10^-2
10^0
x_Mg
Al2O3 (α)
MgO (s)
MgAl2O4 (s)

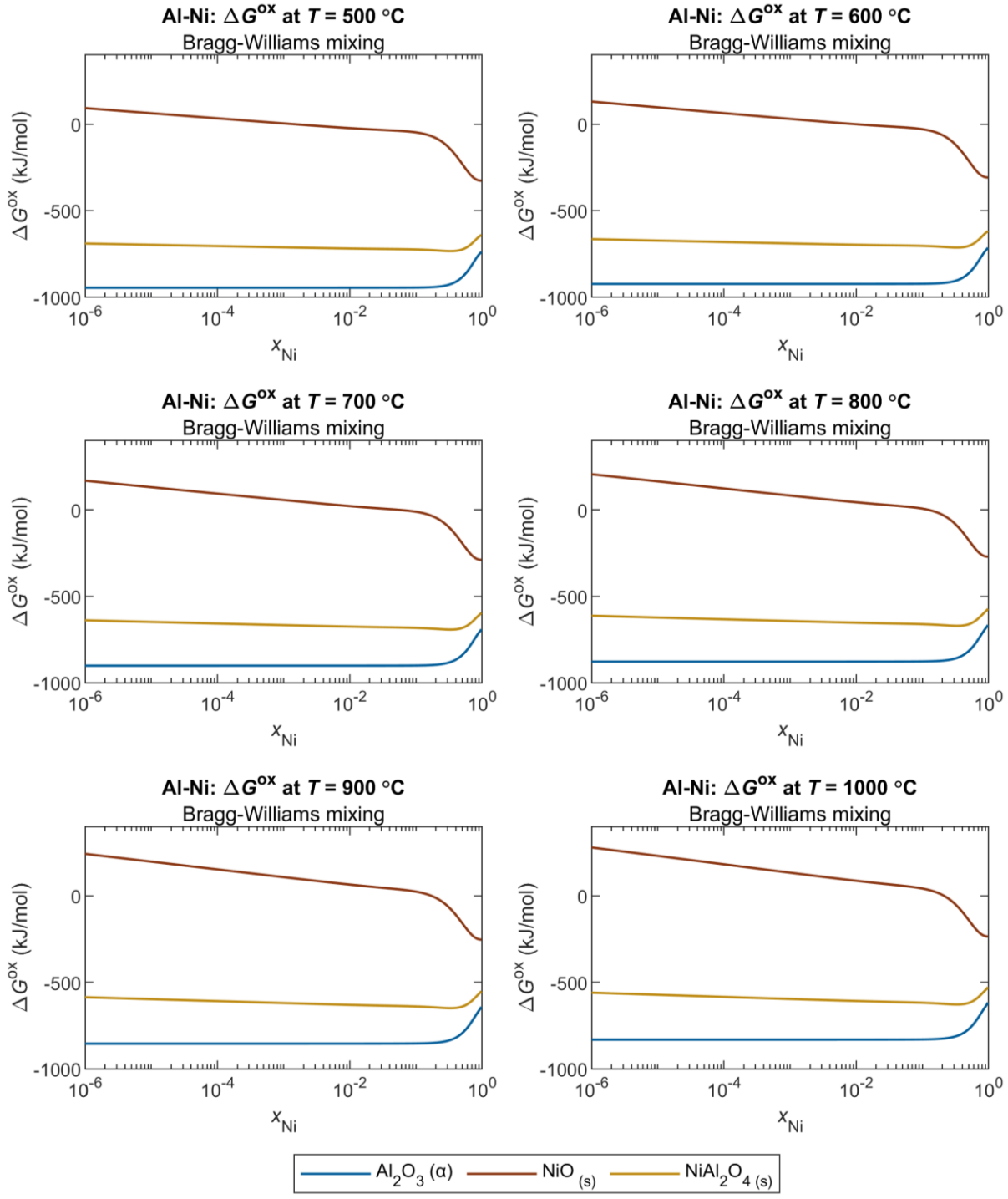
B.4.2.16. Al-Mn


Al-Mn: ΔG^ox at T = 500 °C
Bragg-Williams mixing
Al-Mn: ΔG^ox at T = 600 °C
Bragg-Williams mixing
Al-Mn: ΔG^ox at T = 700 °C
Bragg-Williams mixing
Al-Mn: ΔG^ox at T = 800 °C
Bragg-Williams mixing
Al-Mn: ΔG^ox at T = 900 °C
Bragg-Williams mixing
Al-Mn: ΔG^ox at T = 1000 °C
Bragg-Williams mixing
ΔG^ox (kJ/mol)
x_Mn
0
-200
-400
-600
-800
-1000
10^-6
10^-4
10^-2
10^0
Al2O3 (α)
Mn2O3 (s)
MnO2 (s)
MnO (s)
Mn3O4 (s)
MnAl2O4 (s)

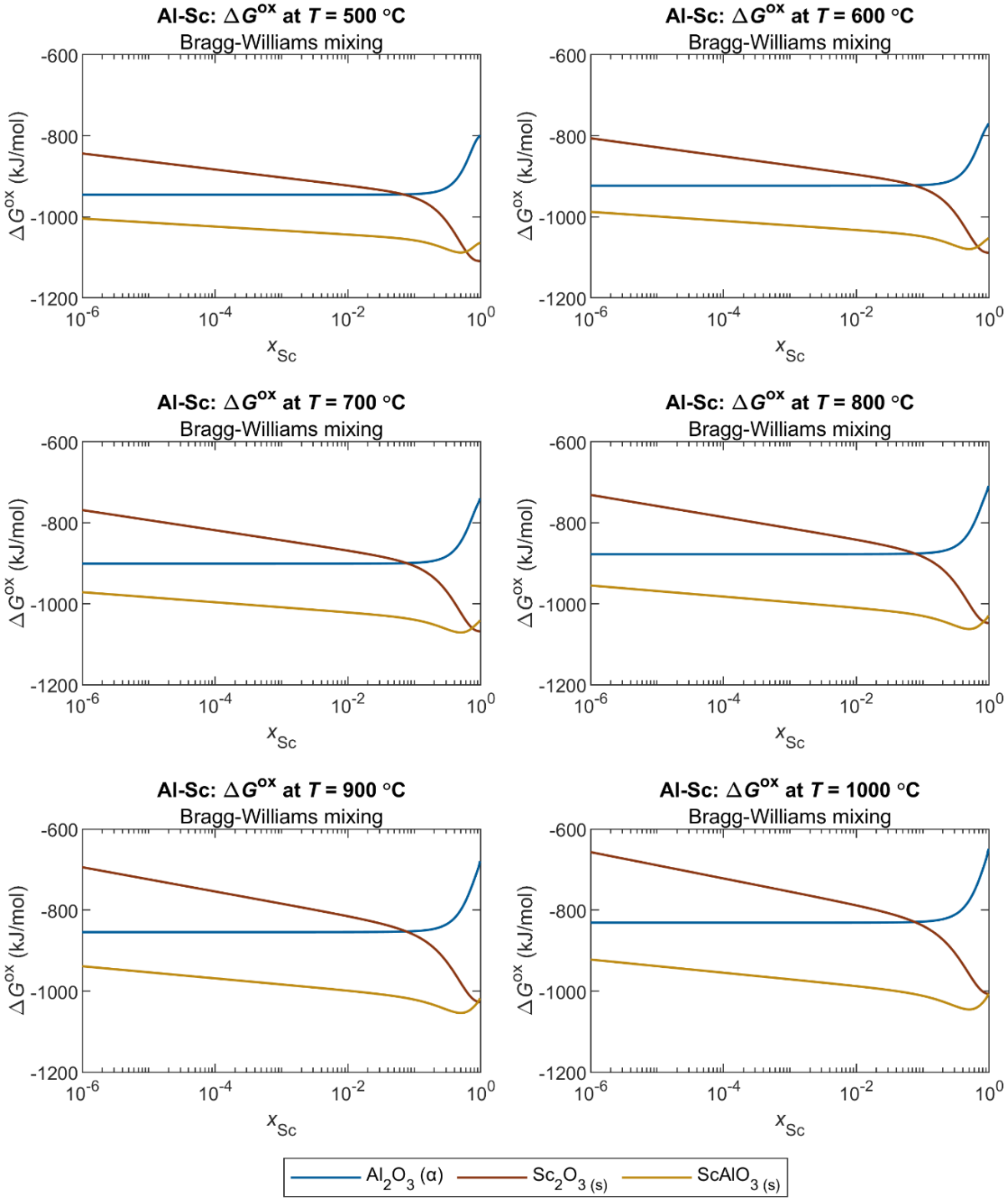
B.4.2.17. Al-Na


Al-Na: ΔG^ox at T = 500 °C
Bragg-Williams mixing
Al-Na: ΔG^ox at T = 600 °C
Bragg-Williams mixing
Al-Na: ΔG^ox at T = 700 °C
Bragg-Williams mixing
Al-Na: ΔG^ox at T = 800 °C
Bragg-Williams mixing
Al-Na: ΔG^ox at T = 900 °C
Bragg-Williams mixing
Al-Na: ΔG^ox at T = 1000 °C
Bragg-Williams mixing
ΔG^ox (kJ/mol)
x_Na
Al2O3 (α)
Na2O (γ)
Na2O
NaAl9O14 (s)
Na2O2 (α)
Na2O (β)
NaAlO2 (α)
Na2Al12O19 (s)
Na2O2 (β)
Na2O (α)
NaAlO2 (β)

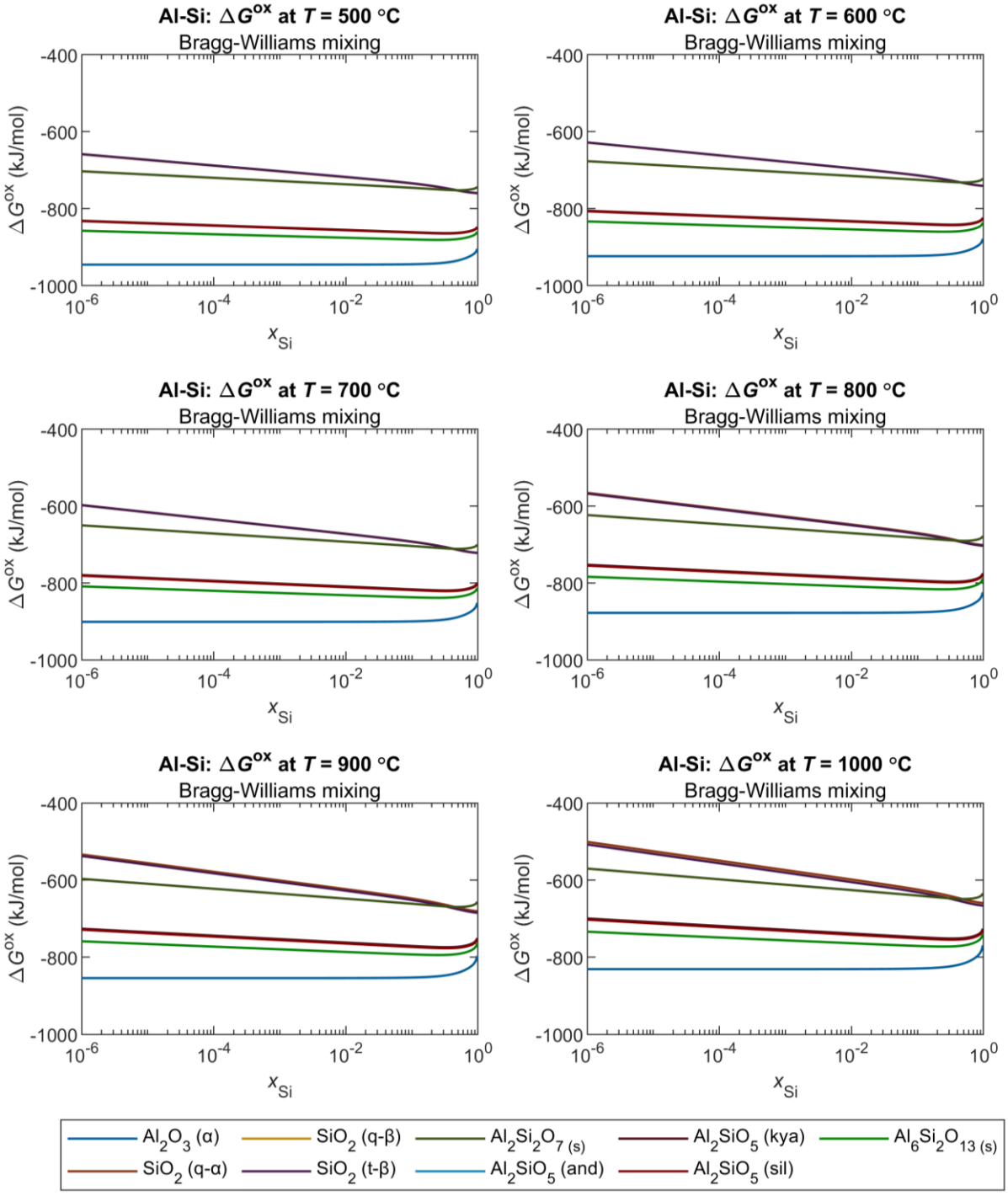
B.4.2.18. Al-Ni


Al-Ni: ΔG^ox at T = 500 °C
Bragg-Williams mixing
Al-Ni: ΔG^ox at T = 600 °C
Bragg-Williams mixing
Al-Ni: ΔG^ox at T = 700 °C
Bragg-Williams mixing
Al-Ni: ΔG^ox at T = 800 °C
Bragg-Williams mixing
Al-Ni: ΔG^ox at T = 900 °C
Bragg-Williams mixing
Al-Ni: ΔG^ox at T = 1000 °C
Bragg-Williams mixing
ΔG^ox (kJ/mol)
0
-500
-1000
10^-6
10^-4
10^-2
10^0
x_Ni
Al2O3 (α)
NiO (s)
NiAl2O4 (s)

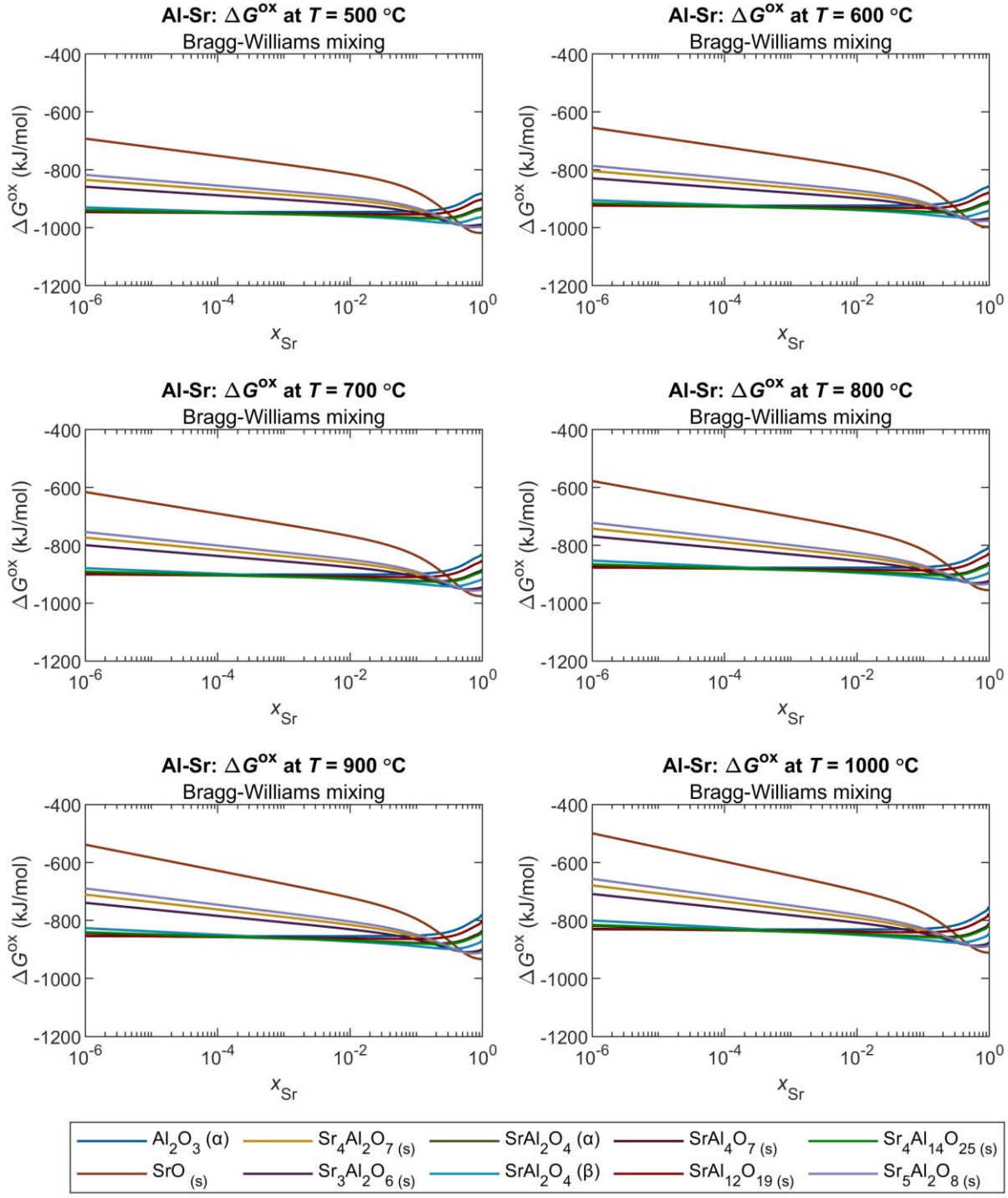
B.4.2.19. Al-Sc


Al-Sc: ΔG^ox at T = 500 °C
Bragg-Williams mixing
Al-Sc: ΔG^ox at T = 600 °C
Bragg-Williams mixing
Al-Sc: ΔG^ox at T = 700 °C
Bragg-Williams mixing
Al-Sc: ΔG^ox at T = 800 °C
Bragg-Williams mixing
Al-Sc: ΔG^ox at T = 900 °C
Bragg-Williams mixing
Al-Sc: ΔG^ox at T = 1000 °C
Bragg-Williams mixing
ΔG^ox (kJ/mol)
-600
-800
-1000
-1200
10^-6
10^-4
10^-2
10^0
x_Sc
Al2O3 (α)
Sc2O3 (s)
ScAlO3 (s)

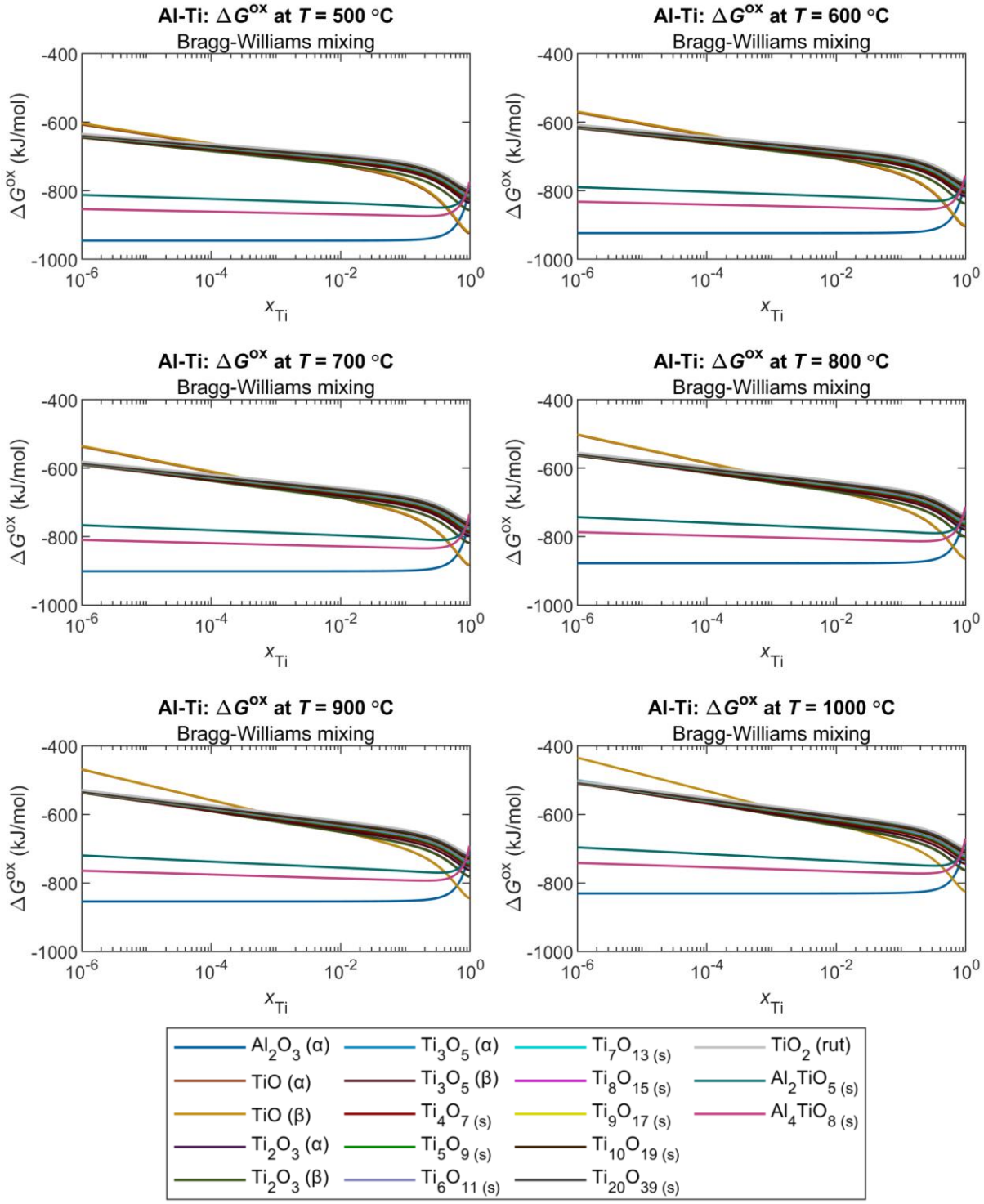
B.4.2.20. Al-Si


Al-Si: ΔG^ox at T = 500 °C
Bragg-Williams mixing
Al-Si: ΔG^ox at T = 600 °C
Bragg-Williams mixing
Al-Si: ΔG^ox at T = 700 °C
Bragg-Williams mixing
Al-Si: ΔG^ox at T = 800 °C
Bragg-Williams mixing
Al-Si: ΔG^ox at T = 900 °C
Bragg-Williams mixing
Al-Si: ΔG^ox at T = 1000 °C
Bragg-Williams mixing
ΔG^ox (kJ/mol)
-400
-600
-800
-1000
10^-6
10^-4
10^-2
10^0
x_Si
Al2O3 (α)
SiO2 (q-β)
Al2Si2O7 (s)
Al2SiO5 (kya)
Al6Si2O13 (s)
SiO2 (q-α)
SiO2 (t-β)
Al2SiO5 (and)
Al2SiO5 (sil)

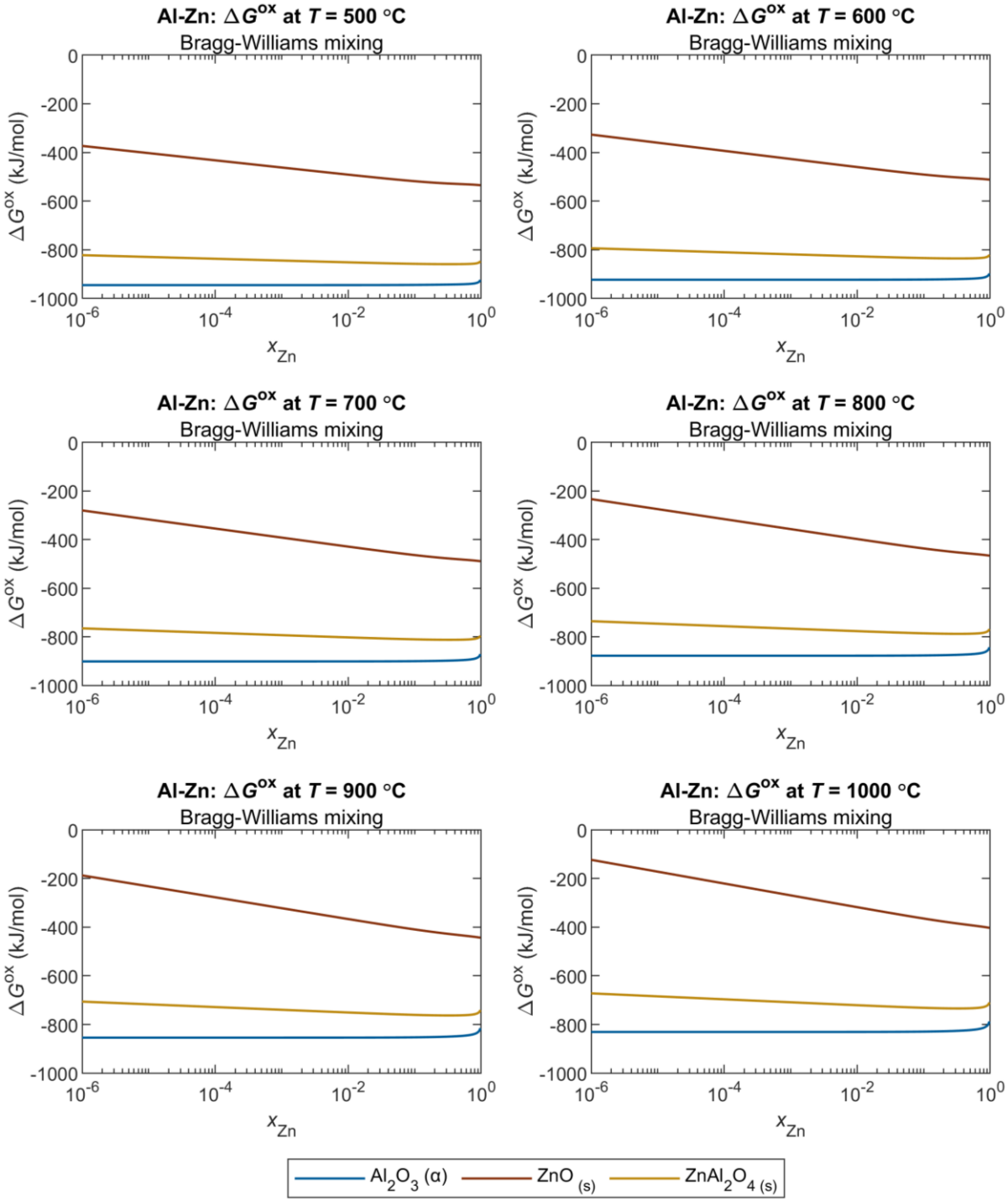
B.4.2.21. Al-Sr


Al-Sr: ΔG^ox at T = 500 °C
Bragg-Williams mixing
Al-Sr: ΔG^ox at T = 600 °C
Bragg-Williams mixing
Al-Sr: ΔG^ox at T = 700 °C
Bragg-Williams mixing
Al-Sr: ΔG^ox at T = 800 °C
Bragg-Williams mixing
Al-Sr: ΔG^ox at T = 900 °C
Bragg-Williams mixing
Al-Sr: ΔG^ox at T = 1000 °C
Bragg-Williams mixing
ΔG^ox (kJ/mol)
-400
-600
-800
-1000
-1200
10^-6
10^-4
10^-2
10^0
x_Sr
Al2O3 (α)
Sr4Al2O7 (s)
SrAl2O4 (α)
SrAl4O7 (s)
Sr4Al14O25 (s)
SrO (s)
Sr3Al2O6 (s)
SrAl2O4 (β)
SrAl12O19 (s)
Sr5Al2O8 (s)

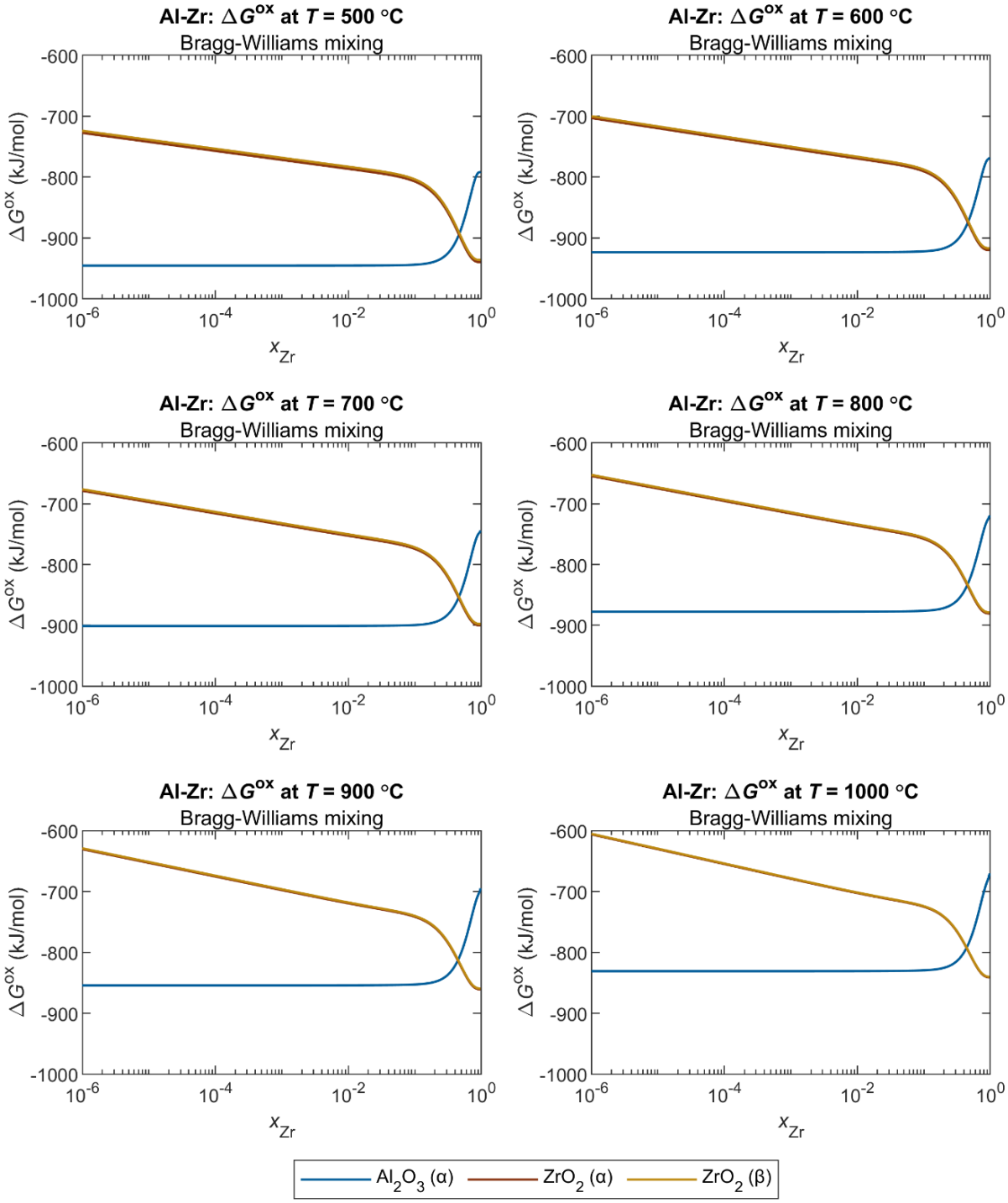
B.4.2.22. Al-Ti


Al-Ti: ΔG^ox at T = 500 °C
Bragg-Williams mixing
Al-Ti: ΔG^ox at T = 600 °C
Bragg-Williams mixing
Al-Ti: ΔG^ox at T = 700 °C
Bragg-Williams mixing
Al-Ti: ΔG^ox at T = 800 °C
Bragg-Williams mixing
Al-Ti: ΔG^ox at T = 900 °C
Bragg-Williams mixing
Al-Ti: ΔG^ox at T = 1000 °C
Bragg-Williams mixing
ΔG^ox (kJ/mol)
-400
-600
-800
-1000
10^-6
10^-4
10^-2
10^0
x_Ti
Al2O3 (α)
TiO (α)
TiO (β)
Ti2O3 (α)
Ti2O3 (β)
Ti3O5 (α)
Ti3O5 (β)
Ti4O7 (s)
Ti5O9 (s)
Ti6O11 (s)
Ti7O13 (s)
Ti8O15 (s)
Ti9O17 (s)
Ti10O19 (s)
Ti20O39 (s)
TiO2 (rut)
Al2TiO5 (s)
Al4TiO8 (s)

B.4.2.23. Al-Zn

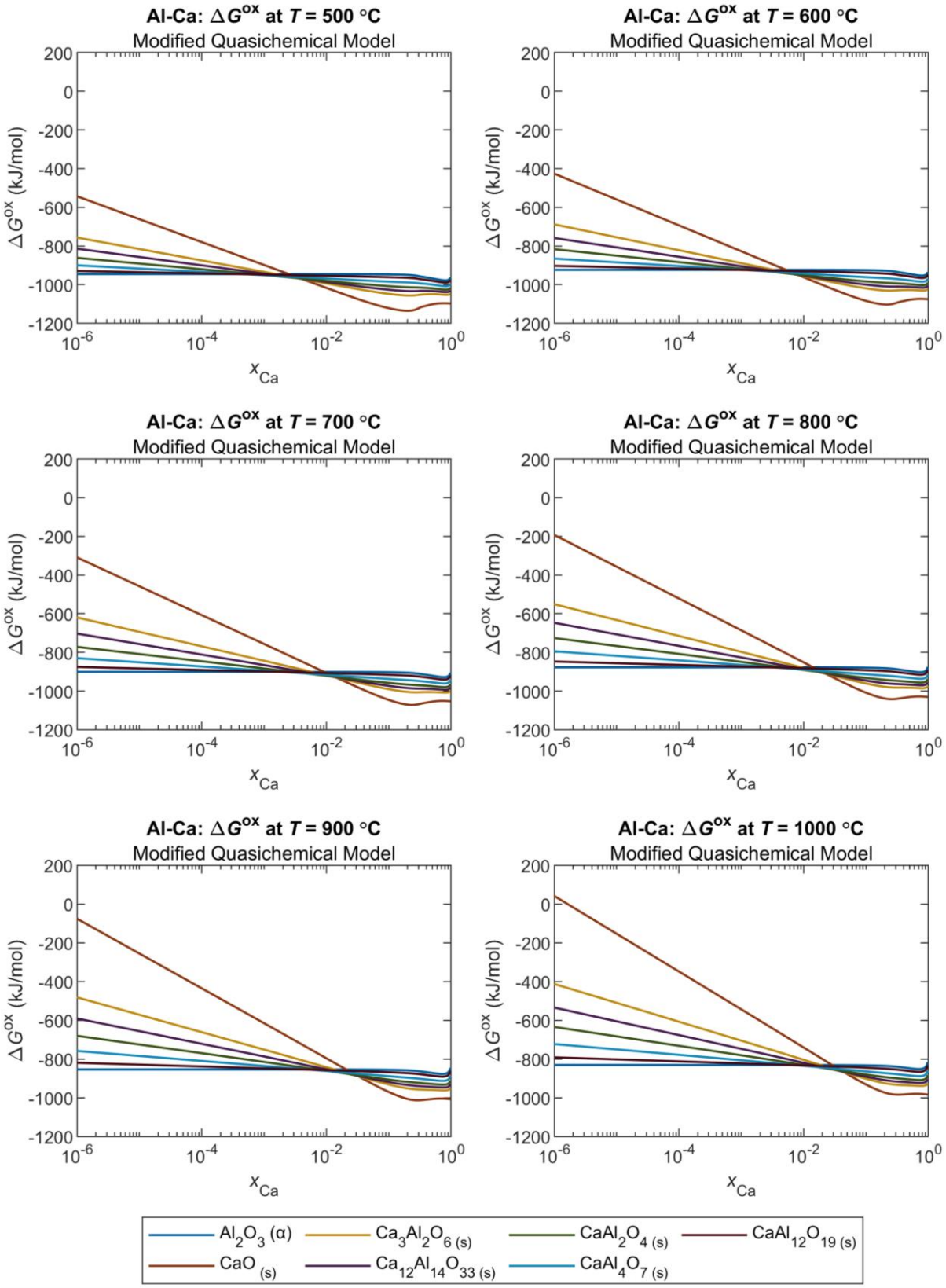

Al-Zn: ΔG^ox at T = 500 °C
Bragg-Williams mixing
Al-Zn: ΔG^ox at T = 600 °C
Bragg-Williams mixing
Al-Zn: ΔG^ox at T = 700 °C
Bragg-Williams mixing
Al-Zn: ΔG^ox at T = 800 °C
Bragg-Williams mixing
Al-Zn: ΔG^ox at T = 900 °C
Bragg-Williams mixing
Al-Zn: ΔG^ox at T = 1000 °C
Bragg-Williams mixing
ΔG^ox (kJ/mol)
x_Zn
0
-200
-400
-600
-800
-1000
10^-6
10^-4
10^-2
10^0
Al2O3 (α)
ZnO (s)
ZnAl2O4 (s)

B.4.2.24. Al-Zr

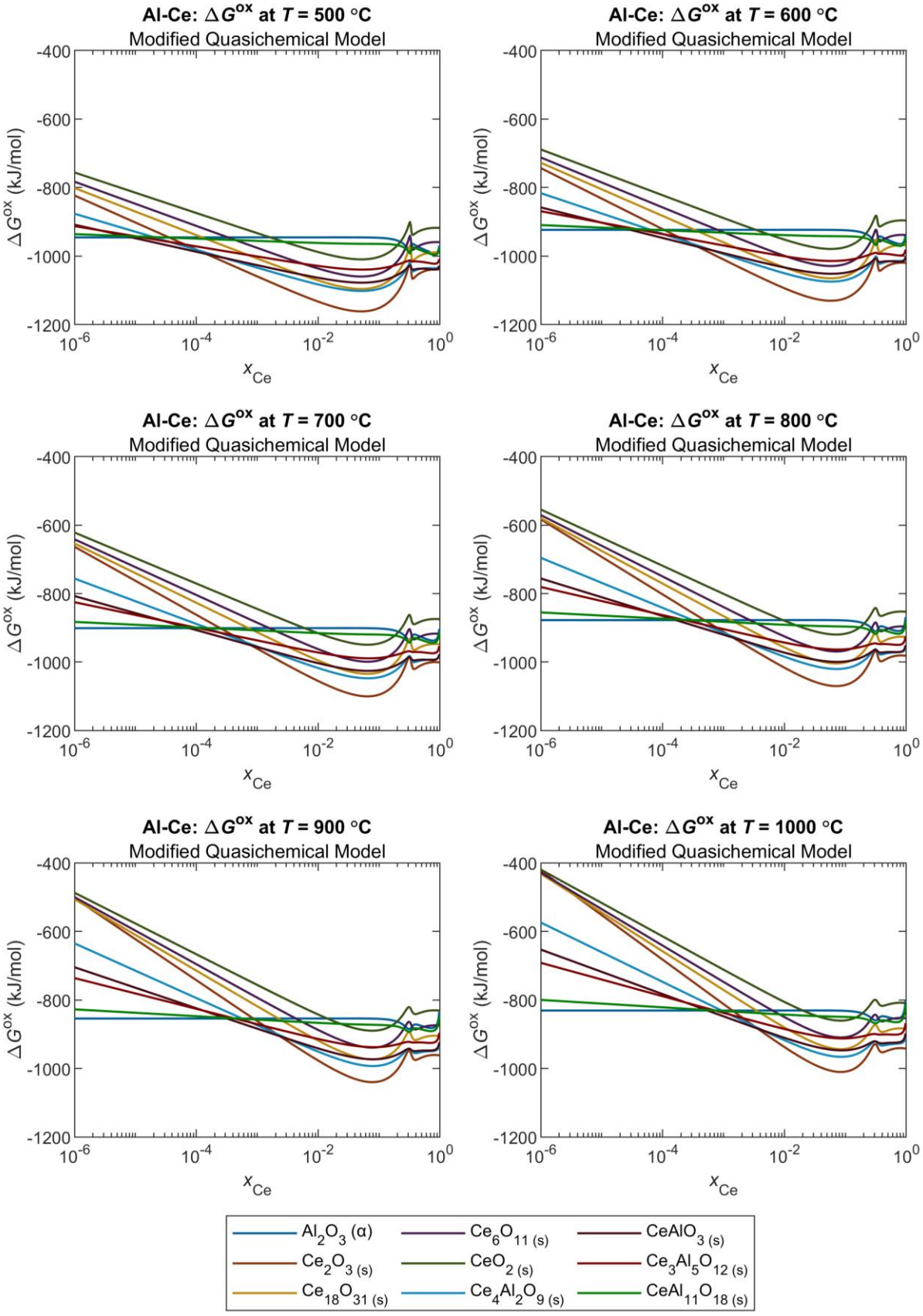

Al-Zr: ΔG^ox at T = 500 °C
Bragg-Williams mixing
Al-Zr: ΔG^ox at T = 600 °C
Bragg-Williams mixing
Al-Zr: ΔG^ox at T = 700 °C
Bragg-Williams mixing
Al-Zr: ΔG^ox at T = 800 °C
Bragg-Williams mixing
Al-Zr: ΔG^ox at T = 900 °C
Bragg-Williams mixing
Al-Zr: ΔG^ox at T = 1000 °C
Bragg-Williams mixing
ΔG^ox (kJ/mol)
-600
-700
-800
-900
-1000
10^-6
10^-4
10^-2
10^0
x_Zr
Al2O3 (α)
ZrO2 (α)
ZrO2 (β)

B.4.3. Modified quasichemical model

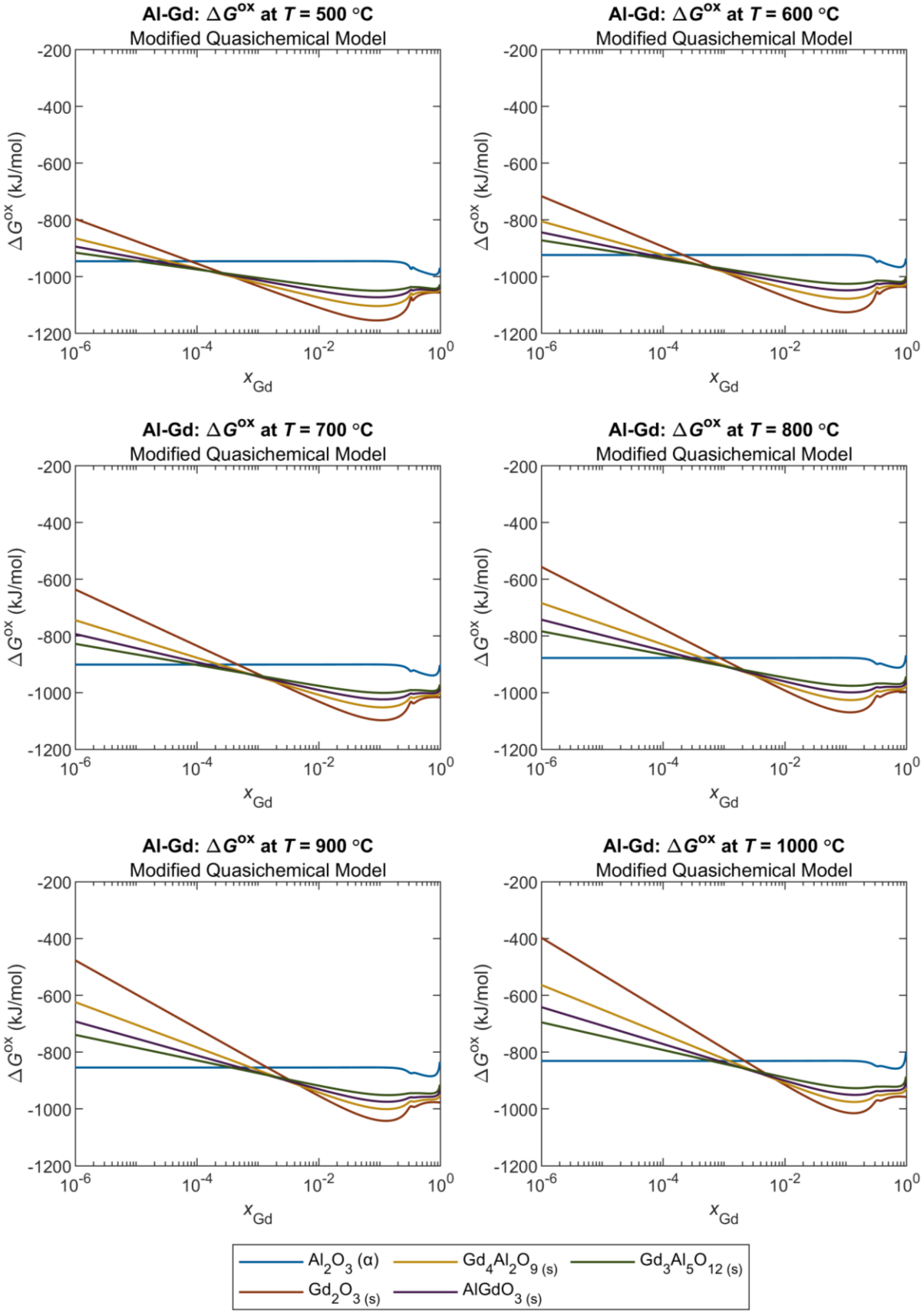
B.4.3.1. Al-Ca



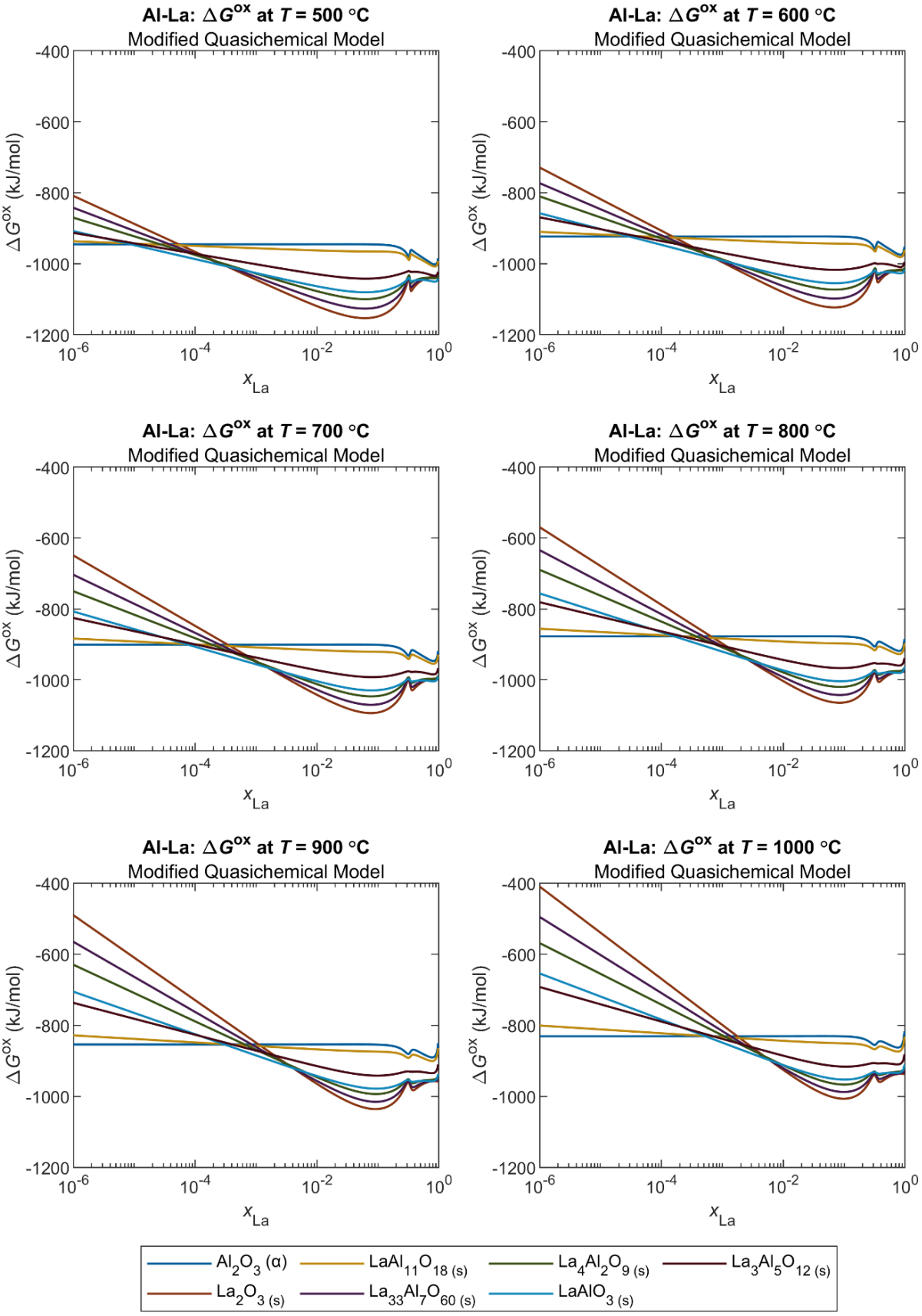
B.4.3.2. Al-Ce


Al-Ce: ΔG^ox at T = 500 °C
Modified Quasichemical Model
Al-Ce: ΔG^ox at T = 600 °C
Modified Quasichemical Model
Al-Ce: ΔG^ox at T = 700 °C
Modified Quasichemical Model
Al-Ce: ΔG^ox at T = 800 °C
Modified Quasichemical Model
Al-Ce: ΔG^ox at T = 900 °C
Modified Quasichemical Model
Al-Ce: ΔG^ox at T = 1000 °C
Modified Quasichemical Model
ΔG^ox (kJ/mol)
-400
-600
-800
-1000
-1200
10^-6
10^-4
10^-2
10^0
x_Ce
Al2O3 (α)
Ce6O11 (s)
CeAlO3 (s)
Ce2O3 (s)
CeO2 (s)
Ce3Al5O12 (s)
Ce18O31 (s)
Ce4Al2O9 (s)
CeAl11O18 (s)

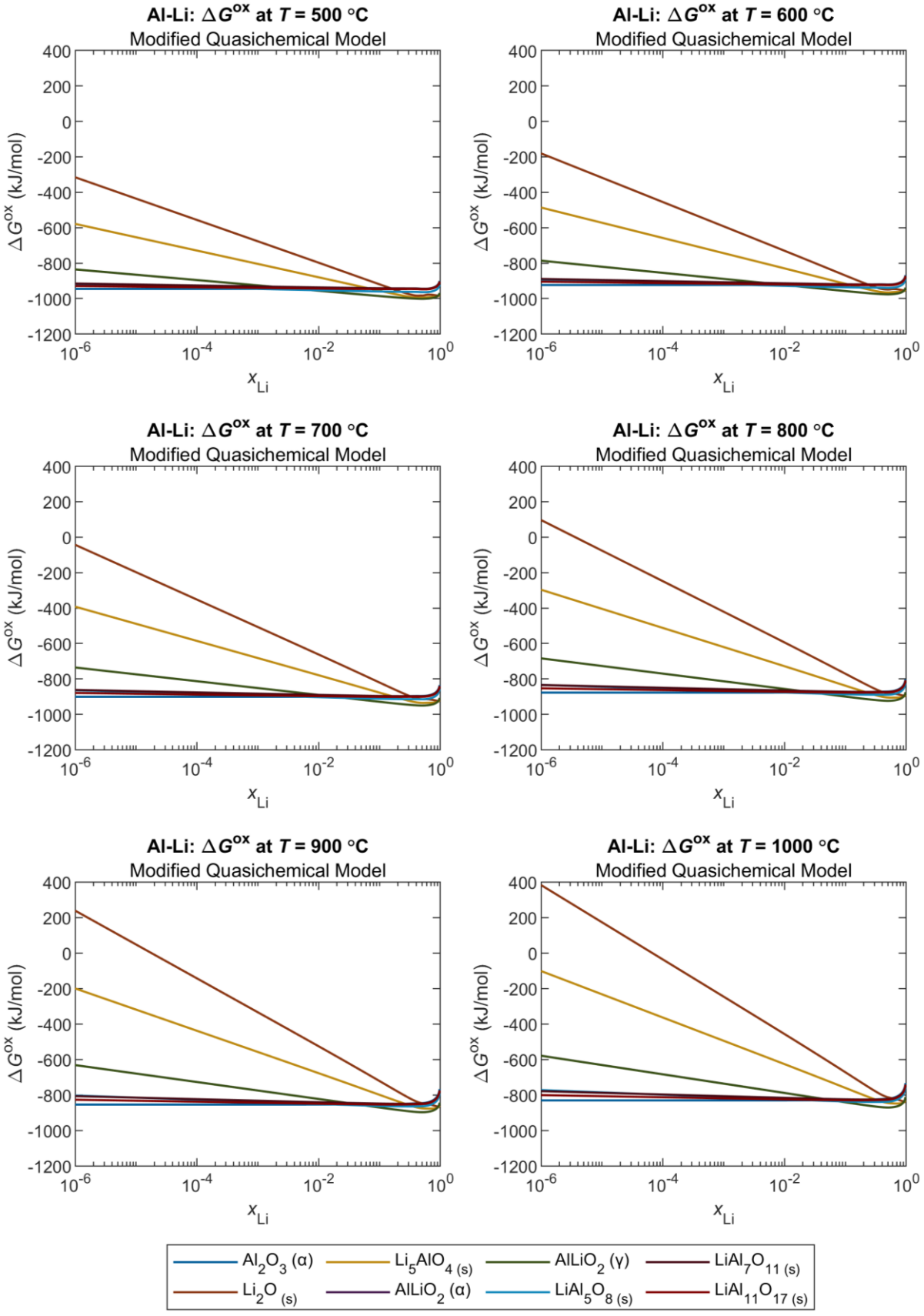
B.4.3.3. Al-Gd


Al-Gd: ΔG^ox at T = 500 °C
Modified Quasichemical Model
Al-Gd: ΔG^ox at T = 600 °C
Modified Quasichemical Model
Al-Gd: ΔG^ox at T = 700 °C
Modified Quasichemical Model
Al-Gd: ΔG^ox at T = 800 °C
Modified Quasichemical Model
Al-Gd: ΔG^ox at T = 900 °C
Modified Quasichemical Model
Al-Gd: ΔG^ox at T = 1000 °C
Modified Quasichemical Model
ΔG^ox (kJ/mol)
-200
-400
-600
-800
-1000
-1200
10^-6
10^-4
10^-2
10^0
x_Gd
Al2O3 (α)
Gd4Al2O9 (s)
Gd3Al5O12 (s)
Gd2O3 (s)
AlGdO3 (s)

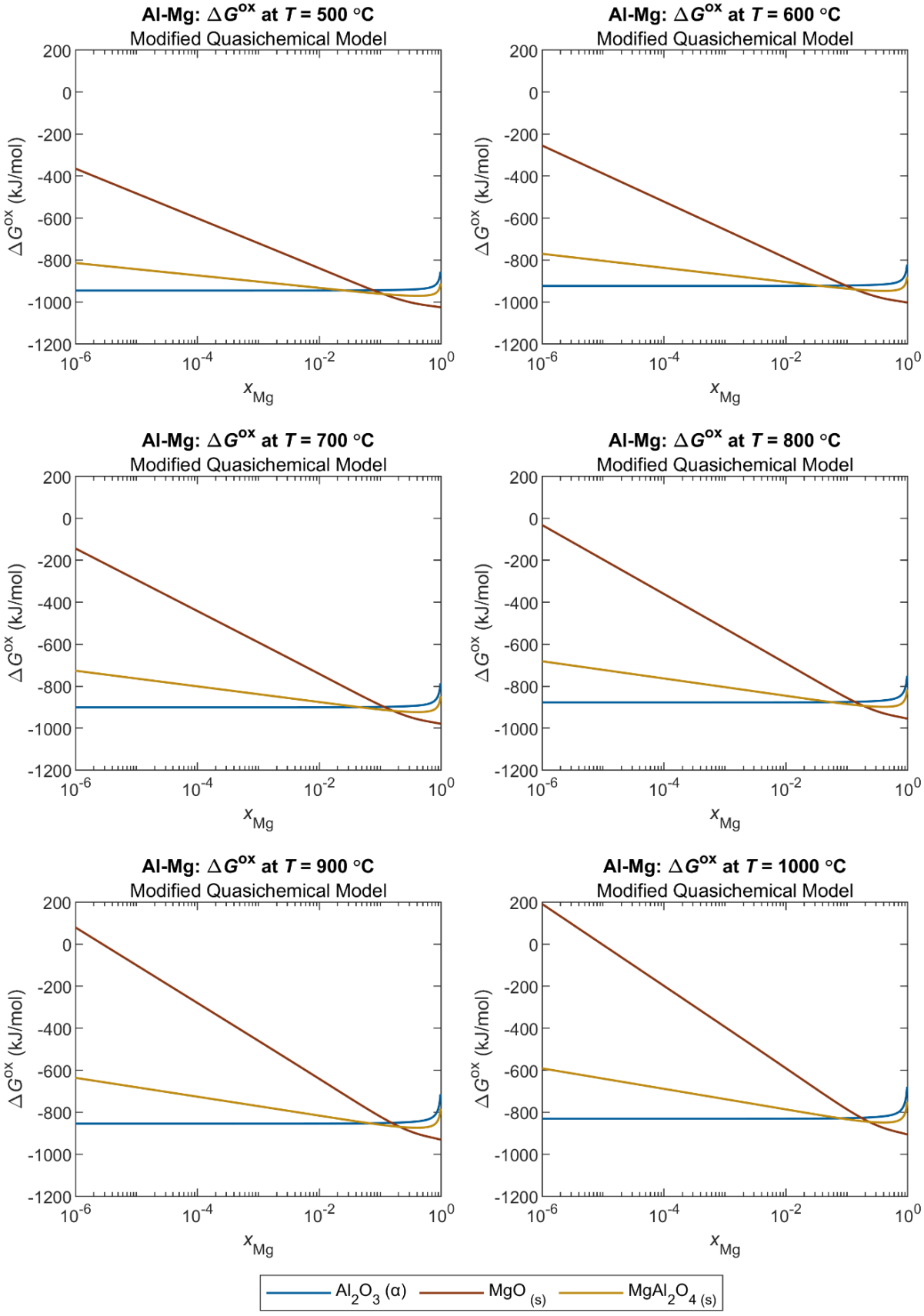
B.4.3.4. Al-La


Al-La: ΔG^ox at T = 500 °C
Modified Quasichemical Model
Al-La: ΔG^ox at T = 600 °C
Modified Quasichemical Model
Al-La: ΔG^ox at T = 700 °C
Modified Quasichemical Model
Al-La: ΔG^ox at T = 800 °C
Modified Quasichemical Model
Al-La: ΔG^ox at T = 900 °C
Modified Quasichemical Model
Al-La: ΔG^ox at T = 1000 °C
Modified Quasichemical Model
ΔG^ox (kJ/mol)
-400
-600
-800
-1000
-1200
10^-6
10^-4
10^-2
10^0
x_La
Al2O3 (α)
LaAl11O18 (s)
La4Al2O9 (s)
La3Al5O12 (s)
La2O3 (s)
La33Al7O60 (s)
LaAlO3 (s)

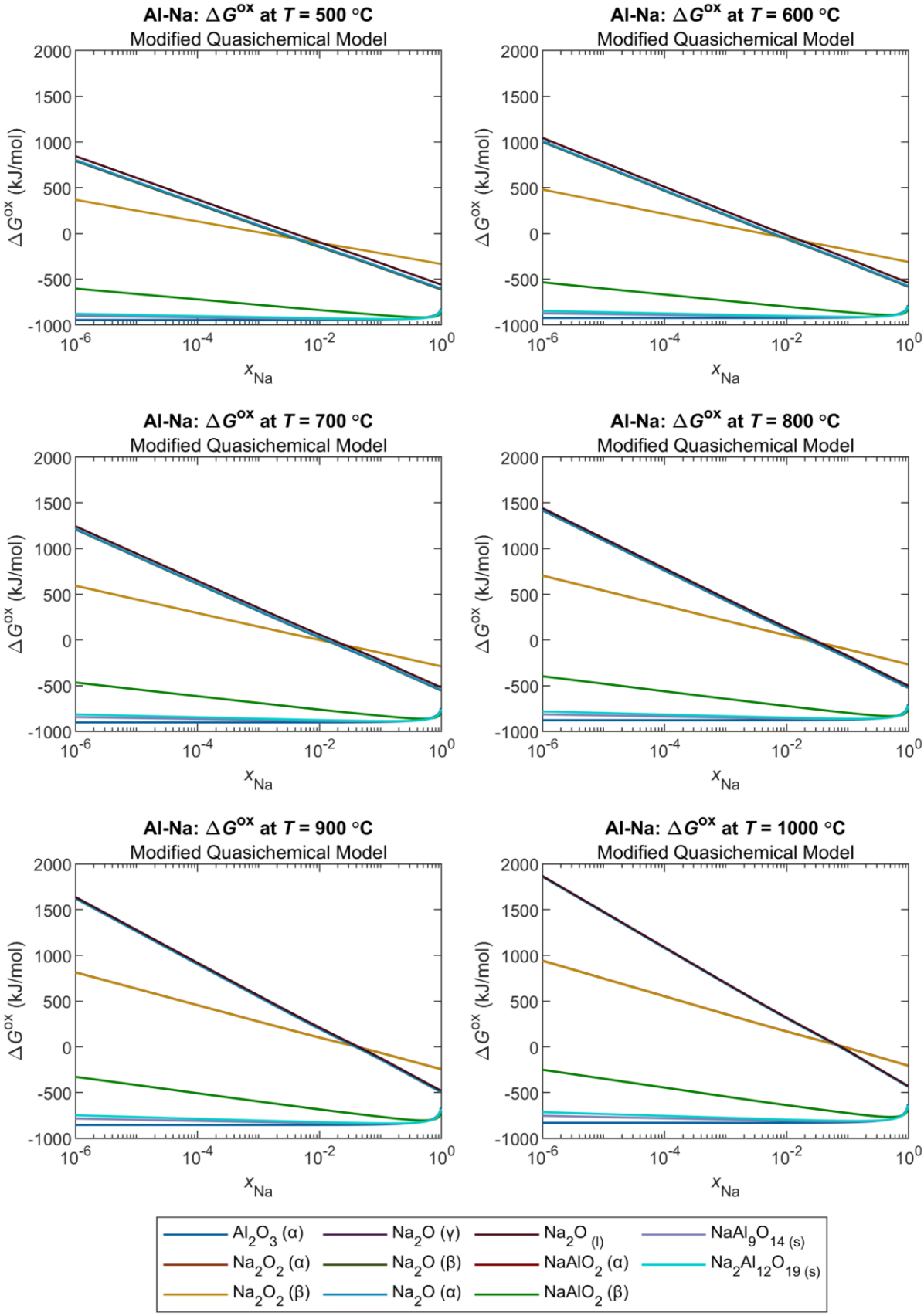
B.4.3.5. Al-Li


Al-Li: ΔG^ox at T = 500 °C
Modified Quasichemical Model
Al-Li: ΔG^ox at T = 600 °C
Modified Quasichemical Model
Al-Li: ΔG^ox at T = 700 °C
Modified Quasichemical Model
Al-Li: ΔG^ox at T = 800 °C
Modified Quasichemical Model
Al-Li: ΔG^ox at T = 900 °C
Modified Quasichemical Model
Al-Li: ΔG^ox at T = 1000 °C
Modified Quasichemical Model
ΔG^ox (kJ/mol)
x_Li
Al2O3 (α)
Li5AlO4 (s)
AlLiO2 (γ)
LiAl7O11 (s)
Li2O (s)
AlLiO2 (α)
LiAl5O8 (s)
LiAl11O17 (s)

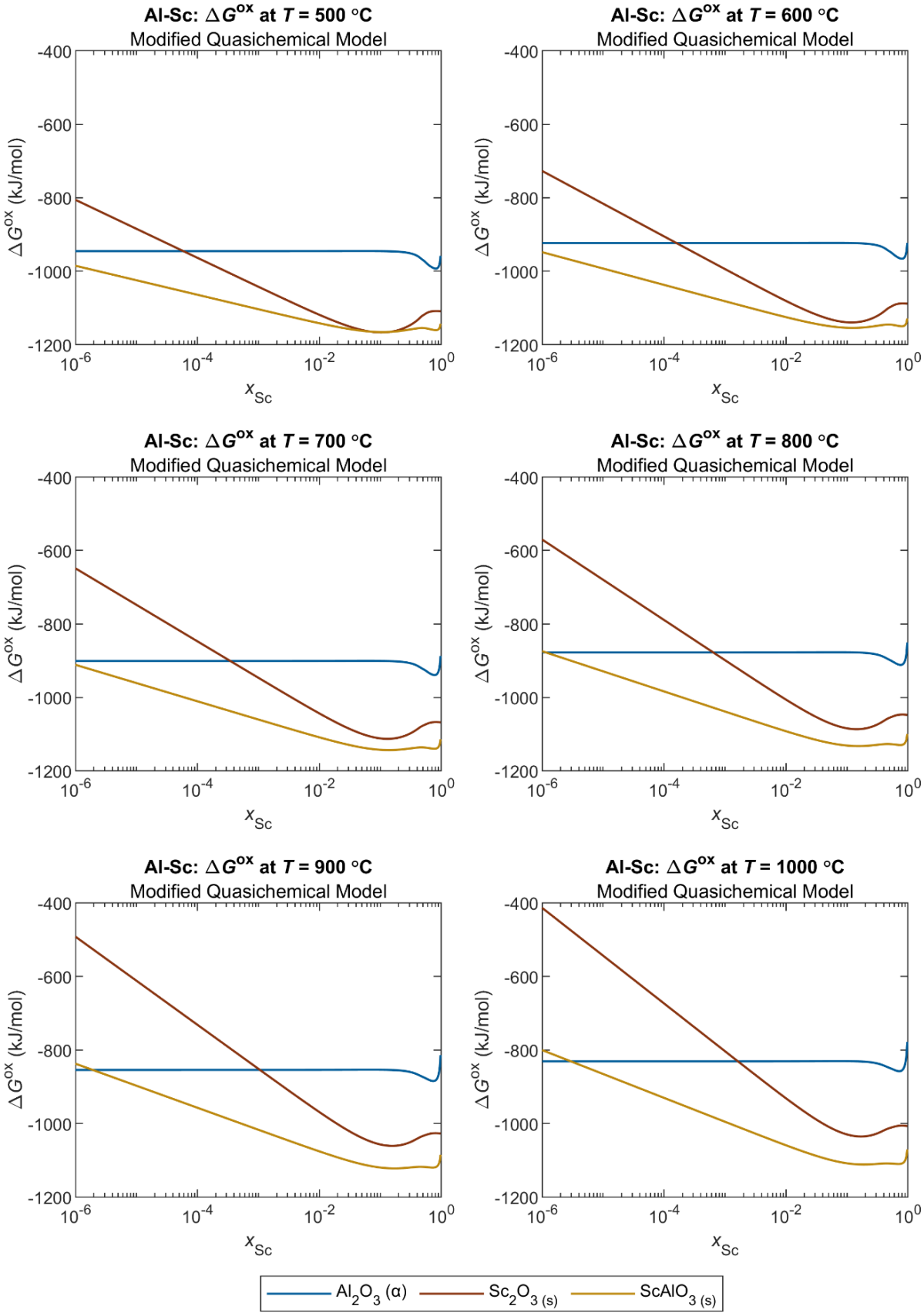
B.4.3.6. Al-Mg


Al-Mg: ΔG^ox at T = 500 °C
Modified Quasichemical Model
Al-Mg: ΔG^ox at T = 600 °C
Modified Quasichemical Model
Al-Mg: ΔG^ox at T = 700 °C
Modified Quasichemical Model
Al-Mg: ΔG^ox at T = 800 °C
Modified Quasichemical Model
Al-Mg: ΔG^ox at T = 900 °C
Modified Quasichemical Model
Al-Mg: ΔG^ox at T = 1000 °C
Modified Quasichemical Model
ΔG^ox (kJ/mol)
200
0
-200
-400
-600
-800
-1000
-1200
10^-6
10^-4
10^-2
10^0
x_Mg
Al2O3 (α)
MgO (s)
MgAl2O4 (s)

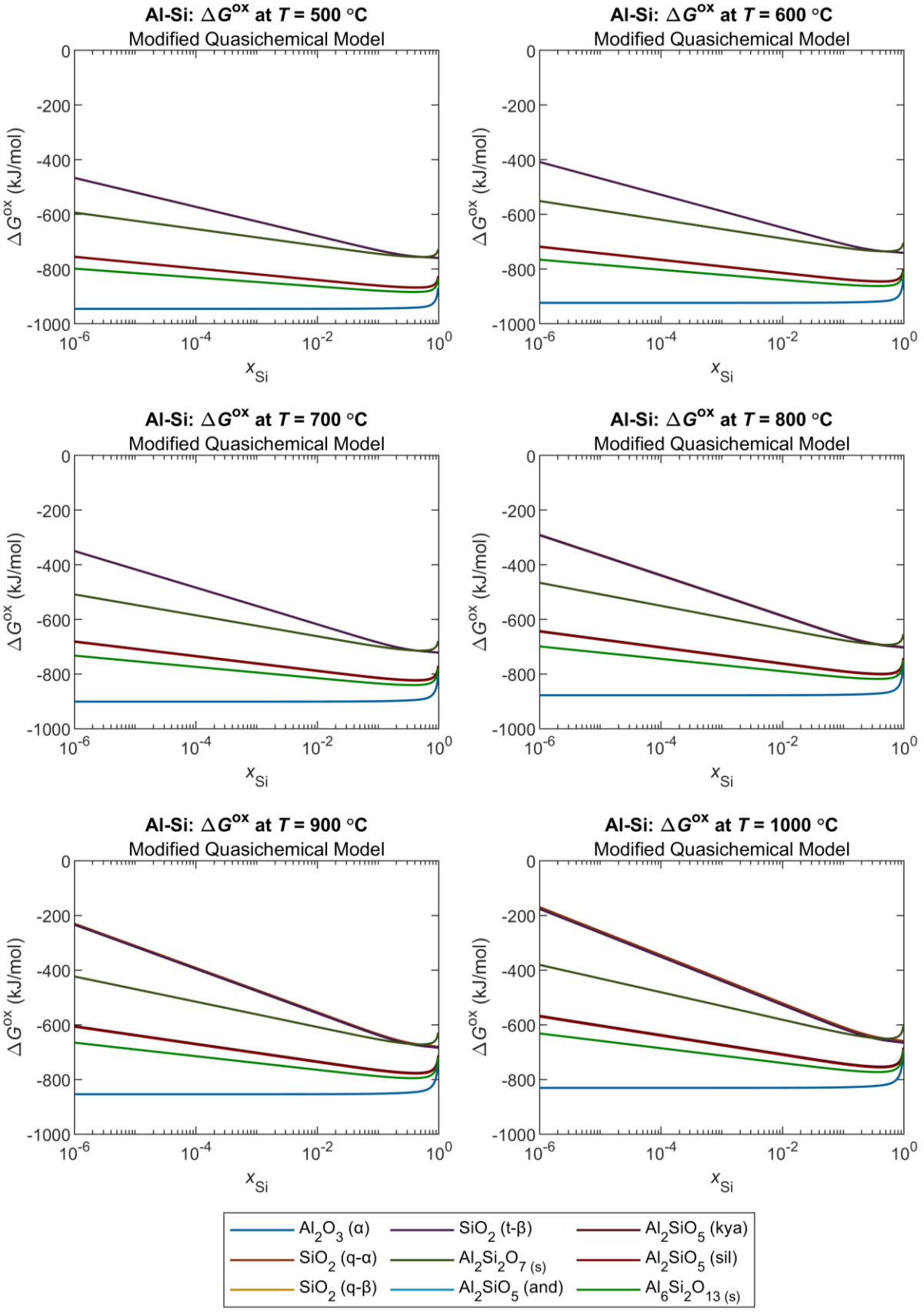
B.4.3.7. Al-Na


Al-Na: ΔG^ox at T = 500 °C
Modified Quasichemical Model
Al-Na: ΔG^ox at T = 600 °C
Modified Quasichemical Model
Al-Na: ΔG^ox at T = 700 °C
Modified Quasichemical Model
Al-Na: ΔG^ox at T = 800 °C
Modified Quasichemical Model
Al-Na: ΔG^ox at T = 900 °C
Modified Quasichemical Model
Al-Na: ΔG^ox at T = 1000 °C
Modified Quasichemical Model
ΔG^ox (kJ/mol)
x_Na
Al2O3 (α)
Na2O2 (α)
Na2O2 (β)
Na2O (γ)
Na2O (β)
Na2O (α)
Na2O (l)
NaAlO2 (α)
NaAlO2 (β)
NaAl9O14 (s)
Na2Al12O19 (s)

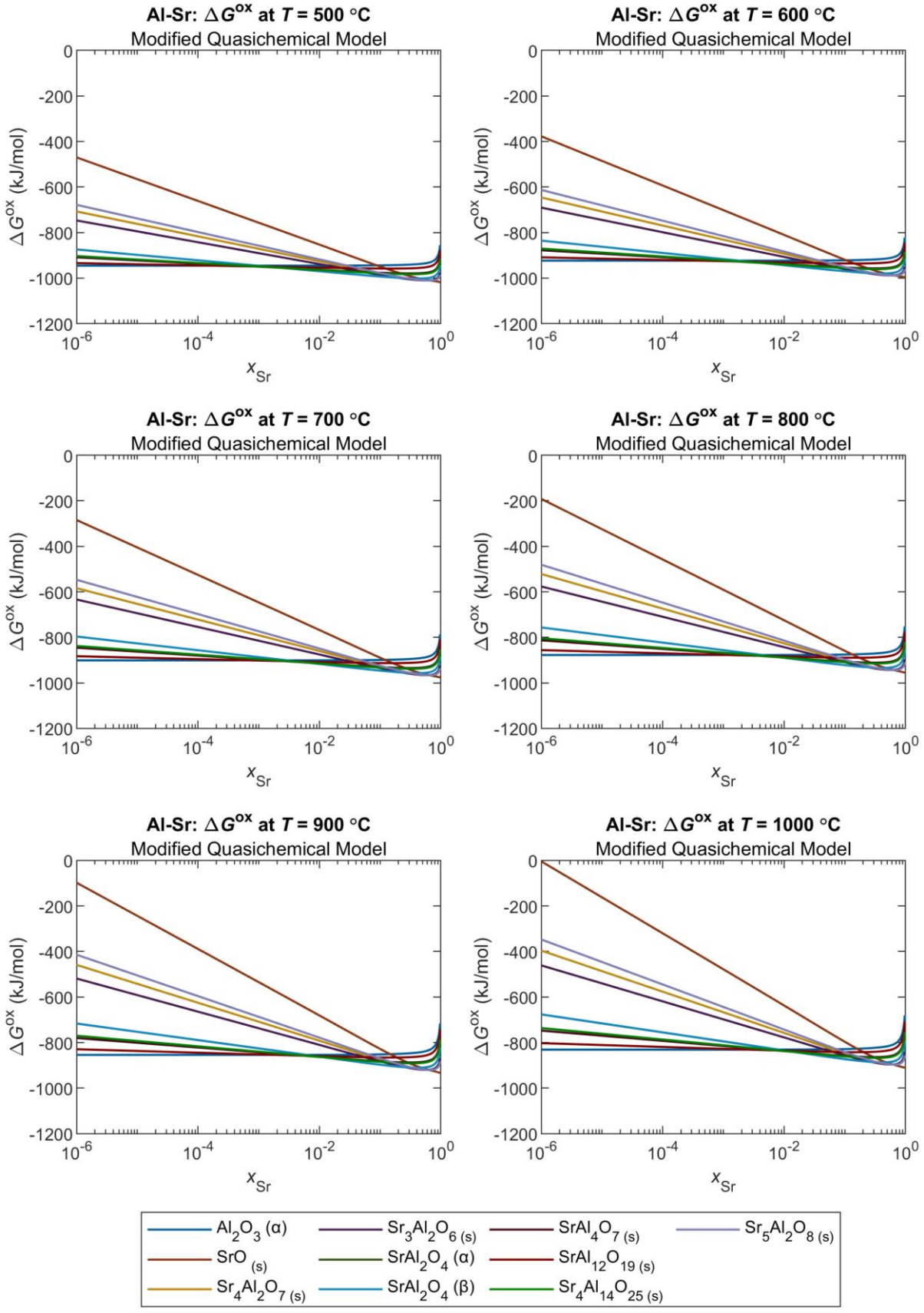
B.4.3.8. Al-Sc


Al-Sc: ΔG^ox at T = 500 °C
Modified Quasichemical Model
Al-Sc: ΔG^ox at T = 600 °C
Modified Quasichemical Model
Al-Sc: ΔG^ox at T = 700 °C
Modified Quasichemical Model
Al-Sc: ΔG^ox at T = 800 °C
Modified Quasichemical Model
Al-Sc: ΔG^ox at T = 900 °C
Modified Quasichemical Model
Al-Sc: ΔG^ox at T = 1000 °C
Modified Quasichemical Model
ΔG^ox (kJ/mol)
-400
-600
-800
-1000
-1200
10^-6
10^-4
10^-2
10^0
x_Sc
Al2O3 (α)
Sc2O3 (s)
ScAlO3 (s)

B.4.3.9. Al-Si


Al-Si: ΔG^ox at T = 500 °C
Modified Quasichemical Model
Al-Si: ΔG^ox at T = 600 °C
Modified Quasichemical Model
Al-Si: ΔG^ox at T = 700 °C
Modified Quasichemical Model
Al-Si: ΔG^ox at T = 800 °C
Modified Quasichemical Model
Al-Si: ΔG^ox at T = 900 °C
Modified Quasichemical Model
Al-Si: ΔG^ox at T = 1000 °C
Modified Quasichemical Model
ΔG^ox (kJ/mol)
x_Si
0
-200
-400
-600
-800
-1000
10^-6
10^-4
10^-2
10^0
Al2O3 (α)
SiO2 (t-β)
Al2SiO5 (kya)
SiO2 (q-α)
Al2Si2O7 (s)
Al2SiO5 (sil)
SiO2 (q-β)
Al2SiO5 (and)
Al6Si2O13 (s)

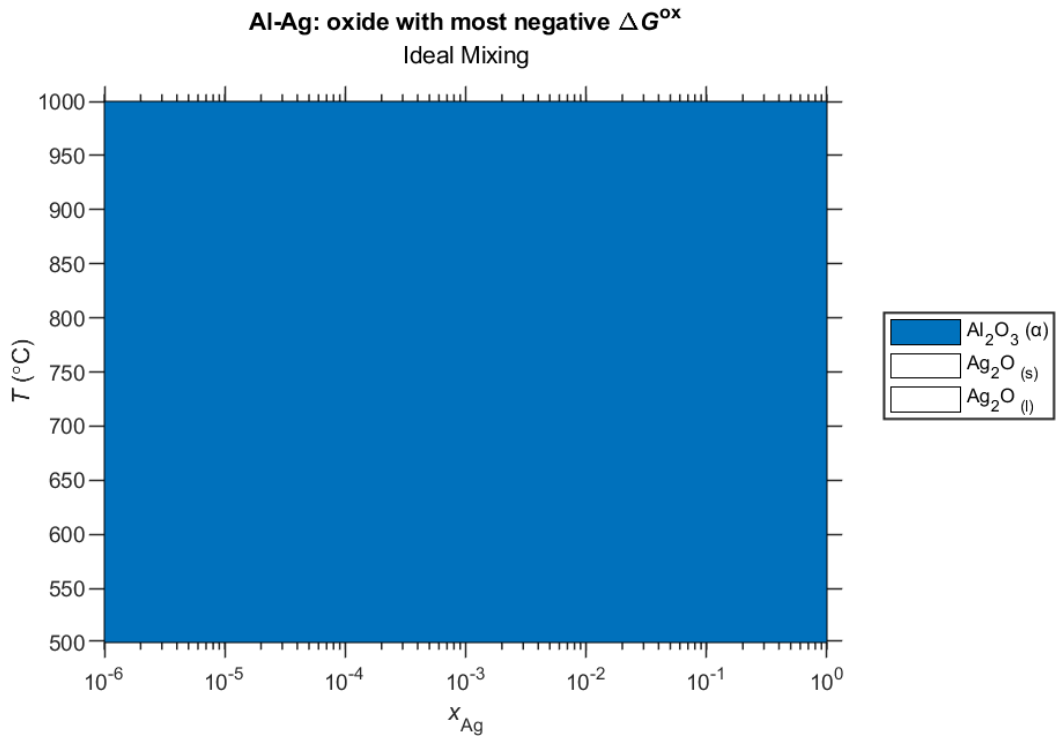
B.4.3.10. Al-Sr


Al-Sr: ΔG^ox at T = 500 °C
Modified Quasichemical Model
Al-Sr: ΔG^ox at T = 600 °C
Modified Quasichemical Model
Al-Sr: ΔG^ox at T = 700 °C
Modified Quasichemical Model
Al-Sr: ΔG^ox at T = 800 °C
Modified Quasichemical Model
Al-Sr: ΔG^ox at T = 900 °C
Modified Quasichemical Model
Al-Sr: ΔG^ox at T = 1000 °C
Modified Quasichemical Model
ΔG^ox (kJ/mol)
x_Sr
Al2O3 (α)
Sr3Al2O6 (s)
SrAl4O7 (s)
Sr5Al2O8 (s)
SrO (s)
SrAl2O4 (α)
SrAl12O19 (s)
Sr4Al2O7 (s)
SrAl2O4 (β)
Sr4Al14O25 (s)

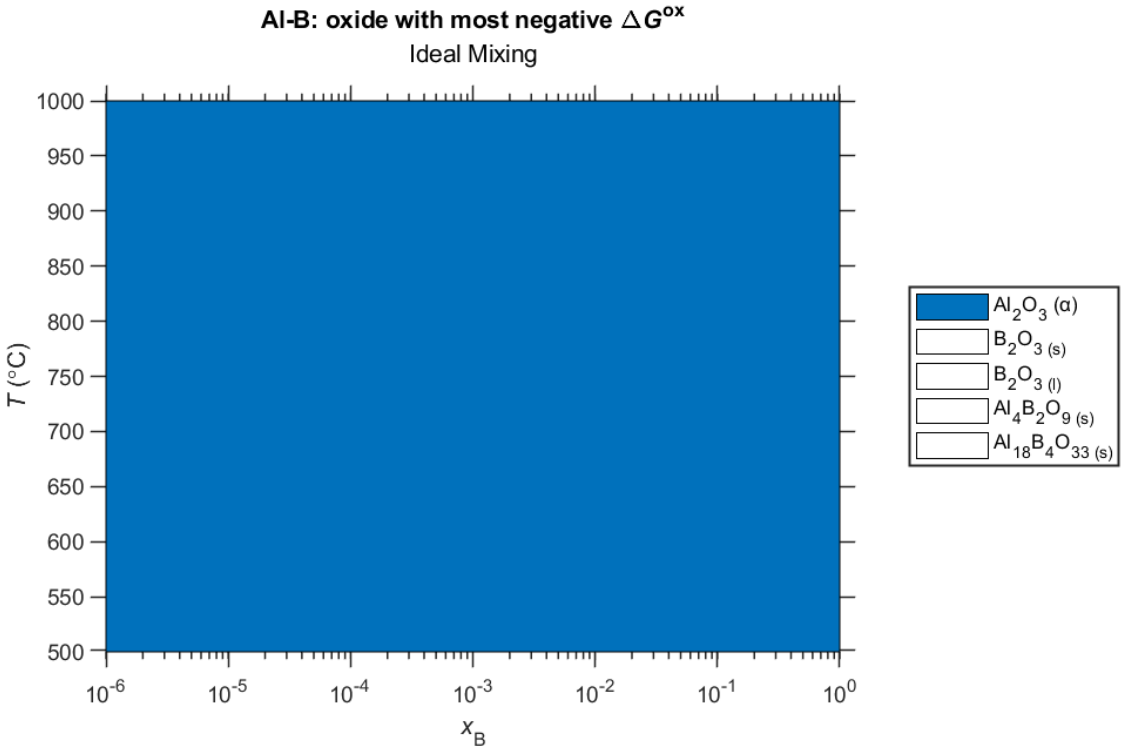
B.5. Oxide stability diagrams

B.5.1. Ideal Mixing

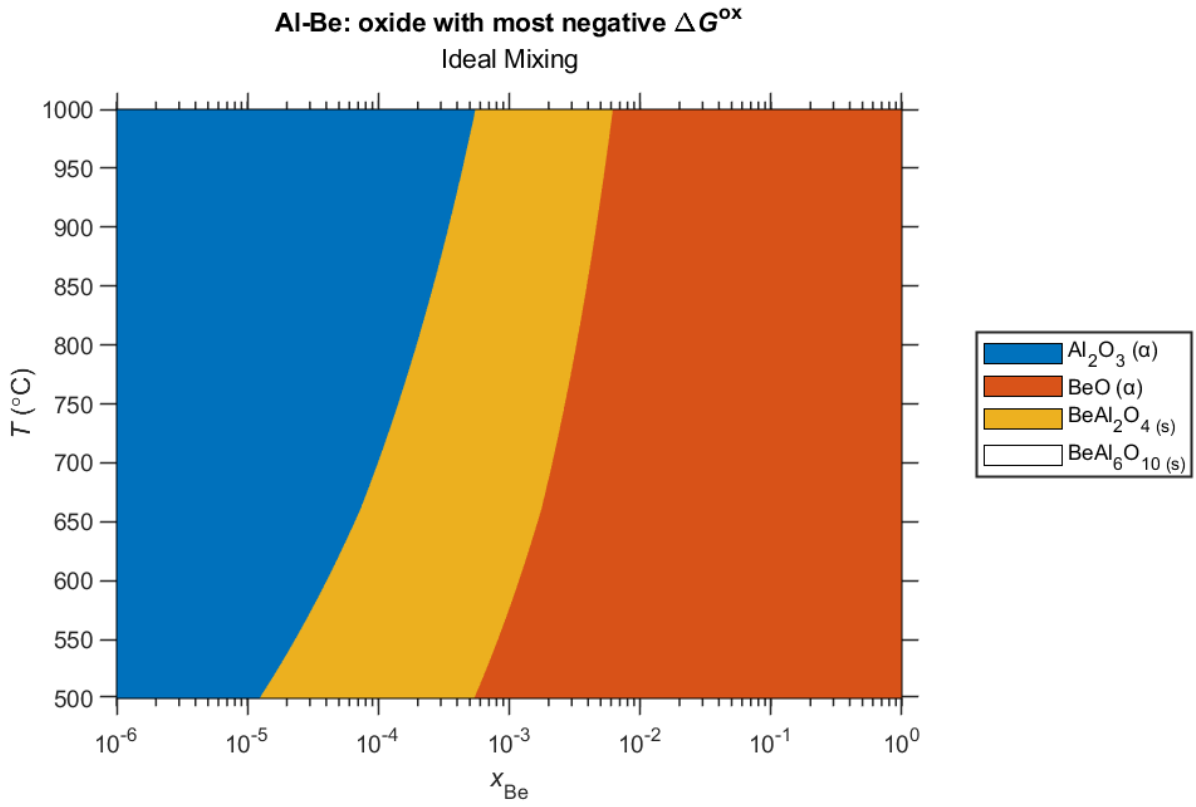
B.5.1.1. Al-Ag



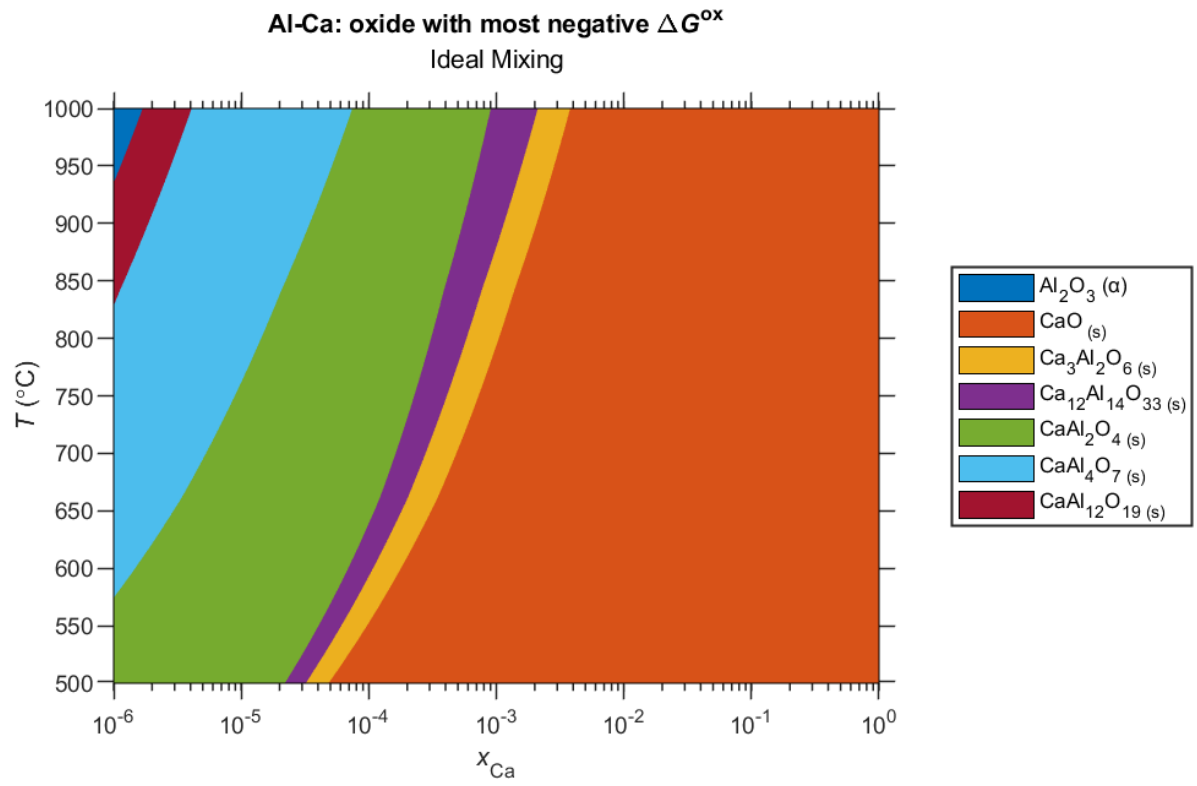
B.5.1.2. Al-B



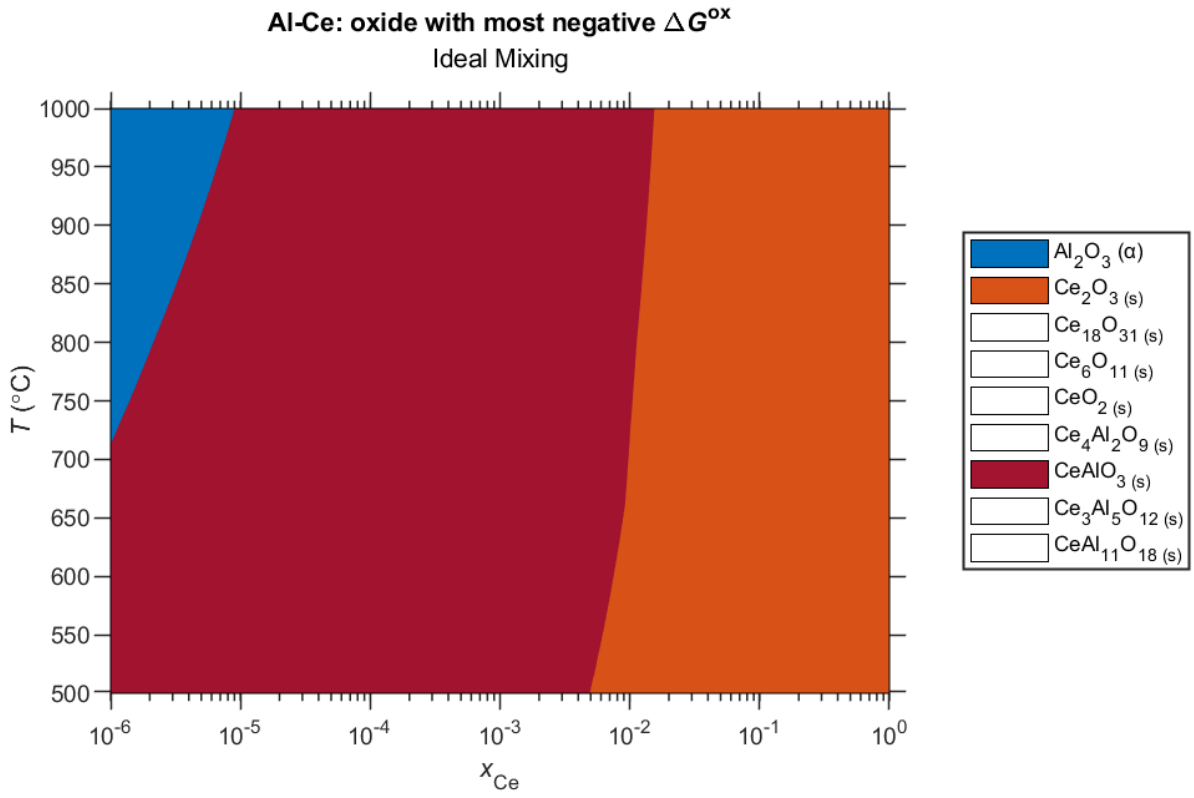
B.5.1.3. Al-Be



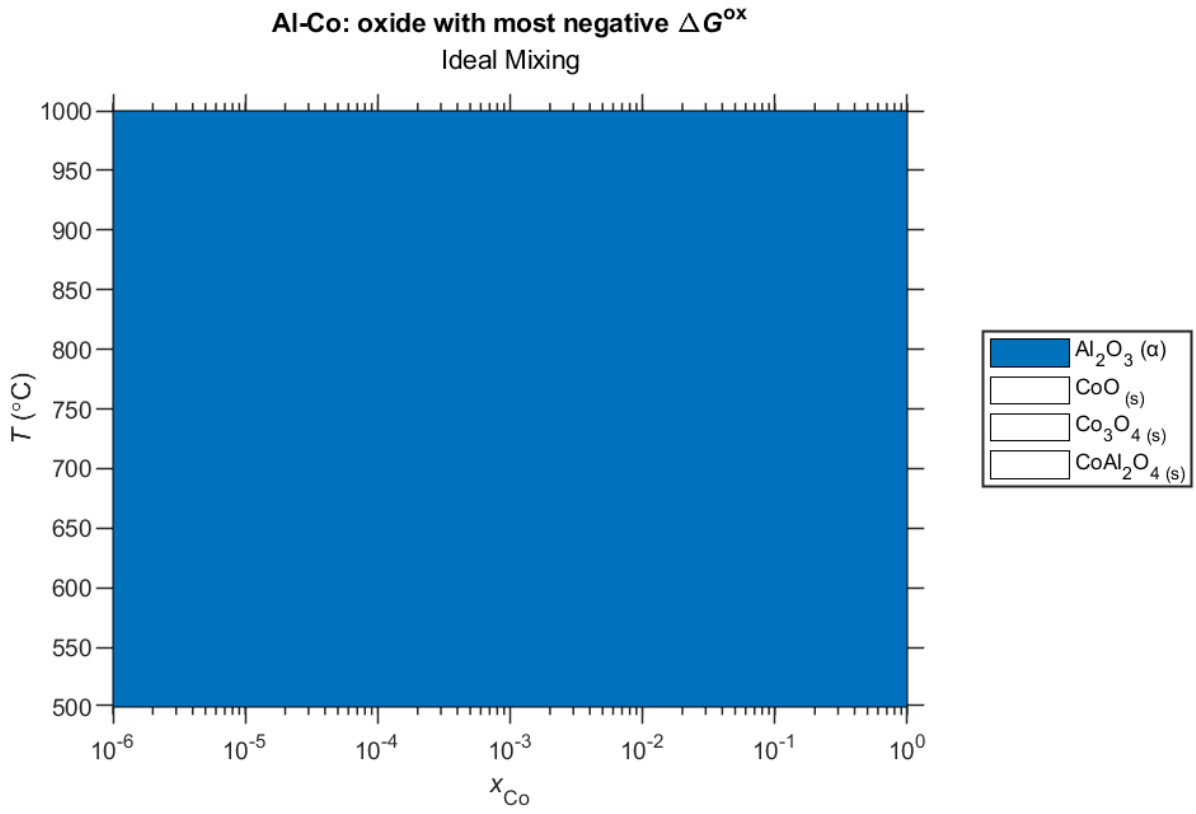
B.5.1.4. Al-Ca



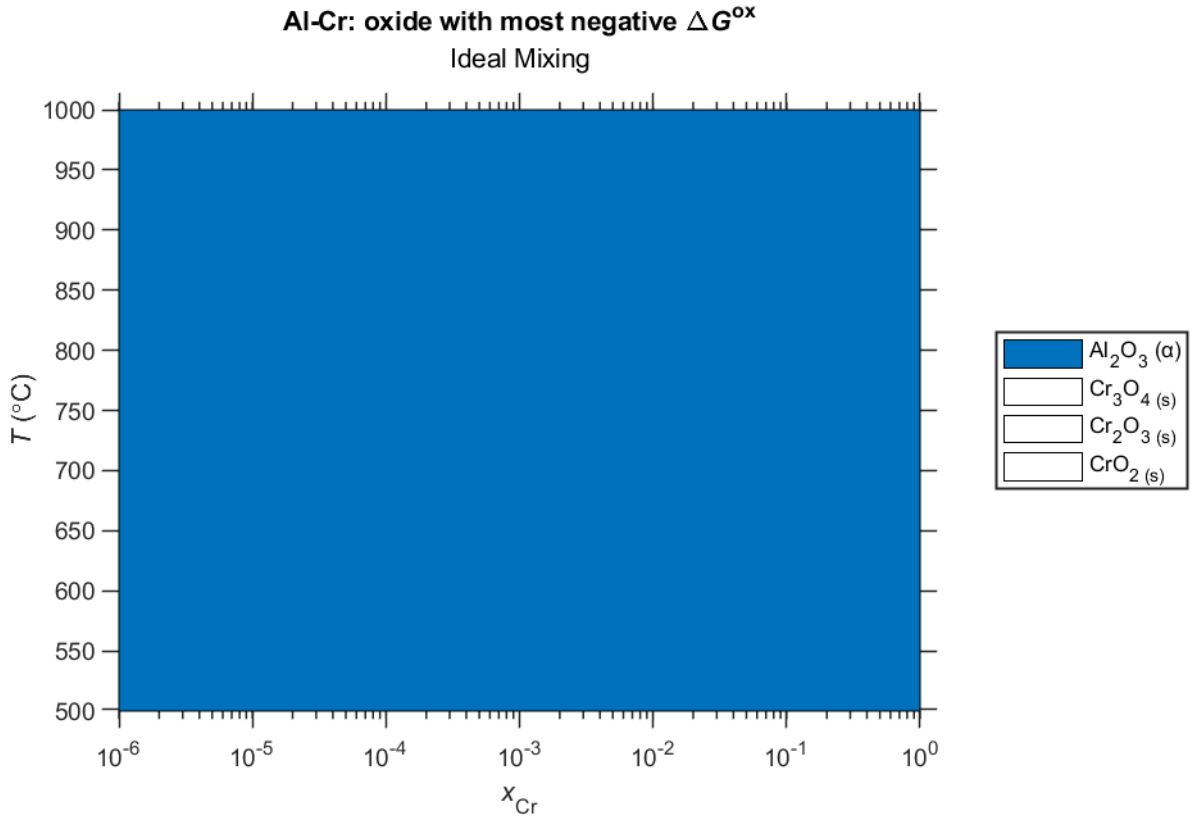
B.5.1.5. Al-Ce



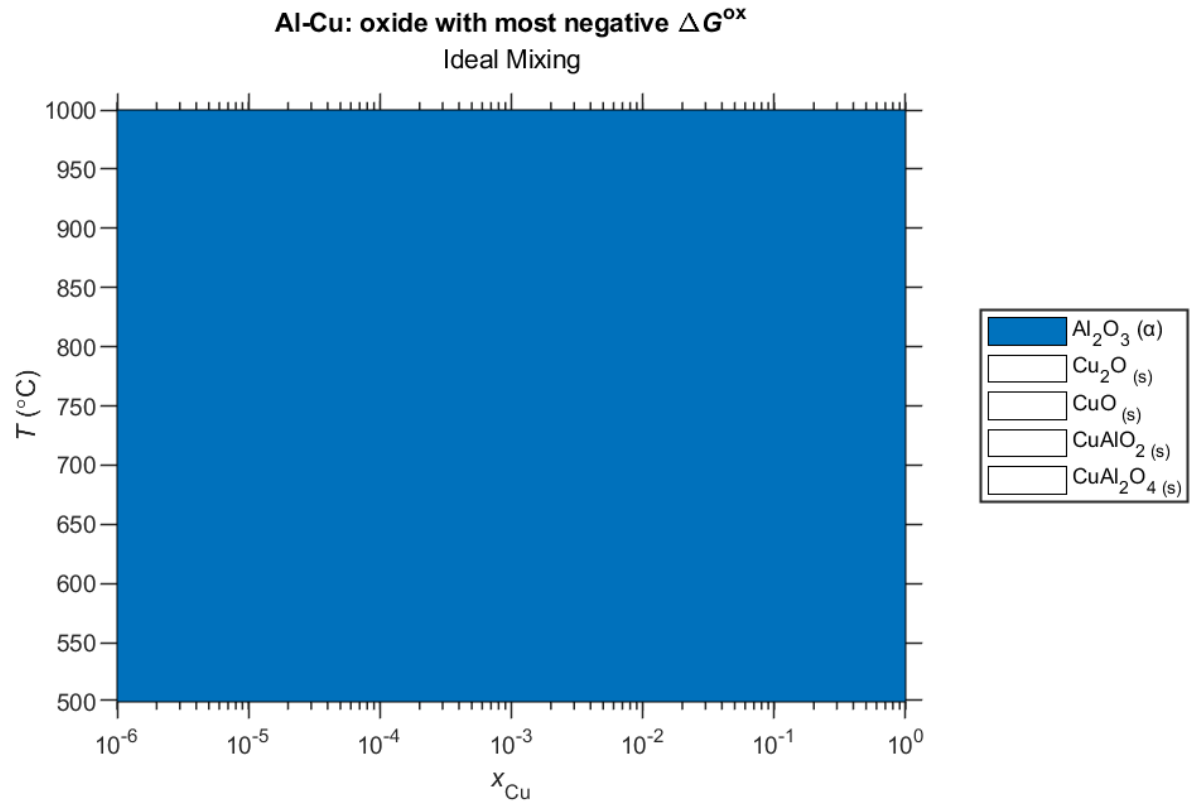
B.5.1.6. Al-Co



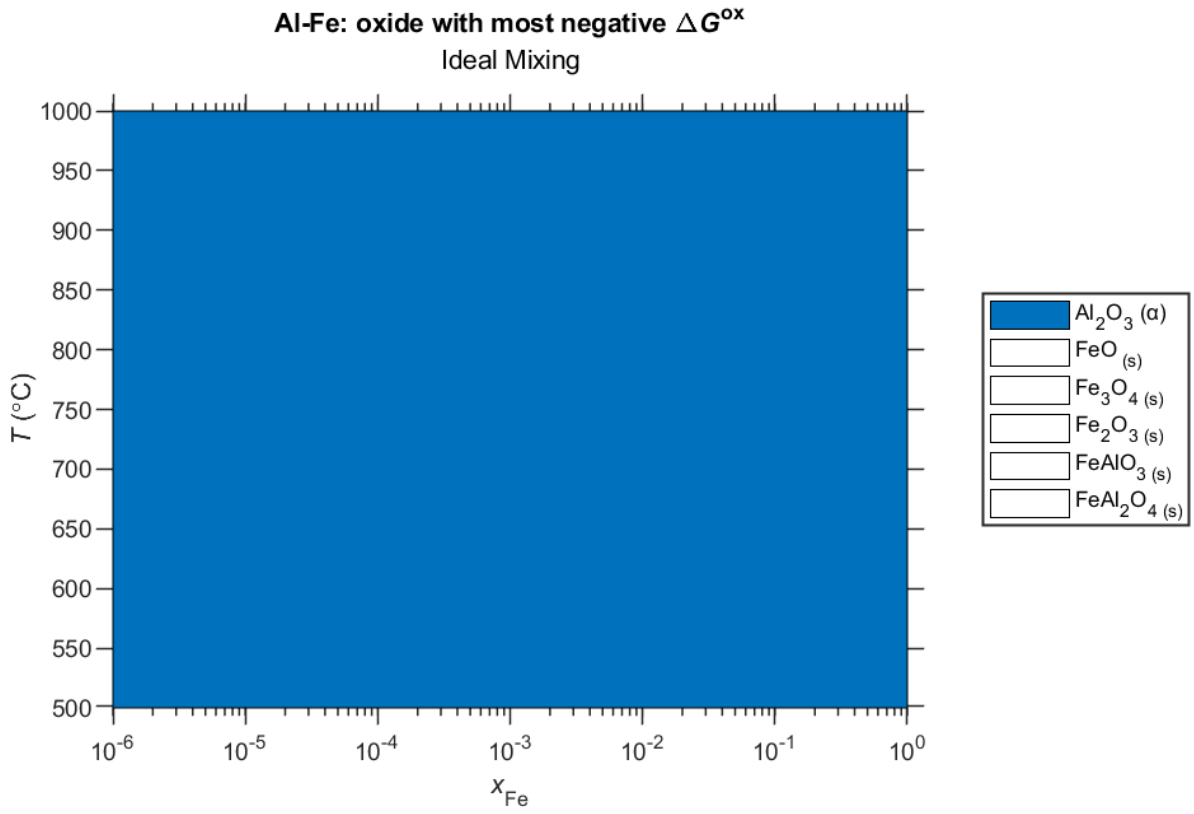
B.5.1.7. Al-Cr



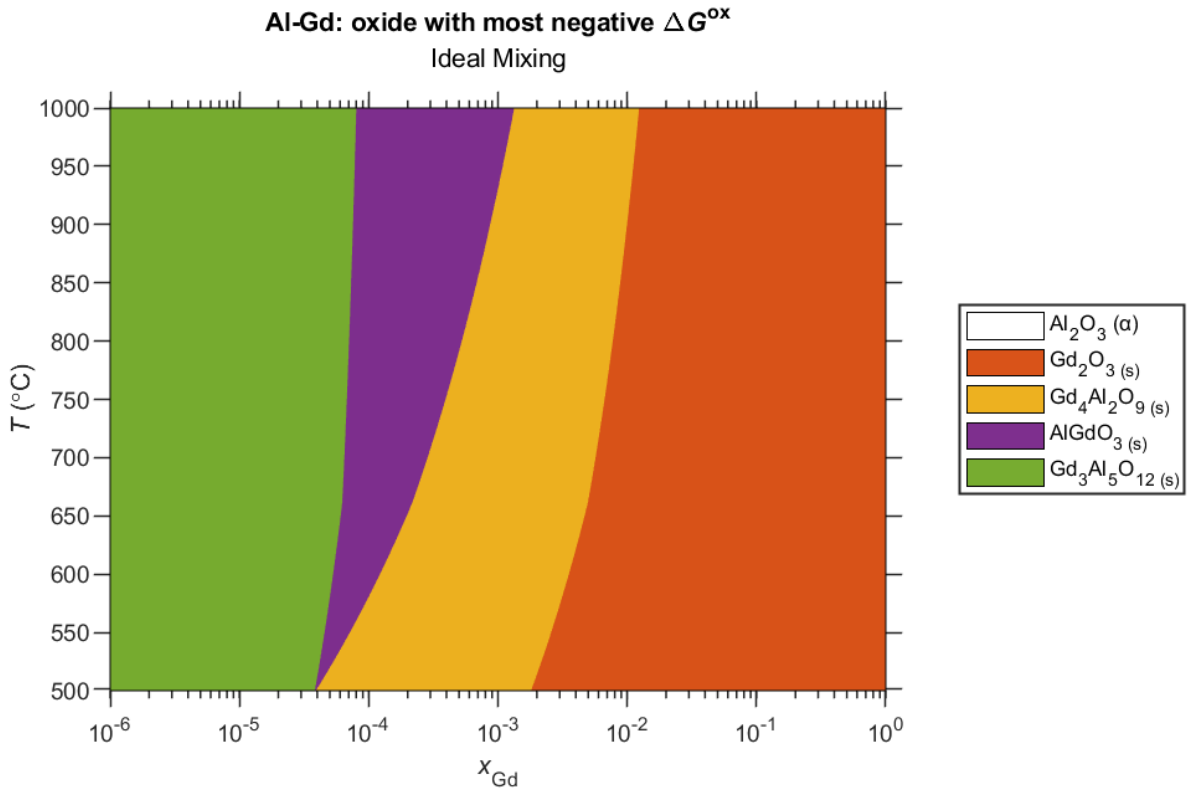
B.5.1.8. Al-Cu



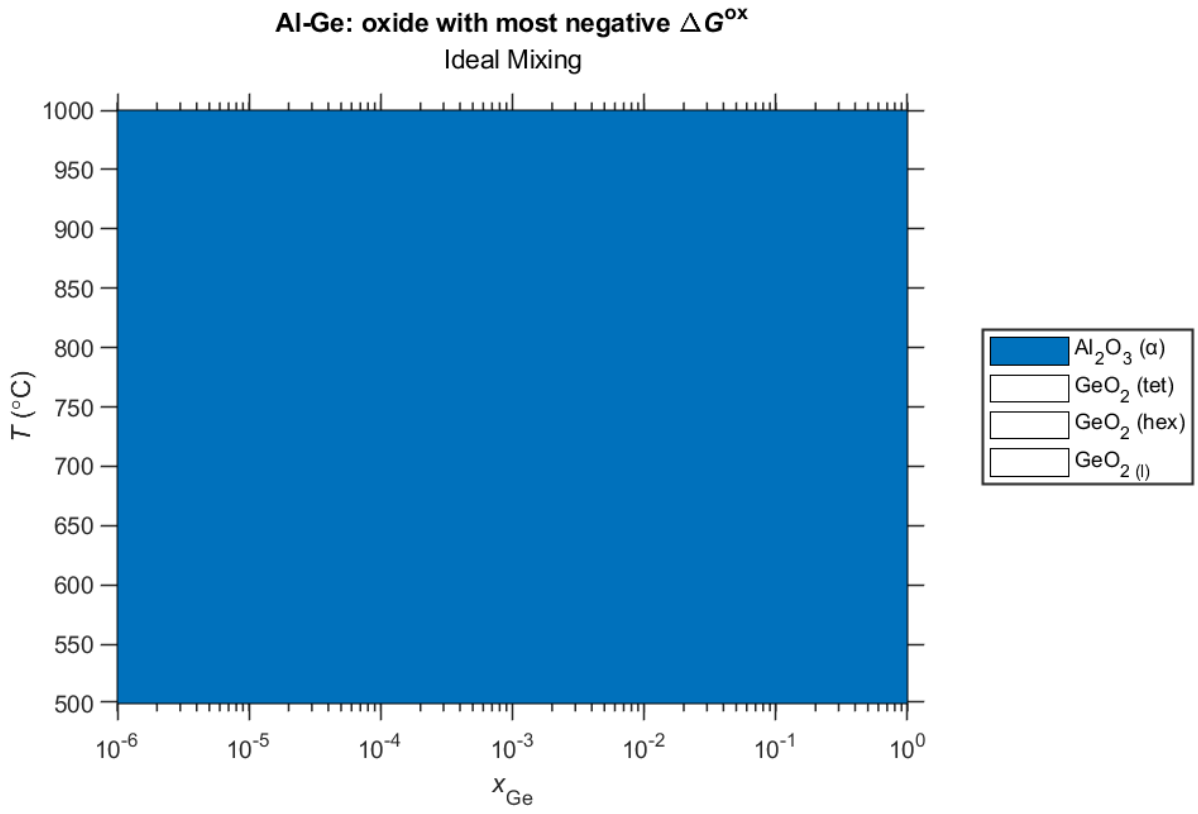
B.5.1.9. Al-Fe



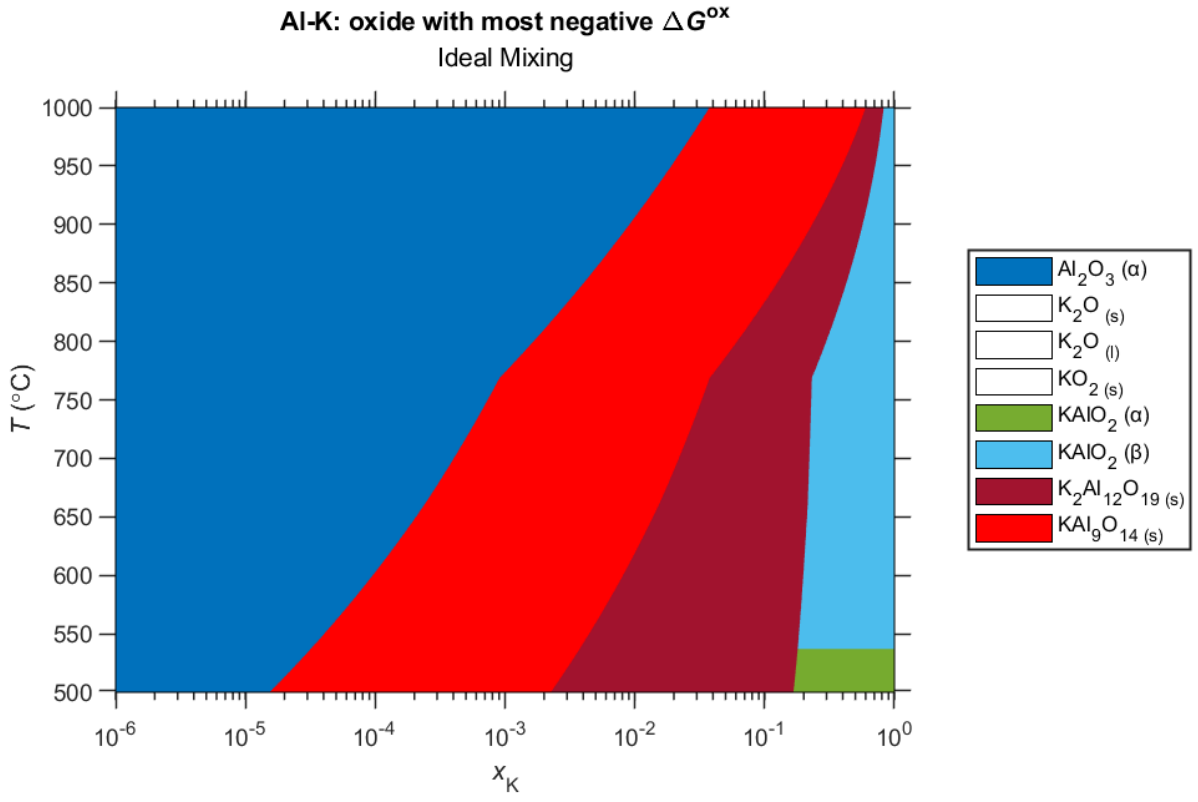
B.5.1.10. Al-Gd



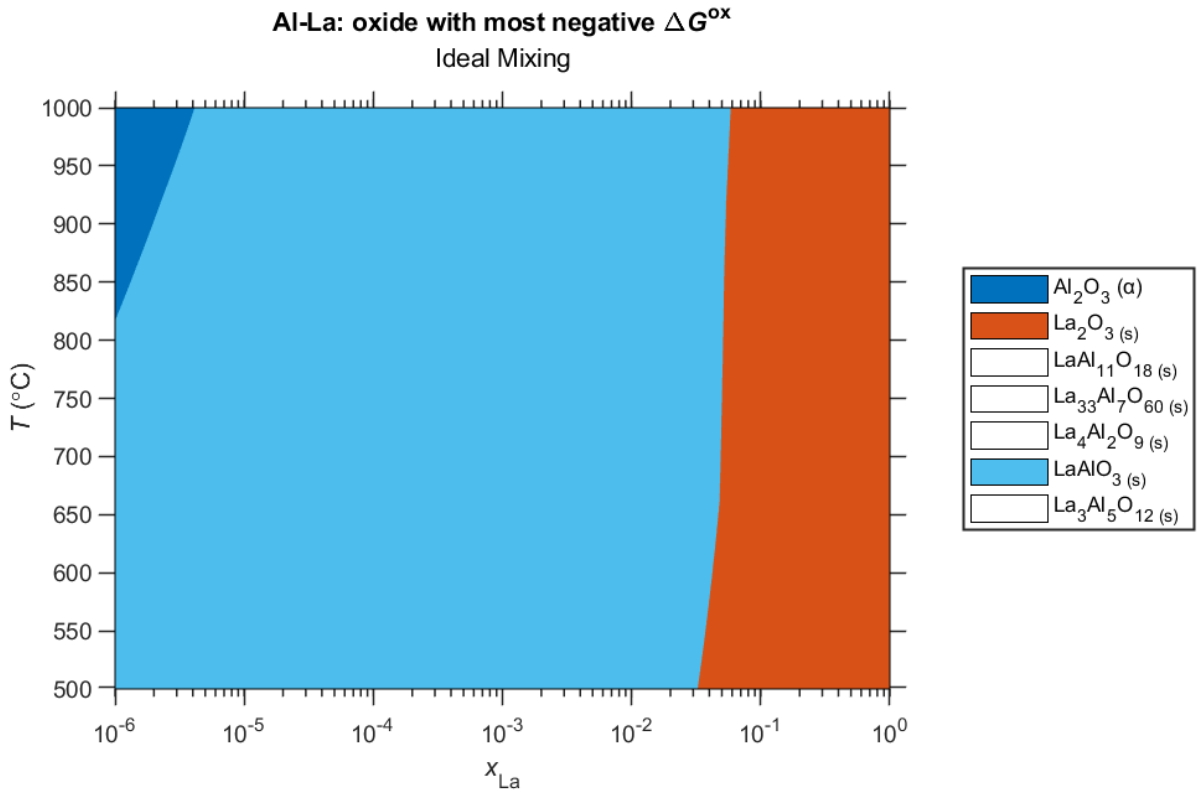
B.5.1.11. Al-Ge



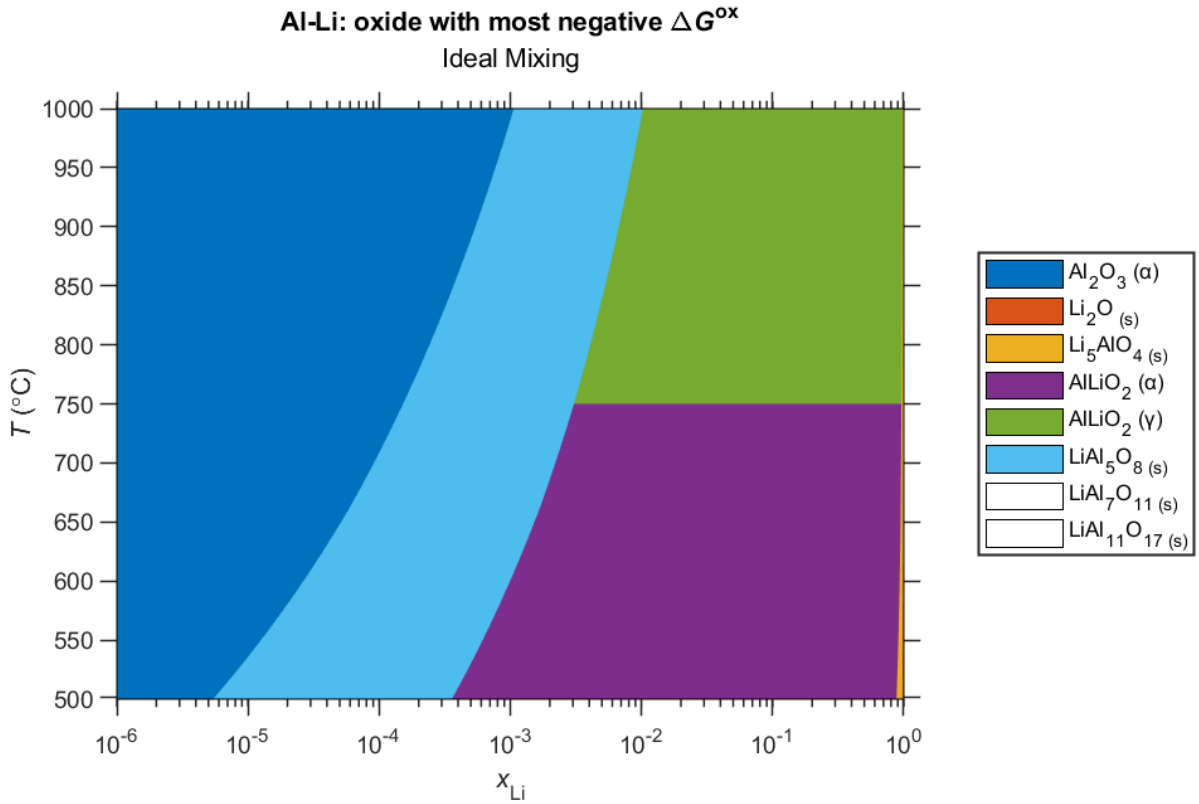
B.5.1.12. Al-K



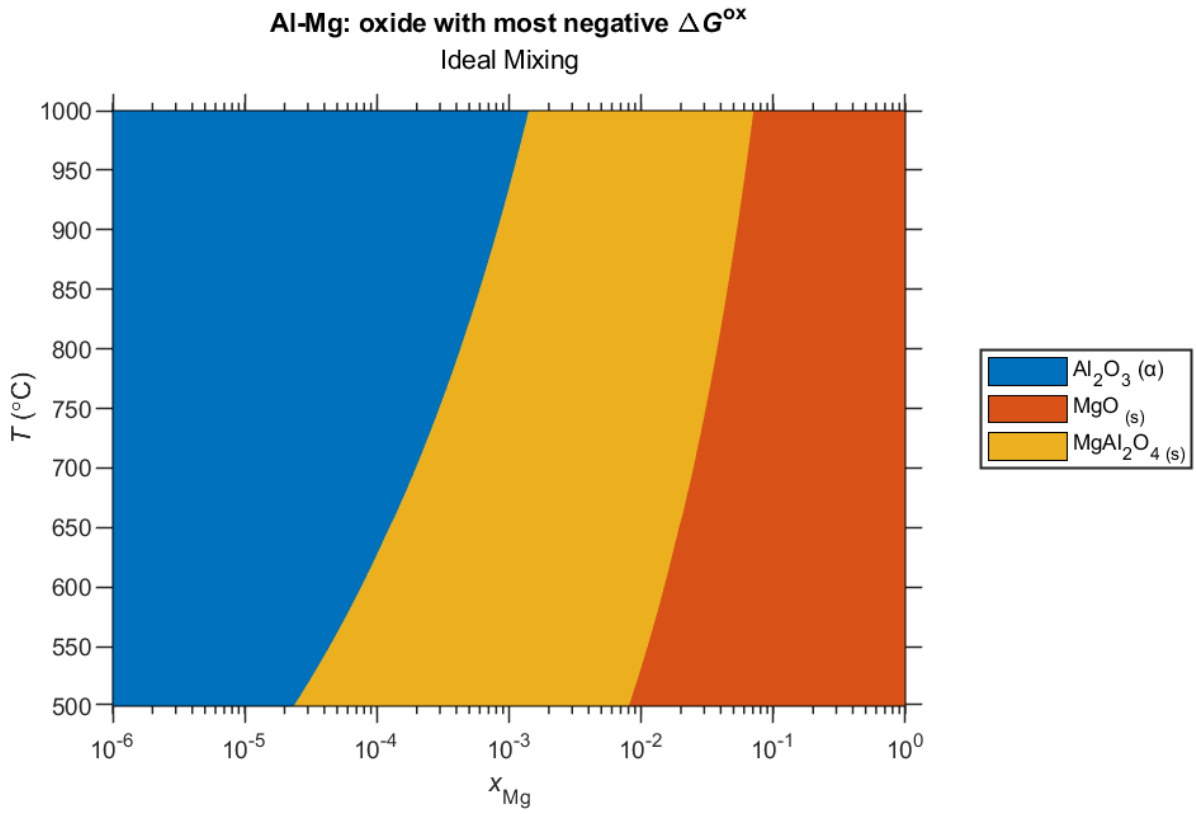
B.5.1.13. Al-La



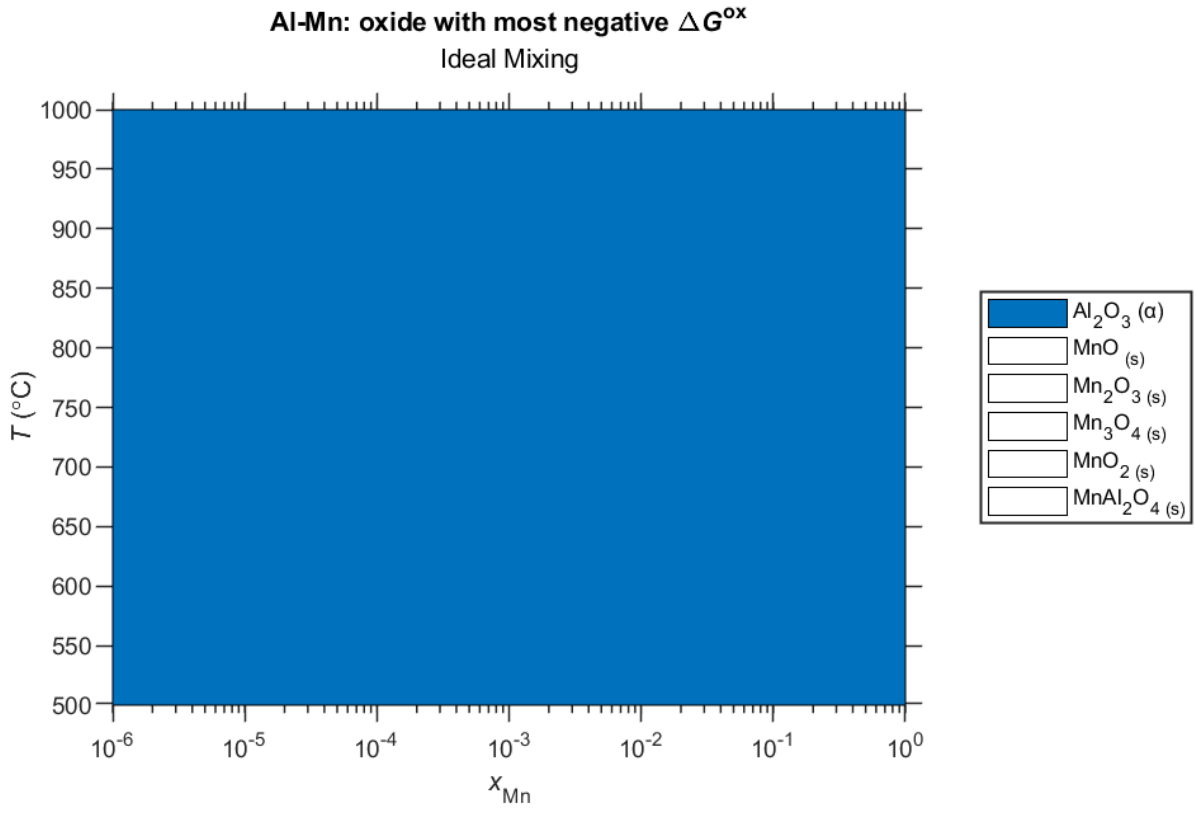
B.5.1.14. Al-Li



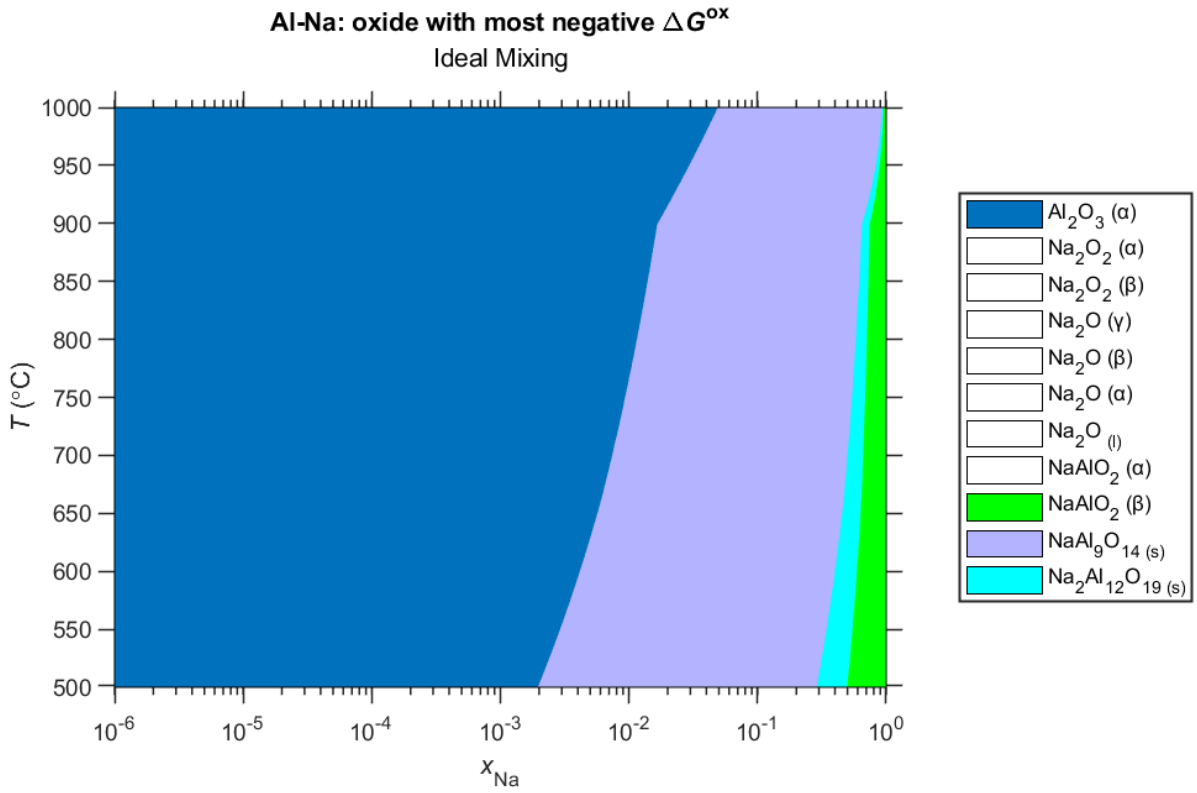
B.5.1.15. Al-Mg



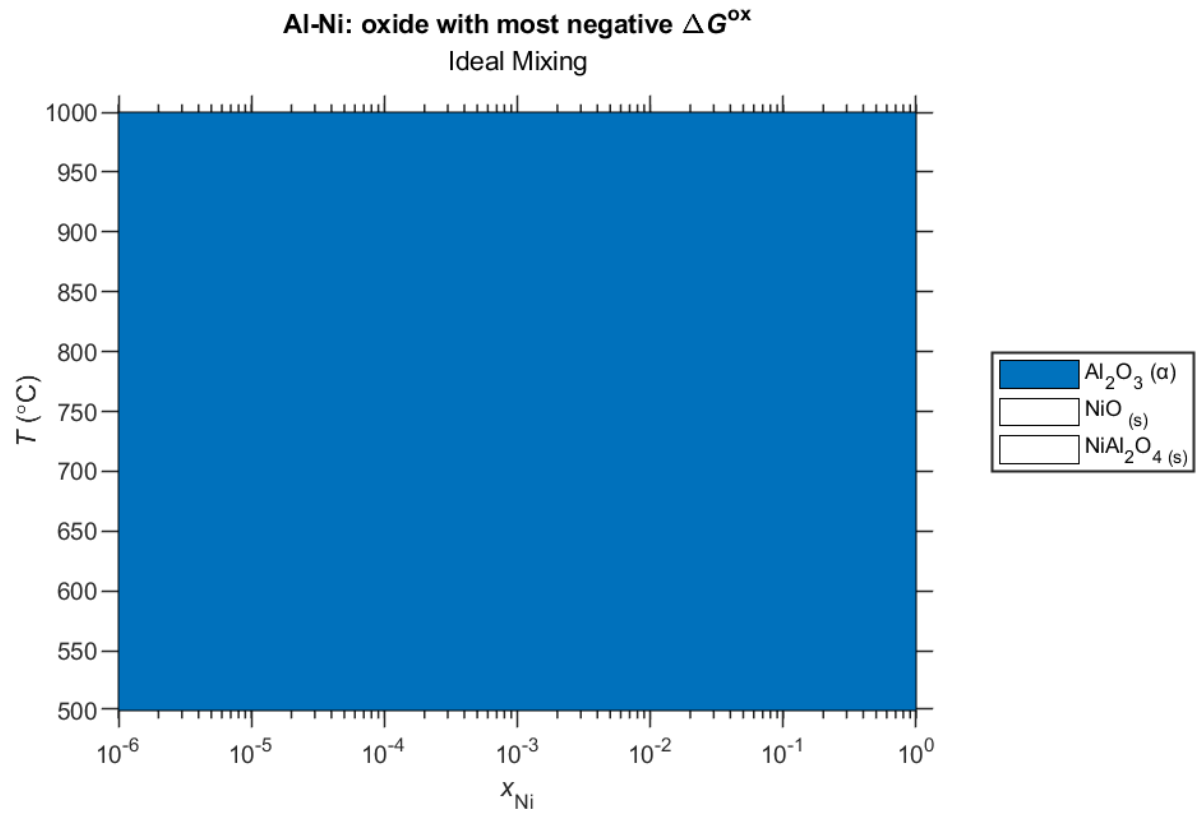
B.5.1.16. Al-Mn



B.5.1.17. Al-Na

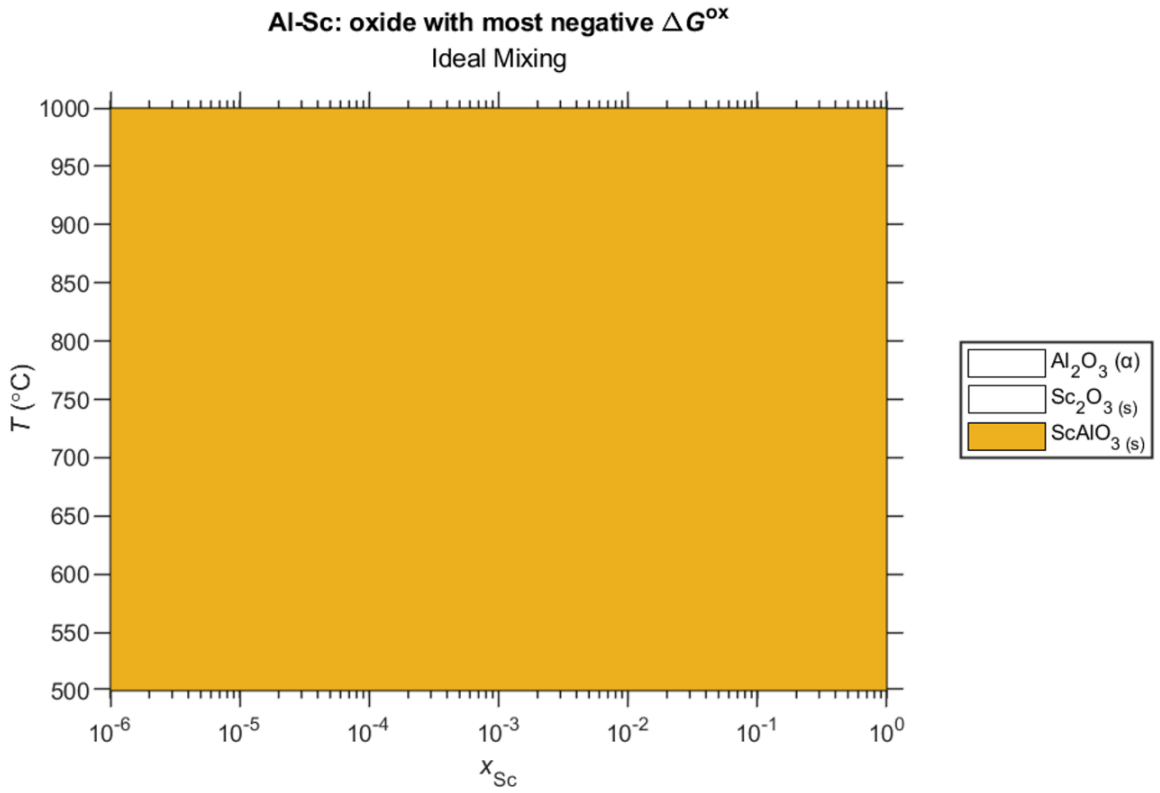


B.5.1.18. Al-Ni

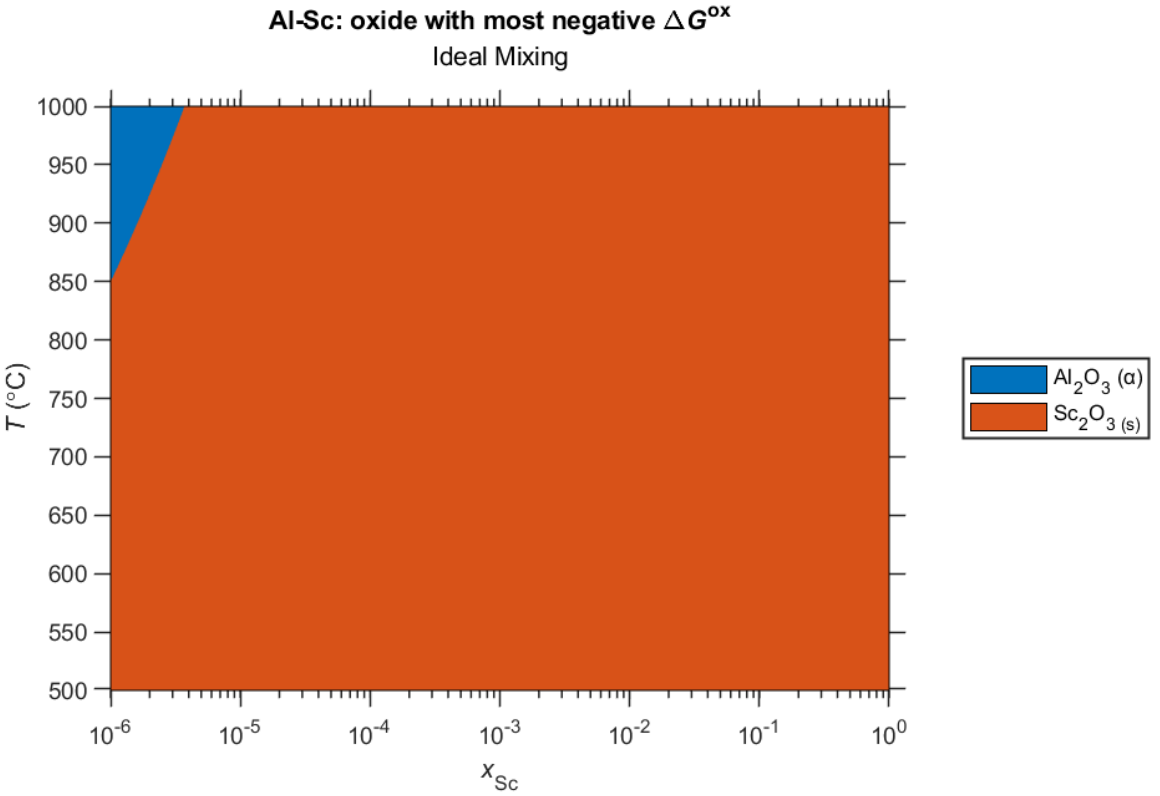


B.5.1.19. Al-Sc

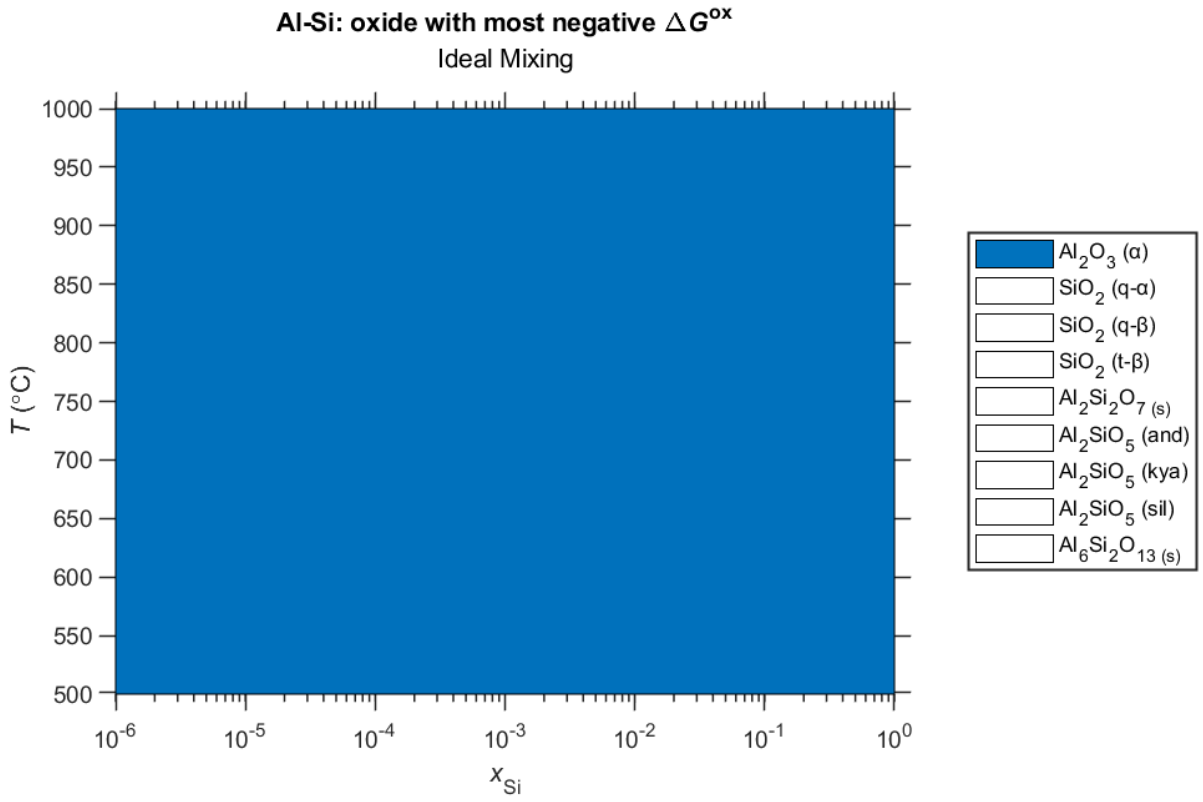
Including $ScAlO_3$



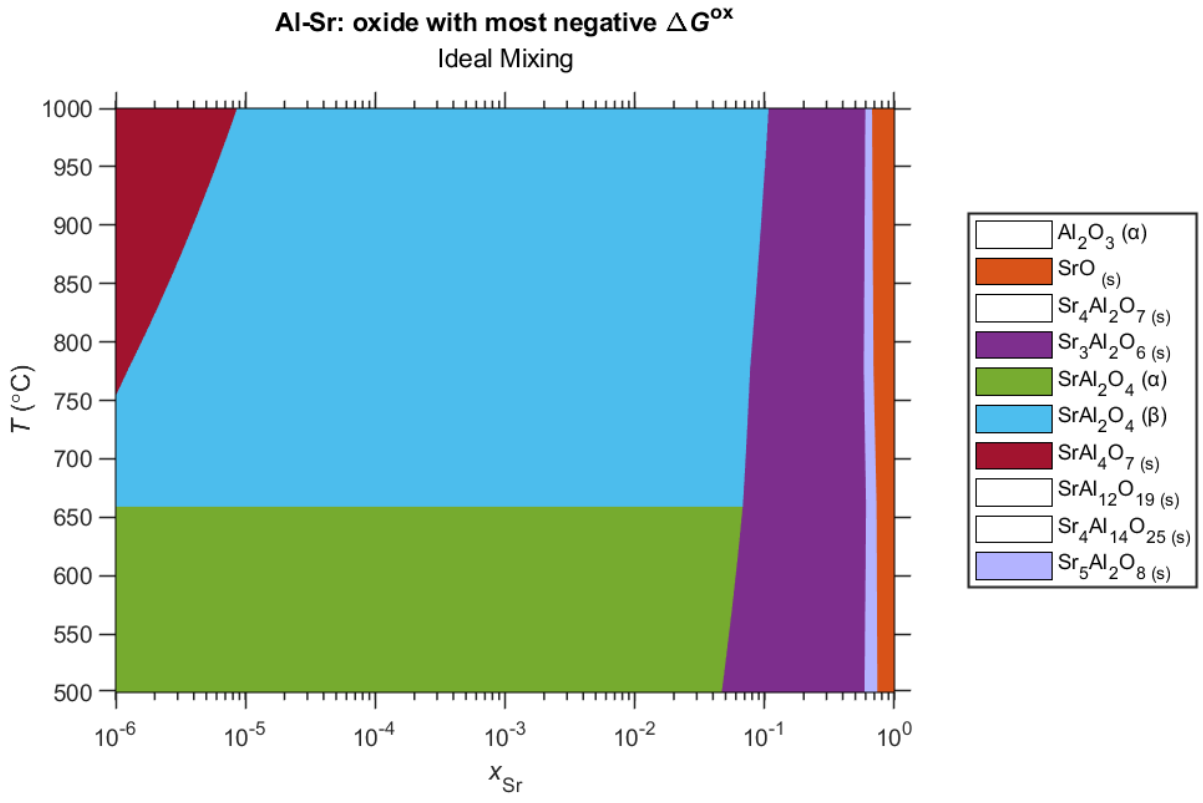
Without ScAlO3



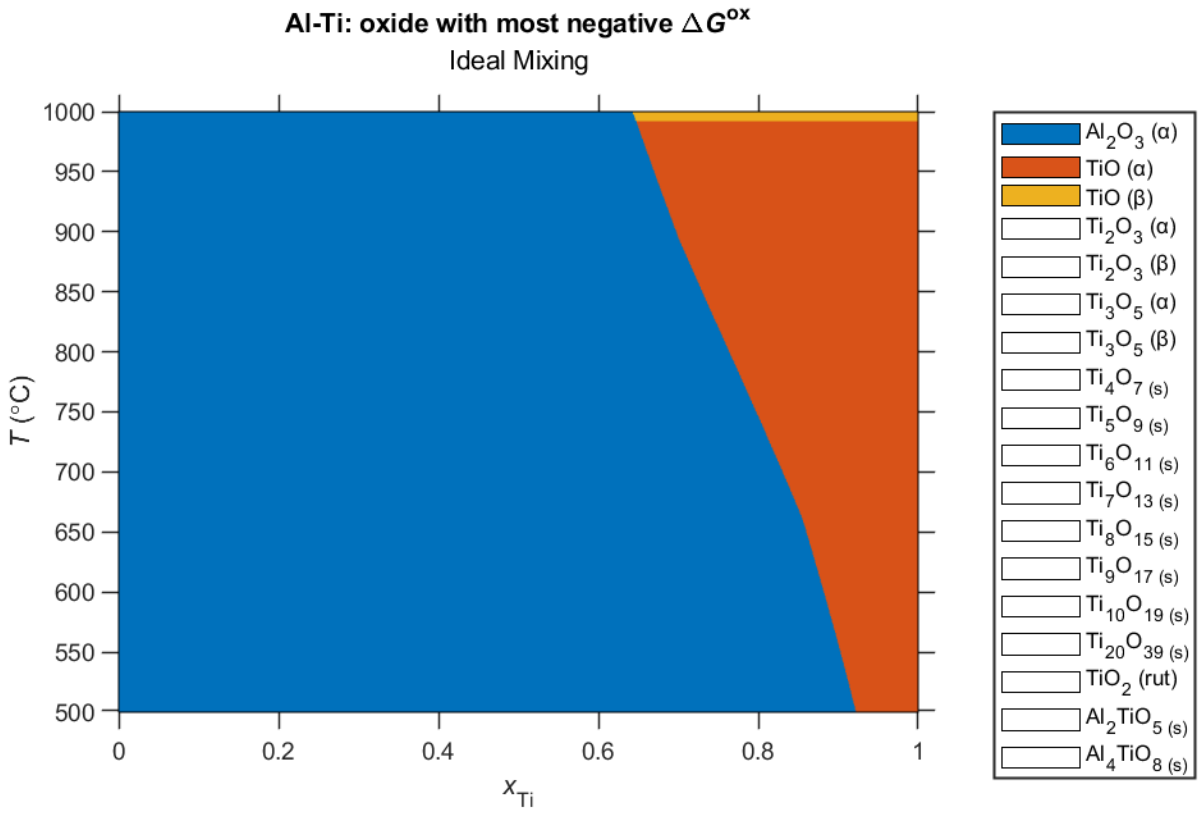
B.5.1.20. Al-Si



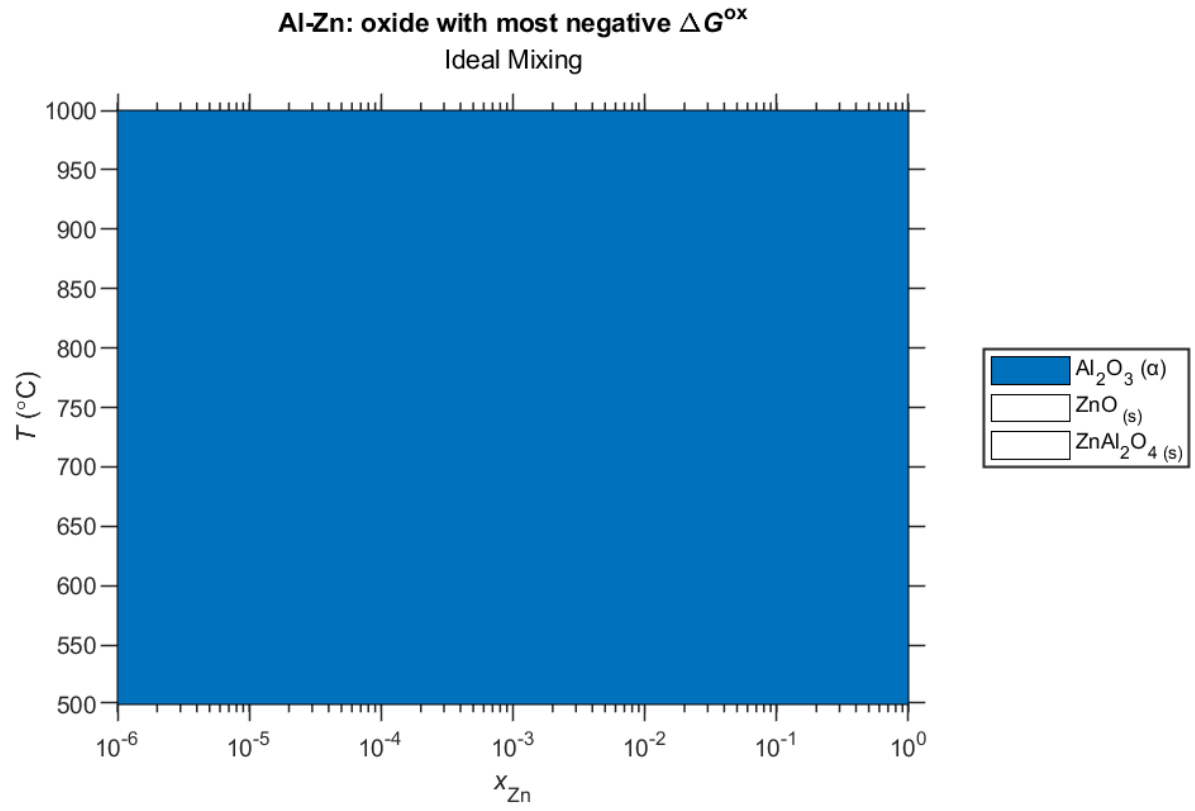
B.5.1.21. Al-Sr



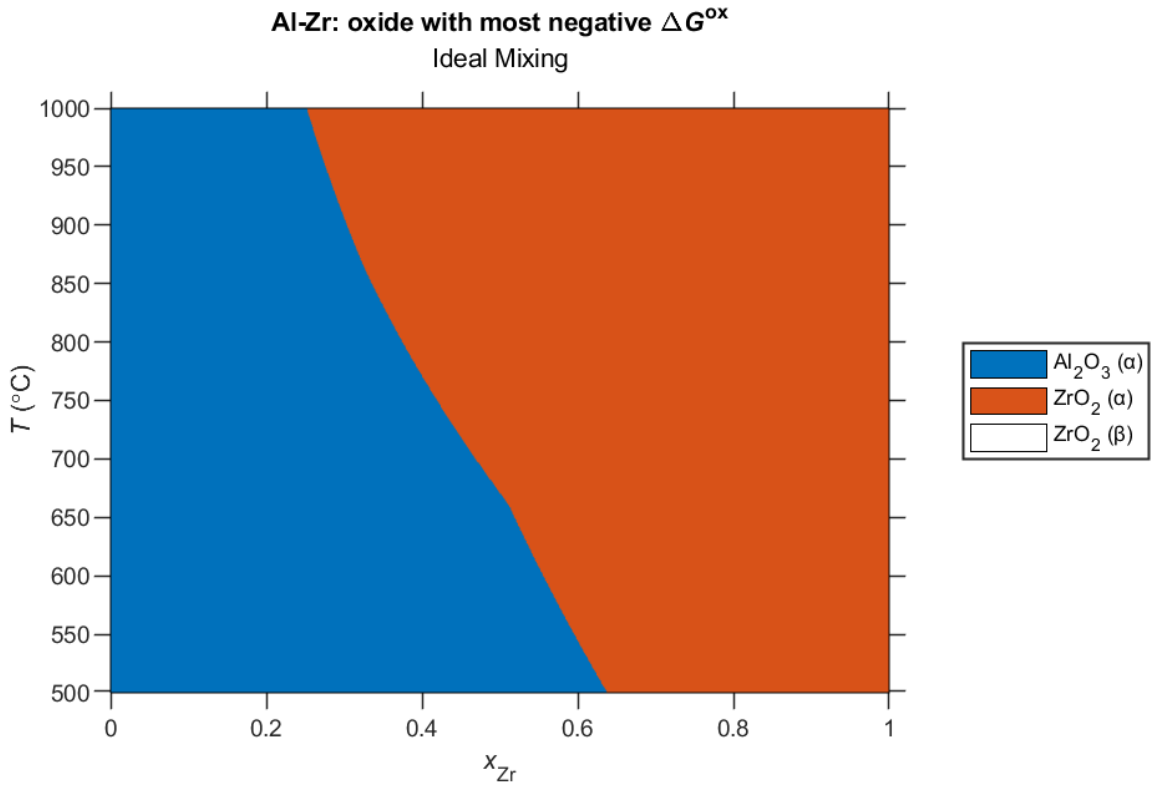
B.5.1.22. Al-Ti



B.5.1.23. Al-Zn

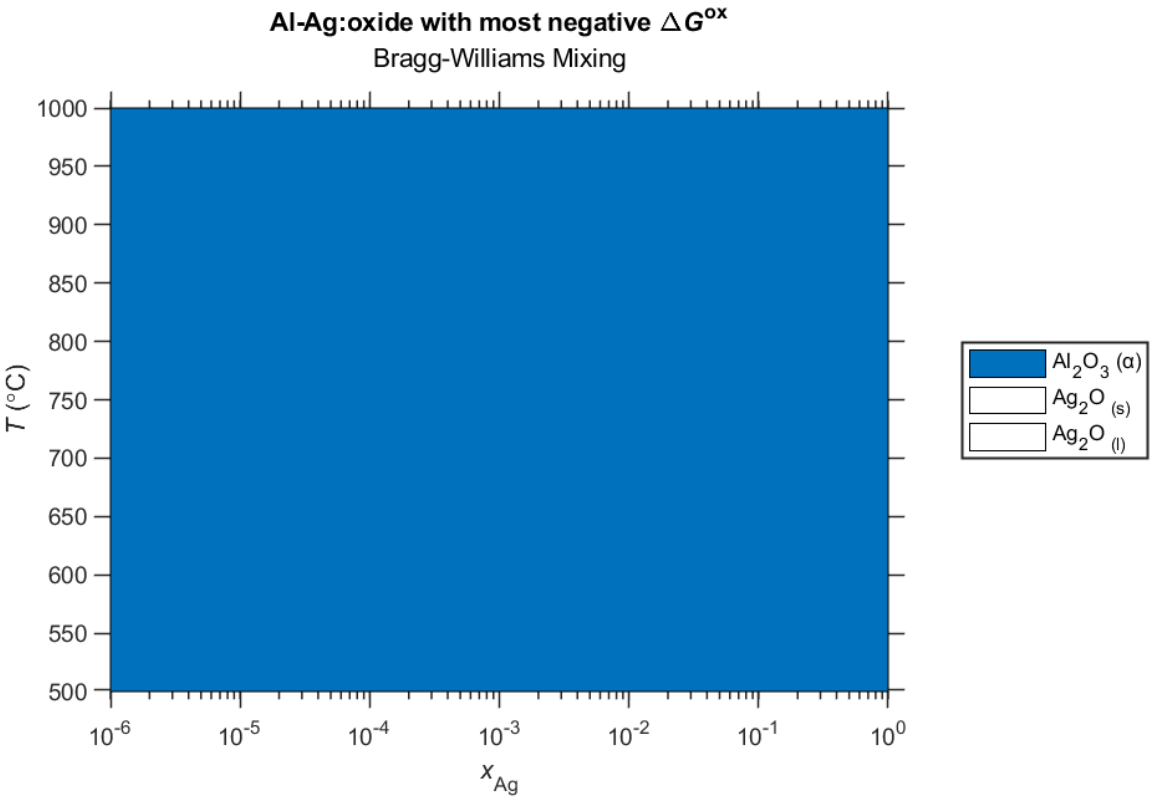


B.5.1.24. Al-Zr

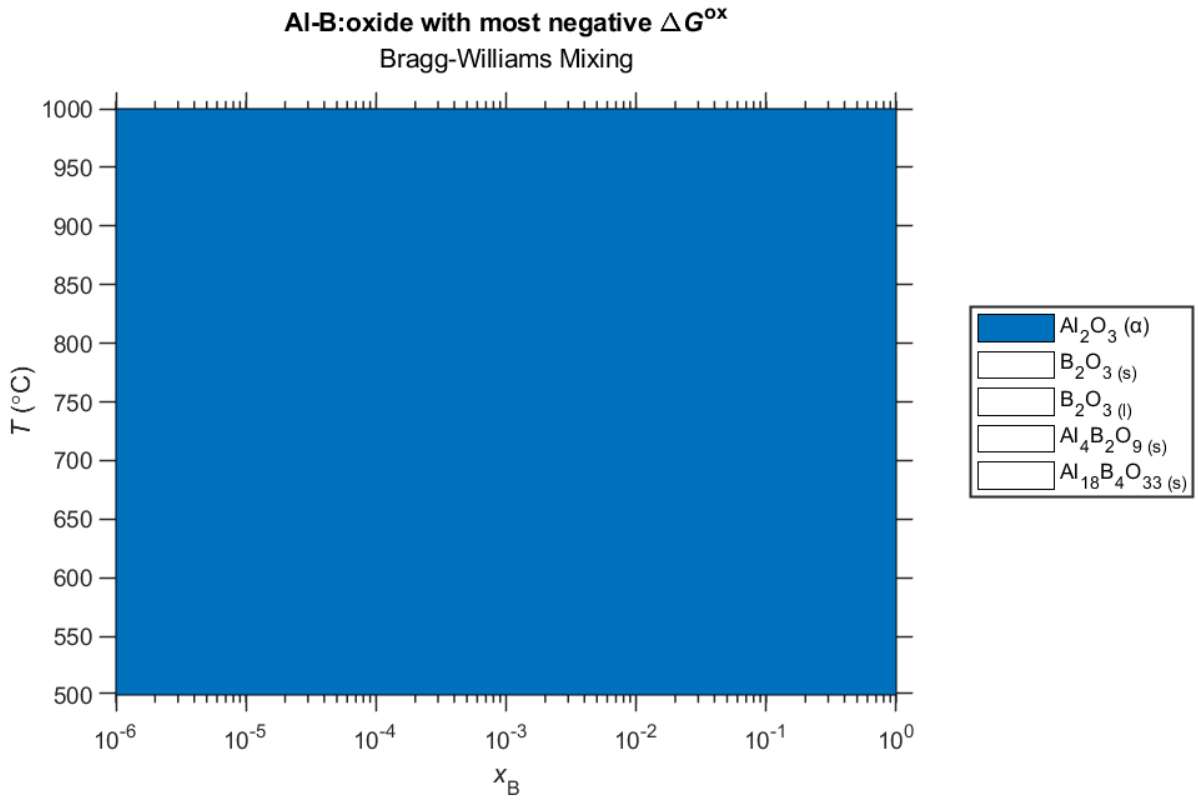


B.5.2. Bragg-Williams mixing

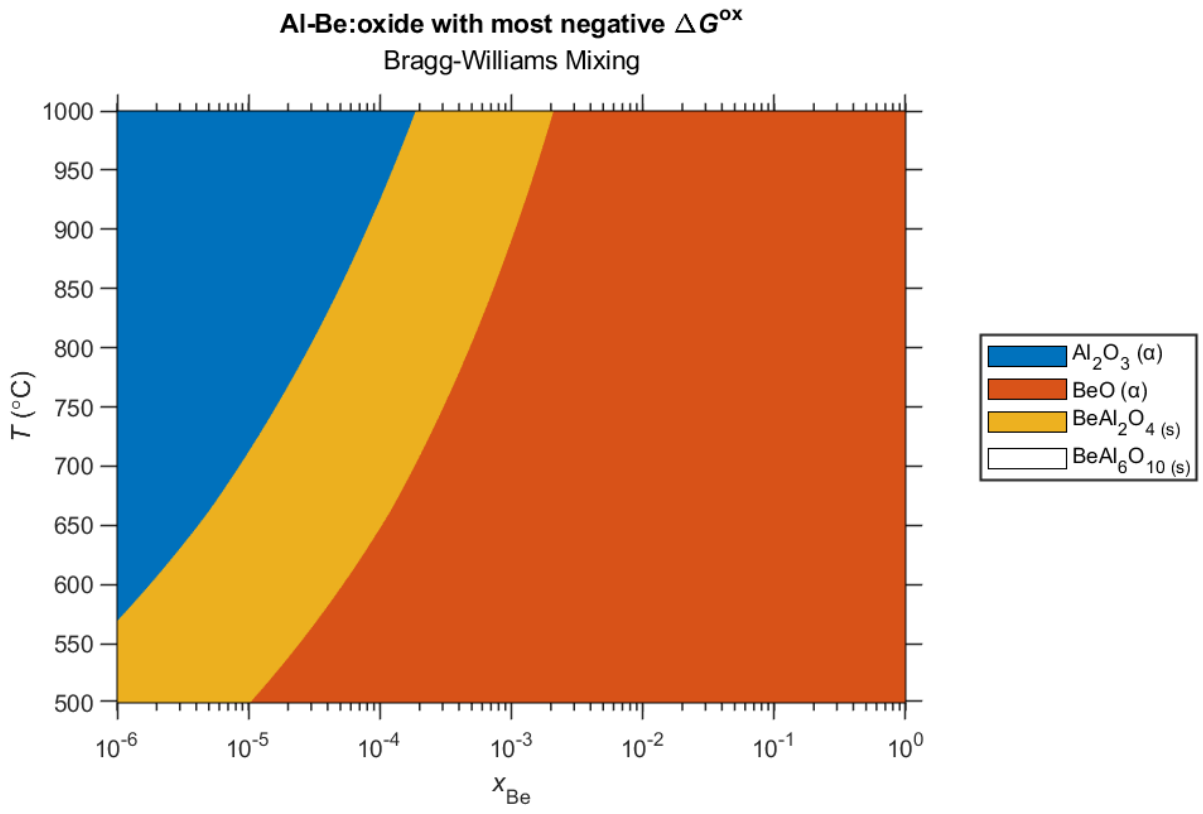
B.5.2.1. Al-Ag



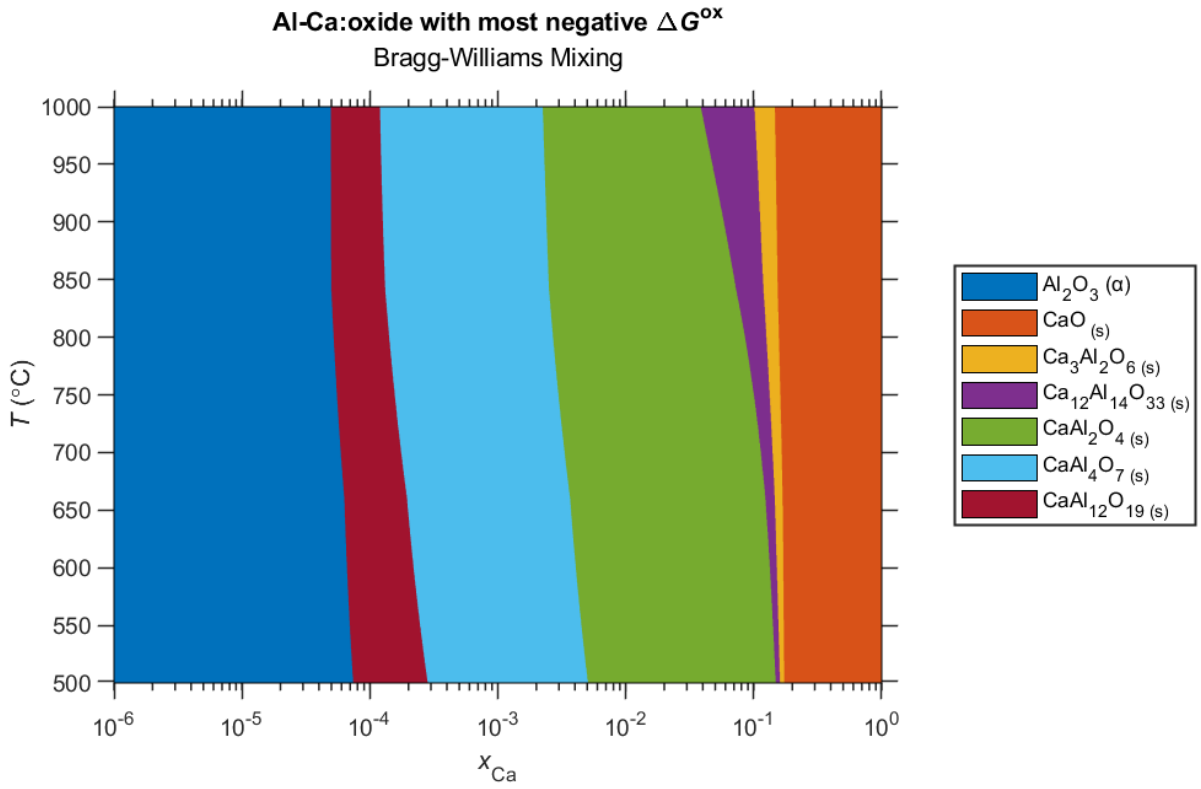
B.5.2.2. Al-B



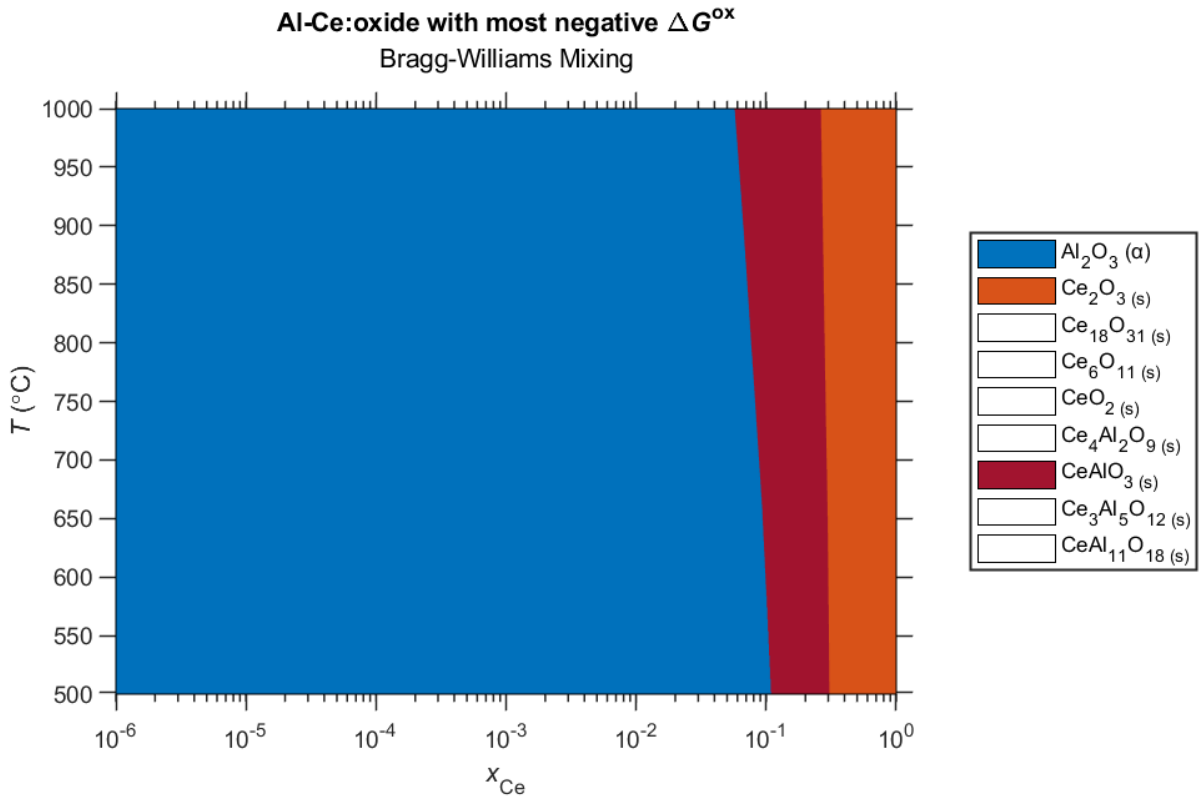
B.5.2.3. Al-Be



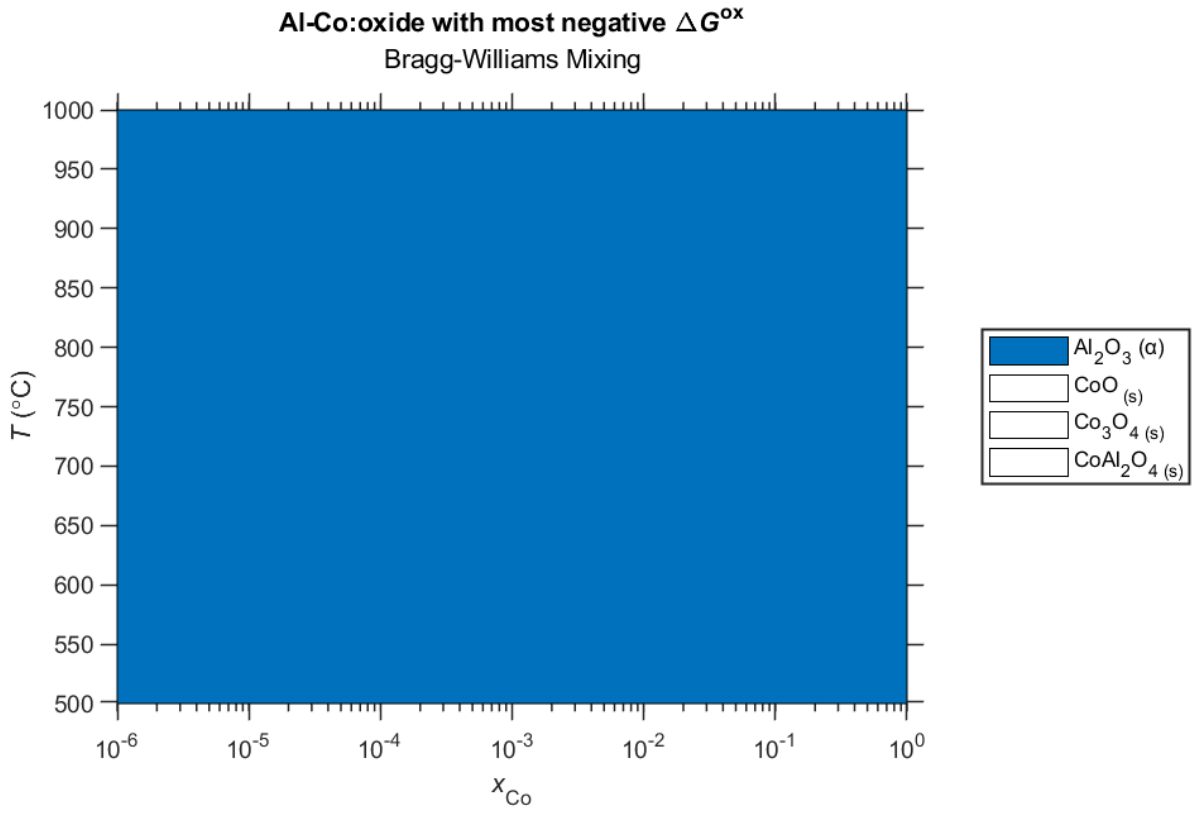
B.5.2.4. Al-Ca



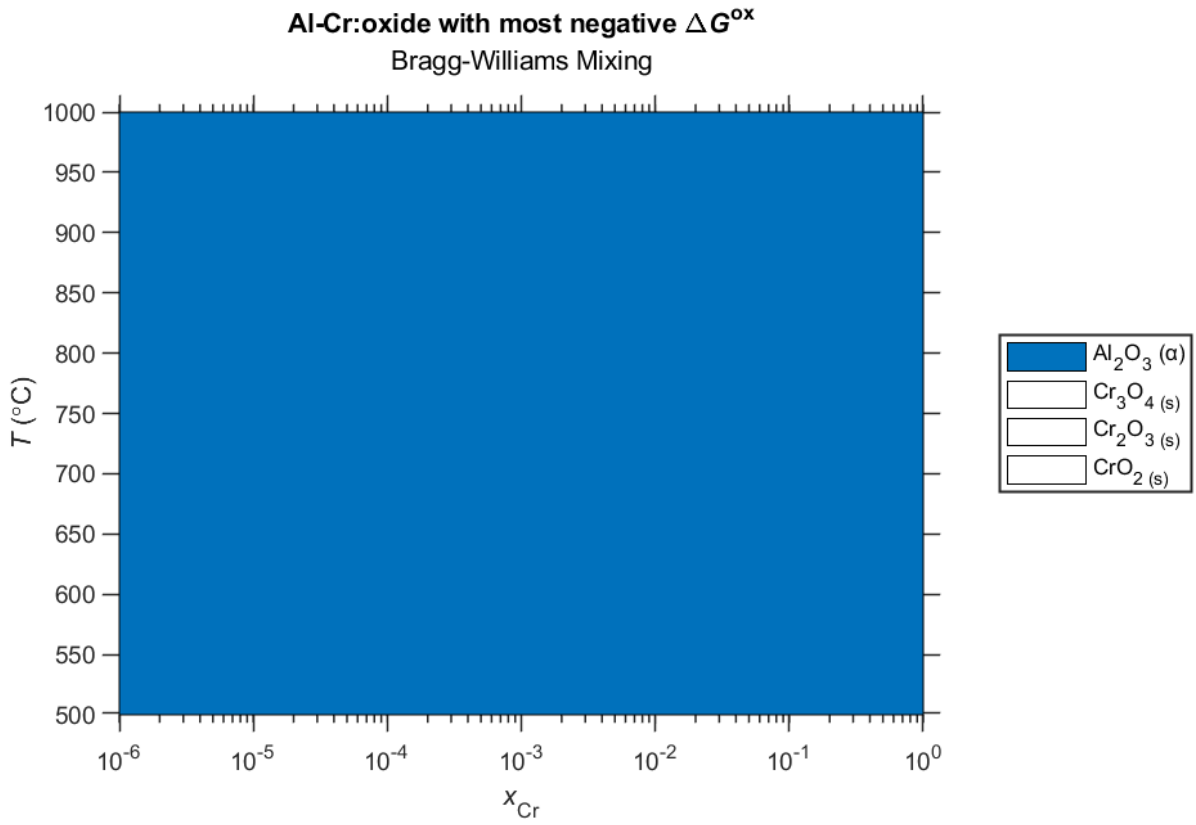
B.5.2.5. Al-Ce



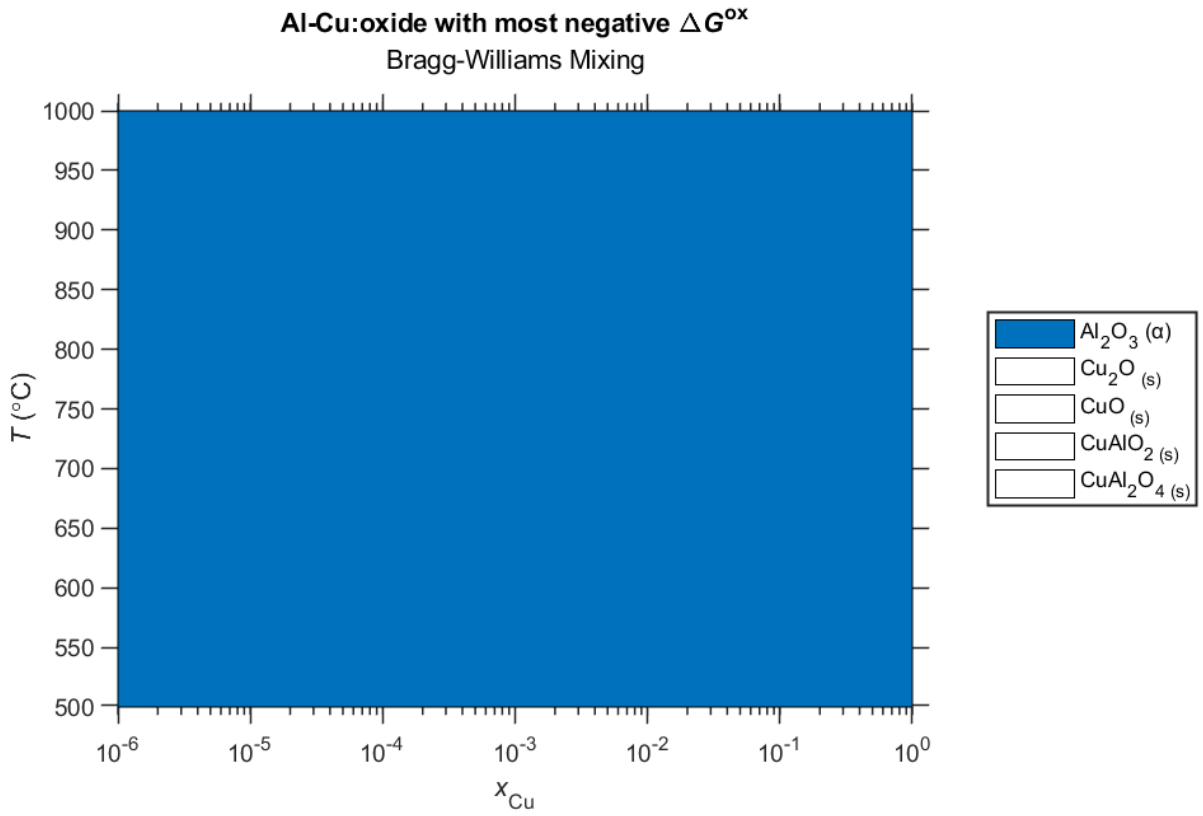
B.5.2.6. Al-Co



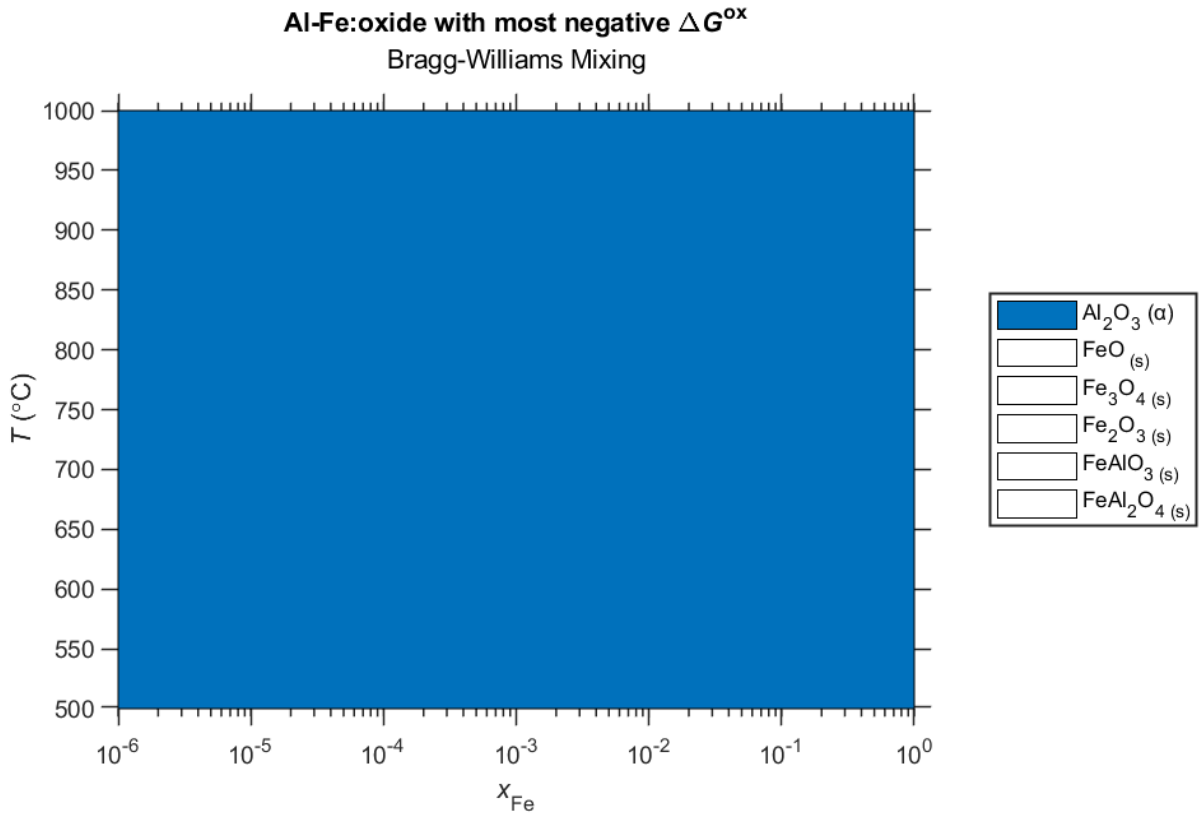
B.5.2.7. Al-Cr



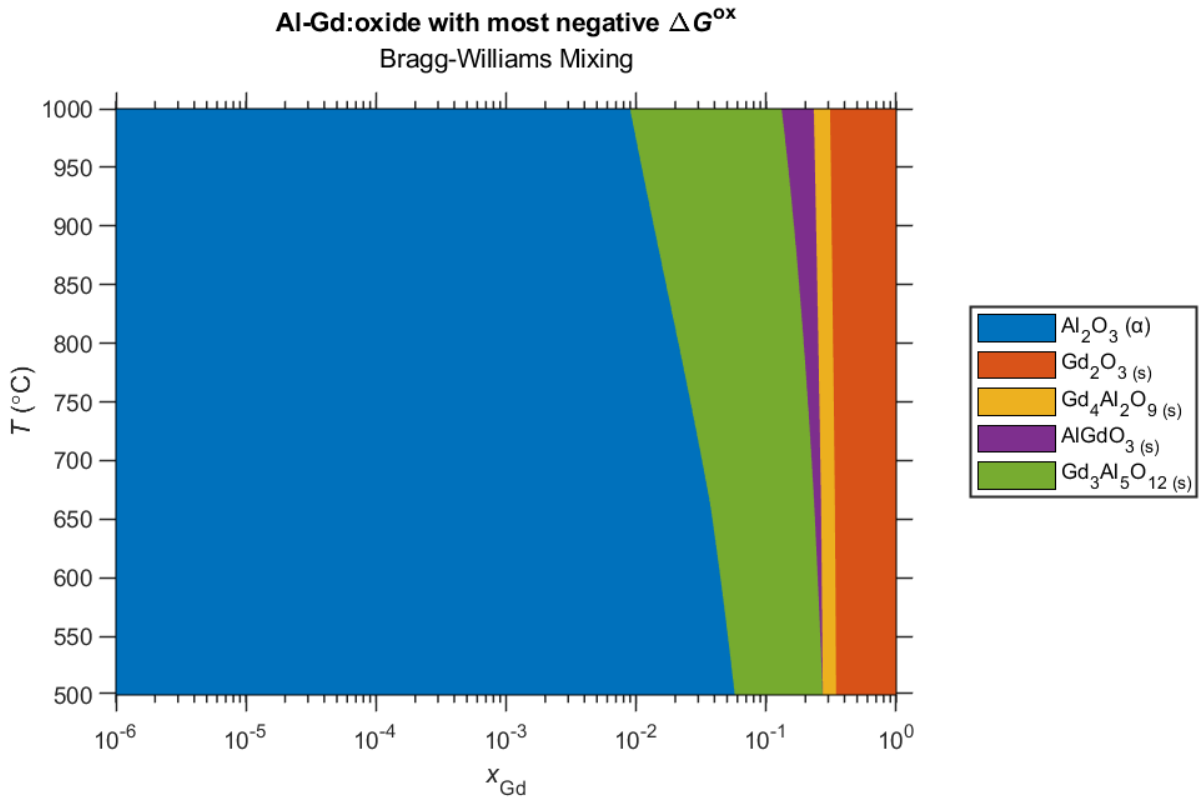
B.5.2.8. Al-Cu



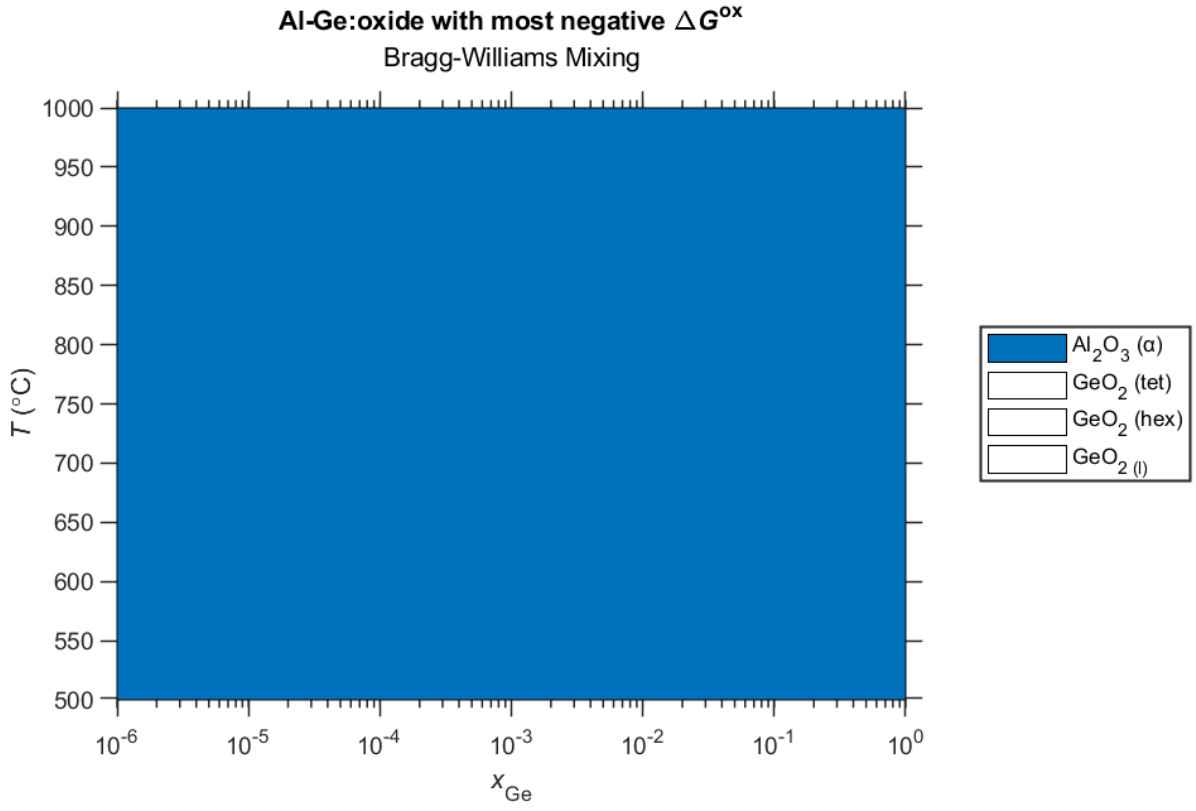
B.5.2.9. Al-Fe



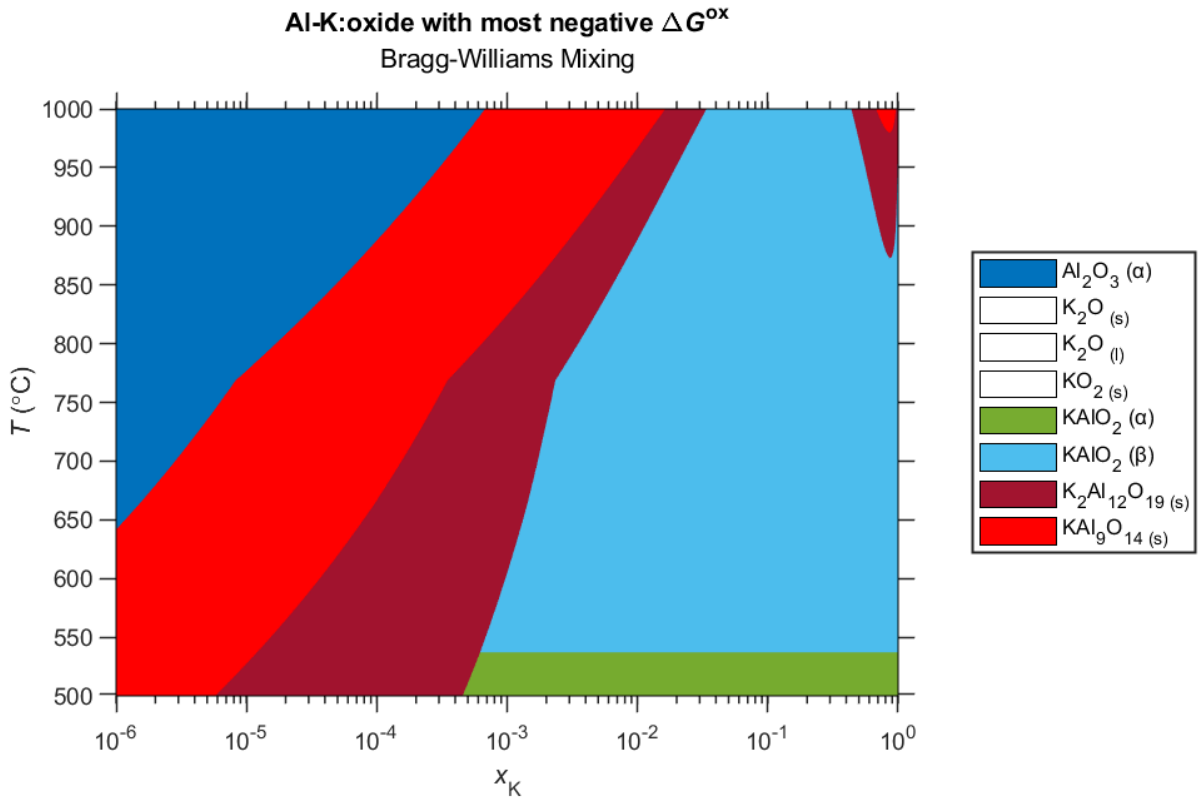
B.5.2.10. Al-Gd



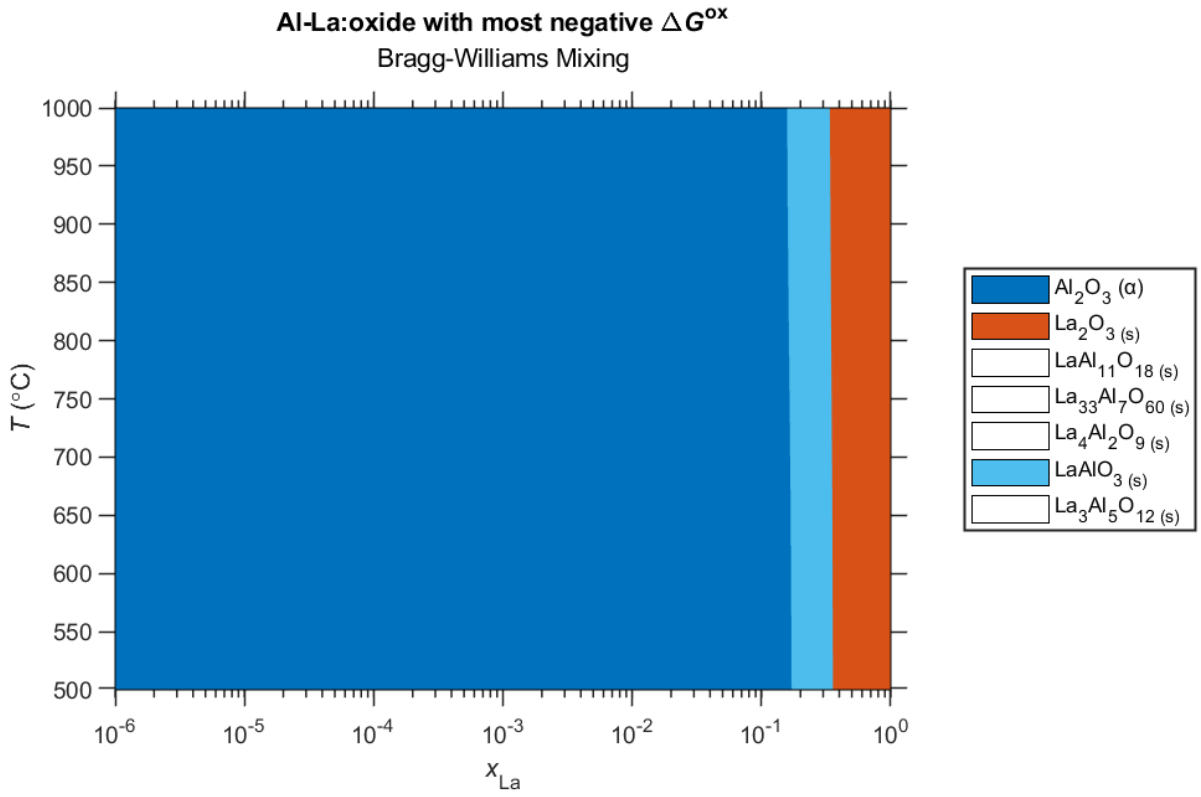
B.5.2.11. Al-Ge



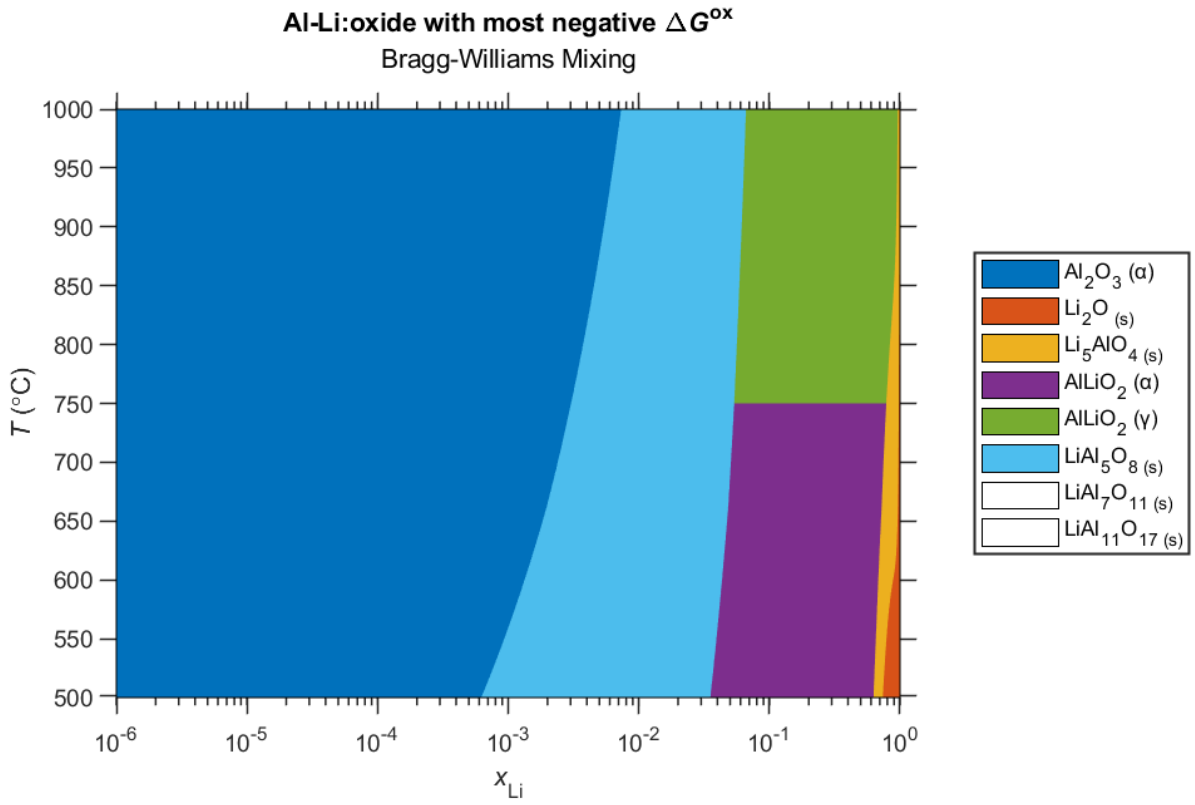
B.5.2.12. Al-K



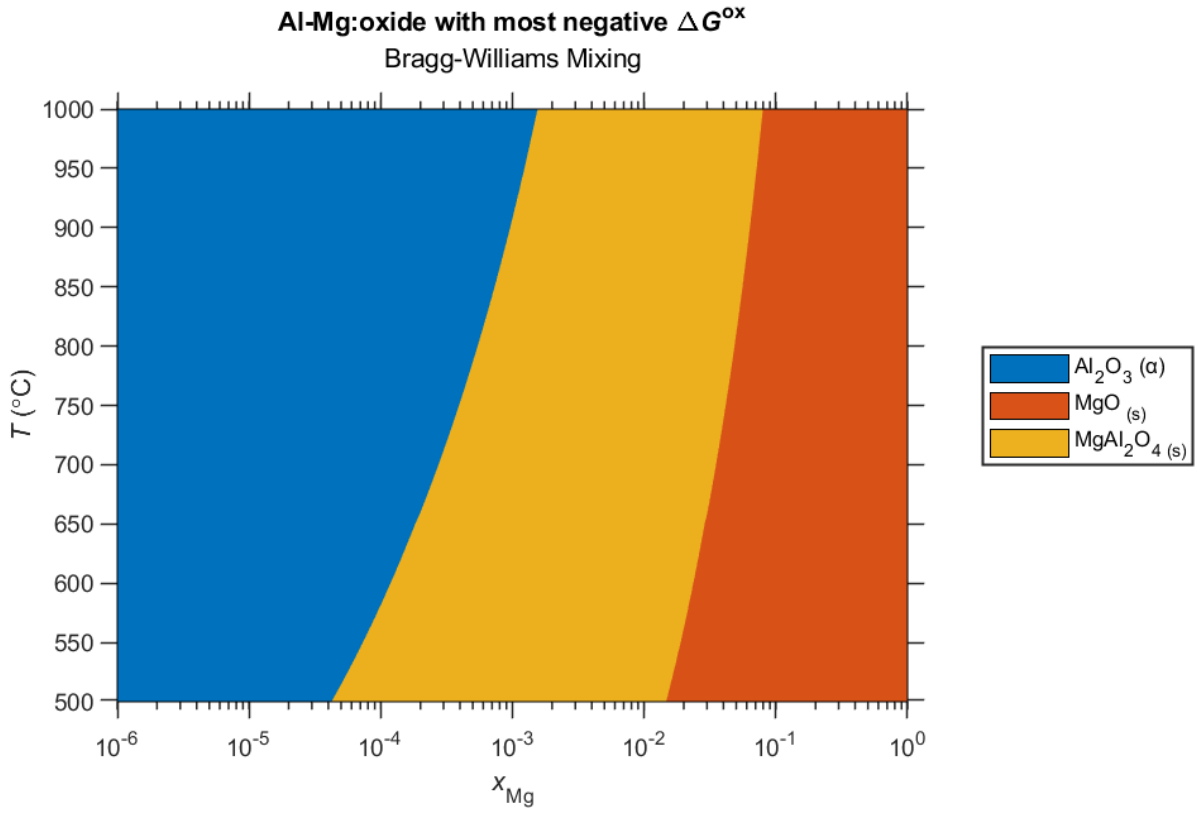
B.5.2.13. Al-La



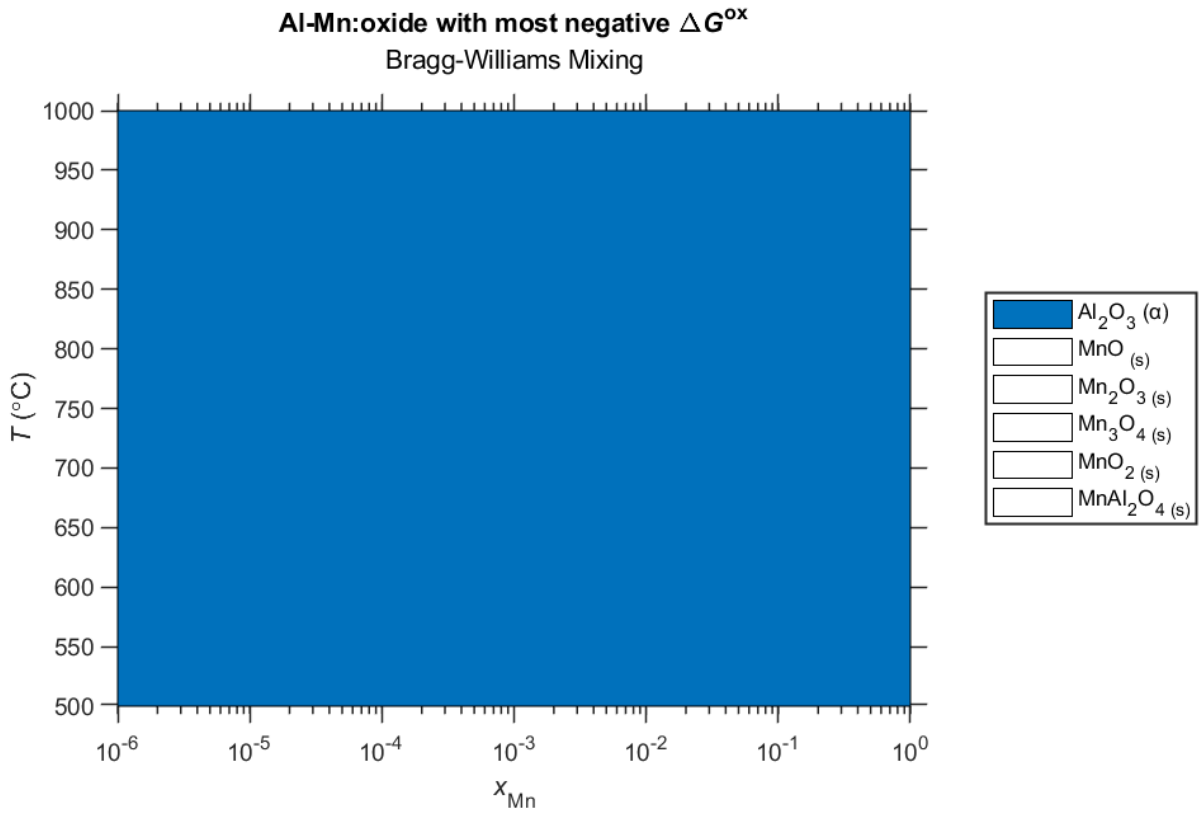
B.5.2.14. Al-Li



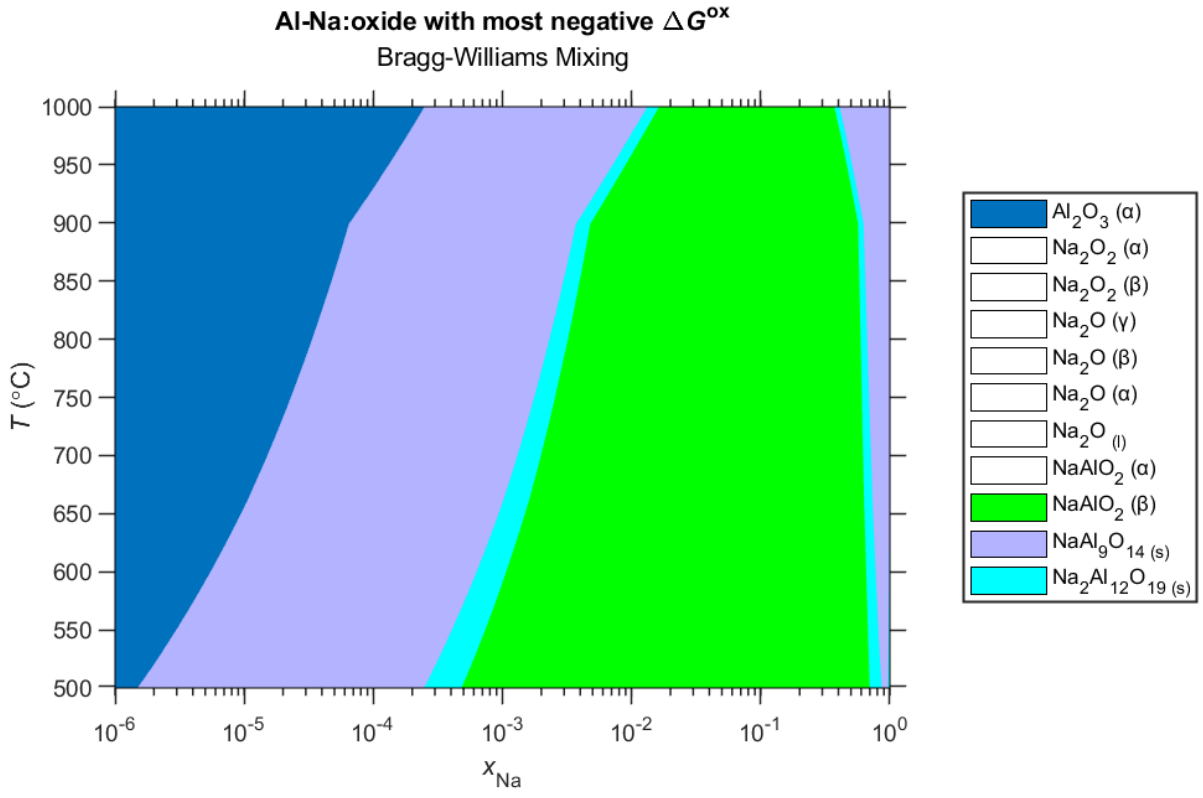
B.5.2.15. Al-Mg



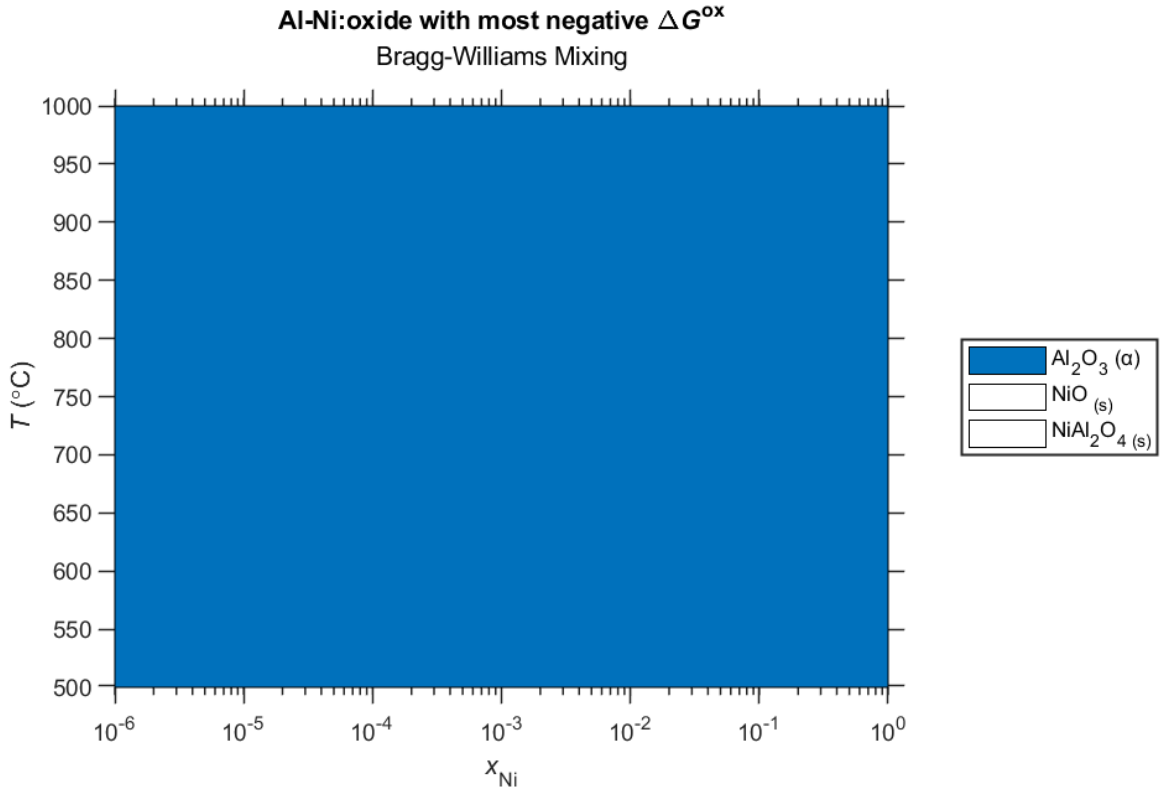
B.5.2.16. Al-Mn



B.5.2.17. Al-Na

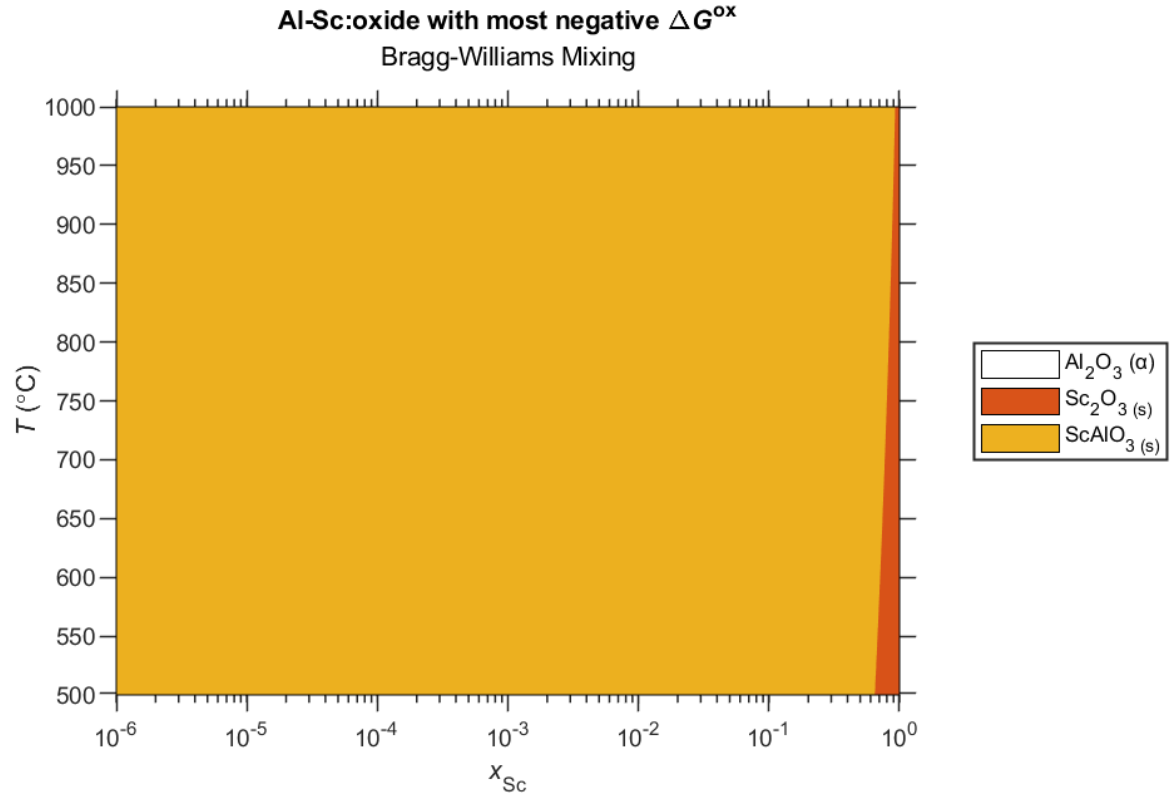


B.5.2.18. Al-Ni

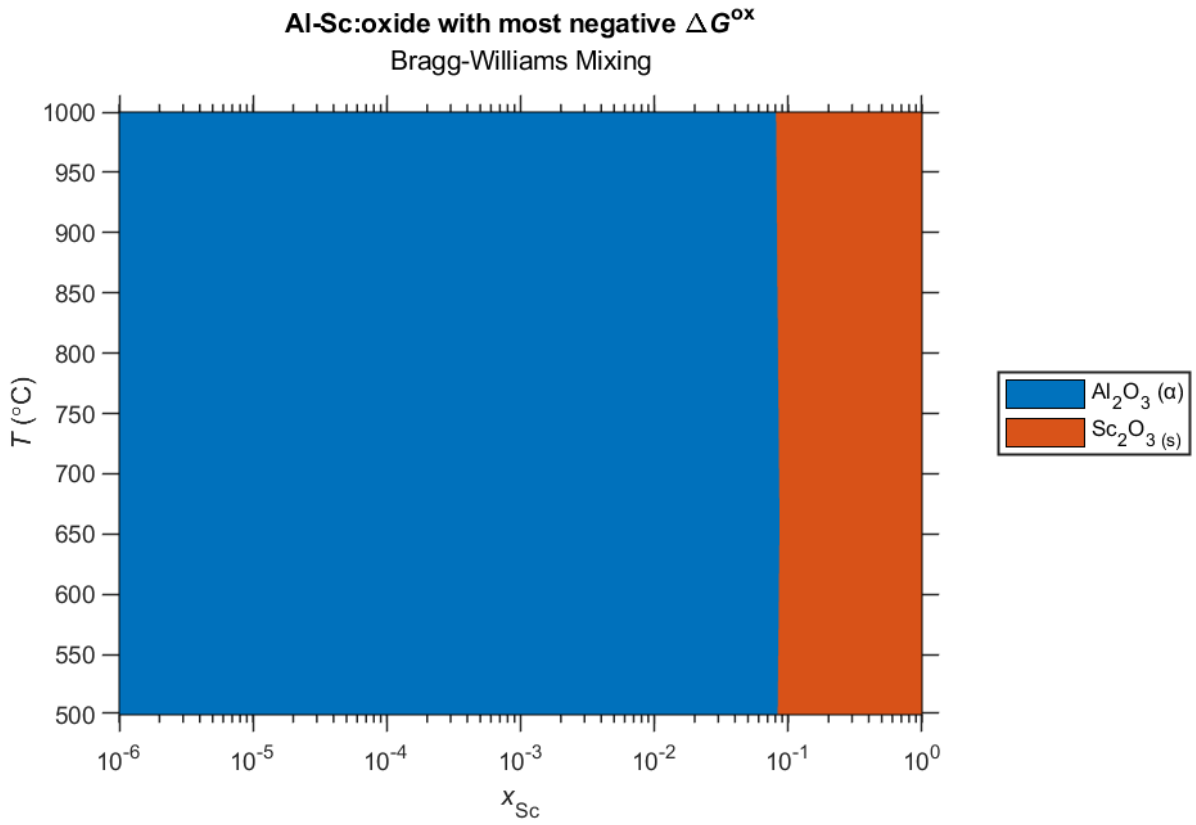


B.5.2.19. Al-Sc

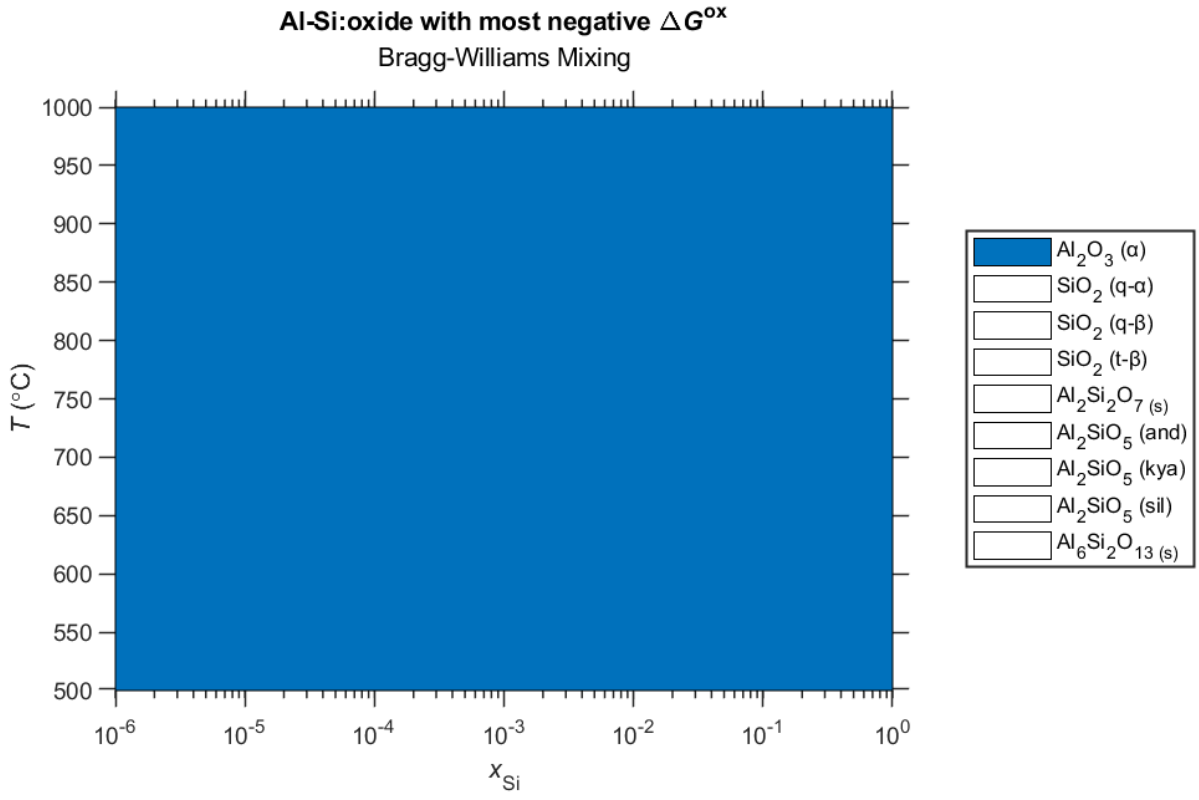
Including $ScAlO_3$



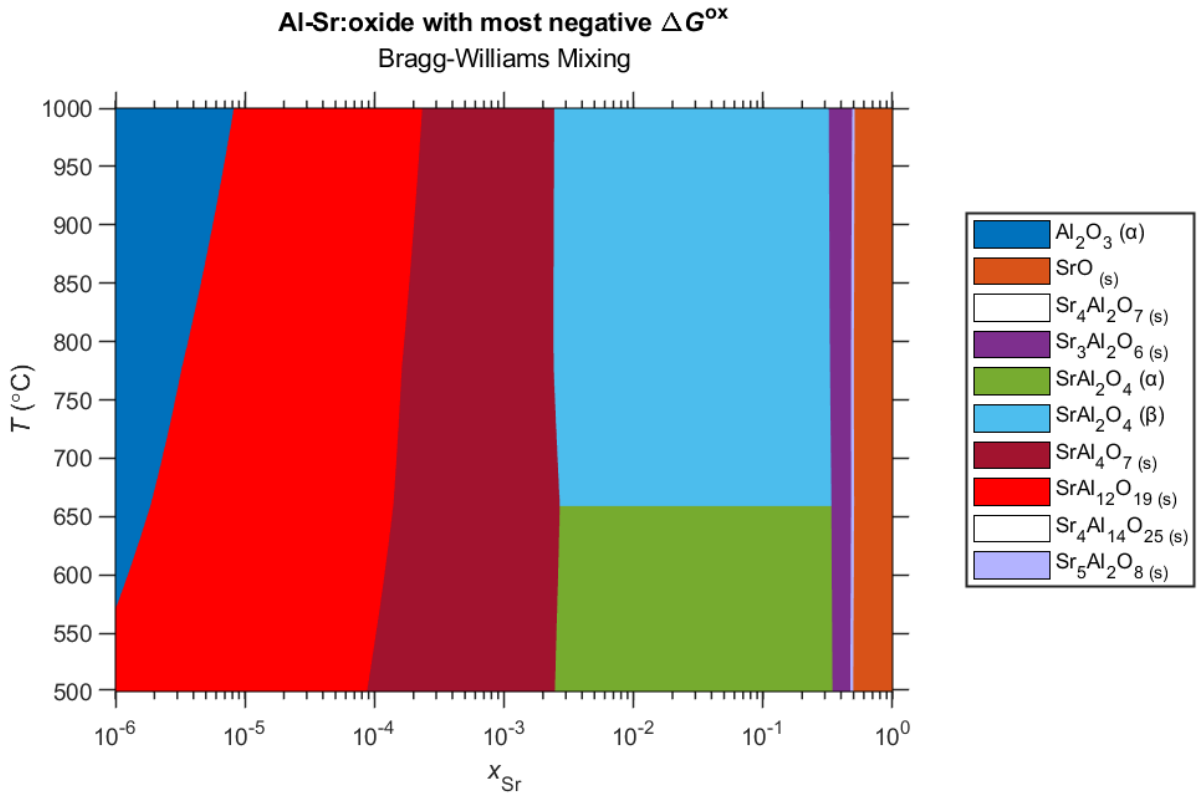
Without $ScAlO_3$



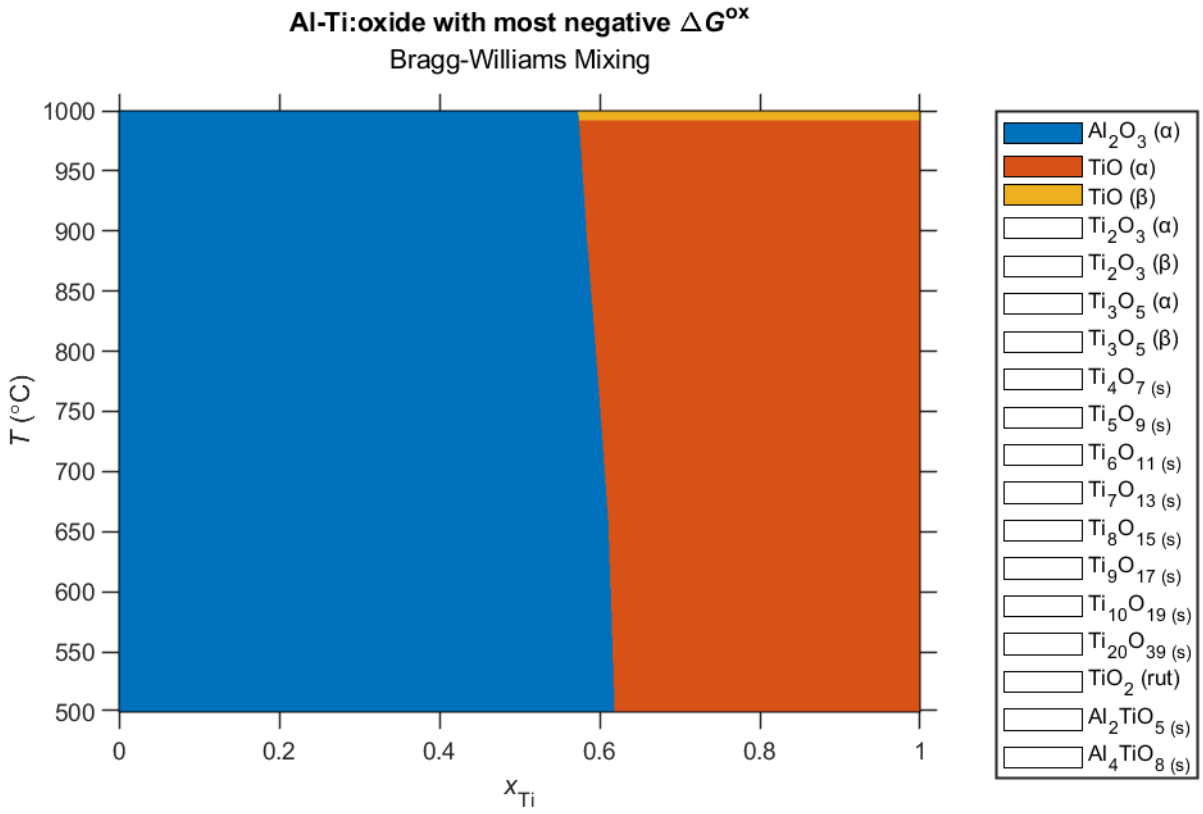
B.5.2.20. Al-Si



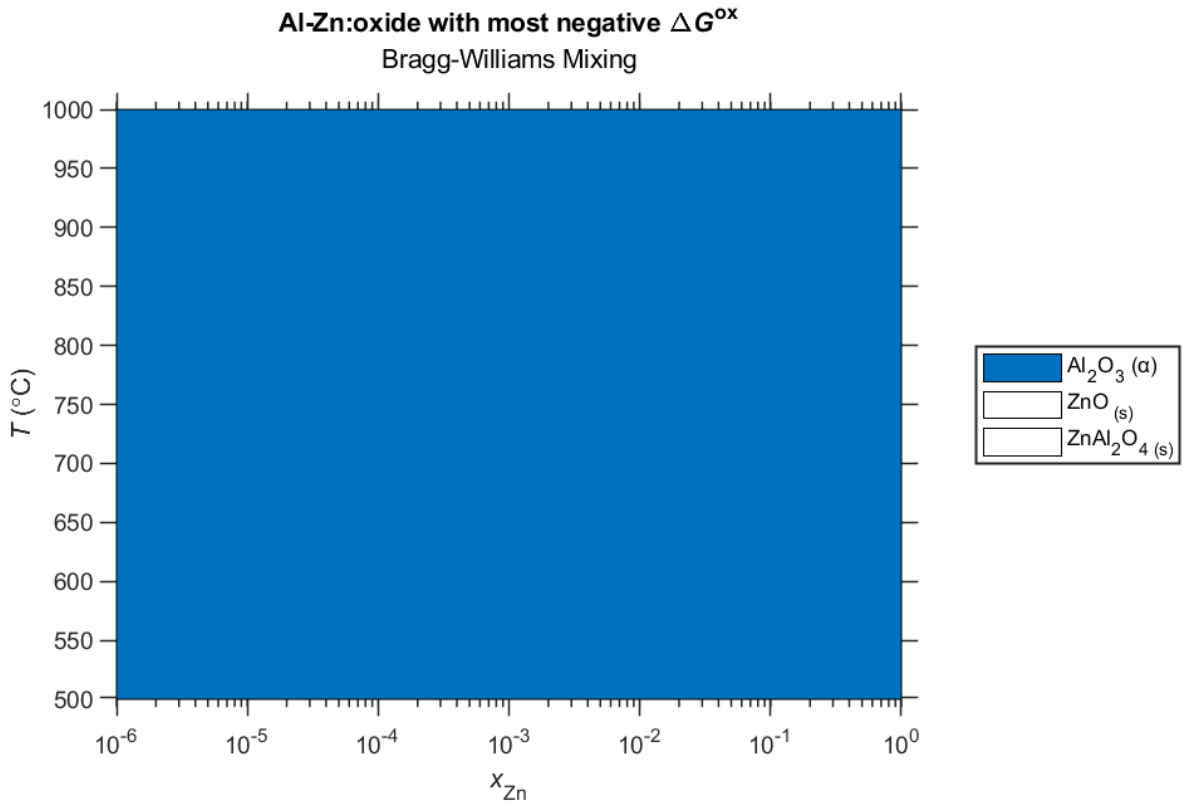
B.5.2.21. Al-Sr



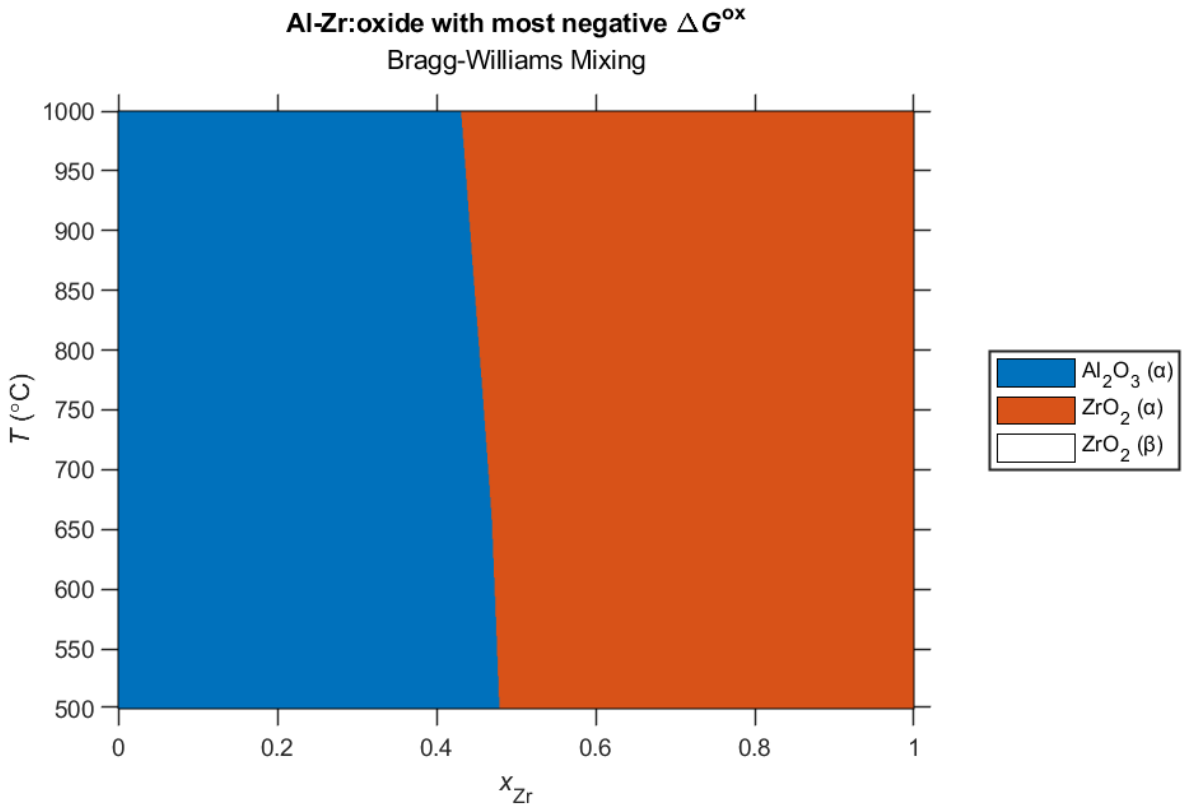
B.5.2.22. Al-Ti



B.5.2.23. Al-Zn

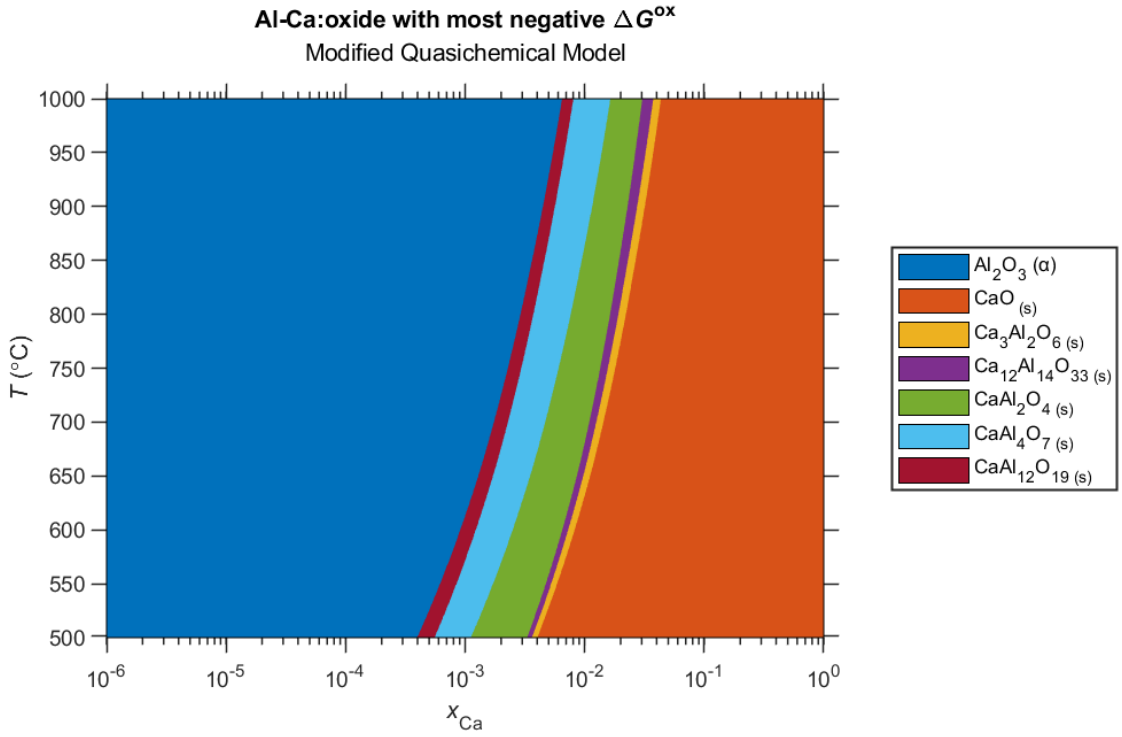


B.5.2.24. Al-Zr



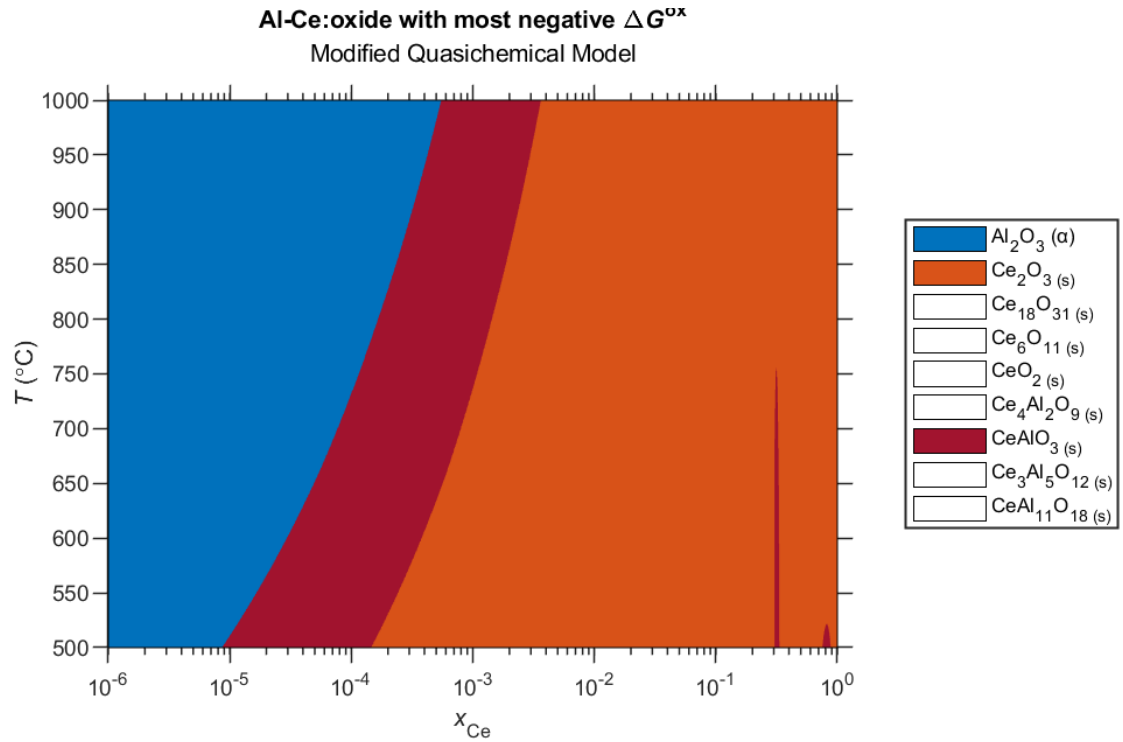
B.5.3. Modified quasichemical model

B.5.3.1. Al-Ca

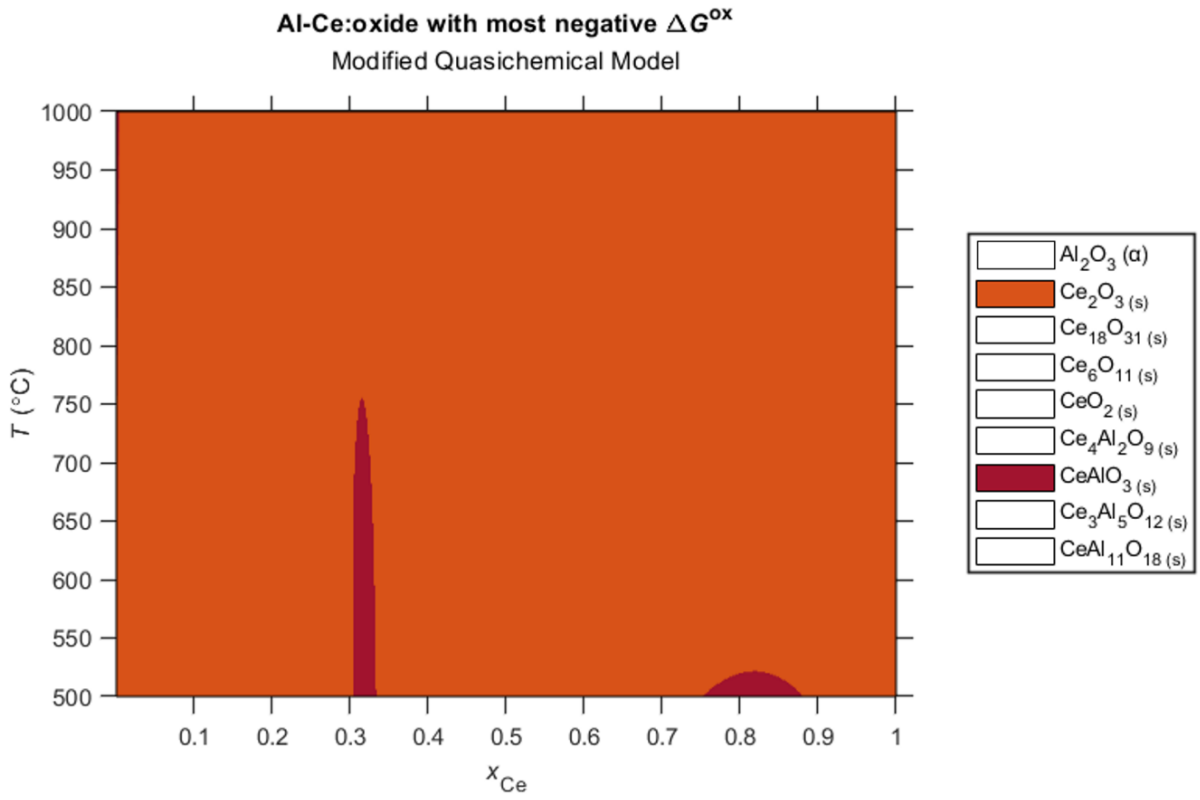


B.5.3.2. Al-Ce

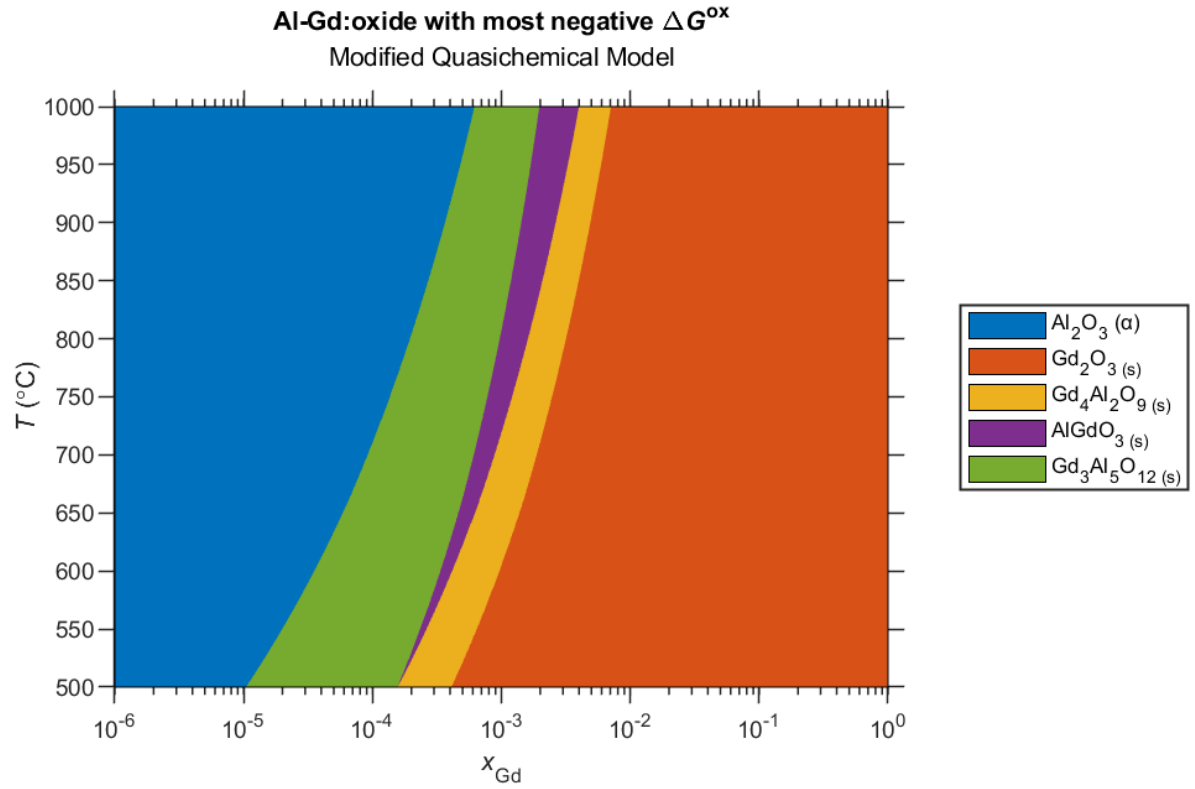
Logarithmic scale



Linear scale

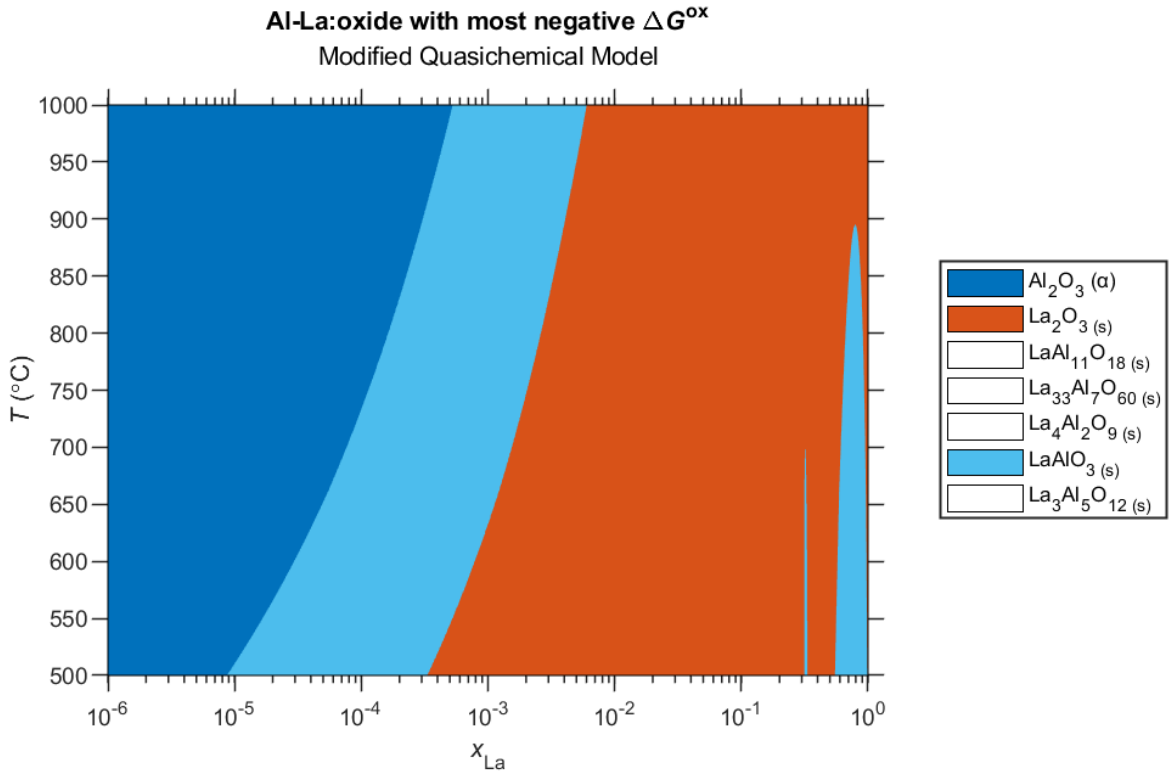


B.5.3.3. Al-Gd

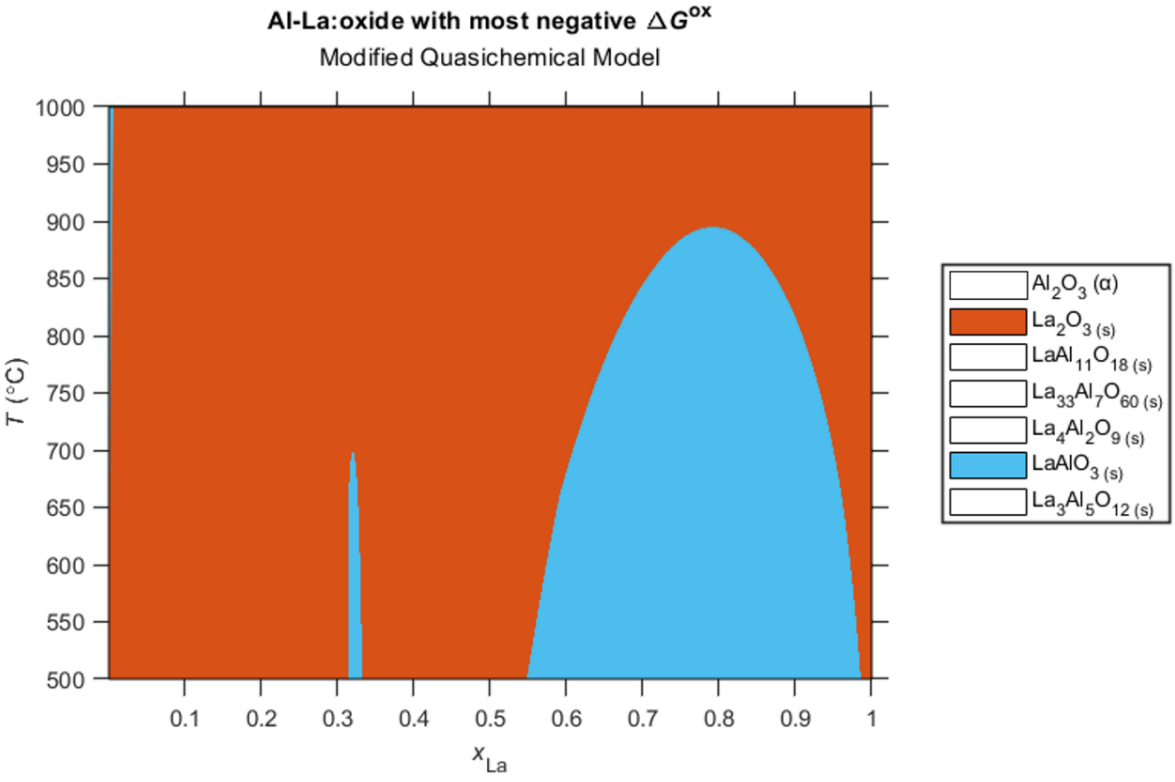


B.5.3.4. Al-La

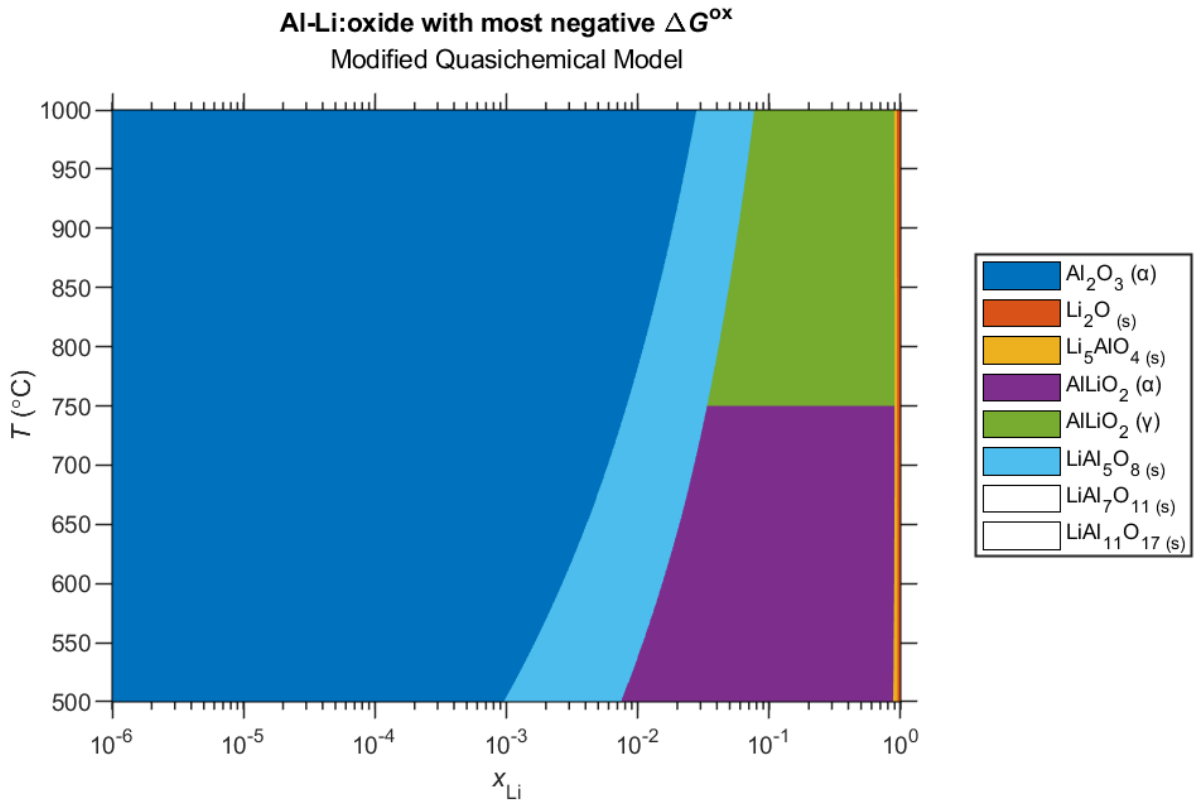
Logarithmic scale



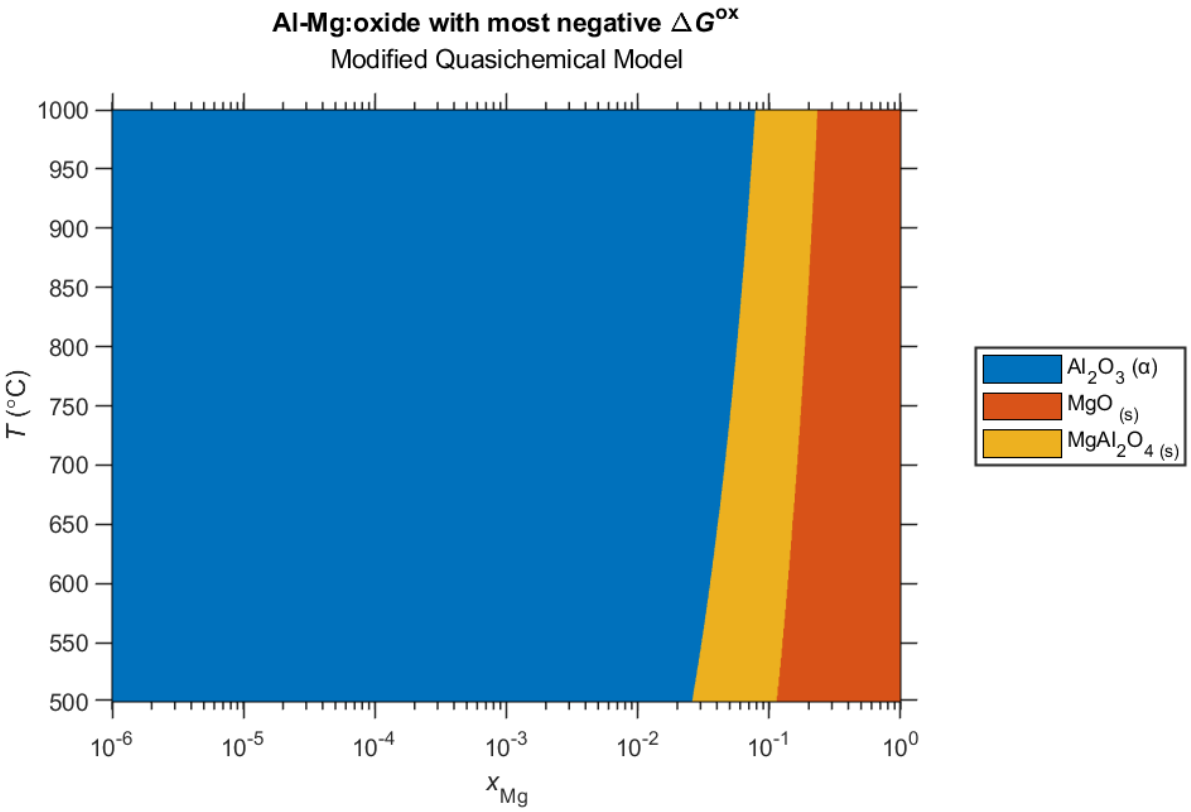
Linear scale



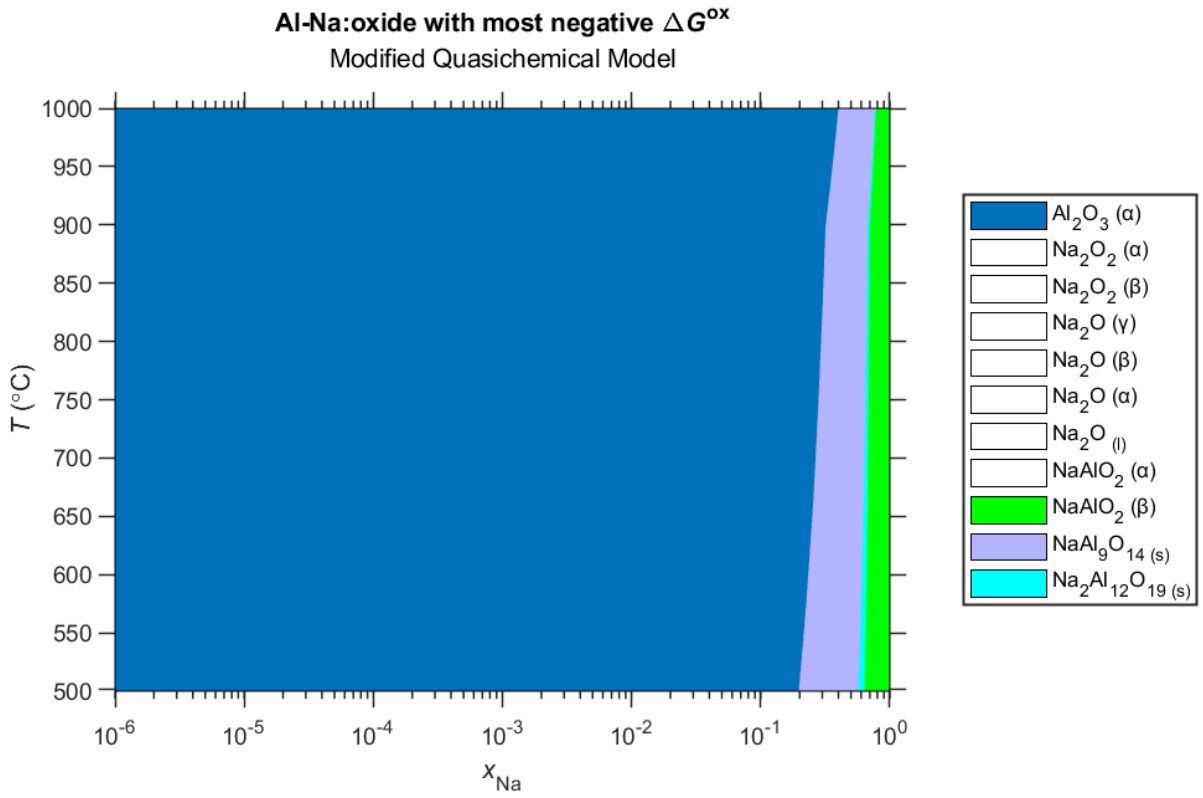
B.5.3.5. Al-Li



B.5.3.6. Al-Mg

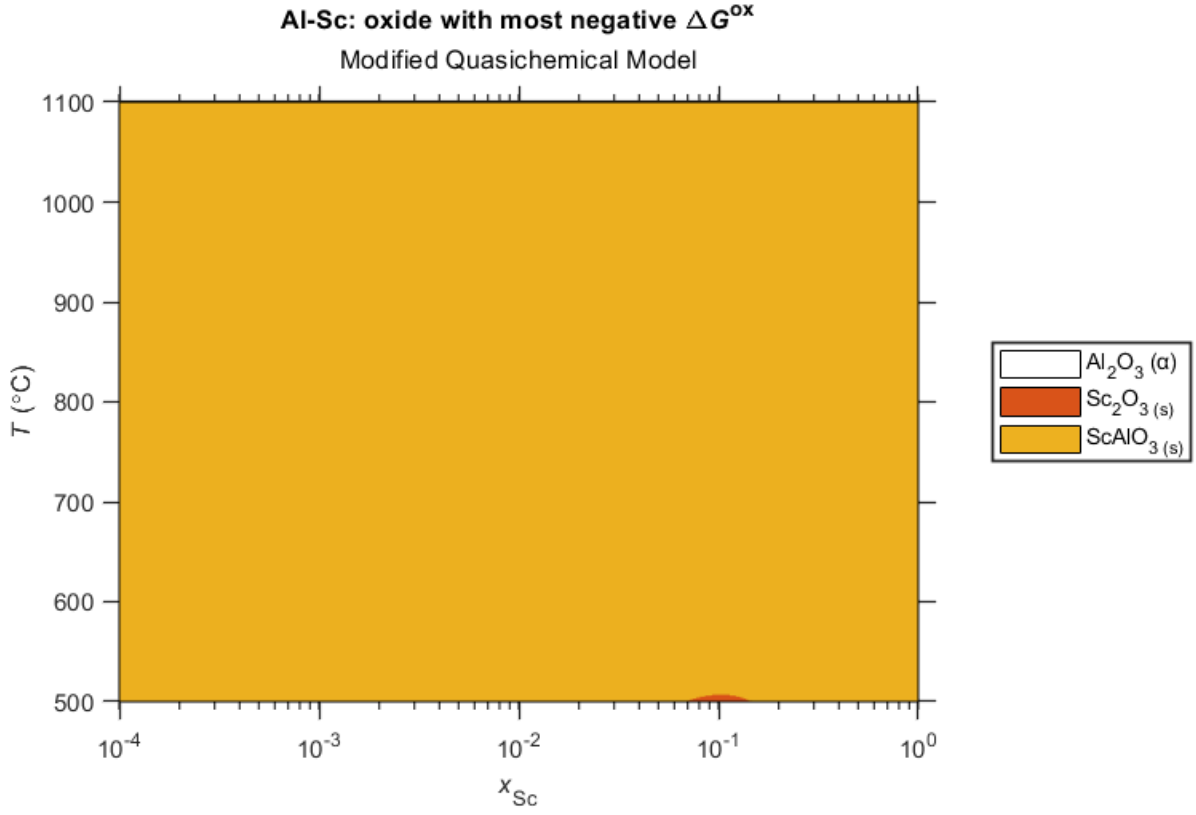


B.5.3.7. Al-Na

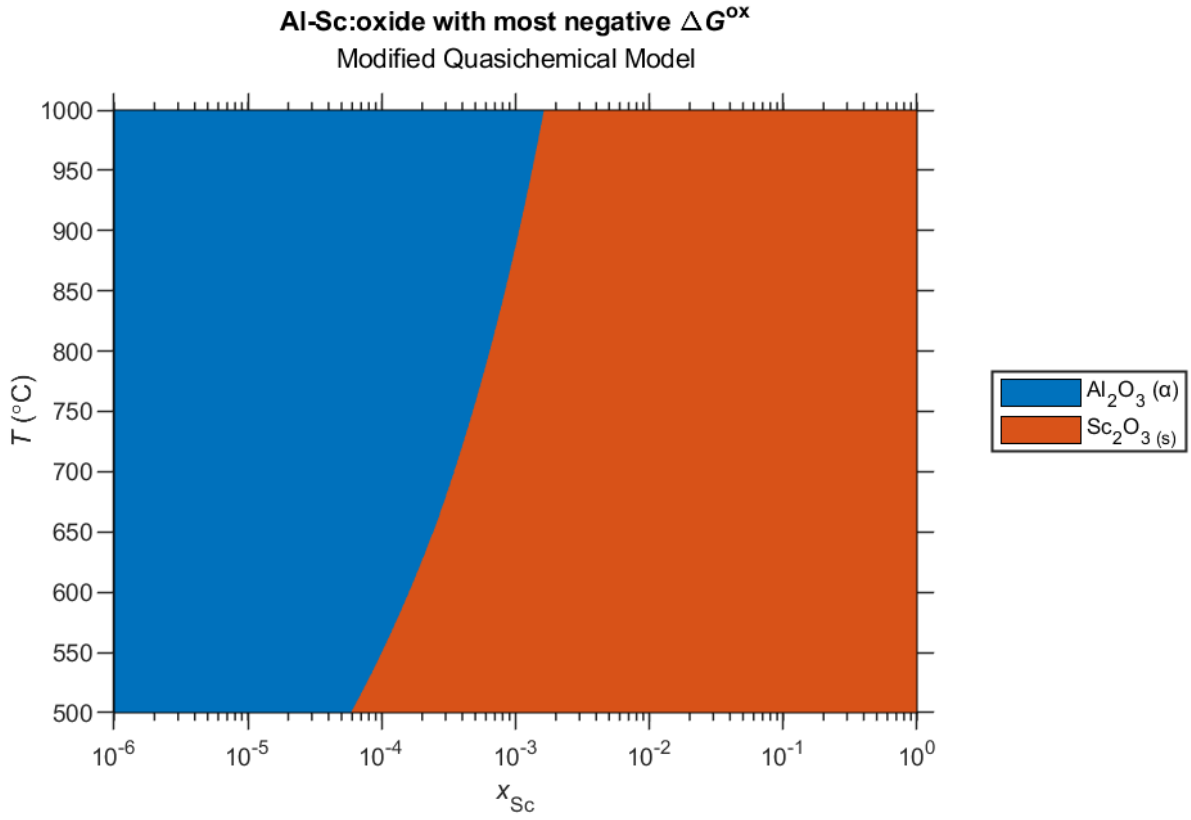


B.5.3.8. Al-Sc

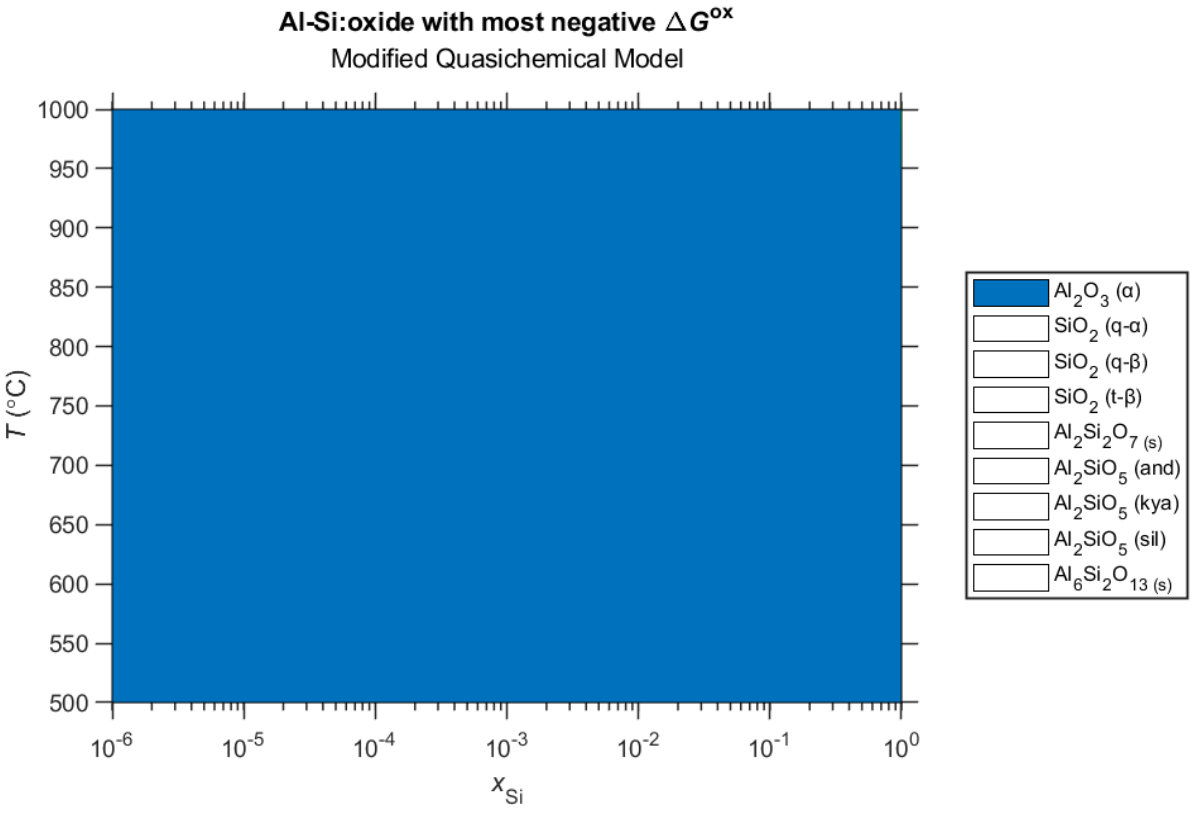
Including $ScAlO_3$



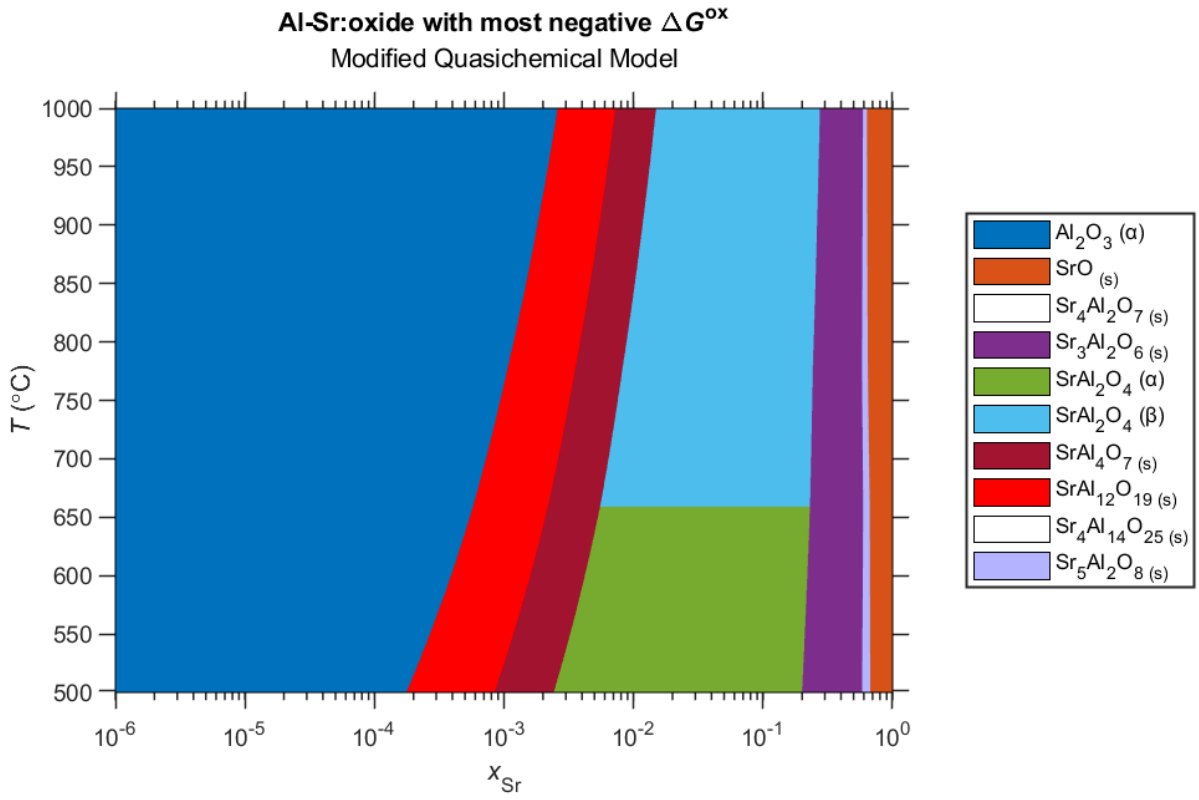
Without $ScAlO_3$



B.5.3.9. Al-Si



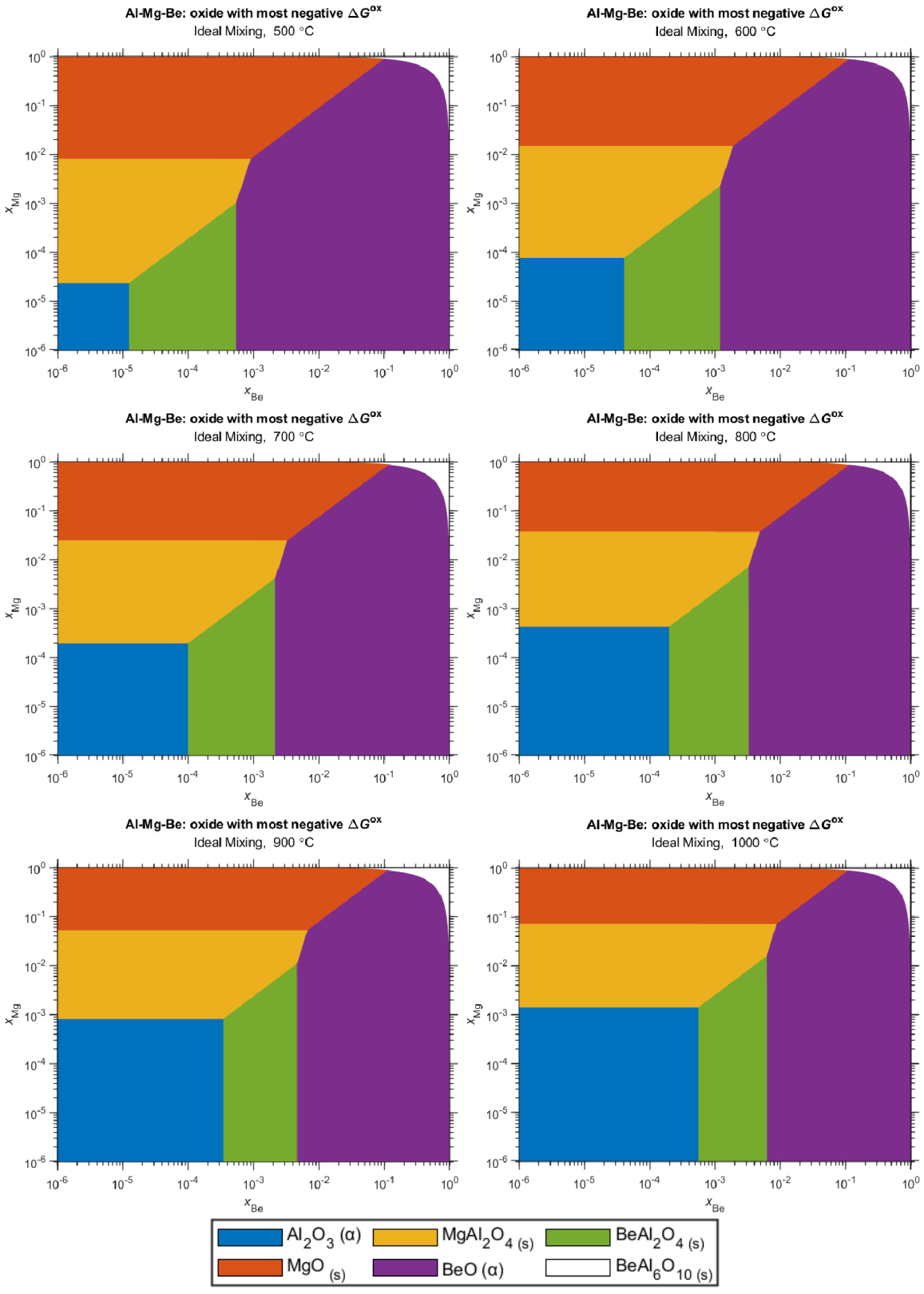
B.5.3.10. Al-Sr


Al-Sr:oxide with most negative ΔG^ox
Modified Quasichemical Model
T (°C)
1000
950
900
850
800
750
700
650
600
550
500
10^-6
10^-5
10^-4
10^-3
10^-2
10^-1
10^0
x_Sr
Al2O3 (α)
SrO (s)
Sr4Al2O7 (s)
Sr3Al2O6 (s)
SrAl2O4 (α)
SrAl2O4 (β)
SrAl4O7 (s)
SrAl12O19 (s)
Sr4Al14O25 (s)
Sr5Al2O8 (s)

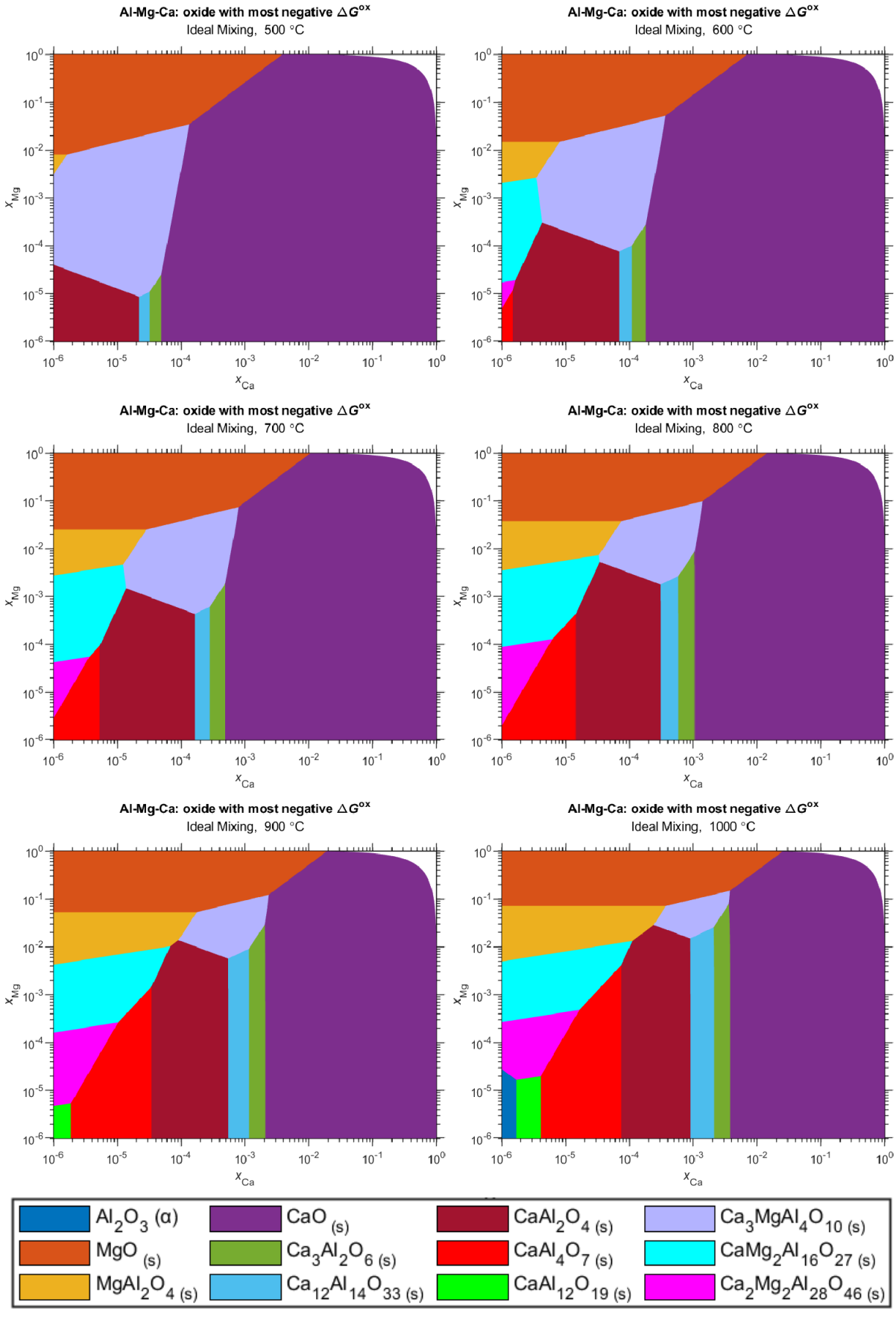
B.6. Ternary systems

B.6.1. Ideal mixing

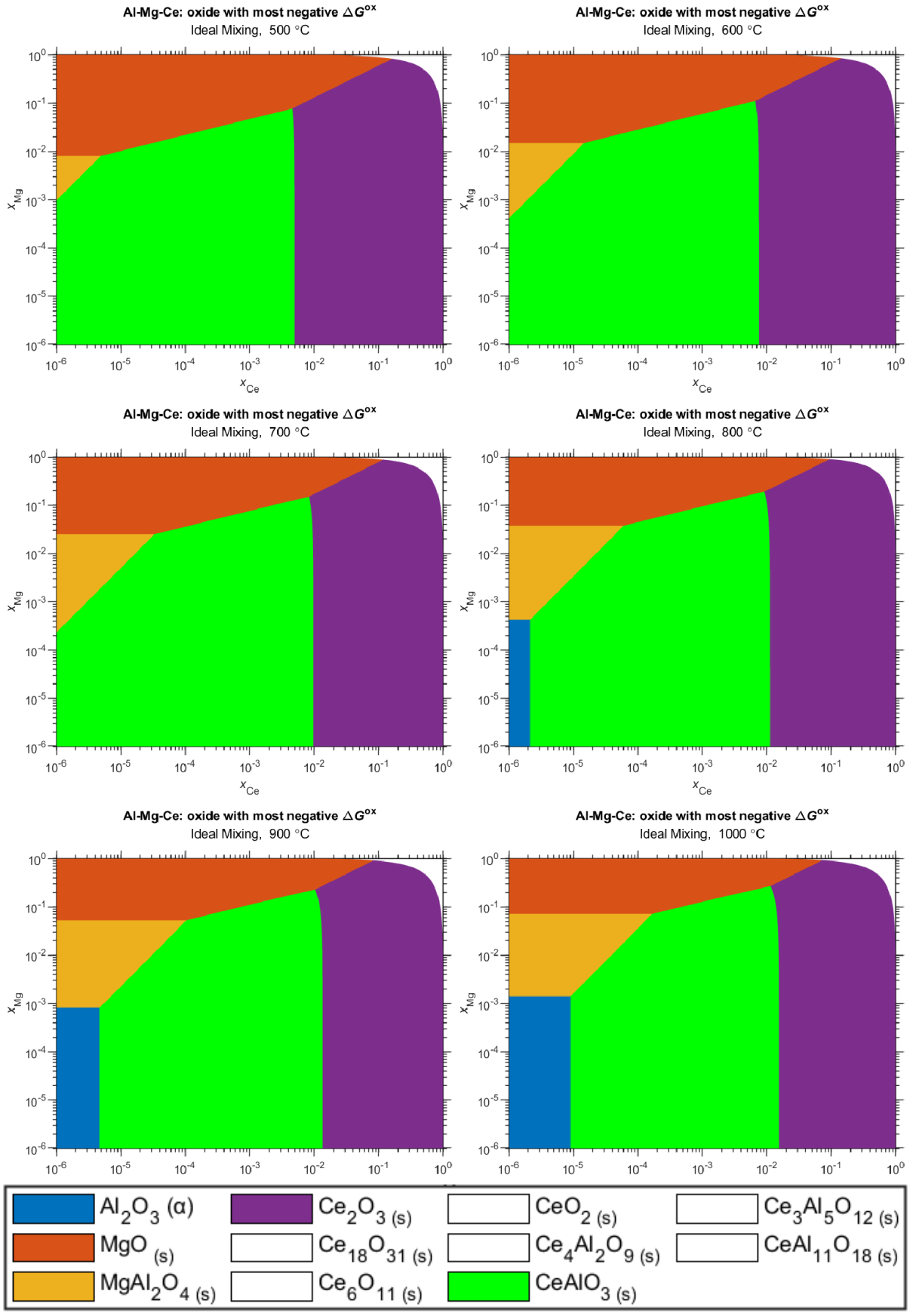
B.6.1.1. Al-Mg-Be



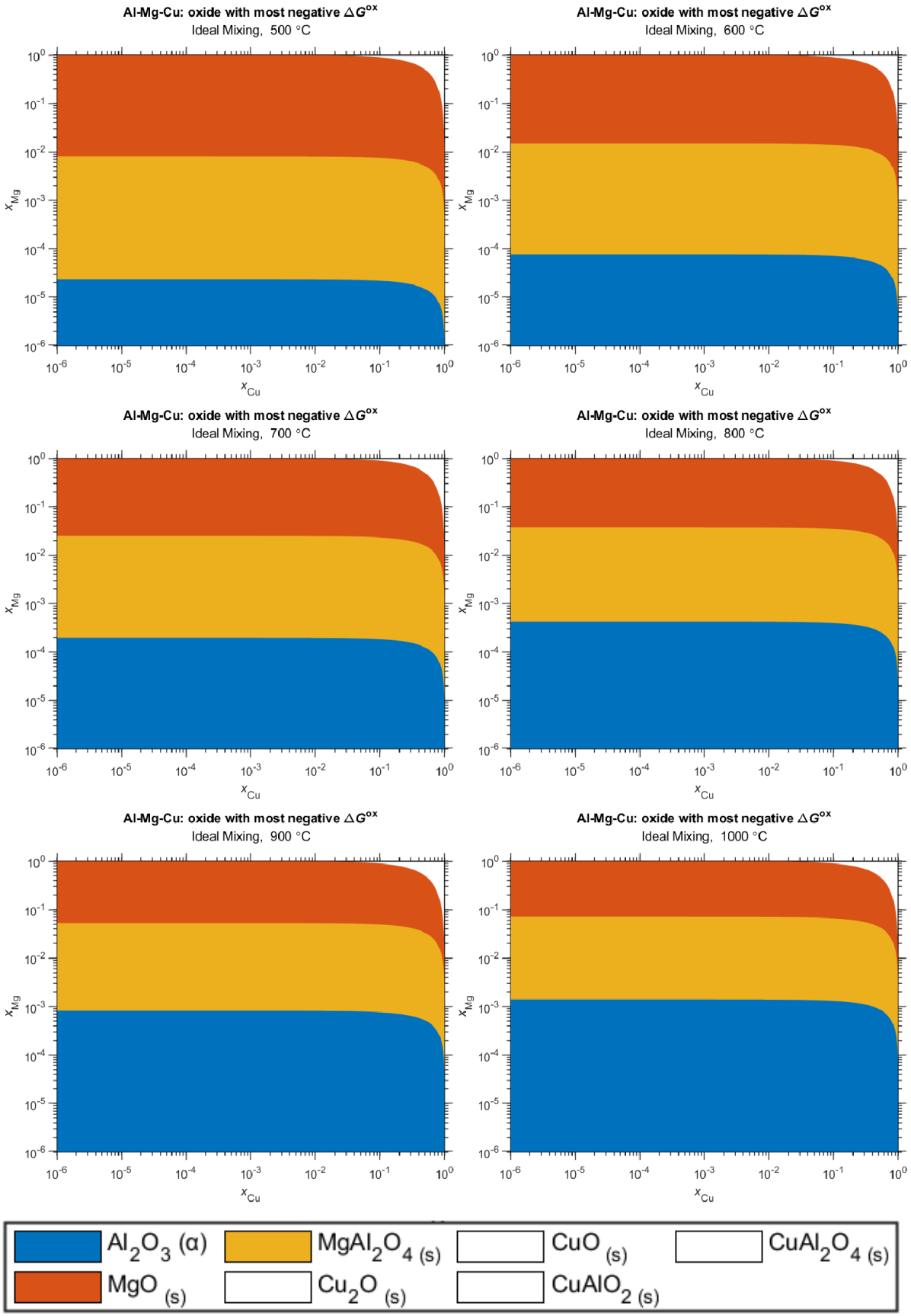
B.6.1.2. Al-Mg-Ca


Al-Mg-Ca: oxide with most negative ΔG°ox
Ideal Mixing, 500 °C
Al-Mg-Ca: oxide with most negative ΔG°ox
Ideal Mixing, 600 °C
Al-Mg-Ca: oxide with most negative ΔG°ox
Ideal Mixing, 700 °C
Al-Mg-Ca: oxide with most negative ΔG°ox
Ideal Mixing, 800 °C
Al-Mg-Ca: oxide with most negative ΔG°ox
Ideal Mixing, 900 °C
Al-Mg-Ca: oxide with most negative ΔG°ox
Ideal Mixing, 1000 °C
x_Mg
x_Ca
Al2O3 (α)
CaO (s)
CaAl2O4 (s)
Ca3MgAl4O10 (s)
MgO (s)
Ca3Al2O6 (s)
CaAl4O7 (s)
CaMg2Al16O27 (s)
MgAl2O4 (s)
Ca12Al14O33 (s)
CaAl12O19 (s)
Ca2Mg2Al28O46 (s)

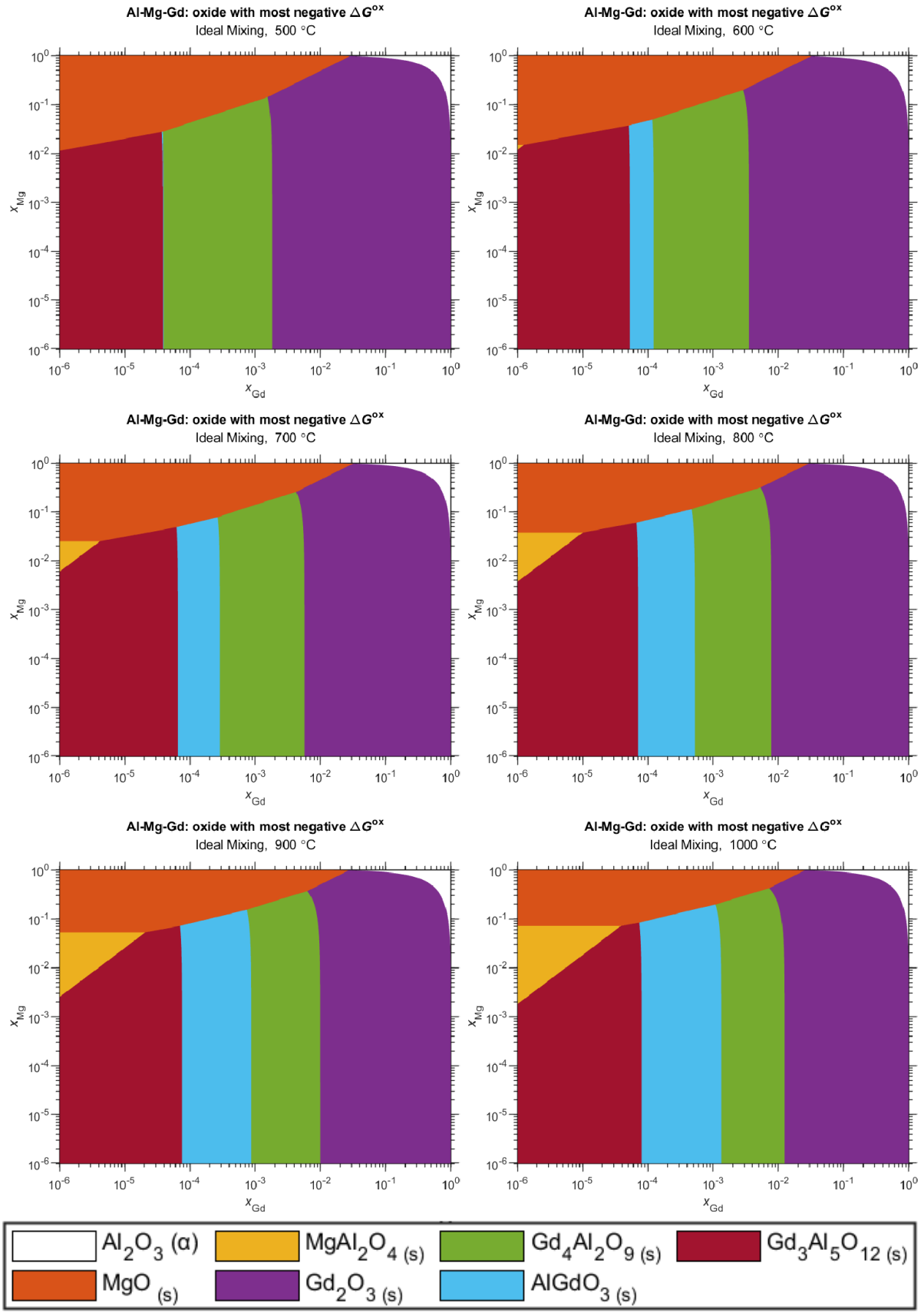
B.6.1.3. Al-Mg-Ce


Al-Mg-Ce: oxide with most negative ΔG°ox
Ideal Mixing, 500 °C
Al-Mg-Ce: oxide with most negative ΔG°ox
Ideal Mixing, 600 °C
Al-Mg-Ce: oxide with most negative ΔG°ox
Ideal Mixing, 700 °C
Al-Mg-Ce: oxide with most negative ΔG°ox
Ideal Mixing, 800 °C
Al-Mg-Ce: oxide with most negative ΔG°ox
Ideal Mixing, 900 °C
Al-Mg-Ce: oxide with most negative ΔG°ox
Ideal Mixing, 1000 °C
x_Mg
x_Ce
Al2O3 (α)
MgO (s)
MgAl2O4 (s)
Ce2O3 (s)
Ce18O31 (s)
Ce6O11 (s)
CeO2 (s)
Ce4Al2O9 (s)
CeAlO3 (s)
Ce3Al5O12 (s)
CeAl11O18 (s)

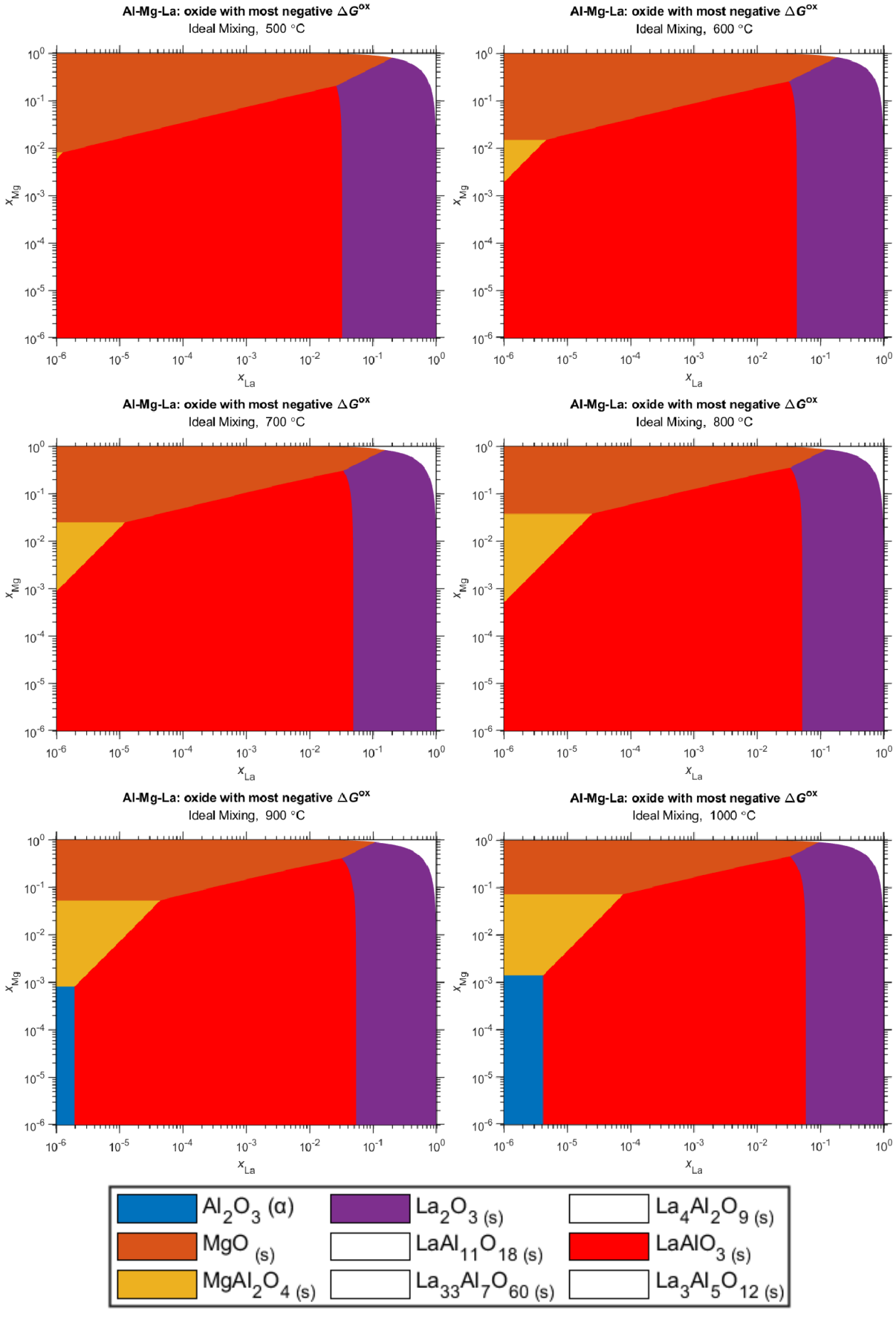
B.6.1.4. Al-Mg-Cu


Al-Mg-Cu: oxide with most negative ΔG^ox
Ideal Mixing, 500 °C
Al-Mg-Cu: oxide with most negative ΔG^ox
Ideal Mixing, 600 °C
Al-Mg-Cu: oxide with most negative ΔG^ox
Ideal Mixing, 700 °C
Al-Mg-Cu: oxide with most negative ΔG^ox
Ideal Mixing, 800 °C
Al-Mg-Cu: oxide with most negative ΔG^ox
Ideal Mixing, 900 °C
Al-Mg-Cu: oxide with most negative ΔG^ox
Ideal Mixing, 1000 °C
x_Mg
x_Cu
Al2O3 (α)
MgAl2O4 (s)
CuO (s)
CuAl2O4 (s)
MgO (s)
Cu2O (s)
CuAlO2 (s)

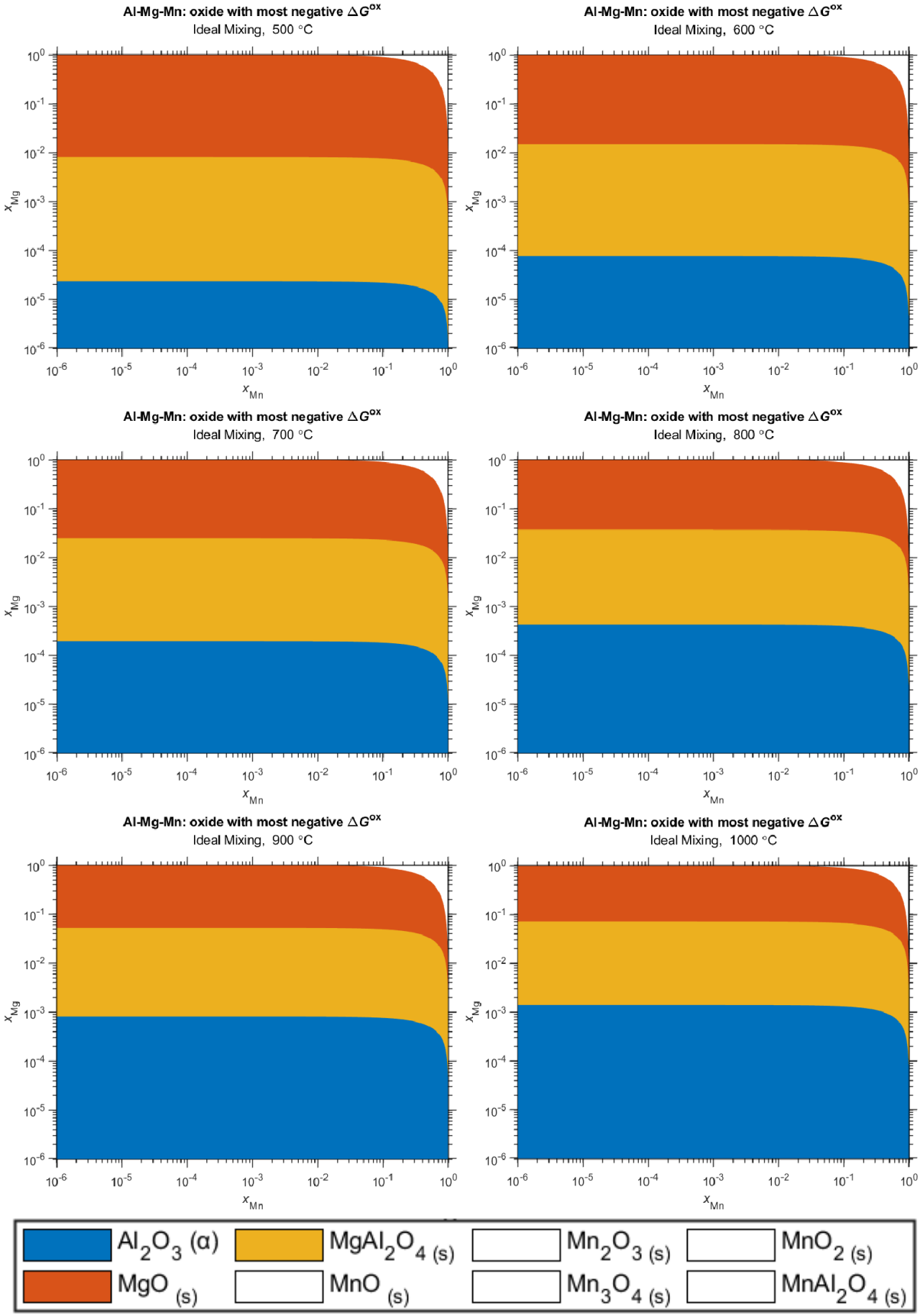
B.6.1.5. Al-Mg-Gd


Al-Mg-Gd: oxide with most negative ΔG^ox
Ideal Mixing, 500 °C
Al-Mg-Gd: oxide with most negative ΔG^ox
Ideal Mixing, 600 °C
Al-Mg-Gd: oxide with most negative ΔG^ox
Ideal Mixing, 700 °C
Al-Mg-Gd: oxide with most negative ΔG^ox
Ideal Mixing, 800 °C
Al-Mg-Gd: oxide with most negative ΔG^ox
Ideal Mixing, 900 °C
Al-Mg-Gd: oxide with most negative ΔG^ox
Ideal Mixing, 1000 °C
x_Mg
x_Gd
Al2O3 (α)
MgAl2O4 (s)
Gd4Al2O9 (s)
Gd3Al5O12 (s)
MgO (s)
Gd2O3 (s)
AlGdO3 (s)

B.6.1.6. Al-Mg-La

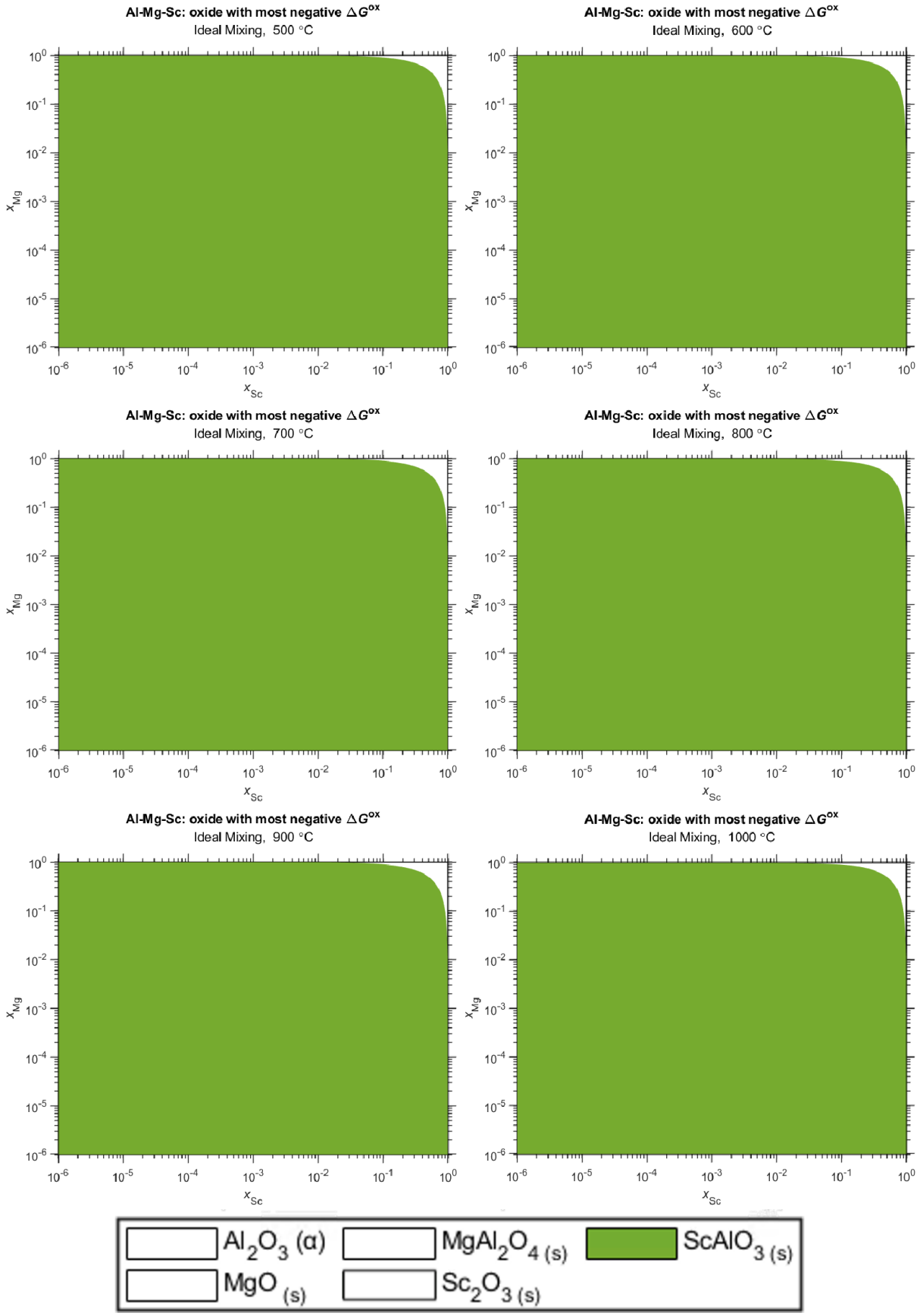

Al-Mg-La: oxide with most negative ΔG^ox
Ideal Mixing, 500 °C
Al-Mg-La: oxide with most negative ΔG^ox
Ideal Mixing, 600 °C
Al-Mg-La: oxide with most negative ΔG^ox
Ideal Mixing, 700 °C
Al-Mg-La: oxide with most negative ΔG^ox
Ideal Mixing, 800 °C
Al-Mg-La: oxide with most negative ΔG^ox
Ideal Mixing, 900 °C
Al-Mg-La: oxide with most negative ΔG^ox
Ideal Mixing, 1000 °C
x_Mg
x_La
Al2O3 (α)
La2O3 (s)
La4Al2O9 (s)
MgO (s)
LaAl11O18 (s)
LaAlO3 (s)
MgAl2O4 (s)
La33Al7O60 (s)
La3Al5O12 (s)

B.6.1.7. Al-Mg-Mn

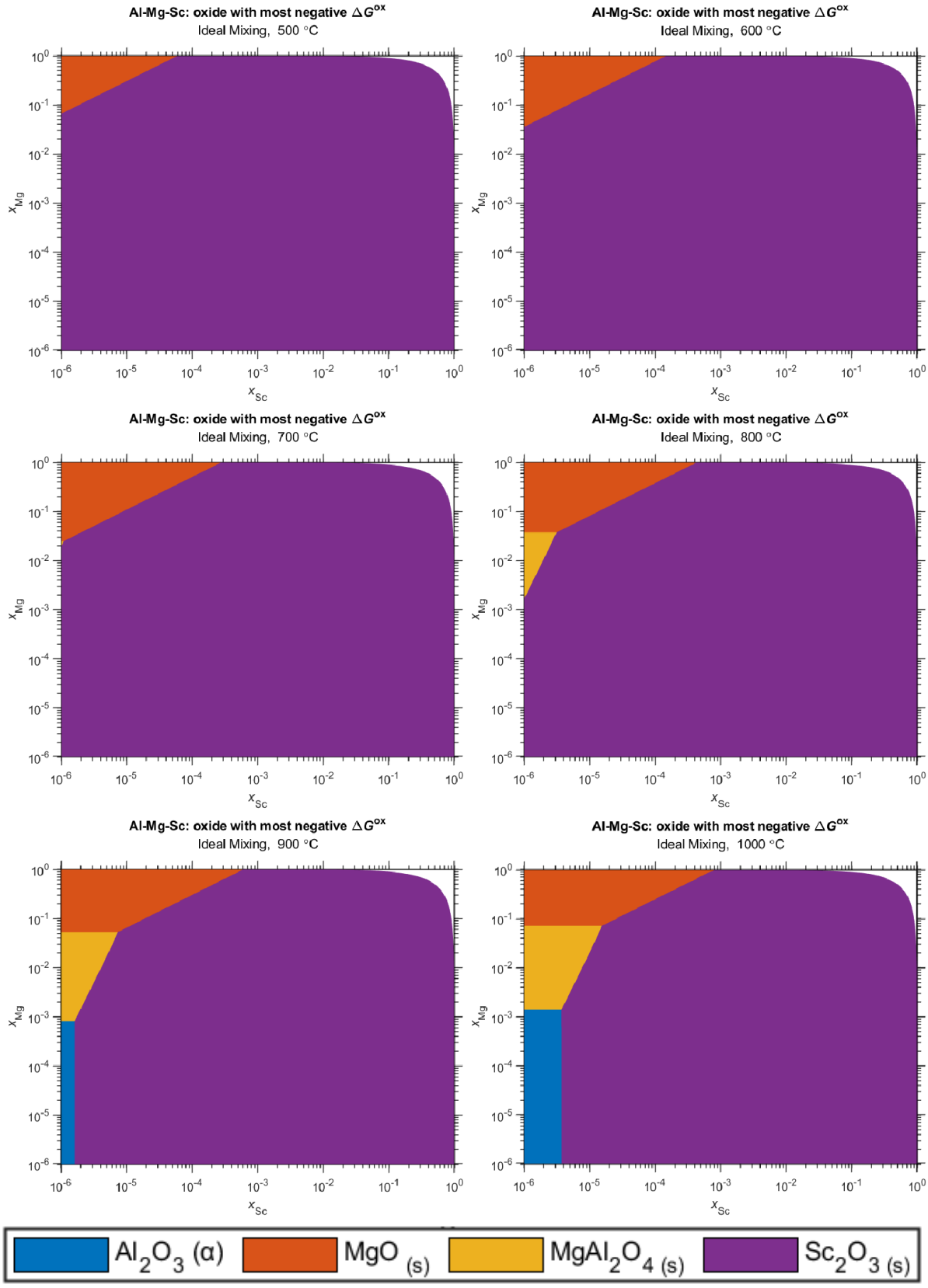

Al-Mg-Mn: oxide with most negative ΔG^ox
Ideal Mixing, 500 °C
Al-Mg-Mn: oxide with most negative ΔG^ox
Ideal Mixing, 600 °C
Al-Mg-Mn: oxide with most negative ΔG^ox
Ideal Mixing, 700 °C
Al-Mg-Mn: oxide with most negative ΔG^ox
Ideal Mixing, 800 °C
Al-Mg-Mn: oxide with most negative ΔG^ox
Ideal Mixing, 900 °C
Al-Mg-Mn: oxide with most negative ΔG^ox
Ideal Mixing, 1000 °C
x_Mg
x_Mn
Al2O3 (α)
MgAl2O4 (s)
Mn2O3 (s)
MnO2 (s)
MgO (s)
MnO (s)
Mn3O4 (s)
MnAl2O4 (s)

B.6.1.8. Al-Mg-Sc

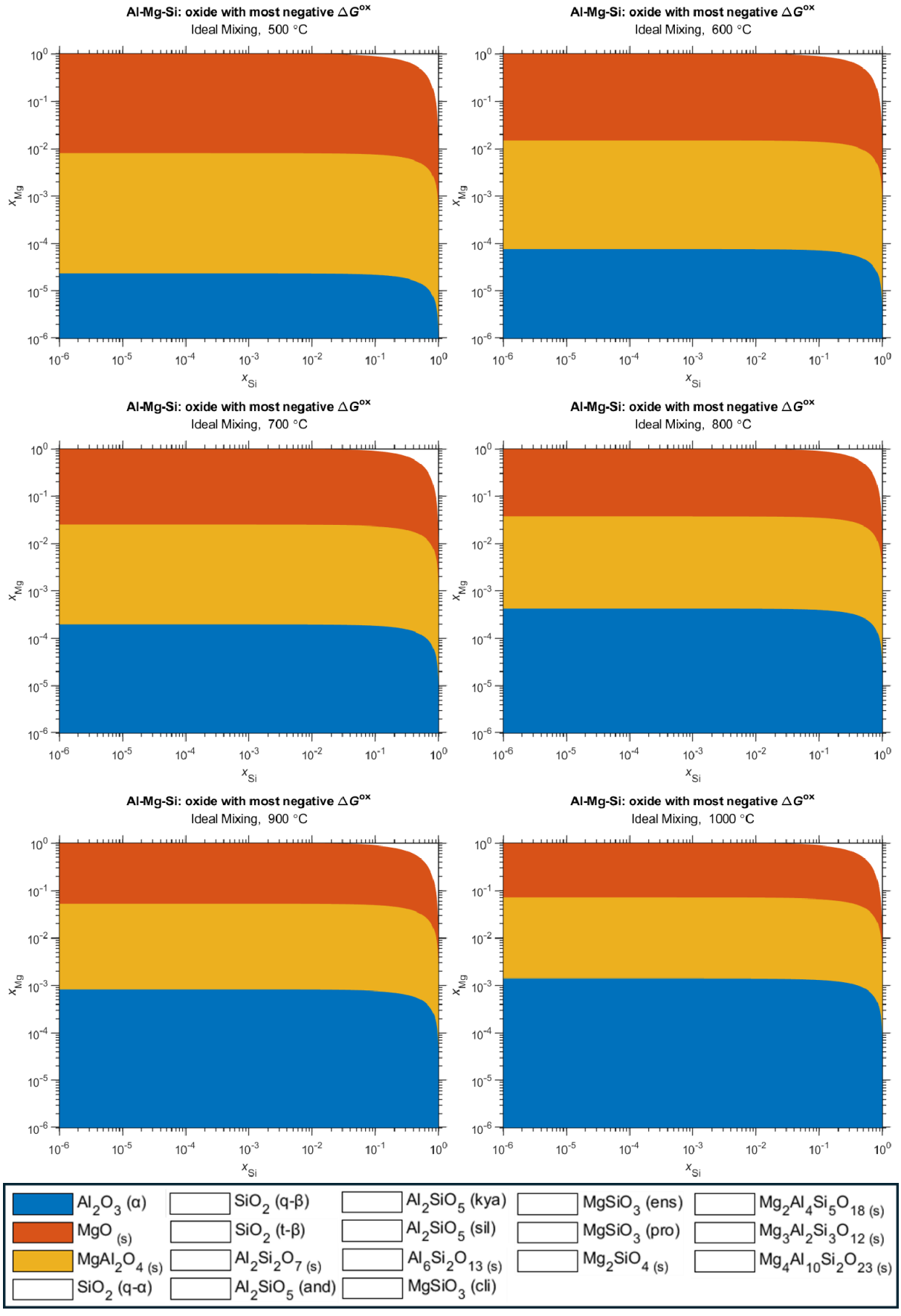
Including $ScAlO_3$



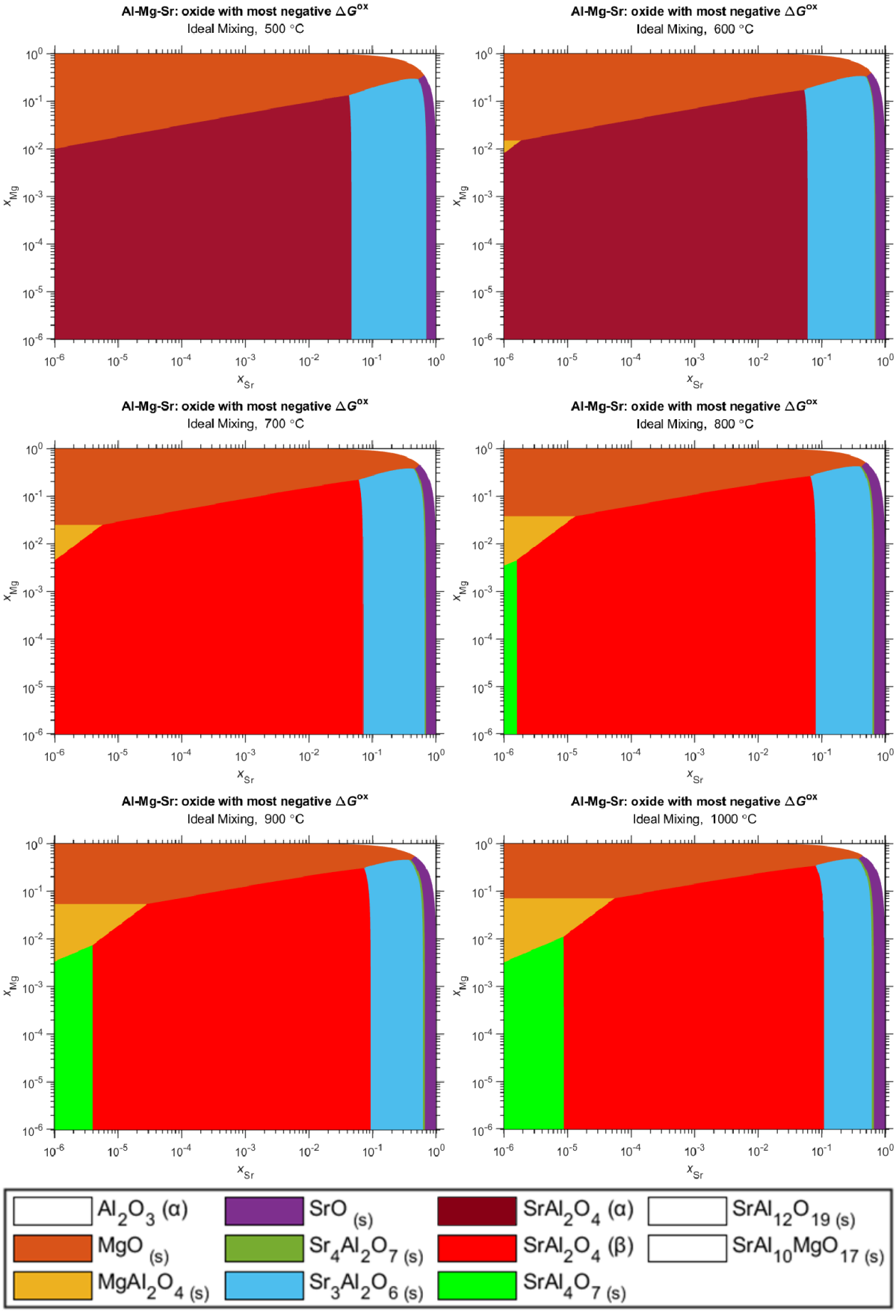
Without $ScAlO_3$



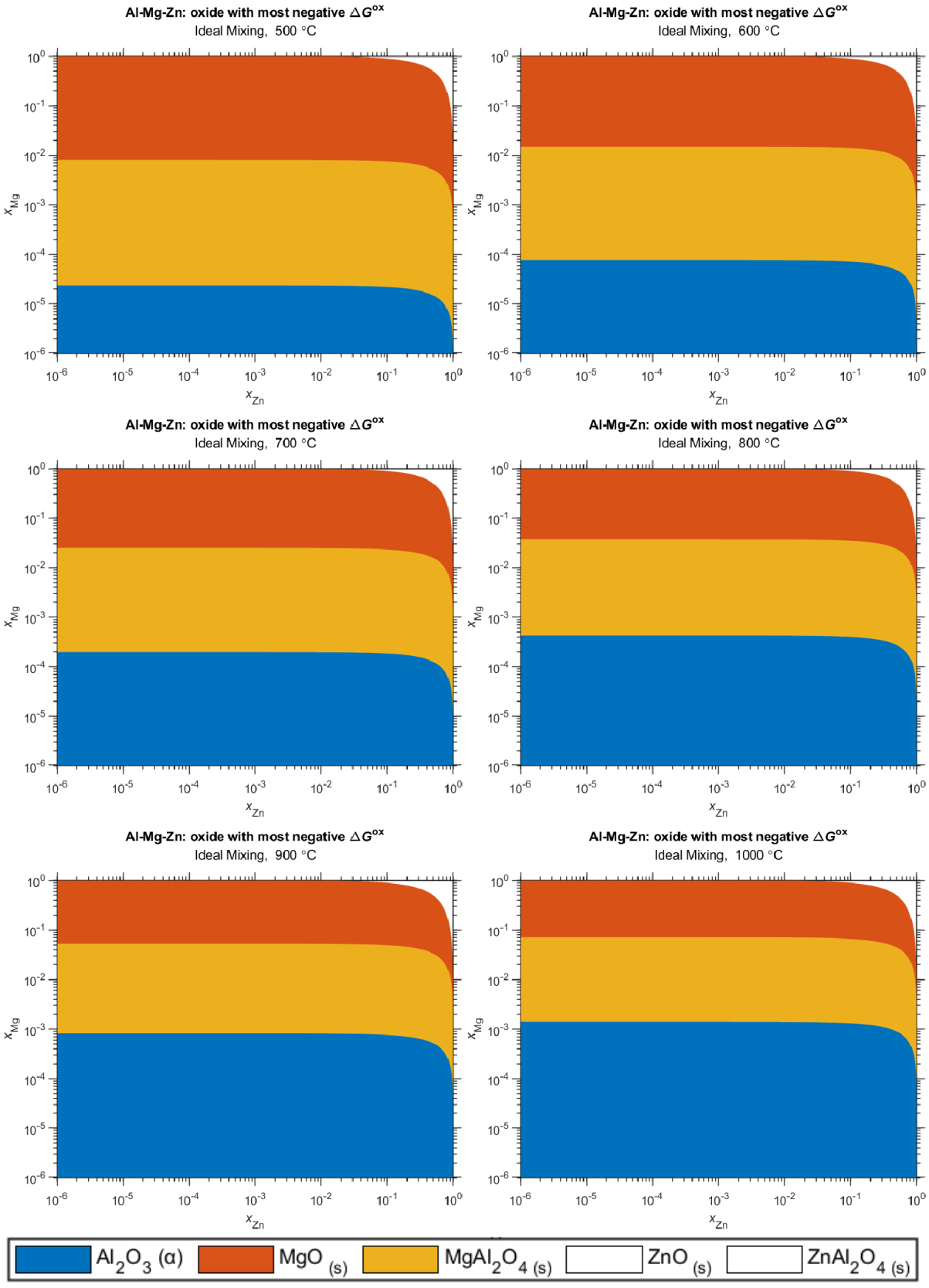
B.6.1.9. Al-Mg-Si


Al-Mg-Si: oxide with most negative ΔG^ox
Ideal Mixing, 500 °C
Al-Mg-Si: oxide with most negative ΔG^ox
Ideal Mixing, 600 °C
Al-Mg-Si: oxide with most negative ΔG^ox
Ideal Mixing, 700 °C
Al-Mg-Si: oxide with most negative ΔG^ox
Ideal Mixing, 800 °C
Al-Mg-Si: oxide with most negative ΔG^ox
Ideal Mixing, 900 °C
Al-Mg-Si: oxide with most negative ΔG^ox
Ideal Mixing, 1000 °C
x_Mg
x_Si
Al2O3 (α)
MgO (s)
MgAl2O4 (s)
SiO2 (q-α)
SiO2 (q-β)
SiO2 (t-β)
Al2Si2O7 (s)
Al2SiO5 (and)
Al2SiO5 (kya)
Al2SiO5 (sil)
Al6Si2O13 (s)
MgSiO3 (cli)
MgSiO3 (ens)
MgSiO3 (pro)
Mg2SiO4 (s)
Mg2Al4Si5O18 (s)
Mg3Al2Si3O12 (s)
Mg4Al10Si2O23 (s)

B.6.1.10. Al-Mg-Sr

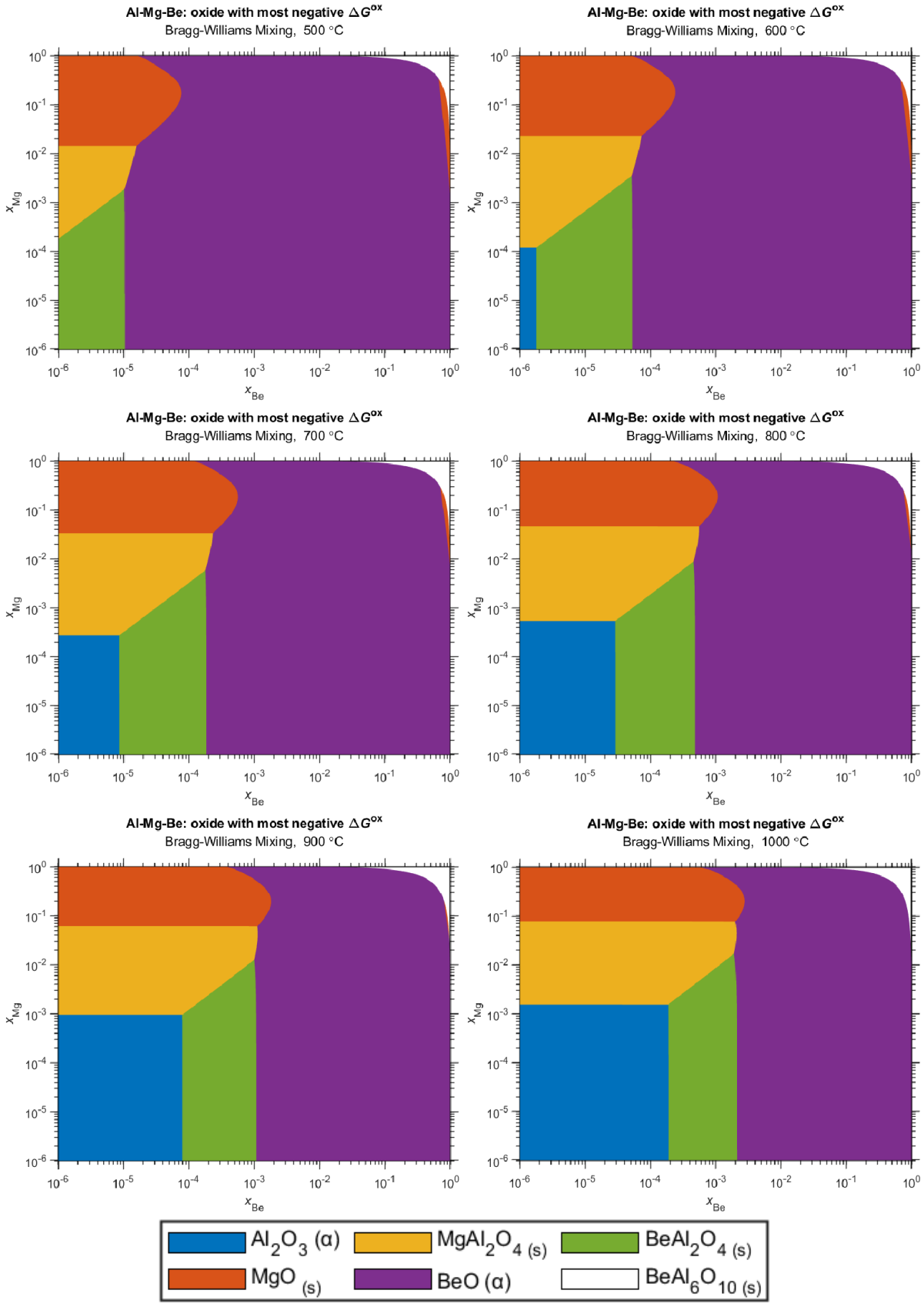


B.6.1.11. Al-Mg-Zn

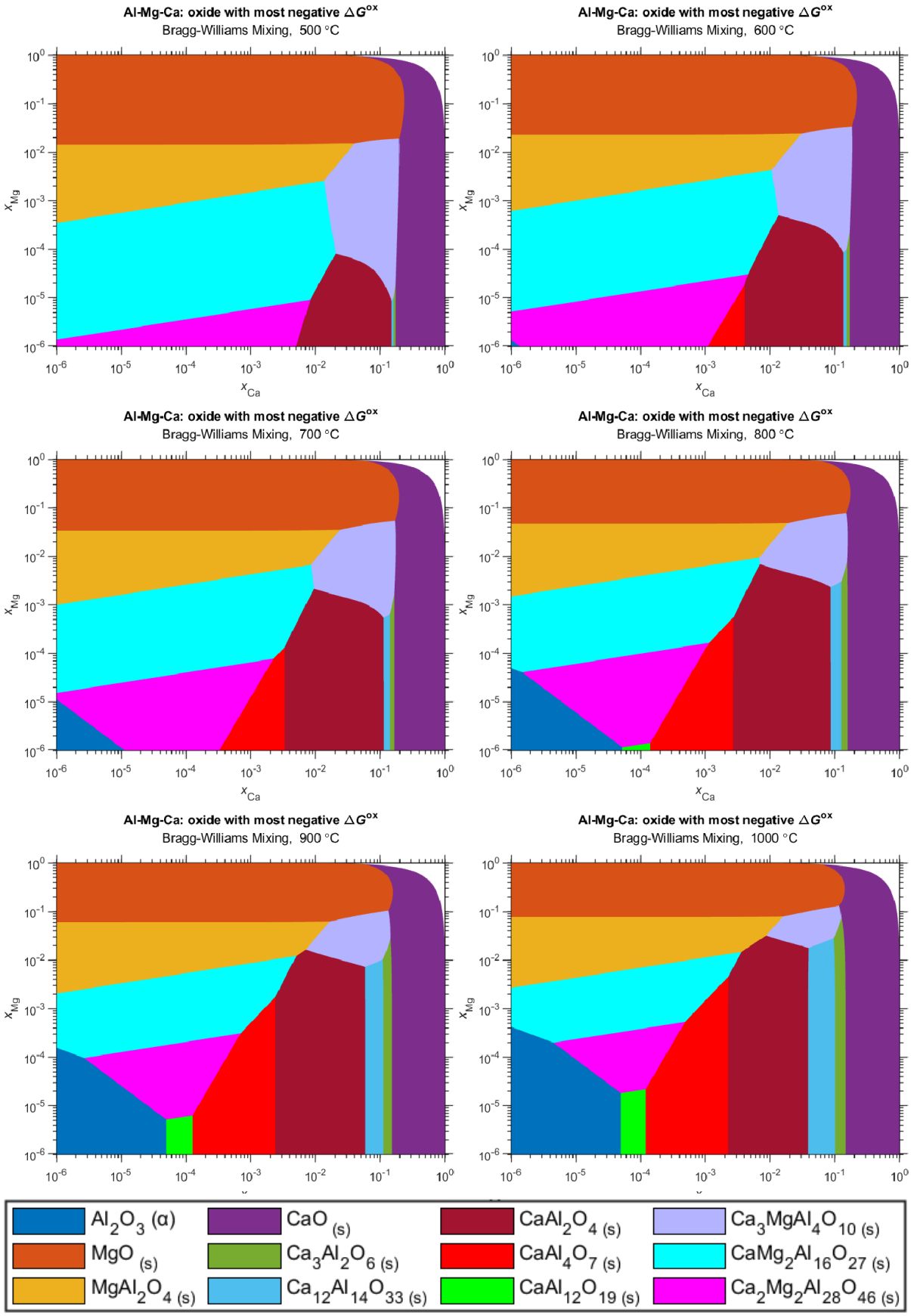


B.6.2. Bragg-Williams mixing

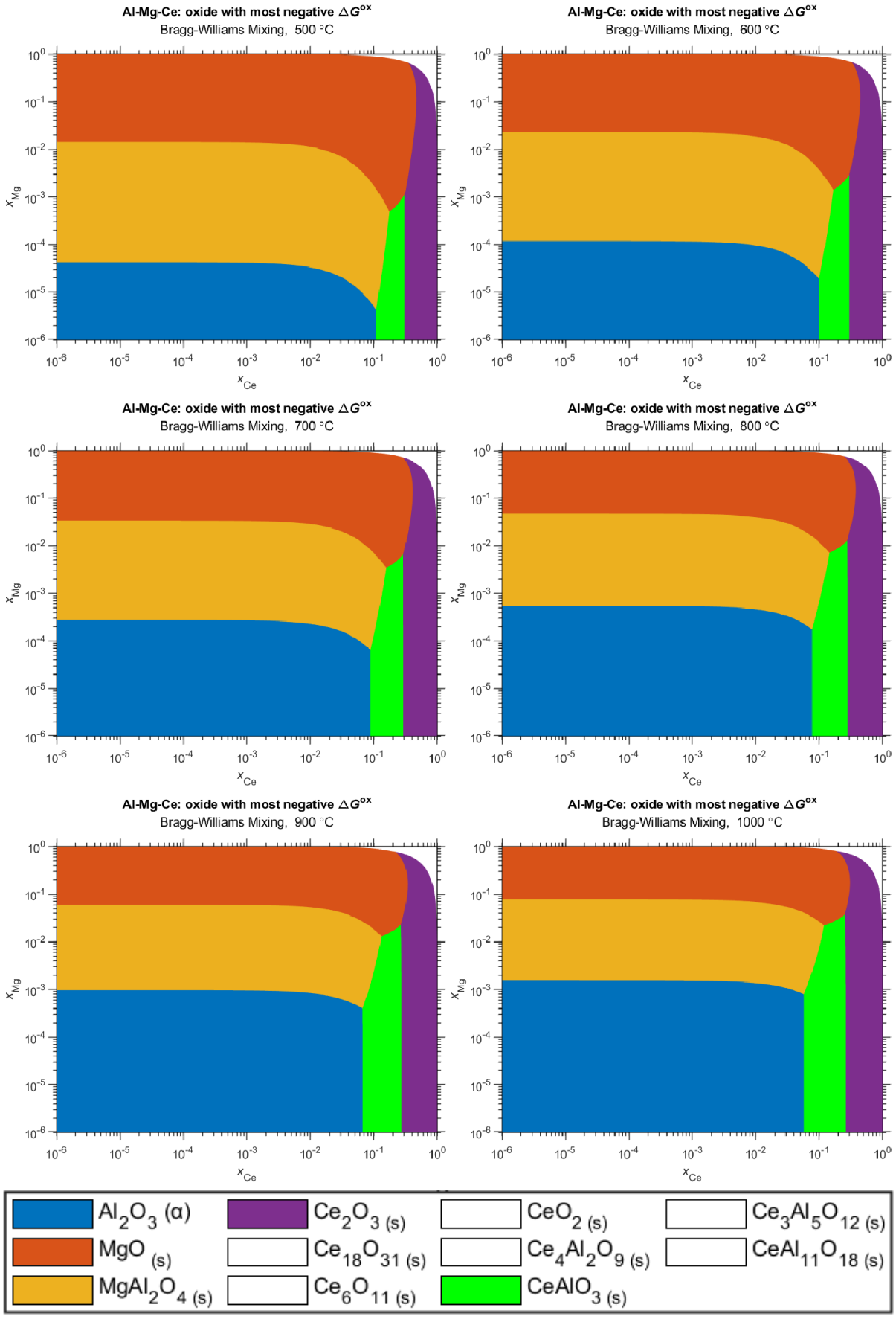
B.6.2.1. Al-Mg-Be



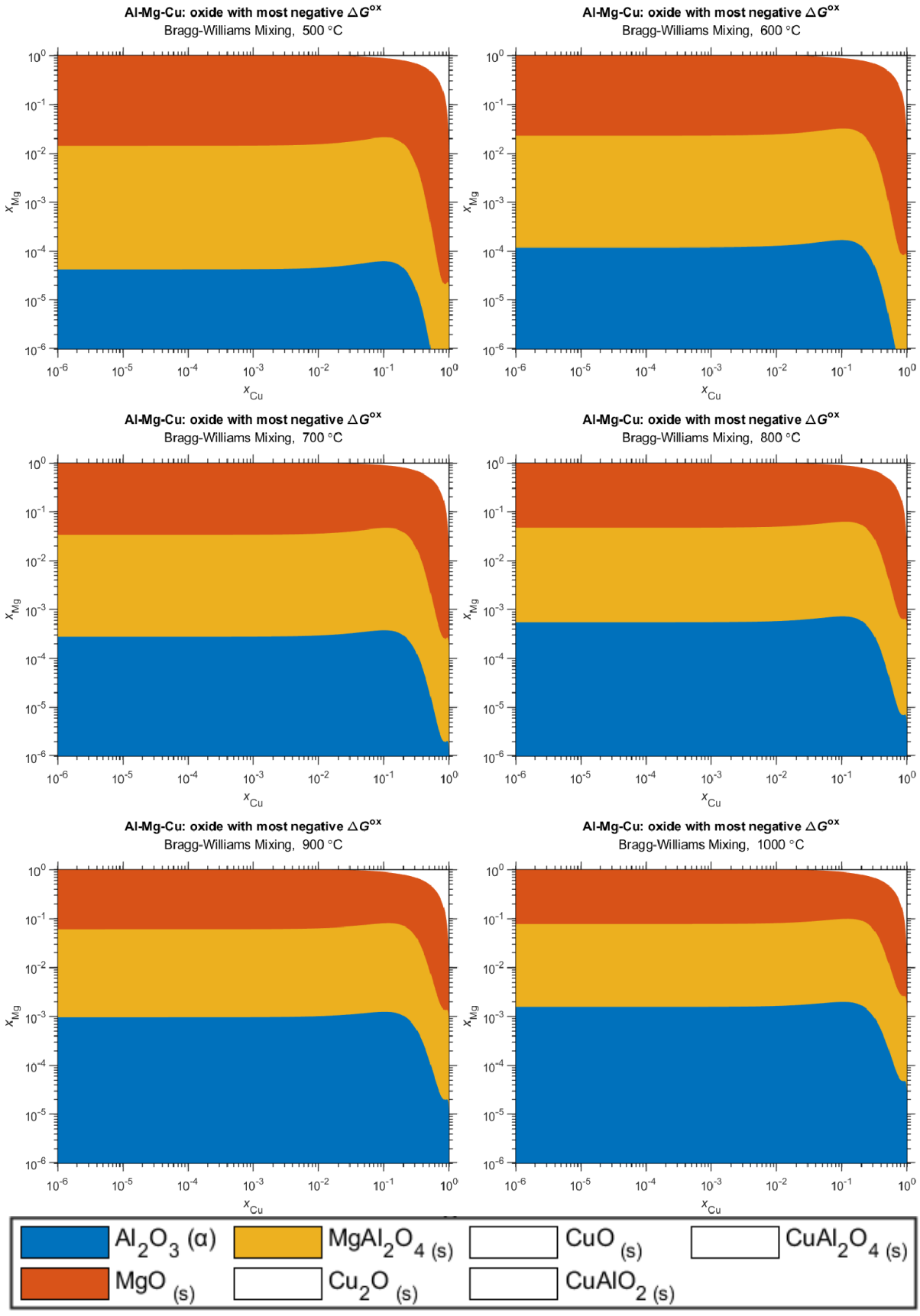
B.6.2.2. Al-Mg-Ca


Al-Mg-Ca: oxide with most negative ΔG°ox
Bragg-Williams Mixing, 500 °C
Al-Mg-Ca: oxide with most negative ΔG°ox
Bragg-Williams Mixing, 600 °C
Al-Mg-Ca: oxide with most negative ΔG°ox
Bragg-Williams Mixing, 700 °C
Al-Mg-Ca: oxide with most negative ΔG°ox
Bragg-Williams Mixing, 800 °C
Al-Mg-Ca: oxide with most negative ΔG°ox
Bragg-Williams Mixing, 900 °C
Al-Mg-Ca: oxide with most negative ΔG°ox
Bragg-Williams Mixing, 1000 °C
x_Mg
x_Ca
Al2O3 (α)
CaO (s)
CaAl2O4 (s)
Ca3MgAl4O10 (s)
MgO (s)
Ca3Al2O6 (s)
CaAl4O7 (s)
CaMg2Al16O27 (s)
MgAl2O4 (s)
Ca12Al14O33 (s)
CaAl12O19 (s)
Ca2Mg2Al28O46 (s)

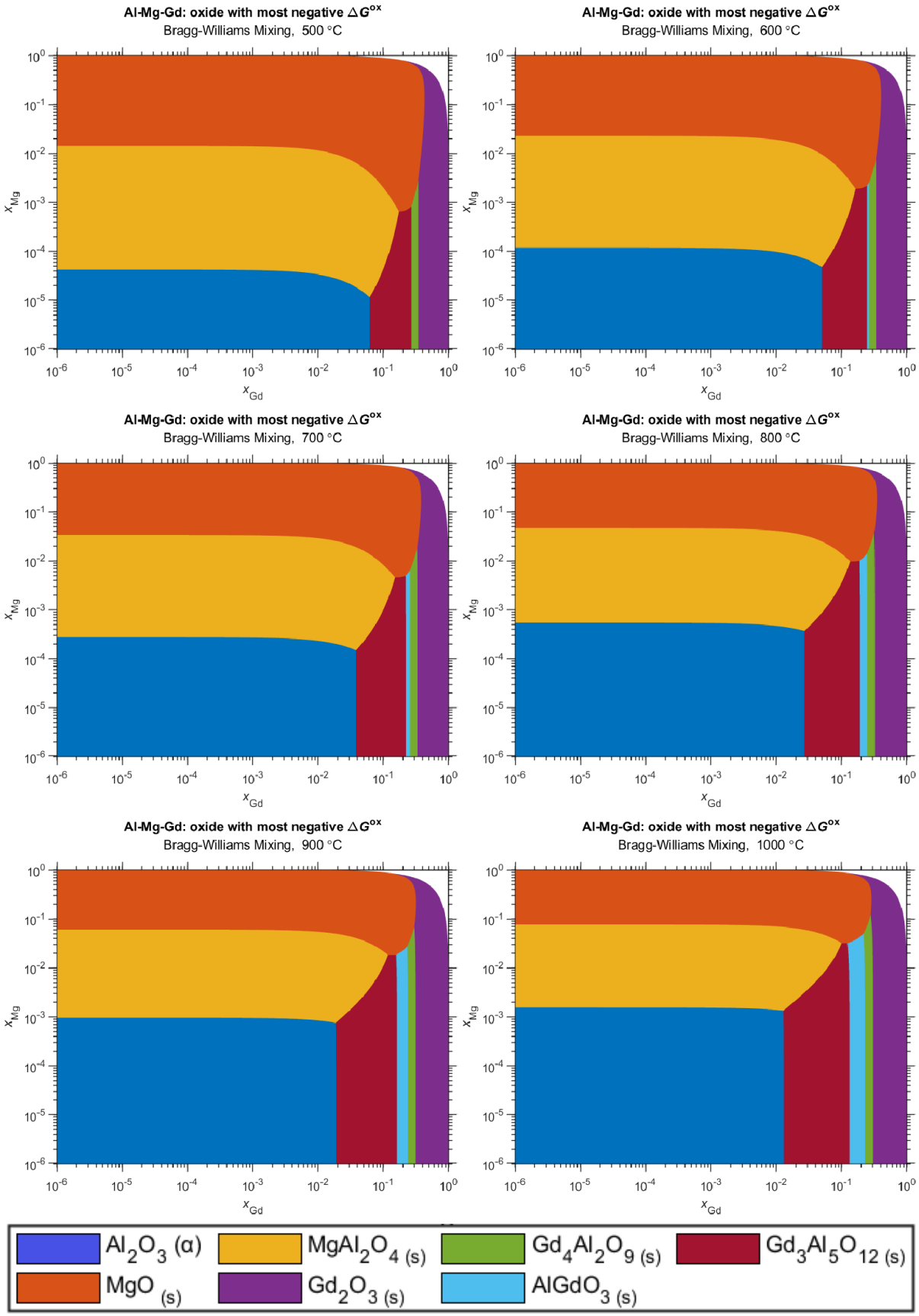
B.6.2.3. Al-Mg-Ce


Al-Mg-Ce: oxide with most negative ΔG^ox
Bragg-Williams Mixing, 500 °C
Al-Mg-Ce: oxide with most negative ΔG^ox
Bragg-Williams Mixing, 600 °C
Al-Mg-Ce: oxide with most negative ΔG^ox
Bragg-Williams Mixing, 700 °C
Al-Mg-Ce: oxide with most negative ΔG^ox
Bragg-Williams Mixing, 800 °C
Al-Mg-Ce: oxide with most negative ΔG^ox
Bragg-Williams Mixing, 900 °C
Al-Mg-Ce: oxide with most negative ΔG^ox
Bragg-Williams Mixing, 1000 °C
x_Mg
x_Ce
Al2O3 (α)
MgO (s)
MgAl2O4 (s)
Ce2O3 (s)
Ce18O31 (s)
Ce6O11 (s)
CeO2 (s)
Ce4Al2O9 (s)
CeAlO3 (s)
Ce3Al5O12 (s)
CeAl11O18 (s)

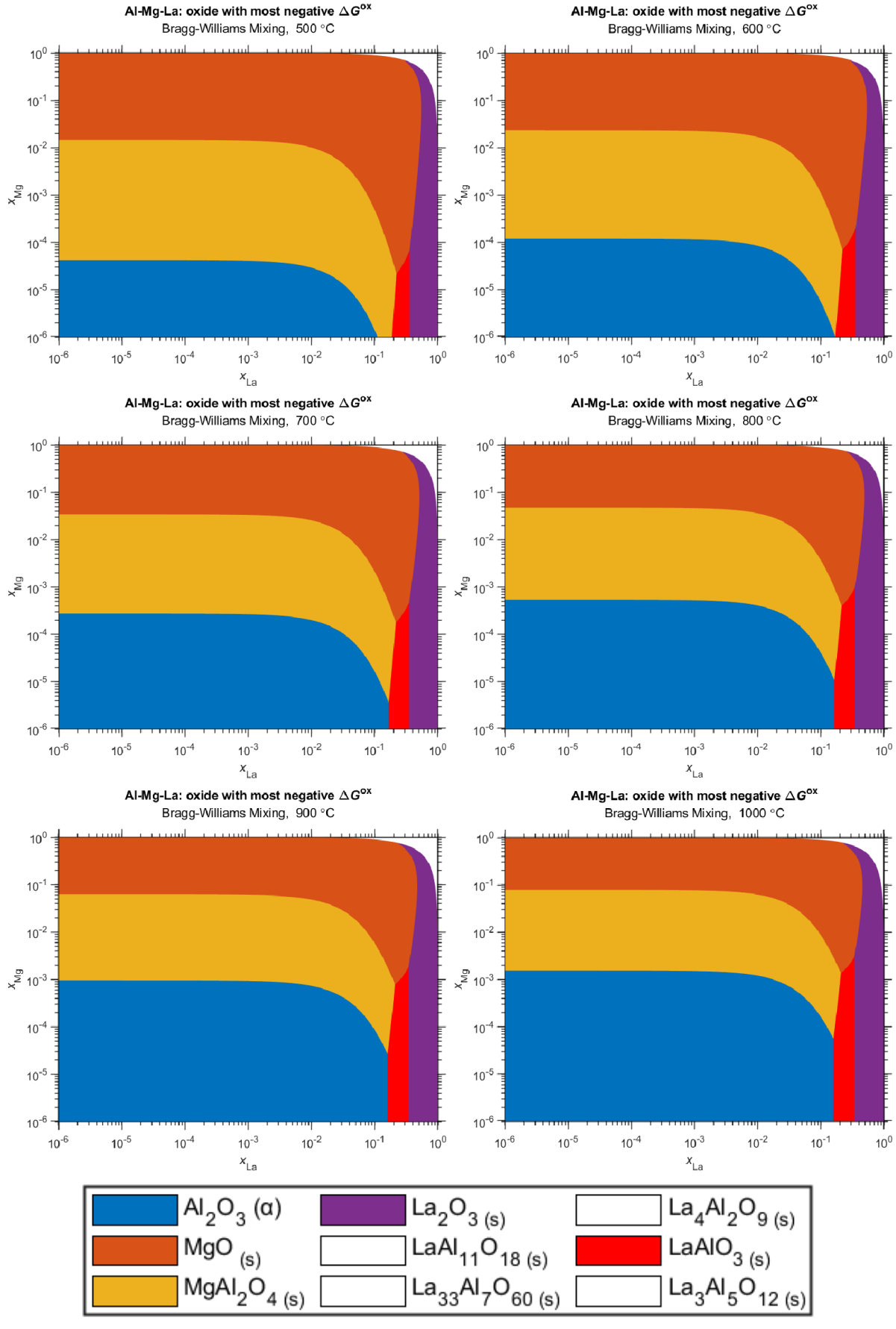
B.6.2.4. Al-Mg-Cu


Al-Mg-Cu: oxide with most negative ΔG°ox
Bragg-Williams Mixing, 500 °C
Al-Mg-Cu: oxide with most negative ΔG°ox
Bragg-Williams Mixing, 600 °C
Al-Mg-Cu: oxide with most negative ΔG°ox
Bragg-Williams Mixing, 700 °C
Al-Mg-Cu: oxide with most negative ΔG°ox
Bragg-Williams Mixing, 800 °C
Al-Mg-Cu: oxide with most negative ΔG°ox
Bragg-Williams Mixing, 900 °C
Al-Mg-Cu: oxide with most negative ΔG°ox
Bragg-Williams Mixing, 1000 °C
x_Mg
x_Cu
Al2O3 (α)
MgAl2O4 (s)
CuO (s)
CuAl2O4 (s)
MgO (s)
Cu2O (s)
CuAlO2 (s)

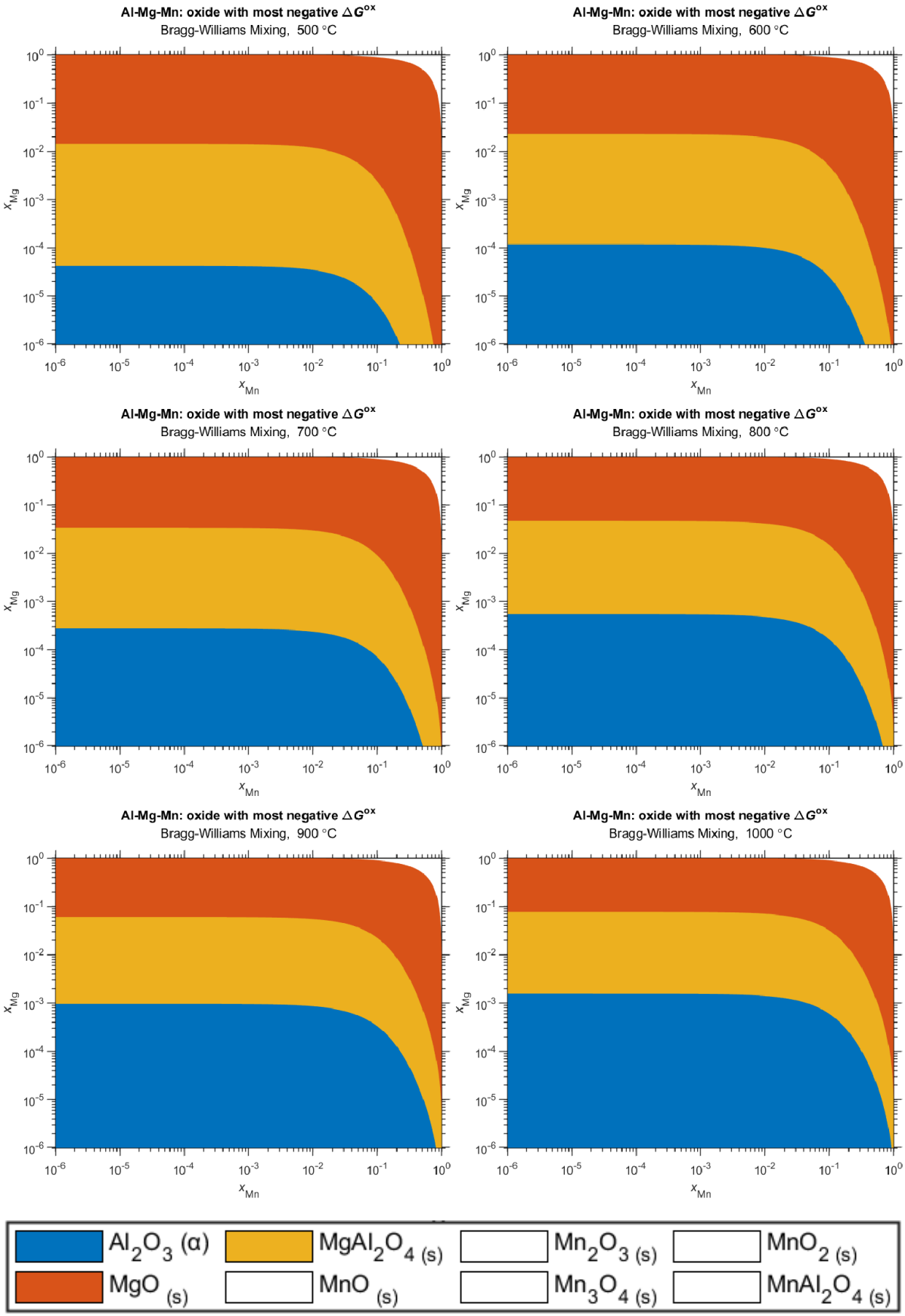
B.6.2.5. Al-Mg-Gd


Al-Mg-Gd: oxide with most negative ΔG^ox
Bragg-Williams Mixing, 500 °C
Al-Mg-Gd: oxide with most negative ΔG^ox
Bragg-Williams Mixing, 600 °C
Al-Mg-Gd: oxide with most negative ΔG^ox
Bragg-Williams Mixing, 700 °C
Al-Mg-Gd: oxide with most negative ΔG^ox
Bragg-Williams Mixing, 800 °C
Al-Mg-Gd: oxide with most negative ΔG^ox
Bragg-Williams Mixing, 900 °C
Al-Mg-Gd: oxide with most negative ΔG^ox
Bragg-Williams Mixing, 1000 °C
x_Mg
x_Gd
Al2O3 (α)
MgAl2O4 (s)
Gd4Al2O9 (s)
Gd3Al5O12 (s)
MgO (s)
Gd2O3 (s)
AlGdO3 (s)

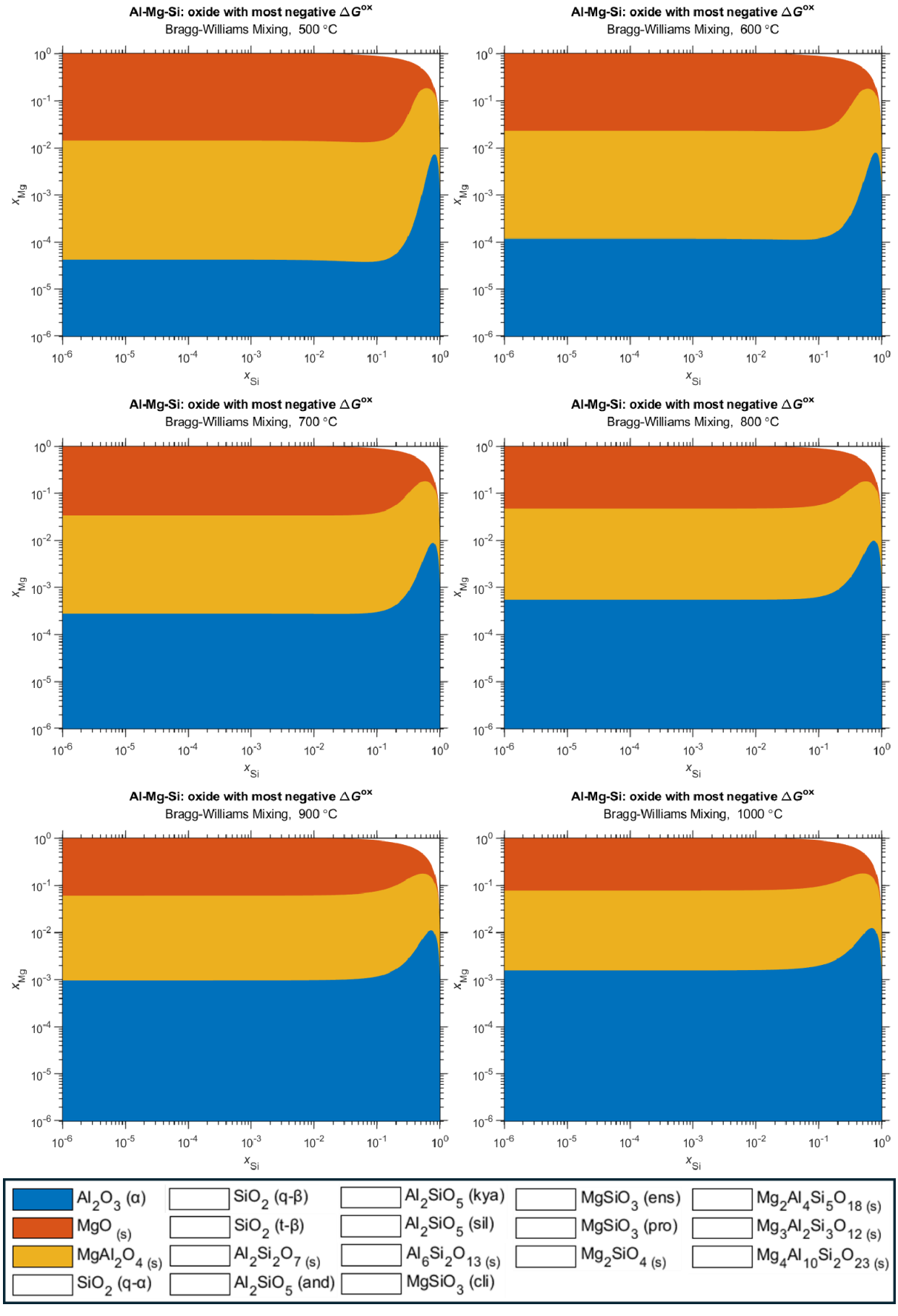
B.6.2.6. Al-Mg-La


Al-Mg-La: oxide with most negative ΔG^ox
Bragg-Williams Mixing, 500 °C
Al-Mg-La: oxide with most negative ΔG^ox
Bragg-Williams Mixing, 600 °C
Al-Mg-La: oxide with most negative ΔG^ox
Bragg-Williams Mixing, 700 °C
Al-Mg-La: oxide with most negative ΔG^ox
Bragg-Williams Mixing, 800 °C
Al-Mg-La: oxide with most negative ΔG^ox
Bragg-Williams Mixing, 900 °C
Al-Mg-La: oxide with most negative ΔG^ox
Bragg-Williams Mixing, 1000 °C
x_Mg
x_La
Al2O3 (α)
La2O3 (s)
La4Al2O9 (s)
MgO (s)
LaAl11O18 (s)
LaAlO3 (s)
MgAl2O4 (s)
La33Al7O60 (s)
La3Al5O12 (s)

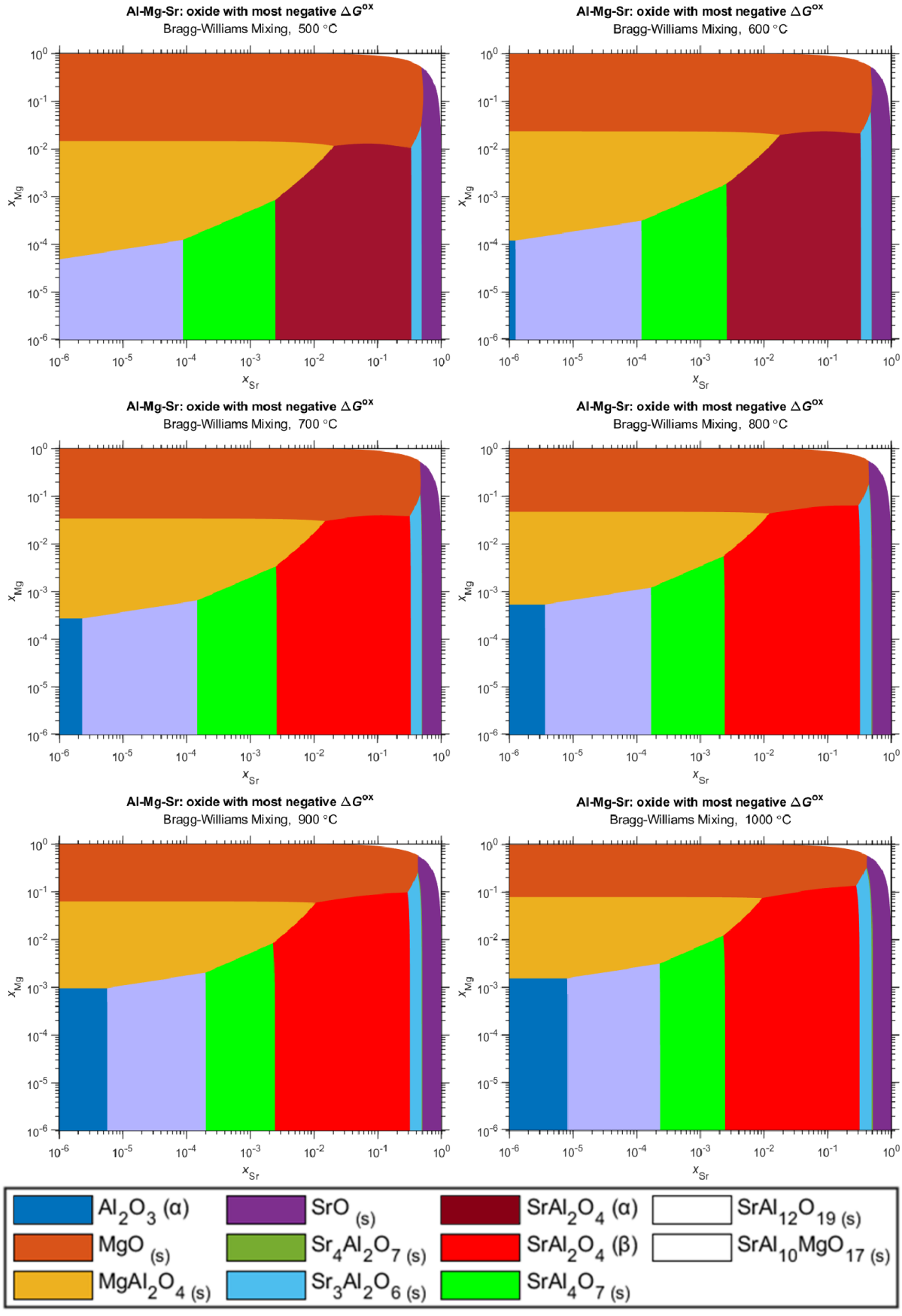
B.6.2.7. Al-Mg-Mn


Al-Mg-Mn: oxide with most negative ΔG°ox
Bragg-Williams Mixing, 500 °C
Al-Mg-Mn: oxide with most negative ΔG°ox
Bragg-Williams Mixing, 600 °C
Al-Mg-Mn: oxide with most negative ΔG°ox
Bragg-Williams Mixing, 700 °C
Al-Mg-Mn: oxide with most negative ΔG°ox
Bragg-Williams Mixing, 800 °C
Al-Mg-Mn: oxide with most negative ΔG°ox
Bragg-Williams Mixing, 900 °C
Al-Mg-Mn: oxide with most negative ΔG°ox
Bragg-Williams Mixing, 1000 °C
x_Mg
x_Mn
Al2O3 (α)
MgAl2O4 (s)
Mn2O3 (s)
MnO2 (s)
MgO (s)
MnO (s)
Mn3O4 (s)
MnAl2O4 (s)

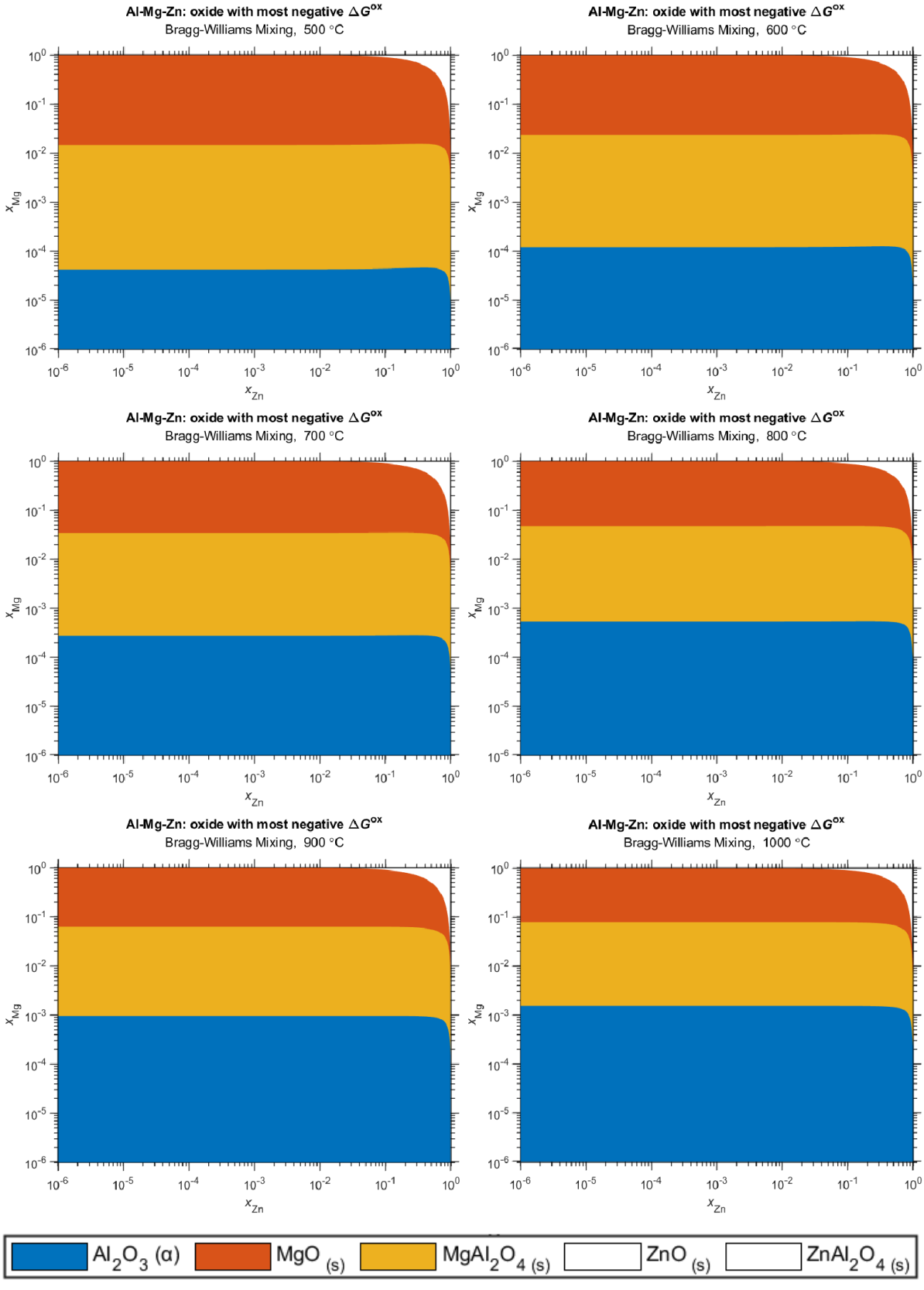
B.6.2.8. Al-Mg-Si


Al-Mg-Si: oxide with most negative ΔG^ox
Bragg-Williams Mixing, 500 °C
Al-Mg-Si: oxide with most negative ΔG^ox
Bragg-Williams Mixing, 600 °C
Al-Mg-Si: oxide with most negative ΔG^ox
Bragg-Williams Mixing, 700 °C
Al-Mg-Si: oxide with most negative ΔG^ox
Bragg-Williams Mixing, 800 °C
Al-Mg-Si: oxide with most negative ΔG^ox
Bragg-Williams Mixing, 900 °C
Al-Mg-Si: oxide with most negative ΔG^ox
Bragg-Williams Mixing, 1000 °C
x_Mg
x_Si
Al2O3 (α)
MgO (s)
MgAl2O4 (s)
SiO2 (q-α)
SiO2 (q-β)
SiO2 (t-β)
Al2Si2O7 (s)
Al2SiO5 (and)
Al2SiO5 (kya)
Al2SiO5 (sil)
Al6Si2O13 (s)
MgSiO3 (cli)
MgSiO3 (ens)
MgSiO3 (pro)
Mg2SiO4 (s)
Mg2Al4Si5O18 (s)
Mg3Al2Si3O12 (s)
Mg4Al10Si2O23 (s)

B.6.2.9. Al-Mg-Sr


Al-Mg-Sr: oxide with most negative ΔG^ox
Bragg-Williams Mixing, 500 °C
Al-Mg-Sr: oxide with most negative ΔG^ox
Bragg-Williams Mixing, 600 °C
Al-Mg-Sr: oxide with most negative ΔG^ox
Bragg-Williams Mixing, 700 °C
Al-Mg-Sr: oxide with most negative ΔG^ox
Bragg-Williams Mixing, 800 °C
Al-Mg-Sr: oxide with most negative ΔG^ox
Bragg-Williams Mixing, 900 °C
Al-Mg-Sr: oxide with most negative ΔG^ox
Bragg-Williams Mixing, 1000 °C
x_Mg
x_Sr
Al2O3 (α)
MgO (s)
MgAl2O4 (s)
SrO (s)
Sr4Al2O7 (s)
Sr3Al2O6 (s)
SrAl2O4 (α)
SrAl2O4 (β)
SrAl4O7 (s)
SrAl12O19 (s)
SrAl10MgO17 (s)

B.6.2.10. Al-Mg-Zn



B.7. Annotated oxide stability diagrams

B.7.1. Binary Al-X systems

B.7.1.1. Data sources

Below is a summary of data used to annotate oxide stability diagrams of binary Al-X alloys (Table B.6). Three methods were generally used in the studies reviewed. Firstly, in 'Melt oxidation' studies, aluminium alloy melts were oxidised, so the data plotted was the products of oxidation against the composition and temperature of the melt. Secondly, in 'Alumina film held in melt' studies, two bars of an aluminium alloy were stacked end to end and melted, causing the alloy melt to react with the native Al_2O_3 layer present at the interface. Over time, the melt reacts with the alumina to form the most thermodynamically favourable oxide, so the data taken was the composition of the alloy, temperature of the melt, and the oxidation products formed after holding. Thirdly, in 'Holding Al_2O_3 against melt' studies, a bulk sample of alumina was held in the melt, which transformed to another, more thermodynamically stable, oxide. Therefore, the data taken was the composition of the melt, temperature of the melt, and the oxide produced.

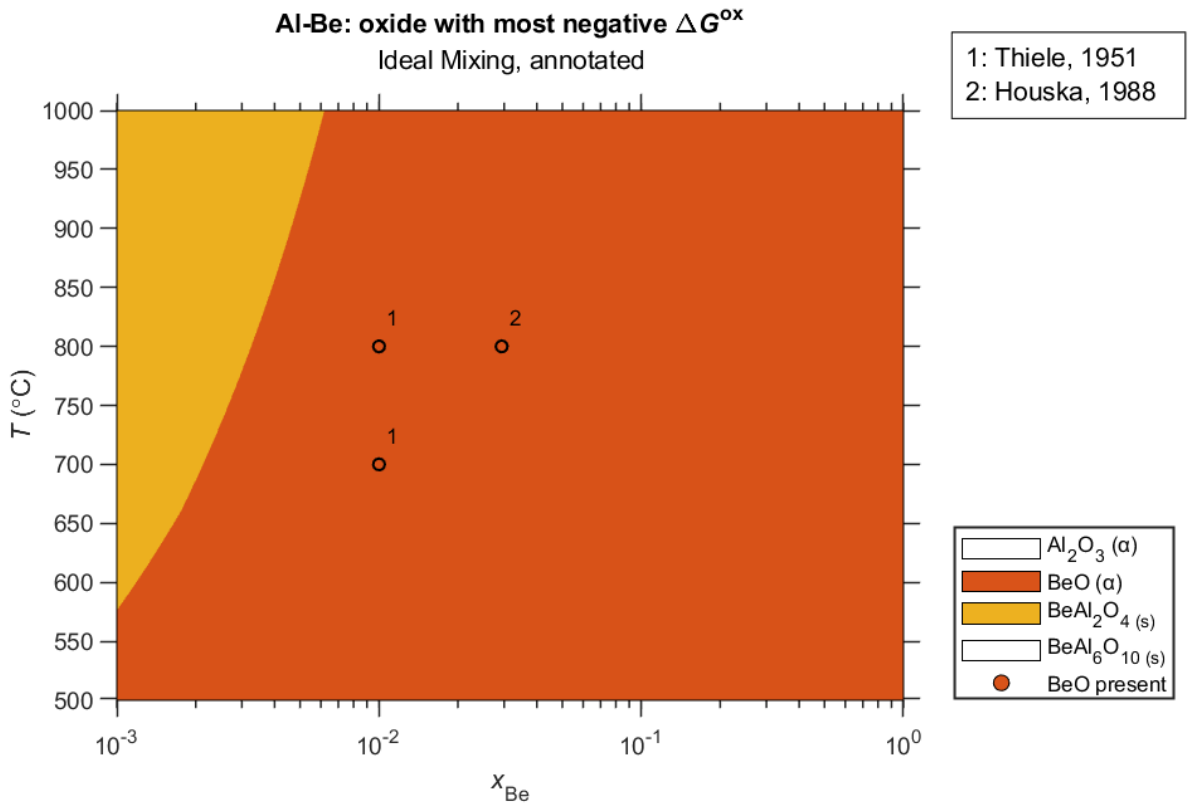
Ref	Text	Elements	Type of study
[48]	Ahmad, 1987	Li	Melt oxidation
[49]	Akbarifar, 2020	Mg	Melt oxidation
[50]	Amirinejhad, 2013	Mg	Alumina film held in melt
[51]	Aryafar, 2010	Mg	Alumina film held in melt
[52]	Bakhtiarani, 2011	Mg	Alumina film held in melt
[53]	Belitskus, 1971	Mg	Melt oxidation
[54]	Brock, 1981	Zn	Melt oxidation
[55]	Cochran, 1977	Mg	Melt oxidation
[56]	Field/Butler, 1983	Li	Melt oxidation
[57]	Field/Scanans, 1983	Li	Melt oxidation
[58]	Fujii, 2003	Sc	Holding Al_2O_3 against melt
[59]	Ganiev, 2018	Ce, La, Sc	Melt oxidation
[60]	Haginoya, 1982	Zn	Melt oxidation
[61]	Haginoya, 1983	Mg	Melt oxidation
[62]	Han, 2023	Li	Holding Al_2O_3 against melt
[63]	Hanabe, 1996	Zn	Melt oxidation
[64]	Hinton, 2016	Mg, Sr	Melt oxidation

[65]	Holdway, 1989	Li	Melt oxidation
[66]	Houska, 1988	Be	Melt oxidation
[67]	Impey, 1990	Mg	Melt oxidation
[68]	Jayaram, 1996	Li, Na	Melt oxidation
[69]	Khaleghifar, 2015	Ca	Alumina film held in melt
[70]	Kim, 2005	Zn	Melt oxidation
[71]	Kouzmichev, 1975	Li	Melt oxidation
[72]	Miresmaeili, 2009	Sr	Melt oxidation
[73]	Nateghian, 2012	Sr	Alumina film held in melt
[74]	Papazian, 1986	Li	Melt oxidation
[75]	Shevchenko, 2017	Ca	Melt oxidation
[76]	Soni, 1991	Li	Melt oxidation
[77]	Thiele, 1951	Be, Ca, Zn	Melt oxidation
[78]	Wu, 2019	Mg	Melt oxidation

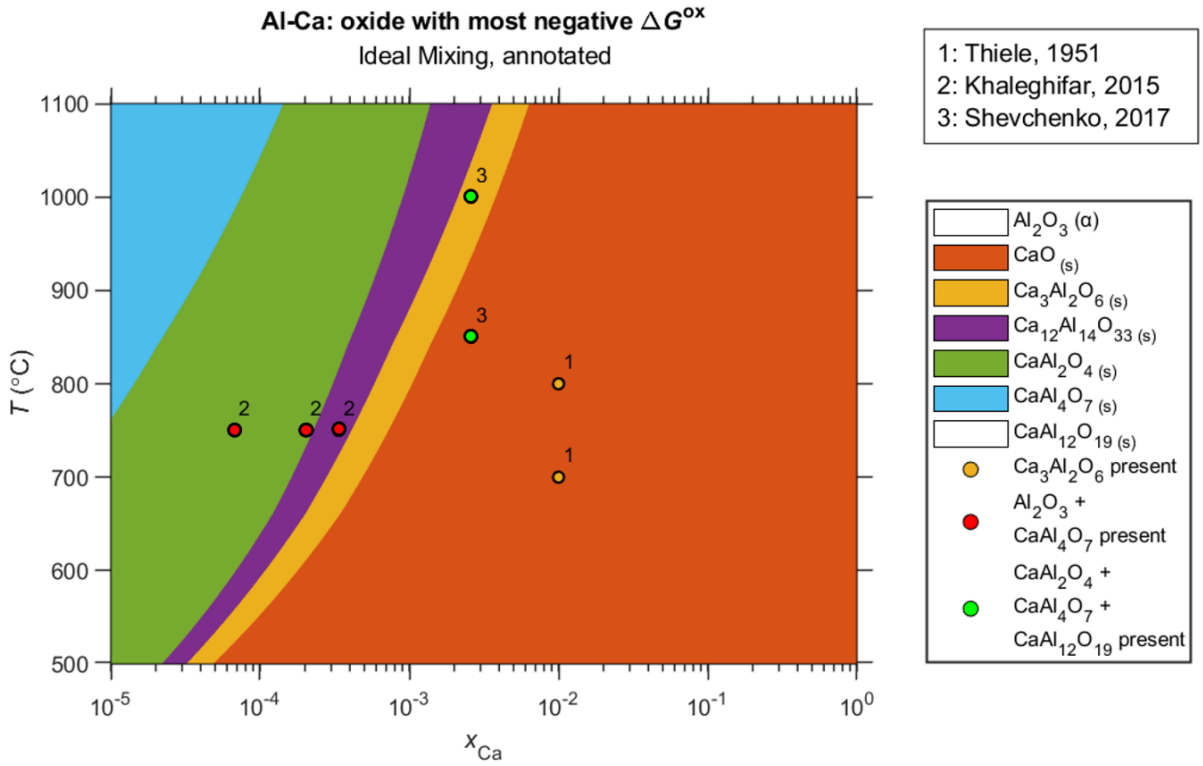
Table B.6. Summary of references and data sources for binary systems, including method used in study.

B.7.1.2. Ideal mixing

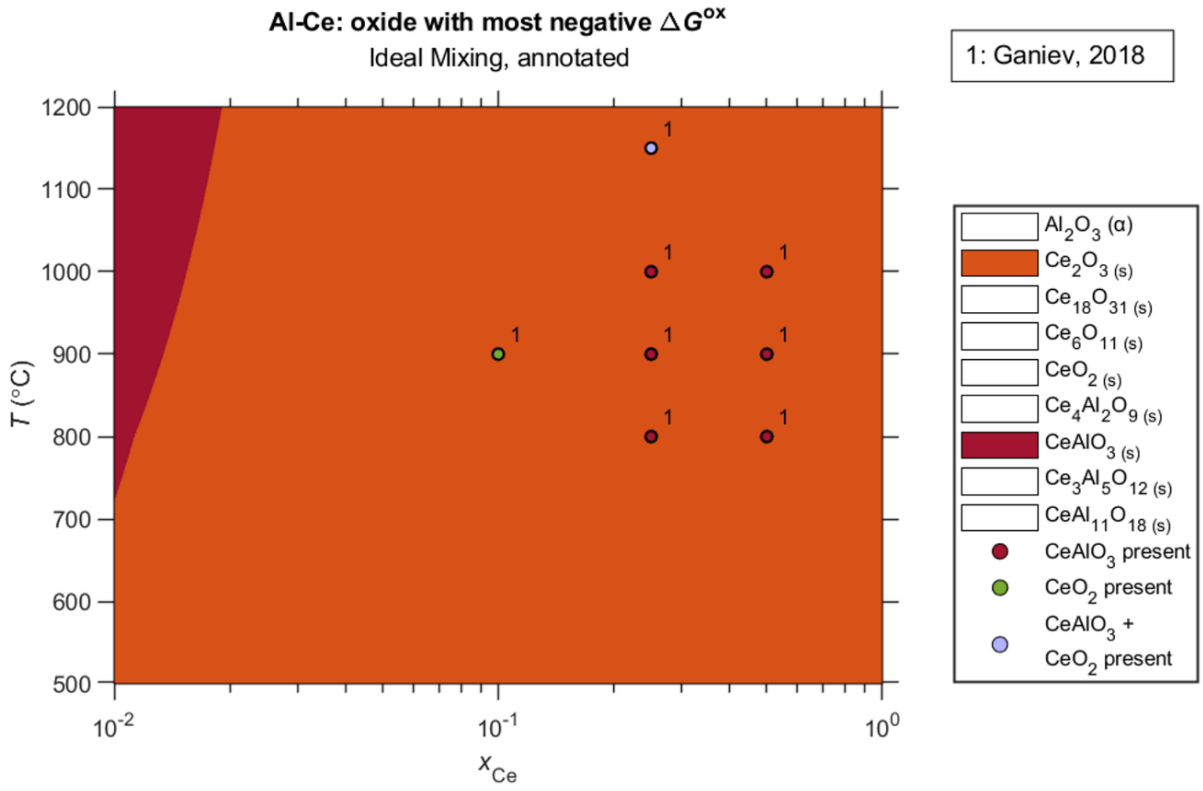
B.7.1.2.1. Al-Be



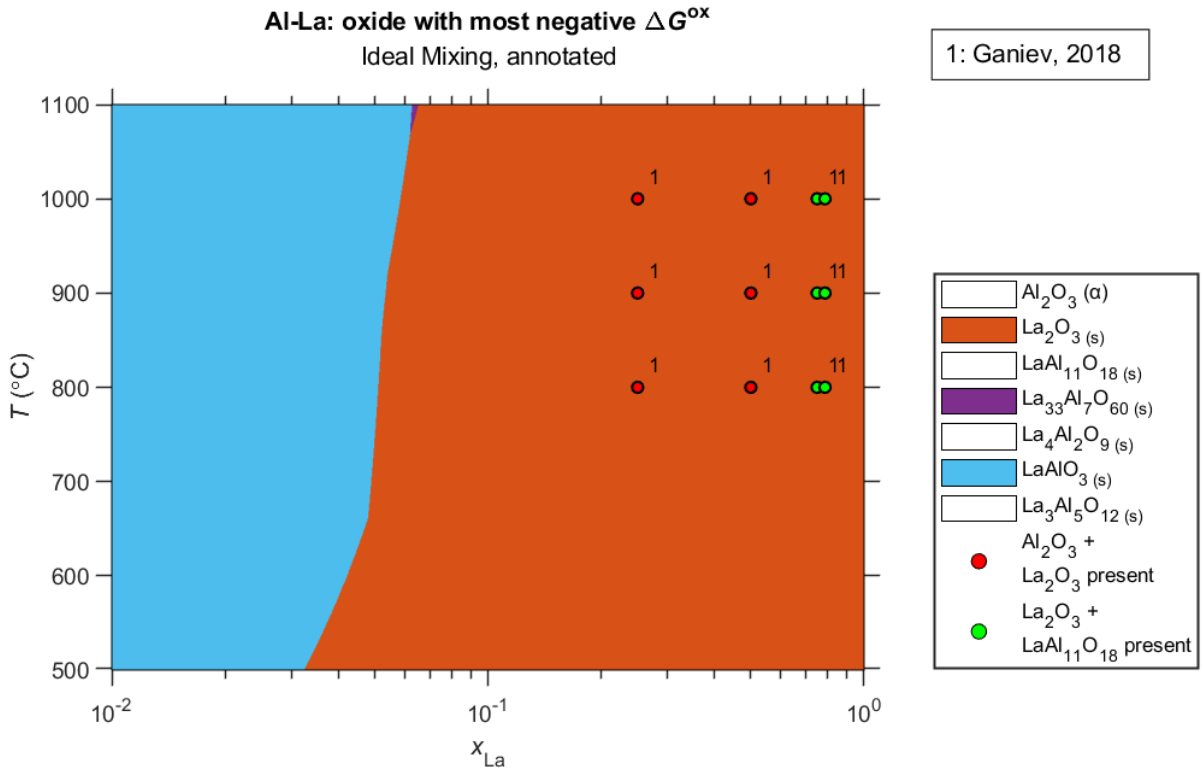
B.7.1.2.2. Al-Ca



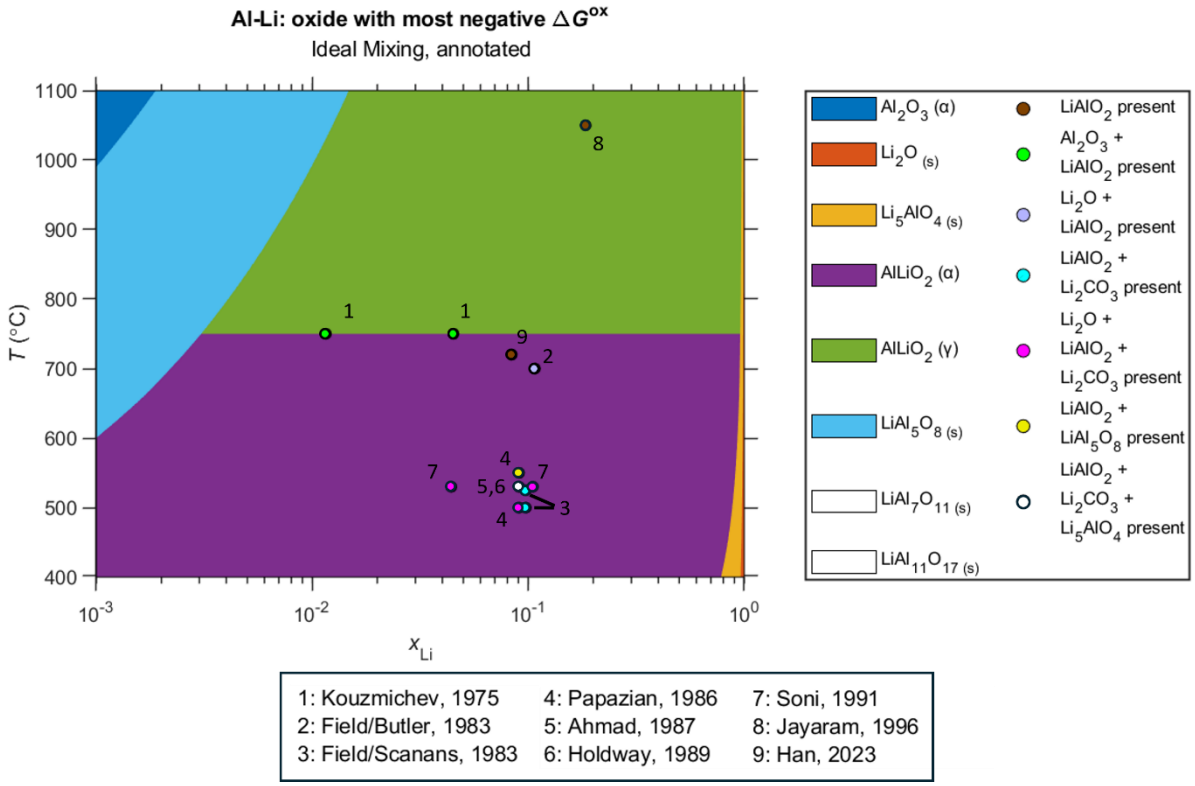
B.7.1.2.3. Al-Ce



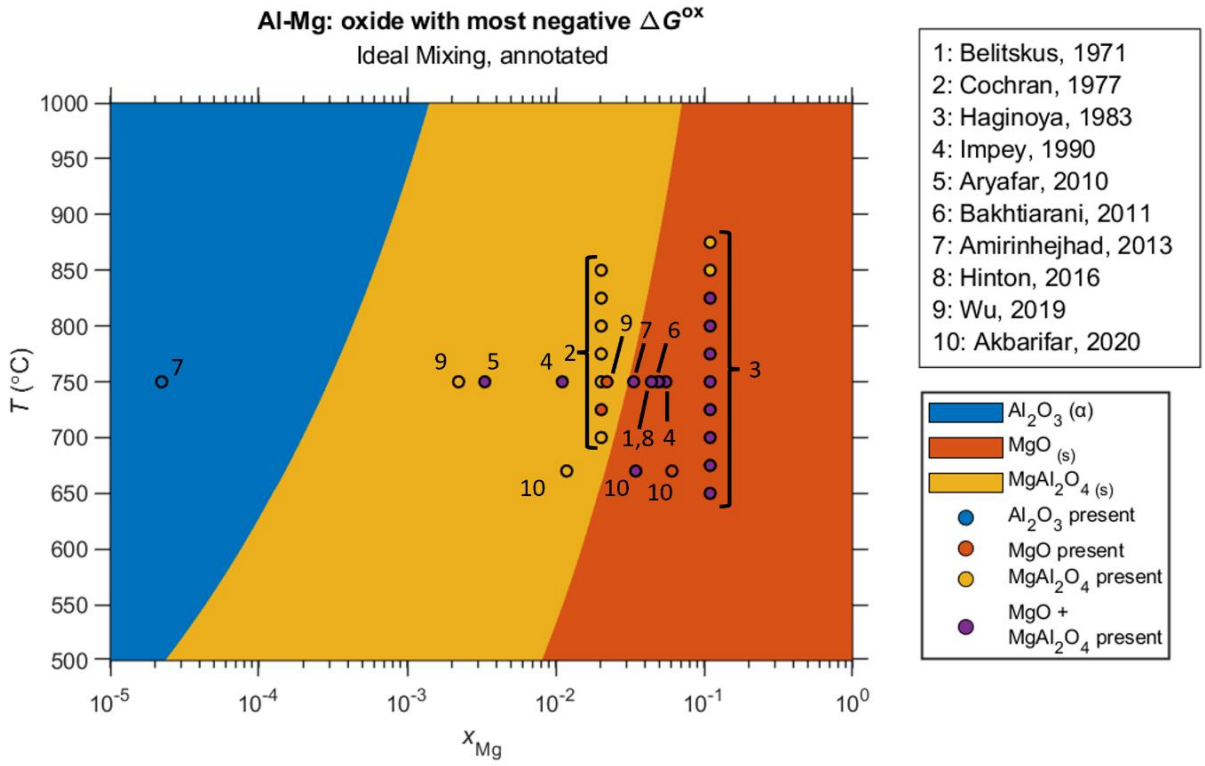
B.7.1.2.4. Al-La



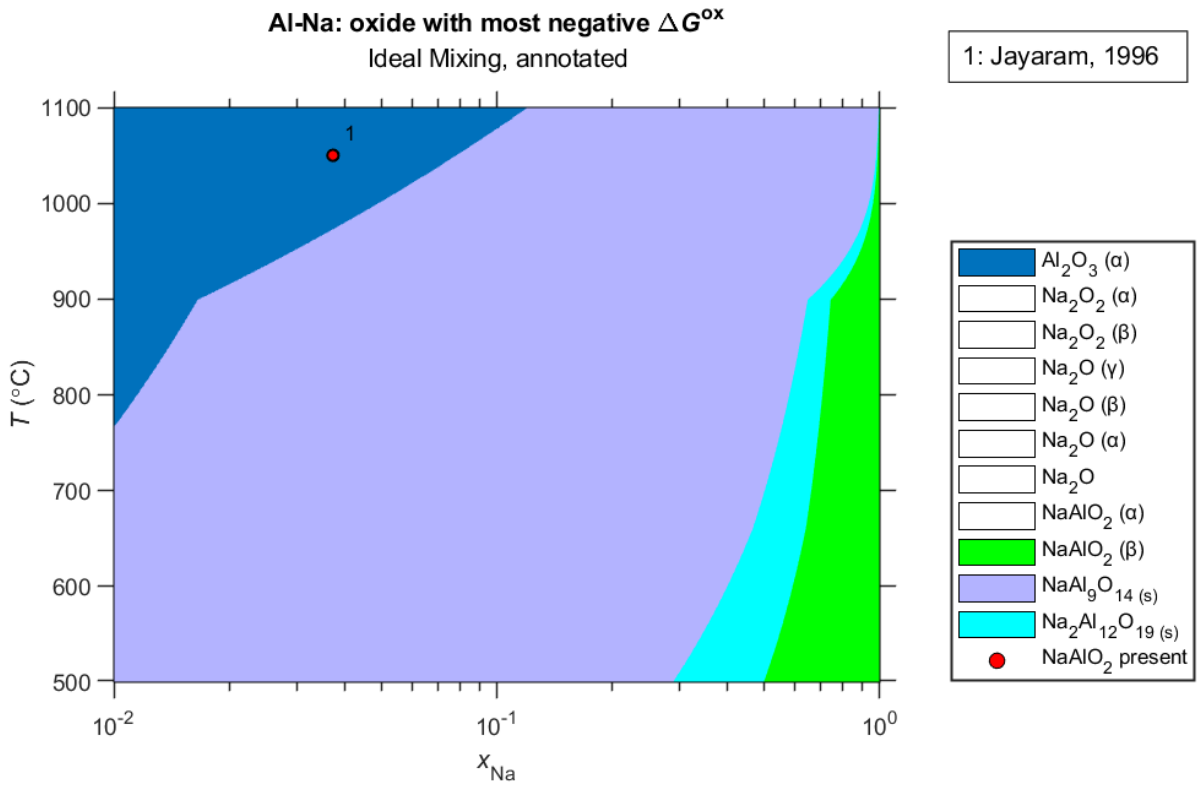
B.7.1.2.5. Al-Li



B.7.1.2.6. Al-Mg

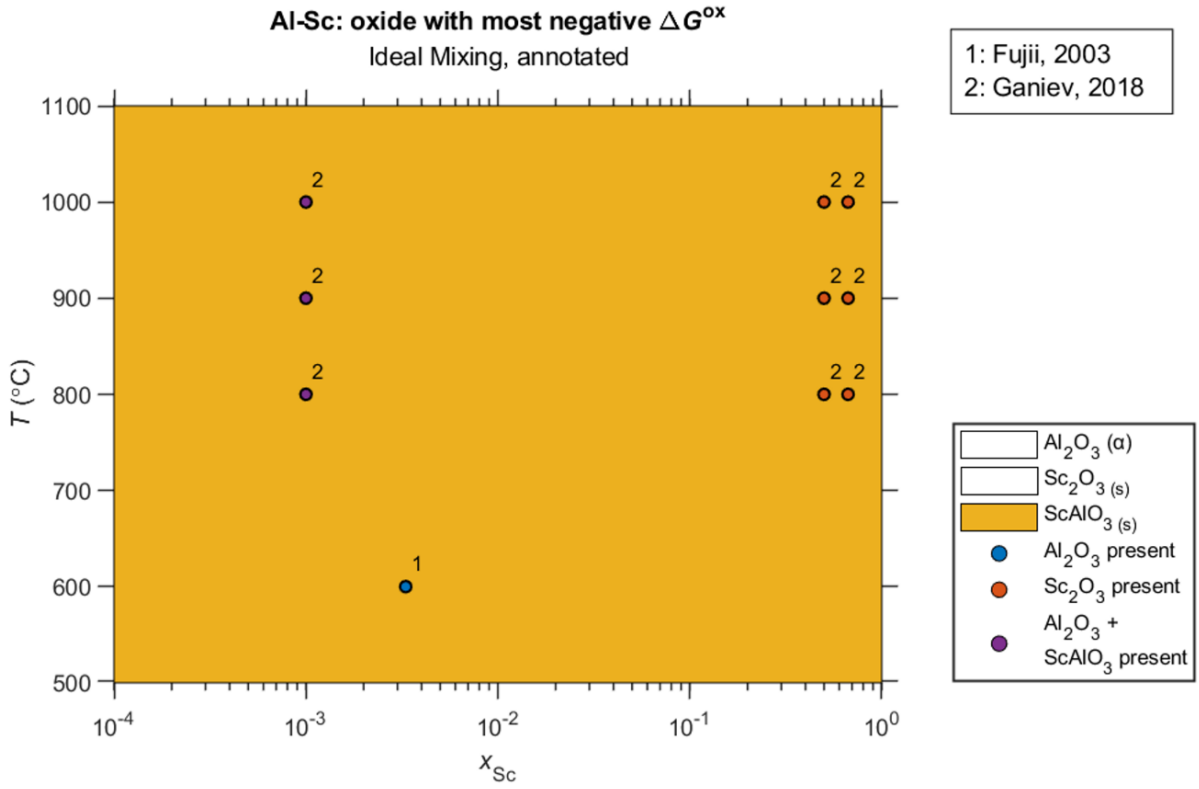


B.7.1.2.7. Al-Na

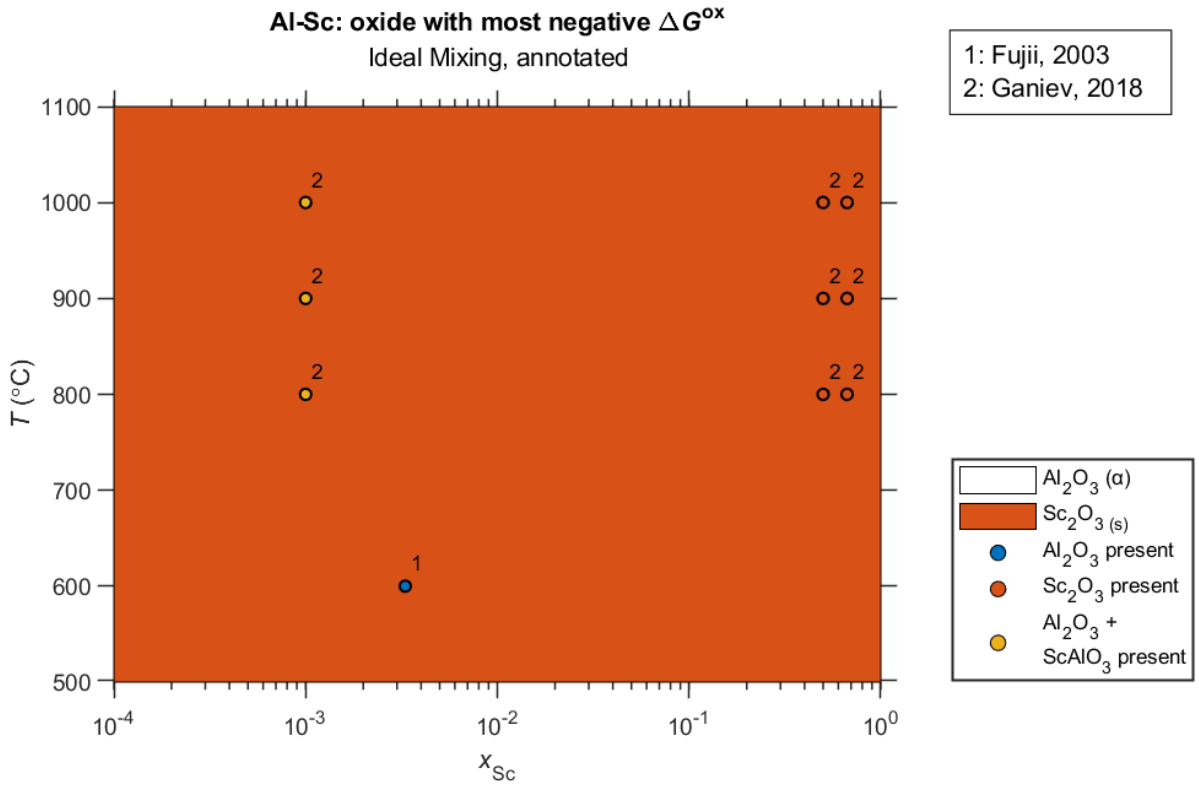


B.7.1.2.8. Al-Sc

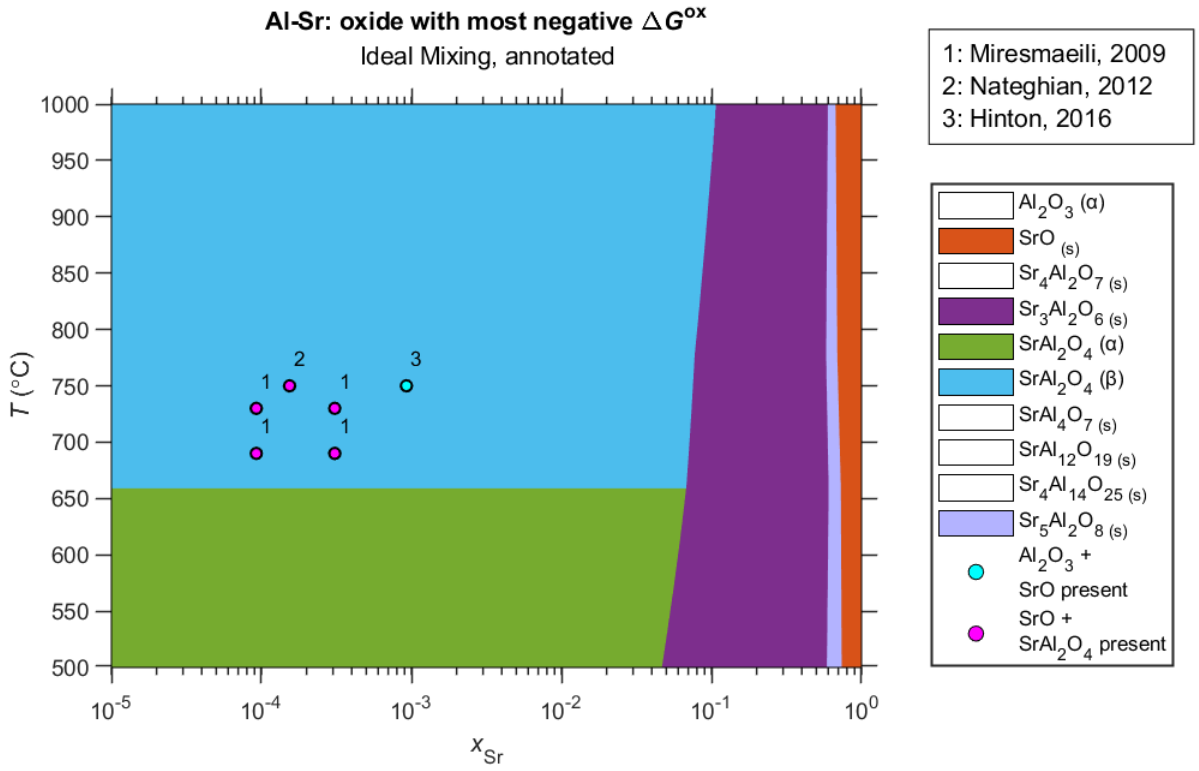
Including $ScAlO_3$



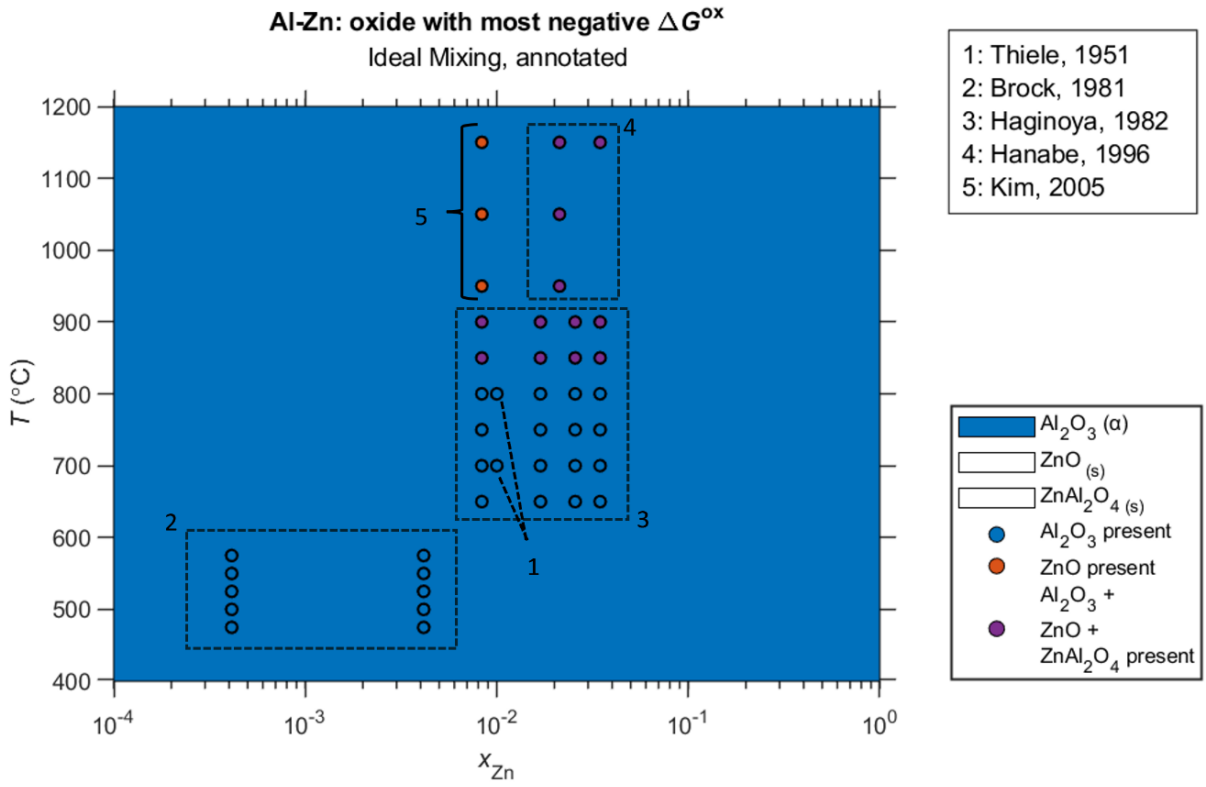
Without $ScAlO_3$



B.7.1.2.9. Al-Sr

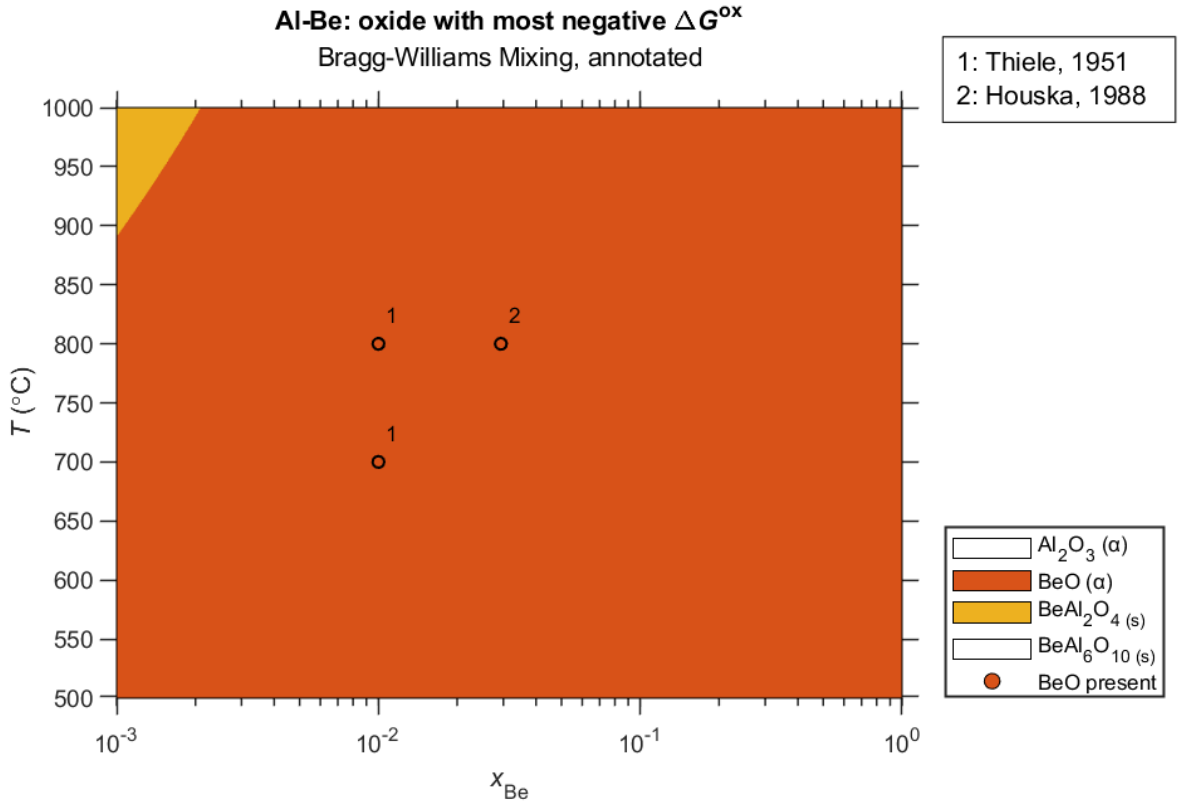


B.7.1.2.10. Al-Zn

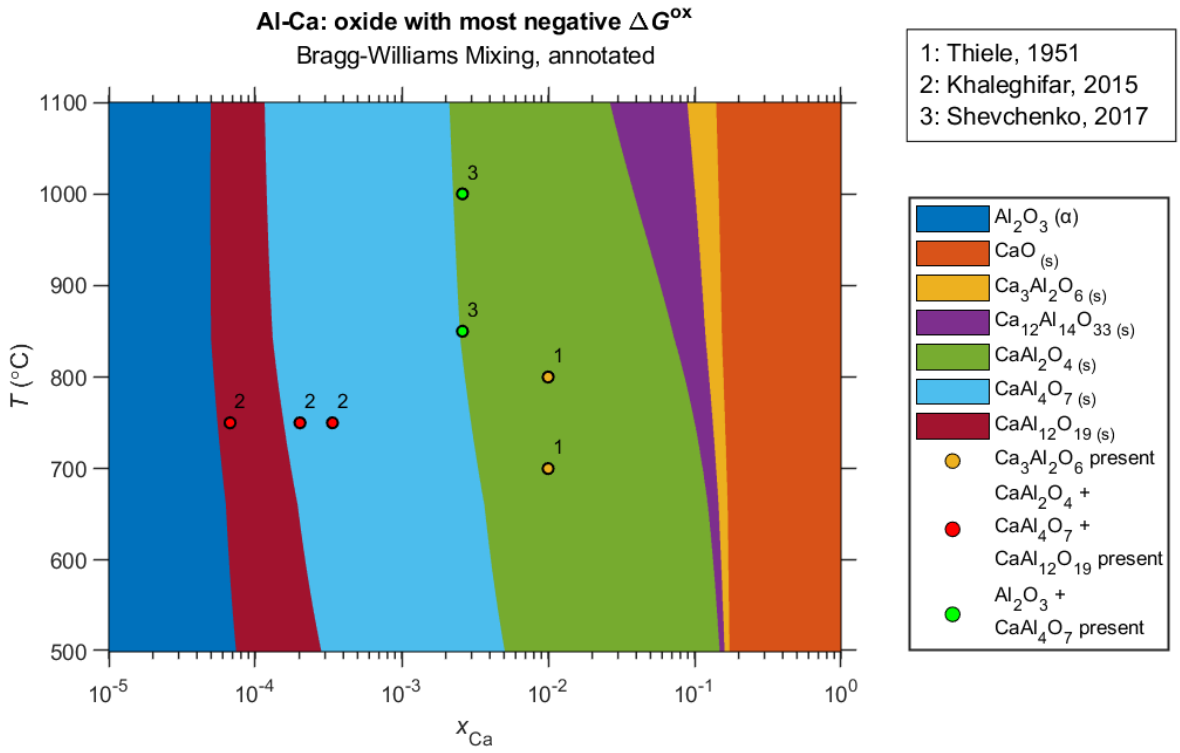


B.7.1.3. Bragg-Williams mixing

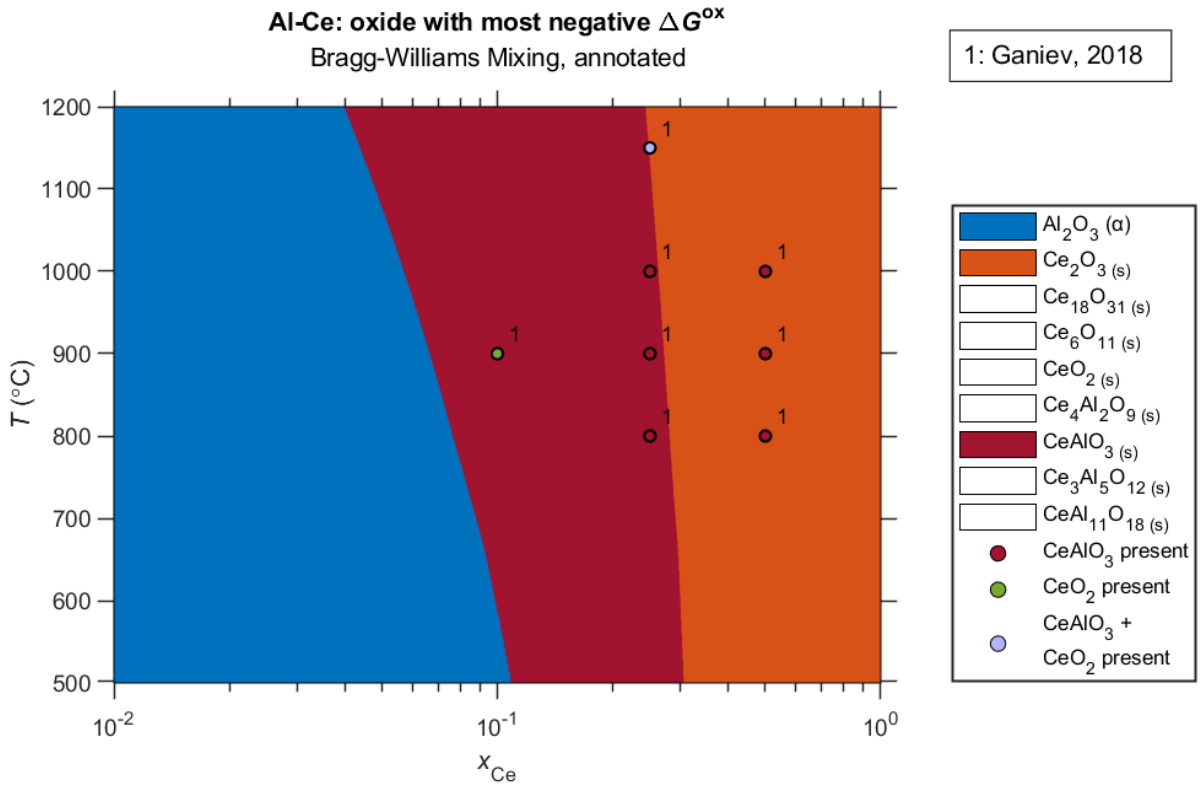
B.7.1.3.1. Al-Be



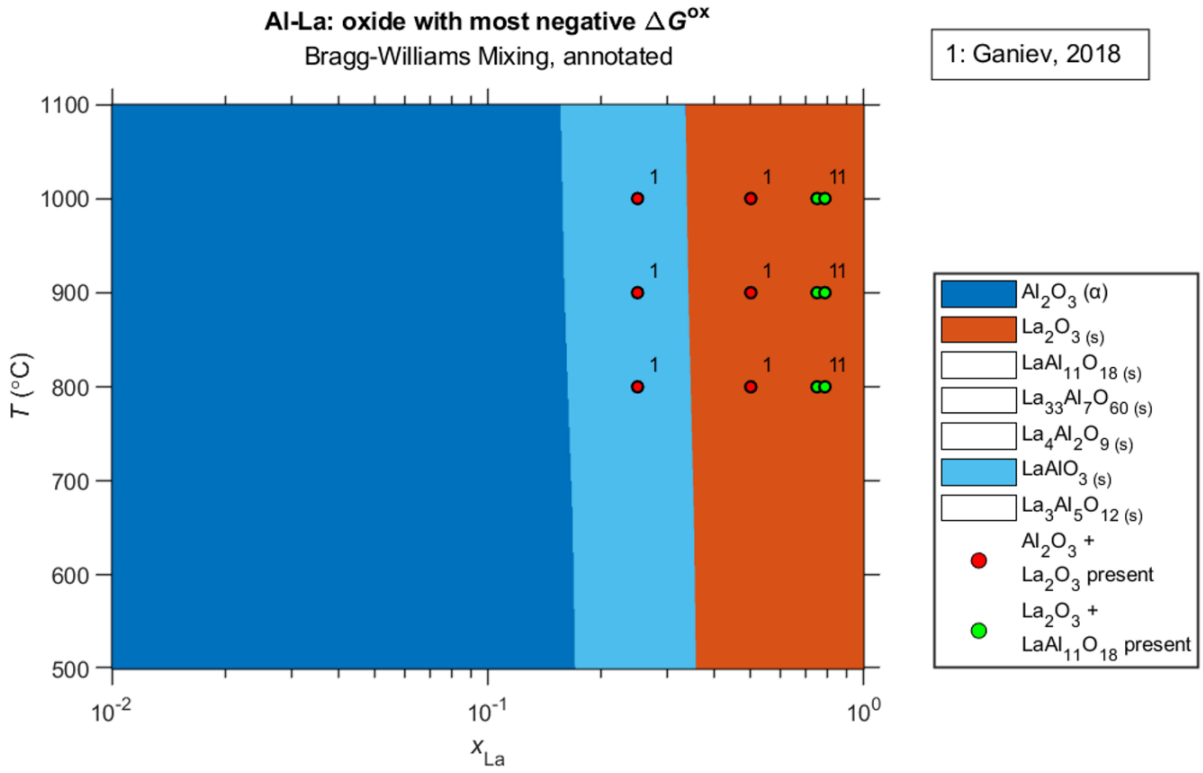
B.7.1.3.2. Al-Ca



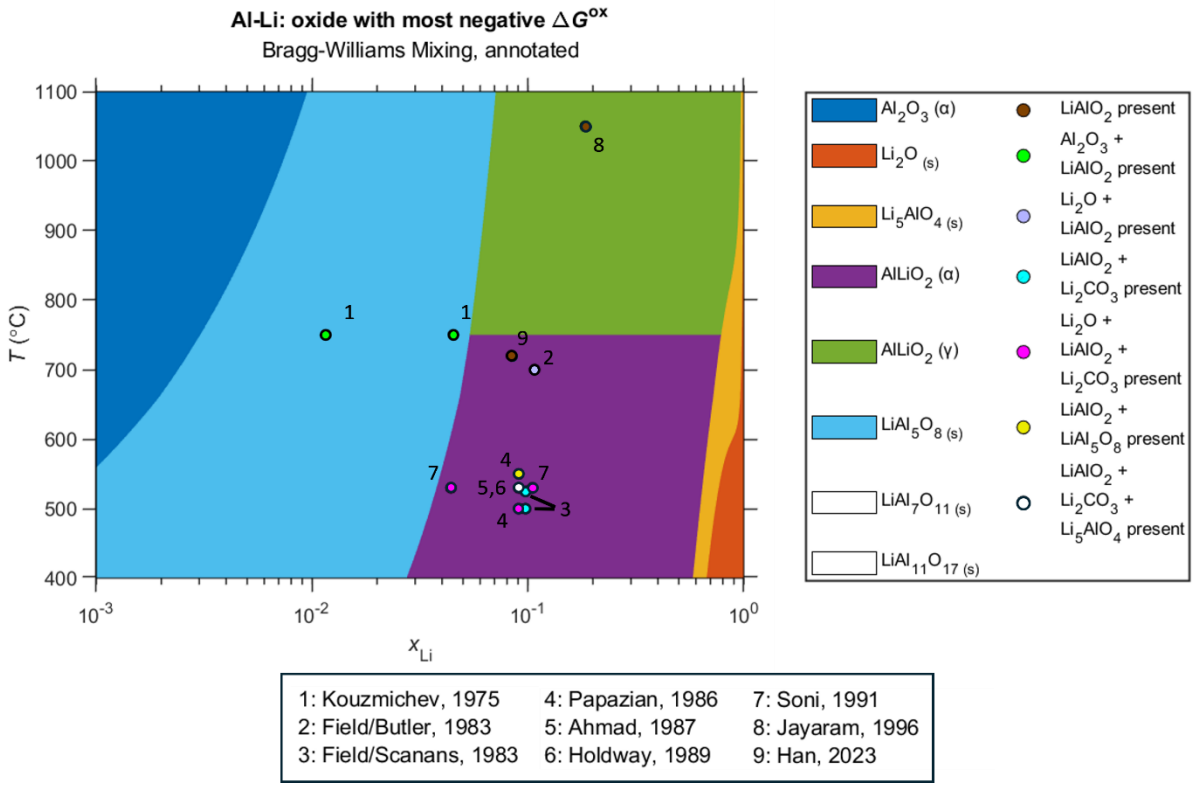
B.7.1.3.3. Al-Ce



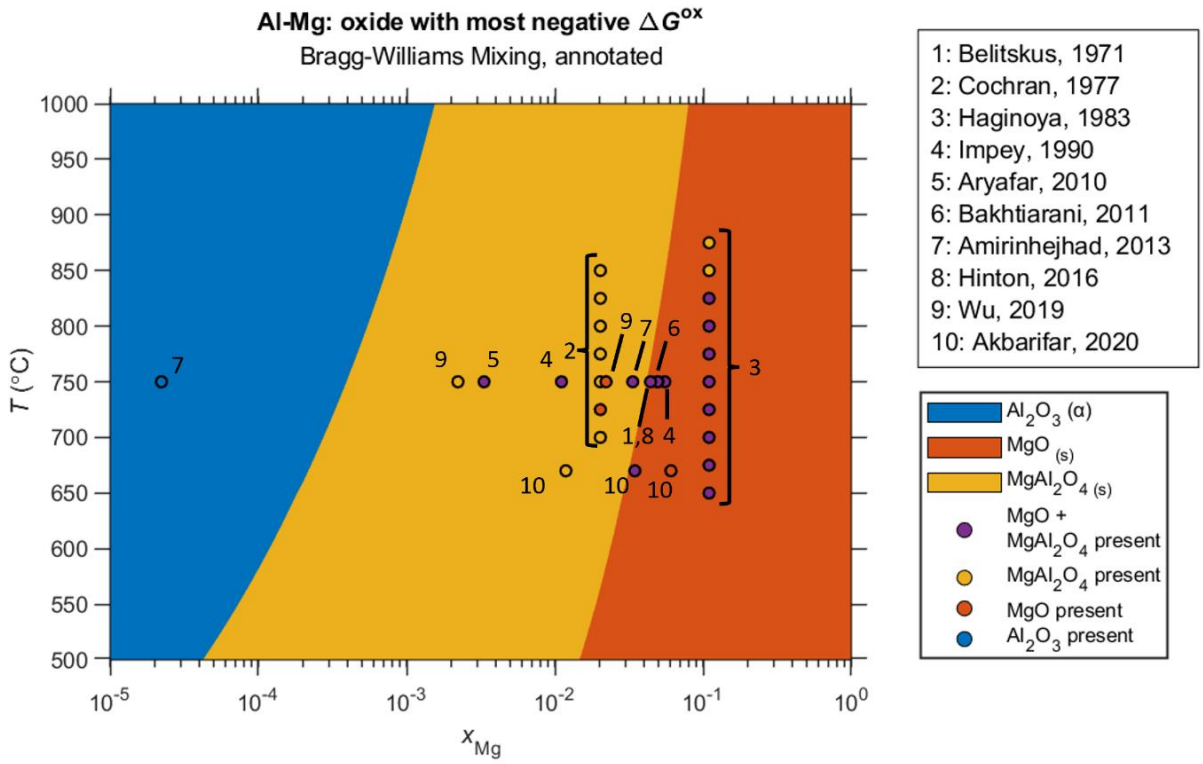
B.7.1.3.4. Al-La



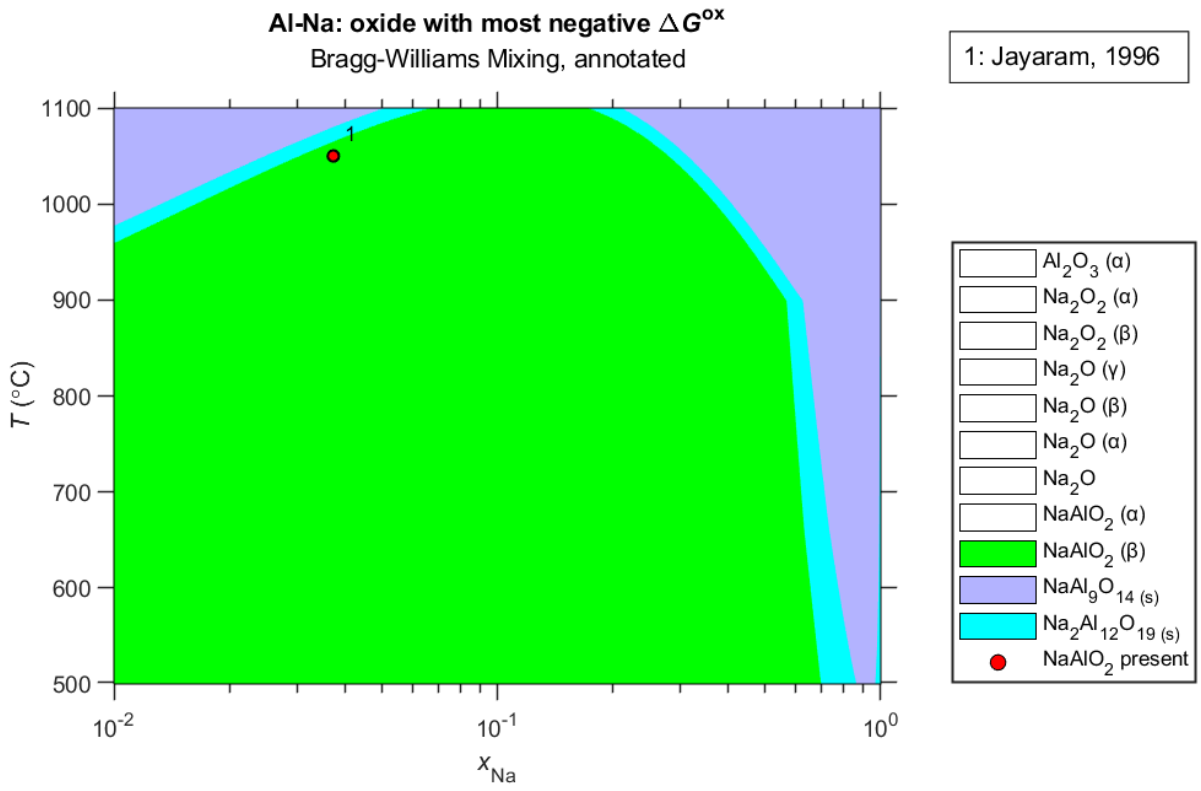
B.7.1.3.5. Al-Li



B.7.1.3.6. Al-Mg

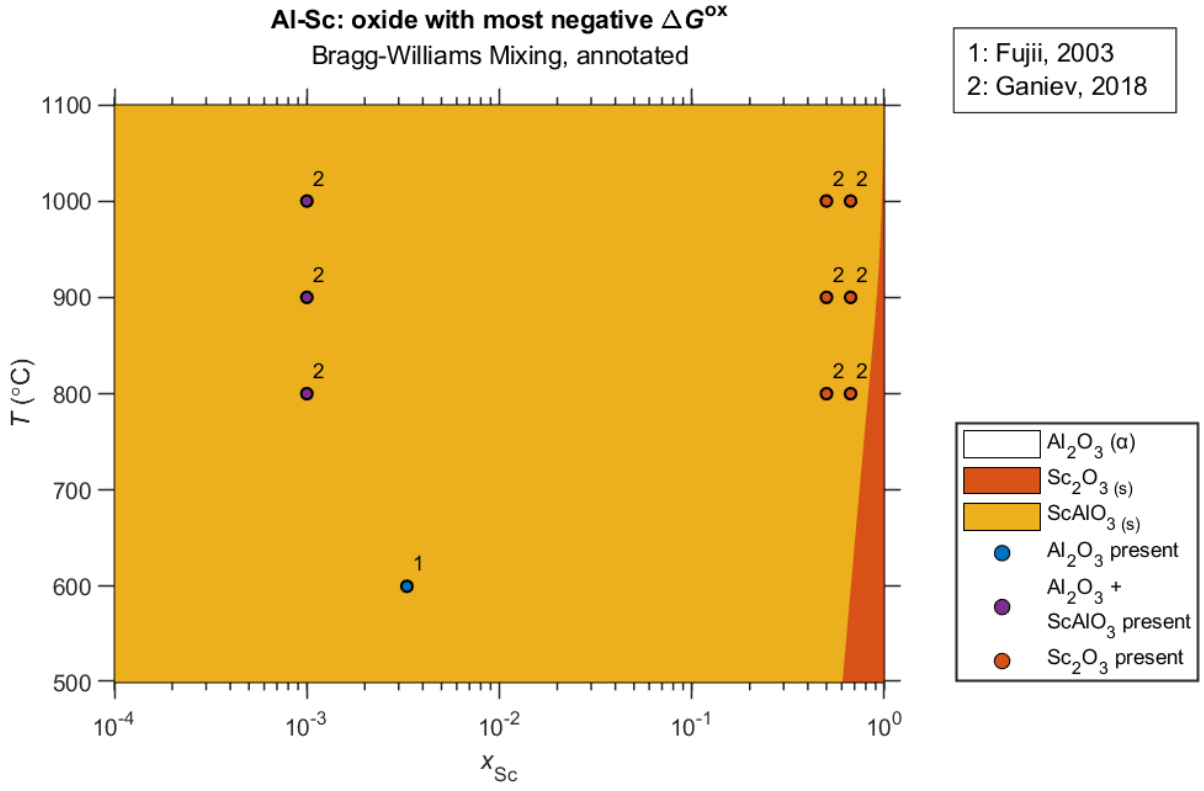


B.7.1.3.7. Al-Na

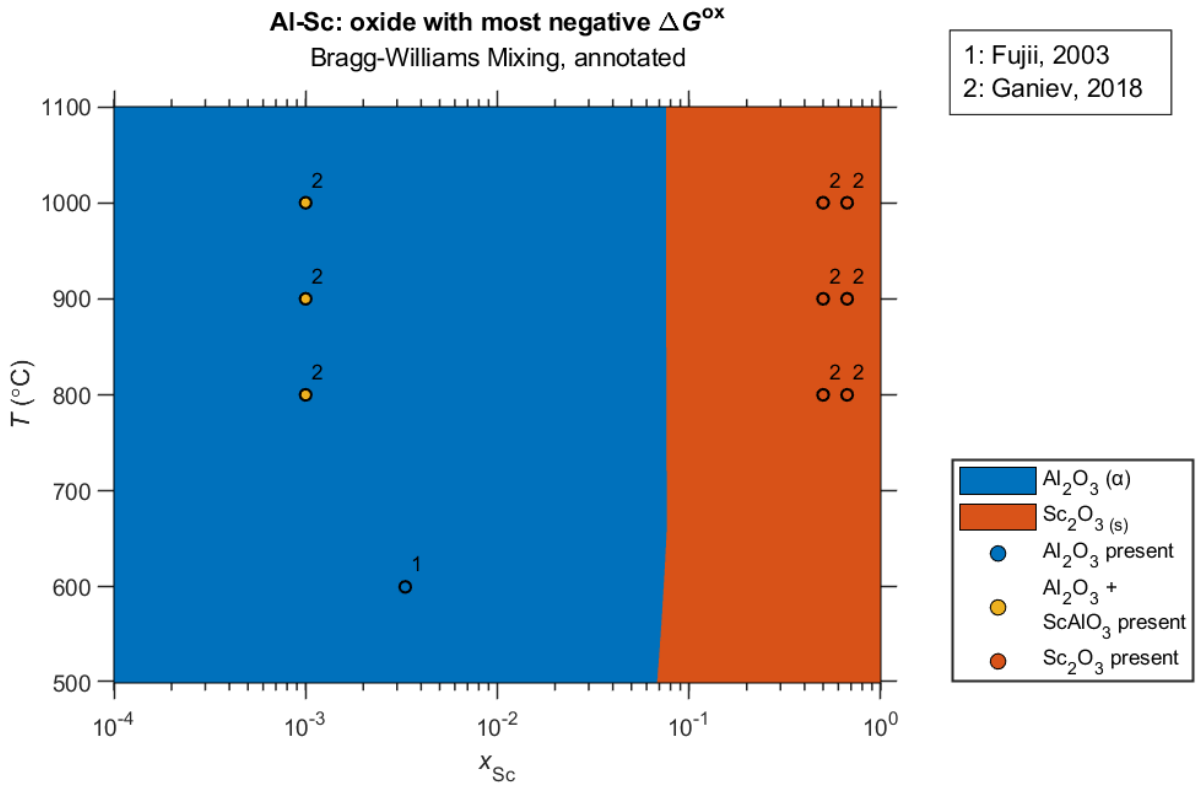


B.7.1.3.8. Al-Sc

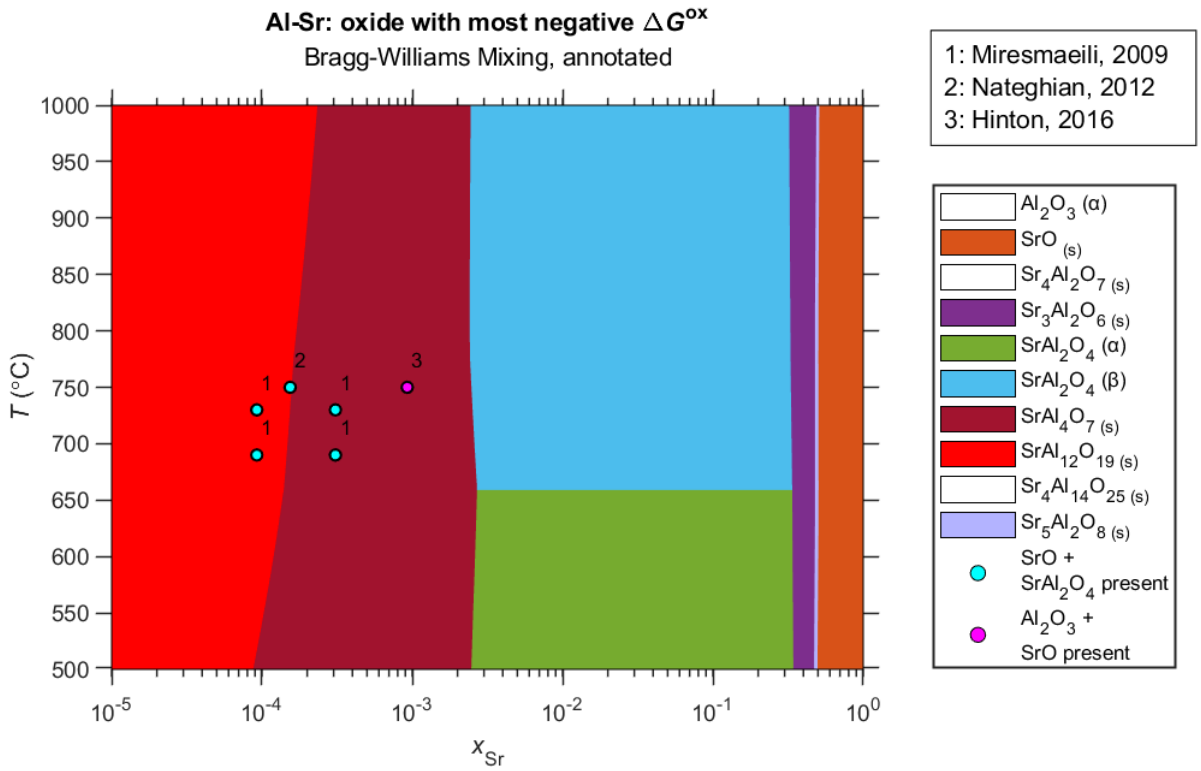
Including $ScAlO_3$



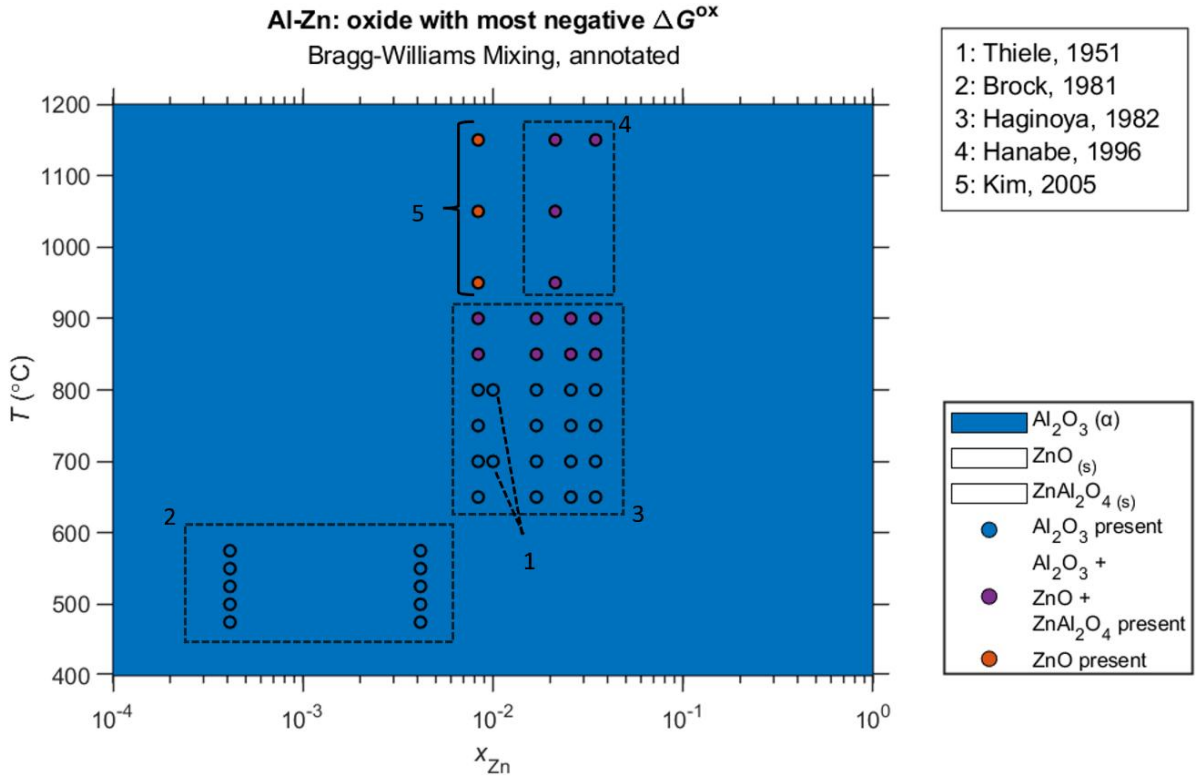
Without $ScAlO_3$



B.7.1.3.9. Al-Sr

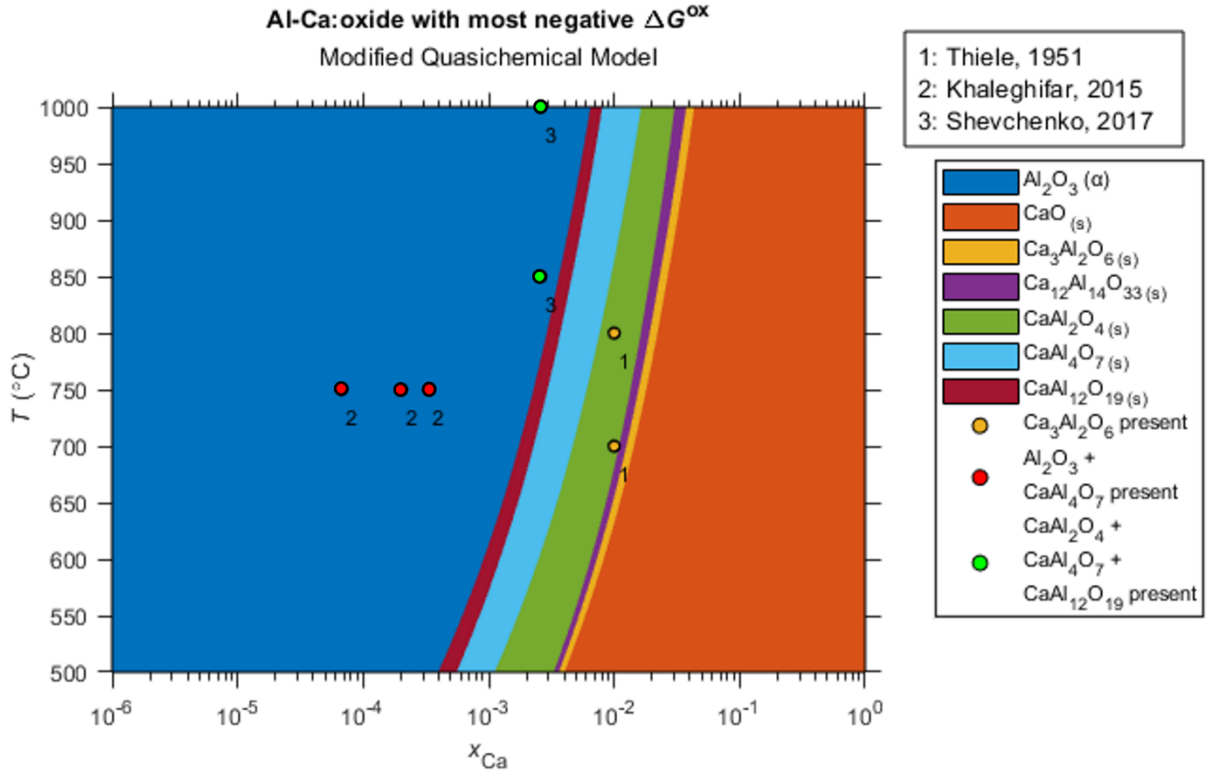


B.7.1.3.10. Al-Zn

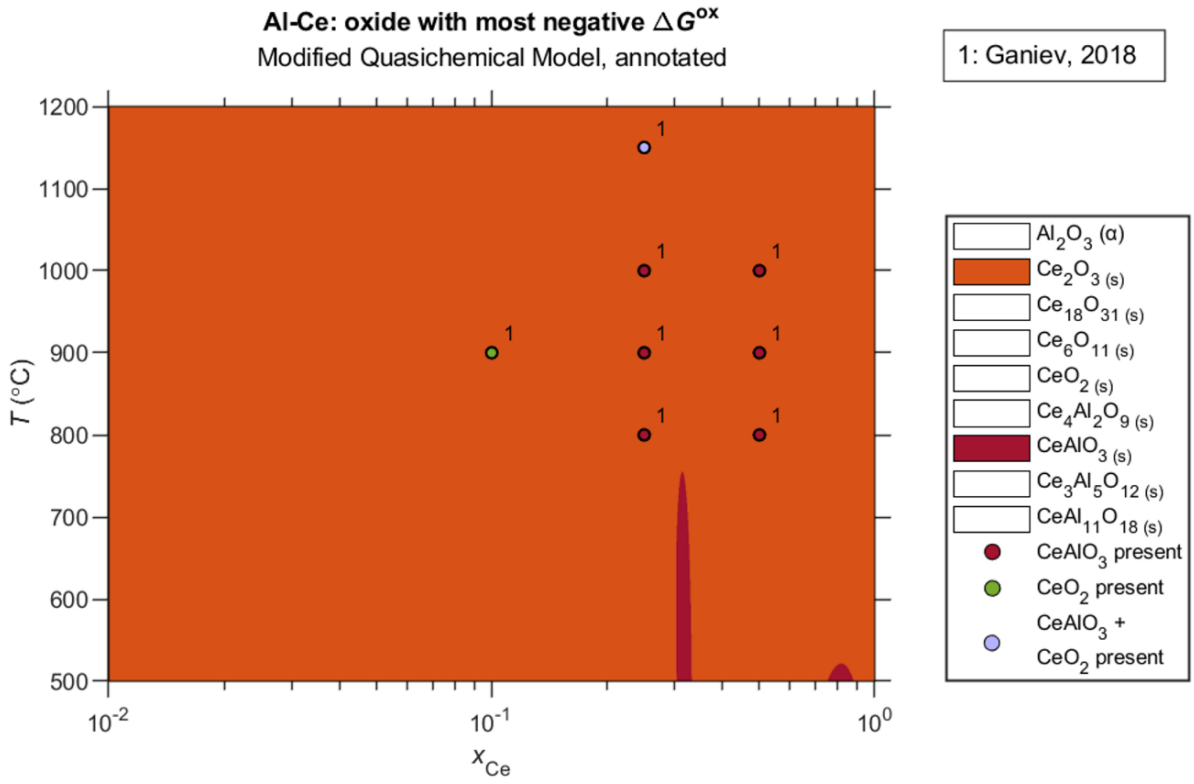


B.7.1.4. Modified quasichemical model

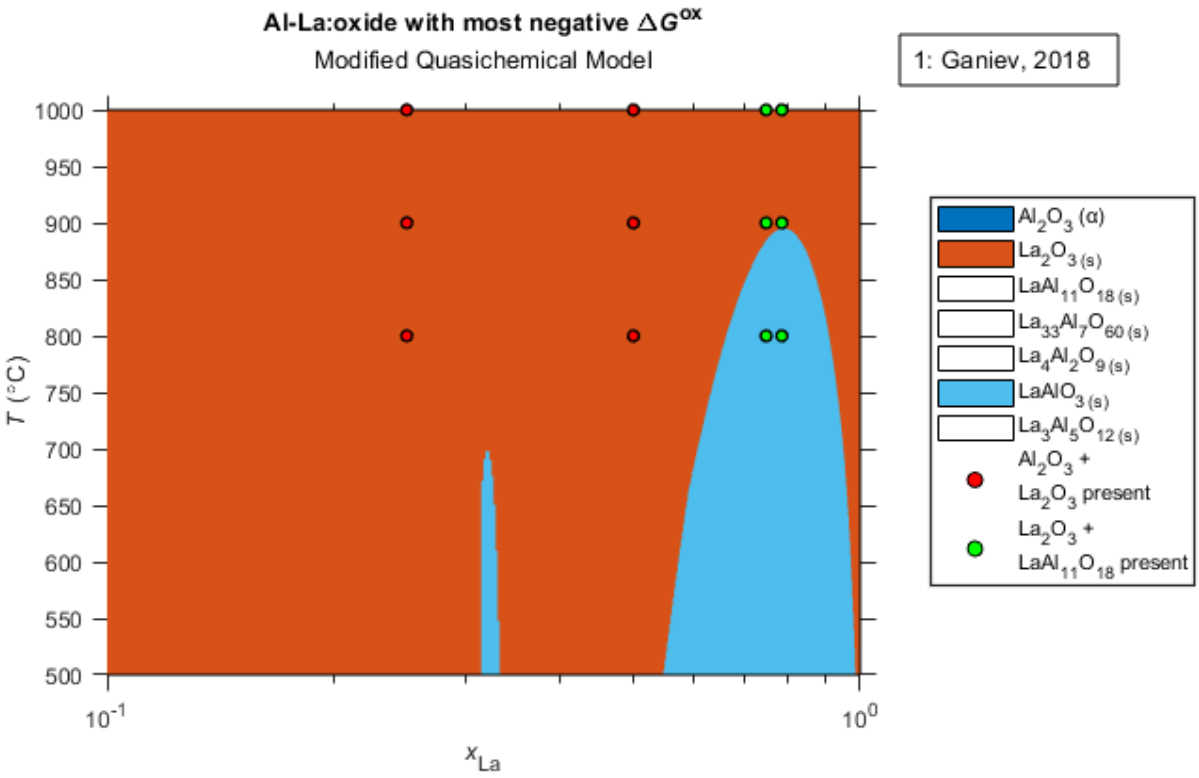
B.7.1.4.1. Al-Ca



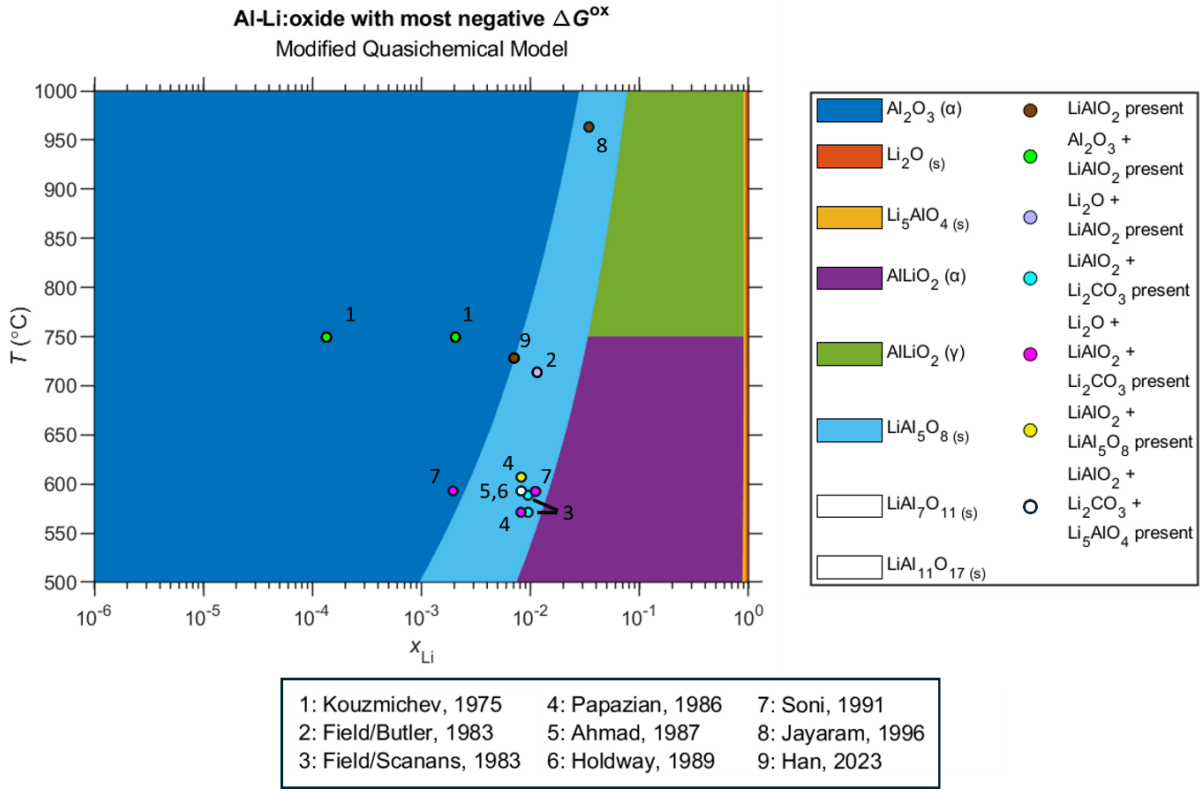
B.7.1.4.2. Al-Ce



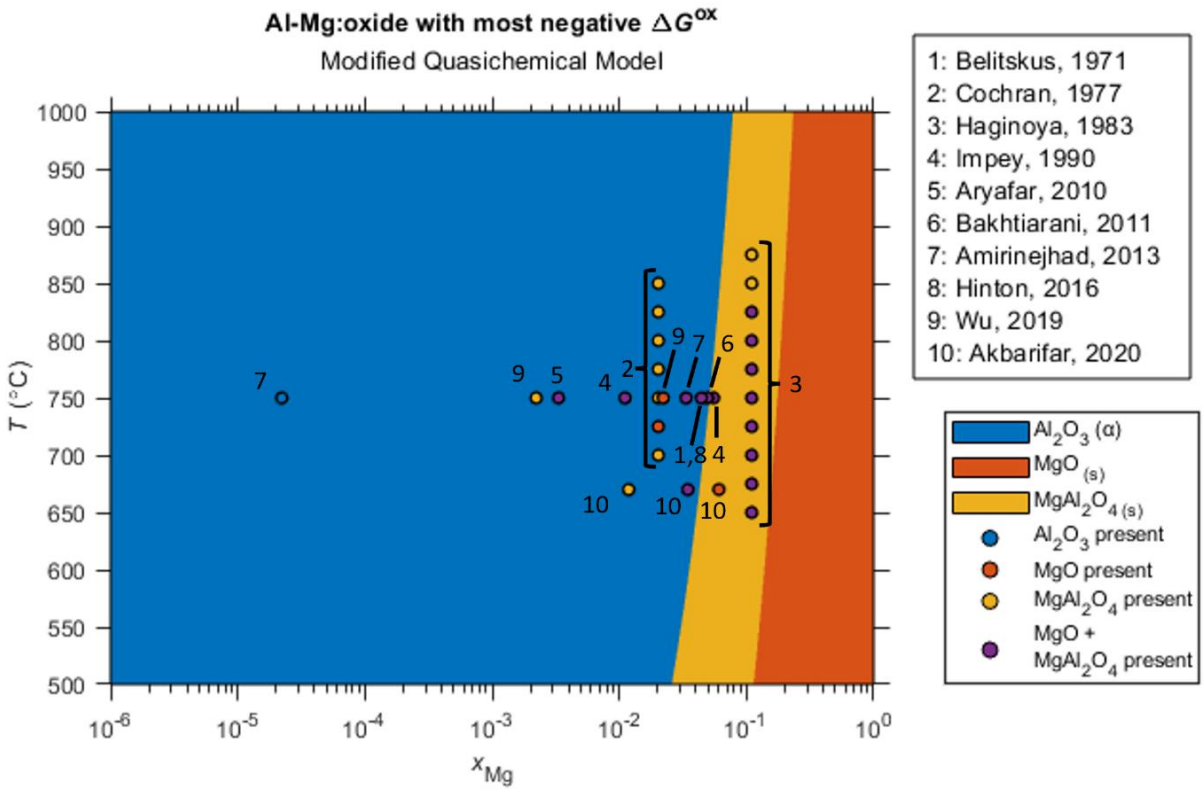
B.7.1.4.3. Al-La



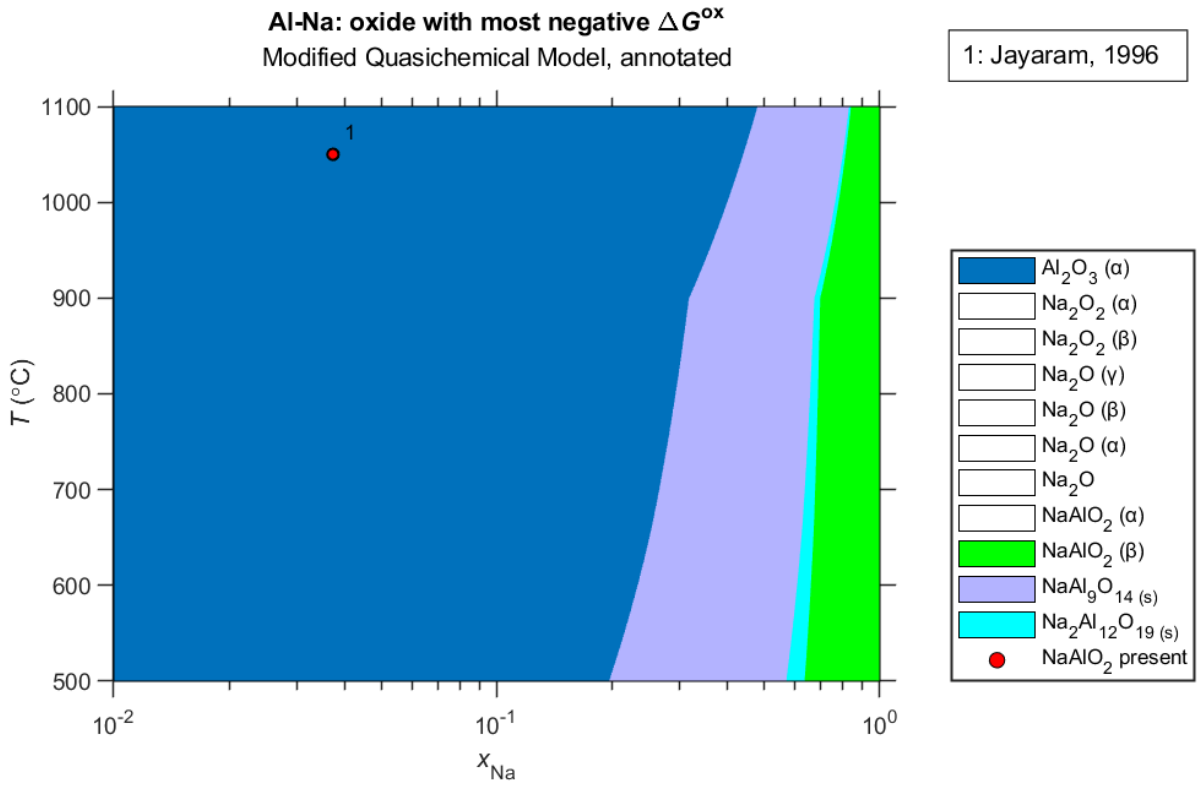
B.7.1.4.4. Al-Li



B.7.1.4.5. Al-Mg

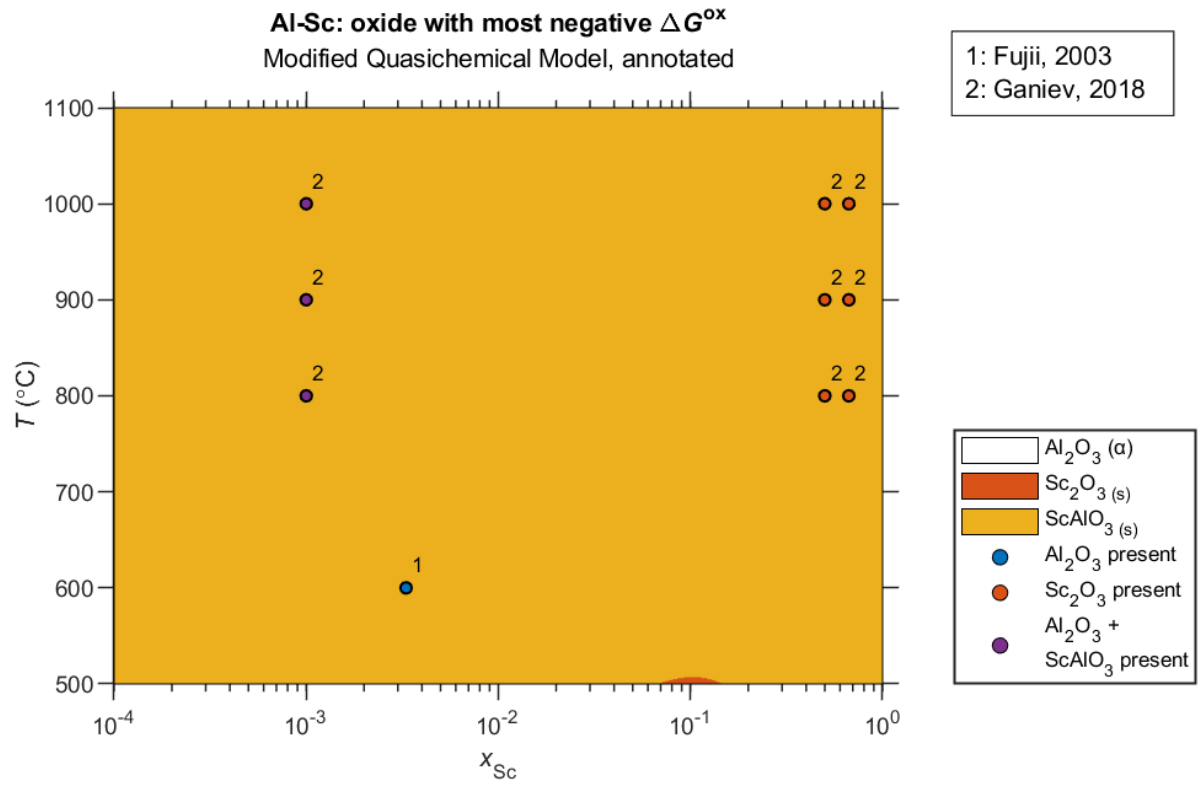


B.7.1.4.6. Al-Na

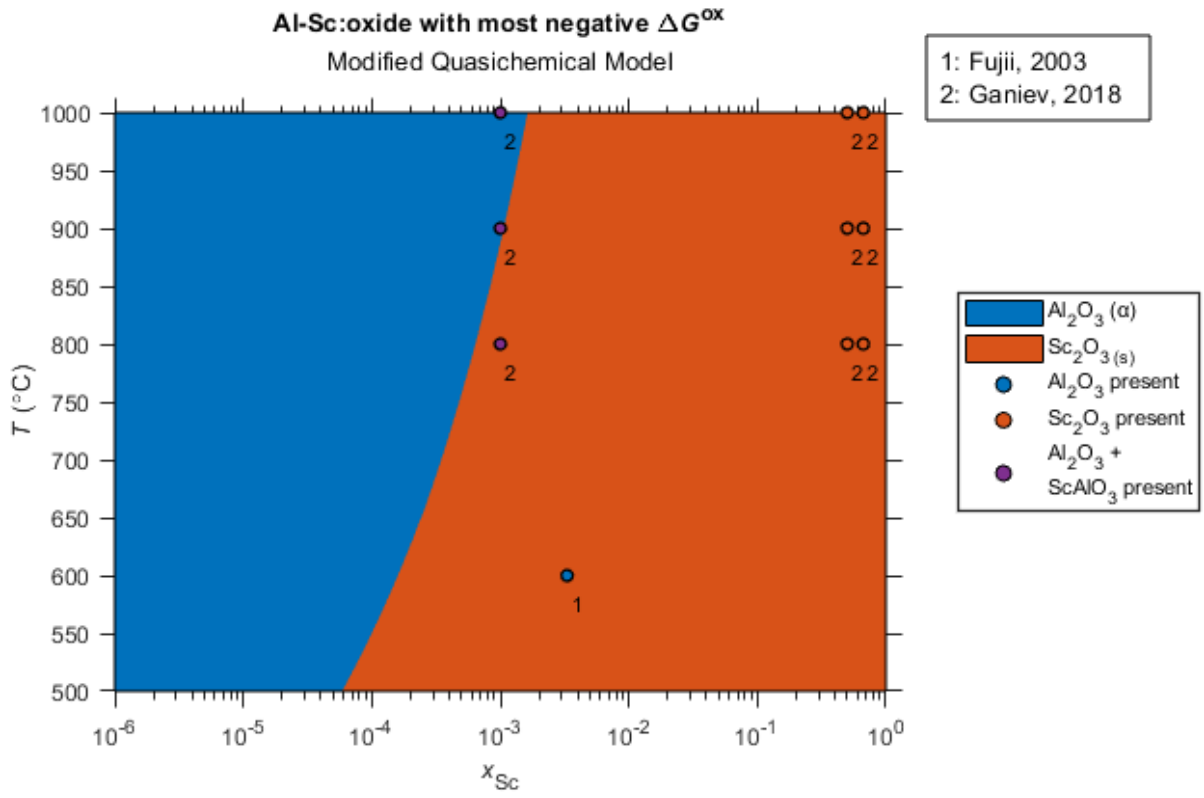


B.7.1.4.7. Al-Sc

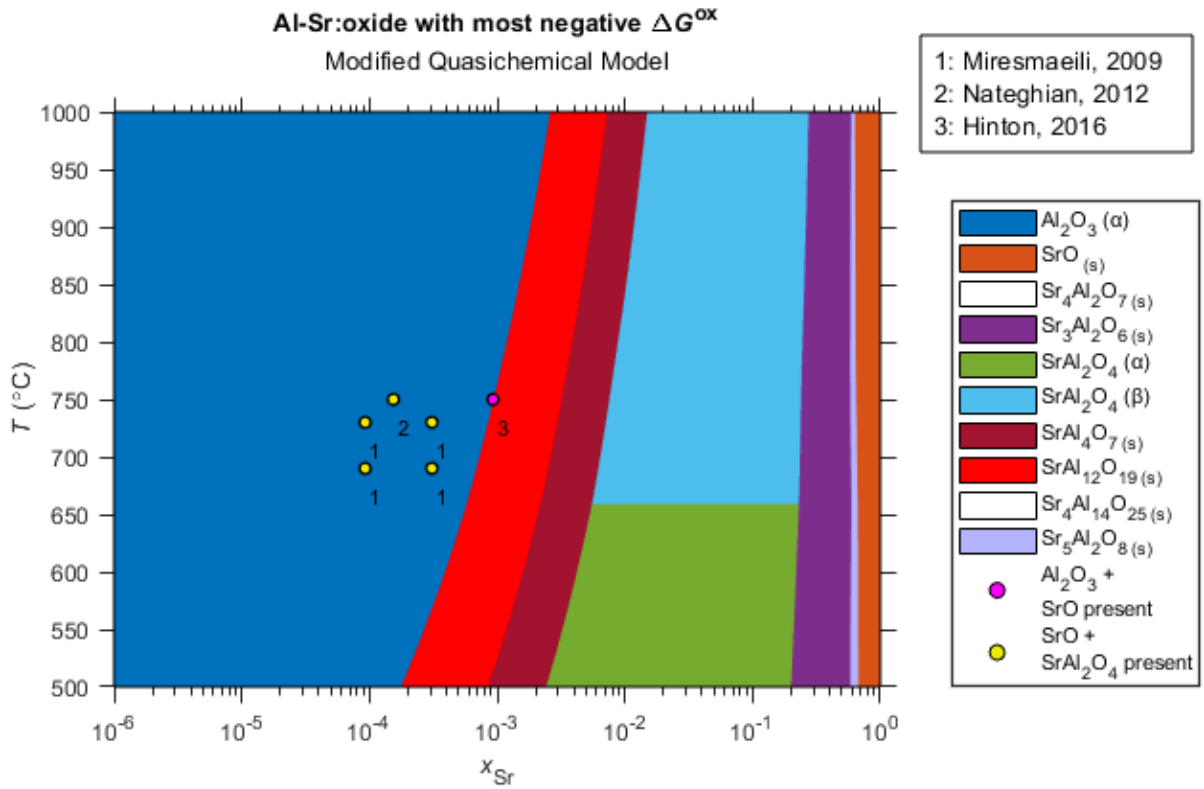
Including ScAlO3



Without ScAlO3



B.7.1.4.8. Al-Sr



B.7.2. Ternary Al-X systems

B.7.2.1. Data sources

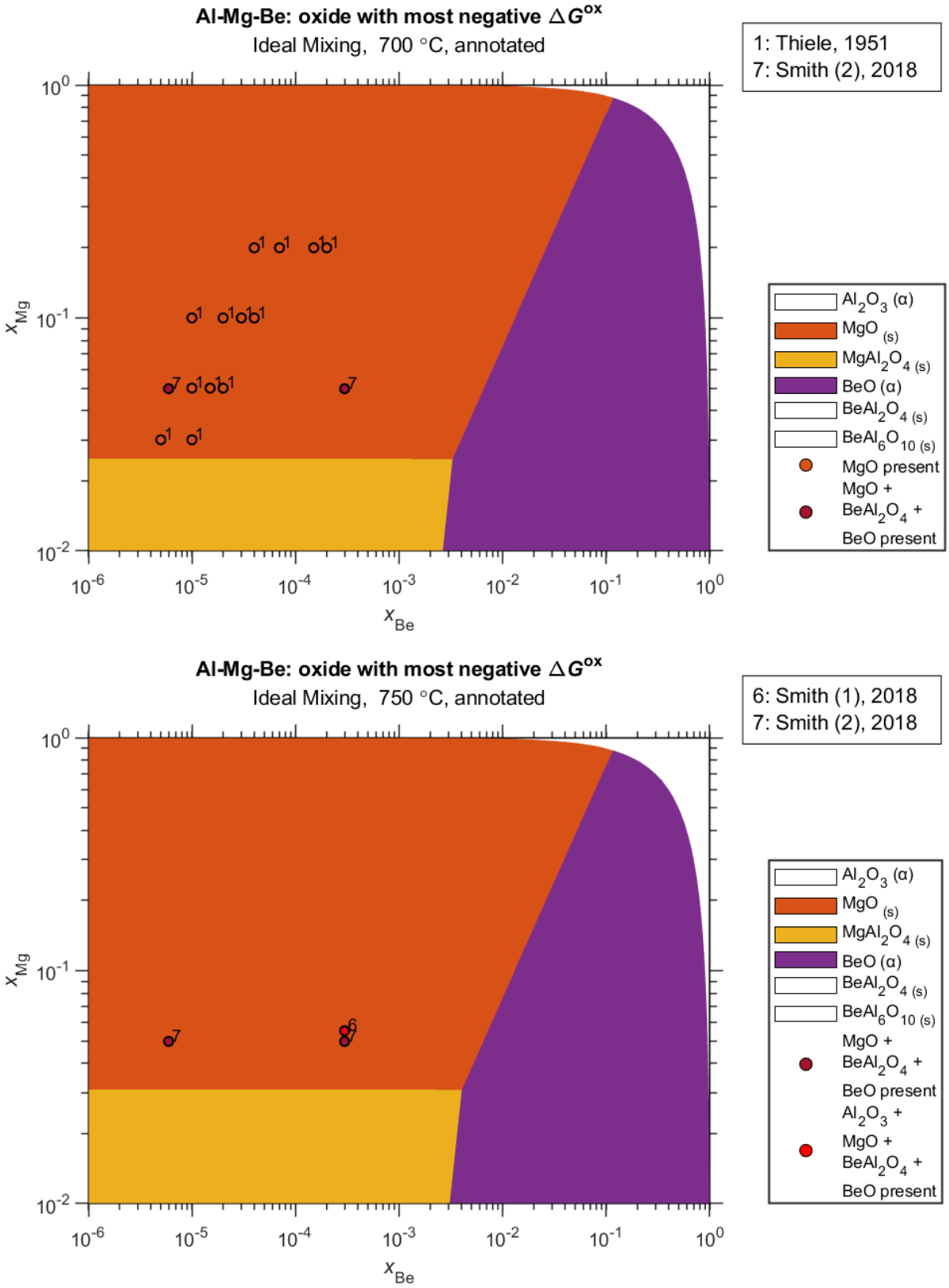
Below is a summary of data used to annotate oxide stability diagrams of ternary Al-Mg-X alloys (Table B.7). All data here was taken from melt oxidation studies, where the melt temperature and composition of the alloy were correlated against oxidation products and whether the melt was protected (i.e. whether the melt underwent breakaway oxidation).

Ref	**Text**	**X**	**Type of study**
[79]	Bahadur, 1987	Be	Melt oxidation
[55]	Cochran, 1977	Be	Melt oxidation
[80]	Ha (1), 2017	Be, Ca	Melt oxidation
[81]	Ha (2), 2017	Ca	Melt oxidation
[82]	Ha, 2014	Ca	Melt oxidation
[83]	Ha, 2019	Ca	Melt oxidation
[84]	Ozdemir, 2009	Sr	Melt oxidation
[85]	Smith (1), 2018	Be	Melt oxidation
[86]	Smith (2), 2018	Be	Melt oxidation
[87]	Smith, 2017	Be	Melt oxidation
[88]	Smith-Hanssen, 2022	Ca, Sr	Melt oxidation
(present work)	Telford, 2025	Ca	Melt oxidation
[77]	Thiele, 1951	Be	Melt oxidation
[89]	Yoon, 2013	Ca	Melt oxidation
[90]	Yuen, 2001	Sr	Melt oxidation

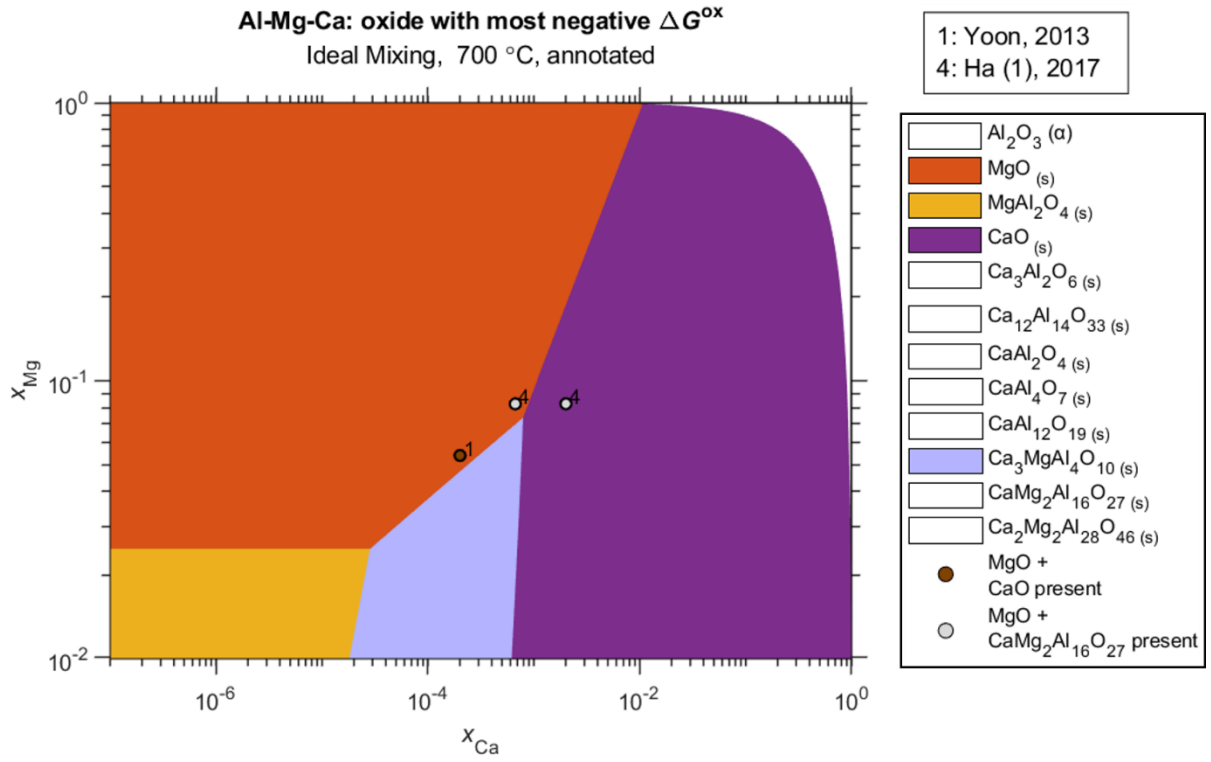
Table B.7. Summary of references and data sources for binary systems, including method used in study.

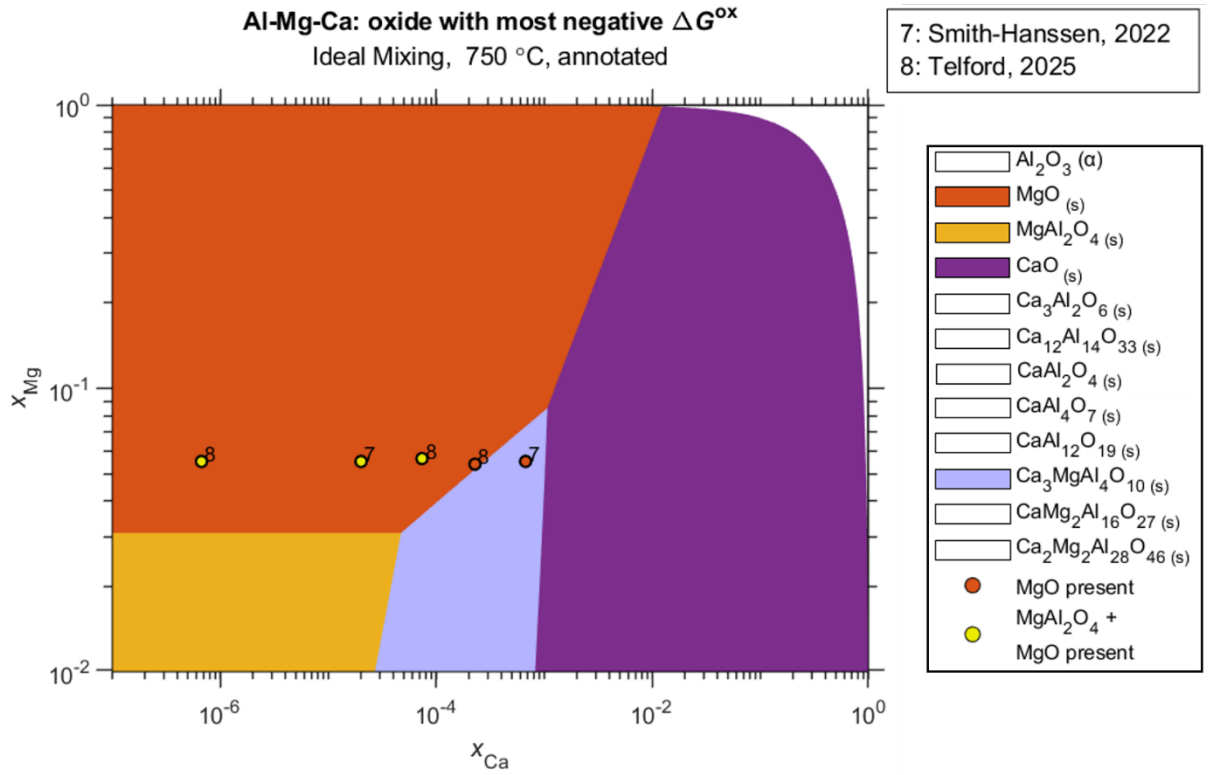
B.7.2.2. Products: Ideal

B.7.2.2.1. Al-Mg-Be

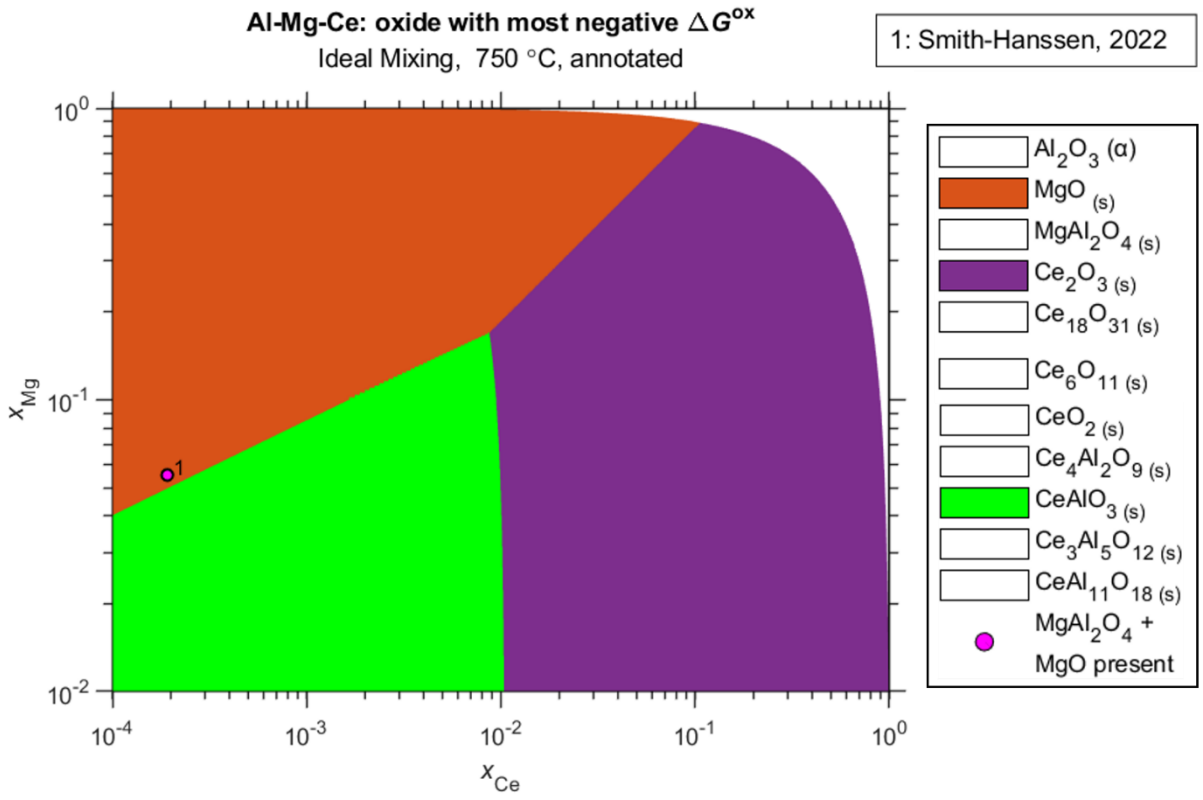


B.7.2.2.2. Al-Mg-Ca

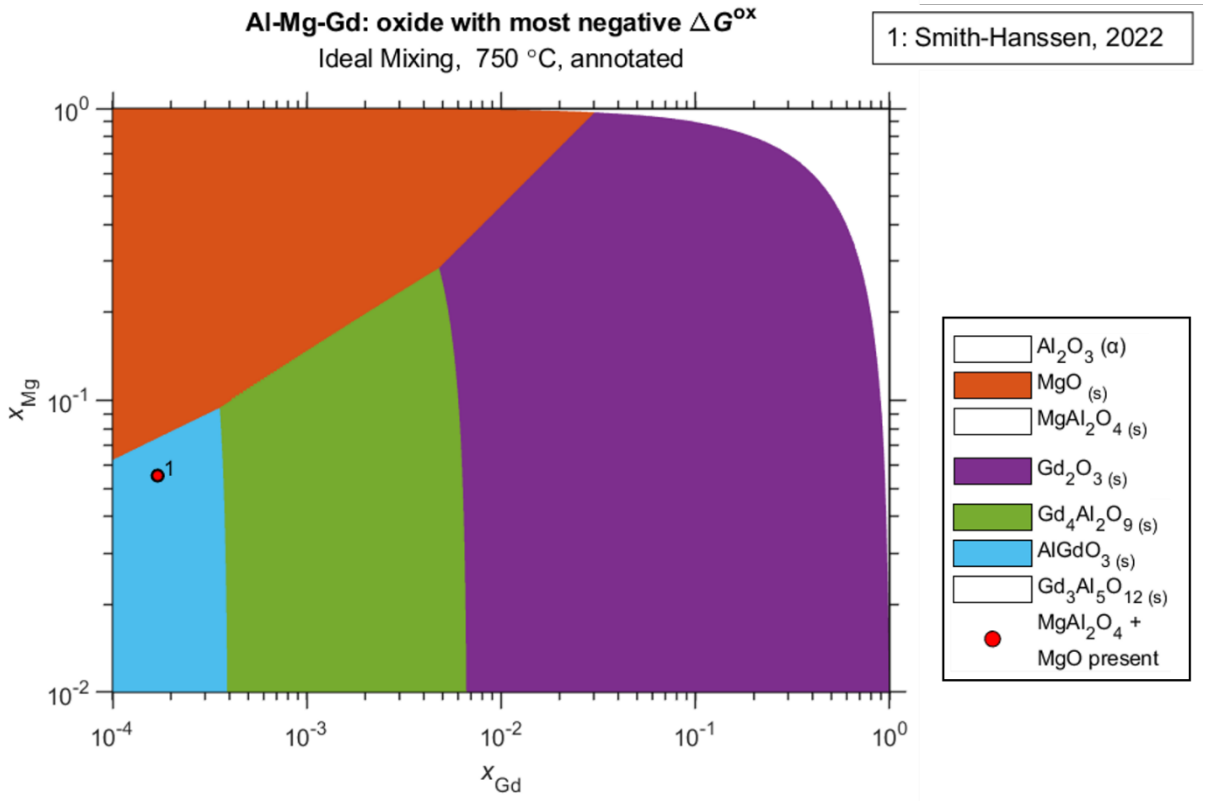




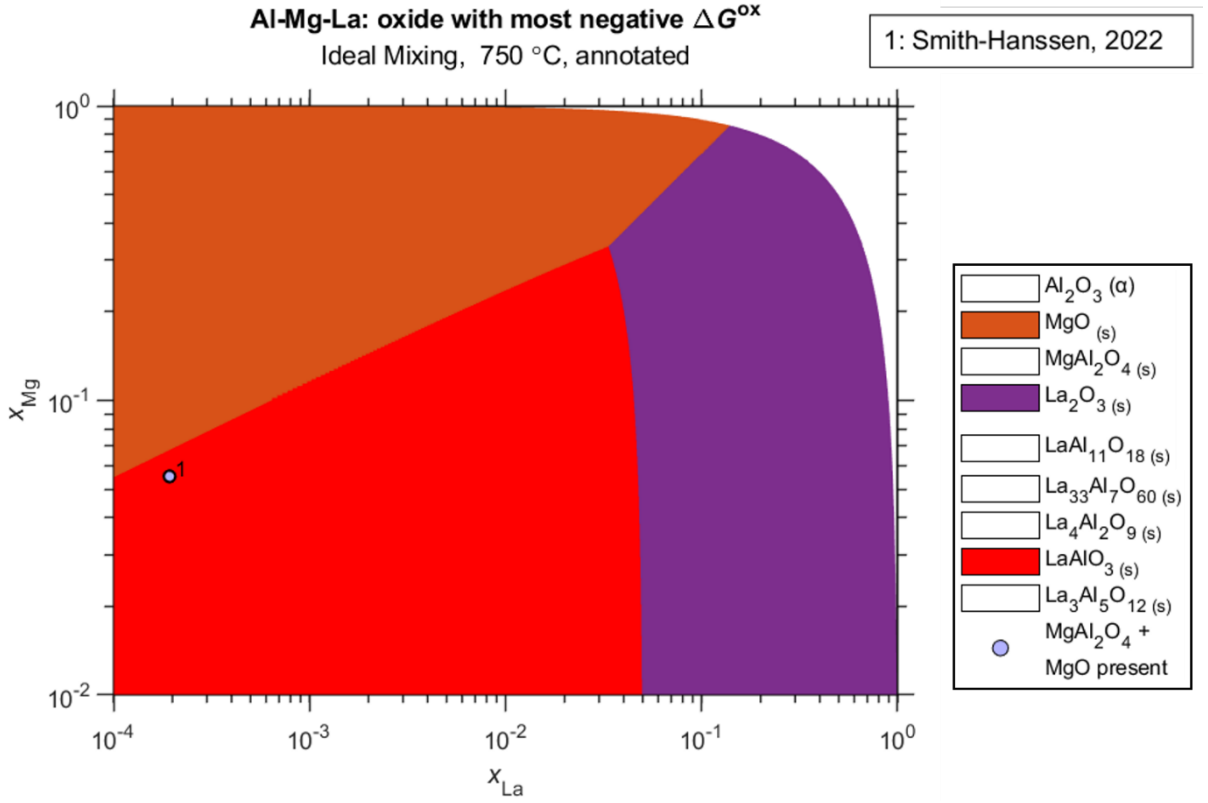
B.7.2.2.3. Al-Mg-Ce



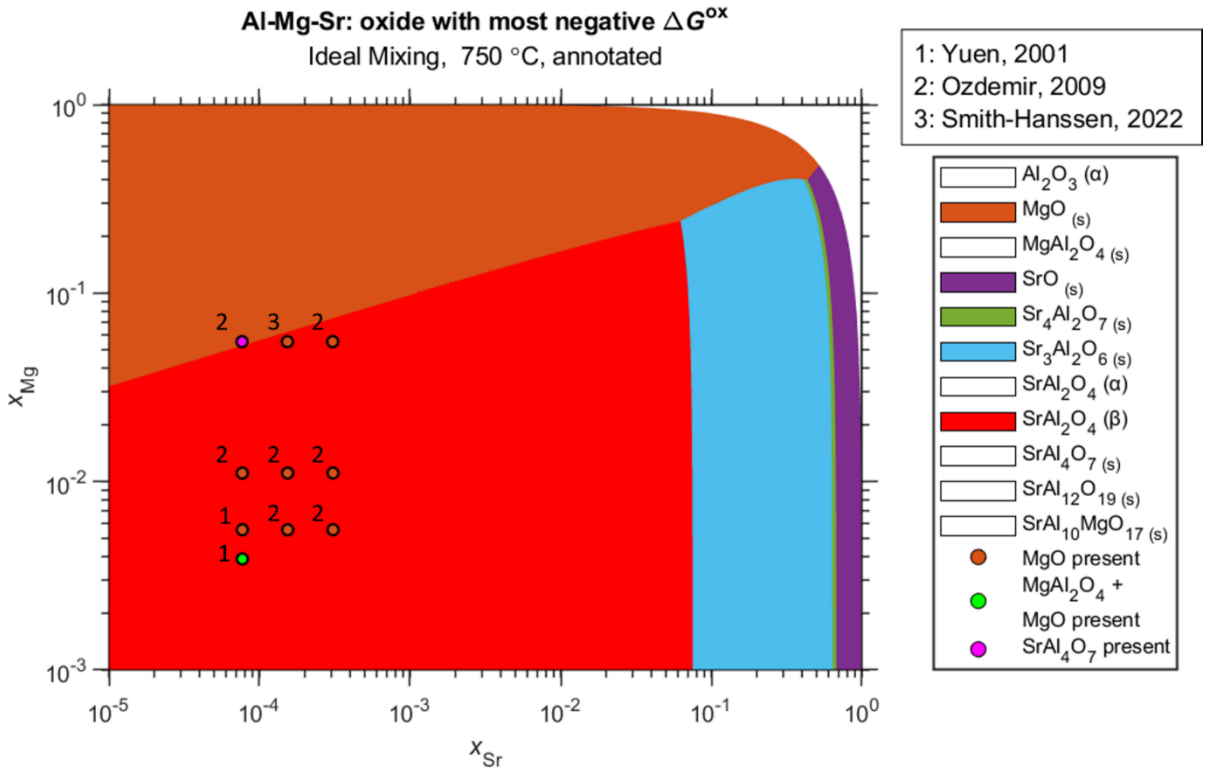
B.7.2.2.4. Al-Mg-Gd



B.7.2.2.5. Al-Mg-La

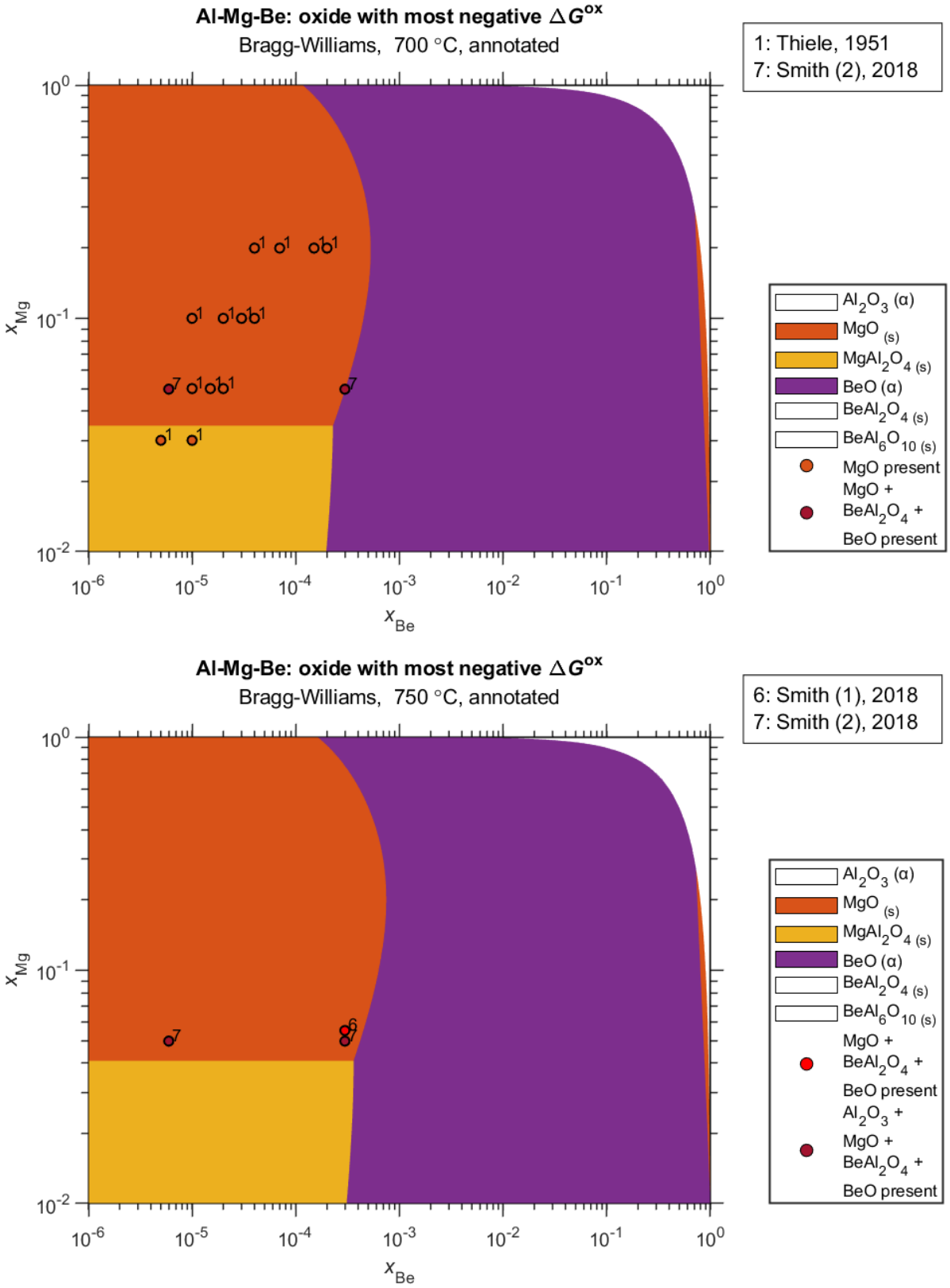


B.7.2.2.6. Al-Mg-Sr

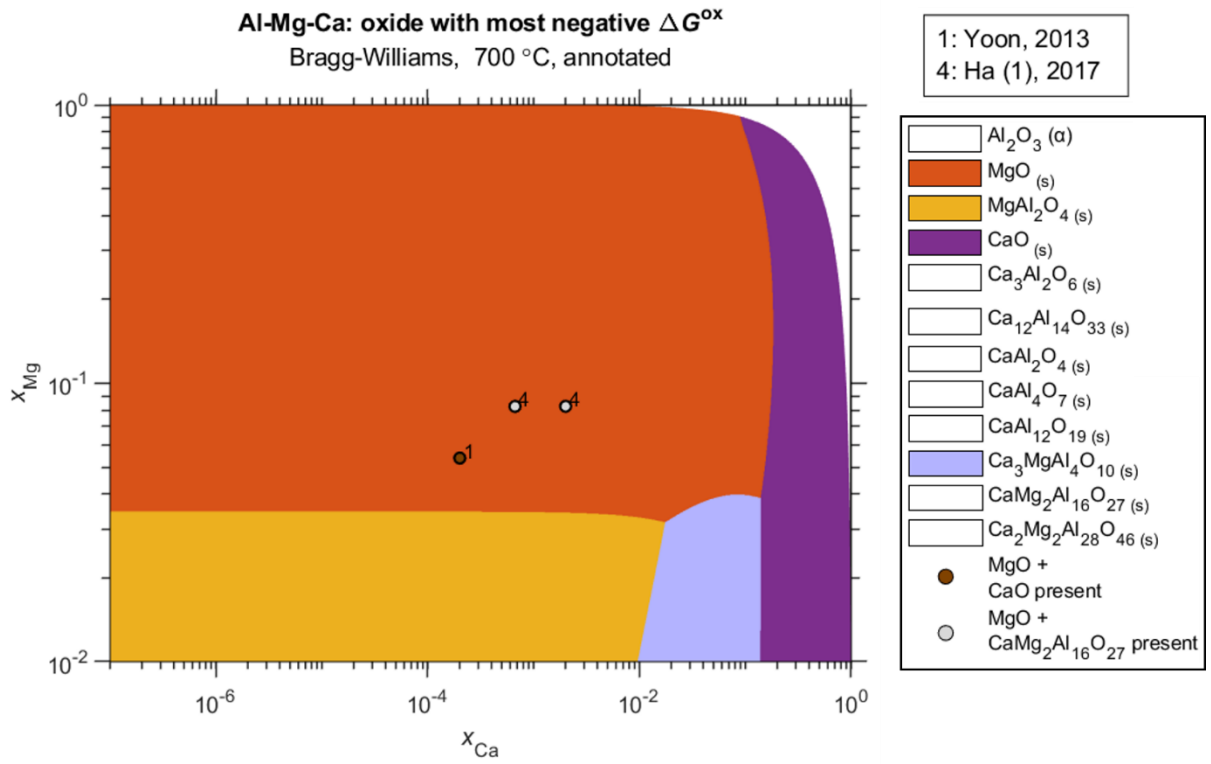


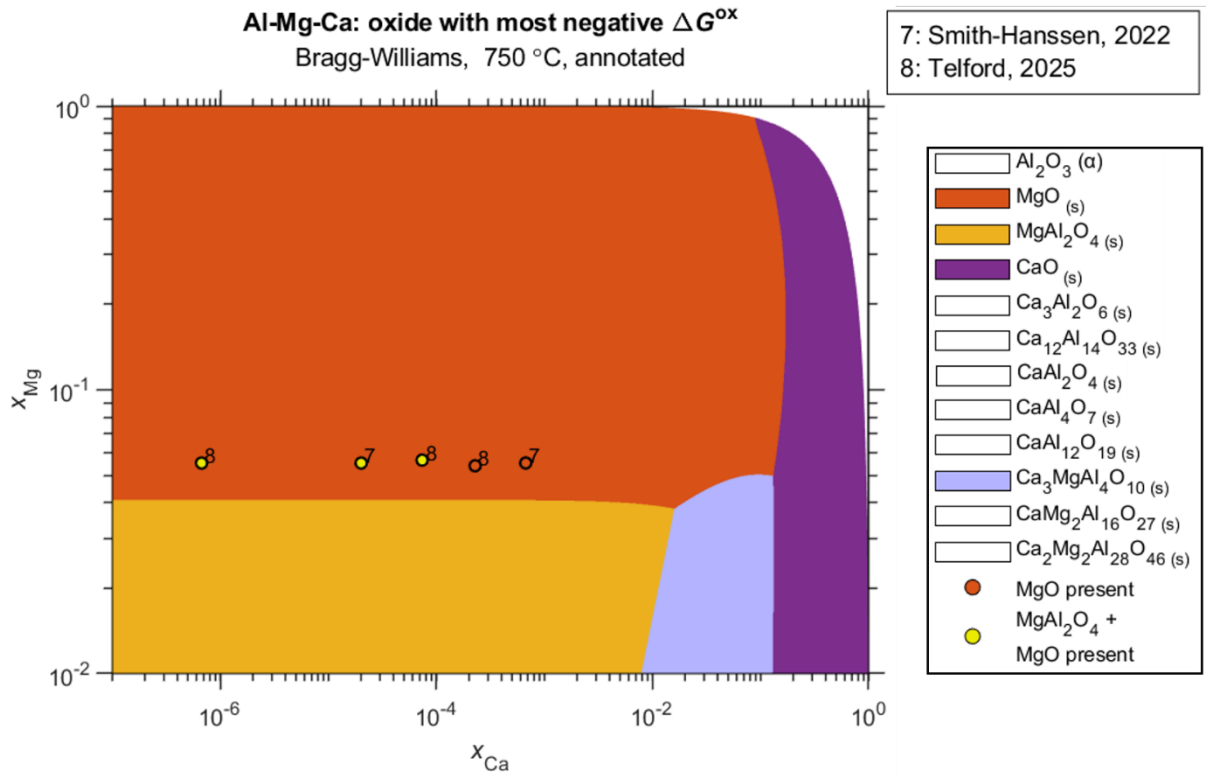
B.7.2.3. Products: Bragg-Williams

B.7.2.3.1. Al-Mg-Be

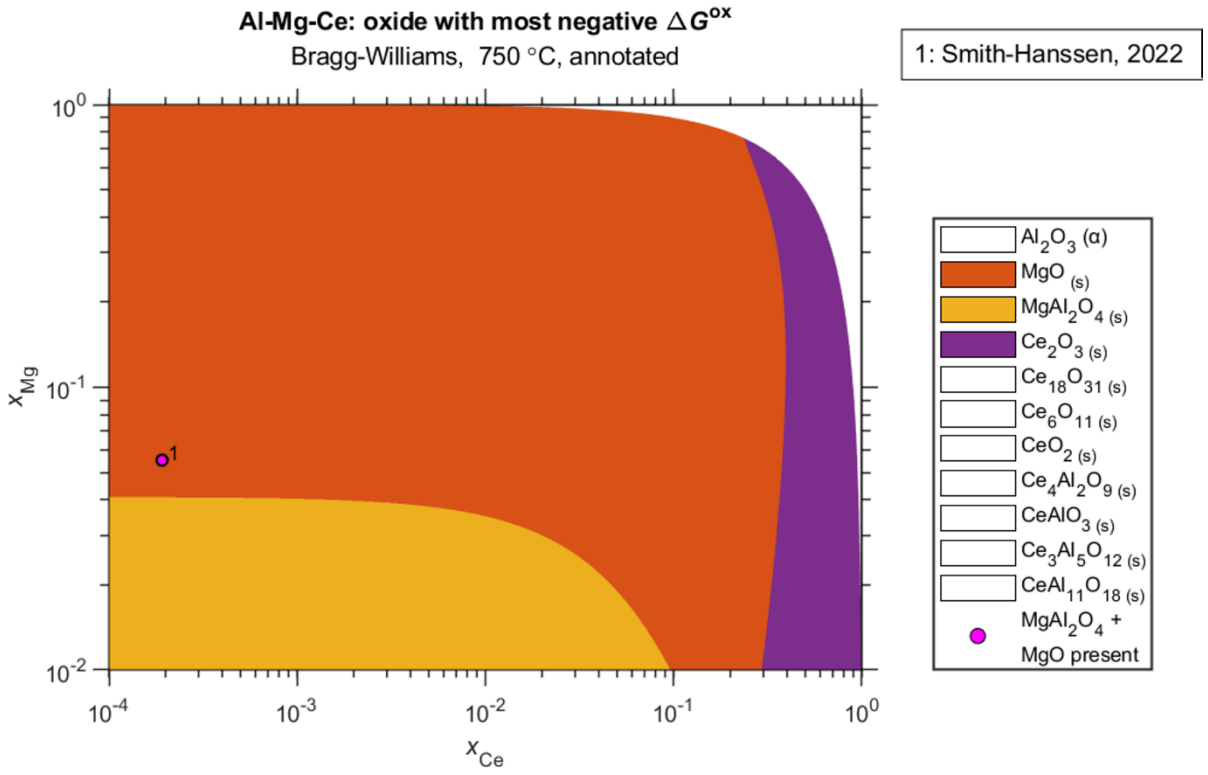


B.7.2.3.2. Al-Mg-Ca

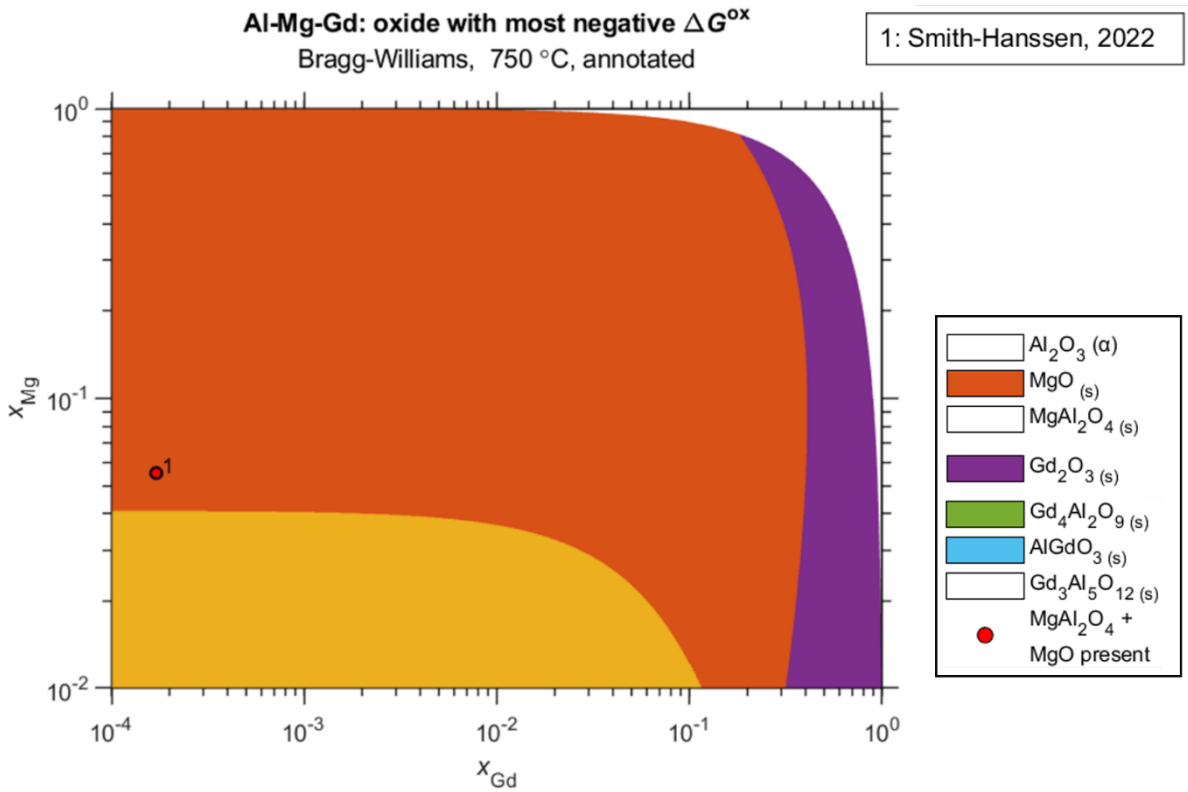




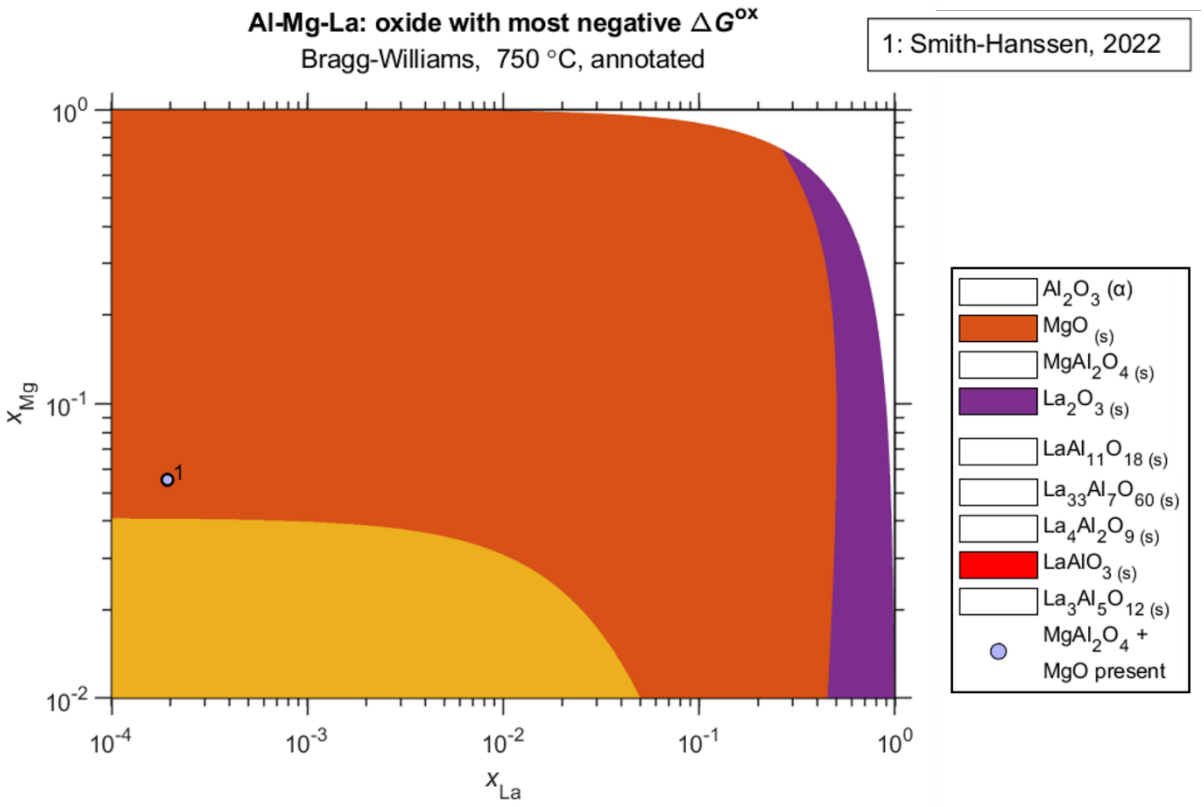
B.7.2.3.3. Al-Mg-Ce



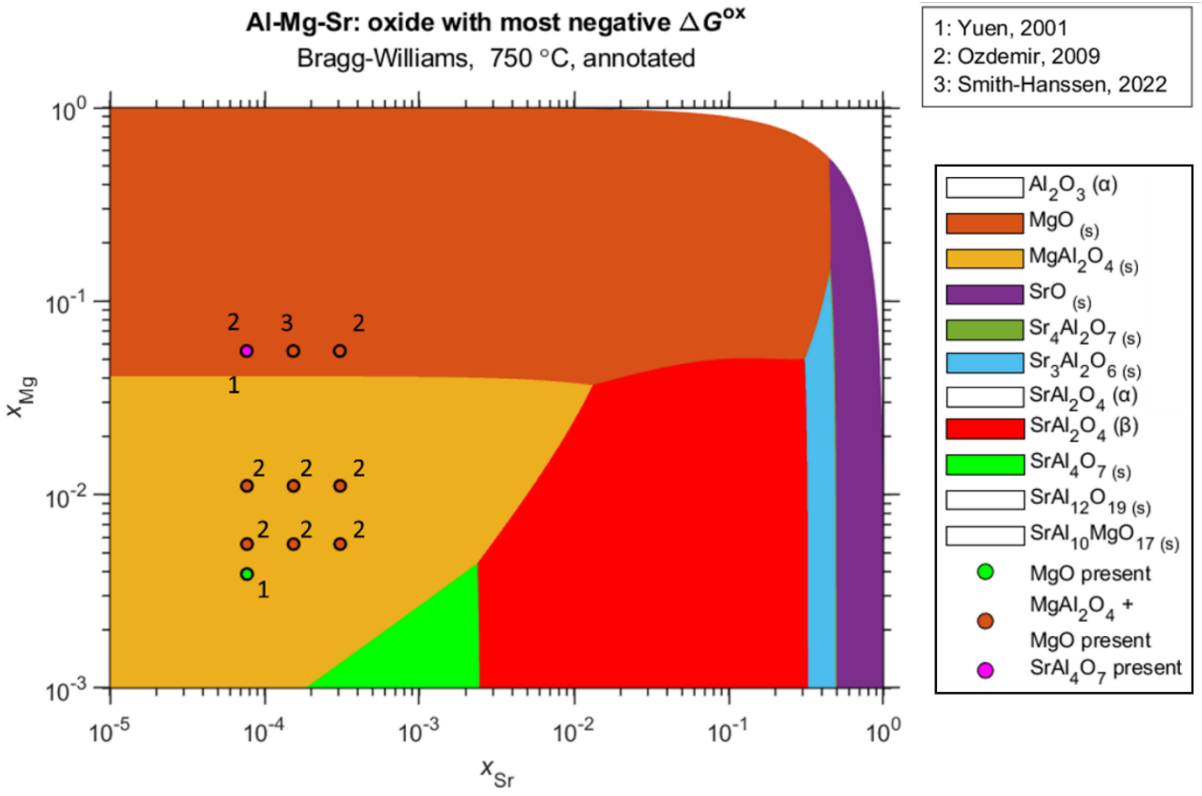
B.7.2.3.4. Al-Mg-Gd



B.7.2.3.5. Al-Mg-La

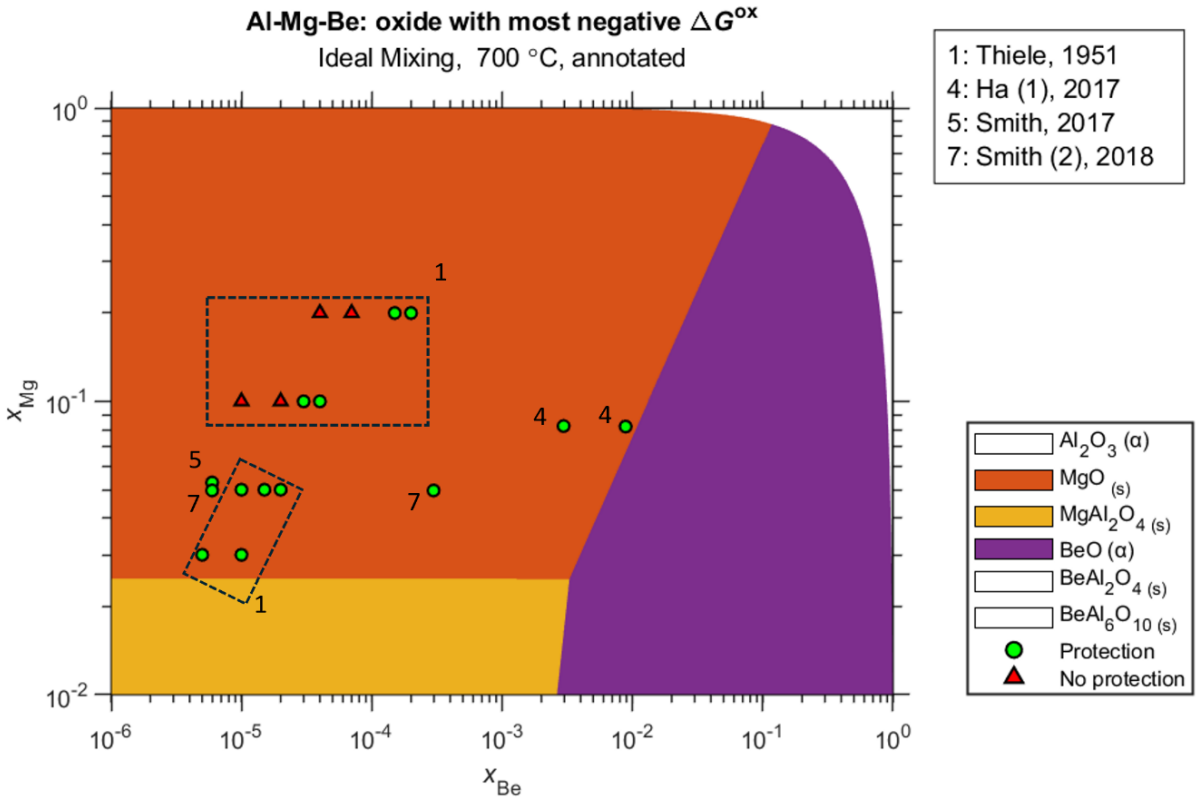


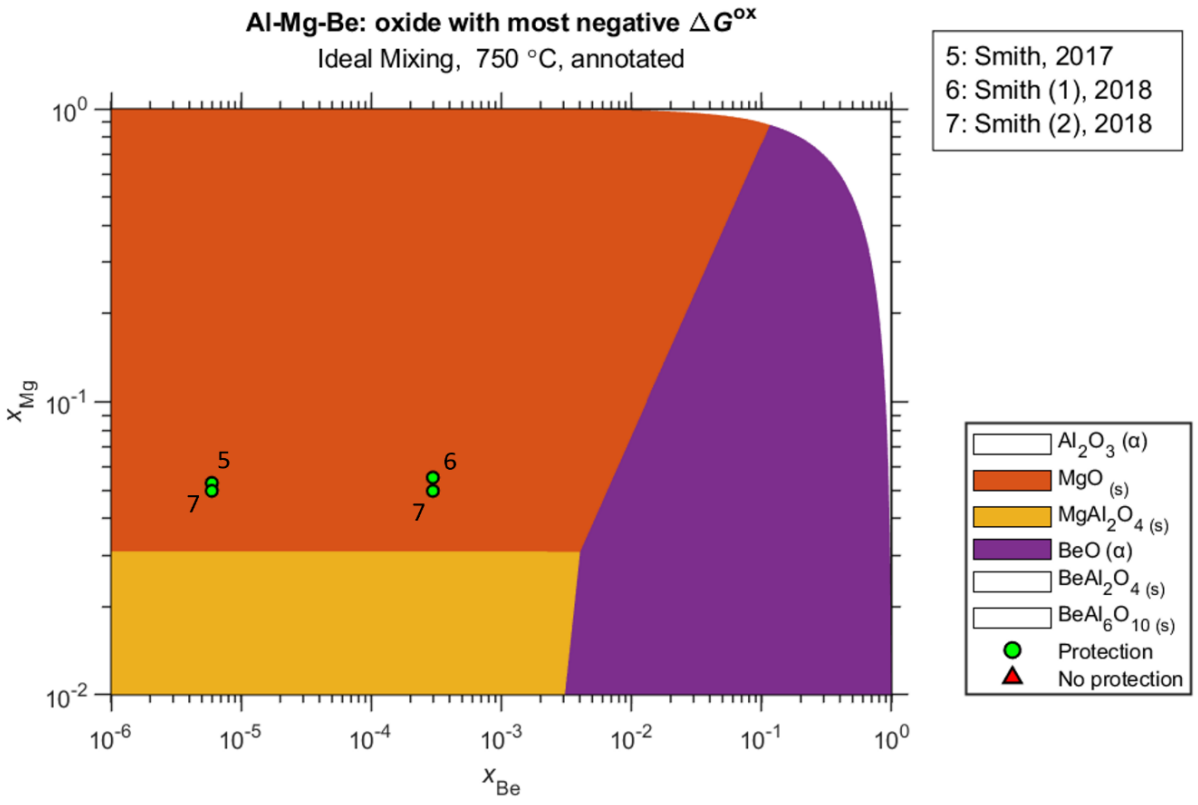
B.7.2.3.6. Al-Mg-Sr

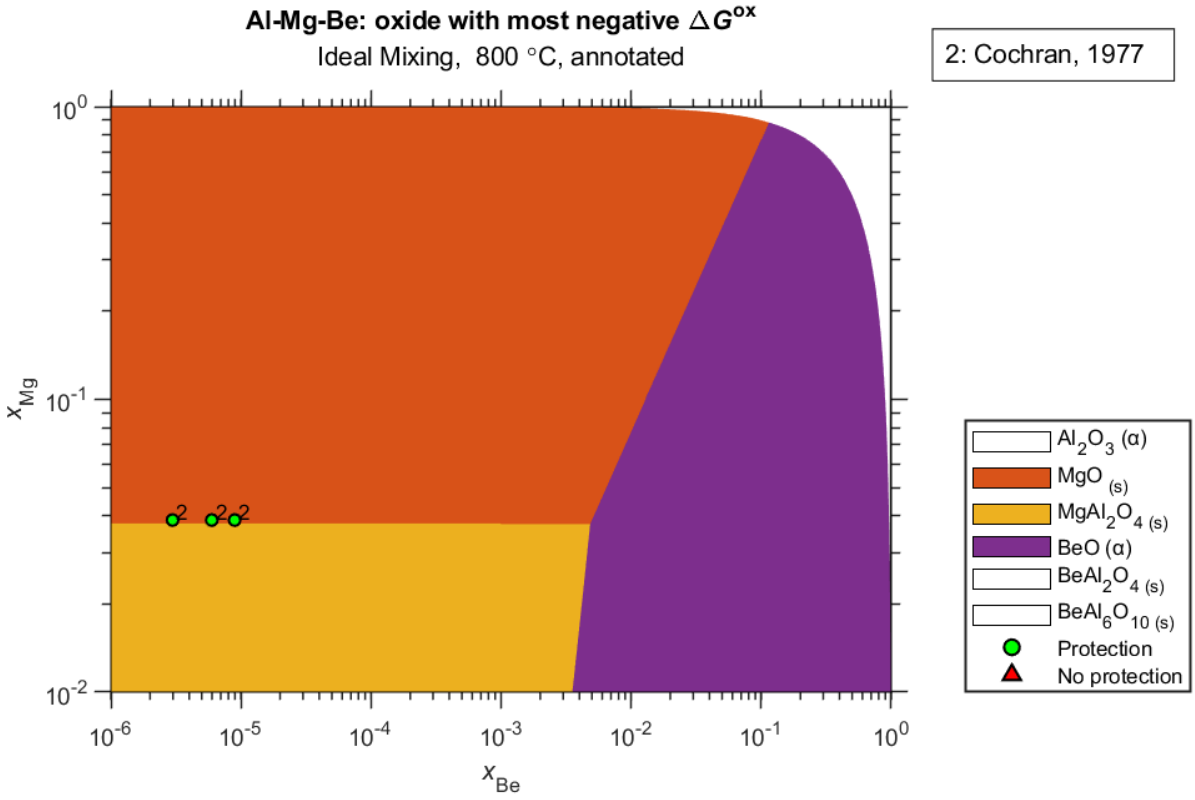


B.7.2.4. Protection: Ideal

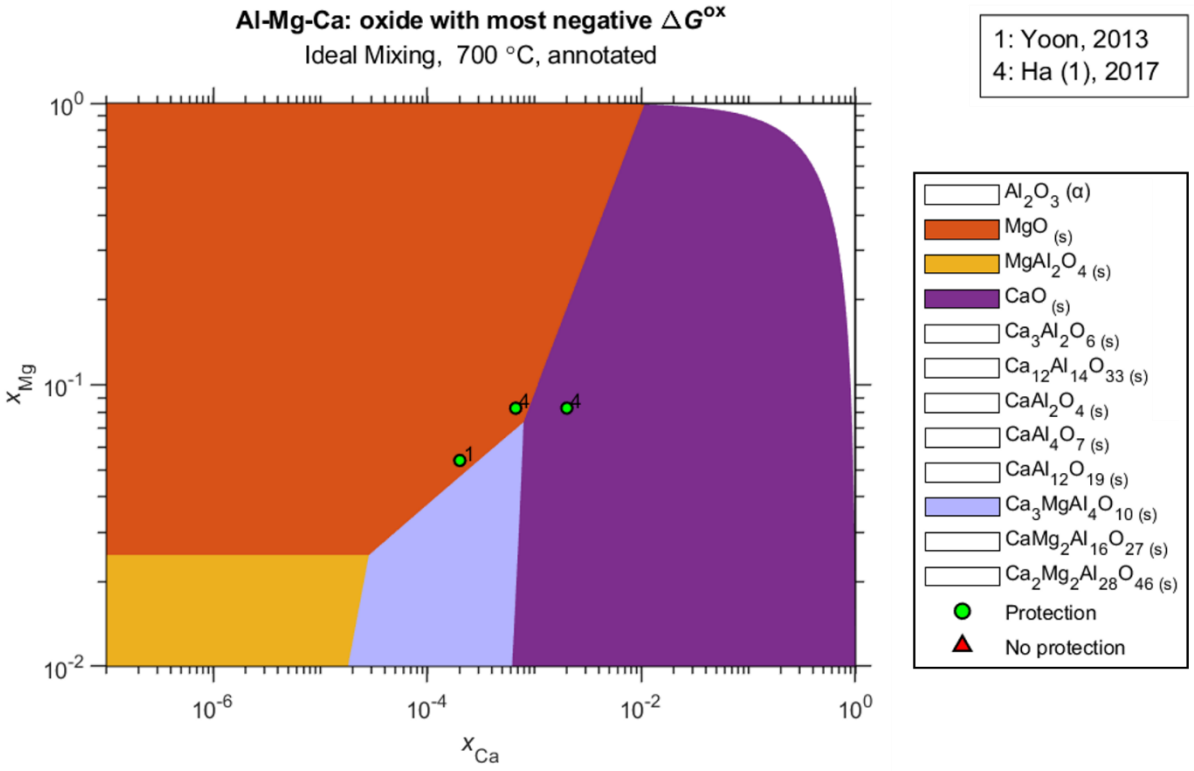
B.7.2.4.1. Al-Mg-Be

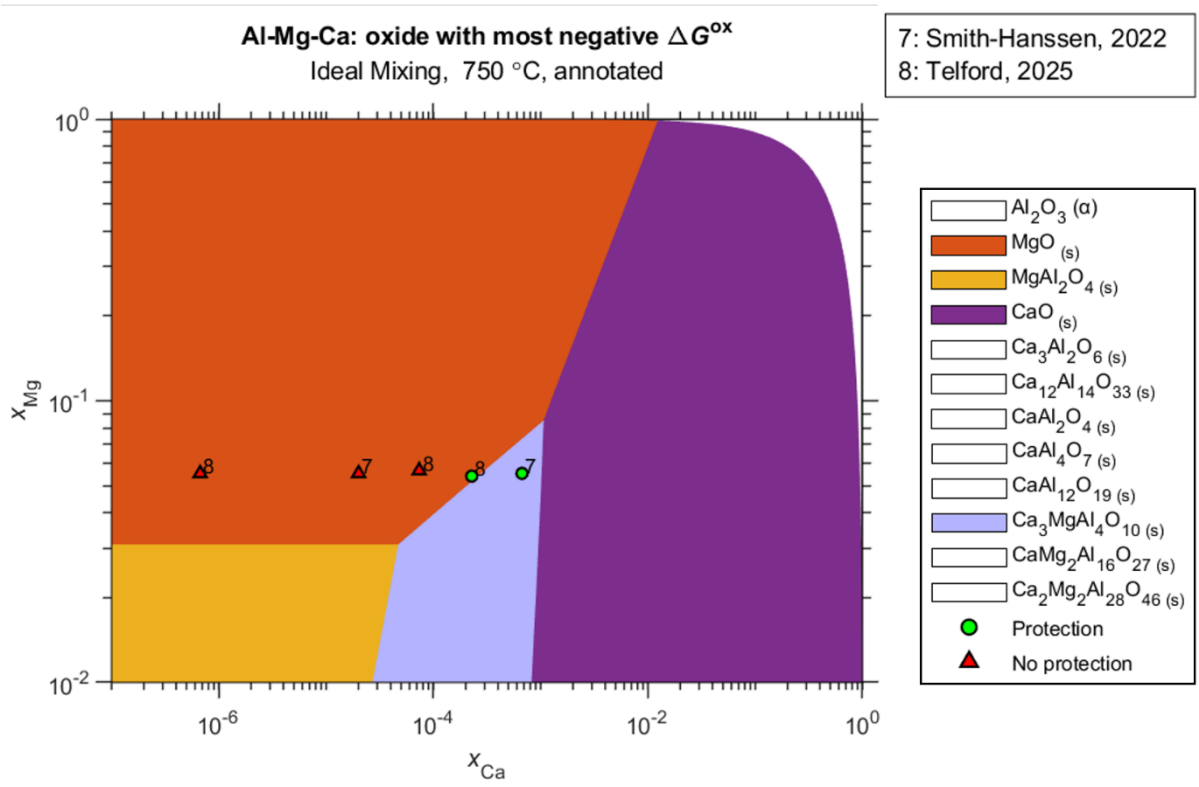




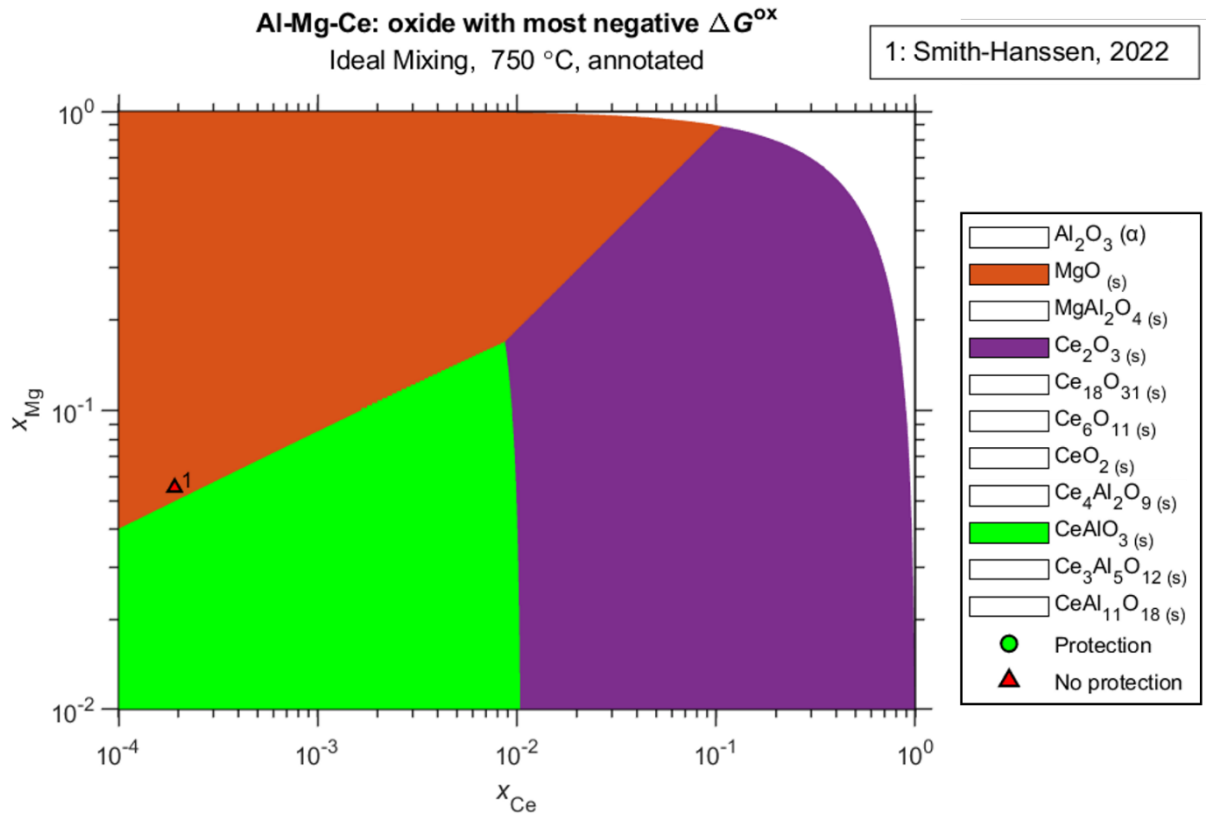


B.7.2.4.2. Al-Mg-Ca

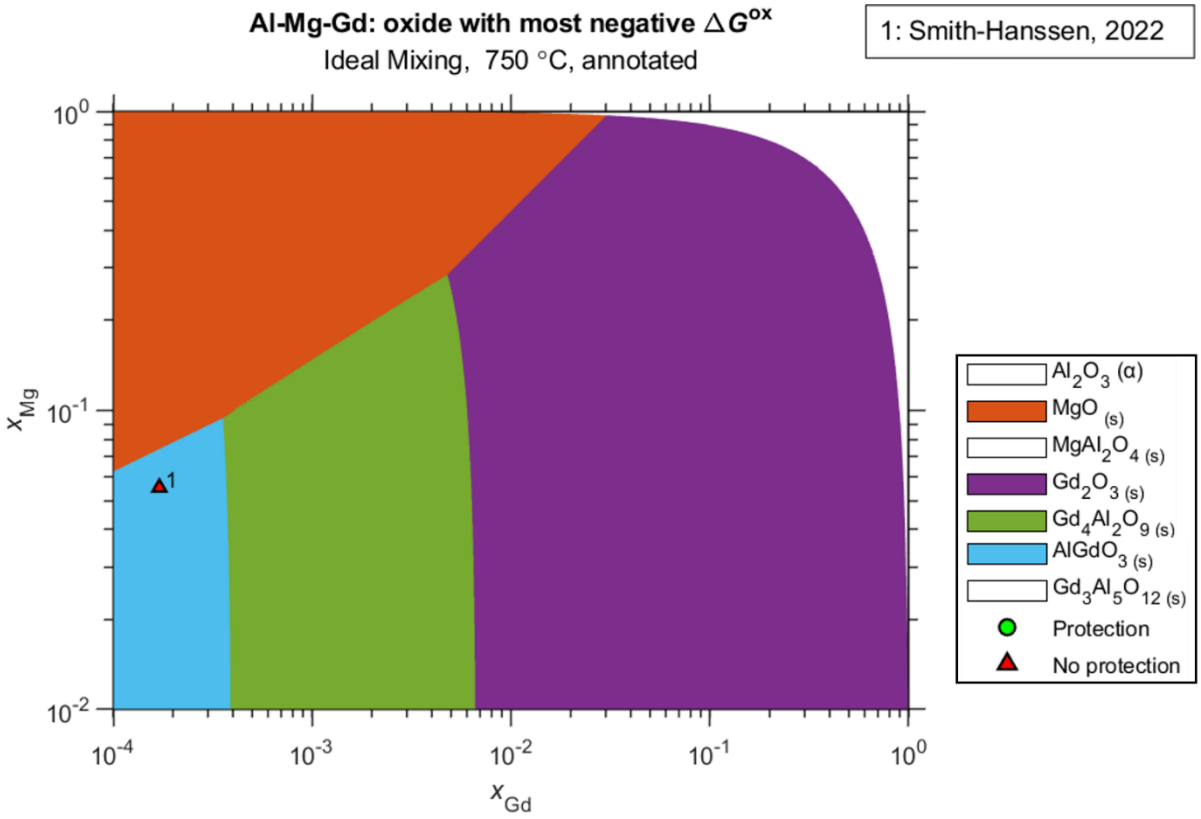




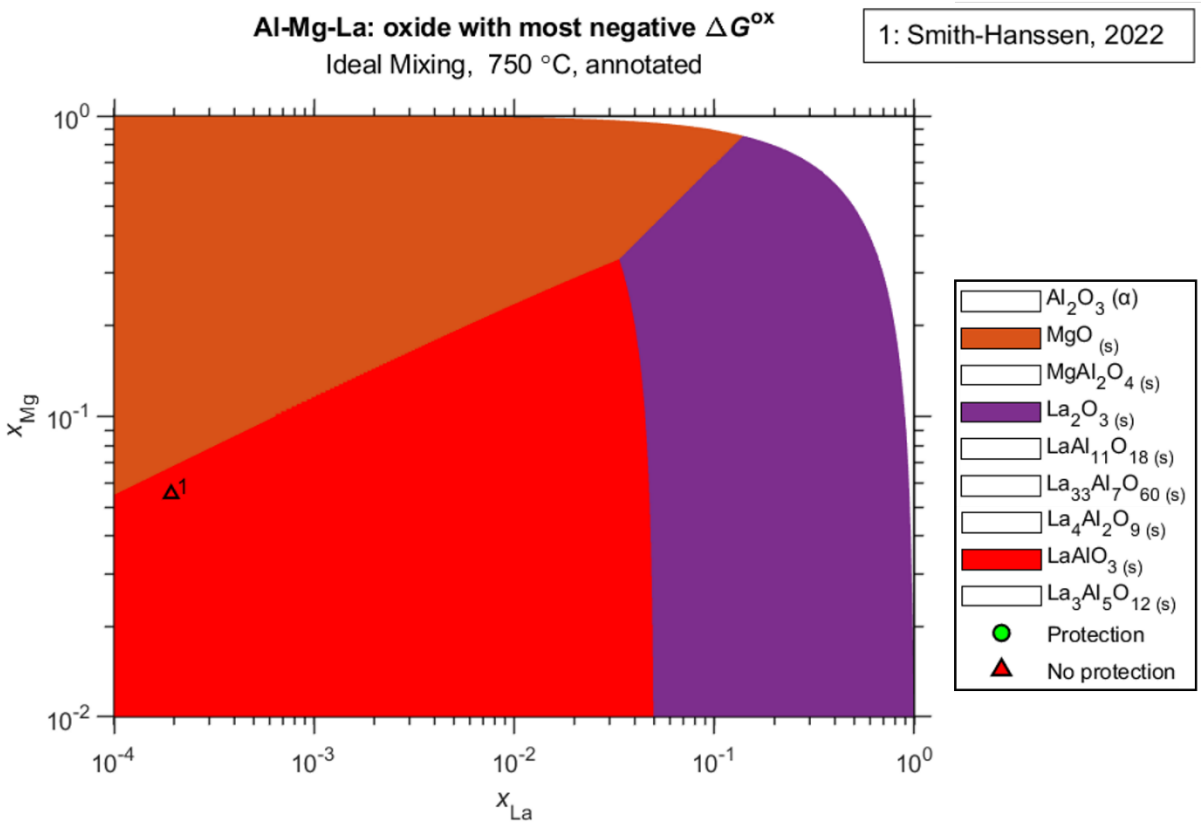
B.7.2.4.3. Al-Mg-Ce



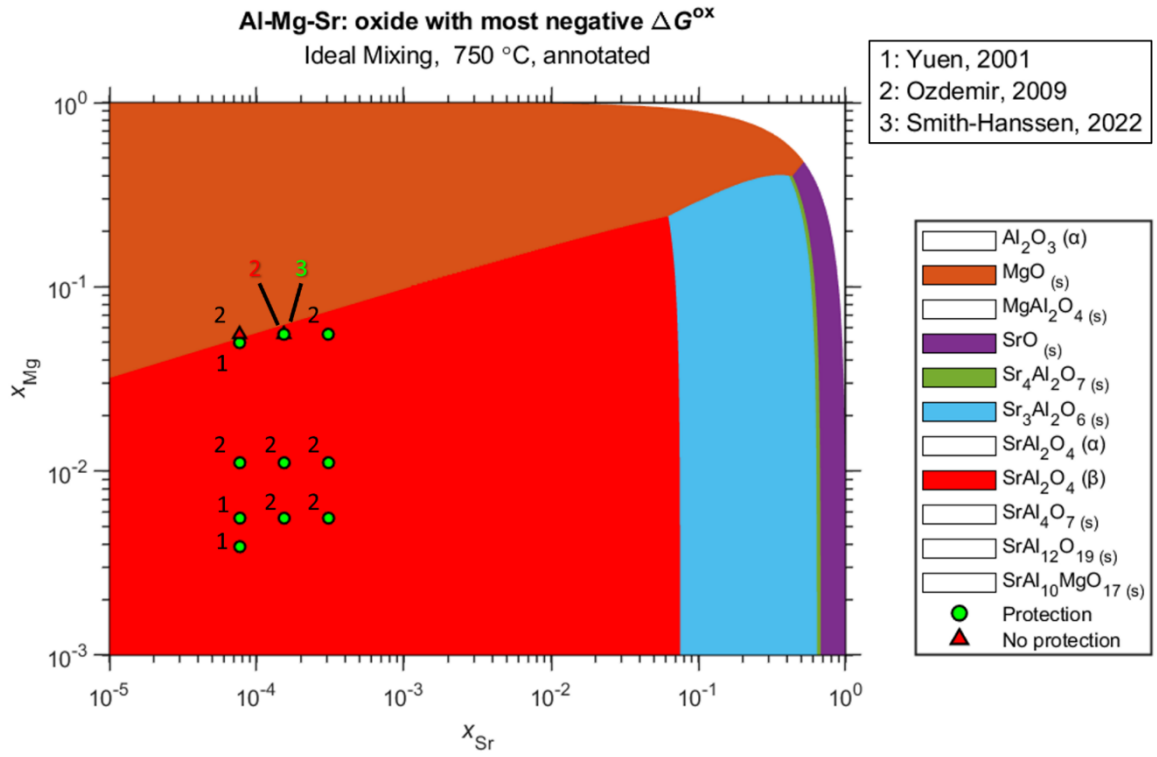
B.7.2.4.4. Al-Mg-Gd



B.7.2.4.5. Al-Mg-La

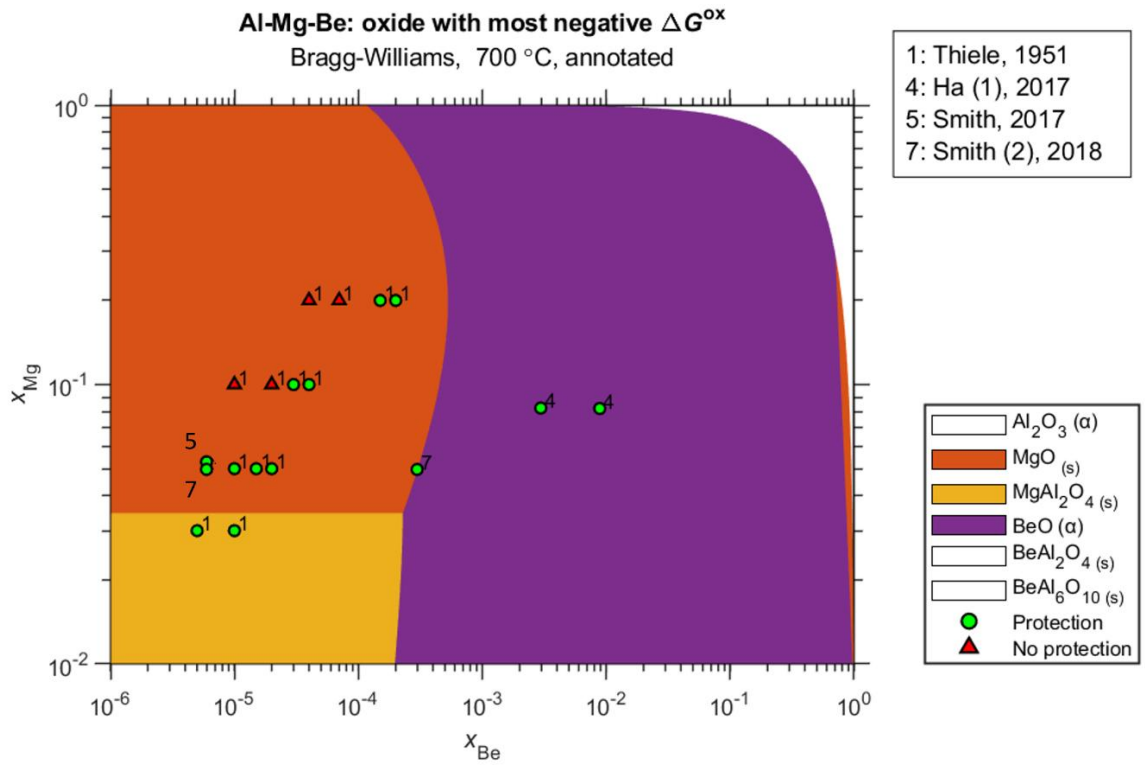


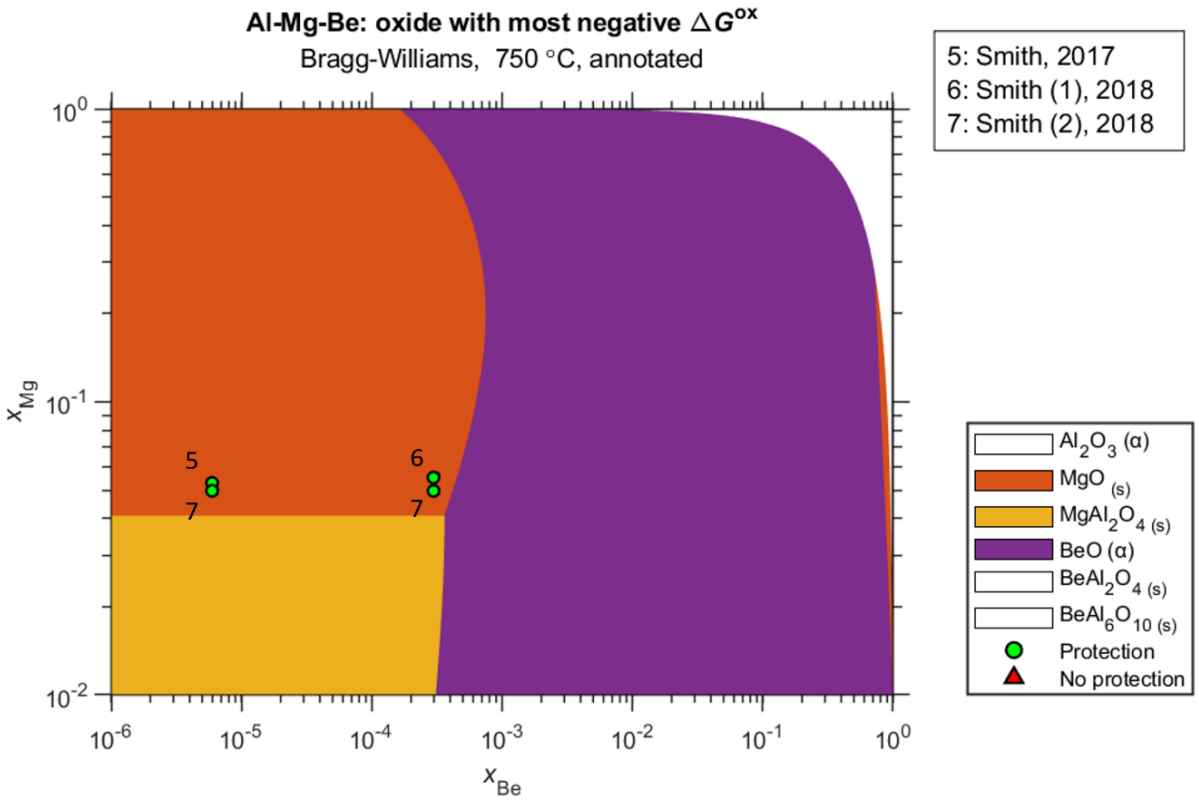
B.7.2.4.6. Al-Mg-Sr

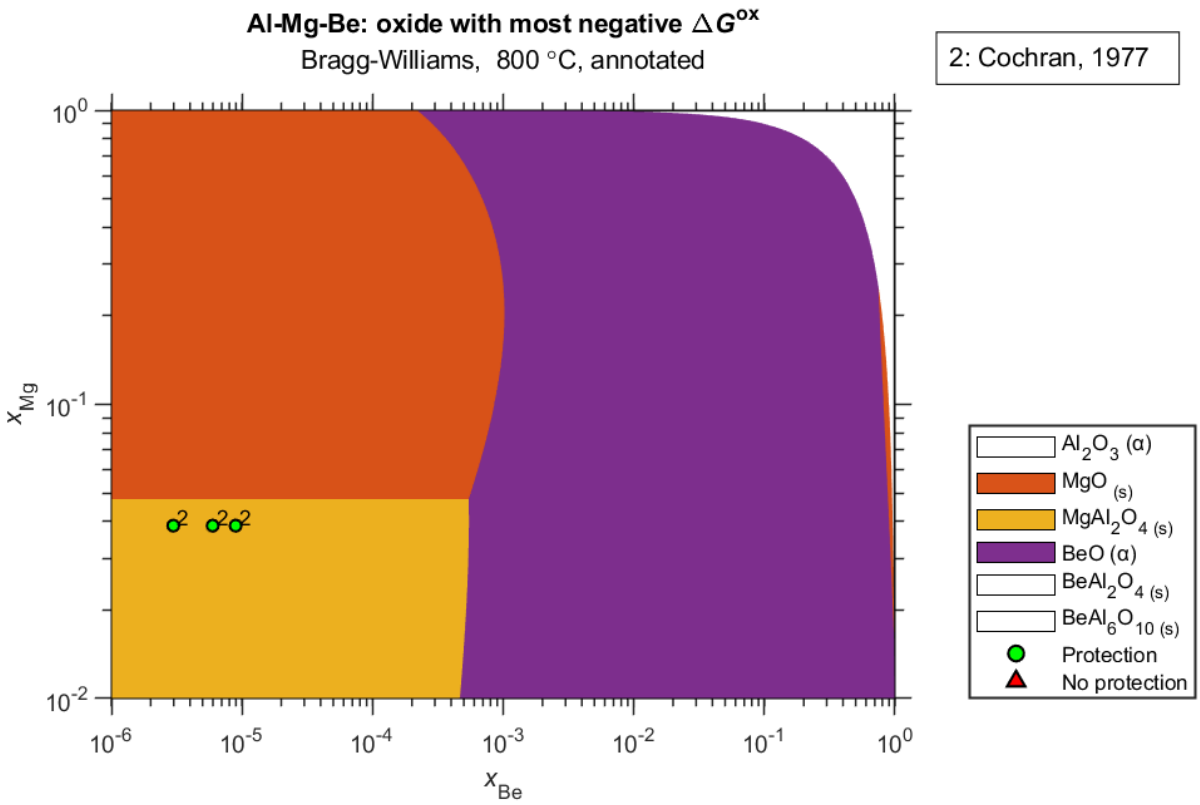


B.7.2.5. Protection: Bragg-Williams

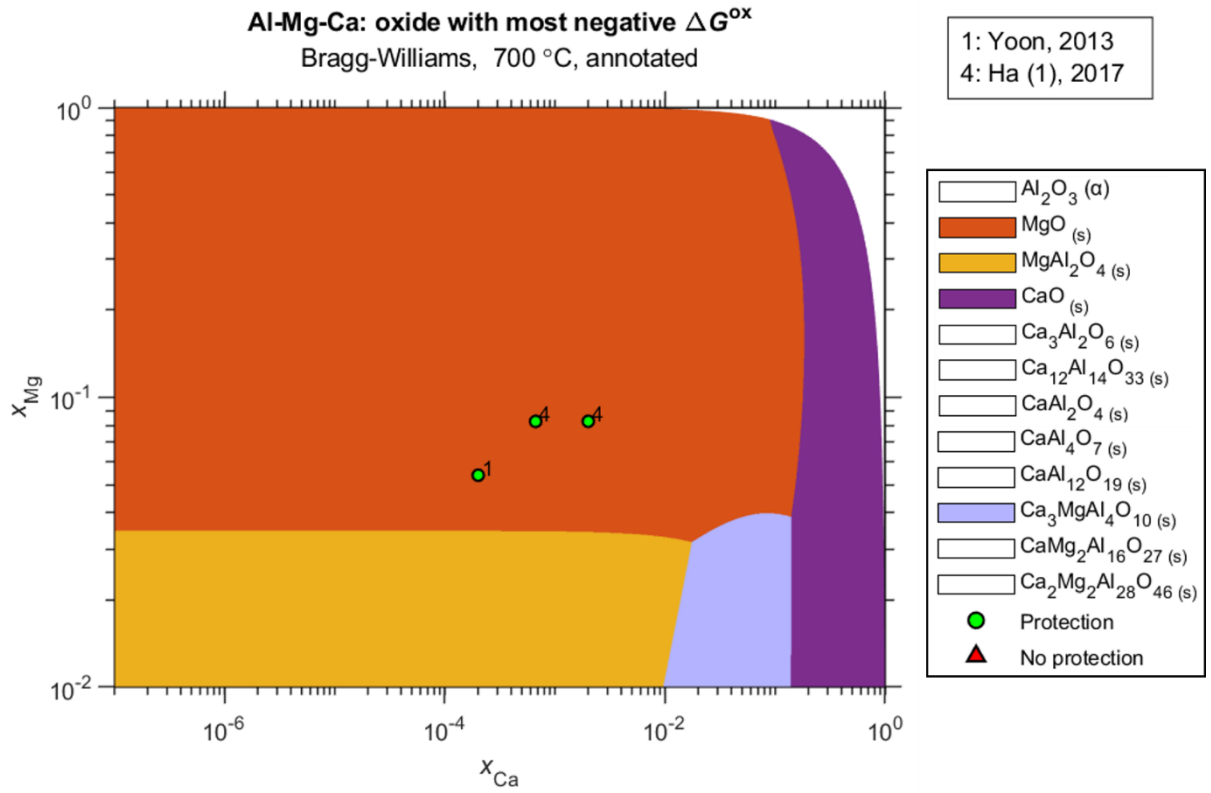
B.7.2.5.1. Al-Mg-Be

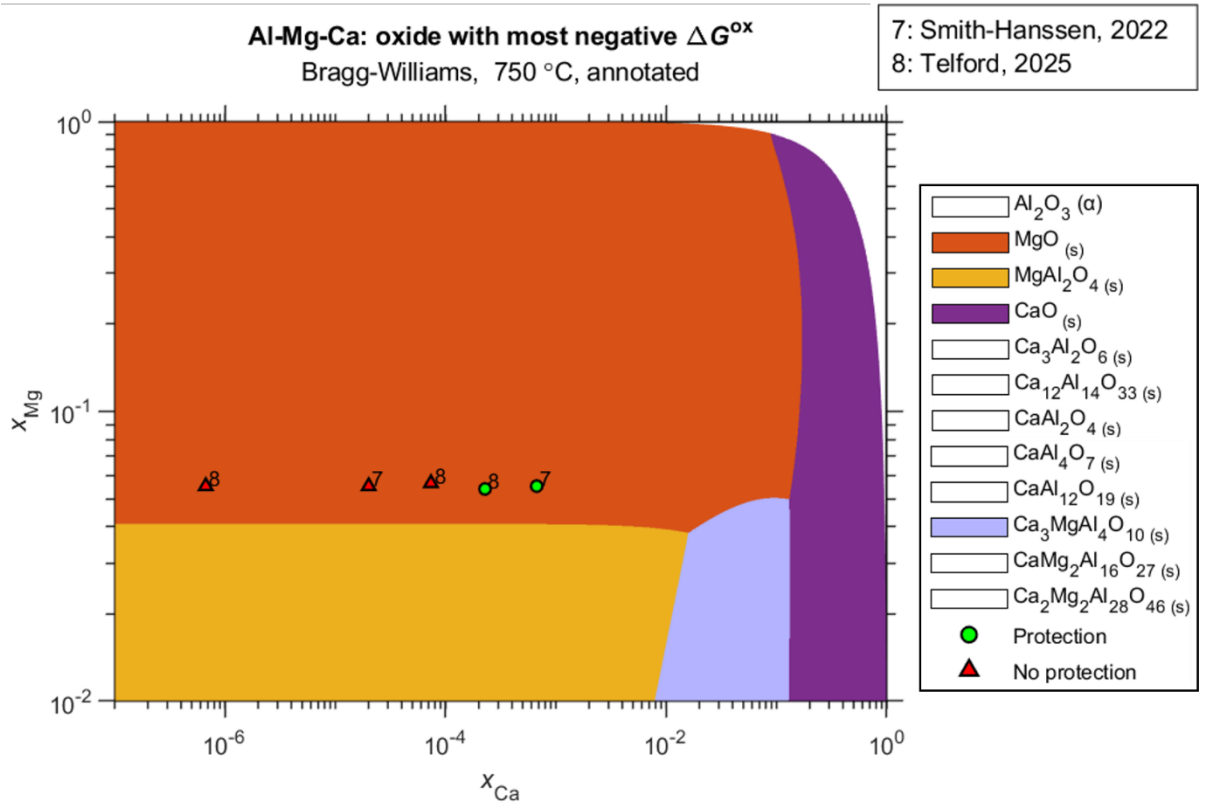



Al-Mg-Be: oxide with most negative ΔG^ox
Bragg-Williams, 750 °C, annotated
5: Smith, 2017
6: Smith (1), 2018
7: Smith (2), 2018
x_Mg
x_Be
Al2O3 (α)
MgO (s)
MgAl2O4 (s)
BeO (α)
BeAl2O4 (s)
BeAl6O10 (s)
Protection
No protection

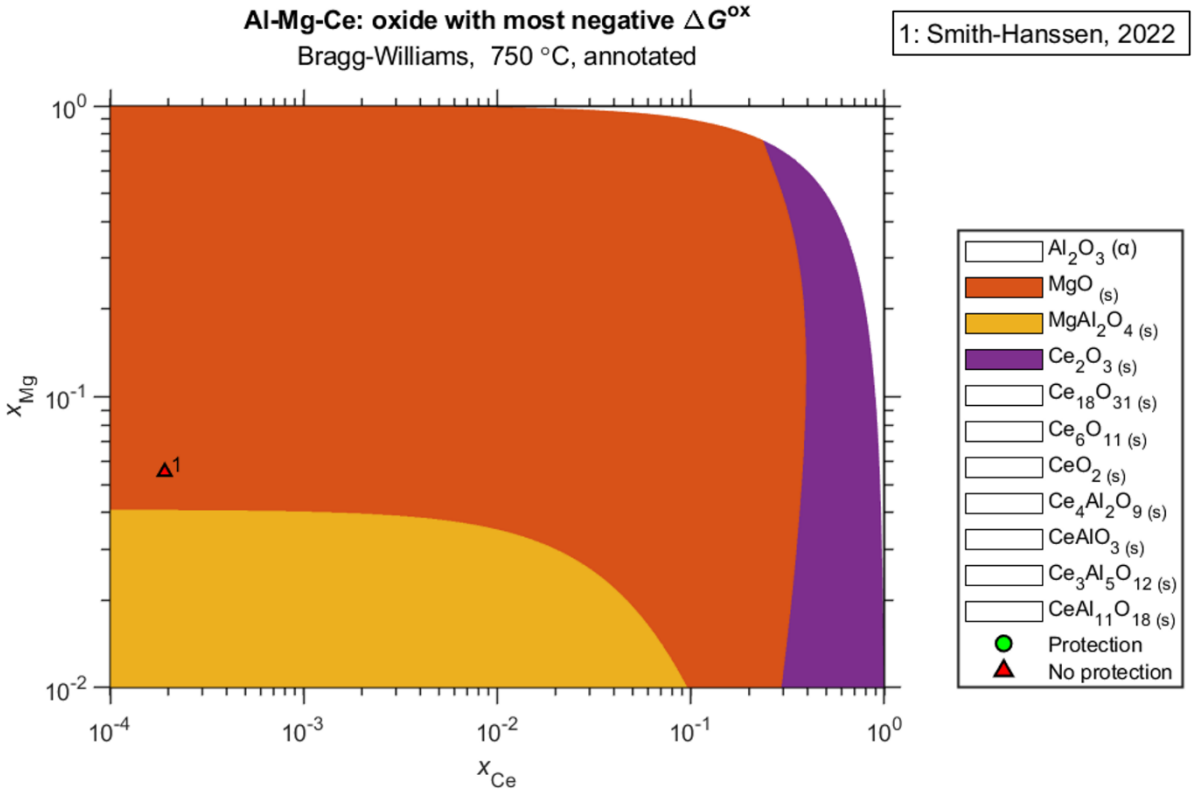

Al-Mg-Be: oxide with most negative ΔG^ox
Bragg-Williams, 800 °C, annotated
2: Cochran, 1977
x_Mg
x_Be
Al2O3 (α)
MgO (s)
MgAl2O4 (s)
BeO (α)
BeAl2O4 (s)
BeAl6O10 (s)
Protection
No protection

B.7.2.5.2. Al-Mg-Ca

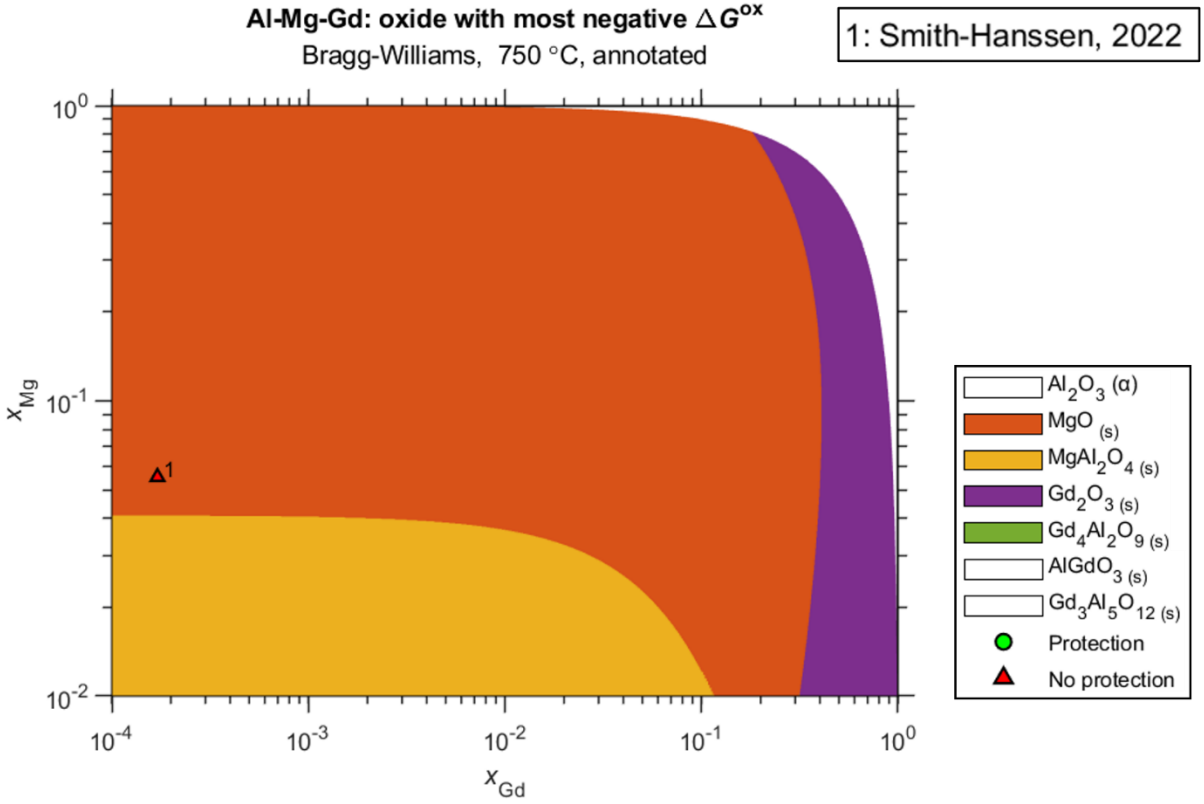




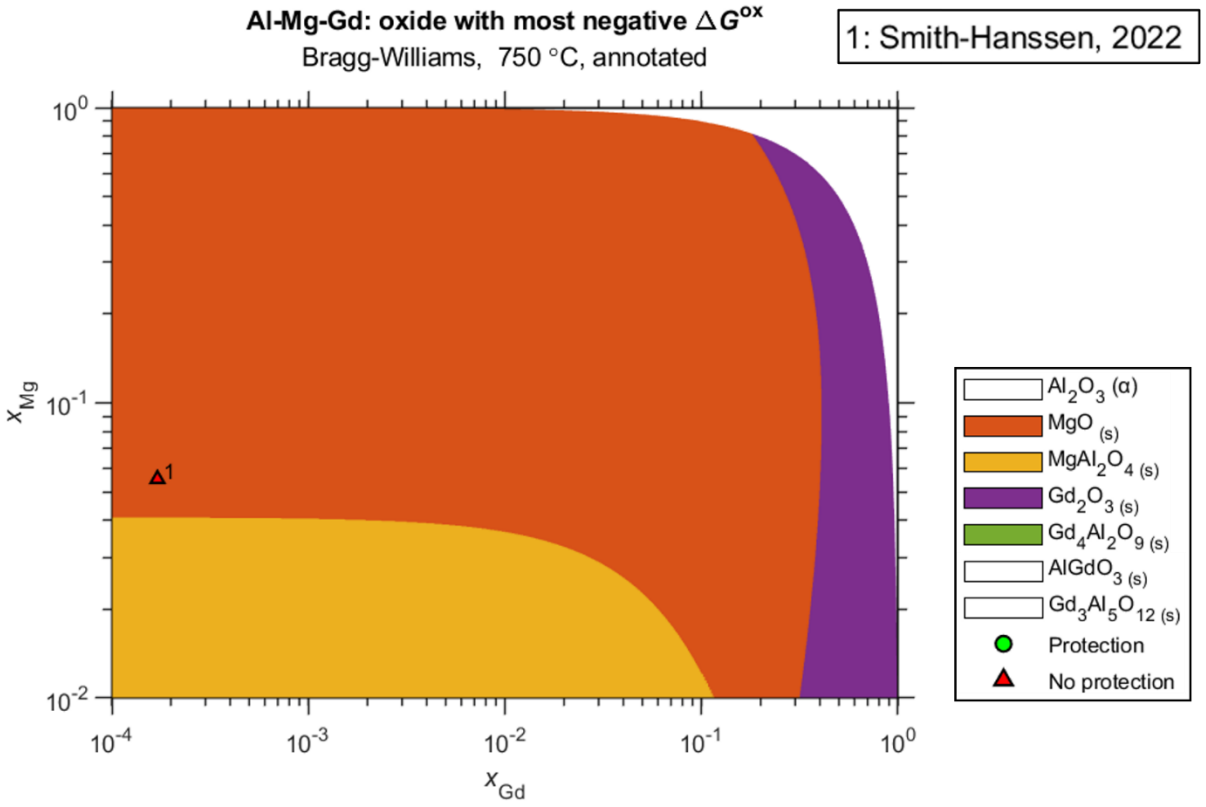
B.7.2.5.3. Al-Mg-Ce



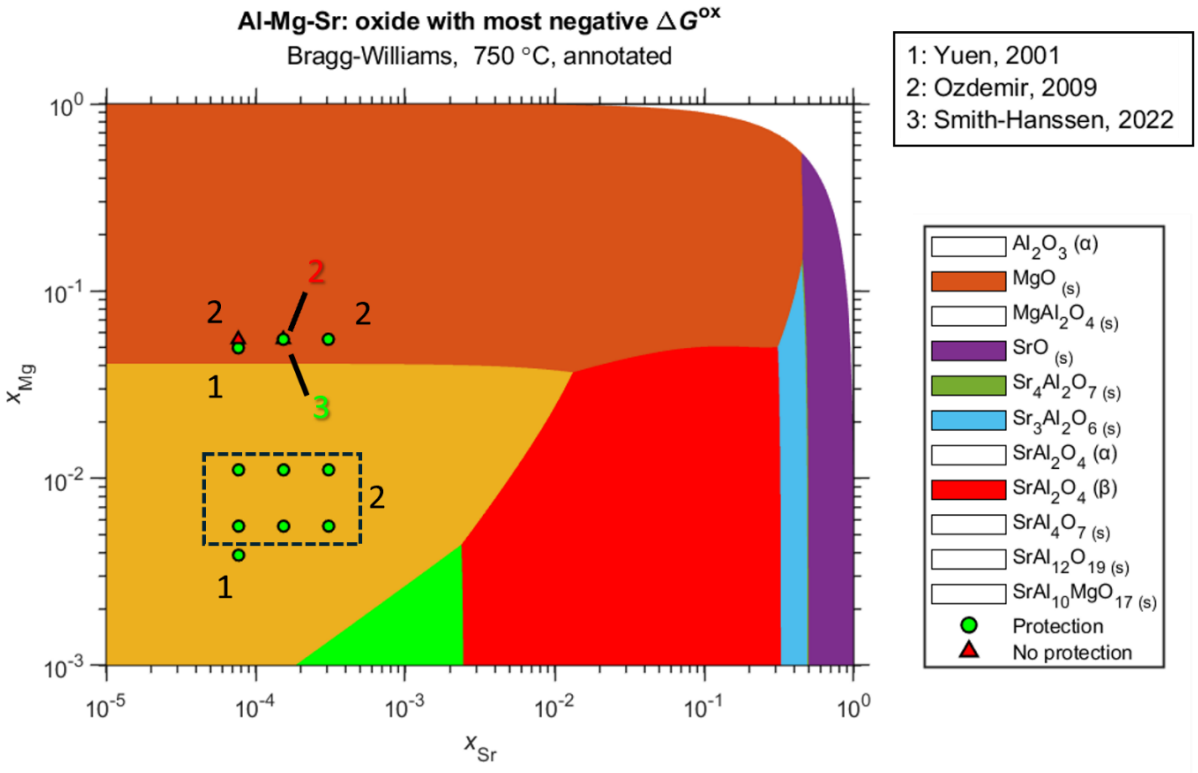
B.7.2.5.4. Al-Mg-Gd



B.7.2.5.5. Al-Mg-La



B.7.2.5.6. Al-Mg-Sr



B.8. References

[1] C.W. Bale, E. Bélisle, P. Chartrand, S.A. Decterov, G. Eriksson, A.E. Gheribi, K. Hack, I.-H. Jung, Y.-B. Kang, J. Melançon, A.D. Pelton, S. Petersen, C. Robelin, J. Sangster, P. Spencer, M.-A. Van Ende, FactSage thermochemical software and databases, 2010–2016, Calphad 54 (2016) 35–53. https://doi.org/10.1016/j.calphad.2016.05.002.

[2] M. Allibert, C. Chatillon, K.T. Jacob, R. Lourtau, Mass-Spectrometric and Electrochemical Studies of Thermodynamic Properties of Liquid and Solid Phases in the System CaO-Al2O3, Journal of the American Ceramic Society 64 (1981) 307–314. https://doi.org/10.1111/j.1151-2916.1981.tb09608.x.

[3] K.T. Jacob, C. Shekhar, G.M. Kale, Phase Equilibria in the System Al2O3-CaO-CoO and Gibbs Energy of Formation of Ca3CoAl4O10, J. Phase Equilib. Diffus. 30 (2009) 2–11. https://doi.org/10.1007/s11669-008-9423-8.

[4] K.T. Jacob, C.B. Alcock, Thermodynamics of CuAlO2 and CuAl2O4 and phase equilibria in the system Cu2O-CuO-Al2O3, J Am Ceram Soc 58 (1975) 192–195. https://doi.org/10.1111/j.1151-2916.1975.tb11441.x.

[5] W. Zhi, F. Wang, X. Chen, Y. Tian, B. Yang, Thermodynamic assessment of the CaO–Al2O3–Sc2O3 ternary system, Calphad 78 (2022) 102454. https://doi.org/10.1016/j.calphad.2022.102454.

[6] S. Terlicka, A. Dębski, W. Gierlotka, A. Wierzbicka-Miernik, A. Budziak, A. Sypien, M. Zabrocki, W. Gąsior, Structural and physicochemical properties of silver-rich Ag–Al alloys, Calphad 68 (2020) 101739. https://doi.org/10.1016/j.calphad.2020.101739.

[7] D. Mirković, J. Gröbner, R. Schmid-Fetzer, O. Fabrichnaya, H.L. Lukas, Experimental study and thermodynamic re-assessment of the Al–B system, Journal of Alloys and Compounds 384 (2004) 168–174. https://doi.org/10.1016/j.jallcom.2004.04.100.

[8] Z. Pan, Y. Du, B.Y. Huang, Y. Liu, R.C. Wang, A thermodynamic description of the Al–Be system: Modeling and experiment, Calphad 28 (2004) 371–378. https://doi.org/10.1016/j.calphad.2004.12.003.

[9] J.C. Anglezio, C. Servant, I. Ansara, Contribution to the experimental and thermodynamic assessment of the AlCaFeSi system-I. AlCaFe, AlCaSi, AlFeSi and CaFeSi systems, Calphad 18 (1994) 273–309. https://doi.org/10.1016/0364-5916(94)90034-5.

[10] M.C. Gao, N. Ünlü, G.J. Shiflet, M. Mihalkovic, M. Widom, Reassessment of Al-Ce and Al-Nd binary systems supported by critical experiments and first-principles energy calculations, Metall Mater Trans A 36 (2005) 3269–3279. https://doi.org/10.1007/s11661-005-0001-y.

[11] Y. Wang, Study on the thermodynamics of the Ni-CoAl-Mo-W system and the diffusion kinetics of its fcc phase, PhD, Shanghai, 2018.

[12] Y. Liang, C. Guo, C. Li, Z. Du, Thermodynamic modeling of the Al–Cr system, Journal of Alloys and Compounds 460 (2008) 314–319. https://doi.org/10.1016/j.jallcom.2007.06.046.

[13] N. Hayashi, K. Nakashima, M. Enoki, H. Ohtani, Thermodynamic Analysis of the Al-Cu-Mg Ternary System, J. Japan Inst. Metals 83 (2019) 378–387. https://doi.org/10.2320/jinstmet.JAW201903.

[14] M. Rank, P. Franke, H.J. Seifert, Thermodynamic investigations in the Al–Fe system: Thermodynamic modeling using CALPHAD, International Journal of Materials Research 110 (2019) 406–421. https://doi.org/10.3139/146.111765.

[15] G. Cacciamani, S. De Negri, A. Saccone, R. Ferro, The Al–R–Mg (R=Gd, Dy, Ho) systems. Part II: Thermodynamic modelling of the binary and ternary systems, Intermetallics 11 (2003) 1135–1151. https://doi.org/10.1016/S0966-9795(03)00151-1.

[16] F. Islam, A.K. Thykadavil, M. Medraj, A computational thermodynamic model of the Mg–Al–Ge system, Journal of Alloys and Compounds 425 (2006) 129–139. https://doi.org/10.1016/j.jallcom.2006.01.050.

[17] Y. Du, X. Yuan, W. Sun, B. Hu, Thermodynamic modeling of the Al-K system, Journal of Mining and Metallurgy, Section B: Metallurgy 45 (2009) 89–93.

[18] F. Yin, X. Su, Z. Li, M. Huang, Y. Shi, A thermodynamic assessment of the La–Al system, Journal of Alloys and Compounds 302 (2000) 169–172. https://doi.org/10.1016/S0925-8388(00)00679-4.

[19] H. Azza, N. Selhaoui, S. Kardellass, A. Iddaoudi, L. Bouirden, Thermodynamic description of the Aluminum-Lithium phase diagram, J Mater Environ Sci 6 (2015) 3501–3510.

[20] P. Liang, T. Tarfa, J.A. Robinson, S. Wagner, P. Ochin, M.G. Harmelin, H.J. Seifert, H.L. Lukas, F. Aldinger, Experimental investigation and thermodynamic calculation of the Al–Mg–Zn system, Thermochimica Acta 314 (1998) 87–110. https://doi.org/10.1016/S0040-6031(97)00458-9.

[21] Y. Du, J. Wang, J. Zhao, J.C. Schuster, F. Weitzer, R. Schmid-Fetzer, M. Ohno, H. Xu, Z. Liu, S. Shang, W. Zhang, Reassessment of the Al–Mn system and a thermodynamic description of the Al–Mg–Mn system, International Journal of Materials Research 98 (2007) 855–871. https://doi.org/10.3139/146.101547.

[22] J.L. Murray, The Al−Na (Aluminum-Sodium) system, Bulletin of Alloy Phase Diagrams 4 (1983) 407–410. https://doi.org/10.1007/BF02868094.

[23] W. Huang, Y.A. Chang, A thermodynamic analysis of the Ni-Al system, Intermetallics 6 (1998) 487–498. https://doi.org/10.1016/S0966-9795(97)00099-X.

[24] H. Bo, L.B. Liu, Z.P. Jin, Thermodynamic analysis of Al–Sc, Cu–Sc and Al–Cu–Sc system, Journal of Alloys and Compounds 490 (2010) 318–325. https://doi.org/10.1016/j.jallcom.2009.10.003.

[25] Z.-K. Liu, Y.A. Chang, Thermodynamic assessment of the Al-Fe-Si system, Metall Mater Trans A 30 (1999) 1081–1095. https://doi.org/10.1007/s11661-999-0160-3.

[26] W. Yi, J. Gao, Y. Tang, L. Zhang, Thermodynamic descriptions of ternary Al–Si–Sr system supported by key experiments, Calphad 68 (2020) 101732. https://doi.org/10.1016/j.calphad.2019.101732.

[27] Q. Luo, Q. Li, J.-Y. Zhang, S.-L. Chen, K.-C. Chou, Experimental investigation and thermodynamic optimization of the Al–Zn–Ti system in the Al-rich corner, Intermetallics 33 (2013) 73–80. https://doi.org/10.1016/j.intermet.2012.09.027.

[28] S.A. Mey, Reevaluation of the Al - Zn System, International Journal of Materials Research 84 (1993) 451–455. https://doi.org/10.1515/ijmr-1993-840704.

[29] Z. Long, D. Cui, H. Hu, Z. Li, F. Yin, T. Fan, Thermodynamic Modeling of the Al-Li-Zr Ternary System, J. Phase Equilib. Diffus. 41 (2020) 623–641. https://doi.org/10.1007/s11669-020-00827-z.

[30] M. Piché, Modélisation thermodynamique des alliages de magnésium avec Al, Mn, Fe et Be, Masters, Polytechnique Montréal, 2002.

[31] R. Agarwal, J.J. Lee, H.L. Lukas, F. Sommer, Calorimetric measurements and thermodynamic optimization of the Ca - Mg system, Zeitschrift Fuer Metallkunde/Materials Research and Advanced Techniques 86 (1995) 103–108.

[32] C. Guo, Z. Du, C. Li, A thermodynamic description of the Ce–La–Mg system, International Journal of Materials Research 101 (2010) 1424–1431. https://doi.org/10.3139/146.110380.

[33] J. Gröbner, D. Mirkovic, M. Ohno, R. Schmid-Fetzer, Experimental investigation and thermodynamic calculation of binary Mg-Mn phase equilibria, J Phs Eqil and Diff 26 (2005) 234–239. https://doi.org/10.1007/s11669-005-0110-8.

[34] D. Kevorkov, R. Schmid-Fetzer, F. Zhang, Phase equilibria and thermodynamics of the Mg-Si-Li system and remodeling of the Mg-Si system, J Phs Eqil and Diff 25 (2004) 140–151. https://doi.org/10.1007/s11669-004-0007-y.

[35] Y. Zhong, J.O. Sofo, A.A. Luo, Z.-K. Liu, Thermodynamics modeling of the Mg-Sr and Ca-Mg-Sr systems, Journal of Alloys and Compounds 421 (2006) 172–178. https://doi.org/10.1016/j.jallcom.2005.09.076.

[36] A. Janz, J. Gröbner, D. Mirković, M. Medraj, J. Zhu, Y.A. Chang, R. Schmid-Fetzer, Experimental study and thermodynamic calculation of Al–Mg–Sr phase equilibria, Intermetallics 15 (2007) 506–519. https://doi.org/10.1016/j.intermet.2006.09.001.

[37] E.E. Moore, P.E.A. Turchi, V. Lordi, D. Weiss, Z.C. Sims, H.B. Henderson, M.S. Kesler, O. Rios, S.K. McCall, A. Perron, Thermodynamic Modeling of the Al-Ce-Cu-Mg-Si System and Its Application to Aluminum-Cerium Alloy Design, J. Phase Equilib. Diffus. 41 (2020) 764–783. https://doi.org/10.1007/s11669-020-00852-y.

[38] C. Qiu, S. Liu, J. Huang, Y. Du, Phase equilibria and solidification behavior of Mg–Al–Gd casting alloys, Transactions of Nonferrous Metals Society of China 34 (2024) 1091–1109. https://doi.org/10.1016/S1003-6326(23)66456-8.

[39] M. Hosseinifar, D.V. Malakhov, On the fabricability of a composite material containing the FCC matrix with embedded ductile B2 intermetallics, Journal of Alloys and Compounds 505 (2010) 459–466. https://doi.org/10.1016/j.jallcom.2010.04.254.

[40] S. Wasiur-Rahman, M. Medraj, A thermodynamic description of the Al–Ca–Zn ternary system, Calphad 33 (2009) 584–598. https://doi.org/10.1016/j.calphad.2009.06.001.

[41] L. Jin, Y.-B. Kang, P. Chartrand, C.D. Fuerst, Thermodynamic evaluation and optimization of Al–La, Al–Ce, Al–Pr, Al–Nd and Al–Sm systems using the Modified Quasichemical Model for liquids, Calphad 35 (2011) 30–41. https://doi.org/10.1016/j.calphad.2010.11.002.

[42] L. Jin, Y.-B. Kang, P. Chartrand, C.D. Fuerst, Thermodynamic evaluation and optimization of Al–Gd, Al–Tb, Al–Dy, Al–Ho and Al–Er systems using a Modified Quasichemical Model for the liquid, Calphad 34 (2010) 456–466. https://doi.org/10.1016/j.calphad.2010.08.004.

[43] J.-P. Harvey, P. Chartrand, Modeling the Hydrogen Solubility in Liquid Aluminum Alloys, Metall Mater Trans B 41 (2010) 908–924. https://doi.org/10.1007/s11663-010-9381-5.

[44] S. Cui, I.-H. Jung, Thermodynamic modeling of the quaternary Al-Cu-Mg-Si system, Calphad 57 (2017) 1–27. https://doi.org/10.1016/j.calphad.2017.02.002.

[45] S. Abdessameud, Thermodynamic Modeling of the Mg-Al-Li-Na-H System for Solid State Hydrogen Storage Applications, PhD, Concordia University, 2016.

[46] Y.-B. Kang, A.D. Pelton, P. Chartrand, C.D. Fuerst, Critical evaluation and thermodynamic optimization of the Al–Ce, Al–Y, Al–Sc and Mg–Sc binary systems, Calphad 32 (2008) 413–422. https://doi.org/10.1016/j.calphad.2008.03.002.

[47] M. Aljarrah, M. Medraj, Thermodynamic assessment of the phase equilibria in the Al–Ca–Sr system using the modified quasichemical model, The Journal of Chemical Thermodynamics 40 (2008) 724–734. https://doi.org/10.1016/j.jct.2007.10.003.

[48] M. Ahmad, Thermal oxidation behavior of an Al-Li-Cu-Mg-Zr alloy, Metallurgical Transactions A 18 (1987) 681–689. https://doi.org/10.1007/BF02649484.

[49] M. Akbarifar, M. Divandari, S.M.A. Boutorabi, S.-H. Ha, Y.-O. Yoon, S.K. Kim, Short-Time Oxidation of Al–Mg in Dynamic Conditions, Oxid Met 94 (2020) 409–429. https://doi.org/10.1007/s11085-020-09999-y.

[50] S. Amirinejhad, R. Raiszadeh, H. Doostmohammadi, Calorimetric study of the oxidation of Al–Mg alloys for the prediction of healing of the double oxide film defect, J Therm Anal Calorim 113 (2013) 769–777. https://doi.org/10.1007/s10973-012-2810-8.

[51] M. Aryafar, R. Raiszadeh, A. Shalbafzadeh, Healing of double oxide film defects in A356 aluminium melt, J Mater Sci 45 (2010) 3041–3051. https://doi.org/10.1007/s10853-010-4308-8.

[52] F.N. Bakhtiarani, R. Raiszadeh, The behaviour of double oxide film defects in Al–4.5 wt.% Mg melt, J Mater Sci 46 (2011) 1305–1315. https://doi.org/10.1007/s10853-010-4916-3.

[53] D.L. Belitskus, Oxidation of molten AI-Mg alloy in air, air-SO2, and air-H2S atmospheres, Oxid Met 3 (1971) 313–317.

[54] A.J. Brock, G.R. Irani, M.J. Pryor, The kinetics of the oxidation of aluminum-zinc alloys in oxygen at high temperature, Oxid Met 15 (1981) 77–100. https://doi.org/10.1007/BF00603756.

[55] C.N. Cochran, D.L. Belitskus, D.L. Kinosz, Oxidation of aluminum-magnesium melts in air, oxygen, flue gas, and carbon dioxide, Metall Mater Trans B 8 (1977) 323–332. https://doi.org/10.1007/BF02657663.

[56] D.J. Field, E.P. Butler, Liquid metal oxidation of Al-3wt.%Li, in: Aluminum-Lithium Alloys II: Proceedings of the Second International Aluminum-Lithium Conference, Metallurgical Society of AIME, Monterey, CA, USA, 1983: pp. 667–673.

[57] D.J. Field, G.M. Scanans, E.P. Butler, The high temperature oxidation of Al-Li alloy, in: Aluminum-Lithium Alloys II: Proceedings of the Second International Aluminum-Lithium Conference, The Metallurgical Society of AIME, Monterey, CA, USA, 1983: pp. 657–66.

[58] H. Fujii, H. Akiyama, J. Kaneko, M. Sugamata, L. Blaz, Al-Sc Master Alloy Prepared by Mechanical Alloying of Aluminum with Addition of Sc2O3, Mater. Trans. 44 (2003) 1049–1052. https://doi.org/10.2320/matertrans.44.1049.

[59] I.N. Ganiev, N.I. Ganieva, D.B. Eshova, Oxidation of Aluminum Melts with Rare-Earth Metals, Russ. Metall. 2018 (2018) 458–464. https://doi.org/10.1134/S0036029518050063.

[60] I. Haginoya, T. Fukusako, Influence of alloying elements on oxidation of molten aluminum alloys, J Jpn Foundrym Soc 54 (1982) 664–669. https://doi.org/10.11279/imono.54.10_664.

[61] I. Haginoya, T. Fukusako, Oxidation of molten Al–Mg alloys, Trans Jpn Inst Metal 24 (1983) 613–619. https://doi.org/10.2320/matertrans1960.24.613.

[62] W. Han, X. Hu, Corrosion of Al-Li alloy melt on oxide refractories, Anti-Corrosion Methods and Materials 70 (2023) 229–235. https://doi.org/10.1108/ACMM-03-2023-2779.

[63] M. Hanabe, V. Jayaram, T.A. Bhaskaran, Growth of Al2O3Al composites from Al-Zn alloys, Acta Mater 44 (1996) 819–829. https://doi.org/10.1016/1359-6454(95)00185-9.

[64] E.M. Hinton, The oxidation of liquid aluminium and the potential for oxides in grain refinement of aluminium alloys, PhD, University of Birmingham, 2016. https://etheses.bham.ac.uk/id/eprint/6508/ (accessed July 14, 2021).

[65] P. Holdway, A.W. Bowen, The measurement of lithium depletion in aluminium-lithium alloys using X-ray diffraction, J Mater Sci 24 (1989) 3841–3849. https://doi.org/10.1007/BF01168945.

[66] C. Houska, Beryllium in aluminium and magnesium alloys, Met Mater 4 (1988) 100.

[67] S. Impey, D.J. Stephenson, J.R. Nicholls, A study of the effect of magnesium additions on the oxide growth morphologies on liquid aluminium alloys, in: Microscopy of Oxidation, The Institute of Metals, Cambridge, UK, 1990: pp. 238–244.

[68] V. Jayaram, The role of volatile solute elements in directed melt oxidation of aluminium alloys, J Mater Sci 31 (1996) 4591–4598. https://doi.org/10.1007/BF00366356.

[69] F. Khaleghifar, R. Raiszadeh, H. Doostmohammadi, Effect of Ca on the behavior of double oxide film defects in commercially pure aluminum melt, Metall Mater Trans B 46 (2015) 1044–1051. https://doi.org/10.1007/s11663-014-0240-7.

[70] S.-J. Kim, W.-J. Lee, B.-C. Shin, I.-S. Kim, G.-H. Lee, Effect of oxidation temperature on the morphology of ZnO nanowires fabricated by directed melt oxidation of Al-Zn alloy, Jpn J Appl Phys 44 (2005) 739–741. https://doi.org/10.1143/JJAP.44.739.

[71] L.V. Kouzmichev, L.Y. Myzlin, A.Y. Radin, B.D. Goopiev, Oxidation of Aluminium/Lithium Alloys and Methods of Protection, Tekhnol. Legk. Splavov, Nauchno-Tekh Byul VILSa. 8 (1975) 18–22.

[72] S.M. Miresmaeili, Effect of strontium on the oxidation behavior of liquid Al–7Si alloys, Oxid Met 71 (2009) 107–123. https://doi.org/10.1007/s11085-009-9136-3.

[73] M. Nateghian, R. Raiszadeh, H. Doostmohammadi, Behavior of Double-Oxide Film Defects in Al-0.05 wt pct Sr Alloy, Metall and Materi Trans B 43 (2012) 1540–1549. https://doi.org/10.1007/s11663-012-9708-5.

[74] J.M. Papazian, R.L. Schulte, P.N. Adler, Lithium depletion during heat treatment of aluminum-lithium alloys, Metall Trans A 17 (1986) 635–643. https://doi.org/10.1007/BF02643982.

[75] V.G. Shevchenko, D.A. Eselevich, A.I. Ancharov, B.P. Tolochko, In Situ Investigation of Oxidation of Aluminum Alloy Powders with Calcium and Barium by Synchrotron Radiation, Universal Journal of Physics and Application 11 (2017) 115–120. https://doi.org/10.13189/ujpa.2017.110404.

[76] K.K. Soni, D.B. Williams, J.M. Chabala, R. Levi-Setti, D.E. Newbury, Morphological and microchemical phenomena in the high-temperature oxidation of binary Al-Li alloys, Oxidation of Metals 36 (1991) 361–378. https://doi.org/10.1007/BF01151586.

[77] W. Thiele, Die oxydation von aluminium und aluminiumlegierungs-schmelzen, PhD, Bergakademie Clausthal, 1951.

[78] G. Wu, K. Dash, M.L. Galano, K.A.Q. O'Reilly, Oxidation studies of Al alloys: Part II Al-Mg alloy, Corros Sci 155 (2019) 97–108. https://doi.org/10.1016/j.corsci.2019.04.018.

[79] A. Bahadur, Behaviour of Al-Mg alloys at high temperature, J Mater Sci 22 (1987) 1941–1944. https://doi.org/10.1007/BF01132920.

[80] S.-H. Ha, Y.-O. Yoon, N.-S. Kim, S.-H. Lim, S.K. Kim, Oxide scale behavior and its effect on oxidation resistance in Al alloys containing alkaline earth metal elements, Defect and Diffusion Forum 380 (2017) 120–123. https://doi.org/10.4028/www.scientific.net/DDF.380.120.

[81] S.-H. Ha, Y.-O. Yoon, B.-H. Kim, T.-W. Lee, S.-H. Lim, S.K. Kim, Precipitation of oxide particles in surface mixed layer of Al–Mg alloys with a trace of Ca during oxidation, J Nanosci Nanotechnol 17 (2017) 8232–8235. https://doi.org/10.1166/jnn.2017.15104.

[82] Ha, Seong-Ho, Yun, Yeong-Ok, Kim, Se-Gwang, Effect of Al_2Ca on Oxidation Resistance and Tensile Property of Al-5Mg Alloy, Journal of Korea Foundry Society 34 (2014) 194–199. https://doi.org/10.7777/JKFS.2014.34.6.194.

[83] S.-H. Ha, Y.-O. Yoon, B.-H. Kim, H.-K. Lim, T.-W. Lee, S.-H. Lim, S.K. Kim, Oxide scale behavior and surface protection of Al–Mg Alloys containing a trace of Ca, Inter J Metalcast 13 (2019) 121–129. https://doi.org/10.1007/s40962-018-0234-3.

[84] O. Ozdemir, J.E. Gruzleski, R.A.L. Drew, Effect of low-levels of strontium on the oxidation behavior of selected molten aluminum–magnesium alloys, Oxid Met 72 (2009) 241–257. https://doi.org/10.1007/s11085-009-9158-x.

[85] N. Smith, A. Kvithyld, G. Tranell, XPS Examination of the Oxide-Metal Interface of an Aluminum–Magnesium Alloy Containing Beryllium, in: O. Martin (Ed.), Light Metals 2018, Springer International Publishing, Cham, 2018: pp. 913–919. https://doi.org/10.1007/978-3-319-72284-9_119.

[86] N. Smith, A. Kvithyld, G. Tranell, The Mechanism Behind the Oxidation Protection of High Mg Al Alloys with Beryllium, Metall Mater Trans B 49 (2018) 2846–2857. https://doi.org/10.1007/s11663-018-1340-6.

[87] N. Smith, B. Gleeson, A. Kvithyld, G. Tranell, Effects of 2 ppm Beryllium on the Oxidation of a 5XXX Aluminum Alloy at Temperatures Between 500 and 750 °C, in:

A.P. Ratvik (Ed.), Light Metals 2017, Springer International Publishing, Cham, 2017: pp. 1465–1474. https://doi.org/10.1007/978-3-319-51541-0_175.

[88] N. Smith-Hanssen, M. Syvertsen, A. Kvithyld, Microalloying to Inhibit Oxidation of Al–Mg Alloys, in: Light Metals 2022, Springer International Publishing, Cham, 2022: pp. 579–586. https://doi.org/10.1007/978-3-030-92529-1_76.

[89] Y.-O. Yoon, S.-H. Ha, G.-Y. Yeom, H.K. Lim, S.K. Kim, Oxidation behavior of Al2Ca added Al-5Mg alloy in the liquid state, in: B.A. Sadler (Ed.), Light Metals 2013, Springer International Publishing, San Antonio, Texas, USA, 2013: pp. 323–326. https://doi.org/10.1007/978-3-319-65136-1_56.

[90] P.K. Yuen, Effects of strontium on the oxidation of molten aluminum alloys containing silicon and magnesium, Masters, McGill University, 2001.

Appendix C
Commentary on Projection Sequence Videos

Overview

This appendix gives commentary on the videos referred to in the tomography chapter, to aid reader understanding and interpretation. Commentary is in the form of a description of each stage with approximate frame numbers and co-ordinates expressed from 0 to 1 going from left to right (x) and bottom to top (y) at which they occur. Videos are described in terms of the first frame (F), last frame (L), and the spacing between frames (S) as $F{:}\,L{:}\,S$ e.g. a film starting at frame 1, showing every 20 frames, and ending at frame 29981 is labelled as "Frames 1:20:29981".

A. Full sequences

Video A1: 0.00Ca full sequence (Frames 1:20:29981)

Frame	Description	x	y
1	Solid Al-5Mg in BN holder.	-	-
8001	Sample begins to melt.	-	-
14601	Sample is fully molten.	-	-
29981	End of sequence.	-	-

Video A2: 0.01Ca full sequence (Frames 1:20:29981)

Frame	Description	x	y
1	Solid Al-5Mg-0.01Ca in BN holder.	-	-
4221	Porous network begins to round off.	0.7	0.3
10001	Highlighted porous network disappears.	0.8	0.1
10501	More networks begin to round off and disappear.	-	-
10681	Cell boundaries become visible as lines through sample.	-	-
14681	Sample expands beyond original boundaries from melting	0.9	0.1

	(frame highlighted is best view).		
15781-16161	Network floats upwards, on left edge, other floating events.	-	-
15961	Last metal melts, can be seen to sink.	0.3	0.3
17341	First bubble forms inside oxide network, others follow.	0.4	0.5
19241	Bubble from inside network dislodges, shoots upwards, bringing network with it.	0.3	0.4
26961	Bubble on side bursts, leaving behind oxide remnants.	0.2	0.1
26981	Bubbles combine due to bubbles bursting.	0.6	0.4
29981	End of sequence.	-	-

Video A3: 0.03Ca full sequence (Frames 1:20:29981)

Frame	Description	x	y
1	Solid Al-5Mg-0.03Ca in BN holder.	-	-
8001	Sample begins to melt.	-	-
9001	Networks round off and disappear.	-	-
11441	Small bubbles start forming throughout.	-	-
12841	Larger bubbles form and start bursting in lower part of sample.	0.5	0.1
13121	Sample expands beyond original boundaries from melting (frame highlighted is best view).	0.5	0.8
13701	More bubble formation in upper part of sample.	0.5	0.7
14001	Bubble formation throughout.	-	-
25441	Last large bubble fully deflates, leaving oxide remnant.	0.4	1
29981	End of sequence.	-	-

B. Sequences from 0.01Ca sample

Video B1: Oxide network flotation during melting (frames 15500:1:16200)

Frame	Description	x	y
15500	Start of sequence: sample partially molten. Clear space at top from liquid expansion, metal and oxide networks visible.	-	-
15501	Network on side begins to float.	0.2	0.4
15592	Small oxide speck dislodges and floats upwards.	0.5	0.8
15642	Small oxide fragment dislodges and floats up slowly.	0.4	0.3
15764	Middle metal network begins to sink.	0.4	0.5
15837	Network on side twists upwards and begins to float.	0.1	0.5
15900	Oxide network rises after metal network begins to fall.	0.3	0.6
15906	Oxide network from below view floats up.	0.5	0
15924	Middle metal network falls rapidly.	0.4	0.4
16065	Another oxide network from below view floats up.	0.5	0
16200	End of sequence.	-	-

Video B2: Bubble dragging oxide network (26961:1:27001)

Frame	Description	x	y
26961	Start of sequence: sample fully molten. Large bubbles present.	-	-
26968	Sample shakes, likely from bubble out of sight bursting.	-	-
26969	Bubble on side rapidly deflates, leaving oxide shell.	0.2	0
26971	Oxide network at top dislodges and begins to move up.	0.5	0.9
26992	Bubble in centre begins to move.	0.7	0.2
26994	Bubble in centre rapidly combines with other two bubbles.	0.6	0.4

27001	End of sequence.	-	-

C. Sequences from 0.03Ca sample

Video C1: Oxide fragments break off (frames 13905:1:14175)

Frame	Description	x	y
13905	Start of sequence: sample partially molten. Focusing on top surface, with metal network near bottom and bubbles attached to top of sample.	-	-
13906	Two oxide fragments begin to float up, slowly (one in foreground, one in background).	0.5	0.6
14030	Oxide fragment on metal network floats up.	0.7	0.1
14151	Oxide fragment reaches top.	0.6	0.9
14175	End of sequence.	-	-

Video C2: Oxide fragments break off (frames 14280:1:14620)

Frame	Description	x	y
14280	Start of sequence: sample fully molten. Focusing on top surface, with metal network near bottom and bubbles attached to top of sample. Bubbles on top surface form throughout sequence.	-	-
14296	Oxide network in foreground twists and moves up.	0.4	0.4
14423	Oxide network twists upwards, left of oxide network mentioned previously.	0.2	0.5
14620	End of sequence.	-	-

Appendix D
Crystallographic Information

Overview

This appendix gives crystallographic data for phases identified in XRD analysis. Crystal structure information was found in the databases of the International Centre for Diffraction Data (ICDD) [1] or Crystallography Open Database (COD) [2]. Information is split into data source (Table D.1) and crystallographic information (Table D.2).

Name	Formula	Database	Code
$Al_{13}Fe_3$	$Al_{13}Fe_3$	ICDD	01-086-3596
$Al_{13}Fe_4$	$Al_{13}Fe_4$	ICDD	01-073-3008
β-AlFeSi	$Al_{4.5}FeSi$	COD	2002891
Bayerite	$Al(OH)_3$	ICDD	01-074-1119
Boehmite	AlO(OH)	ICDD	01-073-9094
Mg_2Si	Mg_2Si	ICDD	00-035-0773
AlN	AlN	COD	1010514
Periclase	MgO	ICDD	00-004-0829
Spinel	$MgAl_2O_4$	ICDD	00-021-1152
CaMgSi	CaMgSi	COD	4000953

Table D.1. References for crystal structures used in XRD analysis.

	Space group		Lattice parameters (Å)			Angles (°)		
Name	Symbol	No.	a	b	c	α	β	γ
$Al_{13}Fe_3$	R3c	161	14.578	14.578	7.702	90	90	120
$Al_{13}Fe_4$	C2/m	12	15.492	8.078	12.471	90	107.69	90
β-AlFeSi	C2/c	15	6.1676	6.1661	20.8093	90	91	90
Bayerite	P21/a	14	5.062	8.671	4.713	90	90.27	90
Boehmite	Cmcm	63	3.691	12.223	2.867	90	90	90
Mg_2Si	Fm-3m	225	6.351	6.351	6.351	90	90	90
AlN	$P6_3mc$	186	3.113	3.113	4.981	90	90	120
Periclase	Fm-3m	225	4.213	4.213	4.213	90	90	90
Spinel	Fd-3m	227	8.083	8.083	8.083	90	90	90
CaMgSi	Pnma	62	7.4752	4.4272	8.3149	90	90	90

Table D.2. Crystallographic information: space groups, lattice parameters, and angles.

References

[1] S.N. Kabekkodu, A. Dosen, T.N. Blanton, PDF-5+: a comprehensive Powder Diffraction File for materials characterization, Powder Diffraction 39 (2024) 47–59. https://doi.org/10.1017/S0885715624000150.

[2] S. Gražulis, D. Chateigner, R.T. Downs, A.F.T. Yokochi, M. Quirós, L. Lutterotti, E. Manakova, J. Butkus, P. Moeck, A. Le Bail, Crystallography Open Database – an open-access collection of crystal structures, J Appl Cryst 42 (2009) 726–729. https://doi.org/10.1107/S0021889809016690.